Sixteenth Symposium on

NAVAL HYDRODYNAMICS

Ship Wakes
Large Amplitude Waves
Real Fluid Effects in Ship Hydrodynamics
Fluid-Structure Interaction
Frontier Problems in Hydrodynamics

edited by
William C. Webster

DISTRIBUTION STATEMENT A
Approved for public release
Distribution Unlimited

Sponsored jointly by:

Office of Naval Research

Naval Studies Board
National Research Council

Department of Naval Architecture & Offshore Engineering
University of California, Berkeley

University Extension
University of California, Berkeley

DTIC QUALITY INSPECTED 2

19971124 059

FORWARD

The Sixteenth Symposium on Naval Hydrodynamics was held at the University of California, Berkeley on July 13-18, 1986 under the joint sponsorship of the Office of Naval Research, the University of California at Berkeley, and the National Research Council. The symposium was the result of two years of dedicated work of many people involved in planning, organizing, and executing the tasks involved.

The five major themes chosen for the symposium were: Ship Wakes; Large Amplitude Waves including Breaking Effects; Real Fluid Effects in Ship Hydrodynamics; Fluid-Structure Interaction; and Frontier Problems in Hydrodynamics. Thirty seven papers of excellent quality were presented in nine sessions. The symposium, as in the past, provided a gathering place for international colleagues who are seriously interested in advancing the state-of-the-art in ship hydrodynamics research. The participants represented as many as eighteen countries. The symposium was highlighted by the variety of new subjects introduced. Some of these subjects are ship wake images by satellites and computer-aided flow visualization. The solutions of these complex problems reflect the developing trend in scientific research in general that multi-disciplinary efforts are required. Also, a noticeable change was the significant increase in the number of young investigators participating in the symposium through paper presentations and discussions. It is an encouraging sign for the ship hydrodynamics research community which shows promise of its future growth. The symposium has also attracted many senior investigators of international reputation, among whom are six distinguished members of the U.S. National Academy of Engineering and National Academy of Sciences. They have certainly contributed to the technical integrity of the Symposium.

It is almost impossible to acknowledge all the contributions made by many people to the success of the Sixteenth Symposium. Only a few contributions can be mentioned here. Among those contributors, the first and foremost is Professor William C. Webster of the Department of Naval Architecture & Offshore Engineering, the University of California at Berkeley. Bill served as the chairman of the Organizing Committee and was the central coordinator for all activities involved in the organization and management of the symposium. He was ably assisted by Ms. Lydia Briedis and Ms. Leslie Service of the Department of Naval Architecture and Offshore Engineering and Ms. Linda Reed and Ms. Karen Anderson of the University Extension of the University of California, Berkeley. This symposium would not have been successful without the dedicated long hours of service provided by some of the Paper Selection Committee: John V. Wehausen, of the University of California, Berkeley, Marshall P. Tulin, of the University of California, Santa Barbara, William B. Morgan, of the David Taylor Naval Ship R&D Center, and V. C. Patel, of the University of Iowa.

Acknowledgement would not serve its full purpose without recognizing the quiet and dedicated behind-the-scenes service provided by Mr. Lee M. Hunt, the Executive Director of the Naval Studies Board of the Naval National Research Council, and Ms. Elizabeth Lucks of his staff. The Naval Studies Board has rendered significant moral and administrative support for the Office of Naval Research in many of the past hydrodynamics symposia and its willingness to continue its assistance in the future is certainly a heartfelt encouragement.

Finally, a special and personal expression of gratitude is extended to Drs. Robert E. Whitehead and Michael M. Reischman of the Office of Naval Research, and Mr. Vincent J. Monacella and Dr. William B. Morgan of the David Taylor Naval Ship R&D Center of their invaluable counsel and encouragement from the beginning to the end of the symposium.

Choung Mook Lee
Office of Naval Research

CONTENTS

Session I
SHIP WAVES & WAKES
M. P. Tulin, Chairman

Surface Wave Wakes and Internal Wave Wakes Produced by Surface Ships — 1
B. A. Hughes

Far Field Features of the Kelvin Wake — 18
A. Barnell and F. Noblesse

Trailing-Vortex Wakes on the Free Surface — 38
T. Sarpkaya

Session II
LARGE WAVE PROBLEMS
T. F. Ogilvie, Chairman

Nonlinear Calculation of Breaking and Non-Breaking Waves Behind a Two-Dimensional Hydrofoil — 51
R. M. Coleman

Some Discussions on the Free Surface Flow Around the Bow — 65
H. Maruo and M. Ikehata

Large, Steep Waves, Wave Grouping and Breaking — 78
M.-Y. Su

A Theory of Spilling Breakers — 98
M. P. Tulin and R. Cointe

Steep and Breaking Deep Water Waves — 106
W. W. Schultz, S. E. Ramberg and O. M. Griffin

Session III
LARGE WAVE PROBLEMS II
R. F. Beck, Chairman

Study of Nonlinear Axisymmetric Body-Wave Interactions — 116
D. G. Dommermuth and D. K. Yue

Nonlinear Wave Maker in a Channel Operating at Cut-Off Frequencies: Theory and Experiment — 137
E. Kit, T. Miloh, and L. Shemer

Steady Flow Past a Step — 151
P. M. Naghdi and L. Vongsarnpigoon

Some Soliton Calculations — 167
R. C. Ertekin and J. V. Wehausen

Generation of Internal Runaway Solitons by Moving Disturbances — 186
J. Zhu, T. Y. Wu, and G. T. Yates

Session IV
FRONTIER HYDRODYNAMICS
V. C. Patel, Chairman

Microbubble Drag Reduction 199
C.L. Merkle, S. Deutsch, S. Pal, and J. Cimbala, W. Seelig

Computer-Aided Flow Visualization 216
D. Rockwell, C. Gumas, P. Kerstens, J. Backenstose,
A. Ongoren, J. Chen, and D. Lusseyran

Session V
REAL FLUID EFFECTS I
W. B. Morgan, Chairman

Optimum Body Profiles with Minimum Drag in Two-Dimensional Oseen Flow 234
M. Bessho, Y. Himeno

Viscous -Flow Computation of Propeller-Hull Interaction 246
F. Stern, V. C. Patel, H. T. Kim, and H. C. Chen

Propeller Interaction with Axisymmetric Sheared Onset Flow 268
T. Brockett

Experimental Investigation of Flow Around a Marine Propeller and Application of Panel Method to the Propeller Theory 289
K. Koyama A. Kakugawa and M. Okamoto

Session VI
REAL FLUID EFFECTS II
M. W. C. Oosterveld, Chairman

Some Time-Dependent Features of Turbulent, Appendage-Body Juncture Flows 312
W. J. Devenport and R. L. Simpson

Numerical Analysis of the Viscous Flow Field Resulting from a Hull-Sail Interaction 336
R. Levy and S. J. Shamroth

Three-Dimensional Flow Separation and the Effect of Appendages 352
M.-S. Chang and L. P. Purtell

Study on the Characteristics of Propeller Cavitation and Its Noise 371
H. Yuasa, H. Kamiirisa, and T. Nojiri

Experimental and Analytical Techniques for the Study of Unsteady Propeller Sheet Cavitation 387
J. Kerwin and S. Kinnas, M. B. Wilson and J. McHugh

Session VII
UNSTEADY FLOW PROBLEMS
H. Maruo, Chairman

Two Dimensional Transient Motions with Large Amplitude by Time Domain Method — 415
Y.-J. Kim & J. H. Hwang

Quadratic Response to Short-Crested Seas — 427
J. F. Dalzell

Wave Drift Forces in Current — 438
R. H. M. Huijsmans

The Dynamics of Waves at the Interface Between a Two-Layer, Viscoelastic Coating and a Fluid Flow — 446
J. H. Duncan

Ship Maneuvering in Waves — 456
W. R. McCreight

Session VIII
FLUID-STRUCTURE INTERACTION
T. Y. Wu, Chairman

Periodic and Multiple Periodic Behavior of Locked-In Vortex Shedding — 470
Y. LeCointe and J. Piquet

Simulation of the Viscous Flow Over a Cylinder in a Wave Field — 490
E. C. Tiemroth

Nonlinear Forces Caused by Breaking Waves — 514
H. Miyata, H. Kajitani, M. Zhu and T. Kawano

Hydrodynamic Impact Loads on Three-Dimensional Bodies — 537
A.W. Troesch and C.-G. Kang

Theoretical Investigation on the Wave Impact Loads on Ships — 559
I. Watanabe

Session IX
STEADY FLOW PAST BODIES
J. V. Wehausen, Chairman

Rankine Source Methods for Numerical Solutions of the Steady Wave Resistance Problem — 575
G. Jensen, Z.-X. Mi, and H. Söding

A Calculation Method for the Lifting Potential Flow Around Yawed Surface-Piercing 3-D Bodies — 583
F. Xia and L. Larsson

Minimization of Resistance of Slowly Moving, Full Hull Forms in Short Waves — 598
T. Sakamoto, E. Baba

Surface Wave Wakes and Internal Wave Wakes Produced by Surface Ships

B. A. HUGHES

Defense Research Establishment Pacific, Canada

ABSTRACT

Measurements are given of Kelvin wakes of the USN Fleet Tug USS QUAPAW operating in Dabob Bay, WN, during the Joint Canada/US Ocean Wave Investigation Project (JOWIP, the Georgia Strait Experiment) in July 1983, and also of internal wave wakes generated by CFAV ENDEAVOUR in Knight Inlet, B.C. in August 1983. Surface wave slopes, internal wave heights and surface currents are given for some of the data sets and the measurements are discussed with reference to SAR imagery. For the Dabob Bay surface Kelvin wakes it is shown that, (a) the slopes are too small for specular reflection to be important in the imagery mechanism, (b) internal waves are too weak to be identifiable in the surface and subsurface measurements, and (c) short surface waves are propagating at a range of angles near the wake axis, not just at the angle given by the traditional Kelvin theory. For the Knight Inlet internal wave wakes, images are strongly multicrested, currents are ~ 0.1 m/s peak-to-peak, and heights are ~ 0.8 m at 4 m depth.

1. INTRODUCTION

As part of the Joint Ocean Wave Investigation Project (JOWIP), also known as the Georgia Strait Experiment, measurements were taken of surface and internal Kelvin ship wakes in order to provide surface truth for comparison with remote SAR imagery. The primary measurement data set consists of surface waveslope and height, and near-surface current, measured along trajectories that cross the wake at oblique angles a few kilometres behind the source ship. Aerial photographs were also taken from a wing-tip stereo system mounted on a Cessna 310, and oblique non-stereo photographs are also available to support the surface truth measurements.

SAR imaging at L- and X-band were taken as coincidentally and simultaneously as possible with the surface measurements. The SAR equipment was flown in a CV580 aircraft at about 7000 m altitude. It was operated, and the imagery was subsequently processed, by personnel from the Canada Centre for Remote Sensing (CCRS), and the Environmental Research Institute of Michigan (ERIM).

The surface Kelvin wake experiments were carried out in Dabob Bay, WN over a three day period (26-28 July 1983) and the internal wake measurements were carried out in Knight Inlet B.C. on the 1st and 2nd of August 1983 (see Fig. 1.) Most of the planning and coordination for the surface wake measurements was done by personnel from the Naval Ocean Systems Center, San Diego, and the source ship, USS QUAPAW, a USN Fleet tug, took part under their authority. Other organizations were also represented, particularly in the planning and execution of the other portions of JOWIP: Applied Physics Laboratory (Johns Hopkins University); TRW, Inc., Los Angeles; Poseidon Inc., Los Angeles; ERIM, Ann Arbor, Michigan.

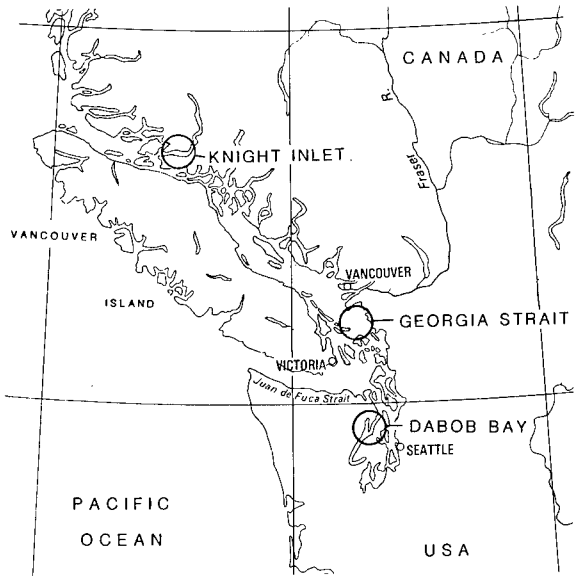


Figure 1. Areas of Operation.

The primary objective of the surface truth comparisons with the SAR imagery for the surface wakes was to determine, if possible, which of several proposed mechanisms is responsible for the formation of the narrow V-angle wake images typical of SEASAT and airborne imagery. The proposed mechanisms are (a) specular reflection (23° from nadir for SEASAT) from relatively steep slopes assumed to exist near the wake axis, (b) scattering from loci of constant Bragg-wavelength in the wake, or (c) steepening of wake or background surface waves by internal wave currents produced simultaneously in the ship's wake.

The primary objective for the internal Kelvin wake measurements was to obtain image modulation data from weak, but known, internal waves. The internal waves that are usually used for modulation measurements are relatively strong and their interaction with surface waves typically produce obvious breaking. The nonlinearities implied by this create difficulties in the modelling and it was anticipated that the use of weaker internal waves would remove these difficulties.

Results obtained by NOSC for surface wakes, with an emphasis on these Dabob Bay measurements, are given by Hammond et al. (1985). A full description of the DREP measurments is given by Hughes and Dawson (1985) for surface wakes, and Hughes and Dawson (1986) for internal wakes.

The following sections of this report provide a description of the equipment, a description of the Kelvin surface wakes concentrating on two of the runs, and a description of the Kelvin internal wakes, again concentrating on two runs, followed by a discussion. The internal wake measurements are incomplete, certainly compared to the surface wake measurements, but are considered to be important because of the general lack of such data sets.

2. EQUIPMENT

For the data to be presented here, the equipment was operated from CFAV ENDEAVOUR. The main equipment package was deployed over the bow, Fig. 2, and a secondary package was deployed over the stern.

The slope measurer is described in detail by Hughes et al. (1984). It was part of the bow equipment and its operating principle is that it measures the amount of refraction that a narrow vertical beam of light experiences as it emerges from the tilted surface. The beam is produced by a small He-Ne laser and it is ~ 1 mm in diameter at the sea surface. The data rates were 400 Hz for each of two orthogonal slope components and a third 400-Hz data set, of secondary importance, measuring beam intensity. Wave height was also measured at 2 Hz and 40 Hz by a wavepole wire attached to this device. Finally, two components of horizontal current were measured at a point about 30 cm

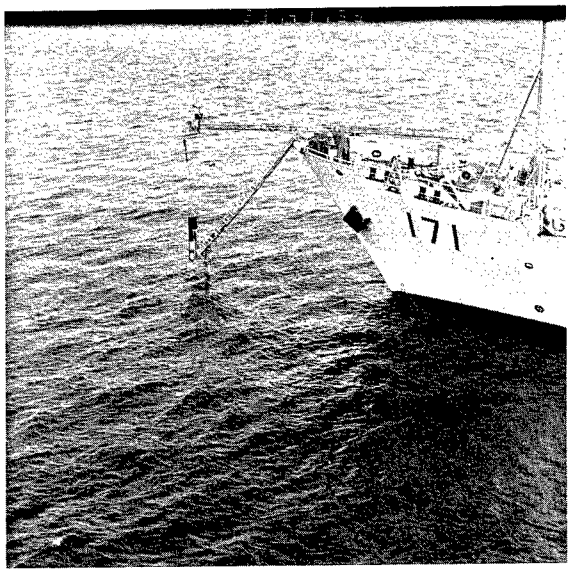


Figure 2a. Bow equipment deployed from CFAV ENDEAVOUR.

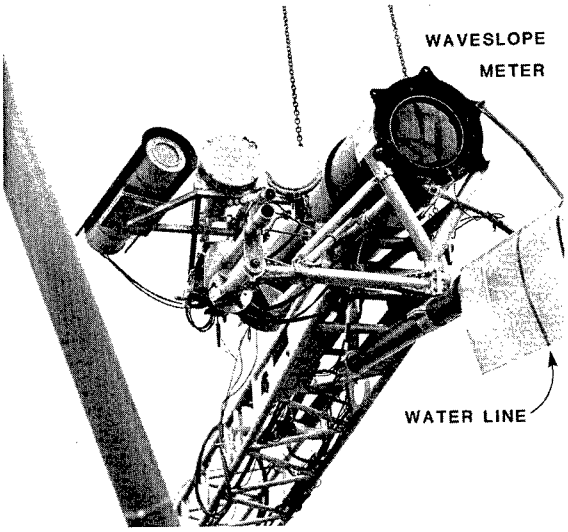


Figure 2b. Closeup of bow equipment showing, from left-to-right, the TRW Inc. TV camera, X-band horn, and light source for glints, and the DREP waveslope meter with its large lens visible. In normal deployment the face of the large lens is horizontal, the strut with the metal fairing running to the right is vertical, and the water line is at the middle tape marker on the fairing.

directly below the laser beam. This equipment is shown schematically in Fig. 3.

A similar current meter and an echosounder were contained in the equipment deployed at stern. Comparisons between the stern and bow current meter records were used to estimate internal wave phase velocities for other portions of JOWIP. The echosounder was used to estimate internal wave amplitudes by monitoring the height changes of scattering layers and identifying these changes with the internal waves.

Wind velocity, ship's heading, air temperature, and ship's position were also measured.

Coherent X-band backscatter, and optical glint measurements were made by TRW, Inc. using near surface equipment (see Fig. 2). A trispar buoy instrumented to measure current, isotherm height, wind and other parameters was deployed by NOSC in Dabob Bay and in Knight Inlet, but recording problems prevented the gathering of primary useful data.

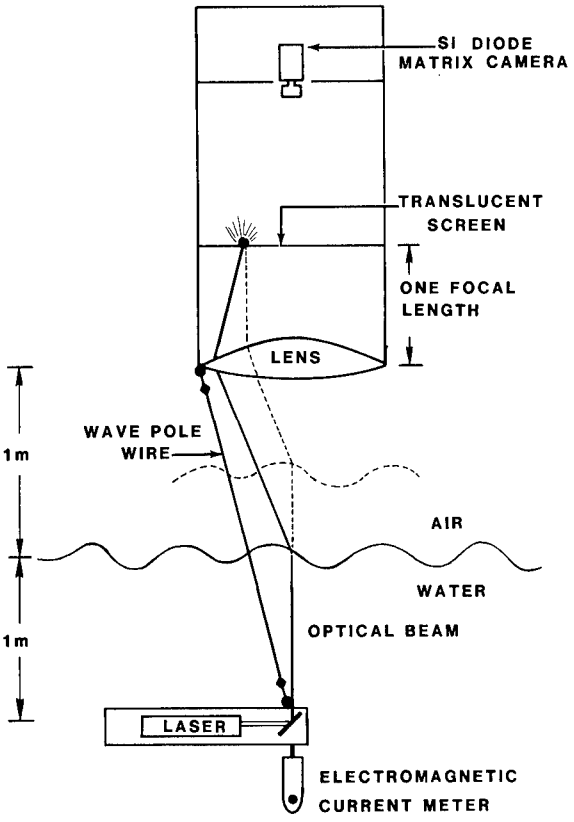


Figure 3. Schematic of waveslope meter, wavepole wire and bow current meter.

3. KELVIN SURFACE WAKES

3.1 GEOMETRY AND OPERATING CONDITIONS

The wakes were produced by USS QUAPAW and were measured from CFAV ENDEAVOUR. The geometry of the experiments is shown in Fig. 4. As USS QUAPAW crossed CFAV ENDEAVOUR's bow, CFAV ENDEAVOUR was brought quickly up to speed (~ 1 knot) and measurements were taken while travelling approximately perpendicularly across the USS QUAPAW wake. Before the bow crossing, CFAV ENDEAVOUR was stationary in the water or was manoeuvring slowly into position. The relative track is also shown in Fig. 4. It can be seen that the actual crossing is at about 12° to the wake axis. Each wake was traversed only once, and over the three day experiment period, fourteen wakes were measured, eight with a USS QUAPAW speed of about $6\frac{1}{2}$ m/s (13 knots) and the remaining six with speeds of about 8 m/s (16 knots). For the first seven runs (26 and 27 July) winds were moderately high (> 10 knots) and for the remaining seven runs, (28 July) winds were light with some patches of very calm water. Except for the run shown in Fig. 4 and one other, all wakes were created with the USS QUAPAW absolute track oriented approximately towards the North, opposite to that shown in Fig. 4, and with CFAV ENDEAVOUR track either as shown or approximately reciprocal. The other wake was created with USS QUAPAW travelling at 90° to the left, i.e. travelling toward 076°T, and CFAV ENDEAVOUR travelling toward 346°T.

3.2 IMAGERY

One SAR image (JOWIP 7/3) was obtained from an East-West flight line with the radar "looking" North. The others were all obtained from North-South flight lines with the radar "looking" West or East.

A typical light wind SAR image (JOWIP 9/2 L-band) is shown in Fig. 5. The narrow V wake is clearly apparent as is modulation along the V-arms (due to the velocity bunching SAR mechanism). The two experiment ships and a power boat travelling parallel and at about the same speed as USS QUAPAW, also producing a narrow V-wake image, are also apparent.

An aerial photograph showing the same wake but taken 3 minutes earlier is given in Fig. 6. Several outstanding features are evident here: modulations or interference effects exist, the steepest waves appear to be at the outer edge, the shorter inner waves are not smooth-crested, and the centre line of the turbulent wake is not straight. The first three features are quite commonly observed in the aerial photographs for the light wind wakes; the last is probably due to steering corrections and is a variable quantity, with most cases showing less deviation than in Fig. 6 (the rms deviation for this wake is 1.2 m).

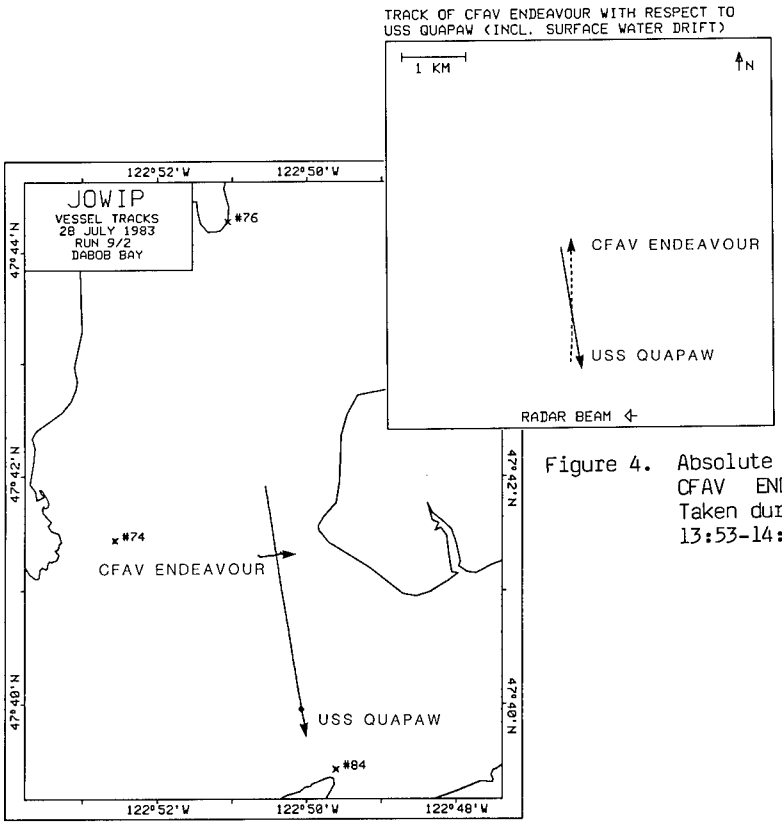


Figure 4. Absolute and relative tracks for CFAV ENDEAVOUR and USS QUAPAW. Taken during JOWIP 9/2 (1983/July/28 13:53-14:02).

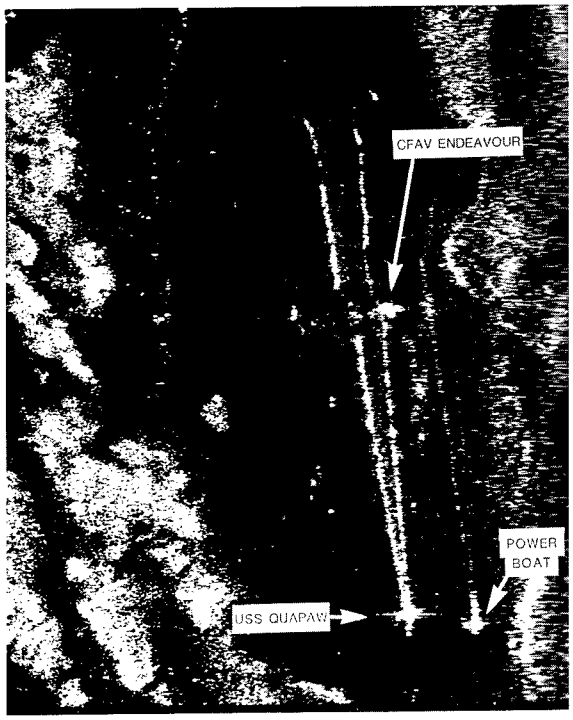


Figure 5. L-band image for JOWIP 9/2. USS QUAPAW at bottom of left V (speed is 7.8 m/s). CFAV ENDEAVOUR mid-right center. 83/7/28 14:00:28 at USS QUAPAW. (Courtesy of ERIM).

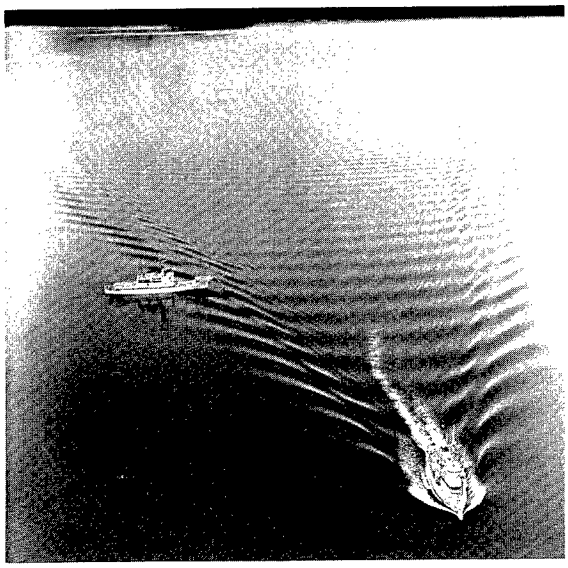


Figure 6. JOWIP 9/2 wake. The source ship is USS QUAPAW (bottom right) with an average speed of 7.8 m/s. CFAV ENDEAVOUR is just entering the outer wake. 83/7/28 13:56:06 PDT.

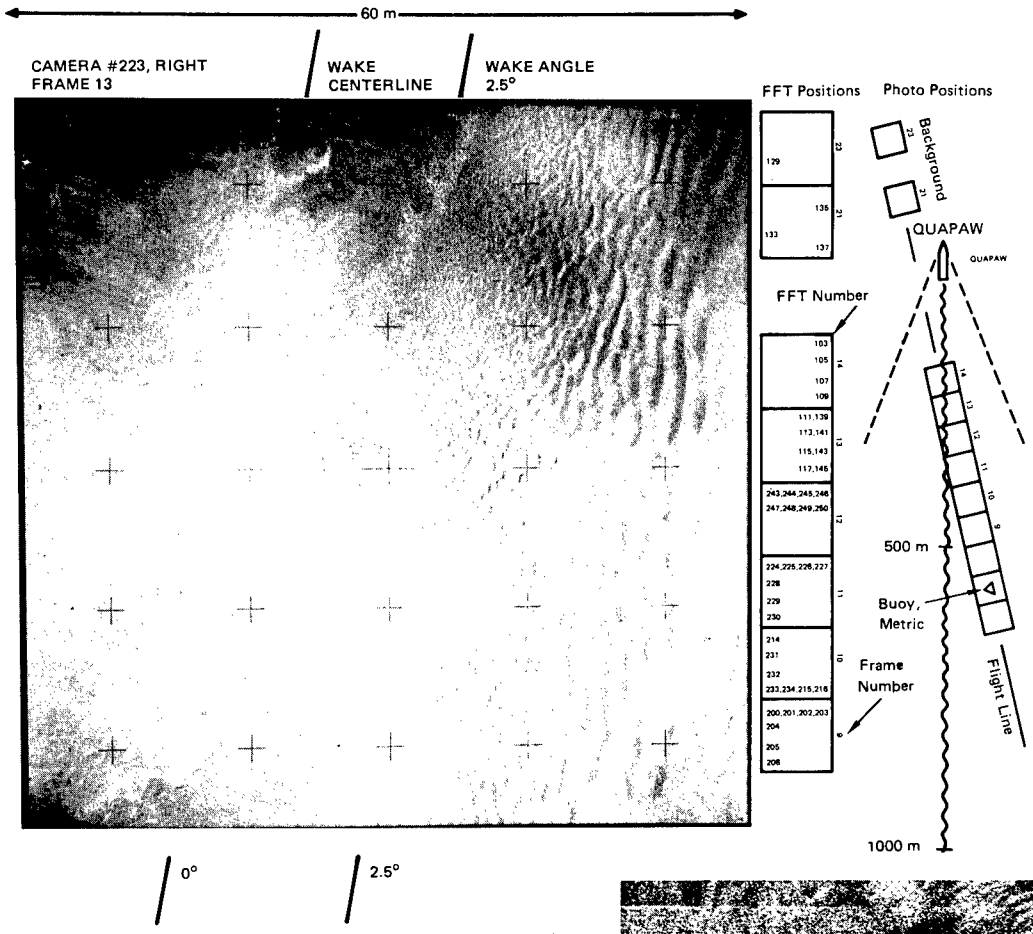


Figure 7. Plan view photograph from JOWIP 8/3 taken approximately 250 m behind USS QUAPAW from an altitude of 60 m. (Courtesy of NOSC).

The nonsmoothness of the crests of the shorter inner waves is perhaps the most important observation as far as the modelling is concerned, because it implies that a simple Kelvin-like treatment, even with an extension to multiple sources over the body of the ship, is probably inadequate. Further evidence of this effect is quite apparent in other oblique photographs (see Hughes and Dawson (1985)), and is shown very clearly in the plan view stereo imagery. An example from one photograph of a stereo pair is shown in Fig. 7 taken during JOWIP 8/3. The longer waves near the right edge are not smooth crested, and the shorter waves near the centre of the photograph are quite obviously propagating over a wide range of angles. The SAR image for this wake is shown in Fig. 8, and similar features to those in Fig. 5 are apparent here. The shorter waves referred to in Fig. 7 are at the location corresponding to the upper V-arm approximately 250 m behind USS QUAPAW, as shown in Fig. 8.

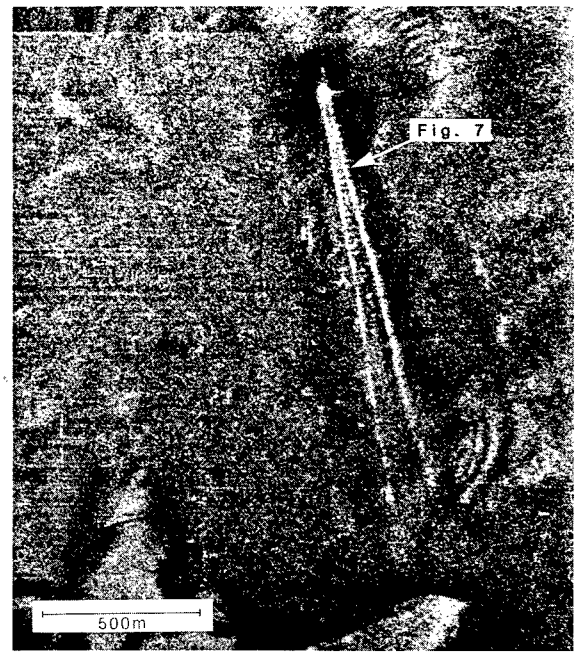


Figure 8. L-band image from JOWIP 8/3. USS QUAPAW is at the tip of the narrow V-wake, and is travelling at 7.9 m/s. The relative location of Fig. 7 is also shown. 83/7/28 09:01:18 at USS QUAPAW. (Courtesy of Erim).

3.3. SLOPE MEASUREMENTS

Time sequences of slope for JOWIP 8/2 are shown in Fig. 9. The East component corresponds quite closely to the component perpendicular to the wake axis. The modulations and the decreasing magnitude towards the wake axis are quite apparent. Frequency can also be seen to increase towards the wake axis. (These features are apparent in all of the light wind wakes, although 8/2 is the only one that is free of wind-ruffled background effects over its entire measurement duration.) For 8/2 the decreasing magnitude effect also remains true when the major wake spreading loss effects are removed by multiplying the slopes by $\sqrt{R}$, where R is the separation distance between source and measurement positions. The wake was crossed at $R \approx 3.3$ km.

The "outermost" waves occur at an angle of about 20^0 to the wake axis, as subtended from a point source located at the center of the source ship. The maximum slope outside of the turbulent wake ignoring occasional spikes in the data, is 0.11 which occurs in the outermost wave group.

The wind speed at 10 m height was 1.7 m/s and, from the aerial photographs, there is evidence of strong spatial variability (patchiness). The air boundary layer was possibly unstable: the temperature at 9 m was less than the temperature of the surface water.

The slopes for JOWIP 9/2 are shown in Fig. 10. The same basic features are evident here as in JOWIP 8/2. The wake crossing here was 0.9 km behind USS QUAPAW, only one-third of the JOWIP 8/2 value. The maximum slope was 0.10 at 16^0 to the wake axis and only 0.20 as measured in the turbulent wake. The wind speed measured only 0.6 m/s and the air thermal boundary layer was stable.

In the seven wakes measured on 28 July, none had maximum slopes along the measurement trajectory that were capable of providing specular reflection of the radar beam from the overflying SAR aircraft. Only one of them, JOWIP 8/3, approaches the necessary value (see Table 1), but that slope occurs in a wind-ruffled area and is not due primarily to the Kelvin wake.

TABLE 1

Maximum Measured Slopes and Required Specular Values for 28 July.

RUN	SAR INCIDENCE ANGLE (°)	REQUIRED SPECULAR SLOPE	MAX MEASURED SLOPE (EAST)	APPROX. ANGLE OFF WAKE AXIS (°)
8/1	29	0.554	0.35	23
8/2	23	0.424	0.11, 0.15	19.5, 0
8/3	23	0.424	0.41	5
8/4	41	0.869	0.36	13
9/1	25	0.466	0.23	6
9/2	22	0.404	0.10, 0.20	16, 0
9/3	27	0.510	0.18, 0.30	18, 2

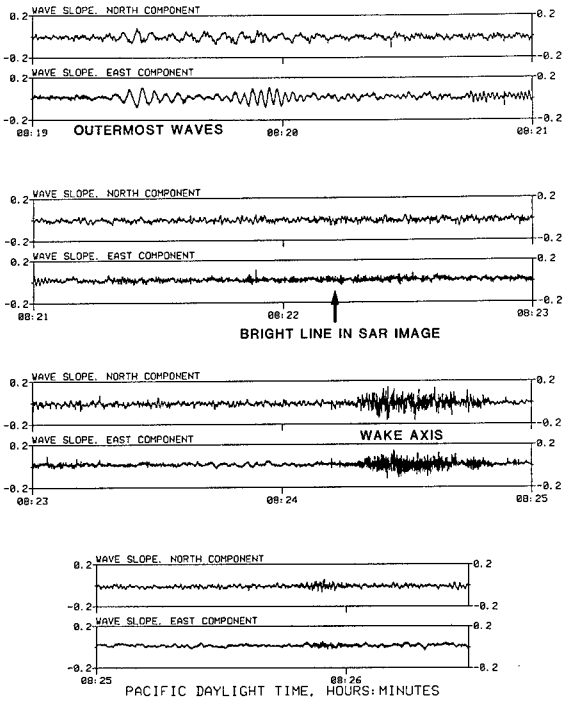


Figure 9. Time-sequences of slope for JOWIP 8/2 shown in contiguous two-minute sections. The East component (approx. perpendicular to the wake axis) is the lower of each pair.

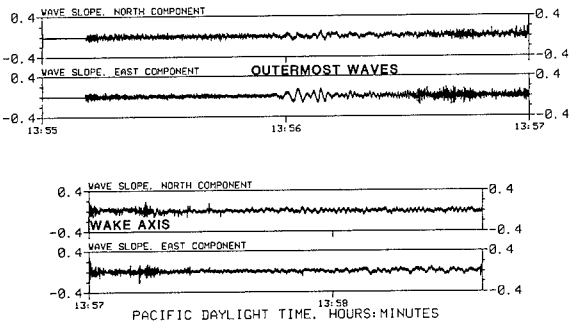


Figure 10. Time-sequences of slope data for JOWIP 9/2. The East component is approximately perpendicular to the wake axis.

3.4 MEASURED BOUNDS ON INTERNAL WAVE CURRENT AND HEIGHT

The bow current meter signals, as measured along each trajectory, have been band-pass filtered to remove low-frequency ship manoeuvring effects (< 0.01 Hz) and high-frequency surface wave effects (> 0.08 Hz). The results are shown for JOWIP 8/2 and 9/2 in Fig. 11. The East component is very closely the same as the cross-track component for each and it can be seen that, between the outer waves and the turbulent wake, the peak-to-peak cross-track current in 8/2 is less than 0.04 m/s, and less than 0.06 m/s, for 9/2. Stronger current excursions are measured in the North components but these are somewhat contaminated by small changes in ship's head which have their maximum effect in the North component and have a minimum effect in the East component. The excursion labelled 'A' in 9/2 is at least half due to this effect. Peak-to-peak current values are given for each run in Table 2.

Estimates of internal wave heights for each run are also given in Table 2. The only observable scattering layers were within a few metres of the instrument and were very indistinct. The direct internal wave height measurements are therefore not highly reliable. There is also an ambiguity of about 1 m in absolute depth because of strong surface scattering overwriting the echosounder chart zero postion. For these reasons the internal wave height data should be used with caution. Examples of echosounder traces for JOWIP 8/2 and 9/2 are given in Fig. 12. The indistinctness of the scattering layer is quite apparent and it can be seen that internal waves with peak-to-peak heights of less than 0.20 metres would not be identifiable. The oceanographic stability profiles for these two cases are shown in Fig. 13. They both show maximum BV frequencies of less than 40 cph at depths of 8-10 m.

4. KELVIN INTERNAL WAKES

4.1 GEOMETRY AND OPERATING CONDITIONS

Two sets of surface-ship-generated internal wave fields have been examined in some detail. One is a transverse set generated by CFAV ENDEAVOUR travelling slowly astern (0.55 m/s) and measured on a return track (referred to as Set 2, Knight Inlet), the other is a diverging wave system generated by CFAV ENDEAVOUR travelling ahead (2.19 m/s) and then measured after executing a wide turn of approximately 250° (Set 6a, Knight Inlet). The geometry for the former is shown in Fig. 14 and the latter in Fig. 15. Nine sets similar to these have been described by Hughes and Dawson (1986), but these two provide the simplest and clearest measurements.

4.2 IMAGERY

Set 2 represents the best (almost the only) measurement of transverse waves, but

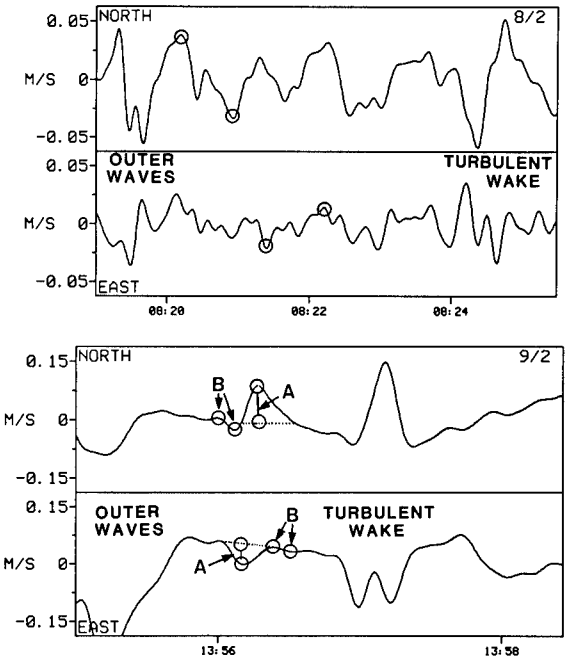


Figure 11. Filtered current data for JOWIP 8/2 (top), and 9/2 (bottom). Values in Table 2 are taken from the encircled points. The cross-wake component is approximately the same as the East component.

TABLE 2

Measured Bounds on Internal Wave Heights and Surface Currents

RUN	peak-to-peak* height (m)	DEPTH (m)	peak-to-peak CURRENT (m/s) NORTH	EAST	TIME
5/3	0.5	at 2.6	0.13	0.12	10:27
5/4	-	-	0.078	0.052	11:09
6/1	0.25	at 2.0	-**	-	-
6/4	0.1	at 1.9	0.19	0.05	16:53
7/3	-	-	0.26	0.068	17:22
7/5	-	-	0.15	0.035	18:33
7/7	0.2	at 1.9	0.14	0.022	19:40
8/1	-	-	0.077	0.034	07:33
8/2	0.25	at 1.9	0.073	0.039	08:22
8/3	0.25	at 1.9	0.071	0.030	09:08
8/4	0.25	at 2.0	0.135	0.025	09:52
9/1	0.2	at 1.9	0.039	0.048	13:19
9/2	0.15	at 1.8	0.120	0.059	13:56
			0.018	0.009	
9/3	-	-	0.038	0.039	14:50

* Missing values are due to absence of coherent scattering layer.
** Completely contaminated by ship manoeuvres.

there are no available aerial photographs or SAR images. It was very similar in shape to Set 1 and a photograph from Set 1 is shown in Fig. 16. In this image, CFAV ENDEAVOUR was starting the measurement phase along a traverse through the waves, which are ahead of the ship, as indicated.

Aerial photography for Set 6a is shown in Fig. 17. The right-hand side of the Kelvin wake is easily apparent and it displays a wavelength of about 30 m. L-band and X-band

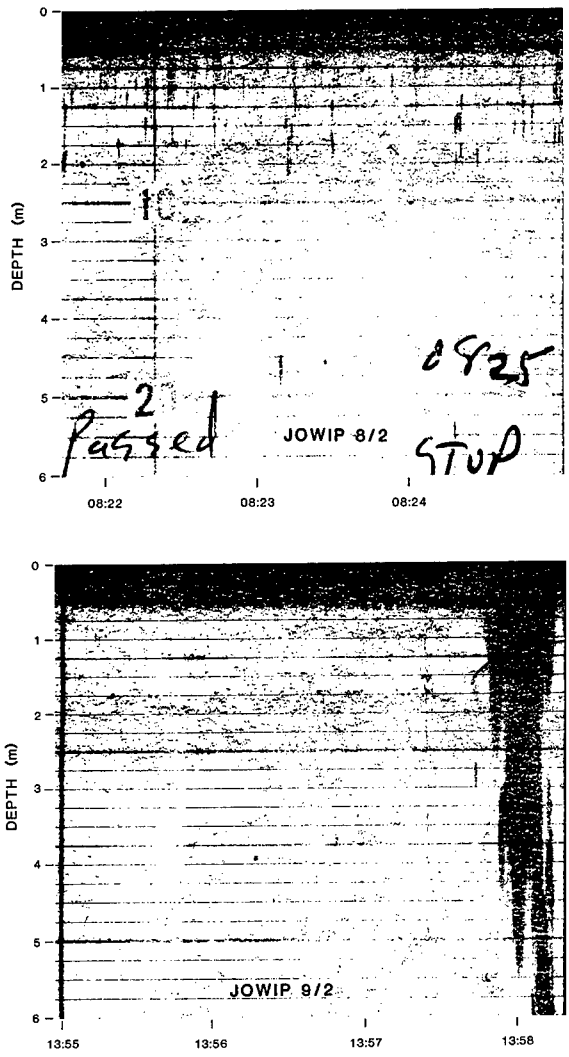


Figure 12. Echosounder traces for JOWIP 8/2 (top) and 9/2 (bottom). The rate of advance of CFAV ENDEAVOUR through the water was about 1.5 m/s giving a horizontal distance scale of about 90 m/min. The echosounder was on the stern of the ship so it crossed the wake about one minute after the forward instruments. The very dark (irregular) band at the surface is due to strong scattering from the (rough) air-water interface and from near-surface foam and bubbles.

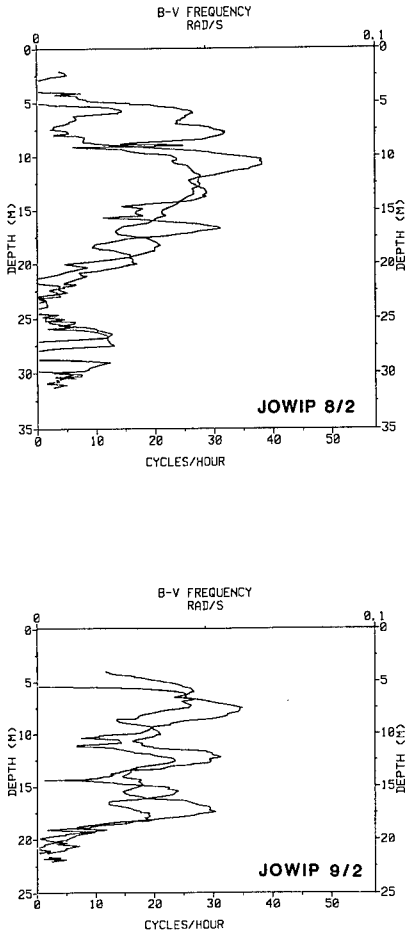
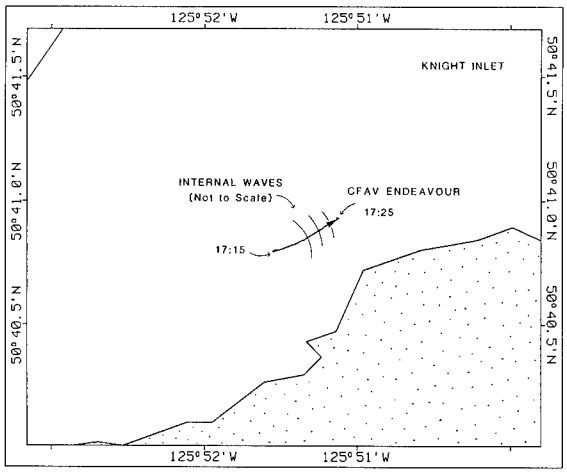


Figure 13. Stability profiles for JOWIP 8/2 and 9/2.

Figure 14. Track of CFAV ENDEAVOUR for Set 2 (Knight Inlet). The upper panel show the land-based track of CFAV ENDEAVOUR during the generation phase, and the lower panel shows the measurement phase (line with crosses) as a track relative to the effective source position (tip of heavy arrow). The crosses locate the relative measurement position every two minutes. Source speed was 0.55 m/s.



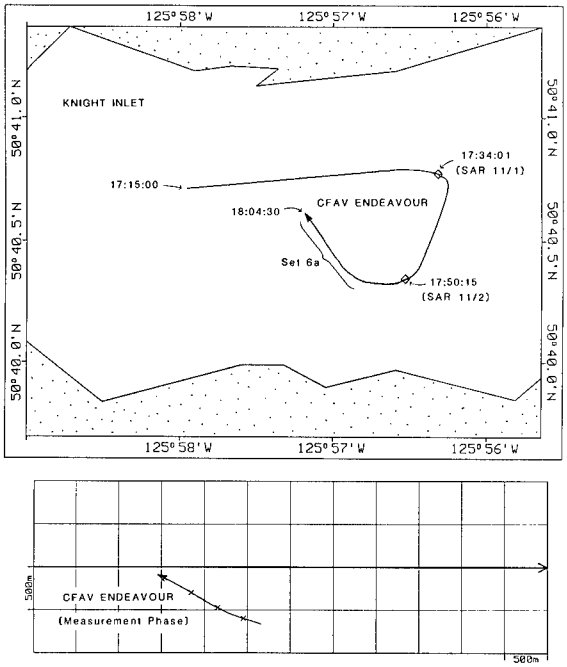


Figure 15. Land-referenced (upper panel) and relative tracks (lower panel) for Set 6a. The open squares in the upper panel locate the vessel at SAR overpass times. Crosses in the lower panel locate the measurement position every two minutes. The effective source position is at the tip of the heavy arrow. Source speed is estimated to be 2.19 m/s.

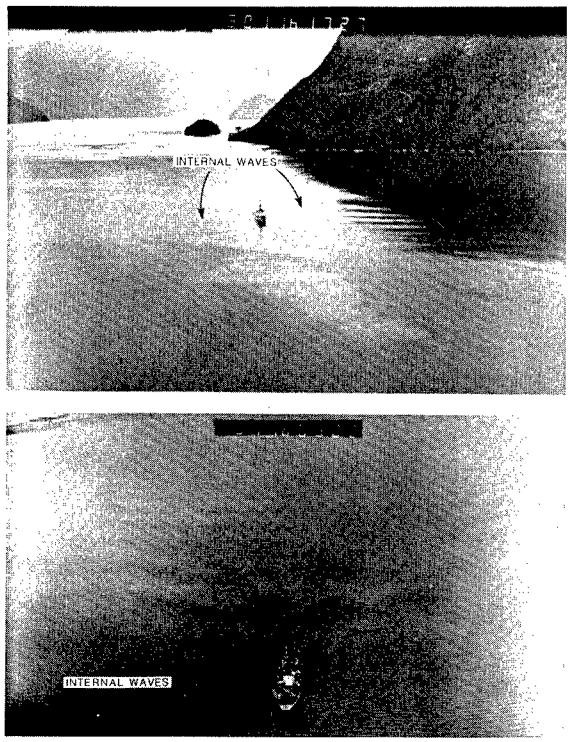


Figure 16. Photograph (from Set 1) showing transverse internal waves similar to those of Set 2 (Knight Inlet). The water line length of CFAV ENDEAVOUR is 67 m.

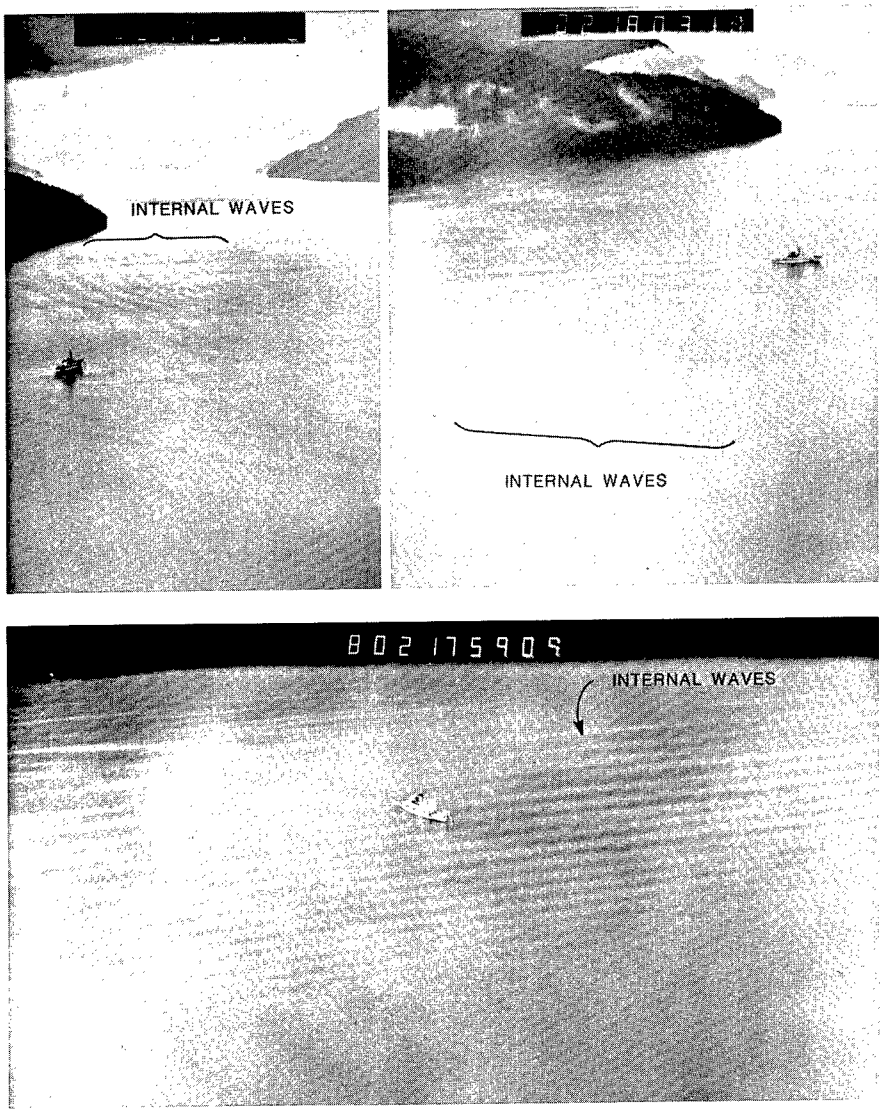


Figure 17. Divergent internal waves of Set 6a (Knight Inlet).

images for Set 6a are shown in Fig. 18. The measured divergent waves are easily apparent at L-band but are almost obscured by noise at X-band. A curved Kelvin wake generated by CFAV ENDEAVOUR during the measurements can also be seen. USS QUAPAW is visible on the right in each image. Local non-uniformities in the background are also apparent and it can be seen that they are quite different in each image.

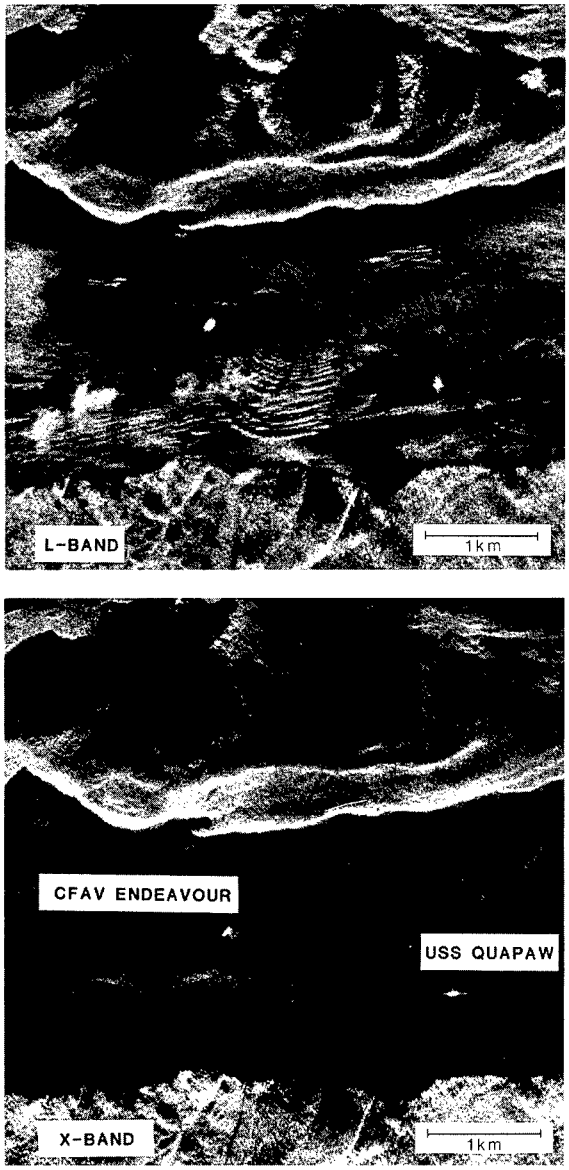


Figure 18. L-band (top) and X-band (bottom) imagery for Set 6a taken from JOWIP 11/3. 1983/8/2 18:05:34 PDT at CFAV ENDEAVOUR.

4.3 MEASURED CURRENTS, INTERNAL WAVEHEIGHTS, SURFACE WAVE SLOPES

For Set 2, the basic measurements are shown in Fig. 19. Total ship's speed including internal wave current is given in the second panel from the top. The bottom three panels show surface wave slope in raw two-component form, and also in mean-square form averaged over consecutive 10 second samples. The internal waves stand out clearly with peak-to-peak mean-square changes of 0.008, i.e. deviations of ±25%. Internal wave current is shown with ship's speed removed in Fig. 20. The component

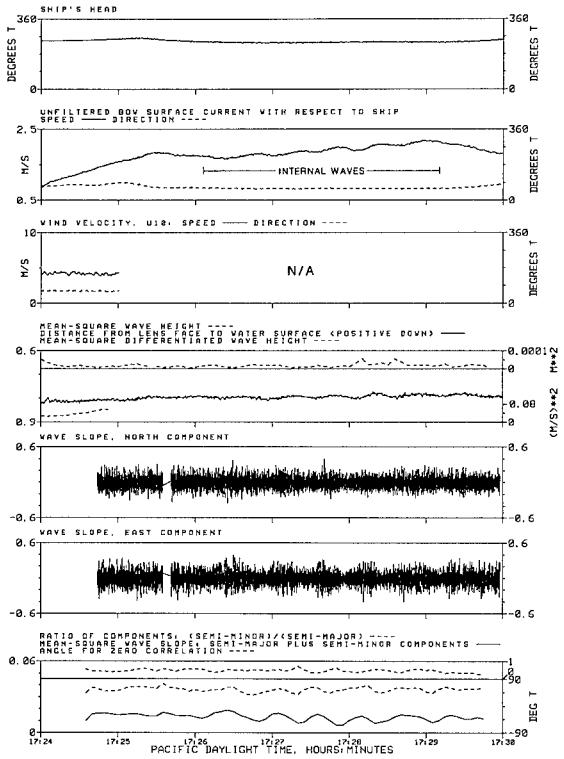


Figure 19. Time sequence data for Set 2 (Knight Inlet). In order from the top, ship's heading (CFAV ENDEAVOUR), surface current at the bow, wind (not available after 17:25), surface wave height, two slope components (not available before 17:24:40), and mean-square slope. The internal waves are evident between 17:26 and 17:29.

shown is parallel to measurement ship's head which is approximately parallel to the wake axis. Peak-to-peak current is ~ 0.20 m/s. Internal wave height is shown in Fig. 21. Internal wave induced changes are quite obvious in the scattering layers between 4.5-m and 9-m depth with a peak-to-peak range of 1.5 m at 8 m depth. Both the current and the height are measured at about 150 m behind the effective source position and 150 m off-axis. The stability profile is shown in Fig. 22. The maximum BV frequency is 80 cph at 7-m depth (very close to the depth of the main scattering layer). The wind speed U_{10} was 2.2 m/s and the air thermal boundary layer was neutrally stable.

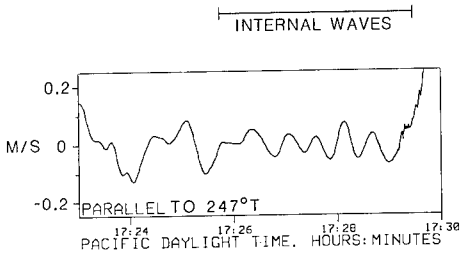


Figure 20. Band-pass filtered surface current for Set 2 measured parallel to 247°T (approximately parallel to the wake axis).

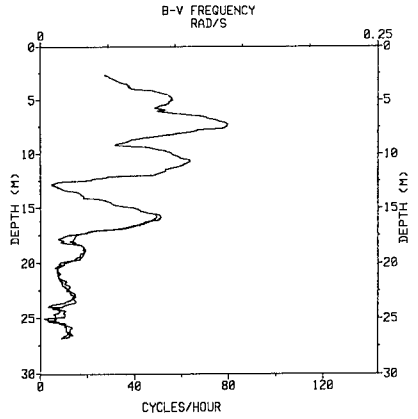


Figure 22. Stability profile for Set 2, 83/8/1 17:46:45-17:50:35.

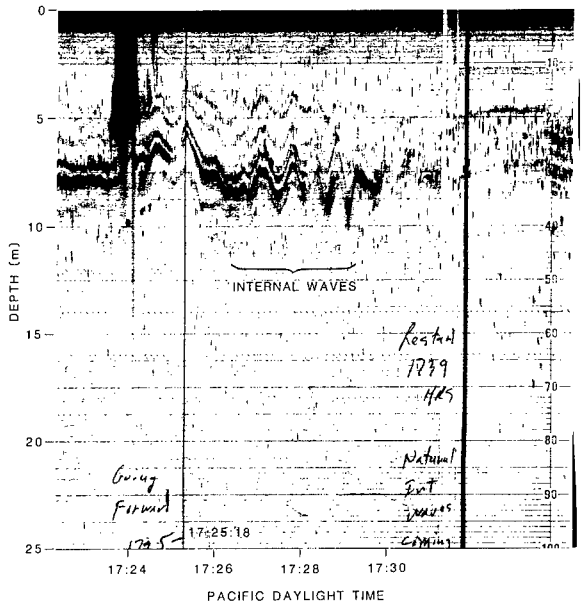


Figure 21. Echosounder traces for Set 2. The echosounder lags behind the bow current and slope signals by about one minute because of its stern mounting position.

Time-sequence data for the divergent-wave case of Set 6a is shown in Fig. 23. Here the internal waves are much weaker than in Set 2 and modulations are not so apparent in the wave slope records. The mean-square slope variations are ±10-to-15% and the modulation periods are much less than in Set 2. The raw slope signals are shown in Fig. 24 against an expanded time scale, and the internal wave modulations are apparent in the North-component (approximately cross-track) between 17:59:30 and 18:01:30. The U_{10} wind speed was 1.58 m/s directed almost across the wake axis (165°T) and the air thermal boundary layer was stable.

Internal wave current is shown in Fig. 25 with the ship's speed and surface wave portions filtered out. The component parallel to the measurement ship's head is shown (344°T) and this is approximately the cross-track component. Peak-to-peak values are about 0.06 m/s and there is an unmistakable decrease in apparent period towards the wake-axis (increasing time) for a major portion of this signal. The amplitude of this decreasing period signal also shows a decreasing tendency.

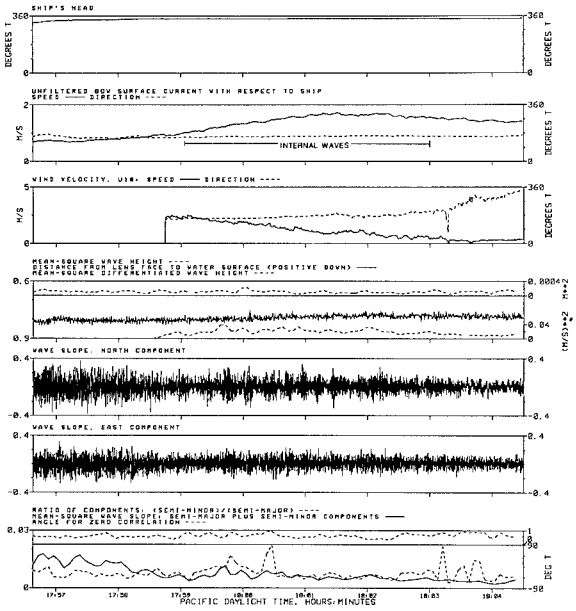


Figure 23. Time-sequence data for Set 6a. Internal waves can be seen in the current (particularly near 18:01) and as modulations in the north wave slope component and mean-square slope before 18:02. Wind data is not available before 17:58:45.

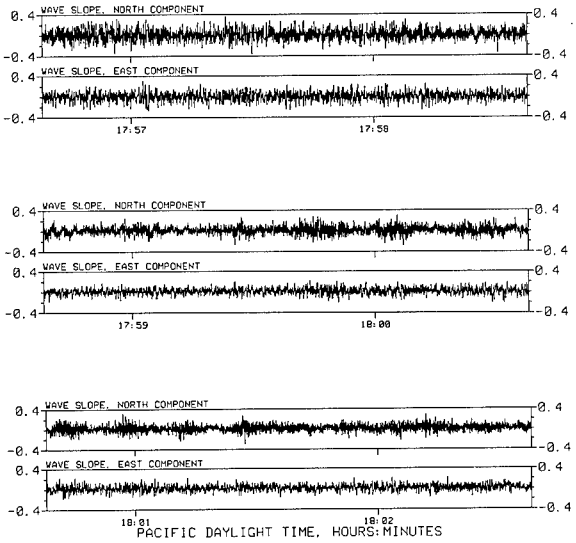


Figure 24. Detailed slope data for Set 6a.

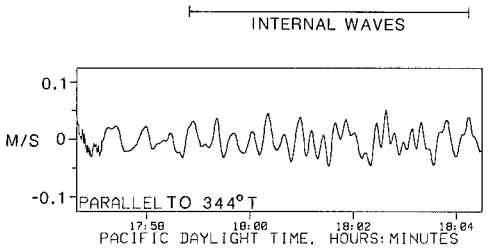


Figure 25. Band-pass filtered currents for Set 6a. The component parallel to measurement ship's head (344°T) is shown (approx. cross-track). The other component is contaminated by noise and ship-steerage effects.

Internal wave heights are evident in the echosounder traces as shown in Fig. 26. Only the longer waves near the outer edge of the wake (17:58) and the very short waves near the wake axis (18:04) are apparent in this case. presumably because of an absence of scatterers near 18:02. Their heights vary from about 1 m for the long waves, to 0.25 m for the short waves, peak-to-peak, at about 4 m depth. The stability profile for this case is shown in Fig. 27 and it displays a maximum BV frequency of 120 cph at 6 m depth.

For Set 6a, the along-track distance during the measurements varied from 3.7 to 4.6 km.

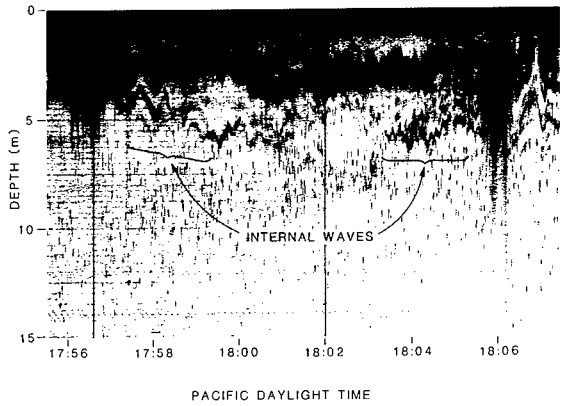


Figure 26. Echosounder traces for Set 6a showing internal waves near 17:58 and 18:04. The ship turned at 18:06.

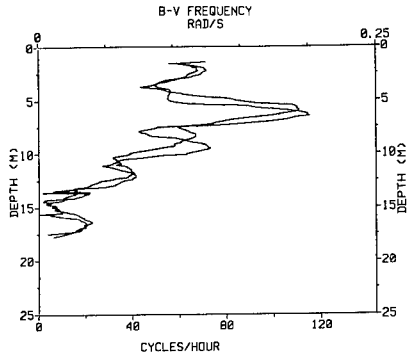


Figure 27. Stability profile for Set 6a. 1983/8/2 17:59:30-18:04:30.

5. DISCUSSION

The surface Kelvin wake data show quite clearly that the wave system near the axis, where the strongest part of the SAR images originate, is quite complicated, with wave energy propagating over a wide range of angles and not just at the angles predicted by simple Kelvin theory. The wavelength gradient perpendicular to the wake axis has the Kelvin appearance, but any distribution of sources along the wake axis near the ship would produce the same gradient because of the dispersive nature of surface waves. It appears that there is an incoherent component to the effective source strength for the short waves, as hypothesized by the JASON group (Brown (1985), Case et al. (1984)). From a careful analysis of the angular width of the imaged "V"'s as performed by Lyden et al. (1985a), it appears that they are somewhat wider than the predictions of first order Bragg theory, assuming linear dispersion, no mean currents, and sources at the position of the ship, although, the measurements can be made to fit the predictions if the sources are placed forward of the ship (Lyden et al. 1985a). Another possibility is that the outer edges of the turbulent wake are acting as incoherent "line" sources near the ship with strengths that are presumably related to the wake turbulence and so to the distance behind the ship. It also seems likely that the turbulent velocity field, particularly near the outer edges of the larger eddies, will exert a significant randomizing effect on the directions of propagation of the shorter Kelvin wake waves. Predictions using these "turbulence" hypotheses are not available.

Examinations of the effect of mean cross-track current gradients have been explored, notably with a vortex model (Lyden et al. 1985b, and Swanson, 1984) and with an internal wave model. The vortex model positions the V-arms correctly and it predicts the cross-track intensity variations correctly, at least for some cases. The model is based on a saturated k^{-4} wind-wave type of spectrum rather than an approximate Kelvin pattern, so presumably it pertains under at least moderately windy conditions or for cases in which the inner Kelvin wake waves are sufficiently randomized that their spectrum has the k^{-4} behaviour. The internal wave model also predicts approximately the right V-shape but correct predictions of the intensity of the V-arms are not available, and, again, it is predicated on the existence of a wind-wave type of spectrum rather than a dominant Kelvin pattern.

The current and internal wave height measurements are not precise enough to support or deny the existence of either vortices or internal waves, however, they do show that, at a few kilometres behind the source ship, models must predict currents that are less than about $3\frac{1}{2}$ cm/s peak-to-peak, and isopycnal height variations that are less than 25 cm peak-to-peak at 2 metres depth.

It does appear that a model based on Bragg scattering from a Kelvin pattern with a random source component, perhaps with the inclusion of mean wake vortex currents and other known mean wake currents, would be quite fruitful in explaining the light wind SAR wake imagery.

The internal Kelvin wakes provide a completely different kind of image pattern, at least for the case that is presented here. Other examples exist in which this is not the situation (Rev 407 SEASAT, LPG tanker JOWIP in Georgia Strait), and this similarity of internal and surface wake imagery has been a source of some complication for people working in this field. Only the multi-crested appearance of internal Kelvin wakes has been used so far to distinguish them from V-like surface wakes. Whether or not this is a reliable indicator has not been proven although it is difficult to imagine how a surface Kelvin wake would give the appearance of multi-crestedness except under special conditions (e.g. multiple-Bragg, or specular and Bragg).

The multiple crestedness of the image for Set 6a (Knight Inlet) is one of its major characteristics. For this case the phase speed of the outer waves is estimated to be about 0.30 m/s and the current fluctuation is about 0.02 m/s rms, thus $u/c \approx 0.07$. The maximum strain rate $2\pi u/\lambda$ is about 0.006 sec^{-1} using a wavelength of 32 metres and a peak u-value of 0.01 m/s. The u/c-ratio indicates that linear propagation theory is probably accurate in this case and the strain rate indicates that wind-wave relaxation times of less than a few minutes will begin to obliterate the surface effect.

A full modelling comparison has not yet been done for this case. However, a comparative analysis of the SAR modulations with surface truth and model predictions is currently being undertaken by other member organizations of JOWIP, for the few Knight Inlet cases that are available.

The ship wakes for Knight Inlet all represent low source speed, high stratification conditions. The speed range is 0.43 m/s to 3.36 m/s and the BV frequency maxima range from 79.6 cph to 119.6 cph. The internal Froude number, defined here as $F_I=V/(Z)(BV)$, ranges from 0.30 to 2.63, all small, and, in fact, subcritical (<1) for two of the sets (one of which is Set 2). Here, Z and BV are depths and value of the BV maximum, and V is the source speed. More typical values for open ocean conditions are V~16 knots, BV max. ~ 10 cph, and Z ~ 100 m, giving F_I ~5. For the surface Kelvin wake of JOWIP 8/2, F_I ~ 11.8, a comparatively large value.

Peak-to-peak current values for the Knight Inlet data set, normalized by the product (Z)(BV), are shown in Fig. 28 as a function of F_I, for all runs with currents distinguishable from noise. To remove spreading "loss" effects, the normalized current has been multiplied by the square root of the number of kilometres from the source position to the measurement position.

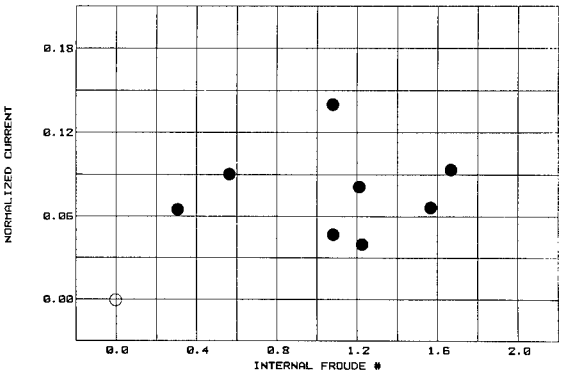


Figure 28. Internal wave current as a function of internal Froude number.

The normalized currents are essentially independent of F_I, with perhaps a slight tendency towards a peak near F_I=1. The average of all the normalized currents is 0.077. It is recognized that more precise forms of F_I can be defined, e.g. with the product (Z)(BV) replaced by the maximum internal wave phase speed, or by $\sqrt{\int Z(BV)^2 dZ}$, etc. Also, other parameters may be equally important in controlling the internal wave current, such as displacement of the source vessel (about 1500T for both CFAV ENDEAVOUR and USS QUAPAW), ambient shear values, etc. and in a full theoretical model all these must be treated.

6. CONCLUSIONS

Three conclusions regaring surface Kelvin wakes have been reached on the basis of the measured data. Firstly, that specular reflection is eliminated as a required mechanism for forming SAR images; secondly, that the inner parts of the Kelvin wake show non-simple along-crest structure, especially for the shorter wavelengths; and thirdly, that internal waves, as a possible source of V-wake modulation, have not been identified, and if present, must exhibit surface currents of less than a few centimetres per second peak-to-peak.

Detailed measurements of slope in one particularly low-background run (8/2) show that, outside of the turbulent wake, maximum slopes occur toward the outer edge of the wave system, i.e. toward the cusp location predicted by traditional Kelvin theory to be at 19.5^0 to the wake axis (using a polar description centred on the source), and further, that interference effects are prominent, but with the expected decrease in wavelength of the diverging wave system towards the wake centre. Because of the complexity of the surface wave field in the inner parts of the Kelvin wake, and the absence of specularly reflecting slope facets, it seems that the Bragg backscattering resonance mechanism is most likely responsible for the V images. An adequate numerical model of this part of the wave wake is not yet available.

Internal Kelvin wakes generated by USS QUAPAW and CFAV ENDEAVOUR in Knight Inlet have been measured and show peak-to-peak currents of order 0.1 m/s and peak-to-peak heights of order 0.8 m at 4-m depth. The shape of the wake patterns are considerably different from the surface Kelvin wakes. An L-band SAR image from Set 6a (JOWIP 11/3) shows strong modulations due to the internal wave surface currents. The modulations are multi-crested as opposed to the simple V-like appearance of the surface Kelvin wake images.

ACKNOWLEDGEMENTS

It is a pleasure to record a special acknowledgement to Rod Buntzen and Bob Hammond of NOSC, San Diego, CA, for being the prime motivators, chief planners and generally taking most of the responsibility for the surface Kelvin wake portion of the JOWIP Georgia Strait Experiment. Many other people were involved and thanks also go to them.

REFERENCES

Brown, E.D. (1985) "Integrated Report on Mechanisms Responsible for Narrow Angle V-Wakes in the Georgia Strait Experiment", Final Report, Science Applications International Corporation, La Jolla, CA.

Case, K., C. Callan, R. Dashen, R. Davis, W. Munk, J. Vesecky, K. Watson, and F. Zachariasen (1984). "SEASAT III and IV", JSR-84-203, The MITRE Corporation, McLean, VA, 22102.

Hammond, R.R., R.R. Buntzen, and E.E. Floren (1985). "Using Ship Wake Patterns to Evaluate SAR Ocean Wave Imaging Mechanisms", Technical Report 978, Naval Ocean System Center, San Diego, CA, 92152-5000.

Hughes, B.A., S.J. Hughes, and T.W. Dawson (1984). "Joint CAN/US Ocean Wave Investigation Project. Objectives, Procedures and DREP Data for the Georgia Strait Experiment (July/August 1983)", Technical Memorandum 84-7, Defence Research Establishment Pacific, Forces Mail Office, Victoria, B.C. V0S 1B0.

Hughes, B.A. and T.W. Dawson (1985). "Joint CAN/US Ocean Wave Investigation Project. DREP Measurements of Surface Ship Wakes in Dabob Bay, WN, July 1983", DREP Report 85-1, Defence Research Establishment Pacific, Forces Mail Office, Victoria, B.C. V0S 1B0.

Hughes, B.A. and T.W. Dawson (1986). "Joint CAN/US Ocean Wave Investigation Project. DREP Measurements of Surface-Ship-Produced Internal Wave Wakes in Knight Inlet, B.C. 1983", Technical Memorandum 85-20, Defence Research Establishment Pacific, Forces Mail Office, Victoria, B.C. V0S 1B0.

Lyden, J.D., D.R. Lyzenga, R.A. Shuchman, and E.S. Kasischke (1985a). "Analyses of Narrow Ship Wakes in Georgia Strait SAR Data", Topic Report 155900-20-T, Environmental Research Institute of Michigan, Ann Arbor, MI, 48107.

Lyden, J.D., D.R. Lyzenga, R.A. Shuchman, and C.V. Swanson (1985b). "SAR Detection of Ship-Generated Turbulent and Vortex Wakes", Technical Memorandum RR-86-112, Environmental Research Institute of Michigan, Ann Arbor, MI, 48107.

Swanson, C.F. (1984). "Radar Observability of Ship Wakes", Cortana Corporation Report, Falls Church, VA.

DISCUSSION

Arthur M. Reed,
David W. Taylor Naval Ship R&D Center

The author states several times that photographs of the wake show waves moving away from the ship. On what does he base this conclusion? Normally, it is difficult to determine wave propagation direction from photographs.

Reply -

Perhaps I have fallen into a possible "trap" in determining propagation direction from wavefront curvature. It can be misleading to do this because non-homogenous current fields can distort wavefront slopes quite independently of the propagation directions, and, especially in our case, the point source optics involved (sun and camera) can conspire to exaggerate wavefront curvatures in images such as the photographs presented here. This latter point has also been emphasized by Bob Hammond of NOSC. Nevertheless, I have used wavefront curvature to determine propagation direction assuming that the waves are propagating away from local centers of curvature, and for the cases presented, believe that this provides a legitimate interpretation.

Michael B. Wilson,
David W. Taylor Naval Ship R&D Center

In one of the photographs there was a stern quarter view of the QUAPAW proceeding across the smooth water of the bay. There appeared to be two narrow tracks or streaks that extended downstream from the stern. These streaks appeared slightly darker than the surrounding water and seemed to be formed into a V-pattern roughly corresponding to the white V of the SAR images. These streaks do not appear to have shown up in any of the other photographs from other camera angles. They probably are visible in this case because of the particular reflection condition (position of the viewer and the light source). Were these streaks associated with ruffled or smoothed water? Are these streaks part of the Kelvin wave pattern in the author's opinion? Or are they formed from bow wave or diverging wave breaking? Are they really in an expanding V-pattern? What relationship could such streaks have with the SAR images?

Reply -

The streaks referred to, Figure 24, (Hughes & Dawson, 1985) do appear in other photographs and have been associated partly with the edge of the turbulent wake and partly to interference effects which can be seen across the whole wave-wake. The dark bands seem to be associated with rufflings or extra-large slopes, and they do appear to be diverging in a V-pattern. It is not known how far downstream they exist or to what extent they have influenced the SAR imagery.

Fred Stern,
Iowa Institute of Hydraulic Research

It seems questionable that the narrow V wake can be attributed to the classical Kelvin wake. In an experiment which is presently underway at the Iowa Institute of Hydraulic Research concerning wave / boundary layer interaction wave generation near the boundary-layer edge has been observed, possibly due to the boundary layer displacement effect. Have any correlations been made between viscous wake length scales and the location of the narrow V?

Reply -

Not to my knowledge.

Far Field Features of the Kelvin Wake

A. BARNELL and F. NOBLESSE

David W. Taylor Naval Ship R&D Center, U.S.A.

ABSTRACT

The classical Kelvin wake trailing a ship advancing at constant speed in calm water is studied. In particular, asymptotic expressions for determining the far-field wake, at large distances behind the ship, are investigated numerically. This analysis, in which surface tension and nonlinearities are ignored, indicates that the divergent waves of a surface ship generally are infinitely steep at the track of the ship, even though their amplitude vanishes there; this result is theoretically possible because the wavelength of the divergent waves vanishes at the track of the ship. Inasmuch as infinitely-steep water waves cannot exist in reality, the linear no-surface-tension analysis presented in this study suggests that no divergent waves can exist within a certain region in the vicinity of the track of the ship, and that the Kelvin wake contains three distinct regions: (i) an inner region where only transverse waves can exist, (ii) an outer region where both transverse and divergent waves are present, and (iii) an intermediate region at the boundary between the inner and outer regions where short steep divergent waves, as well as transverse waves, can be found. Numerical results for a simple bow form show that the inner region is quite narrow, and that the wavelength of the divergent waves at the boundary of the inner region is of the order of 1 to 20 cm, depending on the speed of the ship. These results appear to be consistent with the narrow V-wakes observed in some SAR images of ship wakes. The analysis presented in this study may thus provide a partial explanation for these observations. However, the small wavelengths mentioned above indicate that the divergent waves in the vicinity of the track of the ship are likely to be significantly altered by surface tension, which should therefore be included in a more realistic analysis.

INTRODUCTION

It has been observed, e.g. [1,2,3], that images of ship wakes taken by the SEASAT SAR (Synthetic Aperture Radar) and other airborne SAR systems sometimes reveal long, narrow wakes extending back several miles behind ships. According to Swanson [3], "there appears a narrow, dark band along the centerline of the ship wake, widening slightly with distance away from the ship. Often accompanying these dark regions, at a slightly larger angle, are bright lines, which show up especially well on X-band SAR images". The apparent included angle of this narrow wake is much smaller that that corresponding to the Kelvin cusp line.

Several theoretical explanations of the features observed in SAR images of ship wakes have been proposed [3,4,5,6]. The proposed explanations include interactions between the cross currents created by a ship in its wake and surface gravity waves [3,6] and the occurence of a sharp peak in the amplitude of the divergent waves in the Kelvin wake for a ship form having a large flare angle [5]. However, there currently appears to be no convincing electrodynamic or hydrodynamic explanation of the observations. It thus seems necessary to investigate in detail each one of the proposed possible explanations in order to determine whether one, or possibly a combination of several, of them does in fact provide a satisfactory theoretical interpretation of the SAR images of ship wakes.

The classical Kelvin wake trailing a ship advancing at constant speed in calm water is examined in this study. Viscosity, surface tension and nonlinearities are ignored in this preliminary analysis, and irrotational flow is assumed. The analysis and related numerical results for a simple ship bow form have led to several conclusions and recommendations for further studies which are presented at the end of the paper. Only two conclusions that may be related to some of the features observed in SAR images of ship wakes are discussed here.

It was previously found by Scragg [5] that, for a ship bow form with a large flare angle, the zeroth-order slender-ship approximation to the far-field wave-amplitude

function given in Noblesse [7] predicts a sharp peak in the value of the amplitude of the divergent waves at an angle from the track of the ship equal to approximately half the bow entrance angle. This finding of Scragg has been verified in this study, as may be seen from figures 15, 16 and 18. Furthermore, the magnitude of the wave-amplitude peak has been found to increase very rapidly as the Froude number decreases below a certain threshold value. This peak thus appears to be a large-flare low-Froude-number feature. For the simple ship bow form considered in this study, the peak in the amplitude of the divergent waves in the Kelvin wake occurs along a line at 6° from the track of the ship. It may be found from equation (30a) that the wavelength of the divergent waves along this line varies between 0.7 m and 4.5 m for a ship with speed varying between 10 knots and 25 knots, respectively.

The other conclusion of this study that may be related to the narow V-wakes observed in some SAR images of ship wakes is the result that the divergent waves of a surface ship are infinitely steep at the track of the ship, even though their amplitude vanishes there. This result is theoretically possible because the wavelength of the divergent waves vanishes at the track of the ship. A similar result was previously obtained by Sharma [8] who found that the Michell thin-ship approximation for a thin and deep strut-like ship form predicted infinite slopes for the divergent waves at the track of the ship. Inasmuch as infinitely-steep water waves cannot exist in reality, the foregoing result suggests that no divergent waves can exist within a certain region in the vicinity of the track of the ship, and that the Kelvin wake contains three distinct regions: (i) an inner region where only transverse waves can exist, (ii) an outer region where both transverse and divergent waves are present, and (iii) an intermediate region at the boundary between the inner and outer regions where short steep divergent waves, as well as transverse waves, can be found.

Numerical results for a simple bow form show that the "no-divergent-wave" inner region is quite narrow, as may be seen from figure 20 showing the Kelvin cusp line (angle $\simeq$ 19°28′), the line along which the amplitude of the divergent waves exhibits a peak (angle $\simeq$ 6°), and the three lines along which the steepness of the divergent waves is equal to 1/20, 1/15 and 1/7 (chain line close to the track of the ship). The latter three lines, along which the divergent waves are steep, lie much closer to the track of the ship than the line along which the steepness of the divergent waves exhibits a peak. Figures 21 and 22 show considerable variations among the several "steep-divergent-waves" lines that are represented in these figures. Nevertheless, these lines may be seen to correspond to values of $Y/(-X)$ equal to about 10^{-2} to 2.10^{-2}. For ship speeds varying between 10 knots and 25 knots, the wavelength of the divergent waves corresponding to the foregoing values of $Y/(-X)$ may be shown to vary between 0.7 cm and 4.2 cm for $Y/(-X) = 10^{-2}$, and 2.7 cm and 17 cm for $Y/(-X) = 2.10^{-2}$. These wavelengths are consistent with the wavelengths of the radar pulses used in SAR imaging, so that the foregoing results may provide a partial hydrodynamic explanation for the narrow V-wakes observed in these images.

The tentative nature of this explanation must however be stressed. Indeed, the foregoing results are based on an analysis in which surface tension and nonlinearities have been neglected. Inasmuch as this linear no-surface-tension analysis predicts extremely short and steep waves in the vicinity of the track of the ship, it is evident that both surface tension and nonlinear effects are liable to be significant. In particular, the short wavelengths found along the steep-divergent-wave lines determined in this study, and the brief description of the effects of surface tension upon the Kelvin wake given in Sharma [8], Lamb [9, pp. 468-470] and Wehausen and Laitone [10, pp. 636-637] indicate that the system of divergent waves in the vicinity of the track of the ship is likely to be profoundly affected by surface tension. Effects of surface tension upon the Kelvin wake will be investigated in a sequel to the present study.

APPROACH

This study considers the steady potential flow due to a ship advancing with constant speed in calm water of infinite depth and lateral extent. The far-field Kelvin wake, which is of primary interest here, may be conveniently analyzed in terms of the nondimensional far-field coordinates $\vec{x} = \vec{X}g/U^2$, velocity potential $\phi = \Phi g/U^3$ and velocity vector $\nabla_x\phi = \nabla_X\Phi/U$, where g is the gravitational acceleration and U is the speed of advance of the ship, $\vec{X}$ and Φ represent the dimensional coordinates and velocity potential, respectively, and ∇_x and ∇_X are the nondimensional and dimensional differential operators $\nabla_x = (\partial/\partial x, \partial/\partial y, \partial/\partial z)$ and $\nabla_X = (\partial/\partial X, \partial/\partial Y, \partial/\partial Z)$. The mean free surface is taken as the plane $z = 0$, with

the z axis pointing upwards, and the x axis is chosen in the ship centerplane and pointing towards the bow. The origin of the system of coordinates is placed within the ship. The Froude number is denoted by $F = U/(gL)^{1/2}$, where L is the length of the ship.

Equation (32) in [7] yields the following expression for the velocity potential associated with the Kelvin wake behind the ship

$$\pi\phi(\vec{x}) = \mathrm{Im}\int_0^\infty [E_+(t;\vec{x}) + E_-(t;\vec{x})]K(t)\,dt, \tag{1}$$

where $E_\pm(t;\vec{x})$ is the exponential function

$$E_\pm(t;\vec{x}) = \exp[z(1+t^2) + i(x \pm yt)(1+t^2)^{1/2}], \tag{2}$$

and K(t) is the far-field wave-amplitude function, which depends on the hull shape and the Froude number. Assuming that differentiation under the integral sign is permitted in equation (1), we may obtain

$$\pi \begin{Bmatrix} \phi_x \\ \phi_y \end{Bmatrix} = \mathrm{Im}\, i\int_0^\infty \begin{Bmatrix} E_+ + E_- \\ E_+ - E_- \end{Bmatrix} K(t) \begin{Bmatrix} (1+t^2)^{1/2} \\ t(1+t^2)^{1/2} \end{Bmatrix} dt. \tag{3a, 3b}$$

The nondimensional elevation $e = Eg/U^2$ of the free surface at a sufficiently-large distance behind the ship, such that nonlinearities may be neglected, is given by

$$e(x,y) = \partial\phi(x,y,0)/\partial x. \tag{4}$$

The slopes of the free surface in the directions parallel and perpendicular to the ship course then are

$$\partial e(x,y)/\partial x = \partial^2\phi(x,y,0)/\partial x^2 \tag{4a}$$

$$\partial e(x,y)/\partial y = \partial^2\phi(x,y,0)/\partial x\partial y. \tag{4b}$$

If differentiation under the integral sign in equation (3a) is permitted, we have

$$\pi \begin{Bmatrix} \phi_{xx} \\ \phi_{xy} \end{Bmatrix} = -\mathrm{Im}\int_0^\infty \begin{Bmatrix} E_+ + E_- \\ E_+ - E_- \end{Bmatrix} K(t) \begin{Bmatrix} 1+t^2 \\ t(1+t^2) \end{Bmatrix} dt. \tag{5a, 5b}$$

The vertical velocity ϕ_z is given by

$$\phi_z = -\phi_{xx}. \tag{6}$$

In this study, we are mostly interested in the value of the several flow variables defined above at the mean free surface and behind the ship, so that we have $z = 0$ and $x < 0$. Expression (2) for the exponential function $E_\pm$ then becomes

$$E_\pm = \exp[ix(1 \mp \alpha t)(1+t^2)^{1/2}], \tag{7}$$

where α is defined as

$$\alpha = -y/x. \tag{8}$$

For a ship with port- and starboard-symmetry, as is considered here, the Kelvin wake is symmetric about the ship track $y = 0$. We may then restrict the analysis of the Kelvin wake to the domain $y \geq 0$ and $x < 0$, and assume $\alpha \geq 0$.

Two difficulties associated with the foregoing approach for numerically determining the potential, its gradient, and the free-surface slopes in the Kelvin wake are readily apparent and should be noted here. A first numerical difficulty stems from the oscillations of the exponential function $E_\pm$ given by equation (7), which are very rapid for large values of $|x|$. We have $x = Xg/U^2 = (X/L)/F^2$. For a typical value of the Froude number equal to 0.2, say, we thus have $x = 25\ X/L$; we then have $x = -250$ at 10 ship lengths behind the ship, and much larger values of $|x|$ must be considered at greater distances behind the ship or/and for smaller values of the Froude number. Even for the comparatively-moderate value of x equal to -50, figure 1 shows that the functions E_+ and E_- oscillate quite rapidly. More precisely, figure 1 depicts the real parts of the functions $E_+(t;x,\alpha)$ and $E_-(t;x,\alpha)$ for $x = -50$; $\alpha = .1, .2, 1/2^{3/2}, .4$ and $.5$; and for $0 \leq t \leq 7$ and $0 \leq t \leq 3$ on the left and right sides, respectively. Figure 1 also indicates that the behavior of the function $E_+(t;x,\alpha)$ strongly depends on the value of α.

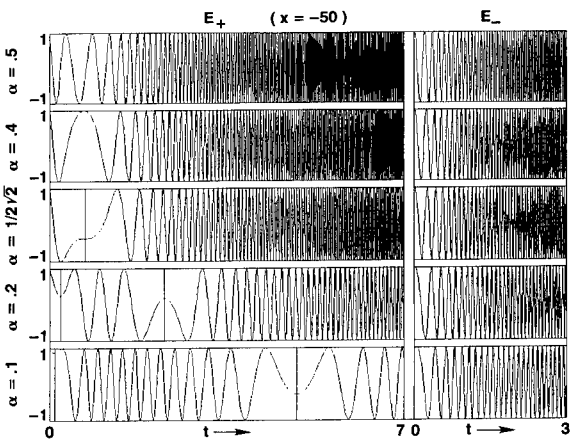


Fig. 1 — Real Parts of the Functions $E_+(t;x,\alpha)$ and $E_-(t;x,\alpha)$ for $x = -50$ and $\alpha = .1, .2, 1/2^{3/2}, .4$ and $.5$

A second, more basic, difficulty is associated with the differentiation under the integral sign which was used for obtaining expressions (3a,b) and (5a,b) from expression (1). For a fully-submerged body, the far-field wave-amplitude function K(t) is exponentially-small as $t \to \infty$, so that the operation of differentiating under the integral sign in expression (1) can be continued indefinitely in principle. Differentiation under the integral sign likewise is justified if $z < 0$. However, the operation must be justified in the limiting case $z = 0$ for a surface ship. Clearly, the operation may not be justified in principle, or feasible in practice, if the far-field wave-amplitude

function K(t) does not vanish sufficiently rapidly as $t \to \infty$. Precise information about the asymptotic behavior of the function K(t) as $t \to \infty$ is required in this respect. Figure 2 depicts the real and imaginary parts of the functions $(1+t^2)K(t)$ and $t(1+t^2)K(t)$ appearing in the integrands of the integrals (5a) and (5b), respectively, for $0 \leqslant t \leqslant 16$ and for a simple ship-bow shape which is considered further on in this study. Differentiation under the integral sign in expression (3a) is clearly not justified in the case corresponding to figure 2.

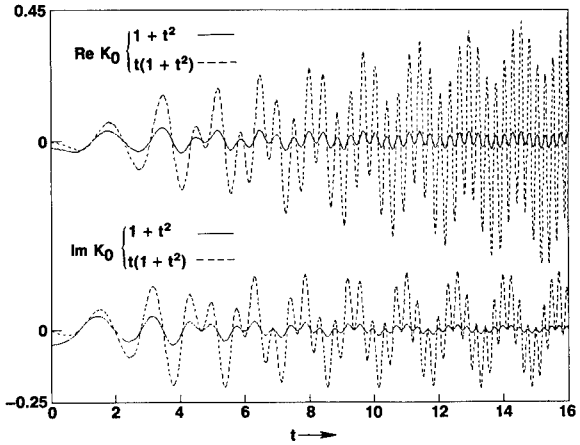


Fig. 2 — Real and Imaginary Parts of the Functions $(1+t^2)K(t)$ and $t(1+t^2)K(t)$ for a Simple Ship Bow Shape in the Zeroth-Order Slender-Ship Approximation

ASYMPTOTIC EVALUATION OF THE KELVIN WAKE

For large values of $|x|$ and $z = 0$, analytical approximations to the integrals (1), (3a,b) and (5a,b) can be obtained by taking advantage of the rapid oscillations of the exponential functions $E_{\pm}$ defined by equation (7). These functions may be expressed in the form

$$E = \exp[ix\theta(t;\alpha)], \tag{9}$$

where $\theta(t;\alpha)$ is defined as

$$\theta(t;\alpha) = (1-\alpha t)(1+t^2)^{1/2}. \tag{10}$$

The functions $E_+(t;x,\alpha)$ and $E_-(t;x,\alpha)$, where $\alpha > 0$, correspond to the function $E(t;x,\alpha)$ with $\alpha > 0$ and $\alpha < 0$, respectively. In the limiting case $\alpha = 0$, we have $E_+ = \exp[ix(1+t^2)^{1/2}] = E_-$. The derivatives of the phase-function $\theta(t;x,\alpha)$ with respect to t are given by

$$\theta'(t;\alpha) = -(\alpha - t + 2\alpha t^2)/(1+t^2)^{1/2}, \tag{11a}$$

$$\theta''(t;\alpha) = (1 - 3\alpha t - 2\alpha t^3)/(1+t^2)^{3/2}, \tag{11b}$$

$$\theta'''(t;\alpha) = -3(\alpha + t)/(1+t^2)^{5/2}. \tag{11c}$$

The phase $\theta(t;\alpha)$ and its first and second derivatives $\theta'(t;\alpha)$ and $\theta''(t;\alpha)$ are depicted in figures 3a, b, c, respectively.

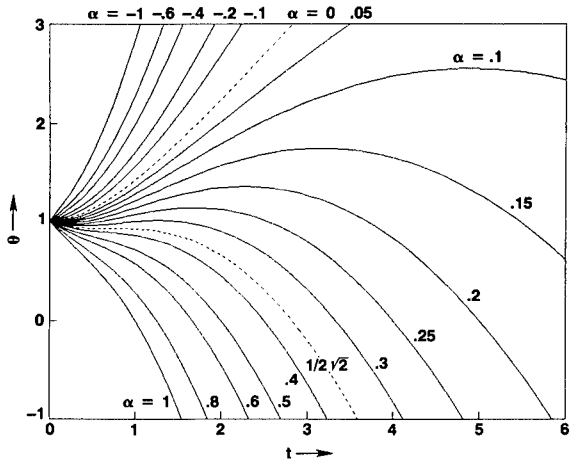


Fig. 3a — The Phase Function $\theta(t;\alpha)$ for $0 \leqslant t \leqslant 6$ and Several Values of α

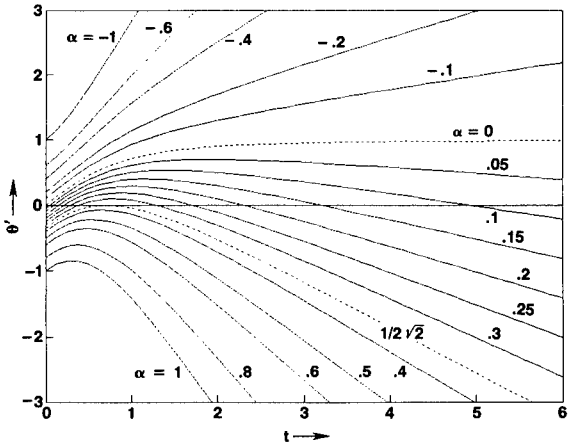


Fig. 3b — The Function $\theta'(t;\alpha)$ for $0 \leqslant t \leqslant 6$ and Several Values of α

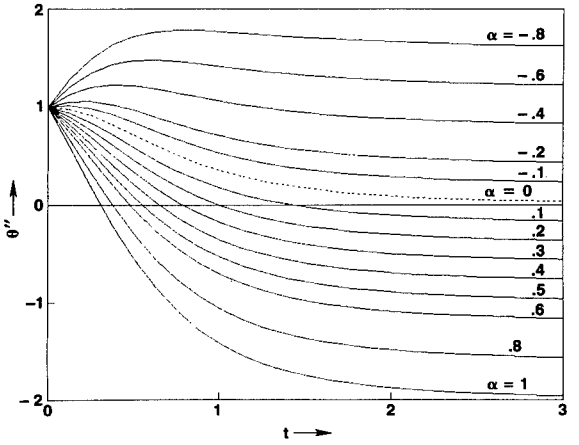


Fig. 3c — The Function $\theta''(t;\alpha)$ for $0 \leqslant t \leqslant 3$ and Several Values of α

It may be seen from figure 3b that the first derivative θ' does not vanish except if $0 \leqslant \alpha \leqslant 1/2^{3/2}$, for which θ' vanishes for 2 values of t. Equation (11a) shows that the 2 points where $\theta' = 0$, that is where the phase θ is stationary, are given by

$$t_{\pm}(\alpha) = [1 \pm (1-8\alpha^2)^{1/2}]/4\alpha. \tag{12}$$

We have $0 \leqslant t_- \leqslant t_+ \leqslant \infty$, with $t_- = 0$ and $t_+ = \infty$ for $\alpha = 0$, and $t_- = 1/2^{1/2} = t_+$ for $\alpha = 1/2^{3/2}$. The 2 points of stationary phase t_- and t_+ are apparent on the left side of figure 1 for $\alpha = .1, .2$ and $1/2^{3/2}$. Figure 3c shows that the second derivative θ'' vanishes for one value of t, say t_0, if $\alpha \geqslant 0$. Equation (11b) yields

$$t_0(\alpha) = (\Gamma - 1/\Gamma)/2^{1/2}, \tag{13}$$

where Γ is defined as

$$\Gamma = \{[1+(1+2\alpha^2)^{1/2}]/2^{1/2}\alpha\}^{1/3}. \tag{13a}$$

The value t_0 for which $\theta'' = 0$, and for which θ' reaches its maximum as figure 3b indicates, is a decreasing function of α. We have $t_0 = \infty$ for $\alpha = 0$, $t_0 = 1/2^{1/2}$ for $\alpha = 1/2^{3/2}$, and $t_0 = 0$ for $\alpha = \infty$. Furthermore, figure 4, where the functions $t_0(\alpha)$, $t_-(\alpha)$ and $t_+(\alpha)$ are depicted, shows that we have $0 \leqslant t_- \leqslant t_0 \leqslant t_+ \leqslant \infty$ for $0 \leqslant \alpha \leqslant 1/2^{3/2}$.

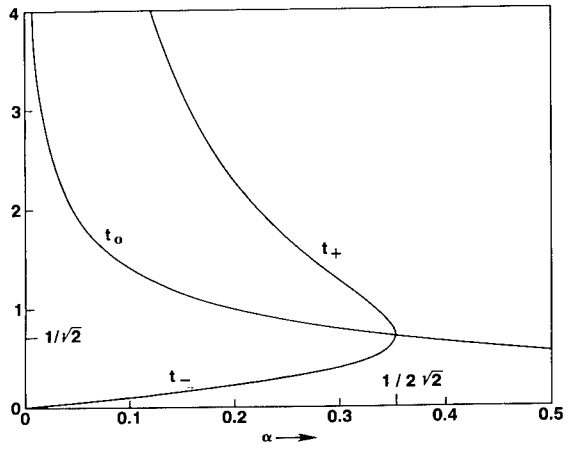


Fig. 4 — The Functions $t_0(\alpha)$, $t_+(\alpha)$ and $t_-(\alpha)$

In the vicinity of the points of stationary phase $t_{\pm}$ the first derivative of the phase-function may be approximated by the two-term Taylor series

$$\theta'(t;\alpha) \simeq (t-t_{\pm})\Theta''_{\pm} + (t-t_{\pm})^2\Theta'''_{\pm}/2, \tag{14}$$

where the function $t_{\pm}(\alpha)$ is defined by equation (12), and $\Theta''_{\pm}$ and $\Theta'''_{\pm}$ represent the values of the functions $\theta''(t;\alpha)$ and $\theta'''(t;\alpha)$ for $t = t_{\pm}(\alpha)$. By using equation (12) in equations (11b) and (11c) we may obtain

$$\Theta''_{\pm} = \pm 2^{3/2}\alpha(1-8\alpha^2)^{1/2}/[1+4\alpha^2 \pm (1-8\alpha^2)^{1/2}]^{1/2}, \tag{15a}$$

$$\Theta'''_{\pm} = \mp 2^{1/2}96\alpha^4/[1+4\alpha^2 \pm (1-8\alpha^2)^{1/2}]^{3/2}. \tag{15b}$$

In the neighborhood of the point t_0, where $\theta'' = 0$, we have

$$\theta'(t;\alpha) \simeq \Theta'_0 + (t-t_{\pm})^2\Theta'''_0/2, \tag{16}$$

where the function $t_0(\alpha)$ is defined by equation (13), and Θ'_0 and Θ'''_0 represent the values of the functions $\theta'(t;\alpha)$ and $\theta'''(t;\alpha)$ defined by equations (11a) and (11c) for $t = t_0(\alpha)$. The functions $t_0(\alpha)$, $t_+(\alpha)$ and $t_-(\alpha)$, $\Theta'_0(\alpha)$ and $\Theta'''_0(\alpha)$, $\Theta''_+(\alpha)$ and $\Theta''_-(\alpha)$, $\Theta'''_+(\alpha)$ and $\Theta'''_-(\alpha)$ are depicted in figure 5. The signs of the functions Θ'_0, Θ'''_0, $\Theta''_{\pm}$ and $\Theta'''_{\pm}$ are readily apparent from this figure. The Taylor-series approximation (14) and (16) are useful for devising an efficient numerical method for evaluating the integrals (1), (3a,b) and (5a,b), as will be examined in detail elsewhere.

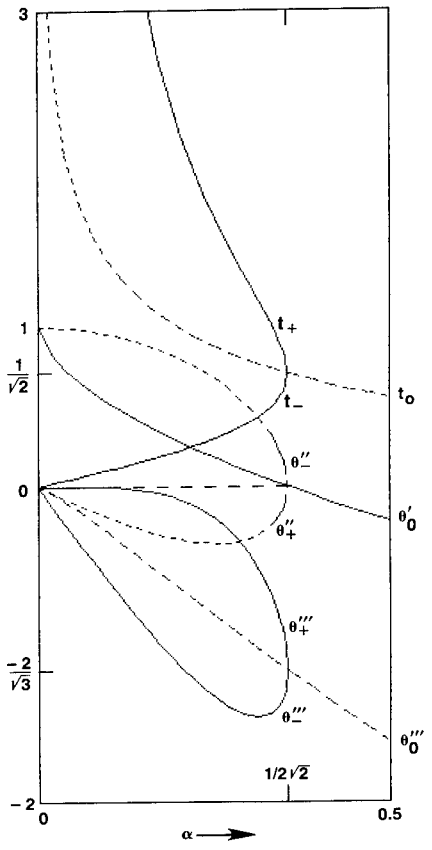


Fig. 5 — The Functions $t_0(\alpha)$, $t_{\pm}(\alpha)$, $\Theta'_0(\alpha)$, $\Theta'''_0(\alpha)$, $\Theta''_{\pm}(\alpha)$ and $\Theta'''_{\pm}(\alpha)$ for $0 \leqslant \alpha \leqslant 0.5$

Asymptotic approximations valid for $z = 0$ and $x \to -\infty$ will now be obtained for the integrals (1), (3a,b) and (5a,b). These five integrals may be expressed in the form

$$\pi\phi_k(x,\alpha) = \mathrm{Im}(c_k^+\psi_k^+ + c_k^-\psi_k^-), \tag{17}$$

where $0 \leqslant k \leqslant 4$, $c_k^{\pm}$ are constants, and $\psi_k^{\pm}$ are the

integrals defined as

$$\psi_k^{\pm}(x,\alpha) = \int_0^{\infty} \exp[ix\theta_{\pm}(t;\alpha)]K(t)a_k(t)\,dt; \quad (18)$$

in this expression, the phase $\theta_{\pm}(t;\alpha)$ is defined by

$$\theta_{\pm}(t;\alpha) = (1 \mp \alpha t)(1+t^2)^{1/2} \text{ with } \alpha \geqslant 0; \quad (19)$$

finally, the constants $c_k^{\pm}$ in equation (17) and the functions $a_k(t)$ in equation (18) are defined in the following table:

k	ϕ_k	a_k	c_k^+	c_k^-	
0	ϕ	1	1	1	(20a)
1	ϕ_x	$(1+t^2)^{1/2}$	i	i	(20b)
2	ϕ_y	$t(1+t^2)^{1/2}$	i	$-i$	(20c)
3	ϕ_{xx}	$1+t^2$	-1	-1	(20d)
4	ϕ_{xy}	$t(1+t^2)$	-1	1	(20e)

In the particular case $\alpha = 0$, that is on the track of the ship, equation (18) yields $\psi_k^+ = \psi_k = \psi_k^-$, with

$$\psi_k(x,0) = \int_0^{\infty} \exp[ix(1+t^2)^{1/2}]\, K(t)a_k(t)\,dt.$$

The major contribution to this integral in the limit $x \to -\infty$ stems from the point of stationary phase at the origin $t=0$. Specifically, we may obtain

$$(\pi/2)^{1/2}(-x)^{1/2}\phi_k(x,0) \sim$$

$$\text{Im } c_k K_0 \exp[i(x-\pi/4)] \text{ as } x \to -\infty, \quad (21)$$

$$\text{with } c_0 = 1,\ c_1 = i,\ c_3 = -1, \quad (21a,b,c)$$

and $c_2 = 0 = c_4$; we thus have

$$\phi_y = 0 = \phi_{xy} \text{ for } \alpha = 0, \quad (22a,b)$$

in accordance with the symmetry of the wave pattern about the axis $\alpha = 0$. In equation (21), K_0 represents the value of the function K(t) at the origin $t = 0$, that is we have $K_0 = K(0)$.

For $0 < \alpha < 1/2^{3/2}$, the phase $\theta_+(t;\alpha)$ is stationary, that is $\theta'_+ = 0$, at the two distinct points $t_-(\alpha)$ and $t_+(\alpha)$ defined by equation (12), whereas $\theta'_-(t;\alpha) > 0$ for $t \geqslant 0$, as may be seen from figure 3b. Equations (17) and (18) then yield

$$\pi\phi_k(x,\alpha) \sim \text{Im } c_k^+ \psi_k^+ \text{ as } x \to -\infty \text{ with } 0 < \alpha < 1/2^{3/2}.$$

The contribution of the two points of stationary phase $t_{\pm}$ can be evaluated by using the method of stationary phase, with the result

$$(\pi/2)^{1/2}(-x)^{1/2}\phi_k(x,\alpha) \sim \text{Im } c_k(A_k^- E_- + A_k^+ E_+)$$

$$\text{as } x \to -\infty, \text{ with } 0 < \alpha < 1/2^{3/2} \text{ and} \quad (23)$$

$$c_0 = 1,\ c_1 = i = c_2,\ c_3 = -1 = c_4; \quad (23a,b,c,d,e)$$

furthermore, $A_k^{\pm}$ and $E_{\pm}$ are the amplitude and exponential functions defined as

$$A_k^{\pm} = K_{\pm} a_k^{\pm}/(\mp\Theta''_{\pm})^{1/2}, \quad (24a)$$

$$E_{\pm} = \exp[i(x\Theta_{\pm} \pm \pi/4)], \quad (24b)$$

where $K_{\pm}$, $a_k^{\pm}$, $\Theta_{\pm}$ and $\Theta''_{\pm}$ are defined as

$$K_{\pm} = K(t_{\pm}),\ a_k^{\pm} = a_k(t_{\pm}), \quad (25a,b)$$

$$\Theta_{\pm} = \theta(t_{\pm};\alpha),\ \Theta''_{\pm} = \theta''(t_{\pm};\alpha), \quad (25c,d)$$

and $t_{\pm}$ is the function of α given by equation (12), that is we have

$$t_{\pm} = [1 \pm (1-8\alpha^2)^{1/2}]/4\alpha. \quad (26a)$$

We may then obtain

$$1+t_{\pm}^2 = [1+4\alpha^2 \pm (1-8\alpha^2)^{1/2}]/8\alpha^2. \quad (26b)$$

The expressions for the terms $a_k^{\pm}$ may readily be obtained from equations (20a-e), (25b) and (26a,b). Equations (25c), (19) and (26a,b) yield

$$\Theta_{\pm} = [3 \mp (1-8\alpha^2)^{1/2}][1+4\alpha^2 \pm (1-8\alpha^2)^{1/2}]^{1/2}/2^{1/2}8\alpha. \quad (26c)$$

Finally, $\Theta''_{\pm}$ is given by equation (15a), that is we have

$$\mp\Theta''_{\pm} = 2^{3/2}\alpha(1-8\alpha^2)^{1/2}/[1+4\alpha^2 \pm (1-8\alpha^2)^{1/2}]^{1/2}. \quad (26d)$$

It may be shown from equations (26a,c,d) and verified from figures 4, 3a, 3c and 5 that we have $t_- = 0$ and $\Theta_- = 1 = \Theta''_-$ in the limit $\alpha = 0$. Furthermore, equations (25b) and (20a-e) show that we have $a_k^- = 1$ for k = 0, 1 and 3, and $a_k^- = 0$ for k = 2 and 4 in the limit $\alpha = 0$. The asymptotic approximation (23) for $\phi_k(x,\alpha)$ therefore becomes identical to the asymptotic approximation given by equations (21), (21a,b,c) and (22a,b) for $\phi_k(x,0)$ in the limit $\alpha = 0$, if the contribution of the second point of stationary phase $t_+ = \infty$ is null, that is if $A_k^+ = 0$ for $\alpha = 0$ and $t_+ = \infty$. In other words, the asymptotic approximation (23) for $\phi_k(x,\alpha)$ is uniformly valid in the vicinity of the track of the ship $\alpha = 0$ if $A_k^+ = 0$ for $\alpha = 0$. Equations (26a) and (26d) yield $t_+ \sim 1/2\alpha$ and $-\Theta''_+ \sim 2\alpha$ as $\alpha \to 0$. We then have $-\Theta''_+ \sim 1/t_+$ as $\alpha \to 0$, and the condition for the asymptotic approximation for $\phi_k(x,\alpha)$ to be uniformly valid in the limit $\alpha = 0$ takes the form

$$t^{1/2}K(t)a_k(t) \to 0 \text{ as } t \to \infty. \quad (27)$$

In the limit $\alpha = 1/2^{3/2}$, we have $t_- = 1/2^{1/2} = t_+$ and $\Theta''_{\pm} = 0$, as may be verified from equations (26a,d) and figure 5. Equation (24a) then shows that we have $|A_k^{\pm}| \to \infty$ as $\alpha \to 1/2^{3/2}$; and the asymptotic approximation (23) is not valid in the vicinity of the boundary of the Kelvin wake. A complementary asymptotic approximation, expressed in terms of Airy functions, valid at and near the Kelvin cusp line is given in Ursell [11] for the particular case of a pressure point at the free surface. However, we are mostly interested in the sector $0 \leqslant \alpha < 1/2^{3/2}$, that is inside the Kelvin wake, in the present study.

The far-field asymptotic approximation (23) shows that the wave pattern at any point (x,α), with $x \ll -1$ and $0 \leqslant \alpha < 1/2^{3/2}$, consists in two elementary plane progressive waves. Specifically, equations (4), (20b), (23)

and (24b) show that the free-surface elevation within the Kelvin wake at a sufficiently-large distance behind the ship is given by

$$(\pi/2)^{1/2}(-x)^{1/2}e(x,\alpha) \sim \mathrm{Re}[A_1^- \exp(i\varphi_-) + A_1^+ \exp(i\varphi_+)], \quad (28)$$

where the phases $\varphi_\pm$ of the two waves are given by $\varphi_\pm = x\Theta_\pm \pm \pi/4$. Curves along which the phases φ_+ or φ_- are constant then are defined by the equation $x\Theta_\pm \pm \pi/4 =$ constant. This relation and equation (8) then yield the following parametric equations for the curves along which the phase is equal to $-2n\pi$:

$$-x_\pm = (2n\pi \pm \pi/4)/\Theta_\pm^2, \quad (29a)$$

$$y_\pm = (2n\pi \pm \pi/4)\alpha/\Theta_\pm, \quad (29b)$$

where $0 \leqslant \alpha \leqslant 1/2^{3/2}$. The ten constant-phase curves corresponding to $1 \leqslant n \leqslant 10$ are depicted in figure 6. The "transverse" and "divergent" waves in this classical representation of the Kelvin wake correspond to the waves $A_1^- \exp(i\varphi_-)$ and $A_1^+ \exp(i\varphi_+)$, respectively, in equation (28).

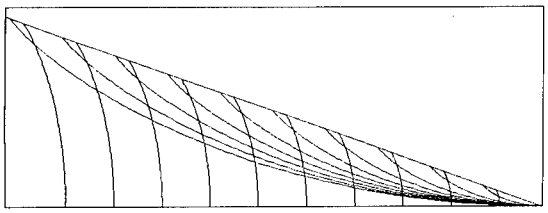


Fig. 6 — The Classical Kelvin Ship Wave Pattern

The wavenumber corresponding to the wave with phase $\varphi_\pm$ is given by $\nabla\varphi_\pm$. The corresponding wavelength, say $\lambda_\pm$, and direction of propagation with respect to the track of the ship, say $\beta_\pm$, then are given by $\lambda_\pm = 2\pi/|\nabla\varphi_\pm|$ and $\beta_\pm = \tan^{-1}(\varphi_y^\pm/\varphi_x^\pm)$, where $\varphi_x^\pm$ and $\varphi_y^\pm$ represent the x- and y-derivatives of $\varphi_\pm$ and $|\nabla\varphi_\pm| = [(\varphi_x^\pm)^2 + (\varphi_y^\pm)^2]^{1/2}$. The relation $\varphi_\pm = x\Theta_\pm \pm \pi/4$ and equation (26c) then yield

$$\lambda_\pm = 2^{1/2}16\pi\alpha^2/[3 \mp (1-8\alpha^2)^{1/2}]\,[1-4\alpha^2 \pm (1-8\alpha^2)^{1/2}]^{1/2}, \quad (30a)$$

$$\beta_\pm = \sin^{-1}\{[1-4\alpha^2 \pm (1-8\alpha^2)^{1/2}]/[1+4\alpha^2 \pm (1-8\alpha^2)^{1/2}]\}^{1/2}. \quad (30b)$$

Equations (30a,b) show that we have $\lambda_- = 2\pi$, $\beta_- = 0$ and $\lambda_+ = 0$, $\beta_+ = \pi/2$ in the limit $\alpha = 0$, and $\lambda_- = 4\pi/3 = \lambda_+$, $\beta_- = \sin^{-1}(1/3^{1/2}) = \beta_+$ for $\alpha = 1/2^{3/2}$. More precisely, we have

$$2\pi \geqslant \lambda_- \geqslant 4\pi/3 \geqslant \lambda_+ \geqslant 0 \text{ and} \quad (31a)$$

$$0 \leqslant \beta_- \leqslant \sin^{-1}(1/3^{1/2}) \leqslant \beta_+ \leqslant \pi/2, \quad (31b)$$

as may be seen from figure 7 where the functions $\lambda_\pm(\alpha)/2\pi$ and $2\beta_\pm(\alpha)/\pi$ are depicted.

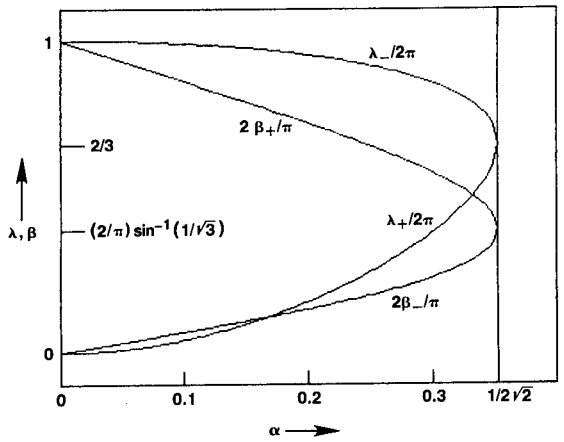


Fig. 7 — The Wavelengths $\lambda_\pm(\alpha)$ and Propagation Angles $\beta_\pm(\alpha)$ of the Transverse and Divergent Waves in the Kelvin Wake

Equation (28) shows that the amplitudes of the transverse and divergent waves in the Kelvin wake are asymptotically given by $(2/\pi)^{1/2}|A_1^\pm|/(-x)^{1/2}$ as $x \to -\infty$. The steepnesses, say $s_\pm$, of these waves then are given by $s_\pm = (2/\pi)^{1/2}|A_1^\pm|/(-x)^{1/2}\lambda_\pm$. Equations (24a), (25a,b) and (20b) then yield

$$(-x)^{1/2}s_\pm \sim \sigma_\pm(\alpha)|K(t_\pm)| \text{ as } x \to -\infty, \quad (32)$$

where $\sigma_\pm(\alpha)$ is defined as $(2/\pi)^{1/2}(1+t_\pm^2)^{1/2}/(\mp\Theta_\pm'')^{1/2}\lambda_\pm$.

Equations (26b,d) and (30a) then yield

$$\sigma_\pm = [3 \mp (1-8\alpha^2)^{1/2}][1-4\alpha^2 \pm (1-8\alpha^2)^{1/2}]^{1/2} \cdot [1+4\alpha^2 \pm (1-8\alpha^2)^{1/2}]^{3/4}/ 64\pi(2^{1/2}\pi)^{1/2}\alpha^{7/2}(1-8\alpha^2)^{1/4}. \quad (33)$$

Equations (12) and (33) yield $t_- = 0$ and $\sigma_- = 1/\pi(2\pi)^{1/2}$ in the limit $\alpha = 0$, for which we have $\lambda_- = 2\pi$ and $\beta_- = 0$ as was noted previously. The steepness of the transverse wave at a point (x,0) on the track of the ship then is given by

$$s_-(x,0) \sim |K(0)|/\pi(2\pi)^{1/2}(-x)^{1/2} \text{ as } x \to -\infty. \quad (34)$$

Equations (12) and (33) also yield $t_+ \sim 1/2\alpha$ and $\sigma_+ \sim 1/16\pi^{3/2}\alpha^{7/2}$ in the limit $\alpha \to 0$, for which we have $\lambda_+ \to 0$ and $\beta_+ \to \pi/2$. We thus have $\sigma_+ \sim t_+^{7/2}/\pi(2\pi)^{1/2}$ as $\alpha \to 0$, and equation (33) shows that the steepness of the divergent wave at a point (x,α) in the vicinity of the track of the ship is given by

$$s_+(x,\alpha) \sim t_+^{7/2}|K(t_+)|/\pi(2\pi)^{1/2}(-x)^{1/2} \text{ as } \alpha \to 0, \text{ with } t_+ \sim 1/2\alpha. \quad (35)$$

The steepness $s_+(x,\alpha)$ then becomes unbounded as $\alpha \to 0$ if

$$t^{7/2}|K(t)| \to \infty \text{ as } t \to \infty. \quad (36)$$

Equations (4), (20b) and (27) show that the asymptotic expansion (23) for the free-surface elevation is valid in the vicinity of the track of the ship if

$$t^{3/2}K(t) \to 0 \text{ as } t \to \infty. \tag{37}$$

Let us assume that we have

$$|K(t)| \sim 1/t^{\mu} \text{ as } t \to \infty. \tag{38}$$

Both conditions (37) and (36) are then satisfied if

$$3/2 < \mu < 7/2. \tag{39}$$

Condition (37) means that the amplitudes of the divergent waves in the Kelvin wake vanish as $\alpha \to 0$, that is as the track of the ship is approached, whereas condition (36) means that the waves become infinitely steep; this is theoretically possible because the wavelengths of the divergent waves vanish as $\alpha \to 0$, as is indicated in equation (31a) and figure 7. However, infinitely-steep water waves cannot exist in reality; indeed, there exists a theoretical upper bound for the steepness of water waves in deep water which is approximately equal to 1/7. Condition (39) therefore suggests that no divergent waves can exist within a certain domain in the vicinity of the track of the ship, and that the Kelvin wake contains three distinct regions: (i) an inner region adjacent to the track of the ship where only transverse waves can exist as was just noted, (ii) an outer region where both transverse and divergent waves are present, and (iii) a region at the boundary between the inner and outer regions where short steep divergent waves, as well as transverse waves, can be found. It must be kept in mind, however, that these conclusions regarding the Kelvin wake are based on condition (39), which was obtained on the basis of an analysis in which surface-tension and nonlinearities are ignored. Inasmuch as this linear no-surface-tension analysis predicts short steep waves, both surface-tension and nonlinear effects are liable to be significant, and these effects should therefore be included in a more realistic analysis. In particular, it is evident from Lamb [9, pp. 468-470] and Wehausen and Laitone [10, pp. 636-637] that the system of divergent waves in the immediate vicinity of the track of the ship may be profoundly affected by surface tension.

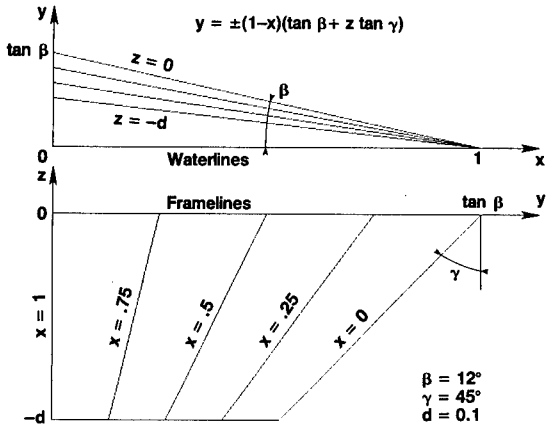


Fig. 8 — Waterlines and Framelines of the Simple Ship Bow Form Considered for Numerical Applications

A SIMPLE TEST CASE: THE FAR-FIELD WAVE-AMPLITUDE FUNCTION

The foregoing theoretical results are investigated numerically for the simple semi-infinite ship form studied previously by Scragg [5]. This ship form consists of a bow region, with length L, followed by a parallel body, with invariant framelines, extending to infinity downstream. All framelines, both in the bow region and downstream from it, are trapezoidal in shape with constant draft D. The waterlines are rectilinear. More precisely, the hull form is defined by the equations

$$y = \pm(\tan\beta + z\tan\gamma)(1-x)$$
$$\text{for } 0 \leqslant x \leqslant 1 \text{ and } 0 \geqslant z \geqslant -d, \tag{40a}$$

$$y = \pm(\tan\beta + z\tan\gamma) \text{ for } x \leqslant 0 \text{ and } 0 \geqslant z \geqslant -d, \tag{40b}$$

where x,y,z and d are nondimensional in terms of the length of the bow region, that is we have $\bar{x} = \bar{X}/L$ and $d = D/L$. Equations (40a,b) require that the condition

$$\tan\beta \geqslant d\tan\gamma \tag{41}$$

be satisfied. Equation (40a) shows that the entrance angle at the bow ($x = 1$, $z = 0$) is equal to 2β, and it may be seen from equations (40a,b) that γ represents the flare angle for $x \leqslant 0$. The four waterlines corresponding to $z = 0, -d/3, -2d/3, -d$ and the five framelines corresponding to $x = 1, 0.75, 0.5, 0.25, 0$ are depicted in figure 8 for $d = 0.1$, $\beta = 12°$ and $\gamma = 45°$. The notation

$\beta_0 = \tan\beta,\ \gamma_0 = \tan\gamma$ (42a,b)

will be used for shortness hereafter.

The far-field wave-amplitude function K(t) for the foregoing semi-infinite hull has been evaluated for two simple approximations defined explicitly in terms of the hull shape and the Froude number, namely the Michell thin-ship approximation and the zeroth-order slender-ship approximation [7], for which the function K(t) is denoted $K_M(t)$ and $K_0(t)$, respectively. The Michell thin-ship approximation is given by the product of two single integrals, as follows:

$$K_M = 2\nu^4 \int_0^1 \exp[-i\nu^2(1+t^2)^{1/2}x]\,dx \cdot \int_{-d}^{0} \exp[\nu^2(1+t^2)z]\,(\beta_0+\gamma_0 z)\,dz.$$

These integrals can be evaluated analytically, with the result

$$K_M(t) = 4[\beta_0-(\beta_0-\gamma_0 d)e-F^2\gamma_0(1-e)/(1+t^2)] \cdot \sin[\nu^2(1+t^2)^{1/2}/2]\,\exp[-i\nu^2(1+t^2)^{1/2}/2]/(1+t^2)^{3/2}, \quad (43)$$

where the term e is defined as

$$e = \exp[-\nu^2 d(1+t^2)]. \quad (44)$$

Equations (43) and (44) yield

$$|K_M(t)| \sim 4\beta_0|\sin(\nu^2 t/2)|/t^3 \text{ as } t \to \infty. \quad (45)$$

The zeroth-order slender-ship approximation may be expressed in the form

$$K_0(t) = K_0^+(t) + K_0^-(t), \quad (46)$$

where $K_0^{\pm}(t)$ is given by the sum of a double integral over the hull surface and a single integral along the top waterline, as follows:

$$K_0^{\pm} = \nu^4 \int_0^1 dx \int_{-d}^{0} dz\,\exp[\nu^2(1+t^2)z] \exp[-i\nu^2(1+t^2)^{1/2}(x\pm yt)](\beta_0+\gamma_0 z) - \nu^2 \int_0^1 dx\,\exp[-i\nu^2(1+t^2)^{1/2}(x\pm yt)]\,\beta_0^3/[1+\beta_0^2+\gamma_0^2(1-x)^2]. \quad (47)$$

The integration in these integrals is carried over the positive half of the hull surface. Equations (40a) and (42a,b) then yield $y = (\beta_0+\gamma_0 z)(1-x)$. We then have

$$x \pm yt = 1-(1\pm\beta_0 t)(1-x)\pm\gamma_0 t(1-x)z.$$

By using this relation into equation (47) we may then obtain

$$\exp[i\nu^2(1+t^2)^{1/2}]K_0^{\pm}(t) = \nu^2 \int_0^1 \exp[i\nu^2(1+t^2)^{1/2}(1\mp\beta_0 t)x] \cdot [\beta_0 I_0^{\pm} - \gamma_0 I_1^{\pm} - \beta_0^3/(1+\beta_0^2+\gamma_0^2 x^2)]\,dx, \quad (48)$$

where $I_n^{\pm}$, with n = 0 and 1, are the integrals defined as

$$(-1)^n I_n^{\pm} = \nu^2 \int_{-d}^{0} \exp[\nu^2(1+t^2)(1\mp i\gamma_0 ux)z]z^n\,dz,$$

with u defined as

$$u = t/(1+t^2)^{1/2}. \quad (49)$$

The integrals $I_n^{\pm}$ may be evaluated analytically with the result

$$I_0^{\pm} = (1-ee_{\pm})/(1+t^2)(1\mp i\gamma_0 ux),$$

$$I_1^{\pm} = [F^2(1-ee_{\pm})/(1+t^2)(1\mp i\gamma_0 ux) - dee_{\pm}]/(1+t^2)(1\mp i\gamma_0 ux),$$

where e is the exponential function given by equation (44) and $e_{\pm}$ is the exponential function defined as

$$e_{\pm} = \exp[\pm i\nu^2 d\gamma_0 t(1+t^2)^{1/2}x]. \quad (50)$$

We then have

$$\beta_0 I_0^{\pm} - \gamma_0 I_1^{\pm} - \beta_0^3/(1+\beta_0^2+\gamma_0^2 x^2) = A_{\pm} - ee_{\pm}B_{\pm}/(1+t^2)(1\mp i\gamma_0 ux), \quad (51)$$

where the terms $A_{\pm}$ and $B_{\pm}$ are given by

$$A_{\pm} = \beta_0/(1+t^2)(1\mp i\gamma_0 ux) - \beta_0^3/(1+\beta_0^2+\gamma_0^2 x^2) - \gamma_0 F^2/(1+t^2)^2(1\mp i\gamma_0 ux)^2,$$

$$B_{\pm} = \beta_0 - \gamma_0 d - \gamma_0 F^2/(1+t^2)(1\mp i\gamma_0 ux).$$

It may be verified that we have

$$A_{\pm} = \beta_0[(1-\beta_0^2 t^2)/(1+t^2) + x^2\beta_0^2\gamma_0^2/(1+\beta_0^2+\gamma_0^2)]/(1+\beta_0^2) + \gamma_0 C_{\pm}, \quad (52a)$$

$$B_{\pm}/(1+t^2)(1\mp i\gamma_0 ux) = \beta_0/(1+t^2) - \gamma_0 D_{\pm}, \quad (52b)$$

where the terms $C_{\pm}$ and $D_{\pm}$ are given by

$$C_{\pm} = [\beta_0^3\gamma_0^3/(1+\beta_0^2)(1+\beta_0^2+\gamma_0^2)]x^2(1-x^2)/(1+\beta_0^2+\gamma_0^2x^2) - [\beta_0\gamma_0 t^2x^2 + F^2(1+t^2-\gamma_0^2t^2x^2)/(1+t^2+\gamma_0^2t^2x^2) \mp it(1+t^2)^{1/2}\{\beta_0 - 2F^2\gamma_0/(1+t^2+\gamma_0^2t^2x^2)\}x]/(1+t^2)(1+t^2+\gamma_0^2t^2x^2), \quad (53a)$$

$$(1+t^2)(1+t^2+\gamma_0^2t^2x^2)D_{\pm} = \beta_0\gamma_0 t^2x^2 + d(1+t^2) + F^2(1+t^2-\gamma_0^2t^2x^2)/(1+t^2+\gamma_0^2t^2x^2) \mp it(1+t^2)^{1/2}[\beta_0 - \gamma_0 d - 2F^2\gamma_0/(1+t^2+\gamma_0^2t^2x^2)]x. \quad (53b)$$

Equation (50) yields

$$\exp[i\nu^2(1+t^2)^{1/2}(1\mp\beta_0 t)x]e_{\pm} = \exp[i\nu^2(1+t^2)^{1/2}(1\mp\beta_d t)x], \quad (55)$$

where β_d is defined as

$$\beta_d = \beta_0 - d\gamma_0 = \tan\beta - d\tan\gamma, \quad (56)$$

as may be obtained from equations (42a,b). By using equations (55), (51), (52a,b) and (44) into equation (48) we may obtain

$$\exp[i\nu^2(1+t^2)^{1/2}]K_0^{\pm}(t) = \beta_0[(1-\beta_0^2t^2)(1+t^2)^{-1}I_0^{\pm}(t;\beta_0) + \beta_0^2\gamma_0^2(1+\beta_0^2+\gamma_0^2)^{-1}I_1^{\pm}(t;\beta_0) - (1+\beta_0^2)\exp\{-\nu^2 d(1+t^2)\}(1+t^2)^{-1}I_0^{\pm}(t;\beta_d)]/(1+\beta_0^2) + \gamma_0[J_{\pm}(t;\beta_0,C_{\pm}) + \exp\{-\nu^2 d(1+t^2)\}J_{\pm}(t;\beta_d,D_{\pm})], \quad (57)$$

where the functions $I_n^{\pm}(t;\beta)$ and $J_{\pm}(t;\beta,A)$, or more

precisely $I_n^{\pm}(t;\beta,\nu)$ and $J_{\pm}(t;\beta,A,\nu)$, are defined in terms of the integrals

$$I_n^{\pm}(t;\beta) = \nu^2 \int_0^1 \exp[i\nu^2(1+t^2)^{1/2}(1\mp\beta t)x]x^{2n}\,dx, \quad (58a)$$

$$J_{\pm}(t;\beta,A) = \nu^2 \int_0^1 \exp[i\nu^2(1+t^2)^{1/2}(1\mp\beta t)x]A(x)\,dx. \quad (58b)$$

The integrals $I_n^{\pm}(t;\beta)$ can be evaluated analytically, with the result

$$I_0^{\pm}(t;\beta) = i(1-E_{\pm})/\sigma_{\pm}, \quad (59a)$$

$$I_1^{\pm}(t;\beta) = -i[(1+2iF^2/\sigma_{\pm})E_{\pm}+2F^4(1-E_{\pm})/\sigma_{\pm}^2]/\sigma_{\pm}, \quad (59b)$$

where $\sigma_{\pm}$ and $E_{\pm}$ are defined as

$$\sigma_{\pm} = (1+t^2)^{1/2}(1\mp\beta t), \quad E_{\pm} = \exp(i\nu^2\sigma_{\pm}). \quad (59c,d)$$

Expressions (59a,b) for $I_0^{+}(t;\beta)$ and $I_1^{+}(t;\beta)$ are not valid in the special case when we have $t = 1/\beta$, for which expressions (59a,b) become

$$I_0^{+}(1/\beta;\beta) = \nu^2, \quad I_1^{+}(1/\beta;\beta) = \nu^2/3. \quad (59e,f)$$

The integrals $J_{\pm}$ defined by equation (58b), where the amplitude function A(x) takes the form of $C_{\pm}$ or $D_{\pm}$ specified in equations (53a,b), cannot be evaluated analytically. These integrals were then evaluated numerically by dividing the integration range $0 \leqslant x \leqslant 1$ into N segments of equal length and using piecewise quadratic approximations for the amplitude function A(x) within each segment. In this manner, we may obtain

$$\sigma_{\pm}J_{\pm}(t;\beta,A) \simeq \sum_{j=1}^{N}(\varepsilon_{\pm})^{j-1}[i(A_j-\varepsilon_{\pm}A_{j+1})$$
$$+(NF^2/\sigma_{\pm})(\varepsilon_{\pm}-1)(A_{j+1}-A_j)+(2NF^2/\sigma_{\pm})$$
$$\{1+\varepsilon_{\pm}+i(2NF^2/\sigma_{\pm})(\varepsilon_{\pm}-1)\}(A_j+A_{j+1}-2A_{j+1/2})], \quad (60)$$

where $\sigma_{\pm}$ is given by equation (59c), $\varepsilon_{\pm}$ is defined as

$$\varepsilon_{\pm} = \exp(i\nu^2\sigma_{\pm}/N), \quad (60a)$$

and A_j, A_{j+1}, $A_{j+1/2}$ represent the values of the amplitude function A(x) at the points $x_j = (j-1)/N$, $x_{j+1} = j/N$, and $x_{j+1/2} = (j-1/2)/N$, respectively. Expression (60) for $J_{+}(t;\beta,A)$ is not valid in the special case when $t = 1/\beta$, for which we have

$$6NJ_{+}(1/\beta;\beta,A) \simeq \sum_{j=1}^{N} A_j + A_{j+1} + 4A_{j+1/2}. \quad (60b)$$

In summary, the zeroth-order slender-ship approximation $K_0(t)$ is determined by equations (46), (57), (59a-f), (60), (60a,b), (42a,b) and (56). In the limiting case $\gamma_0 = 0$, these equations yield

$$K_0(t) = 4\beta_0(1+t^2)^{-3/2}[(1-\beta_0^2t^2)(1+\beta_0^2)^{-1}$$
$$-\exp\{-\nu^2d(1+t^2)\}](R-iI)/(1-\beta_0^2t^2), \quad (61)$$

where the terms R and I are given by

$$R = \sin[\nu^2(1+t^2)^{1/2}/2]\cos[\nu^2(1+t^2)^{1/2}/2]$$
$$-\beta_0 t\sin[\nu^2\beta_0 t(1+t^2)^{1/2}/2]\cos[\nu^2\beta_0 t(1+t^2)^{1/2}/2], \quad (61a)$$

$$I = \sin^2[\nu^2(1+t^2)^{1/2}/2]-\sin^2[\nu^2\beta_0 t(1+t^2)^{1/2}/2]. \quad (61b)$$

In the thin-ship limit $\beta_0 \to 0$, equations (61) and (61a,b) yield

$$K_0(t) \sim 4\beta_0(1+t^2)^{-3/2}[1-\exp\{-\nu^2d(1+t^2)\}].$$
$$\sin[\nu^2(1+t^2)^{1/2}/2]\exp[-i\nu^2(1+t^2)^{1/2}/2] \text{ as } \beta_0 \to 0. \quad (62)$$

The thin-ship limit (62) of the zeroth-order slender-ship approximation $K_0(t)$ may be seen to be identical to the Michell thin-ship approximation (43) in the particular case $\gamma_0 = 0$. However, the thin-ship limit (62) of the slender-ship approximation (61) is not uniformly valid in the limit $t \to \infty$; indeed, equations (61) and (61a,b) yield equation (62) in the limit $\beta_0 t \to 0$. Equation (62) yields

$$|K_0(t)| \sim 4\beta_0|\sin(\nu^2t/2)|/t^3 \text{ for } 1 \ll t \ll 1/\beta_0. \quad (63)$$

More generally, equation (61) yields

$$|K_0(t)| \sim 4\beta_0|R-iI|/(1+\beta_0^2)t^3 \text{ as } t \to \infty. \quad (64)$$

Equations (61a,b) show that $|R-iI| \sim \beta_0 t|\sin(\nu^2\beta_0t^2)|/2$ if $\beta_0 t \gg 1$. We then have

$$|K_0(t)| \sim 2\beta_0^2|\sin(\nu^2\beta_0t^2)|/(1+\beta_0^2)t^2 \text{ for } t \gg 1/\beta_0. \quad (65)$$

In the limit $t\to\infty$, equations (57) and (59a-d) yield

$$\exp(i\nu^2t)K_0^{\pm}(t) \sim \beta_0[(1-\beta_0^2t^2)I_0^{\pm}(t;\beta_0)$$
$$+\gamma_0^2(1+\beta_0^2+\gamma_0^2)^{-1}\beta_0^2t^2I_1^{\pm}(t;\beta_0)]/(1+\beta_0^2)t^2 \text{ as } t \to \infty,$$

where we have

$$I_0^{\pm}(t;\beta_0) \sim i[1-\exp\{i\nu^2t(1\mp\beta_0t)\}]/(1\mp\beta_0t)t \text{ as } t \to \infty,$$
$$I_1^{\pm}(t;\beta_0) \sim -i\exp\{i\nu^2t(1\mp\beta_0t)\}/(1\mp\beta_0t)t \text{ as } t \to \infty.$$

We then have

$$|K_0(t)| \sim 2\beta_0|N|/(1+\beta_0^2)|1-\beta_0^2t^2|t^3 \text{ as } t \to \infty, \quad (66)$$

where the term N is given by

$$N = (1-\beta_0^2t^2)[\sin(\nu^2t)+i\cos(\nu^2t)]$$
$$-(1-\sigma^2\beta_0^2t^2)[\beta_0t\sin(\nu^2\beta_0t^2)+i\cos(\nu^2\beta_0t^2)], \quad (66a)$$

with σ^2 defined as

$$\sigma^2 = (1+\beta_0^2)/(1+\beta_0^2+\gamma_0^2). \quad (66b)$$

We may then obtain

$$|K_0(t)| \sim 4\beta_0|\sin(\nu^2t/2)|/(1+\beta_0^2)t^3 \text{ for}$$
$$1 \ll t \ll F/(\beta_0)^{1/2}, \quad (67a)$$

$$|K_0(t)| \sim 2\beta_0^2|\sin(\nu^2\beta_0t^2)|/(1+\beta_0^2+\gamma_0^2)t^2 \text{ for } t \gg 1/\beta_0. \quad (67b)$$

Equations (67a,b) are identical to equations (63) and (65) in the limits $\beta_0 \to 0$ and $\gamma_0 \to 0$, respectively. More generally, equation (66a) yields the following upper bound for the term |N| in equation (66)

$$|N|^2 \leqslant (1-\beta_0^2t^2)^2+(1+\beta_0^2t^2)(1-\sigma^2\beta_0^2t^2)^2$$
$$+2(1+\beta_0t)^2(1+\sigma\beta_0t)|(1-\beta_0t)(1-\sigma\beta_0t)|. \quad (68)$$

Equations (67a,b) thus show that in the limit $t \to \infty$ we have $|K_0(t)| \sim 1/t^3$ for $1 \ll t \ll F/(\beta_0)^{1/2}$, that is for moderately large values of t, and $|K_0(t)| \sim 1/t^2$ for $1/\beta_0 \ll t$, that is for very large values of t. The asymptotic approximations (67a,b) and (45) show that the Michell approximation $K_M(t)$ corresponds to the thin-ship limit $\beta_0 \ll 1$ of the zeroth-order slender-ship approximation $K_0(t)$,

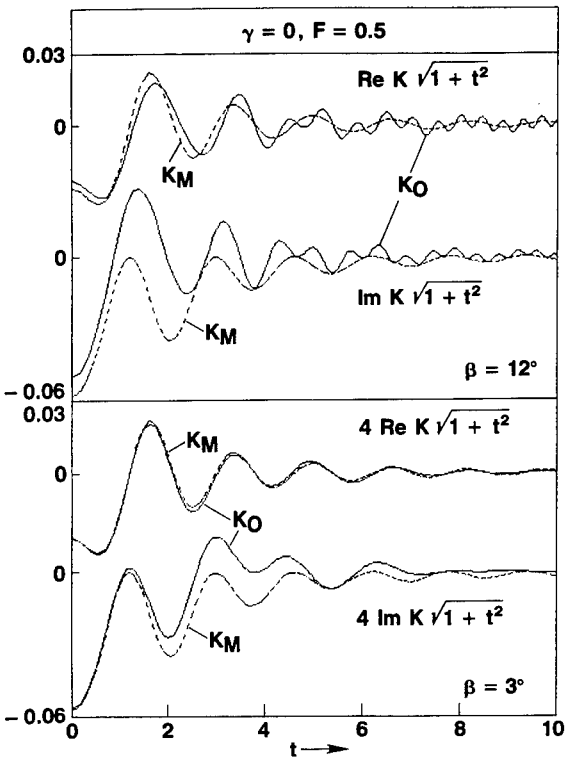


Fig. 9a — Real and Imaginary Parts of the Functions $K_M(t)$ and $K_0(t)$ for a Simple Ship Bow Form with β = 12° (Top) and 3° (Bottom), γ = 0 and F = 0.5

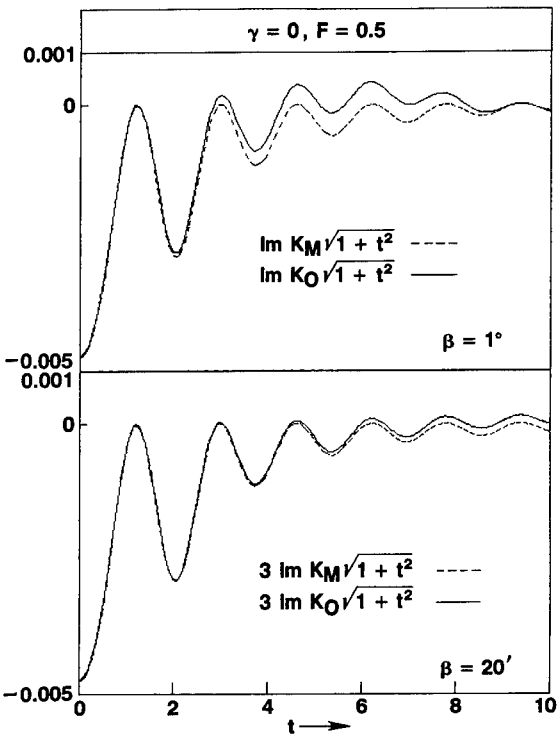


Fig. 9b — Real and Imaginary Parts of the Functions $K_M(t)$ and $K_0(t)$ for a Simple Ship Bow Form with β = 1° (Top) and 20′ (Bottom), γ = 0 and F = 0.5

and that this thin-ship limit is not uniformly valid in the limit $t \to \infty$. More generally, the limiting processes $\beta_0 \to 0$ and $t \to \infty$ cannot be interchanged.

Figures 9a,b depict the real and/or imaginary parts of the functions $(1+t^2)^{1/2}K_M(t)$ and $(1+t^2)^{1/2}K_0(t)$ for the simple bow shape defined by equations (40a,b), where the nondimensional draft d and the maximum flare angle γ are taken equal to d = 0.1 and γ = 0, and four values of the half-entrance-angle β are considered, namely β = 12°, 3°, 1° and 20′. The Froude number based on the length of the bow region is taken equal to F = 0.5 in the numerical results presented in figures 9a,b and in figures 10 and 11 considered further on. The values of $1/\beta_0 = 1/\tan\beta$ corresponding to the values of β equal to 12°, 3°, 1° and 20′ are approximately equal to 4.7, 19, 57 and 172, respectively. The functions $(1+t^2)^{1/2}K_M(t)$ and $(1+t^2)^{1/2}K_0(t)$ are depicted for $0 \leq t \leq 10$ in figures 9a,b. Differences between the approximations K_M and K_0, especially their imaginary parts, can be seen to be substantial in figure 9a corresponding to $\beta = 12°$ and 3°. Figure 9b shows that differences between the imaginary parts of the functions K_M and K_0 remain appreciable even for values of β equal to 1° and 20′, which are quite small, and for values of t that are much smaller than $1/\beta_0$.

The top and bottom parts of figure 10 depict the real and imaginary parts of the functions $(1+t^2)^{1/2}K_M(t)$ and $(1+t^2)^{1/2}K_0(t)$, respectively, for the previously-considered simple bow shape with d = 0.1, β = 12°, F = 0.5 and for two values of the flare angle, namely for γ = 0 and 45°. The top part of the figure shows that differences between the curves corresponding to γ = 0 and γ = 45° are faily small, and are appreciable only for small values of t, for the Michell thin-ship approximation K_M. In particular, the asymptotic approximation $K_M(t) \sim 4\beta_0 \sin(\nu^2 t/2) \exp(-i\nu^2 t/2)/t^3$ as $t \to \infty$, which may be obtained from equations (43) and (44), is independent of γ. The bottom part of figure 10 shows differences between the curves corresponding to γ = 0 and γ = 45° for the slender-ship approximation K_0 that are significantly larger than those for the Michell approximation K_M, especially for intermediate values of t in the vicinity of $t = 1/\tan\beta \simeq 4.7$. The flare angle γ thus has a pronounced effect upon the behavior of the

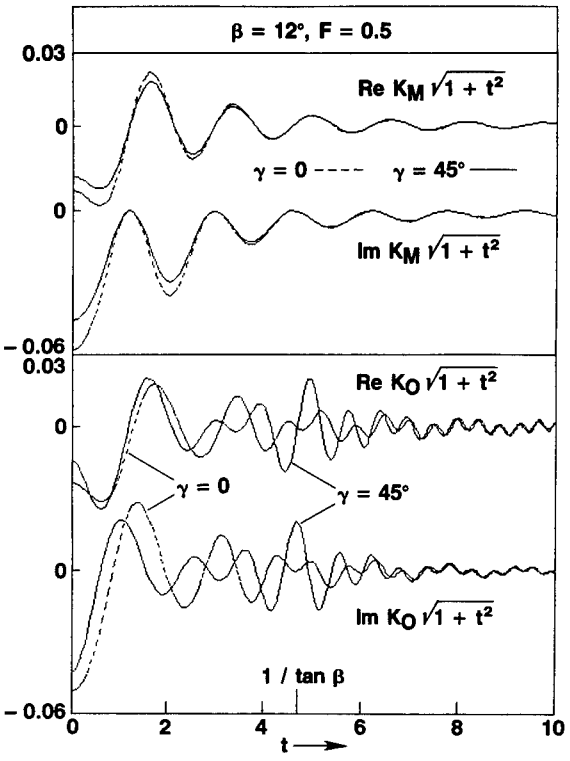


Fig. 10 — Real and Imaginary Parts of the Functions $K_M(t)$ and $K_0(t)$ for a Simple Ship Bow Form with γ = 0 and 45°, β = 12° and F = 0.5

slender-ship approximation $K_0(t)$ for values of t in the neighborhood of $1/\tan\beta$. The influence of γ upon $|K_0(t)|$ for large values of t is explicitly indicated by the asymptotic approximations (67a,b).

Finally, figure 11 depicts the real and imaginary parts of the functions $(1+t^2)^{1/2}K_M(t)$ and $(1+t^2)^{1/2}K_0(t)$ for the simple bow shape depicted in figure 8, for which we have d = 0.1, β = 12° and γ = 45°, at a value of the Froude number F equal to 0.5. Differences between the approximations K_M and K_0 may be seen to be quite substantial. In particular, the function $(1+t^2)^{1/2}K_0(t)$ has a peak at $t = 1/\tan\beta = 1/\beta_0$.

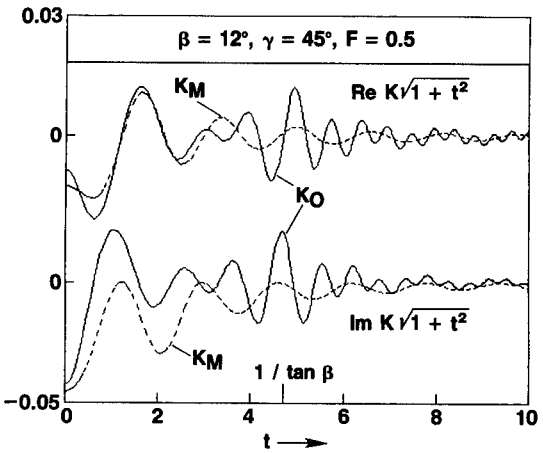


Fig. 11 — Real (Top) and Imaginary (Bottom) Parts of the Functions $K_M(t)$ and $K_0(t)$ for a Simple Ship Bow Form with β = 12°, γ = 45° and F = 0.5

A SIMPLE TEST CASE: THE FAR-FIELD KELVIN WAKE

The expressions for the far-field wave-amplitude function K(t) obtained in the foregoing section for a simple bow shape and for two simple approximations to the function K(t), namely the Michell thin-ship approximation K_M and the zeroth-order slender-ship approximation K_0, may now be used into the previously determined asymptotic approximations for the far-field Kelvin wake.

Far behind the ship, that is for $x \to -\infty$, the functions $\phi_k(x,\alpha)$, where $0 \leq k \leq 4$, defined by equations (17), (18), (19) and (20a-e) are given by the asymptotic approximation (23). The real and imaginary parts of the amplitude functions $A_k^-(\alpha)$ and $A_k^+(\alpha)$ in this asymptotic approximation, given by equation (24a), are depicted in figures 12a and b, 13a and b and 14 for $0 \leq \alpha \leq 1/2^{3/2}$. More precisely, figures 12a,b and 13a,b represent the amplitude functions A_k^- and A_k^+ for k = 0,1,2,3 associated with the potential ϕ and its derivatives ϕ_x, ϕ_y and ϕ_{xx}, and correspond to the approximations K_M and

K_0, respectively. Figure 14 depicts the amplitude functions A_4^- and A_4^+ corresponding to ϕ_{xy} for the approximations K_M and K_0.

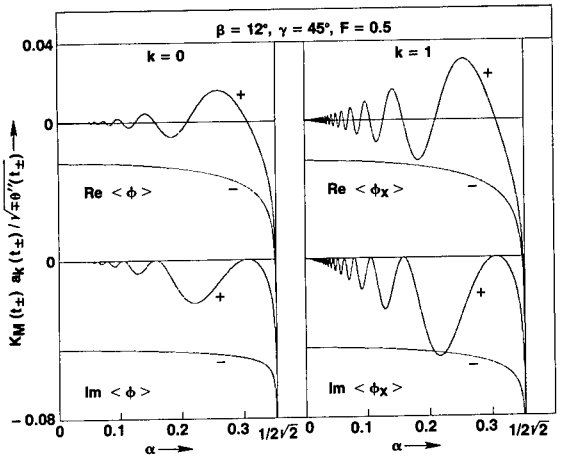


Fig. 12a — Real (Top) and Imaginary (Bottom) Parts of the Functions $K_\pm a_k^\pm/(\mp\Theta''_\pm)^{1/2}$ for k = 0 (Left) and 1 (Right), K = K_M (Michell Thin-Ship Approximation) and a Simple Ship Bow Form with β = 12°, γ = 45° and F = 0.5

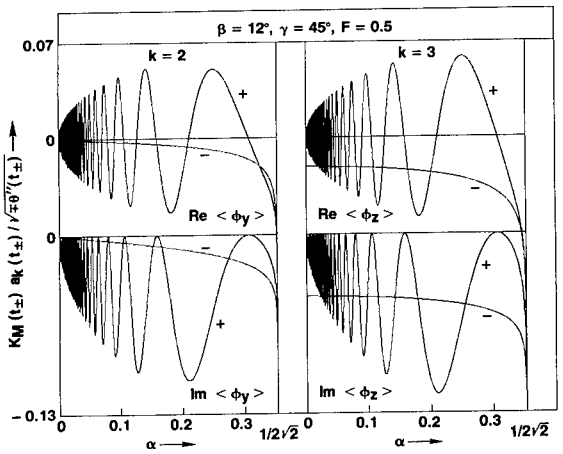


Fig. 12b — Real (Top) and Imaginary (Bottom) Parts of the Functions $K_\pm a_k^\pm/(\mp\Theta''_\pm)^{1/2}$ for k = 2 (Left) and 3 (Right), K = K_M (Michell Thin-Ship Approximation) and a Simple Ship Bow Form with β = 12°, γ = 45° and F = 0.5

It may be seen from figures 12a and b, 13a and b and 14 that the amplitude functions $A_k^-(\alpha)$ and $A_k^+(\alpha)$ become unbounded in the limit $\alpha \to 1/2^{3/2}$. This singularity at $\alpha = 1/2^{3/2}$ stems from the fact that the asymptotic approximation (23) is not uniformly valid in the limit $\alpha \to 1/2^{3/2}$, as was already noted. The amplitude functions $A_k^+(\alpha)$ corresponding to the system of divergent waves in the Kelvin wake also become unbounded in the limit $\alpha \to 0$ in figures 13b and 14 corresponding to k = 2

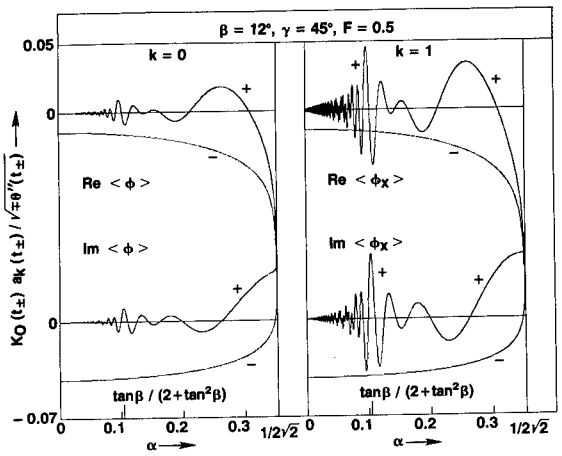


Fig. 13a — Real (Top) and Imaginary (Bottom) Parts of the Functions $K_\pm a_k^\pm/(\mp\Theta''_\pm)^{1/2}$ for k = 0 (Left) and 1 (Right), K = K_0 (Zeroth-Order Slender-Ship Approximation) and a Simple Ship Bow Form with β = 12°, γ = 45° and F = 0.5

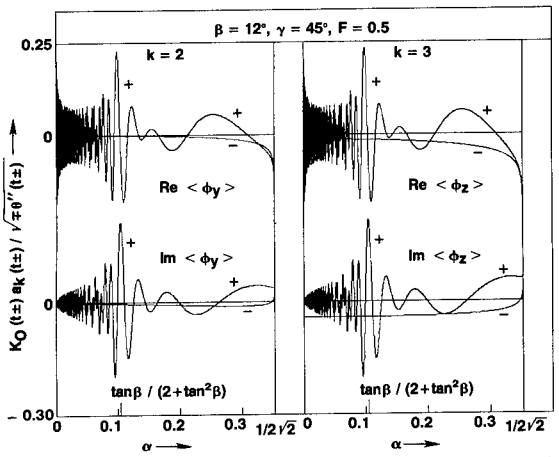


Fig. 13b — Real (Top) and Imaginary (Bottom) Parts of the Functions $K_\pm a_k^\pm/(\mp\Theta''_\pm)^{1/2}$ for k = 2 (Left) and 3 (Right), K = K_0 (Zeroth-Order Slender-Ship Approximation) and a Simple Ship Bow Form with β = 12°, γ = 45° and F = 0.5

and 3 for the slender-ship approximation K_0 and to k = 4 for both approximations K_M and K_0, respectively. This singularity at α = 0 illustrates the previously-noted conclusion that the asymptotic approximation (23) is not uniformly valid in the vicinity of the track of the ship α = 0 if condition (27) is not satisfied. Equations (20a-e) show that we have $a_0 \sim 1$, $a_1 \sim t$, $a_2 \sim t^2$, $a_3 \sim t^2$ and $a_4 \sim t^3$ as $t \to \infty$, and equations (45) and (67b) yield $|K_M| \sim 1/t^3$ and $|K_0| \sim 1/t^2$ as $t \to \infty$, respectively. Condition (27) therefore is not satisfied for $k \geq 4$ and $k \geq 2$ for the approximations K_M and K_0, respectively. Condition (27) however is satisfied for k = 0 and 1,

corresponding to the potential ϕ and the free-surface elevation ϕ_x, for both the approximations K_M and K_0.

Figures 12a and 13a show that the amplitude functions A_0^- and A_1^-, corresponding to the transverse waves in the Kelvin wake, generally are larger in magnitude than the amplitude functions A_0^+ and A_1^+ corresponding to the divergent waves, whereas the reverse may generally be seen to hold in figures 12b and 13b for the amplitude functions $A_2^\pm$ and $A_3^\pm$. The relative importance of the divergent waves with respect to the transverse waves thus increases with k. Indeed, the transverse-wave amplitude function $A_4^-(\alpha)$ is hardly visible on the scale of the divergent-wave-amplitude function $A_4^+(\alpha)$ used in figure 14.

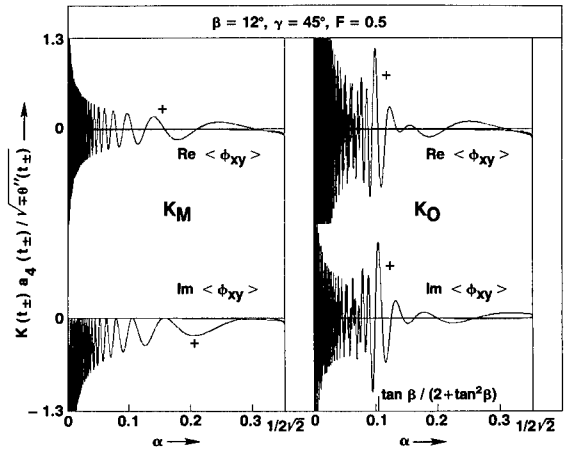


Fig. 14 — Real (Top) and Imaginary (Bottom) Parts of the Functions $K_\pm a_4^\pm/(\mp\Theta''_\pm)^{1/2}$ for K_M (Left) and K_O (Right) and a Simple Ship Bow Form with $\beta = 12°$, $\gamma = 45°$ and F = 0.5

The divergent-wave-amplitude functions $A_k^+(\alpha)$ associated with the approximation K_0 are most notably different from the corresponding functions $A_k^+(\alpha)$ associated with the Michell approximation K_M for values of α in the vicinity of $\alpha = 0$, as was already noted, and of $\alpha = \tan\beta/(2+\tan^2\beta)$. In the vicinity of this value of α, the divergent-wave-amplitude functions $A_k^+(\alpha)$ associated with the approximation K_0 exhibit a peak, which is quite pronounced for $k \geq 1$. The foregoing particular value of α corresponds to the special case when the point of stationary phase t_+, defined by equation (12), is equal to the value $1/\beta_0 = 1/\tan\beta$ for which the function $K_0(t)$ displays a peak, as may be seen from figures 10 and 11.

Figure 15 depicts the amplitude functions $(2/\pi)^{1/2}A_1^-$ and $(2/\pi)^{1/2}A_1^+$ that are associated with the free-surface elevation far behind the ship, as is specifically

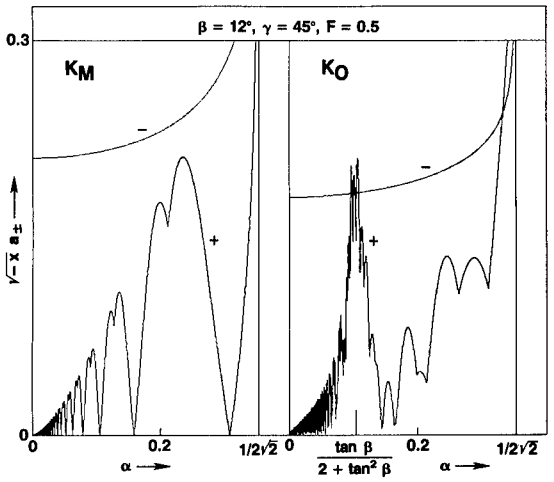


Fig. 15 — Amplitude of the Transverse (−) and Divergent (+) Waves in the Kelvin Wake for a Simple Ship Bow Form, with $\beta = 12°$, $\gamma = 45°$ and F = 0.5, in the Michell Thin-Ship Approximation (Left) and the Zeroth-Order Slender-Ship Approximation (Right)

indicated in equation (28), for the previously-considered ship bow shape. It may be seen that the amplitude $a_+(\alpha)$ of the divergent waves in the Kelvin wake vanishes as $\alpha \to 0$, that is at the track of the ship, and is generally smaller than the amplitude $a_-(\alpha)$ of the transverse waves; this is especially true in the vicinity of the track of the ship. Differences between the wave-amplitude functions $a_\pm(\alpha)$ corresponding to the approximations $K_M(t)$ and $K_0(t)$ are particularly striking for the amplitude $a_+(\alpha)$ of the divergent waves in the vicinity of $\alpha = \tan\beta/(2+\tan^2\beta)$, where the function $a_+(\alpha)$ associated with the approximation $K_0(t)$ exhibits a sharp peak.

Figure 16 depicts the wave-steepness functions $s_-(\alpha)$ and $s_+(\alpha)$, which correspond to the ratios of the wave-amplitude functions $a_-(\alpha)$ and $a_+(\alpha)$ depicted in figure 15 over the wavelength functions $\lambda_-(\alpha)$ and $\lambda_+(\alpha)$ defined by equation (30a); the steepness functions $s_\pm(\alpha)$ are specifically defined by equations (32) and (33). The divergent waves in the Kelvin wake may be seen to be generally steeper than the transverse waves, even though figure 15 shows the transverse waves to be larger in amplitude than the divergent waves. This is especially true near the track of the ship where the steepness of the divergent waves becomes infinitely large, even though figure 15 shows that their amplitude vanishes as $\alpha \to 0$. The divergent waves become infinitely steep at the track of the ship because the wavelength $\lambda_+(\alpha) \to 0$ as $\alpha \to 0$ and condition (36) is satisfied, for both the approximations $K_M(t)$ and $K_0(t)$ as may be seen from

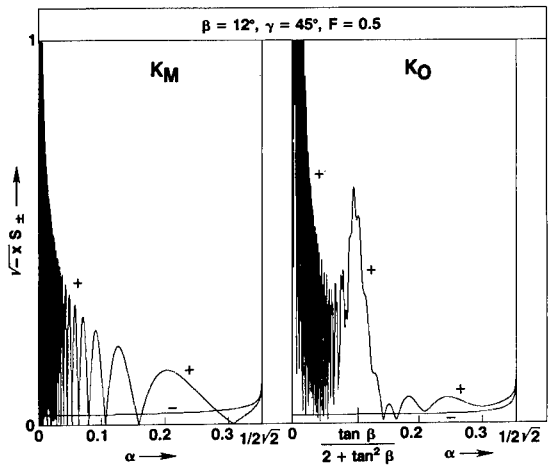


Fig. 16 — Steepness of the Transverse (−) and Divergent (+) Waves in the Kelvin Wake for a Simple Ship Bow Form, with $\beta = 12°$, $\gamma = 45°$ and F = 0.5, in the Michell Thin-Ship Approximation (Left) and the Zeroth-Order Slender-Ship Approximation (Right)

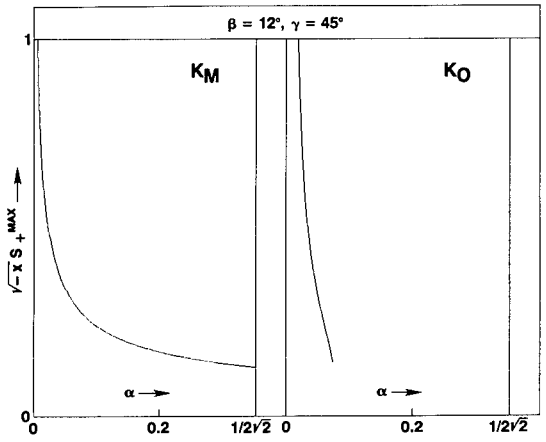


Fig. 17 — Upper Bound for the Steepness of the Divergent Waves in the Kelvin Wake for a Simple Ship Bow Form, with $\beta = 12°$ and $\gamma = 45°$, in the Michell Thin-Ship Approximation (Left) and the Zeroth-Order Slender-Ship Approximation (Right)

equations (45) and (67b). Figure 16 also shows a sharp peak in the steepness of the divergent waves at the value of α equal to $\tan\beta/(2+\tan^2\beta)$.

The steepness $s_+(\alpha)$ of the divergent waves is given by equations (32) and (33). An upper bound for the functions $s_+(\alpha)$ may be obtained by using an upper bound for the function $|K(t_+)|$ in equation (32). Equation (45) yields the following upper bound for the function $|K_M(t)|$ corresponding to the Michell thin-ship approximation: $|K_M(t)| \leqslant 4\beta_0/t^3$ as $t \to \infty$. An upper bound for the function $|K_0(t)|$ is given by equation (66), where the upper bound defined by equation (68) is used for the term |N|. These upper bounds for the functions $|K_M(t)|$ and $|K_0(t)|$ can be expressed in terms of α by using equation (12). The corresponding upper bounds for the steepness function $s_+(\alpha)$ are depicted in figure 17. Comparison of figures 16 and 17 shows that the upper bound for the steepness of the divergent waves in the Kelvin wake depicted in figure 17 is satisfactory for all values of α for the Michell approximation K_M, whereas that corresponding to the slender-ship approximation K_0 is satisfactory for values of α smaller than approximately half the value $\tan\beta/(2+\tan^2\beta)$. In both cases, the upper bounds for the function $s_+(\alpha)$ depicted in figure 17 are satisfactory for the range of small values of α for which the steepness $s_+(\alpha)$ is large. It is noteworthy that these upper bounds for the steepness of the divergent waves are valid for all Froude numbers, since equations (12), (32) and (33), and the upper bounds for $|K_M(t)|$ and $|K_0(t)|$ do not involve the Froude number.

Figure 18 depicts the steepness function $s_+(\alpha)$ of the divergent waves corresponding to the slender-ship approximation $K_0(t)$ for the simple bow shape considered previously in the two cases when the maximum flare angle γ is taken equal to 0 and 45° (at the top and bottom halves of the figure, respectively) and for two values of the Froude number, namely for F = 0.8 and 0.3 (on the right and left halves of the figure, respectively). Comparison of the right and left halves of figure 18 shows no appreciable difference between the values of the steepness function $s_+(\alpha)$ for the range of small values of α for which the steepness is large, in agreement with the previously-noted result that the upper bound for $s_+(\alpha)$ depicted on the right side of figure 17 is independent of the Froude

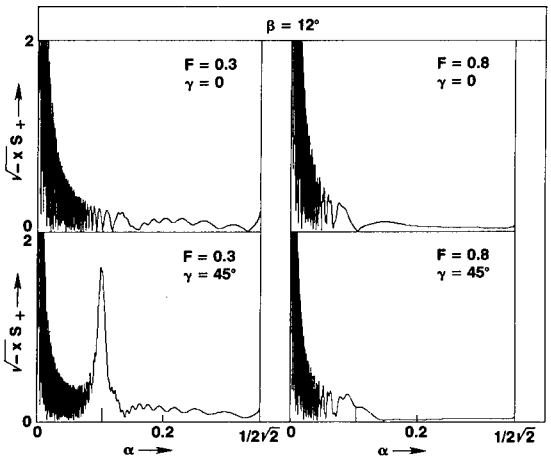


Fig. 18 — Steepness of the Divergent Waves in the Kelvin Wake for a Simple Ship Bow Form with $\beta = 12°$, $\gamma = 0$ (Top) and 45° (Bottom), and F = 0.3 (Left) and 0.8 (Right) in the Zeroth-Order Slender-Ship Approximation

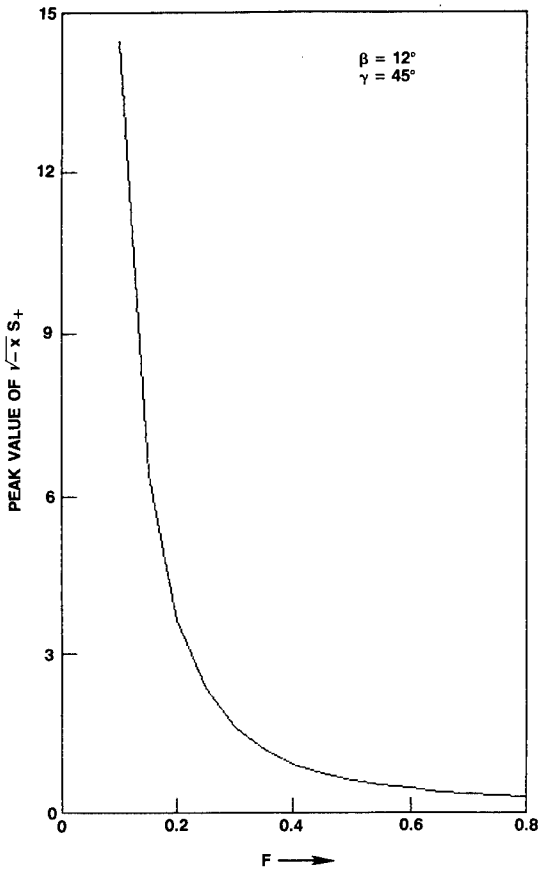


Fig. 19 — Amplitude of the Peak Value of the Steepness of the Divergent Waves in the Kelvin Wake for a Simple Ship Bow Form with $\beta = 12°$ and $\gamma = 45°$ in the Zeroth-Order Slender-Ship Approximation

number. Comparison of the top and bottom halves of figure 18, corresponding to $\gamma = 0$ and 45° as was already noted, shows appreciable differences, especially for F = 0.3 for which the function $s_+(\alpha)$ exhibits a very pronounced peak in the case $\gamma = 45°$. No such peak is apparent in the top half of the figure for $\gamma = 0$, that is in the case when the hull intersects the free surface orthogonally.

The right half of figure 16 and the bottom half of figure 18 show that the magnitude of the peak in the steepness function $s_+(\alpha)$ for $\alpha = \tan\beta/(2+\tan^2\beta)$ strongly depends on the value of the Froude number. Specifically, the peak is very pronounced in figure 18 for F = 0.3, fairly pronounced in figure 16 for F = 0.5, and almost nonapparent in figure 18 for F = 0.8. The magnitude of the peak in the steepness function, that is the value of the function $s_+(\alpha)$ for $\alpha = \tan\beta/(2+\tan^2\beta)$, is represented in figure 19 as a function of the Froude number, which is based on the length of the bow region. This figure shows that the magnitude of the peak increases very rapidly as the Froude number decreases below a certain threshold value in the vicinity of F = 0.3.

Figure 20 depicts the boundary of the Kelvin wake, which corresponds to $\alpha = -y/x = 1/2^{3/2}$ (that is, an angle equal to approximately 19°28′), the line $\alpha = \tan\beta/(2+\tan^2\beta) \simeq \beta/2$ (that is, an angle equal to approximately 6°) along which the steepness of the divergent waves has a peak, and the lines along which the steepness of the divergent waves is equal to 1/20, 1/15, and 1/7 (shown as a chain line close to the track of the ship). The latter three lines were determined by using the upper bound for the steepness function $s_+(\alpha)$ that was determined previously and depicted on the right half of figure 17. The four lines inside the Kelvin wake shown in figure 20 correspond to the zeroth-order slender-ship approximation $K_0(t)$ for the simple bow shape considered previously, with $\beta = 12°$, $\gamma = 45°$ and d = 0.1. The three lines along which the divergent waves are steep lie much closer to the track of the ship than the lines $\alpha \simeq 6°$ along which the steepness of the divergent waves exhibits a peak.

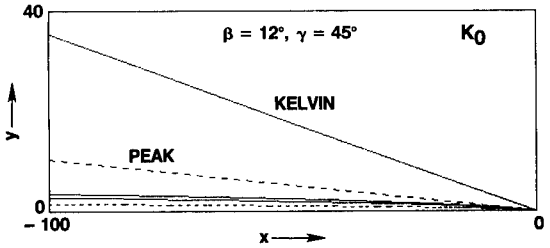


Fig. 20 — The Kelvin Cusp Line, the Line Along Which the Amplitude of the Divergent Waves Exhibits a Peak, and the Three Lines Along Which the Steepness of the Divergent Waves is Equal to 1/20, 1/15 and 1/7 (Chain Line Close to the Track of the Ship) for a Simple Ship Bow Form, with $\beta = 12°$ and $\gamma = 45°$, in the Zeroth-Order Slender-Ship Approximation

The three lines along which the steepness of the divergent waves is equal to 1/20, 1/15 and 1/7, which are depicted in figure 20 for $0 \geq x \geq -100$ and $0 \leq y \leq 40$, are represented again in figure 21 at a distorted scale where $0 \geq x \geq -300$ and $0 \leq y \leq 7$. The corresponding constant-steepness lines predicted by the Michell thin-ship approximation are also shown in figure 21 for comparison. The latter lines were determined from equations (32) and (33) and the upper bound $|K_M(t)| \leq 4\beta_0/t^3$ given by equation (45). Figure 21 shows significant differences between the constant-steepness lines predicted

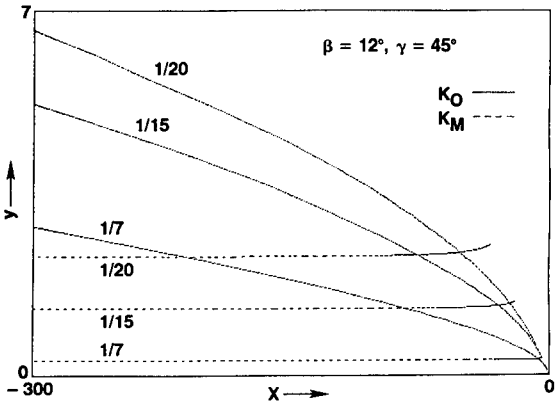


Fig. 21 — Lines Along Which the Steepness of the Divergent Waves is Equal to 1/20, 1/15 and 1/7 for a Simple Ship Bow Form, with $\beta = 12°$ and $\gamma = 45°$, in the Michell Thin-Ship Approximation (— — —) and the Zeroth-Order Slender-Ship Approximation (———)

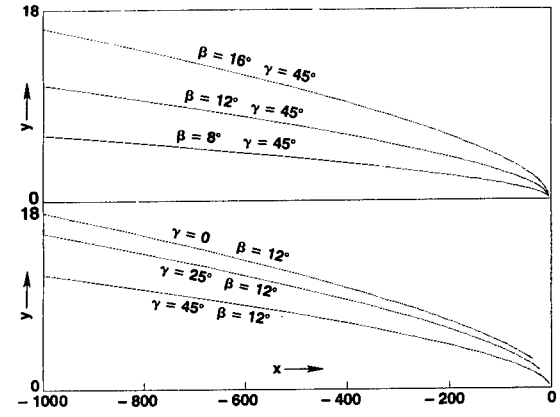


Fig. 22 — Lines Along Which the Steepness of the Divergent Waves is Equal to 1/15 for a Simple Ship Bow Form with $\beta = 8°$, 12°, 16° and $\gamma = 45°$ (Top) and $\gamma = 0$, 25°, 45° and $\beta = 12°$ (Bottom) in the Zeroth-Order Slender-Ship Approximation

by the Michell thin-ship approximation $K_M(t)$ and the zeroth-order slender-ship approximation $K_0(t)$. This figure strongly suggests the need for performing additional calculations based on a more realistic mathematical model than the simple thin-ship and slender-ship approximations used in this study.

Finally, the effect of the entrance angle β and of the flare angle γ on the steepness of the divergent waves is illustrated in figure 22. Specifically, this figure depicts the lines along which the steepness of the divergent waves, as predicted by the slender-ship approximation $K_0(t)$, is equal to 1/15 for $\beta = 8°$, 12°, 16° and $\gamma = 45°$, in the top half of the figure, and for $\gamma = 0$, 25°, 45° and $\beta = 12°$ in the bottom half of the figure. This figure shows that the short divergent waves in the Kelvin wake become steeper as the entrance angle β increases and as the flare angle γ decreases. More generally, figure 22 shows that the short divergent waves in the Kelvin wake are strongly influenced by the hull shape, and it therefore suggests the need for performing additional calculations in which systematic variations in hull shape are considered.

SUMMARY OF RESULTS AND CONCLUSIONS

Asymptotic expressions for determining the velocity potential and its derivatives at a sufficiently-large distance behind a ship advancing at constant speed in calm water are given by equations (23), (23a-e), (24a,b), (25a-d), (20a-e) and (26a-d). The far-field asymptotic approximation (23) is uniformly valid in the vicinity of the track of the ship $\alpha = 0$ if condition (27) is satisfied. For the simple bow shape considered in this study, condition (27) is satisfied for $k = 0$ and 1, corresponding to the potential ϕ and the free-surface elevation ϕ_x, when the far-field wave-amplitude function K(t) is approximated by the Michell thin-ship approximation $K_M(t)$ or the zeroth-order slender-ship approximation $K_0(t)$. However, condition (27) is not satisfied for $k \geqslant 4$ and $k \geqslant 2$ for the approximations K_M and K_0, respectively.

The asymptotic approximations used in this study provide simple explicit analytical expressions for determining the velocity potential and its derivatives for large values of $-Xg/U^2$, that is in the far field, in terms of the far-field wave-amplitude function. However, for small and intermediate values of Xg/U^2, these asymptotic approximations are not useful, and the integrals (18) must be evaluated numerically. For intermediate values of Xg/U^2, the exponential function $E_+(t;\vec{x}) + E_-(t;\vec{x})$ in the integrands of the integrals (1), (3a,b) and (5a,b) oscillates fairly rapidly, as may be seen from figure 1. Accurate and efficient integration rules suited to oscillatory integrands of the type depicted in figure 1 must be used. For small values of Xg/U^2, on the other hand, the oscillations of the exponential function $E_+(t;\vec{x}) + E_-(t;\vec{x})$ are not significantly more rapid than the oscillations of the far-field wave-amplitude function K(t) which also appears in the integrands of the wave integrals (18), so that a different integration rule is required.

The amplitude, a_+, of the divergent waves in the Kelvin wake vanishes at the track of the ship if condition (37) is satisfied. However, it is well known that the

wavelength, λ_+, of the divergent waves also vanishes at the track of the ship, as may be seen from figures 6 and 7. Therefore, the divergent waves can theoretically become infinitely steep at the track of the ship. More precisely, the steepness, $s_+ = a_+/\lambda_+$, of the divergent waves is unbounded at the track of the ship if condition (36) is satisfied. Both conditions (37) and (36) can be satisfied simultaneously if condition (39) is satisfied, where the far-field wave-amplitude function is of order $1/t^\mu$ as $t \to \infty$. Conditions (37) and (36), and consequently also condition (39), are satisfied in the cases of the thin-ship and the slender-ship approximations K_M and K_0 for the simple ship form considered in the study, as may be verified from figures 15 and 16 where $a_+(\alpha) \to 0$ and $s_+(\alpha) \to \infty$ as $\alpha \to 0$.

Infinitely-steep water waves cannot exist in reality. Indeed, there exists a theoretical upper bound for the steepness of water waves in deep water, which is approximately equal to 1/7. Condition (39) thus suggests that no divergent waves can exist within a certain region in the vicinity of the track of the ship, and that the Kelvin wake contains three distinct regions: (i) an inner region adjacent to the track of the ship where only transverse waves can exist, (ii) an outer region where both transverse and divergent waves are present, and (iii) an intermediate region at the boundary between the inner and outer regions where steep short divergent waves, as well as transverse waves, can be found.

Surface-tension and nonlinear effects have been ignored in the analysis presented in this study. This linear no-surface-tension analysis predicts extremely short and steep waves in the vicinity of the track of the ship. Both surface-tension and nonlinear effects therefore are liable to be significant, and these effects should be taken into account. A linear analysis including surface-tension effects should be performed first, since it is evident from the results obtained in the present study and from the brief description of the effects of surface tension upon the Kelvin wake given in Lamb [9, pp. 468-470] and Wehausen and Laitone [10, pp. 636-637] that the system of divergent waves in the vicinity of the track of the ship is likely to be profoundly affected by surface tension.

It was previously found by Scragg [5] that, for a ship bow form with a large flare angle, the zeroth-order slender-ship approximation $K_0(t)$ predicts a sharp peak in the value of the amplitude of the divergent waves at a value of α equal to approximately half the entrance angle β. This finding of Scragg has been verified in this study, as may be seen from figures 15, 16 and 18. Furthermore, the magnitude of the steepness of the divergent waves has been found to increase very rapidly as the Froude number decreases below a certain threshold value, as is shown in figure 19.

The line along which the steepness $s_+(\alpha)$ of the divergent waves has a peak and the lines along which $s_+(\alpha)$ takes the large values 1/7, 1/15 and 1/20 have been determined, for a simple ship form, on the basis of both the zeroth-order slender-ship approximation $K_0(t)$ and the Michell thin-ship approximation $K_M(t)$. Figure 20, corresponding to the slender-ship approximation $K_0(t)$, shows that these lines are well inside the Kelvin angle, and that the large-steepness lines are much closer to the track of the ship than the line corresponding to the peak in the steepness of the divergent waves.

The lines, depicted in figures 20 and 21, along which the steepness of the divergent waves takes large constant values are independent of the value of the Froude number, but they strongly depend on the hull shape, as may be seen from figure 22 where "constant-steepness lines" corresponding to several values of the entrance angle β and of the flare angle γ are depicted. This figure shows that the short divergent waves in the Kelvin wake become steeper as the entrance angle increases and/or as the flare angle decreases.

It was found that the lines, along which the steepness of the divergent waves takes large constant values, predicted by the slender-ship approximation $K_0(t)$ and the thin-ship approximation $K_M(t)$ are quite different from one another, as may be seen from figure 21. This figure therefore indicates the need for performing additional calculations based on a more realistic mathematical model than the simple thin-ship and slender-ship approximations used in this study. These two approximations correspond to simple special cases of the Neumann-Kelvin theory, which should then be used. In particular, it would be useful to determine whether this more realistic theory predicts that the steepness of the divergent waves in the Kelvin wake exhibits a peak (or several peaks), as was found by using the slender-ship approximation $K_0(t)$ for a ship bow form with large flare angle. Figure 21 specifically demonstrates the importance of obtaining accurate predictions of the far-field wave-

amplitude function K(t) for large values of t. Indeed, the short divergent waves in the vicinity of the track of the ship, that is for small values of α, are associated with the value of the function K(t) for large values of t, as may be seen from equations (23), (24a), (25a) and (12). Precise knowledge of the asymptotic behavior of the function K(t) as $t \rightarrow \infty$ therefore is critical.

The behavior of the function K(t) as $t \rightarrow \infty$ has been determined analytically in this study for the simple case of the thin-ship and slender-ship approximations $K_M(t)$ and $K_0(t)$ for an idealized ship bow form. More precisely, the asymptotic behavior of the functions $K_M(t)$ and $K_0(t)$ for the simple ship bow shape considered in this study is specified by equations (45) and (67a,b). These asymptotic approximations show that we have $|K_M(t)| = 0(1/t^3)$ and $|K_0(t)| = 0(1/t^2)$ as $t \rightarrow \infty$. They also show that the Michell thin-ship approximation $K_M(t)$, which corresponds to the thin-ship limit of the slender-ship approximation $K_0(t)$, is not uniformly valid in the limit $t \rightarrow \infty$. It is possible to analytically determine the behavior of the far-field wave-amplitude function K(t) associated with the Neumann-Kelvin theory for an arbitrary ship form, as is shown in [12]. Such an asymptotic approximation for the function K(t) for large values of t is useful because it provides an explicit analytical relationship between the hull form and the Froude number, on one hand, and the amplitude of the short divergent waves in the vicinity of the track of the ship, on the other hand.

ACKNOWLEDGMENTS

This study was funded by the Office of Naval Technology sponsored Exploratory Development Surface Ship Wake Detection Project at the David W. Taylor Naval Ship R&D Center. The authors wish to thank Dr. Arthur Reed and Mr. Seth Hawkins for their interest in the study and for their useful comments.

REFERENCES

1. Fu, Lee-Lueng and Benjamin Holt, "Seasat Views Oceans and Sea Ice with Synthetic Aperture Radar", JPL Publication 81-120, 15 Feb 1982.

2. McDonough, Robert N., Barry E. Raff and Joyce L. Kerr, "Image Formation from Spaceborne Synthetic Aperture Radar Signals", Johns Hopkins APL Technical Digest, Vol. 6, No. 4, Oct-Dec 1985, pp. 300-312.

3. Swanson, Claude V., "Radar Observability of Ship Wakes", Applied Physics Technology Report No. 1, May 1984, 109 pp.

4. Case, K.M., et al, "Seasat Report", MITRE Corporation, Report JSR-83-203, March 1984.

5. Scragg, Carl A., "A Numerical Investigation of the Kelvin Wake Generated by a Destroyer Hull Form", Science Applications, Report No. SAI-83/1216, Oct 1983, pp. 46.

6. Cooper, A.L., "Interactions Between Ocean Surface Waves and Currents", Naval Research Laboratory, NRL Memorandum Report 5755, April 1986, pp. 18.

7. Noblesse, F., "A Slender-Ship Theory of Wave Resistance", Journal of Ship Research, Vol. 27, No. 1, March 1983, pp. 13-33.

8. Sharma, S.D., "Some Results Concerning the Wavemaking of a Thin Ship", Journal of Ship Research, Vol. 13, 1969, pp. 72-81.

9. Lamb, H., "Hydrodynamics", Dover Publications, New York, 1879, pp. 738.

10. Wehausen, J.V. and E.V. Laitone, "Surface Waves", in Encyclopedia of Physics, Springer-Verlag, Berlin, Vol. IX, 1960, pp. 446-778.

11. Ursell, F., "On Kelvin's Ship-Wave Pattern", Journal of Fluid Mechanics, Vol. 8, 1960, pp. 418-431.

12. Noblesse, F., "Analytical Approximations for Steady Ship Waves at Low Froude Numbers", 21st ATTC Resistance and Flow Committee, Washington, Aug. 1986.

DISCUSSION

Robert Beck,
University of Michigan

The wave amplitude in this far field is a function of the derivative of the waterlines for thin ship theory and the derivative of the sectional area curve for slender-body theory. How do you account for the effects of flow (which involve only vertical derivatives of the section shape) in these theories?

Reply -

It should be noted that numerical results are presented for the Michell thin-ship approximation and for the slender-ship approximation proposed in reference [7], and that the latter approximation is different from the slender-body theory which Prof. Beck has in mind. In particular, sources are distributed on the exact position of the ship hull in the slender-ship approximation given in [7], whereas they are distributed on the ship centerplane in the Michell approximation. The presence of flare therefore only affects the density of the source distribution in the Michell approximation, whereas both the distribution surface (support) and its density are affected by flare in the slender-ship approximation. As a result, the influence of flare is much more pronounced for the slender-ship approximation than for the Michell approximation. In particular, the slender-ship approximation predicts that flare may cause a sharp peak is predicted by the Michell approximation. The slender-ship approximation's prediction of a sharp peak for a ship with flare is corroborated by the Neumann-Kelvin theory, as is shown in reference [12].

Blythe Hughes,
Defence Research Establishment Pacific

a. Have comparisons been made between the slender ship theory "extra peak" in slopes, and the Dabob Bay measurements?

b. Would you comment on the infinite slopes predicted by your model compared to the measurements?

Reply -

The Dabob Bay measurements discussed by Dr. Hughes in his paper (see in particular figures 9 and 10) do not appear to indicate the presence of a peak in wave steepness at an angle from the ship track smaller than the Kelvin angle of 19.5 degrees. These measurements thus lend no support to the numerical results obtained in our paper. However, the measurements reported by Dr. Hughes do not necessarily contradict our numerical results. Indeed, a sharp peak in wave steepness was predicted in our study on the basis of the slender-ship approximation for a particular ship bow form with flare provided that the value of the Froude number is sufficiently small, as is shown in figure 19 (see also figures 16 and 18) in our paper. More generally, it is shown in reference [12] that the Neumann-Kelvin theory (of which the slender-ship approximation is a simplified version) predicts the occurrence of a peak in the amplitude of the waves in the far-field Kelvin wake at an angle from the ship track smaller than the Kelvin-cusp angle of 19.5 degrees for a hull form which has a small region of flare and is wall sided elsewhere if the Froud number is sufficiently small. This theoretical prediction of a peak in wave amplitude thus requires that conditions with respect to both the hull form and the Froude number be satisfied. It is uncertain that these two conditions are satisfied for QUAPAW for which measurements are reported in Dr. Hughes' paper. Indeed, this ship has flare gradually varying over a large portion of its waterline, and measurements are reported for fairly-large values of the Froude number (between 0.27 and 0.33).

The theoretical prediction that the steepness of the divergent waves is infinite at the ship track is based on a linear, inviscid, no-surface-tension analysis, which clearly is dubious in the vicinity of the ship track where surface tension and possibly also viscosity are liable to be quite important, as is shown in [a].

We thank Prof. Beck and Dr. Hughes for their interest in our paper.

[a] Wilson, Michael B., "Michell-Oseen Flow Theory for Thin Ships", Ph.D. thesis, California Institute of Technology, Pasadena, California, 1971.

Trailing-Vortex Wakes on the Free Surface

T. SARPKAYA

Naval Postgraduate School, U.S.A.

ABSTRACT

The temporal development of the surface signatures (scars and striations) resulting from the interaction of an ascending inclined vortex pair with the free surface has been investigated. The vortices were generated by towing horizontally various lifting surfaces (delta wings and rectangular foils of different shape and aspect ratio) well below the free surface at prescribed speeds, depths, and negative angles of attack. The evolution of each type of surface signature has been expressed in terms of the depth of generation, mutual induction velocity, and the initial spacing of the vortex pair. It has been shown that V-shaped surface signatures of finite length are created and driven by trailing vortices migrating from depths less than about five initial vortex separation distances. Vortices generated at larger depths gave rise to more complex surface signatures due to the onset of sinusoidal instability, vortex linking, and/or vortex breakdown. The apparent circulation of the vortices, based on the measured characteristics of the scar tracks, was found to be a universal function of a normalized time, measured relative to the inception of the striations.

INTRODUCTION

When a vortex pair approaches the free surface, with or without mutual induction instability [1] and/or vortex breakdown (see e.g., [2-3]) the vortices (or the crude vortex rings) give rise to distinct surface disturbances (waves of very small length). These waves or the local roughening of the free surface are visible because the particle motions they create as they propagate produce a straining field at the surface which modifies the physical characteristics of the sea surface (reflection, refraction and the scattering of sound, heat and light). In fact, in many photographs of the sea surface taken from aircraft or earth resources technology satellites, using passive or active sensors, the differential roughening of the free surface can be seen clearly (see e.g., [4-7]).

The surface signatures produced by a pair of trailing vortices generally occur in the later stages of the vortex lifetimes, and as such, are subject to complex demise mechanisms (Crow instability [1], vortex breakdown and turbulent diffusion).

Previous studies of a vortex (or vortex pair) in ground-or free-surface effect have been generally concerned with the boundary layer development, generation of oppositely signed vorticity, and the so-called 'rebounding' phenomenon, according to which the vortices move at first toward the boundary, as on an inviscid trajectory, and then away from it (see e.g., [8-10]). The boundary surface may be either a rigid boundary at which the no-slip condition is satisfied or a free surface corresponding to zero shear stress. In either case the boundary surface behaves as a vorticity sink and the net circulation of the vortex decrases with time [10].

The trailing vortices are, in general, subjected to sinusoidal instability and/or vortex breakdown which render the vortex motion quickly three dimensional. The interaction of such vortices with their images gives rise to additional deformations. The ability of the free surface to deform under the influence of strain fields increases the complexity of the phenomenon in both degree and kind because the liquid-air interface is moving, the interface is not constrained in its shape, and the velocity gradient decays exponentially away from the positions directly above the vortex.

The scars and striations studied in the present paper were produced by towing various lifting surfaces horizontally below the water surface at a constant speed, depth, and negative angle of attack in a long towing tank. Sample photographs of only the surface signatures are shown in Figs. 1-3. Unless otherwise noted, the vortices are not seeded with dye and thus they do not show in the pictures.

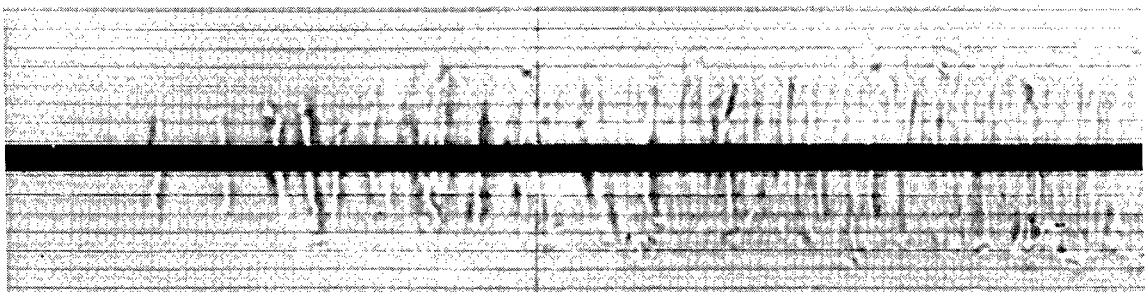


Fig. 1 Evolution of the Striations

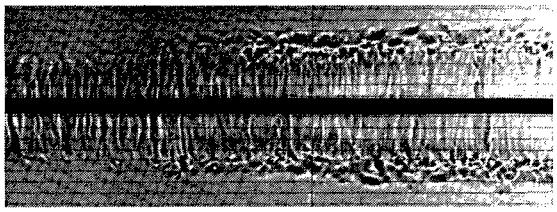


Fig. 2 Transition from Striations to Scars

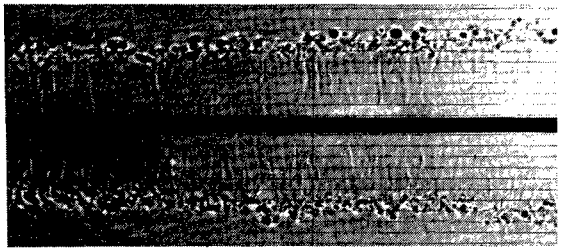


Fig. 3 Evolution of the Scar Tracks

The solid bar in each picture is the narrow slit along the middle of the disturbance management system (to be described below).

EXPERIMENTAL FACILITY

The equipment used to generate the trailing vortices has been described in detail previously [11-13]. Only the salient features, most recent modifications and the adaptation for this work are briefly described in the following.

The system consists essentially of a towing basin. The auxiliary components of the basin are the plumbing for tap water, turbulence management system (a 2.54 cm black polyurethane foam, sandwiched between two perforated aluminum plates), top and bottom carriages, velocity measuring system, lighting system, and the models.

Two parallel rails are mounted along the bottom of the tank. The rails, the carriage and the filling pipes are located under the turbulence management system. The models are mounted on their bases by means of a thin streamlined vertical strut and set at the desired angle of attack. The strut is rigidly attached to the carriage and moves along the slit in the middle of the turbulence management system. The models are pulled by means of a DC motor, pulley, and cable system at the desired speed (ranging from 0.3 to 1.5 m/s).

Seven models were used in the experiments, (see Table I). The first three models are delta wings, made of 3 mm thick aluminum with hollow interiors. The pressure side of the leading edges of delta-1S and delta-2S were made razor sharp. The edges of the suction side were bevelled to an angle of 45 deg. All edges of the remaining delta wings were rounded to a radius of 1.5 mm (half the plate thickness) in order to examine the effect of edge modification on the longevity of the vortices

The fourth and fifth models (RP-1 and RP-2) were of rectangular shape, with a NACA-0012 cross-section. The wing tips were rounded to a radius equal to half the local thickness of the foil. The interior of each model was hollowed and used as a dye reservoir to seed the vortex cores.

The vortices generated by the sharp-edged wings had a larger diameter and relatively rougher surface. The vortices generated by wings with rounded edges had a smaller diameter and smoother surface. It is on the basis of these observations that an elaborate scheme was devised to determine the core size as accurately as possible as described in [11]. The average of at least five measurements per model yielded $r_e/b_o = 0.13 \pm 0.02$ for the sharp-edged models and $r_e/b_o = 0.09 \pm 0.01$ for the wings with rounded edges, (r_e = effective core radius and b_o = initial vortex core spacing). Here and throughout the rest of the paper, the conditions prevailing at ten chord lengths from the trailing edge of the model are designated as the 'initial' conditions.

Model	AR	B	Edges
Delta-1S	1.436	20.0 cm	sharp
Delta-2S	1.675	12.8 cm	sharp
Delta-2R	1.675	12.8 cm	rounded
Delta-3R	1.143	10.2 cm	rounded
Delta-4R	0.837	12.8 cm	rounded
RP-1	1.943	17.3 cm	rounded
RP-2	1.943	11.4 cm	rounded

Table I. The shape, aspect ratio, base width and the edge condition of the test models.

REMOTE SENSING OF THE SURFACE SIGNATURES

Due to the complex nature of the phenomena being investigated and the extreme sensitivity of the vortical structures to external disturbances, flow visualization is one of the few methods available for studying the interaction of vortices with the free surface.

The surface disturbances may be observed and/or detected by a number of active and passive sensors. Some of these are visual (eye), photographic (camera), radar (microwave, synthetic aperature) and infrared radiometry [14].

In the present study both the direct photographing of the scars (through the use of a thin light sheet as described by Scott [15]) and the indirect photographing (shadowgraph technique) were used in order to make sure that the instantaneous position of the surface signatures is determined as accurately as possible through the use of at least two methods.

For the shadowgraph technique, a single collimated light source was positioned along the axis of the basin at a distance far enough to reduce glare and parallax.

Both techniques of measurement were calibrated by photographing a floating grid and its image. Each picture included time accurate to 0.01 seconds (generated by an electronic timer and projected into an inclined mirror). Both methods yielded nearly identical results. However, the shadowgraph technique was more reliable and easier to use. All surface disturbances were recorded on film until they had completely dissipated. Each experiment was repeated at least twice to ascertain that the data were reproducible.

CHARACTERISTICS OF THE SURFACE DISTURBANCES

The physical appearance of the surface signatures produced by an inclined vortex pair approaching the free surface can be characterized in two distinct modes: "striations" and "scars".

The striations appear abruptly sometime after the passage of the lifting surface as ridges perpendicular to the path of the model (see Fig. 1). They grow rapidly to a total length of about $2.6b_o$ to $3.0b_o$ (s/b_o = 1.3 to 1.5 where s is the half width of the scar band). The striation phase of the surface condition lasts for a time interval of $\Delta\tau$ = 0.6 to 1.0 where $\tau = V_o t/b_o$ and Vo is the initial mutual induction velocity of the vortices and t is the time. Shortly thereafter, two distinct signatures or 'scars' appear. They are nearly parallel to the model track and run along the tips of the striations (see Figs. 2 and 3). While the scars become the dominant features of the free surface, the striations remain in the signature band and stretch more or less randomly in the lateral direction.

The scar tracks move sideways, i.e., the width of the signature band increases with time, if unimpeded by other phenomena such as the Crow instability or vortex breakdown (see Fig. 3). The lateral motion of the scars is in phase with that of the vortices. As the scars and striations age, they attenuate, spread over a larger area, and eventually become indistinguishable. The foregoing takes place at relatively small depths (say for less than about $5b_o$). For larger depths of submergence, the Crow instability sets in and amplifies rapidly during the later stages of the rise of vortices. This often leads to the linking of the vortex pair and to the formation of a series of crude vortex rings. The proximity of the free surface may precipitate the occurrence of the Crow instability and vortex linking due to the mutual interaction of the vortices and their images.

Figure 4 is a representative example of the surface signatures created by the vortices which have undergone Crow instability. The dark circular regions correspond to local surface depressions.

The simultaneous observations and measurements of the dye-seeded vortex cores and the surface signatures have shown conclusively that the signatures are indeed created and driven by the vortices moving beneath the free surface. The scar front leads the vortex axis, by an amount to be discussed later. Figure 5 shows the scars and the striations generated by an inclined vortex ring approaching the free surface.

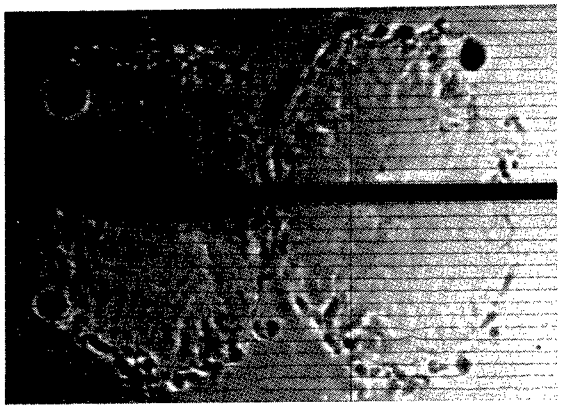


Fig. 4 Crow Instability, Rings and Scars

DIMENSIONAL ANALYSIS

It is easy to show that in a homogeneous medium the position of the trailing vortices ($\pm \xi_v$, η_v) and the position of the scars ($\pm\sigma_s$, 0) are determined primarily by three normalized parameters [11]

$$(\xi_v, \eta_v, \sigma_s) = f_i(\tau, \Delta, r^*) \qquad (1)$$

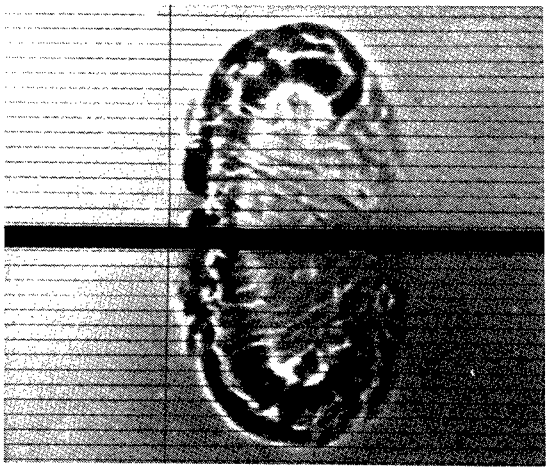


Fig. 5 Scars due to an Inclined Vortex Ring

where $\xi_v = x_v/b_o$, $\eta_v = y_v/b_o$, $\sigma_s = s/b_o$, $\tau = V_o t/b_o$, V_o = the initial mutual-induction velocity, $\Delta = d_o/b_o$, and $r^* = r_e/b_o$. x_v and y_v represent the cooordinates of the vortex at time t, s the half width of the scar band, Γ_o the initial circulation of the vortex ($\Gamma_o = 2\pi b_o V_o$), and d_o the initial depth of the vortex pair. Thus, $\xi_v = 0.5$ and $\eta_v = \Delta$ at $\tau = 0$. The aspect ratio, angle of attack, and the velocity of the model for a given wing-tip shape enter into the analysis only indirectly through τ.

Experiments have shown that [11] the ratio of the initial vortex-core spacing to wing span, b_o/B, is 0.70 for the sharp-edged delta wing, 0.71 for the round-edged delta wing, and nearly equal to $\pi/4$ (its theoretical value) for the rectangular wing (NACA 0012).

The previous measurements [11] have also shown that the parameters V_o^2/gb_o (a Froude number which ranged from 0.003 to 0.03) and $V_o b_o/\nu$ [$= \Gamma o/(2\pi\nu)$] (a Reynolds number which ranged from 3500 to 10,500) are not important within the range of the parameters encountered in the present experiments. Futhermore, of the three parameters appearing in Eq. (1), only τ and Δ may be changed independently. r^* is taken as nature provides it. The primary reason for this is that it has not yet been possible to describe either theoretically and/or experimentally the effect of the wing-tip shape on the rolling-up of vortex sheets, the inception and growth of the helmholtz and Rayleigh instabilities, and the encroachment of the resulting turbulence into the potential flow (until the turbulence reaches the boundaries of the recirculation cell). Here the said influences have been characterized in terms of an effective core radius with full awareness of its shortcomings.

The present investigation has conclusively shown that the surface signatures are not capillary waves but rather disturbances generated and driven by the vortices. Hence the effect of the surface tension (Weber number) on the speed and position of the surface signatures and trailing vortices is considered negligible. The amplitude of the disturbances, which may be affected by the surface tension, has not been studied in the present investigation.

ANALYSIS OF THE MOTION OF TRAILING VORTICES

The growth and propagation of surface scars and striations resulting from the interaction of a turbulent vortex pair with the free surface are largely unexplored.

Peace and Riley [10] calculated the flow induced by a vortex pair in a viscous fluid in the presence of a plane boundary (a free surface or rigid boundary) at very small Reynolds numbers ($Re = \Gamma/\nu = 50$ and 100) for the purpose of explaining the rebounding of the vortices from the boundary. The free surface is assumed to remain undeformed and the vortices are assumed to remain parallel (no large scale instabilities). Thus, their work did not deal with the surface scars.

A relatively simple alternative is to assume the free surface to be undeformable at first and calculate the resulting flow field due to the vortex pair and its image, and then examine the behavior of the free surface due to the velocities induced on it.

For an inviscid line-vortex pair approaching the free surface, the velocity potential may be written as

$$w(z) = -\frac{i\Gamma}{2\pi} \operatorname{Log} \frac{(z - z_v)(z + z_v)}{(z - \bar{z}_v)(z + \bar{z}_v)} \qquad (2)$$

where Γ and z_v represent, respectively, the strength and position of one of the vortices, ($\bar{z}_v$ is the conjugate of z_v).

The velocities may be calculated anywhere in the flow field from

$$u - iv = dw/dz \qquad (3)$$

Of particular interest are the velocities on the free surface and at the center of a vortex. Evaluating Eq. (3) through the use of Eq. (2) and setting $y = v = o$, one has,

$$\frac{u_s}{V_o} = \frac{2\eta_v}{(\xi - \xi_v)^2 + (\eta_v)^2} - \frac{2\eta_v}{(\xi + \xi_v)^2 + (\eta_v)^2} \qquad (4)$$

where u_s is the velocity at the free surface.

The velocity components at the center of a vortex may be obtained from Eq. (3) by omitting the contribution of the vortex itself to the velocity at its center. This procedure yields,

$$\frac{u_v}{V_o} = \frac{(\xi_v)^2}{2\eta_v\,[(\xi_v)^2 + (\eta_v)^2]} \qquad (5)$$

$$\frac{v_v}{V_o} = \frac{-(\eta_v)^2}{2\xi_v\,[(\xi_v)^2 + (\eta_v)^2]} \qquad (6)$$

The trajectories of the ideal line vortices approaching a rigid plane are given by [16],

$$(\xi_v)^{-2} + (\eta_v)^{-2} = 4 + \Delta^{-2} \qquad (7)$$

The vortices do not come to the plane surface a distance closer than

$$\eta_{min} = y_{min}/b_o = [4 + \Delta^{-2}]^{-1/2} \qquad (8)$$

Also, it is easy to show that τ is related to η by

$$\tau = \frac{8\Delta^3}{m^2}\left[\frac{m-2}{2} - \frac{m(\eta_v)^2 - 2\Delta^2}{[m(\eta_v)^2 - \Delta^2]^{1/2}}\right] \qquad (9)$$

where $m = 1 + 4\Delta^2$.

The position x_m of the maximum surface velocity u_m may be obtained by differentiating Eq. (4) with respect to ξ, setting it equal to zero, and combining it with Eq. (7). After considerable simplification, one has

$$\left(\frac{x_m}{b_o}\right)^2 = \frac{(\xi_v)^2}{3}\left[\frac{k(\xi_v)^2-2}{k(\xi_v)^2-1} + \frac{2}{k(\xi_v)^2-1}\left(k^2(\xi_v)^4 - k(\xi_v)^2 + 1\right)^{1/2}\right] \qquad (10)$$

where

$$k = 4 + \Delta^{-2} = (\eta_{min})^{-2} \qquad (11)$$

The foregoing expressions enable one to determine the surface velocity profile, the position and magnitude of the maximum surface velocity, and the instantaneous position of the vortices in terms of $\tau = V_o t/b_o$, $\Delta = d_o/b_o$, and $\xi = x/b_o$.

Figure 6 shows the surface velocity profile at various times for a representative depth of $\Delta = 4$. Evidently, the maximum velocity becomes nearly constant for ξ larger than about 2. This corresponds to the state where the vortex and its image are only weakly affected by the other vortex of the pair and its image. It is exactly for the same reason that the shape of the velocity profile becomes increasingly more symmetrical about a vertical axis.

Figure 7 shows x_m/b_o and u_m/V_o as functions of τ for a relative depth of $\Delta = 4$. Also shown in this figure (with dashed lines)

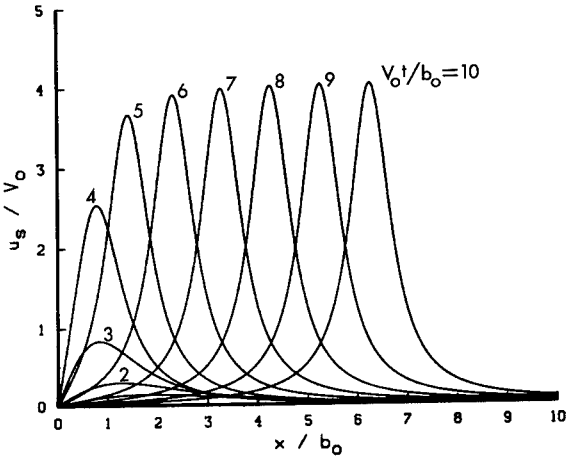


Fig. 6 Surface Velocity at Specific Times for $d_o/b_o = 4$

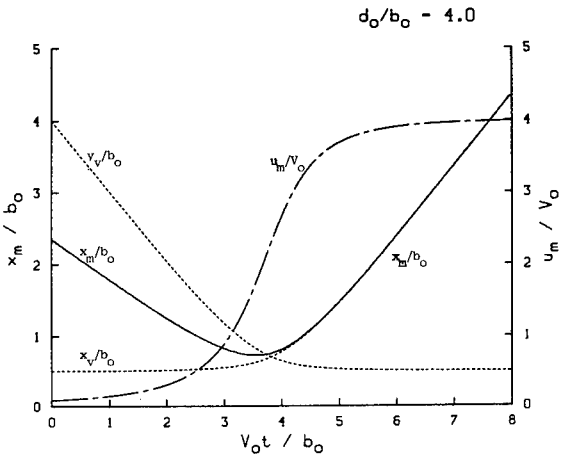


Fig. 7 Vortex Positions and Surface Velocity at Specific Times for $d_o/b_o = 4$

are the variations of ξ_v and η_v with τ. This figure and others (for Δ from 2 to 8) reveal several interesting facts. First, it is noted that the vortices are closer to the vertical axis than the position of the maximum velocity, i.e., $x_v < x_m$, for a time period dependent on Δ. Second, beyond a minimum τ, the position of the maximum velocity and the x-position of the vortex are indistinguishable, i.e., the maximum velocity u_m ,[$\approx \Gamma/(\pi b_o \eta)$], arises from the contributions of the vortex and its image directly above it. Had the vortices migrated from an infinite depth, they could not have come a distance closer than $b_o/2$ to the free surface and the maximum surface velocity would have been $u_m/V_o = \Gamma/(\pi V_o b_o/2) = 4$. Equation (8) shows that $\eta_{min} \cong 0.5$ for $\Delta > 3$. Thus, the asymptotic value of $u_m/V_o = \Gamma/(\pi V_o b_o \eta_{min}) \cong 4$ in Fig. 7 where $\Delta = 4$.

So far the discussion has centered around the motion of a two-dimensional vortex pair parallel to the free surface. The trailing vortices are generated continuously by the model. The older parts of the trail acquire a higher elevation than the more recent parts because they are subjected to mutual induction for a longer time period. Thus, the vortex pair, as viewed from the side, is inclined at an angle $\gamma = \tan^{-1}(V_o/U)$ relative to the horizontal. Consequently, the scars do not appear at the free surface everywhere at once. The scar front (i.e., the striations shown in Fig. 1) moves along the free surface at a speed U, far behind the model. The horizontal distance between the scar front and the model or the time interval between the arrival of the model and the scar front at a specific point along the channel depends primarily on Δ and r^*. Furthermore, as the vortices approach the free surface, they execute ninety-degree turns along their paths and diverge laterally with a speed $V = \Gamma/(4\pi b_o r_{min}) \approx V_o$. However, the older parts of the trail which have approached the free surface earlier move further out laterally because they are subjected to mutual induction with their images a longer time period. Thus, the scar tracks are not parallel and the included angle between them is $2\tan^{-1}(V_o/U)$. As noted earlier, the striations precede the scars and then fill in the region between them like the rungs of a ladder. The entire V-shaped surface signature trails above and behind the lifting surface. The determination of the characteristics of this signature at a given point in time and space as a function of the position and motion of the lifting surface constitutes the essence of the problem.

EXPERIMENTAL DATA

The relative horizontal half spacing s/b_o is shown in Fig. 8 as a function of τ for $\Delta = 4$. The symbol x signifies striations. Other symbols denote scars generated by the lifting surfaces, noted in the figure caption.

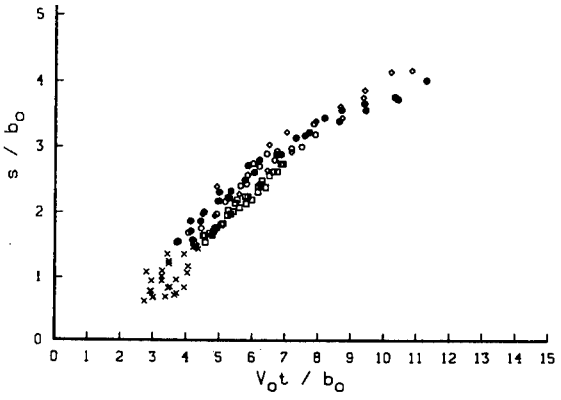


Fig. 8 Scar Front Position as a Function of Time for $d_o/b_o = 4$: x, Striations; o, Delta-4R; ◇, Delta-5R; □, RP-2, ●, Delta-3R.

The data for all Δ reveal the following facts: (i) the surface signatures in the form of striations do not come into existence until a definite time of τ, (e.g., $\tau = 2.7$ in Fig. 8); (ii) For small values of τ, corresponding to the striation phase, the data show larger scatter; (iii) the pure striation phase of the surface signatures ends (as determined from the pictures) after a time interval of $\Delta\tau = 0.6$ to 1.0; and, (iv) the scatter in the latter region (particularly for larger values of Δ) is primarily due to the occurrence of the Crow instability and/or vortex breakdown and the formation of the vortex rings. They give rise to scars of various forms and render the accurate evaluation of s/b_o somewhat more difficult. An inviscid flow analysis, based on the Biot-Savart law (see e.g., [17]), was carried out by dividing up the vortex loop and its image into a number of straight vortex segments in order to study the temporal development of three-dimensional vortex loops in the vicinity of the free surface. However, the difficulty of specifying the initial conditions (transition from Crow instability to vortex linking and the formation of inclined vortex rings) rendered the determination of the surface velocity distribution somewhat arbitrary. It is for this reason that the analytical formulation of the ring problem is not presented here.

ANALYSIS AND DATA

Figure 9 shows a representative plot of x_m/b_o, x_v/b_o and y_v/b_o, as determined from the potential flow analysis [Eqs. (2-11)], and the relative scar position s/b_o, as determined experimentally, for $\Delta = 4$. This figure reveals several interesting facts which are uniformly valid for all the data obtained during this investigation: (i) the position of the maximum velocity (based on the potential flow analysis) trails the scar front for specific normalized times dependent on Δ (e.g., for $\tau < 6$ for $\Delta = 4$) and leads the scar front for

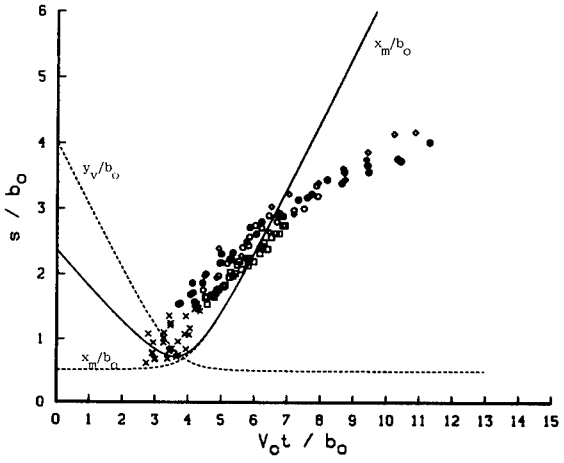


Fig. 9 Scar Front Position and x_m/b_o as a as a Function of Time for $d_o/b_o = 4$

larger times; (ii) the scars come into existence at a time when the vortex pair almost reaches its maximum height and begins to move essentially in the lateral direction; and finally, (iii) the scars cease to exist when the vortices completely dissipate.

The conclusions reached on the basis of Fig. 9 and others for other Δ point out one important fact: If the position of the scars is slaved to the vortices, as shown by numerous test runs, and if the vortices are observed to dissipate in a finite time, then an analysis based on constant vortex strength and potential flow assumption cannot adequately predict either the magnitude or the location of the maximum surface velocity or the positions of the vortices and the scars. Consequently, the arguments which involve the use of formal analytical models for vortex structure and circulation must be set aside and a model must be considered which accounts for the loss of circulation partly due to the mixing of the counter-sign vorticity in the overlapping regions of the vortex pair in the recirculation cell (Parker & Crow [9]), partly due to loss of vorticity at the free surface (Peace & Riley [10]), and partly due to turbulent mixing by convection at inviscid scales (Craik [18]). A theoretical solution is not yet possible. However, the apparent circulation of the vortices may be calculated through the use of the potential flow analysis.

As noted earlier, the surface signatures do not come into existence in the form of striations at the same normalized time, i.e., the relationship between s/b_o and τ for a given depth is shifted relative to the other depths. This observation led to the realization that the evolution of the surface signatures must be examined relative to the time of inception of the striations. Denoting that time with τ^* and plotting s/b_o as a function of $\tau - \tau^*$ in log-log coordinates one obtains Fig. 10. The data shown in this figure (approximately 500 data points) are for $\Delta = 2$ through 8 and for all models. The remarkable feature of Fig. 10 is that there exists a unique relationship between the scar position and the normalized time, measured from the inception of the striations. The solid line drawn through the data may be expressed as,

$$s/b_o = 1.5\ (\tau - \tau^*)^{0.5} \qquad (12)$$

Noting that

$$u_s = ds/dt = \frac{\Gamma_{sc}}{2\pi(2\eta_v)b_o} \qquad (13)$$

and combining with the derivative of Eq. (12), one has

$$\frac{\Gamma_{sc}}{\Gamma_o} = 1.5\,\frac{\eta_v}{(\tau - \tau^*)^{0.5}} \quad \text{for } \tau \geq \tau_{sc} \qquad (14)$$

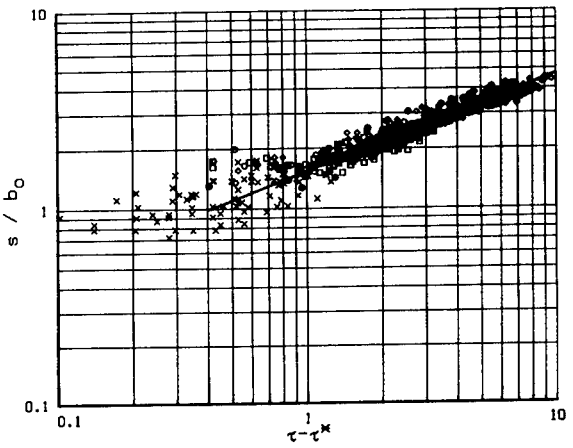


Fig. 10 Scar Front Position as a Function of Relative Time for all Models

in which Γ_{sc} represents the apparent circulation of the vortices in the scar phase of the surface signatures, τ_{sc}, the time of inception of scars and Γ_o, the initial strength of the vortices. Note that $\tau_{sc} > \tau^*$. Equation (14) does not quite represent the true circulation of the vortex since the exact shape of the vorticity containing core has not been accounted for in Eq. (13).

The vortices lose some of their strength gradually during their rise and prior to the formation of the striations. This decrease is a consequence of the loss of vorticity in the overlapping regions of the oppositely-signed vorticity in the recirculation cell. Even though there does not exist an exact solution for the turbulent vortices, numerous approximate models have been proposed in the past to account for the distribution of velocity and vorticity. Among these, the exact solution of the viscous vortex by Lamb [16] is quite well known. However, it does not apply to a turbulent vortex.

Squire [19] suggested that a turbulent trailing vortex could be described by Lamb's solution if the kinematic viscosity ν in it were replaced by an eddy diffusivity ν_t as

$$\frac{\Gamma}{\Gamma_o} = (1-\exp(-\eta^2/4a_o)) \qquad (15)$$

where $\eta^2 = r^2/t\Gamma_o$, r the radial distance from the vortex core and $a_o = \nu_t/\Gamma_o$ which is a function of the vortex Reynolds number, Γ_o/ν. Equation (15) may be reduced to

$$\frac{\Gamma}{\Gamma_o} = 1 - \exp(-A/\tau) \qquad (16)$$

where $A = (r_e/b_o)^2/(8\pi a_o)$. There is no direct measure of the variation of r_e/b_o during the rise of the vortices and the value of a_o was

found to vary within a large range (from 5x10-5 to 7.6x10-3) [20] through the experiments conducted mostly under environmental conditions. Furthermore, it has not been demonstrated either experimentally or theoretically that Squire's proposal should be valid for all turbulent vortices. Partly on the basis of these facts and partly because the loss of circulation prior to the formation of scars is very small, if not negligible, the value of A was determined as follows through the use of the experimental data:

(i) The vertical position of the vortices (i.e., y_v/b_o) at or near the creation of the striations was plotted as a function of Δ for all test models and a mean value of y_v/b_o = 1.1 was obtained (i.e., $\eta_v/\eta_{min} \cong 2.2$). The maximum deviation of the data from this mean value was $\mp$ 0.2. This is primarily due to the fact that it was not always possible to capture on film the exact time at which the first striation came into existence. Furthermore, since the striations are a consequence of the surface strains resulting from the velocity gradients in the x-direction when the inclined vortices come near the free surface and since the vortices differ from run to run even for nearly identical experimental conditions, it is reasonable to expect some variation in y_v/b_o from the mean value of 1.1.

(ii) The time τ^* at which y_v/b_o = 1.1 was then calculated through the use of Eqs. (2-10) for various values of A from 15 to 30 and compared with those obtained experimentally. This resulted in A = 19, ($a_o \cong 2 \times 10^{-5}$).

The foregoing method of determination of the A value may appear to be somewhat subjective since it is not very easy to determine the exact time at which striations are transformed into scars. However, it is important to note that it makes very little or no difference in the determination of the apparent circulation of the vortices. As will be noted shortly, a value of A = 19 or larger means very little or no loss in circulation during the initial rise of the vortices. In fact, in all of the subsequent analysis, the circulation loss for $\tau < \tau_{sc}$ could have been ignored with no loss of generality. It is on the basis of the foregoing that Eq. (16) for $\tau < \tau_{sc}$ and Eq. (14) for $\tau > \tau_{sc}$ were used to calculate the apparent circulation of the vortices.

The relationships between τ^*, τ_{sc} and the corresponding vertical position of the vortices may be summarized as follows:

Inception of striations: $\tau = \tau^*$, $y_v/b_o \approx 1.1$

Inception of scars: $\tau = \tau_{sc}$, $y_v/b_o \approx 0.63$

Figure 11 shows the variation of the normalized circulation as a function of ($\tau - \tau^*$). As expected, the variation of circulation for

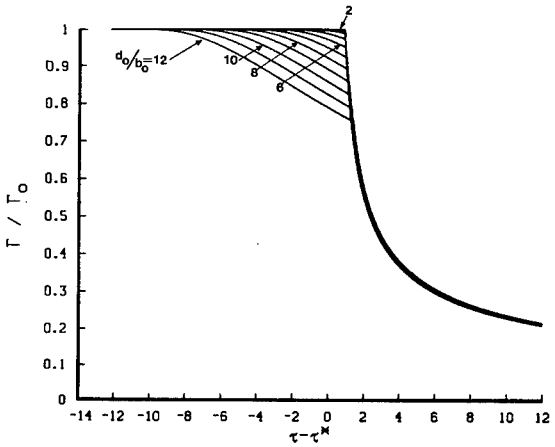


Fig. 11 Normalized Circulation as a Function of Relative Time

times larger than τ^* is a universal function of $\tau - \tau^*$. Apparently, the largest loss of circulation takes place after the inception of the scars partly due to the generation of counter-sign vorticity and partly due to the expenditure of energy to create the surface signatures.

Except for the theoretical work of Peace & Riley [10] at very low Reynolds numbers (Γ/ν = 50 and 100), there are no theoretical predictions or experimental data for the circulation reduction. Peace & Riley found circulation reductions comparable to those shown in Fig. 11 for a laminar vortex in the vicinity of a no-stress boundary. Their Reynolds numbers (Γ/ν = 50 to 100) are considerably smaller than those encountered in the present experiments ($\Gamma/\nu = 22\times10^3 \rightarrow 66\times10^3$) and the circulation reduction is entirely due to the generation of counter-sign vorticity.

The surface velocities were recalculated on the basis of the apparent circulation [Eqs. (14) and (16)]. Figure 12 shows u_s/V_o as a function of x/b_o for Δ = 4. Clearly, the surface velocities and, therefore, the gradients decrease rapidly, eventually leading to the total dissipation of the vortices and their inability to give rise to surface signatures. Thus, even a steady laminar flow solution is not possible even in a frame of reference moving with the vortex. The turbulent nature of the vortices, the deformation of the free surface and the unsteadiness of the entire phenomenon preclude the theoretical determination of the temporal evolution of the vortices. Thus, it is only indirectly that one can estimate the apparent circulation of the vortices in a manner done in the foregoing.

One is now in a position to explore the consequences of the hypothesis that the scars are slaved to the vortices and that the strain field arising from the nonuniform velocity distribution is the cause of the scars. With

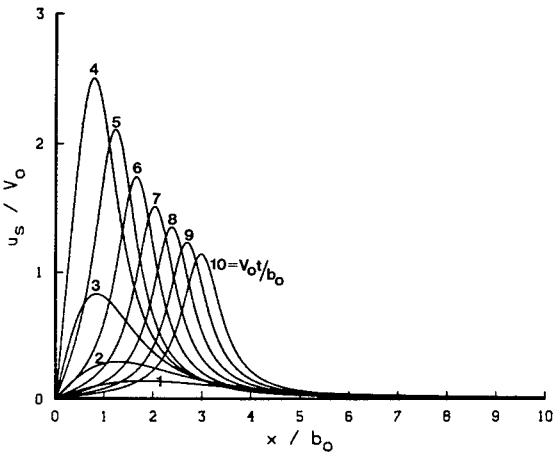


Fig. 12 Surface Velocity Distribution for Various Times with Reduced Circulation for $d_o/b_o = 4$

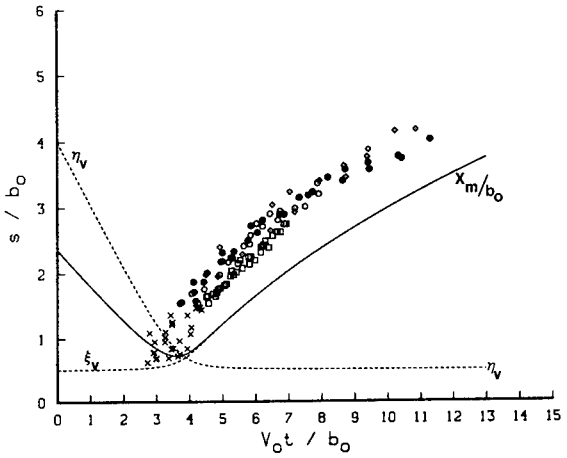


Fig. 13 Comparison of the Scar Front Position with the Vortex Position (Reduced Circulation, $d_o/b_o = 4$)

this objective in mind, the experimental data are compared with the corresponding analytical results. Figure 13 shows a sample plot for $d_o/b_o = 4$. This and all other figures for other Δ show that the position of the maximum surface velocity, predicted through the use of (10), is not coincident with the position of the scars (the position of the maximum velocity is nearly identical with that of the vortices for $x/b_o \geq 1.5$) and the scars lead the vortices by a nearly constant amount. In other words, the x_m/b_o curves are parallel to but not coincident with the data depicting the position of the scars. This is particularly true for depths for which the vortices are not subjected to large scale instabilities.

Figure 14 (corresponding to $\Delta = 4$) shows the data and the original as well as the shifted position (by an amount of 0.86) of x_m/b_o. Leaving aside for the time being the significance of the constant 0.86, it is apparent that the scars and the vortices move in phase and are separated by a constant amount in space.

For larger Δ values, it is not very meaningful to speak of a constant spacing between the scars and the vortices since the velocities used in the calculations have been based on the assumption of linear vortices whereas the scars are ring-shaped. Nevertheless, Fig. 15 shows that even for larger depths a constant shift brings the vortex and scar positions into somewhat unexpected agreement. The shift needed to bring about this agreement is certainly not equal to 0.86 and becomes smaller with increasing Δ. In the following, the relationship between the positions of the scar fronts and the vortices will be amplified, particularly for do/bo ≤ 6.

It is a well-known fact that an inviscid vortex pair moving along a line normal to the line joining them gives rise to a so-called Kelvin oval. In the regions where the motion

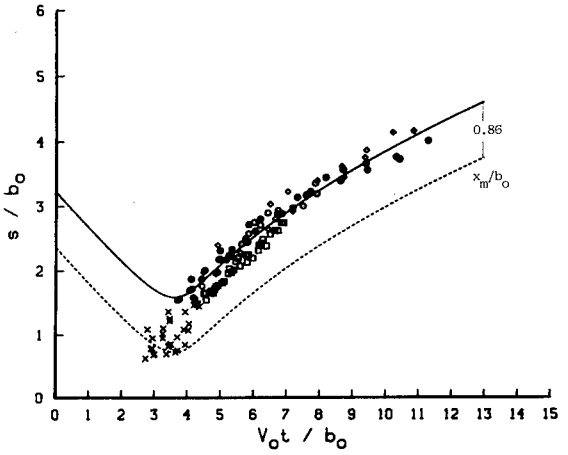


Fig. 14 Relative Position of the Scar Front with Respect to the Maximum Velocity for $d_o/b_o = 4$

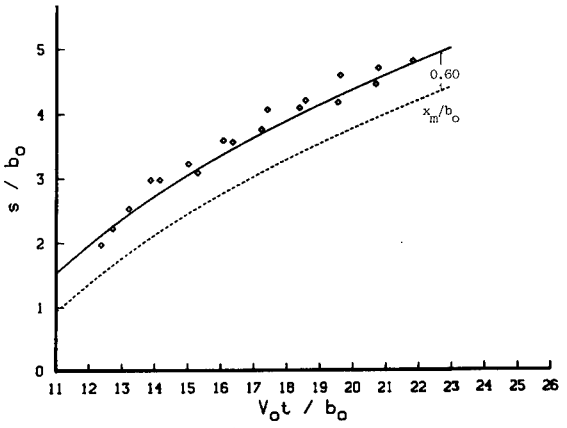


Fig. 15 Relative Position of the Scar Front with Respect to the Maximum Velocity for $d_o/b_o = 10$

of vortices may be regarded as steady or quasi-steady (i.e., subsequent to the formation of the scars or for x/b_o larger than about 2), one of the pair of the trailing vortices and its image encircle a recirculation region in the form of a Kelvin oval. The characteristics of the Kelvin oval are such that the semi-major axis $m/b_o = 1.045$ and the semi-minor axis n/bo = 0.866 [16]. The stagnation points on the Kelvin oval are the points at which the surface strains, resulting from the rapid changes in velocity, are maximum. Thus, one would expect that the scar front will occur at the front stagnation point of the Kelvin oval, particularly when the vortices move as linear vortices and not subjected to large scale instabilities. It has been noted earlier in connection with the discussion of Fig. 14 that a shift of only 0.86 was needed to make the position of the vortices coincide with the position of the scars. It is now evident that the results obtained on the basis of the potential flow analysis and the apparent circulation are in conformity in predicting the position of the scars relative to the vortices, at least for Δ smaller than about 6. The same cannot be said about the rings because the flow cannot be approximated by a steady state and because one can no longer speak of a Kelvin oval.

Special experiments have been carried out in order to determine the relative positions of the scar front and the vortex axis (which corresponds to the position of the maximum velocity). The spacing between them have been determined from photographs and it was found to be equal to 0.86 ∓ 0.05. This result compares exceedingly well with that cited above and provides indirect evidence of the assumptions made regarding the relationship between the vortices, scars and the vortex strengths.

Figure 16 shows the position of the scars, vortices, and the maximum velocity, as deduced from the photographs. Clearly, the position of the vortices is coincident with the calculated position of the maximum velocity and the spatial difference between the position of the vortices and scars is about 0.86.

It was noted earlier that for Δ larger than about 6 or 7, the vortices undergo large scale instabilities: Sinusoidal instability and vortex breakdown. The former has been discussed in sufficient detail in [11]. Here only the observations regarding the occurrence of the vortex breakdown will be noted briefly.

One form of the breakdown followed the bulging and bursting of the vortex core at one or more spots along the vortex trail and remained stationary relative to the ambient fluid. The second form of the breakdown has always started with the development of a U-shaped vortex wrapping around the outside of the core. One or more such breakdowns occurred along the trail either simulataneously

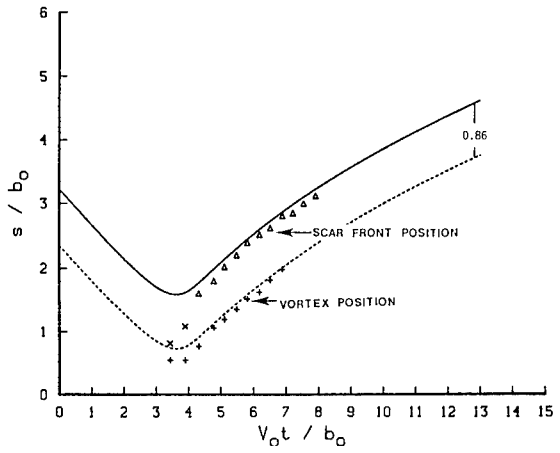


Fig. 16 Comparison of the Measured and Predicted Positions of the Scar Front for $d_o/b_o = 4$ for Delta-2R

or at different times. Each breakdown moved slowly relative to the ambient fluid in a direction away from the model. Strange and Harvey [21] reported similar instabilities in trailing vortices. These observations are in contradiction to those made on single vortices in a tube [2-3]. It appears that much additional work is needed to delineate the characteristics of core bulging and bursting and the evolution of U-shaped instabilities in trailing vortices, (see Figs. 17 and 18).

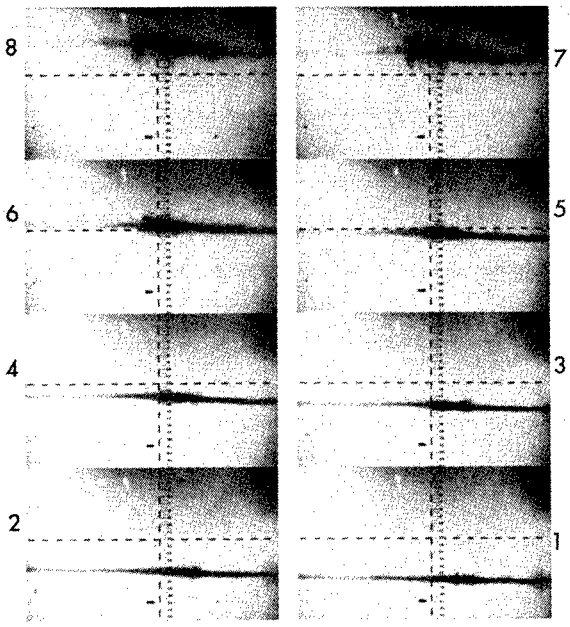


Fig. 17 Evolution of the Core Bulging and Bursting (Note that the Position of the Vortex Breakdown Remains Stationary).

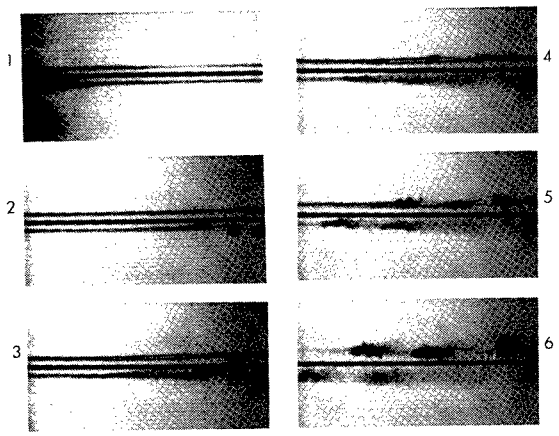


Fig. 18 Evolution of Travelling Breakdowns (Model Moving to the Right and the Breakdown Position Moving to the Left.

CONCLUSIONS

The investigation reported herein warranted the following conclusions:

1. The trailing vortices give rise to surface signatures in the form of striations and scars.

2. The striations come into existence when the vortex pair is at a distance equal to about one initial vortex separation from the free surface.

3. The scars come into existence towards the end of the pure striation phase and when the vortices are at a distance equal to about 60 percent of the initial vortex separation from the free surface.

5. A logarithmic law exists between the normalized separation of the vortices and the normalized time, measured relative to the inception of the striations.

6. The circulation of the vortices decreases slowly at first (prior to the occurrence of scars) and rapidly thereafter.

7. A theoretical model based partly on inviscid flow analysis and partly on the logarithmic law governing the scar-time relationship has shown that the instantaneous position as well as the velocity of propagation of the scars may be predicted with confidence for relative depths smaller than about 6.

8. The formation, the type and the instantaneous position of all surface disturbances are uniquely related to the instantaneous position, velocity, aspect ratio, and the angle of attack of the submerged body.

9. There are two types of vortex breakdowns in a trailing vortex: One due to core bulging and bursting and the other due to U-shaped instabilities.

This research has been supported by the Office of Naval Research through ONR Conract No. 062-776. Special thanks are due D. O. Henderson, W. E. Gray, and Jack Mc Kay for their assistance with the experiments.

REFERENCES

1. Crow, S. C., "Stability Theory for a Pair of Trailing Vortices," AIAA J., Vol. 8, 1970, pp. 2172-2179.

2. Sarpkaya, T., "On Stationary and Travelling Vortex Breakdowns," J. of Fluid Mechanics, Vol. 45, 1971, pp. 545-559.

3. Leibovich, S., "Vortex Stability and Breakdown: Survey and Extension," AIAA J., Vol. 22, 1984, pp. 1192-1206.

4. Gargett, A. E. and Hughes, B. A., "On the Interaction of Surface and Internal Waves," J. of Fluid Mechanics, Vol. 52, 1972, pp. 179-191.

5. Apel, J. R., Bryne, H. M., Proni, J. R., and Charnell, R. L., "Observations of Oceanic Internal and Surface Waves from the Earth Resources Technology Satellite," J. of Geophysical Research, Vol. 80, 1975, pp. 865-881.

6. Maxworthy, T., "Solitary Waves on Density Interfaces," in Waves on Fluid Interfaces, Edited by R. E. Meyer, Academic Press, New York, 1983, pp. 201-220.

7. Nishimura, T., Hatakeyama, Y., Tanaka, S. and Maruyasu, T., "Kinetic Study of Self-Propelled Marine Vortices Based on Remotely sensed Data," in Remote Sensing of Shelf Sea Hyrodynamics (ed. by J. C. J. Nihoul), Elsevier, N. Y., 1984, pp. 69-105.

8. Tombach, I. H., Transport of a Vortex Wake in a Stably Stratified Atmosphere, Aircraft Wake Turbulence and Its Detection, Edited by J. H. Olsen et al., Plenum Press, New York, 1971, pp. 41-57.

9. Barker, S. J. and Crow, S. C., The Motion of a Two-Dimensional Vortex Pair in Ground Effect, J. of Fluid Mechanics, Vol. 82, 1977, pp. 659-671.

10. Peace, A. J. and Riley, N., A Viscous Vortex Pair in Ground Effect, J. of Fluid Mechanics, Vol. 129, 1983, pp. 409-426.

11. Sarpkaya, T., Trailing Vortices in Homogeneous and Density-Stratified Media, J. of Fluid Mechanics, Vol. 136, 1983, pp. 85-109.

12. Sarpkaya, T. and Henderson, D. O., "Surface Disturbances due to Trailing Vortices," Technical Report No. NPS-6984004, March 1984, Naval Postgraduate School, Monterey, CA.

13. Gray, W. E., "Scars and Striations due to Trailing Vortices," MS Thesis, March 1985, Naval Postgraduate School, Monterey, CA.

14. Peltzer, R. D., "Remote Sensing of the USNS Hayes Wake," NRL Memorandum Report 5430, Sept. 1984.

15. Scott, J. C., "Flow Beneath a Stagnant Film of Water: The Reynolds Ridge," J. of Fluid Mechanics, Vol. 116, 1982, pp. 283-296.

16. Lamb, H. (Sir), Hydrodynamics, Dover Publications, New York (6th ed.), 1945, pp. 221-224.

17. Batchelor, G. K., An Introduction to Fluid Mechanics, Cambridge Univ. Press., London, 1967.

18. Craik, A. D. D., "Wind-Generated Waves in Thin Liquid Films," J. Fluid Mechanics, Vol. 26, 1966, pp. 369-392.

19. Squire, H. B., "The Growth of a Vortex in Turbulent Flow," British Aeronautical Research Council, Paper No. 16666, 1955.

20. Govindaraju, S. P. and Saffman, P. G., "Flow in a Turbulent Vortex," Physics of Fluids, Vol. 14, No. 10, 1971, pp. 2074-2080.

21. Strange, C. and Harvey, J. K., "Instability in Trailing Vortices: Flow Visualization Using Hot-Film Anemometry," AGARD Conf. Proc., No. 342, 1983, pp. 4.1-4.11.

DISCUSSION

Terry Brockett,
University of Michigan

The author has presented a wide-ranging investigation of the generation of surface scars and striations by vortex pairs as from a lifting surface. Ships are propelled by screw propellers with similar vortex elements but with more complicated, time dependent geometry. I would like the author to comment on the possibility of similar surface distrubances being generated by the rotating persistant propeller helical vortex system.

James H. Duncan,
Flow Research Company

The photographs show streaks on the free surface that are perpendicular to the axes of the vortices. Have you measured the properties of the streaks and do you have a hypothesis for their origin?

Armin W. Troesch
University of Michigan

The author presented an interesting and informative paper on vortex generated surface disbturbances. In light that the bilge radii on surface ships may act as vortex generators, did you conduct experiments with d_0/b_0 = 0(1) or perhaps d_0/b_0 <1 ? This would be difficult to do since surface waves would also be generated, but does the basic nature of the striations to scars remain the same?

Reply -

The comments and questions of Drs. Brockett, Troesch, and Duncan are very much appreciated. Our experience has shown that the vortex pairs do give rise to scars and striations regardless of their origin (lifting surfaces or screw propellers) and regardless of their proximity to the free surface at the time of their creation. The scars are much closer to the line of motion of the body than the waves generated by the body. Furthermore, the waves did not seem to affect either the occurrence or the subsequent motion of the scars. This is perhaps because of the wide differences in their scales (ship wave length versus Bragg wave length).

We have carried out experiments with d_0/b_0 = 0(1). The basic nature of the surface signatures remained the same, as anticipated by Dr. Troesch. For d_0/b_0 = 1, the surface waves were very small and had no affect on the scars. For d_0/b_0 = 0.5, a standing wave pattern (relative to the lifting surface) was generated. The scars reached the surface almost immediately and rode the waves along the entire length of the towing tank. In another series of experiments, a bi-planer grid (3/8 in x 3/8 in square bars with M = 2.5 in) was towed ahead of the model (at various x/M distances so as to vary the intensity and the integral scale of the turbulence experienced by the vortex pair). At all depths, in particular for d_0/b_0 = 0(1), the scars reached the surface in spite of the turbulence and numerous eddies (between the bars). However, their lifespan was somewhat shorter than those generated in a quiescent medium.

As noted in the paper, the streaks or striations appear abruptly sometime after the passage of the lifting surface as ridges perpendicular to the path of the model. They grow rapidly to a total length of about $2.6b_0$ to $3b_0$. The pure striation phase of the surface condition lasts for a time interval of $DT^* = 0.6$ to 1 where $T^* = V_0 t / b_0$ and V_0 is the initial mutual induction velocity of the vortices. Shortly thereafter, two distinct signatures or 'scars' appear. They are nearly parallel to the model track and run along the tips of the striations. While scars become the dominant features of the free surface, the striations remain in the signature band and stretch more or less randomly in the lateral direction.

The first striation appears when the inclined vortices come near the free surface a distance of about $y_v/b_0 = 1.1$. The fluid ahead of the striation is at rest and the striation front moves along the x-axis with a velocity equal to that of the model. Thus, the striations are a consequence of the surface strains resulting from the velocity gradients in the x-direction. The scars are not parallel and the included angle between them is $2\tan^{-1}(V_0/U)$. The x-component of the velocity of the scar front then gives rise to small surface strains in the x-direction which results in small striations in the scar phase.

Once again, the comments and questions of the discussers are appreciated and it is hoped that the foregoing meets with their approval.

Nonlinear Calculation of Breaking and Non-Breaking Waves Behind a Two-Dimensional Hydrofoil

R. M. COLEMAN,

David W. Taylor Naval Ship R&D Center

Abstract

A finite-difference method is used in conjunction with a numerical mapping technique to compute the two-dimensional unsteady potential flow generated by a submerged hydrofoil in motion below a free surface. Nonlinear boundary conditions are employed for a foil moving horizontally at constant speed and angle of attack. The time-dependent irrotational flow of the incompressible fluid about the hydrofoil is augmented by the solution of an auxiliary potential flow problem used to ensure that the Kutta condition is satisfied at the trailing edge. The time-dependent physical region is transformed into a time-independent computational region made up of the union of rectangular grid segments each with a uniform mesh. Since the geometry of the flow region is not known in advance but is part of the solution, the transformation must be computed simultaneously with the flow field for each time step. Various depths-of-submergence are considered, including those which produce steadily breaking waves. The breaking process is simulated by the application of a pressure distribution on the free surface when the slope reaches a critical value. A comparison of numerical and experimental results shows that an accurate representation of the free-surface flow can be obtained with such a numerical scheme.

I. INTRODUCTION

The energy expended by a body moving in or near a free water surface results in a surface wake which may include both breaking and non-breaking waves. This wake and the associated wave resistance have been the subject of many analytical and experimental studies. While many experiments have dealt with both breaking and non-breaking waves, most of the mathematical/numerical work has focused on the non-breaking free-surface problem. This is true simply because of the difficulties that arise when the air-water interface undergoes large deformations or becomes discontinuous. If large deviations of the free surface from its undisturbed position are to be accurately represented, a fully nonlinear treatment of the free-surface boundary condition is required. New computational tools, such as boundary-fitted coordinates, along with larger and faster computers, have now made the study of these large-amplitude waves feasible. A mathematical/numerical scheme will be able to provide a complete picture of ship-wave phenomena only if the method can account for the effects of breaking waves.

Coleman and Haussling used a finite difference technique in conjunction with boundary-fitted coordinates to calculate large amplitude waves produced by both a submerged circular cylinder [1] and a transom stern hull [2] moving horizontally. The adaptive grid was able to follow the evolution of the free surface up to the point where the forward face of the first wave became vertical and breaking began. A method of applying pressure to the free surface was also investigated in an attempt to simulate breaking, within potential flow theory, by extracting energy from the system [3].

This paper describes the extension of these methods to the calculation of the breaking and non-breaking waves behind a fully submerged hydrofoil moving horizontally at constant speed and angle of attack. A finite difference scheme is used to compute the velocity potential subject to fully nonlinear initial/boundary conditions. In addition, an auxiliary potential equation is solved and used to adjust the circulation around the body in order that the flow at the trailing edge satisfy a Kutta condition. The difficulty of solving this nonlinear problem with a complex geometry is compounded by the fact that the free-surface boundary conditions must be satisfied at the wavy free surface which is not known in advance but is part of the solution. Such geometries are often treated with a rectangular grid using finite-difference formulae for irregular stars at the boundaries. In the present work, a numerical mapping is used to transform the irregular, time-dependent region in physical space onto a regular, time-independent region in computational space made up of the union of several

rectangular grid segments. This mapping is generated by INMESH [4], a computer program developed at DTNSRDC for the creation of boundary-fitted coordinate systems for complicated geometric domains.

Because it is not known in advance whether a particular nonlinear problem will have a steady-state solution, the unsteady problem has been considered. The numerical mapping is recomputed at each time step in order that the finite difference mesh can adapt to the deforming boundaries of the physical region. Steady state results are obtained by progressing in time until the transient effects are no longer significant in the flow region of interest. For depths at which large-amplitude waves are encountered, breaking is simulated by extracting energy from the wave train. This extraction of energy is accomplished by applying a pressure distribution to the front face of the wave when a critical wave slope is reached. The use of such a technique allows the inclusion of the major effects of breaking within a potential flow model, leading to an efficient computer program for hydrofoil analysis.

Duncan [5] has performed extensive experimental studies of the waves generated by a translating two-dimensional hydrofoil moving below a free surface. The computational results are compared with these experimental results as a guide for the development of the methods. In fact, the existence of Duncan's studies for breaking waves was one of the main reasons for the choice of the hydrofoil problem for such an effort.

II. THE FLOW PROBLEM

The flow development due to the acceleration from rest of a cylinder of infinite span in an incompressible fluid bounded above by a free surface and below by a rigid wall is considered. The cylinder has a NACA 0012 shape for its uniform cross section. The fluid is initially at rest and has uniform depth d as defined in Figure 1. The depth of submergence (the distance from the undisturbed free surface to the center of the hydrofoil) is h and the horizontal speed of the foil is u. An (x,y) coordinate system moves with the body and has its origin located at the level of the undisturbed free surface. It is assumed that the flow is irrotational and that the fluid is incompressible and lacks surface tension. It is also assumed that the surface elevation can be described at any time t by specifying y as a single-valued function of x: $y = Y(x,t)$. This assumption is valid only if the free surface remains single valued. In order to accurately calculate the evolution of an overturning wave such as a plunging breaker, a more general free-surface formulation would be necessary. However, since the emphasis here is on steady breaking and non-breaking waves, the simpler formulation is sufficient.

The dimensionless form of the initial/boundary-value problem in the moving reference frame for the free-surface elevation

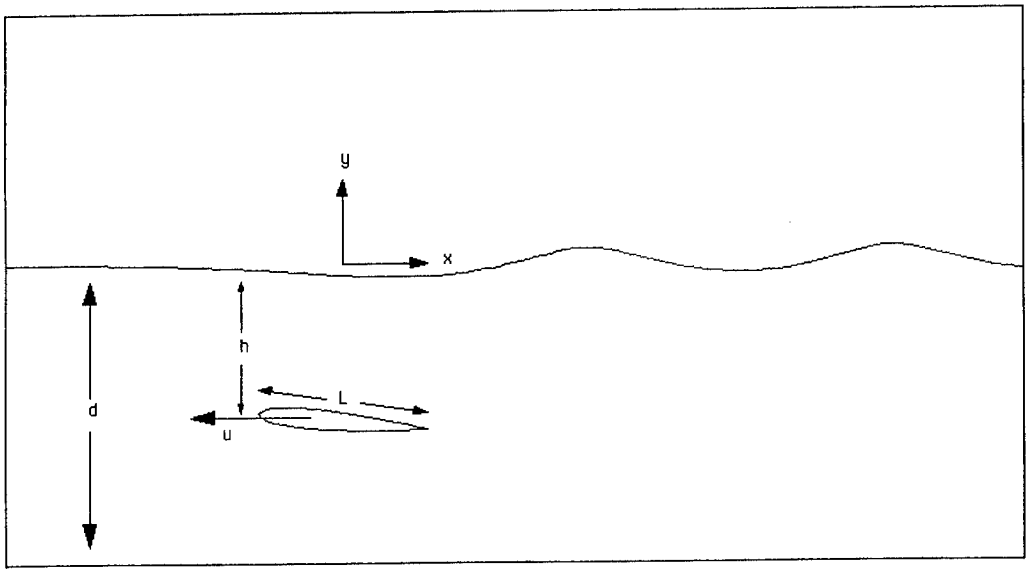


Figure 1: The Flow Regime

Y and potential ϕ for the velocity relative to a frame at rest is the following:

$$\phi_{xx} + \phi_{yy} = 0 \quad -\infty<x<\infty, \quad -d<y<Y \; ; \qquad (1)$$

$$Y_t = [u(t)\phi_x]Y_x + \phi_y \quad \text{at} \quad y = Y; \qquad (2)$$

$$\phi_t = u(t)\phi_x - Y/Fr^2 - p_s - (\phi_x^2 + \phi_y^2)/2 \quad \text{at} \quad y = Y; \qquad (3)$$

$$\nabla\phi\cdot\underline{n} = \begin{cases} 0 & \text{at } y = -d, \\ -u\underline{i}\cdot\underline{n} & \text{at the body;} \end{cases} \qquad (4)$$

$$\phi_x = 0 \quad \text{at} \quad x = \pm\infty; \qquad (5)$$

$$\phi = 0, \quad Y = 0 \quad \text{at} \quad t = 0. \qquad (6)$$

The subscripts x, y, and t denote differentiation. The characteristic length and velocity scales in the dimensionless quantities are L, the chord length of the foil, and U, its final speed. The Froude number is $Fr = U/(gL)^{1/2}$, where g is the gravitational acceleration. The unit normal vector to a boundary is $\underline{n}$, and $\underline{i}$ is a unit vector in the x direction. The pressure at the free surface is denoted by p_s.

In general, the velocity potential will not represent a flow which satisfies the Kutta condition that flow separation occur at the trailing edge. To ensure that the flow satisfies such a condition, an auxiliary potential equation is solved and used to adjust the circulation around the foil so that separation occurs at the proper location.

Solution of the initial/boundary-value problem for the auxiliary potential, ϕ', is carried out simultaneously with the solution for ϕ on the same physical region. For purposes of producing a solution to the Laplace equation that represents a circulation of unity around the foil, an arbitrary cut, R, is made in the physical region extending infinitely far downstream from the trailing edge as shown in Figure 2. A jump in the value of ϕ' equal to 1.0 is enforced across this cut with R^+ representing the upper portion and R^- the lower. The formulation of the initial/boundary-value problem for ϕ' is as follows:

$$\phi'_{xx} + \phi'_{yy} = 0 \quad -\infty<x<\infty, \quad -d<y<Y; \qquad (7)$$

$$\nabla\phi'\cdot\underline{n} = 0 \quad \text{at } y=-d \text{ \& body surface;} \qquad (8)$$

$$\phi'_y = 0 \quad \text{at } y = Y; \qquad (9)$$

$$\phi'_x = 0 \quad \text{at } x = \pm\infty; \qquad (10)$$

$$\phi'\Big|_{R^-} - \phi'\Big|_{R^+} = 1.0 \quad \text{on R;} \qquad (11)$$

Note that ϕ' is a function of time because of the time dependence of the free surface.

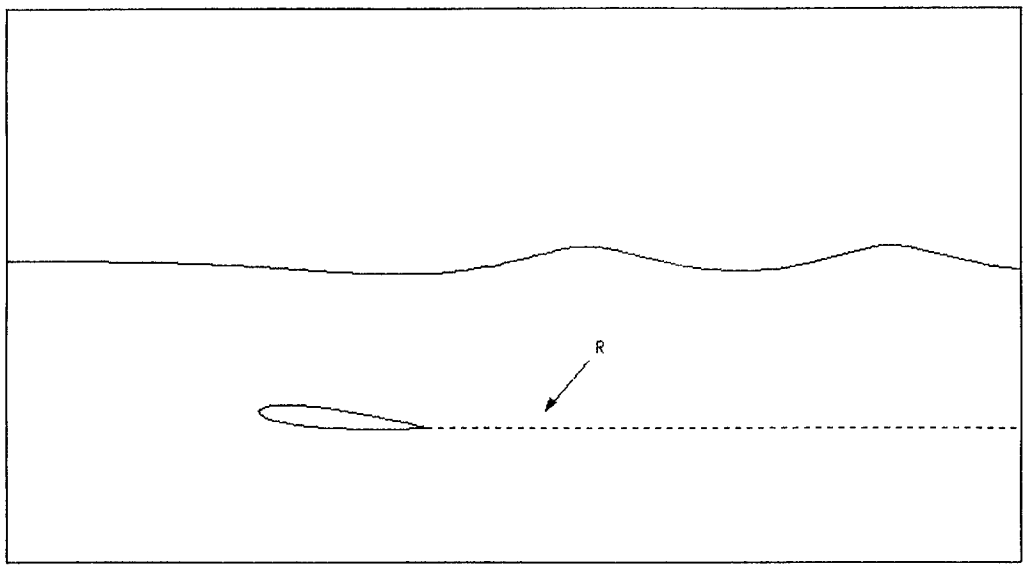


Figure 2: The Flow Regime with Cut

The total potential, Φ, can be found as the sum

$$\Phi = \phi + C\phi' \qquad (12)$$

where the constant C is calculated to provide the correct amount of circulation needed to make the upper and lower velocities at the trailing edge equal. Thus,

$$C = (\phi_u - \phi_\ell)/(\phi'_\ell - \phi'_u) \qquad (13)$$

where the subscripts u and ℓ indicate differentiation along the upper and lower surfaces of the trailing edge respectively. Thus, the free surface conditions for the combined problem become

$$Y_t = [u(t)-(\phi_x+C\phi'_x)]\, Y_x+\phi_y \qquad (14)$$

$$\phi_t+(C\phi')_t = u(t)(\phi_x+C\phi'_x)-Y/Fr^2-p_s \qquad (15)$$
$$-[(\phi_x+C\phi'_x)^2+\phi_y{}^2]/2 + \phi_y Y_t$$

In equation (15) the local time derivative has been replaced by the derivative following the fluid motion and this accounts for the appearance of the final term.

At all depths of submergence the hydrofoil accelerates uniformly from rest to its final speed during one unit of dimensionless time. That is

$$u(t) = \begin{cases} 0 & t<0 \\ t & 0<t<1 \\ 1 & 1<t \end{cases} \qquad (16)$$

The surface pressure is considered to be atmospheric ($p_s = 0$) except when pressure is applied to the surface to simulate wave breaking.

III. METHOD OF SOLUTION

This section presents an outline of the numerical method used to solve the initial/boundary-value flow problem. Details can be found in the previous paper by Haussling & Coleman [3].

To simplify the numerical solution of the problem, the time-dependent physical region in (x,y) space (Figure 2), cut off suitably far upstream and downstream, is transformed to a time-independent computational region in (ξ,η) space composed of 13 rectangles, as shown in Figure 3. These rectangles are overlaid with a uniform mesh and mapped onto sections of grid in the physical region. The sides of the grid segments in computational space are joined together so as to achieve the desired distribution of corresponding grid lines in the physical space seen in Figure 4.

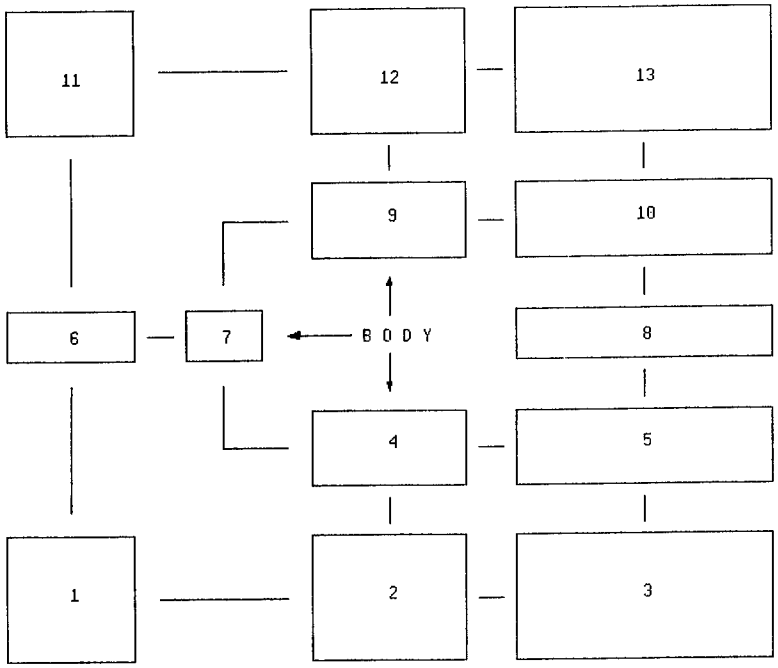


Figure 3: Segmented Computational Region

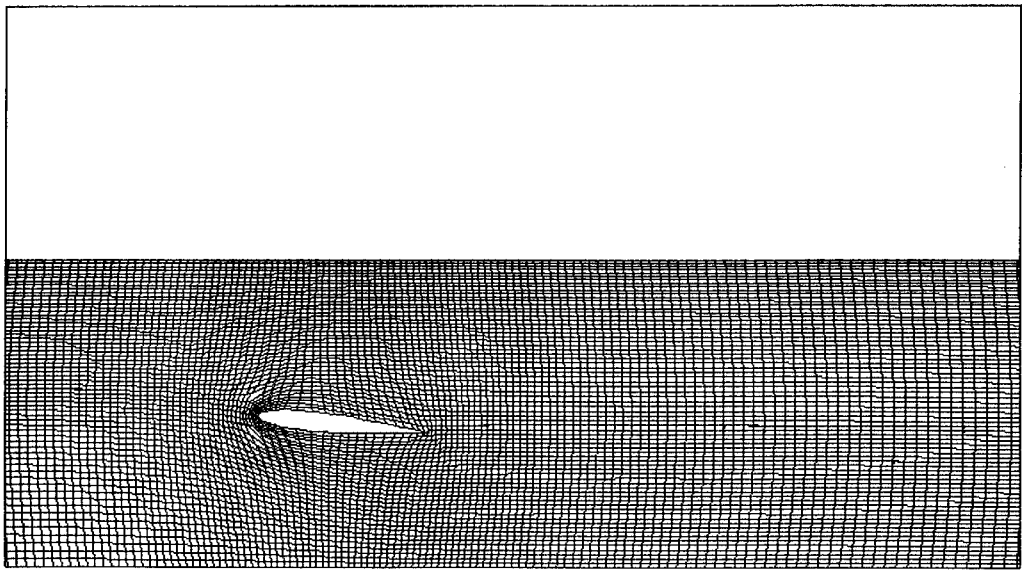


Figure 4: Physical Region Near the Foil at t = 0

Note that this grid has coordinate lines wrapping around the body yet has a more rectangular nature near the outer boundaries. The foil is mapped onto the indicated sides of segments 4, 7, and 8, the free surface to the upper sides of 11, 12, and 13, and the bottom of the fluid to the lower sides of 1, 2, and 3. The upstream boundary is transformed onto the left sides of segments 1, 6, and 11, the downstream boundary onto the right sides of 3, 5, 8, 10, and 13, with the cut R being mapped onto the center horizontal grid line in segment 8.

The INMESH [4] computer program was used to create this boundary-fitted coordinate system. INMESH is not restricted to certain predetermined mapping configurations and therefore can be used to produce many different grid systems for a specific physical problem. This particular configuration was selected as one which is well-suited to the geometry of a hydrofoil moving in a finite-depth fluid near a free surface. This mapping allows grid points to be concentrated in the "C" portion of the mesh close to the foil and directly downstream from its trailing edge. More points may easily be placed in this region by increasing the number of grid lines in segments 4, 5, 7, 9, and 10. In addition, more coordinate lines can be added to the area near the free surface (segments 11, 12, and 13) for better resolution in this critical region.

Through the use of INMESH, the desired transformation, represented by

$$\xi = \xi(x,y,t) \text{ and } \eta = \eta(x,y,t) \qquad (17)$$

is found as a solution to the Poisson generating system

$$\begin{aligned} &\xi_{xx} + \xi_{yy} = P(\xi,\eta,t) \\ \text{and} \quad &\\ &\eta_{xx} + \eta_{yy} = Q(\xi,\eta,t) \end{aligned} \qquad (18)$$

subject to appropriate boundary conditions. The source functions P and Q are specified such that the resulting (ξ,η) coordinate system has spacing that is suitable for the numerical calculations.

For computational purposes, the generating system (18) and the flow problem (1)-(11) are transformed to the (ξ,η) space. Thus the flow problem is solved using a time-dependent (ξ,η) coordinate system which at t = 0, when the fluid is undisturbed, appears as in Figure 4. As stated earlier, the domain of integration in the computational plane is replaced by a uniform network of grid points so that both the transformation and flow problems can be solved numerically. The differential equations are then replaced by difference equations involving values of the dependent variables at these grid points. The control functions P and Q of Equations (18) are used to keep the relative spacing of the grid lines in the physical region constant throughout the calculations even though the free surface undergoes large deformations. Figure 5 shows a finite-difference mesh with a developing free surface for one of the cases considered in the following section.

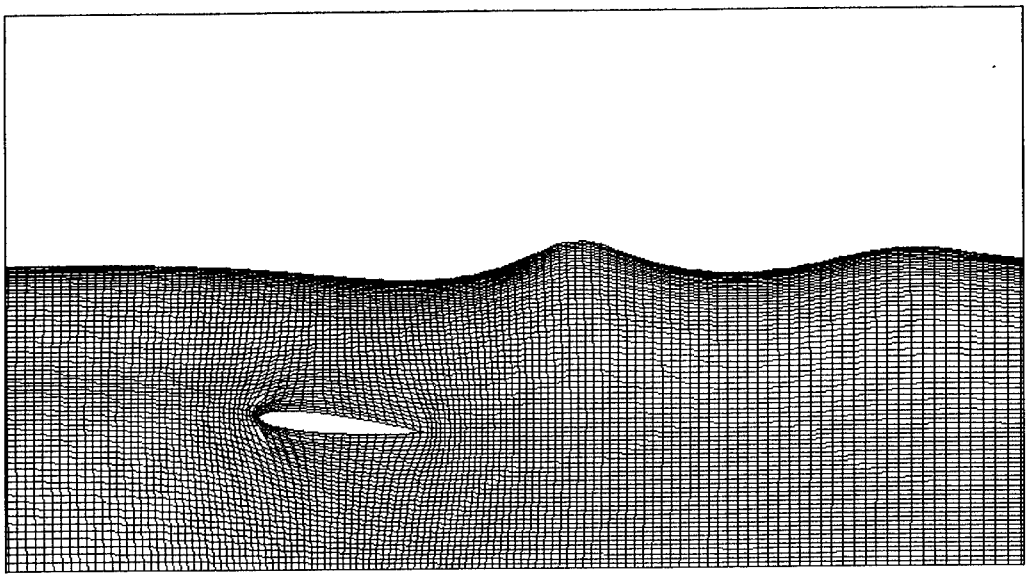


Figure 5: Finite-Difference Mesh With Developing Free Surface

The flow computation is readily performed on the segmented computational region since the same subroutines used to update the mesh at each time step are also used to solve the potential equations.

Euler's modified method of time differencing is used to replace the transformed versions of the combined free-surface boundary conditions (14) and (15) with a suitable implicit marching scheme. The marching equations along with the potential and grid generation equations are used in a combined iterative procedure to solve the unsteady problem.

Numerical filtering was used to eliminate the instability which is usually present in such marching methods for nonlinear water wave problems. Such filtering techniques have been used successfully by the author [1,3,4] to overcome difficulties encountered in the calculation of the development of large amplitude waves. After each advancement of Y and Φ, new values of these quantities are computed according to the formula

$$f_i = [-f_{i+2}-f_{i-2}+4(f_{i+1}+f_{i-1}) +10f_i]/16 \qquad (19)$$

In past work this filtering procedure has been applied at most once between time steps to stablize the calculations. However, as discussed below, extra applications of the smoothing are needed when the surface pressure is applied to simulate breaking. The smoothing was used with care so that it did not change the basic character of the free surface but only removed the unwanted oscillations which gave rise to numerical instability.

The program was written and debugged on an Apollo microcomputer and then was transferred to a Cray XMP mainframe. The code was slightly altered in order to take advantage of the vector processing capabilities of the Cray. Four depths of submergence for the hydrofoil were studied corresponding to those considered by Duncan [5]: h = 1.29, 1.16, 1.03, and 0.95. In all cases the draft-based Froude number was Fr = 0.568 and the angle of attack was 5 degrees. The upstream and downstream boundaries were located a distance of about five chord lengths from the body. The computational region contained about 13,500 points requiring 425K words of memory on the Cray XMP. The free-surface flow in the neighborhood of the foil reached a steady state condition in an average of about 30 minutes of CPU time after about 800 time steps of 0.05.

IV. RESULTS

The experimental studies by Duncan included two-dimensional wave profiles produced by a NACA 0012 shape having a chord length of 20.3 cm moving at 80 cm/s with angle of attack 5 degrees. The foil remained at a fixed distance, 17.5 cm, from the bottom of the towing tank with the depth-of-submergence of the body being determined by the water level in the tank which altered the distance from the foil to the free surface. Duncan states that although the flow field around the foil was influenced by the floor of the tank, the wave dynamics were not significantly affected by the bottom. He also states that the wave slopes in the tank would probably be the same as those produced in an infinitely deep fluid. The numerical studies attempt to duplicate the experiment as accurately as possible. Each numerical case is referred to by its depth of submergence h. (Figure 1)

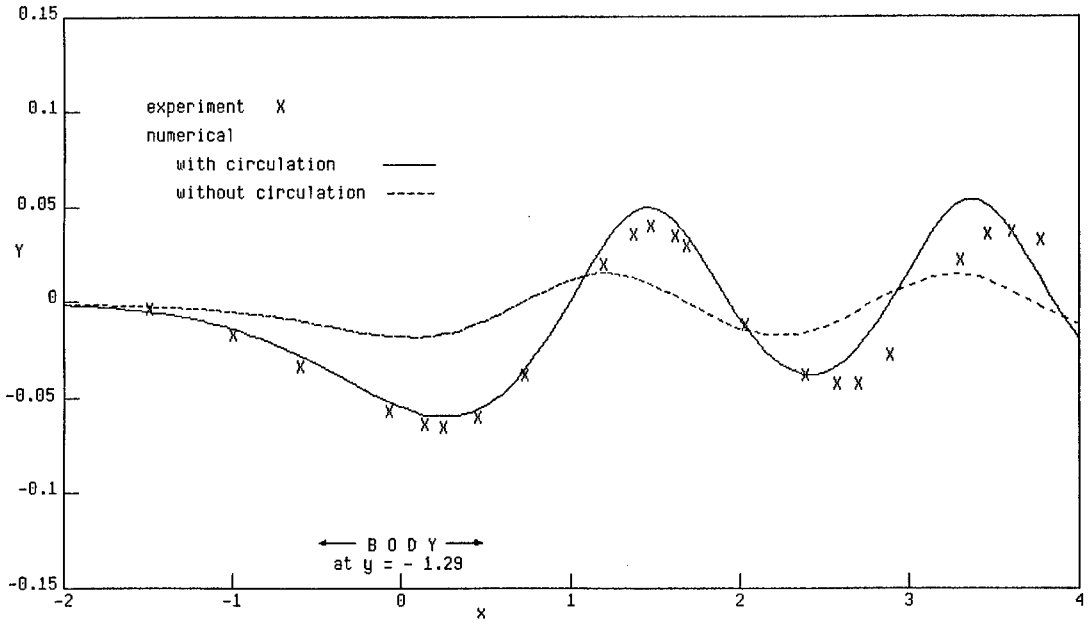


Figure 6: Measured and Computed Wave Profiles, h = 1.29

h = 1.29

The greatest depth of submergence was considered first to test the numerical method on a case which produced only small non-breaking waves. Two separate subcases were considered for this depth: 1) a calculation without circulation (C = 0 for all time) and 2) a calculation with circulation (C determined iteratively as the flow evolves).

Figure 6 provides a comparison of the experimental results with the steady-state wave profiles both with and without circulation. It is evident from Figure 6 that the potential flow solution without circulation does not produce an accurate representation of the free surface. The computed wavelength, λ, agrees very well with the linear theory prediction of 2.03 for this Froude number, even though the computed amplitude is less than half of the experiment. When the auxiliary solution is added to introduce circulation into the calculations, the computed amplitude increases until it is slightly greater than the measured values while the computed wavelength is shortened. The amount of circulation needed for this depth is determined to be C = -0.485, with the minus sign indicating a clockwise direction around the body. The value of C was approximately the same for all cases considered indicating that varying the depth of submergence of the foil has little effect on the amount of circulation needed to satisfy the Kutta condition. Von Kerczek and Salvesen [6] estimated that nonlinear effects would reduce the wavelength to

$$\lambda = \lambda' \, (1 - (A/Fr^2)^2),$$

where A is the crest-to-trough amplitude of the linear waves and λ' is the linear wavelength. This shortening of the wavelength was verified by Salvesen and von Kerczek [7] in experiments dealing with flow past a submerged foil. Using the computed amplitude of A = 0.087 at the second wave downstream, we obtain an estimated wavelength of λ = 1.88 from the perturbation theory. This value can be compared to the numerical wavelength of 1.91, estimated from the first two peaks, and the longer experimental wavelength of 2.13.

The effects of adding circulation to the computations can be seen in Figures 7 and 8 which display computed velocity vectors at steady state near the trailing edge of the hydrofoil. In Figure 7, the solution without circulation shows a definite upward velocity in the fluid near the trailing edge, indicating that the flow turns the corner rather than separating there. The velocity vectors computed with circulation in Figure 8 indicate a better balance between the upper and lower velocities resulting in a flow field which is in better agreement with the physical one.

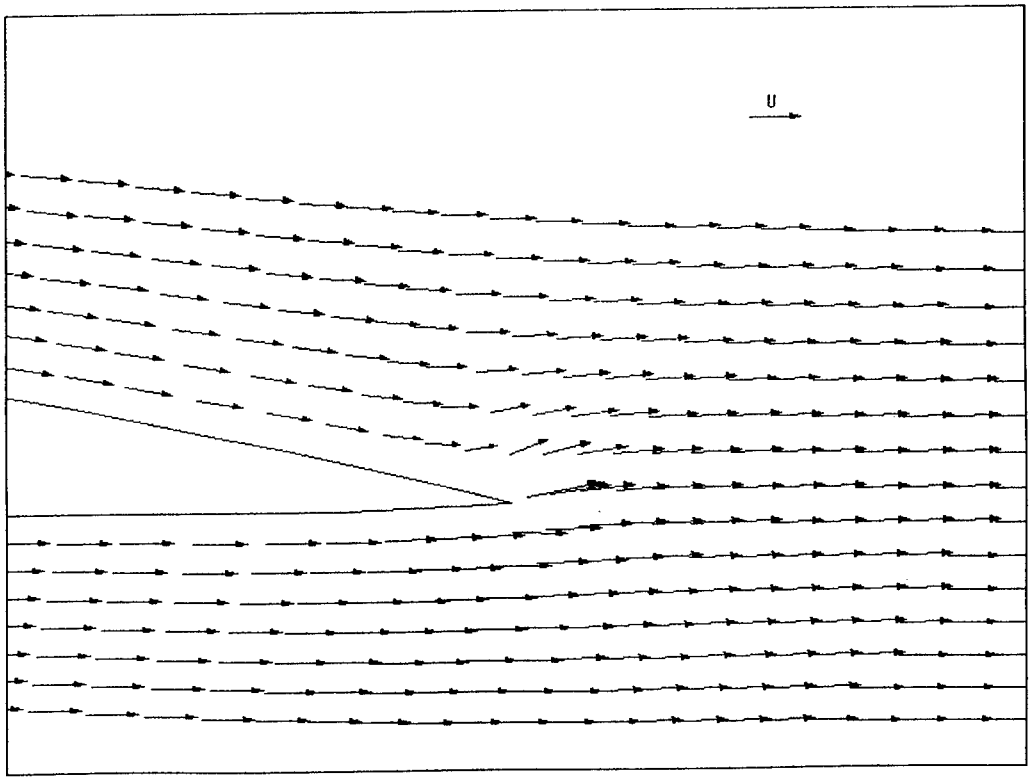


Figure 7: Velocity Vectors Computed Without Circulation, h = 1.29

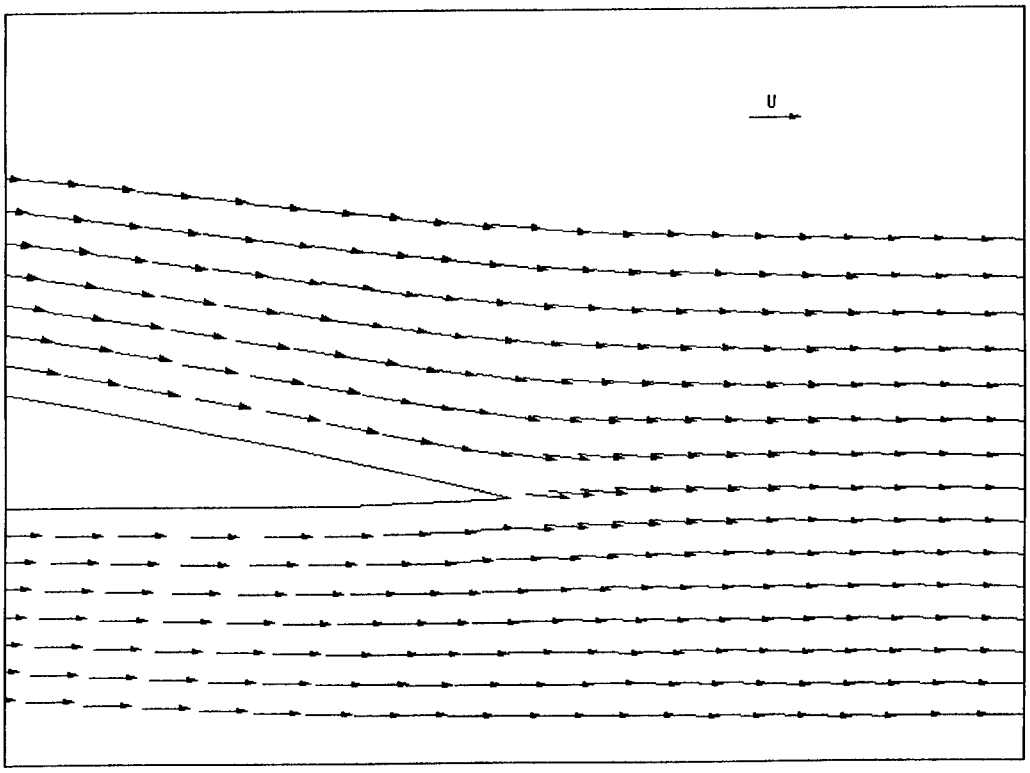


Figure 8: Velocity Vectors Computed With Circulation, h = 1.29

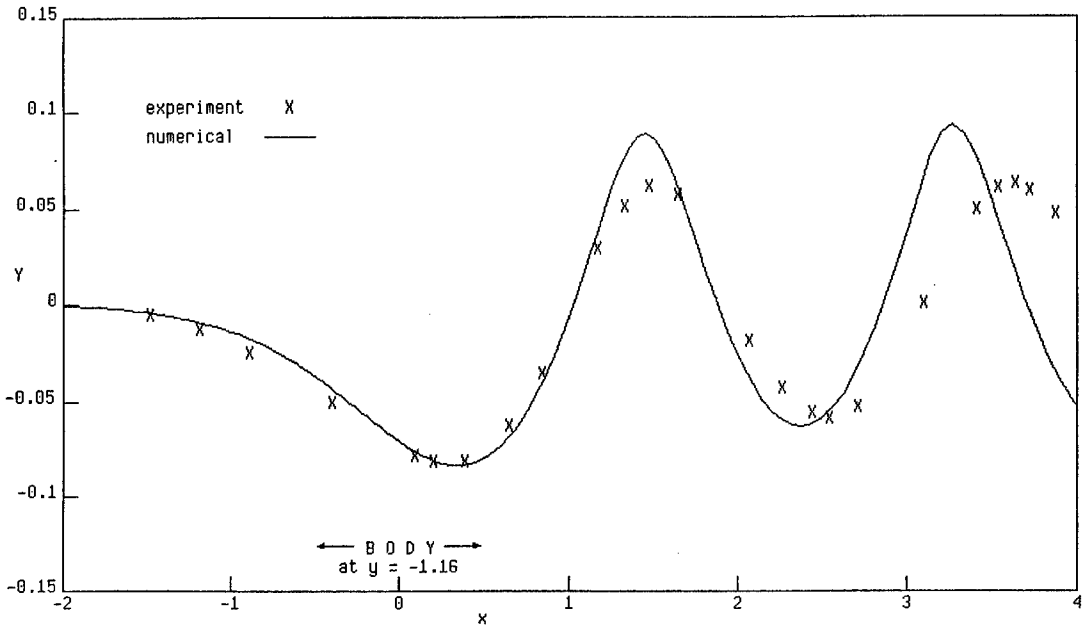


Figure 9: Measured and Computed Wave Profiles, h = 1.16

h = 1.16

The measured and computed steady-state wave profiles for this submergence are given in Figure 9. The experiment yields a wavelength of $\lambda = 2.18$ with an amplitude of $A = 0.12$, while the numerical results give $\lambda = 1.85$ with $A = 0.15$. Both the measured and computed wave profiles show a steeper free surface than for h = 1.29, but with no signs of breaking.

h = 1.03

At this depth the experiment did not produce spontaneous breaking but the computer program would not run until a steady-state condition was achieved. Figure 10 shows the development of the computed free surface as it evolves to a configuration beyond which the numerical scheme cannot proceed. Unfortunately, the calculations cannot be carried out beyond t = 10.0 because of the limitations of the mathematical/numerical model. The assumption of a single-valued free surface means that accuracy deteriorates as the surface slope increases. It seems that the computations predict wave breaking for a somewhat deeper submergence than observed in the experiments which might reflect the approximate nature of the inviscid flow model.

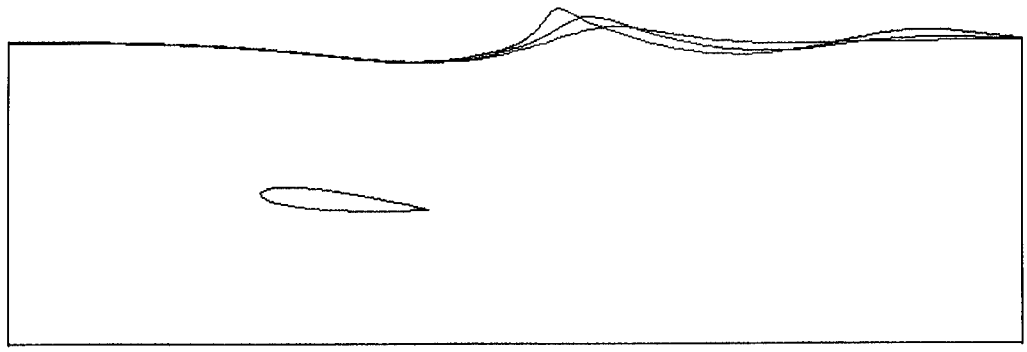


Figure 10: Computed Free-Surface Development, h = 1.03

The use of a surface pressure distribution was investigated as a method of simulating the breaking process for computational purposes. The pressure distribution used had the following form:

$$p_s(x,t) = \begin{cases} K\Phi_n(Y_x - M) & Y_x > M \\ 0 & \text{otherwise} \end{cases} \qquad (20)$$

where K is a constant. This pressure is thus automatically applied whenever the surface slope exceeds M. Because the pressure is proportional to Φ_n, the velocity normal to the free surface (positive away from the water), it always performs negative work on the fluid and therefore removes energy from the flow. Such a pressure distribution can be viewed as a crude parameterization of the breaking process which serves to remove energy from the basic flow and reduce wave heights. This pressure distribution is similar to that used by Haussling & Coleman [3] to suppress the spontaneous wave breaking behind a translating circular cylinder.

The slope used to initiate the surface pressure was based upon Duncan's finding that the free surface could achieve a maximum angle of inclination of about 17 degrees before breaking occurred. Accordingly, the value of M used in the numerical scheme was 0.3 in an attempt to prevent the free surface from exceeding the critical angle. The steady-state wave heights computed using M = 0.3 and K = 1.0 are shown in Figure 11.

The use of this pressure distribution led to a free surface which was not smooth in the area where the slope was the greatest, i.e., the forward face of the first peak. This was most likely due to the fact that the magnitude of the pressure at a point on the free surface depends on only the local slope at that point and no global smoothness criteria is enforced. Any irregularity in the boundaries, however, quickly caused the computations to break down so that care had to be taken to ensure that the flow variables at the free surface were sufficiently smooth at all times. Accordingly, five applications of the filtering formula discussed above were used to smooth the potential and the y-coordinates of the mesh on the free surface and two grid lines into the fluid. The addition of this pressure to the calculations reduces the amplitude of the first peak and forces the second peak downstream slightly yielding computed results that agree well with the experiment.

h = 0.95

At this depth the experiment produced non-breaking waves unless the surface was disturbed, in which case steady breaking occurred. Since the body is closer to the surface than in the previous case, the numerical simulation, as expected, predicted breaking and could not achieve a steady state without surface pressure. Figure 12 compares the breaking wave profile taken from the experiment with the computed free surfaces at steady state when a surface pressure (with smoothing) is used to simulate breaking. The computed wave profile shown in Figure 12 was computed using a pressure with M = 0.1 and K = 6.0.

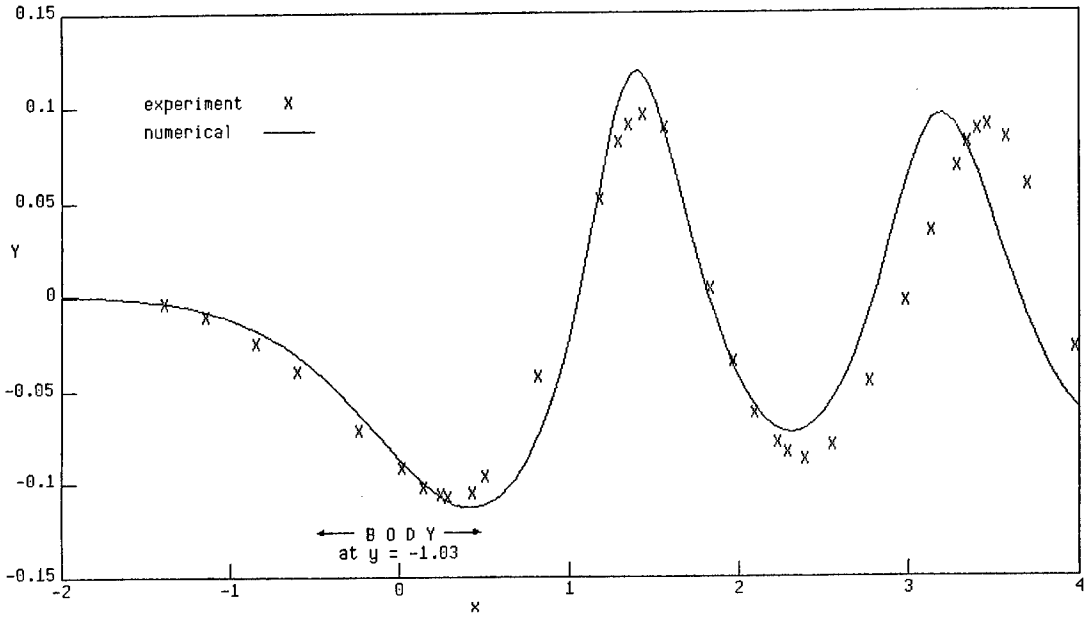


Figure 11: Measured vs. Computed Wave Heights, h = 1.03

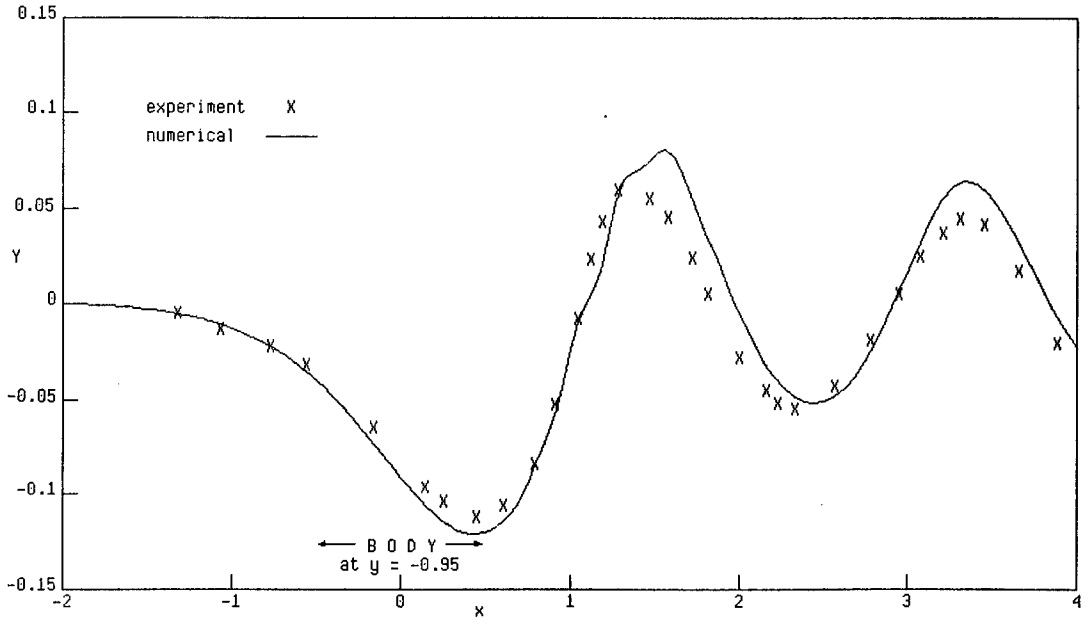


Figure 12: Measured vs. Computed Wave Heights, h = 0.95

Even though a slope of M = 0.3 is the maximum that can be obtained without breaking, Duncan also determined that the slope is often much smaller during the breaking process. The slope of M = 0.1 at which the pressure was applied was based on Duncan's finding of an angle of inclination of 6 degrees as breaking occurs at this depth. The value of K was obtained empirically and appears to be the maximum value that can be used in this case. Application of the pressure on the forward face of the first peak retards its growth which in turn reduces the amplitude of the following wavetrain to a height which is in good agreement with the experiment.

For experimental cases which produced both breaking and nonbreaking flow states, Duncan found the wave resistance on the foil to be essentially independent of whether breaking occurred. Thus, if an automatic method of simulating breaking can be developed within potential flow theory, a steady wavetrain behind the breaker could be calculated giving a good estimate of the wave resistance provided that the body is not too close to the breaking region. Much work remains to be done in order to develop such a method. Perhaps breaking could be predicted numerically by the finding of a slope exceeding the maximum value of 0.3 (17 degrees) at which time a pressure distribution would be used to allow the computations to continue to steady state. Since the angle of inclination of the breaking wave varies with depth and is not known a priori, an accurate wave profile may not be obtainable using a breaking simulation technique based on free-surface slope. If, however, a good approximation of wave resistance on the body does not depend on an accurate wave profile, then a crude simulation of the breaking process may be sufficient for many applications.

V. CONCLUSION

The results discussed in the previous section indicate that the computation of an accurate potential flow solution to the translating hydrofoil problem requires that a Kutta condition be satisfied to insure that flow separation occurs at the trailing edge. These results also illustrate the transition from deep submergence when nonlinear free-surface effects are small to shallow submergence when large-amplitude waves develop and breaking occurs.

For submergence depth h = 1.29 both measured and numerical results yield only non-breaking waves with the numerical amplitude slightly larger and the numerical wavelength slightly shorter than the experimental values. For h = 1.16 both the experiment and the numerical simulation show steeper steady-state waves with no breaking. At a depth of h = 1.03, the experiment produces a steady non-breaking wave train while the computations cannot be continued to steady state unless energy is removed by the application of a pressure distribution. Such removal of energy can be viewed as a method of simulating breaking so that the computations can proceed to a steady-state condition. If the pressure is applied where the slope of the free surface exceeds 17 degrees (the maximum experimental slope which can be achieved without breaking), the numerical calculations yield a steady-state wave profile in good agreement with the

experiment. For h = 0.95 the experiment produces steady breaking if the surface is disturbed while the computed free surface reaches a breaking configuration spontaneously. If the pressure is applied in this case at about 7 degrees (the experimental slope of the breaker), good agreement with the measured wave profile for the breaking case is found.

In order to compute steady breaking using an inviscid flow model, some method of extracting energy from the flow, such as the application of a surface pressure, is necessary. It remains to be determined how to correctly apply a pressure distribution to the free surface to obtain a good representation of the breaking region and the downstream wavetrain. However, Duncan's experiments indicate that breaking may have little effect on wave resistance for a submerged body not too near the breaking region. It may be possible, therefore, to use inviscid theory to obtain a good estimate of wave resistance from a steady-state solution which does not always provide an accurate wave profile.

VI. ACKNOWLEDGMENTS

The author wishes to thank Dr. L. Kurtz for his contributions in the original formulation of the flow problem. The author also acknowledges with gratitude the many useful discussions with Dr. H. Haussling whose encourgement made this study possible. This work was supported by the Numerical Ship Hydrodynamics Program at the David W. Taylor Naval Ship Research and Development Center. This program is jointly sponsored by the Independent Research Program at DTNSRDC and the Fluid Mechanics Program of the Office of Naval Research, Work Unit # 4321001.

REFERENCES

[1] Haussling, H.J. and R.M. Coleman, "Finite-Difference Computations Using Boundary-Coordinates for Free-Surface Potential Flows Generated by Submerged Bodies," Proc. 2nd Int. Conf. Numerical Ship Hydrodyn., University of California, Berkeley, pp. 221-233 (1977).

[2] Coleman, R.M. and H.J. Haussling, "Nonlinear Waves Behind an Accelerated Transom Stern," Proc. 3rd Int. Conf. Numerical Ship Hydrodyn., Palais des Congres, Paris, France, pp. 111-118 (1981).

[3] Haussling, H.J. and R.M. Coleman, "Nonlinear Water Waves Generated by an Accelerated Circular Cylinder," J. Fluid Mech., Vol. 92, Part 4, pp. 767-781 (1979).

[4] Coleman, R.M., "INMESH: An Interactive Program for Numerical Grid Generation", Report DTNSRDC-85/054 (1985).

[5] Duncan, J.H., "The Breaking and Non-Breaking Wave Resistance of a Two-Dimensional Hydrofoil," J. Comp. Phys., Vol. 126, pp. 507-520 (1983).

[6] von Kerczek, C.H., and N. Salvesen, "Numerical Solutions of Two-Dimensional Nonlinear Wave Problems," ONR 10th Naval Hydrodynamics Symposium, Cambridge, MA, pp. 649-663 (1974).

[7] Salvesen, N., and C.H. von Kerczek, Numerical Solution of Two-Dimensional Nonlinear Body-Wave Problems," Proc. 2nd Int. Conf. Numerical Ship Hydrodyn., David W. Taylor Naval Ship Research and Development Center, Bethesda, Md., pp. 279-293 (1975).

DISCUSSION

James H. Duncan,
Flow Research Company

When the depth of submergence of the hydrofoil is small, the momentum flux in the following wave train becomes so large that it can not be convected by the potential flow. In experiments, the wave breaks and the excess momentum in the potential flow appears in the turbulent wake of the breaker. In the calculations, you have used a surface pressure distribution to remove this excess momentum from the flow. The experiments include measurements of the breaker geometry and the momentum deficit in the wake. Thus, it would be possible to compare the pressure imposed in the calculations to the pressure exerted by the weight of the breaker in the experiments and the force imposed in the calculations to the momentum defect of the wake in the experiments. Are you considering making any of these comparisons?

Reply -

We hope to use our computer code to make a more complete study of large amplitude free-surface waves in order to develop a numerical model of the breaking process that could be useful in the design of naval vehicles. This study would contain a detailed comparison of experiments and numerical simulations, including loss of energy due to the presence of the breaker and the effect of breaking on the wave resistance of the body. One step in this investigation might be to impose a surface pressure based on your measurements to see if the present technique produces a breaker geometry similar to that found in the experiments. On the other hand, it remains to be seen how much an accurate prediction of wave resistance depends on an accurate breaker geometry.

K. Mori,
Hiroshima University,

According to the stability analysis, the pressure gradient in the vertical direction is primarily importance and a critical condition for the onset of breaking. I wonder about the introduction of a pressure on the free surface to continue the computation and to make a flow field without breakers. In other words, your computation with an imposed pressure may not always simulate waves with breakers.

Reply -

As long as the pressure is applied so that it does positive work on the water, it will simulate the extraction of energy from the flow by the wave breaking. As indicated in the paper, application of this pressure may result in a wave profile that is not accurate unless the proper pressure is applied in manner which may not be known *a priori*. However, it is our belief that such a numerical scheme can produce a good estimate of important quantities such as wave resistance for a body not too near the breaking region even though the wave heights are less than accurate.

Erik C. Tiemroth,
Ship Research Incorporated

I thank the author for his interesting paper. I think it would add greatly to the paper if the author would give some discussion of his selection of the finite-difference method for solving the boundary value problem over competing methods. It seems to me that it would be advantageous to use a boundary element method because these methods only require discretization of the one-dimensional boundary rather than the entire two-dimensional domain. The number of discretization points will, of course, grow quadratically for the finite-difference method as grid size decreases and/or domain size grows, white the number of points will grow only linearly for boundary methods - an important advantage. Boundary methods only directly provide the solution on the boundaries, however, information about the interior region can always be obtained for potential problems using Green's theorem. While it is true that the use of the Green theory detracts from the previously touted efficiency of the boundary methods, it is generally unnecessary to use it much since one is usually primarily interested in the flow at the boundaries. If an interior method does offer advantages, why not use the finite-element method, since the complicated boundary fitted coordinate system which must be computed at each time-step is unnecessary in the finite element method?

Figure 6 certainly illustrates that incorrect treatment of circulation requirements can lead to large errors. I think it should be pointed out that the transient results, such as figure 10, do not include the effects of the starting vortex or the subsequent vortex shedding that is required by Kelvin's theorem when the circulation around the foil is changed. Thus, I suspect that the transient results predicted by the method will generally be less accurate than the steady results.

Finally, I would like to ask: what boundary conditions were used on the upstream and downstream boundaries and were variations of the mesh size and extent made to ascertain the discretization error?

Reply -

Whether boundary-integral methods are superior to space discretization methods is not a simple question and our experience with both verifies this. The finite-difference method was selected as the solution technique for two reasons: 1) past success of the method due to its rather straightforward use for such water-wave problems with a body present, and 2) the desire to sudy details of the flow in the interior of the region even though the boundary shape may may not be modelled accurately due to the presence of breaking waves. In order to solve the free-surface problem with fully nonlinear boundary conditions, the discretization of the physical region must take place concurrently with the solution of the flow field since the shape and location of the boundary is not known in advance but is part of the flow solution. If an unsteady approach to the problem is taken, a new grid must be obtained as the flow evolves regardless of whether a finite-difference method or finite-element method is used. I have not seen much in the way of finite-element calculations for time-dependent regions. One great advantage of the boundary-fitted

coordinates/finite-difference scheme is the automatic regridding of the flow regime as the boundaries deform. The calculation of new coordinate systems during the time-stepping is a small part of the computations since the shape of the free surface changes very little from time step to time step. In this paper, we use an unsteady approach to obtain a steady-state solution without attempting to ensure the accuracy of the transient effects due to the abrupt start-up of the foil. Wall conditions are imposed at both the upstream and downstream boundaries. Several numerical experiments were performed in which the mesh size and extent were varied. These results were considered in chosing the grid used for the final computations in order to provide an accurate solution to the problem using a reasonable number of points.

Ronald W.Yeung,
University of California,

I want to congratulate the author for devising a rather effective technique of inhibiting the formation of breaking waves in the numerical solution. Introduction of an empirical, and to some extent artificial, pressure distribution does raise the question that numerical modeling requires an *a priori* knowledge of some empirical parameters.

I would also like to comment on that the present treatment of the Kutta condition appears to have ignored the dynamic pressure associated with the term in Euler's integral. This unsteady term leads to the shedding of a trailing vortex sheet whose jump in potential varies spatially over the sheet. It is not clear to what extent the proper inclusion of the sheet may affect the final results. Nevertheless, in a complete unsteady formulation the term should be included and is in fact leading order in linearized theory. Can the author comment on this point?

Reply -

Our objective in this study of the translating hydrofoil was to numerically reproduce both the steady breaking and steady nonbreaking waves seen in the experiment. The unsteady approach that we take does not provide an accurate model of the vortex shed by the body due to its abrupt start from rest. To satisfy the Kutta condition, we make the fluid velocity on the lower surface of the trailing edge the same as that on the upper surface. This is valid only for steady flow and is equivalent to equal pressure on the upper and lower surfaces at steady-state. A proper unsteady treatment of the problem should take into account the time-dependence of the trailing vortex sheet to provide a complete picture of the developing flow. Nevertheless, the steady-state solution should not be affected by this transient disturbance after it has moved off downstream. The transient nature of this vortex is verified by the rapid convergence to a steady value of the time-dependent variable C which is a computed quantity used to control the amount of circulation added to the solution.

Dick K. Yue,
Massachussetts Institute of Technology,

In light of the discussions made by Dr. Euvard and Prof. Birkhoff regarding the use of smoothing or filtering on the free surface by the author, I would like to comment on a new regriding procedure we tested recently which removed the undesirable short-wavelength instabilities. Under this regriding scheme, a new set of equally spaced grid points are created after each time step. This algorithm has good convergence properties as the spatial grid size is decreased and avoids the arbitrariness in the choice of an appropriate smoothing filter.

Reply -

It seems that any smoothing or regriding technique used to remove short-wavelength instabilities raises the same troublesome questions regarding the repositioning of points on the free surface. The filtering scheme of the present work has been used successfully in the past by a number of researchers to eliminate similar instabilities encountered in the numerical calculation of the development of large amplitude waves. The error introduced by any such numerical smoothing or filtering must be analyzed carefully to ensure that the flow solution yields an accurate picture of the physical phenomena being studied.

Some Discussions on the Free Surface Flow Around the Bow

H. MARUO AND M. IKEHATA

Yokohama National University, Japan

ABSTRACT:

In order to elucidate the free surface phenomena around the ship bow, experiments of simple wedge-shaped models are conducted in the towing tank. It is found that the surface tension has a remarkable effect on the free surface pattern around the model. It is shown that the surface activator compound is very effective in order to remove the effect of the surface tension. Free surface configurations free from the surface tension observed by photographs after application of the surface activator are examined in detail. In order to apply the theoretical analysis to the wave pattern under the effect of the surface tension, the ray theory is effectively employed, and a differential equation which determines the curve of the capillary wave front around the wedge is obtained. The ray theory is applied also to the wave pattern at the bow when the surface tension is eliminated, and it is concluded that the wave configuration changes its characteristics, when the entrance angle exceeds 60 degrees. This fact is clearly proved by the experimental observation. Next the effect of surface tension to the resistance of ship models is examined by means of the application of the surface activator to the resistance test. A considerable difference in the resistance is observed when the surface tension is removed. Therefore the scale effect due to the surface tension should be taken into account in the lower speed range.

1. INTRODUCTION

The free surface flow around the ship bow has drawn attention in naval architects in recent years.[1] Among free surface phenomena, the breaking of waves at the bow is of special importance because of its relevance to the resistance of full-hull-forms. There have been several attempts to elucidate the mechanism of wave-breaking at the bow so far, which propose various kinds of hypothesis. However most of these hypotheses are not likely to be acceptable by the rational basis of hydrodynamics of Newtonian fluid, and some critical comments on the various hypotheses so far proposed have appeared in another literature.[2] In consequence, one can regard that the mechanism of the bow-wave-breaking is not yet unvailed. In order to understand the true situation of the physical phenomena, the detailed observation and accurate measurement of the phenomena are indispensable. Photo 1 gives a typical picture of the wave pattern around the bow of a large tanker(VLCC) in full scale. One can observe several wave crests in front of the stem and the breaking waves take place at these wave crests. However this sort of wave pattern is hardly reproduced in model scale in the towing tank. A typical configuration of free surface around the bow of ship model is shown in Photo 2. Although the hull form of the ship in Photo 1 and that of the model are not identical, the difference between these pictures seems to be a common feature in such a comparison. A preliminary observation in the towing tank has indicated the possibility of existence of a scale effect due to the surface tension in the configuration of the free surface. The free surface disturbane under the effect of surface tension was first described by Scott Russel[3] and Kelvin,[4] and mathematical investigation was given by Rayleigh.[5] Typical wave patterns associated with a point disturbance were shown in Lamb's text.[6] It is possible to take account of the surface tension in the thin ship theory as Webster did.[7] According to these theories, the effect of surface tension may be neglected if the speed of advance is sufficiently greater than the critical velocity of gravity-capillarity waves i.e. 0.23m/sec, because the ratio between the lengths of the gravity wave and the capillary ripples is very great. In order to examine how the surface tension influences the configuration of free surface, a series of experiments with wedge-shaped models have been conducted in the towing tank.[8] It has been found that the application of surface activator compound on the water surface reduces the surface tension to a great extent. The comparison between the free surface pattern when the surface activator compound is applied to the water surface in front of the model and that without such process, for

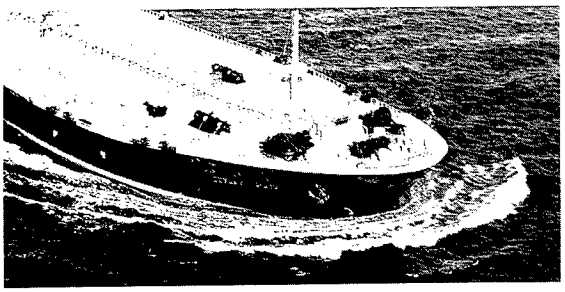


Photo 1 Bow Wave Pattern of a Tanker

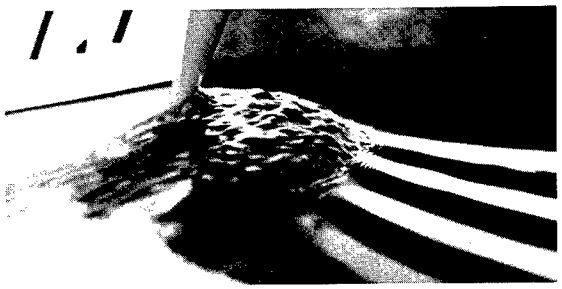


Photo 2 Bow Wave Profile of 5 metre Model of a Bulk Carrier

which the surface tension is intact, indicates that the conclusion of above theories is different from the truth. The difference in free surface pattern in front of the model is significant even if the speed of advance exceeds the critical speed considerably. Specifically, a considerable difference is observed in the wave breaking between two cases.

It is taken for granted in today's practice of ship model test in the towing tank, that Froude's hypothesis is valid, that means the resistance originated from free surface phenomena is a function of Froude number and the change in Reynolds number or Weber number can give only a negligible effect. If the free surface flow around the ship model is subject to the influence of the surface tension to a considerable extent, however, the influence to the model resistance may not be neglected. Since the Weber number for the ship in full scale is extremely great and her resistance is free from the effect of surface tension, the scale effect due to the surface tension seems to be present in the model scale. If this is true, the existing practice of the model-ship correlation method, which is based on the assumption that the resistance coefficient is a function of Reynolds number and Froude number, may need to revise. One of the purpose of the present investigation is to examine how the flow pattern around the model is influenced by the surface tension.

Since the application of the surface activator compound to the free surface almost eliminate the surface tension near the model, the free surface pattern free from the surface tension can be observed. Then one can examine the free surface phenomena free from surface tension, which can be correlated with phenomena in full scale. This process will enable a sound discussion of the mechanism of wave-breaking.

2. OBSERVATION OF THE FREE SURFACE AROUND WEDGE-SHAPED MODELS

It has been found by the preliminary experiment, that the surface activator is very effective to remove the surface tension. For the purpose of comparison of the flow pattern under the effect of surface tension with that free from the surface tension, a solution of surface activator compound is spread on the free surface by a sprayer in front of the model which is towed through the towing tank. Concentration of the compound in the solution is small in order to avoid the pollution of tank water, nevertheless the effect is proved enough to reduce the surface tension to a great extent. Models employed in the experiment are wedges with 230mm breadth and 950mm draft. Entrance angles (1/2 apex angles) of the wedges are 30°, 45°, 60°, 70° and 80°. The models are fixed to the carriage of the towing tank and towed with speed from 0.8m/sec to 1.35m/sec. The free surface is observed by taking pictures from model side and from ahead. In order to reinforce contrast of the picture, a screen board with white and black stripes is placed behind the model. Typical samples of the picture are given in Photo 3-a through Photo 17-b. Stripes on the water surface in the picture are the image of the back screen. Pictures on the left are the case for which the surface activator is not applied while those on the right are the case for which the surface tension is removed by the application of the surface activator. One can observe a remarkable change of the free surface configuration after the process of eliminating surface tension. Photos 3-a, 4-a, 5-a show the case of entrance angle 30° when the surface tension is intact. At lower speed such as 0.8m/sec, there is a curved line of step wave front circumscribing the wedge bow and capillary ripples appear outside the wave front line. Inside this line, there is the silent zone where no wave exists. This type of wave pattern is a characteristic feature of the free surface around the bow at low speed when the surface tension is present. When the speed increases, the wave-breaking takes place at the wave front line above-mentioned (Photo 2-a), and at higher speed, the breaking wave is fully developed until the wedge bow is encircled by a chaotic turbulent zone (Photo 3-a). The free surface after the surface tension is removed by the application of surface activator is shown in Photos 3-b, 4-b, 5-b. The capillary wave front together with ripples disappear and one can observe Kelvin-type diverging wave system starting from the apex of the wedge (Photo 3-b). At slightly higher speed such as 1.0m/sec, a small wave crest appears in front of the bow (Photo 4-b) and as the speed increases, wave-breaking takes place at the position of this wave crest (Photo 5-b). When the speed increases further more, the wave-breaking stretches out on wider area, and the difference between the case under the effect of surface tension and that free from the surface tension

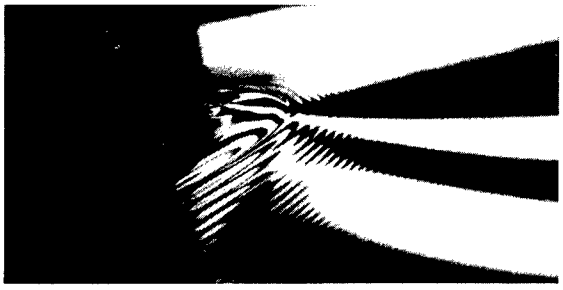


Photo 3-a Wave Pattern under Surface Tension
α = 30°, V = 0.8m/sec

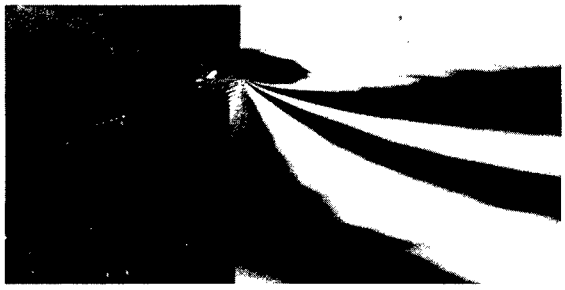


Photo 3-b Wave Pattern free from Surface Tension
α = 30°, V = 0.8m/sec

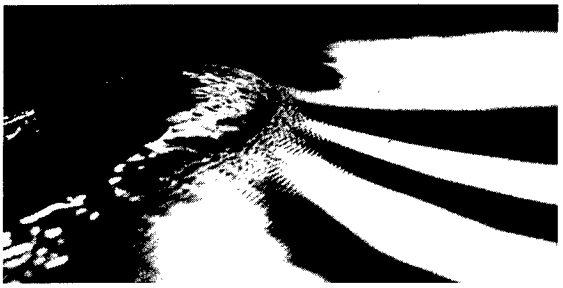


Photo 4-a Wave Pattern under Surface Tension
α = 30°, V = 1.0m/sec

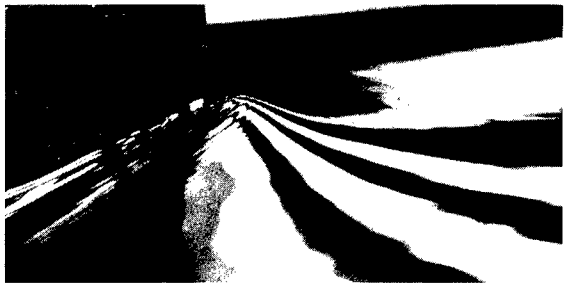


Photo 4-b Wave Pattern free from Surface Tension
α = 30°, V = 1.0m/sec

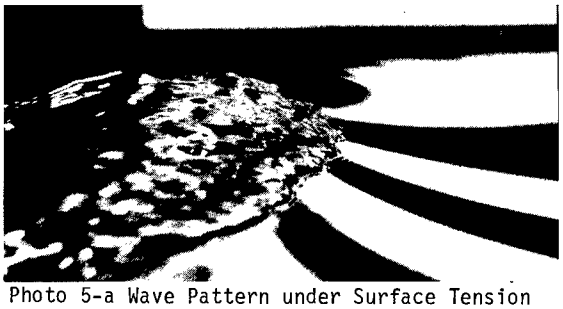


Photo 5-a Wave Pattern under Surface Tension
α = 30°, V = 1.1m/sec

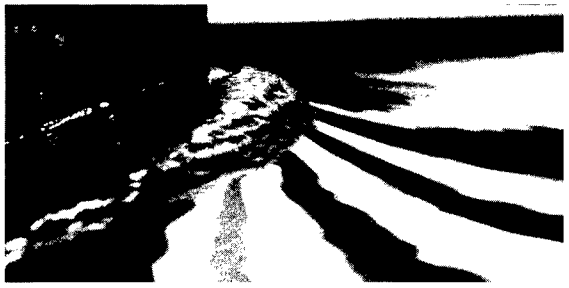


Photo 5-b Wave Pattern free from Surface Tension
α = 30°, V = 1.1m/sec



Photo 6-a Wave Pattern under Surface Tension
α =45°, V = 1.1m/sec



Photo 6-b Wave Pattern free from Surface Tension
α = 45°, V = 1.1m/sec



Photo 7-a Wave Pattern under Surface Tension
α = 45°, V = 1.2m/sec



Photo 7-b Wave Pattern free from Surface Tension
α = 45°, V = 1.2m/sec



Photo 8-a Wave Pattern under Surface Tension
α = 45°, V = 1.3m/sec

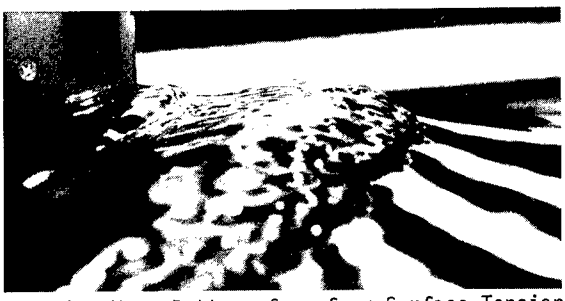


Photo 8-b Wave Pattern free from Surface Tension
α = 45°, V = 1.3m/sec

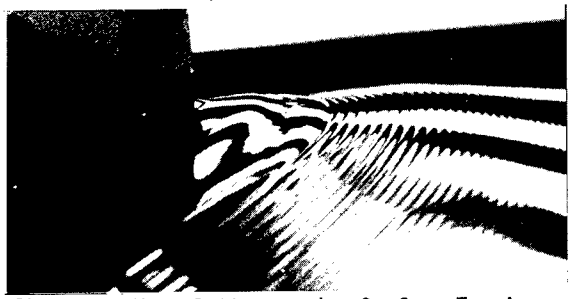


Photo 9-a Wave Pattern under Surface Tension
α = 60°, V = 1.1m/sec

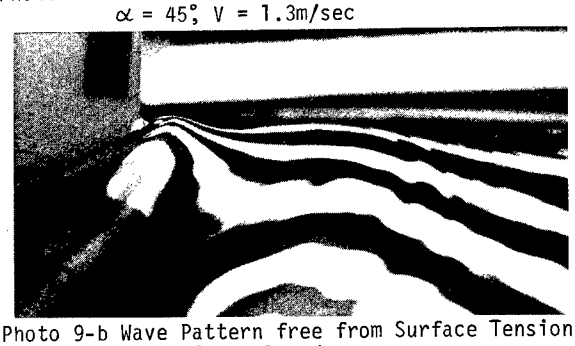


Photo 9-b Wave Pattern free from Surface Tension
α = 60°, V = 1.1m/sec



Photo 10-a Wave Pattern under Surface Tension
α = 60°, V = 1.2m/sec

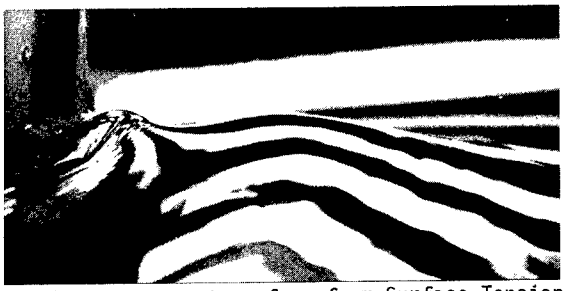


Photo 10-b Wave Pattern free from Surface Tension
α = 60°, V = 1.2m/sec

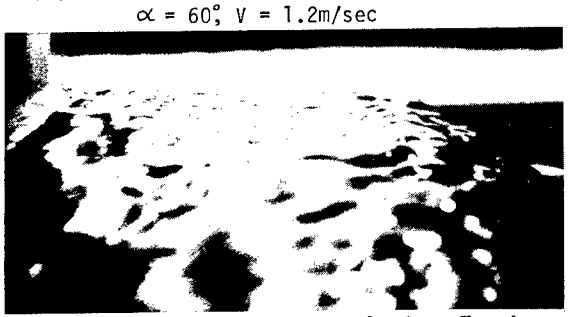


Photo 11-a Wave Pattern under Surface Tension
α = 60°, V = 1.3m/sec



Photo 11-b Wave Pattern free from Surface Tension
α = 60°, V = 1.3m/sec

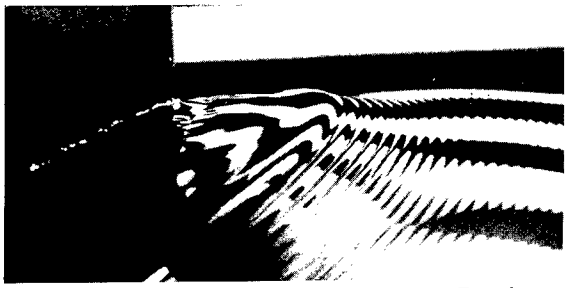


Photo 12-a Wave Pattern under Surface Tension
α = 70°, V = 1.1m/sec

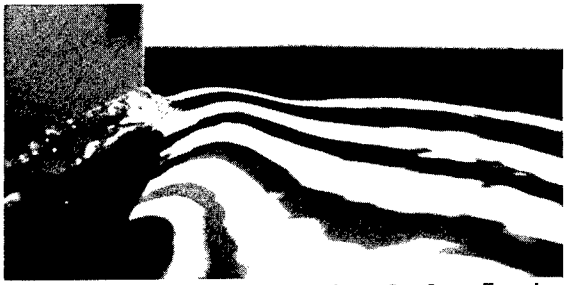


Photo 12-b Wave Pattern free from Surface Tension
α = 70°, V = 1.1m/sec

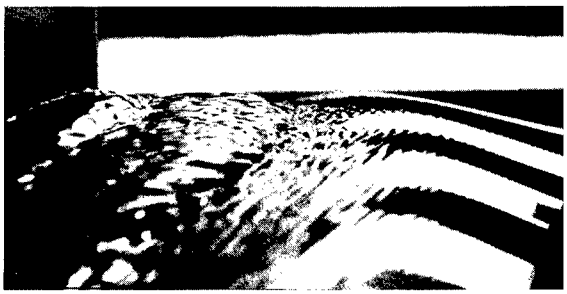


Photo 13-a Wave Pattern under Surface Tension
α = 70°, V = 1.2m/sec

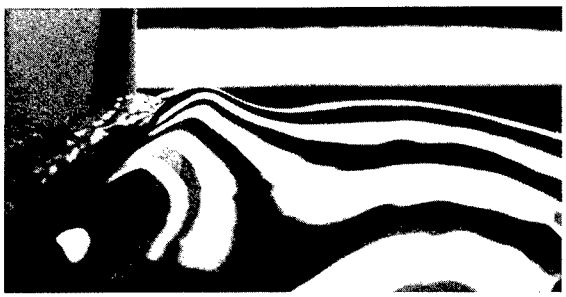


Photo 13-b Wave Pattern free from Surface Tension
α = 70°, V = 1.2m/sec

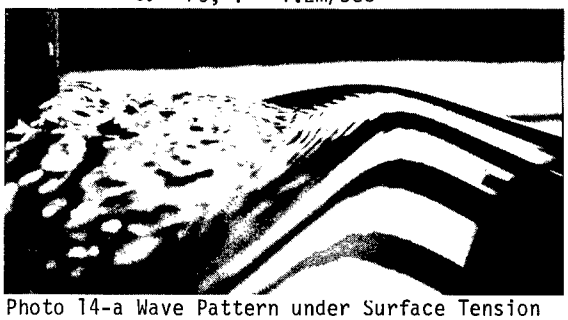


Photo 14-a Wave Pattern under Surface Tension
α = 70°, V = 1.3m/sec

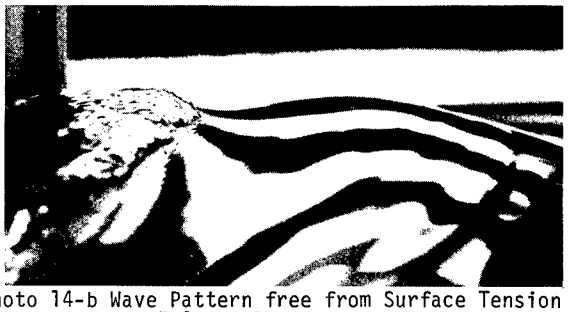


Photo 14-b Wave Pattern free from Surface Tension
α = 70°, V = 1.3m/sec

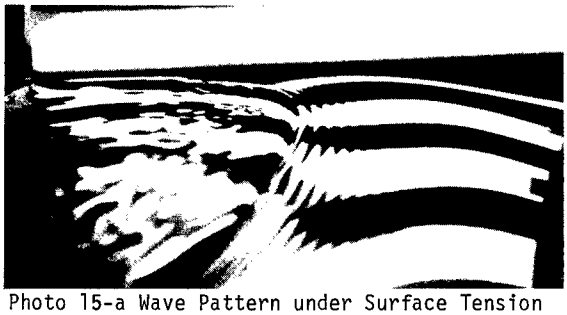


Photo 15-a Wave Pattern under Surface Tension
α = 80°, V = 1.2m/sec

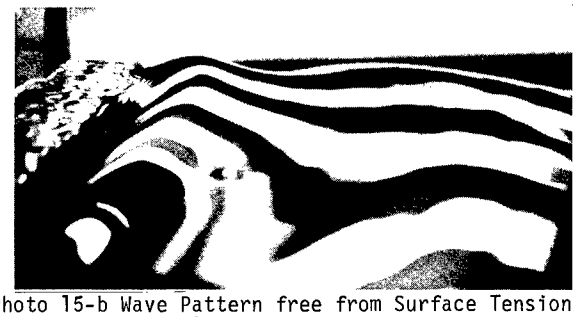


Photo 15-b Wave Pattern free from Surface Tension
α = 80°, V = 1.2m/sec

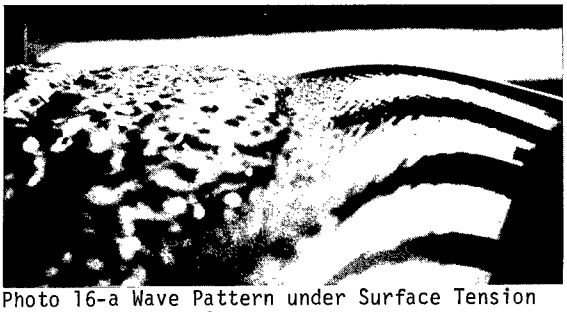


Photo 16-a Wave Pattern under Surface Tension
α = 80°, V = 1.3m/sec

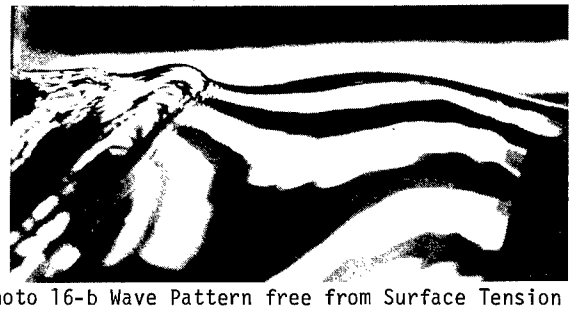


Photo 16-b Wave Pattern free from Surface Tension
α = 80°, V = 1.3m/sec



Photo 17-a Wave Pattern under Surface Tension
α = 80°, V = 1.35m/sec



Photo 17-b Wave Pattern free from Surface Tension
α = 80°, V = 1.35m/sec

disappears. At greater angle of entrance such as 45°, the inception of wave-breaking takes place at higher speed irrespective of the existence of surface tension (Photos 7-a,8-b). The wave crest in front of the bow, which appears when the surface tension is eliminated, is more prominent than that of entrance angle 30°(Photo 7-b). The inception of wave-breaking occurs at further higher speed in greater entrance angle such as 60°. The configuration of the free surface under gravity can be examined clearly by the application of the surface activator. As shown in Photo 9-b, a second crest which is more gently-sloping than the first crest just in front of the model appears forward with the entrance angle 60°, and inception of the wave-breaking takes place at these two wave crests (Photo 11-b). The case of entrance angle 70° shows similar phenomena. When the entrance angle increases to 80°, a third wave crest appears further forward (Photo 15-b). The wave-breaking starts at these crestsat higher speed.

In any case the wave-breaking takes the type of spilling breaker if the surface tension is not present. Other types such as the plunging or surging type breaking waves have not been observed. There has been an opinion such that the wave-breaking is a phenomenon which is analogous to the hydraulic jump or the free surface shock wave[9] in the shallow water flow, but the present observation indicates that such an analogy may not be warranted. The breaking wave in its initial stage as observed in the pictures looks to be similar to the breaking of ocean waves at critical steepness. The instability at the pointed wave crest may become a trigger of the wave-breaking.

Next the measurement of flow velocity in the center plane forward to the model is carried out by means of a small vane wheel of diameter 3mm. Fig. 1 shows the result for the model with entrance angle 30° at 1.1 m/sec in both cases with and without the process of eliminating surface tension. Fig. 2 shows the result for the same model at 1.2 m/sec. No difference is observed in the velocity distribution between two cases in spite of the difference in the free surface shape. In the part where the wave-breaking is fully developed, a remarkable velocity gradient is observed near the free surface (Fig. 2). This phenomenon is shown more clearly in Fig. 3, which gives the result for entrance angle 45° at 1.3 m/sec. However such a remarkable velocity gradient is not observed if the wave-breaking does not take place even if the wavy elevation appears on the free surface in front of the model as shown in Fig. 4, which gives the result for entrance angle 80° at 1.2 m/sec. Therefore the shear layer, which has been observed by several researchers along the free surface, seems to be associated with the presence of wave-breaking. The opinion,[10] that the free surface shear flow is a consequence of the effect of viscosity on the curved free surface without breaking, is doubtful unless the great curvature of the free surface such as the capillary wave front is present. The formation of necklace vortex may not be analogous to the horse shoe vortex at

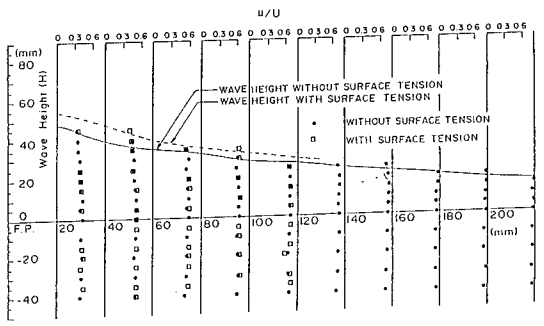


Fig.1 Velocity Distribution α = 30°, V = 1.1m/sec

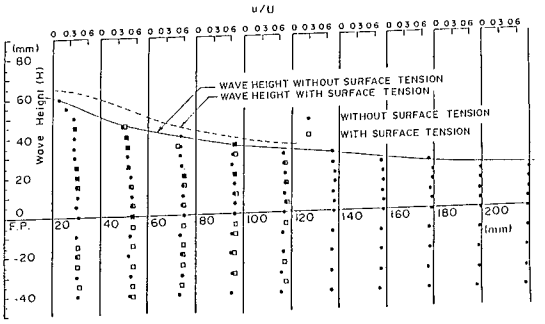


Fig.2 Velocity Distribution α = 30°, V = 1.2m/sec

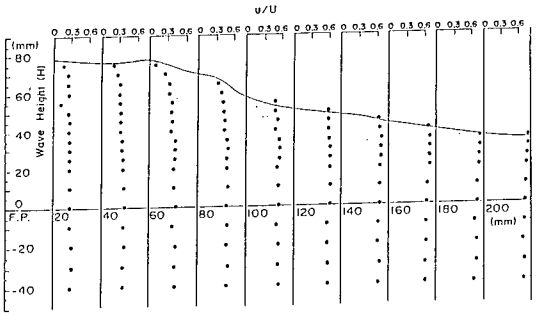


Fig.3 Velocity Distribution α = 45°, V = 1.3m/sec

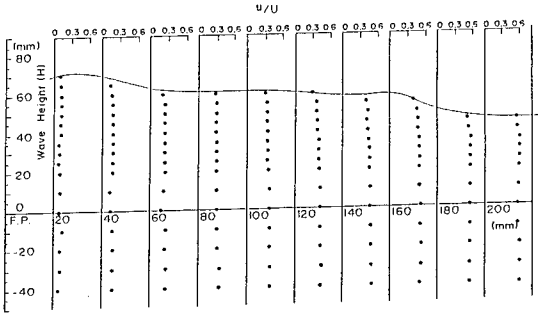


Fig.4 Velocity Distribution α = 80°, V = 1.2m/sec

the base of a body attached to a plane wall,[11] for which the shear flow in the boundary layer plays an important rôle.

3. SOME MATHEMATICAL ANALYSIS

Let us consider the fluid motion around a body fixed in a free surface of a uniform flow of an inviscid incompressible fluid. Take cartesian coordinates x, y, in the undisturbed free surface and the axis of z vertically upwards. The uniform flow is assumed in the direction of positive x. Now we define velocities u_o, v_o, w_o, which are flow velocities when the free surface does not deform as if it were a rigid plane, or they are regarded as velocities around a double body in an unbounded fluid. Because of the free surface elevation, actual flow velocities deviate from u_o, v_o and w_o, and we introduce the velocity potential Φ assuming the irrotational motion in such a way that the velocities are expressed by

$$u = u_o + \Phi_x\,,\quad v = v_o + \Phi_y\,,\quad w = w_o + \Phi_z \qquad (1)$$

where subscripts mean partial derivatives. The velocity potential satisfies the Laplace equation

$$\Phi_{xx} + \Phi_{yy} + \Phi_{zz} = 0 \qquad (2)$$

If we assume the speed of advance is low so that the Froude number is sufficiently small, the free surface elevation is very small and the flow deviates only slightly from the double body flow. Therefore the disturbance velocities, grad Φ are much smaller than the base flow velocities of the double body flow. Further we assume that u_o, v_o and w_o are slowly varying while the disturbance velocities vary more rapidly on account of their wavy nature. Introducing the expression (1) in the boundary condition at the free surface under gravity and surface tension, and taking only terms of the lowest order with the consideration of above assumptions, we obtain the linearized free surface condition for Φ such as

$$u_o^2\Phi_{xx} + 2u_o v_o \Phi_{xy} + v_o^2 \Phi_{yy} + g\Phi_z + \varkappa\Phi_{zzz} = \Psi(x,y) \qquad (3)$$

where g is the acceleration of gravity and $\varkappa$ is the kinematical capillarity defined by $\varkappa = T/\rho$, T being the surface tension per unit length. This equation is regarded to be satisfied on the plane z=0. The function $\Psi(x,y)$ on the right hand side is the forcing function and determined by the base flow velocities u_o and v_o. Now let us apply the ray theory to the present case. Since the ray theory deals with the propagation of free waves, we employ the homogeneous equation by putting $\Psi(x,y)=0$ as the free surface condition. Assume the infinite depth of water and define the wave potential of the form

$$\Phi = Ae^{iF(x,y,z)} \qquad (4)$$

Let us consider the case of short waves and assume

$$\text{grad } F(x,y,z) = O(\varepsilon^{-1})$$

where ε is a small quantity of the first order. Then the Laplace equation results the relation in the lowest order such as

$$[F_x(x,y,0)]^2 + [F_y(x,y,0)]^2 + [F_z(x,y,0)]^2 = 0 \qquad (5)$$

Because Φ gives the free wave without the exponential decay, $F_x(x,y,0)$ and $F_y(x,y,0)$ are real functions, while $F_z(x,y,0)$ is pure imaginary. Therefore one can define the phase function

$$S(x,y) = F(x,y,0) \qquad (6)$$

Since the fluid motion decays downwards, $iF_z(x,y,0)>0$. Then one can define the local wave number

$$iF_z(x,y,0) = \sqrt{S_x^2 + S_y^2} = k \qquad (7)$$

Substituting (3) in the homogeneous free surface condition

$$u_o^2\Phi_{xx} + 2u_o v_o \Phi_{xy} + v_o^2 \Phi_{yy} + g\Phi_z + \varkappa\Phi_{zzz} = 0 \qquad (8)$$

and taking terms of the lowest order, we obtain

$$(u_o S_x + v_o S_y)^2 = \sqrt{S_x^2 + S_y^2}\,[g + \varkappa(S_x^2 + S_y^2)] \qquad (9)$$

This equation defines the dispersion relation of waves under gravity and capillarity, and becomes the basis of the ray theory. Now we define the wave number vector

$$\text{grad } S(x,y) = \underline{k} \qquad (10)$$

and write $\underline{q}$ for the velocity u_o, v_o on z=0. Then the dispersion relation becomes

$$(\underline{q}\cdot\underline{k})^2 = |\underline{k}|(g + \varkappa|\underline{k}|^2) \qquad (11)$$

If the velocity $\underline{q}$ makes an angle Ψ with respect to positive x and the wave number vector makes an angle χ (Fig.5), the following equation is valid.

$$kq^2\cos^2(\Psi - \chi) = g + \varkappa k^2 \qquad (12)$$

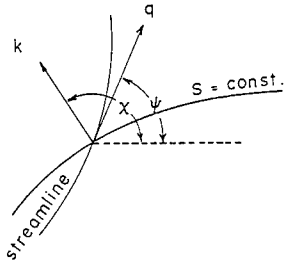


Fig.5 Schematic diagram of the Wave Number Vector

where $q=|\underline{q}|$. The angle χ defines the direction of the ray of elementary waves. Solving the above equation with respect to k, one obtains

$$k = (1/2\kappa)[q^2\cos^2(\psi-\chi) \pm \sqrt{q^4\cos^4(\psi-\chi) - 4g\kappa}] \quad (13)$$

In the case of $q\cos(\psi-\chi)>(4g\kappa)^{1/4}$, there are two wave systems, which have different relations of dispersion. The region where $q\cos(\psi-\chi)<(4g\kappa)^{1/4}$ is the silent zone within which no wave exists. The forward border of the silent zone is the curve of capillary wave front as shown in the pictures of the preceding section. The curve is an iso-phasal line S(x,y)=const. along which the following relation is valid,

$$q\cos(\psi-\chi) = (4g\kappa)^{1/4} \quad (14)$$

and the normal to the curve makes an angle with respect to x axis. If we write the equation of the wave front in the form

$$r = f(\theta) \quad (15)$$

making use of cylindrical coordinates $x=r\cos\theta$, $y=r\sin\theta$, the following relation is derived from (14).

$$\cos(\psi-\theta) - \sin(\psi-\theta)f'(\theta)/r = ((4g\kappa)^{1/4}/q)\sqrt{1+\{f'(\theta)/r\}^2} \quad (16)$$

or

$$\frac{f'(\theta)}{f(\theta)} = \frac{\tau^2\cos(\psi-\theta)\sin(\psi-\theta) - \sqrt{\tau^2-1}}{\tau^2\sin^2(\psi-\theta) - 1} \quad (17)$$

where $\tau=q/(4g\kappa)^{1/4}>1$. The solution of this equation determines the curve of the wave front. In order to apply the above equations to the wedge-shaped model, we employ the two dimensional flow illustrated in Fig. 6 as a flow model. A wedge is placed in a uniform stream and is accompanied by the dead flow bounded by two free streamlines along which the pressure is constant. A complete solution for this flow pattern,[12] obtained by the two-dimensional free streamline theory, is expanded around the stagnation point. Then the conjugate complex velocity u_o-iv_o near the apex of the wedge is expressed by

$$u_o - iv_o = -V(are^{i\theta})^{\alpha/(\pi-\alpha)} \quad (18)$$

where α is the angle of entrance, and a is a coefficient determined by the dimension and the angle of the wedge, given by the equation

$$a = (f/\ell)(1 - \alpha/\pi) \quad (19)$$

where ℓ is the length of each side of the wedge and f is a function of α. In the case of the flow model of Fig. 6, the function f is given by

$$f = 1/4 + \alpha/4\pi + (1/2)(\alpha/\pi)^2[\psi(1-\alpha/2\pi) - \psi(1/2-\alpha/2\pi)] \quad (20)$$

where $\psi(\alpha)$ is the digamma function defined by $\Gamma'(\alpha)/\Gamma(\alpha)$. Then the parameter τ in eq.(17) is expressed by

$$\tau = q/(4g\kappa)^{1/4} = V(ar)^{\alpha/(\pi-\alpha)}(4g\kappa)^{-1/4} \quad (21)$$

The curve of capillary wave front passes the point $x=\ell_c$ on the x axis where $\tau=1$. Therefore we have the relation

$$\ell/\ell_c = f(1-\alpha/\pi)\,\tau_1^{\pi/\alpha-1} \quad (22)$$

where $\tau_1 = V/(4g\kappa)^{1/4}$ (23)

Fig. 7 shows computed results of ℓ/ℓ_c versus τ_1 for several angles of entrance. The curve of capillary wave front is obtained by numerical integration of eq.(17). Fig. 8 shows the result of computation for the cases of the angle of entrance 30°, 45°, and 60°. One may find in these figures that there exists a similarity relation that the curve of wave front for geometrically similar models is determined by the parameter τ_1. Because of the relation

$$\tau_1 = (V/\sqrt{g\ell})((\ell/2)\sqrt{g/\kappa})^{1/2} \quad (24)$$

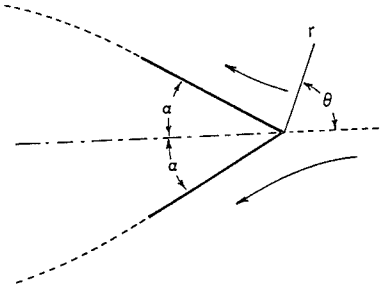


Fig.6 Flow Model around a Wedge

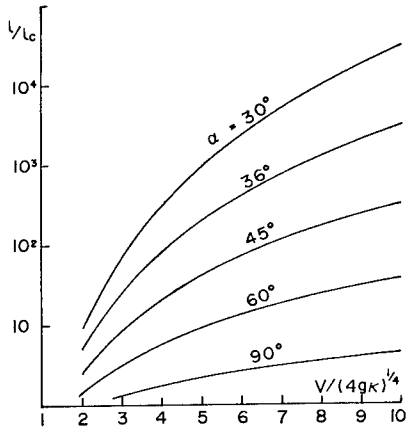


Fig.7 Location of the Capillary Wave Front

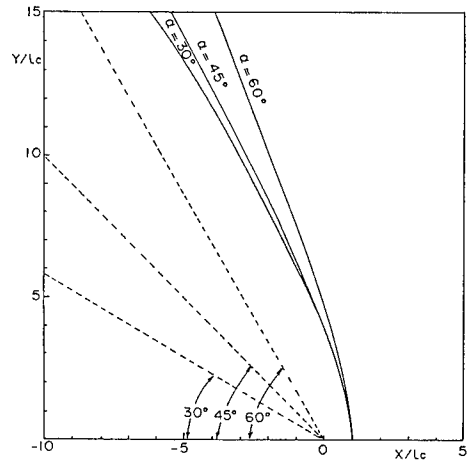


Fig.8 Curves of the Capillary Wave Front

Froude's law is valid under the condition that $\ell\sqrt{g/\varkappa}$ is kept constant.

If the surface tension is eliminated, the dispersion relation of wave becomes much simpler such as

$$(u_o S_x + v_o S_y)^2 = g\sqrt{S_x^2 + S_y^2} \qquad (25)$$

when $\varkappa$ vanishes in eq.(13), the wave number of capillary ripples tends to infinity, while the wave number of gravity waves has the relation

$$k = g/[q\cos(\psi - \chi)]^2 \qquad (26)$$

The ray theory in this condition was applied to ship waves first by Keller[13) 14)] and extended investigations have been carried out by Yim[15)] and Tulin.[16)] According to this theory, the wave pattern is obtained from the solution of the differential equation (25). If we transform (25) in the cylindrical coordinates, we obtain

$$(u_r S_r + u_\theta S_\theta)^2 = g\sqrt{S_r^2 + S_\theta^2} \qquad (27)$$

where u_r, u_θ are velocity components in r and θ direction respectively, and S_r, S_θ are gradients of S in r and θ direction respectively. Let us consider the elementary wave along the wedge boundary $\theta = \pi - \alpha$. Then we can put $S_\theta = 0$, $u_\theta = 0$, so that the phase function becomes

$$S = g\int_0^r (1/q^2)dr \qquad (28)$$

The flow velocity is given by (18) such as

$$q = V(ar)^{\alpha/(\pi-\alpha)} \qquad (29)$$

If $\alpha < 60°$, we have the solution

$$S = (g/V^2)a^{-2\alpha/(\pi-\alpha)} r^{(\pi-3\alpha)/(\pi-\alpha)} \qquad (30)$$

A similar relation is valid along the center line $\theta = 0$. There exist straight rays passing through the apex of the wedge, and caustics describe the wave pattern which is like the Kelvin-wave system as illustrated in Fig. 9. The cusp line of the diverging wave makes an

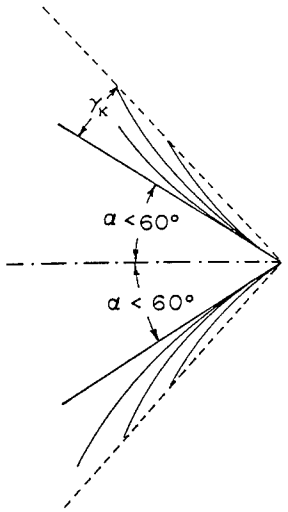


Fig.9 Wave Pattern around the Model $\alpha < 60°$ (schematic)

angle γ with the wedge surface, which is given by

$$\gamma = (1 - \alpha/\pi)\gamma_K$$

where γ_K is the Kelvin angle (19°28′). If $\alpha \geq 60°$, the integral (28) diverges and there is no solution for the phase function around the wedge bow, so that the Kelvin-wave system does not exist, and the disturbance given at the free surface in front of the model does not propagate towards downstream in the form of radiating waves. The bow is encompassed by a turbulent zone as illustrated in Fig. 10 in this case. These phenomena can be observed

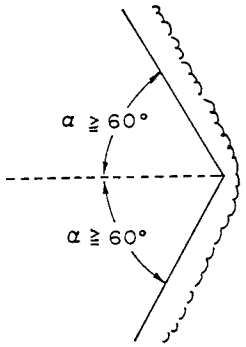


Fig.10 Wave Pattern around the Model $\alpha \geq 60°$ (schematic)

clearly in the experiment by removing the surface tension as shown in Photo 18 for $\alpha < 60°$ and Photos 19, 20 for $\alpha \geq 60°$. The phenomena at the bow of entrance angle not less than 60° may implicate the non-existence of the continuous flow at the bluff bow and relevance to the generation of the necklace vortex around the bow of full hull forms.

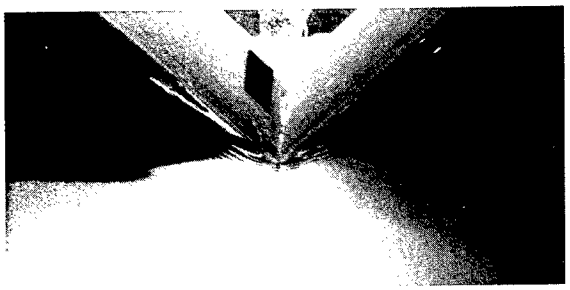


Photo 18 Bow Wave free from Surface Tension
α = 45°, V = 1.1m/sec



Photo 19 Bow Wave free from Surface Tension
α = 60°, V = 1.1m/sec

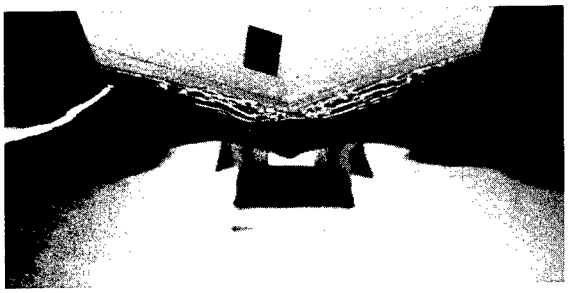


Photo 20 Bow Wave free from Surface Tension
α = 70°, V = 1.1m/sec

4. RESISTANCE OF SHIP MODELS

It has been shown that the free surface configuration around the model is influenced considerably by the surface tension even at moderate speed. Then the effect of surface tension is suspected in the value of the resistance of ship models at the tank test. In order to examine whether the resistance of models is influenced by the surface tension, ship models are towed in the towing tank through water, to which the surface activator compound is applied by spreading on the free surface in front of the models. The resistance measured under this condition is compared with the resistance in unprocessed water in which the effect of surface tension is present. Two models are employed in the experiment. One of them is a 3 metre model of full-hull-form with a cylindrical stem. The other is a 4 metre model of full-hull-form with a wedge-shaped bow of entrance angle 40°. Body plans of the models are shown in Figs. 11, 12. The 3 metre model is tested in two loading conditions,

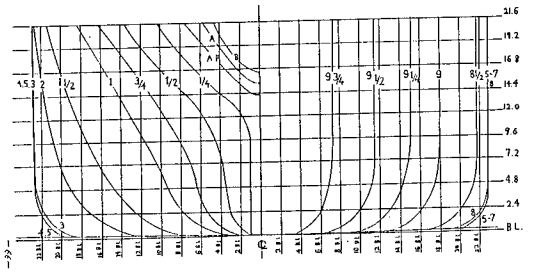


Fig.11 Body Plan of the 3 metre Model

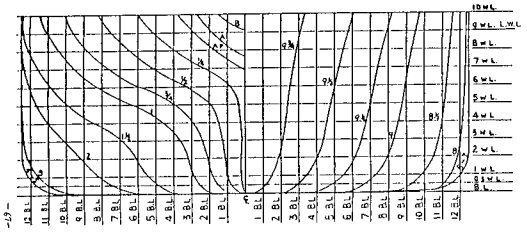


Fig.12 Body Plan of the 4 metre Model

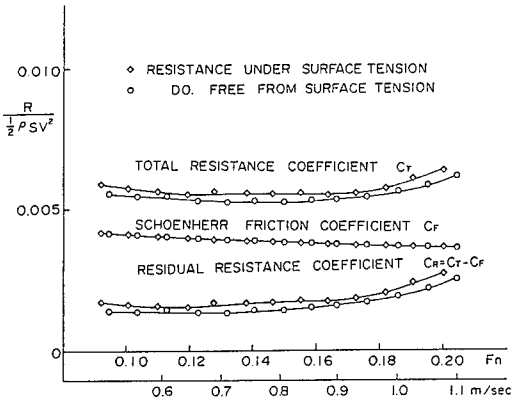


Fig.13 Resistance Curve of the 3 metre Model Full Load Condition

namely full-load and light-load. Fig. 13 shows the result of 3 metre model in full load condition. Consistent difference is observed between the resistance coefficient under the influence of surface tension and that free from surface tension throughout the test speed up to 1.2 m/sec. Photos 21, 22 gives the sample of observation of the free surface, in which we can recognize the effect of surface tension. The turbulent zone around the model which has been explained in the preceding section is observed in Photo 22, in which the surface activator is applied. At higher speed, 0.9 m/sec say, the free surface breaks out even when the surface tension is not present. The difference in the resistance between both cases is possibly due to difference in the area of the wave breaking zone. Fig. 14 shows the resistance coefficients of the same model in light draft. Different from the former case, the effect of surface tension diminishes with increasing speed, and the difference between

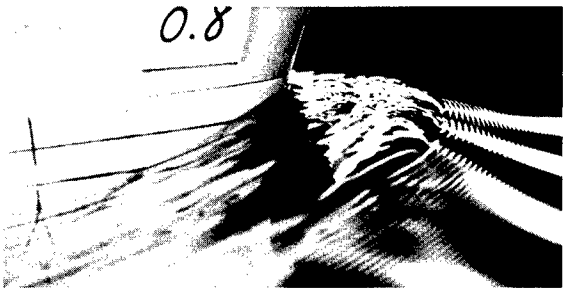


Photo 21 Bow Wave Profile of the 3 metre Model under Surface Tension V = 0.8m/sec

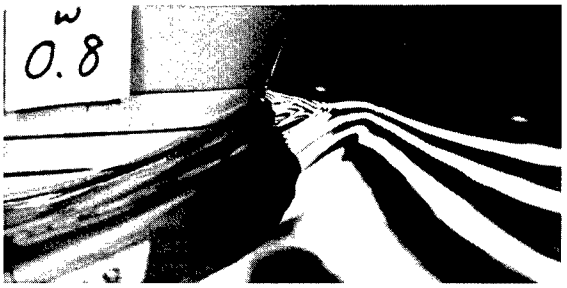


Photo 22 Bow Wave Profile of the 3 metre Model free from Surface Tension V = 0.8m/sec

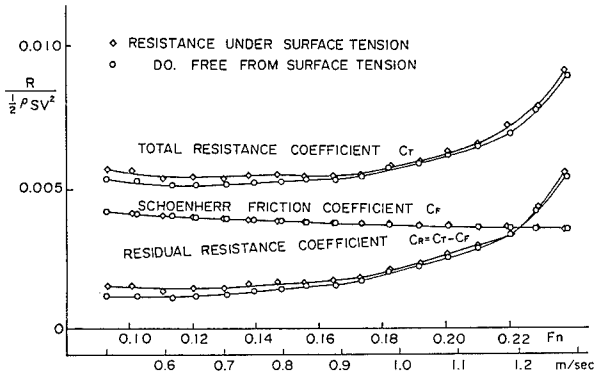


Fig.14 Resistance Curve of the 3 metre Model Light Condition

two curves almost vanish at V=1.0m/sec. The wave breaking takes place at lower speed in the case of light draft than in the case of full load draft. This seems to be one of the reasons of the difference in the effect of surface tension to the resistance curves between the full load draft and light draft. As mentioned in the preceding section, the effect of surface tension is related to the ratio ℓ/ℓ_c given in eq. (22), where f is a function of the entrance angle α. If the draft is finite, f is related to the draft too, in such a way that ℓ/ℓ_c increases as draft decreases. This tendency can be understood by the comparison between a vertical circular cylinder and a sphere with its center on the free surface. Approximate estimates show that

$$r_o/\ell_c \fallingdotseq 2\tau_i \quad \text{for a circular cylinder}$$

$$\fallingdotseq 3\tau_i \quad \text{for a sphere}$$

where r_o is the radius of the cylinder or the sphere. Therefore the effect of surface tension is less in a shallower draft.

The 4 metre model is tested only at the full load condition. Curves of resistance coefficients are shown in Fig. 15. The diffe-

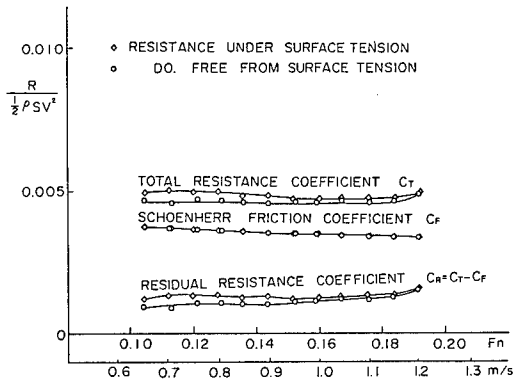


Fig.15 Resistance Curve of the 4 metre Model

rence between the resistance under the effect of surface tension and that free from surface tension decreases as speed increases and vanishes at about 1.15 m/sec, which corresponds to τ_i =5.0. Since the entrance angle of this model is 40°, the corresponding value of ℓ/ℓ_c is about 10^2 according to Fig. 7. Thus the resistance of a ship model is subject to the scale effect due to surface tension, if the tank test is carried out under a certain critical speed. The parameter $V/(4g\kappa)^{1/4}$ may be employed as a criterion for the effect of surface tension. Since Fig. 7 indicates a strong dependence of this effect on the entrance angle, the critical speed is dependent on the entrance angle to a great extent. In the case of the hull form of 4 metre model, the critical speed corresponds to the Froude number greater than 0.18. Therefore the resistance test result is contaminated by the surface tension throughout the whole range of operating speed of full-hull-forms such as oil-tankers and bulk carriers. Even for large models of 6 metre, the critical speed is at the Froude number 0.15, which is still within the important speed range in practice. Another troublesome fact is the difficulty in determination of the form factor for the viscous resistance. If one intends to determine the form factor from the test data at the Froude number 0.10, the error due to the surface tension amounts to more than 20 percent.

5. CONCLUSIONS

Free surface phenomena around the bow are investigated by the use of wedge shaped models. It is found that the free surface configuration is influenced by the surface tension to a great extent. Therefore the free surface phenomena in model scale is not identical with those in full scale, on account of the scale effect due to the surface tension. A particular feature of the existence of surface tension is the capillary wave front which is observed in front

of the model when the wave-breaking does not take place. The wave-breaking starts at the position of this wave front as the speed is increased.

It is found that the surface activator compound is very effective to remove the effect of surface tension. When the surface tension is removed by the application of the surface activator, a remarkable change is observed in the feature of the free surface. Therefore the free surface phenomena in full scale, in which the effect of surface tension is negligible, can be correlated only with model experiments, in which the surface tension is eliminated by the application of the surface activator. The free surface configuration free from the effect of surface tension shows a wave crest or crests in front of the bow. The inception of wave-breaking takes place at these wave crests, showing the spilling type breaking waves, and the hydraulic jump or the free surface shock wave is irrelevant to the wave-breaking at the bow in deep water.

The ray theory is useful to the mathematical analysis of the wave pattern. The curve of the capillary wave front can be calculated by this theory. The wave pattern near the bow of entrance angle less than 60° is like the Kelvin wave system, while such a wave system does not exist when the entrance angle is equal or greater than 60°. In the latter case, the bow is encircled by a chaotic turbulent zone. This phenomenon may be relevant to the generation of the 'necklace vortex' around the bow.

The resistance of ship models is subject to the influence of surface tension. The surface tension results increase in resistance to a considerable extent if the model is towed below a certain critical speed. Then the scale effect due to the surface tension is suspected in the resistance test data at low speed, especially in the case of full-hull-forms with bluff bows. The difference in resistance due to the surface tension vanishes above the critical speed where the breaking waves are fully developed. The critical speed is dependent on the entrance angle and the draft-beam ratio of the model.

ACKNOWLEDGMENTS

The authors wish to express their thanks to Messrs. Z. Takusagawa and I. Okada, staffs of the Marine Hydrodynamic Laboratory, for cooperation. Thanks are also to Messrs. H. Sakamoto, H. Tanikawa, T. Kondo and Y. Morozumi for their participation in the experimental research.

REFERENCES :

1. 17th I.T.T.C. Report of Resistance Committee, Recommendations, Göteborg, 1984
2. Maruo. H., On the breaking of waves at the bow, Symp. on New Developments of Naval Architecture and Ocean Engineering, Shanghai (1983.)
3. Scott Russel, On waves, Brit. Ass. Rep. 1844
4. Thomson, W., Hydrokinetic solutions and observations, Phil. Mag. (4) XVII (1871) 374
5. Reyleigh, Lord, The form of standing waves on the surface of running water, Proc. Lond. Math. Soc. XV (1883) 69
6. Lamb, H., Hydrodynamics, Cambridge Univ. Press. 6th ed. 470
7. Webster, W.C., The effect of surface tension on ship wave resistance, College of Eng. Univ. California, Rep. NA-66-6 (1966)
8. Maruo, H., On the free surface flow around a model bow, Journal Soc. Naval Arch. Japan. 158. (1985) 1-9
9. Inui, T., From bulbous bow to free-surface shock wave-Trends of 20 year's research on ship waves at the Tokyo University Tank, Jour. Ship Res. 25-3 (1981) 147-180
10. Mori, K., Necklace vortex and bow wave around blunt bodies, 15th Symp. Naval Hydro. Hamburg (1985) 303-317
11. Takekuma, K., Eggers, K., Effect of bow shape on free-surface shear flow, 15th Symp. Naval Hydro. Hamburg (1985) 387-405
12. Milne Thomson, Theoretical Hydrodynamics 5th ed. McMilan 347.
13. Keller, J.B., Wave patterns of non-thin or full bodied ships, 10th Symp. Naval Hydro., Cambridge, MA (1974) 543-547
14. Keller, J.B., The ray theory of ship waves and the class of streamlined ships, Jour. Fluid Mech. 91-3 (1979) 465-488
15. Yim, B., A ray theory for nonlinear ship waves and wave resistance, 3rd Internat. Conf. on Numerical Ship Hydro. Paris (1981) 55-70
16. Tulin, M.P., Surface waves from the ray point of view, The Seventh Georg Weinblum Memorial Lecture, Hamburg (1985)

DISCUSSION

Hideaki Miyata,
University of Tokyo

The fine pictures seem to be very interesting and useful for a sound understanding of flow phenomena about a bow.

However, I do not think it is reasonable to discuss bow waves without the parameter of Froude number. Several years ago I found that the Froude number based on draft is very important and it rules the wave formation, at least for wedge models [a]. Since the draft of the author's model is large, the Froude number based on draft may be less than 0.5, while it is from 0.5 to 1.5 for practical ships. This means that the author's experiments were conducted in the very low Froude number range, where wave motions are gentle and consequently the effect of surface tension seems to play a relatively more important role.

With the parameter of Froude number the authors will find more systematical properties of nonlinear bow waves called free-surface shock wave.

[a] H. Miyata and T. Inui, Adv. Appl. Mech. 24.

Reply -

The surface waves under gravity and capillarity around a model are constituted by two wave systems in the speed range under consideration. One of them appears behind the model and the other is observed in front of the model. The former wave system is governed mainly by the gravity and the Froude number is the governing parameter to determine the wave pattern. The latter, on the other hand, is governed mainly by surface tension, so that the Froude number does not become the governing parameter, but the pehenomena can be related to the parameter such as $V(gT/\rho)^{-1/4}$. The Froude number based on the draft does not become a characteristic parameter of the free surface phenomena in front of the model. The effect of change in the draft appears in the change of velocity distribution of the double model flow which determines the free surface pattern. Some discussions in this respect are given in Section 4 of the present paper.

The case of smaller draft is also examined in this paper by the use of ship models of different size. A few examples of the free surface observation are given in Photos 21 and 22. The free surface phenomena in front of models are quite similar to the wedge models. The surface tension has a significant effect even at the speed of 1.1 m/sec. for a 4 meter model. The corresponding Froude number is 0.176, which is by no means a very low speed. The literature [1] mentioned by the discussor deals with only the experiment in which breaking waves are fully developed. Experiments of this kind are of no use for the purpose of elucidating the mechanism of inception of wave breaking. There is no possiblity of shock-like phenomena in deep water waves. Although the superficial feature of the breaking wave has some resemblance with the hydraulic jump in its appearance, the wave breaking at the bow is based on a principle of mechanics which is quite different from that of hydrodynamic shock.

K. Nakatake,
Kyushu University

We appreciate you for your showing the important effect of the surface tension on the model ship resistance. We are conducting cooperative experiments using similar small tanker models (C_b=0.834, GBT-15: L_{pp} = 1.5m and GBT-20: L_{pp}= 2.0m) in the towing tank of Kyushu University and also in the circulating water channel of West Japan Fluid Engineering Laboratory. Since we had the similar results of C_r curves to those of Figs. 14 and 15 in your paper, we would like to show them. We repeated the same experiment two times at different seasons and got nearly the same results. Figs. A and B show C_r curves obtained in the towing tank in case of the full load and ballast conditions. In the full load condition, C_r value of GBT-15 is larger than that of GBT-20, the difference of C_r curves is small in the ballast condition. We used the same turbulence stimulator (stud height: 2mm, spacing: s≈10mm) and could not get such results in the circulating water channel. These tendencies may not be explained by the turbulence stimulation and confuses our common knowledge about C_r value. We think tht these phenomena may be explained by the effect of surface tension on C_r curve. We would like to have some opinion about our results.

Reply -

Thank you for your interesting data. Since our results on the resistance of ship models are very limited, it may not be safe to draw a definite conclusion from them. However, the possibility of a scale effect due to surface tension may be in the right direction. I should like to recommend the model test in the circulating water channel, in which the technique of the surface activator is applied. However repeated application of this technique may not be recommended in the towing tank because of the possible pollution of the tank water.

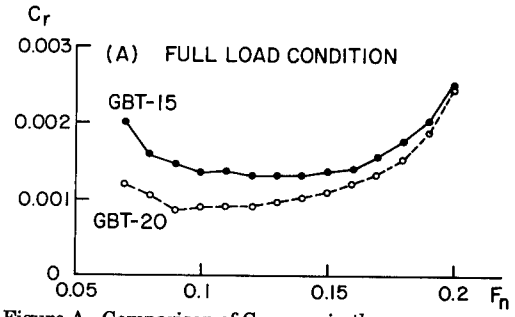


Figure A. Comparison of C_r curve in the full load condition.

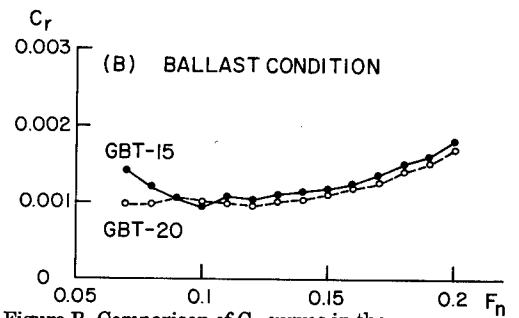


Figure B. Comparison of C_r curves in the ballast condition.

Large, Steep Waves, Wave Grouping and Breaking

M.-Y. SU

Naval Ocean Research and Development Activity, U.S.A.

ABSTRACT

This paper presents a review of the dynamics and statistics of large steep surface waves. In particular, we shall provide strong evidence to support the view that seemingly independent occurrences of large waves, wave grouping and breaking in the open ocean are often different manifestations of the same evolving dynamical process controlled mainly by intrinsic instabilities of steep waves.

These evidences come from three different sources: first, controlled experiments at a very large wave tank and basin, which allow observations of long-distance evolution of steep wave trains and packets; second, theoretical computation of two distinctive types of wave instabilities and their nonlinear coupling; and third, statistical analyses and modeling of wave group characteristics associated with extreme large waves.

INTRODUCTION

For investigation of dynamical responses and design safety of marine vehicles and fixed structures, one needs more than the traditional wave spectra, either one-dimensional or two-dimensional (i.e. direction and frequency/wavemaker). The additional wave features of importance are wave steepness, wave groupiness and wave breaking of large ocean waves. As shall be discussed in this paper based on combined evidence from laboratory experiments, field measurements and theoretical computation, these three important wave characteristics are dynamically related, and often are different aspects of the same evolving wave packets under intrinsic instabilities of steep waves.

We shall first present some observational evidence of large steep ocean waves as reported in the last two decades from various ships and offshore platforms. These selected examples from different parts of oceans and under different local conditions all testify to the enormous wave forcing from their large amplitude and thus inflict great damage to marine vehicles and structures.

A new concept of "Extreme Wave Group" which essentially combines the two separate important features of large waves, extreme waves and wave groupiness, into an integrated one, shall be discussed based on statistical analysis of one large set of ocean wave records collected in the Gulf of Mexico under severe weather conditions. Next a brief summary of experimental results under controlled situations on intrinsic instabilities of regular wave trains and packets shall be given together with available theoretical computations pertaining to these instabilities. These experimental results will then be employed to form a basis for a dynamical interpretation of extreme wave groups as observed in ocean storm waves. The influence of an opposing current to the pre-existing wind-generated waves is another physical mechanism for producing large steep waves and causing wave breaking. These will be also discussed. Finally, some concluding remarks and appeal for importance of stressing statistical analysis of individual waves, in contrast to traditional wave energy spectra, will be made.

LARGE STEEP OCEAN WAVE

Over the last two decades many large ocean waves have been encountered by ocean-going ships, and off-shore marine structure and some have caused much damage. However, only in a limited number of cases, have such large waves been accurately measured by wave gauges. We shall describe below a few cases in order to give a more definite feeling of the ferocity and prevalence of such waves.

The most notorious among these are the so-called "giant waves" in the Agulhas Current on the southeast coast of South Africa (Sanderson, 1974; Mallory, 1974; Schuman,1980). According to reports by oil tankers passing this area, abnormal waves up to 20 meters in height, preceded by a deep trough may be encountered between the edge of the continental shelf and twenty miles seaward thereof. In August 1971, the Moreton Bay reported a 26-meter wave which was unusually steep. On 1 August 1973 the Neptune Sapphire (a 12,000 ton freighter) broken in two in heavy weather. Schuman (1980) has summarized the general

characteristics of such damaging encounters as follows.

"...The captain continued to stare out at the sea, waiting for the next group of big waves he knew would come. The pitching increased, but something seemed different; the size and steepness of this series of waves were greater than anything that had preceded it. The ship struggled up one wave, only to be faced by even larger succeeding one. The bow dig into the roaring form, then was lifted right up the crest; here it hung as the wave slid down the length of the ship. At it came down to meet the next onslaught, the captain stared in disbelief: behind those two enormous waves was a still bigger one, and the ship, now in a downward attitude, was heading straight for the guts of that wall of water. The alarm bells rang even as a deluge of water buried the bow, crashing right up to the bridge..."

The above vivid description summarized field observations revealing the four features of these anomalous huge waves underlying the main themes of this paper:

a. large wave height
b. large wave steepness
c. coming in group
d. wave breaking.

In February 14-15 1982, an anomalous swell of about 50-60 ft height under high winds reaching 90 knots, might have hit the drilling rig "Ocean Ranger" (14,500 tons) and subsequently caused it to capsize on Newfoundland's Grand Banks killing all 84 crewmen, while a 58-foot wave hit two nearby rigs, "SEDCO 706" and Mobil rig, "The Zapata Ugland".

A series of ocean buoys operated by the National Ocean and Atmospheric Administration (NOAA) Data Buoy Center (NDBC) now routinely collects wave conditions along both the east and west coasts of the U.S. and in the Gulf of Mexico. One such buoy (Earle, Bush, Hamilton, 1984) recorded a significant wave height of 12.9 m with the possible maximum wave height of 24 m in February 1983 in the northeast Pacific Ocean. Hamilton (1980) of NDBC further reported the capsizing of two 10 m diameter discus buoys during severe weather conditions in the northeastern Pacific Ocean, of a 5 m buoy in the northwest Atlanic, and of a 12 m buoy north of Bermuda.

During the passage of notorious Hurricane Camille in the Gulf of Mexico in 1968, the maximum wave height recorded by a wave staff on an offshore oil platform, near the mouth of the Mississippi River was 22 m. During fall and winter, the North Sea is well known for its frequently observed very rough high sea state under gale winds. Figure 1 is a composite wave/weather record for 8 days during the winter of 1981 at the Frigg Field in the northern part of the North Sea. Under the maximum wind speed of 41 m/s (82 knots), the maximum wave height of 23 m and the maximum significant wave height ($H_{1/3}$) of 13 m were recorded.

With the increasing number of wave vrecordings on offshore platforms and buoys and the possibility of satellite altimeter measurements of significant wave height on a global coverage, we can certainly expect to gather lots more large amplitude wave data under various weather conditions in the future. In the next sections, we shall make use of one large set of wave data collected on the offshore platform for a statistical characterization of large steep ocean waves.

EXTREME WAVE GROUPS (EWG)

The study of wave groupiness has gained increasing attention in the past decade, because of its importance for long-period excitations to marine fixed and/or floating structures. Statistical analyses of ocean waves in storms (Rye, 1974; Goda, 1976; Cavanie and Ezraty, 1978, Su, et al., 1982) have firmly established the dependence of wave groupiness, such as its distributions and mean length, on the associated spectral bandwidth. Theoretical analyses(Longuet-Higgins, 1984, Kimura, 1980; Goda, 1970, 1983; Nolte and Hsu, 1972) have further related these properties in terms of either the linear narrow-band Gaussian process, or Markovian process. On the other hand, the most important classical design factor for marine structures is the estimation of extreme waves which are usually assumed to occur singly in nature (see Ochi, 1982 for a review on this subject). It can be convincingly argued, however, that a wave group containing an extremely large wave, if exists, would be an even more appropriate environmental design factor than either the single extreme wave or the "regular" wave group. For the sake of easy reference, we shall call this special type of wave groups, each containing an extremely large wave (to be defined more precisely later) by the name of "extreme wave groups" (EWG) in contrast to the "regular wave group" (RWG) which is normally defined to be a sequence of successive waves whose heights all exceed some prescribed critical value (H_c).

Goda (1976) seems to be the first investigator who made a statistical comparison of these two different types of wave groups. He noted that the mean length of runs for EWG is 2.36 when the critical value $H_c=H_{1/3}$, while the corresponding mean length for RWG is only 1.4. In other words, the highest wave does not appear singly, but is frequently accompanied by two to three high waves. Furthermore, the probability for the highest wave occurring in a group is even higher than regular high waves.

Wave Data

The set of wave records used in this investigation was obtained by wave staffs from an offshore platform about 60 miles offshore in the Gulf of Mexico (Ocean Data Gathering

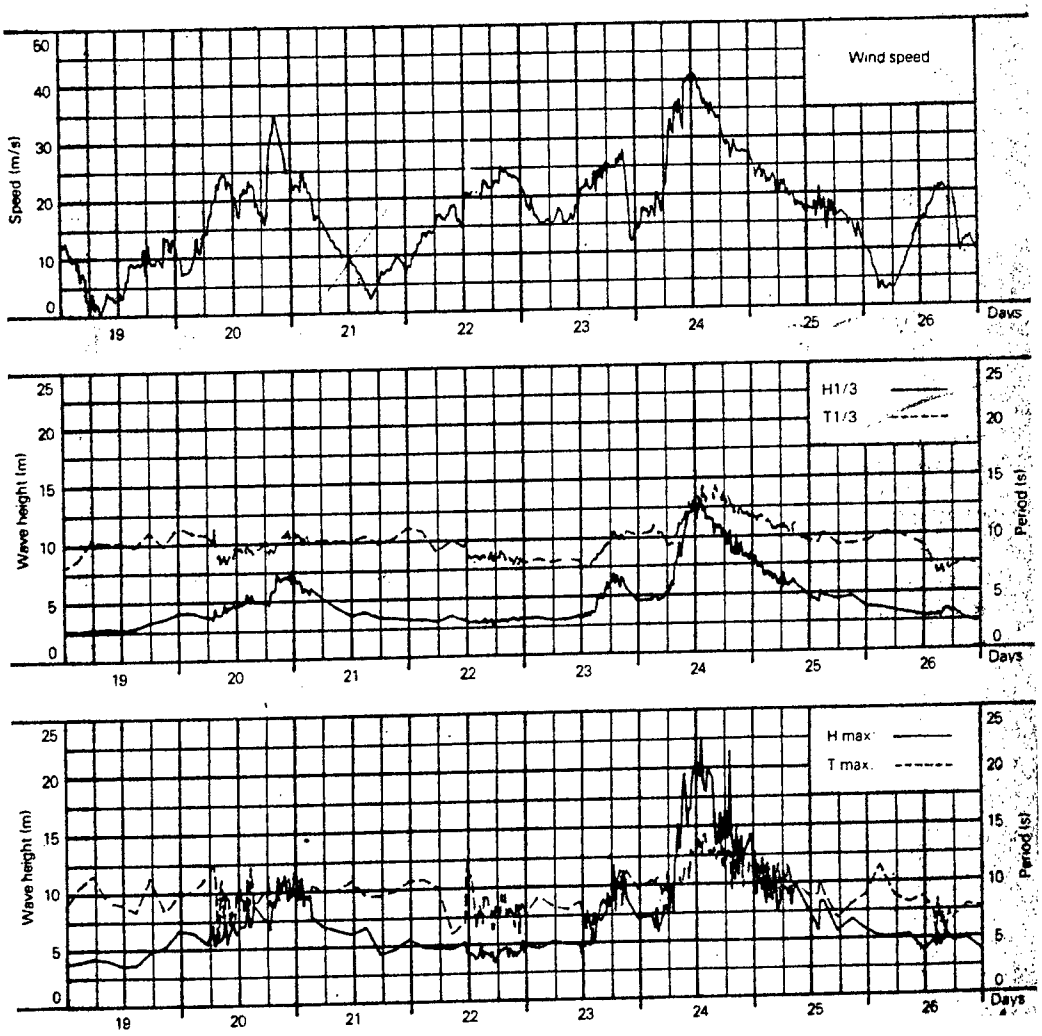


Figure 1. Meteorological and oceanographical data from Frigg Field in the North Sea, January 1981.

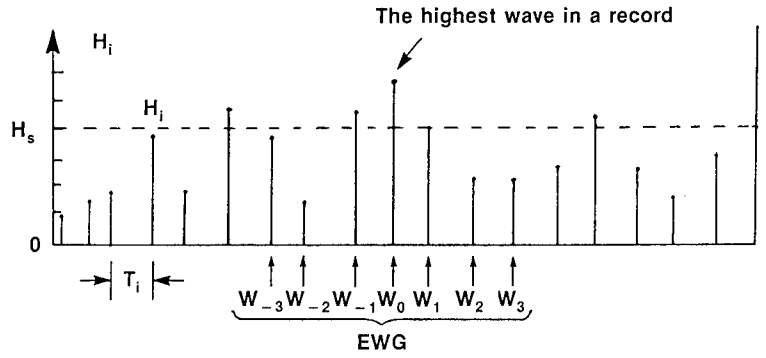


Figure 2. A schematic diagram for definition of extreme wave groups.

Program (ODGP), Station #1) during 1969-1971 under the sponsorship of a consortium of eight oil companies (Ward, 1974). The station is located in South Pass Block 62A, at a depth of about 340 feet.

Each wave record is 19.85 minutes long and has been digitized into 4096 data points at the rate of 3.41 samples per second. For this analysis, we selected a total of 533 wave records, each with the significant wave height ($H_s=H_{1/3}$)$\geq$2 meters in order to emphasize storm waves. These wave records were measured mostly in winter months, with the exception of during three hurricanes occurring in summer months. The eye of one of the hurricanes, Camille, happened to pass within 10 miles of the measuring platform.

Methods

The individual waves with their heights (H_j) and periods (T_j) for j=1,2...N in each wave record are determined by the standard up zero-crossing method. In the set of wave records we used, the value of N lies between 100 and 240 with the average close to 200. The power spectrum E(f) for each wave record is also computed by the Fast Fourier Transform, and is used in turn for computing two parameters indicative of the average bandwidth of the power spectrum. The first parameter was proposed originally by Longuet-Higgins (1983) and called the spectral bandwidth parameter, ν, and defined by

$$\nu = (m_2 m_0/m_1^{-1})^{1/2} \qquad (1)$$

where m_0, m_1 and m_2 are spectral moments as defined by

$$m_i = \int_0^\infty f^i E(f)df \qquad (2)$$

When $\nu^2 << 1$, the power spectrum is said to be narrow. The second parameter was proposed by Goda (1976) and called the spectral peakedness parameter, Q_p, and defined by

$$Q_p = \int_0^\infty 2fE^2(f)df/m_0 \qquad (3)$$

The value of Q_p is always greater than unity, and increases with decreasing spectral bandwidth. We have used certain specified ranges of ν and Q_p, independently, to classify the set of wave records into several subsets in order to see dependence of the statistical characteristics of wave groupiness on the spectral bandwidth.

Definition of Extreme Wave Group (EWG)

For the purpose of our analysis which is constrained by the availability of each wave record being about 20 minutes long, the extreme wave group (EWG) is defined as the wave group containing the largest wave height in the wave record. For convenience of data analyses, we first assume that the EWG may cover up to seven waves and can be expressed as

$$W_{-3}, W_{-2}, W_{-1}, W_0, W_1, W_2, W_3$$

where W_0 is the wave with the largest wave height, the three waves with negative subscripts are waves preceeding W_0, and those with positive subscripts are waves following W_0. The corresponding wave heights, periods, wavelengths, and steepness are denoted by H_i, T_i, L_i and S_i;

$$S_i = a_i k_i = (H_i/2) \times (2\pi/L_i) = H_i/L_i \qquad (4)$$

where a_i is the wave amplitude and k_i the wave number (see Figure 2).

Results

We shall present the computed results which show the mean values (denoted with an overbar) of H_i, T_i and S_i for subsets of wave records with prescribed ranges of Q_p or ν. The majority of the wave records had the values of Q_p between 1.3 and 4.0, or has the values of between 0.40 and 1.0. Based on this distribution, we have classified the wave records into the following subsets: (1) for Q_p;

$$\begin{array}{ll} \text{(a)} & 1.0 \leq Q_p \leq 2.0 \\ \text{(b)} & 2.0 \leq Q_p \leq 3.0 \\ \text{(c)} & 3.0 \leq Q_p \leq 4.0 \\ \text{(d)} & 1.0 \leq Q_p \leq 5.0 \text{ (the entire data set)} \end{array} \qquad (5)$$

and (2) for ν;

$$\begin{array}{ll} \text{(a)} & 0.40 \leq \nu \leq 0.50 \\ \text{(b)} & 0.50 \leq \nu \leq 0.60 \\ \text{(c)} & 0.60 \leq \nu \leq 0.70 \\ \text{(d)} & 0.60 \leq \nu \leq 0.80. \end{array} \qquad (6)$$

Table 1 gives the mean values of the wave heights, periods and steepness of the extreme wave groups for each of the three subsets according to the spectral classification of Q_p, plus the entire data set. Note that the wave heights given here have been normalized by the root-mean square of wave surface displacement $(m_0)^{1/2}$ of each corresponding wave record. The wave periods are normalized by the mean wave period of the corresponding wave record.

We shall start with case (d) in Table 1, which includes the entire set of wave records in order to see the overall mean characteristics first, before discussing their dependence on spectral bandwidth. From the mean values of wave heights, $\bar{H}_j$, on can see the Envelope of the EWG is rather symmetric with respect to the highest wave height, $\bar{H}_0$. The mean wave heights for the three central waves are $\bar{H}_0$ = 6.3 and $\bar{H}_{-1}$, $\bar{H}_1$ = 3.9, while the mean wave heights for outlying waves; $\bar{H}_{-2}$, $\bar{H}_2$ = 2.7

Table 1. Statistics of the Extreme Wave Groups based on the Classification of Spectral Peakedness Parameter, Q_p

	j = -3	-2	-1	0	+1	+2	+3
(a) $\overline{H}_j$	2.335	2.510	3.016	6.284	3.389	2.238	2.322
$\overline{T}_j$	1.093	1.041	1.217	1.369	1.315	1.035	1.003
$\overline{S}_j$	0.152	0.142	0.144	0.186	0.122	0.150	0.143
(b) $\overline{H}_j$	2.491	2.735	3.943	6.335	3.931	2.677	2.361
$\overline{T}_j$	1.024	1.083	1.369	1.289	1.364	1.105	1.014
$\overline{S}_j$	0.154	0.137	0.125	0.195	0.138	0.136	0.146
(c) $\overline{H}_j$	2.667	2.997	4.325	6.352	4.435	3.156	2.704
$\overline{T}_j$	1.085	1.177	1.314	1.233	1.318	1.163	1.059
$\overline{S}_j$	0.122	0.117	0.133	0.208	0.128	0.142	0.136
(d) $\overline{H}_j$	2.506	2.753	3.864	6.325	3.929	2.699	2.418
$\overline{T}_j$	1.047	1.093	1.334	1.291	1.348	1.104	1.022
$\overline{S}_j$	0.153	0.134	0.129	0.196	0.134	0.139	0.143

Table 2. Statistics of the Extreme Wave Groups based on the Classification of Spectral Bandwidth Parameter, ν.

	j = -3	-2	-1	0	+1	+2	+3
(a) $\overline{H}_j$	2.586	2.823	3.971	6.320	3.993	2.739	2.404
$\overline{T}_j$	1.046	1.085	1.324	1.228	1.311	1.088	1.029
$\overline{S}_j$	0.131	0.132	0.122	0.213	0.125	0.140	0.129
(b) $\overline{H}_j$	2.537	2.701	3.703	6.233	3.780	2.532	2.429
$\overline{T}_j$	1.068	1.101	1.335	1.316	1.340	1.086	1.012
$\overline{S}_j$	0.148	0.120	0.109	0.169	0.120	0.128	0.140
(c) $\overline{H}_j$	2.310	2.653	3.895	6.347	3.976	2.874	2.478
$\overline{T}_j$	1.018	1.106	1.327	1.389	1.418	1.190	0.972
$\overline{S}_j$	0.140	0.136	0.125	0.177	0.119	0.122	0.159
(d) $\overline{H}_j$	2.557	2.653	3.982	6.420	4.098	2.890	2.429
$\overline{T}_j$	0.965	1.073	1.320	1.359	1.420	1.143	1.000
$\overline{S}_j$	0.139	0.145	0.133	0.193	0.122	0.139	0.156

and $\bar{H}_{-3}$, $\bar{H}_3$ = 2.5, are much smaller. Recalling that the mean wave height for a linear narrow band Gaussian process is $H = \sqrt{2\pi} = 2.506$ (Arhan et al., 1976), we can infer, based on the height distribution alone, that (W_{-1}, W_0, W_1) is definitely distinctive from (W_{-3}, W_{-2}, W_2, W_3).

The mean wave periods for the three central waves are ($\bar{T}_{-1}$, $\bar{T}_0$, $\bar{T}_1$) = 1.3, while the outlying waves are ($\bar{T}_{-3}$, $\bar{T}_{-2}$, $\bar{T}_2$, $\bar{T}_3$) < 1.1. Since the expected value of the wave periods for a linear random process woule be unity, by definition, we find again that the three central waves (W_{-1}, W_0, W_1) are qualitatively different from the other waves. We also note that $\bar{T}_0$ = 1.29 is appreciably smaller than ($\bar{T}_{-1}$, $\bar{T}_1$) = 1.34.

The mean wave steepness for the highest wave is $\bar{S}_0 = a_0\bar{k}_0 = 0.2$, while the other waves are about 0.14. (The wave steepness for the highest Stokes waves is 0.443.) So, the highest wave turns out to be also the steepest, in the mean, a very significant feature indeed.

Taking together the above observed properties of both wave heights and wave periods, we may suggest that each extreme wave group, in the mean, contains three waves. Furthermore, if we use a threshold wave height $\bar{H}_c = \bar{H}_{1/3} = 4m_0^{1/2}$ for determining a wave group, then the mean (run) group length of the extreme wave group would be slightly less than 2.5. (Since $\bar{H}_{-1}$ = 3.86 and $\bar{H}_{+1}$ = 3.93 are only slightly smaller than the threshold value of 4.0, W_{-1} and W_{+1} will have slightly less than 50% of chance exceeding the prescribed threshold.) This estimated value is thus in good agreement with the value of 2.36 found by Goda (1976). The mean wave group length for EWG is considerably larger than that of regular wave groups (≈1.5) (Goda, 1976; Su and Bergin, 1983).

Next, we shall examine the effects of spectral bandwidth on the above group characteristics by comparing cases (a), (b) and (c) against (d) in Table 1. As the spectral bandwidth becomes narrower, i.e., Q_p increasing from 1.0 to 4.0, or from case (a) to case (c), $\bar{H}_{+1}$ is found to increase from about 3.2 to 4.4, and $\bar{H}_0$ increases from 6.28 to 6.35, and S_0 increases from 0.186 to 0.208, and $\bar{T}_0$ decreases from 1.37 to 1.23. Therefore, one may conclude that the specific features noted for the extreme wave group from the entire data set (case d) becomes even more prominent as the wave power spectra becomes narrower as parameterized by Q_p. In other words, for narrower spectral bandwidth, the mean group length will become longer, and the highest waves become steeper, and, increasingly, the wave period of the central waves become shorter than those of the surrounding waves.

It is well known that power spectra have narrower bandwidth in the fetch-limited growth stages than in either the fully saturated stages or in decaying stages. (Here we have excluded the consideration of swells which could have extremely sharp narrow spectra for which the beat phenomenon can be suitably applied.) One thus expects to find most clearly the unique feature of the extreme wave group in the rapidly growing sea.

Table 2 gives the statistics of the extreme wave groups as given in Table 1 with the exception that the wave records are grouped by the spectral bandwidth parameter, ν. We found much the same group characteristics as noted in Table 1 in all three cases, (a), (b) and (c), for ν = 0.4-0.5, 0.5-0.6, and 0.6-0.8, respectively, but the effects of spectral bandwidth based on ν is not as clear as based on Q_p. One possible reason for this relative sensitivity between the classifications of Q_p and ν is as follows: by its definition, Q_p emphasizes the contribution from the peak of the spectrum due to the square of E(f), while ν, by its definition, considers equally the contribution from the higher frequency range due to the factor of f^2 in the m_2 computation. In our determination of individual waves by the zero-crossing method which acts roughly as a low-pass filter, these individual waves thus obtained are primarily energy-containing lower-frequency waves centering around the spectral peak. Hence, Q_p will be a more sensitive parameter than ν in our analysis.

WAVE BREAKING AND NONLINEAR WAVE INSTABILITY COUPLING

Main Features of Wave Instabilities

We shall follow McLean, et. al. (1981) to call the essentially two-dimensional, side-band modulational instability as Type I instability, and to call the predominantly three-dimensional instability, Type II instability. To easily distinguish the description of the coupling between Type I and Type II, we summarize the important features of these two types of instabilities.

For Type I: (1) The two side-band perturbations are coupled with the unperturbed primary waves to produce a modulation in the wave envelope, (2) the most unstable mode is in the direction of the primary waves and has a wave number about equal to $(a_0k_0)^{-1}k_0$, and (3) usually only the most unstable mode manifests itself in the natural evolution of wave trains and packets.

For Type II: (1) The most unstable mode

has a wavenumber component in the direction of primary waves equal to 1/2 k_0, but it is always three-dimensional; (2) its growth rate is smaller than that of Type I for small a_0k_0 and becomes larger for $a_0k_0 \geq 0.26$, and (3) its two-dimensional manifestations occur only for $a_0k_0 < 0.41$, i.e., close to the Stokes limit. (See Figure 3 for an example at $a_0k_0 = 0.30$.)

So far, Types I and II are described as if they are two independent physical processes in the evolution of wave trains and packets. In reality, they are co-exiting. For the special case of two-dimensional wave evolution, Longuet-Higgins and Cokelet (1978) show, by the time-stepping computation, that subharmonic instabilities of Type I lead to a local steepening of the waves, which then induces instabilities of Type II. Their computations further show that for large $a_0k_0 \geq 0.25$, the combined action of Type I and II lead to two-dimensional wave breaking. In our experiments to be described below, the wave trains are allowed to undergo both two- and three-dimensional modulations. We then observed that the similar combined action can occur at much lower a_0k_0 compatible with the average ocean wave steepness in the rapid growth stage.

Coupling Between Types I and II Instabilities

The experiments to be described here are conducted in a wave tank 167 m long with a cross-section of 3.7 m by 3.7 m. The waves are generated by a plunger-type wavemaker and are measured by the capacitive-type gauges along the length of the tank. The range of wave steepness used if from $a_0k_0 = 0.09$ to 0.20, with the primary wave frequency $f_0 = 1.23$ Hz remaining fixed. More details about the experimental set-up can be found in Su, et al. (1982) and Su (1982).

We shall first describe experimental results for continuous, uniform wave trains. The wave measurements are used to derive power spectra of the surface displacements $E(a_0k_0; f)$, where f denotes the frequency, and analog strip chart records of the surface displacement, $\zeta(a_0k_0; t)$, where t denotes the time. We are particularly interested in the growth of the two side-bands of Type I, with f_1, and f_2 denoting the lower and upper side-band frequency, respectively. Several typical examples of $E(a_0k_0; f)$ and associated $\zeta(a_0k_0; t)$ can be found in Su and Green (1984). We found that the maximum modulation of the wave train due to Type I instability corresponds to the stage when the maximum and equal growth of the two side-band components occur and are approximately equal to one-half of the spectral power at the primary frequency f_0; i.e.,

$$\frac{\text{Max}[E(a_0k_0;f_1)]}{E(a_0k_0;f_0)} = \frac{\text{Max}[E(a_0k_0;f_2)]}{E(a_0k_0;f_0)} = 1/2 \quad (7)$$

The average locations (expressed in actual distance from the wavemaker x, and in the corresponding dimensionless form x/λ_0, where λ_0 is the wave length of the primary waves) of the above condition (1) with respect to a range of a_0k_0 from 0.09 to 0.20 is given by curve (a) in Figure 4. It is obvious that the x/λ_0 for a given a_0k_0 decreases with increasing a_0k_0, since Type I has a larger growth rate for a larger wave steepness. Visual observations during the wave measurements show that wave breaking occurs at locations centered around the maximum wave modulation. Curves (b) and (c) in Figure 3 bound the beginning and ending locations of the observed wave breaking. The shapes of wave breaking are composed of both two-dimensional and three-dimensional forms; the frequency of three-dimensional forms are found to be higher than the two-dimensional forms. Furthermore, this tendency becomes even more dominant as a_0k_0 increases from $a_0k_0 \geq 0.14$. From the ensemble of $\zeta(a_0k_0;t)$, we find that the ratio of the maximum wave amplitude, a_m, to the initial wave amplitude, a_0, is not a monotonic increasing function of a_0k_0, but has a maximum around $a_0k_0 = 0.14$, as shown in Figure 5. It is noted that a_m/a_0 increases very rapidly from $a_0k_0 = 0.09$ to 0.14, with the maximum of a_m/a_0 reaching 1.9; the wave amplitude almost doubles its height from the original due to Type I modulational instability. The decrease of a_m/a_0 with a_0k_0 from 0.14 to 0.20 is equally considerable. Plotted also on Figure 4 is the variation of a_mk_0 vs. a_0k_0. We note that a_mk_0 increase rapidly from 0.11 as a_0k_0 increase from 0.09, but the former level off at 0.29 for $a_0k_0 \gtrsim 0.16$.

We have conducted a series of experiments using wave packets of different lengths (N), i.e., varying the number of waves in the initial generation of wave packets with uniform amplitude. A typical example with $a_0k_0 = 0.16$ and N = 10 is shown in Figure 6 by a sequence of photographs taken from a nearby tower. (This experiment is conducted in a different outdoor wave tank, 150 m long with a cross-section of 3.7 m wide, and 1 m deep. Photographs (a) through (f) show the six sequential stages of the evolution of the same wave packet. Stage (c) corresponds to the maximum modulation of the wave packet with a clear manifestation of two rows of three-dimensional, crescent-shaped, spilling, breaking waves atop the two-dimensional, long wave crest. In stages (d) and (e), further wave breaking with longer crest-wise dimensions are visible. Finally, three separate envelope-

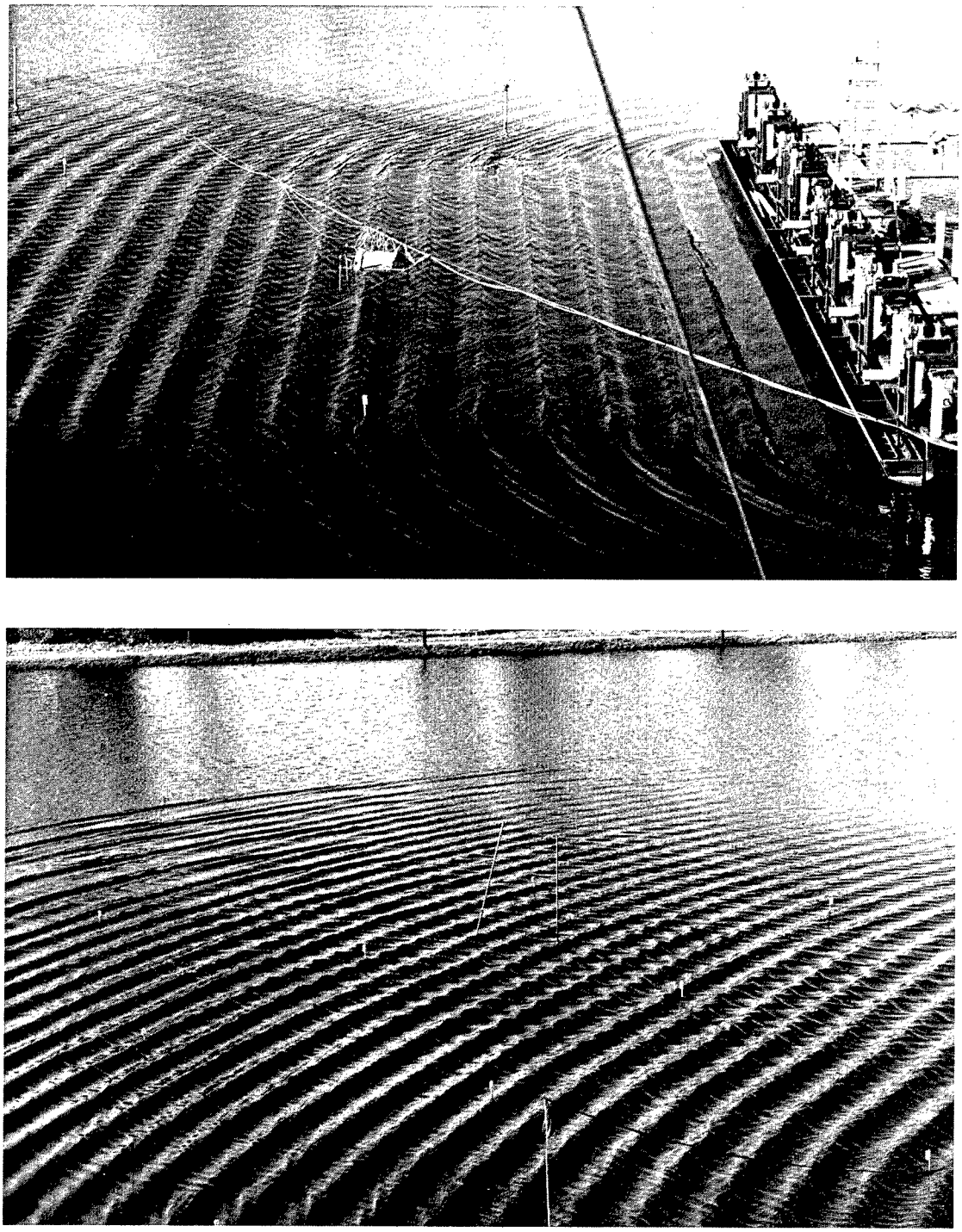


Figure 3. Two photographs showing the evolution of originally two-dimensional uniform wave train, with steepness $a_0k_0 = 0.30$ and frequency $f_0 = 1.2$ Hz, into three-dimensional crescent-shaped breaking waves and subsequently, two-dimensional side-band modulations. Above: The wavemaker in a wide outdoor basin at NORDA and the initial stage of a wave train. Below: The latter of the same wave train.

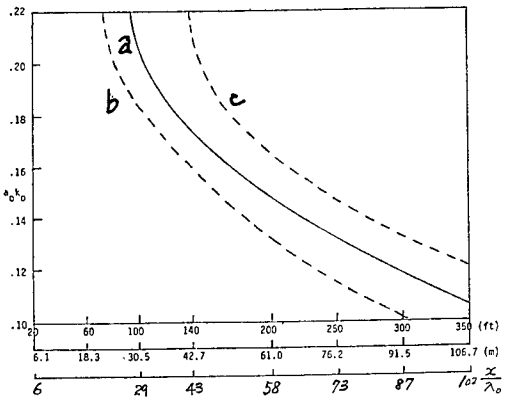


Figure 4. Stages of evolution of wave trains with respect to varying initial wave steepness; a_0k_0: (a) Max $[E(a_0k_0;f_1)]$ = Max $[E(a_0k_0;f_2)]$; (b) Starting distance of observed wave breaking, and (c) Ending distance of observed wave breaking.

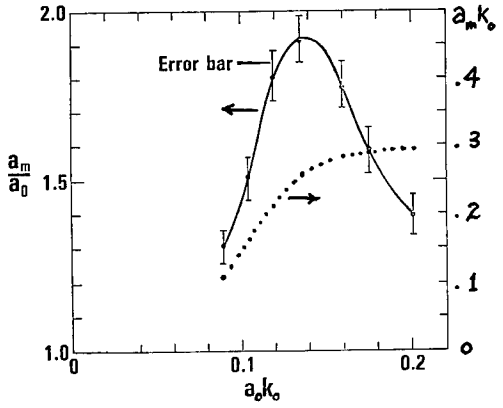


Figure 5. The ratio of the maximum wave amplitude a_m to the initial wave amplitude a_0 for various initial wave steepness a_0k_0. Also shown is the variation of a_mk_0 vs. a_0k_0.

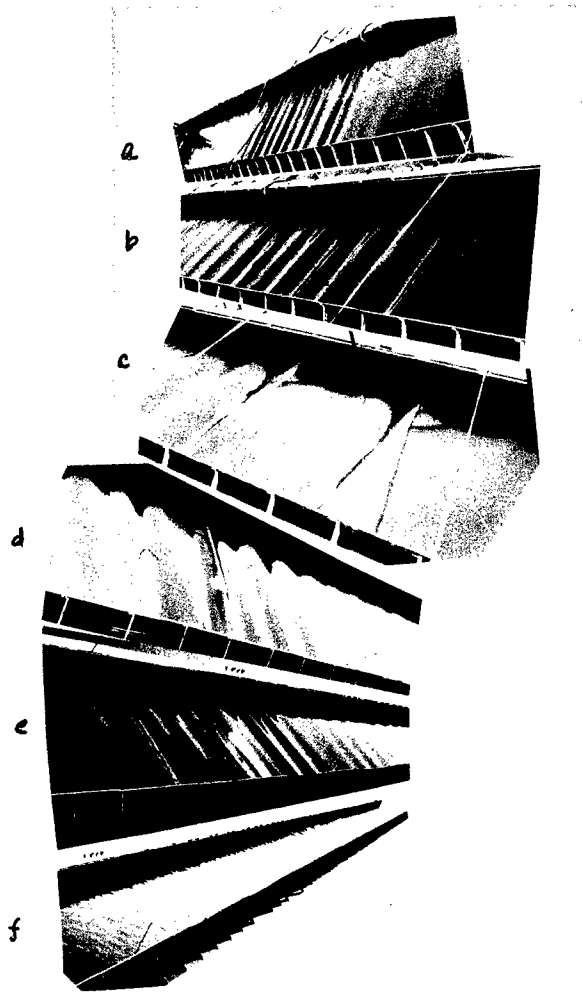


Figure 6. (a-f) A typical sequence of six stages of the evolution of a wave packet with a_0k_0 = 0.16 and N = 10 and f_0 = 1.23 Hz showing three-dimensional wave breaking in a channel of 150 m long and 3.7 m wide and 1 m deep.

soliton like wave groups are formed in stage (f).

For the growth rate of Type I and the stages of beginning and ending of wave breaking of wave packets, the two control parameters a_0k_0 and N are both important. For a fixed a_0k_0, the growth rate is higher and wave breaking occurs sooner for smaller N. The exact characteristics of starting and stopping the wavemaker also plays a role in providing varying degrees of initial perturbations. It certainly deserves more detailed experimental study and will not be discussed further.

We suggest the following physical interpretation for the experimental results described here as the coupling between Type I and Type II instabilities. Under the initial action of Type I instability, the wave trains (or packets) with $a_0k_0 \geq 0.12$ may undergo a considerable modulation in its envelope; subsequently, a few of the waves in the middle of the maximum modulation will have local wave steepness ak > 0.20, which will be high enough to trigger the Type II instability. As $a_0k_0 \geq 0.15$, these locally steeper waves may reach ak $\geq$ 0.30, at which steepness previous experiments (Melville, 1982; Su, et. al., 1982) show extremely fast growth of Type II, thus leading to violent three-dimensional wave breaking. This may explain the leveling off of $a_m a_0$ with respect to a_0k_0 near a_0k_0 = 0.14 in Figure 5 as the transfer of the two-dimensional wave energy to three-dimensional wave form, plus dispersion into three-dimensional higher wavenumber components and dissipation into turbulence is made.

Ocean Wave Breaking

Possible relevance of experimental findings on Type I and II coupling to deep-ocean wave breaking in growing seas will be discussed. First, these natural breaking waves are predominantly three-dimensional crescent-shaped and are spilling rather than plunging forms. Second, Donolan, Longuet-Higgins and Turner (1972) have found, from direct observations, that the average frequency of wave breaking is about equal to half of that of underlying main waves. These authors attributed this feature to the fact that the group velocity is equal to one-half of the phase velocity. Third, the statistical analysis on "extreme wave groups", which are discussed in the previous section, shows that the extreme wave group consists of three zero-crossing waves in the mean, whose average wave steepness is close to 0.16. The average wave steepness of the highest waves is close to 0.20 and, hence, they are very likely near the breaking stage. The three observations from the experimental observations of Types I and II coupling near a_0k_0 = 0.16. As an alternative to the explanation proposed by Donalean, et. al. (1972) on the frequency of wave breaking, we suggest that it is due to the strongest subharmonic perturbation of the wavenumber equal to 1/2 k_0 of Type II instability that has the propagation velocity equal to the phase velocity of primary waves (McLean, 1982; Mieron, Saffman and Yuen, 1982; Su, et al., 1982).

INTERPRETATION OF LARGE WAVES AND EXTREME WAVE GROUPS

Maximum Modulation Due to Wave Instability

Several unique features of the extreme wave group, particularly for the case with narrower spectral bandwidth normally expected for growing seas, prompt us to consider a hypothesis that these extreme wave groups may be caused by nonlinear wave instabilities, rather than simply due to the linear beat phenomenon. In this section we shall present some reasoning in support of this hypothesis.

The side-band instability is characterized by two perturbations with the frequencies $f_1 = f_0 - \Delta f$ and $f_2 = f_0 + \Delta f$, where f_0 is the original primary (unperturbed) freqeuncy of a wave train and/or wave packet under consideration. Furthermore, the Δf is related to the wave steepness, a_0k_0, of the original primary waves by

$$\Delta f = a_0k_0f_0. \tag{8}$$

Experimental observation (Su, 1982) showed that at the maximum modulation due to the side-band instability the amplitudes for the two side-band components, a_1 and a_2, are approximately equal to each other, and further related to the amplitude, a_0, of the primary wave at the particular moment by

$$a_1 \simeq a_2 \simeq 1/2a_0. \tag{9}$$

Hence, the time series of the surface displacement, $\eta(t)$, of the wave train under the maximum modulation of the side-band instability can be expressed as

$$\begin{aligned}\eta(t) &= a_0 \sin(2\pi f_0 t) + a_1 \sin(2\pi f_1 t) + a_2 \sin(2\pi f_2 t)\\ &= a_0 \sin(2\pi f_0 t) + \sqrt{1/2}\, a_0 \sin[2\pi(1-a_0k_0)f_0 t] \sin[2\pi(1+a_0k_0)f_0 t]\\ &= a_0 [1+\sqrt{2}\cos(2\pi a_0k_0f_0t)] \sin(2\pi f_0 t).\end{aligned} \tag{10}$$

Note that the expression in the square bracket is the slower varying envelope of the wave group, which have a repitition period equal to $(a_0k_0)^{-1}$ number of primary wave periods. Now, the mean wave steepness for the

case (c) with 3.0 < 4.0 in Table 1 is equal to $\bar{S}$ = 1/3 (0.133 + 0.208 + 0.128) = 0.156. If we take the average S = 0.16, then the repetition length of the wave group is nearly 6 waves. The corresponding wave heights for the seven waves centering around the maximum of the wave envelope are then given by

$$\begin{aligned} H_0 &= a_0(1 + 2\cos 0^0) = 2.41\, a_0 \\ &= H_0 \\ H_{-1}, H_1 &= a_0(1 + 2\cos 60^0) = 1.707\, a_0 \\ &= 0.7\, H_0 \qquad (11) \\ H_{-2}, H_2 &= a_0\,|(1 + 2\cos 120^0)| = 0.293 \\ &\approx a_0 = 0.121\, H_0 \\ (H_{-3}, H_3) &= a_0\,|(1 + 2\cos 180^0)| \\ &= .41 a_0 = 0.170\, H_0 \end{aligned}$$

The most significant feature of the distribution of the above wave heights is the considerable smallness of $(H_{-3}, H_{-2}, H_2, H_3)$ in comparison to (H_{-1}, H_0, H_1). This feature agrees remarkably well with the observation of the extreme wave group consisting of three high waves, in the mean, as presented in the last section. The ratio $(H_{-1}, H_1)/H_0$ = 4.435/6.352 = 0.698 ≈ 0.7 for case (d) in Table 1 agrees almost exactly with the $(H_{-1}, H_1) = 0.7\, H_0$ of the nonlinear model. The observed fact that $T_0 < (T_{-1}, T_1)$ in Table 1 is also consistent with the experimental observation in the side-band instability.

On the other hand, let's consider a wave train consisting of two sine waves with equal amplitudes but with a difference in frequencies by an amount of $\Delta f = a_0 k_0 f_0$ the same as in the side-band instability. The time series of the corresponding surface displacement for the beat phenomenon will be

$$\eta(t) = a_0 \sin(2\pi f_1 t) + a_0 \sin(2\pi f_2 t)$$

with $f_1 = f_0 - 1/2\, f$, and $f_2 = f_0 + 1/2\, f$. Hence,

$$\eta(t) = a_0[2\cos(\pi a_0 k_0 f_0 t)] \sin(2\pi f_0 t). \qquad (12)$$

The envelope for the beat phenomenon is a simple cosine shape with a repetition period twice longer than the period for the side-band modulation. With the same value of $a_0 k_0$ = 0.16, the seven waves centering around the maximum of the envelope are, approximately,

$$\begin{aligned} H_0 &= 2a_0 \cos 0^0 = 2a_0 = H_0 \\ (H_{-1}, H_1) &= 2a_0 \cos 30^0 = 1.732 a_0 = 0.866 \\ &\approx H_0 \qquad (13) \\ (H_{-2}, H_2) &= 2a_0 \cos 60^0 = a_0 = 0.5\, H_0 \\ (H_{-3}, H_3) &= 2a_0 \cos 90^0 = 0 \end{aligned}$$

Note that $(H_{-2}, H_2) = 0.5\, H_0$ in this case is much larger than the corresponding values for the side-band instability. Of course, when Δf used smaller than the $a_0 k_0 f_0$, the value of H_{+2} will increase, and vice versa.

Wave-Current Interaction

As discussed in the previous section, another possible mechanism for producing large (giant) waves is the effect of an opposing current on waves. It was suggested by Smith (1976) that these giant waves observed on the Agulhas Current, occur where wave groups are reflected by the current. The local behavior of the wave amplitude is modelled by the nonlinear Schrodinger equation. Applying to a typical case with the incoming swell of a wavelength of 200 m and a steepness (ak) of 0.08 in the open ocean and a typical current (-2 m/s) in a current width of 140 km (Mallory, 1974). The corresponding wave height is 5.1 m and wave period 11.2 sec. Smith estimated that there might be about a threefold amplification of the wave height naer the caustic. Thus the crest-to-trough wave height could be as much as 15 m.

We shall suggest another physical mechanism for giant wave generation based on the nonlinear instability. Denote the wave amplitude by a_i, wavelength by λ_i; wave phase speed by c_i, wave frequency by f_i with the subscript I = 1, 2 for the condition, respectively, outside and inside the uniform current region of speed u_i. Longuet-Higgins and Steward (1961) derive the following relations:

$$\left(\frac{a_2}{a_1}\right)^2 = \frac{c_1(u_1 + 1/2\, c_1}{c_2(u_2 + 1/2\, c_2} \qquad (14)$$

$$2\pi f_i = \frac{g}{c_i}(c_i + u_i) \qquad (15)$$

Now, for the example with $u_1 = 0$, $a_1 k_1 = 0.08$

$2a_1 = 5.1$ m, $\lambda_1 = 200$ m

$u_2 = 2$ m/s, and $f_1^{-1} = f_2^{-1} = 12$ sec.

We have

$$a_2/a_1 = 1.342 \qquad (16)$$

$$\lambda_2 = 174 \text{ m}$$

so

$$\frac{a_2 k_2}{a_1 k_1} = \frac{a_2}{a_1} \cdot \frac{\lambda_1}{\lambda_2}$$

$$a_2 k_2 = 0.08 \times 1.546 = 0.124 \qquad (17)$$

For this increase in wave steepness by more than 50%, the maximum wave amplification factor

due to the wave instability alone (a_m/a_2) (see Figure 5) is about 1.7. Hence, the total wave amplitude amplification is

$$\left(\frac{a_2}{a_1}\right)\left(\frac{a_m}{a_2}\right) = 1.342 \times 1.7 = 2.3 \quad (18)$$

Furthermore, for $a_2k_2 = 0.124$, the distance of unstable wave evolution to reach its maximum modulation is less than 100 wavelengths. Thus, it takes less than 40 minutes and 20 km for the original swell becoming giant waves after entering the Agulhas Current. Since the current width is typically of 140 km, the location of the most likely occurrance of giant waves will thus be near the seaward side of the current as actually reported by Mallory (1974).

Comparing to the reflection mechanism of Smith which would take more than 200 km for swell to cross one half of the current width to be reflected by the current shear, this new suggestion based on nonlinear instability is a more direct and quicker mechanism.

CONCLUSIONS

We have analyzed a large set of ocean wave records collected in storm conditions for the structure of wave groups each containing the highest wave height in that wave record, called the extreme wave groups. We found that the extreme wave group predominantly consists of three high waves with heights greater than the significant wave height, and with the mean periods equal about 1.3 times the average period for the entire collection of individual waves determined by the standard up zero-crossing method, and with the mean wave steepness for the highest wave equal to about 0.20. Furthermore, as the spectral bandwidth becomes narrower, these features of the extreme wave groups become more prominent. Based on a previous knowledge of experimental studies on nonlinear side-band instability of finite-amplitude waves, the extreme wave groups are found to be explainable better as the manifestation of the maximum modulation under this type of nonlinear instability, than as the simple linear beat phenomenon.

The experimental results, statistical analyses of field data and theoretical findings, led to suggest that spilling wave breaking for large energy-containing waves near the peak frequency can occur due to nonlinear coupling of instabilities for average wave steepness near 0.14 to 0.18.

In summary, large giant waves, wave groups and wave breaking are most likely the different aspects of the same dynamical process due to the intrinsic instabilities of nonlinear steep waves.

References

1. Benjamin, T.B. and J.E. Feir. 1967. The disintegration of wave trains on deep water. Part 1. Theory. J. Fluid Mech. 27, 417-430.

2. Donelan, M., M.S. Longuet-Higgins, and J.S. Turner. 1972. Periodicity in white caps. Nature 239, 449-450.

3. Earle, M.D., K.A. Bush and G.D. Hamilton. 1984. High-height long-period ocean waves generated by a severe storm in the Northeastern Pacific Ocean during February 1983. J. Physical Oceanography 14, 1286-1299.

4. Elgin, S., R.T. Guza and R.J. Seymour. 1984. Groups of waves in shallow water. J.G.R. 89, 3623-3634.

5. Goda, Y. 1976. On wave groups. BOSS '76, pp. 115-128.

6. Goda, Y. 1983. Analysis of wave grouping and spectra of long-travelled swell. Rep. the Port and Harbour Research Institute, Japan.

7. Hamilton, G.D. 1980. Buoy Capsizing Wave Conditions. Marine Weather Log 24(3).

8. Kimura, A. 1980. Statistical properties of random wave groups. Proc. 17th Int. Conf. on Coastal Eng. pp. 2955-2973.

9. Longuet-Higgins, M.S. 1978b. The instability of gravity waves of finite amplitude in deep water. II. Subharmonics. Proc. R. Soc. Lond. A 360, 489-505.

10. Longuet-Higgins, M.S. 1984. Statistical properties of wave groups in a random sea state. Phil. Trans. R. Soc. Lond. A 312, pp. 219-250.

11. Longuet-Higgins, M.S. and E.D. Cokelet. 1976. The deformation of deep surface waves on water. I. A numerical method of computation. Proc. R. Soc. Lond. A 350, 1-36.

12. Longuet-Higgins, M.S. and E.D. Cokelet. 1978. The deformation of deep surface waves on water. II. Growth of normal-mode instabilities. Proc. R. Soc. Lond. A 364, 1-28.

13. Mallory, J.K. 1974. Abnormal Waves on the South East Coast of South Africa. International Hydrographic Review, 51, No. 2, pp. 99-129.

14. McLean, J.W. 1982. Instabilities of finite-amplitude water waves. J. Fluid Mech. 114, 315-330.

15. McLean, J.W., Y.C. Ma, D.U. Martin, P.G. Saffman and H.C. Yuen. 1981. A new type of three-dimensional instability of finite-amplitude waves. Phys. Rev. Lett. 46, 817-820.

16. Nolte, K.G. and F.H. Hsu. 1972. Statistics of ocean wave groups. Proc. 4th Offshore Tech. Conf., pp. 139-146.

17. Ochi, M.K. 1982. Stochastic analysis and probabilistic prediction of random seas. In Advances in Hydroscience, ed. V.E. Chow, Vol. 13, pp. 217-375.

18. Rye, H. 1974. Wave group formation among storm waves. Proc. 14th Coastal Engineering Conf., Vol. 1, pp. 164-183.

19. Sanderson, R.M. 1974. The Unusual Waves Off Southeast Africa. Marine Observers, Oct., No. 246, pp. 180-183.

20. Schumann, E.H. 1980. Giant Wave. Oceans, July, pp. 27-30.

21. Smith, R. 1976. Giant Waves. J. Fluid Mech. 77, pp. 417-431.

22. Su, M.Y. 1982. Evolution of groups of gravity waves with moderate to high steepness. Phys. Fluids, 25, pp. 2167-2174.

23. Su, M.Y. 1982. Three-dimensional deep-water waves. Part 1. Experimental measurement of skew and symmetric wave patterns. J. Fluid Mech., 124, 73-108.

24. Su, M.Y. 1986. Three-dimensional deep water waves. In Encyclopedia of Fluid Mechanics. Vol. 2. Dynamics of Single-Fluid Flows and Mixing. Chapter 10, ed. N.P. Cheremisinoff, Gulf Pub. Co.

25. Su, M.Y., M. Bergin, R. Myrick and J. Roberts. 1981. Experiments on shallow-water wave grouping and breaking. Proc. First Int. Conf. Meteorology and Air/Sea Interactions of the Coastal Zone, The Hague, Netherlands.

26. Su, M.Y., M. Bergin and S. Bales. 1982. Characteristics of wave groups in storm seas. Proc. Ocean Structural Dynamics Symposium '82. Corvallis, Oregon, pp. 118-132.

27. Su, M.Y. and M.T. Bergin. 1983. Storm Wave Characteristics in the Gulf of Mexico. Proc. 1983 Sym. on Buoy Technology.

28. Su, M.Y. and A.W. Green. 1983. Strong Nonlinear Characteristics of Steep Surface Gravity Waves. 14th Sum. Naval Hydrodynamics. pp. 53-88.

29. Su, M.Y. and A.W. Green. 1984. Coupled two- and three-dimensional instabilities of surface gravity waves. Phys. Fluids 27(11), pp. 2595-2597.

30. Ward, E.G. 1974. Ocean Data Gathering Program - An Overview. Offshore Tech. Conf., pp. 771-780.

31. Yuen, H.C. and B.M. Lake. 1982. Nonlinear dyanmics of deep-water gravity waves. In Advances in Applied Mechanics, Vol. 22, 67-229.

DISCUSSION

H. Maruo,
Yokohama National University

a. You have not mentioned the instability shown by Prof. Saffman of CALTEC which appears in the direction of 90 degrees with respect to the primary wave. This phenomenon may be relevant to your experiment.

b. According to your results, the slope of extreme waves is much less than Stokes highest wave. I have the experience that the highest wave slope which can be generated in laboratory experiment is very close to that of Stokes highest wave. What do you think of the difference between extreme ocean waves and waves generated in the laboratory?

Reply -

a. I checked with Professor Saffman after the symposium, and learned that the instability he discussed earlier was the same three-dimensional instability I presented in the symposium. It is my guess that Professor Maruo has mistaken the "component" in the direction of 90 degrees (with respect to the primary waves) of the above three-dimensional instability to be a separate type of wave instability.

b. Under a carefully controlled, perturbation-free, laboratory condition, it is certainly possible to generate quasi-stationary high-amplitude surface waves which have the slope close to that of Stokes highest wave. However, the extreme waves I discussed in this paper are gravity waves subjected to naturally occurring perturbations, and they are unstable. As such, these extreme waves are totally different from the Stokes waves of permanent form; the latter is unlikely to be existent in open seas.

A Theory of Spilling Breakers

M. P. TULIN and R. COINTE
University of California, Santa Barbara, U.S.A.

ABSTRACT

A physical model for steady spilling breakers is developed and applied, and the results are shown to be in very good agreement with the laboratory experiments of Duncan (1981,3). In this model, the breaker is envisaged as an essentially stagnant eddy held in place on the forward face of the breaking wave by the turbulent shear stresses acting on the streamline which divides the breaker and the underlying flow. Mixing between these regions begins at the front of the breaker, resulting in a discontinuous loss of head on the free surface there. The breaker is trailed by a viscous wake at the free surface which is a direct consequence of the turbulent shear stresses under the breaker. The requirements for force equilibrium and for head loss lead to the determination of breaker height in terms of the crest height of the following wave. The resistance associated with the breaking wave has been determined in two ways: by direct potential wave calculation of the repressive effect of the breaker hydrostatic pressure on the advancing wave, and by a momentum balance. The effect of the trailing wake is considered, and shown to be noticeable. The complete theory reveals that steady breaking wave solutions exist beyond a critical wave steepness, which is less than that of the Stokes limiting wave, and that at the onset of breaking a developed breaker of finite height appears; these predictions are in accord with experimental observations.

INTRODUCTION

Despite their great importance in nature, phenomena related to breaking and breaking waves are poorly understood: Longuet-Higgins, 1980, has characterized breaking as one of the most important basic unsolved problems in hydrodynamics. This is especially true with regard to the ubiquitous spilling[1] breaker, to be distinguished from the unsteady plunging breaker, for which mathematical theories (Longuet-Higgins and Cokelet, 1976, 1978; Vinje, Maogang and Brevig, 1983; New, McIver and Peregrine, 1985) have recently been produced and which is rarely to be found except in the surf, see Figure 1.

The motion of ships is almost always accompanied by spilling breakers in the surrounding water, both at the bow and elsewhere; the white water thus produced is one of the most easily observed features of the ship disturbance, surrounding the ship and trailing aft. Despite this fact, the importance of breaking for ship resistance was noted only in recent times, but then increasingly: (Baba, 1969; Dagan and Tulin, 1970, 1972; Tulin, 1979; Inui, 1981). However, breaking is not only important for resistance, but also in connection with air mixing and its appearance around sonar domes and the ship's screw, and possibly in the remote sensing (SAR) of narrow V wakes behind surface ships.

The physical and mathematical modelling of a "steady" breaker in deep water (as produced by a towed hydrofoil as in Duncan (1981,83), see Figure 1) has been approached in steps within the last 13 years, and this prior work is reviewed in the next section. A major advance was made through the systematic experiments of Duncan referred to above, which for the first time provided not only careful

[1]The classification of breaker types, as now generally employed, was apparently first made by Mason (1952), wherein: the spilling breaker is characterized by white water spilling down the front face, and in contact with it, starting from the crest, and a plunging breaker by a prominent and coherent jet falling in an overturning trajectory from crest to base. Here we emphasize a further distinction, between spilling-like breakers in shallow water (bores) and spilling breakers in essentially deep water. It is the latter which are our interest here.

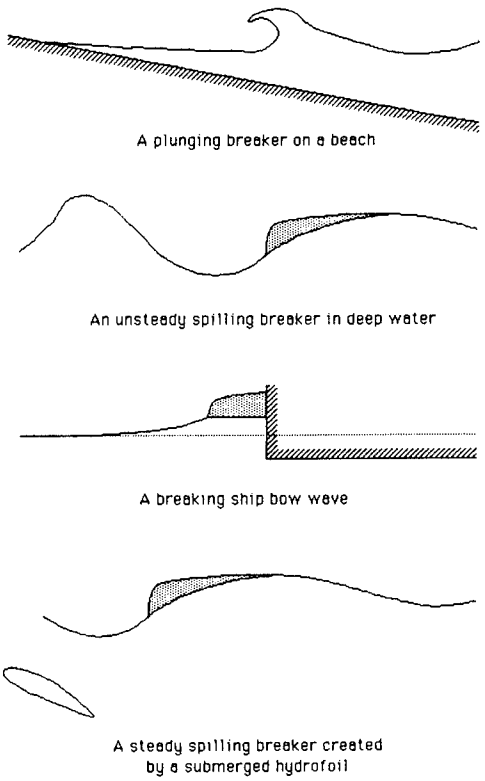


Figure 1 - Various Breaking Waves (Schematic)

qualitative observations but a set of measurements relating breaker and wave dimensions. These data allow a comparison with theory, and have stimulated us to carry out the work reported here.

The Duncan observations give rise to a variety of questions. Some of those which have most intrigued us are:

1. What is the physical nature of a steady spilling breaker? What is an appropriate physical model? Mathematical model?
2. How is the size of the breaker related to the incoming wave resistance?
3. How is onset of breaking determined?
4. What is the relation between the incoming wave resistance and the amplitude of the following waves?
5. How does the breaker suppress the incoming waves?

In this paper [which is an extension of Cointe and Tulin (1986)], the spilling breaker is modelled explicitly as a low energy, essentially stagnant, recirculating eddy riding on the face of the breaking wave and kept in place by the friction between the underlying flow and the eddy; the breaker is trailed by a viscous momentum wake corresponding to the frictional force acting on the breaker mass. In this theory:

- The breaker shape is determined by the balance between hydrostatic pressures and frictional stresses acting on its bounding surface with the underlying wave.
- The viscous (turbulent) region between the breaker and the underlying wave is modelled as a classical mixing region wherein the total head on the dividing streamline is abruptly reduced at the onset point of mixing (leading edge of the breaker), but not thereafter.
- The crest height (amplitude) of the broken wave is determined as a linear declining function of the eddy vertical height by application of Bernoulli's equation (it is argued why this is appropriate) along the dividing streamline. As a result, the larger the breaker the smaller the height of the broken wave.
- Simple force equilibrium considerations determine the vertical height of the eddy in terms of the inclination of the wave front and the magnitude of the friction.
- The relation between the incoming (unbroken) wave and the following (broken) wave is determined through the application of momentum balance or, alternatively with the same result, by utilizing potential wave theory to calculate the wave produced by the breaker (it produces a hydrostatic pressure acting on the surface of the water below) and its subtractive effect on the incoming wave.

The quantitative results are in very good agreement with Duncan's data, and we therefore conclude that our physical model is appropriate.

Among the interesting results and conclusions (which are obtained using linear wave theory in part and therefore subject to future revision):

a) breaking can occur for an incoming wave of amplitude $ga_o/c^2 = 0.69$ or larger, compared to the Stokes limiting $ga_o/c^2 = 0.74$).

b) for steeper incoming waves, two broken states corresponding to a weak and strong breaker can occur; only the strong breaker is observed.

c) breaking would seem not to depend on local, but rather on global considerations.

d) when a breaking solution exists, nature prefers it to the unbroken state.

Directions for extension of the theory are indicated, including the case of breakers before blunt bows.

PREVIOUS WORK

Previous studies of breaking waves have generally been concerned with their limiting form before breaking, both for steady and unsteady waves. Only a few studies concern waves after they have broken. The reason must lie in the fact that potential theory is not sufficient and due account must be taken of viscous processes, notably turbulent shear.

An attempt at a precise description of spilling breakers and their morphology was not made until Longuet-Higgins (1973). He studied the flow near the forward edge of the breaker and modeled the latter as a turbulent wedge sitting on top of the potential flow. The crucial hypothesis in his model was that the leading edge of the breaker is a stagnation point. It leads, for the potential flow, to a solution bearing resemblance to Stokes' limiting wave.

Banner and Phillips (1974) were the first experimentally to study in some detail the flow in a steady spilling breaker. They observed that a turbulent wake extended behind the breaking region. They suggested that a rolling eddy existed in the vicinity of the crest. Unlike the model proposed by Longuet-Higgins, they observed a stagnation point at the crest, and not at the leading edge of the breaker, and took as a breaking criteria the existence of the stagnation point there. They showed, too, that a surface drift current (as due to wind) might be responsible for breaking at lower heights than the Stokes' limiting height, as is commonly observed.

These experimental observations, confirmed in shallow water by those of Peregrine and Svendsen (1978), have led us to consider a physical model at the leading edge of the breaker quite different from that proposed by Longuet-Higgins (1973). We will assume that a discontinuity in velocity occurs at the leading edge, just as at the origin of a classical mixing layer. This concentrated loss in head explains why stagnation can be reached at the crest at a height much lower than Stokes' limiting height: the breaker creates its own drift current.

Longuet-Higgins and Turner (1974) modelled the breaker-eddy itself as a gravity current riding down the forward face of the wave. Under the assumption that the flow was steady in time, they obtained a similarity solution where the whitecap was accelerating uniformly down the slope. They compared their results to a cine film made by Kjeldsen and Olsen (1972), where intermittent breaking was observed. Such modelling has to be performed in order to predict the evolution of the breaking wave. In this paper, we will restrict ourselves to steady breaking. We shall show here that, in this case, the velocity in the breaker can be neglected. Therefore, its shape is determined by a balance between hydrostatic pressures and shear stresses acting on the dividing streamline.

The velocity difference between the flow inside and outside the eddy led us to model quite differently the recirculating region (which is essentially in hydrostatic equilibrium) and the flow underneath. The eddy bears in this model a strong similarity to attached separation regions behind bluff bodies, as modeled by Tulin and Hsu (1980). While modeling the flow in the vicinity of the leading edge of the roller in a manner similar to ours, Madsen and Svendsen (1983) and Svendsen and Madsen (1984) made a numerical model for turbulent bores in shallow water without taking advantage of this distinction.

Duncan (1981 and 1983) made a detailed investigation of the steady spilling breaker created by a towed hydrofoil. His results complemented and extended the observations of Banner and Phillips (1974). He observed that the breaking wave had a small zone of turbulent water riding its forward slope and provided extensive data on the geometry of this breaking region. His measurements supported the hypothesis that the breaking region imparts a shearing force along the forward slope equal to the component of its weight in that direction. This force is responsible for the creation of the wake extending behind the breaking region. An important part of the resistance exerted on the foil is related to the momentum deficit in this wake. Other experimental investigations of the flow in a steady spilling breaker have been performed by Battjes and Sakai (1981) and Mori (1986) for the wave created by a hydrofoil, and by Stive (1980) for a wave on a sloping beach. They confirm the existence of the wake extending behind the roller. However, only Duncan (1981, 1983) related the geometric properties of the breaking wave and the flow field.

In their mathematical modeling, Cointe and Tulin (1986) for the first time studied the effect of the breaker on the wave itself. They showed how the wake is created by the shear distribution at the dividing streamling and how the wave is sharply repressed by the breaker. The present paper is an extension of this work which accounts for most of the experimental observations of Duncan (1981, 1983) concerning the wave train created by a towed hydrofoil.

THE PRESENT MODEL OF THE BREAKER

General Descriptions of the Flow.

Following the observations of Duncan, we visualize the steady spilling breaker as a closed recirculating region (eddy) of aerated

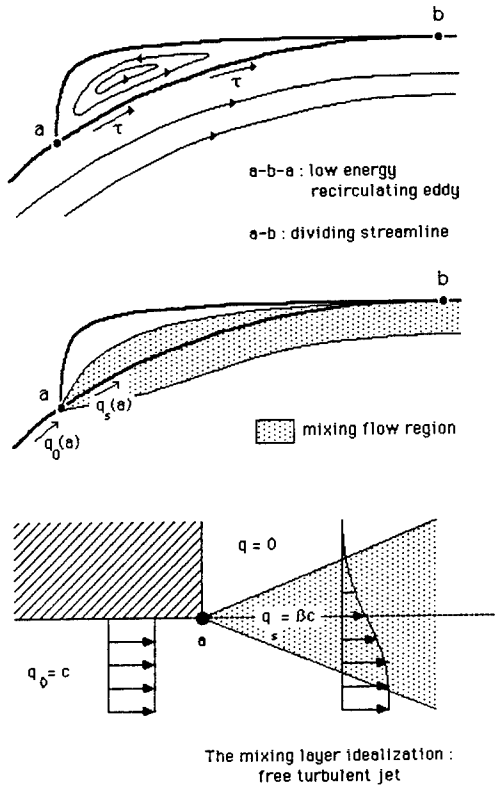


Figure 2 - Physical Model of a Spilling Breaker

water in contact with the underlying wave from the crest at pt. (b), downward over the wave face to its leading edge at pt. (a); we visualize the eddy as essentially flat topped except at its leading edge, where it rises rapidly, see Figure 2. We understand that the flow is turbulent and that exchange takes place from instant to instant between the eddy and the underlying wave, resulting in shear (Reynolds) stresses, but we hereafter refer to the mean (time averaged) steady flow.

In a reference frame fixed in the breaker, the underlying flow moves aft under the breaker, with a speed approaching the wave speed, c, with increasing distance below the wave surface, and we assume that the flow speeds in the body of the breaker are small compared with those in the wave (this assumption is verified in the analysis). As a result of the speed contrast between the fluid in the eddy and beneath it, a strong shear exists along the dividing streamline originating at the onset pt. of mixing (a) and extending to the end of the breaker which coincides with the crest (b); this mixing region is visualized local to (a) as resembling the free turbulent mixing layer between a uniform flow and a stagnant region, see Figure 2.

Inside the breaker the geometry suggests that the flow speed slows and must approach zero as pt. (b) is approached (we assume the speed is continuous there); the assumption that the crest is a stagnation point is critical and is justified by the results and comparison with observations. This assumption is identical to that made by Banner and Phillips (1974) in their analysis of the effects of surface drift on breaking and corresponds of course to the situation in the case of the Stokes limiting potential wave.

We also assume that the fluid within the breaker eddy is aerated due to air mixing, resulting in a substantially lower density, ρ_e, that in the underlying water, ρ. The degree of aeration is not determined from first principles but is estimated from Duncan's observations ($\rho_e/\rho \sim 0.6$).

The shear acting on the free streamline between (a) and (b) results in momentum losses in the underlying flow and as a result there exists just beneath the free surface aft of (b) a turbulent wake which thickens and weakens as it flows aft, as observed and measured by Duncan.

And, finally, the breaker weight causes a positive pressure to exist on the underlying wave and this causes a modification of the wave (as does the following wake to a slighter extent), comprising a strong repression of the incoming wave. This was observed and measured by Duncan and it has been one of the major goals of our theory to explain this effect, as was successfully done.

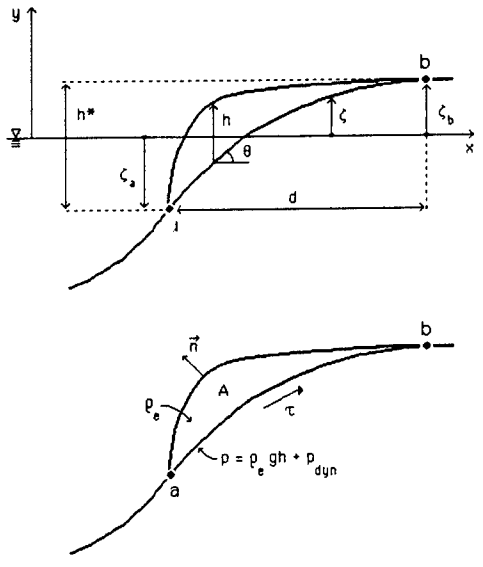


Figure 3 - Definitions

The Mixing Layer and the Dividing Streamline. The height of the wave under the breaker depends upon the head loss experienced by the flow along the dividing streamline, which is a continuation of the free surface. In our model, this flow experiences sudden losses at the leading edge of the breaker (a) where strong initial mixing with the overlying eddy occurs. This flow strongly resembles its mixing layer idealization, see Figure 2, which was first suggested to model the initial mixing of a jet emerging from a nozzle into a chamber. In this flow, which lacks a local length scale and is therefore self-similar, the total head on the dividing streamline experiences a discontinuous loss at (a) and is constant thereafter. We make the same assumptions here[2], so that on the dividing streamline

Before (a), $$q_o^2/2 + g\zeta = c^2/2 \qquad (1)$$

Across (a),

$$\rho_s(a)q_s^2(a) = \beta^2\, \rho(a)q_o^2(a) \qquad (2)$$

Between (a) and (b),

$$p_s + \tfrac{1}{2}\rho_s q_s^2 = \rho_s g(\zeta_b - \zeta) \qquad (3)$$

Note that we have distinguished between ρ_s, the density of the flow on the dividing streamline behind the breaker and ρ, the density of the incoming flow; we expect $\rho_s < \rho$ due to the entrainment of air into the breaker (aeration).

A consequence of (1)-(3) is that the crest height of the breaking wave, ζ_b, becomes determined in terms of the height of the breaker itself, h*:

$$2g\zeta_b/c^2 = 1+2[1-(\rho_s/\rho)\cdot\frac{1}{\beta^2}]\; gh^*/c^2 \qquad (4)$$

Furthermore, the height of the breaking and the following waves are essentially identical, i.e., $\zeta_b = a_f/2$ (this will be confirmed later utilizing potential flow wave calculations). As a result, the prediction (4) can be compared with Duncan's data, see Figure 4. The agreement is excellent[3] for a value[4] $\beta^2 = \rho_s/2\rho$.

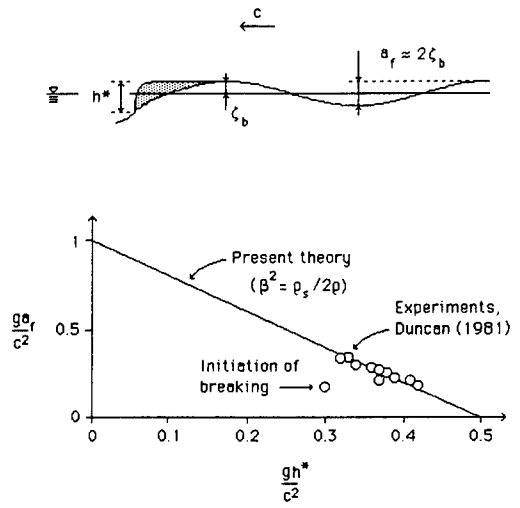


Figure 4 - Breaker Height vs. Following Wave Height

This result can be extended to take into account the effect of surface drift, as due to wind effects, in the same way as in Banner and Phillips (1974). If q_o is the drift velocity at ζ=0, and co-current with the wave velocity, then (we take $\beta^2 = \rho_s/2\rho$):

$$ga_f/c^2 = (1-q_o/c)^2 - 2gh^*/c^2 \qquad (5)$$

Clearly, the effect of drift, q_o, is to reduce the maximum height which can be reached by a wave and to induce early breaking. This was demonstrated by Duncan (1983) where it was shown that early breaking could be stimulated by dragging a sheet on the free surface before the hydrofoil wave system.

This result (5) highlights the fact that the breaker induces its own drift current, i.e., that breaking is self-induced.

Force Equilibria on the Steady Breaker. These equilibria lead to several important conclusions (see Figure 3 for nomenclature):

$$\text{y direction: } \int f_y d(\forall ol) - \int pn_y ds + \int \tau n_x ds = 0 \qquad (6)$$

[2]On a streamline whose curvature is not too great, the flow is given in streamline coordinates by $\rho_s/2\;\partial q_s^2/\partial s + \partial p_s/\partial s = \partial\tau_s/\partial n$. In the idealized mixing flow, the shear stress peaks on the dividing streamline so that $\partial\tau_s/\partial n = 0$, except at the origin of mixing, where it is singular. We assume the same situation in the vicinity downstream of (a), while in the vicinity of (b) we assume that the shear stresses are everywhere small.

[3]The initial data point ($gh^*/c^2 = 0.30$) corresponds to the initiation of breaking, where Duncan has reported to us that the breaker is not fully developed and has a different appearance.

[4]Assuming $\rho_s = \rho_e$ and $\rho_e/\rho = 0.6$ (Duncan's estimate), then $\beta^2 = .55$, in good comparison with the classical mixing layer value, $\beta = .5$.

x direction: $-\int pn_x ds - \int \tau n_y ds = 0$ (7)

where f_y is the vertical body force density (gravitational), and s is the distance along the boundary of the breaker.

The vertical equilibrium simplifies to:

$$\int p_{dyn} dx + \int \tau dy = 0 \quad (8)$$

where the dynamic pressure is due to the circulatory motion within the eddy, as distinct from the hydrostatic pressure acting on the free streamline, $\rho_e gh$. An estimate of p_{dyn} follows from (8) upon assuming that the face of the wave is flat, constant θ, as suggested by Duncan's observations:

$$\left| \frac{\overline{p_{dyn}}}{\rho c^2} \right| = \left(\frac{\bar{\tau}}{\rho c^2} \right) \cdot \tan\theta \tilde{=} 2\times10^{-3} \quad (9)$$

where c is the wave celerity, and the overbars refer to averages over the boundary (a)-(b). We estimate $\bar{\tau}/\rho c^2 = 0(10^{-2})$ based on other data (see later discussion), leading to the estimate (9), and to the conclusion that the circulation within the eddy is very weak, just as in a stable separated zone behind a bluff body (on the other hand, the hydrostatic pressure, similarly non-dimensionalized is observed to be approximately 3×10^{-1}).

The horizontal equilibrium simplifies to:

$$\int \{(\rho_e gh + p_{dyn})\tan\theta - \tau\} dx = 0 \quad (10)$$

or, upon assuming θ constant and neglecting p_{dyn} in comparison to $\rho_e gh$, integration yields,

$$A = \frac{\bar{\tau} d}{\rho_e g \tan\theta} \quad (11)$$

This leads to an estimate for the friction coefficient acting on the dividing streamline near the pt. (a) in the mixing zone, $\bar{c}_f = \bar{\tau}/\rho_o q_o^2(a)$:

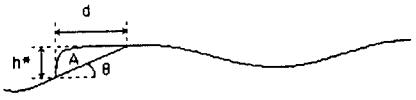
$$\bar{c}_f = \frac{\beta^2}{2} \frac{A}{d^2} \quad (12)$$

We have earlier estimated that $\beta = 0.55$, and Duncan (1981) found experimentally $A/d^2 = 0.11$ (constant), leading to the estimate from (12) that $\bar{c}_f = 0.017$, a value remarkably close to that found experimentally in the mixing zone behind a bluff body (vertical flat plate) by Arie and Rouse (1956), $\bar{c}_f = 0.013$.

Equation (12) also implies:

$$\frac{h^* d}{2A} = \frac{\beta^2}{4} \frac{\tan\theta}{\bar{c}_f} \quad (13)$$

which is compared in Figure 5 with data taken again from Duncan (1981). It would seem that $h^*d/2A$ is, overall, close to unity in value and that the breaker is therefore approximately triangular in shape.



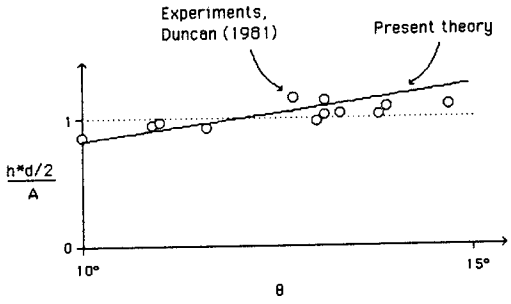


Figure 5 - Breaker Area (Experiments vs. Theory)

Hydrostatic Theory of the Breaker. In view of (9) the dynamic pressure p_d, $0(\bar{p}_d)$, can be neglected in comparison with the hydrostatic, $0(\rho_e gh^*)$, as their ratio $\bar{p}_d/\rho_e gh^* = 0(10^{-2})$. This leads to a very simple theory in which the shape of the breaker is determined by the horizontal balance between the horizontal pressure and the turbulent shear stresses acting on the side and bottom boundaries of a vertical slice of the eddy. As a result, the height of the breaker above the dividing streamline is given by:

$$\rho_e gh dh/dx = \tau - \rho_e gh\tan\theta$$

or,

$$\rho_e gh \frac{d(h+\zeta)}{dx} = \tau \quad (14)$$

Given that $\tau(a)$ is non-zero, as in the mixing layer, then immediately in the vicinity of (a), the front shape of the hydrostatic eddy is parabolic, rising rapidly:

$$h \sim [2\tau(a)(x-x(a))/\rho_e g]^{\frac{1}{2}} \qquad (15)$$

The distribution of τ along the dividing streamline is unknown, but likely falls rapidly with the speed, from a maximum value, $\tau(a)$, near (a) to zero at the stagnation point (b), remaining positive between. As a result, see (14), the upper eddy surface would rise rapidly from (a), flatten out and become horizontal as (b) is approached, as shown in Figures 2 and 3. In fact, the data shown in Figure 5 suggest that a good approximation is given by a right triangular shape, as shown in Figures 6 and 7, as we assume hereafter.

THE EFFECT OF THE BREAKER ON THE FOLLOWING WAVES

General. The breaker causes a pressure to act on the underlying wave as well as shear stresses to act on the free streamline (a)-(b), resulting in the following wake. The action of the shear and its wake can be interpreted as corresponding to a secondary pressure distribution additional to the primary hydrostatic pressure caused by the weight of the breaker eddy. Its effect is noticeable but small.

In lieu of the hydrofoil-wave system it is simpler to consider the more fundamental problem of a non-breaking advancing wave, height, a_o, for which breaking is somehow stimulated on a particular crest, resulting in its repression and a diminished following wave, as shown in Figure 8, for example; the advancing wave may be thought of as generated by a source of resistance, $R = \rho g a_o^2/16$ (small waves).

At the breaking crest, energy is extracted from the underlying wave through the action of the pressure distribution on the forward facing wave, resulting in the following waves repression; the extracted energy is dissipated in the breaker turbulence.

In the following analysis, the effect is calculated in two separate ways with agreement: i) by explicitly calculating the counterwave due to the breaker induced pressure and its subtractive effect on the advancing wave, ii) by a momentum balance taken across the breaking wave, a kind of shock analysis (the balance is actually phrased in terms of the effective wave resistance corresponding to the advancing and following waves, and the resistance due to the breaker).

These analyses follow.

The Wake: Boundary Layer Analysis. The trailing wake behind the spilling breaker seems to behave very much like the turbulent wake behind a two-dimensional body, according to the measurements of Duncan (1981) and Battjes and Sakai (1981). Upon the plausible assumption that the wake is suitably thin, its effect may be calculated by finding the outer potential flow corresponding to the actual physical wave. The major effect is that the outer flow free surface is displaced downward by a distance corresponding to the wake displacement thickness, δ_1; in the case of the wake the latter is well approximated by the wake momentum thickness, δ_2, itself a linear function of the surface stress. The weight of the fluid within the displaced layer then acts upon the outer flow free surface causing an additional secondary pressure distribution; an additional pressure arises due to the curvature of the outer streamlines. Our analysis is closely related to that of Longuet-Higgins (1969) who investigated the effect of wind shear on wave propagation.

As the wake flows along the wavy surface, the outer flow speed fluctuates accordingly (increased in the trough and decreased at the crest), and so therefore does the displacement thickness, see Figure 6, in a manner derived from momentum conservation in the wake (von Karman's boundary layer momentum equation):[5]

$$\delta_1/\Delta = (c/\tilde{q})^3 \qquad (16)$$

where $\tilde{q}$ is the outer flow speed at the wake edge and Δ is the momentum thickness where $\tilde{q} = c$ (i.e. $\zeta=0$); using the momentum equation it is possible to show (we assume $\tilde{q}/c - 1 << 1$) that:

$$\rho\Delta c^2 = \bar{\tau} d \qquad (17)$$

which combined with (11) produces a relation between several experimental observables:

$$\Delta = (\rho_e/\rho)\tan\theta \; gA/c^2 \qquad (18)$$

This relation was first derived by Duncan (1981), who measured Δ using a pitot traverse in the following wave field and otherwise measured θ and A, allowing an indirect experimental determination of the fluid density, ρ_e, within the breaker. He found $\rho_e/\rho = 0.6$, a value we have used here.

The fluctuation in δ_1 and the resulting hydrostatic pressure imposed by it may be shown to modify the dispersion relation for small amplitude waves; this effect is enhanced by the imposed pressure arising from the streamline curvature.[6] The analysis is omitted, but it shows that the wave number k corresponding to a small amplitude wave for celerity c is,

$$k = (1 + 3g\Delta/c^2)g/c^2 \qquad (19)$$

or, combining (18) and (19):

$$k/k_{linear} \sim 1 + 0.9(gh^*/c^2)^2 \qquad (20)$$

---

[5] $d\delta_2/ds + (\delta_1 + 2\delta_2)/\tilde{q} \cdot d\tilde{q}/ds = \tau/\rho\tilde{q}^2$

[6] this pressure is given by $\rho c^2(\Delta/\tilde{q})\partial\tilde{q}/\partial n$

which compares well, see Figure 6, with Duncan's (1981) measurements of the shortened following wavelength, an effect which has not been otherwise explained (the steepness of the following waves, $ga_f/c^2 \sim 0.2$, is too small for the nonlinear effect to explain the observations).

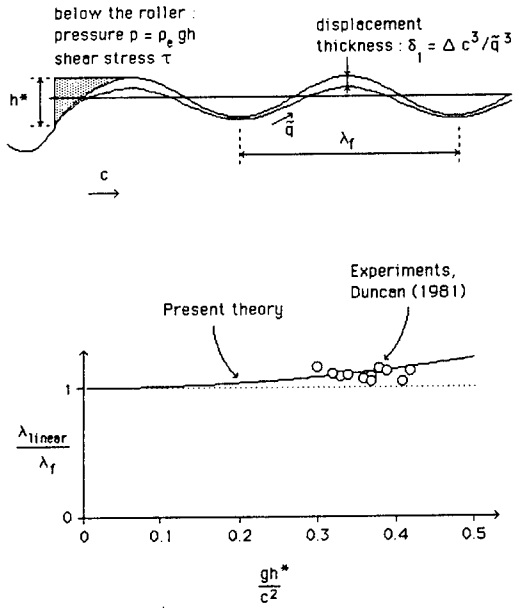


Figure 6 - Effect of Breaker Wake on Following Wave Length

Except for this wavelength change, the effect of the boundary layer thickness modulation will be small and is neglected hereafter.

Potential Flow Wave Calculation. We wish to calculate directly the repressive effect of the breaker upon the advancing wave. Here we take the point of view that this may be done within the framework of potential flow theory, wherein the entire effect of the breaker and wake are to impose on the surface of the wave a hydrostatic pressure (the surface shear and viscous wake momentum balance each other and are otherwise omitted in the model).

The primary pressure due to the breaker is taken corresponding to a flat-topped triangular breaker, being equal to $\rho_e g(h^*-\zeta+\zeta_a)$, where ζ is the elevation of the dividing streamline. The secondary pressure due to the wake will be taken as constant, $\rho g\Delta$, from (b) to ∞ downstream, and it is assumed to grow linearly beneath the breaker, from (a) to (b). See Figure 7.

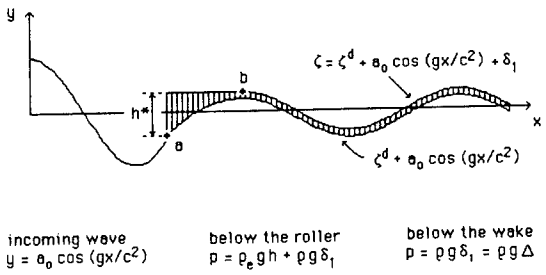


Figure 7 - Effect of Breaker Weight and Wake on Incoming Wave

The advancing wave is steep, although the following wave is not. In any event, we utilize linear-theory, depending upon comparison with experiment for validation. Of course it would be desirable to extend the present theory to include nonlinear effects.

The wave, ζ^*, due to a pressure distribution moving with speed c is given by (see Lamb (1932), Art. 244):

$$\rho c^2\zeta^* = -2\int_{-\infty}^{\infty} p(u)\sin[k(x-u)]du$$

$$+\frac{1}{\pi}\int_{-\infty}^{\infty} p(u)\int_{0}^{\infty} m/(m^2+1)\exp[-m|k(x-u)|]dmdu \qquad (21)$$

where the wavenumber k is g/c^2. The combined pressure due to breaker and wake is:

$$p(x) = \begin{cases} 0 \text{ for } x<x_a \\ \rho_e g(h^*-\zeta+\zeta_a)+\rho g\Delta(x-x_a)/d \\ \qquad \text{for } x_a < x < x_b \\ \rho g\Delta \text{ for } x > x_b \end{cases} \qquad (22)$$

where x_a, x_b, and h^* are unknown and Δ is given by (18).

The resulting wave, ζ, is then given by: $\zeta = \zeta^* + a_0/2\cos(kx) + \delta_1$, where the second term (RHS) represents the incident wave and the last, the assumed displacement thickness. Since (22) involves ζ, the elevation of the free streamline has to be found by iteration. Then, in order to find the unknowns x_a, x_b and h^*, the following conditions are imposed:

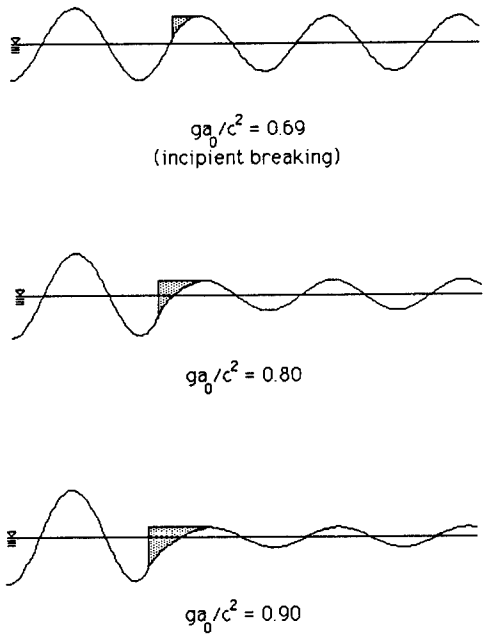


Figure 8 - Computed Wave Profiles

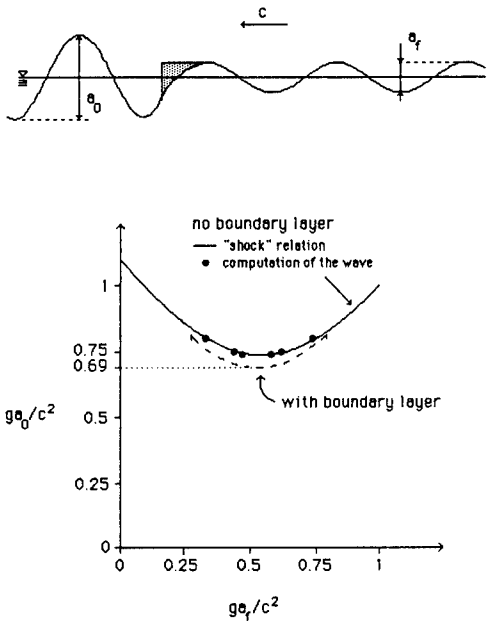


Figure 9 - Incident Wave Height vs. Following Wave Height

$h^*=\zeta_b-\zeta_a$ [the height of the roller is h^*] (23a)

$[d\zeta/dx]_b=0$ [pt. (b) corresponds to a crest] (23b)

$2k\zeta_b=1-2kh^*$ [corresponds to Eq. (5)] (23c)

These equations have been solved numerically, with and without the boundary layer effect. A few computed wave profiles, in the former case, are shown for illustration as Figure 8; note that at incipient breaking a finite breaker exists and that the steeper the advancing wave, the larger the breaker and the weaker the following wave.

The relation between a_f and a_o is shown as Figure 9. We find that: a) a solution exists for advancing waves, as small as $a_o k = 0.69$, which is less steep than the limiting wave which corresponds to $a_o k = 1.0$ (linearized theory); b) two solutions exist for advancing waves corresponding to $a_o k \geq 0.69$, a weak solution with a smaller breaker and larger following waves (to the right of the minimum) and a strong solution (shown in Figure 8); c) the effect of the boundary layer is small but noticeable. The first of these findings, a), is in good agreement with laboratory experiments, which have consistently shown that the maximum deep water wave steepness, a_o/λ, reached prior to breaking for both steady and unsteady waves is in the range 0.10-0.11 [Duncan (1983); Ochi and Tsai (1983); Schultz et al (1986)], in comparison to the Stokes limiting wave for which $a_o/\lambda = 0.14$ [i.e. $(a_o/\lambda)_{exp} \sim 0.75(a_o/\lambda)_{theo}$ at breaking]. It was also observed by Duncan (1981) that at the first appearance of steady breaking, a fully formed breaker already appears, as in the top of Figure 8. Thereafter the breaker grows with increasing hydrofoil resistance, as observed experimentally, corresponding to the strong breaker solution, i.e., the weak breaker is not observed.

Regarding the shape of the breaking wave itself: i) the calculations validate our earlier assumption that the elevation of the breaking and following crests are identical; ii) they allow an estimation of the total height of the breaking wave itself, see Figure 10, and a comparison with experiment. Duncan's (1983) experimental results show that, even before breaking, the first trough behind the hydrofoil is lower than those following. This results in an increase of the height of the first wave of about 20%. We have applied this correction to our result, and this is shown by the dotted line on Figure 10.

Some of the results obtained with the potential wave theory may also be obtained utilizing a momentum balance analysis, at the same time yielding additional insight into the breaking phenomenon.

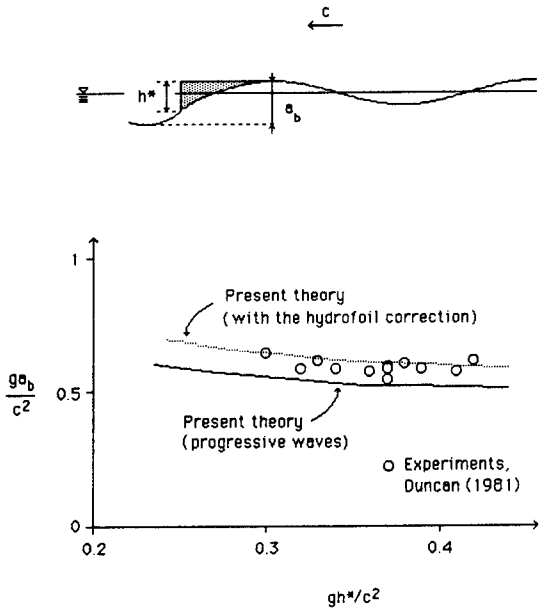


Figure 10 - Breaking Wave Height vs. Height of the Breaker

Momentum Balance; Shock Calculation. Here we calculate the repressive effect of the breaker indirectly. We apply a momentum balance, utilizing the control surface shown at the top of Figure 11, which includes the free surface and the dividing streamling (a)-(b). Conservation of mass is applied and the breaker is assumed flat-topped, and the pressure due to it is taken hydrostatic, $\rho_e gh$. The shear stress on (a)-(b) and the viscous momentum wake are again assumed to balance, and are omitted. The result is:

$$R_o = R_b + R_f \tag{24}$$

where R_o and R_f are the wave resistance associated with progressive waves of amplitude a_o and a_f respectfully, and R_b is the thrust acting on the face (a)-(b) due to the breaker's hydrostatic pressure (i.e., we ignore here the effect of the wake pressure distribution, although it should be included in a more refined theory):

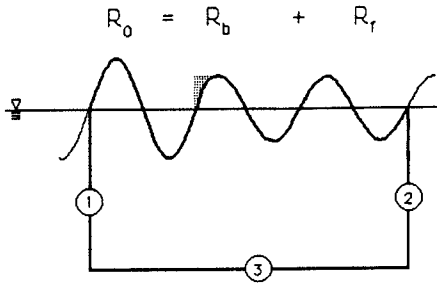
$$R_b = \rho_e g h^{*2}/2 \tag{25}$$

(linear theory) $$R_{o,f} = \frac{\rho g a_{o,f}^2}{16} \tag{26}$$

We note that R_b decreases with increasing a_f while the opposite is true for R_f, see Figure 11. Their sum can be found in terms of a_f by eliminating h^* (using (5)). The sum (R_o is non-dimensionalized) becomes:

$$gR_o/\rho c^4 = \frac{1}{16}(ga_f/c^2)^2 + \frac{1}{8}(\rho_e/\rho)$$
$$[1 - 2(ga_f/c^2) + (ga_f/c^2)^2] \tag{27}$$

which, as shown in Figure 11, has a minimum for $ga_f/c^2 \sim \frac{1}{2}$. In the same figure, the results of the preceding potential wave calculation are shown for the case of no wake effect (solid points) with excellent agreement; and the results including the wake effect are also included again (dashed line).



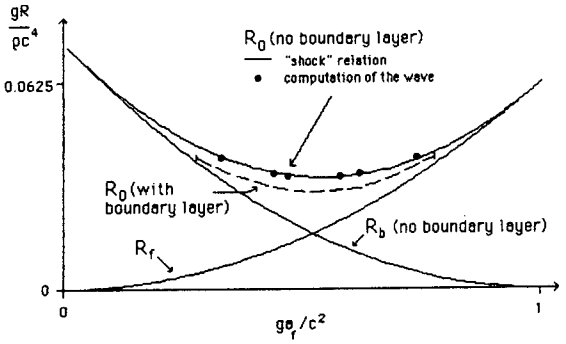


Figure 11 - Total, Wave Associated and Breaking Associated Resistances

The Meaning of the Results; Conclusions. The present results reveal that the existence of the broken wave arises from the fact that it allows the resistance of the advancing wave (i.e., the resistance resulting in the entire wave system) to be balanced by its own breaker resistance plus the residual resistance of the following wave, which is seen to be secondary. This balance is seen to be possible for an initial resistance less than that corresponding to the limiting wave, so that braking is not a consequence of the limiting wave. For a sufficiently small initial resistance, however, no balance is possible, no breaking wave solution exists, and breaking

cannot therefore occur.

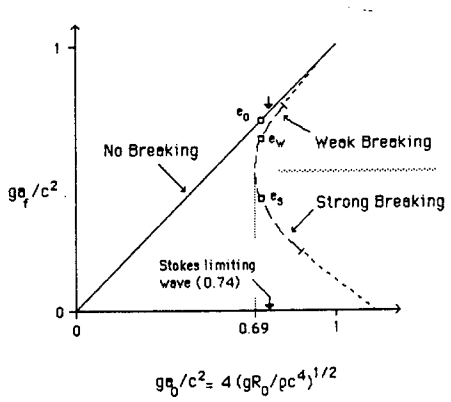


Figure 12 - Following Wave Height vs. Incident Wave Height

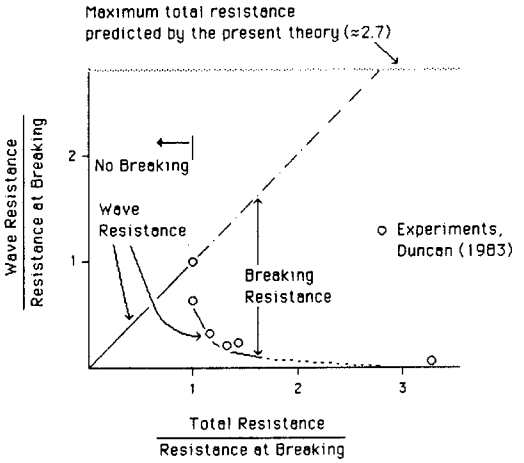


Figure 13 - Wave Resistance vs. Total Resistance

For values of initial resistance larger than that for which breaking can first occur, Figure 11 reveals that two breaking solutions exist (the points e_w and e_s in Figure 12) which we call weak and strong (the breaker is larger in the case of the strong solution). The situation is depicted in Figure 12, showing the jump in a_f which occurs at first breaking, and the strong repression as R_0 is further increased. This strongly resembles Duncan's observations, and in Figure 13 the theoretical prediction based on strong breaking is compared with Duncan's actual data. The fact that we have used linearized theory prevents an exact comparison of data, but when the resistance is non-dimensionalized in terms of the actual resistance at breaking, the agreement between theory and experiment is remarkably good. As a result we can finally conclude that: a breaking solution exists for a wave less steep than the wave of limiting height; nature prefers the broken wave solution; there are actually both a strong and weak breaking solution; the strong breaker is stable and the weak presumably not.

The present model of the spilling breaker would seem well validated in its overall predictions of the actual physical processes which have been observed, it would thus seem to provide an appropriate basis for understanding of these breakers, and has led to answers for all of the five questions presented at the beginning of this paper. Good quantitative comparisons between theory and experiment have also been obtained, see particularly Figures 4, 5, 6, 10 and 13.

Several extensions and applications of the theory suggest themselves: i) reconsideration of the momentum balance utilizing nonlinear wave theory, including the effect of the following wake; ii) theory of the steady spilling breaker before a blunt ship bow; iii) theory of unsteady (transient) spilling breakers as commonly occur in natural waves at sea.

REFERENCES

Arie, M. and Rouse, H., 1956. "Experiments on Two-Dimensional Flow over a Normal Wall," J. Fluid Mech., Vol. 1, pp. 129-141.

Baba, E., 1969. "A New Component of Viscous Resistance," J. Soc. Nav. Arch. Japan, Vol. 125, p. 23.

Banner, M.L. and Phillips, O.M., 1974. "On the Incipient Breaking of Small Scale Waves," J. Fluid Mechanics, Vol. 65, pp. 647-656.

Battjes, J.A. and Sakai, T., 1981. "Velocity Field in a Steady Breaker," J. Fluid Mech., Vol. 111, pp. 421-437.

Cointe, R. and Tulin, M.P., 1986. "An Analytical Model for Steady Spilling Breakers," Proceedings, NSF Symposium on Air-Sea Interaction, Taiwan (in press).

Cokelet, E.D., 1977. "Breaking Waves," Nature, Vol. 267, pp. 769-774.

Dagan, G. and Tulin, M.P., 1970. "Nonlinear Free Surface Effects in the Vicinity of Blunt Ship Bows," Proceedings, 8th Symposium Naval Hydrodynamics, Pasadena, National Academy Press, Washington, DC, pp. 607-626.

Duncan, J.H., 1981. "An Experimental Investigation of Breaking Waves Produced by a Towed Hydrofoil," Proc. R. Soc. London A, Vol. 377, pp. 331-348.

Duncan, J.H., 1983. "The Breaking and Non-Breaking Resistance of a Two-Dimensional Hydrofoil," J. Fluid Mechanics, Vol. 126, pp. 507-520.

Inui, T., 1981. "From Bulbous Bow to Free-Surface Shock Waves - Trends of 20 Years' Research on Ship Waves at the Tokyo University Tank," J. Ship Research, Vol. 25, pp. 147-180 (3rd G. Weinblum Memorial Lecture).

Kjeldsen, S.P. and Olsen, G.B., 1971. "Breaking Waves," 16 mm film. Technical University of Denmark, Copenhagen.

Lamb, H., 1932. Hydrodynamics, Dover Publications, New York.

Longuet-Higgins, M.S., 1969. "Action of a Variable Stress at the Surface of Water Waves," The Physics of Fluids, Vol. 12, pp. 737-740.

Longuet-Higgins, M.S., 1973. "A Model of Flow Separation at a Free Surface," J. Fluid Mech., Vol. 57, pp. 129-148.

Longuet-Higgins, M.S. and Turner, J.S., 1974. "An Entraining Plume Model of a Spilling Breaker," J. Fluid Mech., Vol. 63, pp. 1-20.

Longuet-Higgins, M.S. and Cokelet, E.D., 1976. "The Deformation of Steep Surface Waves on Water. I. A Numerical Method of Computation," Proc. Roy. Soc. London A, Vol. 350, pp. 1-26.

Longuet-Higgins, M.S. and Cokelet, E.D., 1978. "The Deformation of Steep Surface Waves on Water. II. Growth of Normal-Mode Instabilities," Proc. Roy. Soc. London A, Vol. 364, pp. 1-28.

Longuet-Higgins, M.S., 1980. "The Unsolved Problem of Wave Breaking," Proceedings, 17th Int. Conf. Coastal Eng., Sydney, Australia, pp. 1-28.

Madsen, P.A. and Svendsen, I.A., 1983. "Turbulent Bores and Hydraulic Jumps," J. Fluid Mech., Vol. 129, pp. 1-29.

Mason, M.A., 1952. "Some Observations of Breaking Waves," Gravity Waves, U.S. Nat. Bur. Standards, Circular No. 521, pp. 215-220.

Mori, K., 1986. "Sub-Breaking Waves and Critical Conditions for their Appearance," J. Society Naval Architects Japan, Vol. 159, pp. 1-8.

New, A.L., McIver, P. and Peregrine, D.H., 1985. "Computations of Overturning Waves," J. Fluid Mech., Vol. 150, pp. 233-251.

Ochi, M.K. and Tsai, C.-H., 1983. "Prediction of Occurrence of Breaking Waves in Deep Water," J. Physical Oceanography, Vol. 13, pp. 2008-2019.

Peregrine, D.H. and Svendsen, I.A., 1978. "Spilling Breakers, Bores and Hydraulic Jumps," Proceedings, 16th Coastal Eng. Conf., Hamburg, pp. 540-550.

Schultz, W.W., Ramberg, S.E. and Griffin, O.M., 1986. "Numerical and Experimental Studies of Steep and Breaking Gravity Waves in Deep Water," Proceedings, 16th Symposium Naval Hydrodynamics, Berkeley, Calif., July 1986.

Stive, J.J.F., 1980. "Velocity and Pressure Field of Spilling Breakers," Proceedings, 17th Coastal Eng. Conf., Sydney, Australia, pp. 547-565.

Svendsen, I.A. and Madsen, P.A., 1984. "A Turbulent Bore on a Beach," J. Fluid Mech., Vol. 148, pp. 73-96.

Tulin, M.P., 1979. "Ship Wave Resistance - A Survey," Proceedings, U.S. National Congress on Applied Mechanics, UCLA, July 1978.

Tulin, M.P. and Hsu, C.C., 1980. "New Applications of Cavity Flow Theory, 13th Symposium Naval Hydrodynamics, Tokyo, Japan, National Academy Press, Washington, DC, pp. 107-131.

Vinje, T., Maogang, X. and Brevig, P., 1983. "A Numerical Approach to Nonlinear Ship Motion," Proceedings 14th Symposium Naval Hydrodynamics, Ann Arbor, Mich., National Academy Press, Washington, DC, pp. 245-278.

DISCUSSION

William J. Devenport,
Virginia Polytechnic Institute and State University

This problem is in some ways very like the flow over a backward facing step at high Reynolds numbers. This flow also consists of a region of turbulent recirculating flow bounded by a turbulent shear layer. In fact several workers, notably, Chapman and Korst, and more recently Devenport [a] have attempted to model this flow by assuming that the turbulent shear layer behaves like a plane mixing layer positioned on the dividing streamline of the flow. However, if measurements are made in the flow over a backward facing step with instruments sensitive to instantaneous flow reversals, it is found that the turbulent mixing layer is quite different to a plane mixing layer. In particular, the maximum turbulent shear stress is significantly greater than in the plane mixing layer and, in as much as the location of peak turbulent shear stress marks the centre of the shear layer, the centre of the shear layer does not remain coincident with the dividing streamline as reattachment is approached.

[a] Devenport, W.J., "Separation Bubbles at High Reynolds Number: Measurement and Computation," Ph.D. Thesis, Cambridge University, England, 1985.

Reply -

In our paper, we refer to the experiments of Arie & Rouse (1956) for the mixing zone behind a bluff body. In this case, the turbulent mixing layer is very similar to a plane mixing layer near the leading edge. It is remarkable that for the spilling breaker Duncan's experiments lead to a value of the friction coefficient close to that found experimentally by Arie & Rouse (see Eq. [12]). The case of the flow over a backward facing step is somehow different because of the boundary layer which develops before the mixing region and which we of course do not expect to be present in the case of a spilling breaker.

James H. Duncan,
Flow Research Company

The authors are to be commended on their theoretical analysis that illucidates so much about the dynamics of these steady breaking waves. I would like to ask a question concerning an observation made during my experiments on breaking waves produced by hydrofoils. In the experiments, I found that near the point of incipient breaking there were conditions where the wave would break if disturbed but would not break otherwise. Do your calculations show any evidence of this marginal stability zone?

Reply -

In this paper, we did not perform any stability analysis. However, we found that near the point of incipient breaking there are three possible solutions: two breaking and one unbroken. Your experiments seem to show that the weak breaking solution is always unstable, the strong breaking solution stable and the unbroken solution marginally stable (i.e. stable, but less stable tahn the strong breaking solution which is preferred when disturbances are present). Actually, using an argument similar to that of Banner & Phillips (1974) we have shown (see Eq. [5]) how early breaking can be stimulated by a surface drift current. We are presently working on the stability anlaysis to account for your experimental observations.

K. Mori,
Hiroshima University,

The mechanism of the steady breaker is dynamically different from that of the unsteady. In Fig. 8, you gave a mean line including steady breakers measured by Duncan (his symbol +). Careful observation may give a smaller inclination for the steady breakers; my estimation gives 0.016 instead 0.021. It is important not to mix-up all types of breaking.

Reply -

We certainly agree that unsteady breaking is a much more complicated process than steady breaking. However, the purpose of our paper was a more modest one, to develop a theoretical model for steady breaking and to compare these results with Duncan's steady hydrofoil experiments.

Patrick J. Roache,
Ecodynamics Research Associates, Inc.,

To an aerodynamicist, your enlightening and remarkably successful formulation is reminiscent of the Chapman-Korst flow model for base pressure. In that theory, the determination of the ratio of the local velocity along the dividing stream line to the edge velocity if of critical importance. In the Chapman laminar model, it is determined by way of similarity solutions, and in the Korst turbulent model, it is determined by way of an integral solution based upon an error function velocity profile. In the present work, it is empirical. It is surprising to me that the empirical value for two-stream mixing of water would be adequate for the present work in which one stream is 50% aerated. In view of this, have you or do you plan to explicity examine the sensitivity of the solution to this empirical parameter?

Reply -

In our model, the value of B (see Eq.[2]) is not fixed *a priori*. The application of Bernoulli's equation (which is justified by the mixing layer model) leads to a linear relation between the height of the breaker when B is assumed to be a constant. Duncan's experiments confirm the existence of such a linear relation and therefore provide a way to estimate B. As you have noticed, the value of B we obtained is very close to that for two-stream mixing of water. However, we did not attempt to determine directly B by way of a theoretical analysis.

Steep and Breaking Deep Water Waves

W. W. SCHULTZ, University of Michigan, and
O. M. GRIFFIN and S. E. RAMBERG, Naval Research Laboratory, U.S.A.

ABSTRACT

Many Naval applications require a further basic understanding of surface wave hydrodynamics up to and beyond the onset of breaking, and of the energy and momentum transfer processes which take place during and after breaking. In the present paper we describe a technique for the computation of steep asymmetric wave motions up to the incipient or onset stages of breaking. Comparisons are made with related computational schemes and then the method is used for a study of limiting wave conditions and the onset of breaking. The computations are compared with recent measurements made at NRL and elsewhere of the limiting heights of deep water waves and the losses in potential energy density and momentum flux which accompany the breaking process. An estimate of the limiting wave height at breaking in deep water from the computational results is in good agreement with the experiments described where. The potential energy and momentum flux loss rates of plunging breakers are about twice those of spilling breakers in deep water.

1. INTRODUCTION

There are many problems associated with the breaking of waves in deep water which have important Naval applications. The interaction between waves (ship and ambient) and surface currents, including those interactions caused by the passage of a surface ship, often result in the production of waves which steepen to the point of breaking. Other problems include the formation and persistence of white water in the breaking process, and the remotely observable radar and radiometric signatures associated with the breaking phenomena. These applications require a further basic understanding of the wave hydrodynamics up to and beyond the onset of breaking, and of the energy and momentum transfer processes during and after breaking.

In the present paper we consider the steepening and breaking of waves in deep water. First we briefly summarize some of the most recent work concerning the breaking processes in deep water. Extensive summaries of earlier work are readily available (Cokelet, 1977a; Kjeldsen and Myrhaug, 1978; Griffin, 1984). Then we describe a technique for the computation of steep asymmetric waves up to the incipient or onset stages of breaking. Comparisons are made with related computational schemes and then the method is used for a study of limiting wave conditions and the onset of breaking.

The computations then are compared with recent measurements made at NRL and elsewhere of the limiting heights of deep water waves. In the final section of the paper we discuss the energy in steep waves and the losses in potential energy density and momentum flux which accompany the breaking process. Computations of the energy of the waves near and at breaking are compared with the results of the laboratory-scale experiments.

2. SOME RECENT STUDIES OF WAVE BREAKING

Several significant advances toward understanding the causes and characteristics of wave breaking have been made in recent years. These include the experimental observations of instability mechanisms which can lead to wave breaking (Melville 1982; Su, et al., 1982), mathematical models for these instability mechanisms (Longuet-Higgins 1978a,b), and numerical simulations of wave overturning and incipient breaking (Longuet-Higgins and Cokelet 1976, 1978; Vinje and Brevig, 1981a,b; New, McIver and Peregrine, 1985; Schultz, 1985; Jansen, 1986).

Many advanced perturbation techniques have been developed for steep steady waves which are symmetrical, see Cokelet (1977b) and Williams (1981, 1985), for examples. Nonlinear waves approaching the onset of breaking are asymmetric and unsteady, and so numerical simulations must be sought. The most efficient of these available numerical solution algorithms (cited in the preceding paragraph) are based upon some form of boundary integral technique. These numerical approaches at present suffer from the limitations of periodic boundary conditions to limit the extent of the computational domain.

Relatively few detailed experimental studies have been made of the development and subsequent breaking of steep nonlinear waves in deep water. Examples are the work of Ochi and Tsai (1983) and of Bonmarin and Ramamonjiarisoa (1985) to study the onset of breaking for steep, nonlinear waves in a uniform channel; and the work of Ramberg and Griffin (1986) to study the growth of steep waves in a convergent wave channel. These experiments study the conditions which govern the onset of wave breaking. Experimental studies of the growth of steep waves to the onset of breaking are Melville (1982) and by Su, et al. (1982). Measurements of the loss of momentum flux in the spilling and plunging of breakers have been made by Melville and Rapp (1985). Comparable measurements of the loss in potential energy density during and after breaking have been reported by Ramberg and Griffin. Banner and Fooks (1985) have sought to characterize experimentally the radar signature of breaking waves, and to relate the hydrodynamic processes to the microwave back-scattering from the waves.

Experimental studies of steep, nonlinear wave motions are usually three-dimensional by the very nature of the waves

themselves; in some limited cases the flow is quasi-two dimensional, as in the instabilities observed at some of the lower wave steepnesses by Melville and by Su, et al.

3. COMPUTATIONS OF STEEP AND OVERTURNING SURFACE WAVES

Incompressible wave flows such as these usually are viewed as being irrotational up to the stage of breaking when turbulent flow and air entrainment processes are important. This is reasonable either until the formation of aerated white water at the wave crest (spilling); or until the wave's forward face issues into a jet, curls and falls into the surface some distance away from the crest (plunging). Breaking waves are often three-dimensional, but as an initial step many important features can be determined from simpler, two-dimensional approaches.

Although formal analytical techniques have been developed for small-amplitude gravity waves, unsteady and steep waves must be solved numerically. The most efficient of these algorithms are based on some form of boundary integral technique. Even then, the algorithms can be rather time consuming. Hence, no thorough and complete parametric study has been performed on gravity waves. Specifically, there is no agreed-upon criterion for the onset of wave breaking. Even more important, to reduce computational effort, the problem domain is kept as small as possible by applying periodic boundary conditions. Casual observations of breaking waves show that they are not spatially periodic. In this paper, we only present results for the periodic problem.

The numerical schemes to solve irrotational flow problems can be broken into two general approaches: a) domain integration, based on finite differences or finite elements usually combined with Lagrangian movement of the nodes (e. g., Miner, et al., 1983) or b) boundary integration based on Greens functions (Longuet-Higgins and Cokelet, 1976, 1978; Vanden-Broeck, 1980; Baker, Meiron and Orszag, 1982) or based on the Cauchy integral theorem for complex potentials (Vinje and Brevig, 1981a,b). The only published results for breaking waves use boundary integral techniques, due in no small part to the reduction of the problem dimensions by one from a full domain solution. The various boundary integral approaches give equivalent results (McIver and Peregrine, 1981). Recent work (Dold and Peregrine, 1984) has shown that algorithms based on the Cauchy Integral theorem can be up to 50 times faster than Green's function algorithms using sources and 10 times faster than those using vortex methods. Lin, et al. (1984) use the Cauchy formulation when solving two dimensional problems and "revert" to the Greens function algorithm for axisymmetric problems. Apparently, the efficiency of the complex algebra is significant and normal derivatives of the Greens function need not be found.

Here we report on an improvement of an algorithm based on Vinje and Brevig (1981a,b). This highly efficient algorithm allows a thorough study of initial and boundary conditions to determine, for example, the onset of wave breaking, when waves "spill" or "plunge" and ultimately will permit study of non-periodic boundary conditions.

Problem Formulation

The first problem we solve is shown in Fig. 1. The initial boundary value problem solution is described by a complex potential $w(z) = \phi + i\psi$, where ϕ is the velocity potential, ψ is the stream function and $z = x + iy$ represents the two spatial coordinates. At every time step the unknown boundary values of the complex potential (half of the values are known from the boundary conditions) are solved using the Cauchy integral theorem

$$\oint \frac{w\,(z)\,dz}{z - z_0} = 0, \tag{1}$$

where the integral is a closed line integral enclosing the computational domain and z_0 is an arbitrary point nearing the contour from the outside. This integral equation is applied N times as z_0 approaches each node and becomes a system of linear algebraic equations when w is discretized as a piecewise-linear function between the N boundary nodes. Once the complex potential is known along the domain boundary, the solution can be stepped forward in time using Bernoulli's equation and the kinematic boundary conditions on the free surface, respectively, as follows

$$\frac{D\phi}{Dt} = \frac{1}{2}|dw/dz|^2 - y - P \tag{2a}$$

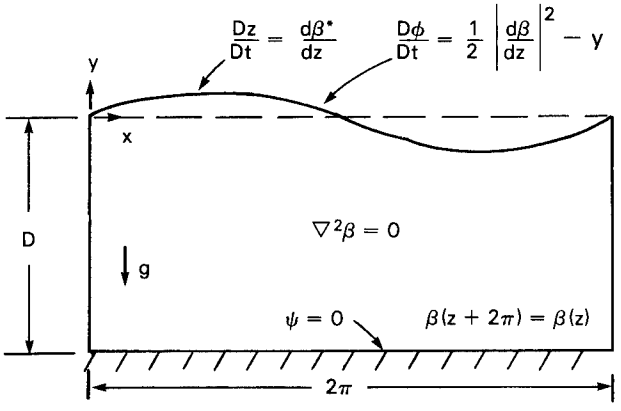


Fig. 1 — The scaled periodic problem

$$\beta = \phi + i\psi$$

$$z = x + iy$$

$$\frac{d\beta}{dz} = u - iv$$

and

$$\frac{Dz}{Dt} = dw^*/dz \tag{2b}$$

Here, P is a prescribed pressure (normally 0 as in this study unless surface tension or wind effects are included), D/Dt is a material derivative, and * denotes complex conjugate. The problem is scaled using gravity and a length scale chosen to make the problem 2π periodic in the horizontal direction. This scaling makes the wavenumber, k, and the linear wave speed, c_0, equal to unity.

Initial conditions are required for the velocity potential, ϕ, and the elevation, η, of the free surface. For purposes of illustration and comparison, we use the same initial conditions as McIver and Peregrine (1981)

$$\eta = -a \sin x \tag{3a}$$

$$\phi = a \cos x. \tag{3b}$$

These initial conditions satisfy linear theory as the amplitude a approaches zero. We successively apply larger values of the initial amplitude a such that the wave will break. The dimensionless potential and kinetic energies are computed in the following way, as

$$P.E. = \frac{1}{2}\int_0^{2\pi} \eta^2 \, dx, \tag{4a}$$

and

$$K.E. = \frac{1}{2}\iint \left|\frac{dw}{dz}\right|^2 dA$$

$$= \frac{1}{2}\oint \phi \frac{\partial \phi}{\partial n} \, ds$$

$$= \frac{1}{2}\oint_0^{2\pi} \phi \, d\psi. \tag{4b}$$

Here we have used Stokes' theorem and the Cauchy-Riemann conditions in order to obtain the final form of the kinetic energy. The integration about the closed contour can be limited to that on the free surface since the periodic contributions cancel.

Numerical Procedure

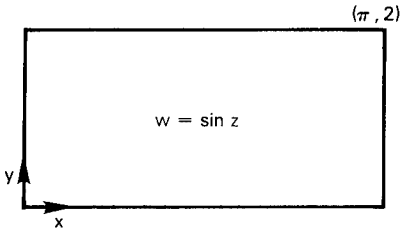
We solve this problem in a similar way to Vinje and Brevig with the following four changes:

1) When the real and imaginary parts of the discretized form of the Cauchy integral theorem are equated, we find that there are essentially 2N real equations and N real unknowns. (There actually can be fewer than N unknowns if some nodes are placed in corners where the real and imaginary parts of w are both known.) Vinje and Brevig (1981a,b) discard half of these equations while we solve the overdetermined system in a least-squares sense.

Numerical experiments compared to a known test case shown in Fig. 2 indicate that the least-squares solution is always better, especially when the node placement is irregular (as will be the case after nodes are convected on the free surface). This test problem is similar to the solution of a potential problem for waves in a container. It is clear from these results that the convergence for the overdetermined system and the Vinje and Brevig approach is order N^2 when the nodes are evenly spaced. However, placing more points in the locations of greatest error (at the upper corners) makes the Vinje and Brevig method solution deteriorate while the least-squares solution significantly improves. Lin, et al. (1984) also find that nodes must be equally spaced, apparently from their use of the same method.

The least-squares approach also eliminates the need to "guess" which equations to discard for the periodic boundary conditions as in Vinje and Brevig. Since much of the time of solving the potential equation is used in developing the complex log terms of the influence functions, little additional computational time is required to solve the overdetermined system if an efficient least-squares algorithm is used.

2) Although our ultimate goal is to eliminate the periodic boundary conditions, it is highly efficient to use conformal mapping for periodic conditions using $\zeta = e^{iz}$ to map a semi-infinite plane to a circle (Longuet-Higgins and Cokelet, 1976, 1978). Conformal mapping has three advantages: a) elimination of periodic and bottom nodes (N is typically reduced by twenty percent), b) elimination of sharp computational corners (All boundary integral techniques suffer when curvature of the boundary becomes large. Our least-squares approach has this difficulty to a lesser extent as shown in Fig.



		Vinje & Brevig Method		Least-Squares Method	
	N	$\|Error\|_2$	$\|Error\|_\infty$	$\|Error\|_2$	$\|Error\|_\infty$
even	8	0.96	1.80		
	16	0.19	0.51	0.12	0.33
	32	0.037	0.12		
uneven	20	0.27	0.61	0.054	0.08

Fig. 2 — Test problem error evaluation. The maximum and rms errors for two methods of solving the potential equation using the Cauchy integral theorem. The maximum errors occured at the upper corners where ψ is assumed to be unknown. The errors are for even placement of the nodes (for example N = 8 has a node at each corner and each midpoint) and uneven placement (N = 20 is the same as N = 16 with nodes placed 0.15 either side of the upper corners).

2. The corner problem is considered in more detail by Jansen (1986)) and c) "linearization" of the linear solution, allowing the linear small-amplitude wave solution to be expressed exactly by a piecewise-linear representation.

3) We use a central difference form for dw/dz (or $dw/d\zeta$) while Vinje and Brevig use a truncated analytic form. Since the solution is piecewise-linear rather than analytic, we have found that some numerical instabilities can develop using Vinje and Brevig's method. One can easily find examples where the derivative dw/dz at a corner of the contour computed using the analytic form lies outside the range computed by the "forward" and "backward" derivatives. This violates the spirit of using piecewise-linear functions and can lead to numerical instabilities. However, the truncated analytic form is more accurate when the contour is smooth.

4) We march fully implicitly in time. Each time step involves full nonlinear iteration between the free surface boundary conditions and the integral equation using an Euler predictor-corrector method. This suppresses numerical instabilities without artificial smoothing. This also allows significantly larger time steps to make the algorithm robust and economical.

Typical Results

Figure 3 shows two typical results of free surface profiles for dimensionless times 0.1 apart for two different initial amplitudes. All computations reported in this paper conserved the total energy to within 0.1 percent all the way to breaking. Breaking can be defined numerically as the time in the computation when the implicit time-stepping procedure fails to converge. The first family of curves for $a = 0.3$ (Eq. 3) has slightly more energy than a steadily progressing traveling wave will support. This results in a "spilling" breaker. When more energy exists initially ($a = 0.544$), the wave becomes a "plunging" breaker. The algorithm breaks down at the last time step shown because of insufficient spatial and/or temporal resolution. This breakdown exhibits itself as a failure of the implicit time stepping procedure to converge. The algorithm has been verified by solving the example problem given in McIver and Peregrine (1981). This comparison is shown in Fig. 4 at a short time before breaking. No numerical filtering was required to inhibit "zigzag" instabilities of the free surface found in some studies (Longuet-Higgins and Cokelet, 1976, 1978; Lin, et al., 1984; Baker, et al., 1982). No direct comparison of computational effort between McIver and Peregrine was made but our algorithm used time steps of a factor of ten to twenty larger.

Numerical Criteria for the Onset of Breaking

We have run many numerical simulations to determine the initial conditions that cause plunging or spilling to occur. We find that waves with initial conditions (3a,b) with the value for $a > 0.28$ will spill and $a < 0.27$ will progress indefinitely. Typical computations use N=60 or 80 and $\Delta t = 0.1$ or 0.05. These results are rather insensitive to the initial conditions in that an initial condition using a 3-term Stokes profile,

$$\eta = a \sin x + 0.5\, a^2 \sin 2x + 0.375\, a^3 \sin 3x, \qquad (5)$$

instead of (3a) does not change whether the wave will spill or not, although the time to breaking and the wave shape differ. Since the total energy is constant throughout an entire computational (and a presumably inviscid) experiment, it would appear to be an promising criterion to determine the onset of breaking. Unfortunately, without a very carefully calibrated and instrumented wavemaker or the ability to measure the velocity everywhere in the flow field, the total energy cannot be measured. Instead, usually a measured steepness criterion (crest-to-trough wave height)/wavelength often is used. We

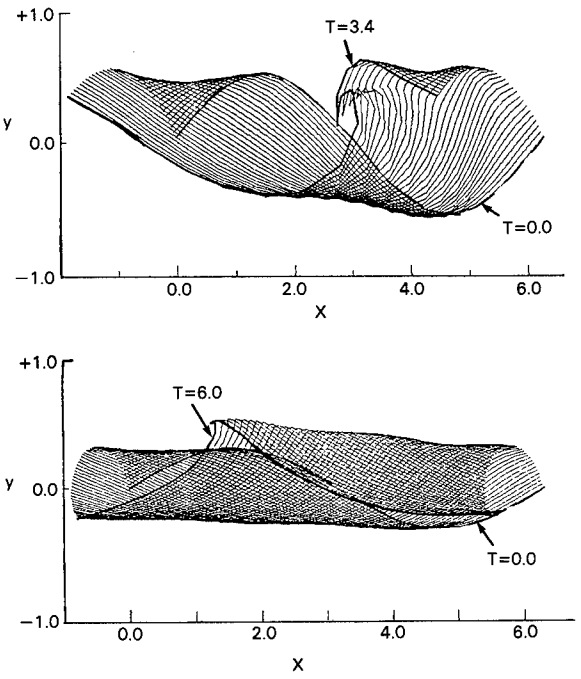


Fig. 3 — Breaking waves. Time history of the development of a plunging breaker (upper plot) and a spilling breaker (lower plot) computed using the present method. The initial conditions were $a = 0.544$ (upper plot) and $a = 0.30$ (lower plot). Our time step between wave profiles is approximately 0.1 .

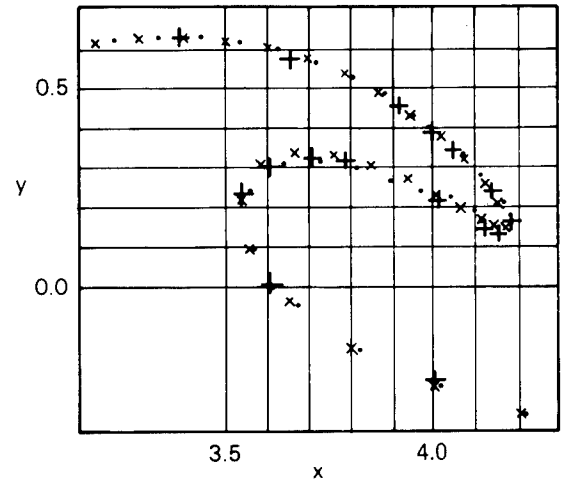


Fig. 4 — Method comparison of results from Vinje and Brevig ×, Longuet-Higgins and Cokelet(•) and our method(+) for the initial value problem with $a = .544$ and at time $t = 3.655$ (modified from McIver and Peregrine, 1981). The depth of Vinje and Brevig and our computations is 10, the depth of the Longuet-Higgins and Cokelet calculation is infinite. Our time step is approximately 0.1 and 60 free surface nodes were used.

see from Fig. 5 that this criterion varies widely in time for the two cases starting with a Stokes wave and $a = 0.27$ and 0.28. In fact, the value for the nonbreaking wave eventually goes slightly higher than the spilling breaker. This should be the case with the variation in space (and time) for the experiments. It should be noted that the maximum and minimum

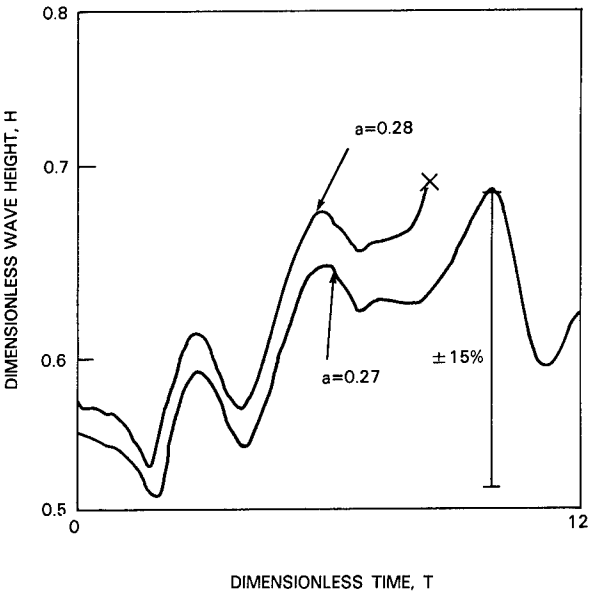


Fig. 5 — Computed wave height. Time history of the growth of the dimensionless peak-to-trough/wave height computed using the present method.

wave heights are determined at the same instant of time at two different locations for the numerical results of Fig. 5 while usually experimental wave heights (with one wave probe) are measured at one location at two different times. The potential energy, although not constant in time, is much less variable and can easily be determined from wave probe data. Figure 6 shows that the potential energies for these same two computations are distinct, indicating that potential energy may be a better criterion for *predicting* whether a traveling surface wave will break. This is discussed further in the following sections of the paper.

4. LIMITING WAVE STEEPNESS

The NRL experiments discussed in this section were conducted in a 30 m long deep water wave channel. The test procedures and the set-up of the experiments are described by Ramberg and Griffin (1986). The channel was fitted with a convergent section with rate 1:16. This generated steep and breaking waves under reasonably well-controlled conditions. Previous breaking wave experiments in a wave channel with a convergent section had been conducted and reported by Van Dorn and Pazan (1975).

The location of wave breaking was established visually during the experiments as the position along the convergent channel where the sharp wave crests were first perceived to be "tripping" into a spilling or plunging mode. It is therefore the point where we first observed an increase in the crest fluid velocity over that of the traveling waveform. These locations were recorded and later compared to the positions where the measured variation of the average wave height $\bar{H}(x)$ exhibited a transition from growth to attenuation along the channel. In all of the cases compared there was good agreement between the two estimated locations. Typical examples of spilling and plunging breakers are given in the photographs of Fig. 7.

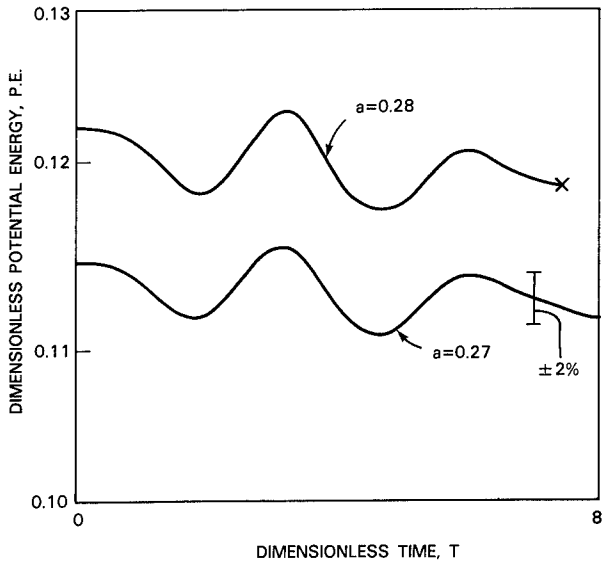
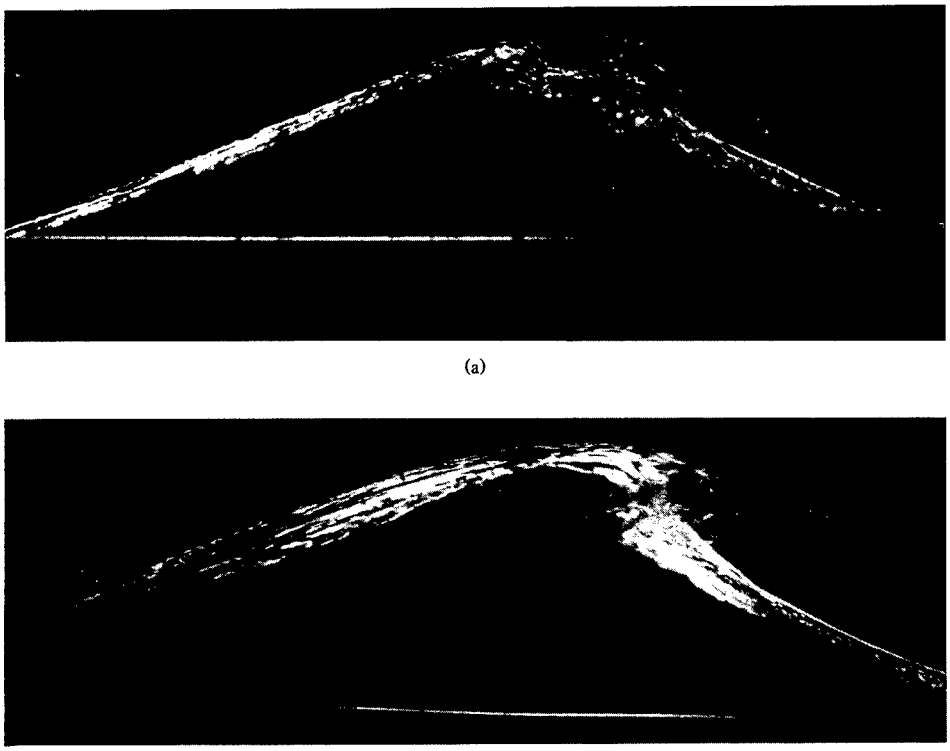


Fig. 6 — Computed wave potential energy. Time history of the growth of the dimensionless potential energy computed using the present method.



(a)

(b)

Fig. 7 — Single breaking deep water waves. (a) Photograph of a spilling breaker; from the experiments of Ramberg and Griffin (1986) and (b) Photograph of a curling or lightly plunging breaker; from the experiments of Ramberg and Griffin (1986).

The limiting wave height or steepness was computed from the data in three ways. First, a spatially-smoothed average was taken of eight recorded wave cycles measured at the observed wave breaking location. This averaged value increased slightly with the dimensionless growth rate of waves in the channel. The second method used the local values of the eight-cycle averages which were used to develop values of the limiting wave height. This calculation reduced the apparent dependence upon growth rate by increasing the observed limiting wave height at the lowest values of growth rate. Subharmonic modulations also produced intermittent breaking at the lowest growth rates (Ramberg and Griffin, 1986), and so the limiting wave heights finally were determined using the third method which considered local values of *only* those individual waves which actually broke. The limiting wave heights obtained by this latter method were essentially constant at a given wave period and showed no dependence upon growth rate.

A wide range of wave heights at the *onset of breaking* are plotted in Fig. 8 for a number of recent investigations corresponding to deep water waves. The data from *all* of the experiments employ a crest-to-preceding-trough value for H. The wave heights measured by Ochi and Tsai (1983) for the breaking of steep nonlinear waves in a uniform channel cover the range $gT^2 = 200$ to 800 cm while the wave heights measured in the NRL experiments cover the range of period parameter $gT^2 = 550$ to 1100 cm. The wave heights measured by Duncan (1983) are in the range $gT^2 = 100$ to 400 cm and those measured by Bonmarin and Ramamonjiarisoa (1985) are in the range $gT^2 = 350$ to 650 cm.[1] The latter experiments were conducted to measure the breaking of waves in a uniform channel, while in the former experiments the breaking waves were generated by towing a hydrofoil through still water at various submergence depths. Above a critical submergence depth of the hydrofoil wave breaking occurred spontaneously (Duncan, 1983). The data in the figure represent considerable overlap between the various experiments.

The Stokes limiting steepness represented in the figure by the solid line

$$H = \alpha\, gT^2, \tag{6}$$

where $\alpha = 0.027$, is based upon the classical limiting wave criterion in the form

$$H = 0.141 L_*, \tag{7}$$

where H = wave height;
L_* = Stokes limiting wave length $= 1.2g\,(T^2/2\pi)$;
T = wave period.

This is the most commonly cited analytical breaking limit (to varying degrees of accuracy) for steep symmetric waves in deep water (Michell, 1893; Dean, 1969; Williams, 1981, 1985). It is clear from the results in Fig. 8 that the measured limiting wave heights at the onset of breaking are well below the Stokes limit. The measured points are clustered about a mean onset breaking wave height given by the dashed line

$$H = \alpha^*\, gT^2, \tag{8}$$

where $\alpha^* = 0.021$, that is shown on the plot. This represents wave heights which are about 78 percent of the Stokes limiting value.

It is clear from all of the results in Fig. 8 that the limiting wave height or steepness at breaking is consistently less

[1]The extensive body of data shown in Fig. 8 was communicated to the authors by Bonmarin (1985, private communication).

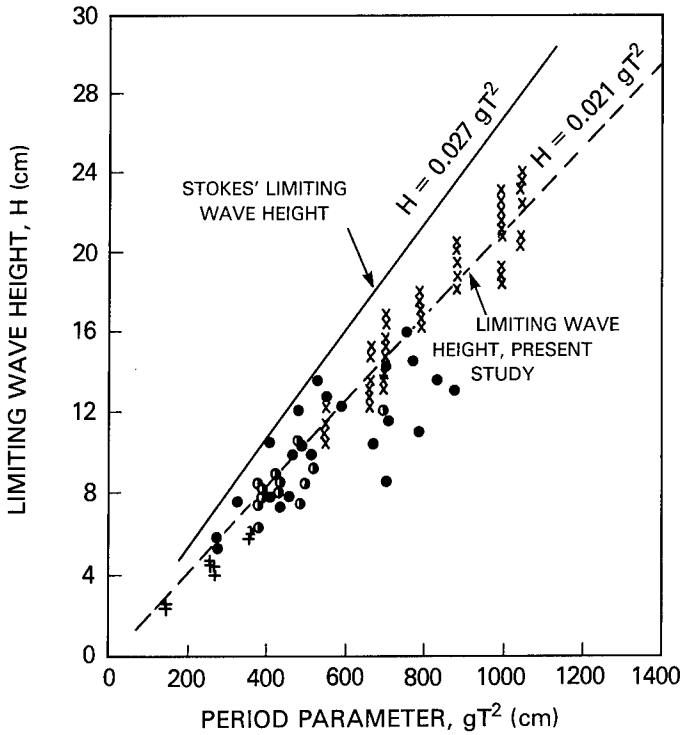


Fig. 8 — Limiting wave height. Relationship between the measured peak-to-trough wave height H and wave period parameter gT^2 for individual breaking occurrences of laboratory-scale deep water waves. Legend for the data points: Ochi and Tsai (1983), • ; Duncan (1983), +; Bonmarin (1985, private communication), ◑; NRL experiments, Ramberg and Griffin (1986), ×.

than the theoretical Stokes limit, $H/L_* \cong 0.14$ for steep symmetric waves and can be taken as $H/L_* = 0.11$ for many practical purposes. It needs to be emphasized that the concept of a limiting wave height or steepness applies to only the onset conditions for a wave breaking event. A breaking wave can still exist at a lower steepness *after* it has begun to break.

The value of the coefficient α^* in the experimental estimate of the limiting wave height dependence on the wave period is $\alpha^* = 0.021$ as based upon the data plotted in Fig. 8. The value of α^* can be determined from the computations if the relationships $H(a)$ and $T(\lambda)$ are known. If we assume that $H = 2a$ for linear waves and note that H typically grows by 20 percent before breaking as shown in Fig. 5, then $H = 2.4a$ at the time of breaking. The wave period T is inversely proportional to the wave's phase speed, $c = \lambda/T$, and a combination of the experiments and computations discussed here suggest is $c = 1.09\ c_o$ for a steep wave just prior to breaking. The resulting estimate of the proportionality coefficient α^* from the computations is $\alpha^* = 0.020$, which is well within the experimental scatter shown in Fig. 8.

5. MOMENTUM AND ENERGY CONSIDERATIONS

It is possible also to compare the results of Ramberg and Griffin (1986) with the measurements of momentum flux losses by Melville and Rapp (1985). The latter reported measurements of wave breaking in packets of waves generated in a uniform channel by the superposition of Fourier components over a small band centered on the frequency f_o. The integrated wave amplitude a^2 was assumed by Melville and Rapp to be a measure of the momentum flux, ΔS, due to breaking and was determined locally by taking the difference between the incipient breaking condition and conditions farther downstream (normalized by the upstream reference value S_o). The *rate* of momentum flux loss R'_b can be expressed as

$$R'_b = \frac{(\Delta\ S/S_o)}{\Delta\ k_o\ (x - x_b)} \tag{9}$$

where $k_o = \omega_o^2/g$ for deep water waves, when ω_o is the radian frequency. A comparison between the experiments of Ramberg and Griffin and those of Melville and Rapp (1985) can be made directly from the results in Table 1. Only the initial *rates* of energy loss are compared here because during the convergent channel experiments the energy/momentum losses rarely reached an asymptotic value, i.e., the waves continued to break throughout the measurement interval. It should be noted that the rate of momentum flux loss from the experiments of Ramberg and Griffin is derived from estimates of potential energy based upon measured wave heights. However, there is only a difference of 2π between the loss rates of potential energy and momentum flux.

The results of the two experiments are in agreement that the initial rates of momentum flux loss due to plunging breakers are typically about twice those of spilling breakers. Moreover, the results of Melville and Rapp also indicate that the *total* losses for the two types of breakers differ by about the same factor. The smaller momentum flux losses reported by Melville and Rapp are expected since their results are for the integral momentum flux of a group of waves. It is possible to qualitatively reconcile the magnitudes of the loss rates given in Table 1 if about half of the most energetic waves in each packet are actually breaking at any given time.

The importance of the potential energy to the overall process of wave breaking is illustrated by the following example based on the results in Figs. 5 and 6. The value of the

Table 1 — Momentum Flux Losses in Wave Breaking

Type of Breaker	Wave Steepness, ak		Rate of Momentum Flux Loss, R'_b	
Spilling	0.30^{+}	$0.31\text{-}0.38^{++}$	0.023^{+}	0.048^{++}
Plunging	0.39	0.33-0.38	0.045	0.089

$^{+}$Melville and Rapp (1985).

$^{++}$Ramberg and Griffin (1986), average of seven wave periods (spilling); and two wave periods (plunging).

wave height H at time $t = 0$ for $a = 0.28$ in Fig. 5 is smaller than the value of H at $t = 3$ for $a = 0.27$. The values of H for both of these points are below the wave height or steepness at the onset of breaking, and as the computed wave height grows with time we would expect the $a = 0.27$ case with the higher value of H to break first. This is obviously is not the case. On the other hand, the potential energies for the two cases are reversed as shown in Fig. 6 and do not cause this confusion. Perhaps a better criterion for the onset of wave breaking than the limiting wave steepness is the potential energy of the wave system. A preliminary estimate from the computations of the dimensionless potential energy at the onset of breaking is $P.E. = 0.12$. This has yet to be confirmed experimentally. Implicit in this proposition is that the temporal growth of the waves in the computations can be modified to compare with the spatial growth in many experiments such as those described in the present paper. This argument concerning the potential energy as a criterion for the onset of wave breaking should apply equally well to the momentum flux of the wave system under the appropriate conditions.

6. SUMMARY AND CONCLUDING REMARKS

We have demonstrated that the complex boundary integral technique for computing the growth of steep and breaking waves is robust and accurate when formulated in an overdetermined system of equations as described in this paper. The numerical algorithm is very stable and economical when it is combined with central difference spatial differentiation and fully implicit time marching.

Also, we have extended the experimental range of measured limiting wave heights for individual deep water wave events. The measured limiting wave heights of Ramberg and Griffin (1986) show considerable overlap and good agreement with other recent laboratory-scale experiments. Computational estimates of the limiting deep water wave height at breaking are in good agreement with the experiments.

The computations indicate that the potential energy of the wave system may be better than the wave height or steepness as an indicator of the onset of breaking for steep nonlinear waves. The wave height or steepness appears from the computations to grow with time, while the potential energy exhibits only small oscillations about a mean value. A criterion such as this for the limiting wave may reduce the apparent scatter which has been observed in laboratory measurements of individual breaking events. However, this proposition has yet to be confirmed experimentally.

The recent experiments of Ramberg and Griffin (1986) and of Melville and Rapp (1985) discussed in this paper have shown that the potential energy and momentum flux loss rates of plunging breakers are about twice those of spilling breakers in deep water.

ACKNOWLEDGMENTS

This study was conducted as part of a research program in free surface hydrodynamics supported by the Naval Research Laboratory.

REFERENCES

G.R. Baker, D.I. Meiron and S.A. Orszag, 1982, "Generalized vortex methods for free-surface flow problems," *J. Fluid Mech.*, Vol. 123, 477-501.

M.L. Banner and E.H. Fooks, 1985, "On the microwave reflectivity of small-scale breaking water waves," *Proc. Royal Soc. London A*, Vol. 399, 93-109.

P. Bonmarin and A. Ramamonjiarisoa, 1985, "Deformation to breaking of deep water gravity waves," *Exp. in Fluids*, Vol. 3, 11-16.

E.D. Cokelet, 1977a, "Breaking waves," *Nature*, Vol. 267, 769-774.

E.D. Cokelet, 1977b, "Steep Gravity Waves in Water of Uniform Depth," *Phil. Trans. Royal Soc.* A, Vol. 286, 183-230.

R.G. Dean, 1969, "Breaking Wave Criteria; A Study Employing a Numerical Wave Theory," *Proc. of the Eleventh Conference on Coastal Engineering*, Vol. I, ASCE: New York, 108-123.

J.W. Dold and D.H. Peregrine, 1984, "Steep unsteady water waves: An efficient computational scheme," University of Bristol School of Mathematics Report AM-84-04.

J. H. Duncan, 1983, "The breaking and non-breaking wave resistance of a two-dimensional hydrofoil," *J. Fluid Mech.*, Vol. 126, 507-520.

O.M. Griffin, 1984, "The Breaking of Ocean Surface Waves," NRL Memorandum Report 5337.

P.C.M. Jansen, 1986, "A Boundary Element Model for Non-Linear Free Surface Pheomena," Delft University of Technology, Department of Civil Engineering Report no. 86-2.

S.P. Kjeldsen and D. Myrhaug, 1978, "Kinematics and Dynamics of Breaking Waves," Norwegian Hydrodynamics Laboratory Report STF60A78100.

W.-H. Lin, J.N. Newman and D.K. Yue, 1984, "Nonlinear forced motions of floating bodies," *Proc. Fifteenth Symp. Naval Hydrodynamics*, National Academy Press: Washington, DC, 33-50.

M.S. Longuet-Higgins and E.D. Cokelet, 1976, "The deformation of steep surface waves on water. I. A numerical method of computation," *Proc. Royal Soc. London A*, Vol. 350, 1-26.

M.S. Longuet-Higgins and E.D. Cokelet, 1978, "The deformation of steep surface waves on water. II. Growth of normal mode instabilities," *Proc. Royal Soc. London A*, Vol. 364, 1-28.

M.S. Longuet-Higgins, 1978a, "The instabilities of gravity waves of finite amplitude in deep water. I. Superharmonics," *Proc. Royal Soc. London A*, Vol. 360, 471-488.

M.S. Longuet-Higgins, 1978b, "The instabilities of gravity waves of finite amplitude in deep water. II. Subharmonics," *Proc. Royal Soc. London A*, Vol. 360, 489-505.

W.K. Melville, 1982, "The instability and breaking of deep-water waves," *J. Fluid Mech.*, Vol. 115, 165-185.

W.K. Melville and R.J. Rapp, 1985, "Momentum Flux in Breaking Waves," *Nature*, Vol. 317, 514-516.

J.H. Michell, 1893, "The Highest Waves in Water," *Phil. Mag.*, Vol. 36, 431-437.

E.W. Miner, M.J. Fritts, O.M. Griffin and S.E. Ramberg, 1983, "Free surface wave motions and interactions," *Int. J. Num. Meth. Fluids*, Vol. 3, 399-424.

J.H. Nath and F.L. Ramsey, 1976, "Probability distributions of breaking wave heights emphasizing the utilization of the JONSWAP spectrum," *J. Phys. Oceanography*, Vol. 6, 316-323.

A.L. New, P. McIver and D.H. Peregrine, 1985, "Computation of overturning waves," *J. Fluid Mech.*, Vol. 150, 233-251.

M.K. Ochi and C.-H Tsai, 1983, "Prediction of Occurrence of Breaking Waves in Deep Water," *J. Phys. Oceanography*, Vol. 13, 2008-2019.

S.E. Ramberg and O.M. Griffin, 1986, "Laboratory Studies of Steep and Breaking Deep Water Waves," *Proc. ASCE, J. WPCO Div.*, submitted for publication.

W.W. Schultz, 1985, "Integral Equation Algorithm for Breaking Waves," *Proc. Eleventh IMACS World Congress, Oslo.* Vol. 2, 219-221.

M.-Y. Su, M. Bergin, P. Marler and R. Myrick, 1982, "Experiments on nonlinear instabilities and evolution of steep gravity-way trains," *J. Fluid Mech.*, Vol. 124, 45-71.

J.M. Vanden-Broek, 1980, "Nonlinear stern waves," *J. Fluid Mech.*, Vol. 96, 603-611.

W.G. Van Dorn and S.E. Pazan, 1975, "Laboratory Investigation of Wave Breaking," Scripps Institution of Oceanography Report 75-21, AD A013 336.

T. Vinje and P. Brevig, 1981a, "Breaking Waves on Water of Finite Depth: A Numerical Study," Ship Research Institute of Norway Report R-111.81.

T. Vinje and P. Brevig, 1981b, "Numerical simulation of breaking waves," *Adv. Water Resources*, Vol. 4, 77-82.

J.M. Williams, 1981, "Limiting gravity waves in water of finite depth," *Phil. Trans. Royal Soc. Lond. A*, Vol. 302, 139-188.

J.M. Williams, 1985, "Near-Limiting Gravity Waves in Water of Finite Depth," *Phil. Trans. Royal Soc. London A*, Vol. 314, 353-377, 1985.

DISCUSSION

K. Mori,
Hiroshima University

Authors give in Fig. 8 a single mean line for limiting wave heights for various waves. A careful observation may convince one that the mean line for a steady breaker, given with the symbol "+" in Duncan (1983), is obviously lower than the given mean line. The experiments by the discussor suggest that the steady breaker is a kind of fluctuating free-surface flow at its early stage whose mechanism is supposed different from that of the progressive wave. In this connection, it would be better not to mix up the data of the steady breaker with those of the progressive wave.

Reply -

The authors wish to thank Professor Mori for his comments and for his interest in their paper. The breaking surface waves observed by Duncan (1983) were produced by the steady motion of a submerged hydrofoil. The character of the individual breaking of the regular and irregular progressive surface waves that are shown in Fig. 8. The important point of the figure is the demonstration that the measured limiting amplitude at the onset of breaking for all of the waves are well below the theoretical Stokes limiting wave amplitudes for steep symmetric waves in deep water. Though Duncan's results are slightly below the dashed trend line drawn through the experimental data, the limiting wave heights measured by him clearly increase monotonically with the period parameter gT^2 and agree well with the approximately linear dependence between the measured limiting wave amplitude and the wave period parameter.

Study of Nonlinear Axisymmetric Body-Wave Interactions

D. G. DOMMERMUTH and D. K. YUE

Massachussetts Institute of Technology, U.S.A.

ABSTRACT

A numerical method is developed for nonlinear three-dimensional but axisymmetric free-surface problems using a mixed Eulerian-Lagrangian scheme under the assumption of potential flow. Taking advantage of axisymmetry, Rankine ring sources are used in a Green's theorem boundary-integral formulation to solve the field equation; and the free surface is then updated in time following Lagrangian points. A special treatment of the free surface and body intersection points is generalized to this case which avoids the difficulties associated with the singularity there. To allow for long time simulations, the nonlinear computational domain is matched to a transient linear wavefield outside. When the matching boundary is placed at a suitable distance (depending on wave amplitude), numerical simulations can, in principle, be continued indefinitely in time. Based on a simple stability argument, a novel regriding algorithm is introduced which removes the instabilities experienced by earlier investigators and eliminates the need for artificial smoothing. The resulting scheme is very robust and stable.

For illustration, three computational examples are presented: (1) the growth and collapse of a vapour cavity near the free surface; (2) the heaving of a floating vertical cylinder starting from rest; and (3) the heaving of an inverted vertical cone. For the cavity problem, there is excellent agreement with available experiments. For the wave-body interaction calculations, we are able to obtain and analyse steady-state results for the force and flow field in the vicinity of the body.

1. INTRODUCTION

Ever since the work of Longuet-Higgins & Cokelet (1976), the mixed Eulerian-Lagrangian method has been used efficaciously for a variety of nonlinear free-surface problems in two dimensions. The algorithm requires two steps: at any instant of time, the field equation is solved in an Eulerian frame, after which Lagrangian points are followed on the free surface to update their positions and potential values. The first step is typically accomplished by writing a boundary integral equation for the velocity potential, and the second by high-order finite-difference time integrators.

Assuming periodic waves, Longuet-Higgins & Cokelet (1976) were able to simulate steep Stokes' waves, as well as realistic overturning and plunging of the wave crest when an asymmetric surface pressure was applied. Faltinsen (1977) applied a similar method to study the nonlinear waves outside and inside moving bodies. For the former, periodic boundary conditions were replaced in favor of matching to a Rankine (non-wave) potential in the far-field. Vinje & Brevig (1981) extended the approach of Longuet-Higgins & Cokelet to include finite water depth and floating bodies but retained the assumption of space periodicity. By applying Cauchy's integral theorem to the complex potential they were able to obtain Fredholm integral equations of the second kind for both the stream function on the free surface and the potential on the body resulting in a substantial gain in efficiency and accuracy of the equation system. The same idea was exploited by Baker et al (1982) who used a dipole distribution on the free-surface (where Dirichlet conditions are posed), and the resulting Fredholm second kind equations were solved using an iterative method. Unlike the complex potential formulation of Vinje & Brevig, this approach can, in principle, be extended directly to three-dimensional problems.

In this paper, we extend the semi-Lagrangian method to vertically axisymmetric free-surface flows. Our ultimate (but ambitious) objective is to be able to simulate fully three-dimensional nonlinear interactions between a free-surface and a body. A number of important difficulties remain to be resolved before such a goal can realistically be reached (see §5). In the present context of axisymmetric problems, we are able to address and satisfactorily solve three of the main outstanding problems: (i) implementation of a far-field closure; (ii) treatment of the body and free-surface intersection line; and (iii) stable representation and time integration of the free surface. In addition, through a number of computational examples, the

usefulness and accuracy of the mixed Eulerian-Lagrangian approach to problems in more than two dimensions is demonstrated. This research paves the way for numerical study of nonlinear three-dimensional diffraction and radiation problems of scientific and engineering importance.

Far-field closure

A satisfactory treatment of the far-field condition is essential to the study of exterior wave motion problems. When the physical problem possesses spatial periodicity, such a difficulty is easily resolved by using periodic boundary conditions (e.g., Longuet-Higgins & Cokelet, 1976). The computation domain is folded onto itself and the exterior boundaries are simply eliminated. When an isolated body is present in an unbounded region, the assumptions of spatial periodicity or of fixed boundaries at some distance are clearly unrealistic. Nevertheless, by keeping a relatively large domain, Vinje & Brevig (1981), Greenhow et al (1982) and others were able to use periodic conditions to study the dynamics of a floating body. Faltinsen (1977) in his study of the heaving motion of a two-dimensional floating body, matched his nonlinear inner solution to that of a Rankine dipole in the far-field. Since wave effects are not present in the latter, Faltinsen found that unless the interior computational domain was increased as a function of simulation time, the computations would soon break down. Assuming a boundary-integral formulation for the nonlinear interior domain with N free-surface points, N must increase approximately linearly with time, T, for both of the above approaches with the associated $O(N^2)$ and $O(N^3)$ increases in storage and computational effort per time step (assuming a direct solution) respectively. For this reason, the cost may become prohibitive even for two-dimensional problems, and Faltinsen's results, for example, were typically restricted to less than one oscillation period. The situation is even more critical for three-dimensional problems with the anticipated $O(T^2, T^4, T^6)$ increase respectively in unknowns N, storage, and number of operations per time step. Thus, in Isaacson's (1982) Eulerian calculation of the nonlinear diffraction by a vertical cylinder, where the fluid velocities were assumed to be zero on a finite truncation boundary, motion for only a fraction of a wave period could be simulated.

In this work, we pose a far-field closure by matching the nonlinear computational solution to a general linear solution of transient outgoing radiated waves. The determination of the linear wavefield as well as specification of the boundary condition for the nonlinear interior problem are obtained through a matching of the two on a fictitious boundary some distance away. Such a scheme is, in principle, untenable in two- dimensional flows since the nonlinearity of the radiated waves persists into the far-field, and a simple matching to linear outer solutions is problematic (e.g. Vinje et al, 1982). In three dimensions, however, the energy density of the radiating waves must necessarily decrease with radial distance so that a matching to a general linear solution is in theory valid at least some distance away. Indeed, for a suitably fixed matching radius (based for example only on motion amplitude) nonlinear simulations can in principle be carried out indefinitely in time. This is confirmed by our numerical experiments where we are able to continue the computations until steady-state conditions are reached for the entire inner computation domain (see §4).

Body and free-surface intersection line

A confluence of boundary conditions exists at the intersection of the free surface and a body moving in it. As a result, the solution exhibits a weak singularity at that point. According to linear theory, the velocity potential for a vertical wall moving horizontally is logorithmically singular at the contact point (Kravtchenko, 1954), and a similar singularity is also present for general three-dimensional flows (Miloh, 1980). This singularity persists even when full nonlinearity is introduced. For example, for a vertical two-dimensional piston moving in a water depth h, Peregrine (1972) derived a perturbation result where the surface elevation displayed a $\log(\tanh(\pi x/4h))t$ behavior for small time, t, where x is the horizontal coordinate measured from the wavemaker. This two-dimensional result has been confirmed by a number of other investigations using both Eulerian and Lagrangian analyses as well as by experiments, and are reviewed in Greenhow & Lin (1983) and Lin (1984). Computationally, this weak singularity along the intersection line has a global influence and numerical difficulties for the nonlinear problem can be expected there. In Vinje & Brevig (1981), the intersection point was treated as part of the body boundary where a kinematic condition but not the free-surface conditions were prescribed, and the position and potential at that point were subsequently obtained via extrapolation. The results using this approach were not completely satisfactory and in a later work by Greenhow et al (1982) using the same method, they found it necessary to use experimental measurements to fix the intersection point locations in their computations to produce acceptable results.

For two-dimensional problems, Lin (1984) developed a novel approach where by specifying both the stream function and the velocity potential at the intersection point in the Cauchy integral-equation solution, the computational difficulties there were, in practice, avoided. In this paper, we adopt a similar idea for the axisymmetric problem where the field equation is solved in terms of the velocity potential and its normal derivative. The resulting scheme is robust and effective as demonstrated, for example, by our computations of a heaving inverted cone (see §4).

Stability of the free surface

In the original work of Longuet-Higgins & Cokelet (1976), a "sawtooth" instability of the free surface was encountered and a smoothing technique was employed to suppress its development. Since then similar smoothing methods have been found necessary by many investigators especially when the local steepness of the waves is large. It is now believed that such high-wavenumber instabilities are nonphysical and are closely related to the accuracy of the velocity calculations for the free-surface particles. The exact mechanism of the instability is, however, quite subtle and may well depend on the details of a particular implementation. In Vinje & Brevig (1981)'s computations using Cauchy's integral formula, no such instability was observed, although using essentially similar schemes Baker et al (1982) and Lin et al (1984) both required a smoothing operator to suppress instabilities when the waves were steep. On the other hand, when a dipole (rather than vortex) distribution was used in Baker et al, the instablity was found to be greatly reduced. Roberts (1983) analysed this problem using Fourier spectral representations for the position and potential of a free shear layer and was able to remove the numerical instablity by a simple modification of the highest (even) Fourier mode. Dold & Peregrine (1984) extended the idea of Vinje & Brevig (1981) by calculating also the higher time derivatives of the complex potential in the Eulerian step. The resulting time integration scheme had an improved accuracy but more importantly showed no apparent short-wavelength instability. Such a scheme is somewhat analogous to a modified Runge-Kutta integration where new values of the potential but not the free surface positions are used in the intermediate steps of the integration (see §3).

We postulate (see §3) that a root cause of the high-wavenumber instability is the concentration of Lagrangian markers in the region of higher gradients so that for a fixed time step, a local Courant condition is inevitably violated as the wave steepens. Thus, we develop a regriding algorithm wherein a new set of equally (arclength) spaced Lagrangian points on the free surface are created after every time step. Such an idea is not new and is not unlike, for example, that used by Fink & Soh (1974) in their simulation of thin vortex sheets. Our numerical experiments indicate that the regriding method is extremely effective and eliminates the instabilities without the use of artificial smoothing. As explained in §3, this regriding approach has important advantages over the traditional smoothing techniques especially in conjunction with a careful treatment of the free surface and body intersection line.

2. MATHEMATICAL FORMULATION

We consider the irrotational flow of an incompressible, inviscid fluid under a free surface. The flow can be described by a velocity potential $\phi(\mathbf{x},t)$ and the fluid velocity is given by $\mathbf{v} = \nabla\phi$. Inside the fluid volume V(t), ϕ satisfies Laplace's equation

$$\nabla^2\phi = 0 \qquad \text{in } V(t) \tag{2.1}$$

On the free surface $F(\mathbf{x},t)$, ϕ satisfies the kinematic boundary condition

$$\frac{D\mathbf{x}}{Dt} \equiv \left(\frac{\partial}{\partial t} + \mathbf{v}\cdot\nabla\right)\mathbf{x} = \nabla\phi \qquad \text{on } F(\mathbf{x},t) \tag{2.2a}$$

and the dynamic boundary condition (assuming zero atmospheric pressure)

$$\frac{D\phi}{Dt} = -gz + \frac{1}{2}|\nabla\phi|^2 \qquad \text{on } F(\mathbf{x},t) \tag{2.2b}$$

where g is the acceleration due to gravity, the vertical coordinate z is positive up, and z = 0 is the undisturbed water surface. On the body surface $B(\mathbf{x},t)$, the normal velocity is continuous,

$$\nabla\phi\cdot\mathbf{n}(\mathbf{x},t) \equiv \frac{\partial\phi}{\partial n} = U(\mathbf{x},t), \text{ prescribed,} \qquad \text{on } B(\mathbf{x},t) \tag{2.3}$$

where $\mathbf{n}$ is the unit normal pointing out of the fluid and n the coordinate along $\mathbf{n}$. On a horizontal bottom B_o at z = -h, (2.3) is satisfied there with U = 0. In addition, we specify zero initial conditions and a suitable far-field condition

$$\phi \to 0 \qquad \text{as } |\mathbf{x}| \to \infty, \quad t < \infty \tag{2.4}$$

We further establish a vertical circular cylindrical matching surface S_o, of a fixed radius A, enclosing B. From (2.1), we have from Green's identity

$$\alpha(\mathbf{x},t)\phi(\mathbf{x},t) = \iint_{S(t)} \left[\frac{\partial\phi}{\partial n'} - \phi\frac{\partial}{\partial n'}\right]\frac{1}{R}\,dx' \qquad \mathbf{x}\in S \tag{2.5}$$

where $R = |\mathbf{x}-\mathbf{x}'|$, $S(t) = B + \bar{B}_o + \bar{F} + S_o$, the overbar denotes that portion of the surface enclosed by S_o, α is the included solid angle at $\mathbf{x}$, and the exclusion of the singular point $\mathbf{x}$ from the integral is implied.

For axisymmetric bodies and motions, and assuming that the radiated waves are circumferentially stable, it follows from (2.3) that ϕ and F are also independent of the angular coordinate θ and (2.5) can be integrated in θ to give

$$\alpha(r,z,t)\phi(r,z,t) = \int_{\partial S} r'\left[\frac{\partial\phi}{\partial n'} - \phi\frac{\partial}{\partial n'}\right]G(r,z;r',z')\,dx' \qquad (r,z)\in S \tag{2.6}$$

The line integral is along the trace $\partial S(t) = \partial B + \partial \bar{B}_o + \partial \bar{F} + \partial S_o$ of S on (r,z). G is the Rankine ring source given by

$$G(r,z;r',z') = \int_0^{2\pi} \frac{d\theta'}{R} = \frac{4}{\rho_1} K(1 - \rho^2/\rho_1^2) \tag{2.7}$$

where $\rho^2 = (z-z')^2 + (r-r')^2$, and $\rho_1^2 = (z-z')^2 + (r+r')^2$ and K is the complete elliptic integral of the first kind (Abramowitz & Stegun, 1964). As $\rho \to 0$, K is logarithmically singular, so that G behaves like a two-dimensional source there. To reduce the number of unknowns, it is convenient in practice to remove the bottom $\partial \bar{B}_o$ from ∂S in (2.6) by augmenting G(r,z;r',z') with its image source with respect to z = -h: G(r,z;r',-z'-2h).

For a particular $\partial S(t)$, (2.6) is a Fredholm integral equation of the first kind for ϕ_n on $\partial \bar{F}$ (where Dirichlet conditions are posed), and of the second kind for ϕ on ∂B. On the outer surface ∂S_o, however, neither ϕ nor $\partial\phi/\partial r$ are in principle known, and we shall obtain a closure by matching them to a general linearized solution $\tilde{\phi}$ outside S_o which satisfies

$$\nabla^2 \tilde{\phi} = 0 \qquad r > A, \; -h < z < 0 \tag{2.8a}$$

$$\left(\frac{\partial^2}{\partial t^2} + g\frac{\partial}{\partial z}\right)\tilde{\phi} = 0 \qquad r > A, \; z = 0 \tag{2.8b}$$

$$\frac{\partial \tilde{\phi}}{\partial n} = 0 \qquad r > A, \; z = -h \tag{2.8c}$$

$$\tilde{\phi} \to 0 \qquad r \to \infty, \; t < \infty \tag{2.8d}$$

and initial conditions

$$\tilde{\phi}, \; \frac{\partial \tilde{\phi}}{\partial t} = 0 \qquad r > A, \; z = 0, \; t = 0 \tag{2.8e}$$

Details of the solution for $\tilde{\phi}$ are given in the Appendix. The important result is that the transient history of the potential $\tilde{\phi}$ and the normal derivative $\tilde{\phi}_n$ of any linear wavefield outside a closed surface S_o can be directly related when evaluated on S_o. Thus we can write in general

$$\tilde{\phi}|_{S_o} = H\,\tilde{\phi}_n|_{S_o} \tag{2.9}$$

where H is a known operator (depending only on S_o) which accounts for both the impulsive motion of the fluid and the memory effect of the free surface outside S_o. Typically, H involves integration over the surface S_o as well as a convolution of the operand for the memory effects (see Appendix). For a circular cylindrical S_o (radius A, depth h), for example, the form of (2.9) is given by (A.8). Eq.(2.9) now provides the closure for ϕ on S_o upon imposing the matching conditions

$$\phi = \tilde{\phi} \quad \text{and} \quad \phi_n = \tilde{\phi}_n, \quad \text{on } S_o \tag{2.10}$$

Implicit in (2.10) is the assumption that S_o is sufficiently large so that the nonlinear radiated waves can be matched to a linear field without appreciable errors or reflection. The validity of this matching scheme must finally be demonstrated, say, by comparing results obtained using different values of the matching radii A for S_o. Substituting (2.9) into (2.6) using (2.10) we finally obtain

$$a(r,z,t)\phi(r,z,t) = \tag{2.11}$$

$$\int_{\partial B+\partial \bar{F}} r'\left[\frac{\partial \phi}{\partial n'} - \phi \frac{\partial}{\partial n'}\right] G \, dx' + \int_{\partial S_o} r'\left(G - \frac{\partial G}{\partial r'}H\right)\frac{\partial \phi}{\partial r'}, \qquad (r,z)\in\partial S$$

Following a semi-Lagrangian approach, we have at a given time, the position of the body $\partial B(t)$ and the normal derivative ϕ_n on it given from the body boundary condition (2.3); the position $\partial \bar{F}(t)$ and ϕ on $\partial \bar{F}$ from time integration of (2.2); and a history of all previous values of ϕ_r on ∂S_o. Eq.(2.11) can then be solved for ϕ on ∂B, ϕ_n (and hence $\nabla\phi$) on $\partial \bar{F}$ and (the present value of) ϕ_r on ∂S_o. The process is then repeated for successive time steps. We remark here that the linear wavefield $\tilde{\phi}$ is completely general subject to (2.8) and appears in the formulation only through the function H in (2.11).

3. NUMERICAL IMPLEMENTATION

3.1 Solution of the field equation

To discretize (2.11), we (a) subdivide ∂S into a number of small segments ∂S_j, j=1,2,...,J; (b) represent the boundary values of ϕ and ϕ_n by local basis functions; and (c) collocate (2.11) at selected points on ∂S. An important consideration here is the treatment of the intersection point between $\partial \bar{F}$ and ∂B (and also between $\partial \bar{F}$ and ∂S_o) because of the anticipated weak singularity there. To avoid numerical difficulties at the intersection points, we follow the idea of Lin (1984) for the two-dimensional problem and seek to satisfy both the free-surface and body boundary conditions at the intersection. The most direct extension of the idea is to prescribe both ϕ from the condition on $\partial \bar{F}$ and ϕ_n from the body boundary condition at that point. This requires that the end points of the segments be specified as collocation points and that the approximation for ϕ be continuous across these points. We adopt the simplest choice of piecewise linear variations of (ϕ,ϕ_n) along each segment, prescribed by their values, (ϕ_j,ϕ_{nj}), j=1,2,...,J+1, at the segment end points. For consistency in approximation, and also to satisfy the need for continuous normal derivatives ϕ_n on $\partial \bar{F}$ where Dirichlet conditions are specified, we require that ∂S be at least piecewise quadratic with continuous slopes across segment boundaries. To avoid the degeneracy of quadratic splines, the portions of ∂S (∂B, $\partial \bar{F}$, ∂S_o) are approximated by cubic splines with prescribed end slopes.

Thus within a particular segment j, ϕ^j, $\phi_n{}^j$ are linear functions of arc-length, s,

$$[\phi_j(\xi),\ \phi_{n_j}(\xi)] = (1-\xi)\ [\phi_j,\ \phi_{n_j}] + \xi\ [\phi_{j+1},\ \phi_{n_{j+1}}] \tag{3.1}$$

where ξ=s/L, and s,L are respectively the arc-length and total length of the segment given by

$$s(\varsigma) = \int_0^{\varsigma} J(\varsigma')d\varsigma' \qquad 0 \le \varsigma \le 1 \tag{3.2a}$$

$$L = \int_0^{1} J(\varsigma')d\varsigma' \tag{3.2b}$$

and J is the Jacobian

$$J(\varsigma) = \sqrt{\left(\frac{dr}{d\varsigma}\right)^2 + \left(\frac{dz}{d\varsigma}\right)^2} \qquad 0 \le \varsigma \le 1 \tag{3.2c}$$

which are all functions of the cubic spline parameter ς, $0 \le \varsigma \le 1$, for that segment. The difference between using a linear function of arc-length ξ, and ς in the interpolation (3.1) is nontrivial, since they differ, in general, even to leading order in L. Expanding (3.2a), for example, we have

$$\xi = (J(0)/L)\ (\varsigma + 0(L)) \tag{3.3}$$

Computationally, (3.1) is found to have a greater accuracy and more rapid convergence with segment length than linear basis functions based on ς.

Following standard procedures, (2.11) can now be discretized and evaluated at successive collocation points, $\mathbf{x}_j$, j=1,2,...,J+1, to obtain a system of algebraic equations for the values of the unknowns (ϕ_j or ϕ_{nj}), j=1,2,...,J+1. The quadrature over each segment typically involves products of the ring source G or its derivative, the interpolation functions in (3.1) and the Jacobian (3.2c) so that the integration is with respect to the parameter ς. When the collocation point is an end point of the segment being integrated, special care is required to account for the singularities of the kernel. For the logarithmic singularity of G, the singular portions of the kernel up to and including $\varsigma\ln(\varsigma)$ are subtracted out and integrated analytically. There is no Cauchy singularity in $\partial G/\partial n$ when the collocation point $\mathbf{x}$ is on the interior of the boundaries ∂B, $\partial\bar{F}$ or ∂S_o, where the slope is continuous. The kernel can be evaluated (except at $\mathbf{x}'=\mathbf{x}_j$) and the included angle is simply $\alpha=2\pi$. At the intersections of ∂B and $\partial\bar{F}$, and $\partial\bar{F}$ and ∂S_o, where the slopes are in general discontinuous, the integrand still exists at either side of $\mathbf{x}_j$ although somewhat more care is required to evaluate the included angle. When the body (or free surface) intersects the centerline r=0, the integral is evaluated readily in a spherical coordinate system, so that for an inverted cone of half vertex angle θ_o, for example, the angle α at the vertex is $\alpha=2\pi(1+\cos\theta_o)$. The evaluation of all the regular integrals are performed using 4-point Gaussian quadratures, whose accuracies are confirmed against those obtained from convergent Romberg integrations.

For a given matching radius A, fixed (Eulerian) collocation points on ∂S_o, and prescribed time steps, the evaluation of the functions in H need not be repeated for different interior problems. For the impulsive part, the first two terms of (A.5) are evaluated and inverted once at the beginning of each problem. The singularities involved there are similar to those for G and will not be elaborated. The memory effects of H are evaluated via the last term of (A.8). A simple trapezoidal rule is used to perform the convolution integration, and the value $\phi_r(\tau=t)$ at the upper limit does not appear from this term on account of (A.11). When $z,z'\neq 0$, the integrand in the Fourier integral in (A.11) diminishes exponentially and Filon's method is used for its evaluation. For z=z'=0, however, the integrand decreases only algebraically, and the convergence using Filon's quadrature is accelerated by subtracting out analytically the leading contributions in terms of sine and cosine exponential integrals.

3.2 Time Integration and Stability

Once (2.11) is solved for (ϕ,ϕ_n) on ∂S, $\nabla\phi$ can be evaluated on $\partial\bar{F}$, and the kinematic and dynamic boundary conditions (2.2) integrated in time. Provided that the desired accuracy is achieved, the specific time integration formula used appears not to be critical and a variety of different schemes have been employed by previous investigators typically using higher-order explicit (e.g. Runge-Kutta) or multi-step (e.g. Adam-Bashford-Moulton) methods or a combination of the two. In our simulations, we adopt a modified fourth-order Runge-Kutta scheme wherein the unknowns associated with the potential (ϕ,ϕ_n), but not the position of the boundary ∂S, are updated in the intermediate steps. This is not unlike the approach used by Dold & Peregrine (1984) where, for a given free-surface boundary, the (complex) potentials and its time derivatives are solved via Cauchy's integral theorem which are then combined in a higher-order time integration formula. In the present case, computation time is dominated by that required to calculate the coefficients of the matrices associated with (2.11) so that the modified scheme, which maintains the same matrix coefficients during one complete time step, represents a substantial savings in effort but at a slightly decreased accuracy compared to exact Runge-Kutta integration. Furthermore, the extra complication of tracing Lagrangian points which cross the computation boundary during the intermediate steps is avoided. To obtain the gradient $\nabla\phi=(\phi_r,\phi_z)$ or (ϕ_n,ϕ_s), the tangential derivatives ϕ_s are calculated by second-order finite-difference formulas in terms of arc lengths. At the matching boundary, the position and potential value of the free-surface point on ∂S_o for the new time step are obtained by Lagrangian extrapolation.

Unless special care is taken, short-wavelength numerical instabilities, similar to those experienced by Longuet-Higgins & Cokelet (1976) and others for the two-dimensional problem, are also observed in our computations. The exact cause of these instabilities is uncertain although we believe that an important mechanism is the instability associated with concentration of Lagrangian points in regions of high flow gradients. If we perform a von Neumann stability analysis for the fourth-order Runge-Kutta scheme, for example, with linearized forms of the free-surface conditions (2.2), we obtain for stability the Courant condition

$$\Delta t^2 \leq \frac{8}{\pi} \frac{\Delta x}{g} \tag{3.4}$$

where Δt is the time step, and Δx the local grid spacing. This suggests that for fixed Δt such instabilities may be avoided if the minimum grid size can be effectively controlled. Thus, we propose a scheme where a new set of equal arc-length spaced Lagrangian points on $\partial\overline{F}$ are created after every time step. Using this algorithm, the earlier instabilities are completely removed and no smoothing is required. Such a regriding idea is not new and has been used in related work by Fink and Soh (1974), for example, to improve the accuracy of their principal value integrals and extend the simulation time of their calculation of two-dimensional unsteady vortex sheets. The main disadvantage of regriding is the potential loss of resolution which is usually provided by more closely spaced Lagrangian points in areas of large gradients. The advantages of regriding over smoothing especially in the present context are, however, substantial: (i) regriding can potentially remove less energy from the system especially in the limit of very small grid sizes; (ii) the arbitrariness in the choice of a smoothing formula for a particular problem is avoided; (iii) smoothing can not be easily applied at the intersection points between the free surface and body or matching boundaries; and (iv) the difficulties associated with the loss or gain of Lagrangian points as they cross the matching boundary are completely avoided if the free surface is regrided after every time step.

3.3 Numerical Accuracy

The overall accuracy of our numerical scheme can be considered in three parts: that associated with the solution of the field equation (2.11); that associated with the integration of the evolution equations (2.2); and that due to linear matching. Both the field equation solver and the time stepping procedure can be checked independently against known (prescribed) solutions. Our numerical experiments show that when forty segments are used per wavelength, the relative error in (2.11) is less than 1%. The convergence with grid size is quadratic everywhere except at the intersections of the free surface with the body or the matching boundary where it is linear. Similarly, the modified fourth-order Runge-Kutta scheme has less than 1% relative error when forty time steps are used in a wave period. Discretizations comparable to these are used in all our computations. To assess the errors introduced by the matching boundary, our simulations are typically performed with two or more matching radii A, and convergence for results near the body to within several percent is achieved (e.g. see Figure 8).

In addition to the above checks for convergence with respect to temporal and spatial discretizations and matching radii, the global accuracy of our computations is also evaluated for conserved fluid volume and conserved energy:

$$\iint_B p \frac{\partial\phi}{\partial n}\, dx = -\frac{d}{dt}\left[\iint_{B+F+S_o} \frac{1}{2}\rho\phi \frac{\partial\phi}{\partial n}\, dx + \iint_{B+F} \frac{1}{2}\rho r z^2 n_z\, dx \right] + \iint_{S_o} \rho \frac{\partial\phi}{\partial t}\frac{\partial\phi}{\partial n}\, dx \tag{3.5}$$

The first term is proportional to the power expended by the body B, the second term the rate of change of kinetic and potential energy in the fluid volume $\overline{V}$, and the last term the energy flux across the matching boundary S_o. The pressure p on the body can be evaluated using Bernoulli's equation

$$-\frac{p}{\rho} = \frac{\partial\phi}{\partial t} + \frac{1}{2}|\nabla\phi|^2 + gz \tag{3.6}$$

$$= \left(\frac{\partial}{\partial t} + \mathbf{V}\cdot\nabla\right)\phi + \frac{1}{2}(\nabla\phi - \mathbf{V})\cdot\nabla\phi + gz$$

where the second form is more useful when following moving Eulerian points (with velocity V) on the body. For all the examples in §4, such quantities are typically conserved to within a few percent (e.g. see Figure 10).

4. NUMERICAL RESULTS

To demonstrate the usefulness and accuracy of our numerical method for axisymmetric problems involving free surfaces, we present results here for three different applications of interest. (1) Growth and collapse of an initially spherical cavity bubble near a free surface. For the non-bouyant case, excellent experimental data are available from Blake & Gibson (1981) which allow us to make a detailed comparison and validation of our code. It is found that the inclusion of gravity can have a profound effect on the evolution of the cavity. (2) Large-amplitude periodic heaving motions of a floating vertical circular cylinder starting from rest. Our primary interests here are steady-state results for the reaction forces and flow field in the vicinity of the cylinder. Since a large number of periods must be simulated, especially for the latter, this is a particularly useful test of the effectiveness of the matching boundary. (3) Forces and run-up on a heaving inverted cone. In addition to

engineering applications such as the use of these devices as wavemakers, this problem also provides a demonstration that our treatment at the body and free surface intersection line is satisfactory.

4.1 Dynamics of a cavity bubble near a free surface

We study the growth and collapse of a vapour cavity near an initially plane free surface under the assumptions of potential flow, negligible surface tension, vertical axisymmetry, and uniform and constant (in time) cavity-vapour pressure. The last assumption is made for simplicity and is not critical to our simulation. Physically, these assumptions are valid for cavities that are not too small (to ignore viscosity and surface tension), and for small liquid and vapour Mach numbers (to neglect compressibility effects and to assume constant cavity pressure). On the other hand, the assumption of axisymmetry may be unrealistic if the maximum volume of the bubble is greater than a few c.c. beyond which there may be considerable circumferential variations in the bubble shape. The relevent parameters for this problem are $\eta=R_m/h$ and $\gamma=\sqrt{(gR_m)}/U$, where R_m is the maximum radius the bubble will attain if the fluid is unbounded, h the initial depth of the centroid of the bubble, $U^2=\Delta p/\rho$, and $\Delta p=p_a-p_v$, the (constant) difference between the atmospheric and cavity-vapour pressures. All velocities and lengths are scaled by U and R_m respectively. To begin the simulation, a spherical bubble of small initial radius $R_o \ll h$ is used, whose velocity of expansion $\dot{R}_o$ is given by (Rayleigh,1917)

$$\dot{R}_o^2 = \frac{2}{3} U^2 \left(R_m^3 / R_o^3 - 1 \right) \qquad (4.1)$$

In our simulations, $R_o/R_m=.25$ is used, which corresponds to a time t_o = .0154 R_m/U measured from an instant when the bubble has negligible volume.

For the non-buoyant case, $\gamma=0$, detailed observations were made by Blake & Gibson (1981) who took 11000 frames/s cine pictures of the bubble under free-fall conditions. Figure 1 shows comparisons between the experiments (reproduced directly from Blake & Gibson, figure 8) and our computations for the bubble profiles in the expansion and collapse phases for $\eta=1.02$, and dimensionless times t_kU/R_m = .087,.173,.260,.347,.520,.604,.867,1.040,1.214, 1.300,1.387,1.474,1.508; for the labels k=1,2, ...,13. The collapse phase is marked by a rapid involution of the bubble in the form of a downward jet accompanied by a continuely rising free surface which develops into a jet in the opposite direction. The correspondence between the experiments and calculations is satisfactory up to the last reported frame when the imploding jet is close to the bottom of the bubble. Our simulation, in fact, continues on to the time when the jet meets the far side of the bubble. These comparisons are substantially better both in terms of accuracy and duration of simulation than those of Blake & Gibson (1981) and Blake et al (1985) using similar methods. To obtain some understanding of the underlying dynamics, the centerline fluid velocity and total pressure are presented in Figures 2 and 3 respectively for time instants corresponding to k=6,9,11,12,13. (In this and later results, the velocity in the fluid is obtained directly from taking the gradient of Green's identity, Eq.2.6). Note the large negative (downward) velocities of the jet above and a small distance away from the bubble. The magnitude, which increases with time, is close to 4U at k=13, tU/R_m=1.508. For $\Delta p \sim 1$ atmosphere and ρ = density of water,

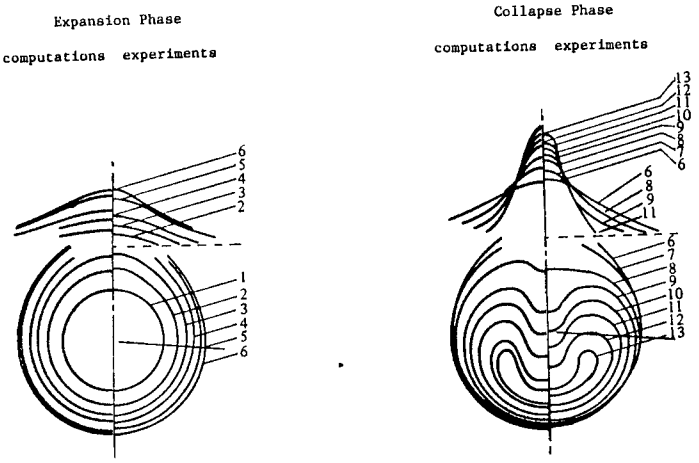


Figure 1. Comparison of profiles between measurements (Blake & Gibson, 1981) and computations for the growth and collapse of a cavity bubble beneath a free surface: γ = 0 (no gravity) and η = 1.02; for different time instants.

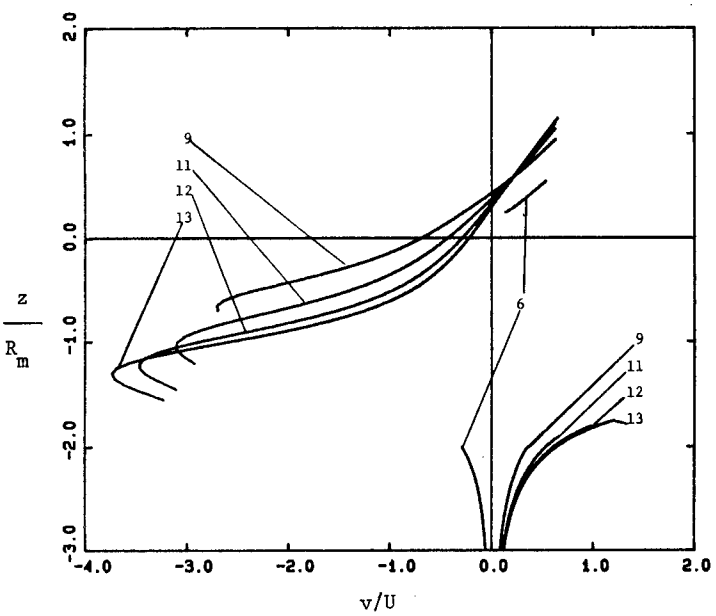


Figure 2. Centerline (vertical) fluid velocity near a cavity bubble collapsing beneath a free surface: $\gamma = 0$ (no gravity), and $\eta = 1.02$; for different time instants. Note that the curves are discontinued inside the bubble and above the free surface.

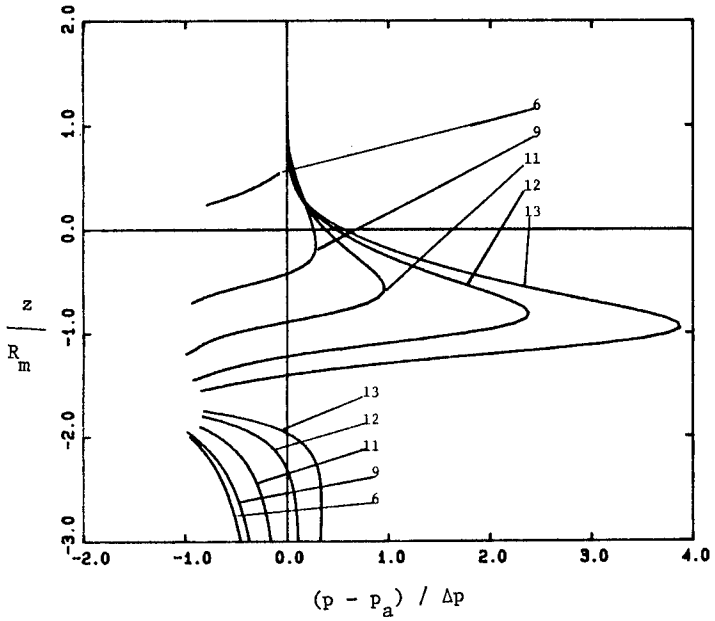


Figure 3. Centerline fluid pressure near a cavity bubble collapsing beneath a free surface: $\gamma = 0$ (no gravity) and $\eta = 1.02$; for different time instants. The pressure coefficient inside the bubble (-1) and above the free surface (0) are not plotted.

this is approximately 40 m/s, a value which is somewhat smaller than but of the same magnitude as observed maximum velocities of bubble jets collapsing near a solid boundary (Plesset & Chapman, 1971). The velocity below the bubble is relatively small but positive, indicating a rising of the bottom as the cavity collapses.

Throughout the collapse phase, the total fluid pressure (Figure 3) has a maximum value above the bubble which explains the directions of the free-surface and bubble-implosion jets. At the last time instant plotted, the pressure reaches a maximum value of $(p-p_a)/\Delta p \sim 4$ which can be quite significant for small p_v.

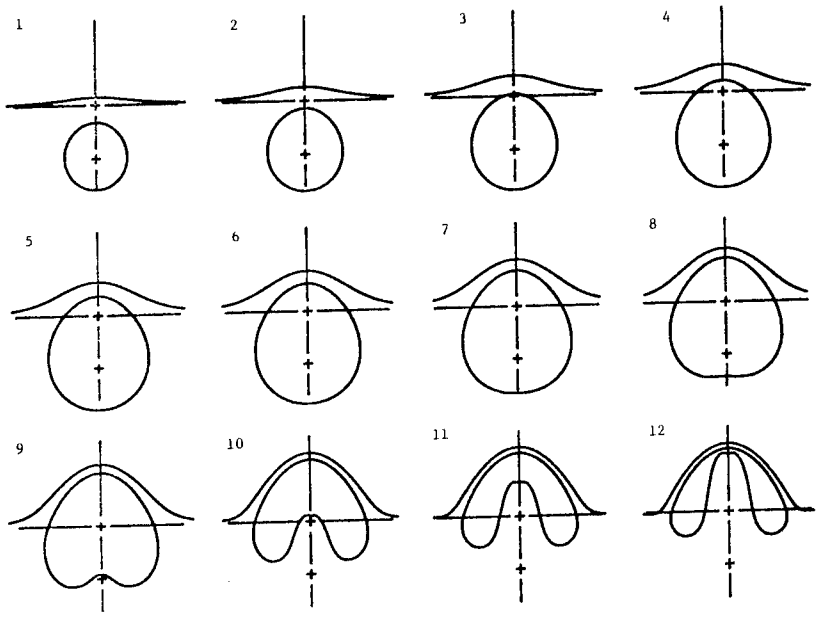


Figure 4. Profiles showing the growth and collapse of a vapour bubble beneath a free surface: γ = 1 (gravity present) and η = 1; for different time instants. Note that the crosses mark the initial free surface and bubble centroid locations.

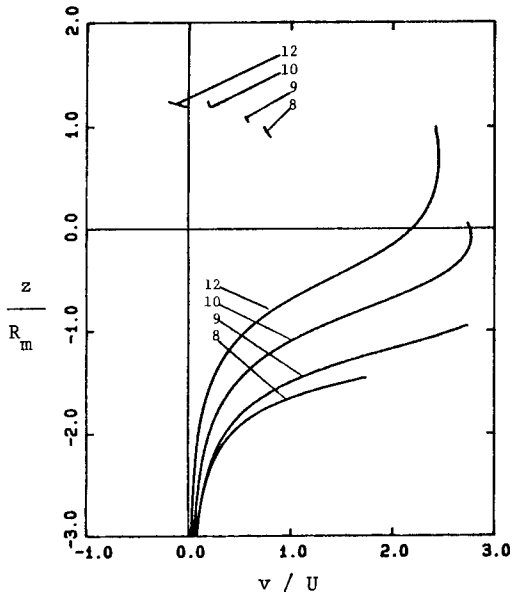


Figure 5. Centerline (vertical) fluid velocity near a cavity bubble beneath a free surface: γ = 1 (gravity present) and η = 1; for different time instants. Note that the curves are discontinued inside the bubble and above the free surface.

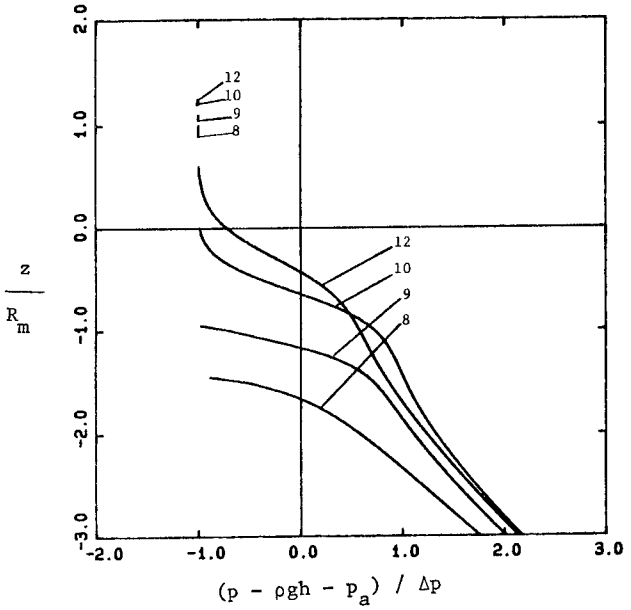


Figure 6. Centerline fluid pressure near a cavity bubble beneath a free surface: γ = 1 (gravity present) and η = 1; for different time instants. The pressure coefficients inside the bubble and above the free surface (both equal -1) are not plotted.

When gravity is present, the evolution of the bubble can be changed dramatically (Blake et al, 1985). This is shown in Figures 4-6 for the case $\eta=\gamma=1$ (the definition is now $\Delta p=p_a+\rho gh-p_v$, and in fact $p_a=p_v$ in this case). Figure 4 shows the profiles of the cavity at dimensionless times $t_k U/R_m$=.134,.215,.311,.412, .521,.641,.777,.939,1.148,1.516,1.716,1.896; for the plots k=1,2,...,12. Because of the presence of buoyancy, the bubble (centroid) continues to rise through the growth and collapse phases eventually becoming entrained under an elevated free surface. The bubble collapse is now accompanied by the involution of its bottom surface into a jet which is directed upwards towards the free surface. At the last stages of our simulation, in fact, all three free surfaces are almost in contact with each other. In the centerline velocity plots, Figure 5, the maximum velocities are associated with the upward jet but have magnitudes only about half of those in the non-buoyant case. The total centerline pressures (Figure 6), which are dominated by hydrostatics at large depth, vary smoothly to the prescribed value p_v at the bubble, and also between the bubble and the free surface ($p_a=p_v$), in contrast to the profiles in Figure 3. Furthermore, the maximum pressure is clearly no longer above the cavity, so that the implosion jet is directed from the bottom of the bubble upwards.

Provided that axisymmetry is maintained, it is seen that the present method is well suited to the study of the dynamics of cavity bubbles and their interactions with a free surface. The latter, in particular, may have useful applications, for example, to the generation of sub-sea acoustic signals using bubbles, and to the understanding of spray formation by entrained air.

4.2 Forced heaving of a floating circular cylinder starting from rest

We consider large-amplitude forced periodic heaving motions of a floating vertical circular cylinder of radius R_o, initial draft H, in water depth h, where $H/R_o=.5$ and $h/R_o=1$. The vertical velocity of the cylinder is prescribed by

$$U(t) = \begin{cases} 0 & t < 0 \\ -\omega a \cos \omega t & t \geq 0 \end{cases} \qquad (4.2)$$

where the excitation frequency $\omega=2\pi/T$ is chosen to correspond to an Airy wavelength of $2R_o$, i.e.

$$\omega^2 h/g = \pi \tanh \pi \qquad (4.3)$$

Three different (half) stroke amplitudes a/H = .125, .25 and .5 are considered. In the simulation for the largest amplitude a/H=.5 case, the cylinder is found to be already very close to aerating at the top of the stroke. When a matching radius of $A=10R_o$ (i.e. roughly 5 Airy wavelengths) is used, simulations have been carried out to beyond 12 wave periods. Uniform grid spacings are used on the free surface and matching boundary, while a cosine distribution of segment lengths are used on the cylinder in anticipation of the singular flow at the corner. In this case, we use a total of N=237 unknowns (36,180 and 20 segments on $\partial B, \partial\bar{F}$ and ∂S_o respectively), and the solution time, which is roughly proportional to N^2, is of the order of 15 seconds per time step on the Cray 2, or approximately 10 minutes per motion period.

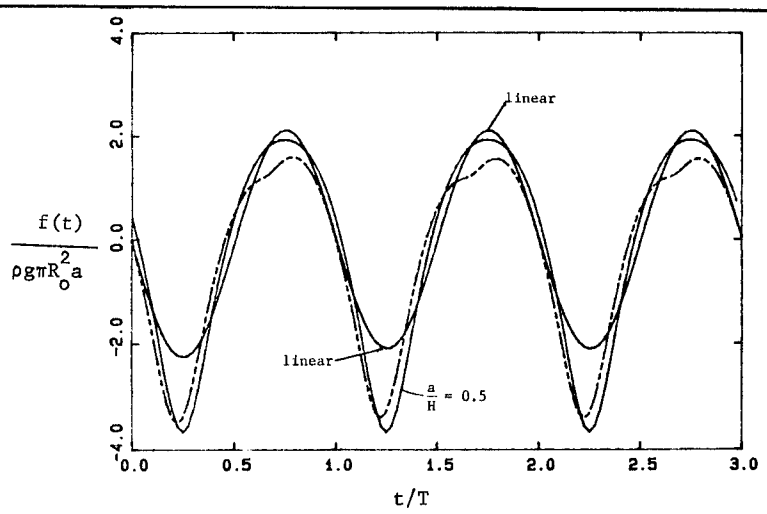


Figure 7. Time history of the vertical force on a floating cylinder for a/H= 0.5. — — — — : the impulsive force $f_I(t)$ (Eq.4.4); ———— : the linear and nonlinear force histories.

Figure 7 shows time histories of the vertical force f(t) on the cylinder for different motion amplitudes. Note that steady state for the force is reached within one or two periods. A relatively good estimate of the force can be obtained by considering only the impulsive force, f_I, associated with the instantaneous submerged portion of the body, $\underline{B}(t)$, below the still-water level. From momentum balance, we have

$$f_I(t) = -\rho \frac{d}{dt} \iint_{\underline{B}(t)} \psi n_z dS + \frac{\rho}{2} \iint_{B_o} \psi_r^2 \, dS \qquad (4.4)$$

where $\psi(t)$ is the potential corresponding to the linear impulse (infinite-frequency) problem for $\underline{B}(t)$ satisfying $\psi=0$ on $z=0$, $r>R_o$, and $\psi_n=U(t)n_z$ on $\underline{B}(t)$. This is also computed and plotted in figure 7 for the a/H=.5 case. The rather close agreement indicates that the reaction force is dominated by added-mass effects as may be suggested by the rapid approach to steady state. In contrast, the linear time-domain result (obtained by keeping the free surface at z=0 and ignoring nonlinear terms in our nonlinear code) shows fairly large discrepencies especially at the troughs. The difference between f_I and the nonlinear force represents radiated wave effects which show distinct higher-harmonic contributions. To see this, we perform harmonic analysis on the steady-state portion of the force, and define Fourier force coefficients

$$\frac{1}{T_o} \int_t^{t+T_o} f(t')dt' = (\rho g \pi R_o^2 H)(a/H)^2 \, f_o^*$$

and

$$\frac{2}{T_o} \int_t^{t+T_o} f(t')e^{in\omega t'}dt' = (\rho g \pi R^2 H)(a/H)^n \, f^* \qquad n = 1,2,... \qquad (4.5)$$

These are presented in Table 1 where the hydrostatic force has been subtracted from f_1^*. Note that for the a/H=.5 case, the magnitudes of the mean, second and third harmonic forces are up to 11%, 28% and 7% respectively of the first harmonic force. For comparison, we also calculate the mean and first-order force coefficients from a linear frequency-domain semi-analytic method which uses matched eigenfunction expansions outside and underneath the cylinder (e.g. Garrett, 1971). Because of the scaling with respect to stroke amplitude in (4.5), the coefficients show only small deviations with decreasing strokes and approach the linear value for the first-harmonic force. The comparison to the frequency-domian mean force is not as close and is partly due to the difficulty in integrating the pressure near the corner. For $s=(R_o-r)/R_o \ll 1$, $\phi_r \sim s^{-1/3}$, and $p \sim \phi_r^2 \sim s^{-2/3}$; so that even for the linear calculation, the eigenfunction amplitudes theoretically have only a -5/3 power convergence.

	f_o^*	$\lvert f_1^* \rvert$	$\lvert f_2^* \rvert$	$\lvert f_3^* \rvert$
Nonlinear Computations				
a/H = .5	-.45	2.19	1.3	.6
a/H = .25	-.42	2.14	1.2	.6
a/H = .125	-.40	2.11	1.2	.7
Linear Frequency-Domain Results				
	-.31	2.118	-	-

Table 1. Harmonic Force Coefficients for the Forced Heaving of a Floating Cylinder.

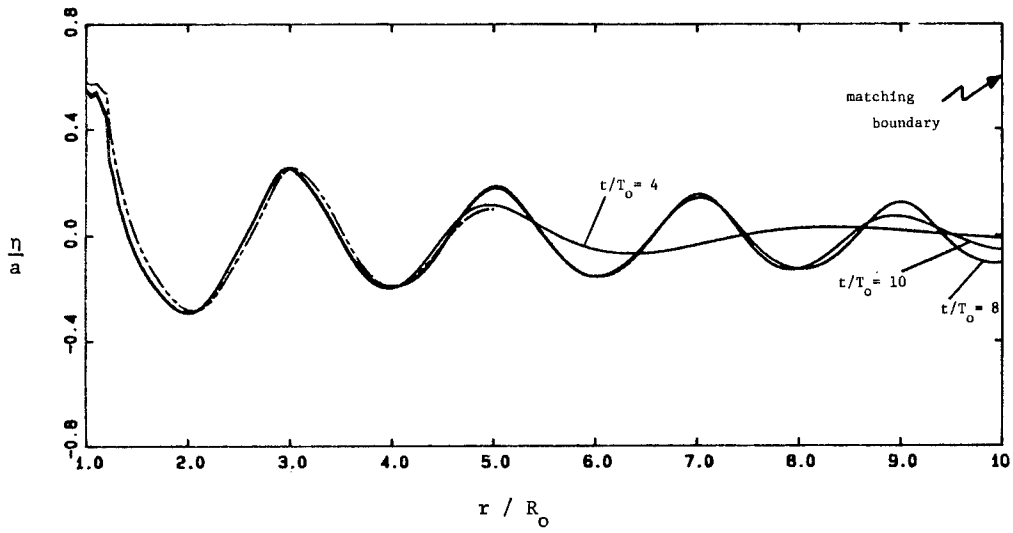


Figure 8. Instantaneous free-surface profiles outside a heaving vertical cylinder for a/H = 0.5 at different time instants, for a matching radius A/R_o = 10. —— – – —— : surface profile at t/T_o = 4 for A/R_o = 5.

For the flow field around the cylinder, the convergence to steady state is much slower. Figure 8 plots the instantaneous free-surface positions, $\eta(r,t)$, at specific instants t/T=4,6,8 and 10 for the case a/H=.5. Note that the matching boundary is located at A/R_o=10. The absence of reflections from that boundary is evidenced by the fact that the correspondance among the profiles, which indicates their approach to steady state, improves with increasing radius and time. To give an illustration of the convergence with matching radius A, the free-surface profile at t/T=4 obtained using a much smaller computational domain A/R_o=5 is also shown. The use of the larger matching radius is clearly conservative.

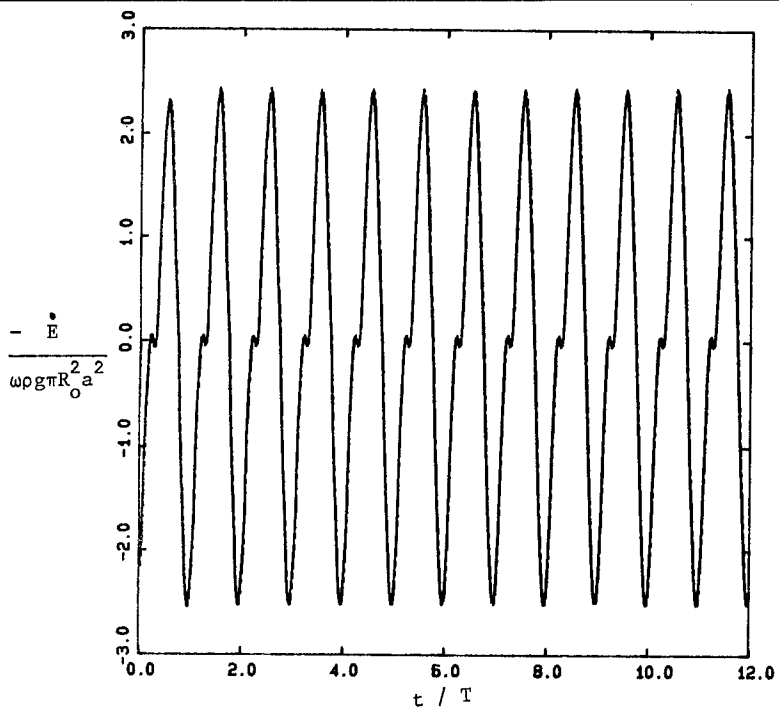


Figure 9. Comparison between the power expended by the body, E (————); and the rate of total energy decrease in the fluid plus energy flux out of the fluid volume (—— – – ——) for a heaving vertical cylinder a/H = 0.5.

The left and right sides of (3.5), which represent a balance between the power input into the fluid and the rate of change of total energy in the fluid, are plotted in Figure 9, for 12 periods of simulation for a/H=.5. The two curves are almost indistinguishable and total energy is conserved to within a few percent throughout. The small jump near t=(n+1/4)T, n=0,1,2,..., occurs at the bottom of the stroke where the clearance is only $R_o/4$. The added mass there is strongly affected by the bottom and the jump reflects the steep gradient of the added mass with small clearance.

The steady-state mean set-down associated with the nonlinear radiated waves is of some interest, and harmonic analyses of the steady-state surface profile histories are performed to obtain the coefficients $\eta_n^*(r)$, $R_o < r < A$, defined by

$$\frac{1}{T_o}\int_t^{t+T_o} \eta(r,t')dt' = \eta_o^*(r)\ H\ (a/H)^2 (R_o/r) \qquad (4.6)$$

and

$$\frac{2}{T_o}\int_t^{t+T_o} \eta(r,t')e^{-in\omega t'}dt' = \eta_n^*(r)\ H\ (a/H)^n (R_o/r)^{n/2} \qquad n=1,2...$$

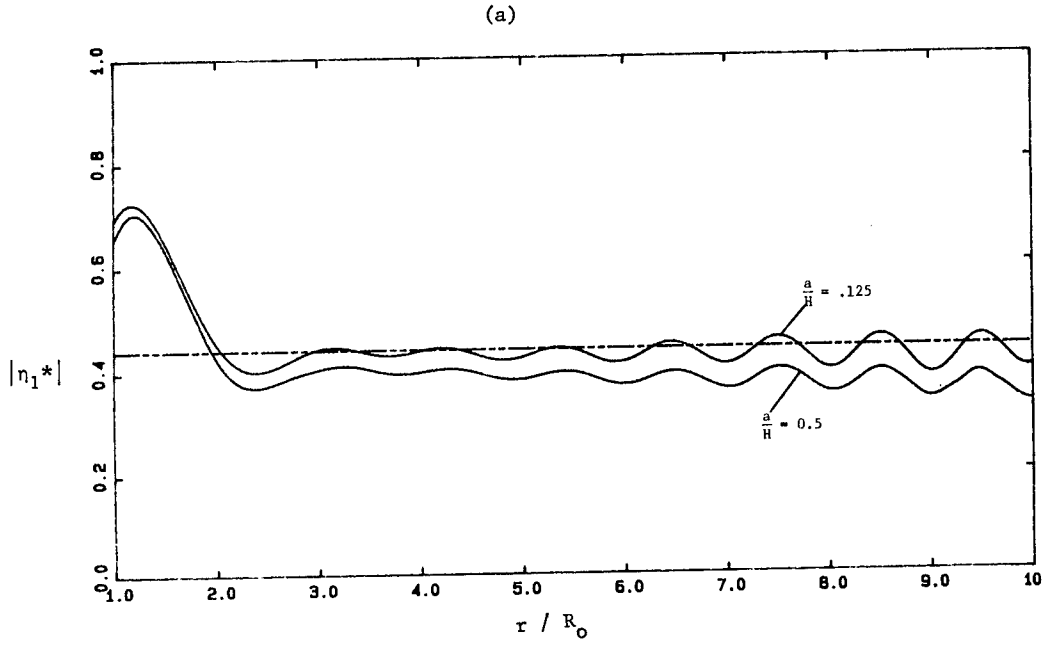


Figure 10. Surface elevation outside a heaving vertical cylinder for different stroke amplitudes. —— - - —— : constant values predicted by linear theory (Eq. 4.7). (a) first harmonic coefficient amplitude; (b) mean set-down coefficient.

(b)

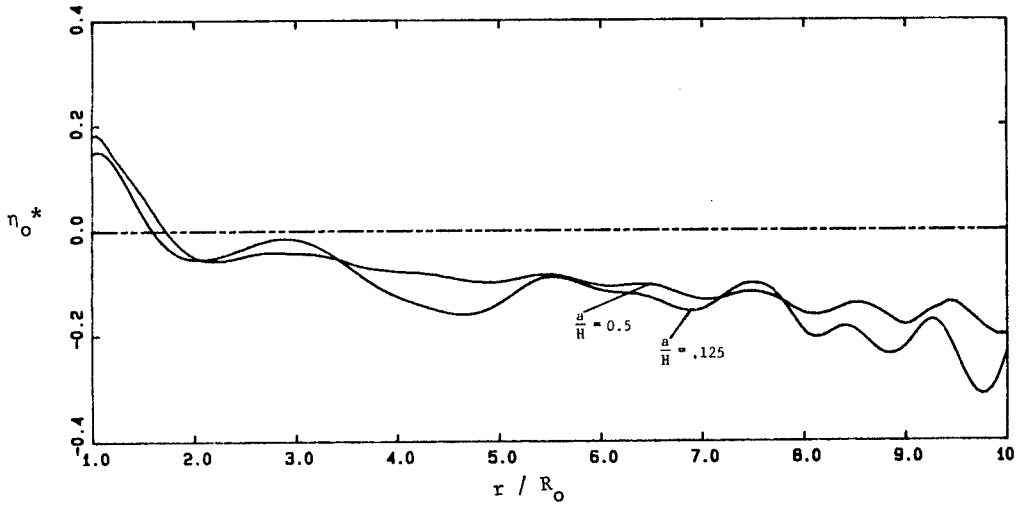


Figure 10. Surface elevation outside a heaving vertical cylinder for different stroke amplitudes. —— - - —— : constant values predicted by linear theory (Eq. 4.7). (a) first harmonic coefficient amplitude; (b) mean set-down coefficient.

The forms of (4.6) are suggested by the asymptotic behavior of the surface elevation, $\tilde{\eta}_n^*$, based on first-order (frequency-domain) results assuming steady state. Thus, for a radiated wave of wavenumber k, (satisfying $\omega^2=gk\tanh(kh)$), we have (e.g. Mei, 1983)

$$\left|\tilde{\eta}_1^*\right| \sim c \qquad kr \gg 1 \qquad (4.7)$$

and the mean set-down,

$$\left|\tilde{\eta}_o^*\right| \sim \frac{|c|^2 kH}{2\sinh 2kh} \qquad kr \gg 1$$

The amplitude coefficient c is a complex constant from linear frequency-domain analysis. Using the value of c from our semi-analytic linear calculations, the harmonic amplitudes η_n^* obtained from nonlinear simulations can be compared to the linear asymptotics (4.7). This is shown in figures 10 for the first-harmonic and mean set-down. The comparison for η_1^* is quite satisfactory, reaching constant asymptotics whose values approach the linear estimate as stroke amplitude is decreased. The growing oscillations with radial distance give indications that steady state is not fully reached at the larger distances, while the oscillations themselves may be related to those behind an advancing wave-front (e.g. Longuet-Higgins, 1974). The result for η_o^* (Figure 10b) is not as reasonable, with the nonlinear mean set-down remaining almost constant with increasing r. Although the magnitudes involved are quite small, this does indicate that the matching boundary does not adequately account for the mean second-order volume fluxes crossing it - a conclusion not completely surprising in view of the assumptions implicit in the matching conditions (2.11).

Finally, we show results for the fluid velocities near the body. Figure 11 is a vector plot of the steady-state time-averaged horizontal velocities in the fluid for a/H=.5. Near the surface, there is a mean outgoing Stokes' drift velocity compensated by a weaker return current which has almost a constant amplitude through the remaining water depth. A careful analysis of the magnitudes reveal that the mean velocities decrease with radial distance roughly as 1/r and quadratically with decreasing stroke amplitudes as expected.

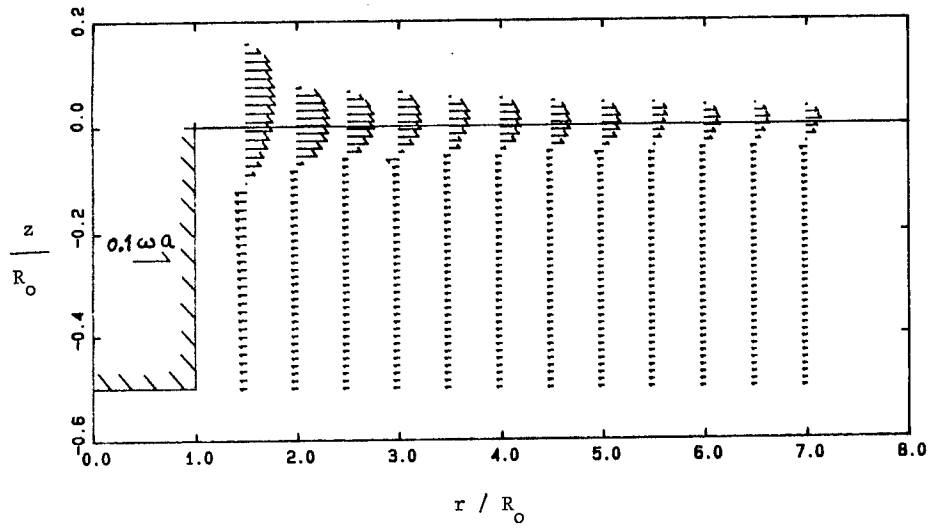


Figure 11. Mean horizontal velocities outside a heaving vertical cylinder for a/H = 0.5. The velocities continue almost constant to the bottom at $z/R_o = -1$.

4.3 Forced heaving motion of a floating inverted cone starting from rest

To test the validity of our treatment of the body and free-surface intersection line when the wall of the heaving body is not vertical, we consider the periodic forced motions of an inverted cone, initial waterplane radius R_o, draft $H=2R_o$, and water depth $h=2H$. We keep the same forcing velocity and frequency (4.2) and (4.3), and half stroke amplitudes a/H = .05, .1, and .2 are considered. When larger amplitudes are used for this cone angle and frequency, a thin jet of fluid is observed to rise sharply up the side of the body, and the simulations can not be continued much further. The matching boundary is placed at $A=20R_o=5h$ and uniform segment lengths are used throughout.

Our primary interests here are the forces and run-up on the cone which reaches steady state rapidly and computations beyond four periods are not found to be necessary for our analyses. The reaction force coefficients as defined earlier are given in Table 2. (Note that the hydrostatic component is now included in the coefficients.) The linear frequency-domian results for comparison are now obtained using an axisymmetric hybrid element method (Yue et al, 1978). As the motion amplitudes decrease, the coefficients compare well with linear predictions for both the mean and first-harmonic force, and there are no difficulties with large potential gradients. (For the third-harmonic coefficient, the force for the smallest stroke is insignificant and therefore not reliable).

	f_o^*	$\lvert f_1^* \rvert$	$\lvert f_2^* \rvert$	$\lvert f_3^* \rvert$
Nonlinear Computations				
a/H = .2	.43	.8270	.24	.072
a/H = .1	.44	.8242	.25	.073
a/H = .05	.44	.8238	.25	-
Linear Frequency-Domain Results				
	.441	.8237	-	-

Table 2. Harmonic Force Coefficients for the Forced Heaving of an Inverted Cone.

The behavior at the contact point is very smooth, and Figure 12 plots its position, (r_c,z_c), as a function of time after steady state is reached for $T \leq t \leq 3T$ for a/H=.2. Note the rapid approach to steady state indicated by the closed contour. The skewed shape of the particle orbit is due to the presence of nonlinearity. In general, if the vertical displacement of the cone is $\zeta(t)$ and the elevation of the free surface on the body is $\eta(r_c,t)$, then we have simply $z_c = \eta$ and $r_c - R_o = (R_o/H)(\eta-\zeta)$. Now for the linear harmonic problem, if the forcing motion $\zeta(t)$ is sinusoidal, $\eta(r_c,t) \simeq \overline{\eta}(R_o,t)$ will also be sinusoidal with a particular magnitude and phase with respect to ζ. In this case, then, (r_c,z_c) describes the locus of an ellipse inclined at an angle to the vertical plane. Such a curve using the magnitude and phase values from our linear theory calculation is also shown in Figure 12. The difference between the linear and nonlinear predictions is quite significant.

5. CONCLUSION

A numerical method which extends the mixed Eulerian-Lagrangian approach to nonlinear axisymmetric body (or bubble) and wave interaction problems is presented. For illustration, three problems involving nonlinear free surface effects are studied in some detail to bring out the important physical features and to demonstrate the effectiveness and accuracy of the method. In particular, novel ideas in the implementation of a linear far-field matching boundary, in the treatment of the free surface and body intersection line, and in a regriding algorithm to suppress the instabilities are tested and validated.

Our eventual objective is to develop accurate (quantative) computational models for fully three-dimensional nonlinear body free-surface interactions such as those associated with offshore structures in steep waves, large-amplitude ship motions, bow and stern flows, and nonlinear ship waves and wave resistance. To accomplish this, a number of important issues must be addressed:

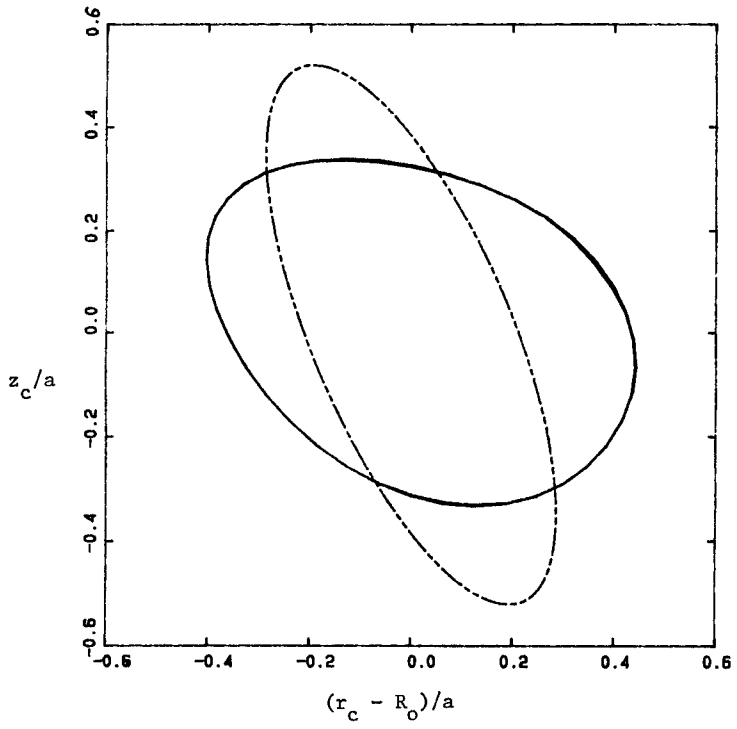


Figure 12. Steady-state locus of the intersection point between the free-surface and the surface of a heaving cone for a/H = .2. ——— : particle orbit predicted from linear theory. Note that three periods of motion ($T \leq t \leq 3T$) are plotted for the nonlinear problem.

1) Treatment of the nonlinear free surface. The semi-Lagrangian method has been shown to be remarkably successful, in both two-dimensions and beyond, especially in predicting highly nonlinear phenomena such as wave breaking and jets. The idea is directly applicable to three-dimensional flow, although refinements in the field equation solver to achieve the necessary stability, accuracy and efficiency may be important.

2) The body and free-surface intersection line. Difficulties associated with the intersection points have been practically resolved by the method of Lin et al (1984) in two dimensions in the context of complex potential formulation, and extended to axisymmetric flows using Green's identity in the present work. Furthur generalization to fully three-dimensional problems can be anticipated without special difficulties.

3) Far-field closure of the computational domain. The successful implementation of a far-field matching boundary has made feasible the long-time simulation of body generated waves. For three-dimensional problems, the more general formulation (see Appendix) is still applicable. Algorithms for the efficient evaluation of the (linear) transient wave-source potential will be valuable.

4) Efficient solution of the field equation. The present formulation of the mixed boundary-value problem as a Fredholm integral equation of the first kind has required direct solutions of the resulting algebraic system. To discretize the computational boundary of realistic fully three-dimensional problems, $N=O(10^4)$ unknowns can be anticipated - a prohibitive number for direct solution even on modern supercomputers. Our experiences towards formulating the mixed problem entirely as second kind Fredholm integral equations (Burton & Miller, 1971; Baker et al, 1982), for which iterative solution procedures are applicable, have not been completely successful. This is partly due to difficulties associated with proper treatment of the intersection of the free surface with the body and the matching boundary. The development of an efficient iterative solution to the field equations in an irregular domain, perhaps even by non-boundary-integral methods, is of critical importance.

5) Stability of the time integration. The regriding idea is very satisfactory at removing short-wavelength instabilities and should be directly extendable to three-dimensional problems (say with a two-dimensional spline of the surface). The exact mechanism of the instabilities is, however, still not well understood. A more fundamental treatment of this problem would be very desirable.

6) Implementation of a nonlinear incident wave for the diffraction problem. The difficulty here is to achieve this in a way consistent with a linear matching in the far-field. Several promising ideas can be pursued: (a) generate steep incident waves in the interior through directional and/or frequency focussing of linear waves imposed on the matching circumference; (b) prescribe as initial conditions large amplitude localized disturbances inside the computational domain; (c) introduce a wavemaker (for example a pressure patch or heaving cone) in the interior of the domain. However, since a good wavemaker will necessarily also be an efficient scatterer, simulation time will again be limited by the proximity of the wavemaker and thus the size of the computational region - a situation, ironically, not unlike what one may encounter in a physical wavetank.

Although a complete solution to these problems is still some time away, this work addresses many of the important issues and takes a useful step towards the simulation of realistic nonlinear free surface and body interactions.

This research was supported by the National Science Foundation (NSF Grant MEA 8210649) and the Office of Naval Research (Contract N00014-82-K-0198). Most of the computations were performed at the NSF sponsored Minnesota Supercomputer Institute. D.K.P.Y. also acknowledges partial support from the Henry L. Doherty Chair.

APPENDIX: SOLUTION OF THE LINEAR OUTER PROBLEM

The requisite relationships (2.9) for the linear outer potential can be obtained by applying Green's theorem in the region $r > A$, $-h < z < 0$ and using the boundary conditions (2.8) to give

$$2\pi\,\tilde{\phi}(x,t) + \int_{S_o} \left[\tilde{\phi}(t)\,\frac{\partial}{\partial r'},- \frac{\partial\tilde{\phi}(t)}{\partial r'}\right] G_R\,dS' \qquad (A.1)$$

$$+ \int_0^t d\tau \int_{S_o} \left[\tilde{\phi}(\tau)\,\frac{\partial^2}{\partial\tau\partial r'} - \frac{\partial\tilde{\phi}(\tau)}{\partial r'}\,\frac{\partial}{\partial\tau}\right] G_F(t-\tau)\,dS' = 0,$$

$$x \in S_o$$

where G_R, G_F are respectively the impulsive (Rankine) and memory (free-surface) parts of the transient Green function source given by (Wehausen and Laitone, 1960),

$$G_R(x,y,z;x',y',z') = \frac{1}{R} + \frac{1}{R_1} - \frac{1}{R_2} \qquad (A.2)$$

$$- \int_0^\infty dk\, J_o(k[(x-x')^2+(y-y')^2]^{1/2})$$

$$\cdot\left[2\,\frac{\cosh k(z+h)\,\cosh k(z'+h)e^{-kh}}{\cosh kh} - e^{k(z+z')}\right]$$

$$G_F(x,y,z;\, x',y',z';t) \qquad (A.3)$$

$$= 2\int_0^\infty dk\, \frac{\cosh k(z+h)\, \cosh k(z'+h)}{\sinh kh \cosh kh}$$

$$\cdot \{1 - \cos([gk \tanh kh]^{1/2} t)\}$$

$$\cdot J_o(k[(x-x')^2+(y-y')]^2)^{1/2}$$

In (A.2), $R_1^2=(x-x')^2+(y-y')^2+(z+z'+2h)^2$ and $R_2^2=(x-x')^2+(y-y')^2+(z+z')^2$ are associated respectively with Rankine source singularities at image points about the bottom and free surface.

When the flow is vertically axisymmetric, the integrals over θ' in (A.1) can be performed analytically. Using (2.7) and the identity (Watson, 1952),

$$\int_0^{2\pi} J_o(k[(r'\cos\theta'-r)^2+r'^2\sin^2\theta']^{1/2})\, d\theta'$$

$$= 2\pi J_o(kr)J_o(kr') \qquad (A.4)$$

we have

$$2\pi\, \tilde{\phi}(r=A,z,t) + \int_{-h}^{o} dz' \left[\tilde{\phi}(t)\, \frac{\partial}{\partial r'} - \frac{\partial \tilde{\phi}(t)}{\partial r'}\right] \bar{G}_R \Big|_{r=A} \qquad (A.5)$$

$$+ \int_o^t d\tau \int_{-h}^{o} dz' \left[\tilde{\phi}(\tau) \frac{\partial}{\partial r' \partial \tau} - \frac{\partial \phi(\tau)}{\partial r'}\, \frac{\partial}{\partial \tau}\right] \bar{G}_F(t-\tau) \Big|_{r=A} = 0$$

with the "ring" transient Green functions given by

$$\bar{G}_R(r,z;r',z') = G(r,z;r',z') + \qquad (A.6)$$

$$G(r,z;r',-z'-2h) - G(r,z;r',-z')$$

$$-2\pi r \int_0^\infty dk \left[2\, \frac{\cosh k(z+h) \cosh k(z'+h) e^{-kh}}{\cosh kh} - e^{k(z+z')}\right] J_o(kr)J_o(kr')$$

$$\bar{G}_F(r,z;r',z',t-\tau) = \qquad (A.7)$$

$$4\pi r \int_0^\infty dk\, \frac{\cosh k(z+h) \cosh k(z+h')}{\sinh kh \cosh kh}$$

$$\cdot \{1 - \cos[(gk \tanh kh)^{1/2}(t-\tau)]\} J_o(kr)J_o(kr')$$

Computationally, the integral in (A.6) converges rapidly with k because the Rankine singularities are subtracted out. The quadrature in (A.7), however, requires special care because of the oscillatory nature of both the cosine and Bessel functions. Note that (A.5) is not explicitly in the form of (2.9) because of the appearance of $\tilde{\phi}(t)$ under the first integral. ($\tilde{\phi}_r(t)$ does not come from the convolution integral since $\bar{G}_F(x,x';0) = 0$ as required). Numerically, one simply inverts the kernel associated with $\tilde{\phi}(t)$ after discretization to obtain H explicitly. Since ∂S_o is fixed, that kernel is a function only of h and A (and the discretization of ∂S_o) and the inversion needs to be performed once only for a given simulation.

Alternatively, one can seek an equation of the form (2.9) directly. For any linearized axisymmetric wavefield, $\tilde{\phi}$ and $\tilde{\phi}_r$ on a fixed vertical cylinder of radius A can, in general, be related by an equation of the form (Lin et al, 1984):

$$\tilde{\phi}(A,z,t) = \int_{-h}^{o} dz'\, D_R(z,z')\, \tilde{\phi}_r(A,z',t) \qquad (A.8)$$

$$+ \int_o^t d\tau \int_{-h}^{o} dz'\, D_F(z,z',t-\tau)\, \tilde{\phi}_r(A,z',\tau)$$

$$-h < z < 0$$

where D_R represents the impulsive contributions, and D_F the free-surface memory effects of the "Green function" $D(r,z,t;r',z',\tau)$ which satisfies the linearized exterior problem (2.8) with the condition

$$\frac{\partial D}{\partial r} = \delta(z-z')\delta(t-\tau) \qquad r = A$$

$$-h < z,z' < 0 \qquad (A.9)$$

The result is similar to that of Lin et al (1984) for infinite depth and is simplified when values on r = A only are required. The final forms are

$$D_R(z,z') = -\frac{2A}{\pi^2} \int_0^\infty dk \left[e^{-k|z-z'|} + e^{-k(z+z'+2h)} - \frac{2 \cosh k(z+h) \cosh k(z'+h) e^{-kh}}{\cosh kh}\right]$$

$$\cdot \frac{1}{(kA)^2[J_1^2(kA) + Y_1^2(kA)]} \qquad (A.10)$$

and

$$D_F(z,z',t-\tau) = \qquad (A.11)$$

$$-\frac{4g}{\pi^2}\int_0^\infty dk\,\frac{\sin\left[(gk\tanh kh)^{1/2}(t-\tau)\right]}{(gk\tanh kh)^{1/2}}$$

$$\cdot\,\frac{(1+\tanh kh)\cosh k(z+h)\cosh k(z'+h)\,e^{-kh}}{\cosh kh\,(kA)(J_1^2(kA)+Y_1^2(kA))}$$

As expected, D_R is logarithmically singular as $z\to z'$, while at $\tau=t$, we have $D_F(z,z',0)=0$.

Comparing the earlier Green's theorem formulas (A.5,6,7) to the present results (A.8,10,11), we note that the former can be more readily generalized to three-dimensional problems although (A.11) for D_F is in a more efficient form for quadrature than (A.7) for G_F. Both results are equally valid, and since portions of the Rankine kernel (A.6) are almost identical to that already required for the interior problem, we use (A.6) for the impulsive part, and (A.11) for the free-surface memory part of H in (2.9) for our computations.

REFERENCES

Abramowitz, M. & Stegun, I.A. (1964). Handbook of Mathematical Functions, Government Printing Office, Washington.

Baker, G.R., Meiron, D.I. & Orszag, S.A. (1982). Generalized vortex methods for free-surface flow problems. J. Fluid Mech., **123**: 477-501.

Blake, J.R. & Gibson, D.C. (1981). Growth and collapse of a vapour cavity near a free surface. J. Fluid Mechanics. **111**: 123-140.

Blake, J.R., Taib, B.B., & Doherty, G. (1985). Transient cavities near boundaries. Part II - Free Surface. University of Wollongong Preprint No. 5/86.

Burton, A.J. & Miller, G.F. (1971). The application of integral equation methods to the numerical solution of some exterior boundary-value problems. Proc. Roy. Soc. Lond. A. **323**: 201-210.

Dold, J.W. & Peregrine, D.H. (1984). Steep unsteady water waves: an efficient computational scheme. University of Bristol Report No. AM-84-04.

Faltinsen, O.M. (1977). Numerical solution of transient nonlinear free-surface motion outside or inside moving bodies. Proc. 2nd Intl. Conf. on Num. Ship Hydro., U.C. Berkeley.

Fink, P.T. & Soh, W.K. (1974). Calculation of vortex sheets in unsteady flow and applications in ship hydrodynamics. Proc. 10th Symp. on Naval Hydro., Cambridge.

Garrett, C.J.R. (1971). Wave forces on a circular dock. J. Fluid Mech., **46**: 129-139.

Greenhow, M. & Lin, W.M. (1983). Nonlinear Free Surface Effects: Experiments and Theory, MIT, Dept. of Ocean Engineering, Rpt. No. 83-19.

Greenhow, M., Vinje, T., Brevig, P. & Taylor, J. (1982). A theoretical and experimental study of the capsize of Salter's duck in extreme waves. J. Fluid Mech., **118**: 221-239.

Isaacson, M. de St. Q. (1982). Nonlinear-wave effects on fixed and floating bodies. J. Fluid Mech., **120**: 267-281.

Kravtchenko, J. (1954). Remarques sur le Calcul des Amplitudes de la Houle Lineaire Engendree par un Batteur. Proc. 5th Conf. on Coastal Engineering, Grenoble, France, 50-61.

Lin, W.M. (1984). Nonlinear Motion of the Free Surface Near a Moving Body. Ph.D. Thesis, M.I.T., Dept. of Ocean Engineering.

Lin, W.M., Newman, J.N. & Yue, D.K. (1984). Nonlinear forced motions of floating bodies. Proc. 15th Symp. on Naval Hydro. Hamburg.

Longuet-Higgings, M.S. (1974). Breaking Waves - in Deep or Shallow Water. Proc. 10th Symp. Naval Hydro., 597-605.

Longuet-Higgins, M.S. & Cokelet, E.D. (1976) The deformation of steep surface waves on water. I. A numerical method of computation. Proc. R. Soc. Lond. A., **350**: 1-26.

Mei, C.C.. (1983). The Applied Dynamics of Ocean Surface Waves, John Wiley & Sons, New York.

Miloh, T. (1980). Irregularities in Solutions of Nonlinear Wave Diffraction Problem by Vertical Cylinder. Proc. ASCE Journal of the Waterway, Port, Coastal and Ocean Division. **106**: 279-284.

Peregrine, D.H. (1972). Flow Due to Vertical Plate Moving in a Channel. Unpublished notes.

Plesset, M.S. & Chapman, R.B. (1971). Collapse of an initially spherical vapour cavity in the neighborhood of a solid boundary. J. Fluid Mech., 47: 283-290.

Rayleigh, Lord (1917). On the pressure developed during the collapse of a spherical cavity. Phil. Mag., 34: 94-97.

Roberts, A.J. (1983). A Stable and accurate numerical method to calculate the motion of a sharp interface between fluids. Journal of Applied Mathematics, 31: 13-35.

Vinje, T. & Brevig, P. (1981). Nonlinear ship motions. Proc. 3rd Intl. Symp. Num. Ship Hydro., Paris.

Vinje, T., Maogang, X. & Brevig, P. (1982). A Numerical Approach to Nonlinear Ship Motion. Proc. 14th Symp. on Naval Hydro., pp. 245-278.

Watson, G.N. (1952). A Treatise on the Theory of Bessel Functions, Cambridge University Press.

Yue, D.K., Chen, H.S. & Mei, C.C. (1978). A Hybrid Element Method for Diffraction of Water Waves by Three-Dimensional Bodies. International Journal for Numerical Methods in Engineering, 12: 245-266.

DISCUSSION

Garrett Birkhoff,
Harvard University

The growth and collapse of a bubble in a liquid acted on by gravity provide a fascinating, deceptively simple looking class of problems, to which the methods of Longuet-Higgins and Cokelet should certainly be applied. The more complicated problems of vertical water entry of a sphere, first studied photographically by A.M. Worthington (Phil. Trans. London 194 (1900), 175-90), is at least as fascinating. In particular interest are: (1) the contrast between "deep seal" and "surface seal", already observed by Worthington, (2) the effects of air density, and (3) the effect of capillarity.

It has been noted [a] (Chap. XI, 4) that a basis for "effective approximate calculation" is provided by the assumption that "the water is constrained to flow between concentric spheres, centered at the point of entry." The range of validity of this essentially empirical assumption was tested [b]. With modern computers and computing methods, it should be possible to obtain much more definitive results.

[a] G. Birkhoff and E.H. Zarantonello, "Jets, Wakes and Cavities", Academic Press, 1960.
[b] G. Birkhoff and R. Isaacs, "Transient cavities in air- water entry", Navord Report 1490, 1951.

Reply -

We thank Professor Birkhoff for pointing out the very interesting problem of water entry of a sphere, and we agree that numerical methods similar to the present one can indeed be exploited to obtain more definitive quantitative results. Our preliminary computational results for the entry of a vertical cone (Shiffman and Spencer, 1951, Comm. Pure App. Math, 4) are already promising, although the condition at the intersection line may need to be reexamined, and a suitable model for jet formulation may also be important.

Patrick J. Roache,
Ecodynamics Research Associates, Inc.

Could you provide some details on the algorithm for redistribution of free surface points? Is it perhaps based on equidistribution in arc length?

Reply -

Yes, our regriding is achieved by calculating a new set of free-surface points which are equidistant from each other with respect to arc length which is calculated in terms of cubic splines.

Nonlinear Wave Maker in a Channel Operating at Cut-Off Frequencies: Theory and Experiment

E. KIT, T. MILOH, and L. SHEMER

Tel Aviv University, Israel

ABSTRACT

Experimental and theoretical studies of sloshing waves in a rectangular channel at the vicinity of second cut-off frequency are presented in this paper. The experiments were performed in a wave tank which is 1.2m wide, 18m long and 0.9m deep. Sloshing waves were generated by a computer-controlled segmented wavemaker consisting of four independent modules. Experimental results are compared with numerical solutions of the appropriate nonlinear Schrödinger equation, a derivation of which is also presented. The importance of dissipation effects on the physical processes of wave evolution is discussed, and a simple dissipative model is suggested and incorporated in the governing equations.

1. INTRODUCTION

It is well known (e.g. Barnard, Mahony and Pritchard (1977), to be referred to as BMP in the sequel) that resonant waves with crests parallel to the channel walls and with wavelengths $\lambda = \frac{2b}{n}$, n being an integer representing the mode number, may appear in a semi-infinite channel of depth h and width b. These waves may be generated by a nonplanar wavemaker, whose shape in the direction normal to the channel walls has a typical wave length λ, and which operates at frequency close to the cut-off value defined by $\omega^2 = \frac{2g\pi}{\lambda} \tanh \frac{2\pi}{\lambda} h$. Waves formed in this manner are usually referred to as "sloshing waves". An alternative way of generating similar waves is by their parametric excitation by a plane wavemaker at subharmonic frequency, Garrett (1970), Barnard and Pritchard (1972). These waves are known as "cross-waves". Linear theory of sloshing waves given, e.g. in Wehausen (1974), fails to describe correctly the wave response in the vicinity of the cut-off frequencies, (Shemer, Kit and Miloh 1986), since it yields infinite amplitudes at these frequencies. In order to account for the finite wave amplitude observed experimentally at the cut-off frequency, both nonlinear effects and dissipation have to be considered in the theoretical model.

The most extensive experimental work reported on sloshing waves is due to BMP. They have performed measurements covering a wide range of forcing amplitudes in the vicinity of the 1st cut-off frequency by using a pointer-type wave gauge. BMP have observed that two distinct steady wave patterns may exist in the channel at identical forcing conditions. In some experiments the maximum of the wave height distributions along the channel was found to be shifted downwards from the wavemaker. A similar result was also reported by Barnard and Pritchard (1972) in their experiments on cross waves. Miles (1985) claimed that this type of distribution may be interpreted as a trapped soliton.

A steady soliton-like solution was observed experimentally by Wu, Keolian and Rudnick (1984). An attempt to analyse this non-propagating soliton was made by Larraza and Putterman (1984) by employing the well-known nonlinear Schrödinger equation.

A consistent to third-order derivation of the nonlinear Schrödinger equation (NLS) for the propagation of an acoustic wave in a duct, including a wavemaker-like forcing, was given by Aranha, Yue and Mei (1982). The numerical solutions of the obtained equation revealed that in the case which is analogous to deep water in the channel, no steady solution of the NLS equation can be obtained. The solution of an initial boundary value problem gave a wave pattern which can be decomposed into two parts: an unsteady decaying wave adjacent to the wavemaker and a single soliton which propagates away from the wavemaker. The unsteady character of the solution obtained numerically by Aranha, Yue and Mei (1982) is in contrast with the steady distribution observed experimentally by BMP.

This contradiction between the only experimental results known to us on sloshing waves and the numerical predictions, triggered our interest in this problem and was the main motivation for the present study. We decided to take advantage of our considerably larger wave tank, compared with the one used by BMP,

E. Kit, T. Miloh, L. Shemer, Faculty of Engineering, Tel-Aviv University, Tel-Aviv, 69978, Israel

which was about 30cm wide.

In a bigger facility one can generally expect lower dissipation rates. It is plausible to assume that the strong dissipation in BMP experiments is at least partially responsible for the evident discrepancy between their reported results and the numerical predictions of Aranha et al. By using our modular wavemaker it is possible to generate both the 1st and the 2nd modes of sloshing waves. Our present experiments were restricted to the 2nd mode, where detailed computer-based measurements of waveforms in the vicinity of the second cut-off frequency were performed. The experimental results are supplemented by a derivation of the nonlinear Schrödinger equation which is found to be appropriate for sloshing waves. Numerical solutions of this equation are also presented.

2. EXPERIMENTAL PROCEDURE

Experiments were performed in a wave tank which is 18m long, 1.2m wide, and 0.9m deep, which was filled to a mean water level of 0.6m. Waves were generated by a modular paddle-type wavemaker which consisted of four independent sections. A beach for wave energy absorption was placed at the far end of the tank. The detailed description of the experimental facility is given in Shemer, Kit and Miloh (1986).

Following the discussion of BMP, a stable wavemaker frequency with the possibility of fine tuning is indispensable for obtaining accurate and repeatable results in the close vicinity of the cut-off frequency. These features are extremely important since the most intriguing nonlinear phenomena occur in a very narrow frequency band and depend critically on previous history. For this reason it was decided to operate the wavemaker using a 1 MHz quartz clock of PDP 11/23 minicomputer. A total of 32 data points were used to emulate the sinusoidal signal. The output of D/A converter was low-pass filtered using Krohn-Hite filter. In this way a period resolution of 32 μs was obtained. Since the forcing period for the second cut-off frequency, where the measurements were made, is about 880 ms, the tuning accuracy $\frac{\Delta\omega}{\omega}$ which could be attained was as low as $3.6.10^{-5}$. In order to obtain second-mode sloshing wave with a zero net displacement, and thus to eliminate the contamination of the wave field by a plane propagating wave, all wavemaker sections were operated at identical amplitudes with a 180° phase shift between the two inner and the two outer wavemaker segments.

The instantaneous position of each wavemaker section could be monitored using the output signals of the position potentiometers. The instantaneous surface elevation of the induced wavefield was measured by four conductance-type wave height gauges which were located along the center line of the channel. The gauges were placed on a bar and could be moved by a carriage along the tank.

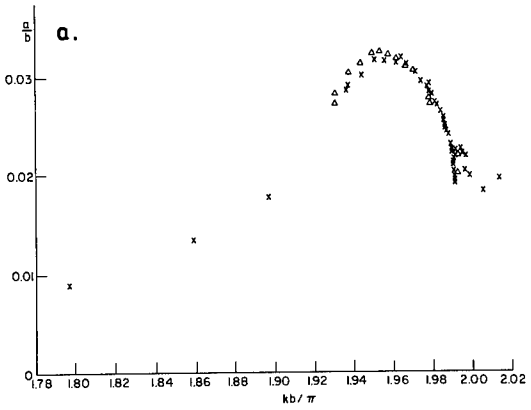
The outputs of 4 wave gauges, 4 wavemaker position potentiometers and the forcing signal which served as phase reference, were sampled instantaneously using A/D converter of the same minicomputer. All information was recorded on a magnetic tape for further processing. This procedure enabled one to perform long-time measurements. On a later stage the recorded time series for each data channel were phase averaged and the corresponding amplitudes and phases were obtained from these phase averaged signals using the Fourier transform. The data processing procedure is given in detail in Shemer, Kit and Miloh (1986).

In order to present the experimental results in dimensionless form, channel width b is used as a length scale. Following BMP, the small parameter of this study ε is defined as $\varepsilon = fs/b$, where s is the wavemaker stroke at the water surface level, and the dimensionless coefficient f is related to the wavemaker shape. For our facility, operating at the second cut-off frequency, $f = 1.762$, as shown in Section 4. In order to compare the experimental results taken at different forcing amplitudes ε, the distance x from the wavemaker has to be related to ε, so that the slow dimensionless X is defined by $X = \varepsilon^{1/2} x/b$ (see eq. (4.8).

3. EXPERIMENTAL RESULTS

The general behavior of sloshing waves for frequencies away from the cut-off, is described reasonably well by the linear theory (Shemer, Kit and Miloh, 1986). In the present work we are interested in the sloshing wave response in the close vicinity of the cut-off frequency, where nonlinear effects become dominant. Linear theory suggests the existence of two distinct wave regimes in the channel. Below the cut-off frequency, one can expect an a wave field whereas a radiating wave is generated at frequencies above the cut-off. The critical frequency range, where transition from one wave regime to another occurs, is amplitude-dependent and down-shifted relative to the linear cut-off value, (Penney and Price 1952). In view of the fact that the exact boundary conditions on the beach at the far end of the tank are not well defined, it was decided to restrict the experiments to conditions where no influence of the far end can be observed and the water close to the beach remains practically still. Detailed waveform measurements were thus performed mainly at frequencies below the cut-off value were the wave amplitude decays along the channel.

In order to isolate the frequency range where most interesting nonlinear phenomena can be observed, measurements were first performed covering a relatively wide frequency region. Figures 1 show the wave number dependence of the amplitudes, a (Fig.1a) and the phase angles relative to the phase of central sections of the wavemaker, ϕ



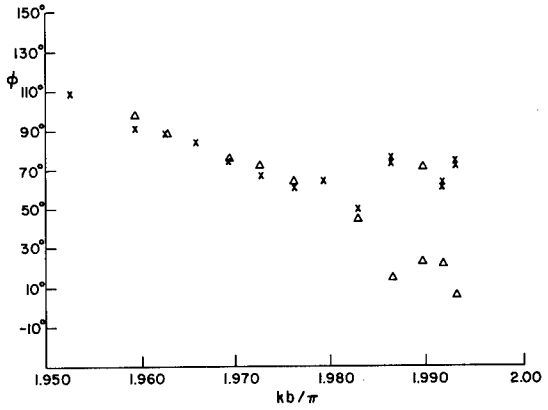


Figure 2: The dependence of phase angles of probes located at 11cm, X = 0.0078 - x; and 160cm, X = 0.113 - Δ, on wave number, forcing amplitude ε = 0.0072.

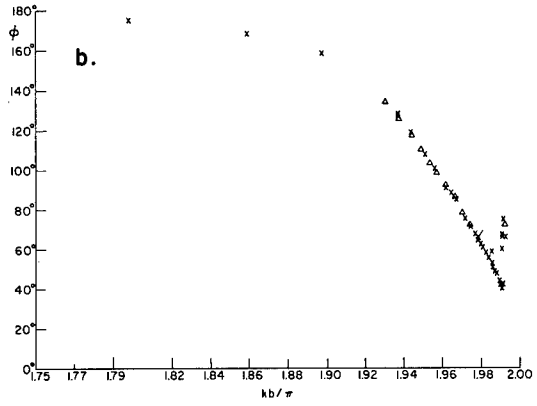


Figure 1: The dependence of wave amplitudes (Fig. 1a) and wave phase angles (Fig. 1b) on wavenumber. Probe location x = 11cm, forcing amplitude ε = 0.0052; X = 0.0066; x - increasing frequency; Δ - decreasing frequency.

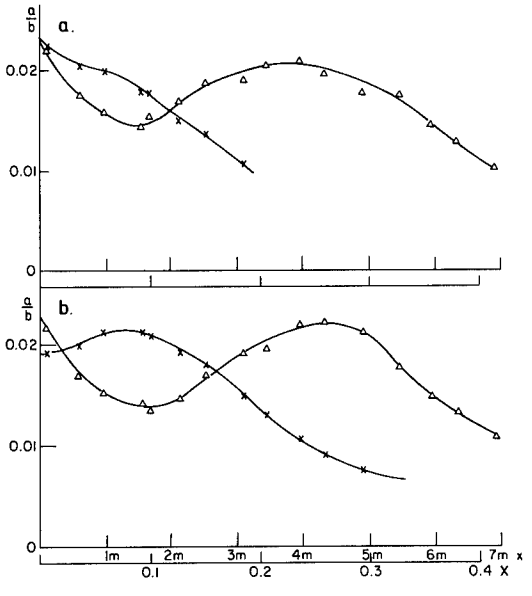


Figure 3: The distribution of wave amplitudes along the tank at k/k_0 = 1.9900 (Fig. 3a) and k/k_0 = 1.9913 (Fig. 3b), ε = 0.0052; x - steady regime; Δ - unsteady regime.

(Fig.1b), measured by the wave gauge located at a distance of 11cm from the wavemaker.

Linear theory predicts a 180° phase shift between the amplitudes of the wavemaker and the surface elevation for the decaying regime and a 90° phase shift for the radiating wave. Figure 1b indicates that the linear limit is approached at a relatively low frequency ($kb/\pi \leq 1.8$). Increasing the frequency of the wavemaker results in a further decrease of the phase shift ϕ. It is important to note that the energy rate introduced into the system by the wavemaker when operating at frequency ω and with a stroke s, is proportional to the product $\omega s \cdot a \sin\phi$. The deviation of ϕ from 180° in the vicinity of the resonance clearly indicates that there exists an energy feed mechanism into the wave field. Contrary to the radiating mode, no energy transfer to infinity occurs in the decaying regime, thus energy dissipation, being the only possible energy sink, plays an important role in this range of frequencies.

The wave amplitude attains a maximum at $kb/\pi \approx 1.95$ and then decreases. It is interesting to note that at approximately the same value of kb/π the phase shift ϕ crosses the 90° line and thus the energy flux exhibits there a pronounced maximum.

At $kb/\pi \approx 1.991$ a dramatic transition in the wave field pattern is observed which manifests itself in Figures 1 in the form of a jump in both amplitude and phase angle. Observation of the wave field in the tank suggests that a wave pattern of radiating nature is generated. The increase in the phase angle ϕ, which now approaches the value of 90°, supports this suggestion. The detailed investigation of the transition process, is one of the main goals of the present work.

A similar transition at higher forcing amplitude is shown in Figure 2 from a different point of view. The phase angles relative to the wavemaker are shown here for two probes located at 11cm and 160 cm (corresponding to a dimensionless slow X = 0.0066 and X = 0.096, respectively). One can immediately see that for $kb/\pi < 1.986$ the phase angles are identical, as expected for a standing wave. The transition at this higher amplitude occurs at a lower value of kb/π than in Figure 1. The wave field, beyond transition is characterized by an increased value of ϕ close to the wavemaker, similar to the results displayed in Figure 1b. On the other hand, the phase angle at the downstream position continues to decrease. Significant phase differences measured at different locations indicate that energy is propagating along the channel. It is observed in the experiments that the amplitude of the propagating wave decays well before the beach due to dissipation.

A most interesting nonlinear phenomena is to be expected in the transition region where the history of the wave field may be of importance. A possibility of existence of two distinct wave patterns at identical forcing conditions, was first observed by BMP. Examples displaying two different wave amplitude distributions along the channel at the same amplitudes and frequencies of forcing, are presented in Figures 3a and 3b. In order to obtain these distributions, special care was taken to vary the forcing frequency monotonically. This could be achieved as a result of the special features provided by the computer control of the wavemaker.

In Figures 3, distribution I was obtained when the desired frequency was approached from below, while distribution II represents the case where the same frequency was approached from above. Curves I represent the "decaying" wave regime. At a lower frequency the wave amplitude decays monotonically (although the decay is not exponential and an inflection point in the longitudinal wave amplitude distribution is clearly seen). The slight increase in the frequency, which amount to an increase in kb/π by 0.06%, results in a qualitatively different distribution where the maximum amplitude was found to be detached from the wavemaker. The wave amplitudes at this frequency, after attaining a maximum, decrease along the channel in a similar manner to that displayed in Fig. 3a. In both cases the waves vanish already far from the beach. No measurements were performed in the monotonically decreasing region far from the wavemaker. It is important to stress here that distributions of type I represent wave regimes which are essentially steady.

In contrast with regime I, the family of curves labelled as II represent basically an unsteady wave field, which is characterized by a modulation on a slow time scale. Before dealing with the details of the long-time modulation, we shall restrict our analysis to values averaged over times longer than the typical modulation period. The distinct property of a type II distribution shown in Figure 3, is that the amplitude first decreases significantly, attains a minimum at a distance which is comparable with the width of the tank (and hence with the wave length), and then increases again reaching a maximum at a substantial distance from the wavemaker. From that location on, the wave amplitude decay monotonically towards the beach.

Amplitude distributions of type I and II will be referred to in the sequel as "decaying" and "radiating" modes, respectively. In the transition region the "radiating" mode is quite different from the linear solution which gives a propagating wave having a constant amplitude and a 90° phase shift. The sharp transition between the two observed modes, on one hand, and the gradual change in the wave parameters when the frequency is further increased, on the other hand, seems to justify this notation. The "decaying" mode in the vicinity of the transition is also different in essence from the linear solution and may be considered as a trapped soliton, discussed by Miles (1985). The presence of a trapped soliton may also explain the shift in the location of the maximum amplitude away from the wavemaker. A similar phenomenon was also observed in the cross-waves experiments

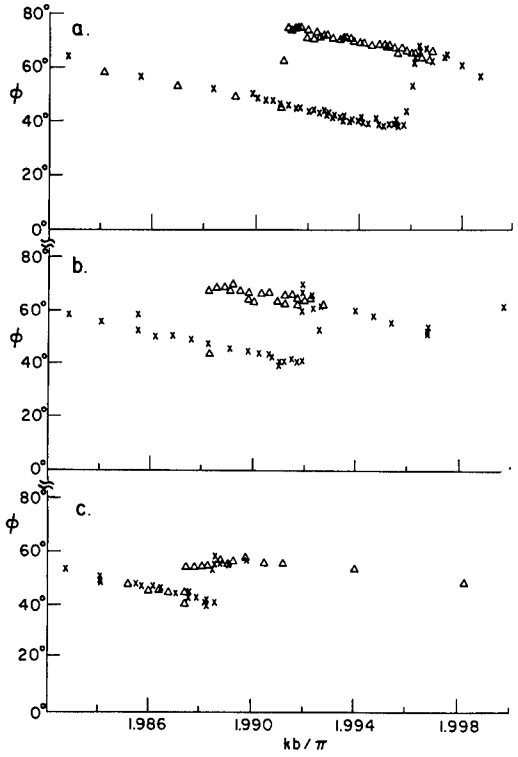


Figure 4: The dependence of phase angles of probe located at x = 11cm on wave number, x - for increasing frequency; Δ - for decreasing frequency. Forcing amplitude: Fig. 4a ε = 0.0036; Fig. 4b ε = 0.0052; Fig. 4c ε = 0.0072.

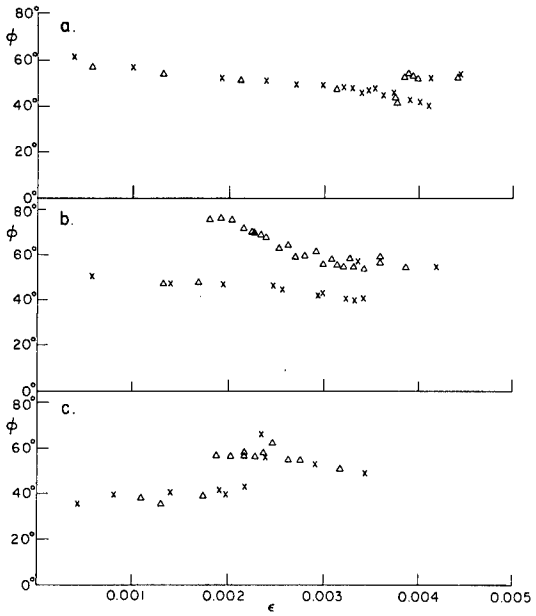


Figure 6: The dependence of wave-phase angle φ on amplitude of forcing for x = 11cm. k/k_0 = 1.9869 (Fig. 6a), 1.9900 (Fig. 6b) and 1.9950 (Fig. 6c) x - increasing amplitude, Δ - decreasing amplitude.

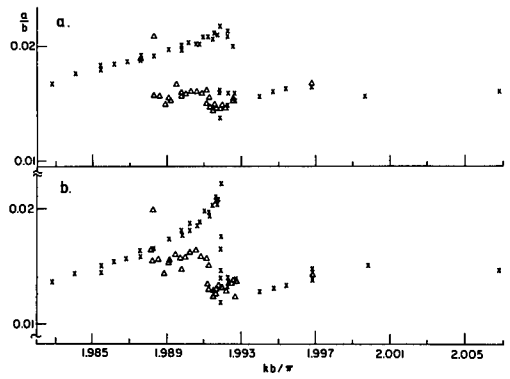


Figure 5: The dependence of wave amplitude at x = 111cm; X = 0.067 (Fig. 5a) and at x = 160cm; X = 0.096 (Fig. 5b) on wave number. x - results for increasing frequency; Δ - decreasing frequency; amplitude of forcing ε = 0.0052.

reported by Barnard and Pritchard (1972), and Miles (1985).

Figures 4 show in the expanded scale, the dependence of the phase angle, measured by the probe located at 11cm from the wavemaker at three forcing amplitudes. The hysteresis type behavior is evident in all three cases, and the transition from the "decaying" to the "radiating" mode occurs at frequencies which are slightly higher than those at which a reverse transition is observed. Generally speaking, the transition region is shifted towards lower frequencies with increasing amplitudes. The hysteresis loop becomes narrower with increasing forcing amplitude. It is interesting to note that close to the transition point the phase angle of the "decaying" mode, in all three cases, attains practically the same value of approximately 40^{o}, while the phase of the "radiating" mode decreases significantly with increasing amplitude.

Although the phase hysteresis at a distance of 11cm from the wavemaker is clearly seen in the experiment, the amplitude measurements at this location do not give a clear picture. The reason for that can be understood from a close scrutiny of the amplitude distributions shown in Figures 3. One can see that close to the wavemaker the absolute difference in the wave amplitude between the "decaying" and the "radiating" modes is small. Moreover, the sign of this difference changes in a narrow range of frequencies. For this reason it is more instructive to demonstrate the behavior of the amplitudes in the vicinity of the transition at some distance from the wavemaker.

In Figures 5 the dependence of wave amplitudes on the wave number is shown at a distance of 111cm (Figure 5a) and 160cm (Figure 5b) from the wavemaker. A well-defined hysteresis loop can be seen in both cases. In Figure 5a the amplitude of the "decaying" mode is always higher than that of the "radiating" mode. In Figure 5b, on the other hand, the backward transition from the "radiating" to the "decaying" mode occurs practically without any amplitude change, and the hysteresis loop has a form which resembles a triangle. The explanation for such a form may be obtained again from Figure 3. One can see that there exists a crossing point between the amplitude distributions in the two modes; the location of the point where the amplitudes of both modes are equal moves closer to the wavemaker with decreasing frequency. At $kb/\pi = 1.987$, this point is apparently located at a distance of about 160cm from the wavemaker. At more distant locations, the amplitude will increase when a transition from the "decaying" to the "radiating" regime occurs. This may explain the difference between our results and the amplitude dependence on frequency, given by BMP, (see their Fig. 5).

In Figures 4 and 5 the hysteresis loop was obtained by keeping the forcing amplitude constant. The same phenomenon could be obtained by varying the forcing amplitude at a constant frequency (Figures 6). At the lowest wavemaker frequency (Figure 6a), very high amplitudes and thus strong nonlinear effects, are necessary in order to generate a "radiating" regime. On the contrary, at high frequencies (Figure 6c), the "decaying" mode can be observed only for very low forcing amplitudes. At an intermediate frequency (Figure 6b), a wide hysteresis loop was obtained. One can notice that here again the transition from "decaying" to "radiating" mode, for all values of forcing, occurs when the phase shift is about 40^{o}.

Special attention was also paid to the detailed analysis of the unsteady behavior of the wave field. Since the unsteady character of the wave field is more pronounced at higher amplitudes of forcing, the data for $\varepsilon = 0.0072$ is presented first. The time dependence of the wave amplitudes measured simultaneously by four wave gauges, which are fixed to the probe carriage, are presented in Figure 7. These measurements cover the range of wave gauge locations from 11cm to 9m from the wavemaker, corresponding to 5 different carriage positions and for a total duration of 2114 sec (corresponding to 2400 wave periods).

The existence of a well defined periodicity on the long-time scale for all locations is evident. The period of the slow amplitude modulation is about 495 sec. The periodic modulation observed everywhere in the tank, is supplemented by a clear envelope soliton-type waveform which is developed at $x > 2m$. The soliton propagation velocity (estimated from the measured shift in the position of the maximum amplitude at different probes), is about 3.5 cm/sec. One can also see from Figure 7a that close to the wavemaker the modulation is relatively weak and it becomes more pronounced with increasing x. The increase in the modulation depth (ratio between maximum and minimum amplitudes) is accompanied by a growth in the maximum wave amplitude, which at $x > 2m$ becomes nearly twice as large as the value in the vicinity of the wavemaker. At $x > 5m$ the wavy disturbance in front of the soliton nearly vanishes, and the wave amplitude differs notably from zero only when the soliton is present.

One can assume that the increase in the height of the envelope soliton results from extracting energy from the background wave field. When the waves leading the soliton gradually disappear, the soliton height remains nearly constant ($2.5\ m < x < 5.5m$). For larger x, the soliton height decreases and this process is accompanied by a transfer of energy to background waves trailing the soliton (Figure 7e, $x = 897$ cm). The total wave energy decay rate along the channel is obviously due to dissipation (on the boundaries as well as in the bulk).

It is quite surprising to realize that at lower forcing amplitude, $\varepsilon = 0.0052$, the modulation period measured from Figures 8, is about 505 sec which is nearly the same as the value measured at significantly higher amplitude. In the lower forcing-amplitude

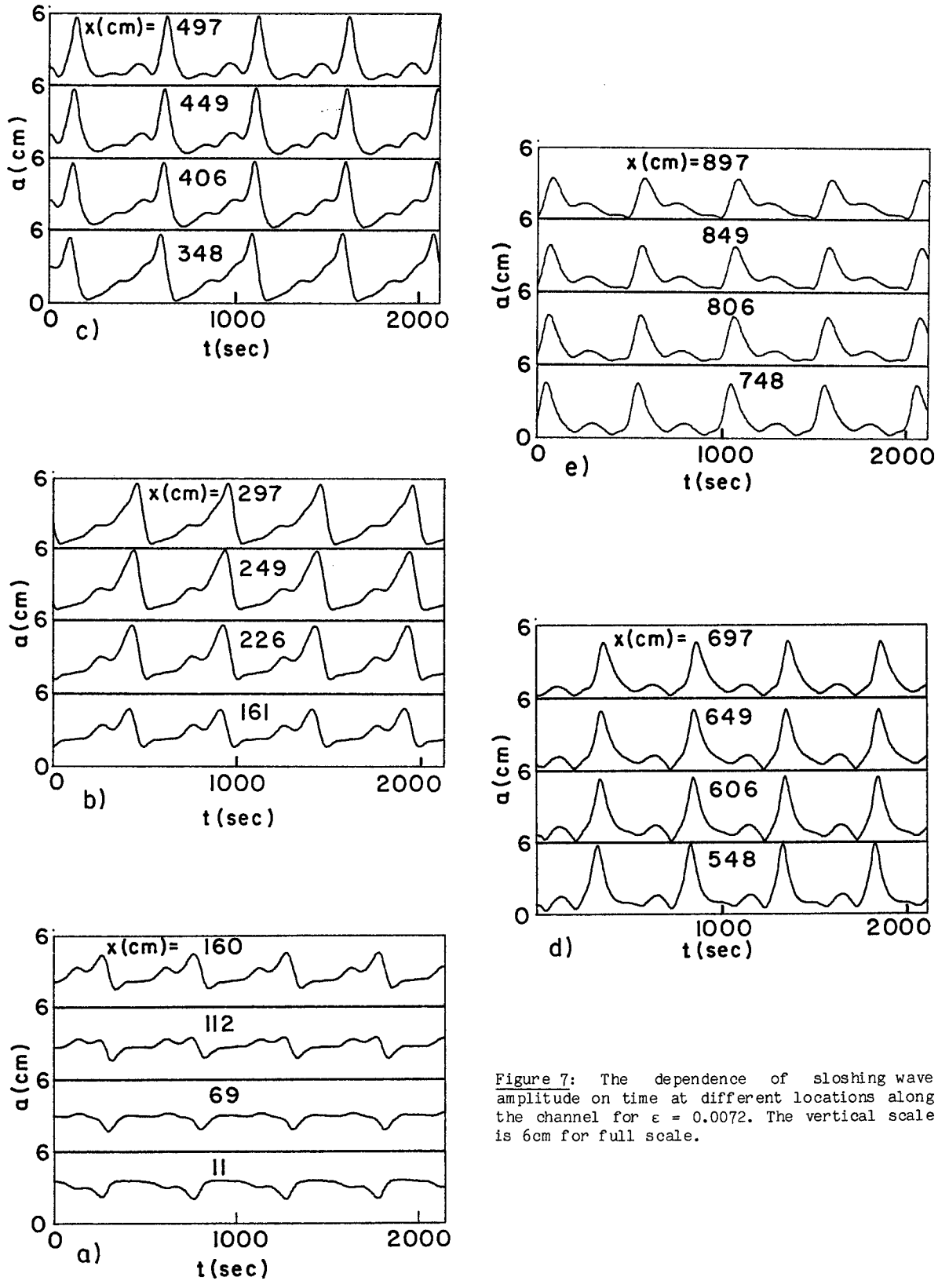
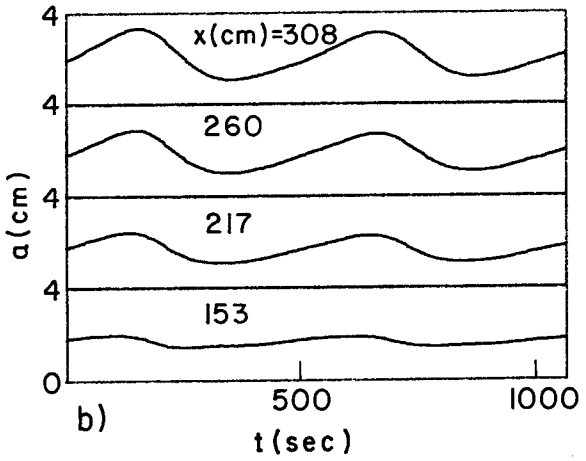
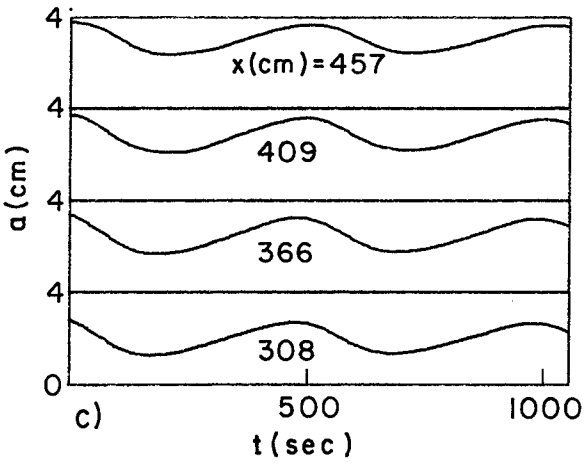


Figure 7: The dependence of sloshing wave amplitude on time at different locations along the channel for $\varepsilon = 0.0072$. The vertical scale is 6cm for full scale.





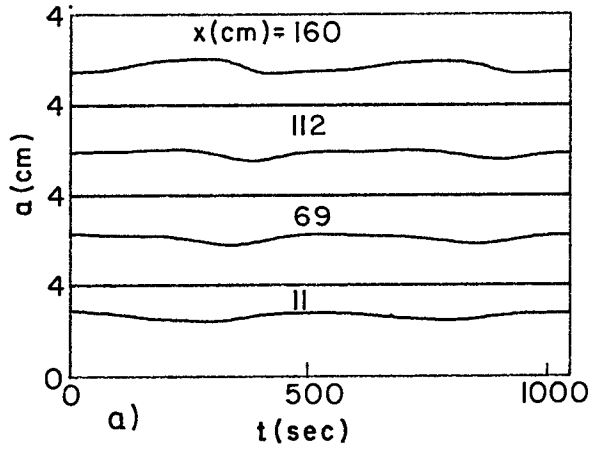


Figure 8: Same as in Figures 7; $\varepsilon = 0.0052$; vertical scale 4cm for full scale.

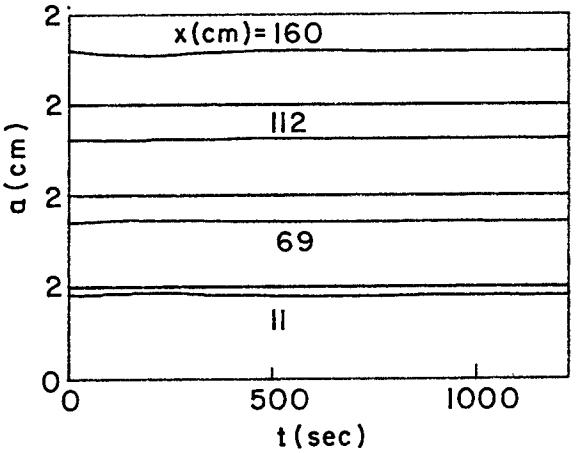


Figure 9: Long time modulation for $\varepsilon = 0.0036$, vertical scale 2cm for full scale.

range no clear soliton-like waveforms could be observed and the general pattern of the maximum amplitude variation with x, is quite similar to the strong forcing case. At even lower forcing, the modulation is extremely weak and could hardly be detected (Figure 9), for this reason no clear conclusions regarding the modulation period could be drawn.

4. THEORETICAL CONSIDERATIONS

Consider a semi-infinite rectangular wave tank of width b and water depth h equipped with a wavemaker situated at x=0. In a Cartesian coordinate system (x,y,z), the undisturbed free-surface is z=0 (with z pointing vertically upward), z = - h is the bottom and the two parallel channel walls lie at y=0 and y=b. Let the fluid be inviscid and the flow irrotational. The governing equation and the free surface boundary conditions, relating the induced velocity potential $\phi(x,y,z,t)$ and the resulting free-surface elevation $\eta(x,y,t)$, are as follows:

$$\nabla^2\phi = 0 \tag{4.1}$$

$$\eta_t + \phi_x \eta_x + \phi_y \eta_y = \phi_z \qquad z = \eta(x,y,t) \tag{4.2a}$$

$$\phi_t + g\eta + \frac{1}{2} \nabla\phi\cdot\nabla\phi = 0 \tag{4.2b}$$

This should be supplemented by the impervious boundary conditions on the channel wall:

$$\phi_y = 0 \quad ; \quad y = 0,b \tag{4.3a}$$

$$\phi_z = 0 \quad ; \quad z = - h \tag{4.3b}$$

Eliminating the free-surface displacement from (4.2) and using Taylor expansion about z=0, yields the following relationship correct to third order in the displacement (Newman 1977),

$$\phi_{tt}+g\phi_z+2\nabla\phi\ \nabla\phi_t+\frac{1}{2}\ \nabla\phi\cdot\nabla(\nabla\phi\cdot\nabla\phi)$$

$$- \frac{1}{g}\ \phi_t(\phi_{tt}+g\phi_z+2\nabla\phi\ \nabla\phi_t)_z \tag{4.4}$$

$$- \frac{1}{g}\ (-\frac{1}{g}\ \phi_t\phi_{zt} + \frac{1}{2}\ \nabla\phi\cdot\nabla\phi)\cdot(\phi_{tt}+g\phi_z)_z$$

$$+ \frac{1}{2g^2}\ \phi_t^2\ (\phi_{tt}+g\phi_z)_{zz} = 0$$

The boundary condition on the wavemaker is

$$\phi_x = \varepsilon(\xi_t + \phi_y\ \xi_y + \phi_z\ \xi_z) \quad \text{on } x = \varepsilon\ \xi\ (y,z,t) \tag{4.5}$$

where ε is a small parameter related to the amplitude of the wavemaker. The condition at infinity is

$$\phi \to 0 \qquad \text{as} \qquad x \to \infty \tag{4.6}$$

and the initial condition is given by

$$\phi(x,y,z,0) = \phi_o(x,y,z) \tag{4.7}$$

where ϕ_o is a known function. In order to analyze the channel response in the vicinity of the second cut-off frequency it is advantageous to introduce slow variables in the following manner;

$$X = \varepsilon^{1/2}\ x; \quad T = \varepsilon\ \ (\frac{b}{g})^{1/2}\ \frac{t}{2\omega},$$

$$\Omega = \omega + \varepsilon\ \frac{g}{b}\ \frac{\lambda}{2\omega} \tag{4.8}$$

This particular ordering between physical and slow variables, as well as the relationship between the forcing frequency Ω and the cut-off frequency ω, was chosen so as to eliminate secular first harmonic terms in the third order, (Aranha et al 1982). The cut-off frequency ω satisfies the dispersion relation

$$\omega^2 = gk \tanh kh\ , \qquad k = \frac{b}{2\pi} \tag{4.9}$$

A three-term expansion of ϕ can be represented as:

$$\phi = \varepsilon^{1/2}\ \phi_1 + \varepsilon\ \phi_2 + \varepsilon^{3/2}\ \phi_3 + O(\varepsilon^2) \tag{4.10}$$

We look for solutions of (4.1) with harmonically oscillating wavemaker, correct to order $\varepsilon^{3/2}$, which satisfies the boundary conditions (4.2) to (4.4) in the form

$$\phi_1 = C(X,T) \cos ky\ \frac{\cosh k(z+h)}{\cosh kh}\ ^{-i\Omega t} + c.c \tag{4.11}$$

so that the complex amplitude C depends only on the slow variables X and T and c.c. denotes complex conjugate.

Following a procedure similar to the one outlined in Aranha et al, (1982), and using the appropriate alternative theorem given in Stakgold (1979), one can show that the complex amplitude is governed by the following cubic Schrodinger equation

$$\frac{i}{2}\ \ (\frac{g}{b})^{1/2}\ \frac{\partial C}{\partial T} + \frac{g}{2k}\ \frac{\partial^2 C}{\partial X^2} + \frac{\lambda g}{b}\ C + K\ |C|^2\ C = 0 \tag{4.12}$$

where for $kh \to \infty$ (deep water)

$$K = k^4 \tag{4.13}$$

The appropriate boundary condition to be applied on the wavemaker is

$$\frac{1}{b}\ \frac{\partial C}{\partial X} = - i\Omega \qquad \text{at} \qquad X = 0 \tag{4.14}$$

It follows from (4.14) that the small parameter ε should be defined as

$$\varepsilon = f\ \frac{s}{b} \tag{4.15}$$

where f is a dimensionless coefficient, related to the wavemaker displacement amplitude $\xi_m(y,z)$ normalized by the wavemaker stroke s by

$$f = \frac{4\kappa^2 \cosh^2 kh}{\pi(\sinh 2kh + 2kh)}$$

$$\int_0^b \int_{-h}^{0} \frac{\xi_m(y,z)}{s} \cos ky \, \frac{\cosh k(z+h)}{\cosh kh} \, dydz \qquad (4.16)$$

The deep water approximation (4.13) was found to hold in our experimental facility ($kh = 2\pi \frac{h}{b} = \pi$). The detailed derivation and the appropriate value of the coefficient K for arbitrary water depth will be given elsewhere.

Rendering all variables dimensionless by using b as length scale and $\sqrt{b/g}$ as time scale, (4.12) yields,

$$i \frac{\partial \hat{C}}{\partial \hat{T}} + \frac{\partial^2 \hat{C}}{\partial \hat{X}^2} + \hat{\lambda} \hat{C} + 2\left|\hat{C}\right|^2 \hat{C} = 0 \qquad (4.17)$$

with the condition on the wavemaker

$$\frac{\partial \hat{C}}{\partial \hat{X}} = -i \qquad \text{at} \qquad \hat{X} = 0 \qquad (4.18)$$

where the renormalized dimensionless quantities are related to the corresponding physical values by

$$\hat{X} = (2\pi)^{5/2} \hat{\varepsilon}^{1/2} \, x/b \; ; \qquad \hat{T} = (2\pi)^4 \hat{\varepsilon}/2\omega \; g/b \; t; \qquad (4.19)$$

$$\hat{C} = (b^3 g)^{1/2} C \; ; \qquad \hat{\lambda} = \frac{4\omega(\Omega-\omega)}{(2\pi)^4 \hat{\varepsilon}} \frac{b}{g}$$

The normalized value of $\hat{\varepsilon}$ is related to the value of ε defined in (4.15) by

$$\hat{\varepsilon} = (2\pi)^{-5/2} \omega \left(\frac{b}{g}\right)^{1/2} \varepsilon/2 \qquad (4.20)$$

The value of f calculated for our wavemaker from (4.16), is f = 1.762.

Equation (4.17) with the boundary condition (4.18) was solved numerically using a semi-implicit Crank-Nicolson type scheme and by employing explicit estimation of the nonlinear term. Since the normalized NLS equation (4.17) is identical with the one solved numerically by Aranha et al, we adopted their numerical approach. The step sizes were similar or less than those checked by Aranha et al (i.e., $\Delta \hat{X} \leq 0.2$; $\Delta \hat{T} \leq 0.025$). In most of the runs presented in the sequel, we chose $\Delta \hat{X} = 0.1$ and $\Delta \hat{T} = 0.01$. In order to compare the numerical results with the experimental data, it is necessary to relate the physical scales to the normalized dimensionless quantities. Using the value of $\varepsilon = 0.0052$, corresponding to an intermediate amplitude in our experiments, one obtains the following relations;

$$\hat{X} = 0.8 \; x/b \quad ; \qquad \hat{T} = 0.05 \; \Omega t/2\pi \qquad (4.21)$$

Hence, the length of the channel from the wavemaker to the beach is $\hat{X} \approx 12$. In order to eliminate the influence of the far end of the channel, the calculations were performed for $0 \leq \hat{X} \leq 100$, which is equivalent to a channel, at least 8 times longer than the present one. The results, however, are presented only for $\hat{X} \leq 40$. In view of the fact that the experiments were performed at frequencies below the cut-off, we have restricted our numerical calculations to negative values of λ. Zero initial conditions and a continuous oscillating forcing were used in the numerical scheme.

Figure 10a shows the space time evolution of $\left|C(\hat{X},\hat{T})\right|$ for $\hat{\lambda} = -0.1$. A propagating soliton, similar to the one found by Aranha et al for positive and zero values of λ, was obtained. The "width" of the soliton calculated from Figure 10a, is in agreement with the experimental observations (about 4 - 6 m in the calculations and 3-5 m in the experiments). Once generated, the soliton propagates with a constant velocity down the channel, in accordance with the experiment. The calculated value of the propagation velocity is about 10 cm/s compared to about 3.5 cm/s found in the experiments. The evolution of the wave form was found to be in good qualitative agreement with the experiment. The height of the soliton increases initially (up to about $\hat{T}$=10), and then decreases again with some of the energy apparently transferred to the background waves at $\hat{T} > 10$.

Similar calculations for which were performed for $\hat{\lambda} = -0.2$, gave a much flatter soliton with a substantially lower height. However, it is important to note that the propagation velocity remains essentially unchanged compared with that measured from Figure 10a. For $\hat{\lambda} = -0.5$, no soliton like solution was obtained, and the solution resembles the reported results of Aranha et al for $\lambda = -1.$ and $\lambda = -2$.

The numerical solutions given in Figures 10 differ qualitatively from the experimental observations in two aspects: i) in contrast with the numerical results the solitons observed in the experiments were generated periodically at the wavemaker and ii) the numerical solutions for the wave amplitude at the wavemaker, were found to be much higher than in the rest of the wavefield, while in the experiments a quite different pattern was obtained (see Figures 7).

As pointed out in the previous section, the inviscid model is, in principle, incapable to describe correctly all wavefield features which are observed experimentally. In order to get a better qualitative agreement between experiments and theory, it seems important to include dissipation effects in some way. Following Ursell (1952), a dissipation on the channel walls is a dominant mechanism in a real system and should be included in the analysis. In most cases, e.g., Ursell (1952), BMP, which deal with a relatively deep channel, only dissipation on the side walls is considered. The numerical results, yielding

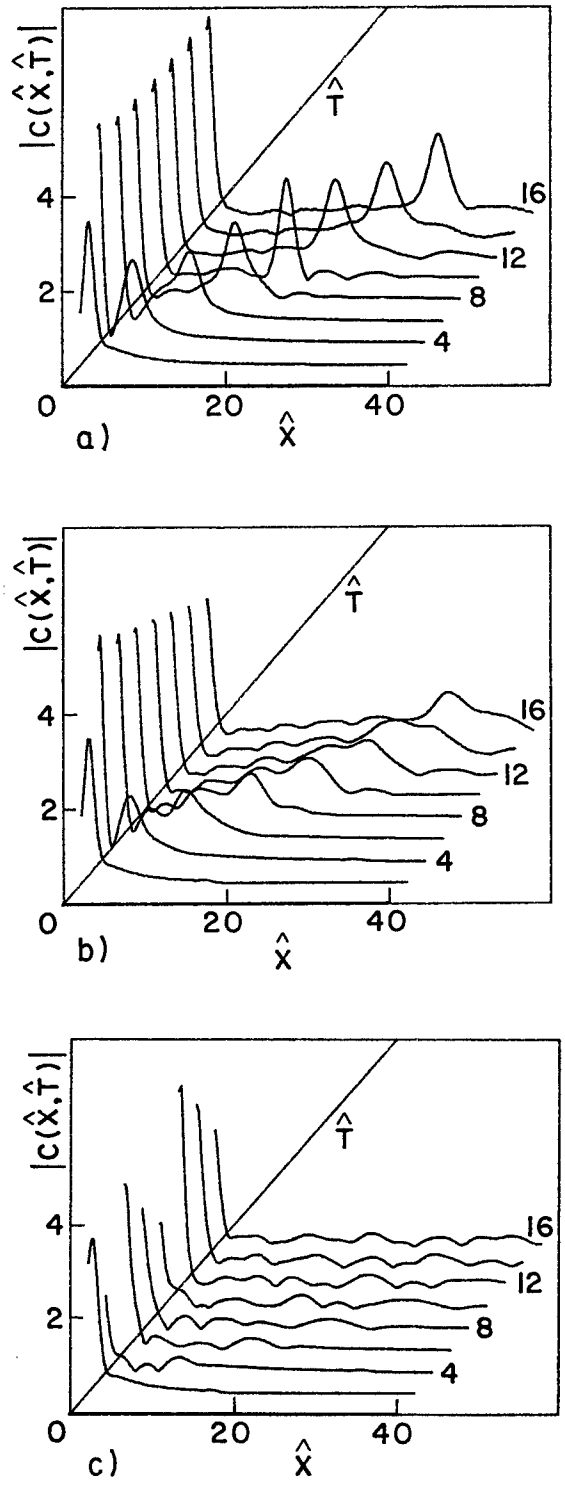


Figure 10: Space-time evolution of $|C(\hat{X},\hat{T})|$ for the inviscid case; a) $\hat{\lambda} = -0.1$; b) $\hat{\lambda} = -0.2$; c) $\hat{\lambda} = -0.5$.

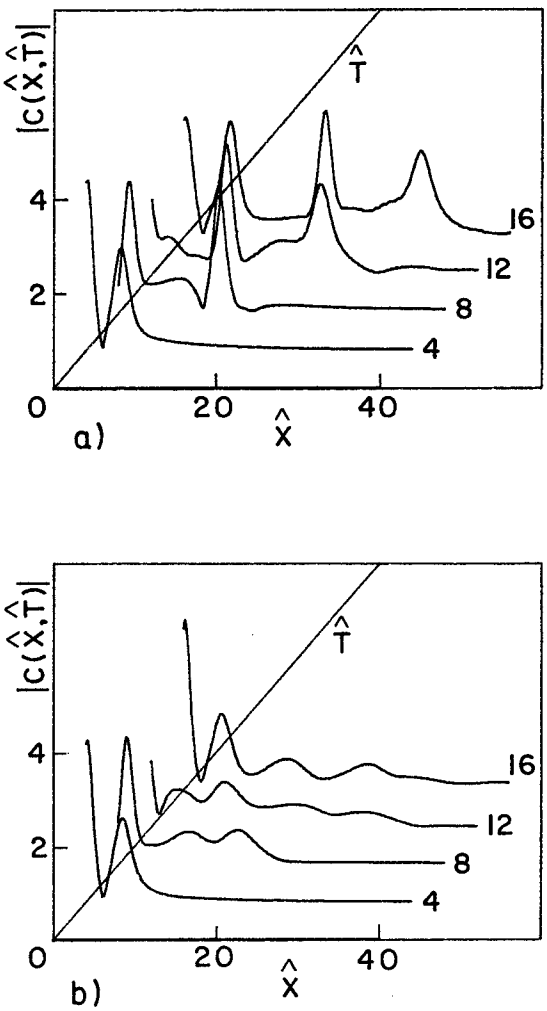


Figure 11: Space-time evolution of $|C(\hat{X},\hat{T})|$ for the dissipative model; $\hat{\lambda} = -0.1$; a) $a_1 = 0$; $a_2 = 0.1$; b) $a_1 = 0.1$; $a_2 = 0$.

extremely high amplitudes at $\hat{X} = 0$, indicate, however, that dissipation at the wavemaker can not be disregarded.

In the present work we do not attempt to give a full solution of the dissipation problem, but rather try to incorporate some crude dissipation models in the NLS equation and in the boundary conditions. It is well known that viscous dissipation in any oscillatory flow occurs in the Stokes layer, which in our case, has the width, Schlichting (1975),

$$\delta_{ST} = (\nu/\omega)^{1/2} \approx 3mm << b \qquad (4.22)$$

The phase shift between the potential flow velocity and the shear stress on the wall, is 45°. On the basis of these simple considerations we adopt the heuristic form used by BMP to model the effect of dissipation on the walls and add to (4.17) a term $a_1 (1+i) \hat{C}$, where a_1 is some real positive number. In order to account for dissipation at the wavemaker, the boundary condition (4.18) is modified in the following way:

$$\partial\hat{C}/\partial\hat{X} + a_2(1+i)\,\hat{C} = -i \qquad (4.23)$$

where again a_2 is some positive number. The solution of (4.17) with $a_1 = 0$ (no side wall dissipation) and $a_2 = 0.1$ (dissipation on wavemaker) is given in Figure 11a. One can immediately see that adding effective dissipation on the wavemaker, results in a dramatic change in the wavefield. The periodic generation of solitons at the wavemaker can now be clearly seen. These periodically generated solitons propagate with the same velocity as the single soliton shown in Figure 10a. The numerical results displayed in Figure 11a now resemble strongly the experimental observations.

In Figure 11b an attempt was made to take into account the side wall dissipation ($a_1 = 0.1$) while neglecting the dissipation on the wavemaker ($a_2=0$). There again, periodic generation of solitons can be noticed. However, the solitons thus generated disappear very fast in the course of their motion down the channel due to strong dissipation.

5. DISCUSSION

Our numerical results tend to support the conjecture made by Aranha et al that the inviscid cubic Schrodinger equation with a positive nonlinear term (corresponding to the deep water case) does not yield steady solutions. Both experimental measurements and numerical calculations were limited mostly to negative values of $\hat{\lambda}$. In the range of $\hat{\lambda}$ tested, two different types of numerical solutions were obtained. For $\hat{\lambda} \leq -0.5$, no propagating solitons appeared in the numerical solutions, and the wavefield was restricted to the region close to the wavemaker. For $\hat{\lambda} > -0.5$, a single soliton moving down the channel with a constant speed, was obtained.

Experimentally, the observed behavior of the wavefield, described in Section 3, is somewhat different from the numerical predictions. In the experiments, as well as in the numerical solution, there exists a critical frequency below which a unique wave pattern of a purely decaying mode, is observed. Above this value, a transition zone exists, where two different wave regimes could appear, depending on the history of the flowfield. The dimensionless tuning parameter $\hat{\lambda}$, corresponding to the value of this critical frequency, was ε (amplitude) dependent. From Figures 4 one can deduce that $\hat{\lambda} = -0.81$ for $\varepsilon = 0.36.10^{-2}$, $\hat{\lambda} = -0.73$ for $\varepsilon = 0.52\ 10^{-2}$ and $\hat{\lambda} = -0.56$ for $\varepsilon = 0.72\cdot10^{-2}$. Thus, the agreement between experiments and theory is improved with increasing forcing amplitude. It is also worthwhile to recall here that the lateral extend of the hysteresis region shrinks with increasing ε, and that pronounced solitons were obtained experimentally only for high forcing amplitudes.

All these facts seem to indicate that the inviscid nonlinear Schrodinger equation provides a better prediction of experimental observations at strong forcing. This can be also understood when one realizes that the relative importance of nonlinearity, as compared with essentially linear dissipation effects, increases with amplitude. The inviscid approach is thus more justifiable at high wave amplitudes. Nevertheless, the inviscid solution still does not correspond to the observations even for the highest amplitude employed in the experiment.

The inviscid equation includes a single tunable parameter $\hat{\lambda}$, which represents the ratio between the frequency detuning $\Omega-\omega$ and the forcing ε (see 4.8). No direct dependence on ε appears in the NLS equation. The experimental results, however, were found to depend on ε and not only on λ. At $\varepsilon = 0.36\cdot10^{-2}$ for example, a steady or weakly modulated wavefield was observed experimentally, while at $\varepsilon = 0.72\cdot10^{-2}$ periodic envelope soliton was found to propagate down the channel. The periodicity of soliton formation can not be explained within the framework of inviscid theory. The very crude dissipation model incorporated both in the Schrodinger equation and in the boundary condition on the wavemaker, yields a qualitative agreement with high amplitude observations, and exhibits a periodic appearance of solitons. As a matter of fact, including dissipation in the model introduces an additional tunable parameter and effectively decouples frequency detuning and amplitude. A refined dissipation model will hopefully give even better agreement with the experiment, in particular at lower amplitudes of forcing.

These considerations can help us to understand the differences between the experimental results of BMP and those reported here. Since the wave tank used by BMP was narrower by a factor of 4 compared with our flume, the effective dissipation in their experiments was much stronger. That might be the reason why BMP did not report on any propagating solitons and on the existence

of a long-time modulation in their experimental work. From the results presented by BMP one can deduce, however, that a hysteresis phenomenon similar in nature to one discussed in our work, was also present in their experiments. One can speculate that the reason for this hysteresis stems from a strong interaction between dissipation and nonlinear effects.

6. CONCLUSIONS

1. A well-defined hysteresis phenomenon by amplitude or frequency was observed experimentally at the vicinity of the cut-off frequency, in a relatively narrow frequency band. The observation of the hysteresis loop was made possible only due to the fact that the operation of the wavemaker was extremely stable, with the possibility of very fine frequency tuning.

2. Two distinct wave regimes at identical forcing, depending on previous history and on frequency, were observed in the channel for all wavemaker amplitudes.

3. At relatively low forcing amplitude the observed wave field was essentially steady. Increasing the forcing results in an amplitude modulation on a long time scale. At highest forcing amplitude, solitons were generated periodically at the wavemaker and then propagated down the channel with constant speed.

4. A cubic Schrödinger equation, valid for a semi-infinite deep rectangular channel with a proper boundary condition at the wavemaker, was derived.

5. The numerical solutions of this NLS equation were checked against experimental observations. Quantitative comparison of soliton propagation velocity, soliton width and location of transition, showed reasonably good agreement, in particular for high amplitudes of forcing.

6. The inviscid NLS equation was found inadequate in explaining the periodicity of soliton generation at the wavemaker and the direct amplitude dependence of the observed wave field. The NLS equation and the boundary conditions on the wavemaker were therefore modified to incorporate, in a qualitative manner, the effect of dissipation.

7. The numerical solution of the modified nonlinear Schrödinger equation gave periodic appearance of propagating solitons similar to those observed in the experiments.

7. REFERENCES

1. Aranha, J.A., Yue, D.K.P. and Mei, C.C., "Nonlinear waves near a cut-off frequency in an acoustic duct - a numerical study", J. Fluid Mech., Vol. 121, 1982, 465-485.

2. Barnard, B.J.S., Mahony, J.J. and Pritchard, W.G., "The excitation of surface waves near a cut-off frequency," Phil. Trans. R. Soc. London, Vol. A286, 1977, 87-123.

3. Barnard, B.J.S. and Pritchard, W.G., "Cross-waves. Part 2. Experiments", J. Fluid Mech., Vol. 55, 1972, 245-255.

4. Garrett, C.J.R., "On cross-waves", J. Fluid Mech., Vol. 41, 1970, 837-849.

5. Larraza, A and Putterman, S., "Theory of non-propagating surface-wave solitons", J. Fluid Mech., Vol. 148, 1984, 443-449.

6. Miles, J.W., "Note on parameterically excited trapped cross-wave", J. Fluid mech., Vol. 151, 1985, 391-394.

7. Newman, J.N., Marine Hydrodynamics, MIT Cambridge, 1977, p. 247-248.

8. Penney, W.G. and Price, H.T., "Part II. Finite periodic stationary gravity waves in a perfect fluid", Phil. Trans., Vol. A244, 1952, 254-284.

9. Schlichting, H., Boundary Layer Theory, 1975, McGraw-Hill.

10. Shemer, L., Kit, E., and Miloh, T., "Measurements of two-and three-dimensional waves in a channel, including the vicinity of cut-off frequencies", to appear in Experiments in Fluids, 1986.

11. Stakgold, I., Green's functions and boundary value problems, 1979, J. Wiley, N.Y., pp. 207-214.

12. Ursell, F., "Edge waves on a sloping beach," Proc. R. Soc. London, Vol. A214, 1952, 79-97.

13. Wehausen, J.V., "Methods for boundary-value problems in free-surface flows", 1977. The third D.W. Taylor Lecture, DTNSRDC Report 4622, Bethesda, Maryland

13. Wu, J., Keolian, R and Rudnick, I., "Observation of a nonpropagating Hydrodynamic Soliton", Phys. Rev. Lettrs, Vol. 52, 1984, 1421-1424.

DISCUSSION

Dick K. Yue,
Massachussetts Institute of Technology

First I would like to thank the authors for this important contribution and especially for providing the sought for experimental confirmation of the predictions of the Aranha, Yue and Mei (1982) for a closely related problem. I would like Prof. Miloh to comment on two points:

a. The nonlinear Schrödinger equation and method of numerical solution you used is similar to Aranha, Yue and Mei but you seem to suggest some quantitative discrepancies in the results with respect to the tuning coefficient. Could you comment on that?

b. In our earlier work, a discussion of the effect of dissipation was made primarily from the point of view of the large modulation lengths implied by the theory. In that regard, the dissipation values you use appear to be large since the disturbance is strongly damped downstream in contrast to your own experiments. Have you tried somewhat smaller values of dissipation and, if so, are the quantitative changes still observed?

Reply -

a. In the paper of Aranha, Yue and Mei results for continuous forcing and $K > 0$ case (corresponding to deep water waves) are presented for a single value of the detuning coefficient $\lambda = 0$. There is no discrepancy between our results for this value of λ and those of Aranha et al. The solutions obtained for other values of λ differ quantitatively from the case $\lambda = 0$ (see our Fig. 10). This is, however, in agreement with the results of Aranha et al., obtained for a positive value of K (see their Fig. 8).

b. Our experiments seem to indicate that the governing dissipation mechanism is that at the wavemaker (Fig. 11). Smaller values of a_2, which correspond to weaker dissipation at the wavemaker, still give qualitatively similar results. A more detailed analysis of the dissipation effects is necessary in order to obtain a better estimate of the appropriate numerical values of the coefficients a_1 and a_2.

Steady Flow Past a Step

P. M. NAGHDI and L. VONGSARNPIGOON
University of California, Berkeley, U.S.A.

ABSTRACT

This paper is concerned with the problem of steady two-dimensional flow, under the action of gravity, of an incompressible inviscid fluid sheet past a step of finite height. The effect of surface tension is neglected and attention is confined mainly to the case in which the top free surface is continuous everywhere. The problem is formulated here by a direct approach with the use of the theory of a directed fluid sheet which includes appropriate jump conditions within the scope of the basic theory. A nonlinear steady state solution of the problem, which also allows for the possibility of energy loss at the step, is used to predict the downstream values of the free surface waveheight for the full range of the far upstream Froude number. In particular, given the far upstream conditions, it is shown that a steady flow exists only if the step height is below a certain value. Detailed numerical results are obtained, which exhibit the effect of loss of energy at the step.

1. INTRODUCTION

The flow of an incompressible, inviscid, fluid past a step over a fixed bottom has been discussed by several authors. A treatment of the problem, in the context of linearized theory and with particular reference to reflection and transmission of waves, can be found in Lamb (1932, Section 176, 187) who cites additional references. A related discussion of reflection and transmission of plane waves with the use of a linear shallow water theory is included in a recent paper of Tuck (1978), while Green & Naghdi (1976, 1977) with the use of a nonlinear steady state solution have considered a step in formulating the problem of hydraulic jump when the free surface waveheight is discontinuous directly above the step. Utilizing the restricted theory of a directed fluid sheet (Green & Naghdi, 1976, 1977) we discuss in the present paper a general nonlinear steady state solution of the problem for two-dimensional flow in the x-z plane over a finite step, but with emphasis placed on the case in which the top free surface is continuous everywhere.

For the sake of clarity, we include here a brief statement of the problem. Consider a two-dimensional steady flow past a step in the x-z plane of rectangular Cartesian coordinates $x_i = (x,y,z)$, with associated base vectors $\underset{\sim}{e}_i = (\underset{\sim}{e}_1,\underset{\sim}{e}_2,\underset{\sim}{e}_3)$, $i = 1,2,3$. The bottom surface is defined by $z = H(x)$, with $H(x)$ specified by

$$H = \begin{cases} 0 & \text{for } -\infty < x < 0, \\ d = \text{const.} & \text{for } 0 < x < \infty . \end{cases} \tag{1.1}$$

The bottom surface defined by (1.1) is a step of finite constant height d at x = 0 as shown in Fig. 1. The physical region of space then conveniently separates into the upstream region $-\infty < x < 0$ ahead of the step (labeled I in Fig. 1) and the downstream region $0 < x < \infty$

to the right of the step (labeled II in Fig. 1). In the upstream region as $x \to -\infty$, the flow approaches the far upstream uniform flow with the uniform fluid height h_o and uniform velocity u_o. In the formulation of the problem, we neglect the effect of surface tension and take the atmospheric pressure at the top free surface to be zero everywhere without loss in generality. As noted in the opening paragraph, the nonlinear steady state solution of the problem can be discussed in such a manner that the free surface waveheight may exhibit discontinuity directly above the step. However, we are interested here mainly in the case for which the top free surface of the fluid remains continuous everywhere.

In Section 2, we briefly consider a nonlinear differential equation for the free surface waveheight h appropriate for two-dimensional steady motion over a level bed. This differential equation (see Eq. (2.1)) can be derived from the system of basic equations of the theory of a directed fluid sheet (Green & Naghdi, 1976, 1977) where the director is assumed to remain always parallel to the e_3-direction. A brief discussion of the upstream flow in region I is also included in Section 2.

The flow in the downstream region is considered in detail in Section 3. Allowing for the possibility of energy loss at the step, it is shown that the downstream flow is completely determined if the value of one of the constants of integration, namely S_2, is known. This constant can be determined from the knowledge of the free surface waveheight h and its gradient at any one point in region II, e.g., at the point immediately to the right of the step (see Fig. 1). In particular, for given far upstream information (h_o, F^2), where h_o is the far upstream height and F is the Froude number defined by Eq. (2.2), a steady flow is possible in region II only if the constant S_2 is bounded from above and below by the values S_2^+ and S_2^-, respectively, i.e., $S_2^- \leq S_2 \leq S_2^+$. For the upper bound value S_2^+, the flow above the step is subcritical uniform flow everywhere. On the other hand, for the lower bound value S_2^-, the downstream flow approaches a supercritical uniform flow far downstream. For a value of $S_2^- < S_2 < S_2^+$, the downstream flow has the form of stationary cnoidal waves. Making use of the fact that the constant S_2 is bounded from above and below, it is demonstrated that --for given upstream conditions (h_o, F^2)--a steady flow is not possible if the step height d is above a certain value. Equivalently, for a fixed step height, a steady flow is not possible if the upstream height h_o is below a certain value for a given F^2.

For purposes of illustration, we consider an example in Section 4 and present the results of certain calculations, carried out both in the presence, or absence, of energy loss. These calculations which are obtained for a particular Froude number ($F^2 = 0.05$), represent the maximum and minimum waveheights of the cnoidal wave solution (in the downstream region) as functions of the step height. The corresponding results for other admissible values of the Froude number have similar features and hence are not included here.

2. BASIC EQUATIONS. THE UPSTREAM FLOW

For an incompressible, homogeneous, inviscid fluid and for steady motions confined to the x-z plane of the rectangular Cartesian coordinates (x,y,z), the basic equations of the restricted theory of a directed fluid sheet (Green & Naghdi 1976, 1977) in the absence of surface tension can be integrated to yield (see, e.g., Naghdi & Vongsarnpigoon 1986a):

$$hh_{xx} - \frac{1}{2}h_x^2 + \frac{3h^3}{F^2h_o^3} - \frac{3h^2}{F^2h_o^3}\left(\frac{R}{g} - H\right) + \frac{3}{2}\left(H_{xx} + \frac{H_x^2}{h}\right) + \frac{3}{2} = 0 \quad . \tag{2.1}$$

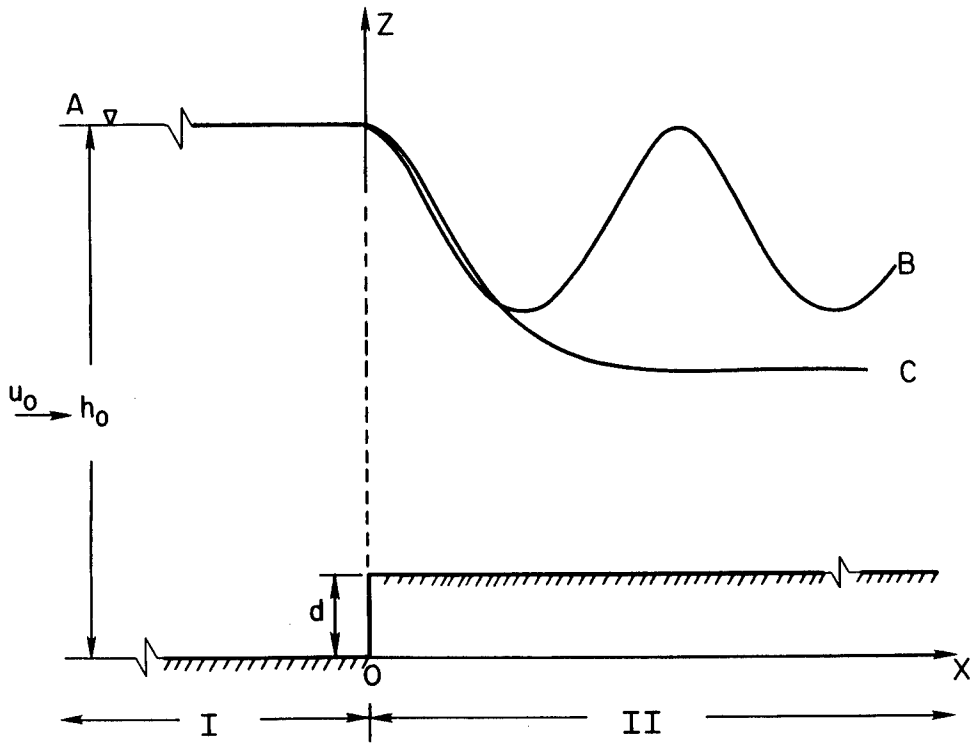


Fig. 1: A sketch of steady flow over a step in the x-z plane of the rectangular Cartesian coordinate system showing the upstream and downstream regions labeled I and II, respectively. Also shown are the far upstream vertical height h_o, the far upstream velocity u_o and the step height d. Depending on the step height, the downstream flow: (a) may be a standing cnoidal wave such as AB or (b) may approach a uniform flow of diminishing height such as AC.

In the above differential equation, h is the waveheight, H the vertical distance to the variable bottom surface of the fluid sheet, g the constant gravitational acceleration, F the far upstream Froude number defined by

$$F^2 = u_o^2/gh_o \ , \qquad (2.2)$$

and R in the fourth term of (2.1) is a constant of integration. Also in writing (2.1), we have assumed that the pressure $\hat{p}$ at the top surface of the fluid sheet is the constant atmospheric pressure taken to be zero without loss in generality. We also recall that for an incompressible fluid, the conservation of mass can be reduced to

$$hu = Q = h_o u_o \ , \qquad (2.3)$$

where u is the horizontal component of velocity and Q is the constant flow rate which has been determined from the far upstream conditions for uniform flow.

For flow over a level bed with H = constant, (not necessarily equal to zero), $H_x = H_{xx} = 0$, the differential equation (2.1) reduces to

$$hh_{xx} - \frac{1}{2}h_x^2 + f(h)=0 \ , \qquad (2.4a)$$

$$f(h) = \frac{3h^3}{F^2h_o^3} - \frac{3h^2}{F^2h_o^3}\left(\frac{R}{g} - H\right) + \frac{3}{2} \ . \qquad (2.4b)$$

By a standard procedure, (2.4a) can be integrated to yield

$$h_x^2 + q(h) = 0 \qquad (2.5a)$$

$$q(h) = \frac{3h^3}{F^2h_o^3} - \frac{6h^2}{F^2h_o^3}\left(\frac{R}{g} - H\right) + \frac{6Sh}{F^2gh_o^3} - 3 \quad , \qquad (2.5b)$$

where S is another constant of integration. [Note that our notations for u,h,ρ^*,Q in the present paper (which are the same as those in Naghdi & Vongsarnpigoon 1986a) correspond, respectively, to u,ϕ,ρ^*,k of a number of previous papers, e.g. Green & Naghdi (1976, 1977) and Naghdi & Rubin (1981)].

Let R_1 and S_1 be the values of R and S, respectively, in the upstream region where $x < 0$ and let the level bottom be specified by $H = 0$. Making use of the far upstream conditions, it follows from (2.4) and (2.5) that

$$R_1 = \frac{1}{2}u_o^2 + gh_o = gh_o\left(\frac{F^2}{2} + 1\right) \quad , \qquad (2.6)$$

$$S_1 = \frac{1}{2}F^2gh_o^2\left(2 + \frac{1}{F^2}\right) \quad , \qquad (2.7)$$

respectively. In what follows we restrict our attention to a subcritical upstream flow in which $F_2 < 1$. Then, with this stipulation, it is well-known that the upstream height ahead of the step is given by

$$h = h_o = \text{constant} \quad (x < 0) \quad . \qquad (2.8)$$

It may be emphasized here that the basic theory involves also appropriate jump conditions, which arise naturally in the context of the theory of a directed fluid sheet. A summary of these conditions is given in the Appendix at the end of the paper. They provide matching conditions at the transition boundary between the upstream and downstream regions. Moreover, the right-hand sides of these conditions are not necessarily zero and in general require constitutive equations. It should be noted also that the right-hand sides of the jump conditions in the (relatively simple) direct theory used here are not all independent: The right-hand side of (A4a) is related to the right-hand side of (A5) by (A7). Also, with the condition (A8), the right-hand sides of (A4b,c) are related by (A10).

3. THE DOWNSTREAM FLOW

We consider now the flow in region II over the step. The underlying physics in the determination of the downstream flow is the fact that a change in momentum is imparted at the step, giving rise to a resultant force $\underset{\sim}{F} = F_1\underset{\sim}{e}_1 + F_3\underset{\sim}{e}_3$ which acts on the step. Of course, this change in momentum is accompanied also by a dissipation of energy at the step. Within the scope of the theory of a directed fluid sheet, it is possible to account for the effect of energy dissipation (for example due to viscosity) by specifying a nonvanishing Φ on the right-hand side of (A5). In the presence of energy dissipation, the differential equation for the flow in the downstream region follows from(2.4a,b), (A6) and (2.6) and is given by (Naghdi & Vongsarnpigoon 1986b)

$$hh_{xx} - \frac{1}{2}h_x^2 + \overline{f}(h) = 0 \quad , \qquad (3.1a)$$

$$\overline{f}(h) = \frac{3h^3}{F^2h_o^3} - \frac{3h^2}{h_o^2}\left(\frac{1}{F^2} + \frac{1}{2} - \frac{d}{F^2h_o} - \frac{\Phi h_o^2}{\rho^* Q^3}\right) + \frac{3}{2} \quad , \qquad (3.1b)$$

where we have made use of the fact that H=d for x>0 as defined in (1.1). Similarly, from (2.5a,b) we obtain

$$h_x^2 + \overline{q}(h) = 0 \quad , \qquad (3.2a)$$

$$\overline{q}(h) = \frac{3h^3}{F^2h_o^3} - \frac{3h^2}{h_o^2}\left(1 + \frac{2}{F^2} - \frac{2d}{F^2h_o} - \frac{2\Phi h_o^2}{\rho^* Q^3}\right) + \frac{6S_2h}{F^2gh_o^3} - 3, \qquad (3.2b)$$

where S_2 is the value of S in the downstream region.

Consider first the nature of the solution when the flow approaches a uniform flow far downstream. Since h_x and h_{xx} both approach zero far downstream, it follows from (3.1a) that far downstream h must approach a root of the function $\bar{f}(h)$ given by (3.1b). We note in passing that by setting d=0 and Φ=0, the function $\bar{f}(h)$ in (3.1b) reduces to the corresponding function f(h) with two positive roots h_0 and γh_0 (see Naghdi & Vongsarnpigoon 1986a), with the parameter γ given by

$$\gamma = \frac{1}{4}[F^2 + (F^4+8F^2)^{1/2}]. \qquad (3.3)$$

It can be shown that the function $\bar{f}(h)$ also has two positive roots $h = \gamma_1 h_0$ and $h = \gamma_2 h_0$ (the details of the calculations are similar to those used in Green & Naghdi 1976, Sec. 8) with

$$\gamma < \gamma_2 < \gamma_1 < 1 \quad , \qquad (3.4)$$

provided that the combination of d and Φ satisfy the condition

$$0 < d + \frac{\Phi}{\rho^* g Q} < D \quad , \qquad (3.5)$$

where the upper bound D is given by

$$D = \frac{h_0}{\tau^2}(1-\tau)(\tau-\gamma)(\tau+\gamma-\frac{F^2}{2}) = h_0(1+\frac{F^2}{2}-\frac{3}{2}\tau),$$

$$\tau = F^{2/3} \quad . \qquad (3.6a,b)$$

Before proceeding further, we note that since (3.1a) with $h_x = h_{xx} = 0$ must be satisfied for values of $h = \gamma_1 h_0$ and $h = \gamma_2 h_0$ we have

$$\Phi = \rho^* Q g\{h_0(1+\frac{F^2}{2}) - \gamma_1 h_0(1+\frac{F^2}{3\gamma_1})-d\}, \qquad (3.7a)$$

$$= \rho^* Q g\{h_0(1+\frac{F^2}{2}) - \gamma_2 h_0(1+\frac{F^2}{3\gamma_2})-d\}. \qquad (3.7b)$$

Thus, if the far upstream waveheight h_0 and Froude number F^2 are known, and if we know that the far downstream flow indeed approaches a uniform flow, then the far downstream waveheight must be equal to either $\gamma_1 h_0$ or $\gamma_2 h_0$ and the value of Φ (as a measure of energy dissipation) can be determined from either (3.7a) or (3.7b).

For a downstream flow which approaches a uniform flow with far downstream height equal to $\gamma_1 h_0$, the value of the constant S_2 can be calculated from (3.2) by setting $h_x = 0$ and $h = \gamma_1 h_0$. We denote this value of S_2 by S_2^+. By elimination of h_x^2 between (3.1a) and (3.2a) we have (Naghdi & Vongsarnpigoon 1986a):

$$h_{xx} + \frac{1}{2}\frac{d\bar{q}}{dh} = 0 \quad . \qquad (3.8)$$

Hence, if the flow approaches a uniform flow of height $\gamma_1 h_0$ far downstream, it follows from (3.2) and (3.8) that $\gamma_1 h_0$ must be a double root of the function $\bar{q}(h)$ in (3.2b) with $S_2 = S_2^+$, i.e., we can factorize $\bar{q}(h)$ in the form

$$\bar{q}(h) = \frac{3}{F^2 h_0^3}(h-\gamma_1 h_0)^2(h-\frac{F^2 h_0}{\gamma_1^2}) \quad . \qquad (3.9)$$

Similarly, let S_2^- be the value of S_2 calculated from (3.2) for the flow which approaches a uniform flow of height $\gamma_2 h_0$ far downstream. By a similar reasoning, with the help of (3.2) and (3.8), we may conclude that $\gamma_2 h_0$ must be double root of the function $\bar{q}(h)$ in (3.2b) with $S_2 = S_2^-$ so that we can factorize $\bar{q}(h)$ in the form

$$\bar{q}(h) = \frac{3}{F^2 h_0^3}(h-\gamma_2 h_0)^2(h-\frac{F^2 h_0}{\gamma_2^2}) \quad . \qquad (3.10)$$

We discuss now the nature of the cubic function $\bar{q}(h)$. First we observe that the

coefficient of the cubic term is positive and that $\bar{q}(h)$ has a double root when the graph of $\bar{q}(h)$ plotted against h becomes tangential to the h-axis. Thus, when $\bar{q}(h)$ has a double root at $\gamma_1 h_0$, this double root is also the largest root and the function $\bar{q}(h)$ increases and is always positive for $h > \gamma_1 h_0$. Furthermore, since $\bar{q}(h)$ is tangential to the h-axis at $\gamma_1 h_0$, we conclude that $\bar{q}(h)$ is nonnegative for h greater than $F^2 h_0/\gamma_1^2$, which is the other root of the function $\bar{q}(h)$. It then follows that for $S_2 = S_2^+$ the only possible solution of (3.2a) is given by

$$h = \gamma_1 h_0 = \text{const. everywhere } (x>0). \quad (3.11)$$

On the other hand, with $S_2 = S_2^-$ and $\bar{q}(h)$ given by (3.10), the remaining root

$$F^2 h_0/\gamma_2^2 = \gamma^* h_0 \text{ (say)}$$

is greater than $\gamma_2 h_0$ i.e., $\gamma_2 h_0 < \gamma^* h_0$, and the function $\bar{q}(h)$ is negative for $\gamma_2 h_0 < h < \gamma^* h_0$. Hence, in addition to the trivial solution $h = \gamma_2 h_0$, two other possible solutions of (3.2) when $h_x \neq 0$ everywhere are (see, e.g., Naghdi & Vongsarnpigoon 1986a):

$$h = \gamma_2 h_0 + \gamma_2 h_0 \left(\frac{F^2}{\tau_2^3} - 1\right) \operatorname{sech}^2 \left\{\left[\frac{3(F^2-\gamma_2^3)}{4F^2}\right]^{1/2} \left(\frac{x}{\gamma_2 h_0} + a_1\right)\right\}, \quad (3.12a)$$

$$h = \gamma_2 h_0 + \gamma_2 h_0 \left(\frac{F^2}{\tau_2^3} - 1\right) \operatorname{csch}^2 \left\{\left[\frac{3(F^2-\gamma_2^3)}{4F^2}\right]^{1/2} \left(\frac{x}{\gamma_2 h_0} + a_2\right)\right\}, \quad (3.12b)$$

where a_1 and a_2 are constants of integration.

Clearly, for a value of S_2 such that

$$S_2^- < S_2 < S_2^+ , \quad (3.13)$$

the function $\bar{q}(h)$ has three positive real roots $h_1 > h_2 > h_3$, with possible ranges

$$\frac{F^2 h_0}{\gamma_1^2} < h_3 < \gamma_2 h_0 < h_2 < \gamma_1 h_0 < h_1 < \frac{F^2 h_0}{\gamma_2^2} . \quad (3.14)$$

Since $\bar{q}(h)$ has three positive roots, (3.2a) can be written as

$$h_x^2 + \frac{3}{F^2 h_0^3}(h-h_1)(h-h_2)(h-h_3) = 0 \quad (3.15)$$

and has a cnoidal wave solution (see Abramowitz & Stegun 1965, p. 597) in the form

$$h = h_2 + (h_1-h_2)\,\mathrm{cn}^2\left\{\frac{1}{2}(h_1-h_3)^{1/2}\left(\frac{3}{F^2 h_0^3}\right)^{1/2} (x-a_3)\right\} , \quad (3.16)$$

where a_3 is the value of x when $h = h_1$ and cn is the Jacobian elliptic function with modulus $m = (h_1 - h_2) / (h_1 - h_3)$.

For a value of the constant S_2 such that $S_2 > S_2^+$ or $S_2 < S_2^-$, the function $\bar{q}(h)$ has only one positive root which is not a double or triple root, then it can be shown by a standard argument that h must vanish at some point in the region $x > 0$ and a steady solution is not possible. It should be noted here that if, instead of the condition (3.5), we assume

$$d + \Phi/\rho^* g Q > D , \quad (3.17)$$

where D is given by (3.6), then it can be shown that the function $\bar{q}(h)$ in (3.2b) has only one real positive root which is not a double or triple root regardless of the value of S_2, and hence, a steady solution is not possible.

From the preceding discussion, we have shown that similarly to the result in Naghdi & Vongsarnpigoon (1986a, Sec. 4), a steady flow in the region over the step is possible if and

only if the constant S_2 is bounded from above and below, i.e.,

$$S_2^- < S_2 < S_2^+$$

with

$$\begin{Bmatrix} S_2^+ \\ S_2^- \end{Bmatrix} = \frac{1}{2} gh_o F^2 \begin{Bmatrix} [2/\gamma_1 + \gamma_1^2/F^2] \\ [2/\gamma_2 + \gamma_2^2/F^2] \end{Bmatrix} ,$$

provided that (3.5) is satisfied. Thus, the downstream flow from the step is completely determined once the value of the constant S_2 is known.

In order to obtain a complete solution for a steady flow over a step, we need to make use of the jump conditions to match the upstream and downstream flows at x=0 in Fig. 1. The relevant jump conditions are those given in (A4a-c) and (A5). Before proceeding further, we recall that Green and Naghdi (1976) have discussed a steady flow over a fluid bed which changes from one constant level to another such that the difference in the two levels is small. They have also discussed the problem of hydraulic jump at a finite step but with conditions equivalent to setting the right-hand sides of (A4a-c) and (A5) equal to zero (see Eqs. (8.2)-(8.6) of Green & Naghdi 1976). Further Green & Naghdi (1977) reexamined the problem of hydraulic jump at a step in the context of a nonhomogeneous incompresible fluid with conditions equivalent to setting the right-hand sides of (A4b,c) and (A5) equal to zero while retaining a nonzero F_1 which arises from the right-hand side[1] (A4a). In the present paper, we are mainly interested in a steady flow with no discontinuity in the free surface waveheight and postpone any additional comment for the case in which the free surface is allowed to be discontinuous at the step (x = 0).

Since the free surface waveheight is assumed to be continuous everywhere, the waveheight immediately to the right of the step is

$$h^+ = h_o - d \quad , \qquad (3.18)$$

where in line with (A2) of the Appendix the notation h^+ stands for $h = h\Big|_{x=0^+}$. Furthermore, since H_x is equal to zero on both sides of the step, with the help of (2.8), it follows from (A12) that

$$h_x^+ = 0 \quad . \qquad (3.19)$$

Thus, the slope of the free surface waveheight is also continuous over the step so that in the present development the slope at $x = 0^+$ of the top surface of the fluid sheet is level. A similar conclusion in regard to the slope of the top free surface immediately to the right of the step was reached by Tuck (1977) who, with the use of a linearized shallow water theory and on the basis of stretched coordinate in the "inner region," argued that the top free surface over the step can be replaced by a rigid level surface. While Tuck's (1977) conclusion appears to be similar to (3.18) and (3.19), it should be noted that the two are derived from entirely different bases. It should also be noted that if the bottom surface to the right of the step is not level, i.e., if $H_x^+ \neq 0$, then (3.19) will not be valid and the top surface will not be level above the step.

With the help of (3.18) and (3.19), the relationship (A7) between Φ and F_1 becomes

$$\frac{\Phi}{Q} + \frac{F_1}{h_o - d} = \frac{1}{2}\rho^* gh_o^2 \left[\frac{1}{h_o} - \frac{1}{(h_o-d)}\right] + \frac{1}{2}\rho^* Q^2 \left\{\frac{-2}{(h_o-d)}\left[\frac{1}{h_o} - \frac{1}{(h_o-d)}\right] + \frac{1}{h_o^2} - \frac{1}{(h_o-d)^2}\right\} - \frac{1}{2}\rho^* gd \quad , \qquad (3.20)$$

[1] The notation F_1 of the present paper corresponds to X in Eq. (67) of Green & Naghdi (1977).

where use has been made of the expression for the pressure p in the upstream region. For given upstream conditions $\{h_o, F^2\}$ and given step height d, if Φ is known, e.g., by a prescribed constitutive equation, the quantity F_1 can be determined from(3.20), and vice versa. It is worth noting here that because of (3.19), $F_3 = L_3 = 0$ [see (A4b,c)] and the resultant force at the step has only a horizontal component, i.e., $\underset{\sim}{F} = F_1 \underset{\sim}{e}_1$.

Recall that if the far downstream flow approaches a uniform flow, the far downstream waveheight is equal to either $\gamma_1 h_o$ or $\gamma_2 h_o$ which are the two positive roots of the function $\bar{f}(h)$ in (3.1b). In general, it is unlikely that the value of h^+ in (3.18) would be equal to either $\gamma_1 h_o$ or $\gamma_2 h_o$, and hence a downstream (x>0) uniform flow with $h = h_o - d$ is also unlikely. However, the values of h^+ and h_x^+ in (3.18) and (3.19), respectively, can be used as the boundary conditions for the integration of (3.1) in region $x > 0$ once Φ is known. Alternatively, since the flow in the region past the step is known once the value of the constant S_2 is known, with the use of (3.18) and (3.19) we can calculate the value of S_2 from (3.2a,b) at $x = 0^+$. Equivalently, with Φ known, the value of F_1 can be calculated from (3.20) and the value of S_2 determined from (A15). The value of S_2 can then be compared with the values S_2^+ and S_2^- discussed earlier and the downstream flow is then determined. To elaborate further, we recall that it is unlikely for the downstream flow to be uniform, i.e., $h = \gamma_1 h_o$ everywhere, and, thus, it is unlikely that S_2 will be equal to S_2^+. For the value $S_2^- < S_2 < S_2^+$, the downstream flow is cnoidal waves of the form (3.16). It should be noted that since $h_x = 0$ at $h = h_o - d$ by (3.17) and (3.18), the value $(h_o - d)$ is one root of the function $\bar{q}(h)$ in (3.2b); and, in fact, represents its largest root. The two other roots of $\bar{q}(h)$ can easily be determined and the next largest root of $\bar{q}(h)$ represents the minimum waveheight. Finally, if S_2 is equal to S_2^-, the downstream flow in region II has the form of a solitary wave given by[2] (3.12a). In this case, the remaining root of $\bar{q}(h)$ in (3.2b) is a double root at $h = \gamma_2 h_o$ and it follows that for particular values of the upstream conditions $\{h_o, F^2\}$ as well as the step height d and Φ, the value of $F^2 h_o / \gamma_2^2$ in (3.10) is equal to $(h_o - d)$ or equivalently

$$\gamma_2^2 = \frac{F^2 h_o}{(h_o - d)} \quad . \tag{3.21}$$

We conclude this section with a brief discussion for the case of steady flow with discontinuous top surface. If we assume that (A8) is valid, then (A12) follows and we again have (3.19). If $h^+ [\neq (h_o - d)]$ is known, then a discussion parallel to that following (3.18) holds also in this case. On the other hand, if h^+ is not known and is to be determined as part of the solution for a given d, then the knowledge of Φ but not F_1 is insufficient to obtain a complete solution and additional information is needed. However, the complete solution can be obtained if both F_1 and Φ are known. For example, in the discussion of hydraulic jump over a step (Green & Naghdi 1976, Sec. 8) both F_1 and Φ are taken to be zero and h^+ is determined as part of the solution of the problem.

4. AN EXAMPLE

In the rest of this paper, we consider an example and provide some calculations both in the presence, and absence, of energy loss at the step. For definiteness, we suppose that the energy loss at the step is proportional to the upstream value[3] R_1 of the constant R, i.e.,

---

[2]The solution of the form (3.12b) can be ruled out since $(h_o - d)$ is larger than $\gamma_2 h_o$.

[3]Recall that the quotient R_1/g represents the total head of the upstream flow.

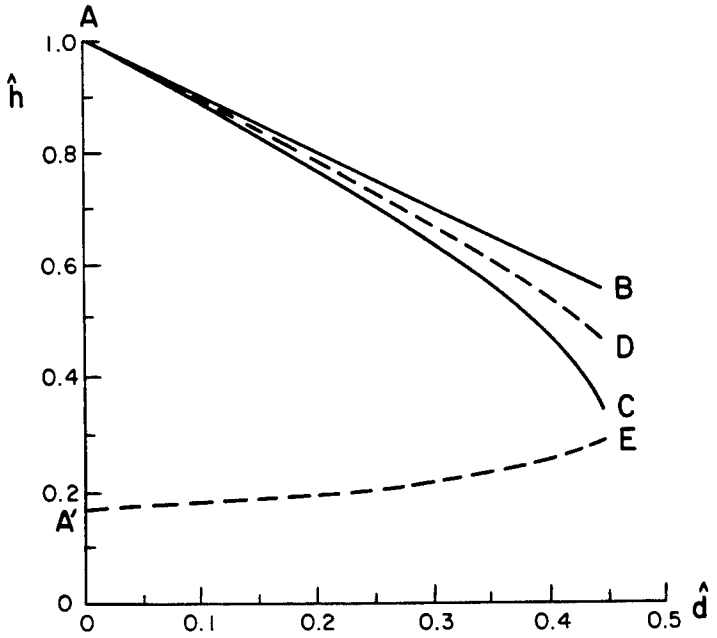


Fig. 2(a): Representative plots of the maximum (curve AB) and minimum (curve AC) fluid heights of the resulting cnoidal waves in the downstream region as functions of the normalized step height $\hat{d}$ for a given upstream Froude number (The curves shown in the figure are for F^2 = 0.05) and without loss at the step. Also shown for comparison purposes are the dashed lines (---) representing the hypothetical far downstream fluid heights for flows which would approach a uniform flow far downstream for the given upstream conditions: For the higher value (curve AD), the downstream flow would be a uniform flow of constant height everywhere; for the lower value (curve A'E), the downstream flow would approach a supercritical uniform flow far downstream. Curve AC approaches A'E at a value of $\hat{d}$ representing a maximum step height d^* beyond which no steady flow is possible.

$$\frac{\Phi}{\rho^* Q} = \kappa\, R_1 = \kappa g h_0 \left(\frac{F^2}{2} + 1\right), \qquad (4.1)$$

where the coefficient κ must in general be specified by a constitutive equation. However, for our present purpose we restrict our attention to the case in which κ = constant. In the absence of energy loss, both κ and Φ vanish and the relation (4.1) is identically satisfied.

In order to indicate some of the features of the solution, the maximum and minimum heights of the resulting cnoidal wave in region II are calculated as functions of the step height d. These calculations are carried out in terms of normalized variables, defined by

$$\hat{h} = \frac{h}{h_0}\ , \quad \hat{d} = \frac{d}{h_0}\ , \quad \hat{x} = \frac{x}{h_0}\ , \qquad (4.2)$$

and for a specified value of F^2. The results of such calculations are shown in Figs. 2(a) and 2(b) with F^2 = 0.05, but corresponding results for other admissible values of F^2 exhibit similar characteristics.

The results of the calculations in the case of no energy loss (κ = 0) are shown in Fig. 2(a). The maximum normalized height of the cnoidal wave in Fig. 2(a) is given by the

straight line $\hat{h} = (1-\hat{d})$. Also, as might be expected, for small values of $\hat{d}$ the maximum and minimum heights of the cnoidal wave solution are close to one another. As $\hat{d}$ increases, the value of S_2 decreases and leads to a larger difference between the roots h_1 and h_2 of $\overline{q}(h)$ in (3.2b). Consequently, the amplitude of the cnoidal waves increases as $\hat{d}$ increases. Also shown in Fig. 2(a) are the dashed line curves $\hat{h} = \gamma_1$ and $\hat{h} = \gamma_2$ which represent the nondimensionalized fluid heights for flows which would approach uniform flow far downstream. As S_2 approaches the values S_2^-, the minimum waveheight of the cnoidal wave solution approaches the value γ_2. Clearly when the value $\hat{d} = d^*$ at which $S_2 = S_2^-$, the flow in region II has the form of a solitary wave (3.12a) and this represents the maximum possible step height for the given upstream Froude number. This is because for $\hat{d} > d^*$, the constant S_2 would become smaller than S_2^-; and, as mentioned earlier, no steady flow is possible. [In carrying out the actual numerical calculation, it was difficult to obtain a precise value of d^* since S_2 approaches S_2^- rapidly for $\hat{d}$ close to d^*. Thus, a small increase in the value of $\hat{d}$ may render S_2 smaller than S_2^- implying that d^* has been exceeded.]

Results similar to those in Fig. 2(a) but in the presence of energy loss ($\Phi \neq 0$) are plotted in Fig. 2(b), again for the same far upstream Froude number ($F^2 = 0.05$) but with

$$\kappa = 0.1 \ , \qquad (4.3)$$

which corresponds to $\Phi/\rho^* Q$ being 10% of the upstream R_1. The curves A_1B and A_3C in Fig. 2(b) represent the maximum and minimum normalized waveheights of the cnoidal waves. Also shown in Fig. 2(b) are the (dashed line) curves $A_2D(\hat{h} = \gamma_1)$ and $A_4E(\hat{h} = \gamma_2)$ which represent the nondimensionalized heights for flows which would approach uniform flow far downstream.

A direct comparison between Fig. 2(a) and Fig. 2(b) clearly shows that the amlitude of the cnoidal waves for the same value of step height $\hat{d}$ is larger for the case in which $\Phi \neq 0$ than when $\Phi = 0$. In addition, the maximum height d^* of the step is reached earlier for $\Phi \neq 0$ than for $\Phi = 0$.

As noted following (4.2), for a given upstream Froude number, there exists a maximum step height $\hat{d} = d^*$ beyond which no steady flow is possible so that all possible combinations of (F^2, d^*) represent a curve above which no steady flow is possible. The location of the curve depends, however, on the value of the energy loss Φ at the step, i.e., on the value of κ in (4.1). In this connection two curves are shown in the plot of F^2 versus d^* in Fig. 3: one curve (dashed line) with the value of $\Phi = 0$ (or $\kappa = 0$) and the other (solid line) for $\Phi \neq 0$ ($\kappa = 0.1$). Clearly, for the same upstream Froude number, the maximum step height for the flow without energy loss ($\Phi = 0$) is larger than that in the presence of energy loss ($\Phi \neq 0$). However, since the calculations for these curves are carried out in terms of the nondimensionalized quantity $\hat{d} = d/h_0$, where h_0 is the far upstream waveheight, for a fixed step height $d = d_1$ (say), the curves in Fig. 3 also give information on the minimum upstream waveheight h_0^* below which no steady flow is possible. This is because d_1/h_0^* must be equal to d^* for a given Froude number.

ACKNOWLEDGEMENT

The results reported here were obtained in the course of research supported by the U.S. Office of Naval Research under Contract N00014-86-K-0057, Work Unit 4322 534 with the University of California, Berkeley.

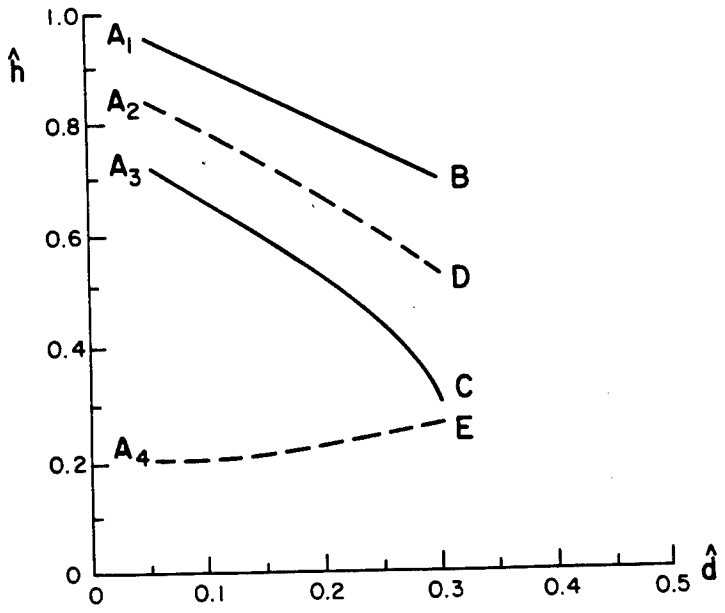


Fig. 2(b): Representative plots of maximum (curve A_1B) and minimum (curve A_3C) fluid heights of the resulting cnoidal waves in the downstream region as functions of the normalized step height $\hat{d}$ for a given upstream Froude number (the curves shown in the figure are for $F^2 = 0.05$) and with energy loss at the step (in this case 10%). Also shown for purposes of comparison are the dashed lines (--) representing the hypothetical far downstream fluid heights for flows which would approach a uniform flow far downstream for the given upstream conditions: For the higher value (curve A_2D), the downstream flow would be a uniform flwo far downstream. Curve A_3C) approaches A_4E at a value of $\hat{d}$ representing a maximum normalized step height d^* beyond which no steady flow is possible. Note that the maximum step height here is smaller than that in Fig. 2(a).

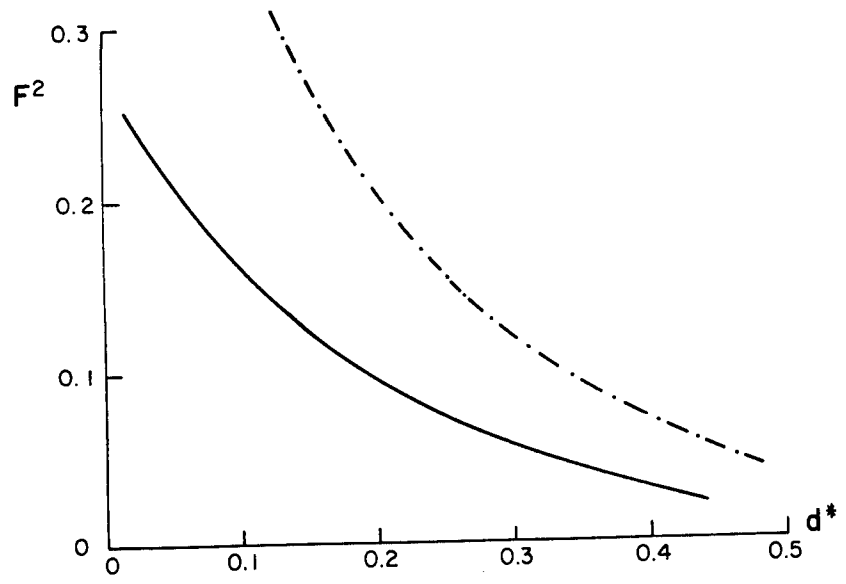


Fig. 3: Plots of the upstream F^2 versus the maximum normalized step height d^* beyond which no steady flow is possible in the presence of (10%) energy loss (——) and without energy loss (—·—). The plots represent the combination of upstream Froude numbers and step height such that the downstream flow approaches a supercritical flow far downstream.

REFERENCES

Abramowitz, M. & Stegun, I. A. (editors) 1965 Handbook of Mathematical Functions with Formulas, Graphs and Mathematics Tables, Dover Publications.

Green, A. E. & Naghdi, P. M. 1976 Directed fluid sheets. Proc. R. Soc. Lond. A 347, 447-473.

Green, A. E. & Naghdi, P. M. 1977 Water waves in a nonhomogeneous incompressible fluid. J. Applied Mech. 44, 523-528.

Lamb, H. 1932 Hydrodynamics, 6th ed. Cambridge University Press.

Naghdi, P. M. & Rubin, M. B. 1981 On the transition to planing of a boat. J. Fluid Mech. 103, 345-374.

Naghdi, P. M. & Rubin, M. B. 1986 The effects of energy dissipation and changes in propulsion angle on the transition to planing of a boat (in manuscript form).

Naghdi, P. M., & Vongsarnpigoon, L. 1986a The downstream flow beyond an obstacle. J. Fluid Mech. 162, 223-236.

Naghdi, P. M. & Vongsarnpigoon, L. 1986b On steady flow past a sluice gate. Phys. Fluids, to appear.

Tuck, E. O. 1977 Some classical water-wave problems in varying depth. In Symposium on Waves in Water of Varying Depth (eds. Provis. D. G. & Radok, J.R.M.), Lecture Notes in Physics, Vol. 64, Springer-Verlag, pp. 9-20.

APPENDIX

The purpose of this appendix is to recall the basic jump conditions associated with the restricted theory of a directed fluid sheet and derive certain results utilized in the main text. For our present purpose, it will suffice to let the singular curve (or the curve of discontinuity) be a stationary curve on the reference surface of a directed fluid sheet and identify its fixed location by the line $x = x_0$. The relevant jump conditions across $x = x_0$ are then given by (see Naghdi & Rubin 1981, 1986)[4]

$$[\![\rho^* hu]\!] = 0 \quad , \quad [\![\rho^* hu^2+p]\!] = F_1 \quad , \qquad \text{(A1a,b)}$$

$$[\![\rho^* hu\,\lambda]\!] = F_3 \quad , \quad [\![\tfrac{1}{12}\rho^* huw]\!] = L_3 , \qquad \text{(A1c,d)}$$

$$[\![\tfrac{1}{2}\rho^* hu(2\varepsilon+u^2+\lambda^2+\tfrac{1}{12}w^2+2g\psi) + pu + a^{1/2}q^1]\!] = -\Phi \quad , \qquad \text{(A1e)}$$

where the notation f is defined by

$$[\![f]\!] = f^+ - f^- \quad , \quad f^+ = f|_{x=x_0^+} \quad ,$$

$$f^- = f|_{x=x_0^-} \quad , \qquad \text{(A2)}$$

ε is the internal energy per unit mass and $a^{1/2}q^1$ represents the component of the heat flux vector per unit length along $\underset{\sim}{e}_1$. Also, $\lambda = \dot{\psi}$, where $\psi = H + 1/2h$ with H represen- the vertical position of the bottom bed. The quantities F_1, F_3, L_3 and Φ serve to balance, respectively, the jump in the horizontal component of linear momentum, the vertical component of the linear momentum, the vertical component of director momentum and energy. In addition, the quantity Φ can be used to represent the effect of dissipative mechanisms, e.g., viscosity, which do not explicitly occur in the equations for an inviscid fluid sheet.

In general, F_1, F_3, L_3 and Φ require constitutive equations. On the other hand, by utilizing the identification of the assigned force and moment with quantities from the three-dimensional theory, the quantitites F_1, F_3 and L_3 can be identified with (see Naghdi & Rubin 1981, Appendix)

$$F_1 = \lim_{\delta\to 0}\int_{x_0-\delta}^{x_0+\delta} (\hat{p}\beta_x - \bar{p}H_x)dx \quad , \qquad \text{(A3a)}$$

$$F_3 = \lim_{\delta\to 0}\int_{x_0-\delta}^{x_0+\delta} (\bar{p}-\hat{p})dx \quad , \qquad \text{(A3b)}$$

$$L_3 = \lim_{\delta\to 0}\int_{x_0-\delta}^{x_0+\delta} [-\tfrac{1}{2}(\bar{p}+\hat{p})]dx \quad . \qquad \text{(A3c)}$$

Consider now a steady motion on either side of the line discontinuity. Since $\rho^* =$ constant, it follows from (A1a) that the constant $Q = hu$ resulting from the continuity equation does not change across $x = x_0$. Next, the jump conditions (A1b-d) become

$$[\![\rho^* Q^2 \tfrac{1}{h} + p]\!] = F_1 \qquad \text{(A4a)}$$

$$[\![\rho^* Q^2(\tfrac{H_x}{h} + \tfrac{1}{2}\tfrac{h_x}{h})]\!] = F_3 \quad , \qquad \text{(A4b)}$$

$$[\![\tfrac{1}{12}\rho^* Q^2(\tfrac{h_x}{h})]\!] = L_3 \quad . \qquad \text{(A4c)}$$

Further, assuming that there is no discontinuity in ε and q^1, (A1e) reduces to

$$[\![\tfrac{1}{2}\rho^* hu(u^2+\lambda^2+\tfrac{1}{12}w^2+2g\psi)+pu]\!] = -\Phi. \qquad \text{(A5)}$$

With the use of the basic equations of motion, it can be shown that for a steady flow (A5) can be written in the form

[4] The quantities h and Φ in (A1a-e) correspond, respectively, to ϕ for the wave height and to $-\Phi$ in the Appendix of Naghdi & Rubin (1986). The latter quantity has a different meaning than $-\Phi$ on the right-hand side of (A4) in the Appendix of Naghdi & Rubin (1981).

$$[\![\rho^* RQ]\!] = -\Phi \quad , \tag{A6}$$

i.e., Φ determines the change in the constant R across the singular curve. For a nonzero Φ, it follows from (A4a) after the elimination of p^+ that Φ and F_1 must be related by

$$\frac{\Phi}{Q} + \frac{F_1}{h^+} = p^-\left(\frac{1}{h^-} - \frac{1}{h^+}\right) + \frac{1}{2}\rho^* Q^2$$

$$\left\{-\frac{2}{h^+}\left(\frac{1}{h^-} - \frac{1}{h^+}\right) + \left(\frac{1}{h^-}\right)^2 - \left(\frac{1}{h^+}\right)^2 + \left(\frac{H_x^-}{h^-}\right)^2\right.$$

$$\left. - \left(\frac{H_x^+}{h^+}\right)^2 + \frac{H_x^- h_x^-}{(h^-)^2} - \frac{H_x^+ h_x^+}{(h^+)^2} + \frac{1}{3}\left(\frac{h_x^-}{h^-}\right)^2 - \frac{1}{3}\left(\frac{h_x^+}{h^+}\right)^2\right\}$$

$$+\rho^* g\left(H^- - H^+ + \frac{1}{2}h^- - \frac{1}{2}h^+\right). \tag{A7}$$

For a flow with a free top surface and $\hat{p}$ identified with the constant atmospheric pressure p_o, we consider a special case in which the top surface is assumed to be continuous, i.e., there is no jump in the top surface. Since $\hat{p} = p_o$ is finite, it follows immediately that[5]

$$\lim_{\delta \to 0} \int_{x_o-\delta}^{x_o+\delta} \hat{p}\,dx = 0 \quad . \tag{A8}$$

Making use of (A8) in the right-hand sides of (A3b,c) we obtain

$$F_3 = \lim_{\delta \to 0} \int_{x_o-\delta}^{x_o+\delta} \overline{p}\,dx \quad , \tag{A9a}$$

$$L_3 = \lim_{\delta \to 0} \int_{x_o-\delta}^{x_o+\delta} \left(-\frac{1}{2}\overline{p}\right)dx. \tag{A9b}$$

[5]The conclusion (A8) may not be valid if the top surface is allowed to be discontinuous or if $\hat{p}$ is not bounded everywhere.

Comparison of the right-hand sides of (A9a,b) yields

$$F_3 = -2L_3 \quad , \tag{A10}$$

and it follows from (A4b,c) and (A10) that

$$[\![\rho^* Q^2\left(\frac{H_x}{h} + \frac{1}{2}\frac{h_x}{h}\right)]\!] = -2[\![\frac{1}{12}\rho^* Q^2\left(\frac{h_x}{h}\right)]\!]. \tag{A11}$$

Since Q is unchanged across the line of discontinuity, (A11) can be rewritten in the form

$$[\![\frac{h_x}{h}]\!] = -\frac{3}{2}[\![\frac{H_x}{h}]\!] \quad , \tag{A12}$$

which gives the magnitude of the jump in the slope of the fluid height in terms of the jump in the slope of the bottom surface of the fluid sheet.

For the case in which the top surface of the fluid sheet is discontinuous, the result (A12) will remain valid if we assume that $\hat{p}$ in (A8) is bounded everywhere including the point of discontinuity.

Recalling the expression for the pressure p for the flow over a level bottom, i.e., H = constant which is not necessarily zero, we have

$$p + \rho^* \frac{Q^2}{h} = -\rho^* \frac{Q^2}{6}\left\{\frac{h_x^2}{h} - \frac{3}{h} + \frac{3h^2}{F^2 h_o^3} - \frac{6h}{F^2 h_o^3}\left(\frac{R}{g} - H\right)\right\}. \tag{A13}$$

Since the flow on either side of x = 0 is characterized by a differential equation of the same form as (2.5a,b), it follows from (A13) and (2.5a,b) that

$$p + \rho^* \frac{Q^2}{h} = \rho^* S \quad . \tag{A14}$$

But in view of the jump (A4a), we conclude that the change in the value of the constant S across the line of discontinuity is

$$[\![S]\!] = \frac{1}{\rho^*} F_1 \quad . \tag{A15}$$

We recall that the value of the constant $S = S_2$ in the downstream region can be determined from (3.2a,b) once the waveheight and its slope are known at one point, e.g., at the point $x = 0^+$ immediately to the right of the step. It can be easily shown that the value of F_1 calculated from (A15) is identical to that calculated from (A7) if Φ known, i.e., (A15) is not a separate condition independent from (A7).

DISCUSSION

Garrett Birkhoff,
Harvard University

In general, steady plane flows of a liquid in a uniform gravity field, bounded by free streamlines and polygonal fixed boundaries, can be determined by solving numerically an integral equation of a type discovered by Villat. The case of a symmetric jet from a slot was worked out by Kenneth Wilson, and the flow under a vertical sluice gate was computed by Carl de Boor. Brief descriptions of the method may be found in [a] and [b] below.

[a] G. Birkhoff and E. H. Zarantonello, "Jets, Wakes, and Cavities", Chap. VIII, 10, 11.

[b] G. Birkhoff, "Calculation of potential flows with free streamlines", Paper #2977 (J. Hydraulics Div.), Proc. Am. Soc. Civ. Eng. pp. 17-21 (Nov., 1961).

Reply -

We thank Professor Birkhoff for his comments and for providing the above references.

The integral equation due to Villat (see Eq. (15) of Ref. [a]) appears to be a numerical procedure and should not be regarded similar to a theory such as the theory of a directed fluid sheet (with a single constrained director) which has its own conservation laws and its own jump conditions.

As remarked in a number of previous papers (see, for example, Ref. [c] below), the theory of directed fluid sheets (with K directors) is based on a three-dimensional model called a Cosserat (or directed) surface. This model is not just a two-dimensional surface alone but is, in fact, endowed with some structure in the form of additional kinematical vector fields called directors. The theory of directed fluid sheets is constructed directly by postulates similar to those used in obtaining the basic equations of the three-dimensional theory.

Although it is an interesting question, the justification for construction of direct theories is not in regarding them as approximations to the three-dimensional theory, but rather in their use an independent theories to predict some of the main features and properties of (three-dimensional) fluid flow problems in hydrodynamics, including those arising in water wave theory. Of course, in the special case of the direct theory for which only a single director is utilized (as in the paper in this proceedings), one would expect the theory to be valid only for depths which are small in the sense that the velocity field (of the three-dimensional theory) can be reasonably approximated by a linear dependence on the depth coordinate; in this connection, see also Part C of Ref. [d].

The predictive capabilities of the direct approach during the past ten years have been examined with the use of the simplest direct theory for inviscid incompressible sheet-like fluid flow problems (see, for example, some of the references cited in the paper). However, the basic capabilities of the direct approach is not limited to only this class of problems and has been explored in connection with viscous fluid flow problems in [c] and in connection with finite amplitude waves over waters of finite and infinite depths [d]. With references to the last remark by Professor Birkhoff, it is perhaps also of interest to note a recent paper by the present authors [e] concerning the steady flow under a sluice gate with the use of the theory of a directed fluid sheet (with a single constrained director) for an incompressible inviscid fluid. This latter paper contains a theoretical explanation for the determination fo the contraction ratio, along with detailed comparison with experimental results of Benjamin [f].

[c] A. E. Green and P. M. Naghdi, "A direct theory of viscous fluid flow in channels," Arch. Rational Mech. Anal., '86, 39-63 (1984).

[d] A. E. Green and P. M. Naghdi, "A nonlinear theory of water waves for finite and infinite depths, Phil. Trans. Royal Soc., London, Ser. A, 320, 37-70 (1986).

[e] P. M. Naghdi and L. Vongsarnpigoon, "Steady flow past a sluice gate," Phys. Fluids, 29, 3962-3970 (1986).

[f] T. B. Benjamin, "On the flow in channels when rigid obstacles are placed in the stream," J. Fluid Mech., 1, 227-248 (1956).

Some Soliton Calculations

R. C. ERTEKIN, University of Hawaii, and
J. V. WEHAUSEN, University of California, Berkeley, U.S.A.

Abstract

Several soliton calculations often studied by means of the Korteweg-de Vries and related equations have been repeated using the equations of A. E. Green and P. M. Naghdi. For small amplitudes and disturbances the results are similar to those based on these other equations, as is to be expected. For larger amplitudes and disturbances differences are discussed in the paper.

Introduction

In order to explain certain phenomena observed in the towing tank, we have been making calculations with the Green-Naghdi shallow-water equations since 1983 (Ertekin, 1984; Ertekin et al., 1984, 1986). These calculations seemed to explain fairly well, certainly qualitatively, the observed phenomena. However, others, using different equations, also were able to show calculations agreeing qualitatively with the observations (Wu & Wu, 1982;Akylas, 1984; Cole, 1985; Lee, 1985). Since there have been only few numerical studies based upon the Green-Naghdi (hereafter G-N) equations and since there is a considerable literature devoted to exploring numerically the consequences of the other equations, especially the Korteweg-de Vries (hereafter KdV) equation, it seemed timely to make a similar investigation for the G-N equations. There is a particular interest in doing this because of the difference in the derivation of the G-N equations from that of the other, Boussinesq-like equations, and especially the KdV equation. This difference will be discussed presently. In addition, there is a rich literature in which the applicability of inverse-scattering theory to the KdV equation is exploited, yielding asymptotic results of physical significance. It is of interest to know to what extent these results carry over to the G-N equations, even if the investigation is only numerical.

In order to explore such questions we have selected a set of numerical experiments, ones that also lend themselves to physical experimentation, as test cases for the G-N equations. Each of the configurations has been studied by means of other equations, sometimes extensively. The configurations are all two-dimensional, and all are initial-value problems. They are as follows. (1) A soliton passing over a bump on the bottom. (2) A soliton approaching a shelf with a smooth transition between the two depths. (3) Collision of solitons. (4) Reflection of solitons from a wall. (5) Overtaking of one soliton by another. (6) Disturbance produced by an initial hump of water. For the first four we have varied physical parameters over a range that covers most practical situations. Since the last two were rather costly in computer time, only one case was computed for each.

It has been mentioned above that the derivation of the G-N equations is quite different from that of the other equations used for shallow-water problems. The most noticeable difference is the lack of any perturbation parameter in the derivation. There is no indication that the equations provide more accurate solutions, the smaller some parameter becomes. For most fluid dynamicists a familiar approximation method close to the "direct

method" of Green and Naghdi is the integral method in boundary-layer theory. In the latter one assumes a functional form (usually a polynomial) for the dependence of the velocity along the surface upon the distance perpendicular to the surface. Boundary conditions at the surface and at the edge of the boundary layer determine some of the coefficients in the functional form; the rest are determined by using the momentum integral and higher moments if necessary. There is no parameter associated with this approximation, but a tacit assumption (and the possibility of a theorem) that the approximation will be better, the more complex the assumed functional form. Levich & Krylov(1969, esp. pp. 312-313) describe a shallow-water theory similar to Green and Naghdi's that is explicitly based upon analogy with integral methods in boundary-layer theory. The G-N equations are given in the next section. The assumption made there concerning the functional form of the velocity corresponds to the assumed functional form in boundary-layer integral methods. Within the hierarchy of G-N equations this is the simplest; others are possible. The equations of motion are then derived by invoking conservation of mass, conservation of momentum in a depth-integrated form and conservation of moment of momentum. Boundary conditions are satisfied exactly. The pressure within the fluid cannot be determined from the equations used here, only its average over depth. A derivation of the equations has been presented at an earlier Symposium (Naghdi,1978).

The Green-Naghdi Equations

The equations are presented here only in their two-dimensional form. We use a right-handed coordinate system with Oz directed against gravity and Ox to the right. The equilibrium free surface is taken as $z = 0$, the free surface as $z = \zeta(x,t)$, and the bottom as $z = -h(x,t)$. For the problems to be treated here $h = h(x)$. We shall take h_0 as a reference depth and as the actual depth in the region on either side of a bump or before a shelf. The pressure on the free surface is denoted by $\hat{p}(x,t)$. In all our calculations it will be taken as zero. For the Green-Naghdi theory for a single restricted director it is assumed for the velocity components (u,w) that

$$u = u(x,t),\ w = w_0(x,t) + zw_1(x,t).$$

Let $D = \partial/\partial t + u\partial/\partial x$. The G-N equations for a sheet of inviscid and incompressible fluid are then the following:

$$\zeta_t + \{(\zeta + h)u\}_x = -h_t,$$

$$Du + g\zeta_x + \rho^{-1}\hat{p}_x = -(1/6)[-D^2h(2\zeta - h)_x + D^2\zeta(4\zeta + h)_x + (\zeta + h)(2D^2\zeta - D^2h)_x].$$

The three-dimensional version of these equations is given in Ertekin et al. (1986). We note that the motion described by the G-N equations is not irrotational. We shall make the equations dimensionless with the dimensionally independent set h_0, g, ρ. In the equations above one need only replace these constants by 1 in order to have the dimensionless equations. Henceforth we shall suppose that all variables are dimensionless unless otherwise stated.

As initial conditions we shall prescribe $\zeta(x,0)$, and $u(x,0)$. As an open-boundary condition, wherever this is necessary, we shall take (in dimensional variables) $\Omega_t + c\Omega_x = 0$, where Ω may be u or ζ and $c = \pm\sqrt{gh_d}$, where h_d is the depth at the place where the open-boundary condition is being applied. In dimensionless variables $c = -1$ at a left-hand boundary where $h_d = h_0$ and at a right-hand boundary, where perhaps $h_d = h_1$, $c = \sqrt{h_1/h_0}$.

In many of the calculations we shall be starting with a solitary wave. We may write this in the following form:

$$\zeta(\bar{x}) = A\,\mathrm{sech}^2[[3A/4(1+A)]^{1/2}\bar{x}],$$

where $\bar{x} = x - x_0 - Ut$, U being the velocity of the soliton and x_0 its center at time $t = 0$. We recall that for the G-N equations (and some others)

$$A = U^2 - 1 = \mathrm{Fr}^2 - 1,$$

where Fr is the Froude number, defined in

dimensional numbers by $Fr^2 = U^2/gh_0$. Hence one can also define the solitary wave in terms of the Froude number:

$$\zeta(\bar{x}) = (Fr^2 - 1)\,\mathrm{sech}^2\{[3(Fr^2 - 1)]^{1/2}\bar{x}/2Fr\}, \quad Fr > 1.$$

It can be verified that this function ζ satisfies the G-N equations when the bottom is flat and $\hat{\rho} = 0$. The expression for $u(x, 0)$ associated with ζ is determined by $u = U\zeta/(\zeta + 1)$. Strictly speaking, ζ does not satisfy the equations in the conditions in which it is used, for either the bottom is not really flat or else there are two solitons present. However, at the initial instant a soliton is sufficiently far from either any bottom variation or from another soliton so that the error is negligible.

Numerical Procedures

The calculations have been carried out by replacing the partial differential equations by second-order difference equations. The procedure is described in detail in Ertekin (1984) and summarized in Ertekin et al. (1984). For 2-dimensional problems this leads to a set of linear equations with matrix in tridiagonal form, so that the calculations are not very time-consuming.

One of the special attractions of the G-N equations as a model for a physical phenomenon is that all mechanical conservation laws are exactly satisfied in a depth-integrated formulation. The associated difference equations do not inherit this property. Computer experiments indicate that the loss of mass or energy during the time interval of a calculation is associated with the size of Δx: the smaller Δx is, the smaller the loss, as one expects. Although one must have $\Delta t < \Delta x$ for stability, decreasing Δt while holding Δx constant does not appreciably increase the accuracy. We have chosen grid sizes that keep the fluctuation in mass less than about 0.05%. For $A < 0.6$ we have taken $\Delta x = 0.12$, $\Delta t = 0.10$, but for $A \geq 0.6$ we have had to take $\Delta x = 0.06$, $\Delta t = 0.05$.

One rather surprising aspect of our calculations has been the amount of mass that is lost through the open boundaries, in particular at the left boundary as a result of a reflected wave when a soliton passes from left to right over a bump or onto a shelf of smaller depth. Even though the reflected wave may appear quite small, a substantial part of the initial excess mass associated with the initial soliton(s) may be lost through the boundary. On the other hand, if x_L and x_R are the abscissae of the fixed left and right boundaries, respectively, then the quantity

$$\int_{x_L}^{x_R} \zeta(x, t)\,dx - \int_0^t u(x_L, t)[\zeta(x_L, t) + h_L]\,dx + \int_0^t u(x_R, t)[\zeta(x_R, t) + h_R]\,dx$$

remains constant within 0.05%. In our applications $h_L = 1$ and $h_R = 1$ or h_1.

The slope leading up to the shelf presents a small dilemma. In order that it should be easy to construct, we have chosen a straight line for the slope. On the other hand, the equations involve third derivatives of the function $h(x)$, and in order to avoid dealing with jump conditions, we have smoothed the bottom with a five-point smoothing formula. Hence the slope to the shelf is somewhat different from the nominal one near the junctures with the flat regions.

All the computations were performed with single precision on a VAX 8600 computer of the University of California, Berkeley.

Results

The several numerical experiments listed in the Introduction will now be discussed separately. The calculations of the free surface ζ will be presented in a uniform fashion for each case. In the middle of each figure one finds the initial configuration approximately to scale. Stacked above it are shown snapshots of the surface at a selected sequence of dimensionless times. At the very top is shown the last snapshot with the vertical scale magnified tenfold. The bottom part of each figure shows as a function of time the readings on numerical wave gauges located at positions indicated by the triangles on the initial configuration. In the captions we shall give only the relevant parameter information. Other graphs based upon an analysis of these results vary according to the subject.

Bump on the Bottom

In order that derivatives of $h(x)$ through the third order should be continuous, we have chosen an eighth-order polynomial as the profile of the bump. Let $L=2\ell$ be the length and B the height of the bump. Then its equation is given by

$$h(x) = -h_0 + (B/L^8)[4(x^2-\ell^2)]^4, \quad -\ell<x<\ell.$$

Calculations have been made for $A = 0.3$ and 0.6 ($Fr = 1.1402,\ 1.2649$) and for $B=0.2,\ 0.4$, and 0.6. The length was kept constant at $L=10$. Qualitatively the behavior was the same in every case. After passing the bump, the soliton loses some amplitude, but remains as a single soliton followed by a train of dispersive waves of decreasing wavelength. In addition, there is a reflected train of dispersive waves, with a crest leading. Figures 1 to 4 show snapshots of ζ at various times indicated on the figures and for $B=0.2$ and 0.6. In conformity with experience with the Korteweg-deVries equation one might expect a change in phase of the soliton, that is, that its maximum would lag behind the position anticipated from the initial velocity and position. However, this anticipated behavior is complicated by the fact that the amplitude, and hence the velocity, of the soliton decreases as it passes the bump, some of its energy having gone into the generation of the reflected waves and the trailing waves. Table 1 shows the phase shift and final amplitude for the calculated values of A and B. Phase shift is clearly a function of soliton amplitude at a given instant of time. Nevertheless, we give only the final phase shift without considering the reduction in soliton amplitude. It can be seen from Table 1 that the phase shift experienced by the soliton seems to depend on the bump amplitude only and not the initial soliton amplitude.

B \ A	0.3		0.6	
	Δx	A_F	Δx	A_F
0.2	0.283	0.299	0.324	0.578
0.4	0.618	0.297	0.620	0.565
0.6	1.061	0.289	1.066	0.537

Table 1. Phase shift and final amplitude as functions of soliton and bump amplitude.

Propagation onto a Shelf

As mentioned earlier, the transition from the bottom to the shelf has been assumed plane. It extends over a length 10 so that its slope steepens as the shelf becomes shallower. With h_f as the (dimensionless) depth of the shelf, the following values were chosen for h_f: 0.2, 0.3 0.451, 0.5, 0.614, 2. The values 0.451, 0.5, 0.614 were chosen in order to allow comparison with results in papers by Madsen & Mei (1969), Johnson (1972, 1973) and Schember (1982). Two amplitudes were used: 0.12, 0.3. However, for depth 0.2 and amplitude 0.3 the computation stopped at the shelf because the amplitude became unbounded. This apparent breaking of the soliton is consistent with the analysis of Grimshaw (1971) and the experiments of Camfield & Street (1969). The qualitative behavior was similar to that predicted in Johnson's paper for his modified KdV equation: several solitons of decreasing amplitude on the shelf followed by trailing dispersive waves; there is also a reflected wave. Figures 5 to 8 show the results for $A= 0.12$ and Figures 9, 10, 11 show them for $A=0.3$.

Johnson's analysis predicts 2 and 3 solitons, respectively, for the depths 0.614 and 0.415 with no trailing dispersive waves in either case. For depth 0.5 he predicts 3 solitons on the shelf plus trailing dispersive waves. For depth 0.2 his formula (3) implies 9 solitons with the 9th being very weak, and also trailing dispersive waves. Since the derivation of Johnson's equations is based upon an assumed small disturbance, one expects better agreement with his predictions for $A=0.12$ than for $A=0.3$, and this is indeed the case. Nevertheless, they conform remarkably well even for $A=0.3$ except for the presence of the trailing dispersive waves. For A=0.12 and h_f=0.2 only 6 solitons were observed, but further ones may not have developed by the time the computation was terminated. Table 2 shows the amplitudes of the first three successive solitons on the shelf (counting from the right) together with Johnson's predicted values and also values computed by Schember using Boussinesq-like equations derived by T. Y. Wu (1981). (We note as a curiosity that the G-N values for the amplitudes agree better with

A	h_1	A_1		A_2		A_3	
0.12	0.614	0.168	0.181 0.170	0.041	0.045 0.040		
	0.5	0.184	0.207 0.203	0.066	0.079 0.071	0.013	0.012 0.014
	0.451	0.190	0.220 0.205	0.080	0.098 0.077	0.020	0.024 0.017
	0.3	0.183	0.270 -	0.130	0.173 -	0.069	0.097 -
	0.2	0.156	0.320 -	0.141	0.246 -	0.112	0.182 -
0.30	0.614	0.352	0.452	0.094	0.113		
	0.5	0.331	0.517	0.149	0.198	0.030	0.029
	0.451	0.311	0.549	0.174	0.244	0.050	0.061
	0.3	0.223	0.676	0.206	0.432	0.145	0.243
	0.2	-	0.800	-	0.615	-	0.456

Table 2. Amplitudes of successive shelf solitons. Left column: present calculations; right column, top, $A = 0.12$: Johnson (1972); right column, bottom, $A = 0.12$: Schember (1982); right column, $A = 0.3$: Johnson (1972).

Johnson's predicted values if we do not include the factor $h_1^{-1/4}$.) The computed and experimentally measured values of Madsen & Mei (1969) are not in the table. They are as follows. For $A=0.12$ and $h_1=0.5$ they give $A_1=0.2\ (0.13)$; $A_2=0.09\ (0.04)$; $A_3=0.02$ (experimental values in parentheses).

The computation for $h_1=2$ shows a behavior quite different from that observed for $h_1<1$. This is , in fact, predicted by Johnson. However, although the leading wave in the deeper region appears to be a part of a wave train, its velocity is supercritical and we assume that eventually a soliton will develop from it. It is shown in Figure 12.

Interacting Solitons

These configurations have been much studied in the literature, particularly in the case when the two solitons are of equal amplitude, corresponding to a single soliton running up against a wall. For our calculations we have chosen the following values of A: 0.1, 0.3, 0.45, 0.6. The results for colliding solitons of different amplitudes are shown in Figures 13, 14, 15 for $A = 0.1, 0.3, 0.6$

Although asymptotic results based upon the KdV equations show the solitons eventually passing through each other and regaining their initial amplitudes, we find that each loses some amplitude and is followed by trailing dispersive waves. We have determined for each pair of colliding solitons the maximum height attained during the interaction. This is shown in Table 3.

A_L \ A_R	0.1		0.3		0.45		0.6	
0.1	0.205	0.206						
0.3	0.415	0.420	0.649	0.665				
0.45	0.568	0.582	0.823	0.856	1.004	1.007		
0.6	0.715	0.746	0.988	1.051	1.189	1.291	1.390	1.542

Table 3. Maximum run-up of colliding solitons. Left columns determined from present computations, right columns from Su & Mirie (1980).

A_L \ A_R	0.1		0.3		0.45		.0.6	
0.1	0.452	0.397						
0.3	-0.340 0.224	-0.352 0.226	0.910	0.798				
0.45	-0.670 0.244	-0.438 0.247	-0.524 0.436	-0.496 0.435	1.311	1.079		
0.6	-0.760 0.250	-0.514 0.267	-0.744 0.438	-0.581 0.411	-0.774 0.582	-0.632 0.547	1.846	1.364

Table 4. Phase shift for each of the colliding solitons; left column present computation, right column Su & Mirie. Top row: slow soliton. Bottom row: fast soliton. For wall case phase shift is total.

The right-hand entries in the double columns are values calculated from a third-order analytical result of Su & Mirie (1980). Table 4 shows the phase shift experienced by each of the colliding waves, again according to the G-N equations and Su & Mirie's result. In each table the agreement appears to deteriorate as the amplitudes increase.

When the colliding solitons are of equal amplitude, the behavior at the midpoint, that is at an equivalent vertical wall, has been frequently studied (Street & Camfield, 1966; Chan & Street,1970; Byatt-Smith, 1971; Oikawa & Yajima, 1973; Maxworthy, 1976; Su & Mirie,1980; Mirie & Su, 1982; Power & Chwang, 1984; Renouard et al., 1985). Figures 16, 17, 18 show the free surface for $A= 0.1, 0.3, 0.6$. Figure 16 shows no trailing waves behing the reflected soliton, in conformity with predictions from the KdV equation. In the others the trailing waves are evident. The run-up, also included in Table 3, is plotted in Figure 19 together with experimental and analytical results of others. The agreement with the analytical result of Byatt-Smith is notable. Figure 20 shows the phase shift, together with experimental data and analytical results of others. The G-N results conform to other results for smaller values of A but go their own way for larger values. Figure 21 shows the time at which the soliton reaches its maximum amplitude as a function of initial soliton amplitude. The G-N results and the numerical and analytical results of Power & Chwang agree well, with some small divergence beginning at $A=0.3$. Figure 22 shows the time phase lag at the wall together with numerical and analytical results of Power & Chwang and a single experimental point of Maxworthy. Except for $A=0.1$ there is at best qualitative agreement.

Figure 23 shows our sole calculation for one soliton overtaking another. Because of the large (12%) decrease in amplitude of the fast soliton and the long period of time during which this interaction takes place we conjecture that round-off and truncation error may have made this computation less reliable than the others. We plan to repeat it at a later time with a higher-order numerical scheme and double precision. We note, however, that the phase shift (-3.344) experienced by the slow soliton, whose final amplitude is reduced by only 1%, agrees rather well with that obtained from an analytical expression (-3.166) based on the KdV equation and given by Whitham (1974, Sec.17.2). Because of the considerable reduction in amplitude of the fast soliton our computations predicted a phase shift of -0.887, contradicting the well known result that the fast soliton experiences a forward shift, which has been confirmed by the experiments of Weidman & Maxworthy (1978).

Initial Mound of Water

Figure 24 shows the results of our single calculation for an initial mound of water. As initial configuration we have taken a rectangular hump with the water being at rest. One can calculate the expected number of solitons according to the KdV equation. Following Segur (1973), the number lies between $LA^{1/2}/\pi$ and $LA^{1/2}/\pi + 1$, that is between 3.42 and 4.42 in our case, where $L=24$ and $A=0.2$. In fact, from Figure 24 one can see that four solitons have been formed although they are not yet well separated. Their amplitudes and speeds are shown in Table 5. For comparison we also show the speed according to the formula $(1+A_j)^{1/2}$. Since the speeds of the last two solitons are not supercritical, it seems reasonable to conclude that they are not yet fully developed.

	A	c	$(1+A_j)^{1/2}$
A_1	0.1565	1.076	1.075
A_2	0.1249	1.047	1.061
A_3	0.0853	0.991	1.042
A_4	0.0324	0.933	1.016

Table 5. Soliton amplitudes and speeds as determined from solution and formula.

Concluding Remarks

As was stated at the outset, our principal aim has been to test the G-N equations in a number of situations where there already exist extensive calculations using other shallow-water equations. Since the G-N equations reduce to these others when the disturbances are small, we expected to find reasonable agreement in such cases, and this has been so. Divergences appear for larger disturbances, but in such cases there is often at least qualitative agreement with higher-order shallow-water theories. We recall that the G-N equations that we have used are based upon a single restricted director. Recent calculations by Shields (1986) using two full and one restricted director have shown remarkable agreement with numerical calculations based upon the exact (Euler's) equations.

References

Akylas, T. R. 1984.
On the excitation of long nonlinear water waves by a moving pressure distribution. J. Fluid Mech. vol. 14, pp. 455-466.

Byatt-Smith, J. G. B. 1971.
An integral equation for unsteady surface waves and a comment on the Boussinesq equation. J. Fluid Mech. vol. 49, pp. 625-633.

Camfield, F. E.; Street, R. L. 1969.
Shoaling of solitary waves on small slopes. Proc. ASCE J. Waterways Harbors Div. vol. 95, pp. 1-21.

Chan, R. K. C.; Street, R. L. 1970.
A computer study of finite-amplitude water waves. J. Comput. Phys. vol. 6, pp. 68-94.

Cole, S. L. 1985.
Transient waves produced by flow past a bump. Wave Motion vol. 7, pp. 579-587.

Ertekin, R. C. 1984.
Soliton generation by moving disturbances in shallow water: theory, computation and experiment. Ph. D. dissertation, Univ. Calif., Berkeley. v+352 pp.

Ertekin, R. C.; Webster, W. C.; Wehausen, J. V. 1984. Ship-generated solitons. Proc. 15th Symp. Naval Hydrodynamics, Hamburg, 1984, pp. 347-361; disc. 361-364.

Ertekin, R. C.; Webster, W. C.; Wehausen, J. V. 1986. Waves caused by a moving disturbance in a shallow channel of finite width. J. Fluid Mech. In press.

Grimshaw, R. 1971.
The solitary wave in water of variable depth. Part 2. J. Fluid Mech. vol. 46, pp.611-622.

Johnson, R. S. 1972.
Some numerical solutions of a variable-coefficient Korteweg-de Vries equation (with applications to solitary wave development on a shelf). J. Fluid Mech. vol. 54, pp. 81-91.

Johnson, R. S. 1973.
On the development of a solitary wave over an uneven bottom. Proc. Cambridge Philos. Soc. vol. 73, pp. 183-203.

Lee, Seung-Joon 1985.
Generation of long water waves by moving disturbances. Ph.D. thesis, Calif. Inst. Tech., 1985. xiv+155pp.

Levich, V. G.; Krylov, V. S. 1969
Surface-tension-driven phenomena. Ann. Rev. Fluid Mech. vol. 1, pp. 293-316.

Madsen, O. S.; Mei, C. C. 1969.
The transformation of a solitary wave over an uneven bottom. J. Fluid Mech. vol. 39, pp. 781-791.

Maxworthy, T. 1976.
Experiments on collisions between solitary waves. J. Fluid Mech. vol. 76, pp. 177-185.

Mirie, R. M.; Su, C. H. 1982.
Collision between two solitary waves. Part 2. A numerical study. J. Fluid Mech. vol. 115, pp. 475-492.

Naghdi, P. M. 1978.
Fluid jets and fluid sheets: a direct formulation. Proc.12th Symp. Naval Hydrodynamics, Washington, D. C.,1978, pp. 500-515.

Oikawa, M.; Yajima, N. 1973.
Interactions of solitary waves--a perturbation approach to nonlinear systems. J. Phys. Soc. Japan vol. 34, pp. 1093-1099.

Power, H.; Chwang, A. T. 1984.
On reflection of a planar solitary wave at a vertical wall. Wave Motion vol. 6, pp. 183-195.

Renouard, D. P.; Seabra Santos, F. J.; Temperville, A. M. 1985. Experimental study of the generation, damping, and reflexion of a solitary wave. Dynam. Atmosph. Oceans vol. 9, pp. 341-358.

Schember, H. R. 1982.
A new model for three-dimensional dispersive waves. Ph.D. thesis, Calif. Inst. Tech., 1982. vii+141pp.

Segur, H. 1973.
The Korteweg-de Vries equation and water waves. Solutions of the equaton. Part 1. J. Fluid Mech. vol. 59, pp.721-736.

Shields, J. J. 1986.
A direct theory for waves approaching a beach. Ph.D. dissertation, Univ. of Calif., Berkeley. iv+137 pp.

Street, R. L.; Camfield, F. E. 1966.
Observations and experiments on solitary-wave deformation. 10th Conf. Coastal Engng., Tokyo, 1966, pp. 1.13/1-1.13/5.

Su, C. H.; Mirie, R. M. 1980.
On head-on collisions between two solitary waves. J. Fluid Mech. vol. 98, pp. 509-525.

Weidman, P. D.; Maxworthy, T. 1978.
Experiments on strong interactions between solitary waves. J. Fluid Mech. vol. 85, pp. 417-431.

Whitham, G. B. 1974.
Linear and Nonlinear Waves. Wiley, New York. xvi+676pp.
Wu, T. Y. 1981.
Long waves in ocean and coastal waters. J. Engng. Mech. Div. ASCE vol. 107, pp. 501-522.
Wu, D.-M.; Wu, T. Y. 1982.
Three-dimensional nonlinear long waves due to moving surface pressure. Proc. 14th Symp. Naval Hydrodynamics, Ann Arbor, 1982, pp. 103-125; disc. 126-129.

Acknowledgement

This research has been sponsored in part by the Office of Naval Research under Contract N000014-84-K-0026.

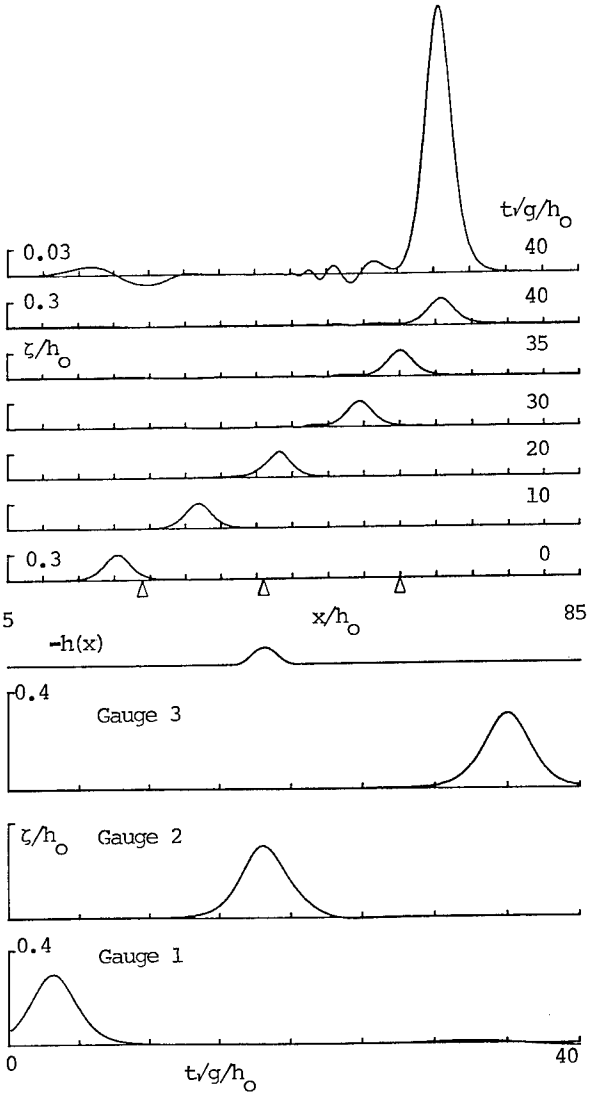


Figure 1. Soliton moving over a bump: soliton amplitude $A=0.3$; bump amplitude $B=0.2$. Initial position of soliton: $x_0=20.4$. Position of bump: $x=41.04$. Wave gauges: no. 1 at $x=24$; no.2 at $x=41.04$; no. 3 at $x=60$.

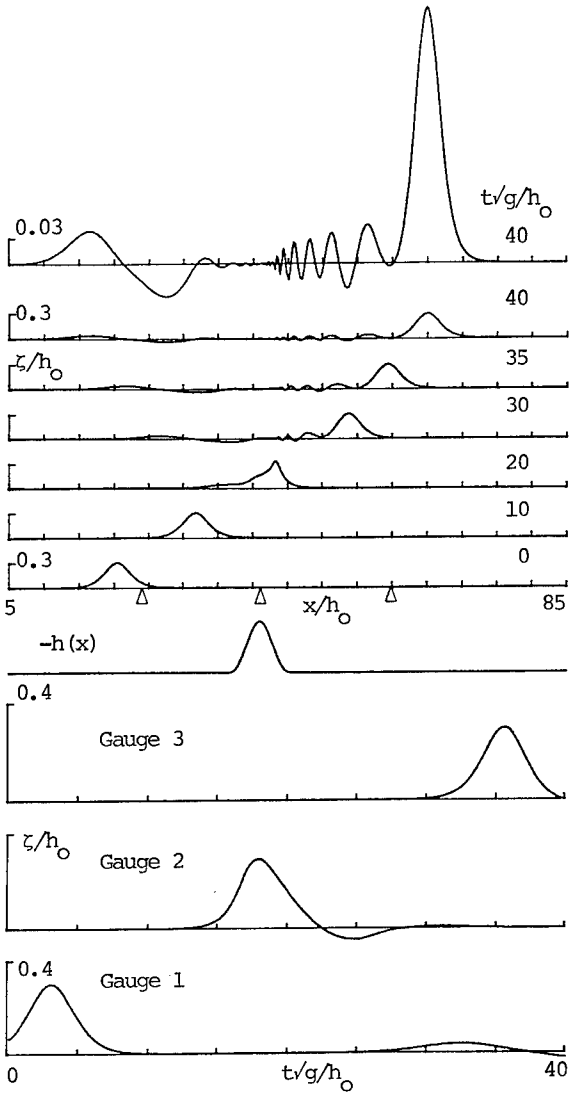


Figure 2. Soliton moving over a bump: $A=0.3$; $B=0.6$. See Figure 1 for other information.

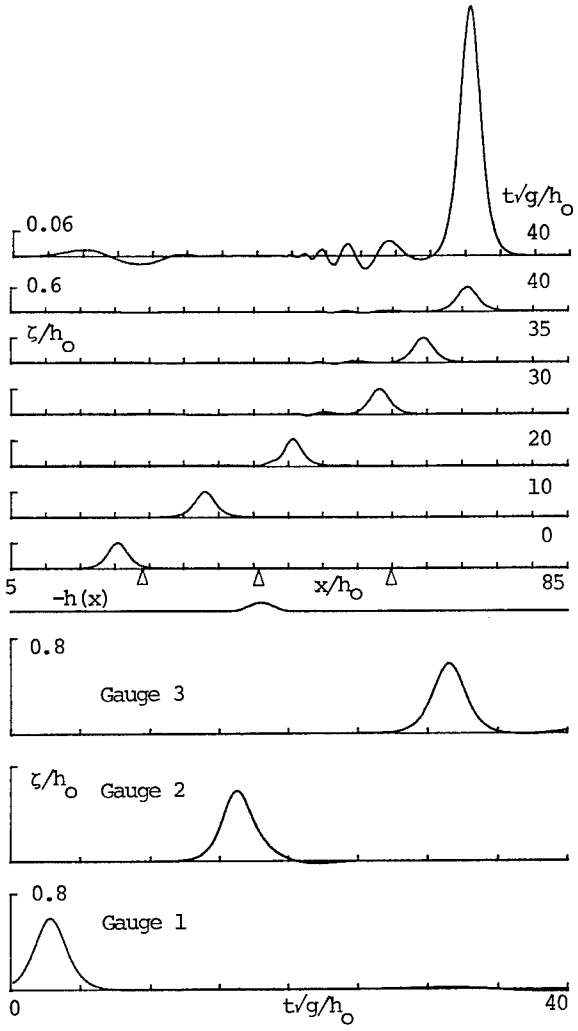


Figure 3. Soliton moving over a bump: *A=0.6; B=0.2.* For other information see Figure 1.

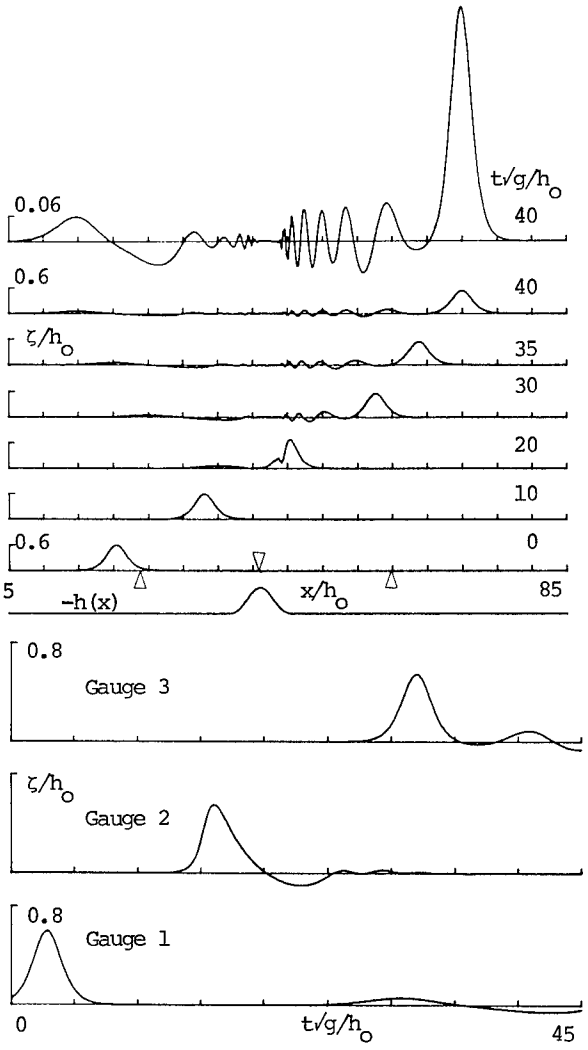


Figure 4. Soliton moving over a bump: *A=0.6; B=0.6.* For other information see Figure 1.

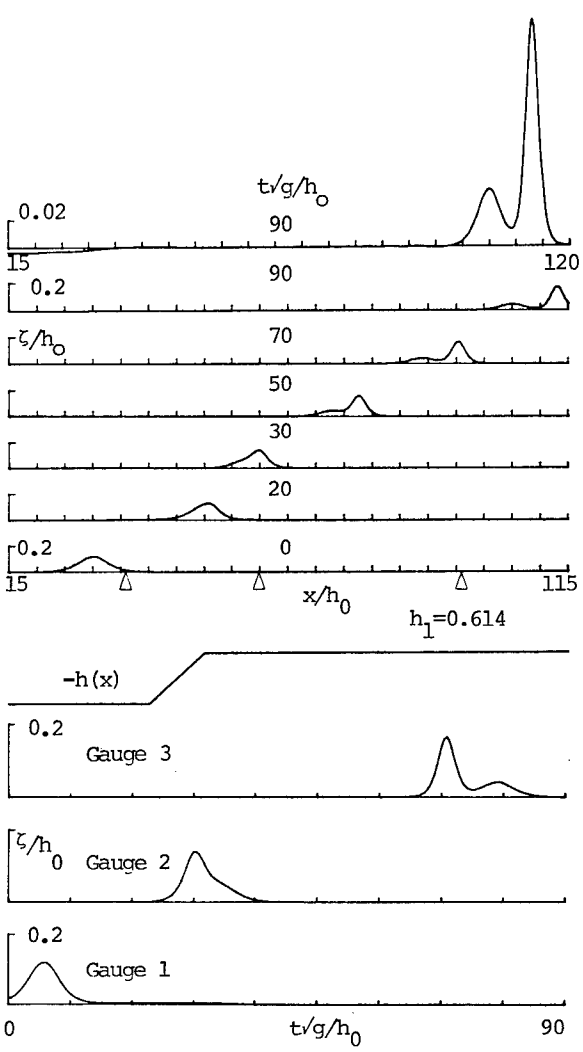


Figure 5. Soliton approaching a shelf. Soliton amplitude $A=0.12$, shelf depth $h_1=0.614$. Initial position of soliton: $x_0=30$. Wave gauges: no. 1 at $x=36$; no. 2 at $x=60$; no.3 at $x=96$.

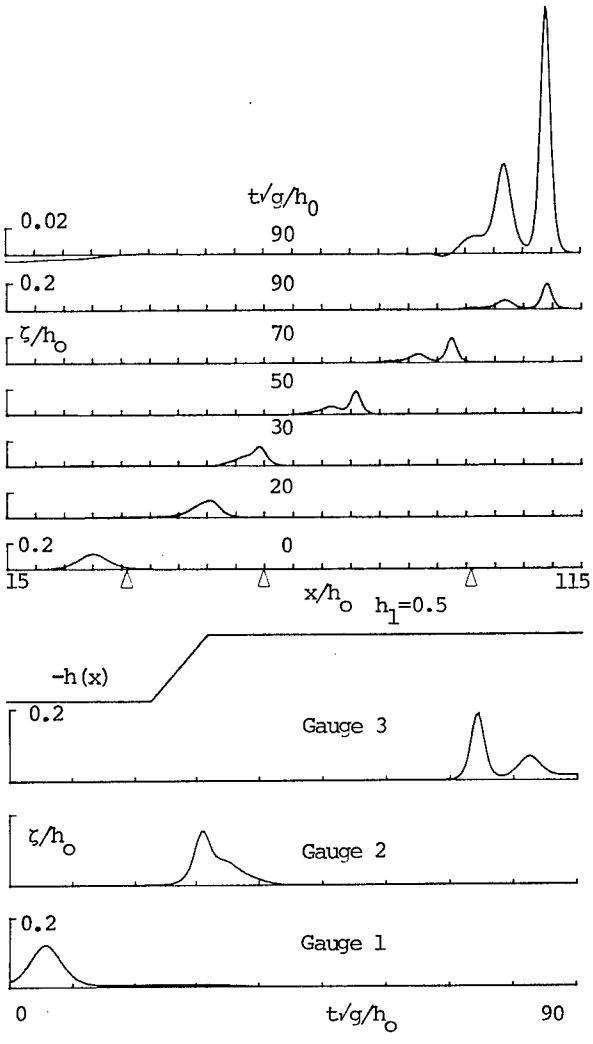


Figure 6. Soliton approaching a shelf: $A=0.12$, $h_1=0.5$. For other information see Figure 5.

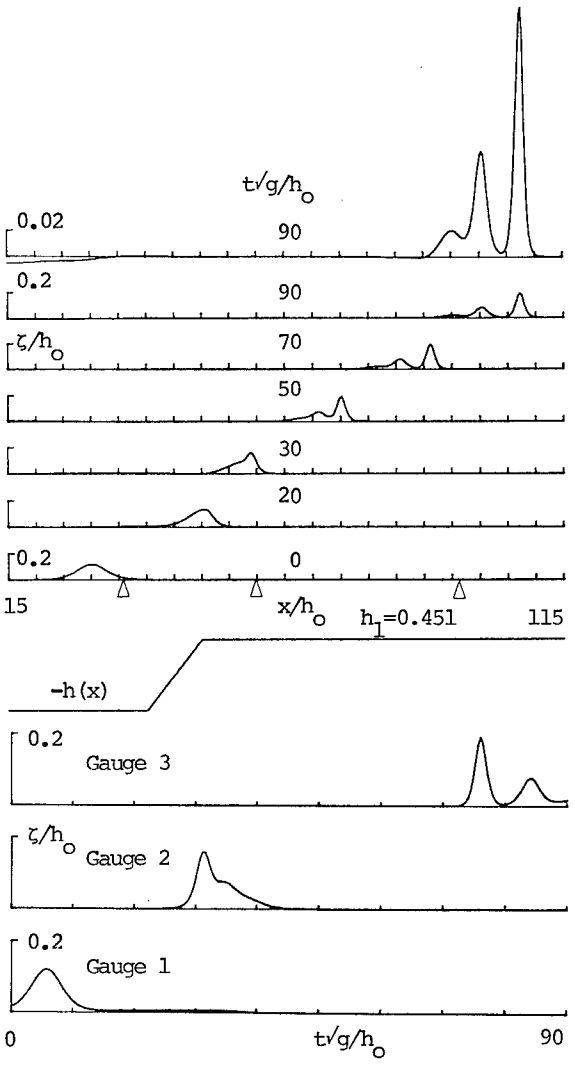


Figure 7. Soliton approaching a shelf: $A=0.12$, $h_1=0.451$. For other information see Figure 5.

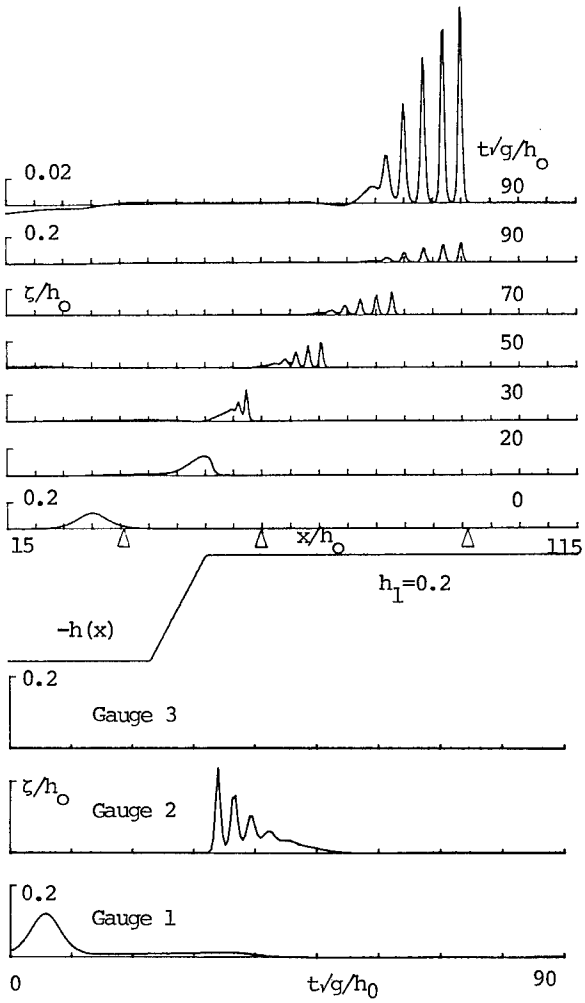


Figure 8. Soliton approaching a shelf: $A=0.12$, $h_1=0.2$. For other information see Figure 5.

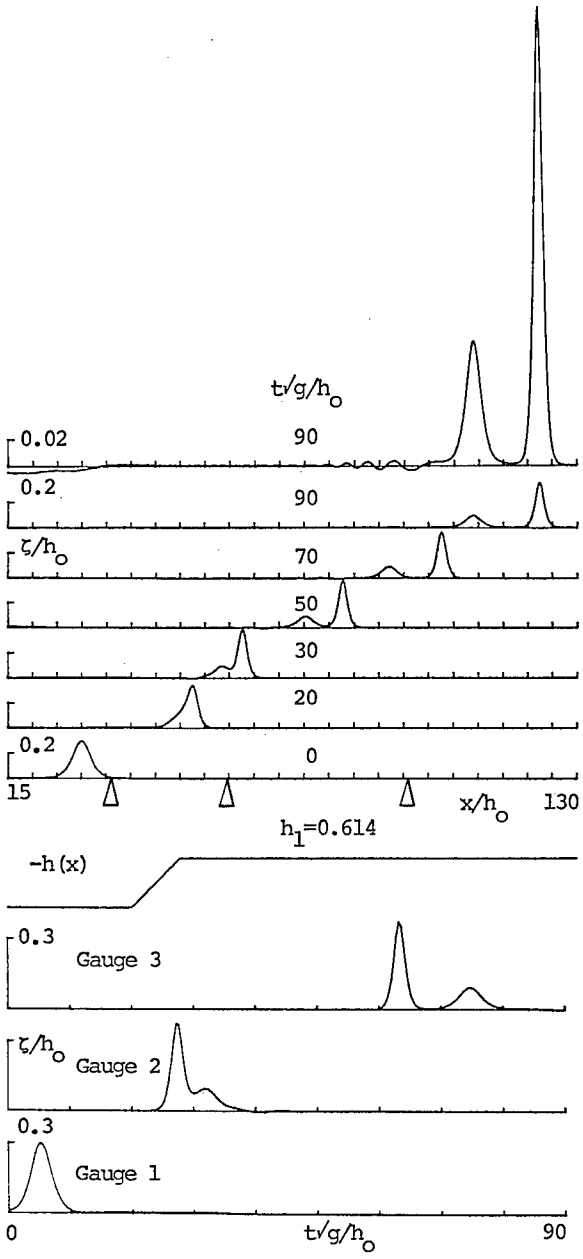


Figure 9. Soliton approaching a shelf: $A=0.3$, $h_1=0.614$. For other information see Figure 5.

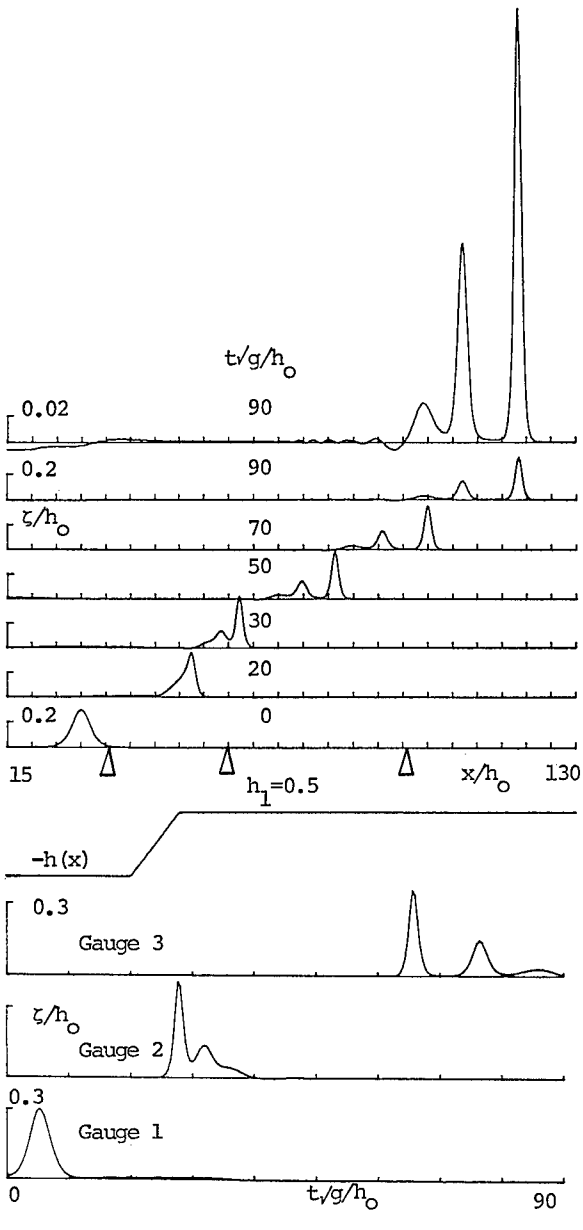


Figure 10. Soliton approaching a shelf: $A=0.3$, $h_1=0.5$. For other information see Figure 5.

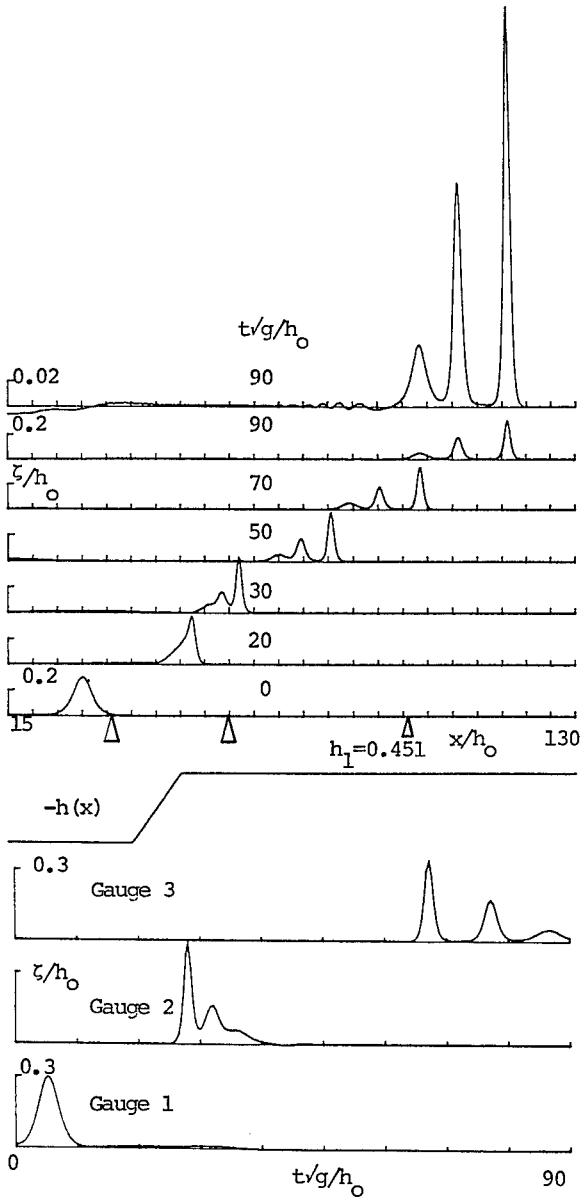


Figure 11. Soliton approaching a shelf: $A=0.3$, $h_1=0.451$. For other information see Figure 5.

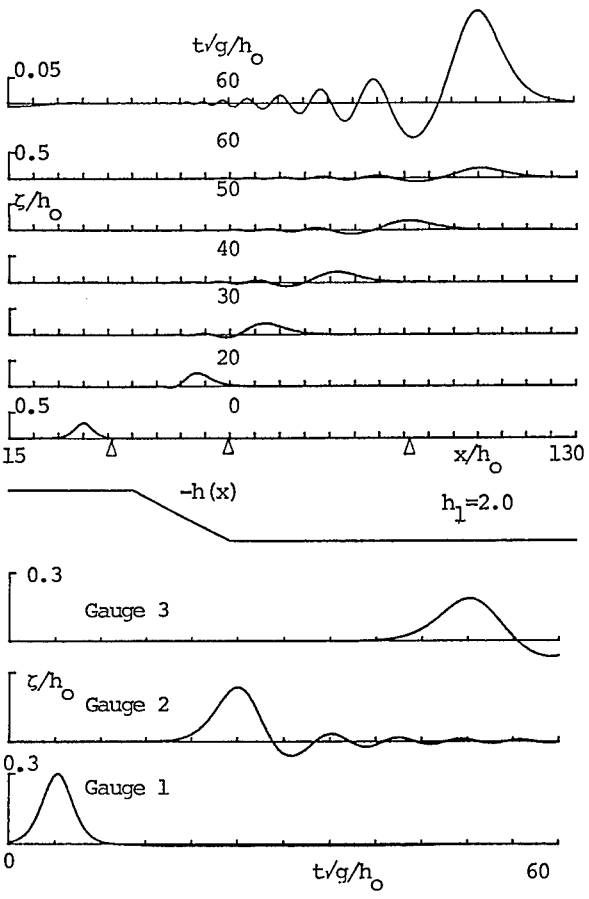


Figure 12. Soliton passing from a shelf to deeper water: $A=0.3$, $h_1=2$. For other information see Figure 5.

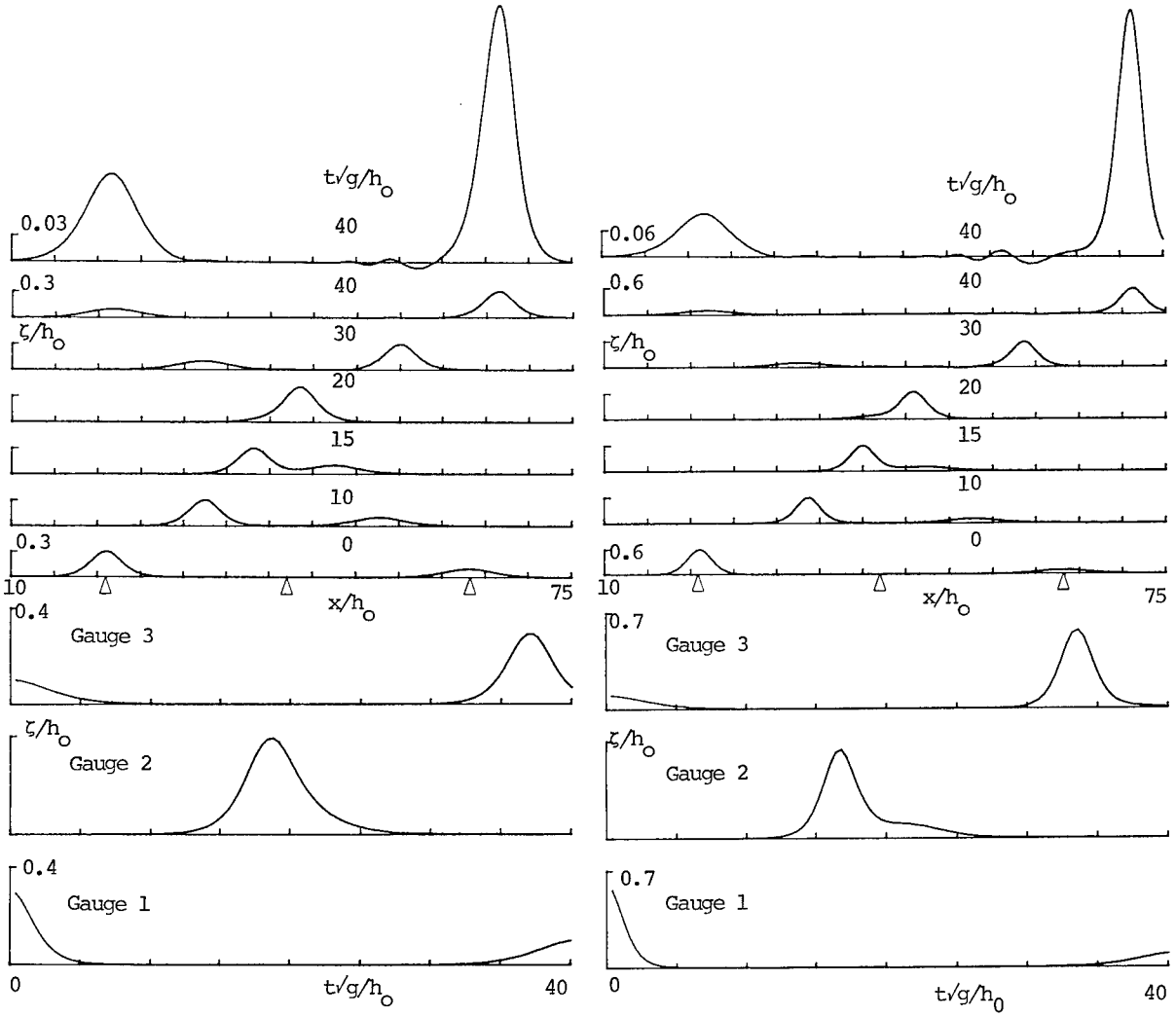


Figure 13. Two colliding solitons of different amplitudes: left soliton A_L=0.3; right soliton A_R=0.1. Initial position of left soliton: x_{0L} = 21; of right soliton: x_{0R} = 63. Wave gauges: no.1 at x=21, no.2 at x=42, no.3 at x=63.

Figure 14. Two colliding solitons: A_L=0.6, A_R= 0.1. For other information see Figure 13.

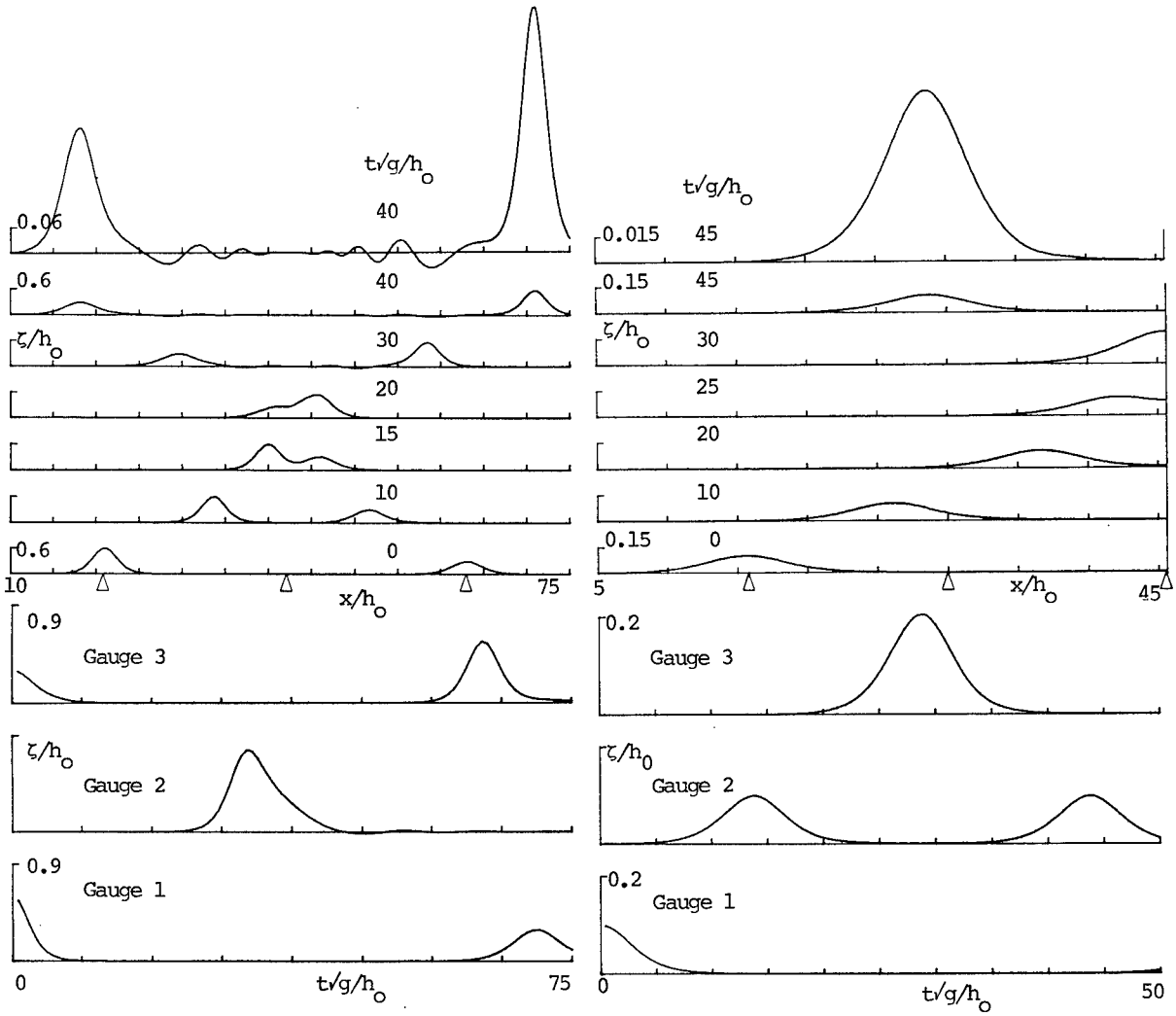


Figure 15. Two colliding solitons: A_L=0.6, A_R=0.3. For other information see Figure 13.

Figure 16. Soliton reflecting from a vertical wall: amplitude A=0.1. Initial position of soliton: x_0=15.6. Wall at x=45.6. Wave gauges: no. 1 at x=15.6, no. 2 at x=30, no. 3 at x=45.6.

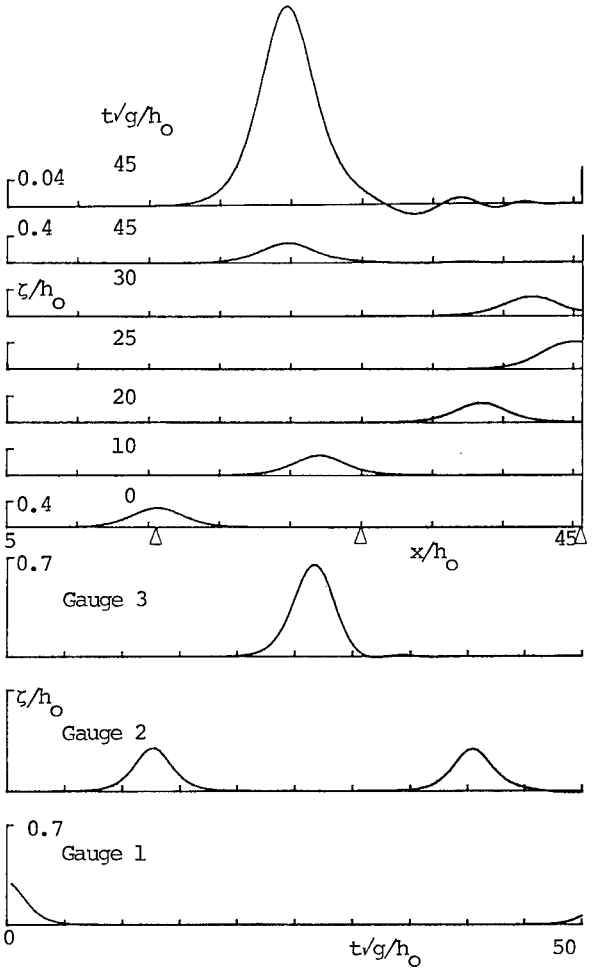


Figure 17. Soliton reflecting from a vertical wall: $A=0.3$. For other information see Figure 16.

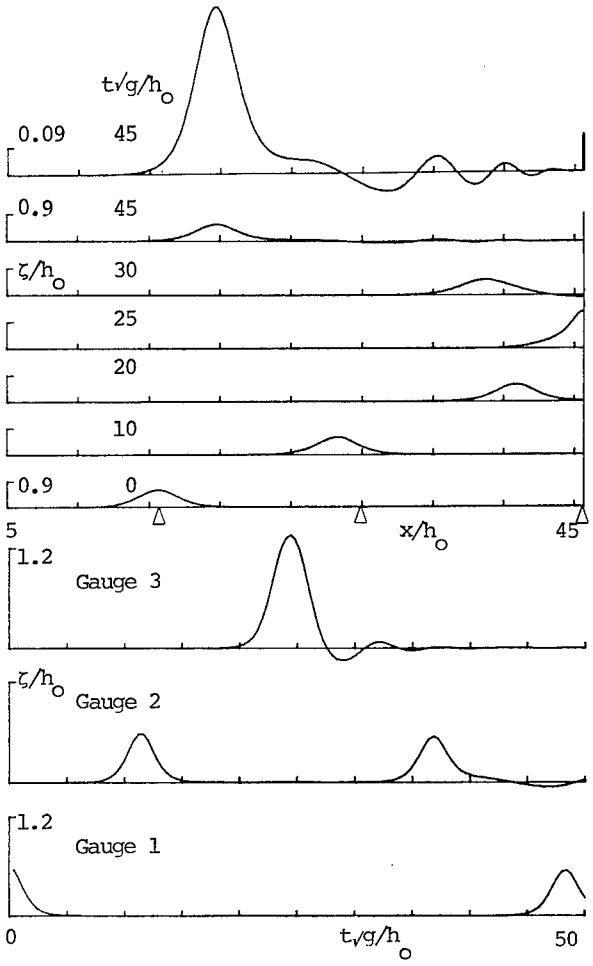


Figure 18. Soliton reflecting from a vertical wall: $A=0.6$. For other information see Figure 16.

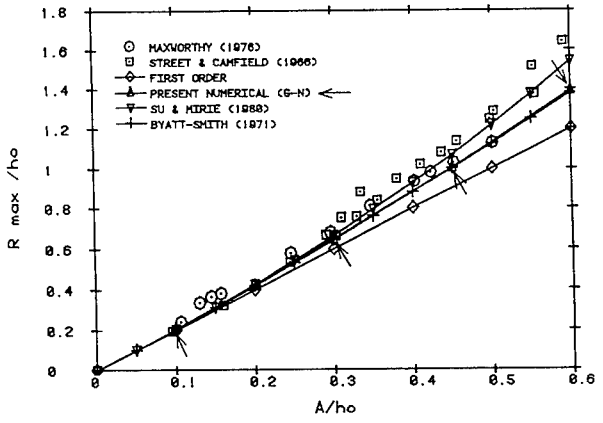


Figure 19. Soliton run-up against a vertical wall as a function of initial amplitude.

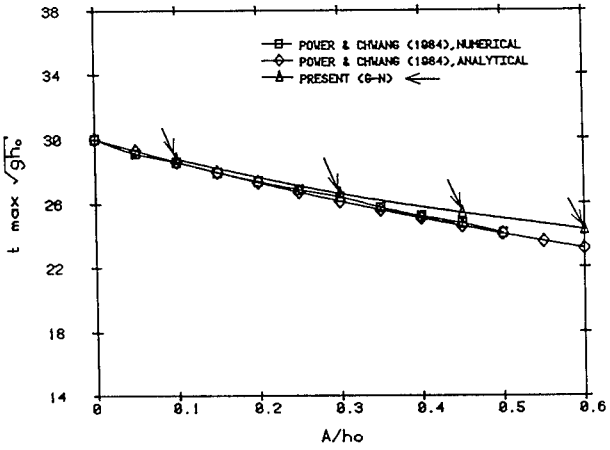


Figure 21. Time at which soliton amplitude reaches its maximum during reflection from a vertical wall as a function of initial amplitude.

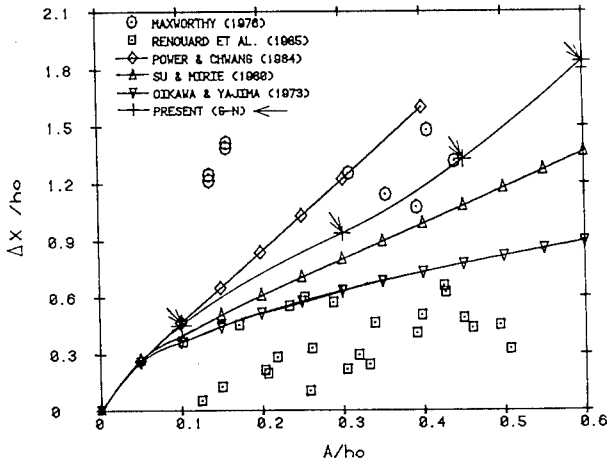


Figure 20. Spatial phase shift of soliton after reflection from a vertical wall as a function of initial amplitude.

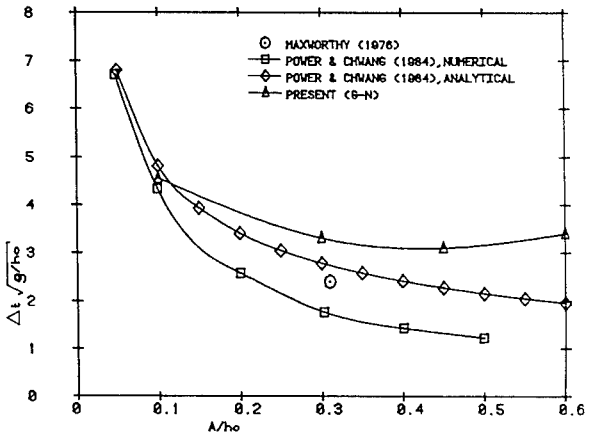


Figure 22. Time soliton maximum remains on wall during reflection as a function of initial amplitude.

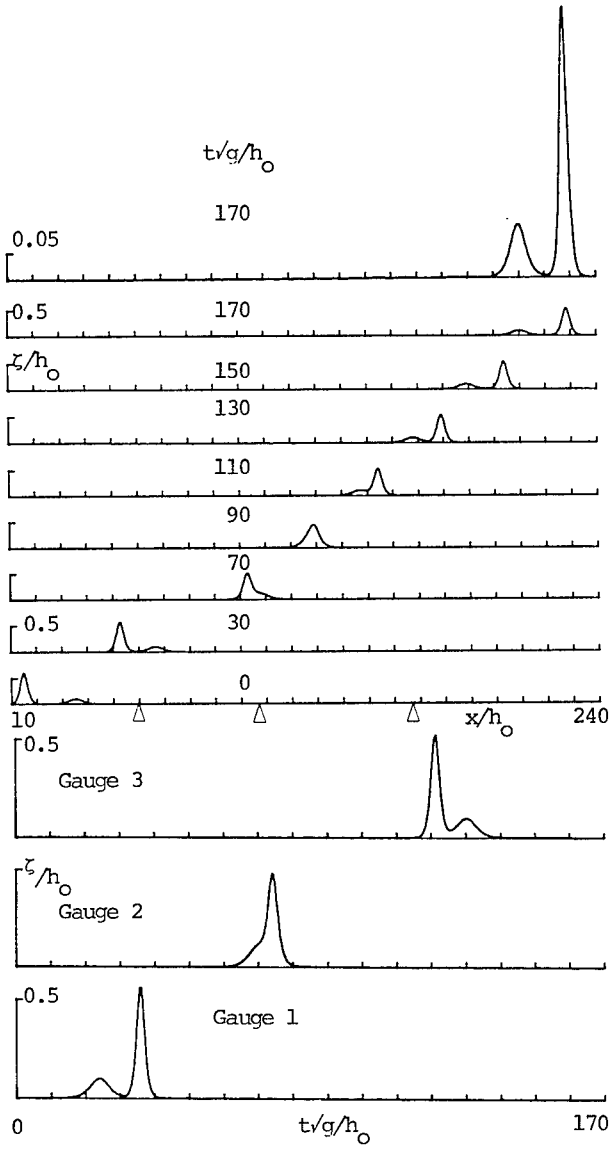


Figure 23. Soliton of amplitude 0.6 overtaking one of amplitude 0.1. Initial position of fast soliton: $x_F=14.88$, of slow one: $x_S=34.92$.

Wave gauges: no.1 at $x=60$, no. 2 at $x=108$, no. 3 at $x=168$.

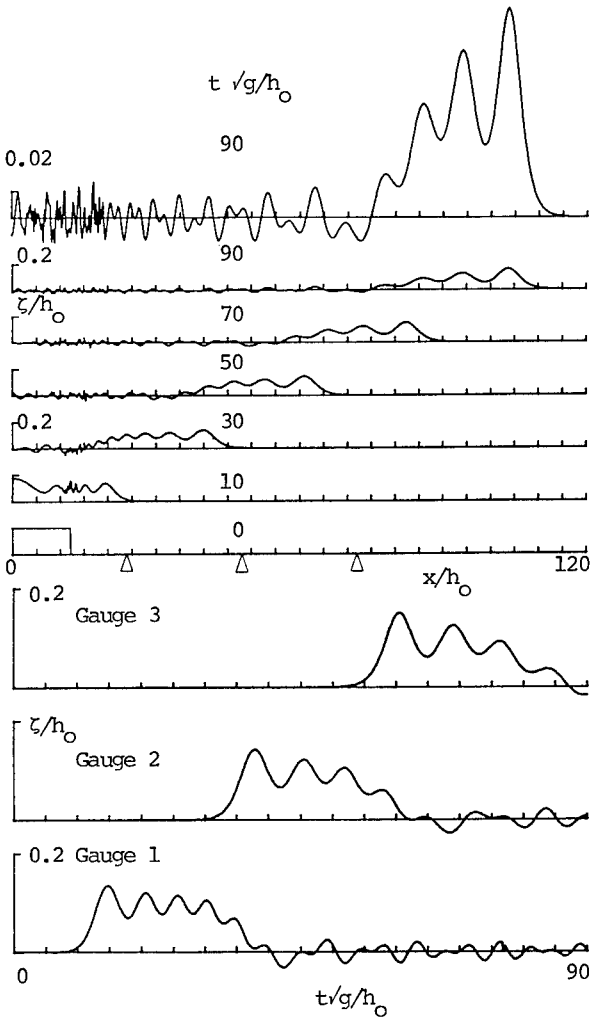


Figure 24. Waves generated by an initial rectangular mound of water. Wave gauges: no. 1 at $x=24$, no. 2 at $x=48$, no.3 at $x=72$.

DISCUSSION

Fred Stern,
Iowa Institute of Hydraulic Research

What was the reason for not extending your calculations to greater values of time?

Reply -

The reason for not extending the calculations to greater values of time was partly financial, but also a belief that not much additional insight would be gained by more extended calculationos. In several cases, however, e.g., in Figures 12 and 24, a longer time span might have clarified what is happening.

Generation of Internal Runaway Solitons by Moving Disturbances

J. ZHU, T. Y. WU, and G. T. YATES

California Institute of Technology, U.S.A.

ABSTRACT

A theoretical, numerical and experimental study has been carried out on the phenomenon of internal solitary waves generated in a two-layer stratified fluid by moving disturbances, such as a moving submerged obstacle or a pressure distribution moving over the upper fluid surface. A forced KdV equation (generalized from the classical Korteweg-de Vries family) has been derived for predicting the forced motions of weakly nonlinear and weakly dispersive long waves propagating in two layers of incompressible and immiscible fluids or in a continuously stratified fluid system. This provides the theoretical model for our numerical computations of the results.

Experimentally, the two-layer system consists of an upper layer of fresh water and a lower layer of strong brine in a horizontal rectangular water tank. The obstacle has a circular-arc top and a flat bottom, and moves horizontally, after an impulsive start, with a constant velocity along the floor of the fluid layer. Within a range of the lower transcritical speed, it has been found, both numerically and experimentally, that a sequence of internal solitons are generated to surge upstream, periodically one after another from the moving bump, and are centered along the interface. The upper free water surface, inasmuch as discernible, remained horizontal. Satisfactory agreement has been found between experiment and the present numerical results based on a finite-difference scheme. The amplitude and period of generation of the resulting solitary waves are found to depend on the distribution and the Froude number of the moving disturbance as well as on the depth ratio and density ratio of the two-layer fluids.

INTRODUCTION

Stable stratified fluids can support not only top-surface waves as in the ocean, but also internal wave modes which propagate within the fluid bulk below the free water surface due to internal density variations. These internal waves have been a subject of keen interest in geophysics, ocean engineering, applied mathematics and hydrodynamics. The oceans are a complex stratified fluid system widely distributed with pycnoclines, commonly located about 50-150 meters below the surface. Osborn, Burch & Scarlet (1978), Osborn & Burch (1980) and Locke (1980) reported field observations of internal waves of finite amplitude in the deep waters of the Andaman Sea off the West Coast of Thailand. Other investigations of large internal waves have been conducted by Perry & Schimke (1970) near the Northwest Coast of Sumatra, by Ziegenbein (1969, 1970) and Farmer & Armi (1986) in the Strait of Gibralter, Eriksen (1978) in the Bermuda waters, Gargett (1976) and Farmer & Smith (1980) in the West Coast Area of Canada and by Halpern (1971), Haury (1979) and Chereskin (1983) in the Massachusetts Bay. A significant feature of these observations is the discovery of the great amplitude of these apparently ubiquitous internal waves occurring in nature. Internal solitary waves as high as 200m or more have been reported although the top surface waves that accompany such giant internal waves are invariably very small. These internal waves have been responsible for increased resistance of surface ships (Long, 1970), and have caused the flexing of drilling risers of offshore drilling rigs (Locke, 1980).

Important experimental studies on internal waves have been reported by Yih & Guha (1955), Lee & Beardsley (1974), Hurdis & Pao (1975), Baines (1977, 1979), Maxworthy (1979), Hammack (1980), Koop & Butler (1981), Lansing & Maxworthy (1984), Kao, Pao & Renouard (1985) and Gilreath & Brandt (1985). Internal waves have been investigated theoretically by Keulegan (1953), Long (1956), Peters & Stoker (1960), Benjamin (1966, 1967) and Koop & Butler (1981) for two-layer fluid systems, and Peters & Stoker (1960), Benny (1966), Benjamin (1966, 1967), Wu (1966), Wu & Mei (1967), Ono (1975), Joseph (1977), Kubota, Ko & Dobbs (1978) and by Liu, Kubota & Ko (1980) for continuously stratified fluid systems.

Most of these research studies are concerned with steady state solution and with "free" wave propagation; i. e., propagation and evolution of nonlinear long waves without being

subject to external forcing disturbances except for the conservative gravity field acting as the only restoring force. Among the few who have considered external forcing disturbances, Lansing & Maxworthy (1984) investigated both theoretically and experimentally, the generation and evolution of internal waves in a two-layer system by towing an obstacle with a to-and-fro sinusoidal motion.

The phenomenon of soliton generation by steadily moving disturbances was first reported for the homogeneous one-layer case by Wu & Wu (1982) who identified the phenomenon from their numerical calculations and was later confirmed by experiments with both two and three-dimensional disturbances in homogenous one-layer fluids by Huang et al. (1982), Sun (1980), Ertekin (1984), Lee (1985), and by Ertekin et al. (1985). Further theoretical investigations have been pursued on this phenomenon by Akylas (1984), Cole (1985), Grimshaw & Smyth (1985), Mei (1986), Wu 1984, 1986), Smyth (1986) and by Zhu (1986). Grimshaw & Smyth (1985) investigated the flow of a stratified fluid over localized topography and obtained a forced KdV equation to model the generation and evolution of internal waves by moving bottom configurations. From their forced KdV equation they showed solitons can be generated to surge ahead of the disturbance in resonant cases.

The objective of this paper is to study the runaway soliton phenomenon in stratified fluid systems theoretically, numerically and experimentally. It is intended to discover some new behaviors and to verify similar behaviors to those already known for the homogeneous one-layer case. With this intent, we hope to elucidate the theoretical models for investigating weakly nonlinear and weakly dispersive internal waves in incompressible, inviscid, and stratified fluid systems.

We have developed a KdV equation for evaluating generation and evolution of internal waves of finite amplitude in continuously stratified fluid systems with two very general types of external forcing disturbances. The system can have an arbitrary bottom topography in motion and a moving pressure disturbance applied on the top surface, provided they are not excessively strong. This model can be simplified for the special case of two-layer fluid systems and for small density differences between the two layers, in which cases some simple qualitative features of the internal waves can be easily explored. Numerical integration of the theoretical models for both the continuously stratified and the two-layer systems are performed and are compared to each other as well as with experimental measurements. In the experiments reported here, the external forcing was provided by a bottom bump which was driven along the floor of a flume filled with a stratified fluid consisting of fresh water lying above a salt water solution. The salient features of this phenomenon are examined in this comparative study.

THE FORCED KdV MODEL FOR STRATIFIED FLUID SYSTEMS

The theoretical model to be developed here is for study of two-dimensional weakly nonlinear and weakly dispersive long waves generated in a stratified fluid system by external forcing functions in unidirectional motion through the fluid. The fluid system may be as simple as one consisting of two layers of distinct, immiscible, homogeneous fluids or as general as a shallow layer of continuously stratified fluid of arbitrary but stable density distribution. With the fluids assumed incompressible and inviscid, the system has at least two or may have infinitely many normal modes of free oscillations as determined on linear theory. Our particular interest in this study is to investigate the resulting motion generated by one or more forcing disturbances moving with a transcritical speed of any one of the normal modes, in particular the first internal-wave mode. The objective is to determine the roles played by the nonlinear and dispersion effects in such a near-resonant state of motion. We shall first deal with the general case of arbitrary density distribution and then deduce from the general result the basic equations for the case of two-fluid-layer systems.

For continuously stratified fluid, the primary density distribution, which prevails when at rest, is assumed given,

$$\rho = \rho_o(z) , \qquad (0 \le z \le h) , \tag{1}$$

where z is the vertical of the Oxz-coordinate system and h is the total constant water depth (figure 1). The two-dimensional equations of continuity and motion are

$$\frac{d\rho}{dt} = \rho_t + u\rho_x + w\rho_z = 0 , \tag{2}$$

$$u_x + w_z = 0 , \tag{3}$$

$$\rho(u_t + uu_x + wu_z) = -p_{e_x} , \tag{4}$$

$$\rho(w_t + uw_x + ww_z) = -p_{e_z} - (\rho - \rho_o)g , \tag{5}$$

where u and w are the x- and z- velocity components, the subscripts x, z, and t denote partial differentiation, and p_e represents the excess pressure above the local hydrostatic pressure in the state of rest, related to the total pressure p by

$$p = p_o + p_e , \qquad p_o = -g\int_h^z \rho_o(z_1)dz_1 \tag{6}$$

g being the gravity constant. With a forcing pressure $p_a(x, t)$ acting on the fluid at its top surface and a bottom bump $z = b(x, t)$ moving along the floor of the water layer, the boundary conditions are

$$w = d\hat{\zeta}/dt = \hat{\zeta}_t + u\hat{\zeta}_x \qquad (z=h+\hat{\zeta}) , \tag{7}$$

$$p = p_a(x, t) \qquad (z=h+\hat{\zeta}) , \tag{8}$$

$$w = db/dt = b_t + ub_x \qquad (z=b) \tag{9}$$

where $\hat{\zeta}$ is the wave elevation at the top surface $(z=h+\hat{\zeta})$.

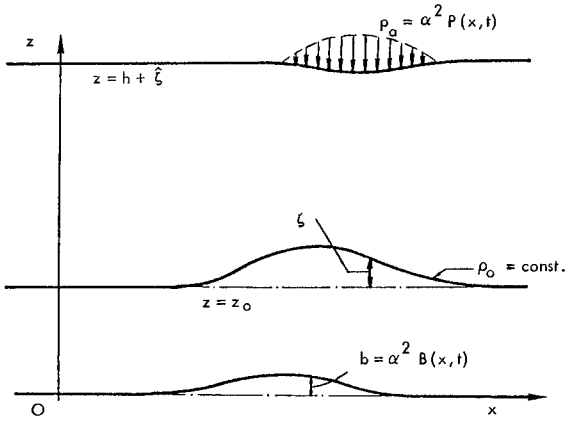


Fig. 1. Definition sketch for a continuously stratified fluid system.

From (2), which asserts the assumption of incompressibility in terms of the invariance of the density as a material property (for its general validity, see Yih 1965), it follows that

$$\rho(x, z, t) = \rho_o(z-\zeta(x, z, t)), \tag{10}$$

where $\zeta(x, z, t)$ is the vertical displacement of a fluid particle, here regarded as a Eulerian field variable, such that

$$w=d\zeta/dt=\zeta_t+u\zeta_x+w\zeta_z \qquad (b \le z \le h+\hat{\zeta}). \tag{11}$$

We note that in terms of the variable ζ, the assumption of incompressibility, (2) is automatically satisfied, the top surface kinematic condition (7) is also satisfied at $z= h+\hat{\zeta}$, and (9) becomes

$$\zeta = b(x, t) \qquad (z=b) . \tag{12}$$

Now we will scale x by λ, a typical wavelength, z and ζ by h, t by λ/c_o, and u and w by c_o, where $c_o = (gh)^{1/2}$, which is taken here as a reference velocity. We further scale ρ by a typical density ρ_c, and p by $\rho_c gh$. This scaling gives rise to two dimensionless flow parameters;

$$\alpha = a/h , \qquad \epsilon = h/\lambda , \tag{13}$$

where α characterizes the nonlinear effects for waves of typical amplitude a and ϵ, the dispersion effects. As in the case of classical Boussinesq and Korteweg-de Vries models for weakly nonlinear and weakly dispersive long waves, we shall assume that

$$\alpha = O(\epsilon^2) ,$$

and take α and $\epsilon^2 = \alpha$ alternatively as being equivalent.

In order to have the nonlinear and the dispersion effects play a well balanced role interacting with the leading terms in the basic equations governing a left-going (or right-going) wave system in a specific normal mode, we apply the transformation

$$\xi = (x+ct) , \qquad \tau = \epsilon^2 t , \tag{15}$$

to the system of basic equations, where c is the positive characteristic wave velocity of this normal mode and is normalized with respect to c_o. We further assume the dependent variables to have the expansions:

$$\begin{aligned} u &= \alpha[u_1(\xi, \tau, z)+ \epsilon^2 u_2(\xi, \tau, z)+\dots] , \\ \zeta &= \alpha[\zeta_1(\xi, \tau, z)+ \epsilon^2 \zeta_2(\xi, \tau, z)+\dots] , \\ p_e &= \alpha[p_1(\xi, \tau, z)+ \epsilon^2 p_2(\xi, \tau, z)+\dots] , \end{aligned} \tag{16}$$

(For right-going waves the same holds with a change of sign for c.) The expansion for w can then be deduced from (11) and (16) to give

$$w = \alpha\epsilon[c\zeta_{1\xi}+ \alpha(c\zeta_{2\xi}+\zeta_{1\tau}+ u_1\zeta_{1\xi}+ c\zeta_{1\xi}\zeta_{1z}) + \dots] . \tag{17}$$

For the external forcing functions we further assume that

$$p_a = \alpha^2 P , \qquad b = \alpha^2 B . \tag{18}$$

It is in this order that the two disturbances can first appear as arbitrary distributions, according to what is required by the solvability condition encountered in the analysis.

By substituting these expansions into equations (3)-(5) for the three variables u, ζ, and p, and incorporating Taylor's series expansion of the density relation (10), we obtain

$$(u_1+c\zeta_{1z})_\xi+\alpha\{(u_2+c\zeta_{2z})_\xi+ (\zeta_{1\tau}+ u_1\zeta_{1\xi} + c\zeta_{1\xi}\zeta_{1z})_z\} = 0 , \tag{19}$$

$$(\rho_o- \alpha\zeta_1\rho_o')\{cu_{1\xi}+ \alpha(cu_{2\xi}+ u_{1\tau}+ u_1u_{1\xi} + c\zeta_{1\xi}u_{1z})\}+(p_1+ \alpha p_2)_\xi = 0 \tag{20}$$

$$p_{1z}+ \alpha(p_{2z}+ c^2\rho_o\zeta_{1\xi\xi})- \{\rho_o'\zeta_1+ \alpha(\rho_o'\zeta_2- \tfrac{1}{2}\rho_o''\zeta_1^2)\} = 0 , \tag{21}$$

in which ρ_o' means $d\rho_o(z)/dz$, and $\alpha=\epsilon^2$ is used as understood. For the top surface boundary conditions we have

$$p_1- \rho_o\zeta_1+ \alpha\{p_2+\zeta_1p_{1z}-P-\rho_o(\zeta_2+\zeta_1\zeta_{1z}) - \tfrac{1}{2}\rho_o'\zeta_1^2\} = 0 \qquad (z=h) , \tag{22}$$

in which $\hat{\zeta}$ has been expanded about z=h, and for the bottom boundary condition,

$$\zeta_1 + \alpha\zeta_2 = \alpha B \qquad (z=o)\ , \tag{23}$$

The above system of equation (19)-(23) each holds with an error of $O(\alpha^2)$.

The First-order Equations

By equating the terms with like powers in α, we obtain, under the boundary conditions that u_j, ζ_j and p_j vanish at $|\xi| = \infty$, the first order equation as

$$u_1 = -c\zeta_{1z}\ , \tag{24}$$

$$p_1 = -c\rho_o u_1\ , \tag{25}$$

$$p_{1z} = \rho_o'\zeta_1\ , \tag{26}$$

and accordingly, upon eliminating u_1 and p_1 from the above equations,

$$(\rho_o\zeta_{1z})_z = \frac{1}{c^2}\rho_o'\zeta_1 \qquad (o \le z \le h=1), \tag{27a}$$

$$\zeta_{1z} = \frac{1}{c^2}\zeta_1 \qquad (z=h)\ , \tag{27b}$$

$$\zeta_1 = 0 \qquad (z=0)\ . \tag{27c}$$

The system of equations (27) is in fact a problem of ordinary differential equation in z and ξ and τ only appear here as parameters of the problem. The solution can therefore assume the form by separation of variables as

$$\zeta_1 = \phi(z)\eta(\xi,\tau)\ , \tag{28}$$

which reduces the system (27) to the Sturm-Liouville problem for $\phi(z)$ as

$$L\phi \equiv (\rho_o\phi')' - \mu\rho_o'\phi = 0 \quad (o \le z \le h,\ \mu = 1/c^2)\ , \tag{29a}$$

$$B_h\phi \equiv \phi' - \mu\phi = 0 \qquad (z=h)\ , \tag{29b}$$

$$\phi = 0 \qquad (z=o)\ , \tag{29c}$$

where the prime denotes differentiation with respect to z. The system of equations (29) defines an eigenvalue problem whose solution will determine the eigenvalue c and the corresponding eigenfunction $\phi(z)$. For arbitrary distribution of $\rho_o(z)$ this problem has in general infinitely many eigenvalues ($\mu=\mu_j$, j = 1, 2, . . .) and corresponding eigenfunctions ($\phi=\phi_j(z)$, j=1, 2, . . .) of which each pair (μ_j and ϕ_j for given j) represents one normal mode of free oscillation in z that the system can perform. It can be shown that all μ_j's are real and positive, so that for each mode, $c_j = \pm 1/\sqrt{\mu_j}$. At this stage, however, the horizontal motion represented by $\eta(\xi,\tau)$ remains undetermined; its solution, as will be seen, must be resolved together with the second-order problem.

The Second-order Equation

From (19)-(21) and boundary conditions (22) and (23) we obtain the second-order equations as

$$(u_2 + c\zeta_{2z})_\xi = -\zeta_{1\tau z}\ , \tag{30}$$

$$(p_2 + c\rho_o u_2)_\xi = cu_{1\xi}(\rho_o\zeta_1)_z - \rho_o(u_{1\tau} + c\zeta_{1\xi}u_{1z})\ , \tag{31}$$

$$(p_{2z} - \rho_o'\zeta_2) = -c^2\rho_o\zeta_{1\xi\xi} - \frac{1}{2}\rho_o''\zeta_1^2\ , \tag{32}$$

$$p_2 - \rho_o\zeta_2 = P + \rho_o\zeta_1\zeta_{1z} - \frac{1}{2}\rho_o'\zeta_1^2 \quad (z=h), \tag{33}$$

$$\zeta_2 = B \qquad (z=o)\ . \tag{34}$$

The equation for ζ_2 is readily found as

$$L\zeta_{2\xi} = F \qquad (o \le z \le h)\ , \tag{35a}$$

where the operator L is defined in (29a) and

$$F = -\frac{2}{c}(\rho_o\phi')'\eta_\tau + \{\frac{\partial}{\partial z}(3\rho_o\phi'^2 - 2\rho_o\phi\phi'') - 2\rho_o\phi'\phi''\}\eta\eta_\xi - \rho_o\phi\eta_{\xi\xi\xi}\ , \tag{35b}$$

$$B_h\zeta_{2\xi} = \frac{1}{\rho_o c^2}P_\xi - \frac{2\mu}{c}\phi\eta_\tau + 3\mu^2\phi^2\eta\eta_\xi \qquad (z=h)\ , \tag{35c}$$

$$\zeta_2 = B(\xi,\tau) \qquad (z=o)\ , \tag{35d}$$

where the operator B_h is defined in (29b). In (35b) and (35c), use has been made of (29a) and (29b). This system of equations constitute an inhomogeneous Sturm-Liouville problem for ζ_2, whose homogeneous part is the same as the first-order problem (29a, b, c). It therefore follows from Fredholm's Alternative Theorem that in order to have a solution for ζ_2 for the same eigenvalue c determined with ϕ from solving the first-order problem, the system (35) must satisfy the required solvability condition which yields for η, after some manipulation, the equation

$$\tilde{a}_1\eta_\tau + \tilde{a}_2\eta\eta_\xi + \tilde{a}_3\eta_{\xi\xi\xi} + \phi(h)P_\xi + c^2\rho_o(0)\phi'(0)B_\xi = 0, \tag{36a}$$

where

$$\tilde{a}_1 = -2c\int_o^h \rho_o\phi'^2 dz\ , \tag{36b}$$

$$\tilde{a}_2 = 3c^2\int_o^h \rho_o\phi'^3 dz\ , \tag{36c}$$

$$\tilde{a}_3 = c^2\int_o^h \rho_o\phi^2 dz\ . \tag{36d}$$

This equation is the forced KdV equation for continuously stratified fluid systems. When the required solution of (36) is obtained, the internal wave displacement is given by

$$\zeta \simeq \alpha\zeta_1 = \alpha\phi(z)\eta(\xi,\tau)\ . \tag{37}$$

Finally, the forced KdV equation for ζ follows as

$$\zeta_t - c\zeta_x + A_2\zeta\zeta_x + A_3\epsilon^2\zeta_{xxx} = A_4 p_{a_x} + A_5 b_x \,, \tag{38}$$

$$A_2 = \tilde{a}_2/[\tilde{a}_1\phi(z)] \,,\quad A_3 = \tilde{a}_3/\tilde{a}_1 \,, \tag{39}$$

$$A_4 = -\phi(h)\phi(z)/\tilde{a}_1 \,,\quad A_5 = -c^2\rho_o(0)\phi'(0)\phi(z)/\tilde{a}_1 .$$

The system of waves generated by the external forcing disturbances is left- or right-going according as c is positive or negative. If the surface pressure term is absent, (36) agrees with the equation obtained by Grimshaw & Smyth (1985) and with that derived by Benney (1966) if $p_a = b = 0$.

For the case of continuously stratified fluid systems with a rigid top surface, the eigenvalue c and the eigenfunction ϕ also satisfy (29a) but with the boundary conditions modified as

$$\phi(0) = \phi(h) = 0 \,. \tag{40}$$

Consequently, the corresponding forced KdV equation has the same form as (36) except that the term with P_ξ is deleted because of (40).

The Homogeneous One-layer Analogy

Having obtained the forced KdV model for the general case of a continuously stratified fluid layer of arbitrary density distribution, we may deduce the corresponding equations for the homogeneous one-layer system and for the two-fluid-layer systems as special cases.

For a homogeneous one-layer system, ($\rho = \rho_o$ = const., h = const.), we obtain at once from (29a) the eigenfunction ϕ and from (29b) the eigenvalue c, after restoring physical dimensions,

$$\phi = z, \qquad (0 < z < h) \,, \tag{41}$$

$$c = c_o = \sqrt{gh} \,. \tag{42}$$

The corresponding free surface elevation $\zeta = \zeta^*$ then satisfies, after restoring the original independent variables x and t, the equation

$$\zeta^*_T - (1+\tfrac{3}{2}\zeta^*)\zeta^*_X - \tfrac{1}{6}\epsilon^2\zeta^*_{XXX} = \tfrac{1}{2}\frac{\partial}{\partial X}(p_a^* + b^*) \tag{43}$$

where x and t are written in upper cases, *'s are used to identify this one-layer system as the reference case. Equation (43) agrees with that derived by Lee (1985).

For a two-fluid-layer system with density distribution,

$$\rho_o = \rho_2 + (\rho_1 - \rho_2)H(z - h_2) \qquad (0 < z < h = h_1 + h_2 = 1) \,, \tag{44}$$

where $H(z)$ is the Heaviside step function, defined as usual. For simplicity, the total water depth will be normalized to unity, $h_1 + h_2 = 1$. With this primary density distribution and with the top surface free, we readily derive from (29a, b, c) for the two eigenvalues the result:

$$\left.\begin{matrix}\mu_1 \\ \mu_2\end{matrix}\right\} = \frac{1}{2r\sigma}\left[1 \mp (1-4r\sigma)^{1/2}\right] \tag{45}$$

where

$$\sigma = 1 - \rho_1/\rho_2, \quad r = h_1h_2/(h_1+h_2)^2 = h_1h_2. \tag{46}$$

Consequently, the two critical velocities are

$$c_j = (\mu_j)^{-1/2}, \quad (j = 1, 2) \,. \tag{47}$$

The corresponding eigenfunctions are found as

$$\begin{aligned}\phi &= z + b_1 \qquad (h_2 \le z \le 1) \\ &= b_2 z \qquad (0 \le z \le h_2) \,,\end{aligned} \tag{48a}$$

where

$$b_1 = \frac{1}{\mu} - 1 \,,\quad b_2 = 1 + \frac{1}{h_2}\left(\frac{1}{\mu} - 1\right) \,, \tag{48b}$$

and $\mu = \mu_1$ (for the free-surface wave mode) or μ_2 (for the internal wave mode) as given by (45).

The coefficients of equation (36a) are readily determined, yielding for this case the forced KdV equation as

$$\zeta_t - c_j\zeta_x + a_2\zeta\zeta_x + \epsilon^2 a_3\zeta_{xxx} = a_4 p_{ax} + a_5 b_x, \tag{49a}$$

where $\zeta = \tilde{\zeta}_1$ for the elevation of the top surface, $\zeta = \tilde{\zeta}_2$ for the interface, and the coefficients a_n's have different values for the two cases. For the top free surface, $\zeta = \tilde{\zeta}_1$, we have, with reference density $\rho_c = \rho_1$,

$$a_2 = 3\left[c_j^2\left(\frac{h_1}{h_2} - 2\right) + h_1\sigma + 1 - \frac{h_1}{h_2}\right]/a_1$$

$$a_3 = \left[-\left(\frac{1}{3} - r\sigma\right)c_j^2 + r\sigma\left(\frac{1+r}{3} - r\sigma\right)\right]/a_1$$

$$a_4 = \left[(1-h_2\sigma)c_j^2 - r\sigma\right]/a_1$$

$$a_5 = +c_j^4/a_1 \,,\quad a_1 = c_j(4c_j^2 - 2) \,. \tag{49b}$$

For the interface, $\zeta = \tilde{\zeta}_2$ also satisfies (49a), except that the coefficients are now given by

$$a_2 = -\frac{3}{(1-\sigma)c_j}\left\{c_j^2\left(\frac{h_1}{h_2} + 1 - 2\sigma\right) - \sigma[(2-\sigma)h_1 - h_2]\right\}/a_1,$$

$$a_3 = -\frac{1}{c_j}\left\{\left(\frac{1}{3} - \sigma r\right)c_j^2 - \sigma r\left(\frac{1+r}{3} - \sigma r\right)\right\}/a_1 \,,$$

$$a_4 = c_j(1-\sigma)h_2/a_1 \,,$$

$$a_5 = (c_j^2 - h_1)c_j/a_1 \,,\quad a_1 = 4c_j^2 - 2 \,. \tag{49c}$$

It is of great practical value to draw the analogy between the motions in a two-layer system and that in a one-layer system according to the forced KdV model. Comparison of the system (49) with (43) establishes their equivalence if their respective counterparts satisfy the following law of correspondence:

$$\zeta = -\frac{3c_j}{2a_2}\zeta^* ,$$

$$x = \left(-\frac{6a_3}{c_j}\right)^{1/2} X ,$$

$$t = \frac{1}{c_j}\left(-\frac{6a_3}{c_j}\right)^{1/2} T , \qquad (50)$$

$$p_a = -\frac{3c_j^2}{4a_2a_4} p_a^* ,$$

$$b = -\frac{3c_j^2}{4a_2a_5} b^* .$$

Thus, to each two-layer case there corresponds a one-layer system according to the scaling rule (50). It is essential to note that the Froude number remains invariant under this rule as the characteristic velocity for the one-layer case is normalized to unity.

We further stress the point that this law of correspondence is also applicable to the system of continuously stratified fluids if the correspondence is sought for any one horizontal plane, $z=z_o$=const. $(0< z_o<h)$ say, at a time, with $\zeta=\zeta(x, z_o, t)$ to the leading term and with $a_n(n=2, 3, 4, 5)$ in (50) replaced by $A_n(z_o)$ given by (39), in which $c=c_j$ and $\phi=\phi_j(z_o)$ refer to the jth normal mode of interest. The numerical results for one-layer systems can thus be used very effectively to predict the behavior of wave motions in stratified fluid systems. Based on this analogy we can therefore draw the conclusion that in stratified systems, disturbances moving with transcritical velocities (with respect to a specific normal mode) will generate a series of solitons surging ahead of the disturbance similar to the phenomenon known for the one-layer case.

This model can be applied to the important and commonly occurring case when the density difference between the upper and lower fluids is small and when the pycnocline is rather thin compared with the other physical length scales so that it can be represented in first approximation by the two-layer model. Then, under the assumption that $\sigma \ll 1$, the internal-wave mode has the eigenvalue (see eqs. 45 and 47) and critical velocity

$$\mu_2 = (r\sigma)^{-1}, \quad c_2 = \sqrt{r\sigma} \quad (r=h_1h_2). \qquad (51)$$

We note that $\mu_2 \gg 1$ and $c_2 \ll 1$ for $\sigma \ll 1$. In this internal-wave mode with $\sigma \ll 1$, the wave elevations in the upper and lower layers, denoted by $\tilde{\zeta}_1=\zeta(x, z=1, t)$ and $\tilde{\zeta}_2=\zeta(x, z=h_2, t)$ respectively, and the horizontal velocities in the two layers, denoted by $\tilde{u}_1$ and $\tilde{u}_2$ respectively, are related by

$$\tilde{\zeta}_1 = -h_2\sigma\tilde{\zeta}_2 , \qquad (52)$$

$$\tilde{u}_1h_1 = -\tilde{u}_2h_2 . \qquad (53)$$

Relation (52) follows at once from (28), (48) and (51) which yield, for $\sigma \ll 1$, $\tilde{\zeta}_1 = \eta/\mu_2$ and $\tilde{\zeta}_2 = -h_1\eta$, whence (52). The relation (53) is obtained by also using (24).

Clearly, (52) shows that the top surface wave is much weaker than the interfacial wave since σ is small. This result will imply vanishing net mass flux across any vertical plane, which is precisely (53). Since the two horizontal velocities are always opposite in direction, the interface is a vortex sheet (whose concentrated vorticity would diffuse if the viscous effects should be taken into account). Since the velocity ratio is inversely proportional to the depth ratio of the two layers, the shallower the shallow layer, the larger will be its horizontal velocity and the greater will be the strength of the interfacial vortex sheet, other parameters being equal.

Furthermore, under the condition of small density difference $(\sigma \ll 1)$ between the two layers, the scaling rule (50), which renders the correspondence to a one-layer KdV system, reduces to the rule:

$$\tilde{\zeta}_2 = [r/(h_1-h_2)]\zeta^* \qquad (r=h_1h_2) ,$$

$$x = \sqrt{r}\, X , \qquad t = T/\sqrt{\sigma} \qquad (54)$$

$$b = [h_2/(h_1-h_2)]\, b^*, \quad p_a = [h_1/(h_2-h_1)]p_a^* .$$

This rule holds when the top surface of the two-layer system is free, as assumed, and in fact also remains valid even if the top surface is rigid, which is expected in view of the negligible ratio of $\tilde{\zeta}_1/\tilde{\zeta}_2$ given by (52), provided the last equation in (54) correlating the forcing pressures is released for the latter case.

Several general conclusions can be drawn from these relations. In the one-layer system, the solitons which are generated periodically to surge ahead of a moving disturbance, are always positive in elevation regardless of whether the forcing is positive or negative (Lee, 1986). By the scaling relation (54), the corresponding interfacial wave is positive or negative according as h_1 is greater or smaller than h_2. This, of course, is expected on physical grounds that solitons in two-layer fluid systems always displace away from the thinner layer into the thicker one.

The specified density difference parameter σ takes part (when $\sigma \ll 1$) only in the time scaling. Therefore, all the other parameters being the same, changes in σ do not alter the wave behavior except with respect to the scaled time.

In the one-layer fluid model, Lee (1985) found that the one-layer surface pressure p_a and the bottom bump b of the same distribution and relative magnitude are exactly equivalent, as shown by (43). For the two-layer systems, however, we see from (54) that the pressure forcing p_a and the bump forcing b have different effects on internal waves. These formulas indicates that if we interchange the values of h_1 and h_2 and at

the same time interchange the top-surface and bottom-bump disturbances, equal but opposite internal waves will result. Furthermore, the effects of bottom bump or top-surface pressure on the generated wave magnitude are found to be inversely proportional to the distance between the forcing and the interface. In fact, if $p_a = b$, we have

$$p_a^*/b^* = -h_2/h_1 \ .$$

Physically, this means that the closer the interface is to one of the two forcing disturbances, the larger the interfacial waves will be, the two disturbances being equal in strength, though acting separately.

Numerical computations for the two-layer system have been carried out for a range of the physical parameters including the disturbance strength b_m and length L (measured relative to the water depth h), density difference σ, upper-to-lower-layer thickness ratio (h_1/h_2), and the Froude number

$$Fr = \frac{U}{c} \qquad (55)$$

where the disturbance is taken to move at a constant speed U, and c is for a specific mode.

In the numerical computations, we first change the KdV equation (38) to the so-called regularized form (Benjamin et al., 1972), which is obtained by using the leading order terms to convert the dispersive term from ζ_{xxx} to ζ_{xxt}/c. As elucidated by Whitham (1974), the regularized form gives the correct dispersive relation for small wavenumber k, yet is superior for numerical calculations because it can effectively curtail numerical errors associated with the grid sizes (large values of k). A finite difference method with a predictor-corrector procedure was adopted. Spatial derivatives were approximated by central differences and temporal derivatives by forward differences, and resulted in a tri-diagonal system of linear algebraic equations. The same window shifting procedure and open-boundary conditions were used as described in Wu & Wu (1982). The calculations were performed on a CRAY X-MP/12 at the Naval Research Laboratory and a typical case took about 7 seconds of CPU time. Further details of the numerical method can be found in Lee (1985) and Zhu (1986).

The numerical calculations are found in satisfactory agreement with the above observation and two examples are presented here (for more examples see Zhu, 1986). The internal waves and wave resistance for a bottom bump moving at Froude number 1 are shown in figure 2, and for a bottom trough (negative bump) in figure 3. The wave resistance is evaluated at fixed t and is defined here in dimensional form as

$$C_R = \frac{1}{\rho_c g h^2} \int p b_x dx \ . \qquad (56)$$

For these computations, we used cosine bump with

$$b(x,t) = \frac{1}{2} b_m \{1 - \cos[\frac{2\pi}{L}(x - x_o + Ut)]\}$$

$$\text{for } (0 < x - x_o + Ut < L) \qquad (57)$$

and $b = 0$ outside this moving region. The dominant parameter influencing the wave behavior is the Froude number, and the numerical results for various Froude numbers will be discussed in detail with the experimental results.

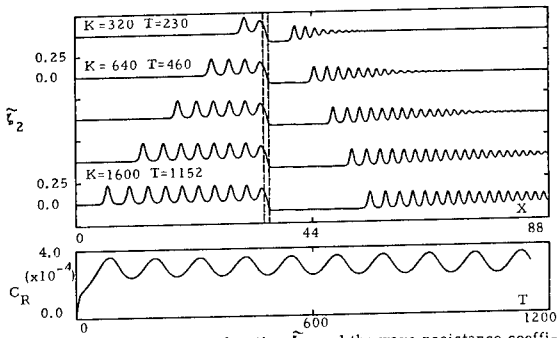


Fig. 2. The interface wave elevation $\tilde{\zeta}_2$ and the wave resistance coefficient C_R for the bottom bump given by the numerical KdV model for the two-layer system. $\tilde{\zeta}_2$, X, T and c_2 are referenced to h and $c_o = \sqrt{gh}$ as units. K is the number of time steps calculated. $h_2 = 0.2$, $\sigma = 0.03$, $L = 1$, $b_m = 0.1$, $Fr = U/c_2 = 1.0$ and $c_2 = 0.069$.

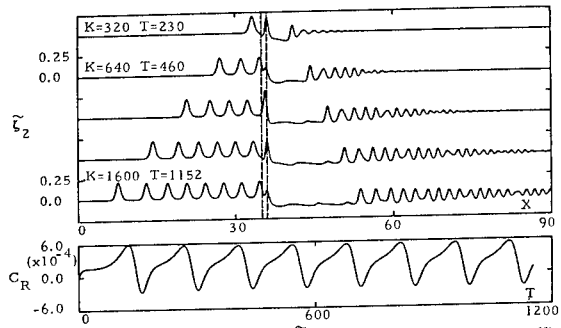


Fig. 3. The interface wave elevation $\tilde{\zeta}_2$ and the wave resistance coefficient C_R for the bottom bump given by the numerical KdV model for the two-layer system. $\tilde{\zeta}_2$, X, T and c_2 are referenced to h and $c_o = \sqrt{gh}$ as units. K is the number of time steps calculated. $h_2 = 0.2$, $\sigma = 0.03$, $L = 1$, $b_m = -0.1$, $Fr = 1.0$ and $c_2 = 0.069$.

EXPERIMENTS

A series of experiments were conducted in a wave tank which is 7.5 meters long, 76 cm wide, 60 cm deep, and is located in the Engineering Science Laboratory at Caltech. A two-dimensional disturbance was fabricated of aluminum and had a circular-arc top surface and a flat bottom. In cross section it was 0.66 cm in height at its midchord and had a chord length of 4.9 cm. The disturbance was supported from an overriding carriage by thin vertical struts along the tank sidewalls and its vertical location was adjusted so that there was a minimum clearance of about 0.05 cm from the tank floor which had an unevenness of less than $\pm$ 0.1 cm over the entire length of the tank. In this way, a two-dimensional bump was closely approximated, which could be moved along the bottom of the wave tank at any

prescribed speed by using an overhead carriage and motor drive system.

The tank was first filled to a desired depth (nominally 6 cm) with tap water. Then a brine solution with a specific density of about 1.03 was slowly fed into the tank bottom using eight feeding tubes located at equal spacing along the tank. With some care, we were able to obtain suitably stratified systems with an upper layer of fresh water, a lower layer of brine, and a narrow mixed layer between them, across which the density increased monotonically from the fresh water to the brine density. Following this procedure we found the resulting system to be quite stable, the pycnocline to be relatively thin, and the demarcation surface between the colorless fresh-water layer and the underlying colored brine to be quite sharp. This sharp layer of separation could be maintained, apparently with negligible growth in thickness due to cross-layer mass diffusion for several hours. The pycnocline was generally about 1.5 cm thick at the beginning of a series of experiments and about 2 cm at the end of the series that usually lasted about four hours.

The density profiles in the rest state were measured by a density probe, which consisted of a centered stainless steel wire of 1/32 inch (0.08 cm) diameter as one electrode, surrounded by a grounded aluminum ring of 0.4 cm inner diameter, 0.1 cm thick, and 0.6 cm in height as the grounded electrode, with both electrodes fixed to a thin Plexiglass support. The immersed part of the central stainless wire above the ring was electrically insulated by a coating of Varsity spray enamel No. 1140. The entire probe was further platinized according to standard chemical methods (Water, 1965) before its use in the experiment. Four 'standard' saline solutions with specific densities accurately set at 1.01, 1.02, 1.03 and 1.04 were prepared and placed in four beakers for calibration in addition to tap water.

A set of one top surface and six internal wave gauges, of resistance type, were used to measure the elevations of both the top surface waves and the internal waves primarily centered about the pycnocline. Four internal-wave gauges (G1, G2, G3 and G4) were fixed relative to the tank and were located at distances of 20ℓ, 40ℓ, 80ℓ and 100ℓ respectively (ℓ being the chord length of the bump; 4.9 cm) along the tank from the starting position of the bump. Two internal-wave gauges moved with the bump and were fixed to the carriage; MG1 was located at 1.8ℓ ahead of the leading edge of the bump and MG2 was held at 2.8ℓ behind the leading edge. All wave gauges were made of parallel stainless wires of various lengths, 1/16 inch (0.16 cm) in diameter, and typically separated by 0.5 cm. For the interfacial wave gauge, the upper part of the parallel wires of the gauge was coated with GC red GLPT insulating varnish so that only the lower uncoated parts of the wires would provide a measurement of the conductivity of the surrounding fluid. During experimental measurements, these conductive parts were always kept below the top surface so that the top surface variation would not affect the interfacial wave gauge signal. The vertical location of the interfacial wave gauges were set such that their conducting parts would pierce through the interface and the top surface wave gauges would be so located as to never reach the interface. In addition, the fixed interfacial wave gauges G1-G4 were specially made by using one wire placed at the center to serve as one end to the bridge circuit, surrounded by four grounded wires connected to the grounded end of the bridge, and further using three tinned copper wires to weld together the conducting parts of the surrounding wires and thus forming a sparse grounded net.

Extensive testing was performed on the internal wave gauges to document their response to both internal waves and changes in density profile. Calibration was done by raising and lowering the gauges by known amounts and measuring the output signal which was taken as the elevation of the mean density, $(\rho_1+\rho_2)/2$. As the pycnocline thickened the gauge sensitivity was found to decrease slightly. Thus, after every four experimental runs, a selective withdrawal of fluid from the pycnocline was performed, thereby making the pycnocline effectively thinner. Accordingly, the total depth of the stratified water was slightly reduced. The wave gauges were calibrated and the density profile measured before and after each selective withdrawal, and the calibration most immediate to an experiment was used to scale the data acquired from that run. Additional error was introduced into the internal wave measurements, because the pycnocline may vary slightly in its thickness during the course of an experiment. To estimate this error, we compared the gauge calibrations for the thinnest and thickest pycnocline and estimated the overall uncertainty in locating the internal wave elevation to be about $\pm$ 2 mm. More details on the experimental procedures are available in Zhu (1986).

RESULTS AND DISCUSSION

A typical density profile for the stratified fluid in our experiments is shown in figure 4, where the data points are curve-fitted, by the method of least-square errors, to a hyperbolic tangent function

$$\rho_o(z)=\frac{1}{2}(\rho_1+\rho_2)+\frac{1}{2}(\rho_1-\rho_2)\tanh k(z-h_2). \qquad (58)$$

Using this curve, the coefficients of the KdV equation and c_2, the eigenvalue (or rather the characteristic speed) of the first internal wave mode was obtained from numerical computation of the eigenvalue problem (29); for details see Zhu (1986). The eigenfunction corresponding to the first internal wave mode has only one interior zero at $z=0.996$, which is very close to the undisturbed free surface (at $z=1.0$). Since the wave elevation of any initially horizontal level is proportional to the eigenfunction according to (37), and since the eigenfunction is very small at the top surface,

the waves on the top surface are negligibly small. For this internal-wave mode, the eigenfunction reaches a maximum at a point slightly above the level of the mean density and thus the largest wave amplitudes will occur at this location. Furthermore, other numerical results indicate that c_2 decreases (from $c_2 = 0.061$ for the density distribution shown in figure 4) as the pycnocline becomes thicker. In addition, the eigenfunction $\phi_3(z)$ corresponding to $c_3 = 0.02$ for the second internal-wave mode is included in figure 5; it has two interior zeros at $z = 0.252$ and at $z = 0.995$ and has two extrema.

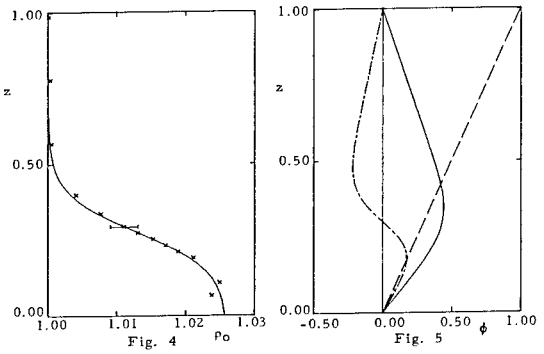


Fig. 4 Fig. 5

Fig. 4. A typical density distribution measured in a stratified fluid at rest (shown with x); the solid curve is given by eq. (58) with $\rho_1=1$, $\rho_2=1.026$, $k=7.78$, and $h_2=0.278$.

Fig. 5. The first three eigenfunctions calculated for the stratified fluid density distribution shown in figure 4; – – – the first mode; —— the second mode; –·–·– the third mode.

The experimental and numerical results are compared in order of increasing Froude number in figures 6-11. The upper part of each figure depicts two snapshots of the numerical results of the internal wave elevation evaluated at $z = h_2$. The lower part presents the experimental data, recorded from the internal wave gauges, and the corresponding numerical results plotted together for comparison (solid lines give numerical results and dashed lines, experimental data). Although the selection withdrawal causes some slight changes in the specific density-difference parameter σ, the position of the mean density contour (originally at $z = h_2$) and the total water depth, which in turn after the strength of the disturbance b and nondimensional bump chord length L, the predominant parameter, however, is the Froude number, which varies from 0.66 in figure 6 to 1.18 in figure 11. In all cases, the top surface remained nearly flat, varying less than 0.2 mm, and this data has been omitted from the plots.

These results show satisfactory qualitative agreement between theory and experiment for all the main features observed for internal runaway solitons. At low Froude numbers, the trailing waves are quite large and have a mean value very near the undisturbed depth of the maximum $\rho_o'(z)$ initially at $z = h_2$. The upstream-running internal waves are then small but the period of generation is short. With increasing Froude number, the generated

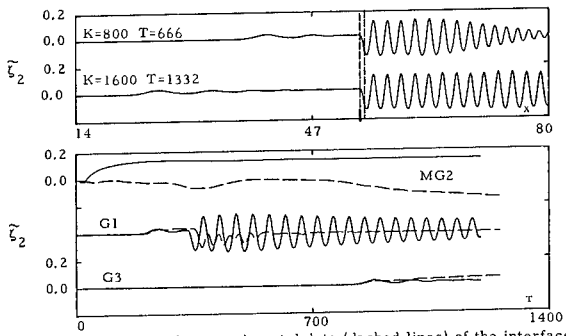


Fig. 6. Comparison of the experimental data (dashed lines) of the interface (or pycnocline) elevations with the numerical solutions (solid curves) given by the KdV model for a continuously stratified fluid system. ζ_2, X, T, and c_2 are referenced to h and $c_o=\sqrt{gh}$ as units; K is the number of time steps calculated; $Fr=0.66$, $h_2=0.28$, $\sigma=0.025$, $L=0.67$, $b_m=0.09$, $c_2=0.061$.

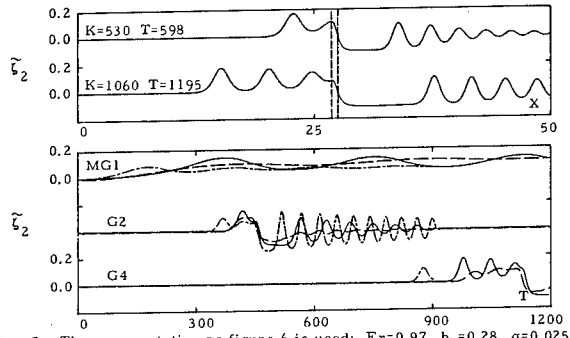


Fig. 7. The same notation as figure 6 is used; $Fr=0.97$, $h_2=0.28$, $\sigma=0.025$, $L=0.67$, $b_{max}=0.09$, $c_2=0.061$. Dash-dot lines denote the corresponding numerical results given by the KdV equation for two-layer-fluid systems.

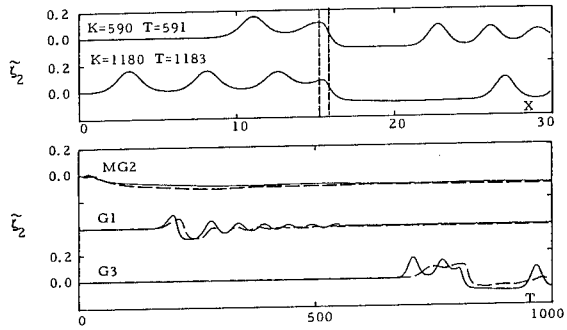


Fig. 8. The same notation as figure 6 is used; $Fr=0.985$; $h_2=0.24$, $\sigma=0.03$, $L=0.61$, $b_{max}=0.083$, $c_2=0.062$.

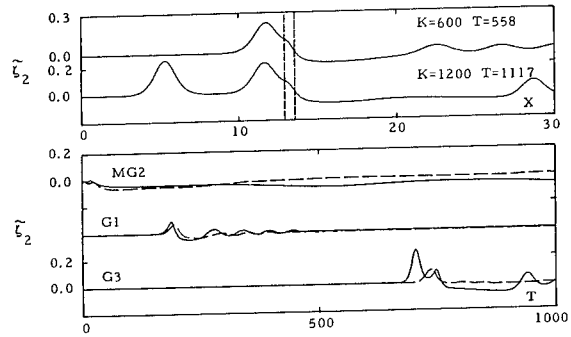


Fig. 9. The same notation as figure 6 is used; $Fr=1.09$; $h_2=0.27$, $\sigma=0.027$, $L=0.65$, $b_{max}=0.087$, $c_2=0.064$.

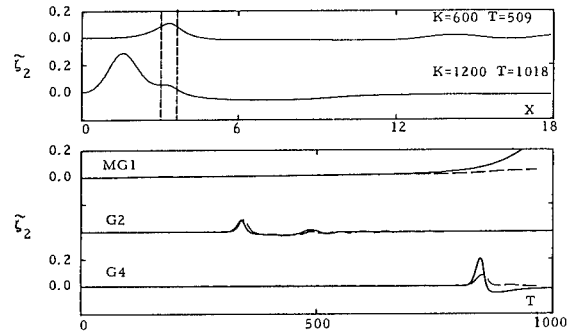


Fig. 10. The same notation as figure 6 is used; Fr=1.16; h_2=0.24, σ=0.03, L=0.61, b_{max}=0.083, c_2=0.062.

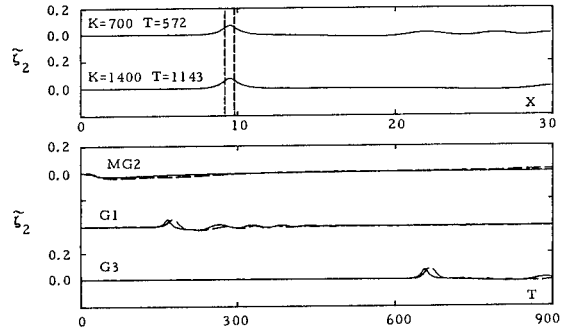


Fig. 11. The same notation as figure 6 is used; Fr=1.18; h_2=0.27, σ=0.03, L=0.61, b_{max}=0.083, c_2=0.064.

upstream-running internal solitons become larger in amplitude and the period of generation increases accordingly, until finally no upstream internal waves are generated when a certain supercritical Froude number is reached (about 1.2). The presence of a depressed and nearly uniform region immediately behind the bump followed by a train of trailing cnoidal-like waves was also found in satisfactory agreement between experiments and numerical computations.

To evaluate the distinction between a continuous stratification and its approximate representation by a step-function distribution, the limiting case of the KdV model for a very sharp density profile was computed. The results of this two-layer model (with densities and interfacial position chosen to best approximate the experiment) are plotted in figure 7. Clearly, the two-fluid model predicts a shorter generation period than both the continuously stratified model and the experimental measurements. This indicates that details of the density stratification are important in making accurate predictions of internal wave generation periods and other physical quantities.

Quantitatively, most of the cases investigated show that the internal solitons so generated have smaller amplitudes and larger generation periods observed in the experiments than those predicted by numerical calculations. Since our theoretical model is inviscid, the viscous effects can not be readily accounted for without having these models appropriately modified and these effects are thought to be a most likely cause of the discrepancies between theory and experiment. To give a crude estimate of the viscous effects, the decay formula for free internal solitons in a two-layer system, given by Leone, Segur & Hammack (1982), was used to calculate the decay of the first soliton in figure 7, with the kinematic viscosity of water taken as 0.01 cm^2/s. If the measured amplitude of the first soliton at G2, ζ=0.1, is taken as the initial amplitude, the calculated amplitude when this soliton reaches the G4 position, after traveling 60ℓ, is about 0.038, whereas its recorded amplitude is about 0.077. Thus, in this case, the estimated decay rate for the leading solitary wave is considerably stronger than that measured. There are two possible explanations for this difference. First, the decay rate may be higher in two-layer systems than in continuously stratified fluids, even though they are equivalent by an analogy which precludes an account of the viscous effects. The truth of this variance between the two categories of fluid systems remains to be seen. Second, the external forcing may still be influencing the wave, contributing to its growth (probably at a rate slower than that without the viscous effects) and thus reducing its decay rate. Some fine structures of the flow field were observed about the position of the first trailing wave crest during the experiment. They are believed to be related to wave breaking, which in turn enhanced the viscous mixing process, and may contribute to the discrepancies between the experimental data and the numerical results in the trailing wave region. To achieve definitive clarification of the viscous effects on the internal wave generation in continuously stratified fluids, further research is required.

Acknowledgments

This work was jointly sponsored by ONR Contract N00014-85-K-0636, NR 655-005, and NSF Grant MSM-8118424, A03. Numerical results presented here were partly performed on a CRAY X-MP/12 at the Naval Research Laboratory, Washington, D.C. and partly carried out with the Computing Support Services at Caltech. We are indebted to Raymond Mak for his assistance in conducting the experiments. We also appreciate very much the commendable help of Helen Burrus.

REFERENCES

Akylas, T.R. 1984 On the excitation of long nonlinear water waves by a moving pressure distribution. J. Fluid Mech. vol. 141, pp. 455-466.

Baines, P.G. 1977 Upstream influence and Long's model in stratified flows. J. Fluid Mech. vol. 82, pp. 147-159.

Baines, P.G. 1979 Observation of stratified flow over two-dimensional obstacles in fluid of finite depth. Tellus. vol. 31, pp. 351-371.

Benjamin, T.B. 1966 Internal waves of finite amplitude and permanent form. J. Fluid Mech. vol. 25, pp. 241-270.

Benjamin, T.B. 1967 Internal waves of permanent form in fluids of great depth. J. Fluid Mech. vol. 29, pp. 559-592.

Benjamin, T.B., F.R.S., Bona, J.L. and Mahony, J.J. 1972 Model equations for long waves in nonlinear dispersive systems. Phil. Trans. Roy. Soc. London, vol. 272, pp. 47-78.

Benney, D.J. 1966 Long non-linear waves in fluid flows. J. Math. & Phys. vol. 45 pp. 52-53.

Chereskin, T.K. 1983 Generation of internal waves in Massachusetts Bay. J. Geophys. Res. vol. 88 (c4), pp. 2649-2661.

Cole, S.L. 1985 Transient waves produced by flow past a bump. Wave Motion. vol. 7, pp. 579-587.

Eriksen, C.C. 1978 Measurements and models of fine structure, internal gravity waves, and wave breaking in the deep ocean. J. Geophys. Res. vol. 83, pp. 2989-3009.

Ertekin, R.C. 1984 Soliton generation by moving disturbances in shallow water: Theory, computation and experiments. Ph.D. Dissertation, University of California, Berkeley.

Ertekin, R.C., Webster, W.C. and Wehausen, J.V. 1985 Proc. 15th Symp. on Naval Hydrodynamics. National Academy of Sciences, Washington, D.C., pp. 347-364.

Farmer, D.M. and Armi, L. 1986 Maximal two-layer exchange over a sill and through the combination of a sill and contraction with barotropic flow. J. Fluid Mech., vol. 164, pp. 53-76.

Farmer, D.M. and Smith, J.D. 1980 Tidal interaction of stratified flow with a sill in Knight Inlet. Deep-Sea Res. vol. 27A, pp. 239-254.

Gargett, A.E. 1976 Generation of internal waves in the Strait of Georgia, British Columbia. Deep-Sea Res. vol. 23, pp. 17-32.

Gilreath, H.E. and Brandt, A. 1985 Experiments on the generation of internal waves in a stratified fluid. AIAA J. vol. 23, pp. 693-700.

Grimshaw, R.H.J. and Smyth, N. 1985 Resonant flow of a stratified fluid over topography. Res. Rep. No. 14. Dept. of Math., Univ. of Melbourne, Australia.

Halpern, D. 1971 Observations on short-period internal waves in Massachusetts Bay. J. Marine Res. vol. 29, pp. 116-132.

Hammack, J.L. 1980 Baroclinic tsunami generation. J. Phys. Oceano. vol. 10, pp. 1455-1467.

Haury, L.R. 1979 Tidally generated internal wave packets in Massachusetts Bay. Nature. vol. 278, pp. 312-317.

Huang, D-B, Sibul, O.J., Webster, W.C., Wehausen, J.V., Wu, D-M, & Wu, T.Y. 1982 Ship moving in the transcritical range. Proc. Conf. on Behavior of Ships in Restricted Waters. vol. 2, 26.1-26.12, Varna, Bulgaria.

Hurdis, D.A. and Pao, H.P. 1975 Experimental observation of internal solitary waves in a stratified fluid. Phys. Fluids. vol. 18, pp. 385-386.

Joseph, R.J. 1977 Solitary waves in a finite depth fluid. J. Phys. A, Math. Gen., vol. 10, pp. L225-L227.

Kao, T.W., Pan, F-S and Renouard, D. 1985 Internal solitons on the pycnocline: generations, propagation, and shoaling and breaking over a slope. J. Fluid Mech. vol. 159, pp. 19-53.

Keulegan, G.H. 1953 Characteristics of internal solitary waves. J. Res. Natl. Bur. Stand. vol. 51, pp. 133-140.

Koop, C.G. and Butler, G. 1981 Internal solitary waves in a two fluid system. J. Fluid Mech. vol. 112, pp. 225-251.

Kubota, T., Ko, D.R.S. and Dobbs, L.D. 1978 Weakly-nonlinear, long internal gravity waves in stratified fluids of finite depth. J. Hydronaut. vol. 12, pp. 157-165.

Lansing, F.S. and Maxworthy, T. 1984 On the generation and evolution of internal gravity waves. J. Fluid Mech. vol. 145, pp. 127-149.

Lee, C-Y, and Beardsley, R.C. 1974 The generation of long nonlinear internal waves in a weakly stratified shear flow. J. Geophys. Res. vol. 79, pp. 453-462.

Lee, S-J. 1985 Generation of long water waves by moving disturbances. Ph.D. Thesis, California Institute of Technology, Pasadena, CA.

Lee, S-J. 1986 Personal communication.

Leone, C., Segur, H. and Hammack, J.L. 1982 Viscous decay of long internal solitary waves. Phys. Fluids. vol. 25, pp. 942-944.

Liu, A.K., Kubota, T. and Ko, D.R.S. 1980 Resonant transfer of energy between nonlinear waves in neighboring pycnoclines. Studies Appl. Math. vol. 63, pp. 25-45.

Locke, L. 1980 Waves beneath the sea. Lamp. Summer 1980. Publ., Exxon Corp.

Long, R.R. 1956 Solitary waves in the one- and two-fluid systems. Tellus, vol. 8, pp. 460-471.

Long, R.R. 1970 Stratified flow. The NCFMF Book of Film Notes. 1972 The MIT Press.

Maxworthy, T. 1979 A note on the internal solitary waves produced by tidal flow over a three-dimensional ridge. J. Geophys. Research. vol. 84, pp. 338-346.

Mei, C. C. 1986 Radiation of solitons by slender bodies advancing in a shallow channel. J. Fluid Mech. vol. 162, pp. 53-67.
Ono, H. 1975 Algebraic solitary waves in stratified fluids. J. Phys. Soc., Japan. vol. 39, pp. 1082-1091.
Osborne, A. R. and Burch, T. L. 1980 Internal solitons in the Andaman Sea. Science. vol. 208, pp. 451-460.
Osborne, A. R., Burch, T. L. and Scarlet, R. I. 1978 Influence of internal waves on deep-water drilling. J. Petro. Tech., vol. 30, pp. 1497-1504.
Perry, R. B. and Schimke, G. R. 1970 Large-amplitude internal waves observed off the Northwest Coast of Sumatra. J. Geophys. Res. vol. 70, pp. 2319-2324.
Peters, A. S. and Stoker, J. J. 1960 Solitary waves in liquids having nonconstant density. Comm. Pure Appl. Math. vol 13, pp. 115-164.
Sun, M. -G. 1980 Personal communication with photos, paper published 1985 in Proc. 60th Anniv. Volume of Zhongshan University, Guangzhow, China.
Smyth, N. 1986 Modulation theory solution for resonant flow over topography. Dept. of Math. Research Rep. 3-1986, University of Melbourne, Melbourne, Australia.
Water, I. 1965 Standard methods for the examination of water and wastewater.
Whitham, G. B. 1974 Linear and Nonlinear Waves. John Wiley & Sons, Inc., New York, N. Y.
Wu, T. Y. 1966 Radiation and dispersion of internal waves. Proc. 6th Symp. Naval Hydrodynamics, Washington, D. C.
Wu, T. Y. 1984 New birth to runaway solitons. Symp. on frontier in applied mechanics and biomechanics, UCSD, La Jolla, CA
Wu, T. Y. 1986 On generation of solitary waves by moving disturbances. IUTAM Symposium on "Fluid Mechanics in the Spirit of G. I. Taylor" Cambridge, England, 23-29 March 1986.
Wu, T. Y. and Mei, C. C. 1967 Two-dimensional gravity waves in a stratified ocean. Phys. Fluids, vol. 10, pp. 482-486.
Wu, D-M and Wu, T. Y. 1982 Three-dimensional nonlinear long waves due to moving surface pressure. Proc. 14th Symp. Naval Hydrodyn., National Academy Press, Washington, D. C., pp. 103-125.
Yih, C-S. 1965 Dynamics of nonhomogeneous fluids. Macmillan, New York.
Yih, C-S and Guha, C. R. 1955 Hydraulic jump in a fluid system of two layers. Tellus. vol. 7, pp. 358-366.
Zhu, J. 1986 Internal solitons generated by moving disturbances. Ph. D. Thesis, California Institute of Technology, Pasadena, CA.
Ziegenbein, J. 1969 Short internal waves in the Strait of Gibraltar. Deep-Sea Res. vol. 16, pp. 358-366.
Ziegenbein, J. 1970 Spatial observations of short internal waves in the Strait of Gibraltar. Deep-Sea Res. vol. 17, pp. 867-875.

DISCUSSION

Michael B. Wilson,
David Taylor Naval Ship R&D Center

For the case of the forcing by a "negative bump" or bottom depression, wave resistance results are included in Figure 3. It is seen that the oscillating variation of C_R shows some minus values. Could you comment on the feature of negative resistance in this case. Is the mean value of C_R positive?

Reply -

We thank Dr. Wilson for his comments. The example of negative forcing may be obtained by the motion of a trough along an otherwise flat bottom or (by transformation of reference frame) the uniform flow of shallow water over a fixed transverse trough. For small disturbances this is also equivalent to the application of a moving suction (negative) pressure on the free surface. As pointed out by Dr. Wilson, in the case of negative forcing, the wave resistance may take on negative values during a part of the cycle (figure 3). This means that the waves are then actually pushing the disturbance forward and hence generating thrust during this part of the cycle. The mean value of the wave resistance in all numerical calculation are however always positive, which agrees with general energy considerations for flows starting from an initially undisturbed free surface. This is easily demonstrated by multiplying equation (38) by ζ and integrating from $x = -\infty$ to $+\infty$,

$$\frac{d}{dt}\left[\int_{-\infty}^{+\infty} \zeta^2 \, dx\right] = A_4(h)\, D = A_4(h)\,(D_p + D_b)$$

where D_p and D_b are the drag force acting on the surface pressure and the bottom topography respectively and $A_4(h) \geq 0$ is evaluated at $z = h$ and is given by (39). Thus, the time average drag is

$$\bar{D} = \frac{1}{T}\int_0^T D \, dt = \frac{1}{T\,A_4(h)}\left[\int_{-\infty}^{+\infty} \zeta^2 \, dx\right]_{t=0}^{t=T}$$

which is always greater than or equal to zero for motions starting with an initially undisturbed free surface ($\zeta = 0$ for $t = 0$). This result is expected since the perpetual motion of the disturbance is not possible.

Microbubble Drag Reduction

C.L. MERKLE, S. DEUTSCH, S. PAL and J. CIMBALA

Applied Research Laboratory, Pennsylvania State University, U.S.A

W. SEELIG, AVCO Systems Inc.

ABSTRACT

Photographic and optical surveys of microbubble boundary layers are presented. The results show that the outer edge of the bubble cloud diffuses away from the wall as the bubbles are swept downstream. The plate-on-bottom orientation contains a bubble-free region near the wall that cannot be discerned for the plate-on-top configuration. Skin friction measurements made when the bubble-free region extends to y^+=100 show there is no longer any C_f reduction present suggesting bubbles are not effective when they are in the outer portion of the boundary layer. Bubble size measurements show sizes from 200 to 1100 μm. Bubble size increases with airflow and decreases with freestream velocity. Bubble coalescence with distance from the injection section appears to be significant.

INTRODUCTION

Methods for decreasing the drag of hydrodynamic vehicles are of paramount interest because they translate directly into improved performance and more efficient operation. In general, the drag on a vehicle is composed of viscous-, pressure-, and wave-drag components. For many present-day hydrodynamic vehicles it is the viscous drag that dominates and, for this reason, the present study is focused on the control of this component of the drag. The viscous drag on a moving vehicle arises because of the net momentum added to the fluid as the vehicle passes through. Under high Reynolds number conditions this momentum addition occurs in a thin region near the surface of the vehicle. The character of this boundary layer may be laminar or turbulent depending on the conditions present (including the size, shape and speed of the vehicle).

Numerous previous studies have also looked at the control of viscous drag. These studies may be subdivided into laminar flow control (LFC) and turbulent flow control (TFC) concepts. Laminar flow control studies have included suction, body shaping, and surface heating (surface cooling in air). The general aim of these LFC concepts is to delay transition to turbulence, hence taking advantage of the inherently lower skin friction in a laminar boundary layer. Turbulent flow control concepts have attempted to mitigate the increased momentum transfer that is characteristic of turbulent boundary layers by controlling the turbulence or the "events" that give rise to the turbulence. The various TFC concepts that have been studied include the addition of small quantities of long-chain polymers, the use of special surface geometries such as riblets, the insertion of mechanical devices such as LEBU's into the boundary layer; and the use of viscoelastic surface coatings. The volume by Hough[1] and the review papers by Bushnell[2,3] and co-workers represent recent summaries of much of the work in both the LFC and TFC areas.

The present paper deals with an alternative concept for controlling turbulent shear stress that has not been discussed in the summaries cited above. Here, we are concerned with the introduction of a large number of small bubbles ("microbubbles") into a turbulent boundary layer. Because this concept relies upon the presence of two phases, its application is limited to liquid boundary layers. Investigations into microbubble drag reduction have been limited, but the experiments to date have been strongly encouraging.

Work on microbubbles started with McCormick and Bhattacharya's drag measurements on a towed body of revolution[4]. These measurements were followed by a series of skin friction measurements on flat plates by Soviet researchers[5-8] and more recently by similar experiments in our laboratory[9-12]. A summary of much of this work is given in Ref. 13, and preliminary attempts at

modeling the phenomena are given in Refs. 14 and 15.

The McCormick-Bhattacharya experiments showed that the introduction of bubbles into the boundary layer could lead to a reduction in the total drag of a vehicle. Because of the nature of their experiment, they were unable to separate the reduction into skin friction and form drag components. In addition, it appears that the bubbles may also have affected the transition location, thus further complicating the interpretation of their results.

The flat plate experiments initiated by the Soviets[4-8] were designed to give more detailed understanding of the manner in which the bubbles affected skin friction. Their results showed that local C_f reductions of as much as 90% could be obtained for a wide range of flow conditions and for injection surfaces with various porosities. In general, they showed that the C_f reduction increased with airflow rate until some maximum "saturation" level was reached. These results were for the most part corroborated by the measurements in our laboratory[9-12] and were extended in numerous ways including wider velocity ranges, different gravitational orientations, and additional types and sizes of porous surfaces. Both flat plate and axisymmetric geometries were tested. The most significant aspects of both sets of measurements is that they demonstrate unequivocally that the introduction of microbubbles reduces skin friction.

Although the effectiveness of microbubbles has been demonstrated, the mechanism that leads to this reduction is only poorly understood. In particular, the interaction between the bubbles and the boundary layer has not been studied extensively. As a step in providing this necessary insight, the present paper presents a photographic survey of the microbubble boundary layer, some measurements of the location and trajectory of the bubble cloud, and some preliminary measurements of the bubble sizes that have been obtained from the photographs. In addition, some new local C_f measurements are also presented.

EXPERIMENTAL FACILITY

The results given in the present paper were taken on a flat plate mounted in the round test section of the 12-inch water tunnel at The Pennsylvania State University. The previously reported flat plate measurements[9-11] were made on one wall of the rectangular test section of the same tunnel. Because of the limited visual access in the rectangular test section, detailed observations of bubble sizes, dynamics and coalescence rates and of bubble cloud trajectories could not be made. The round test section allows much improved optical access and for this reason a flat plate has been constructed for this test section.

The flat plate is 1100 mm in length, is centered in the test section, and spans the width of the tunnel. Air is injected through a 76 x 51 mm porous section flush-mounted on the surface of the plate. The leading edge of the porous section is 254 mm downstream of the leading edge of the plate as shown in Fig. 1. The porous material used for these experiments was a 3-mm thick piece of sintered stainless steel. This material is manufactured for use as a filter and is nominally rated as a 40 μm filter. Because of the manufacturing process, the pore sizes are irregular and the flow passages are winding and tortuous.

The tunnel is capable of operation over a range of velocities (4-18 m/s) and pressures (0.5 to 3.0 atm). In addition, the test section can be rotated, thus enabling the study of gravitational effects. With the plate mounted so that the injection section is on the upper side (hereafter referred to as the "plate-on-bottom" position) buoyancy tends to cause the microbubbles to rise out of the boundary layer. By rotating the test section through 180° (this position will hereafter be referred to as the "plate-on-top" position) the opposite buoyant effect is induced. The relative sensitivity to buoyancy is, of course, dependent on the tunnel velocity. Our experiments range from high speeds where buoyancy has no effect to low speeds where it becomes dominant.

The tunnel also has a 0.2 m^3/s bypass system that removes a substantial fraction of the recirculating water from the closed circuit tunnel and replaces it with fresh water, a process necessary for keeping the freestream relatively air-free.

PHOTOGRAPHS OF BUBBLE FLOWFIELD

As air is injected into the boundary layer through the porous injection section, the air is quickly broken up into bubbles which are then swept downstream by the fluid. Some representative photographs of the bubble cloud at low air injection rates are given in Figs. 2-5. Because of the bubble densities, no photographs at high airflow rates are given. These photos are for a flow velocity of 4.6 m/s and include side and top views of the bubbles for the plate-on-bottom configuration. The photos were taken with a 35 mm camera using a 55 mm Nikon lens and Kodak Tri-X, 20 exposure film. A stroboscope with a flash duration of 40 ms was used for lighting. Top lighting was used for both the side and top views. The location of the photos with respect to the

injection section is shown on the schematic in Fig. 1.

Figures 2 and 3 show the bubble cloud at an airflow rate that produces a maximum skin friction reduction of roughly 10% (C_f/C_{fo} = 0.90). Figure 2 shows a side view 450 mm downstream of the injection section while Fig. 3 is a top view at the same location. For reference, the approximate thickness of the undisturbed boundary layer is given on Fig. 2. At this location, the edge of the bubble cloud fluctuates between one and two delta (undisturbed) in a manner reminiscent of typical flow visualizations of turbulent boundary layers. A major feature of both the side and top views is the presence of a few very large bubbles. Photos taken at airflow rates below those that produce C_f reduction (see Figs. 4 and 5) show a complete absence of such large, distorted bubbles. The large bubbles at the higher flow rate may be the result of bubble coalescence because the bubbles are so close together or may be formed at injection. Other photographs (not included here) show that large, irregular bubbles are absent at higher speeds. Although the widely separated bubble field shown in Fig. 5 is not representative of drag reducing conditions, it is useful for studying the characteristics of individual bubbles.

MEASUREMENTS OF THE BUBBLE CLOUD LOCATION AND TRAJECTORY

The characteristics of the bubble cloud including the bubble sizes and size distributions, the bubble concentration profile across the boundary layer, and the bubble cloud trajectory are clearly of interest for understanding the microbubble-laden boundary layer. Measurements of these quantities are, however, very difficult because of the high bubble concentrations (such as those shown in Fig. 2) that make optical access extremely difficult. As a means of getting a first-order estimate of the bubble cloud location, a laser transmission measurement was devised. A schematic of this measurement is shown in Fig. 6. A 1 mm diameter beam from a low power He-Cd (325 nm) laser was passed through the bubble cloud perpendicular to the flow and was received on the opposite side of the tunnel by a photomultiplier. The combined laser-photomultiplier system was mounted on a precision jack that allowed traversing in the distance normal to the plate surface. The movement of the beam was monitored by a dial gage with 0.0254 mm gradations. To determine the location of the bubble cloud, the laser beam was typically traversed from the plate surface to the outer edge of the bubbles. The strength of the transmitted beam was converted to a voltage by the photomultiplier. In a typical bubble cloud at concentration levels corresponding to significant C_f reduction, the laser beam was totally obscured by the bubbles and the photomultiplier output dropped (nearly) to zero. As the beam neared the outer edge of the bubble cloud, beam transmission increased toward its level in clear water (no bubbles) and the photomultiplier voltage increased accordingly.

In principle, the attenuation of the laser beam could provide a quantitative measure of the integrated bubble concentration along the line of sight of the beam. Such quantitative measurements are, however, virtually impossible because of the absence of a calibration procedure. The laser beam attenuation is influenced by both absorption and scattering with scattering presumably being the dominant effect. With bubble diameters ranging from 200 μm and upward as described later, Fraunhofer and Fresnel diffraction plus reflection all take place. Bouguer's law[16] states that the intensity of the transmitted beam depends upon the path length, the bubble size distribution and the number density of bubbles as,

$$i'_\delta(s) = i'_\delta(0) \exp\left[-\int \sigma_{s\delta}(s^*)ds^*\right]$$

where $i'_\delta(0)$ = intensity at x = 0
$i'_\delta(s)$ = intensity at x = s
$\sigma_{s\delta}$ = scattering coefficient
$= s_\delta N_s$

where s_δ = average scattering cross section
N_s = number density of the particles

The lack of information on bubble sizes, number densities, and the average scattering cross sections prohibits the construction of actual bubble density profiles. In addition, the fact that the beam was totally obscured would make such a determination difficult even if a calibration were available, although this could possibly have been rectified by reducing the span-wise extent of the bubble injection section. Because of these limitations, the laser transmission measurements were limited to qualitative measurements. Such information does, however, allow us to record for the first time the location of the bubble cloud. A number of measurements of this type are presented below.

Laser transmission measurements were made at three locations and at two velocities for four air injection rates. Both plate-on-top and plate-on-bottom measurements were made and are compared below. The three locations were 76 mm, 203 mm and 356 mm, respectively, downstream of the leading edge of the injection section as shown on Fig. 1. The two velocities were 4.7 and 10.7 m/s. These conditions correspond to Reynolds numbers (based on

distance from the plate leading edge) of 1.5 and 3.6 million at the upstream location and 2.8 and 6.5 million at the downstream location. The four airflow rates used were 0.5×10^{-4}, 1.4×10^{-4}, 2.8×10^{-4}, and 4.6×10^{-4} m^3/s. For convenience, these airflows will be referred to as airflow rates I-IV, respectively. The amount of C_f reduction corresponding to these airflows has been determined from hot film measurements made at these same locations. The results of these measurements for airflow rates of interest to this study are shown in Figs. 7 and 8 on which these four specific airflow values are marked. Note that at the higher velocity, C_f/C_{fo} continues to decrease until the airflow is some four times larger than that shown on Fig. 8. For convenience, the values of C_f/C_{fo} for each wall location and airflow rate are summarized in Table I. Detailed comparison of these initial C_f measurements in this new flat plate facility with previous measurements in the previous facility[9-11] have not been made, but it is noted that they are at least qualitatively similar.

TABLE I

Airflow	Airflow Rate (m^3/s)	C_f/C_{fo}			
		Velocity = 4.6 m/s		Velocity = 10.7 m/s	
		76 mm (Location)	356 mm (Location)	76 mm (Location)	356 mm (Location)
I	0.5 x 10-4	0.98	1.0	0.97	1.0
II	1.4 x 10-4	0.93	1.0	0.94	1.0
III	2.8 x 10-4	0.84	0.98	0.90	0.98
IV	4.6 x 10-4	0.30	0.93	0.87	0.96

Plate-on-Bottom Laser Transmission Profiles

Laser transmission measurements for the plate-on-bottom configuration are given in Figs. 9-12 for the upstream and downstream measurement stations. The abscissa on these figures represents the distance normal to the surface while the ordinates represent the photomultiplier voltages. The results of six traverses are shown on each figure. The four traverses corresponding to airflow rates I-IV are bounded by two reference traverses. The constant, near-zero voltage on each figure corresponds to the photomultiplier reading with the laser beam turned off. Ideally, this voltage should be zero, but the small voltages shown were generated by minor room-light leakage into the system. The nearly constant high voltage shown on each figure is the laser transmission through clear water. Fluctuations in this upper voltage level are mostly associated with imperfections in the (low-quality) tunnel windows. These fluctuations with distance from the surface were quite repeatable and are not thought to impact the present measurements. In general, the photomultiplier voltage generated when the beam is transmitted through a high bubble concentration region will correspond to the voltage generated when the beam is turned off (the beam is totally obscured), and, of course, the voltage will approach the clear water voltage as the beam emerges from the top edge of the bubble cloud.

Figure 9 shows laser transmission traverses for the low speed (4.6 m/s) condition at the nearest (76 mm) measurement section. In general, all traverses rise from "zero" transmission near the wall (the bubble cloud is optically thick) to full transmission at the edge (attenuation drops to zero in the clearwater region outside the bubble cloud). Comparison of the four airflow rates shows that this transition occurs further away from the plate as the airflow is increased. This implies that the bubble cloud extends farther from the wall at higher airflow rates. The increased volume of bubbles is accommodated by encompassing a larger fraction of the boundary layer, but it is also likely that the local bubble concentration near the wall also increases as the airflow rate is increased. The results at the lowest airflow rate show the bubble cloud remains translucent at this concentration. The slightly increased transmission right at the wall is the result of gravitational motion of the bubbles away from the surface as is seen more clearly later.

Figure 10 shows similar transmission measurements at the near-injector location for a velocity of 10.7 m/s. These results are qualitatively like those at 4.6 m/s. The partial transmission and the increase in intensity near the wall are again seen at the low airflow rate (I), but in general the transmission rises from zero to 100% as the laser beam is traversed through the bubble cloud. The major difference between these two velocity cases is that the bubble cloud is thinner at the higher velocity (Fig. 10). There are two major reasons for this. The first is because the convection time is shorter for the faster velocity so that bubble movement by buoyancy, diffusion and turbulent convection is decreased. The second is that although the volumetric flow rate of air is the same for the two cases, the volumetric ratio of airflow to water flow is smaller at the higher speed because of the increased volumetric flow rate of water. Thus, the relative concentration of bubbles is smaller at the higher speed.

Corresponding transmission measurements at the farthest downstream injection section are shown in Fig. 11 for the 4.6 m/s case and Fig. 12 for the 10.7 m/s case. The increased distance from the injection section has caused major changes in the transmission profiles at both speeds. At the lowest airflow rate, the cloud has diffused considerably. The minimum transmission is about 60% here. Even at the highest airflow rate, some laser light is still transmitted. In addition, the bubble concentration near the surface is virtually zero at all airflow rates. Visual inspection at all plate-on-bottom conditions

showed a distinct clear water region between the bubble cloud and the plate that is large enough to be detected by the 1 mm laser beam at 4.6 m/s. Finally, the gradients near the outer edge are also much less steep indicating the outer edge of the bubble cloud is becoming less well-defined. This major difference between the near-injector location and the downstream location is primarily caused by buoyancy although bubble diffusion and turbulent convection effects are also present. In this regard, it is noted that buoyancy would not only tend to move the centroid of the bubble cloud away from the surface, but it would also tend to diffuse and thicken the cloud because the larger bubbles would rise much faster than the smaller ones. This argument is reinforced later by our plate-on-top measurements at the same location.

The effects of increasing the velocity at this same downstream station can be seen by comparing the results on Fig. 11 with those on Fig. 12. The results are qualitatively similar, but the extent of the bubble diffusion is much less. This is a consequence of the smaller convection time at the higher speed.

Plate-on-Top Laser Transmission Profiles

Companion results for the plate-on-top orientation are shown on Figs. 13-16. The near-injector measurements on Figs. 13 and 14 are quite like the plate-on-bottom results of Figs. 9 and 10 except there is no indication of increased transmission near the wall. In fact, the bubble concentration appears to reach a maximum near (or very near) the wall. This result is further verified by the downstream measurements shown in Figs. 15 and 16. Visual observations also support this conclusion in that a clear water region next to the wall was never seen with the plate on top.

Comparison of the near-injector, plate-on-top data in Figs. 13 and 14 with the downstream data in Figs. 15 and 16 shows that even when buoyancy inhibits movement away from the wall, the bubble cloud diffuses further from the wall and thickens as it moves downstream. The rate of diffusion in the plate-on-top data is, however, not as rapid as in the plate-on-bottom cases shown in Figs. 9-12, especially at the lower (4.6 m/s) velocity. The major effect of buoyancy is thus to augment the diffusion and rate of thickening of the bubble cloud for the plate-on-bottom orientation, and in addition to introduce a clear water region near the wall.

This variation in bubble cloud development suggests an intriguing possibility as to the effect of gravity on the bubble size distribution in the boundary layer. It is well-known that larger bubbles drift faster under the action of buoyancy than do small ones. This fact, coupled with the observations noted above, suggests that for the plate-on-bottom configuration, the larger bubbles may migrate towards the outer edge of the boundary layer leaving the smaller bubbles near the wall and the larger bubbles near the free stream. For the plate-on-top configuration, the opposite size gradient might be generated. Here, the larger bubbles will be retained near the wall and the smaller ones will be convected and diffused toward the free stream. The extent of such a bubble-size stratification effect, or indeed even its existence, cannot be verified from our present measurements. Further, its potential impact on C_f reduction (if it does occur) is not clear, but it does pose an interesting possibility which may be of importance in understanding microbubble boundary layers.

Streamwise Trajectories of the Bubble Cloud

A more concise description of the evolution of the bubble cloud is given on Figs. 17-20. Representative bubble density contours were obtained by connecting regions of constant photomultiplier voltage outputs on Figs. 9-16, as well as the intermediate measurement station (not shown). Results are shown for both plate-on-bottom and plate-on-top orientations. In these figures, the abscissa represents the distance from the plate surface while the ordinate represents the distance along the surface from the leading edge of the injection section. The regions of darkest cross-hatching correspond to regions where no laser transmission was detected ("zero" photomultiplier voltage) and, hence, where the bubble concentration was maximum. Regions of lighter cross-hatching correspond to increased amounts of laser transmission and lower bubble concentration. In general, the region of maximum bubble concentration for the plate-on-bottom configuration does not touch the wall, but appears as an "island" in the boundary layer. By contrast, the plate-on-top data show no measurable low concentration region adjacent to the wall. Recall, however, that the diameter of the measuring beam is 1 mm so resolution below this distance is precluded. All figures also show that the thickness of the bubble cloud increases with distance from the injection section. Thus, regardless of the direction of gravity, the bubbles diffuse away from the wall. The rate of diffusion is, however, enhanced for the plate-on-bottom results.

The low airflow, low velocity results on Fig. 17 show that the region of maximum bubble density for the plate-on-bottom results extends only a few hundred millimeters downstream and then terminates as the bubbles spread out reducing the concentration at the peak. As the airflow is increased, this region of maximum density

(no laser signal reaching the photomultiplier) grows wider and persists much further downstream (Fig. 18). The streamwise extent of the high concentration region at the 10.7 m/s condition (Fig. 19) is about the same as for the 4.6 m/s case (Fig. 17), but both the region of high concentration and the overall bubble cloud are thinner. Also, the overall thickness of the plate-on-top cloud at this higher speed is much nearer to that for the plate-on-bottom orientation than it was at 4.6 m/s. This illustrates the diminishing effect of buoyancy at the higher speed. Similar conclusions can be made about the bubble cloud trajectories at the higher airflow rate as shown on Figs. 18 and 20.

Laser Transmission Plots in Inner Variables

To test the manner in which these laser "concentration" profiles scale, and to place the bubble cloud thicknesses in more conventional turbulent boundary layer notation, the plate-on-bottom results presented on Figs. 9-12 have been replotted in inner variables (voltage versus y^+) and are shown on Figs. 21-24. The actual C_f values as measured in the presence of bubbles (see Table I) have been used to define the friction velocity for these plots. One major conclusion is that the outer edge of the bubbles lies near $y^+=1000$ at the near-injector location (76 mm from the injection section) as shown on Figs. 21 and 22. Even in inner variables, the outer edge of the bubble cloud moves further from the plate as more air is added.

The results at the downstream location (356 mm from the injection section) show the outer edge of the bubbles has migrated to y^+ values of several thousand for both freestream velocities (see Figs. 23 and 24). As shown in Table I, there is virtually no C_f reduction remaining at this plate-on-bottom location. Interestingly enough, these figures show that there are also no bubbles remaining in the near wall region ($y^+<100$) at this location. This would suggest the bubbles must remain in the near-wall region to be effective drag reducing agents. This trend was predicted by the computational study reported in Ref. 13. Careful placement of polymers in the near wall region have shown[17] they must be inside the buffer layer to be effective. Resolution at sublayer scales cannot be achieved without present measurement techniques, however, similar sensitivities to microbubble location might be expected.

BUBBLE SIZE ANALYSIS

An accurate knowledge of bubble sizes is critical in understanding the interaction between bubble dynamics, turbulence, and the boundary layer. The size distribution is primarily determined by flow parameters in the system including the strain rate at the wall[12,17,18] and the turbulence characteristics. In addition, a weak dependence on the injection process is expected. As an initial estimate of bubble sizes we have used top-view photographs like those shown in Figs. 3 and 5. These size measurements were made manually by projecting these photos on the wall, counting and marking them and measuring their diameter with a ruler. The accuracy of such measurements is only nominal, and it is certainly not possible to obtain enough samples to give an accurate statistical picture of the bubble size distribution.

Pictures were taken for airflows ranging from 4.6×10^{-5} m^3/s to 5.4×10^{-4} m^3/s (the range of Cases I-IV), but the high density of the bubbles made it nearly impossible to decipher information on bubble diameter at the higher airflow conditions. Therefore, two low airflow conditions (i.e., 4.6×10^{-5} m^3/s and 1.9×10^{-4} m^3/s) were chosen. Bubble size measurements were made at two velocities (i.e., 4.6 m/s and 14.7 m/s). At these conditions, the bubbles have at most a 5% effect on C_f, but these size measurements at least give us an indication of the bubble size range that is encountered at drag reducing airflow conditions. The bubble diameter measurements were conducted for both gravitational orientations and at the two locations downstream of the injection section discussed earlier. A synopsis of the information is presented on Fig. 25 and in Table II.

TABLE II

LOCATION from leading edge of porous section	AIRFLOW RATE (m^3/s)	VELOCITY (m/s)	PLATE ON BOTTOM		PLATE ON TOP	
			$\bar{x}$ μm	σ μm	$\bar{x}$ μm	σ μm
76 mm	0.46×10^{-4}	4.6	420	120	460	100
76 mm	1.86×10^{-4}	4.6	610	370	630	200
76 mm	0.46×10^{-4}	14.6	150	-	180	-
76 mm	1.86×10^{-4}	14.6	300	-	370	-
356 mm	0.46×10^{-4}	4.6	930	350	870	230
356 mm	1.86×10^{-4}	4.6	1170	420	1170	360
356 mm	0.46×10^{-4}	14.6	360	90	310	80
356 mm	1.86×10^{-4}	14.6	450	120	600	110

Several general conclusions can be deduced from these bubble size measurements. In all cases, the average bubble size increased as the airflow rate was increased. As was pointed out earlier, this trend is also visible directly from the photographs. Second, the measurements indicate that bubble size increases with distance from the injection section, an observation that can again be made directly from the photographs. This suggests that substantial bubble coalescence is taking place. Third, bubble sizes decrease with increasing freestream velocity. In general, the standard deviation of the bubble sizes (only given in Table II) also increases as the bubble diameters increase. Differences between plate-on-bottom and plate-on-top appear to be within the scatter of the data.

The sample sizes upon which these conclusions are based range between 50 and 100, as noted in Table II. The average bubble size ranges from 150 to 1200 μm. For reference, the inner scale ($y^+=1$) in the boundary layer is about 2 μm at these conditions, and the outer scale, δ, is around 10 mm.

CONCLUSIONS

Initial results from a new flat plate experiment for the study of microbubble phenomena have been reported. The new plate offers much improved optical access as compared to our earlier experimental configuration[9-11], and the present results have concentrated on the optical and photographical aspects of the microbubble cloud. Several significant new conclusions can be drawn from the results. These include the following.

Both laser transmission measurements and direct visual and photographic evidence show the existence of a clear, bubble-free region between the bubble cloud and the plate when the plate-on-bottom orientation is tested. This clear water region does not occur for the plate-on-top orientation. Hence, it is reasonable to conclude that the clear water region is the result of buoyancy effects. An important observation concerning this bubble-free region is that for the one case reported here the inner edge of the bubbles had moved to about $y^+=100$ (no bubbles inside $y^+=100$) and there was no longer any drag reduction present. This suggests that the bubbles are effective only when they are near the wall, but additional data must be obtained before this observation can be verified completely.

Both plate-on-bottom and plate-on-top results show that the outer edge of the bubbles spreads further into the stream with increasing distance from the injection section and that the bubble cloud becomes correspondingly thicker. The spreading rate is faster for the plate-on-bottom configuration demonstrating that buoyancy is a factor, but the persistence of spreading for the plate-on-top configuration where buoyancy inhibits such motion shows that some other diffusion mechanism is present also. This mechanism undoubtedly includes turbulent convection effects, but it is probably the mechanism which leads to the reduction in the effectiveness of the bubbles with distance from the injection section. Additional measurements of the thickness of the bubble cloud show that it becomes thinner as the freestream velocity is increased. This would suggest that the bubbles are more effective at higher speeds, but their effectiveness is also offset by the fact that a given volumetric flow rate of air produces lower bubble concentrations in the boundary layer at higher speeds.

Finally, bubble size measurements made from the photographs show bubble sizes ranging from 200 to 1100 μm. In all cases measured, the bubble sizes increased with distance from the injection section indicating significant coalescence was taking place. The bubble size also increases with air flow rate. Freestream velocity appears to be the most significant variable controlling bubble size with a sizeable decrease in bubble size as freestream velocity is increased.

ACKNOWLEDGEMENT

This work was sponsored by the Office of Naval Research under Contract Number N00014-81-K-0481.

REFERENCES

1. Hough, G. R., Viscous Flow Drag Reduction, Progress in Astronautics and Aeronautics 72, 1980.

2. Hefner, J. N., Bushnell, D. M., Whitcomb, R. T., Cary Jr., A. M. and Ash, R. L., "Concepts for Aircraft Drag Reduction", AGARD/VKI Special Course on Concepts for Drag Reduction, Rhode-St-Genese, Belgium, March 1977, AGARD-R-654.

3. Bushnell, D. M., "Turbulent Drag Reduction for External Flows", AIAA Paper 83-0227, AIAA Aerospace Sciences Meeting, Reno, NV, Jan. 10-13, 1983.

4. McCormick, M.E. and Bhattacharya, R., "Drag Reduction of a Submersible Hull by Electrolysis", Naval Engineers Journal 85, 1973, pp. 11-16.

5. Migirenko, G. S. and Evseev, A. R., "Turbulent Boundary Layer with Gas Saturation", Problems of Thermophysics and Physical Hydrodynamics (in Russian), (Novosibirsk), Nauka, 1974.

6. Dubnischev, Yu., Evseev, A. R., Sobolev, V. S., and Utkin, E.N., "Study of Gas-Saturated Turbulent Streams Using a Laser-Doppler Velocimeter", J. Appl. Mech. Tech. Phys. 16, No. 1, 1975, p. 114. Translated from Zhur. Prikl. Mech. Tekh. Fiz., No. 1, 1975, p. 147.

7. Bogdevich, V.G. and Malyuga, A.G., "The Distribution of Skin Friction in a Turbulent Boundary Layer in Water Beyond the Location of Gas Injection", in Investigations of Boundary Layer Control (in Russian), edited by S.S. Kutateladze and G.S. Migirenko (Thermophysics Institute Publishing House, Novosibirsk, 1976), p. 62.

8. Bogdevich, V.G. and Evseev, A.R., "Effect of Gas Saturation on Wall Turbulence", in Investigations of Boundary Layer Control (in Russian), edited by S.S. Kutateladze and G.S. Migirenko (Thermophysics Institute Publishing House, Novosibirsk, 1976), p. 49.

9. Madavan, N.K., Deutsch, S. and Merkle, C.L., "Reduction of Turbulent Skin Friction by Microbubbles", Physics of Fluids, Vol. 27, No. 2, February 1984, pp. 356-363.

10. Madavan, N.K., Deutsch, S. and Merkle, C.L., "The Effects of Porous Material on Microbubble Skin Friction Reduction", AIAA Paper 84-0348, AIAA 22nd Aerospace Sciences Meeting, Reno, NV, Jan. 9-12, 1984.

11. Madavan, N.K., Deutsch, S. and Merkle, C.L., "Measurements of Local Skin Friction in a Microbubble Modified Turbulent Boundary Layer", J. Fluid Mech. (1985), Vol. 156, pp. 237-256.

12. Deutsch, S. and Castano, J., "Microbubble Skin Friction Reduction on an Axisymmetric Body", submitted for publication in the Physics of Fluids.

13. Merkle, C.L. and Deutsch, S., "Drag Reduction by Microbubbles: Current Research Status", AIAA Paper 85-0348, AIAA Shear Flow Control Conference, Boulder, CO, March 12-14, 1985.

14. Madavan, N.K., Merkle, C.L. and Deutsch, S., "Numerical Investigations into the Mechanisms of Microbubble Drag Reduction" Journal of Fluids Engineering, Vol. 107, September 1985, pp. 370-377.

15. Legner, H.H., "A Simple Model for Gas Bubble Drag Reduction", Phys. Fluids, Vol. 27, December 1984, pp. 2788-2790.

16. Siegel, R. and Howell, J.R., Thermal Radiation Heat Transfer, McGraw-Hill, Inc., New York, NY 1981, pp. 412-434.

17. Tiederman, W. G., Luchik, T. S. and Bogard, D. G., "Wall-Layer Structure and Drag Reduction", J. Fluid Mech., Vol. 156, 1985, pp. 419-437.

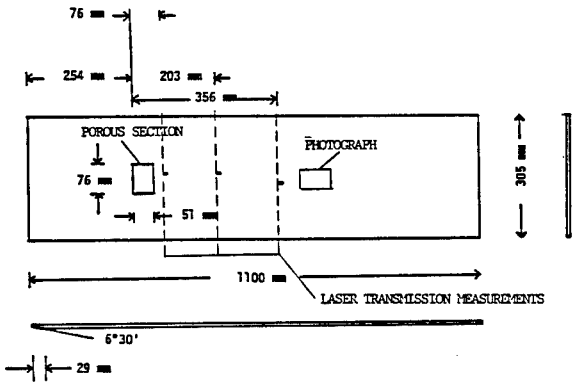


Fig. 1 A schematic of the flat plate with hot-film and photograph locations.

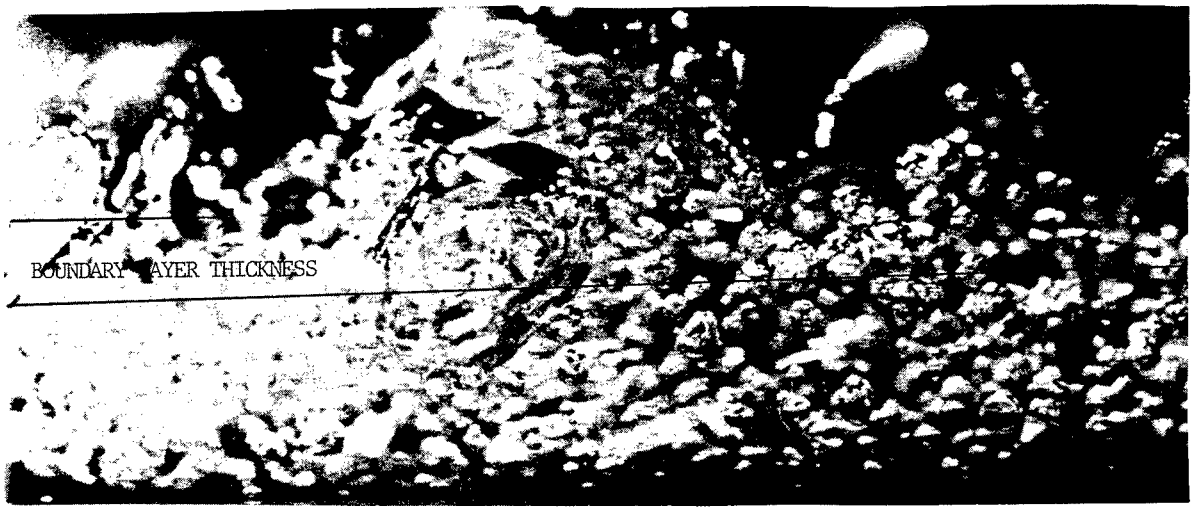


Fig. 2 Side view photograph of the 76 mm deep bubble cloud, 444 mms downstream of the leading edge of the porous plate at a freestream velocity of 4.6 m/s. The airflow rate is 3.2 x 10^{-4} m^3/s and the corresponding local C_f/C_{fo} is 0.98. Flow is from left to right. Note thickness of undisturbed boundary layer is superimposed on photograph.

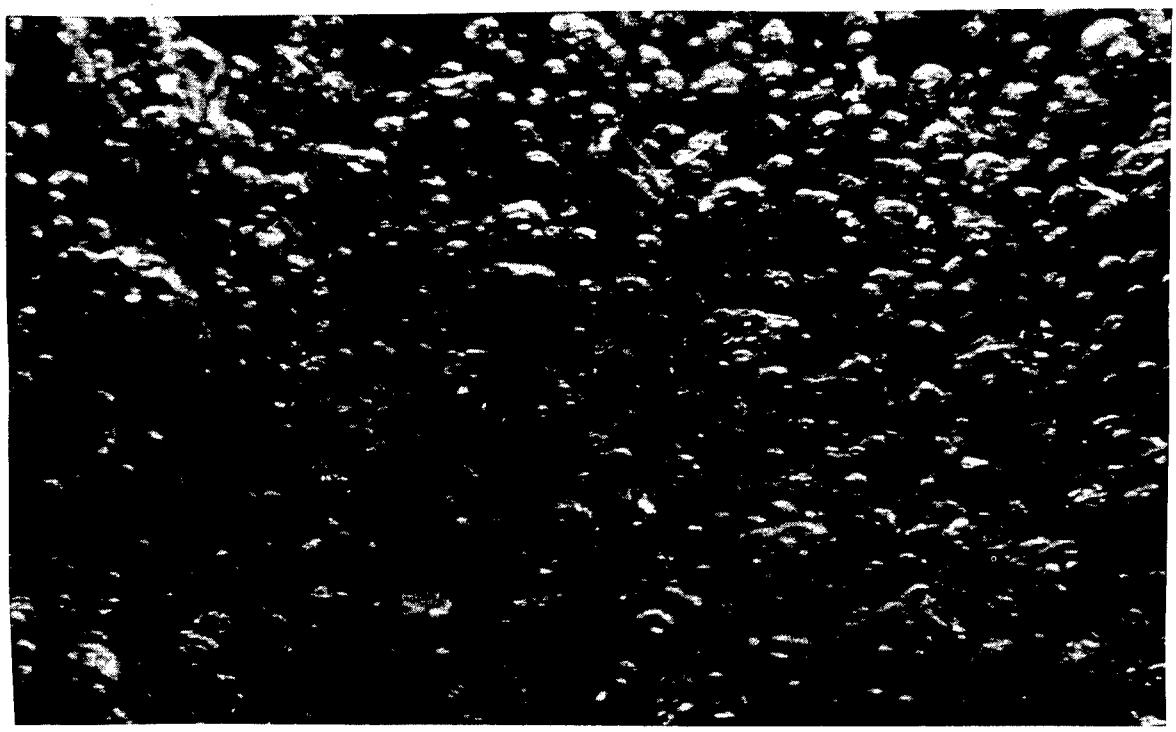


Fig. 3 Top view photograph at the same conditions as Fig. 2.

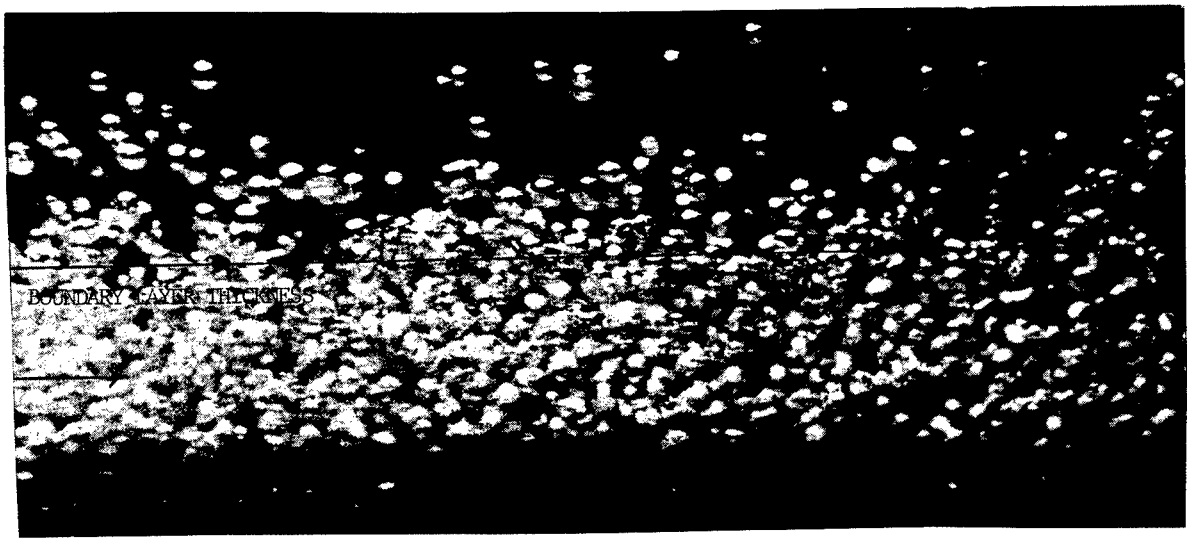


Fig. 4 Side view photograph of the 76 mm deep bubble cloud, 444 mms downstream of the leading edge of the porous plate at a freestream velocity of 4.6 m/s. The airflow rate is 0.5×10^{-4} m^3/s and the corresponding local C_f/C_{fo} is 1.0. Flow is from left to right. Note thickness of undisturbed boundary layer is superimposed on photograph.

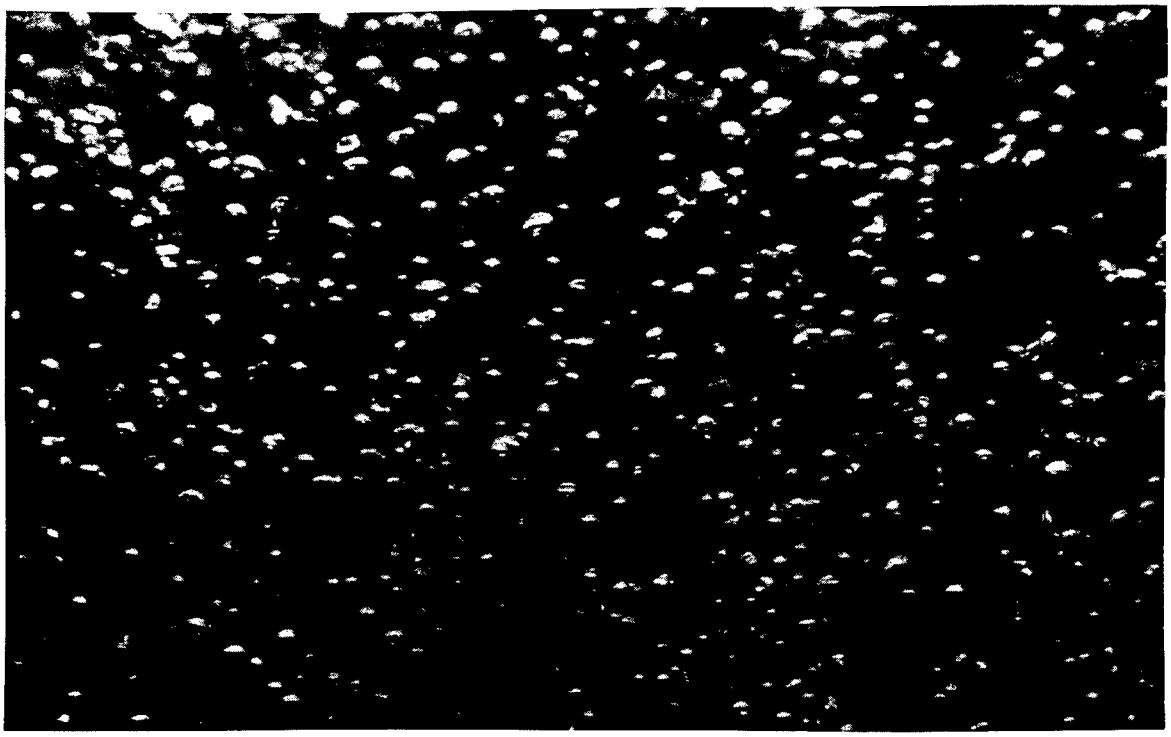


Fig. 5 Side view photograph at the same conditions as Fig. 4.

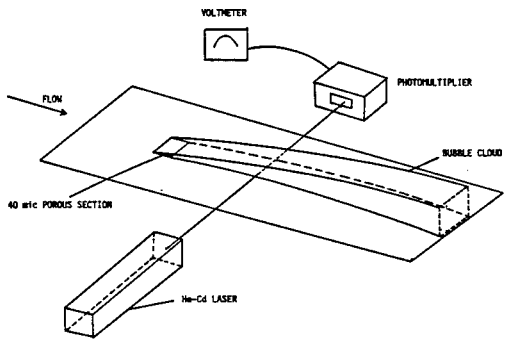


Fig. 6 Schematic of experimental measurement of bubble cloud location.

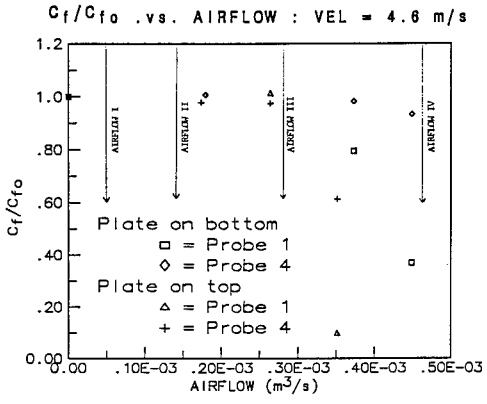


Fig. 7 C_f/C_{fo} as a function of airflow for a freestream velocity of 4.6 m/s. Note: C_f/C_{fo} for airflows I-IV are tabulated in Table I.

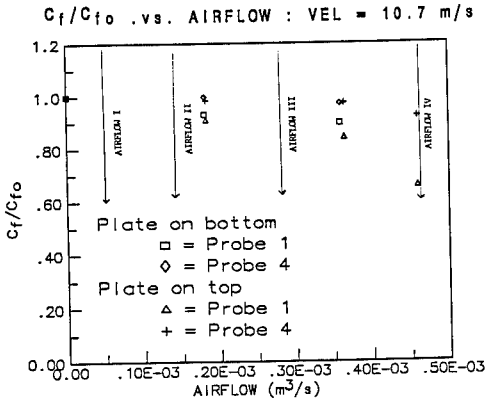


Fig. 8 C_f/C_{fo} as a function of airflow for a freestream velocity of 10.7 m/s. Note: C_f/C_{fo} for airflows I-IV are tabulated in Table I.

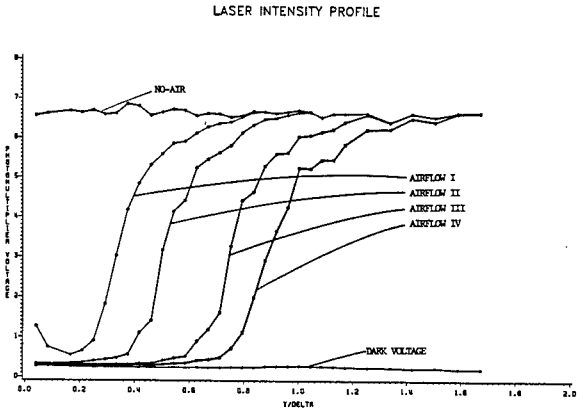


Fig. 10 Photomultiplier voltage versus y/δ for the four airflows. The freestream velocity is 10.7 m/s and the axial distance is 76 mm from the leading edge of the porous section. "Plate-on-bottom" case.

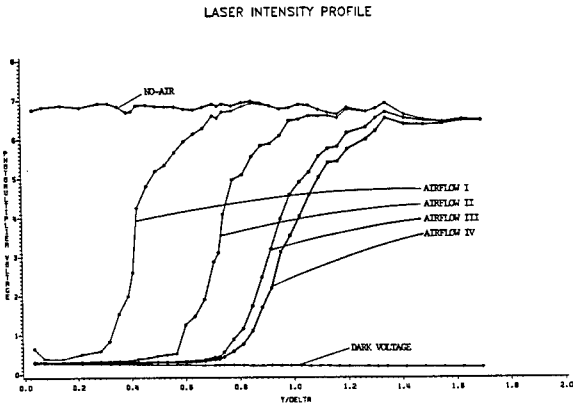


Fig. 9 Photomultiplier voltage versus y/δ for the four airflows. The freestream velocity is 4.6 m/s and the axial distance is 76 mm from the leading edge of the porous section. "Plate-on-bottom" case.

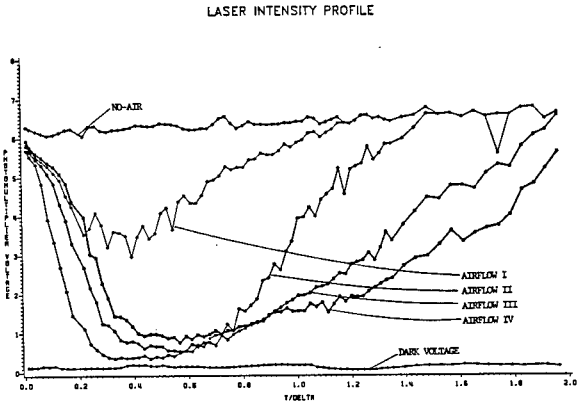


Fig. 11 Photomultiplier voltage versus y/δ for the four airflows. The freestream velocity is 4.6 m/s and the axial distance is 356 mm from the leading edge of the porous section. "Plate-on-bottom" case.

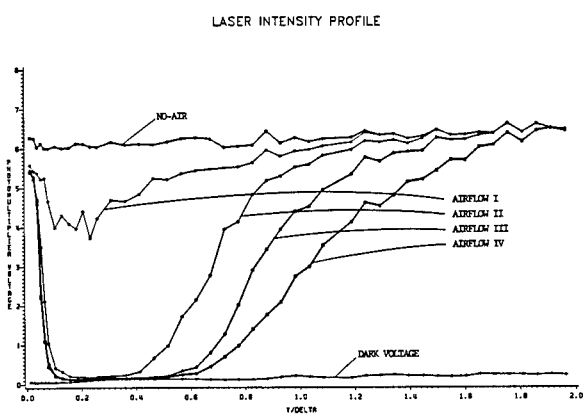


Fig. 12 Photomultiplier voltage versus y/δ for the four airflows. The freestream velocity is 10.7 m/s and the axial distance is 356 mm from the leading edge of the porous section. "Plate-on-bottom" case.

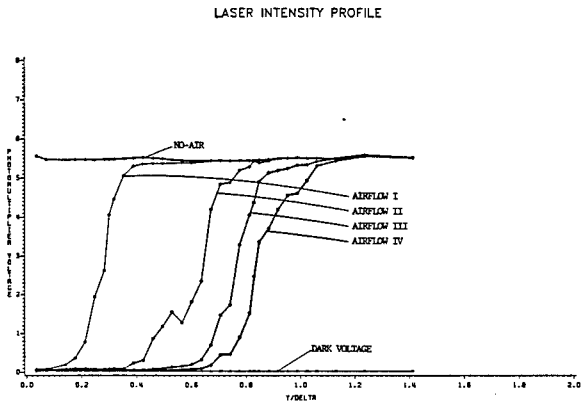


Fig. 13 Photomultiplier voltage versus y/δ for the four airflows. The freestream velocity is 4.6 m/s and the axial distance is 76 mm from the leading edge of the porous section. "Plate-on-top" case.

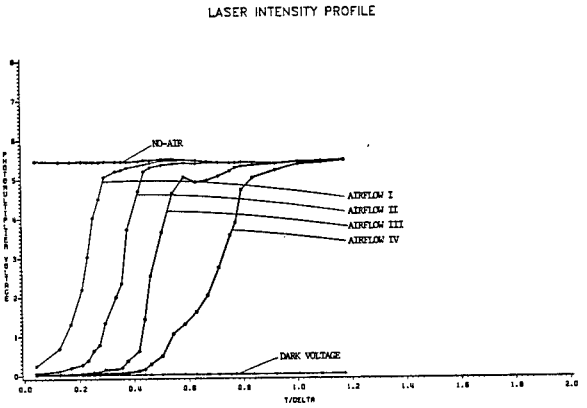


Fig. 14 Photomultiplier voltage versus y/δ for the four airflows. The freestream velocity is 10.7 m/s and the axial distance is 76 mm from the leading edge of the porous section. "Plate-on-top" case.

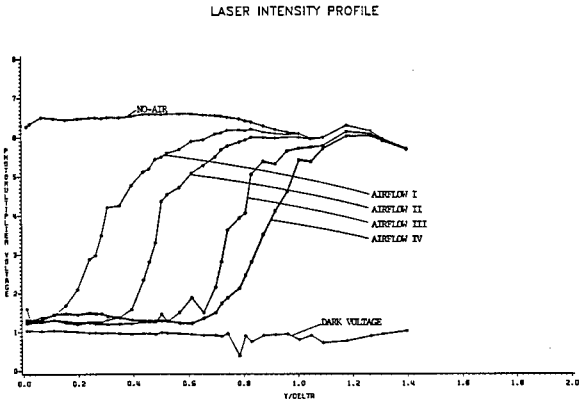


Fig. 15 Photomultiplier voltage versus y/δ for the four airflows. The freestream velocity is 4.6 m/s and the axial distance is 356 mm from the leading edge of the porous section. "Plate-on-top" case.

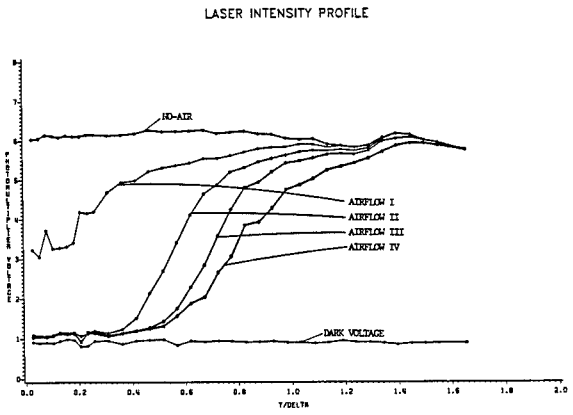


Fig. 16 Photomultiplier voltage versus y/δ for the four airflows. The freestream velocity is 10.7 m/s and the axial distance is 356 mm from the leading edge of the porous section. "Plate-on-top" case.

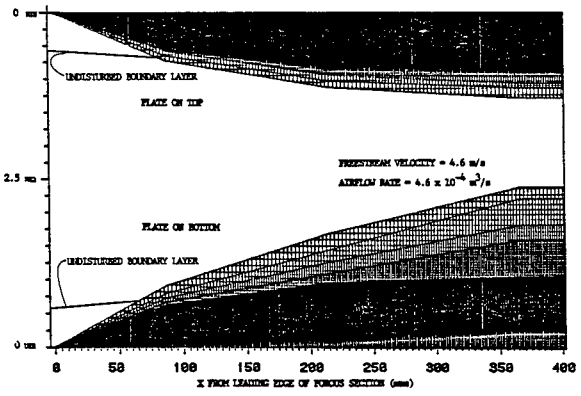


Fig. 18 Bubble density contours for both "Plate-on-Bottom" and "Plate-on-Top" cases at a freestream velocity of 4.6 m/s and an airflow rate of 4.6×10^{-4} m^3/s.

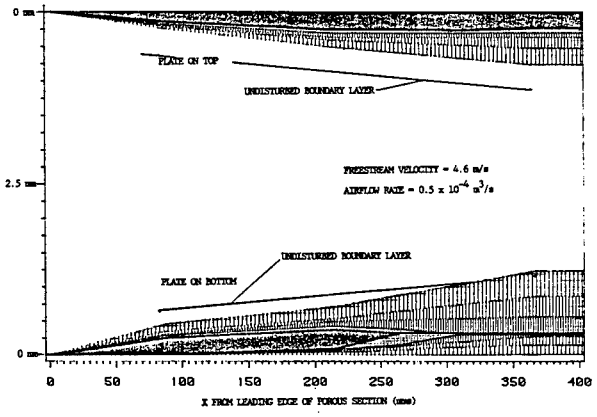


Fig. 17 Bubble density contours for both "Plate-on-Bottom" and "Plate-on-Top" cases at a freestream velocity of 4.6 m/s and an airflow rate of 0.5×10^{-4} m^3/s.

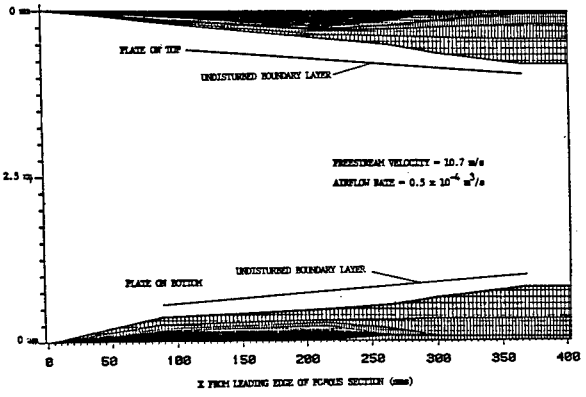


Fig. 19 Bubble density contours for both "Plate-on-Bottom" and "Plate-on-Top" cases at a freestream velocity of 10.7 m/s and an airflow rate of 0.5×10^{-4} m^3/s.

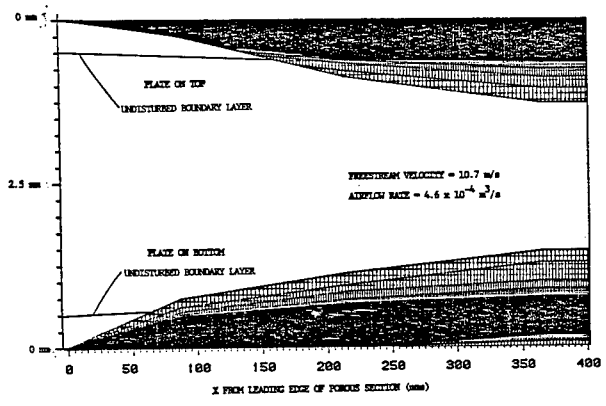


Fig. 20 Bubble density contours for both "Plate-on-Bottom" and "Plate-on-Top" cases at a freestream velocity of 10.7m/s and an airflow rate of 4.6×10^{-4} m^3/s.

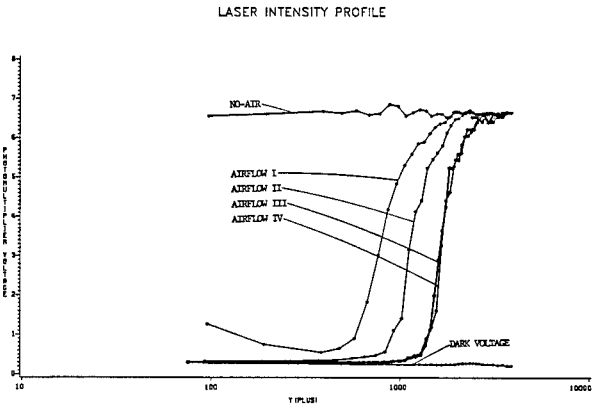


Fig. 22 Photomultiplier voltage versus $y^+(yu^*/\nu)$ ("Plate-on-Bottom") for a freestream velocity of 10.7 m/s and at a distance of 76 mm from the leading edge of the porous section. Note that the reduced C_f values given in Table I have been used to define u^*.

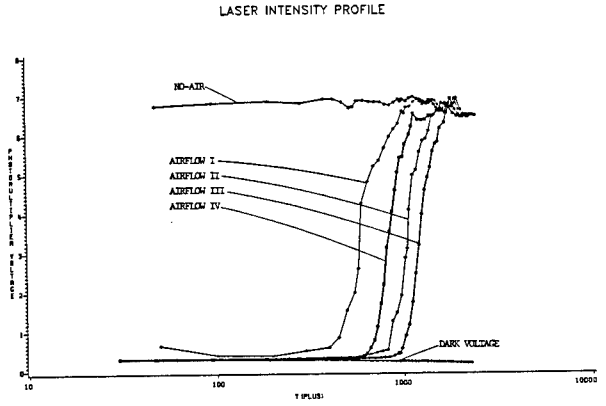


Fig. 21 Photomultiplier voltage versus $y^+(yu^*/\nu)$ ("Plate-on-Bottom") for a freestream velocity of 4.6 m/s and at a distance of 76 mm from the leading edge of the porous section. Note that the reduced C_f values given in Table I have been used to define u^*.

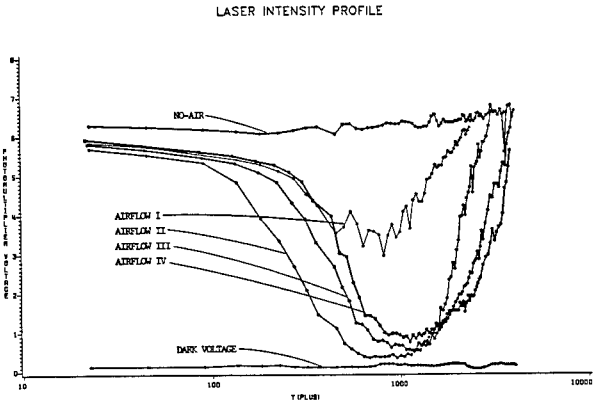


Fig. 23 Photomultiplier voltage versus $y^+(yu^*/\nu)$ ("Plate-on-Bottom") for a freestream velocity of 4.6 m/s and at a distance of 356 mm from the leading edge of the porous section. Note that the reduced C_f values given in Table I have been used to define u^*.

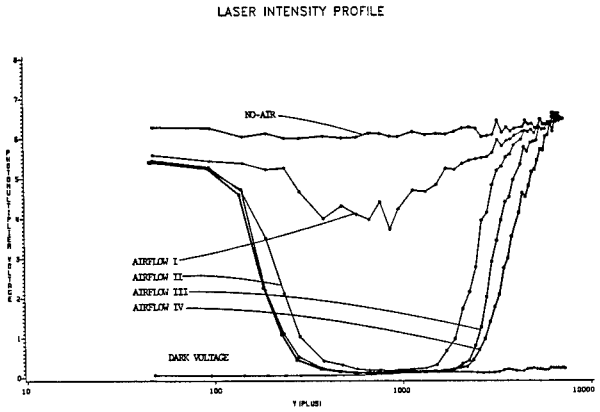


Fig. 24 Photomultiplier voltage versus $y^+(yu^*/\nu)$ ("Plate-on-Bottom") for a freestream velocity of 10.7 m/s and at a distance of 356 mm from the leading edge of the porous section. Note that the reduced C_f values given in Table I have been used to define u^*.

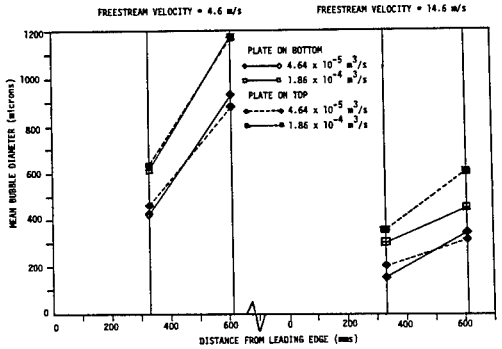


Fig. 25 Bubble diameters as a function of distance from leading edge of flat plate. Bubble diameters range from 150 to 1200 μm for the velocity and airflow ranges encountered here.

DISCUSSION

Eiichi Baba,
Mitsubishi Heavy Industries, Ltd.

The Nagasaki Experimental Tank of Mitsubishi Heavy Industries made some experiments to confirm the drag reduction effect by a method different from the authors' experimental setup (Floating element). That is, a direct drag measurement was made by towing a 4 meter flat plate in the towing tank 285 meters long at speeds up to 9m/sec. On this flat plat two pieces of porous sections (150 x 70 mm) were flush-mounted for the plate on top configuration. The results are shown in figures below. A drag reduction up to 70% was realized and a similar tendency was observed in the drag reduction rate as those of the authors' previous results (References 9-10). In this experimental study, photographs were taken from a camera fixed on the towing tank bottom and also a paint test was made to determine the extent of areas where drag reduction was thought to be effective. It was observed that in the areas covered by microbubbles the extension of paint was smaller. This suggests that the shear stress acting on the paint surface is reduced. The discusser would suggest the authors to attempt to use paint testing techniques for a better understanding of the flow mechanism of the micro-bubble boundary layers.

Reply -

I would like to thank Dr. Baba for his comments and his very interesting experimental results. They complement our measurements in several ways. Our experiments are concerned with measurements of skin friction while Dr. Baba's have to do with measurements of drag. Although there are no fundamental physical arguments to suggest that the C_f reductions would not also translate into drag reductions, these direct measurements provide concrete assurance that they do. Dr. Baba's measurements also complement ours in that the two measurement techniques he has used are distinct from the two we have used, yet all provide similar conclusions. (In addition to a floating element balance, we have also made extensive use of flush-mounted hot films for C_f measurements.) Finally, I would like to comment that the paint testing technique is a very clever qualitative method for detecting C_f reductions in extremely harsh environments like the present one. The concept may prove helpful for some of the more difficult experimental conditions for which quantitative techniques begin to fail, and I appreciate Dr. Baba's calling this to my attention.

V. C. Patel,
Iowa Institute of Hydraulic Research

In your introduction you mentioned that most of the observed effects of microbubbles could be explained on the basis of the changes in the fluid properties. Can you elaborate on that?

Reply -

The comment was based upon the results of an analytical model of the microbubble boundary layer (Ref. 14). In this model, we simulated the effect of the bubbles on the mean density and the mean viscosity in the boundary layer. Both of these property changes were in the direction to cause an increase in the kinematic viscosity. Numerical results based upon a simple turbulence model showed that the reduced turbulence Reynolds numbers caused by this modified viscosity led to increased dissipation and, hence, reductions in C_f. This modification was most effective when the bubbles (i.e., the turbulence Reynolds number reduction) were in the vicinity of the buffer layer and the predicted C_f reductions were in qualitative agreement with experiments. An interesting sidelight of the present measurements is that the measured bubble cloud trajectories reported here can be used as an input to a model of this sort to make it somewhat more representative of experimental conditions.

Karen Scott,
C.S. Draper Laboratory, Inc.

The high reductions in C_f illustrated in this study are remarkable, as is the flow visualization of the bubble clouds. It would be useful, however, to put this drag reduction method in the context of possible energy savings in actual implementation. That is, when air flow rate is included in the balance, what are the power savings possible in implementating this scheme in, say, a submersible?

Reply -

Our primary interest is in studying the physics of the microbubble boundary layer rather than on a system study of its effectiveness for a particular application, but some general comments may be useful to you. The tradeoff between pumping power required for an injection and the energy reduction because of reduced drag depends upon two primary parameters: pumping power per unit mass of gas, and the total volume of gas required. Previous results have shown that the type of porous material used is relatively unimportant so the material may be chosen at least in part up to minimize the Δp. The pumping power then depends primarily upon the pressure difference across the shell of the submersible. This pressure difference should be readily calculable for a particular application.

The second parameter, namely the volumetric flow rate, is very difficult to estimate primarily because the arclength of the body over which the C_f reduction persists is largely unknown. In other words, we don't know how far downstream of the first injector the second injector should be placed. The four meter plate results just shown by Dr. Baba suggest that this distance is quite long for his case whereas our smaller scale results whould suggest somewhat shorter distances. The answer you get concerning overall effectiveness is totally controlled by this factor. I am aware of several back of the envelope estimates of net energy reductions and they range from marginally effective (pumping power about equal to the drag reduction) to very favorable (pumping power small compared with drag reduction) depending upon the assumptions made concerning the replenishment distance.

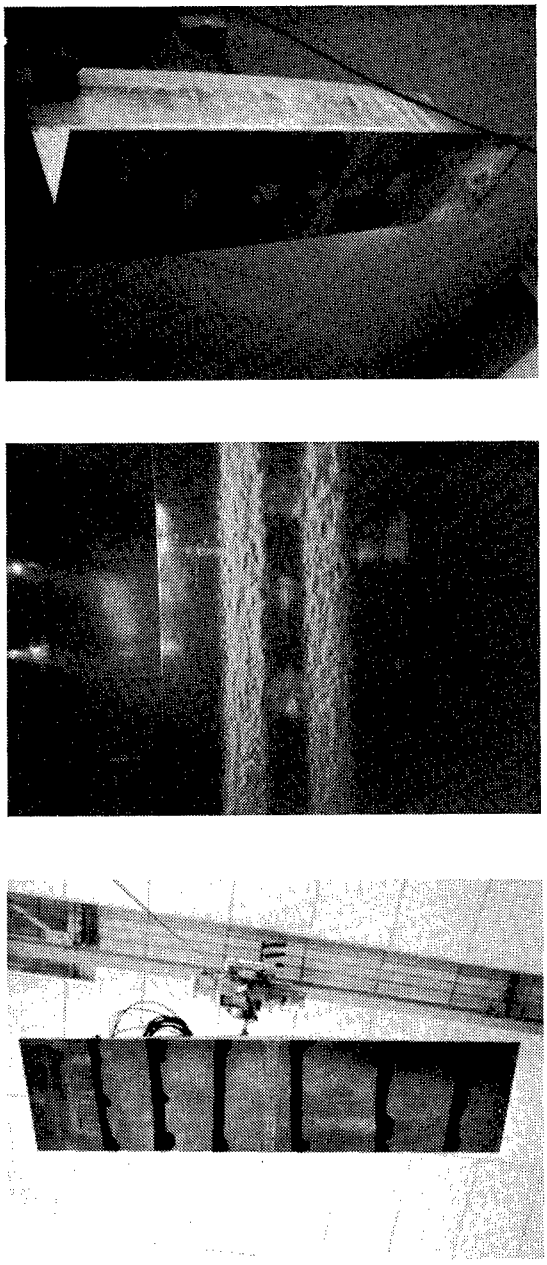


Figure A. Experimental setup at Nagasaki Experimental Tank of Mitsubishi Heavy Industries.

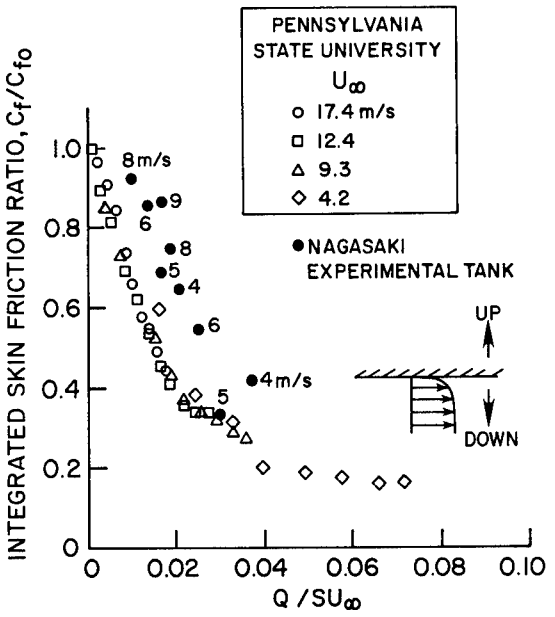


Figure B. The integrated skin friction ratio as a function of the nondimensional air flow parameter. The plate is above the layer.

Computer-Aided Flow Visualization

D. ROCKWELL, C. GUMAS, P. KERSTENS, J. BACKENSTOSE,

A. ONGOREN, J. CHEN, and D. LUSSEYRAN

Lehigh University, U.S.A

ABSTRACT

This overview describes some recent progress on processing and analysis of flow visualization images. Attention is focussed on recently developed techniques for: curve-tracking of images; visual correlation and ensemble-averaging both within a given image and between images; recognition of patterns of flow structure in images; determination of three-dimensional flow structure from single- and dual-view images; estimates of velocity eigenfunctions from images; and determination of flow structure-surface pressure relations from images and pressure measurements acquired simultaneously.

INTRODUCTION

Interpretation of flow visualization, employing a wide variety of techniques, has received considerable attention in recent years. Valuable overviews of a range of techniques for quantitatively determining complex features of unsteady flow fields are given by Emrich (1) and Merzkirch et al (2). Among the diverse possibilities for visualizing the flow are: smoke and dye injection; laser-induced fluorescence; and density gradients induced in heated flows or mixing in dissimilar fluids. These visualization techniques and corresponding methods of interpreting them are addressed by, for example, Hernan and Jiminez (3), Bernal, Hernan, and Sarohia (4), Keffer, Kowal, and Shokr (5), and Wallace, Balint, Ladahara, and Morel (6).

Depending upon the visualization medium and the type of flow, there are a number of possible means of effectively marking defined regions of the fluid. Perhaps the simplest and most widely popular technique of visualization involves injection of dye or smoke, and its illumination by either diffuse light or laser sheets. With these techniques, there are a number of fallacies in interpreting the visualized unsteady flow relative to the actual vorticity field (7). Another approach involves generation of timeline markers in the flow by pulsing, for example, voltage through a small wire whose axis is orthogonal to the primary flow direction. The advantage of this approach is that the time of flight of each timeline segment is related to the local flow velocity. Consequently, in principle, it is possible not only to determine quantitative features of the unsteady velocity field, but also to formulate pattern recognition and reconstruction techniques for two- and three-dimensional unsteady flows. In essence, patterns of timelines in a flow image represent a physically meaningful basis for applying a variety of techniques to interpretation of complex flow fields; the purpose of this overview is to provide a synopsis of some recent progress in this area. In doing so, we first describe means of quantitatively defining the timeline patterns in flow images, then proceed to methods for describing and recognizing patterns of the flow structure and techniques for quantitative interpretation of the velocity and vorticity fields.

EXPERIMENTAL TECHNIQUES

Figure 1 gives an overview of the essential elements of the experimental system: a wire for generating timelines located at an arbitrary position in a three-dimensional vortical flow; synchronized video cameras interfaced with the mainframe of the video system; a digitizer; and the CAD processing system.

Hydrogen bubble timelines were generated from a one mil diameter platinum wire stretched across the flow. The width of each timeline, and distance between timelines, was controlled by a function generator; it produced a voltage waveform in accord with the desired timeline pattern. The bubble timelines were illuminated by two stroboscopic (90 watt) lights interfaced with the mainframe of the video system.

The Instar (Videologic) video system has a split-screen capability. Two video cameras,

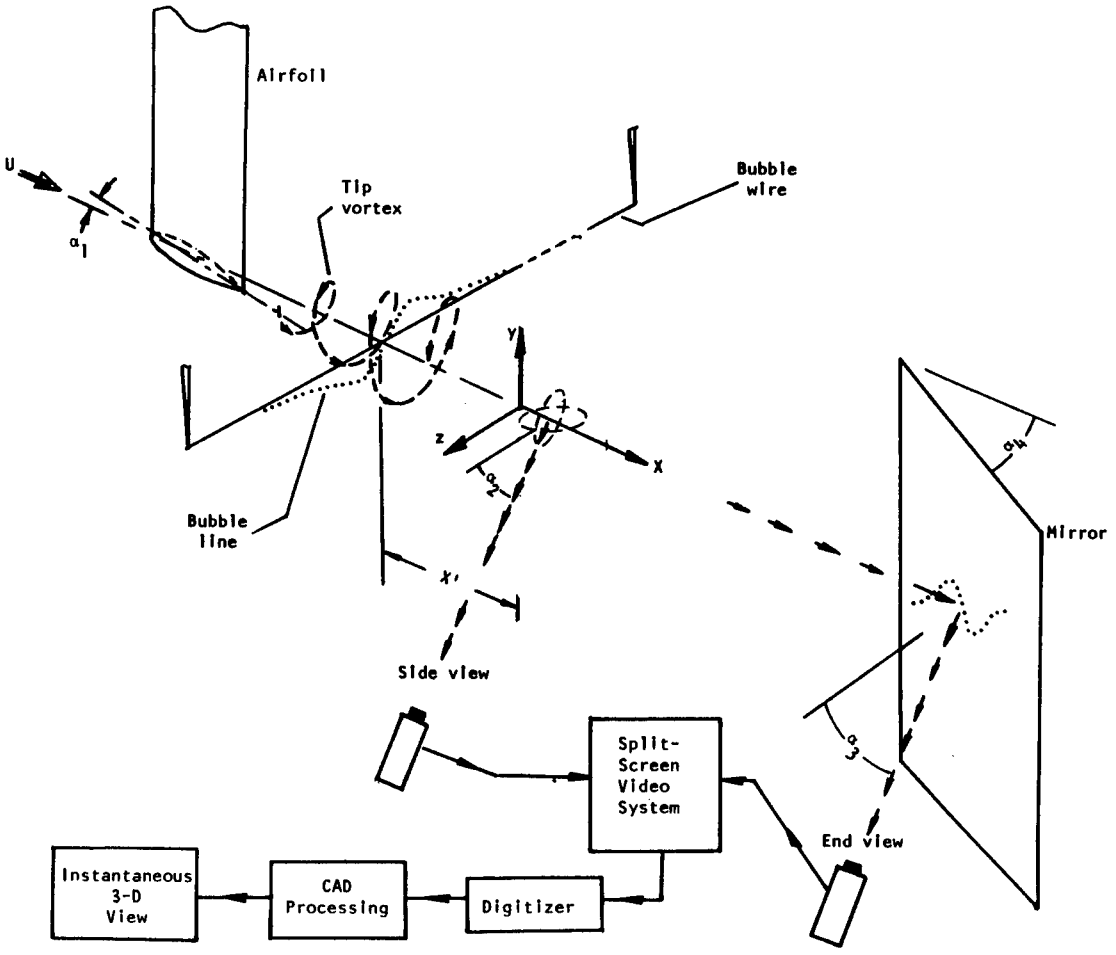


Figure 1: Overview of technique for acquiring and processing flow visualization using two-camera, split-screen video system, digitizer, and computer-aided design system. In the example shown, a tip vortex is generated, and its side and end views are recorded simultaneously.

oriented in arbitrary directions, provide simultaneous images to the mainframe. The desired views of the flow structure were greatly facilitated by various arrangements of mirrors external to, as well as within, the flow. Once the images were acquired on the Instar mainframe, they were digitized using a Colorado video (model 270A) digitizer. In turn, the digitized images were put on file in the computer-aided design (CAD) laboratory, which is driven by two VAX 11/780 computers. The advantage of performing image evaluation in the CAD laboratory is that image processing operations can be employed in conjunction with available CAD techniques such as Unigraphics. In the following we define techniques for image definition, their interpretation, and corresponding techniques for reconstruction of the flow.

IMAGE ENHANCEMENT AND DEFINITION

With a digitized image at hand, it is necessary to define the timeline pattern in binary form before proceeding with techniques of image interpretation. Figure 2 shows a typical, digitized image in raw form. A series of image processing operations can be employed to bring out the essential features of the time-line pattern from the raw image; a partially-processed image is shown in Figure 2. Possible processing operations include application of: a "band-pass" spatial filter; a thresholding operation; a thinning algorithm; a two-dimensional, low-pass filter; and other related

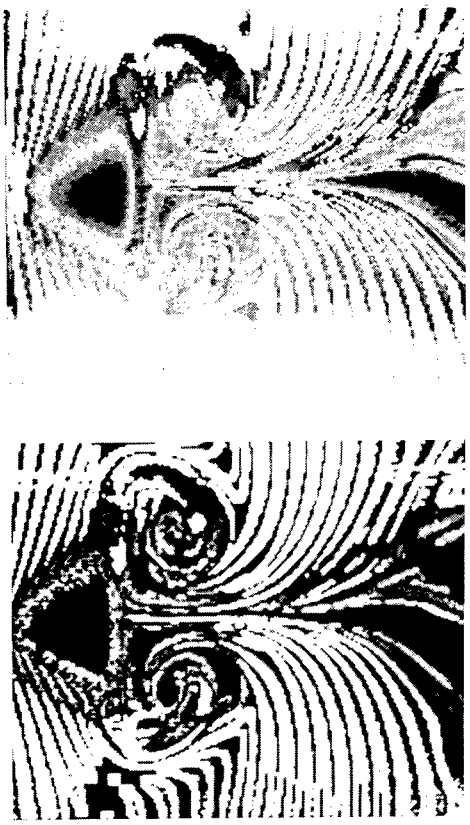


Figure 2: Raw digitized and processed images of vortex generation from a prism oscillating in the streamwise direction (8).

techniques described by Gumas and Rockwell (9).

Once the image has been enhanced to its optimal form, it is then possible to proceed with the process of curve-tracking, whereby the coordinates of each timeline are defined. If the processed image were in a purely binary form, then tracking of each timeline and generation of the corresponding chain codes would be a relatively simple matter. However, for the multi-level digital images of typical interest, the complexity of the curve-tracking process increases with the number of intensity levels of the image. There are 256 grey levels of intensity information per pixel. Moreover, despite application of the image processing techniques described in the foregoing, there is still residual noise from the digitization process as well as from non-uniform illumination of the originally acquired flow image. Consequently, it is necessary to formulate a curve-tracking technique that can account for these complexities of the multi-level image.

Gumas (10) has developed a simple curve-tracking algorithm that effectively defines most curves, or timelines, in the flow image. The tracking algorithm is based on the concept of linear predictive coding (LPC); it is described in detail by Gumas (10) and summarized by Gumas and Rockwell (9). In essence, the tracking algorithm moves from one pixel of the flow image to the next in accord with certain criteria. That is, the path of the timeline is defined on a point-by-point basis, with each point corresponding to a given pixel. During the tracking process, the last point on the current path is designated as the point of interest (POI). At each POI, there is a direction of arrival (DOA), which in turn is calculated from the previous values of the DOA. Furthermore, this DOA determines the set of points, or pixels, that are considered in the search for the next point along the path of the timeline. This particular set of pixels is made up of a number of shells; each of the interlocking shells contains possible points to which the path of the timeline can move. In carrying out the actual curve-tracking process, each shell is given a certain weight. The point to which the defined timeline moves is in the direction of maximum intensity; in turn, it is defined in terms of the sum, over all shells, of the product of maximum pixel intensity of a shell, the direction weight for that pixel, and the shell weight. Using this technique, the entire pattern of timelines in the given flow image can be automatically determined.

VISUAL CORRELATION AND ENSEMBLE-AVERAGING OF IMAGES

With defined timelines of the sort shown in Figure 2 at hand, it is possible to consider quantitative means of correlating successive images, or portions of images, as well as ensemble-averaging them. Correlations of velocity and pressure at a single point, or between two points, in a flow have been extensively undertaken and interpreted in recent decades. However, the concept of visual correlation of defined flow domains of images, as well as averaging of such domains, has received relatively little attention. Images of timeline patterns provide a quantitative basis for determining visual correlations and averages.

To quantitatively define the timelines in the xy plane, we employ the concept of a tangent angle function ϕ, which is simply the local tangent to the curve at a given position. Figure 3 shows the discretized form of a curve and the corresponding function ϕ. An extensive discussion of interpretation of the continuous and discrete forms of ϕ is given by Gumas and Rockwell (9). It is our objective here to correlate two curves, or timelines, by determining the correlation of the tangent angle function at respective locations along each of the two curves. However, a complication arises from the fact that any two curves rarely have the same length. Consequently, in comparing curves, there are two possible options: normalize

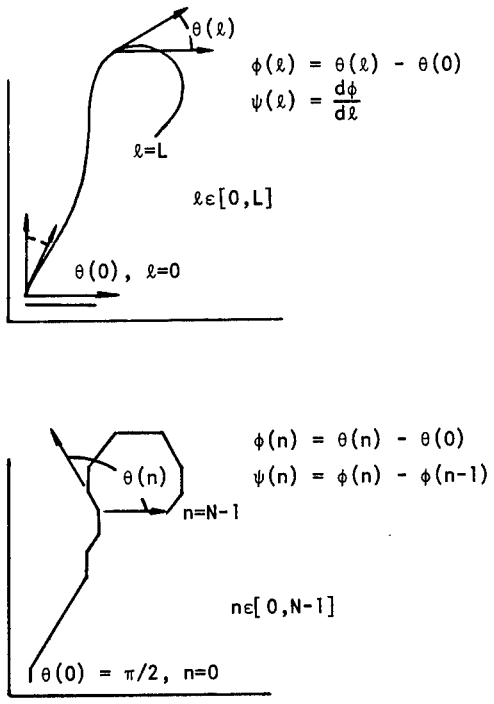


Figure 3: Definition of absolute θ and relative φ tangent angle function for continuous and discretized curves (9).

the length of one curve with respect to the other; or compare a portion of the longer curve with the shorter curve. We refer to these techniques as the normalized curve and shorter curve methods respectively. For the normalized curve technique, codes were written for curve normalization, such that points on the shorter curve are spread out on a wider spacing on the longer curve; the incremental distance along a given curve is the same, but different from that of the adjacent curve. For the shorter curve technique, the incremental spacing is the same on both curves.

In actual implementation of the curve comparison technique, there are additional complications that must be accounted for (11). They include, for example, directional ambiguity, arising from the fact that a curve is defined in its digitized form with a given chain of pixels oriented in an arbitrary direction; consequently, a different number of pixels is required to represent a continuous curve of given length, depending upon the orientation of the curve. This aspect, as well as a binary search routine that determines the pixel whose location gives the length L of the curve in comparison with a reference curve, is addressed by Kerstens and Rockwell (11).

In determining the correlation between two curves, where each curve is defined by its tangent angle function as in Figure 3, the logical first step is to define a cross-correlation function analogous to that used in classical point measurements (12). For two curves a and b with tangent angle functions $\phi_a(\ell)$ and $\phi_b(\ell)$, the cross-correlation extending over the interval from -A to A of the normalized curves is:

$$R_{\phi_a\phi_b} = \int_{-A}^{A} \phi_a(\ell)\phi_b(\ell-\tau)d\ell \qquad (1)$$

in which τ is a shift operator. For the discretized curves, we interpret τ as the number of discretized curve segments, by which ϕ_b is shifted with respect to ϕ_a. However, as discussed by Kerstens and Rockwell (11), this traditional definition, as well as its normalized form, is inadequate for several reasons. Among them are the inability to distinguish the same angle between two curves when the curves are oriented at different absolute angles and failure to distinguish properly the mirror image of the curve with respect to its original. We employ a new type of correlation, or similarity, function based on the difference rather than the product of tangent angle functions. In discretized form, the normalized correlation function is:

$$S_{\phi_a\phi_b} = \sum_{k=1}^{N} A^*(k, \tau)/N \qquad (2)$$

where

$$A^*(k,\tau) = 1 - 2|\phi_a(k) - \phi_b(k-\tau)|/\pi \qquad (3)$$

in which k designates a particular element, N is the number of discrete elements along the curve, and τ is the spatial phase shift between curves defined in terms of the number of elements. With the definition of equation (2), it is possible to determine various types of auto- and cross-correlations between any two curves in a given image or between specified curves in two successive images.

The visual average of several successive images may be obtained from the spatial averages of respective timelines in a number of successive images. If each of the images corresponds to a defined phase of a periodic forcing function, such as displacement of a body, etc., then the average of successive images is termed an ensemble-average. Once the x,y coordinates of each of the curves in a series of images is defined, then the average curve is calculated by averaging the respective coordinates in successive images. The averaged x and y coordinates

are simply given by:

$$x_{i,ave} = \Pi x_{i,j} w_j / \Pi w_j$$

$$y_{i,ave} = \Pi y_{i,j} w_j / \Pi w_j \qquad (4)$$

$$\Pi \equiv \sum_{j=1}^{n}$$

in which $x_{i,ave} \equiv$ the x coordinate of point i on the average curve, $x_{i,j} \equiv$ the x coordinate of point i on curve j, and so on. The total number of curves that are averaged is indicated by n, and the weighting factor for curve j by w_j; this weighting factor accounts for possible recurrence of a given curve. The points on the average curve will not necessarily be equally spaced. However, the average curve can be represented by a continuous string of pixels that closely approximate the calculated point locations (13). Redundant pixels are then removed from the resultant image by application of the corner cutting matrix of Freeman (14, 15).

To illustrate the correlation and ensemble-averaging operations described in the foregoing, we consider the flow past a circular cylinder subjected to controlled, sinusoidal oscillations in the streamwise direction as indicated in Figure 4. Timelines were generated by pulsing a bubble wire located upstream of the oscillating cylinder. The interesting feature of this flow is that even though the oscillations are in the streamwise direction, thereby inducing a symmetrical perturbation field, the inherently unstable mode of the vortex formation is antisymmetrical. Consequently, there is competition between symmetrical and antisymmetrical modes of vortex formation (16). A remarkable feature of the flow structure is that, for certain values of excitation frequency, there is deterministic decay from a highly ordered symmetrical mode of vortex formation to an antisymmetrical mode over a number of controlled oscillation cycles of the cylinder. It is evident that over seven cycles of the controlled oscillation, there is a gradual decay from symmetrical to antisymmetrical vortex formation. Correspondingly, the timeline patterns are highly symmetrical in the first photo and very asymmetrical in the seventh photo.

Digitized representation of the upper halves of these timeline patterns are shown in Figure 5. Using these timeline patterns as well as additional ones between them, we can quantitatively define the degree of symmetry of each image as well as the degree to which a portion of the flow changes in going from one image to the next. Use of the basic definition of the correlation function $S_{\phi_a\phi_b}$ of equation (2) allows formulation of, for example: autocorrelation of a timeline, providing an index of how rapidly the timeline distorts in the streamwise direction; and cross-correlation of timelines on opposite sides of the image, indicating the degree of asymmetry of the developing flow. Of course, these correlation concepts can be applied between, as well as within, images. It is also possible to introduce the concept of delay τ in the correlation functions. We note here that in actually calculating the correlations, a geometrical scaling factor whould be employed; this factor is the ratio of the length scales of the curves a and b.

A simple illustration of the correlation $S_{\phi_a\phi_b}$ can be taken as the correlation of each successive timeline with the first timeline in the right image of Figure 5. $S_{\phi_a\phi_b}$ rapidly decays, in accord with the rapid distortion shown in the right hand photograph of Figure 5, as verified by calculations.

To illustrate the concept of ensemble-average for the flow in Figure 4, we first of all know that each of the photos therein was acquired at the maximum-negative position of the cylinder during a sinusoidal oscillation cycle. Consequently, averaging a number of images taken at this phase of the oscillation will give an ensemble-averaged image. We consider here the much-simplified case of an ensemble-average of two images, the first and seventh images of Figure 4. In doing so, equation 4 is employed. Figure 6 shows the top halves of the first and third images of Figure 4 and the averaged image.

Clearly, in order to relate these correlations and ensemble-averaging techniques to traditional parameters of the unsteady velocity field, it is useful to generate segmented timelines. This approach would allow tracking defined segments of bubbles. Segmented timelines are discussed subsequently in the section on three-dimensional reconstruction. Even without segmented timelines, it is possible to gain quantitative insight into the velocity field represented by a given image using a time of flight technique; it considers the streamwise distance between adjacent timelines. This aspect is addressed in the section on velocity eigenfunction and vorticity.

PATTERN RECOGNITION USING IMAGES

In unsteady, non-periodic flows, it is desirable to determine which of the large-scale features of the flow recur on an orderly basis. Consequently, it is desirable to define a library of basic types of flow patterns; then, by continuously comparing the observed, instantaneous flow structure with the basic patterns, it would be possible to make physically meaningful interpretation of the unsteadiness. In essence, this approach represents a type of pattern recognition technique. There are a number of possible approaches to formulating a pattern recognition technique in conjunction with the timeline visualization method.

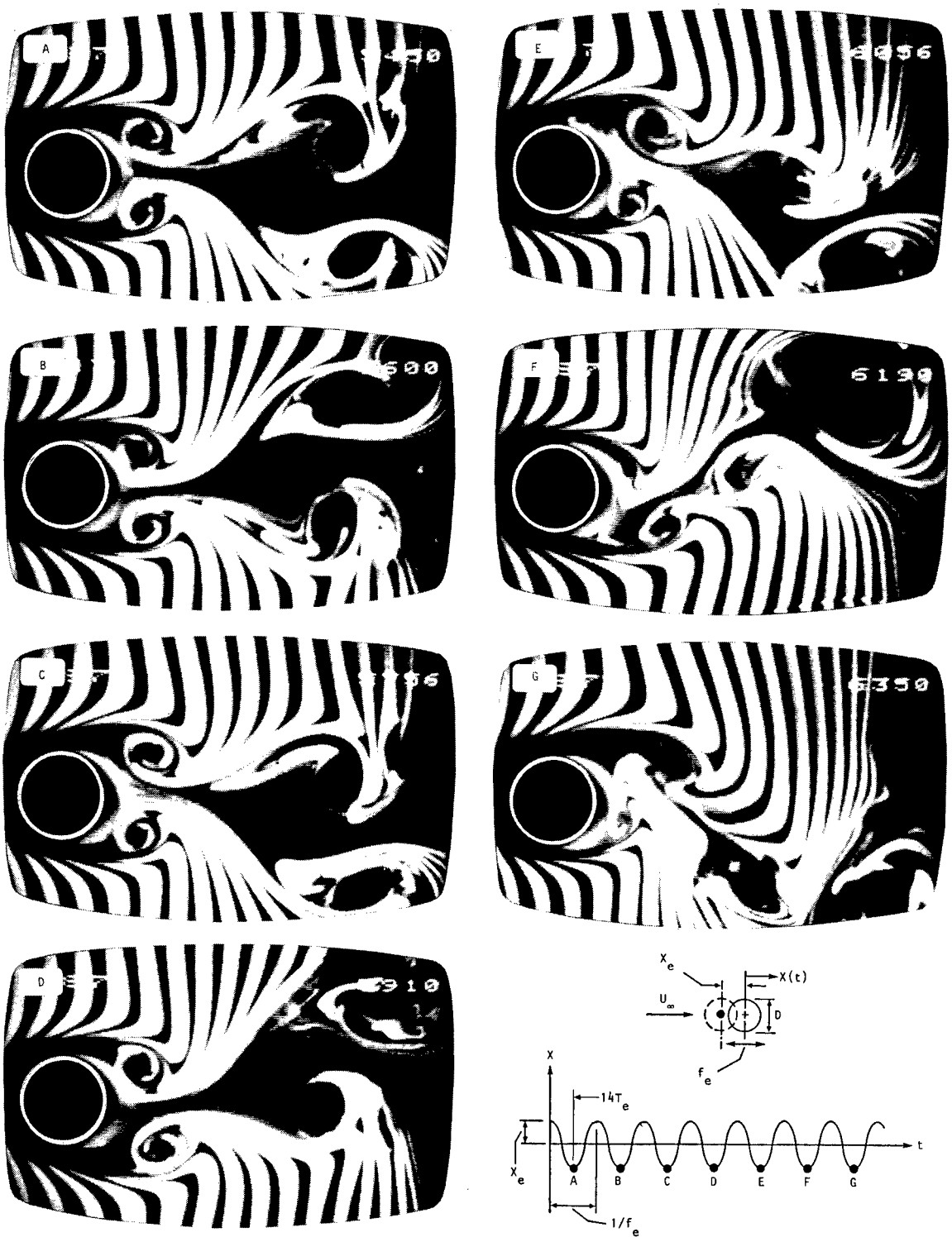


Figure 4: Ordered sequence of decay from symmetrical to antisymmetrical mode of vortex formation over a number of cycles of cylinder oscillation in the streamwise direction. All photographs are phase-locked to the maximum-negative position of the cylinder.

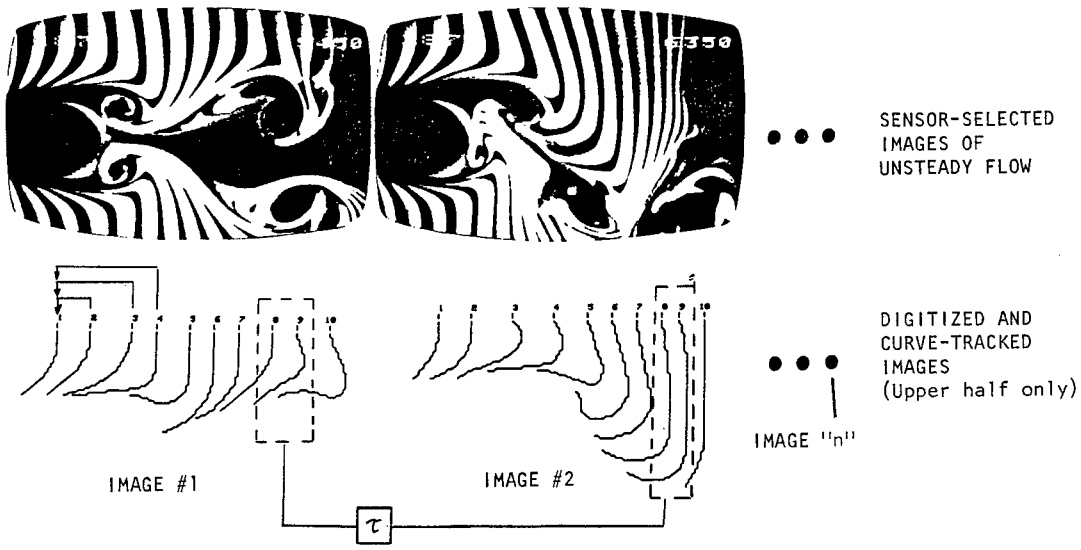


Figure 5: Illustration of correlation between a defined region in two successive images; correlation can be carried out with delay τ. For each photograph, only the upper half of the photo has been digitized and curve-tracked (13).

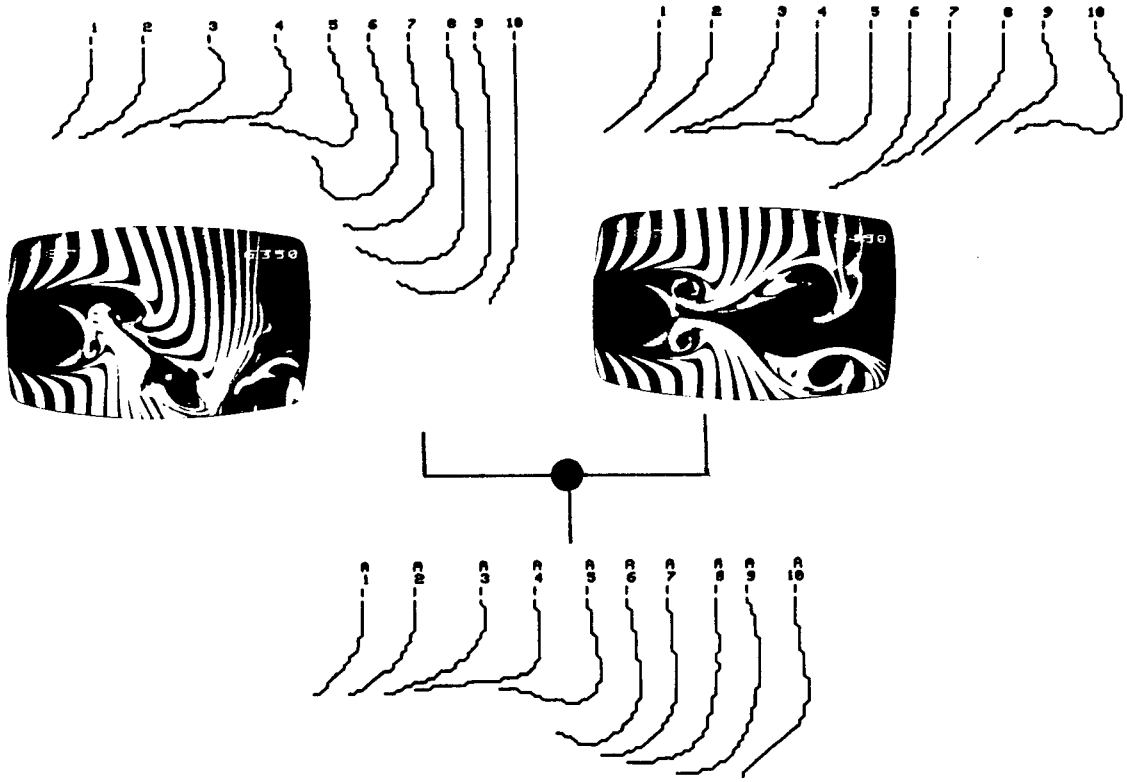


Figure 6: Depiction of concept of ensemble-averaging of two-flow images. The maximum negative position of the cylinder serves as a phase reference for triggering the ensemble-averaging. Digitized images are averaged using the tangent angle function concept (13).

An intriguing possibility is that employed in classifying patterns of fingerprints (17, 18). The images are similar in form to the timeline patterns generated in vortical flows. Although the preprocessing techniques used in fingerprint analysis appear to be directly applicable to typical images of unsteady flows, the types of classification techniques employed for fingerprint analysis have not been fully assessed with application to images of timelines.

Another approach, which directly follows from the tangent angle function concept described in conjunction with Figure 3, is to store the coordinate positions and tangent angle functions of all timelines in a given image; by comparing certain reference positions within the images, it should be possible to identify recurring patterns of the flow structure. The basis for this technique has already been established in the previous section.

Finally, we consider still another approach; it involves the Fourier transform of the tangent angle function ϕ of a given curve (timeline) defined in Figure 3. The Fourier "descriptor" of a timeline, or curve, provides the basis for comparison of timelines of successive images. The Fourier descriptor $\Phi(\omega)$ of the tangent angle function ϕ is discussed and derived by Gumas and Rockwell (9). Figure 7 shows a typical curve in physical space and its tangent angle function

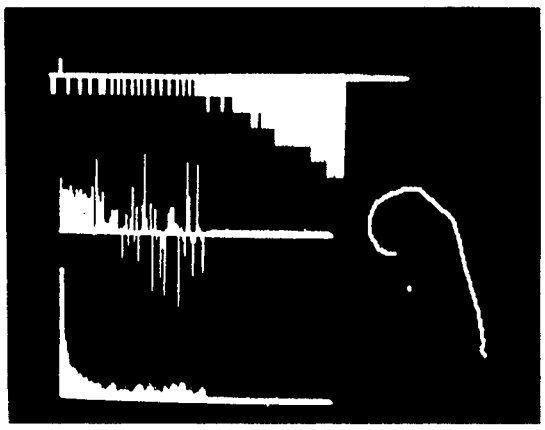


Figure 7: Typical curve appearing in a digitized image and corresponding distributions of tangent angle function (top plot); and spectra of phase (middle plot) and amplitude (bottom plot) resulting from calculation of the Fourier-descriptor of the tangent angle function.

ϕ (top) and the phase (middle) and amplitude (lower) distributions of its Fourier descriptor Φ. In most cases, it is adequate to employ only the first few coefficients of the Fourier descriptors in order to achieve a reasonable definition of the curve (9).

In concept, it is possible to define a library of these Fourier descriptors for a series of images, and by comparing a number of images with the library of descriptors, one could determine the coherent, recurrent patterns of the flow structure. In fact, this technique is commonly used for recognition of aircraft silhouettes (19), hand print character recognition (20), and machine part identification (21). Fourier descriptors of the silhouette of an aircraft, for example, are determined from various spatial perspectives, and by comparing an unidentified aircraft silhouette with the library descriptors of known aircraft, it is possible to rapidly recognize an unidentified aircraft. In principle, the same approach could be used to define and recognize types of large-scale structures. A primary advantage of this approach is that the curve description can be made independent of orientation, position, and scale of the curve. The feasibility of this approach for open curves of the type represented by timelines has been demonstrated by Gumas and Rockwell (9).

THREE-DIMENSIONAL RECONSTRUCTION FROM IMAGES

In the foregoing, the flow is taken to be quasi-two dimensional. In the event that the unsteady flow structure has a pronounced three-dimensional character, it is possible to construct a three-dimensional representation of it using the timeline technique. There are several possible approaches to constructing three-dimensional time-surfaces from patterns of timelines. Smith and Paxson (22) have generated timelines from a single wire whose axis is parallel to the spanwise direction. Using a two-camera system and obtaining two simultaneous views, a three-dimensional surface was constructed; it provided insight into the three-dimensional character of a turbulent boundary layer.

It is, however, possible to determine multiple surfaces representing the three-dimensional flow structure by use of a single wire and a single camera. Ongoren, Chen, and Rockwell (23) employ a wire whose axis is aligned with the cross-stream (y) direction in conjunction with a single camera view in the spanwise direction in order to determine a family of three-dimensional time-surfaces; time-surfaces are formed by connecting timelines in the spanwise (z) direction. This is accomplished using a phase reference technique, whereby phase-locked photos are taken for successive wire locations in the spanwise direction, thereby allowing construction of phase-referenced time-surfaces.

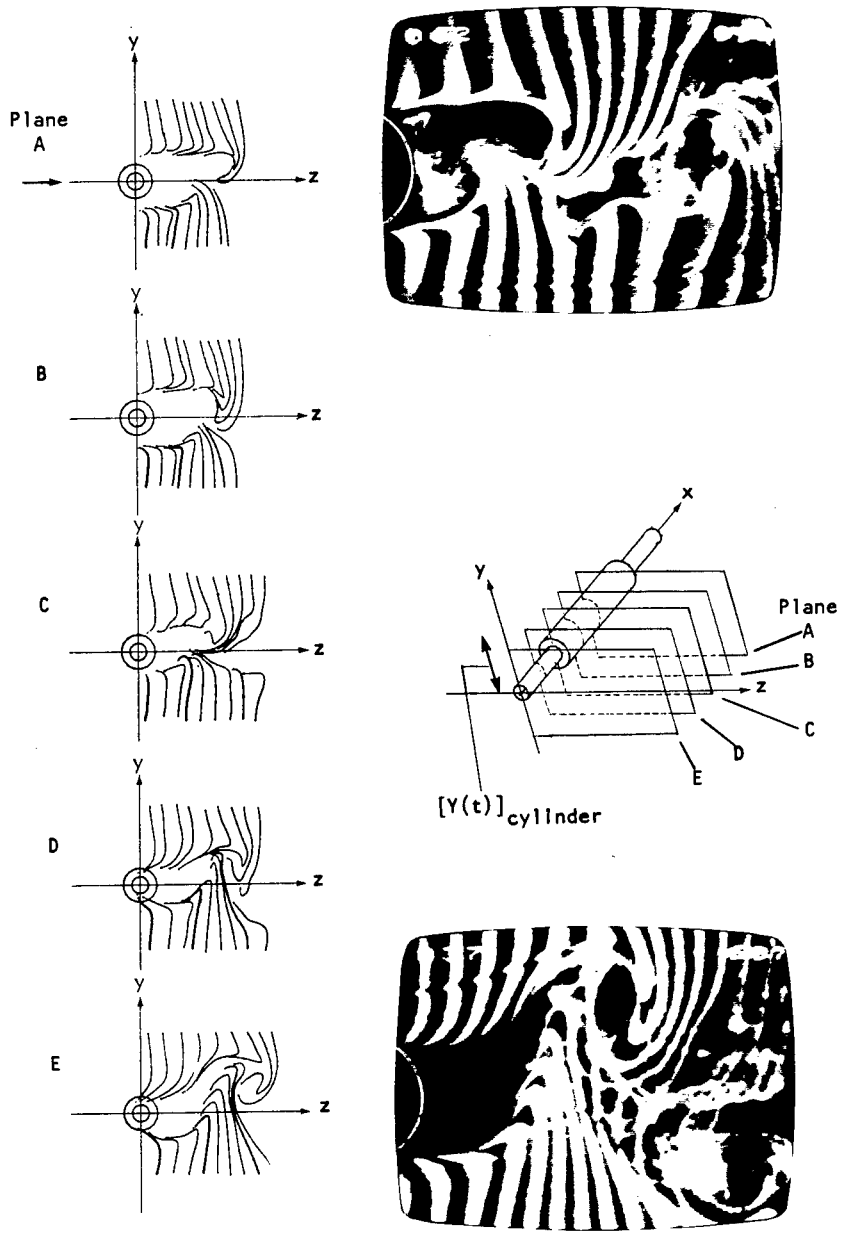


Figure 8a: Flow past a three-dimensional obstacle such as a segmented cylinder strongly distorts the vortex shedding process. Using the cylinder displacement Y(t) as a phase reference, bubble timelines (i.e. material lines) are converted to digitized form, allowing construction of three-dimensional material surfaces using a CAD technique (23).

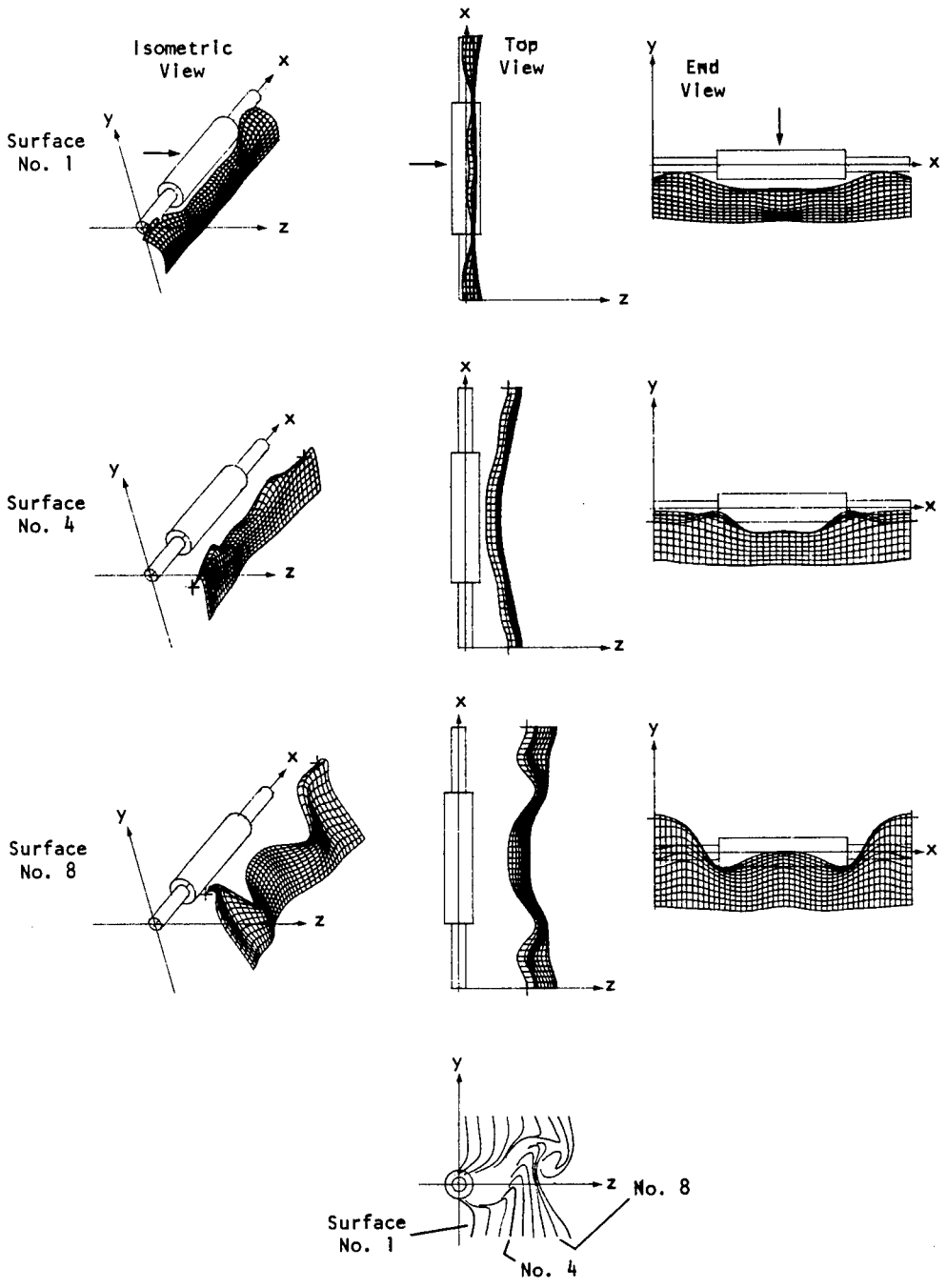


Figure 8b: Streamwise evolution of the three-dimensional vortex shedding is represented by increased distortion of time-surfaces 1, 4, and 8. These three-dimensional surfaces were constructed from the information in Figure 8a (23).

Figure 8a shows the concept for this technique, whereby a severely distorted three-dimensional flow was generated by separation from a segmented cylinder. Phase-locked photos were taken for seventeen planes extending from the mid-section of the small-diameter segment to the mid-section of the large diameter segment; during the reconstruction of the three-dimensional flow structure, it was assumed that symmetry about the midplane of the large-cylinder segment was satisfied, an assumption verified by subsequent hot-film measurements. In Figure 8a, five of these planes are shown and designated as planes A through E. Phase-locked photos were acquired at the maximum-negative displacement of the cylinder; two representative photos are shown. From images of this sort, it is possible to obtain the digitized images illustrated in the left column of Figure 8a.

With the timeline patterns of Figure 8a at hand, it is possible to determine the corresponding three-dimensional time-surfaces by connecting timelines that are originally generated at the same instant in planes A through E. The resultant three-dimensional surfaces are termed time-surfaces as opposed to timelines in a single plane. The three-dimensional surfaces were obtained with use of Unigraphics, a widely used program in the mechanical design area. In essence, this program employs a bicubic spline technique to interpolate between the finite number of timelines in the spanwise direction. Once the three-dimensional surfaces are constructed, it is then possible to view them from any arbitrary direction using the UG-2 work station of the CAD laboratory.

In Figure 8b, we show isometric, plan, and end views of time-surfaces formed by connecting defined timelines, which we designate as timelines 1, 4, and 8. It is evident that there is significant three-dimensional distortion, even at a location relatively close to the three-dimensional cylinder. In particular, the top view shows that the vortex shedding from the large-cylindrical segment lags that from the small-cylindrical segment. In fact, these cross-stream distortions of the time-surface can be related to corresponding cross-stream variations of the velocity (23).

In concept, this technique can be employed in any unsteady flow where a suitable phase reference is available. Considering the wide variety of experimental configurations for which external forcing is applied in the form of oscillating flaps, heating elements, etc., there is considerable potential for further development.

Another approach to determining the three-dimensional structure involves use of the two-camera, dual view system already described in Figure 1. Two views of the three-dimensional flow are acquired simultaneously. Figure 9 shows visualized plan and end views of a tip vortex. The platinum wire is kinked such that it generates spanwise periodic nonuniformities in the bubble sheet. In the plan view, the bubble sheet is relatively long. It shows that the vortex core has a significantly lower axial velocity than that of the free-stream. From these plan and end views, it is possible to estimate the unsteady velocity field. In addition, three-dimensional surfaces can be constructed using the CAD system. The three-dimensional representations of Figure 9 are for the same flow viewed at different perspectives.

Real time, three-dimensional simulation of this tip vortex structure and the foregoing wake structure of Figures 8 and 9 can be displayed on the Evans and Sutherland PS-300 terminal and Unigraphics UG-2 terminals in the Lehigh University CAD Laboratory.

IMAGE EVALUATION FOR VELOCITY EIGENFUNCTION AND VORTICITY

Since the timelines generated from a fixed (wire) in the flow field are convected downstream at a rate proportional to the flow velocity, it is possible to employ a time of flight analysis of the timelines in order to determine the velocity field across the flow; subsequently, for certain classes of flow, distributions of vorticity and circulation follow. The technique of velocity determination via the timeline technique is addressed by Schraub et al (25).

Recently, Lu and Smith (26) have considered this concept in detail and demonstrated its feasibility for determining higher order statistics of a turbulent boundary layer.

With the timeline technique, the mean and fluctuating velocity components are determined from the displacement of timelines on the image in conjunction with the pulsation frequency of the bubble wire. The primary advantage of this approach is that the same data sample is used to determine the instantaneous velocity across the flow at successive instants, thereby circumventing the loss of information characteristic of traditional single- and two-point measurements of velocity.

Figure 10 shows a timeline at two successive instants of time, t and $t + \Delta t$. A possible source of uncertainty is that the actual path of an elemental portion of the original timeline may depart significantly from the streamwise direction. The uncertainty associated with this departure has been analyzed by Lusseyran and Rockwell (27). It obviously depends on the characteristic ratio of the cross-stream v to streamwise u velocity component; this error can be minimized by calculating the velocity in those regions of the flow where the local tangent to the timeline is nearly vertical (i.e. $\gamma \sim 180^{\circ}$). In practice, this accuracy can be achieved by

carrying out measurements close to the bubble generating wire, properly accounting for wake defect corrections.

In typical unsteady shear layers, there are strong gradients of both amplitude and phase of the velocity fluctuations across the layer. Particularly dramatic is the occurrence of a phase jump; timeline techniques are ideally suited to these abrupt phase variations in the cross-stream direction. As shown in Figure 10, phase can be determined by taking the fast Fourier transform (FFT) of the time-dependent u fluctuations at defined values of y across the shear layer. From these Fourier coefficients at each respective value of y, the local phase Φ follows from taking the ratio of the imaginary to real coefficients. Then, the relative phase shift ϕ between successive y locations is simply the difference between the local values of phase Φ. The success of this technique in predicting the location and magnitude of the phase jump is evidenced in Figure 10. The abrupt change in phase of approximately π is in agreement with that predicted from linear stability theory applied to the wake flow downstream of a thin trailing-edge. The streamwise u and cross-streamwise v fluctuating velocity components can also be estimated. Experimental values of u are determined directly from the time of flight technique and values of v by application of the continuity equation assuming harmonic velocity fluctuations. These distributions of u and v are in reasonable agreement with linear theory for an unstable wake flow. Finally contours

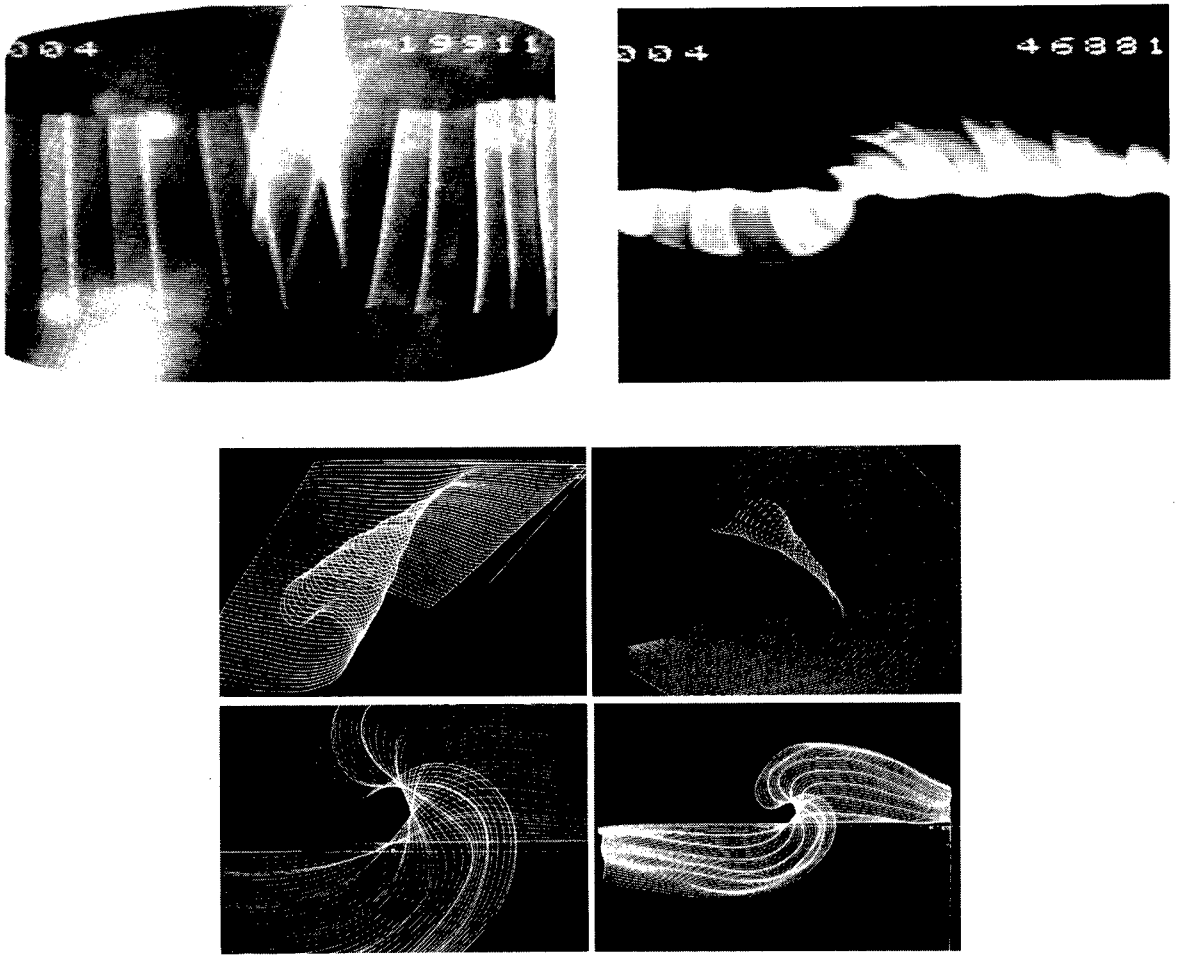
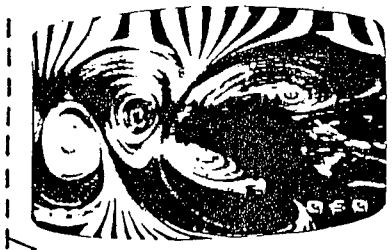
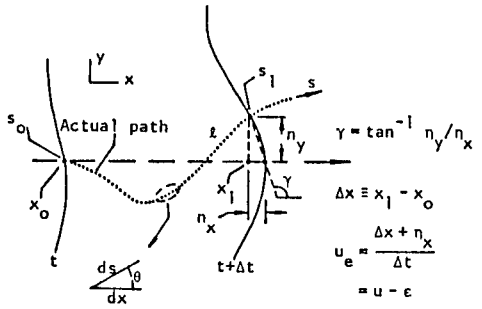


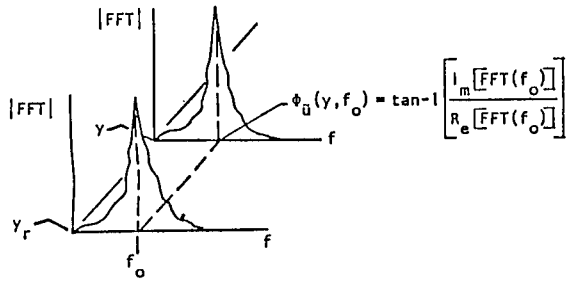
Figure 9: Plan (upper left photo) and end (upper right photo) views of structure of tip vortex obtained by liberation of hydrogen bubbles from pulsed, segmented bubble wire. These synchronized plan and end views allow determination of the instantaneous three-dimensional flow structure using a computer-aided design technique (lower set of photos). This three-dimensional pattern can be viewed from a variety of perspectives (24).



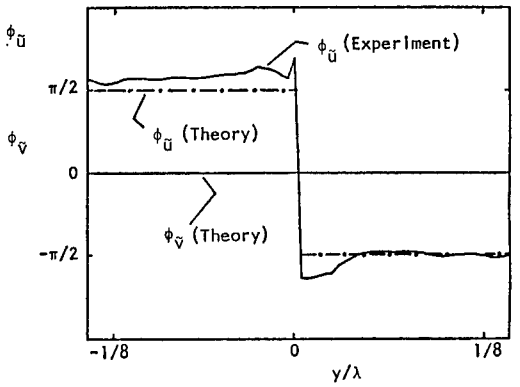
TIMELINE GENERATOR
(VORTICAL STRUCTURES
APPROACHING BODY)



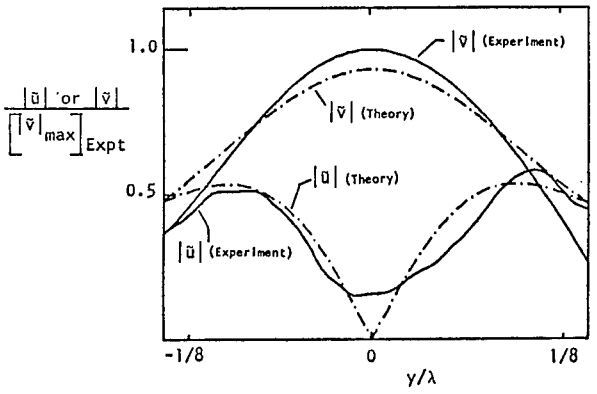
TIMELINE TRACKING



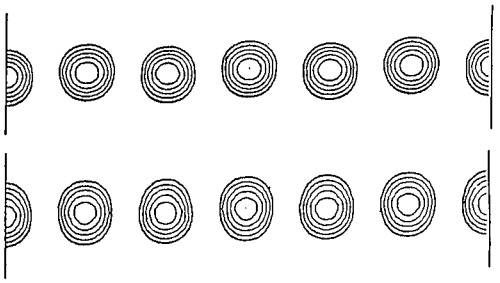
CROSS-SPECTRUM → CROSS-STREAM
PHASE DISTRIBUTION



CROSS-STREAM PHASE



CROSS-STREAM AMPLITUDE



CONTOURS OF CONSTANT VORTICITY
(Theory - top; experiment - bottom)

Figure 10: Tracking of timelines, and use of time-of-flight technique leads to direct determination of the cross-stream phase and amplitude distribution, as well as approximations to contours of constant vorticity for the case of an unstable wake flow (27).

of constant vorticity follow from knowledge of the u and v components of experiment and theory.

FLOW IMAGE-SURFACE PRESSURE CORRELATIONS

The relation between the visualized, instantaneous flow structure and corresponding instantaneous surface pressure requires a means of continuously recording the visualized flow simultaneously with measurement of the instantaneous pressure along the surface of a body. Flow images can be recorded, digitized and processed in a manner similar to that prescribed in the foregoing; on the other hand, determination of the instantaneous pressure distribution along the surface requires either a large array of transducers or a suitable phase reference technique whereby the pressure fluctuations at successive stations are related to each other, then to the flow image. Here we address a simplified technique requiring a single pressure transducer and a two-camera video system. By employing water as the working fluid and restricting experiments to ranges of parameters involving relatively low frequencies, it is possible to obtain accurately the amplitude and phase information of the pressure fluctuations. Using an LDA or hot-film signal in the flow as a phase reference, the phase shift between pressure fluctuations can be determined by cross-spectral analysis. It then remains to determine the phase shift between any one of the surface pressure fluctuations and the flow image at a defined instant. In the event that the flow-surface interaction is sinusoidal, then the oscilloscope trace from the transducer can be viewed through one camera, and the flow image through another camera; then, both images can be displayed simultaneously on the split-screen television system. It is this split-screen capability that provides the link between the instantaneous flow structure and the surface pressure. Obviously, there are several other ways of indirectly determining this crucial phase link.

Visual representation of the flow structure-surface pressure correlation is obtained by processing the images and pressure data in the CAD laboratory. A program has been written which properly accounts for: the phases and amplitudes of the fluctuating pressure at discrete locations along the surface; the phase between the pressure and flow image; and the digitized image. It provides a composite view of the flow structure-surface pressure correlations. The evolution in time of the flow structure and surface pressure field due to primary-secondary vortex formation is shown in Figure 11.

CONCLUDING REMARKS

In the foregoing, we have addressed image analysis techniques that are applicable to a variety of visualization methods; of primary interest herein is the timeline visualization technique. Since this technique marks material elements at defined instants of time, the spacing between, and distortion of, these timelines provides a meaningful basis for interpreting flow images.

Ensemble-averaging of successive images can be achieved rapidly by using the free-stream portions of timelines as a means of identifying and tracking them within an image and between images. The ensemble-averaging process requires use of a phase reference or trigger; in principle, it can take the form of a repetitive, coherent portion of the image or a velocity, pressure, or shear stress signal from the flow.

Various visual correlation techniques can be formulated, again taking advantage of the timeline technique for explicitly identifying lines, or localized regions, of the flow. Autocorrelation of successive timelines within a given image can provide an index of the degree to which the flow pattern undergoes distortion in space and time. Possible extensions of the autocorrelation technique described herein involve its use in identifying the wavelength, frequency, and other quantitative parameters of the large-scale flow structure. Cross-correlation techniques within any given image can provide an index of the degree of asymmetry of the flow structure, and its variation over longer periods of time. This approach has potential for study of the competition between symmetrical and antisymmetrical modes of large-scale flow structures. More detailed formulations of these correlation techniques, involving cross-correlation with the time delay τ, are currently underway. In general, these correlation techniques can be applied not only within a given image, but also between successive images, or portions of images.

Pattern recognition of flow structure within images can be expedited by using the timeline visualization technique; it involves use of the tangent angle function of successive points along a given timeline, and for an entire family of timelines. With this approach, it should be possible, in principle, to establish a library for basic patterns of timelines that correspond to identifiable features of the flow structure. Alternately, it may be desirable to employ the Fourier descriptor technique, whereby each timeline is expressed in Fourier space; then, a library of Fourier descriptors can be established for identifying basic types of flow structure.

Three-dimensional reconstruction of unsteady flow structure can be achieved effectively either by considering flow images taken from two different viewing angles at successive instants of time, or by processing a sequence of images taken from a single viewing angle in conjunction with a phase reference in the flow. Central to the success of both of these techniques is use of a computer-aided design (CAD) technique for construction and displaying three-dimensional views.

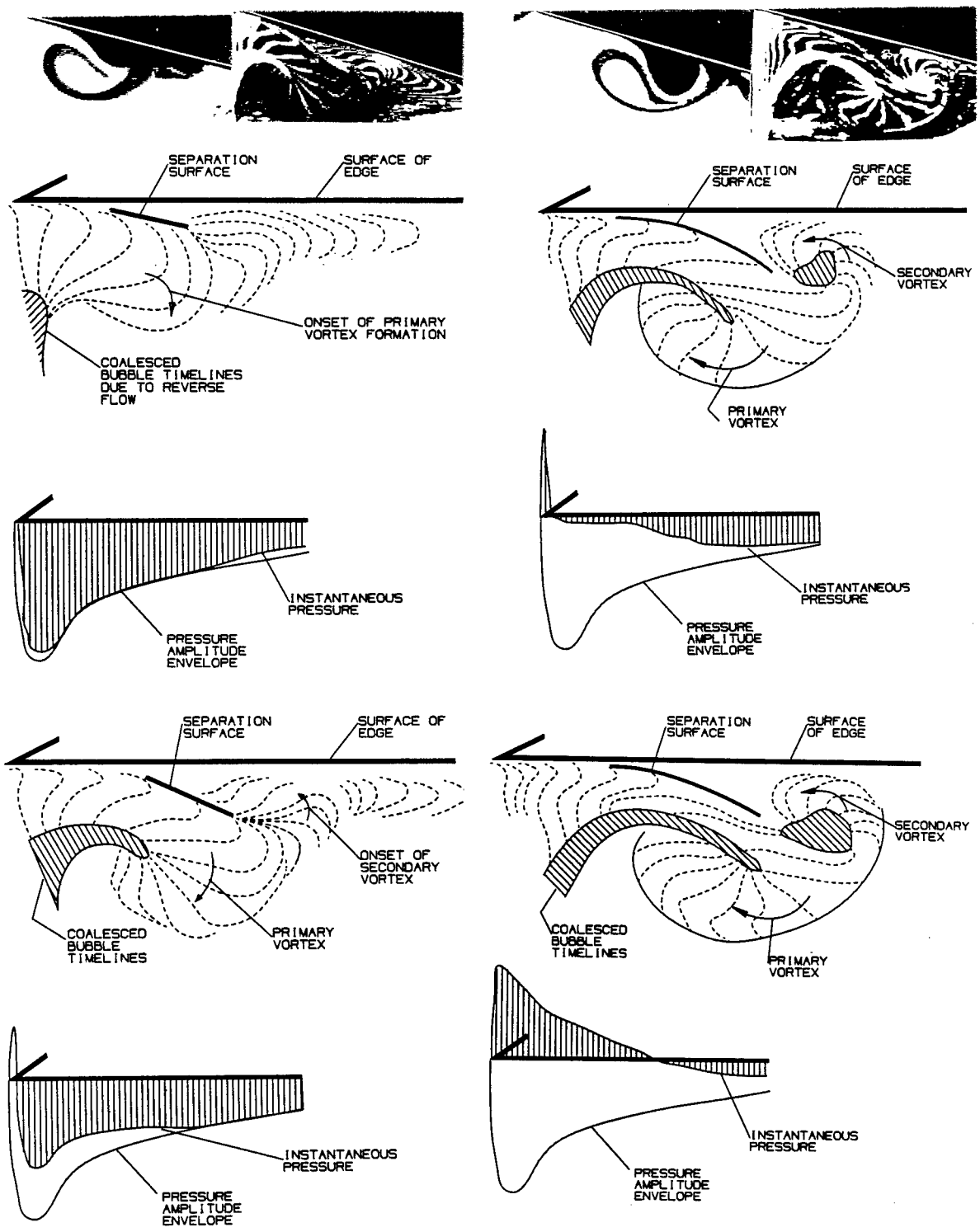


Figure 11: Visualization of primary vortex development in conjunction with flow separation and onset of secondary vortex formation; this visualized flow structure is shown with the corresponding instantaneous pressure fields along the surface of the edge. The top row of photos shows raw flow visualization images obtained from dye injection at the tip of the edge and timeline generation at the tip. The time-dependent timeline patterns were digitized and the synchronized, instantaneous surface pressures were determined in order to construct the flow structure-surface pressure correlations shown above (28).

The unsteady velocity field across the flow can be estimated rapidly from analysis of successive flow images using a time of flight technique. Since the timeline technique provides instantaneous information across the flow, it is particularly well suited to analyzing unsteady shear layers where large gradients of amplitude and phase occur across the layer. In the case of quasi-periodic flow, estimates of the vorticity field follow.

The relation of the unsteady flow structure described in the foregoing to the surface pressure field can be determined by image anlaysis of the visualized flow in conjunction with simultaneous, instantaneous measurements of the surface pressure field. This approach allows determination of the phase shift between local flow distortions and peaks in the surface pressure field.

Obviously, there are a number of interesting avenues that await exploration. Among them are generation of segmented timelines allowing tracking of defined material elements; use of chopped and swept laser illumination in conjunction with timeline generation; and employment of multiple-timeline generators to gain further insight into the three-dimensional flow structure.

ACKNOWLEDGEMENTS

The authors are pleased to acknowledge principal support of the Office of Naval Research, as well as supplemental support from the National Science Foundation and the Volkswagen Foundation.

REFERENCES

1. Emrich, R. J., Methods of Experimental Physics: Fluid Dynamics, Vol. 18, Part A, Academic Press, New York, 1981.

2. Merzkirch, W., Chassery, J. M., Hesselink, L., Schon, J. P., Lourenco, L. and Monti, R., "Flow Visualization and Digital Image Processing" in von Karman Institute for Fluid Dynamics Lecture Series Monographs (1985-1986). Based on June 9-13, 1986, Lecture Series, Designated as 1986-09 Monograph,

3. Hernan, M. A. and Jiminenz, J., "Computer Analysis of a High-Speed Film of the Plain Turbulent Mixing Layer", Journal of Fluid Mechanics, Vol. 119, 1982, pp. 323-345.

4. Bernal, L. P., Hernan, N. A., and Sarohia, V., "Characterization of Coherent Structures in a Turbulent Mixing Layer by Digital Image Analysis", Third International Symposium on Flow Visualization, September 6-9, University of Michigan, Ann Arbor, Michigan, 1983, pp. 407-411.

5. Keffer, J. F., Kowal, J., and Shokr, M., "Image Processing Technique for Determining Properties of Turbulent Flow", Third International Symposium on Flow Visualization, September 6-9, 1983, University of Michigan, Ann Arbor, Michigan, pp. 305-309.

6. Wallace, J. M., Balint, J.-L, Ladahari, F. and Morel, R., "Obligations of Image Processing Analysis to the Study of Turbulent Boundary Layer Structure", Third International Symposium on Flow Visualization, September 6-9, 1983, University of Michigan, Ann Arbor, Michigan, pp. 310-314.

7. Hama, F. R., "Streaklines in a Perturbed Shear Flow", Physics of Fluids, Vol. 5, No. 6, June 1962, pp. 644-650.

8. Gumas, C., Ongoren, A. and Rockwell, D. 1985, Unpublished Image Processing.

9. Gumas, C. and Rockwell, D., "The Fourier Descriptor Technique: A Means of Pattern Description and Recognition In Fluid Mechanics", 1986, to be submitted for publication.

10. Gumas, C., "A General Pattern Recognition Technique for Open Curves", M.S. Thesis, Department of Computer Science and Electrical Engineering, Lehigh University, 1985.

11. Kerstens, P. and Rockwell, D., "Ensemble-Averaging on Correlation Techniques for Flow Visualization Images", 1986, to be submitted for publication.

12. Carlson, A. B. Communication Systems, 2nd Edition, McGraw-Hill, 1975.

13. Kerstens, P. Manual for Spatave: An Image Processing and Pattern Recognition Program for Fluid Flow Analysis, Department of Mechanical Engineering, Lehigh University, September, 1985.

14. Freeman, H., "On the Encoding of Arbitrary Geometric Configurations", IRE Transactions on Electronic Computers, Vol. EC-10, 1961, pp. 260-268.

15. Freeman, H., "Techniques for the Digital Computer Analysis of Chain Encoded Arbitrary Plane Curves", Proceedings of the National Electronics Conference, Vol. 17, 1961, pp. 421-432.

16. Ongoren, A and Rockwell, D., "Flow Structure from an Oscillating Cylinder. Part III: Mode Competition", 1986, to be submitted for publication.

17. Rao, K., and Balck, K., "Type Classification of Fingerprints: A Syntatic Approach", IEEE Transactions on Pattern Analysis and Machine Intelligence, Vol. PAMI-2, No. 3, May, 1980, pp. 223-231.

18. Lerner, E. J., "Sleuthing by Computer" IEEE Spectrum, July, 1983, pp. 44-49.

19. Wallace, T. P. and Mitchell, O. R., "Analysis of Three-Dimensional Movement Using Fourier Descriptors", IEEE Transactions on Pattern Analysis and Machine Intelligence, Vol. PAMI, No. 2 - No. 6, November, 1980, pp. 583-588.

20. Granlund, G. H., "Fourier Processing for Hand Print Character Recognition", IEEE Transactions on Computers, Vol. C-21, February 1972, pp. 195-201.

21. Persoon, E. and Fu, K.-S., "Shape Discrimination Using Fourier Descriptors", IEEE Transactions on Systems, Man, and Cybernetics, Vol. SMC-7, No. 3, March 1977, pp. 170-179.

22. Smith, C. R. and Paxson, R. D., "A Technique for Evaluation of Three-Dimensional Behavior in Turbulent Boundary Layers Using Computer Augmented Hydrogen Bubble-Wire Flow Visualization", Experiments in Fluids, Vol. 1, 1983, pp. 43-49.

23. Ongoren, A., Chen, J., and Rockwell, D., "Multiple Time-Surface Characterization of Time-Dependent, Three-Dimensional Flows", 1986, to be submitted to Experiments in Fluids.

24. Kramer, L. and Rockwell, D., "Visualization of the Three-Dimensional, Time-Dependent Flow Structure of a Tip Vortex", Department of Mechanical Engineering and Mechanics, Lehigh University, 1986, unpublished.

25. Schraub, F. A., Kline, S. J., Henry, J., Runstadler, D. W., and Littell, A., "Use of Hydrogen Bubbles for Quantitative Determination of Time-Dependent Velocity Fields in Low Speed Water Flows", ASME Transactions, Journal of Basic Engineering, Vol. 87, Series D, June 1965, pp. 429-444.

26. Lu, L. J. and Smith, C. R., "Image Processing of Hydrogen Bubble Flow Visualization for Determination of Turbulence Statistics and Bursting Characteristics", Experiments in Fluids, Vol. 3, 1985, pp. 349-356.

27. Lusseyran, D. and Rockwell, D., "Estimation of Velocity Eigenfunction and Vorticity Distributions from the Timeline Visualization Technique", 1986, to be submitted to Experiments in Fluids.

28. Kaykayoglu, R., and Rockwell, D., "Unstable Jet-Edge Interaction. Part I: Instantaneous Pressure Fields at a Single Frequency", Journal of Fluid Mechanics (in press), 1986.

DISCUSSION

William J. Devenport,
Virginia Polytechnic Institute & State University

Over what range of Reynolds numbers can this technique provide useful results?

Reply -

The limiting parameter of this electrolysis technique for generating hydrogen bubbles is actually the absolute speed of the flow. At higher flow speeds, it is necessary to generate more bubbles in order to obtain adequate reflection from bubble sheets in the flow. With a voltage across the electrodes of about one hundred volts, it is possible to attain quality visualization up to flow speeds of one to two feet per second. At substantially higher voltage, taking care to ensure that the power of the generator is also sufficiently high, visualization can be achieved at much higher speeds.

We are currently developing high-speed laser scanning techniques to be employed in conjunction with multiple bubble sheets. In these cases, it is possible to obtain high resolution visualization images of a desired cross-section of a three-dimensional flow.

Yoji Himeno,
University of Osaka Prefecture

Would it be possible to create the instantaneous streamline patterns and also the contours of the vorticity? Would there be any problem for creating those patterns?

Reply -

Of course, for both the instantaneous streamline patterns and the contours of constant vorticity, it is necessary to determine the instantaneous velocity field. We have demonstrated that if the flow is quasi-periodic, the u component can be determined directly from tracking the bubble lines. Then, by use of the continuity equation, the instantaneous v component can be calculated. These instantaneous velocities lead to contours of constant vorticity in the space-time domain.

We are currently developing a technique based on segmented, or periodically insulted, bubble wires, allowing segments of bubbles to be tracked throughout the flow domain. By tracking these individual segments, it will be possible to determine the instantaneous velocity throughout the flow domain, and thereby the corresponding values of vorticity and stream function.

Optimum Body Profiles with Minimum Drag in Two-Dimensional Oseen Flow

M. BESSHO, National Defense Academy, and

Y. HIMENO, University of Osaka Prefecture, Japan

ABSTRACT

The present paper deals with an inverse problem for obtaining optimum body profile with minimum drag in two-dimensional Oseen flow. The flow quantity is at first represented and determined by integral equations using Oseen kernel function and taking stresses on the body surface as variables. Then the variation of the drag due to a slight arbitrary deformation of the profile is calculated and expressed in terms of the flow quantities and the deformation vectors on the surface, also in an integral representation. A Newton-Raphson type iterative scheme is proposed to obtain an optimum distribution of the deformation vectors for mimimizing the drag. The treatment of multi-restriction condition is also described and several numerical results are shown.

NOMENCLATURE

A	Area of body profile
b	Half beam
B	Breadth
C	Body contour
Ci	Coefficients
D	External domain
E	Integral for reciprocity theorem
k	$= 1/(2\nu)$
K_0, K_1	Modified Bessel functions
l	Half length
L	Length
n	Normal coordinate to surface
N	Number of segments
p	Pressure
P,Q	Points (x,y) and (x',y')
Pi	Kernel function for pressure
r	Distance from P to Q
R	Drag of body
Rn	Reynolds number
s	Tangential coordinate along C
Ts,Tn	Stresses in s and n directions
u,v	Velocities in x and y directions
U	Uniform Velocity
Ui,Vi	Kernel functions for u and v
x,y	Coordinates of point P
x',y'	Coordinates of point Q
X,Y	Stresses in x and y directions
Xi,Yi	Kernel functions for X and Y
Zi	Kernel functions for vorticity
β	Beam-length ratio = B/L
δ	Prefix representing variation
ν	Kinematic viscosity
ρ	Fluid density
ζ	Vorticity
Superscript '	Different flow field
Superscript *	Reverse flow quantity
Subscript n,s	Derivatives or components in n and s directions
Subscript x,y	Derivatives w.r.t. x and y
Subscript i	Natural number (1 or 2)

1. INTRODUCTION

In the field of ship wave resistance, a variety of inverse methods for the improvement of ship hull form based on linear wave theory have been established and are widely used in ship design. In the ship viscous resistance field, on the other hand, very few work has been done yet, because of the difficulty of evaluating the viscous resistance itself. The present work is an attempt of fundamental approach to the inverse problem of drag minimization in Oseen flow field.

In early time Bessho (1) showed a method of minimizing crosswise potential flow energy in a ship section which was assumed to be related to ship viscous resistance and obtained optimum frame line configuration. Hess (2) proposed a scheme for obtaining optimum body shape in which he used Squire and Young's formula for evaluating viscous resistance. Nagamatsu (3) applied direct search method for the same optimization problem in which he used boundary layer calculation to determine the drag. Nowacki's recent work (4) also seems to be along this line although he applied his optimization technique to evaluate optimum ship dimensions with ordinary hull form. Such a method of nonlinear programming based on a ship boundary layer calculation will become a useful tool of practical ship design.

On the other hand, it would also be interesting to make fundamental analysis on drag minimization as a pure hydrodynamic problem. Recently Bessho (5) developed a scheme for optimizing boundary shape in boundary element

method in plane stress analysis and applied it to the problem of finding an opimized boundary shape with least stress concentration (6). The method was applied to a flow problem by Bessho and Kyozuka (7) to obtain a cavity shape. They also applied the method to a drag minimization problem based on an empirical boundary layer type formula to obtain optimum shapes in two--dimensional and axisymmetric flows (8,9). Bessho and Himeno (10,11) also applied the method to two-dimensional and axisymmetric Stokes flows to find optimum body shapes. The present work is an extention of the method to two-dimensional Oseen flow.

After Oseen's original work (12), Oseen flow has been studied from various points of view, for instance, Filon's infinite Reynolds number flow (13), Imai's solution (14) by multipole expansion method, Miyagi's integral equation method (15), and so on. Attempts of expanding Navier-Stokes equation by the use of Oseen's kernel function have recently been made by Bessho (16,17,18,19) and Kida (20). Therefore study on Oseen flow seems still to be useful for the understanding of viscous fluid flow.

The procedure of the present inverse method can briefly be stated as follows. The first step is an ordinary method for solving the flow quantities and the drag on a prescibed body shape by integral equation. The secod step is an inverse procedure in which the deviation of the drag due to a small deformation of the body shape is formulated and then inversely the deformation is solved so that the drag is minimized. The third step is an iterative scheme to deform the body profile and to return to the first step until it converges. Thus the present scheme can be regarded as a Newton-Raphson's method in which the drag is a nonlinear function of the body profile.

In the following chapter this scheme is applied to two-dimensional Oseen flow.

2. BASIC EQUATIONS AND RECIPROCITY THEOREM

2.1 Basic Equations

Let us consider a body contour C, the external domain D, and the interior domain $\bar{D}$ as shown in Fig.1. The uniform velocity U is supposed to be in the positive x direction. Let all stresses in the fluid be normalized by the fluid density ρ, then the basic 2-d Oseen equations can be written in terms of the perturbation velocityies u and v, and the pressure p,

$$\begin{aligned} Uu_x &= -p_x + \nu\nabla^2 u \\ Uv_x &= -p_y + \nu\nabla^2 v \end{aligned} \tag{1}$$

and

$$u_x + v_y = 0. \tag{2}$$

The adjoint equation which corresponds to the reverese flow can also be expressed in the following form by replacing U to -U.

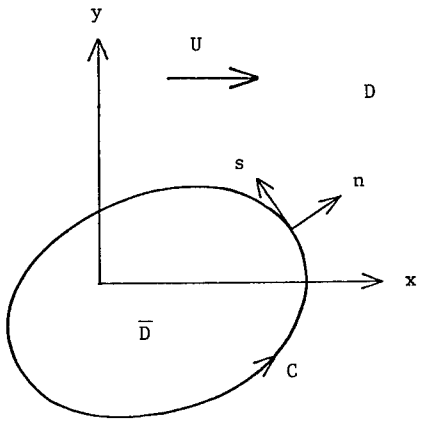


Fig.1 Coordinate system

$$\begin{aligned} -Uu^*_x &= -p^*_x + \nu\nabla^2 u^* \\ -Uv^*_x &= -p^*_y + \nu\nabla^2 v^* \end{aligned} \tag{3}$$

and

$$u^*_x + v^*_y = 0 \tag{4}$$

The boundary conditions are:

$$u = -U,\ v = 0,\ u^* = U,\ v^* = 0 \text{ on } C. \tag{5}$$

The stress components X and Y per unit length on arbitrary plane in D are defined as

$$\begin{pmatrix} X \\ Y \end{pmatrix} = \begin{pmatrix} -p+2\nu u_x, & (u_y+v_x) \\ (u_y+v_x), & -p+2\nu v_y \end{pmatrix} \begin{pmatrix} x_n \\ y_n \end{pmatrix} \tag{6}$$

where x_n and y_n represent directional cosines of the normal $\vec{n}$ of the plane. On C, eq.(6) can be transformed into the following form by using the boundary condition (5), the continuity (2), and the vorticity ζ (= $v_x - u_y$).

$$X = -px_n - \nu\zeta y_n,\ Y = -py_n + \nu\zeta x_n \tag{7}$$

The tangential and normal components of the stress Ts and Tn on C become the form,

$$Ts = Xx_s + Yy_s = \nu\zeta,\ Tn = Xx_n + Yy_n = -p. \tag{8}$$

Similar expressions also hold for the reverse flow quantity.

The relationship between the pressure and the vorticity on the contour C can be derived from equation (1) and the boundary conditions as follows.

$$p_n = -\nu\zeta_s,\ p_s = \nu\zeta_n - \zeta x_n \tag{9}$$

The last term should disappear if we take Navier-Stokes equation instead of Oseen's one, so that the pressure and the vorticity are conjugate each other on C in real fluid.

Other flow properties in Oseen flow are well known through many text books, and are not stated here.

2.2 Reciprocity Theorem

Let us take two arbitrary velocity fields (u,v) and (u',v') in the domain D and introduce the following double integral E.

$$E(u,v;u',v')= \nu \iint_D 2(u_x u'_x + v_y v'_y) + (u_y + v_x)(u'_y + v'_x)\, dxdy \qquad (10)$$

The integral E would be related to the dissipation energy in the fluid if the two fields should coincide. It is obvious that reciprocity between the two fields holds in the expression E.

$$E(u,v;u',v') = E(u',v';u,v) \qquad (11)$$

If we assume (u,v) satisfies eq.(1) and (u',v') coincides with (u^*,v^*), i.e., the reverse Oseen flow in eq.(3), we can substitute these equations into eq.(10) and perform partial integration, by utilizing eq.(6). Then we can obtain a line integral form.

$$\int_C (u^*X+v^*Y)ds = \int_C (uX^*+vY^*)ds - U\int_C (uu^*+vv^*)ds \qquad (12)$$

If we apply the boundary condition (5), the last term vanishes and we obtain the form,

$$U\int_C X\, ds = -U\int_C X^* ds \qquad (13)$$

which means that the drags in the positive flow and in the reverse flow are the same, and that it is independent of the body shape.

2.3 Velocity Field

In eq.(12), the reverse flow velocities u^* and v^* can be replaced to the Oseen kernel functions like Ui(P,Q), Vi(P,Q), where the point P(x,y) lies on the boundary C and the singularity lies at the point Q(x',y') in the domain D. Thus we have

$$u(Q)=-\int_C (X(P)U_1(P,Q)+Y(P)V_1(P,Q) - u(P)X_1(P,Q)-v(P)Y_1(P,Q) - (u(P)U_1(P,Q)+v(P)V_1(P,Q))x_n)ds(P),$$
$$v(Q)=-\int_C (XU_2+YV_2-uX_2-vY_2-(uU_2+vV_2)x_n)ds. \qquad (14)$$

In eq.(14), the contour of the line integration has been extended to include a small circle around the singularity point Q, and the stress singularities Xi and Yi correspond to those of velocities Ui and Vi satisfying eq.(6). All of the singularities are listed in APPENDIX.

If the point Q lies inside of C, a similar expression to eq.(14) holds and then bringing the point Q to the external region D the left-hand side of the expression will be zero, which can be added to the original eq.(14). Then the result will be the following form in which the boundary condition is also taken into account.

$$u(Q) = -\int_C (XU_1(P,Q)+YV_1(P,Q))ds(P)$$
$$v(Q) = -\int_C (XU_2(P,Q)+YV_2(P,Q))ds(P) \qquad (15)$$

Equation (15) holds in the entire domain $D+\bar{D}$, and means that the flow is at rest in the internal region. This is the fundamental expression for 2-d. Oseen flow with the stresses on the surface as unknown variables.

If the point Q lies on C, we have a set of integral equations for solving the stresses X(P) and Y(P) on C.

$$\int_C X(P)U_1(P,Q)+Y(P)V_1(P,Q)\, ds(P) = 1$$
$$\int_C X(P)U_2(P,Q)+Y(P)V_2(P,Q)\, ds(P) = 0 \qquad (16)$$

Eq.(16) can be solved by any numerical scheme. Then we can determine the flow quantities, the velocities by eq.(15), and the vorticity and the pressure by the following equations.

$$\zeta(Q) = -\int_C (XZ_1(P,Q)+YZ_2(P,Q))ds(P) \qquad (17)$$
$$p(Q) = -\int_C (XP_1(P,Q)+YP_2(P,Q))ds(P) \qquad (18)$$

It should be noted here that in eqs.(15) to (18) the pressure constant p_0 remains undetermined, which can be fixed by prescribing the pressure inside of C to be zero, for instance.

From the procedure mentioned above, we can evaluate all the flow quantities once the body profile is prescribed. This is the first step of the present inverse analysis.

3. BODY DEFORMATION AND DRAG MINIMIZATION

3.1 Drag Variation Due to Body Deformation

Let us assume that the body profile is deformed by an amount of δn in the normal direction to the contour C as shown in Fig. 2. The new domain is denoted as D', and correspondingly the velocities become u' and v', which can be analytically continued to the original contour C if the deformation is very small. We can define velocity variations δu and δv on C and approximate them to the first order as in the following form.

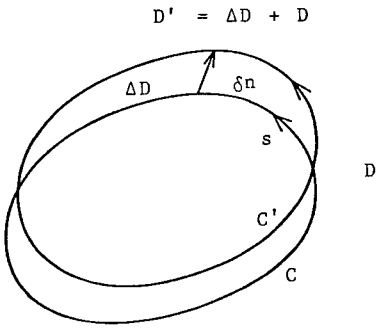


Fig.2 Body deformation

$$\delta u = u'(\text{on C}) - u(\text{on C}) = -u_n(\text{on C})\delta n = \zeta_y \delta n, \text{ on C}$$
$$\delta v = -v_n \delta n = -\zeta_x \delta n \quad (19)$$

Similar expression also holds for the reverse flow velocities u* and v*.

The drag R can be defined by using the reciprocity integral (10) as the following form.

$$UR = U\int_C X ds = -E_D(u,v;u^*,v^*) - U\iint_D (u^* u_x + v^* v_x)dxdy \quad (20)$$

The drag R' in the new domain D' can also be defined by putting the prime ' to all the quantities in eq.(20). Thus the deviation of the drag δR due to δn can be defined as

$$\delta R = R' - R \quad (21)$$

and utilizing the definition of R and R' we obtain the following form.

$$U\delta R = I_1 + I_2 \quad (22)$$

$$I_1 = E_D(u,v;u^*,v^*) + U\iint_D (u^* u_x + v^* v_x)dxdy \quad (23)$$

$$I_2 = E_D(u,v;u^*,v^*) - E_{D'}(u',v';u^{*'},v^{*'}) - U\iint_D (u^{*'}u_x' + v^{*'}v_x' - u^* u_x - v^* v_x)dxdy \quad (24)$$

The first integral (23) represents the effect of deviation of the domain, whereas the second integral (24) corresponds to the effect of the velocity change due to the body deformation.

After reduction and linearization of the above equations we can first obtain the form,

$$I_1 = \int_C (\nu\zeta\zeta^* + U^2 u_x)\delta n \, ds \quad (25)$$

in which the vorticity definition and the continuity equation on C are used for the derivation. And for the second integral we can make partial integration of eq.(24) and obtain

$$I_2 = \int_C (u^{*'}X' + v^{*'}Y' - u^*X - v^*Y) ds = \int_C (\delta u^* X + \delta v^* Y + u^* \delta X + v^* \delta Y) ds. \quad (26)$$

For the deviations of the stresses X and Y in eq.(26), we can use the following equation as a variation of eq.(12).

$$\int_C (u^* \delta X + v^* \delta Y) ds = \int_C (\delta u X^* + \delta v Y^*) ds - U\int_C (u^* \delta u + v^* \delta v) x_n \, ds \quad (27)$$

Substituting eq.(27) into eq.(26), and using eq.(19) we finally obtain the form for the second integral.

$$I_2 = -\int_C (2\nu\zeta\zeta^* - U^2 u_x)\delta n \, ds \quad (28)$$

The expression for the drag variation δR is consequently derived in the following form,

$$U\,\delta R = -\int_C (\nu\zeta\zeta^* - 2U^2 u_x)\delta n \, ds \quad (29)$$

where the first term in the righthand side corresponds to the same expression in Stokes flow (Bessho and Himeno, 10), and the last term to an inertia effect. Similar equation can be obtained for the drag variation δR^* in the reverse flow,

$$U\,\delta R^* = +\int_C (\nu\zeta\zeta^* - 2U^2 u_x^*)\delta n \, ds \quad (30)$$

and from eq.(13)

$$\delta R + \delta R^* = 0. \quad (31)$$

Combining these three equations we finally obtain the following form.

$$\int_C (\zeta - \zeta^*) x_n y_n \delta n \, ds = 0 \quad (32)$$

$$U\delta R = -\int_C (\nu\zeta\zeta^* + U^2(\zeta+\zeta^*) x_n y_n)\delta n \, ds \quad (33)$$

3.2 Drag Minimization

An optimum profile in the present problem should have minimum drag, so that the variation of the drag should be zero.

$$U\delta R = -\int_C (\nu\zeta\zeta^* - 2U^2 u_x)\delta n \, ds = 0 \quad (34)$$

As the least requirement for the restriction condition, we assume here the area A of the body profile to be specified as a constant, which means that the variation δA becomes zero.

$$\delta A = \int_C \delta n \, ds = 0 \quad (35)$$

Therefore from eqs.(34) and (35) we obtain

$$\nu\zeta\zeta^* - 2U^2 u_x = \text{const.} = C_0 \quad (36)$$

or,

$$\nu\zeta\zeta^* + (\zeta+\zeta^*) x_n y_n = C_0 \quad (37)$$

It is noted that as the viscosity increases only the first term remains, which corresponds to the case in Stokes flow. In the high Reynolds number range, however, eq.(36) becomes

$$u_x = \text{const. on C} \quad (38)$$

which will lead to meaningless solution because of the boundary condition, i.e., lead to a numerical divergence in the solution procedure.

The edge angle of the optimum body can also be analyzed in the same manner as in Stokes flow, and the requirement condition at the edge is found to be a finite value for the vorticity which results that the half edge angle is proved to be 51.3 degree, same to Stokes flow, though the proof is omitted here.

3.3 Iterative Solution Procedure

Since eq.(36) or (37) is nonlinear for the unknown vorticities, we cannot solve the equation system directly. An iterative scheme is required to obtain the optimum profile. Let us take a deviation of eq.(37), then we obtain the

form,

$$\delta\zeta(\nu\zeta^*+x_n y_n)+\delta\zeta^*(\nu\zeta+x_n y_n) = C_0 - \nu\zeta\zeta^*-(\zeta+\zeta^*)x_n y_n, \text{ on C} \quad (39)$$

where the variations of the vorticity $\delta\zeta$ and $\delta\zeta^*$ are related to the variations of the stress using eq.(17).

$$\delta\zeta = -\int_C(\delta X Z_1(P,Q)+\delta Y Z_2(P,Q))ds, \text{ on C} \quad (40)$$

Similar relation holds for the reverse flow. We can also take the variation of eq.(15) for the velocity, and substitute it into eq.(19).

$$\delta u = -\int_C(\delta X U_1+\delta Y V_1)ds = \zeta y_n \delta n$$
$$\delta v = -\int_C(\delta X U_2+\delta Y V_2)ds = -\zeta x_n \delta n \quad (41)$$

Therefore, once we obtained the flow quantities on a prescibed initial body profile, we can obtain the variations of the stresses δX and δY, the linearized optimum body deformation n, and the unknown constant C , by solving eq.(35) and eqs.(39) to (41) at the same time. We would also have to combine the similar expressions for the reverse flow if the body shape should be asymmetric. All the equations are in integral form so that they can be converted into a set of simultaneous equations. And the kernel functions are almost the same to those in solving the flow quantities.

After the deformation vector is obtained on the body contour, we can deform the profile and obain a new shape as the next step. This procedure should be iterated until it converges within a prescribed error allowance.

In case that the body profile is symmetric about the origin, a great deal of the reduction of the number of the unknowns can be made. We thus have

$$\zeta(x,y)= -\zeta(-x,y),\ \zeta^*(x,y)= -\zeta^*(-x,y)$$
$$\delta n(x,y)= \delta n(-x,y) \quad (42)$$

and eq.(32) is satisfied automatically. So the unknowns are distributed only in the upper quadrants of C and it is not necessary to calculate the reverse flow quantity.

3.4 Multi-Restriction Condition

It is not difficult to introduce other type of restriction condition. The length of the body can be specified in the following form.

$$\delta n(y=0) = 0 \quad (43)$$

The beam can also be specified as

$$\delta n(x=0) = 0 \quad (44)$$

in case of symmetric body.

Any other condition like the above can be added to the original equations for determining the deformation vector, although eq.(37) should be changed to include additional terms in order to compansate the increased number of equation. Thus we may assume

$$\nu\zeta\zeta^*+(\zeta+\zeta^*)x_n y_n = C_0 + C_1 x^2 + C_2 x^4 + .. \quad (45)$$

Considering eq.(34), the additional terms in eq.(45) correspond to the conditions for specifying higher order moments of the profile such as the following forms, in the after body.

$$\int_C x^2\delta n\, ds = 0,\ \int_C x^4\delta n\, ds = 0\ ,,,. \quad (46)$$

We thus have additional unknown coefficients for the additional restriction conditions.

4. NUMERICAL PROCEDURE

4.1 Panel Method

For the first step of the inverse analysis in the 2-d. Oseen flow, only right-left and fore-aft symmetric body profile is treated here. The contour C in the upper plane is divided into N segments (N is about 30), on which the variables are assumed to be constant. When the area is to be specified, the value is taken to be the same to that of a circle of unit radius, i.e., π. For solving eq.(16) to determine the flow field, the number of the unknowns is 2N for the stresses X and Y in the upper plane. And for determining the deformation vector, 2N unknowns for δX and δY in the upper plane, N/2 for δn in the first quadrant, and a few unknowns for the additional conditions are needed. All the integral equations are transformed into simultaneous linear equations and are solved by Gauss-Jordan method with double precision digit.

The initial profile for the iteration is prescribed as an ellipse with an appropriate beam-length ratio. The number of the iteration is from 5 to 20 according to the initial shape and to the error allowance for convergence, which is about 0.003 for max. of δn.

4.2 Singularity Treatment

As will be shown in APPENDIX, all the Oseen kernels like Ui, Vi, Zi, Pi includes the modified Bessel functions of the zeroth and first orders, $K_0(kr)$ and $K_1(kr)$, where $k=1/2\nu$, and r denotes the distance between the points P and Q. For small kr we have

$$K_0(kr) = -\log(kr) + O(1) \quad (47)$$

$$K_1(kr) = 1/(kr) + O(kr). \quad (48)$$

These singularities can be treated only in self-induced segment (P=Q), in which the singular part is analytially integrated and the rest is treated by Gaussian numerical integration.

For high Reynolds number, an asymptotic expansion for the Bessel functions can be utilized for larger value of kr.

$$K_0(kr) = K_1(kr) = (\pi/2kr)^{1/2}\exp(-kr) \quad (49)$$

Singular behavior like step function appears in

the wake region of a segment, which can be treated separately both for the upper and lower parts in the wake. This effect becomes severe when the segment lies parallel to x-axis and kr becomes large.

5. CALCULATION RESULTS AND DISCUSSIONS

5.1 Flow Around Elliptic Cylinder

Before proceeding to optimum profiles, it is useful to calculate the Oseen flow around elliptic cylinders in order to understand the flow property and to confirm numerical accuracy.

Fig.3 shows the Reynolds number effect on the pressure and vorticity distributions on the circular cylinder. As Reynolds number increases the stagnation pressure and the vorticity peak decreases and approaches to Filon's limiting flow. This situation also holds for an elliptic cylinder of beam-length ratio B/L=0.3 as shown in Fig.4. The drag coefficient for elliptic cylinders of various B/L ratio is calculated and shown in Fig.5. When the length L is specified there is no optimum B/L ratio with minimum drag so that flat plate has smallest drag for any Reynolds number. However when the area is specified there is an optimum B/L ratio in very small Reynolds number range, though the figure is not shown here. For moderate Reynolds number, therefore, the flat plate has smallest drag among the elliptic cylinders of same length or same area in Oseen flow.

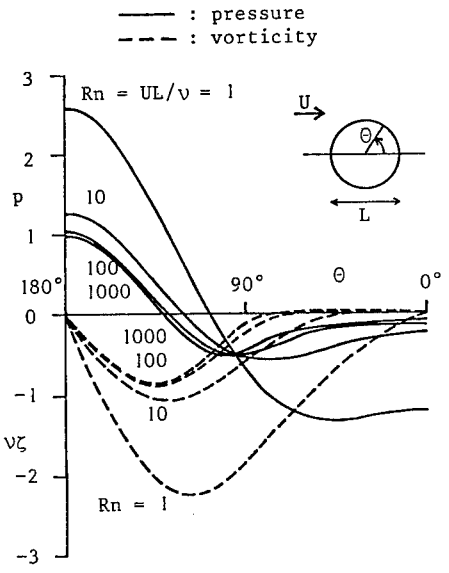


Fig.3 Pressure and vorticity distribution on circular cylinder

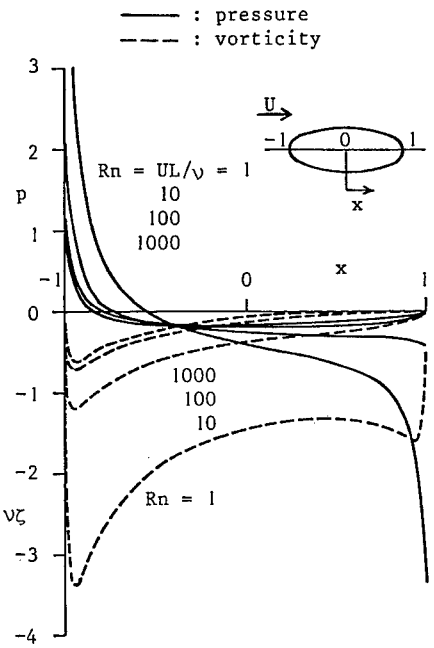


Fig.4 Pressure and vorticity distribution on elliptic cylinder (B/L = 0.3)

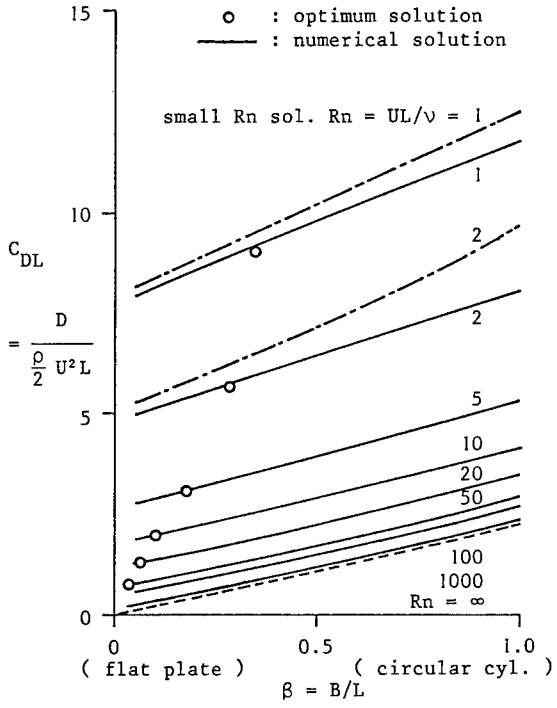


Fig.5 Drag coefficient of elliptic cylinders

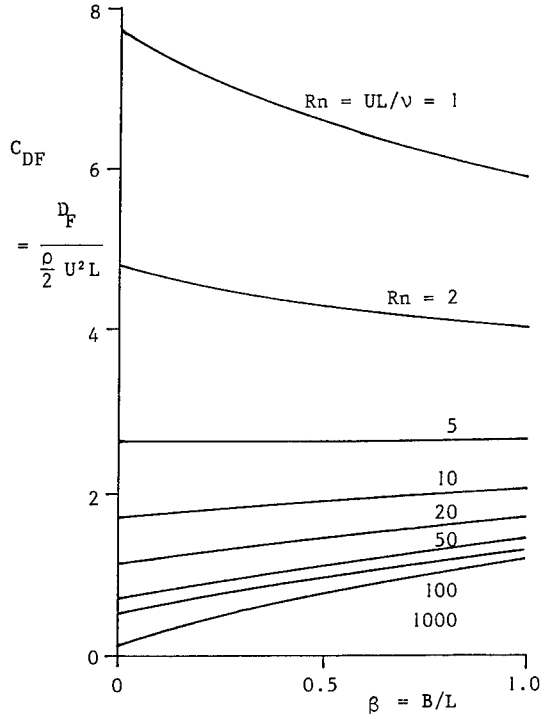


Fig.6 Friction drag coefficient

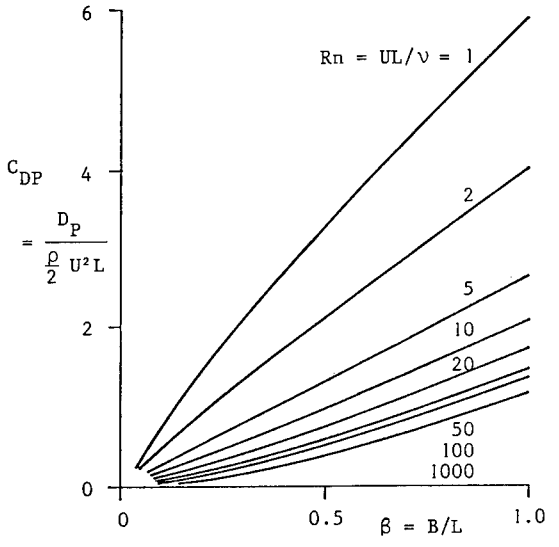


Fig.7 Pressure drag coefficient

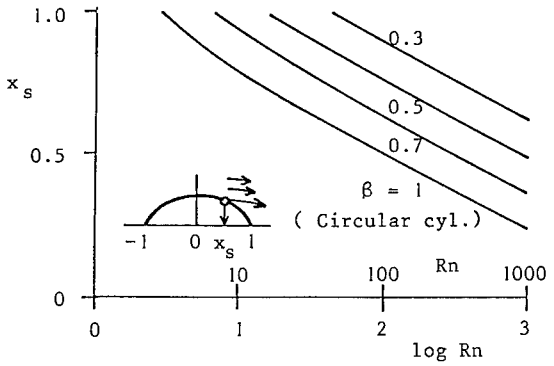


Fig.8 Location of separation point

Optimum B/L points for the optimum profile which will be stated later, are also plotted in Fig.5. Optimum profiles have a little smaller drag than the elliptic cylinder of same B/L ratio and also approach to flat plate as Reynolds number increases.

Figs. 5 and 6 illustrate the friction and pressure drag coefficients of the elliptic cylinders. The friction drag does not show rapid change against B/L and at high Reynolds number it seems to be proportional to B/L. The pressure drag, on the contrary, seems roughly proportional to the beam at moderate Reynolds number. For the relationship between the friction and pressure drags, the following formula

$$D_P = (B/L)\, D_F \qquad (50)$$

is numerically confirmed for elliptic cylinder at arbitrary Reynolds number in 2-d. Oseen flow, although the proof has not been done here.

The location of the separation point on the elliptic cylinders are shown in Fig.8. As Reynolds number increases the separation point moves upstream and approaches to maximum beam position, i.e., to the limiting flow pattern.

5.2 Optimum Profiles

The calculation is made here only for the symmetric profiles about origin, for simplicity and for the first step of the present problem.

Fig.9 shows the calculated results of elementary optimum profiles which have one ristriction condition, for instance, the area being specified to be π, same to that of the circular cylinder of unit radius. Only the first quadrant is shown in the figure. All the profiles have sharp edge at both ends where the half edge angle should be 51.3 degree according to the theoretical analysis. As Reynolds number increases the shape becomes elongated and approaches to flat plate.

The case when the length is specified to be 2 is shown in Fig.10. The Reynolds number dependency is similar to the former case of area specified. The profile should also be

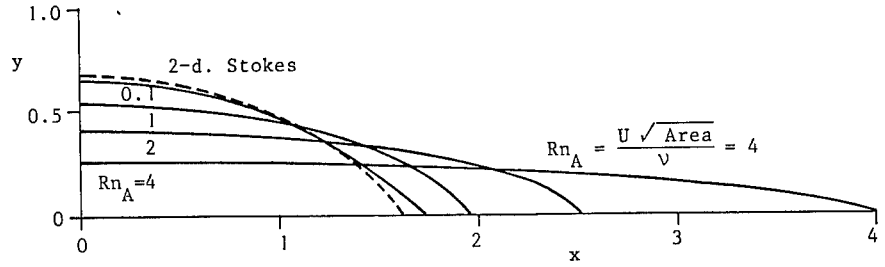


Fig.9 Optimum shape in 2-d. Oseen flow (Area = π)

similar to the former case when the corresponding Reynolds number is the same, since the same equation (37) is adopted for thr requirement of the vorticity. The drag has already been shown in Fig.5, where the drag reduction is quite small compared to that of elliptic cylinder of same B/L ratio.

Fig.11 shows the pressure and vorticity distribution on the profile, which has similar tendency to that of elliptic cylinder in Fig.4, although the vorticity has finite value at both ends of the profile. Fig.12 shows the half beam value which tends to that of Stokes flow (abt 0.4) for small Renolds number and approaches to zero, i.e., flat plate. The profile curve is normalized by the half beam and by the half length as shown in Fig.13. The normalized profiles in Oseen flow is somewhat elongated probably by the influence of the inertia term, compared to that in Stoke flow.

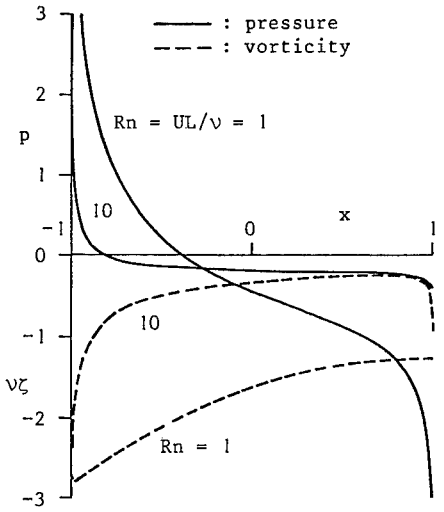


Fig.11 Pressure and vorticity distributions on optimum profiles

5.3 Optimum Profiles with Multi-Restriction

When the number of the ristriction condition is increased the freedom of deformability decreases as experienced in the Stokes flow problem. Here only the results with the length and the beam specified are shown as examples of the multi-restriction case. The length is fixed to be 2 in all cases and the beam is specified to be the value of the elementary optimum profile for a prescribed Reynolds number.

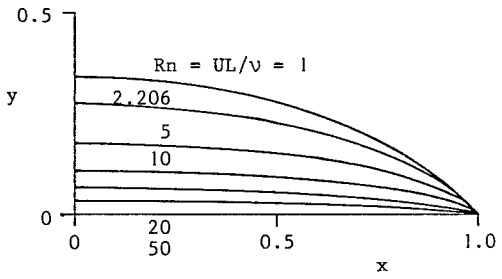


Fig.10 Optimum shape in 2-d. Oseen flow (fore-aft symmetric and length-specified)

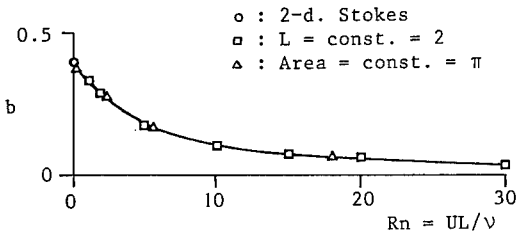


Fig.12 Half beam of optimum shape (L = 2.0)

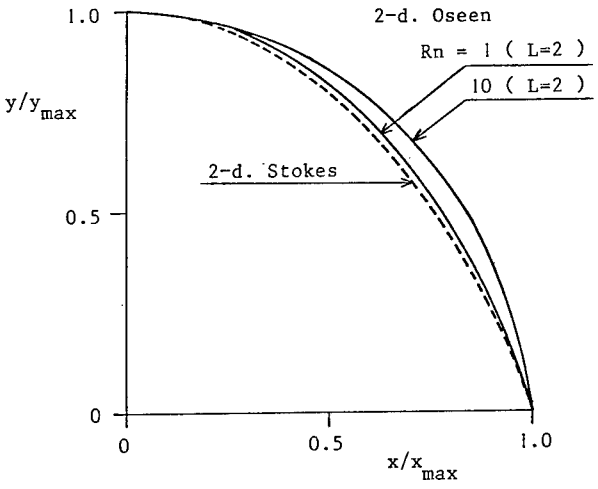


Fig.13 Normalized optimum shape

Figs.14 and 15 show the cases when the half beams are fixed to be 0.343 and 0.287 which correspond to the optimum values for the elementary optimum shape at Reynolds numbers 1 and 2 respectively. When Reynolds number increases with length and beam fixed, profiles with blunt nose are obtained and at higher Reynolds number the iteration does not converge. It can be considered that the blunt nose is a numerical solution with a cirtain accuracy and it may not be an exact solution, since the half nose angle must be 51.3 degree if the vorticity remains finite there. Therefore the appearance of the blunt nose seems to be due to the non-uniqueness of the solution at high Reynolds number. In any case, the increase of drag near the separated end for the blunt-nose profile seems to compensate with the drag decrease in the smoothened side area. A similar situation was also experienced in Bessho and Kyozuka's analysis on the optimum profiles based on the boundary layer concept (8).

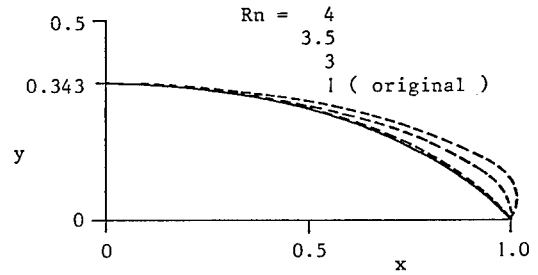


Fig.14 Optimum profiles (l=1, b=0.343)

The cases when narrower beams are specified are shown in Figs.16 to 18. The beams correspond to the elementary solutions at higher Reynolds number. When the beam becomes smaller, the blunt nose no longer appears and convergence is not achieved at high Reynolds number. Instead, round curves appear in the side region at lower Reynolds number. This is a quite similar result to that of Stokes flow (10) with multi-restriction.

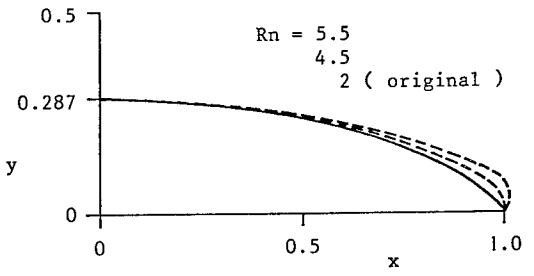


Fig.15 Optimum profiles (l=1, b=0.287)

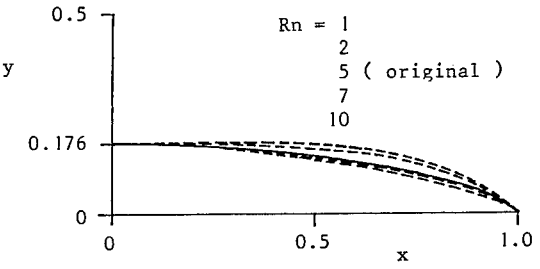


Fig.16 Optimum profiles (l=1, b=0.176)

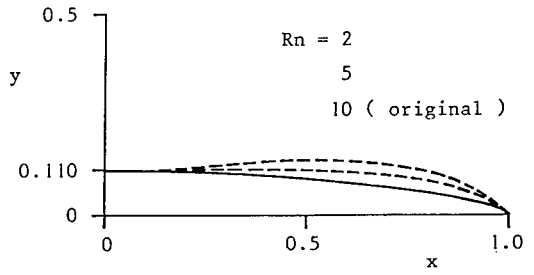


Fig.17 Optimum profiles (l=1, b=0.110)

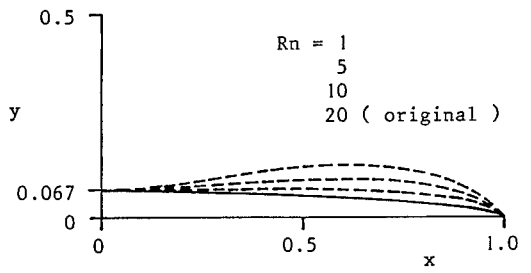


Fig.18 Optimum profiles (l=1, b=0.067)

6. CONCLUSIONS

Bessho's inverse scheme for obtaining optimum boundary shape by boundary element method is applied to two-dimensional Oseen flow. The optimum profiles with minimum drag are obtained in case of symmetric body. The following conclusions can be made.

i) In case when the area is specified the optimum profile becomes rather elongated than that in Stokes flow, and approaches to flat plate at high Reynolds number.

ii) The optimum profile has sharp edge at both ends where the half angle is 51.3 deg.

iii) For the case of the length specified similar results are obtained.

iv) When multi-restriction is specified, blunt-nose shapes are numerically obtained for the case of relatively large beam specified. For smaller beams, on the contrary, round shape in the side region appears which are similar to that in Stokes Flow.

v) All the iterative calculation do not converge at High Reynold number.

Further studies should be necessary on the asymmetric optimum profiles, axisymmetric case, application of the present scheme to Navier-Stokes flow, and so on.

REFERENCES

1. Bessho, M., "Study into Frame Line Configuration," Jour. Soc. Naval Archi. Japan, Vol.122, 1967 (in Japanese)

2. Hess, J. L., "On the problem of shaping an axi-symmetric body to obtain low drag at large Reynolds numbers," Jour. Ship Res., Vol.20, No.1, 1976

3. Nagamatsu, T. et al., "Study on the Minimization of Ship viscous Resistance," Jour. Soc. Naval Archi. Japan, Vol.154, 1983

4. Nowacki, H., "Optimization Methods Applied to Viscous Drag Reduction," Proc., Osaka Int. Coll., Osaka, 1985

5. Bessho, M. and Kawabe, H., "Singularity Method in Boundary Value Problem in the Theory of Elasticity," Part 1, Kansai Soc. Naval Archi., Japan, No.177, 1980 (in Japanese)

6. Bessho, M., "On the Stress Intensity Factor in the Erasto-Dynamics," Kansai Soc. Naval Archi., Japan, No.189, 1983 (in Japanese)

7. Bessho, M., Kyozuka, Y., et al., "On a Computation of Riabouchinski's Axi-Symmetric Cavity Flow," Trans. West-Japan Soc. Naval Archi., No.67, 1984 (in Japanese)

8. Bessho, M., Kyozuka, Y., et al., "Study into the Shape of Minimum Viscous Resistance," 1st Report, Trans. West-Japan Soc. Naval Archi. No.68, 1984 (in Japanese)

9. Bessho, M., Kyozuka, Y., et al., "Study into the Shape of Minimum Viscous Resistance," 2nd Report, Trans. West-Japan Soc. Naval Archi. No.70, 1985 (in Japanese)

10. Bessho, M. and Himeno, Y., "On Optimum Profiles in Two-Dimensional Stokes Flow," Jour. Kansai Soc. Naval Archi., Japan, No.193, 1984 (in Japanese)

11. Bessho, M. and Himeno, Y., "Study on Drag Minimization in Stokes Flow," Proc., 2nd Int. Symp. Ship Viscous Resist., Gothenberg, 1985

12. Oseen, C. W., "Hydrodynamik", Akad. Ver., Leipzig, 1927

13. Filon, L. N. G., "The Forces on a Cylinder in a Stream od Viscous Fluid," Proc. Roy. Soc., Ser.A, Vol.113, 1926

14. Imai, I., "A new method of solving Oseen's equation and its application to the flow past an inclined elliptic cylinder," Proc. Roy. Soc., Ser.A, Vol.224, 1954

15. Miyagi, T., "Oseen flow past a Circular Cylinder at High Reynolds Number," Jour. Phys. Soc. Japan, Vol.37, No.6 1974

16. Bessho, M., "Study of Viscous Flow by Oseen's Scheme," 1st Report, Jour. Soc. Naval Archi. Japan, No.156, 1984 (in Japanese)

17. Bessho, M., "Study of Viscous Flow by Oseen's Scheme," 2nd Report, Jour. Soc. Naval Archi. Japan, No.157, 1985 (in Japanese)

18. Bessho, M., "Study of Viscous Flow by Oseen's Scheme," 3rd Report, Jour. Soc. Naval Archi. Japan, No.158, 1985 (in Japanese)

19. Bessho, M., "On the Viscous Flow around A Thin Cylinders," Proc. Osaka Int. Colloquium on Ship Viscous Flow, Osaka, 1985

20. Kida, T., "A New Perturbation Approach to the Laminar Fluid Flow Behind a Two-Dimensional Solid Body," Soc. Ind. Appl. Mech., Jour. Appl. Math., Vol.44, No.5, 1984

APPENDIX: OSEEN'S KERNEL FUNCTIONS

The kernel functions in the 2-d. Oseen flow is well known and the following expressions are adopted here, in which the coefficients are determined so as to make the integral of the stress kernel X_1 around the point Q be unity.

$$2\pi U_1(P,Q) = (\ln r + F)_x + 2kF \tag{51}$$

$$2\pi U_2 = 2\pi V_1 = (\ln r + F)_y \tag{52}$$

$$2\pi V_2 = -(\ln r + F)_x \tag{53}$$

In the above,

$$r^2 = (x-x')^2 + (y-y')^2 \tag{54}$$

$$F(P,Q) = K_0(kr)\exp(k(x'-x)) \tag{55}$$

$$k = 1/(2\nu) \tag{56}$$

where K_0 is modified Bessel function of zeroth order. The kernel functions for pressure can be derived by taking harmonic part of the velocity kernel.

$$2\pi P_1(P,Q) = -(\ln r)_x \tag{57}$$

$$2\pi P_2(P,Q) = -(\ln r)_y \tag{58}$$

And the vorticity kernel is defined as

$$Z_i(P,Q) = V_i(P,Q)_{x'} - U_i(P,Q)_{y'} \tag{59}$$

so that we obtain

$$2\nu\pi Z_1(P,Q) = F_y \tag{60}$$

$$2\nu\pi Z_2(P,Q) = -F_x. \tag{61}$$

The kernels for the stresses can be derived from eq.(6) in the preceeing chapter.

DISCUSSION

William B. Morgan,
David W.Taylor Naval Ship R&D Center

From your work on optimum body profiles, can you give any guidance into the optimization of body profiles in turbulent flows? And, do you see any possibility of extension of your techniques to these flows?

Reply -

Thank you for the discussion. The key point of the present method is whether variational expressions both for the flow and the drag are possible or not. Therefore a direct extension of the present method to the real turbulent flows seems to be difficult. As cited in the references in the paper, however, an extension is possible if we use an approximate formula from turbulent boundary layer theory to obtain the drag, like Squire and Young's formula. Another possibility of this method is an extension to Navier-Stokes flow, on which Bessho has recently made some progress. The result would appear in the near future.

Dr. Jacek S. Pawlowski,
Institute for Marine Dynamics, NRCC,

I share the authors' interest in inverse hydrodynamic problems and therefore I have found their paper most interesting. I would like to point out that the inverse problems can be understood in a broader sense as problems of optimum form description rather than finding the optimum geometrical form for a particular regime of motions [a]. In practice the form of a body can rarely be optimized with respect to one hydrodynamic force, besides it seems that the optimum form description approach leads to a richer mathematical structure.

[a] Jacek S. Pawlowski, Form Parameters for Ship Design, Based upon Hydrodynamic Theory, International Symposium on Ship Hydrodynamics and Energy Saving, El Pardo, September 6-9, 1983.

Reply -

As you pointed out, it would be important to take many parameters into account for the purpose of finding optimum ship form in actual ship design. However, the aim of the present work is not such a practical application but is to offer a basic feature of the problem of finding the body form of minimized drag in viscous fluid flow. We believe that this kind of basic study would provide a physical base of understanding real flow to ship-form designers.

Viscous-Flow Computation of Propeller-Hull Interaction

F. STERN, H. T. KIM, V. C. PATEL and H. C. CHEN
University of Iowa, U.S.A.

ABSTRACT

A partially-parabolic method for calculating ship-stern flow is coupled with a propeller-performance program in an interactive and iterative manner to predict the combined flow field. The overall computational method is described including the use of a body-force distribution to represent the propeller. Results are presented for both axisymmetric and three-dimensional body geometries. The axisymmetric geometries are simple propeller-shaft configurations for which extensive experimental data are available. The steady-flow calculations are in excellent agreement with the experimental data and show that the present procedures are able to predict many details of the flow field including the formation of the hub vortex and its dependence on the propeller loading. The unsteady-flow calculations, which are in reasonable agreement with the experimental data, point out the limitations of the present approach for simulating the complex blade-to-blade flow. The three-dimensional geometry combines the DTNSRDC 3:1 elliptical body with a propeller. Although no experimental data are available for this case, the results are physically realistic and indicate many interesting features, including the propeller-induced flow asymmetry.

1. INTRODUCTION

When a propeller operates in the nonuniform wake of a ship, the resulting flow field is interactive; that is, the propeller-induced flow is dictated by the incoming flow which is itself altered by the presence of the propeller. The fluid velocity, and the forces and moments acting on both the propeller and hull, fluctuate periodically with time. The steady components of the propeller-hull flow field, and forces and moments, pertain to the propulsive performance of the ship; that is, for fixed ship speed and propeller rpm, to the resulting propeller thrust (hull resistance) and torque (powering requirements) and the effective propeller inflow. The unsteady components concern both the propeller bearing and excited surface forces which are mainly related to hull vibration and the characteristics of the propeller slipstream. The situation can be further complicated by the occurrence of cavitation. An accurate knowledge of both the steady and unsteady components of the propeller-hull flow field has become imperative for the ship designer due to the more stringent modern performance criteria.

Since the time of R.E. Froude (1883), propeller-hull interaction has been analyzed in terms of three propulsion factors: effective wake, thrust deduction and relative rotative efficiency. The effective wake refers to the alteration of the nominal wake (velocity field in the propeller plane not including the effect of the propeller) by the action of the propeller. The thrust deduction refers to the modification of the hull resistance (usually augmented compared to the towed condition) due to the action of the propeller. The relative rotative efficiency refers to the difference in propeller torque when operating behind the hull from that in open water. Traditionally, these factors have been determined by combining the results from model resistance and self-propulsion tests, nominal-wake surveys, and propeller open-water tests. These tests, like all towing-tank tests, suffer from Reynolds-number scaling effects. Also, the complete effective-wake velocity field in the propeller plane, needed by the propeller designer, is not provided.

The first major theoretical work on propeller-hull interaction was done by Dickmann (1938), who separated the wake and thrust-deduction fractions into three components: zero-Froude-number potential effects; viscous effects due to the boundary layer and wake; and wave effects due to the presence of the free surface. Dickmann postulated that the most significant wake components were the zero-Froude-number potential and viscous ones, and the most significant thrust-deduction component was the zero-Froude-number potential one.

Almost all subsequent work on thrust deduction has followed Dickmann's example, differing only in that modern potential-flow

calculation methods are used to represent the hull and propeller (Cox and Hansen, 1977). For deeply submerged axisymmetric bodies with streamlined tails, these methods appear to show good agreement with experimental data. Dinavahi and Landweber (1981) have pointed out that this may be fortuitous since the errors due to the numerical inaccuracy of the conventional panel methods used for the zero-Froude-number potential-flow calculation are of the same order as the neglected viscous pressure drag and the thrust deduction itself. For a three-dimensional body, or blunt afterbody axisymmetric forms, and when the free-surface is present, the agreement with experimental data has generally not been good and the potential-flow approach is questionable. Under these conditions, viscous-inviscid interaction effects are important and the viscous pressure drag can become large. Consequently, the interaction between the propeller and the hull boundary layer may be important.

Huang et al. (1976, 1980), Nagamatsu and Tokunaga (1978), and Toda et al. (1982) have developed methods for correcting the nominal wake distribution of deeply submerged axisymmetric bodies to account for the propeller. These methods assume that the influence of the propeller is inviscid in nature. The results show good agreement with experimental data. An extension of such procedures to three-dimensional forms has been attempted by Toda et al. (1984) with encouraging results for the simple Wigley hull.

More rigorous investigations utilizing the complete Reynolds equations have also been performed for axisymmetric bodies with propellers by Schetz and Favin (1977, 1979), Pelletier and Schetz (1985), and Zhou and Yuan (1984). Although results from these methods are quite limited, they do show good agreement with experimental data. However, extensions of these methods to three-dimensional flow and arbitrary hull forms have not been made.

Investigations which also take into account free-surface effects have been performed by Yamazaki and Nakatake (1980, 1981, 1983) and by Nowacki and Sharma (1971). Nowacki and Sharma combined experimental and computational results to show that the wave component of the effective-wake and thrust-deduction fractions can be significant at higher Froude numbers (Fn ~ .3) and that the viscous component of the thrust deduction is appreciable at all Froude numbers. Yamazaki (1980) outlined a method for calculating propeller-hull-rudder interactions by combining various potential- and viscous-flow computation methods; however, no results were given. Nakatake (1981) simplified the Yamazaki method and circumvented viscous and wave calculations entirely by using experimental data. The results were only fair, although some experimentally observed trends were reproduced. Nakatake and Yamazaki (1983) investigated free-surface effects for a thin-ship sink-propeller combination and showed significant free-surface effects for high Froude number or shallow propeller immersion.

Recently, the authors (Stern et al., 1985), have taken a more comprehensive approach to the problem of propeller-hull interaction. The partially-parabolic method of Chen and Patel (1985) for calculating ship-stern flow has been coupled with a propeller-performance program in an interactive and iterative manner to predict the combined flow field. In the previous paper, results were presented for steady rotationally-symmetric flow about propeller-driven axisymmetric bodies. These were found to be in good agreement with the rather limited experimental data that are available.

The present paper is concerned with further work on this research project. First, more detailed validation of the overall method is provided by comparing the results with extensive steady-flow measurements for two propeller-shaft configurations. Second, extensions for unsteady flow, which include the effects of blade rotation, have been made. Here again, results are presented for one of the above mentioned propeller-shaft configurations although only very limited unsteady flow experimental data are available. Third, extensions have been made for three-dimensional bodies and results are presented for steady flow about a propeller-driven DTNSRDC 3:1 elliptical body (Huang et al., 1983). Unfortunately, only very limited experimental data are available for three-dimensional bodies and none for the present application.

2. COMPUTATIONAL METHOD

Consider the boundary layer and wake of a ship which is advancing at constant speed U_o through an incompressible fluid under the action of a propeller rotating at constant angular velocity ω. As a first approximation, the free-surface waves are ignored and the free surface is considered a plane of symmetry (zero-Froude-number approximation). This is appropriate, since the focus of attention is specifically on the interaction between the propeller-induced velocity field and the boundary layer and wake. For computational purposes, the flow field is divided into four regions, as depicted in figure 1. Region I is outside the boundary layer and wake and the flow is considered inviscid and irrotational. Region II contains the propeller. Region III is the thin boundary layer on the hull, and ends at a station x^* where the boundary-layer approximations are no longer valid. Region IV ($x > x^*$) is the thick boundary-layer and wake region.

Appropriate computational methods can be used for each of the four regions. They are connected through their boundary conditions

and are not necessarily independent. In particular, the propeller and the thick boundary-layer and wake flow fields are interdependent such that the complete solution has to be determined by iteration. Quite advanced solution methods are available for regions I-III. Herein, the primary focus is on region IV and the interactive analysis to obtain the combined propeller-hull flow field.

2.1 Partially Parabolic Method for Calculating Ship-Stern Flow

In the thick boundary layer over the stern and in the wake the usual thin boundary-layer assumptions are no longer valid and the review of Patel (1982) indicates that the partially-parabolic Reynolds equations, in which only the streamwise diffusion terms are neglected, are more appropriate. The primary effect of an operating propeller on the aforementioned flow field is to accelerate the fluid in the vicinity of the propeller in both the axial and tangential directions and this reinforces the partially-parabolic assumptions. Recently, Chen and Patel (1985) have developed a novel method for solving the partially-parabolic equations. This method has been modified to include the effects of an operating propeller. The details of the basic partially-parabolic method for bodies without a propeller have been provided by Chen and Patel (1985) and will not be reproduced here. However, for completeness, and to aid in understanding the necessary modifications and procedures for the incorporation of an operating propeller, a brief review of the method is given below.

In its present form, the method of Chen and Patel solves the transport equations for momentum, turbulent kinetic-energy k, and its dissipation-rate ε, in conjunction with the continuity equation, for the mean velocity $\underline{V}=(U,V,W)$, pressure p, and turbulence parameters k and ε. The five transport equations for $\phi = (U,V,W,k,\varepsilon)$ are written in cylindrical polar coordinates (x,r,θ) in the physical domain, and transformed into numerically-generated, body-fitted, nonorthogonal, curvilinear coordinates such that the computational domain forms a simple rectangular region with equal grid spacing. The transformation is a partial one since it involves the coordinates only and not the dependent variables ϕ. Referring to figure 1, the specified boundaries of the solution domain are the hull surface S_h, the inlet plane S_i, the exit plane S_e, the symmetry planes S_w and S_f (calm waterline) and the outer boundary S_o. The outer boundary is placed at a sufficiently large distance from the body so that uniform-stream conditions can be assumed there. This eliminates the need of both a potential-flow solution and a viscous-inviscid matching procedure. The transport equations are discretized using a staggered grid and solved using the finite-analytic method which reduces false numerical diffusion and instability as compared with more conventional methods. The velocity-pressure coupling is accomplished through the use of a two-step global pressure-correction procedure derived from the equation of continuity. The equations are written and solved in the unsteady form. For steady flow applications time simply serves as an iteration parameter.

The partially-parabolic assumption is made in the transformed coordinates; that is, second-derivatives of the transport quantities in the longitudinal coordinate direction are neglected. As a result of this assumption, only the pressure field p is fully elliptic and the velocity field is elliptic only in the transverse plane. A solution may be obtained by marching in the downstream direction; however, multiple global iterations are necessary for the influence of the downstream pressure to propagate upstream. The boundary conditions for a body without a propeller are as follows:

(1) on the inlet plane (S_i), (U,V,W,k,ε) are given from thin boundary-layer calculations (Region III).

(2) on the outer boundary (S_o), the uniform-flow condition is applied, i.e. $U = U_o$, $W = k = \varepsilon = 0$.

(3) on the exit plane (S_e), a zero-pressure-gradient condition is applied ($\partial p/\partial x=0$).

(4) on the symmetry planes (S_w and S_f), $W = 0$,

$$\frac{\partial}{\partial \theta}(U,V,k,\varepsilon) = 0.$$

2.2 Representation of the Propeller and Interaction Procedure

The manner in which the interaction between the propeller-induced velocity field (region II) and the thick boundary layer and wake velocity field (region IV) is modelled is of crucial importance. In the present approach, as a first approximation, the propeller is represented in region IV not by its actual physical presence but rather by its induced effects. Therefore, for specified propeller geometry, operating conditions, and nonuniform inflow-velocity distribution, the propeller induced effects, i.e., the velocity field and forces, are assumed known. The vortex-lattice lifting-surface method developed by Kerwin (Kerwin and Lee 1978) for predicting propeller performance is used for this purpose.

There are, in fact, a number of possible approaches for representing the propeller in the partially-parabolic formulation of region IV. It is expected that different representations may highlight different propeller effects and that some representations may be more difficult to implement than others. Three alternative methods are under investigation: inner boundary-condition method; body-

force distribution method; and velocity-field interaction method. A part of the present research project is to evaluate the various alternatives and determine the most appropriate propeller representation. To date, the best results have been obtained through the use of the body-force distribution method. This method has been used in the present calculations and will be described in detail. For further details concerning the other two methods the reader is referred to Stern et al. (1985).

In the body-force distribution method, following Schetz and Favin (1977, 1979), and others, the influence of the propeller is accounted for by the addition of body force terms $\underline{fb} = \underline{fb}(x,r,\theta,t)$ in the source functions of the momentum equations. Modifications to the turbulence-model equations for the effects of the body force (or rotation) have not been made although, in principle, they can be readily introduced. The body-force distribution is obtained from the region II calculation for given effective inflow velocities. The only other additional boundary condition required is that on the propeller hub S_{ph}: $\underline{V} = \omega r_h \underline{e}_\theta$, where r_h is the hub radius and $\underline{e}_\theta$ is the unit vector in the tangential direction. The hub boundary condition is applied by using the relative velocity in the "wall-function" approach used in the basic method. Thus, it is assumed that the log-law remains valid for a flow with a spinning boundary provided it is referenced to the relative velocity. This assumption has been verified experimentally by Lohmann (1976) even for large values of $\omega r_h/U_o$. Since the body-force distribution depends on the effective inflow velocities (i.e., the partially-parabolic solution) which, in turn, depends on the body-force distribution, the complete solution must be obtained iteratively.

The axial (fb_x) and the tangential (fb_θ) components of the body force are related to the propeller thrust T and torque Q as follows:

$$T(t) = \int_{r_h}^{r_p} \int_{\theta_{te}(r)}^{\theta_{le}(r)} \int_{x_p(r,\theta)}^{x_s(r,\theta)} fb_x \, dx r d\theta dr \quad (1)$$

$$Q(t) = \int_{r_h}^{r_p} \int_{\theta_{te}(r)}^{\theta_{le}(r)} \int_{x_p(r,\theta)}^{x_s(r,\theta)} fb_\theta \, r dx r d\theta dr \quad (2)$$

where the integration is over the instantaneous volume of the propeller. Equations (1) and (2) are the most general form appropriate for unsteady flow simulations. For steady flow simulation, it is more appropriate to use a distribution over a disc ($r_h \le r \le r_p$) of finite thickness (Δx), i.e.

$$T = 2\pi \Delta x \int_{r_h}^{r_p} fb_x \, r dr \quad (3)$$

$$Q = 2\pi \Delta x \int_{r_h}^{r_p} fb_\theta \, r^2 dr \quad (4)$$

In the results to be presented, both prescribed and interactive body-force distributions have been used. In the former case, the overall solution procedure is noniterative, i.e., the partially-parabolic solutions are carried out only once. This is because equations (1) and (2), or (3) and (4), are independent of the effective inflow. In the latter case, several iterations are required, on both the partially-parabolic and the propeller solutions, since $\underline{fb}$ now depends on the effective inflow.

The prescribed body-force distributions used in the present investigation are based on the situation in which the propeller thrust coefficient C_T (or K_T), torque coefficient K_Q, speed of advance J, and radial circulation distribution $\Gamma(r)$ are known. In this case,

$$fb_x = \frac{C_T L \, r_p^2 \, G(r)}{4\Delta x \int_{r_h}^{r_p} G(r) \, r dr} \quad (5)$$

$$fb_\theta = \frac{4K_Q L \, r_p^3 G(r)}{\pi r J^2 \Delta x \int_{r_h}^{r_p} G(r) \, r dr} \quad (6)$$

where L is the length of the body, and $G = \Gamma(r)/2\pi U_o r_p$. These distributions were derived assuming a lightly loaded propeller.

3. APPLICATIONS FOR AXISYMMETRIC BODIES

It should be emphasized that the overall computational method described in Section 2 is applicable to the most general situation of unsteady flow about propeller-driven three-dimensional bodies. However, for validation purposes it is both appropriate and necessary to perform calculations for simple configurations such as propeller-driven axisymmetric bodies. This is because almost no experimental data are available for three-dimensional flow. In fact, even for axisymmetric flow, the available data are quite limited.

In the previous work (Stern et al., 1985), calculations were performed for an axisymmetric body with afterbody 1 fitted with DTNSRDC propeller 4577 and the results were compared with the experimental data of Huang

et al. (1976, 1979, 1980) which were limited to upstream of the propeller for the with-propeller condition. The results were found to be in good agreement with the available data with respect to the surface pressure distribution, wall-shear velocity, axial velocity profile in the stern boundary layer, and thrust deduction. Both analytically-prescribed body-force distributions and those obtained numerically through the use of a lifting-surface propeller performance program (Kerwin and Lee 1978) were used. In the latter case, the nature of an interactive solution was explicated.

In the present paper, results are presented for a simple propeller-shaft configuration. In this case, the upstream body is simply the propeller shaft. Although this is clearly an idealization of the practical circumstance, it will be shown that, the flow field exhibits all the distinctive features of interest. Most importantly, it is for this configuration that the most extensive experimental information is available.

Recently, Wang (1985) has performed experiments with two distinctly different propeller-shaft configurations: propeller P4660 which has zero loading near the root, and P4498 which has finite loading near the root. Steady (circumferential-mean) velocity profiles were obtained both in the immediate downstream vicinity of the propeller and in the near and intermediate wake regions. The unsteady (periodic) velocity measurements were made in a plane immediately downstream of the propeller. The focus of these experiments was on the formation of the hub vortex and its relationship to the loading characteristics of the propeller near the root. Also, numerical predictions of the propeller circulation distribution, using a modified version of the Greely and Kerwin (1982) lifting-surface propeller program to include hub effects, were shown to be in good agreement with circulation distributions obtained from the measured swirl velocity component and Kelvin's circulation theorem.

In the present study, calculations have been performed for conditions corresponding to the complete program of experiments by Wang (1985). Body-force distributions based on the propeller circulation distributions presented by Wang were used. Both steady and unsteady flow calculations have been performed. Since the results are rather extensive, a detailed account of all aspects is beyond the scope of the present paper. Therefore, only an overview of the results is provided here. A complete report describing all the results is in preparation (Stern et al., 1986).

3.1 Steady Flow

The results to be presented in this section were obtained using the rotationally symmetric version of the more general three-dimensional partially-parabolic method described in Section 2. This is appropriate for steady (circumferential-mean) flow around an axisymmetric body fitted with a propeller. As previously mentioned, calculations have been performed for two propeller-shaft configurations: propeller P4660 which is a controllable pitch propeller from the DD-963 class destroyer; and propeller P4498 which is a research propeller. P4660 has a larger hub ratio (.3) than P4498 (.2) and, a lower pitch and camber at sections near the root. As will be shown below, the latter geometric characteristics have a large influence on the flow field, especially with regard to the formation of the hub vortex.

The calculation conditions were selected to simulate the experimental conditions as closely as possible; however, this was made somewhat difficult due to the lack of sufficient information for viscous-flow calculations, particularly with regard to the upstream flow (e.g., boundary-layer thickness). The following conditions were employed for P4660: C_T = .7458, K_T = .279, K_Q = .0647, J = .976, and ω = 300 rpm and for P4498: C_T = .78, K_T = .242, K_Q = .0659, J = .889, and ω = 900 rpm. Based on these, and assuming a shaft length L=2m and a water temperature of 15°C, the shaft-length Reynolds numbers for P4660 and P4498 were determined as $Rn = U_o L/\nu = 2.7 \times 10^6$ and 8×10^6, respectively. In the discussion to follow, all coordinates are nondimensionalized using the shaft length L, with x = 0 at the shaft nose, and velocities and pressure are normalized using the free-stream velocity U_o and fluid density. In many of the figures the radial coordinate is normalized by the propeller radius r_p i.e., $Y = r/r_p$.

A partial view of the grid used in the calculations for P4660 is shown in figure 2. This is a fine grid. Referring to figures 1 and 2 for notation: the inlet boundary S_i is at x_u = .55; the exit boundary S_e is at x_d = 16; the outer boundary S_o is at y_o = .4; the first grid point off the body surface is located in the range $50 \leq y^+ \leq 80$; the number of axial grid points is 85; and the number of transverse grid points is 48. Turbulent flat-plate profiles were used to specify the initial conditions with the inlet boundary layer thickness estimated to be δ = .006. Calculations were performed for conditions corresponding to the shaft with a fixed hub and no propeller, the shaft with a spinning hub and no propeller, and the shaft with a spinning hub and propeller. For the with-propeller condition, two different body-force distributions were used. These are shown in figure 3. Both of these were derived from the circulation distributions presented by Wang (1985) using the procedures described in Section 2.2. One of these corresponds to results from the propeller lifting-surface program modified to include hub effects (PSF2-HUB) and the other corresponds to results obtained using

the measured swirl velocity component and Kelvin's circulation theorem. Note that there are some differences between the two body-force distributions particularly near the hub.

Figure 4 provides an overview of the results through the variation of some properties in the longitudinal direction, figure 5 shows some characteristics of the solutions in the far wake, and figure 6 shows radial distributions of the various quantities of interest at two sections behind the propeller.

Before discussing the influence of the propeller on the flow field it is of interest to examine the characteristics of the basic flow, i.e., without the propeller. Referring to figure 4, it is seen that for the shaft with a fixed hub, the flow characteristics are consistent with a trailing-edge flow in the presence of a thin boundary layer. The solution indicates a weak viscous-inviscid interaction and the other usual features associated with such a flow. Although the flow on the shaft with a spinning hub shows similar characteristics, there are some important differences. We observe a decrease in pressure in the vicinity of the tail such that the pressure recovery in the wake occurs with a favorable as opposed to an adverse gradient; a large increase in the magnitude of the shear stress on the spinning portion of the hub; the generation of swirl; and an increase in turbulence levels in the near and intermediate wake (not shown here). The axial and radial velocities showed only a minimal influence of spin. This is indicated by the insignificant change in the wake centerline velocity.

Swirling turbulent shear flows are classified as weak or strong depending on the magnitude of the rotation parameter $\omega r_h/U_o$. For weak swirl, i.e. $\omega r_h/U_o << 1$, the axial velocity is not appreciably affected by swirl. Reynolds (1962) has shown that the asymptotic forms for weakly swirling wakes and jets are identical to the nonswirling cases due to the fact that the swirl decreases more rapidly than the axial velocity or velocity defect. This has been confirmed experimentally for swirling jets (Rose, 1962) and for wakes (Liu, 1971). The present results are plotted in the format of the asymptotic velocity decay laws in figure 5, in which: D_s = shaft diameter, D_p = propeller diameter, $\Delta U_{CL} = U_o - U_{CL}$ is the velocity defect, and $\Delta U_{max} = U_o - U_{max}$ is the velocity excess. It is seen that the axial velocity defect follows the $x^{-2/3}$ power and the swirl velocity decays as x^{-1}, as expected from asymptotic analysis. Experimental studies indicate that the axial velocity defect (or excess) is decreased by swirl, presumably due to an increase in entrainment and mixing. It should be recognized that such behavior is related to the structure of turbulence; since, for laminar flow, the axial and swirl velocities develop independently. The present results with the fixed and spinning hub do not follow the experimental trend with regard to the dependence of the axial velocity defect (or excess) on the rotation parameter. This is presumably because the swirl is relatively small and the basic k-ε turbulence model used here does not explicitly contain any effects of rotation.

Returning to figure 4, it is seen that, as expected from physical considerations, a major influence of the propeller is a jump in pressure across the propeller plane associated with the propeller thrust and a large decrease in pressure along the wake centerline due to the large propeller-induced swirl velocity. The distribution of the wall-shear velocity u_τ on the body indicates an increase over both the fixed- and spinning-hub conditions due to the propeller. Also, a sharp decrease is shown at the propeller plane. The wake centerline velocity also indicates an increase over the no-propeller conditions and an overshoot, i.e., values greater than the free-stream velocity, are observed. The swirl velocity, which is of course zero in the absence of a propeller and for the fixed-hub condition, attains quite large values just downstream of the propeller, but decays rapidly with downstream distance. Finally, we note that the pressure and wall-shear variations are quite sensitive to the body-force distribution. The results for the PSF2-HUB body-force, which has larger values of fb_θ and fb_x near the hub, indicate a larger reduction in pressure and shear velocity and larger swirl velocities in the near wake, than the results for the experimental body force. It is believed that the latter is more accurate, since for this application, PSF2-HUB appears to overpredict the circulation near the hub.

Figure 6 shows the radial distributions of the axial, radial and tangential velocity components (U,V,W), pressure (p), and turbulence parameters (k,ε) at two stations downstream of the propeller: $x/r_p = .28$ which is just downstream of the propeller trailing edge and $x/r_p = 1.053$ which is at the hub apex. Comparisons are made with the experimental data wherever possible. In general, all the results are consistent with the previous discussion. However, it is of interest to note some special features of the solutions. First, we see that the calculations are in excellent agreement with the experimental data for all three velocity components. Second, the increase in U and p, the decrease in V, and the generation of W are all consistent with expectations from physical considerations. Third, the shape of the V profile just downstream of the propeller is dominated by the propeller loading characteristics whereas further downstream its shape is more affected by the body trailing edge and transition into the wake. Fourth, the shape of the W profile indicates that the propeller-generated swirl and the hub-generated swirl initially develop independently but subsequently merge through

the action of turbulent diffusion. This effect is due to the fact that P4660 has zero loading at the hub (see figure 3). The experimental data indicates basically no interaction and merging of the propeller and spinning hub swirl velocities even as far downstream as $x/r_p = 1.252$ (figure not shown). This is rather surprising since, from physical considerations, a rapid mixing would have been expected. Other important results deduced from the calculations but not shown in the present figures are: (a) the calculations indicate a negligible influence of the propeller for $x/r_p < -2$; (b), the overshoots in U and p, and the magnitude of the swirl velocity W, which are quite marked in the slipstream and in the near wake decrease with downstream distance; (c) the turbulence parameters are greatly increased in the wake over the values observed without a propeller, especially near the wake centerline in the near wake and all across the wake in the intermediate and far wake. Unfortunately, no experimental data is available to verify the turbulence parameter predictions. The limited experimental data that is available for other configurations (Ravindranath and Lakshminarayana, 1981; Schetz and Jakubowski 1976; Jessup et al., 1984; Kotb and Schetz, 1985) indicate an increase in turbulence due to the propeller. This increase is due both to the larger gradients in the mean flow profiles for the with-propeller condition and to the turbulence production on the blades. Only the former effect is included in the present calculations.

The velocity components in the wake with the propeller are also shown on figure 5. Here again, the correct asymptotic forms are recovered. The fact that a propeller wake decays at the same rate as the nominal wake of a bare body has been confirmed experimentally by Aron (1960). However, we note that the analysis of Reynolds (1962) indicates that a momentumless swirling wake (the practical circumstance) decays at different rates than the condition considered here. This has not been confirmed experimentally.

Calculations were performed for P4498 using both a fine and a coarse grid. As will be discussed subsequently, the reason for using a coarse grid is that it was not possible to make calculations for the with-propeller condition with the fine grid due to the large loading near the root of P4498. The fine grid was very similar to that described earlier for P4660 and shown in figure 2. In the coarse grid the first grid point off the body surface was located in the range $170 \leq y^+ \leq 220$; the number of axial grid points was 70; and the number of transverse grid points was 40. The initial and flow conditions for the P4498 calculations are similar to those described earlier for P4660. This is also true for the derivation of the body-force distributions which are shown in figure 7. The very different characteristics of the body-force distributions for P4660 and P4498 are evident from a comparison of figures 3 and 7. In particular, P4498 has finite and large values of fb_x and fb_θ at the root. Note that for this case the differences between the experimental and PSF2-HUB body-force distributions are minimal. The format for the presentation of the results for P4498 is similar to that described earlier for P4660. Also, many aspects of the two solutions are similar and will not be discussed again. The focus of the discussion to follow is on the differences between the two solutions.

A comparison of figures 8 and 4 shows that the drop in the pressure for P4498 is considerably larger than for P4660. This is the result of the increased swirl velocities for P4498, the maximum swirl velocity at the hub apex being almost twice as large than for P4660.

A comparison of figures 9 and 6 shows the differences in the detailed solutions for the two propellers. In particular, the development of the swirl velocity component is quite different. For P4498 the propeller generated swirl and the spinning-hub generated swirl do not develop independently, but interact such that a large hub vortex is formed at the hub apex. Also, the axial velocity component for P4498 is much fuller near the root than with P4460. These effects are a direct result of the differences in the loading distributions.

As mentioned previously, the results with the P4498 propeller were obtained using a coarser grid. Calculations were made using both the fine and the coarse grids for the spinning-hub condition. Results from both these calculations are also shown on figure 9. It is seen that the coarse-grid solution leads to a large under prediction of the swirl velocity. Thus, if it had been possible to obtain a fine-grid solution with the propeller for P4498, it is expected that an even closer agreement with the experimental data would have resulted. The difficulties associated with the fine-grid solution for P4498 can be attributed to the use of "wall-functions" in the turbulence model. The present results underscore the need for further work on near-wall turbulence modeling in order to resolve the details of the solution in this region.

The calculations described above were performed on a Prime 9950 minicomputer and took about 30 minutes of cpu time. A time relaxation factor $\alpha_t = .3$ was used on the body and $.03 \leq \alpha_t \leq .3$ for the wake. A total number of 80 global sweeps were used. With the propeller, the solutions were obtained in stages, starting with the no-propeller condition and building up to the final values of C_T and K_Q. Five stages were required for P4660 and nine stages were required for P4498.

3.2 Unsteady Flow

Unsteady-flow calculations in which the effects of blade rotation are simulated have also been performed for P4660. In this case, the fully three-dimensional version of the partially-parabolic method was used. However, since this was the first application of this method for unsteady flow some modifications were required. First, in order to obtain time-accurate solutions a true iteration parameter was introduced and the use of time for this purpose was removed. This procedure was first developed and tested using the rotationally-symmetric version of the computer program with a sinusoidally time varying body force. Second, the specifications of the boundary conditions in the transverse plane required modification from the previously used symmetry conditions on the waterline and keel. If the upstream flow is three-dimensional and the propeller and body axis coincide (submarine application), then there are no planes of symmetry and a full-plane solution is required. If the upstream flow is three-dimensional and the propeller axis is below the body axis (surface ship application), then the waterline can be regarded as a periodic symmetry plane within the zero-Froude-number approximation. If the upstream flow is axisymmetric (as in the present application), then periodic boundary conditions are appropriate at blade spacing intervals. Initially, full plane solutions were obtained so as to validate the procedures for the more general circumstance; however, this proved to be too time consuming on the minicomputer presently being used. Therefore, the results to be presented were obtained using periodic boundary conditions. For future applications to three-dimensional upstream flows it may be necessary to use a supercomputer.

In the present approach, the unsteady turbulent flow is treated by the so-called quasi-steady approximation insofar as the basic k-ε turbulence model derived from simple steady flows is retained. In other words, any direct interaction between the turbulence structure and the unsteadiness induced by the propeller, or its wake, is ignored. Little experimental or theoretical information is available at the present time to quantify this interaction for such complex flows. Generally, it is believed that the quasi-steady approximation is valid if the frequency parameter $\beta = f\delta/U_o$ (where f is the imposed frequency and δ is a characteristic boundary-layer thickness) is small compared to a characteristic turbulence frequency, such as the turbulent-burst frequency, $\beta = .2$. This has been observed experimentally for simple boundary layers with oscillating external flows (Telionis 1981, Cousteix 1986). For the results to be presented, the value of the frequency parameter is $\beta = .03$.

The flow and initial conditions used for the unsteady calculations were identical to those described earlier for steady flow. The radial grid distribution was somewhat coarser than that used for the steady-flow calculations (see figure 2) but similar to that described earlier for P4498. In general, for unsteady flow, the body-force distributions are distributed over the instantaneous propeller volume and are time dependent as indicated by equations (1) and (2). However, consistent with the axisymmetric inflow and the periodic boundary conditions used in the present application, the body-force distributions are independent of time but are imposed over the instantaneous location of the propeller blade. In other words, a rotating constant strength body-force distribution is used. Calculations were performed using both a coarse and a fine cross-section grid and propeller representation. In the case of the coarse cross-section grid, the propeller was represented by a single radial distribution (see figure 10), and only three time steps per period were used. In the case of the fine cross-section grid, the propeller was represented by four radial distributions, and six time steps per period were used. In both cases, the radial body-force distributions were based on the experimental circulation distribution as previously described. In the latter case, the chordwise loading was distributed based on the NACA .8 mean line. The time accuracy of the solution is influenced not only by the number of time steps per period but also by the number of global iterations used in the partially-parabolic method per time step, and the total number of periods calculated. Presently, 15 global iterations per time step and a total number of 6 periods have been used. Only the results with the coarse cross-section grid will be presented here.

Figure 11 shows the body surface and wake centerline pressure, wall-shear velocity, wake centerline velocity, and maximum wake swirl velocity obtained at the 17th time step and for all three grid lines over one blade spacing interval (i.e. one period). These are to be compared with the corresponding steady-flow results shown in figure 4. The unsteady solution shows distinct characteristics at each of the grid lines over the blade spacing interval: for grid line 2, the propeller is in the "right on" position, and its influence is maximum , i.e. the flow field variations are larger than the steady-flow solution; for grid line 3, the propeller has "not arrived" yet and the results are closer to the no propeller solution; and for grid line 1, the propeller has "just passed" and the solution shows a residual influence of the propeller.

Figure 12 shows the radial distributions of (U,V,W,p,k,ε) at $x/r_p = .28$, which is just downstream of the propeller trailing edge, for all 18 time steps (except the first) at grid line 2. The corresponding results for steady flow are shown in figure 6. The results in figure 12 clearly show the influence of blade

position as described with reference to figure 11. The small differences shown between some of the solutions at the same blade spacing grid line but different time steps is due to the influence of transients during the first few periods.

Figure 13 shows the time history of the velocity components (U,V,W) at x/r_p=.28 for two radial positions $Y=r/r_p$=(.417, .833) at grid line 2. Also shown for comparison are the experimental results. A blade angle coordinate $\theta = \omega t$ measured from the generator line of the key blade has been used instead of time for the abscissa. Referring to figure 10, $\theta = 0$ corresponds to the key blade at grid line 1. It is believed that the experimental blade angle is approximately consistent with this; however, it was not possible to confirm the experimental blade angular coordinate. Consistent with the steady-flow predictions, the mean values are well predicted; however, there are large differences in both the magnitude and phase of the unsteady component. This is especially true for the radial (V) component. The trends shown by the calculations have already been described with reference to figure 11. The body-force representation of the propeller simulates the thrust and torque but is unable to capture all of the details of the complex blade-to-blade flow seen in the experimental data. The experimental data reveal many interesting features of the blade-to-blade flow, including radial variations resulting from the effects of the propeller loading, blade wakes, and tip vortices. In order to predict such effects a more detailed representation of the propeller is required. One possibility, which is similar to the present approach, is the velocity-field interaction method as described by Stern et al. (1985). Alternatively, a solution can be pursued in which the actual propeller is embedded in a viscous flow method and the no-slip condition satisfied on the rotating blades.

Lastly, the calculations indicate that the unsteady-flow effects are limited to $-1 \leq x/r_p \leq 2$. Although Wang's (1985) unsteady-flow data are not extensive enough to confirm this, the earlier MIT experiments of Min (1978) and Kobayashi (1981) seem to indicate a similar extent of the unsteady effects (excluding the tip vortex).

These calculations were also performed on the Prime 9950 minicomputer and took about 530 minutes of cpu time. Time relaxation was of course not used, but a relaxation factor of $\alpha_p = .3$ was used for the pressure in the wake.

4. APPLICATIONS FOR THREE-DIMENSIONAL BODIES

Preliminary results will now be presented for a propeller-driven three-dimensional body. In this case, only steady-flow calculations have been made thus far. The body-force distributions were obtained from the propeller-performance program of Kerwin and Lee (1978). This allows for an interaction with the partially-parabolic solution since the body-force distributions depend on the propeller inflow.

The body geometry selected for the calculations is the DTNSRDC 3:1 elliptical body of Huang et al. (1983). Note that the parent form for this body is afterbody 1 for which calculations were reported in the previous paper (Stern et al., 1985). In fact, the propeller geometry, location, and loading conditions for the present calculations were chosen to simulate the afterbody 1 conditions: i.e., DTNSRDC propeller 4577 with C_T = .37 and K_Q = .0453; $R_n = 5.9 \times 10^6$. A small modification to the tail geometry ($.98 \leq x \leq 1$) of the 3:1 body was made in order to allow for a cylindrical hub. The grid resolution was similar to that used previously for afterbody 1. The grid in the plane of the major axis is shown in figure 14 and is representative of the grid as a whole. Referring to figures 14 and 1 for notation: the inlet boundary S_I is at x_u = .5; the exit boundary S_e is at x_d = 16.25; the outer boundary S_o is at y_o = .89; the first grid point off the body surface is located in the range $140 \leq y^+ \leq 270$; the number of axial grid points is 60; and the number of transverse grid points is 19. Calculations with and without the propeller were performed. In the absence of the propeller, the calculations were performed for a quarter of the cross-section only since in this case there are two planes of symmetry. Five girthwise grid points were used. For the with-propeller condition there is one plane of periodic symmetry (the waterline) and the calculations are for a half plane. Nine girthwise grid points were used. In both cases, a finer grid spacing was used near the keel. Turbulent flat-plate profiles were again used to specify the initial conditions, with the inlet boundary layer thickness δ = .004.

Besides the inflow-velocity distribution, the propeller geometry and operating conditions, the propeller program also requires the specification of three parameters related to the geometry of the trailing vortex wake; namely the radius of the ultimate wake r_w; the pitch angle of the outer extremity of the transition wake B_T; and the pitch angle of the ultimate tip-vortex helix B_U. A more recent version of this propeller program (Greeley and Kerwin, 1982) performs a calculation to determine B_T and B_U, leaving only r_w to be specified. In either case, and as is generally the case with other methods, the predicted propeller performance, including the propeller-induced velocities, thrust, and torque, are strongly influenced by the prescribed wake geometry. When comparing predictions with experimental results the wake descriptors are often adjusted so as to obtain the measured thrust.

In the previous calculations, for afterbody 1, two types of interaction were investigated: (1) wake descriptors adjusted to obtain the measured thrust, and (2) the thrust determined using estimated wake parameters. In both cases, the iteration procedure began with the calculated nominal inflow used as input to the propeller program to obtain the distributions of fb_x and fb_θ, and the propeller-induced axial and tangential velocities, u_a and u_t, respectively. Next, the viscous flow was recalculated using these fb_x and fb_θ to obtain the total velocity $\underline{V_T}$ at the propeller plane. The effective wake, defined as

$$\underline{V_e} = \underline{V_T} - (u_a \underline{i} + u_t \underline{e_\theta})$$

(where u_a and u_t are midchord values) was then used as input to the propeller program to obtain updated body-force distributions and propeller-induced velocities. The procedure was repeated twice to obtain convergence: i.e., until V_T, $\underline{fb}$ and (u_a, u_t) were unchanged. It was found that with the present grid resolution the differences in the partially-parabolic solutions when using the body-force distributions obtained from the propeller program when the nominal wake or either type 1 or 2 effective wakes were used, were not appreciable. On the other hand, the differences in propeller performance corresponding to the nominal and effective wakes were found to be significant. Furthermore, the type 1 interaction led to unrealistically high values for B_T and B_U in order to maintain the measured thrust, whereas the type 2 interaction led to a 10% reduction in thrust and torque as compared to the experimental values. It is believed that even though the type 2 interaction did not reproduce the measured thrust and torque it is a more realistic simulation than the type 1 interaction; therefore, only type 2 interaction calculations have been performed for the present three-dimensional body. Also, for convenience, the steady option of the propeller program with only the zeroth harmonic of the inflow-velocity distribution was used. This approximation neglects the influence of the higher harmonics of the inflow-velocity distribution and the propeller-induced velocities on the body-force distributions. In future applications, especially for unsteady flow, such an approximation will not be made.

The type 2 interaction procedure requires estimates for the wake parameters. Herein, the standard-practice estimates were used: B_T = ½ (advance angle + hydrodynamic pitch angle); $B_U = 1.15 B_T$; $r_w = .83$. The first step in the interaction procedure is to calculate the propeller performance using the nominal wake. In this case, it was found that B_T = 24°, $C_T = .371$, and $K_Q = .0431$. The interaction procedure described above converged in just two iterations resulting in B_T = 24°, $C_T = .4$, and $K_Q = .0456$ which represents about a 10% change in propeller performance. The body-force distributions obtained using the nominal wake and the converged effective wake are shown in figure 15. Consistent with the previous interaction calculations for afterbody 1, the changes in the body-force distributions are quite small. These, in turn, lead to rather small changes in the flow field. Therefore, only the solutions with the converged body-force distribution will be shown below.

Figure 16 shows a comparison of the velocity vectors in the propeller plane without and with the propeller. Figures 17 (without propeller) and 18 (with propeller) provide an overview of the results through the variation of some properties in the longitudinal direction. Figures 19 and 20 show the corresponding radial distributions of the various quantities of interest at the tail of the body. Here, the focus is on the differences between the flow-field characteristics for the without- and with-propeller conditions. The reader is referred to Chen and Patel (1985) for a comparison of the results for the without-propeller condition with the experimental data of Huang et al. (1983). Good agreement is shown between the calculations and the experimental data along the symmetry planes with respect to the surface and wake centerline pressure distribution, the wall-shear velocity, and profiles of the (U,V) velocity components and turbulent kinetic energy.

Referring to figures 17 and 19, which are for the without-propeller condition, it is seen that the flow field about the 3:1 body shows similar characteristics to the thick boundary-layer flow about axisymmetric bodies but with a faster boundary-layer growth rate along the keel (θ = 90°) than the waterline (θ = 0°). For $0° \leq \theta \leq 33°$ the flow is almost two-dimensional. For $33° \leq \theta \leq 90°$ the flow is weakly three-dimensional and shows a smooth variation between the waterline and keel. Consistent with the above, the surface pressure increases and the wall-shear velocity decreases continuously from $\theta = 0°$ to $\theta = 90°$. Consistent with the fact that the flow is only weakly three-dimensional, the maximum swirl velocity in the wake is quite small.

Referring to figures 18 and 20 which are for the with-propeller condition, it is seen the influence of the propeller is similar to that discussed in Section 3.1 with reference to the simple propeller-shaft configuration, i.e., a reduction in the pressure on the body surface and along the wake centerline, an increase in wall-shear velocity, especially on the spinning hub, and a large increase in the wake centerline and maximum swirl velocities. The detailed radial distributions also show the previously discussed large increase in (U,W,p,k) and decrease in V due to the influence of the propeller. Note that figures 16, 18, and 20 clearly show the propeller-induced flow asymmetry.

The three-dimensional flow calculations were also performed on a Prime 9950 minicomputer and took about 90 minutes of cpu time. The time relaxation factor α_t=.3 and the pressure relaxation factor α_p =.3 was used. A total of 40 global sweeps were used.

5. CONCLUDING REMARKS

The feasibility of coupling a propeller-performance method (or more simple propeller models) with a state-of-the-art viscous flow calculation method has been demonstrated at various levels of flow field complexity: rotationally-symmetric steady and unsteady flows, and three-dimensional steady flow. The steady-flow results for the simple propeller-shaft configuration are in excellent agreement with experimental data and show that the present procedures are able to predict many details of the flow field including the formation of the hub vortex and its dependence on propeller loading. The previous steady-flow results for afterbody 1, which showed good agreement with the experimental data, suggest that the present steady-flow results for the DTNSRDC 3:1 elliptical body are quite realistic. Based on the above steady-flow applications it is concluded that the present procedures can accurately simulate the steady part of the combined propeller-hull flow field and can be used with some confidence for predictions of thrust deduction and effective wake, as well as other flow quantities of interest. Of course, much more work needs to be done, especially for three-dimensional flow, to extend the method to realistic ship geometries.

The unsteady-flow results are in reasonable agreement with the experimental data. However, they point out the limitations of the present approach for simulating the complex blade-to-blade flow. A more detailed representation of the propeller than the body force is required. Two alternative approaches need to be investigated. The first, is the velocity-field interaction method as described by Stern et al. (1985), which is similar to the present approach, in that different methods are used for the propeller and viscous flow and the complete solution is obtained iteratively and interactively. The second, is the development of a method in which the actual propeller is embedded in a viscous flow method and the no-slip condition is satisfied on the surface of the rotating blades.

Validation of the computational results is made difficult by the lack of detailed experimental data for combined propeller-hull flow fields. This is especially true for turbulence quantities, the slipstream velocity field, and the entire flow field for three-dimensional bodies. An experimental project is also underway at the Iowa Institute of Hydraulic Research with the goal of obtaining such data.

ACKNOWLEGEMENTS

This research was sponsored by the Office of Naval Research, Accelerated Research Initiative (Special Focus) Program in Propeller-Hull Interaction, under Contract N00014-85-K-0347. The Graduate College of The University of Iowa provided a large share of the computer funds.

REFERENCES

Aron, A., (1960), "Decay of Turbulent Wakes Behind a Propeller", M.S. Thesis, Dept. of Mech. and Hydraulics, University of Iowa.

Chen, H.C. and Patel, V.C., (1985), "Calculation of Trailing-Edge, Stern and Wake Flows by a Time-Marching Solution of the Partially-Parabolic Equations", Iowa Inst. Hydraulic Research, IIHR Report No. 285.

Cousteix, J., (1986), "Three-Dimensional and Unsteady Boundary Layer Computations", Annual Review of Fluid Mechanics, Vol. 18, pp. 173-196.

Cox, B.D. and Hansen, A.G., (1977), "A Method for Predicting Thrust Deduction Using Propeller Lifting Surface Theory", DTNSRDC Report SPD-77-0087.

Dickmann, H.E., (1938), "Thrust Deduction, Wave Resistance of a Propeller, and Interaction with Ship Waves", (in German), Jahrbuch STG, Vol. 40, pp. 234-291.

Dinavahi, S.P.G. and Landweber, L., (1981), "Effect of Boundary Layer on Thrust Deduction", Iowa Inst. Hydraulic Research, IIHR Report No. 239.

Froude, R.E., (1883), "A Description of a Method of Investigation of Screw Propeller Efficiency", Transactions RINA, Vol. 24, pp. 231-255.

Greeley, D.S. and Kerwin, J.E., (1982), "Numerical Methods for Propeller Design and Analysis in Steady Flow", Trans. SNAME, Vol. 90, pp. 415-453.

Hough, G.R. and Ordway, D.E., (1965), "The Generalized Activator Disk", Developments in Theoretical and Applied Mechanics, Vol. II.

Huang, T.T., Wang, H.T., Santelli, W. and Groves, N.C., (1976), "Propeller/ Stern/ Boundary-Layer Interaction on Axisymmetric Bodies: Theory and Experiment", DTNSRDC Report 76-0113.

Huang, T.T., Santelli, N. and Belt, G., (1979), "Stern Boundary-Layer Flow on Axisymmetric Bodies", Proc. 12th ONR Sym. Naval Hydrodynamics, Washington, D.C., pp. 127-157.

Huang, T.T. and Groves, N.C., (1980), "Effective Wake: Theory and Experiment", Proc. 13th ONR Sym. Naval Hydrodynamics, Tokyo, pp. 651-673.

Huang, T.T., Groves, N.C., and Belt, G.S., (1983), "Stern Boundary-Layer Flow on Two Three-Dimensional Bodies Having Elliptic Transverse Cross-Sections", Proc. 2nd Sym. Num. and Physical Aspects of Aerodynamic Flows, Long Beach.

Jessup, S.D., Schott, C., Jeffers, M., Kobayashi, S., (1984), "Local Propeller Blade Flows in Uniform and Sheared Onset Flows Using LDV Techniques", Proc. 15th ONR Symp. Naval Hydrodynamics, Hamburg, pp. 221-237.

Kerwin, J.E. and Lee, C.S., (1978), "Prediction of Steady and Unsteady Marine Propeller Performance by Numerical Lifting-Surface Theory", Trans. SNAME, Vol. 86, p. 218-253.

Kobayashi, S., (1981), "Experimental Methods for the Prediction of the Effect of Viscosity on Propeller Performance", MIT, Dept of Ocean Eng., Report No. 81-7.

Kotb, M.A. and Schetz. J.A., (1986), "Measurements of Three-Dimensional Turbulent Flow Behind a Propeller in a Shear Flow", AIAA Journal, Vol. 24, pp. 570-577.

Liu, C.-Y., (1971), "Wake of an Axially Symmetrical Body With Spinning", Proc. 9th Int. Symp. on Space Tech. and Sci., Tokyo, p. 373.

Lohmann, R.P., (1976), "The Response of a Developed Turbulent Boundary Layer to Local Transverse Surface Motion", Trans. ASME, J. Fluids Eng., Vol. 98, pp. 354-363.

Min, K.S., (1978), "Numerical and Experimental Methods for the Prediction of Field Point Velocities Around Propeller Blades", MIT, Dept. of Ocean Eng., Report no. 78-12.

Nakatake, K., (1981), "A Practical Method to Calculate Propulsive Performance of Ships", Memoirs, Faculty of Engineering, Kyushu University, Vol. 41, No. 1.

Nakatake, K. and Yamazaki, R., (1983), "Effect of the Free Surface on the Propulsive Performance of a Ship", Trans. Japan Soc. Naval Arch., Vol. 152.

Nagamatsu, L. and Tokunaga, K. (1978), "Prediction of Effective Wake Distribution for a Body of Revolution", J. Soc. Naval Arch., Japan, Vol. 143.

Nowacki, H. and Sharma, S.D., (1971), "Free-Surface Effects on Hull Propeller Interaction", University of Michigan, Dept. NA & ME, Report 112.

Patel, V.C., (1982), "Some Aspects of Thick Three-Dimensional Boundary Layers", Proc. 14th ONR Sym. Naval Hydrodynamics, Ann Arbor, pp. 999-1040.

Pelletier, D.H. and Schetz, J.A., (1985), "A Navier-Stokes Calculation of 3-D Trubulent Flow Near a Propeller in a Shear Flow", AIAA 23rd Aerospace Sciences Meeting, Reno.

Ravindranath, A. and Lakshminarayana, B., (1981), "Structure and Decay Characteristics of Turbulence in the Near and Far-Wake of a Moderately Loaded Compressor Rotor-Blade", ASME Eng. for Power, Vol. 103, pp. 131-140.

Reynolds, A.J., (1962), "Similarity in Swirling Wakes and Jets", J. Fluid Mech., Vol. 14, p. 241.

Rose, W.G., (1962), "A Swirling Round Turbulent Jet", J. Appl. Mech. Vol. 29, p. 616.

Schetz. J.A. and Jakubowski, A.K., (1975), "Experimental Studies of the Turbulent Wake behind Self-Propelled Slender Bodies", AIAA Journal, Vol. 13, pp. 1568-1575.

Schetz, J.A. and Favin, S., (1977), "Numerical Solution for the Near Wake of a Body with Propeller", AIAA, J. Hydronautics, Vol. 11, pp. 136-141.

Schetz, J.A. and Favin, S., (1979), "Numerical Solution of a Body-Propeller Combination Flow Including Swirl and Comparisons with Data", AIAA, J. Hydronautics, Vol. 13, pp. 46-51.

Stern, F., Patel, V.C., Chen, H.C. and Kim, H.T., (1985), "The Interaction Between Propeller and Ship-Stern Flow", Proc. Osaka Int. Colloq. on Ship Visc. Flow, pp. 468-495.

Stern, F., Kim, H.T., Patel, V.C.and Chen, H.C., (1986), "Viscous-Flow Computations of Propeller-Shaft Configurations", IIHR Report, in preparation

Telionis, D.P., (1981), "Unsteady Viscous Flow", Springer-Verlag New York Inc.

Toda, Y., Tanaka, I. and Iwasaki, Y. (1982), "Distortion of Axisymmetric Boundary Layer Due to Propeller Suction", J. Kansai Soc. Nav. Arch., Japan, Vol. 185, p. 39.

Toda, Y., Tanaka, I., Suzioka, H. and Mori, H. (1984), "Distortion of Three-Dimensional Boundary Layer Due to Propeller Suction", J. Japanese Soc. Nav. Arch., Japan, Vol. 172.

Wang, M.H., (1985), "Hub Effects in Propeller Design and Analysis", MIT Dept. of Ocean Eng. Report no. 85-14.

Yamazaki, R., (1980), "A New Direction in Propulsion Theory of Ships on Still Water", Memoirs, Faculty of Engineering, Kyushu University, Vol. 40, No. 1.

Zhou, L.D. and Yuan, J.L. (1984), "Calculation of the Turbulent Flow Around the Stern and in the Wake of a Body of Revolution with the Propeller in Operation", Proc. 15th ONR Sym. Naval Hydrodynamics, Hamburg, pp. 279-290.

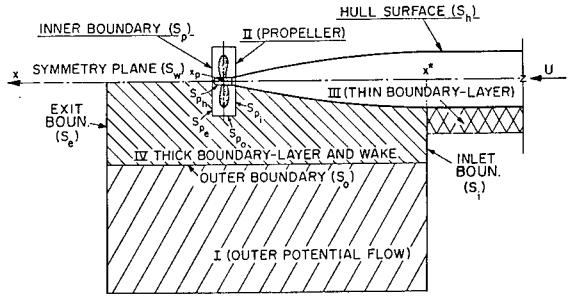


Fig. 1. Flow field region definition sketch.

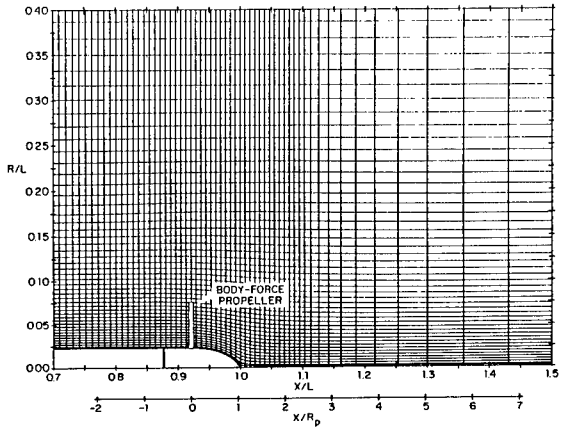


Fig. 2. P4660 fine grid (partial view).

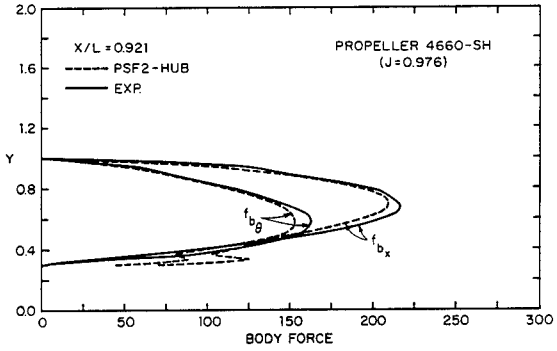
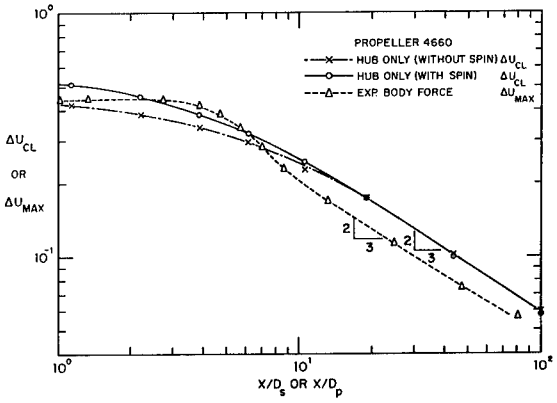


Fig. 3. Body-force distributions.



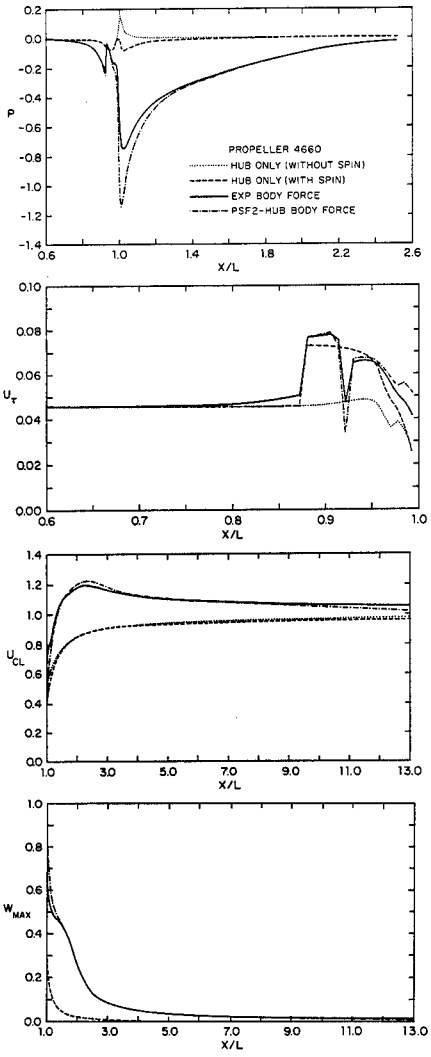


Fig. 4. Body surface and wake centerline pressure, and wall-shear, wake centerline, and maximum swirl velocities.

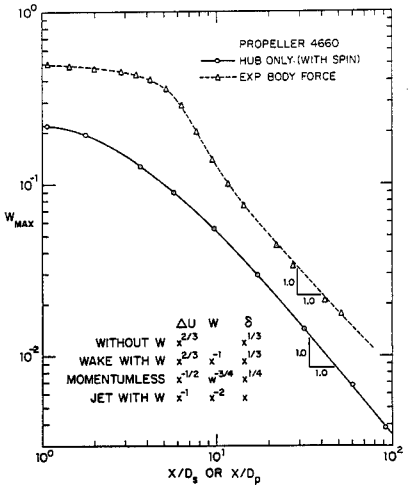


Fig. 5. Far wake asymptotic forms.

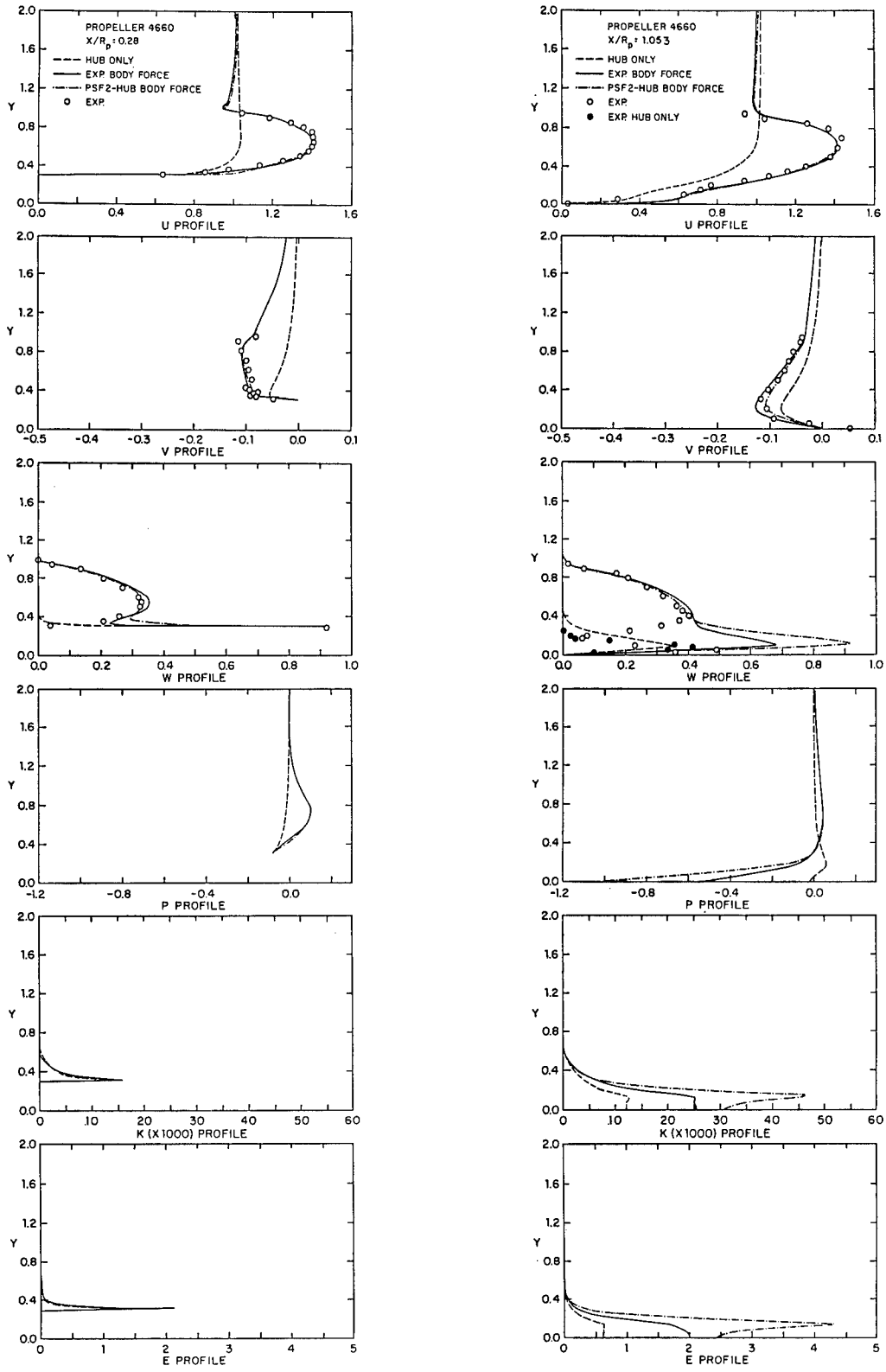


Fig. 6. Velocity profiles, pressure, and turbulence parameters.

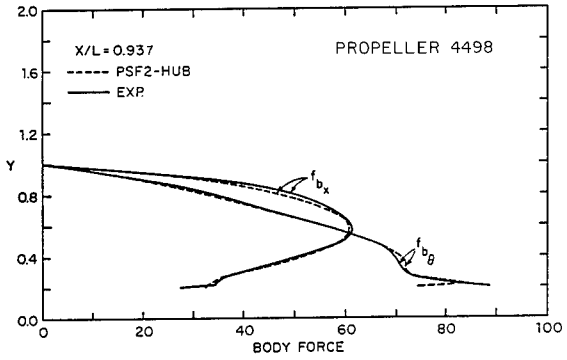


Fig. 7. Body-force distributions.

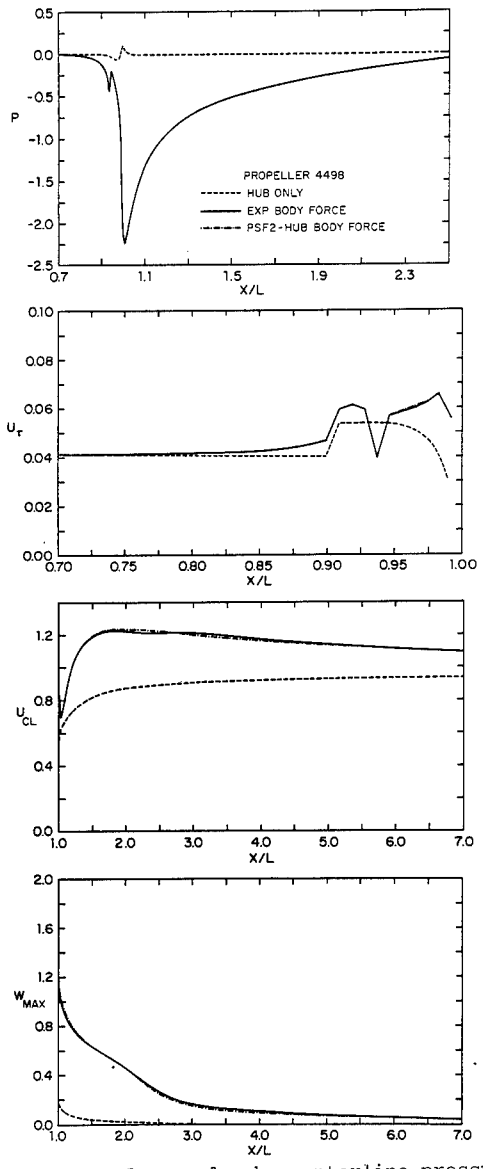


Fig. 8. Body surface and wake centerline pressure, and wall-shear, wake centerline, and maximum swirl velocities.

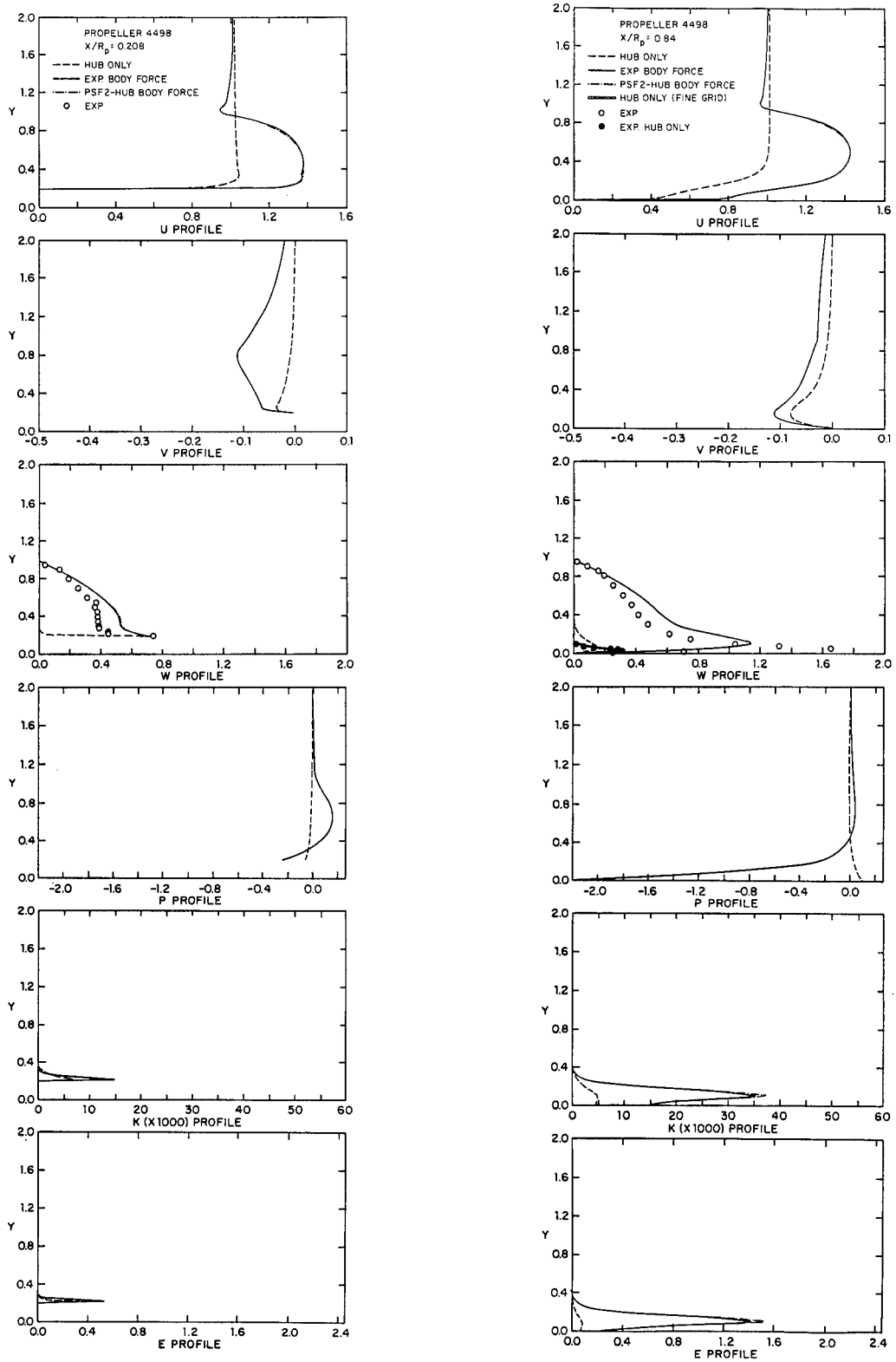


Fig. 9. Velocity profiles, pressure, and turbulence parameters.

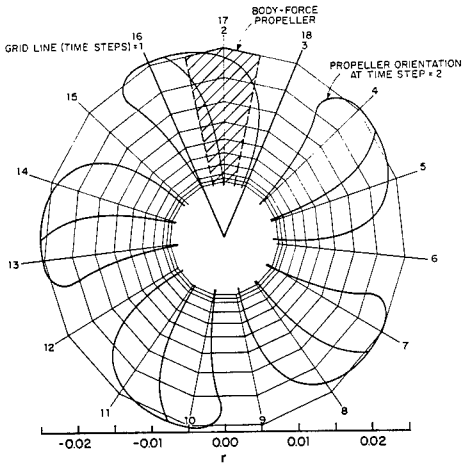


Fig. 10. Unsteady flow cross-section grid (partial view).

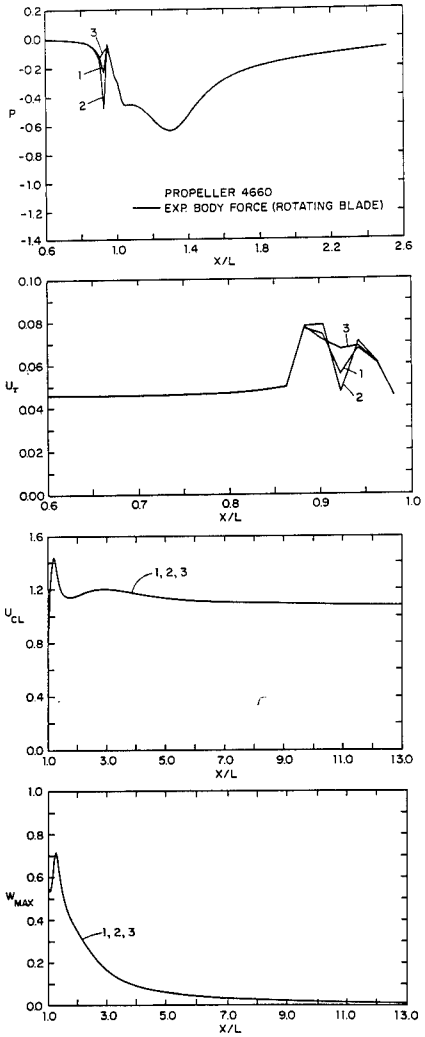


Fig. 11. Body surface and wake centerline pressure, and wall-shear, wake centerline, and maximum swirl velocities.

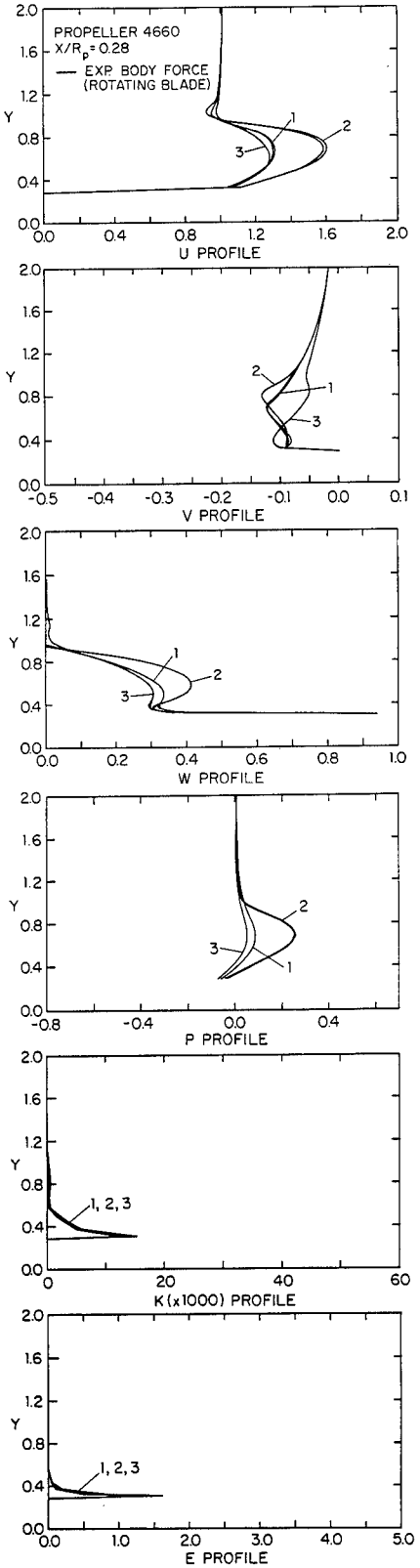


Fig. 12. Velocity profiles, pressure, and turbulence parameters.

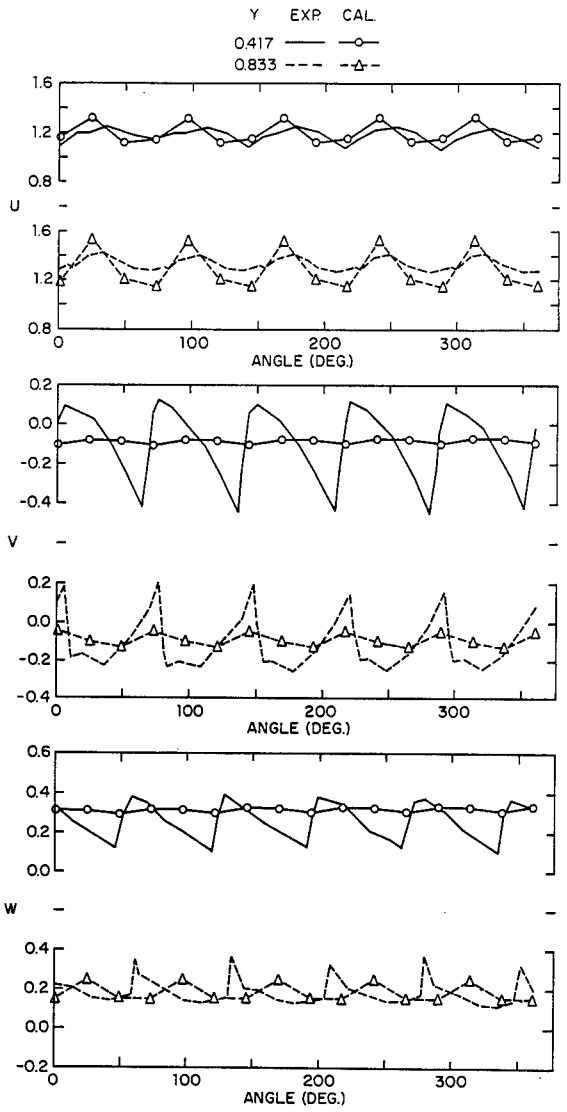


Fig. 13. Time history of the velocity components at $x/R_p = .28$.

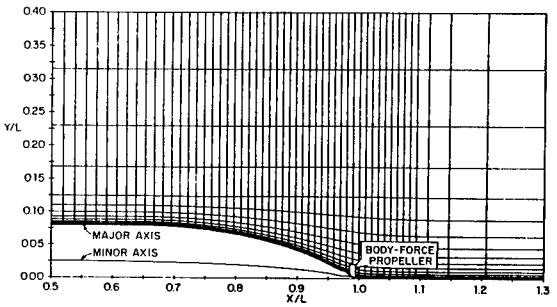


Fig. 14. 3:1 Elliptical body grid: major axis plane (partial view).

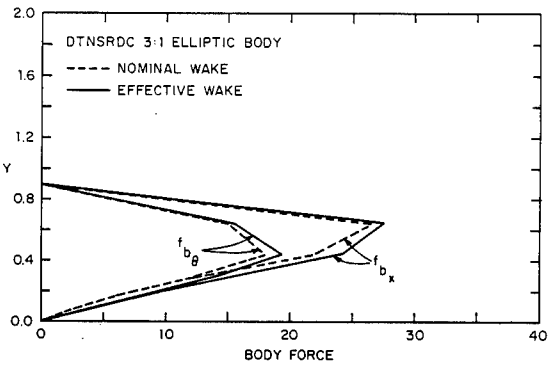


Fig. 15. Body-force distributions.

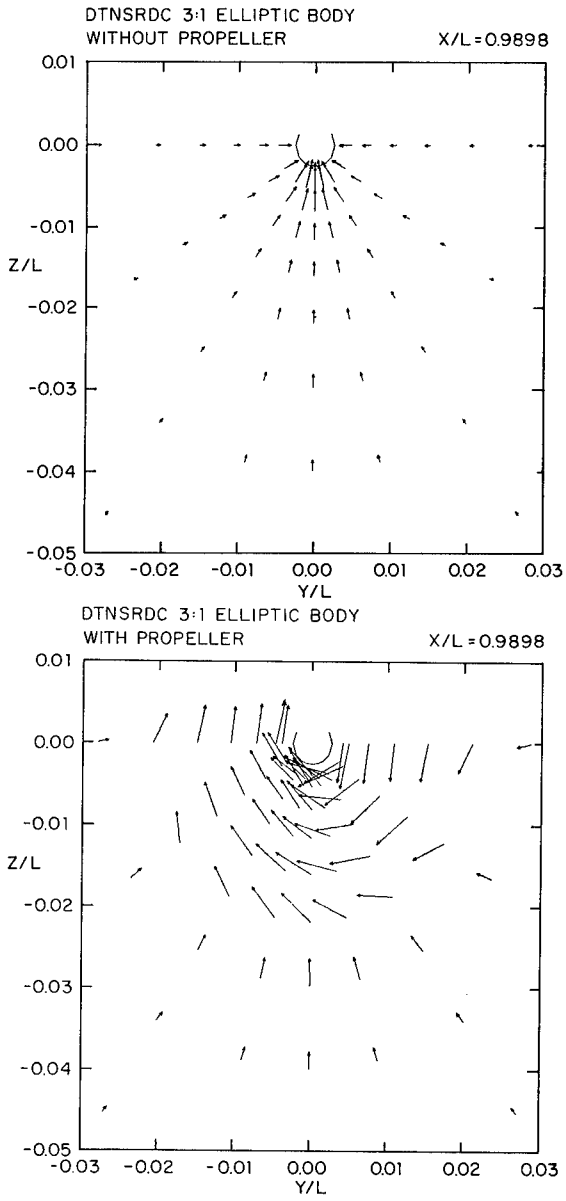


Fig. 16. Velocity vectors in the propeller plane.

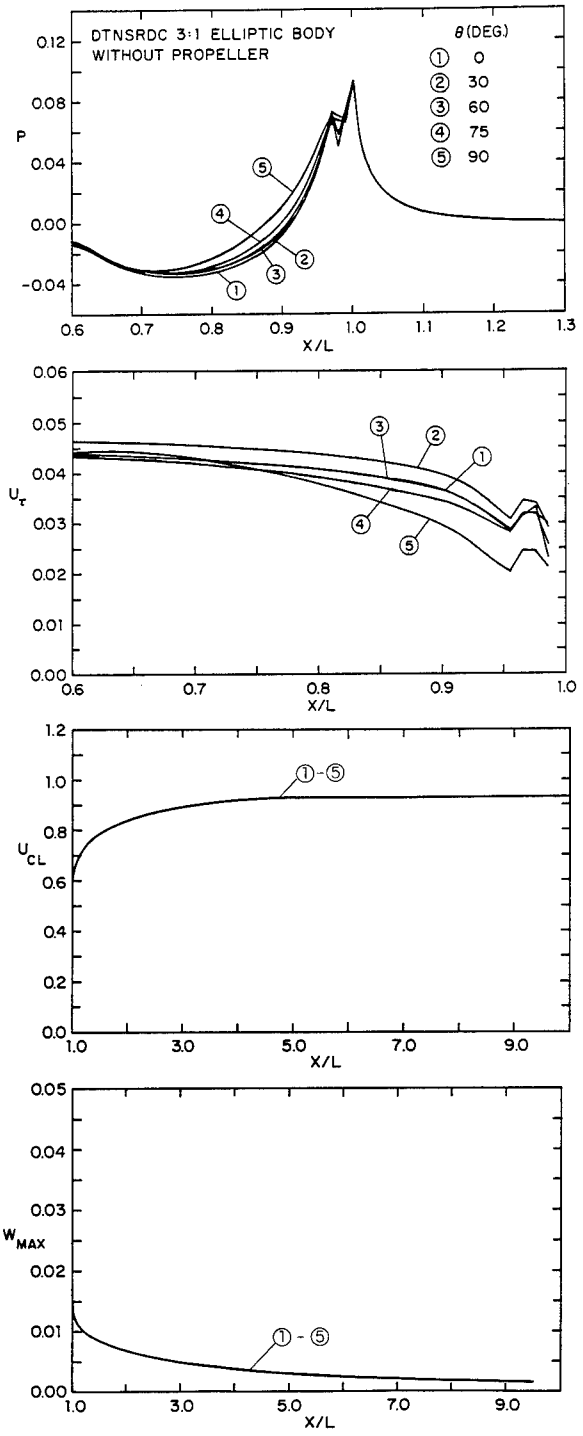


Fig. 17. Body surface and wake centerline pressure, and wall-shear, wake centerline, and maximum swirl velocities.

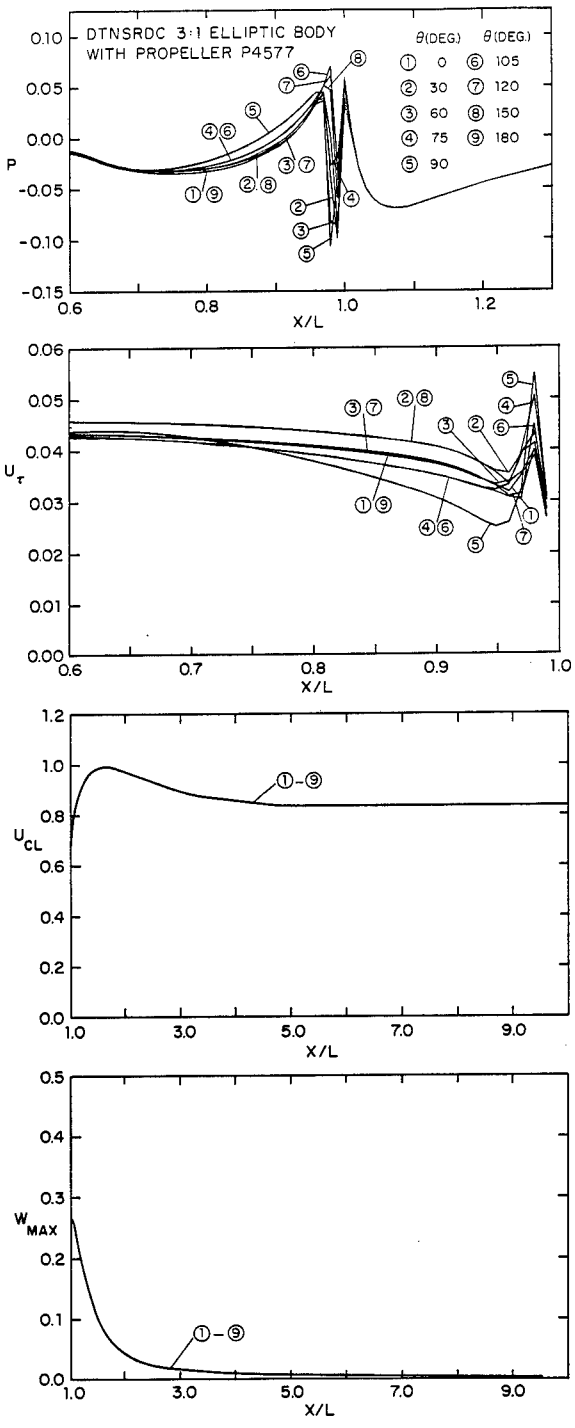


Fig. 18. Body surface and wake centerline pressure, and wall-shear, wake centerline, and maximum swirl velocities.

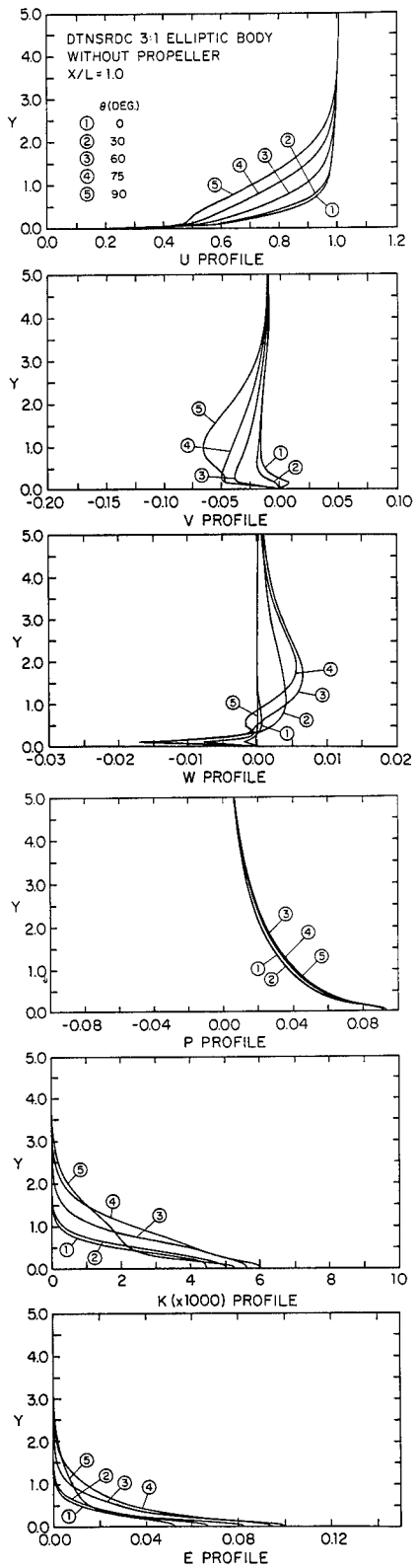


Fig. 19. Velocity profiles, pressure, and turbulence parameters.

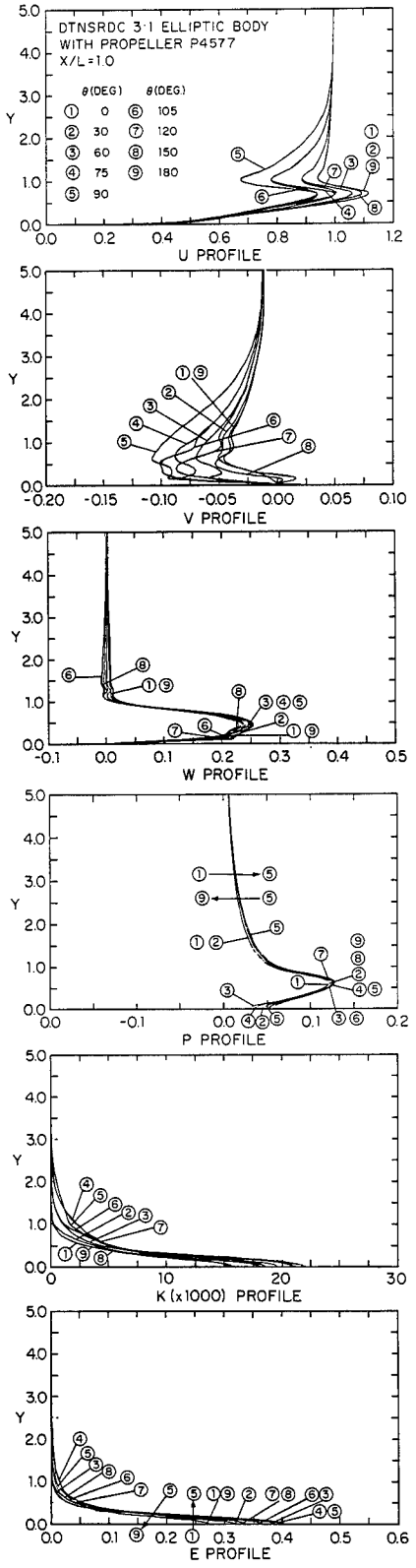


Fig. 20. Velocity profiles, pressure, and turbulence parameters.

DISCUSSION

Terry Brockett,
University of Michigan

The authors have undertaken a comprehensive investigation of the flow about a hull/propeller combination and presented impressive correlation with experimental data. For the most part, their approach is the analysis of the flow field. For the design of a propulsor, subcomponents of the analysis are required. Can the authors present such information as the effective wake at points on the propeller blade surface and the thrust deduction? For the thrust-deduction computation, I wonder about the contribution from the suction on the fairwater downstream of the propeller. Do the authors find this to be an important contribution? Again I compliment the authors on their comprehensive investigation.

Reply -

In response to Professor Brockett, we note that the complete flow field including velocity, pressure, and turbulence parameter profiles as well as the body surface shear-stress and pressure distributions are provided by the present solution. The thrust deduction is obtained by using the latter two quantities to calculate the axial force on the body for both the with and without propeller conditions. In our previous work with DTNSRDC, on afterbody 1 (Stern et al., 1985), the results for thrust deduction were shown to be in good agreement with the available experimental data. Since no data for thrust deduction were available for the present applications, thrust deduction was not calculated. It is expected that for root-loaded propellers with large hub vortices the contribution to thrust deduction (if it is defined to include the fairwater) from the suction on the fairwater downstream of the propeller may be significant. We shall make a point of quantifying this contribution in the future. However, possibly an even more important consequence of the swirl-induced low pressure in the propeller slipstream is the reduction in propeller efficiency (i.e., reduction in thrust for a given shaft horsepower). Lastly, we have not presented effective-wake profiles since they are dependent on the method used to obtain the propeller-induced velocities, and instead prefer total velocity profiles. Of course, effective wake values can be obtained at any field point from the results presented by simply subtracting the propeller-induced velocity.

Brian Clayton,
University College London

The development of turbulence models and the experimental verification of them is notoriously difficult. The authors use a k-ε model to ascertain the stern boundary layer characteristics that develop naturally on a body. I should be grateful if the authors could discuss in a more quantitative way the form of the k-ε model that was used, especially as it was applied to a thick boundary layer region. How do the induced rotational velocities from the subsequently installed propeller modify the initial model? Bearing in mind the general lack of experimental data on k and ε for the type of flows being examined would the authors care to speculate on the type of experiments they would like to see performed in order to furnish details that could be used to verify and then refine their turbulence models.

Reply -

We note that we have used the standard k-ε turbulence model without modifications for thick-boundary-layer or propeller-induced effects such as nonisotropy, curvature, rotation, vortex flow, and unsteady flow. This is justified since it is believed that the present flow is basically pressure driven, and for the initial development of methodology such a turbulence model is adequate. Furthermore, present procedures for including these additional factors in turbulence models are not sufficiently well developed that they can be considered as improvements. With regard to the required experiments for the verification and refinement of turbulence models, detailed measurements of both the velocity and turbulence profiles upstream and downstream of the propeller are necessary including mean and phase-averaged values. Particular attention should be given to the flow in the immediate vicinity of the propeller in order to explicate the nature of the unsteady flow and the evolution of the blade wakes in the propeller slipstream. Such an experimental program is presently underway at the Iowa Institute of Hydraulic Research.

Michael Mendenhall,
Nielsen Engineering & Research

a. What order of computer time is required for the unsteady calculation with the fine grid?

b. Is the fine grid arrangement converged; i.e., is it worth the effort to further refine the grid?

Reply -

We have not performed unsteady flow calculations with the finer grid (i.e., Fig. 2) so we cannot be certain of the required computer time. However, based on previous experience it is expected that it will increase by a factor of 3.2. The steady-flow P4660 fine grid results are fully converged.

K. Nakatake,
Kyushu University

In the future, you will take into consideration the effects of the rudder and the free surface. Is it easy to apply your method to that case?

Reply -

Of course we would like to include such effects as appendages and the free surface; however, we recommend first including such effects in viscous-flow methods without the complication of the propeller to focus on the basic aspects an then study the modifications due to the inclusion of the propeller.

Stephen Shamroth,
Scientific Research Associates

Have you tried various turbulence models and can you comment on the sensitivity of results to turbulence modelling assumptions.

Reply -

To date we have not used other turbulence models so we cannot comment on the sensivity of the results to turbulence modeling assumptions (see the previous response to Dr. Clayton). With regard to turbulence modeling, the most critical aspect at the present time is felt to be in the near-wall modeling; thus, future studies will focus on this aspect. If time permits, more sophisticated Reynolds stress models will be investigated.

Propeller Interaction with an Axisymmetric Sheared Onset Flow

T. BROCKETT
University of Michigan, U.S.A.

ABSTRACT

A mathematical model and some numerical analysis are presented for the interaction between a conventional propeller and an axisymmetric onset flow. In a coordinate system rotating with the blades, the steady flow field is treated as inviscid but one possessing vorticity. The total velocity field consists of the rotational onset flow, the potential interaction and propeller-induced velocity, and a rotational interaction term. The onset flow and potential velocity fields are assumed known, and hence our concern is with the three-dimensional shear-interaction term. If the interaction components were added to the onset flow, the effective velocity field is defined and the remaining velocity component may be properly represented by one of a number of existing potential-flow models for the propeller.

Two other aspects of operation in an axisymmetric shear flow are described. One is the conservation of the Bernoulli head H , along streamlines. Since the body streamline divides and takes different directions on each side of the blade, there is an added term in the loads that involves the difference in H across the blade section. Representative calculations show that a significant effect on pressure distribution may occur even though the overall loads are negligibly influenced. The second aspect is the presence of the variable Bernoulli head in the force-free condition employed to define the equation governing the position vector of the shed vortex sheet filaments. Estimates given for the influence of this effect on the orientation of filaments leaving the trailing edge show it may be of equal importance as the constant-head analysis at the trailing-edge departure point.

PRINCIPAL NOMENCLATURE

$c_p=(p-p_o)/(\rho V^2/2)$	Pressure coefficient
$C_P=2\pi Qn/(\rho V^3 \pi D^2/8)$	Power-loading coefficient, based on reference speed
$C_{Th}=T/(\rho V^2 \pi D^2/8)$	Thrust-loading coefficient, based on reference speed
$c(x_R)$	Blade-section chord length
D	Propeller diameter
$E(x_c,x_R) = E_c \pm E_T$	Profile shape function
$E_c(x_c,x_R)$	Meanline shape function
$E_T(x_c,x_R)$	Thickness shape function
$(\underline{e}_1,\underline{e}_2,\underline{e}_r)$	Unit base vectors in a helical reference system
$\underline{f}$	Offset in $\underline{e}_2$ direction in specification of shed vortex sheet filament trajectory
$G(x_R) = \Gamma/(\pi DV)$	Non-dimensional circulation
$H(\underline{r})$	Bernoulli head, conserved along a streamline in steady flow with vorticity

$i_T(x_R)$	Total rake: axial displacement of blade-section mid chord point from x = 0 plane
$(\underline{i},\underline{e}_r,\underline{e}_\theta)$	Unit base vectors in a cylindrical polar reference system
$(\underline{i},\underline{j},\underline{k})$	Unit base vectors in a Cartesian reference frame
$J_V = V/nD$	Advance coefficient based on reference speed
$\underline{N}$	Normal to surface
n	Propeller rotational speed, revolutions per unit time
p	Pressure
$P(x_R)$	Pitch of blade section
Q	Torque absorbed by blades
$\underline{q}=\underline{q}_o+\underline{v}_p+\underline{v}_o+\Delta\underline{v}$	Velocity vector in rotating coordinate system
$\underline{q}_E=\underline{q}_o+\underline{v}_o+\Delta\underline{v}$	Effective velocity
$\underline{q}_o$	Velocity vector field without propeller, rotating system
R = D/2	Propeller radius
r_h	Radius of propeller hub
$\underline{r}$	Position vector of field point
$\underline{r}_o$	Position vector of field point on blade reference surface
T	Thrust produced by blades
$\underline{T}$	Tangent vector along lines of constant vortex strength in shed vortex sheet
$\overline{U}_T(x_R)$	Average preswirl component in onset flow to propeller
V	Reference speed
$\underline{v}_o$	Potential interaction velocity
$\underline{v}_p$	Velocity component due to presence of the blades, potential flow
$w_R(x_R)$	Radial velocity component in nominal onset flow, fraction of V
$w_T(x_R)$	Tangential velocity component in nominal onset flow, fraction of V
$w_x(x_R)$	Local axial wake fraction for nominal onset flow
(x,y,z)	Cartesian coordinates
x_h	Hub radius, fraction of tip radius
x_R	Fraction of radius, measured from axis of rotation
Z	Number of blades
$\beta(x_R)=\tan^{-1}\frac{J_V(1-w_x)}{x_R\pi}$	Advance angle of blade section
$\beta_w(x_R)$	Pitch angle of reference helix used to define shed vortex sheet
$\Delta\underline{v}$	Velocity component due to interaction with sheared onset flow
Δx_{Ro}	Non-dimensional displacement of constant strength vortex filaments from constant radius
$\Delta\underline{\omega}$	Vorticity associated with $\Delta\underline{v}$
$\Gamma(x_R)$	Circulation distribution
$\underline{\zeta}_w(n,x_R)$	Position vector of point on constant-strength vortex filament in shed vortex sheet
$\theta = \tan^{-1}\frac{-y}{z}$	Angular coordinate in cylindrical reference frame

$\theta_b = 2\pi(b-1)/Z$	Angular coordinate of blade-reference line of b^{th} blade
$\theta_s(x_R)$	Skew angle; circumferential displacement of blade-section midchord point from y = 0 plane
(ξ_1,ξ_2,r)	Helical coordinates on pitch reference surface
ρ	Fluid density
$\phi_p(x_R)$	Geometric pitch angle
$\underline{\omega}$	Vorticity vector in flow field

INTRODUCTION

The mathematical model and numerical analysis procedures for an isolated propeller operating in an otherwise uniform onset flow field are at an advanced state of development (Cox and Morgan (1), Kerwin (2)). Such situations are adequately modeled with potential-flow analysis for local lift and pressure distributions plus a local viscous drag (often an empirical approximation). The potential-flow model employs surface distributions of singularities which are usually approximated with distributions on representative surfaces for the blades and shed vortex sheet. However, marine propellers are almost universally placed at the stern of the hull form and hence operate in close proximity to the hull as well as in a local flow field, called the nominal wake, that is both radially and circumferentially variable. These velocity variations coexist with vorticity and hence a potential-flow model is no longer applicable.

Treatment of the propeller in this onset field involves two considerations: time-average pressure/loads and fluctuating performance. The time-average performance is determined with the axi-symmetric component of the onset flow, and the fluctuating performance is determined with the circumferential variations. The time average dependence on only the axisymmetric onset flow is a first-order approximation. That is, the pressure is a non-linear function of speed and thus components of the response to the circumferential variations in the onset flow will also contribute to the steady loads. For the approximation of linear dependence of pressure on induced velocity, the above assumption is appropriate.

In the present investigation, a fundamentally consistent investigation of the interaction of a propeller operating in an axisymmetric onset flow is defined.

The flow field is considered to be composed of two essential components: (1) the nominal onset flow which is taken as given in terms of both a velocity field, $\underline{q}_o(\underline{r})$, and a pressure field, $p_o(\underline{r})$, and (2) the propeller induced velocity $\underline{v}(\underline{r})$ and pressure fields, $p(\underline{r})$, which are superimposed on the nominal fields. Our concern is to define the propeller-induced velocity field since the pressure field can be determined from the conservation of the upstream radially-variable Bernoulli head along streamlines once the velocity field is known.

The propeller-induced velocity field is further subdivided: a potential term due to the presence of the propeller, $\underline{v}_p(\underline{r})$; a potential term due to the interactions of the propeller with the hull and other nearby surfaces, $\underline{v}_o(\underline{r})$; and a shear-interaction term due to the presence of the propeller, $\Delta\underline{v}(\underline{r})$. Hence the total velocity field $\underline{q}(\underline{r})$ is given by

$$\underline{q}(\underline{r}) = \underline{q}_o(\underline{r}) + \underline{v}_p(\underline{r}) + \underline{v}_o(\underline{r}) + \Delta\underline{v}(\underline{r}) \tag{1}$$

The terms $\underline{v}_p(\underline{r})$ and $\underline{v}_o(\underline{r})$ are represented with conventional techniques. Our concern is with the shear-interaction term, $\Delta\underline{v}(\underline{r})$, which we will show to be a three-dimensional quantity, as is any other propeller-induced velocity component.

It is sometimes convenient to think of the total velocity vector minus the irrotational component of the propeller-induced velocity as an effective velocity field:

$$\underline{q}_E(\underline{r}) = \underline{q}(\underline{r}) - \underline{v}_p(\underline{r}) = \underline{q}_o(\underline{r}) + \underline{v}_o(\underline{r}) + \Delta\underline{v}(\underline{r}) \tag{2}$$

The effective velocity field at $\underline{r}_o = (r,\xi_1)$, a point on the blade, is the non-dimensional effective onset flow to the propeller blade:

$$\frac{\underline{q}_E(\underline{r}_o)}{V} = [1-w_E(r,\xi_1)]\underline{i} + w_{RE}(r,\xi_1)\underline{e}_r + w_{TE}(r,\xi_1)\underline{e}_\theta \tag{3}$$

where r is the radius measured from the axis of rotation and ξ_1 is the helical coordinate along the nose-tail line at constant radius, and the various w_{iE} are effective wake values corresponding to cylindrical polar directions (i.e., radial, and circumferential). This definition is

essentially that given by the International Towing Tank Conference (Dyne, et al, (3)).

It has long been recognized that the circumferential average onset flow together with a potential-flow model of the propulsor is inadequate. A correction is often made from a comparison of performance of the same propeller in open water and behind the hull. The resulting correction is often applied as a multiplicative correction to the circumferential average axial component of the nominal flow. More recent procedures treat the shear-interaction term as an axisymmetric axial velocity component. Pioneering work in this area is that of Nelson (4), followed by Huang (5), Pelletier and Shetz (6), Stern et al (7) and van Gent(8). Each of these investigations treats the propulsor as an axisymmetric field and thus is significantly different than the present analysis of the three-dimensional interaction.

In addition to the velocity field, a derivation of the loads acting on the blade reveals a here-to-fore neglected term that is essentially the integral of the Bernoulli head difference across the blade. This effect arises from a consideration of the dividing-streamline locations on the two sides of the blade. Since these streamlines are in slightly different directions and the chord may be relatively long, the pressure along a fixed radius section may be significantly influenced by the variable Bernoulli head convected across this section. Generally, the sign of this integrand is different in the hub and tip region and thus the overall loads - but not local pressures - are nearly the same as without inclusion of this term. Example computations are given to demonstrate the magnitude of this effect.

A further aspect of the axisymmetric onset flow analysis is a modification of the location of the predicted position of the shed-vortex sheet. The two boundary conditions on the shed vortex sheet are that the normal component of velocity be zero and that there be no pressure difference across the sheet. Part of the pressure difference is due to the Bernoulli head difference at a point and hence this difference ultimately is involved in the differential equation governing the position of the shed-vortex sheet. The previous example computations of the Bernoulli head difference across the blade surface give a value at the trailing edge that is used to define the change in initial orientation of the filament. Some representative computations are given to confirm its importance.

The following analysis is concerned with defining the three aspects of interaction just described. Since these are sub-elements of the complete description of the flow, a lifting-surface code is also required. Several such codes are described by Kerwin(2). The one selected for the present analysis was developed by Brockett(9).

In the following paragraphs, the mathematical model for the three shear-interaction effects is defined, some representative computations are presented for the Bernoulli-head effect, numerical schemes for the three-dimensional effective wake are mentioned, and conclusions are drawn.

MATHEMATICAL MODEL - THICK, LIFTING BLADES IN AXISYMMETRIC SHEAR FLOW

Statement of Problem, Basic Equations

We consider a set of blades rotating with constant angular speed in an axisymmetric onset flow that is radially variable and may have a small radial flow component. An observer in an inertial reference frame notes that the flow field is unsteady but that it is steady[1] for a coordinate system fixed to the blades. In a coordinate system rotating with the propeller, the onset velocity, $\underline{q}_o$, can be expressed in polar components $(\underline{i}, \underline{e}_r, \underline{e}_\theta)$ as

$$\underline{q}_o(\underline{r}) = V_x(r,x)\underline{i} + V_R(r,x)\underline{e}_r + \Omega r\underline{e}_\theta \tag{4}$$

$$\frac{\underline{q}_o(\underline{r})}{V} = [1-w_x(r,x)]\underline{i} + w_R(r,x)\underline{e}_r + \frac{\pi x_R}{J_V}\underline{e}_\theta \tag{5}$$

where $\underline{r} = (x,r,\theta)$ is the position vector of a point in the flow field expressed in a coordinate system rotating with the propeller, positive x is measured downstream along the axis of rotation, and θ is measured counterclockwise from the upward vertical when looking upstream, and

[1] The flow is steady only if the onset flow were axisymmetric, as assumed. In a nonuniform onset flow and/or for a case with preswirl produced by upstream blades, the flow will be unsteady. In addition, preswirl vanes introduce vortex sheets across which the flow field is discontinuous and hence must be taken as a boundary of the flow field (as are the propeller vortex sheets). These nonuniform/unsteady effects are not treated.

V = constant value of reference speed in the axial direction
V_X = is the axial component of the onset velocity, $(1-w_X)V$
Ω = is the constant rotational speed, $2\pi n$
V_R = is the radial component of the onset flow, $w_R V$, and is of small order (i.e., it is comparable to the components of velocity introduced by the propeller)
x_R = r/R, non-dimensional radius
J_V = $V/(nD)$, advance coefficient based on reference speed

In the vicinity of the propeller, the axial component is assumed to vary significantly in the radial direction but only slightly in the axial direction. Far upstream both V_R and the axial variation in V_X tend to zero. We assume $\underline{q}_o$ is given.

In addition to this onset flow, there may be another identifiable steady component that is introduced locally by an interaction with the hull, other nearby appendages or lifting surfaces (e.g., those from another row of blades):

$$\underline{v}_o(\underline{r}) = v_{ox}(\underline{r})\underline{i} + v_{or}(\underline{r})\underline{e}_r + v_{o\theta}(\underline{r})\underline{e}_\theta \qquad (6)$$

We assume this component can be adequately represented by a potential[2]:

$$\underline{v}_o(\underline{r}) = \nabla\phi_o(\underline{r}) \qquad (7)$$

We also assume $\underline{v}_o$ tends to zero far ahead of the propeller and is known at all required spatial points. The tangential velocity component, $\underline{v}_o \cdot \underline{e}_\theta$, may contain an axisymmetric preswirl component $\bar{U}_{T_o}(x,r)$ that is of large order. A reference value of this tangential component at the blade is $\bar{U}_T(r)$.

When the propeller is modeled in this flow field, two components of velocity are identified, one potential in nature (associated with the nearly potential flow about the blades) and one rotational in nature (associated with the redistribution of the vorticity in the onset flow). Let these two terms be $\underline{v}_p$ and $\Delta\underline{v}$. Hence the total velocity, $\underline{q}$, is given in Equation (1).

[2] Any shear-interaction velocity contribution resulting from this component is included in $\Delta\underline{v}$.

If a small parameter ε were to represent the magnitude of the disturbance introduced by the propeller, then we assume $\underline{v}_p$, $\underline{v}_o - \bar{U}_T\underline{e}_\theta$, $\Delta\underline{v}$ and the axial variation of V_X (i.e., $\partial\bar{V}_X/\partial x$), and the radial component of the onset flow V_R, are of order ε.

It has been shown (10,11) that an arbitrary solenoidal vector field, $\underline{u}$, can be represented by the following combination of boundary and volume integrals

$$\underline{u}(\underline{r}) = \frac{1}{4\pi}\oiint_{S_V}\left[(\underline{n}\cdot\underline{u})\frac{\underline{r}-\underline{s}}{|\underline{r}-\underline{s}|^3} + (\underline{n}\times\underline{u})\times\frac{\underline{r}-\underline{s}}{|\underline{r}-\underline{s}|^3}\right]d\sigma_s + \frac{1}{4\pi}\lim_{\varepsilon\to 0}\iiint_{V-B(\underline{r},\varepsilon)}\underline{\omega}\times\frac{\underline{r}-\underline{s}}{|\underline{r}-\underline{s}|^3}\,dV_s \qquad (8)$$

where S_V is the surface bounding the volume V,
$\underline{s}$ is the variable of integration,
$\underline{n}(\underline{s})$ is a unit vector normal to the surfaces directed into the fluid,
$d\sigma_s$ and dV_s are differential elements of surface area and volume,
$B(\underline{r},\varepsilon)$ is a small volume about $\underline{r}$ with characteristic dimension ε, and
$\underline{\omega} = \nabla\times\underline{u}$ is the vorticity.

This representation satisfies the continuity equation everywhere in the flow field. The first term in the surface integral can be interpreted as a source distribution of variable strength $(\underline{n}\cdot\underline{u})/4\pi$ and the second term can be interpreted as a vortex distribution of variable strength $(\underline{n}\times\underline{u})/(4\pi)$. In the literature dealing with propellers (e.g., Kerwin (2)), this is the representation considered, and hence we take it as known. We will show that $\Delta\underline{v}$ is associated with the volume integral. On surfaces of fluid discontinuity in the flow field, $\underline{v}_p$ will have a jump but $\Delta\underline{v}$ may be continuous (and will be taken so at the outset).

If the whole flow field were treated as viscous, only the volume integral of the vorticity would exist, since in viscous flow the velocity is zero on a fixed boundary. For lifting surfaces with attached flow, a region of intense vorticity exists in the boundary layer region near the surface, with much less change in the field vorticity outstide this region. When this near-surface region is thin, Equation (8) shows that the surface integrals are equivalent to the volume integral over this narrow region, and hence they provide an adequate representation of the flow field.

There exist several procedures (3, 4,5,8) for determining $\Delta\underline{v}$ when it is

assumed to be an axial component that is a function of radius only, i.e., if $\Delta\underline{v} = \Delta v(r)\underline{i}$ only. In the analysis presented here, the increment in velocity $\Delta\underline{v}$ is a spatial variable, and may consist of axial, radial, and tangential components.

So far we have described the components of the flow field. Now we describe the conditions that govern this flow field. These are predominately the continuity equation:

$$\nabla\cdot\underline{q} = 0 \tag{9}$$

and the momentum equation for the steady relative flow in a rotating coordinate system:

$$\underline{q}\cdot\nabla\underline{q} = -\frac{1}{\rho}\nabla p - 2\underline{\Omega}\times\underline{q} - \underline{\Omega}\times(\underline{\Omega}\times\underline{r}) \tag{10}$$

This equation is valid in a coordinate system rotating with constant angular velocity $\underline{\Omega} = -\Omega\underline{i}$. In this equation p is the pressure. It will be required later to know an expression governing the vorticity vector, $\underline{\omega} = \nabla\times q$. One can take the curl of the momentum equation to obtain the required expression. Following Batchelor (12) the equation governing the vorticity in the rotating coordinate system can be expressed:

$$\underline{q}.\nabla(\underline{\omega}+2\underline{\Omega}) = (\underline{\omega}+2\underline{\Omega})\cdot\nabla\underline{q} \tag{11}$$

The momentum equation can be integrated to obtain a general Bernoulli equation:

$$\nabla\left(\frac{1}{2}\underline{q}\cdot\underline{q} + \frac{p}{\rho} - \frac{1}{2}\Omega^2 r^2\right) = \underline{q}\times(\underline{\omega} + 2\underline{\Omega}) \tag{12}$$

Since the vector cross product on the right-hand side produces a vector normal to both components, the directional derivative along a streamline will be zero (i.e., $\underline{q}\cdot(\text{L.H.S.})=0$). Hence

$$\frac{1}{2}\underline{q}\cdot\underline{q} + \frac{p}{\rho} - \frac{1}{2}\Omega^2 r^2 = H(\zeta_\psi) \tag{13}$$

Here $H(\zeta_\psi)$ is the general Bernoulli function that is constant along a particular streamline (conservation of the left-hand side of this equation would also take place along curves aligned with the $(\underline{\omega} + 2\underline{\Omega})$ direction field if desired.)

If a propeller were introduced into a uniform stream, the total flow field will be determined by integrals of appropriate terms over the boundary (the first integral on the right-hand side of Equation (8)). This solution will be complete and unique for potential flow once some account has been made of the Kutta condition and the shed vortex sheet position is specified (13). Experience has shown that in real viscous fluid involving a uniform onset flow, this representation adequately describes the flow. However, if vorticity exists in the onset flow field, a field description for the solution must be added to terms arising from the surface integrals (i.e., the volume integral in Equation (8) is the required term). Our approach here will be to consider the solution to be the sum of terms described by Equation (8). This solution is exact for inviscid flow and is believed an adequate representation of the flow field outside the thin boundary layer on the lifting surface in real flow. A portion of this solution consists of boundary integrals for which significant analysis and numerical codes exist (2). It is anticipated that the volume integral due to the presence of shear flow represents a small contribution that can be adequately evaluated using some straightforward approximations. An alternative to the approach taken here would be to treat the whole detailed flow field numerically using the full governing equations. Such an approach is believed to be prohibitively time consuming.

Propeller Geometry and Boundary Condition on Blade

Coordinate systems are constructed with the same orientation as in (9,11, and 13). The helical coordinate system (ξ_1,ξ_2,r) rotating with the blades is shown in Figure 1. Unit base vectors in a right-handed Cartesian reference frame are the customary $(\underline{i},\underline{j},\underline{k})$ where $\underline{i}$ is along the x axis and is positive pointing aft, $\underline{j}$ is along the y axis and $\underline{k}$ is along the z axis that is generally along the reference blade. Unit vectors along the helical coordiates are

$$\underline{e}_1 = \sin\phi_p\,\underline{i} + \cos\phi_p\,\underline{e}_\theta \tag{14}$$

$$\underline{e}_2 = -\cos\phi_p\,\underline{i} + \sin\phi_p\,\underline{e}_\theta \tag{15}$$

$$\underline{e}_r = -\sin\theta\,\underline{j} + \cos\theta\,\underline{k} \tag{16}$$

where

$$\underline{e}_\theta = -\cos\theta\,\underline{j} - \sin\theta\,\underline{k} \tag{17}$$

The blade surface is given by

$$\xi_2 = E(\xi_1,r) \tag{18}$$

$$= E_C(\xi_1,r) \pm E_T(\xi_1,r) \tag{19}$$

where

E_C is the meanline shape, and

E_T is the thickness shape

In the analysis it is convenient to change the variables to non-dimensional ones (x_c, x_R) instead of (ξ_1, r), where

$$\xi_1 = c(x_c - 0.5) \tag{20}$$

$$r = D\, x_R/2$$

c = chordlength at radius r

and

D = propeller diameter

The position vector of a point on the blade surface described by Eq. (18) is

$$\underline{s}(x_c, x_R) = D\{[\frac{i_T}{D} + \frac{c}{D}(x_c - 0.5)\sin\phi_p - \frac{E}{D}\cos\phi_p]\,\underline{i} + \frac{x_R}{2}\,\underline{e}_r(\theta)\} \tag{21}$$

and a normal, directed out from the blade surface, is (9,10)

$$\underline{N} = \pm\, D^2\, \frac{\partial \underline{s}/D}{\partial x_c} \times \frac{\partial \underline{s}/D}{\partial x_R} \tag{22}$$

where the plus sign is used for the suction side of the blade and the negative sign for the pressure side. With some effort, one can show that

$$\underline{N} = \pm\, \frac{D^2}{2}\left[\frac{c}{D}\,\underline{e}_2 - \frac{\partial E/D}{\partial x_c}\,\underline{e}_1 + N_R\,\underline{e}_r\right] \tag{23}$$

where the radial component is given by a lengthy expression (see Equation 10 of (9)). The normal to the blade reference surface, $\xi_2 = 0$, $0<x_c<1$, $x_h<x_R<1$ is

$$\underline{N}_o = \pm\frac{D^2}{2}\,\frac{c}{D}\,[\underline{e}_2 + N_{Ro}\,\underline{e}_r(\theta_o)] \tag{24}$$

where the radial component N_{Ro} is given by Equation 11 of (9)). In the derivation of the first-order expressions for numerical analysis, the reference surface (E=0) is often employed. Generally no specific mention will be made of differences between variables on the blade surface and on the reference surface.

The boundary condition on the blade is that there be no flow through the surface:

$$\underline{q} \cdot \underline{N} = 0 \quad \text{for } \underline{r} \text{ on } S \tag{25}$$

This condition applies to both the upper (suction) and lower (pressure) surface:

$$\underline{q}^+ \cdot \underline{N}^+ = 0$$
$$\underline{q}^- \cdot \underline{N}^- = 0 \tag{26}$$

The velocity on the blade surface consists of both even and odd components. The components $\underline{q}_o$ and $\underline{v}_o$ are assumed continuous throughout space (and hence continuous over the thin blade surface). The velocity component $\underline{v}_p$ will experience a jump across the blade surface (because the blade is lifting). Since $\Delta\underline{v}$ is associated with a volume integral without directional components of the integrand, it may be continuous across the thin blade surface. Hence one can specify the velocity at points on the blade surface, $\underline{r}_o(x_{co}, x_{Ro})$ as

$$\underline{q}^{\pm}(x_{co}, x_{Ro}) = \bar{\underline{q}}(x_{co}, x_{Ro}) \pm \langle \underline{q}(x_{co}, x_{Ro})\rangle \tag{27}$$

where

$$\bar{\underline{q}} = \underline{q}_o + \underline{v}_o + \Delta\underline{v} + \bar{\underline{v}}_p$$
$$= \underline{q}_o + \bar{U}_T(r)\,\underline{e}_\theta + O(\varepsilon)$$

$\bar{U}_T(r)$ = reference tangential velocity component at blade

$$\langle \underline{q}\rangle = \langle \underline{v}_p\rangle$$
$$= O(\varepsilon)$$

$$\bar{\underline{v}}_p = (\underline{v}_p^+ + \underline{v}_p^-)/2$$

$$\langle \underline{v}_p\rangle = (\underline{v}_p^+ - \underline{v}_p^-)/2 \tag{28}$$

The sum of Equations (26) is:

$$\{\underline{q}_o + \underline{v}_o + \bar{\underline{v}}_p + \Delta\underline{v} + \langle \underline{v}_p\rangle\}\cdot\underline{N}^+ + \{\underline{q}_o + \underline{v}_o + \bar{\underline{v}}_p + \Delta\underline{v} - \langle \underline{v}_p\rangle\}\cdot\underline{N}^- = 0 \tag{29}$$

If this equation were rearranged, one obtains (with $\underline{q}_E$ from Equation 3)

$$(\underline{q}_E + \bar{\underline{v}}_p)\cdot(\underline{N}^+ + \underline{N}^-) + \langle \underline{v}_p\rangle\cdot(\underline{N}^+ - \underline{N}^-) = 0$$

Now

$$(\underline{q}_E + \bar{\underline{v}}_p)\cdot(\underline{N}^+ + \underline{N}^-) = D^2\,\frac{\partial E_T/D}{\partial x_c}\,.$$

$$\{(\underline{q}_o + \bar{U}_T\underline{e}_\theta)\cdot\underline{e}_1 + O(E, w_R, \underline{v}_o - \bar{U}_T\underline{e}_\theta, \Delta\underline{v})\}$$

If ϕ_p were the local pitch angle and

β were the local advance angle ($\beta = \tan^{-1}[V(1-w_x)/(2\pi nr+\bar{U}_T)]$) then

$$\frac{\underline{q}_o}{V} + \frac{\bar{U}_T \underline{e}_\theta}{V} = \sqrt{(1-w_x)^2 + \left(\frac{\pi x_R}{J_V}\frac{\bar{U}_T}{V}\right)^2} \cdot \{\cos(\phi_p-\beta)\underline{e}_1 + \sin(\phi_p-\beta)\underline{e}_2\} + w_r \underline{e}_r \quad (30)$$

Thus, to first order in $w_R, E, \underline{v}_o - U_T\underline{e}_\theta$, $\phi_p-\beta$, or $\Delta\underline{v}$, (i.e., to first order in ε)

$$D^2 V \sqrt{(1-w_x)^2 + \left(\frac{\pi x_R}{J_V}\frac{\bar{U}_T}{V}\right)^2} \cos(\phi_p - \beta).$$

$$\frac{\partial E_T/D}{\partial x_c} = 2\,\underline{N}_o^+ \cdot \langle \underline{v}_p \rangle \quad (31)$$

This expression sets the values of the source terms in Equation (8).

The difference of Equations (26) is:

$$(\underline{q}_E^+ \bar{\underline{v}}_p) \cdot (\underline{N}^+ - \underline{N}^-) + \langle \underline{v}_p \rangle \cdot (\underline{N}^+ + \underline{N}^-) = 0$$

or, to first order

$$(\underline{q}_o + \bar{U}_T \underline{e}_\theta) \cdot (\underline{N}^+ - \underline{N}^-) + \left((\underline{v}_o - \bar{U}_T \underline{e}_\theta) + \Delta\underline{v} + \bar{\underline{v}}_p\right) \cdot 2\underline{N}_o^+ = 0$$

Now

$$(\underline{q}_o + \bar{U}_T \underline{e}_\theta) \cdot (\underline{N}^+ - \underline{N}^-) = (\underline{q}_o + \bar{U}_T \underline{e}_\theta) \cdot \left(2\underline{N}_o^+ - D^2 \frac{E_c/D}{\partial x_c} \underline{e}_1 + O(E)\underline{e}_r\right)$$

$$= D^2 V \left[\sqrt{(1-w_x)^2 + \left(\frac{\pi x_R}{J_V}\frac{\bar{U}_T}{V}\right)^2} \cdot \left(\frac{c}{D}(-\sin(\phi_p-\beta)) - \frac{\partial E_c/D}{\partial x_c}\cos(\phi_p-\beta)\right) + \frac{c}{D} w_R N_{Ro}\right] \quad (32)$$

This expression can be rearranged to give the slope of the meanline:

$$\frac{\partial E_c/D}{\partial x_c} = \frac{c}{D}\left[\tan(\phi_p-\beta) + \frac{2\underline{N}_o^+}{D^2(c/D)} \cdot \frac{\bar{\underline{v}}_p}{V} + \frac{\Delta\underline{v}}{V} + \frac{\underline{v}_o - \bar{U}_T\underline{e}_\theta}{V} + w_R N_{Ro}}{\cos(\phi_p-\beta)\sqrt{(1-w_x)^2 + \left(\frac{\pi x_R}{J_V}\frac{\bar{U}_T}{V}\right)^2}}\right]$$

or

$$\frac{\partial E_c/c}{\partial x_c} = \left[\tan(\phi_p-\beta) + \frac{(\underline{e}_2 + N_{Ro}\underline{e}_r) \cdot \left\{\frac{\bar{\underline{v}}_p}{V} + \frac{\Delta\underline{v}}{V} + \frac{\underline{v}_o - \bar{U}_T\underline{e}_\theta}{V}\right\} + w_R N_{Ro}}{\cos(\phi_p-\beta)\sqrt{(1-w_x)^2 + \left(\frac{\pi x_R}{J_V}\frac{\bar{U}_T}{V}\right)^2}}\right] \quad (33)$$

This is the fundamental equation that is used to determine the pitch and meanline shape (and has been included in the code described in (9)) or to determine the pressure and loads on a given propeller. For design, the slope of the meanline is determined as a function of known geometry and inflow quantities (as long as $\Delta\underline{v}$ is given) plus the normal component of the average potential induced velocity on the blade surface. Hence it is clear that the shear-interaction term must be explicitly known at points on the blade surface rather than as an axisymmetric component in the propeller plane.

Velocity Component Due to Interaction with Shear Flow ($\Delta\underline{v}$)

The second term of Equation (8) is the integral of the vorticity over the entire fluid volume. The term $\Delta\underline{v}$ can be computed from this integral. The surface integral term satisfies the boundary conditions of the flow field and this additional term $\Delta\underline{v}$ will satisfy the vorticity equation, Equation (11).

The vorticity in the flow field is

$$\omega = \nabla \times \underline{q} = \nabla \times (\underline{q}_o + \underline{v}_o + \underline{v}_p + \Delta\underline{v}) \quad (34)$$

$$= \nabla \times \underline{q}_o + \nabla \times (\Delta\underline{v}) = \underline{\omega}_o + \Delta\underline{\omega} \quad (35)$$

where $\underline{\omega}_o$ is the vorticity in the undisturbed flow and $\Delta\underline{\omega}$ is the increment in vorticity arising from the presence of the propeller. The undisturbed onset flow satisfies the relations:

$$\underline{q}_o(\underline{r}) = \frac{1}{4\pi} \iiint_V \underline{\omega}_o \times \frac{\underline{r}-\underline{y}}{|\underline{r}-\underline{y}|^3} dV_y \quad (36)$$

$$+ \frac{1}{4\pi} \oiint_{S_\infty} \left((\underline{n}\cdot\underline{q}_o)\frac{\underline{r}-\underline{s}}{|\underline{r}-\underline{s}|^3} + (\underline{n}\times\underline{q}_o)\times\frac{\underline{r}-\underline{s}}{|\underline{r}-\underline{s}|^3}\right) d\sigma_s$$

and (from Equation (11))

$$\underline{q}_o \cdot \nabla(\underline{\omega}_o + 2\underline{\Omega}) = (\underline{\omega}_o + 2\underline{\Omega}) \cdot \nabla \underline{q}_o \quad (37)$$

For the flow field when the propeller is present, both $\underline{v}_o$ and $\underline{v}_p$ are associated with the surface integral of

Equation (8) and the components $\underline{q}_o$ and $\Delta\underline{v}$ are due to the volume integral (and an integral over a far distant surface):

$$\underline{q}_o+\Delta\underline{v} = \frac{1}{4\pi}\iiint_V (\underline{\omega}_o+\Delta\underline{\omega})\times\frac{\underline{r}-\underline{y}}{|\underline{r}-\underline{y}|^3}dV_y \qquad (38)$$

$$+\frac{1}{4\pi}\iint_{S_\infty}\left((\underline{n}\cdot\underline{q}_o)\frac{\underline{r}-\underline{s}}{|\underline{r}-\underline{s}|^3}+(\underline{n}\times\underline{q}_o)\times\frac{\underline{r}-\underline{s}}{|\underline{r}-\underline{s}|^3}\right)d\sigma_s$$

and hence, since $\underline{q}_o$ is determined by Equation (36):

$$\Delta\underline{v}(\underline{r}) = \frac{1}{4\pi}\iiint_V \Delta\underline{\omega}\times\frac{\underline{r}-\underline{y}}{|\underline{r}-\underline{y}|^3}dV_y \qquad (39)$$

With the propeller present, the equation governing the vorticity (Equation 11) becomes:

$$(\underline{q}_o+\underline{v}_o+\underline{v}_p+\Delta\underline{v})\cdot\nabla(\underline{\omega}_o+\Delta\underline{\omega}) =$$

$$(\underline{\omega}_o+\Delta\underline{\omega}+2\underline{\Omega})\cdot\nabla(\underline{q}_o+\underline{v}_o+\underline{v}_p+\Delta\underline{v})$$

If Equation (37) were subtracted from this expression, one obtains

$$\underline{q}_o\cdot\nabla(\Delta\underline{\omega}) + (\underline{v}_o+\underline{v}_p+\Delta\underline{v})\cdot\nabla(\underline{\omega}_o+\Delta\underline{\omega})$$

$$= \Delta\underline{\omega}\cdot\nabla(\underline{q}_o+\underline{v}_o+\underline{v}_p+\Delta\underline{v})$$

$$+ (\underline{\omega}_o+2\underline{\Omega})\cdot\nabla(\underline{v}_o+\underline{v}_p+\Delta\underline{v}) \qquad (40)$$

To first order in the velocity terms, this expression becomes[3]

$$(\underline{q}_o+U_{T_o}\underline{e}_\theta)\cdot\nabla(\Delta\underline{\omega}) + \underline{v}\cdot\nabla\underline{\omega}_o$$

$$= \Delta\underline{\omega}\cdot\nabla(\underline{q}_o+U_{T_o}\underline{e}_\theta) + (\underline{\omega}_o+2\underline{\Omega})\cdot\nabla\underline{v} \qquad (41)$$

where $\underline{v} = \underline{v}_p + \Delta\underline{v} + \underline{v}_o - U_{T_o}\underline{e}_\theta$ (42)

This equation can be further simplified by recalling the assumption that the radial velocity component in the onset flow is a small term as are the axial variations of $\underline{q}_o$. Now the vorticity in the onset flow is

$$\underline{\omega}_o = \nabla\times\underline{q}_o = \left(-\frac{\partial V_x}{\partial r}+\frac{\partial V_R}{\partial x}\right)\underline{e}_\theta + 2\Omega\underline{i}$$

and thus to lowest order,

$$\underline{\omega}_o = -\frac{\partial V_x}{\partial r}\underline{e}_\theta + 2\underline{\Omega} \qquad (43)$$

In cylindrical polar coordinates with $\underline{v} = v_x\underline{i} + v_r\underline{e}_r + v_\theta\underline{e}_\theta$ and $\Delta\underline{\omega} = \Delta\omega_x\underline{i} + \Delta\omega_r\underline{e}_r + \Delta\omega_\theta\underline{e}_\theta$, Equation (41) has the three first-order terms:

$$V_x\frac{\partial\Delta\omega_x}{\partial x} + \left(\Omega+\frac{U_{T_o}}{r}\right)\frac{\partial\Delta\omega_x}{\partial\theta}$$

$$= \frac{1}{r}\left(-\frac{\partial V_x}{\partial r}\right)\left(\frac{\partial v_x}{\partial\theta} - r\,\Delta\omega_r\right)$$

$$V_x\frac{\partial\Delta\omega_r}{\partial x} + \left(\Omega+\frac{U_{T_o}}{r}\right)\frac{\partial\Delta\omega_r}{\partial\theta}$$

$$= \frac{1}{r}\left(-\frac{\partial V_x}{\partial r}\right)\frac{\partial v_r}{\partial\theta} \qquad (44)$$

$$V_x\frac{\partial\Delta\omega_\theta}{\partial x} + \left(\Omega+\frac{U_{T_o}}{r}\right)\frac{\partial\Delta\omega_\theta}{\partial\theta}$$

$$= \frac{1}{r}\left(-\frac{\partial V_x}{\partial r}\right)\left(\frac{\partial v_\theta}{\partial\theta} + v_r\right) + \Delta\omega_x\frac{\partial U_{T_o}}{\partial x}$$

$$+ \Delta\omega_r\, r\frac{\partial(U_{T_o}/r)}{\partial r} + v_r\frac{\partial^2 V_x}{\partial r^2}$$

These are the equations that govern the rate of change of $\Delta\underline{\omega}$ in space and they can be used to solve for the polar coordinates of $\Delta\underline{\omega}$. Since $\underline{v}$ contains both $\Delta\underline{v}$ and $\underline{v}_p$, and since $\underline{v}_p$ depends on $\Delta\underline{v}$, they are coupled. The boundary condition on $\Delta\underline{\omega}$ is that it tends to zero far upstream and far out from the propeller axis. The linear left-hand side is approximately the rate of change along a streamline and hence a solution procedure that involves integration along the nearly helical lines may be desirable.

Once the components of $\Delta\underline{\omega}$ are determined, the velocity $\Delta\underline{v}$ can be computed (from equation (39)):

$$\Delta\underline{v} = \Delta v_x\,\underline{i} + \Delta v_r\underline{e}_r + \Delta v_\theta\,\underline{e}_\theta \qquad (45)$$

If the position vectors and differential volume element were expressed in cylindrical polar coordinates, one has

$$\underline{y} = y\,\underline{i} + \rho\underline{e}_\rho(\phi)$$

$$\underline{r} = x\,\underline{i} + r\,\underline{e}_r(\theta) \qquad (46)$$

$$dV_y = \rho\,d\rho\,d\phi\,dy$$

$$|\underline{y}-\underline{r}|^2 = |y-x|^2 + \rho^2+r^2 - 2r\rho\cos(\phi-\theta)$$

[3] The zeroth order term arising from the preswirl component in $\underline{v}_o$ is identically satisfied:

$$U_{T_o}\underline{e}_\theta\cdot\nabla\underline{\omega}_o = (\underline{\omega}_o+2\underline{\Omega})\cdot\nabla(U_{T_o}\underline{e}_\theta)$$

$$= \frac{1}{r}U_{T_o}(x,r)\frac{\partial V_x}{\partial r}\underline{e}_r$$

since $d\underline{e}_\theta/d\theta = -\underline{e}_r$.

and the velocity components become

$$\Delta v_x = \Delta \underline{v}\cdot\underline{i} = -\frac{1}{4\pi}\iiint \frac{\Delta\omega_\rho r\sin(\phi-\theta)+\Delta\omega_\phi(r\cos(\phi-\theta)-\rho)}{|\underline{y}-\underline{r}|^3}\,\rho d\rho d\phi dy$$

$$\Delta v_r = \Delta \underline{v}\cdot\underline{e}_r = -\frac{1}{4\pi}\iiint \frac{-\Delta\omega_y\rho\sin(\phi-\theta)+[\Delta\omega_\rho\sin(\phi-\theta)+\Delta\omega_\phi\cos(\phi-\theta)](y-x)}{|\underline{y}-\underline{r}|^3}\,\rho d\rho d\phi dy \quad (47)$$

$$\Delta v_\theta = \Delta \underline{v}\cdot\underline{e}_\theta = -\frac{1}{4\pi}\iiint \frac{\Delta\omega_y(\rho\cos(\phi-\theta)-r)+[-\Delta\omega_\rho\cos(\phi-\theta)+\Delta\omega_\phi\sin(\phi-\theta)](y-x)}{|\underline{y}-\underline{r}|^3}\,\rho d\rho d\phi dy$$

Thus, once $\Delta\underline{\omega}$ is known, Equation (47) can be employed to compute the velocity $\Delta\underline{v}$. Since the equations for $\Delta\underline{v}$ and $\Delta\underline{\omega}$ are coupled and they are small, an iteration scheme, with some approximation, is a possibility.

In the literature, several procedures have been proposed for solving a problem that has $\Delta\underline{v} = \Delta v_x(r)\,\underline{i}$ only. If this were so, $\Delta\underline{\omega} = -\frac{\partial \Delta v_x}{\partial r}\underline{e}_\theta$ and the right hand side of Equation (44) governing $\Delta\omega_\theta$ will in general not be satisfied. The interaction velocity will be consistent only with the volume integral of Equation (8) since velocity will be given by

$$\Delta\underline{v} = \Delta v_x\underline{i} = -\frac{1}{4\pi}\iiint \frac{\Delta\omega_\phi(r\cos(\phi-\theta)-\rho)}{|\underline{y}-\underline{r}|^3}\,\underline{i}\;\rho d\rho d\phi dy \quad (48)$$

As yet no solution of Equations (44) and (47) has been attempted. Significant numerical difficulties are anticipated.

Pressure and Loads

The pressure along a streamline is given by Equation (13). If at some point along the streamline the pressure and velocity were known, then the value of the general Bernoulli head would also be known. Assume that $\underline{q}_o(\underline{r})$ is predominately inviscid, and the pressure is known at some point far upstream. Then the non-dimensional Bernoulli head can be explicitly computed at this point:

$$\frac{H(\zeta_\psi)}{V^2/2} = \frac{p^*(x_R^*)}{\rho V^2/2} + \left[\frac{\underline{q}_o(x_R^*)\cdot\underline{q}_o(x_R^*)}{V^2} - \left(\frac{\pi x_R^{*2}}{J_V}\right)\right]$$

$$= \frac{p^*(x_R^*)}{\rho V^2/2} + \left[(1-w_x(x_R^*))^2 + w_R^2(x_R^*)\right] \quad (49)$$

where x_R^* is the non-dimensional radius of the streamline ζ_ψ far upstream. The value of $H(\zeta_\psi)$ is constant along the streamline, ζ_ψ, and thus along the streamline a pressure coefficient is

$$c_p^* \equiv \frac{p-p^*}{\rho V^2/2} = \left[(1-w_x(x_R^*))^2+w_R^2(x_R^*)\right] - \left[\frac{\underline{q}\cdot\underline{q}}{V^2} - \left(\frac{\pi x_R}{J_V}\right)^2\right]_{\zeta_\psi} \quad (50)$$

This equation gives the pressure coefficient at a point in the flow field that lies on the streamline ζ_ψ. However, this streamline is not a constant radius line. As we shall determine in the following paragraphs, the first-order blade loads will depend upon the pressure difference across the blade section.

To define the pressure coefficient at an arbitrary point in space or on the blade, an appropriate reference is the far field constant pressure, speed and head:

$$\frac{H_o}{V^2/2} = \frac{p_o}{\rho V^2/2} + 1 \quad (51)$$

The pressure coefficient is:

$$c_p \equiv \frac{p-p_o}{(\rho V^2/2)} = \frac{H-H_o}{V^2/2} + \left\{1+\left(\frac{\pi x_R}{J_V}\right)^2\right\} - \frac{\underline{q}\cdot\underline{q}}{V^2} \quad (52)$$

The first-order pressure difference across the blade is:

$$\Delta c_p = \frac{p^- - p^+}{\rho V^2/2}$$

$$= 2\sqrt{(1-w_x)^2 + \left(\frac{\pi x_R}{J_V} + \frac{\bar{U}_T}{V}\right)^2}\ \frac{\gamma}{V} + 2\frac{H^- - H^+}{V^2}$$

$$= 2\pi\sqrt{(1-w_x)^2 + \left(\frac{\pi x_R}{J_V} + \frac{\bar{U}_T}{V}\right)^2}\ G(x_R)\ \frac{\gamma^*(x_c)}{c/D}$$

$$+ 2\frac{H^- - H^+}{V^2} \qquad (53)$$

The first term of this expression depends on only the onset flow field and assigned load and geometry variables. It is independent of rake, skew or pitch variations. The difference in Bernoilli head is dependent on the total solution for streamline trajectories (see Appendix of (9)).

The Bernoulli head difference across the blade must be determined from a series of steps. First, the streamline that convects the known Bernoulli head at the upstream reference position to the blade leading edge must be defined. The constant value of head along these line can be interpolated to find a variable head along the chordine on each side of the blade. This problem is illustrated schematically in Figure 2.

Once the distribution on the blade surface is known, the thrust and torque in inviscid flow may be calculated:

$$T_i = Z \int_{x_h}^{1} dx_R \int_0^1 (p^+\underline{N}^+ + p^-\underline{N}^-)\cdot\underline{i}\ dx_c \qquad (54)$$

$$Q_i = -Z \int_{x_h}^{1} r\ dx_R \int_0^1 (p^+\underline{N}^+ + p^-\underline{N}^-)\cdot\underline{e}_\theta\ dx_c$$

or in terms of a thrust and power coefficient:

$$C_{T_i} = \frac{T_i}{\rho V^2 \pi D^2/8}$$

$$= \frac{2Z}{\pi}\int_{x_h}^{1} dx_R \int_0^1 dx_c\left[\Delta c_p\left(\frac{c}{D}\cos\phi_p\right.\right.$$

$$\left. + \frac{\partial E_c/D}{\partial x_c}\sin\phi_p\right) - \bar{c}_p \frac{\partial E_T/D}{\partial x_c}\sin\phi_p\Big] \qquad (55)$$

$$C_{P_i} = \frac{2\pi n Q_i}{\rho V^3 \pi D^2/8}$$

$$= \frac{2Z}{J_V}\int_{x_h}^{1} x_R dx_R \int_0^1 dx_c\left[\Delta c_p\left(\frac{c}{D}\sin\phi_p\right.\right.$$

$$\left. - \frac{\partial E_c/D}{\partial x_c}\cos\phi_p\right) + \bar{c}_p \frac{\partial E_T/D}{\partial x_c}\cos\phi_p\Big]$$

where

$$\Delta c_p = \frac{p^- - p^+}{\rho V^2/2}$$

$$\bar{c}_p = \frac{p^- + p^+}{\rho V^2/2}$$

To first order, the thrust and power coefficients involve only the pressure difference across the blade at a constant radius section:

$$C_{T_i} = \frac{2Z}{\pi}\int_{x_h}^{1} dx_R \frac{c}{D}\cos\phi_p \int_0^1 \Delta c_p\ dx_c$$

$$= 4Z\int_{x_h}^{1}\sqrt{(1-w_x)^2+\left(\frac{\pi x_R}{J_V}+\frac{\bar{U}_T}{V}\right)^2}\ G(x_R)\cos\phi_p dx_R$$

$$+ \frac{4Z}{\pi}\int_{x_h}^{1} dx_R \frac{c}{D}\cos\phi_p \int_0^1 \frac{H^- - H^+}{V^2}\ dx_c \qquad (56)$$

$$C_{P_i} = \frac{2Z}{J_V}\int_{x_h}^{1} dx_R\ x_R \frac{c}{D}\sin\phi_p \int_0^1 \Delta c_p\ dx_c$$

$$= \frac{4\pi Z}{J_V}\int_{x_h}^{1} x_R\sqrt{(1-w_x)^2+\left(\frac{\pi x_R}{J_V}+\frac{\bar{U}_T}{V}\right)^2}\cdot$$

$$\sin\phi_p G(x_R) dx_R$$

$$+ \frac{4Z}{J_V}\int_{x_h}^{1} x_R \frac{c}{D}\sin\phi_p dx_R \int_0^1 \frac{H^- - H^+}{V^2}\ dx_c \qquad (57)$$

These performance coefficients are dependent on the assigned circulation distribution and difference in Bernoulli head along the blade section. The difference in Bernoulli head is dependent on the streamline positions along the blade surface and hence is dependent on the overall

solution. For those flow problems with a potential onset flow (e.g., uniform onset flow), the Bernoulli head is constant everywhere and the second terms of both Equation (56) and (57) will vanish.

A viscous blade section drag coefficient is added to this inviscid expression to produce an equation that can be employed to produce a better representation of the loads. These corrections are given by Equations (82) and (83) of (9) with an additional correction for possible preswirl.

Position Vector of Filaments in Shed Vortex Sheet

The boundary conditions on the shed vortex sheet can be used to determine the trajectory of the constant strength vortex elements comprising the sheet. On the shed-vortex sheet two conditions apply:

1. the pressure is continuous across the sheet, $p+ = p-$, and
2. the normal component of velocity is zero, $(\underline{q}\cdot\underline{n})^{\pm} = 0$.

These two conditions are sufficient to produce a definition of the trajectories of the lines of constant vorticity in the shed-vortex sheet. These lines are of interest since integration can be performed along them independent of the strength of the vorticity. Let the position vector of the curve of constant vortex strength be expressed in a helical coordinate system. One representation of these curves is that they emerge from the blade at the trailing edge at a radius $r_o = x_{Ro} D/2$ and trail aft at a radius $r_o + \Delta r = (x_{Ro} + \Delta x_{Ro})D/2$ as a function of $\xi_1 - c/R = \eta D$, the distance measured along a helical filament at a constant radius x_{Ro} and pitch angle $\beta_w(x_{Ro})$. The nondimensional coordinate of a point along the filament is:

$$\frac{\underline{\zeta}_w}{D}(\eta, x_{Ro}) = \frac{x_{TE}(x_{Ro}) + X(\eta, x_{Ro})}{D}\,\underline{i} + (x_{Ro} + \Delta x_{Ro}(\eta, x_{Ro}))/2\ \underline{e}_r(\eta, x_{Ro}) \quad (58)$$

where

$x_{TE}(x_{Ro})$ is the axial coordinate of the trailing edge point at nondimensional radius x_{Ro}

$X(\eta, x_{Ro}) = (\eta \sin\beta_w(x_{Ro}) - f(\eta, x_{Ro}) \cos\beta_w(x_{Ro})) \cdot D$

$\xi_2 = f(\eta, x_{Ro}) \cdot D$, distance on cylinder of radius x_{Ro}, measured normal to the pitch line with a positive component in the upstream direction

$\Delta x_{Ro}(\eta, x_{Ro})$ = change in radius from the value at the trailing edge

$\theta(\eta, x_{Ro}) = \theta_{TE}(x_{Ro}) + \theta_b + 2(\eta \cos\beta_w + f \sin\beta_w)/x_{Ro}$

and $\theta_{TE}(x_{Ro})$ = angular coordinate of trailing edge point at radius x_{Ro}

This representation of the filament specification is illustrated in Figures 3 and 4. A vector tangent to the lines of constant vorticity (not necessarily of unit magnitude) is

$$\underline{T} = D \frac{\partial \underline{\zeta}_w/D}{\partial \eta}$$

$$\underline{T} = D\Big[\Big(1+\frac{\Delta x_{Ro}}{x_{Ro}} \cos\beta_w\Big(\cos\beta_w + \frac{\partial f}{\partial \eta}\sin\beta_w\Big)\Big)\underline{e}_1 + \Big(\frac{\partial f}{\partial \eta}\frac{\Delta x_{Ro}}{x_{Ro}} - \sin\beta_w\Big(\cos\beta_w + \frac{\partial f}{\partial \eta}\sin\beta_w\Big)\Big)\underline{e}_2 + \frac{1}{2}\frac{\partial \Delta x_{Ro}}{\partial \eta}\underline{e}_r\Big] \quad (59)$$

where the helical unit vectors ($\underline{e}_1, \underline{e}_2, \underline{e}_r$) are defined on and normal to the surface of a cylinder of constant radius x_{Ro}. Similarly a vector (not necessarily of unit magnitude) normal to the surface of the shed vortex sheet defined by the variable η and parameter x_{Ro} is

$$\underline{N}_w^+ = D^2 \frac{\partial \underline{\zeta}_w/D}{\partial \eta} \times \frac{\partial \underline{\zeta}_w/D}{\partial x_{Ro}} \quad (60)$$

where $\underline{N}_w^+$ is constructed to have a positive component in the upstream direction. In several texts (e.g., (10)), it is shown that $\underline{n} d\sigma = \underline{N}_w^+ d\eta\, dx_{Ro}$.

Since the trajectory of the shed vortex sheet filaments will be used in the calculation of the velocities induced by the sheet, it is convenient to look ahead at the form of this equation. From Equation (8), the induced velocity due to the shed vortex sheet will be defined by the second term in the surface integral. This can be expressed as a summation (over the number of blades) of integrals over each individual sheet:

$$\frac{\underline{v}_w(\underline{r})}{V} = \sum_{b=1}^{Z} \int_{x_h}^{1} dx_{Ro} \int_{o}^{\infty} \Big(\frac{\underline{N}_w^+ \times \langle \underline{v}_{pw} \rangle}{2\pi D^2 V}\Big) \times$$

$$\frac{\frac{r}{D} - \frac{\zeta_{wb}}{D}}{\left|\frac{r}{D} - \frac{\zeta_{wb}}{D}\right|^3} d\eta \qquad (61)$$

where $\langle \underline{v}_{pw} \rangle = \frac{1}{2}(\underline{q}_w^+ - \underline{q}_w^-)$, half the velocity jump across the shed vortex sheet

and

$$\eta = \xi_1/D - c/2D$$

Let the expression for the nondimensional vortex strength be

$$\frac{\underline{N}_w^+ \times \langle \underline{v}_{pw} \rangle}{2\pi D^2 V} = \underline{\Lambda}_w(\eta, x_{Ro})$$

$$= \Lambda_w(x_{Ro})\ \underline{T}(\eta, x_{Ro}) \qquad (62)$$

Note: $|\underline{\Lambda}_w| \neq \Lambda_w$ since $\underline{T}$ is not generally a unit vector. The magnitude of $\underline{\Lambda}_w$ is determined by equating the strength of the vorticity in the shed vortex sheet to that leaving the blade at radius x_{Ro}.

Since $\underline{T}$ is directed along the trajectory of the vortex filament,

$$\underline{T} \times \underline{\Lambda}_w = 0 \qquad (63)$$

$$= \underline{T} \times \left(\frac{\underline{N}_w^+}{2\pi D^2} \times \frac{\langle \underline{v}_{pw} \rangle}{V}\right)$$

$$= \left(\underline{T} \cdot \frac{\langle \underline{v}_{pw} \rangle}{V}\right)\frac{\underline{N}_w^+}{2\pi D^2} - \left(\underline{T} \cdot \frac{\underline{N}_w^+}{2\pi D^2}\right)\frac{\langle \underline{v}_{pw} \rangle}{V}$$

$$= \left(\underline{T} \cdot \frac{\langle \underline{v}_{pw} \rangle}{V}\right)\frac{\underline{N}_w}{2\pi D^2}$$

Since, in general, neither $\underline{T}$ nor $\langle \underline{v}_{pw} \rangle$ is zero, the vectors $\underline{T}$ and $\langle \underline{v}_{pw} \rangle$ must be perpendicular:

$$\underline{T} \cdot \langle \underline{v}_{pw} \rangle = 0 \qquad (64)$$

From the kinematic boundary condition, $\underline{q} \cdot \underline{n} = 0$, there results:

$$\underline{N}_w^+ \cdot \langle \underline{v}_{pw} \rangle = 0 \qquad (65)$$

Hence in the orthogonal vector system $(\underline{N}_w^+, \underline{T}, \underline{N}_w^+ \times \underline{T})$, the difference in the velocity vector across the shed vortex sheet is

$$\langle \underline{q} \rangle = \langle q_1 \rangle \underline{N}_w^+ + \langle q_2 \rangle \underline{T} + \langle q_3 \rangle \underline{N}_w^+ \times \underline{T}.$$

for which the Equations (64 and 65) have shown that there is a component in only the $\underline{N}_w^+ \times \underline{T}$ direction:

$$\frac{\langle \underline{v}_{pw} \rangle}{V} = \frac{\langle \underline{q} \rangle}{V} = \frac{\langle q_3 \rangle}{V}\ \underline{N}_w^+ \times \underline{T} \qquad (66)$$

and from Equation (62)

$$\Lambda_w(x_{Ro})\underline{T}(\eta, x_{Ro}) = \frac{\underline{N}_w^+}{2\pi D^2} \times \left(\frac{\langle q_3 \rangle}{V}\ \underline{N}_w^+ \times \underline{T}\right)$$

$$= -\left(\frac{\langle q_3 \rangle}{V}\ \frac{|\underline{N}_w^+|^2}{2\pi D^2}\right)\underline{T} \qquad (67)$$

The component of the velocity difference across the shed vortex sheet in the $\underline{N}_w^+ \times \underline{T}$ direction is thus

$$\frac{\langle q_3 \rangle}{V} = -\left(\frac{\Lambda_w(x_{Ro})\ 2\pi D^2}{|\underline{N}_w^+|^2}\right) \qquad (68)$$

Let the average velocity along the shed vortex sheet be expressed

$$\bar{\underline{q}} = (\underline{q}^+ + \underline{q}^-)/2 \qquad (69)$$

$$= \bar{q}_1\ \underline{N}_w^+ + \bar{q}_2\ \underline{T} + \bar{q}_3\ \underline{N}_w^+ \times \underline{T}$$

(Again note that the individual terms are expressed relative to non-unit vectors). The kinematic boundary condition $\underline{q} \cdot \underline{n} = 0$ leads to the result:

$$\underline{N}_w^+ \cdot \bar{\underline{q}} = 0 \qquad (70)$$

or

$$\bar{q}_1 = 0 \qquad (71)$$

The difference in speed across the shed vortex sheet is

$$(\underline{q}^+)^2 - (\underline{q}^-)^2 = 4\ \bar{\underline{q}} \cdot \langle \underline{q} \rangle$$

$$= -4\ \bar{q}_3\ |\underline{N}_w^+ \times \underline{T}|^2\ \frac{\Lambda_w V\ 2\pi D^2}{|\underline{N}_w^+|^2} \qquad (72)$$

From the dynamic boundary condition (equal pressure) and the general Bernoulli equation (Equation 13), one has

$$(q^+)^2 - 2H^+ = (\underline{q}^-)^2 - 2H^-$$

or

$$(\underline{q}^+)^2 - (\underline{q}^-)^2 = 2(H^+ - H^-) \qquad (73)$$

Hence Equation (72) and Equation (73) produce the result:

$$\frac{\bar{q}_3}{V} = -\frac{(H^+ - H^-)|\underset{+}{N_w}|^2}{4|\underset{+}{N_w}\times\underline{T}|^2\Lambda_w V^2\pi D^2} = -\frac{H^+ - H^-}{4|\underline{T}|^2\Lambda_w V^2\pi D^2} \quad (74)$$

So that the equation governing the lines of constant vortex strength in the shed vortex sheet is

$$\underline{\bar{q}} \times \underline{T} = \bar{q}_3 \,(\underset{+}{N_w}\times\underline{T})\times\underline{T}$$

$$= -\bar{q}_3 \underset{+}{N_w} |\underline{T}|^2$$

$$= \frac{H^+ - H^-}{4\Lambda_w V\pi D^2}\underset{+}{N_w} \quad (75)$$

or

$$(\underline{\bar{q}} + \frac{H^+ - H^-}{4\Lambda_w V\pi D^2}\frac{\partial\zeta_w/D}{\partial x_{Ro}})\times\underline{T} = 0 \quad (76)$$

For an onset flow that can be derived from a potential, the Bernoulli head H is a fixed value in space and the right-hand side of Equation (75) is zero. This case has been previously derived in (13).

Equation (76) is sufficient to define the equations governing Δx_{Ro} and f . However, the expressions are complicated and lengthy. First-order equations can be obtained that are sufficient to illustrate the effect. Without derivation we present the results. The first-order differential equation for Δx_{Ro} is:

$$\frac{1}{2}\frac{\partial\Delta x_{Ro}}{\partial\eta} \approx \frac{q_{or}}{q_{o1}}\frac{\Delta x_{Ro}}{x_{Ro}}\cos^2\beta_w + \frac{q_{Er} + \bar{v}_{pr} + \frac{H^+-H^-}{8\pi\Lambda_w VD}(1+\frac{\partial\Delta x_{Ro}}{\partial x_{Ro}})}{q_{E1} + \bar{v}_{p1}} \quad (77)$$

and for f it is:

$$\frac{\partial f}{\partial\eta} \approx \frac{\Delta x_{Ro}}{x_{Ro}}(\frac{q_{o2}}{q_{o1}}\cos^2\beta_w - \sin\beta_w\cos\beta_w) + \frac{q_{E2} + \bar{v}_{p2} + \frac{H^+ - H^-}{4\pi\Lambda_w VD}\Pi}{q_{E1} + \bar{v}_{p1}} \quad (78)$$

where

$$\Pi = -\frac{\partial x_{TE}}{\partial x_{Ro}}\cos\beta_w - \eta\frac{d\beta_w}{dx_{Ro}} + \frac{\partial f}{\partial x_{Ro}} + \frac{1}{2}(x_{Ro}+\Delta x_{Ro})\sin\beta_w(\frac{d\theta_{TE}}{dx_{Ro}} - \frac{2\eta\cos\beta_w}{x_{Ro}^2}) - \eta\frac{\Delta x_{Ro}\sin^2\beta_w}{x_{Ro}}\frac{d\beta_w}{dx_{Ro}} - f\frac{\sin^2\beta_w}{x_{Ro}} \quad (79)$$

Even these first-order equations are complicated and involve radial gradients of the unknown Δx_{Ro} and f as well as the derivatives along the trajectory.

DISCUSSION

The formulation presented herein defines the interaction of a lifting surface operating in an otherwise known axisymmetric shear flow with the fluid interaction treated as inviscid in nature. The interaction aspects are in addition to those presently available from three-dimensional lifting-surface codes based on potential flow. As described, there are three separate, but coupled, aspects of the shear interaction:

(1) the induced shear-interaction velocity component.
(2) the loads and pressure field developed on the propeller, and
(3) the vortex sheet location.

The formulation for the shear-interaction velocity component, as obtained from the volume integral of Equation (8), is a three-dimensional field value, as are all perturbation velocity component arising from the presence of the propulsor in the otherwise known nominal velocity field. This three-dimensional dependence on the value of the shear-interaction term is also suggested by the experimental data of Jessup, et al, (15). In their tests, noticable differences were found between the circumferential variations of the induced velocity computed with the three-dimensional model of the potential flow and axisymmetric shear-interaction term. It is also clear (from the boundary condition, Equation 33) that an essential piece of information about this velocity component is its value at points on the blade surface: if these were known, then only a potential-flow model is needed to represent the rest of the blade for design and performance analysis. For compound propulsors, this velocity increment must be determined on all surfaces of the unit. For operation in a non-uniform onset flow, the shear-

interaction term will be unsteady at points on the blade and hence a suitable average value must be defined. Note that there are two three-dimensional effects of the propeller-wake interaction: the propeller and wake. Previous efforts have not addressed the three-dimensional aspects of the propeller.

The formulation presented for this component may not be a desirable one for numerical analysis since multiple integrations over space are required to compute values. An alternative approach based on the finite difference or finite element approach may be more direct. We are currently exploring these alternatives.

To determine the possible magnitude of the second aspect defined above, the effect of the radially variable Bernoulli head on the loads and pressure, representative calculations were performed. The Bernoulli head variation at the leading edge of the blade was taken as that given by the data of Huang, et al, (16) at the stern of an axisymmetric body. From the measured non-dimensional velocity components and static pressure coefficient, the variable Bernoulli head can be expressed:

$$\frac{H - H_o}{V^2/2} = c_p + \left[(1-w_x)^2 + w_R^2 - 1\right] \qquad (80)$$

The individual terms are greatest near the hull and tend to zero far from the body. The lift-hand side term is generally negative, with a value near -0.75 at the hub, and the value of C_p is about +0.15 at the hub. These values are assumed representative at the leading edge of the blade also. The radial distribution of H/H_o from (16) is shown in Figure 5. A blade shape similar to NSRDC propeller 4498 was designed (see 2, 9) to operate in the wake measured by Huang (16). The streamlines were computed on each side of the blade (see 9) and the constant Bernoulli head along each of these lines interpolated to define values along the constant-radius blade section. Since H increases with distance from the hub, in the tip region H will increase on the suction side along the chordline from the leading-edge to trailing edge and decrease on the pressure side. In the hub region the opposite trend will occur. The difference in the Bernoulli head along three radii (x_R = 0.254, 0.669, and 0.946) are shown in Figure 5. As can be seen, there are different signs in the root and tip region. The component of loads due to the H difference (Equations 56 and 57) were computed based on these data. The value of $C_T = T/(\pi\rho V^2 D^2/8)$ was reduced by 0.007 and $C_P = P_D/(\pi\rho V^3 D^2/8)$ was reduced by 0.003. These reductions are negligibly small compared to the design values. (Based on the effective average speed, the design C_{Th} is 0.69). Hence there is little reason to compute this component of the loads for similar cases. However, the (linear) pressure distribution along the blade-section can also be computed (from Equation 52). Pressure distributions for the same three radii are shown in Figure 6. The pressure is increased on both sides of the blade relative to consideration of the constant H case. This effect is primarily a result of the drop in head from the reference value H_o to that at the blade section since only minor variation along the blade occurs. Hence there may be some importance of this term for cavitation predictions but most other hydrodynamic consequences are a result of pressure differences and for that only minor effects are found.

The third aspect defined for the interaction is the effect of the variable Bernoulli head on the position of the vortex sheet filaments. Some calculated results (e.g., 9, 14, 17) indicate a significant (but small) effect of vortex-sheet geometry on propeller design and analysis. Generally the dependence on the f variation is more than the Δx_{Ro} variation. Hence it is appropriate to quantify the effects of head on the filament orientation. The complicated equations governing the sheet are considerably simplified at the trailing edge starting point and are sufficient to describe the change in filament orientation as it leaves the blade (see Equations 77 and 78).

The two angles δ_1 and δ_2 shown in Figure 4 are the initial inclination of the filaments. These angles are given by the following equations:

$$\delta_1 = \tan^{-1}\left[-\frac{\partial(R\Delta x_{Ro})}{\partial x}\right]_{\eta=0}$$

$$= \tan^{-1}\left[-2\frac{\partial \Delta x_{Ro}}{\partial \eta}/(\sin\beta_w - \frac{\partial f}{\partial \eta}\cos\beta_w)\right]_{\eta=0} \qquad (81)$$

$$\delta_2 = \tan^{-1}\left[-\frac{\partial f}{\partial \eta}\right]_{\eta=0} \qquad (82)$$

With the average propeller-induced velocity components expressed in helical coordinates:

$$\bar{v}_p = \bar{U}_1 \underline{e}_1 + \bar{U}_2 \underline{e}_2 + \bar{U}_R \underline{e}_r \qquad (83)$$

and the resultant onset speed in uniform flow:

$$\frac{\underline{q}_E}{V} = \underline{q}_o = V\sqrt{1+\left(\frac{\pi x_{Ro}}{J_V}\right)^2}\,[\cos(\beta_w-\beta)\underline{e}_1 + \sin(\beta_w-\beta)\underline{e}_2] \qquad (84)$$

and for the case $\beta_w \approx \beta$, the first-order components of δ_1 and δ_2 are

$$\delta_1 = \tan^{-1}\left[-\frac{1}{\left(\sin\beta_w - \frac{\partial f}{\partial \eta}\cos\beta_w\right)} \frac{\frac{\bar{U}_R}{V} + \frac{\delta}{2}}{\sqrt{1+\left(\frac{\pi x_{Ro}}{J_V}\right)^2} + \frac{\bar{U}_1}{V}} \right]_{\eta=0} \qquad (85)$$

$$\delta_2 = \tan^{-1}\left[\sin(\beta_w-\beta)\sqrt{1+\left(\frac{\pi x_{Ro}}{J_V}\right)^2} + \frac{\bar{U}_2}{V} + \delta\Pi \right]_{\eta=0} \qquad (86)$$

where $\delta = (H^+-H^-)/(4\pi\Lambda_w V^2 D)$ and Π is given in Equation (79).

Sample calculations are presented for a redesign of NSRDC propeller 4498 operating in uniform flow so that some of the computed data can be compared with the measurements of Min (18,19) for the tip-vortex trajectory. The effect of head difference, as defined in Figure 5, is added to these uniform-flow results to access the impact of the new terms.

Table 1 summarizes the calculations for three radii (x_R = 0.254, 0.669, and 0.946). The various induced velocity components at the trailing-edge were taken from reference (9) and the Bernoulli head differences at the trailing edge were taken from Figure 5. For comparison, induced velocities at the lifting line and the experimental data from Min (18,19) are also shown (these data were selected from the detailed plots given in (18) for the unskewed propeller 4381 since the geometry for 4498 was not designed with consideration of zero total rake, (20)) There are significant differences between the induced velocities from the lifting line model (at the bound vortex line) and the lifting-surface model at the trailing edge (as expected) and the computed filament orientation leaving the trailing edge, $\beta_w + \delta_2$, is about the same as if twice the induced velocities computed at the lifting line were acting. There are large differences between the radial-contraction angle δ_1 measured by Min (18) at the tip and our calculated value near the tip. Although rather large gradients are expected in these angles in the tip region, this difference is quite large. Calculations by Koumbis (21) are more in line with our computations than with the experimental data. The experimental data were obtained in a closed jet test section and may be influenced by the confined flow but it is equally possible that the calculations are incomplete. The equations are based on linearized, inviscid theory and data for the design case were employed in the computations. The actual geometry of the blades may not be such as to produce the local design loads in the tip region (e.g., the last 5% of the blade geometry is extrapolated from design computations). Hence more computational and experimental data of the type presented must be obtained to determine if better agreement were possible.

The second half of the table indicates a possibly significant effect of the head difference in the filament orientation, with more influence on δ_1 and δ_2. The vortex sheet specification is expected to generally be unimportant for conventional propellers but may be signifcant for multiple blade-row propellers (17). The present effect will be greater further downstream, since the head difference will be greater and the filament orientation more influenced. Hence a significant effect may occur for the interaction of compound propulsors.

CONCLUSIONS

Three coupled but distinct effects of a propeller operating in an axisymmetric sheared onset flow field are identified:

A. a three dimensional interaction component that is the essential quantity to be computed to define the effective wake,
B. a contribution to loads and pressure distribution from the variable Bernoulli head on the blades, and
C. a modification to the position of shed vortex sheet filaments due to the variable Bernoulli head.

The first of these effects has been addressed in the literature in an approximate way (i.e., the circumferential average limited to the axial velocity component), but neither the three-dimensional aspects nor the modification of an axisymmetric tangential or radial velocity component have been

determined. In addition, it is shown that the essential value to use with a potential-flow representation is the value on the blade. Analysis procedures for this component must be carefully selected to produce an efficient computational procedure.

Representation calculations for the second aspect have shown it to be of significance for the pressure distribution along the blade span but that the overall loads are nearly the same as when the difference is set to zero.

The position vector of the shed vortex-sheet filaments is too complex an undertaking to explore all along the path. Representative calculations of the initial orientation as the filaments leave the blade show a possibly significant effect on the orientation.

ACKNOWLEDGMENTS

The work reported herein was sponsored by the U.S. Navy, Office of Naval Research, Special Focus Program in Ship Hydrodynamics, under contract N00014-85-K-0018, NR-655-004, and Accelerated Research Program in Hull/Propeller Interaction, under contract N00014-86-K-0058, administered by Dr. C.-M. Lee. Some of the information presented is taken from unpublished work performed with the U.S. Navy, David Taylor Naval Ship R&D Center. Able assistance in the various aspects of the analysis was provided by C. Tseng (DTNSRDC), M.-H. Kim (U of M), and R. Korpus (U of M).

REFERENCES

1. Cox, G.G. and Morgan, W.B., "The Use of Theory in Propeller Design," Marine Technology, Vol. 9, No.4, October 1972.

2. Kerwin, J.E., "Marine Propellers," Annual Review of Fluid Mechanics, 1986.

3. Dyne, G., et al, "Report of Propeller Committee," Proceedings 17th ITTC, Goteborg, 1984.

4. Nelson, D.M., "Development and Application of a Lifting-Surface Design Method for Counterrotating Propellers," Naval Undersea Center, NUC TP 326, November, 1972. Also "A Computer Program Package for Designing Wake Adapted Counterrotating Propellers: A User's Manual," Naval Undersea Center, NUC TP 494, December, 1975.

5. Huang, T.T. and Groves, N., "Effective Wake: Theory and Experiment," 13th Symposium on Naval Hydrodynamics, Tokyo, 1980.

6. Pelletier, D.H. and Schetz, J.S., "A Navier-Stokes Calculation of 3-D, Turbulent Flow Near a Propeller in a Shear Flow," AIAA 23rd Aerospace Sciences Meeting, AIAA-85-0365, Reno, January, 1985.

7. Stern, F., et al, "The Interaction Between Propeller and Ship-Stern Flow," Osaka Int. Coll. Ship Visc. Flow, Osaka, October, 1985.

8. van Gent, W., "A Model of Propeller-Ship Wake Interaction," Proceedings of the International Symposium on Propeller and Cavitation, Wuxi, 1986.

9. Brockett, T., "Lifting-Surface Hydrodynamics for Design of Rotating Blades," Propellers '81 Symposium, SNAME, May 1981; also DTNSRDC Report 81/081.

10. Phillips, H., Vector Analysis, Wiley, London, 1933.

11. Brockett, T., "Propeller Lifting-Surface Computations; Part I: Thickness Effects," DRTNSRDC/SPD-0872-01, September 1981; also Defense Research Establishment Atlantic, Technical Memorandum 80/I, November 1980.

12. Batchelor, G.K., An Introduction to Fluid Dynamics, Cambridge, London, 1967.

13. Brockett, T., "Propeller Perturbation Problems," NSRDC Report 3880, October 1972.

14. Greeley, D.S. and J.E. Kerwin, "Numerical Methods for Propeller Design and Analysis in Steady Flow," SNAME Transactions, Vol. 90, 1982.

15. Jessup, S.D., et al, "Local Propeller Blade Flows in Uniform and Sheared Onset Flows using LDV Techniques," 15th Symposium on Naval Hydrodynamics, Hamburg, 1984; also U.S. Navy DTNSRDC-85/007, February 1985.

16. Huang, T.T., et al, "Stern Boundary-Layer Flow on Axisymmetric Bodies," 12th Symposium on Naval Hydrodynamics, Washington, June 1978.

17. Brockett, T., and Korpus, R., "Parametric Evaluation of the Lifting-Line Model for Conventional and Preswirl Propulsors," Proceedings International Symposium on Propeller and Cavitation, Wuxi, 1986.

18. Min, K.-S., "Laser Measurements of Field Point Velocities for Four NSRDC Propellers in the MIT Variable Pressure Water Tunnel," MIT Dept. of Ocean Engineering, Report No. 77-17, July 1977.

19. Min, K.-S., "Numerical and Experimental Methods for the Prediction of Field Point Velocities Around Propeller Blades," MIT Dept. of Ocean Engineering, Report No. 78-12, June 1978.

20. Nelka, J.J., "Experimental Evaluation of a Series of Skewed Propellers with Forward Rake," NSRDC Report 4113, July 1974.

21. Koumbis, A., "On the Effect of the Slipstream on the Mathematical Representation of Open Propellers," RINA, 1983.

TABLE 1

Induced Velocities and Vortex Filament Orientation
Near Trailing Edge for Redesign of Propeller 4498

INDUCED VELOCITIES

x_R	β_w degrees	β	$\sqrt{1+(\frac{\pi x_R^2}{J_v})}$	$\bar{U}_1/V$ L.S.	$\bar{U}_1/V$ L.L.	$\bar{U}_2/V$ L.S.	$\bar{U}_2/V$ L.L.	$\bar{U}_R/V$ L.S.	$\bar{U}_R/V$ L.L.
0.254	56.4	48.1	1.344	0.036	0.188	-0.417	-0.046	0.080	N/A
0.669	29.3	22.9	2.567	0.020	0.236	-0.510	-0.161	0.026	N/A
0.946	18.7	16.5	3.489	-0.029	0.073	-0.232	-0.087	-0.072	N/A

UNIFORM FLOW, CONSTANT HEAD

Min data (18) for 4381

x_R	$\delta_1=\tan^{-1}[-2\frac{\partial \Delta x_{Ro}}{\partial (x/D)}]$ deg.	$\delta_2=\tan^{-1}[-\frac{\partial f}{\partial \eta}]$ deg.	$\beta_w + \delta_2$ deg.	pitch angle deg.	δ_1 deg.
0.254	-3.6	9.2	65.6	-	-
0.669	-1.0	5.0	34.3	-	-
0.946	3.4	1.6	20.3	-	-
1.0	-	-		16.3	37

UNIFORM FLOW PLUS VARIABLE HEAD

x_R	$\frac{H^- - H^+}{V^2/2}$	$\delta_1=\tan^{-1}[-2\frac{\partial \Delta x_{Ro}}{\partial (x/D)}]$ deg.	$\delta_2=\tan^{-1}[-\frac{\partial f}{\partial \eta}]$ deg.
0.254	0.111	-6.5	8.8
0.669	-0.039	-3.7	4.3
0.946	-0.011	3.1	1.6

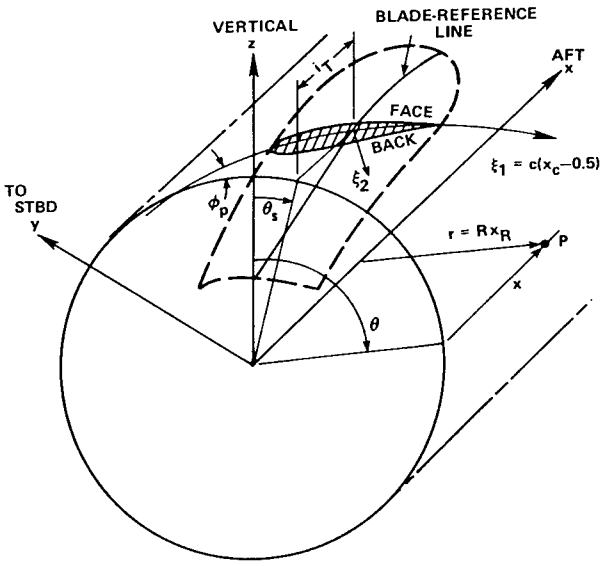


Figure 1 Lifting-Surface Geometry

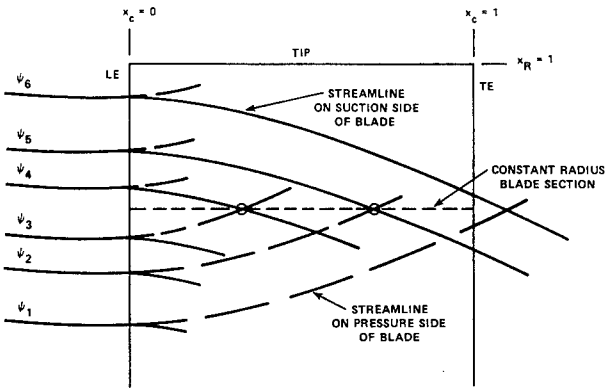


Figure 2 Schematic of Streamline in (x_c, x_R) Coordinates

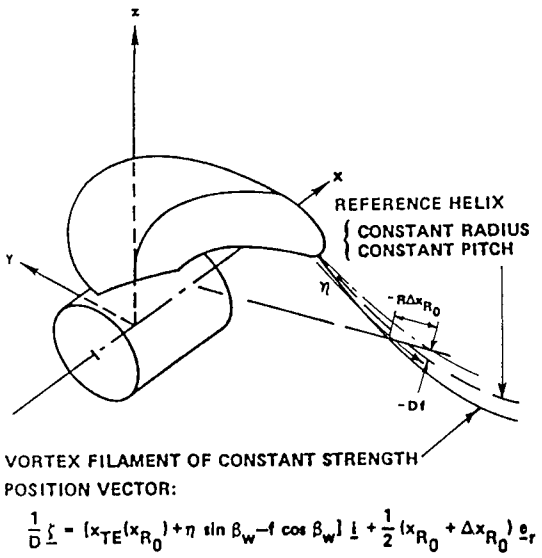


Figure 3 Schematic of Constant-Strength Filaments in Shed-Vortex Sheet

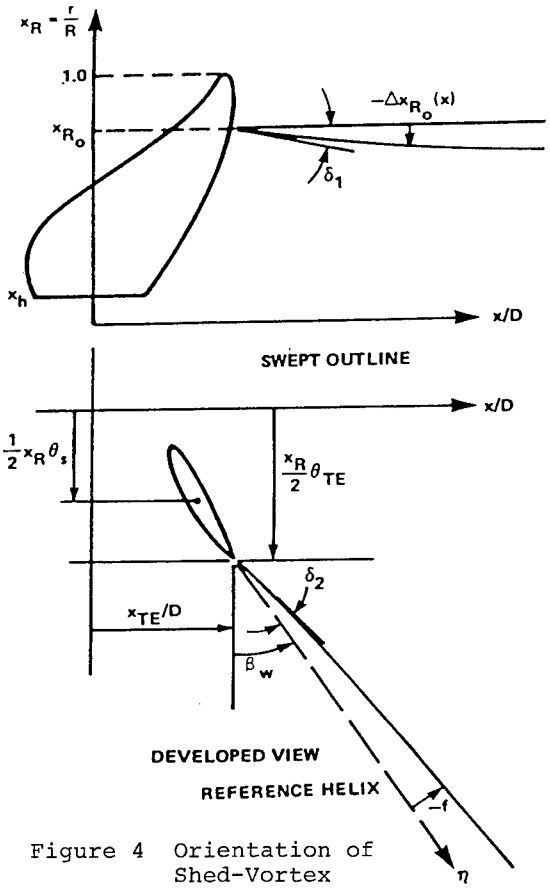


Figure 4 Orientation of Shed-Vortex Sheet Filament Trajectory

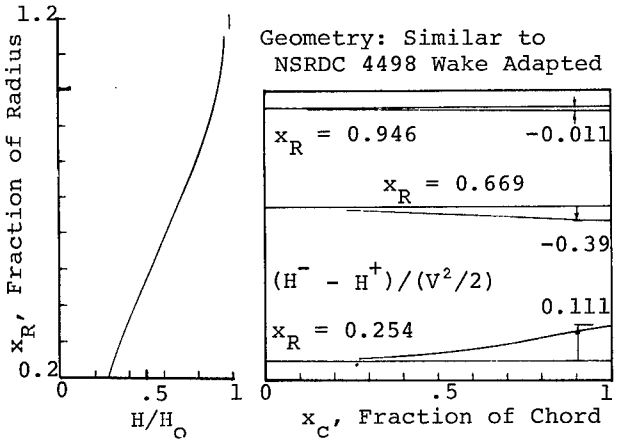


Figure 5 Assumed Head Variation along Leading Edge and Computed Difference along Three Blade Sections

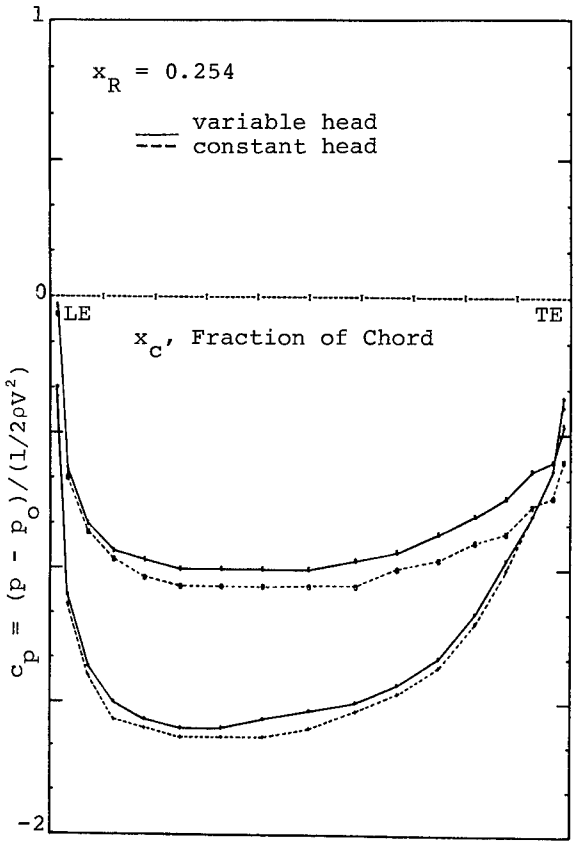
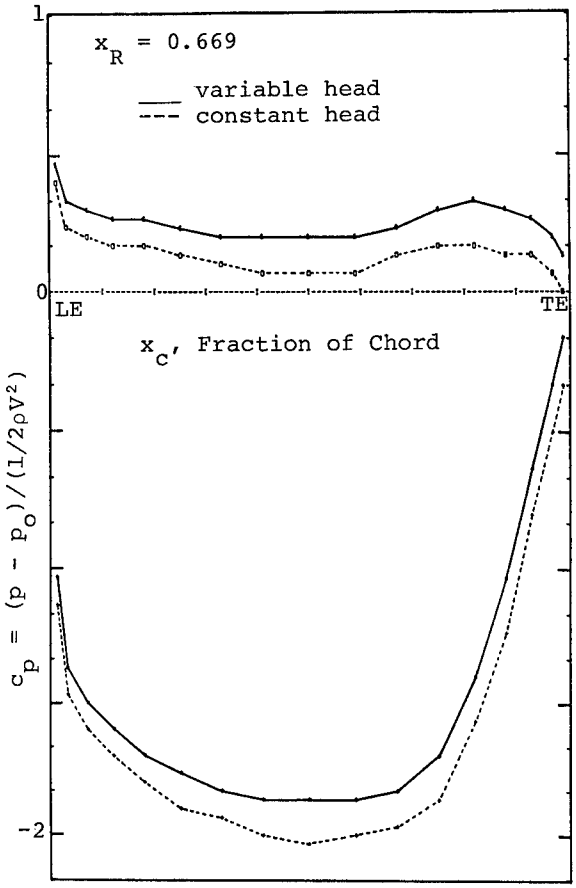
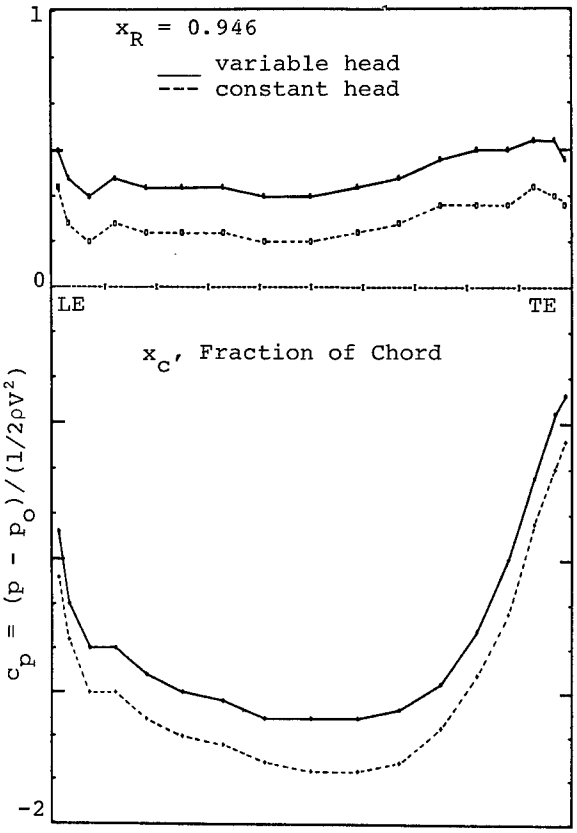


Figure 6 Pressure Distributions along Three Blade Sections





DISCUSSION

E. Baba,
Mitsubishi Heavy Industries,

In the present study the nominal onset flow is treated as a given quantity. However, the viscous boundary layer at stern region may change, since a propeller is operating in close proximity to the hull. The discussor would like to hear the author's opinion about the effect of propeller on the stern viscous boundary layer when determining effective velocity field for propeller.

Reply -

Dr. Baba's question addresses the initial assumption made in the present analysis: namely that an inviscid but rotational model of the fluid flow is sufficient to produce an acceptable value of the interaction velocity component. For an axisymmetric nominal flow field that is not separated and for a propulsor that develops its major load-bearing at outer radii, the viscous forces (those associated with the gradients of the velocity) can be neglected away from a very thin layer along the hull surface. For sure, the modification of the pressure field on the hull surface due to the propulsor produces increased vorticity that will diffuse into the flow but this process should be confined to a region near the hull surface since the upstream pressure modification is of about a diameter in extent. This argument is of course similar to that used to justify the use of potential flow for a uniform onset stream. The treatment of real turbulent flows from a time-average standpoint leads to the concept of the Reynolds stresses. These "stresses" have been measured for a variety of bodies and based on such data we believe they may be of significant importance in the flow field for nearly the entire span of the propulsor and hence should be included in the mathematical model of the interaction. Eventually we intend to address this interaction component but at present we feel that first priority is to address the inviscid rotational term as described in the paper.

Hyoung-Tae Kim,
Iowa Institute of Hydraulic Research

a. I understand that in pracitcal propeller design, it is usual to consider only the axial component of the effective velocity field. Can you tell me the magnitude of the tangential component of the calculated effective velocity vector and its effects?

b. In more general situation, when a propeller is operating in the thick boundary layer of ship stern, the onset shear flow is not axisymmetric, thus the velocity field (in Eq. (1),(2)) is not only a function of r, but a function of θ also. Is it possible to apply your method to this case?

Reply -

Mr. Kim notes that conventional practice is concerned with defining only the axial component of the effective wake. Our efforts have been aimed at describing all three components of the shear interaction velocity and their circumferential variation. For field points on the blade, the three components of effective wake could be defined by adding this vector to the nominal velocity. Since a numerical solution has not been obtained yet, I am not able to quantify the magnitude of the presently neglected components. The ultimate effect of including all velocity components in the design problem will be to produce a geometry specification that better meets the assigned loading distributions.

If the onset flow field were also circumferentially variable, then the flow field as observed in a coordinate system fixed to the propeller would no longer be steady and appropriate consideration of the time dependence must be included in the analysis. Much of the philosophy of the present approach should still be applicable, but the nominal flow and the shear interaction component will be time dependent at points on the blade and, hence it may be more appropriate to define average values for use in design.

Experimental Investigation of Flow Around a Marine Propeller and Application of Panel Method to the Propeller Theory

K. KOYAMA, A. KAKUGAWA and M. OKAMOTO

Ship Research Institute, Japan

ABSTRACT

Flow around a marine propeller was investigated experimentally. Measurement of pressure distributions on blades of model propellers was performed in a cavitation tunnel Measurement of velocity distribution around propeller blades was also carried out using an LDV (Laser Doppler Velocimeter) measurement system. The investigation into the measured velocities revealed the vortex system around propeller blades.

Experimental results were compared with the results calculated by the ordinary theoretical method based on the lifting surface theory. The comparison shows that it is necessary to take into account the three dimensional blade thickness effect and the separated flow in the region near the blade tip. The development of a propeller theory based on a panel method is presented, in order to improve the ordinary theoretical method. In the results of the calculations we can see the state of the accuracy level of the propeller analysis method based on the potential theory.

1. INTRODUCTION

In analyzing the hydrodynamic characteristics of marine propeller, the numerical method based on the lifting surface theory is very useful. At present the numerical methods employing high speed computer are widely used for the analysis. Although the experimental proof of the theoretical method has been carried out in many studies, it is not considered that there are many comparisons between theory and experiment in the microscopic value such as pressure distribution on a blade and velocity distribution around blades. So the measurement of pressure on the blade and velocity around blades is considered to be worthy now. In this paper, experimental study was performed in order to throw light on the hydrodynamics of propeller. The comparison between theory and experiment in the pressure on a blade and the flow around a blade shows the new direction of the improvement of the propeller theory. One of the direction of the improvement is the application of the panel method. In the calculation of the propeller lifting surface, the application of the discrete loading function method far outnumbers that of the mode function method, as the high speed computer with large capacity becomes popular. This means the application of panel method is available, because the unknown of the panel method is only twice the number of the discrete loading function method of the lifting surface theory. In this paper the application of the panel method to the propeller analysis is discussed.

In section 2 of the main body of this paper the results of measurement of pressure on propeller blades are presented and discussed with the comparison with the ordinary theoretical method based on the lifting surface theory. In section 3 the results of measurement of the flow field around a propeller by Laser Doppler Velocimeter are presented and discussed. In section 4 the results of oil flow observation on the blade surface are shown and the separated flow on the blade is discussed. The direction of the improvement of the propeller theory is groped, from section 2 through section 4. In section 5 the panel method is investigated and applied to the analysis of the propeller. The panel method surmounts the shortcomming appeared in the ordinary method based on the lifting surface theory.

2. PRESSURE DISTRIBUTION ON PROPELLER BLADES

Pressure distribution on propeller blades is important characteristics of marine propellers from the view point of the performance of blade and of cavitation. At the same time the pressure distribution is very useful for the investigation of the analysis method. So there are some papers dealing with the measurement of pressure on propeller blades (1)~(4). The results of the measurement are very interesting from the view point of evaluation of analysis method.

In this section measurement of pressure on a propeller blade operating in uniform flow was performed for some propellers, including the measurement in the region near the blade tip. The results of the measurement

Table 1 Particulars of Model Propellers

MODEL PROPELLER NO.	MP0123	MP0221	MP0222	MP0199
DIAMETER (m)	0.250	0.300	0.300	0.300
BOSS RATIO	0.180	0.313	0.313	0.313
PITCH RATIO	1.264(0.7R)	0.850	0.850	0.850
EXP. AREA RATIO	0.800	0.515	0.515	0.515
BLADE THICKNESS R.	0.050	0.048	0.048	0.048
ANGLE OF RAKE (deg.)	7.5	0.0	0.0	0.0
NUMBER OF BLADE	6	3	3	3
BLADE SECTION	SRI-a	NACA 4 digit	NACA 16	Circular arc

are compared with the ordinary theoretical calculation based on the lifting surface theory and discussed. In the ordinary theoretical calculation, the pressure on the blade is obtained by thick airfoil theory for the equivalent airfoil section whose mean camber line is deformed so that the loading distribution corresponds to that obtained by propeller lifting surface theory (5).

2.1 Model Propellers

Measurement was carried out for the model propellers MP0123, MP0221, and MP0199. Particulars and configurations of the model propellers are shown in Table 1 and Fig. 1 respectively. Propeller MP0123 is a conventional 6 bladed propeller, though the section form is new series in development. Propellers MP0221 and MP0199 have three blades of low aspect ratio, and the blade has no camber unlike the conventional marine propeller. The form of blade section of MP0221 is NACA 4 digit type. The form of blade section of MP0199 is circular arc, hence it is symmetrical about midchord.

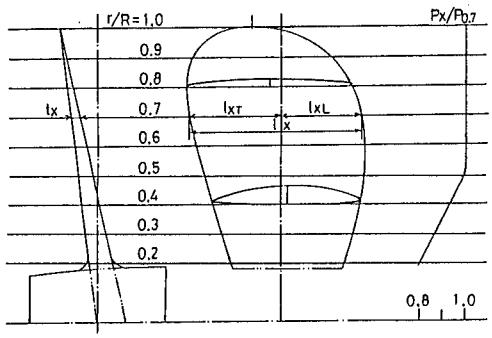
2.2 Measurement System

The experiment was performed in the cavitation tunnel with a test section of 0.75 m diameter (Fig.2) (3). The measurement of pressure distributions on the blade was carried out using very small pressure gauges made of semi-conductor. In case of MP0123 the diaphragm of the pressure gauge was exposed to the flow on the blade surface. In case of MP0199 and MP0221, the diaphragm was in the small chamber inside the blade (Fig.3). A small hole was drilled at the measuring point on the blade into the chamber. The center of the hole and that of the diaphragm are set at the same radius of the propeller. The latter mounting method has the advantage that the blade surface for the measurement is kept smooth.

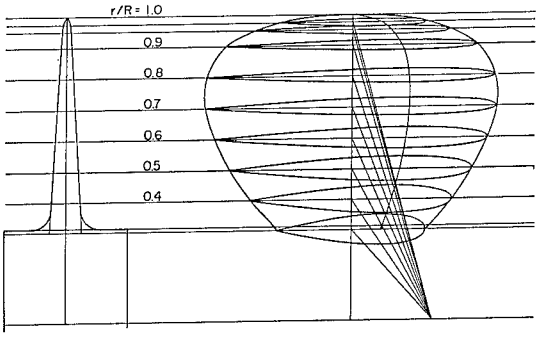
Measured positions are 0.77R section for MP0123, 0.9R and 0.95R sections for MP0221, and 0.9R and 0.962R sections for MP0199.

The effect of the tunnel wall was taken into consideration by using the theoretical relation between velocity upstream of the

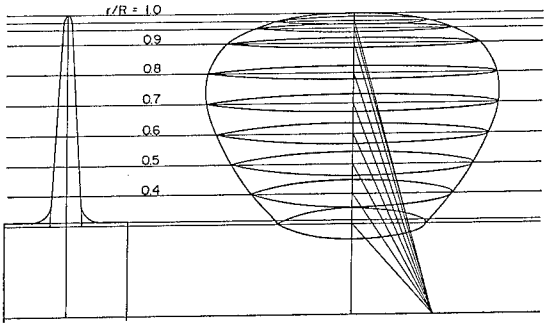
MP0123



MP0221



MP0222



MP0199

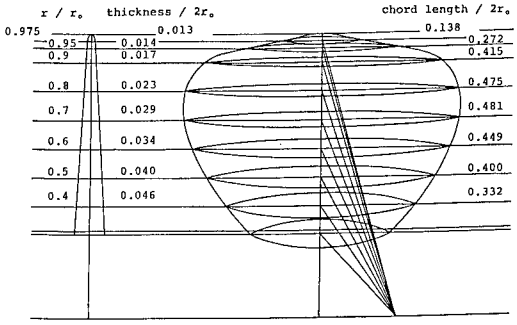


Fig. 1 Geometry of Model Propellers

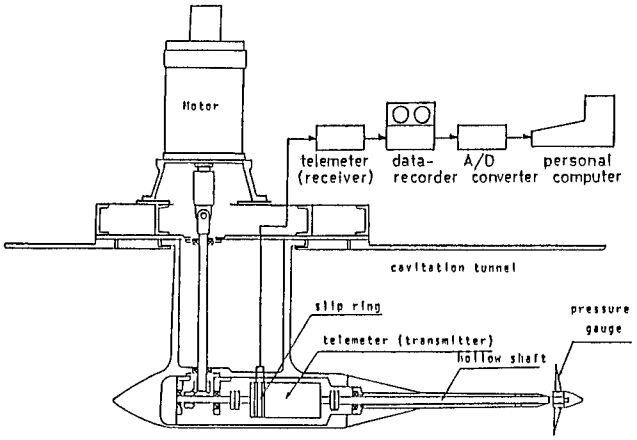


Fig. 2 Pressure Measurement System

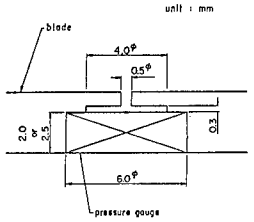


Fig. 3 Setting of Pressure Gauge

propeller in tunnel V_V and velocity upstream of the propeller in infinite region V (6),

$$\frac{V_V - V}{V} = \frac{2}{\pi}\left(\frac{R}{R_T}\right)^2 \frac{K_T}{J^2}$$

where R and R_T are radius of the model propeller and that of tunnel, respectively, and K_T is thrust coefficient and J is advance coefficient.

2.3 Results of Measurement

The results of the measurement for MP0123 are shown in Fig.4 . The agreement between the value calculated by the ordinary theoretical method and the measured value is considered to be satisfactory in general, although the calculated value for $-C_p$ is a little higher than the measured value.

The results for MP0221 are shown in Fig.5. The agreement between the calculated value and the measured value seems to be good for the results in the fore part on back side. But the calculated value for $-C_p$ is higher than the measured value in general.

The results for MP0199 are shown in Fig.6. In case of r/R=0.9, the calculated value for $-C_p$ is higher than the measured value. However in case of r/R=0.962, the measured value on back side is complicated. It is remarkable that the measured value for $-C_p$ on back side is very high in case of highly loaded condition (J=0.4), and that even in case of moderately loaded condition (J=0.6) the value is also high in the region near the leading edge.

The values measured at some positions are shown in Fig.7, as an example. The measured values plotted in Fig.5 and Fig.6 are the value obtained from the mean curve of the

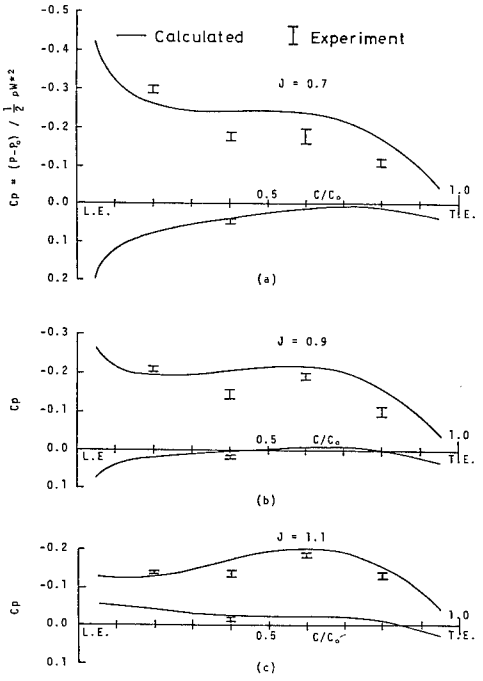


Fig. 4 Pressure Distribution on Blade (MP0123, r/R = 0.77)

figure such as Fig.7. In case of measuring position near the leading edge, the mean curves for back side and face side crosses each other at the J point where the thrust equal nearly zero. In the aft part, the pressure is little varied with the change of the advance coefficient J, and the discrepancy of the pressure between back side and face side is very small.

2.4 Discussions

The pressure calculated by the ordinary theoretical method is lower than the measured value in general as shown in the previous section.

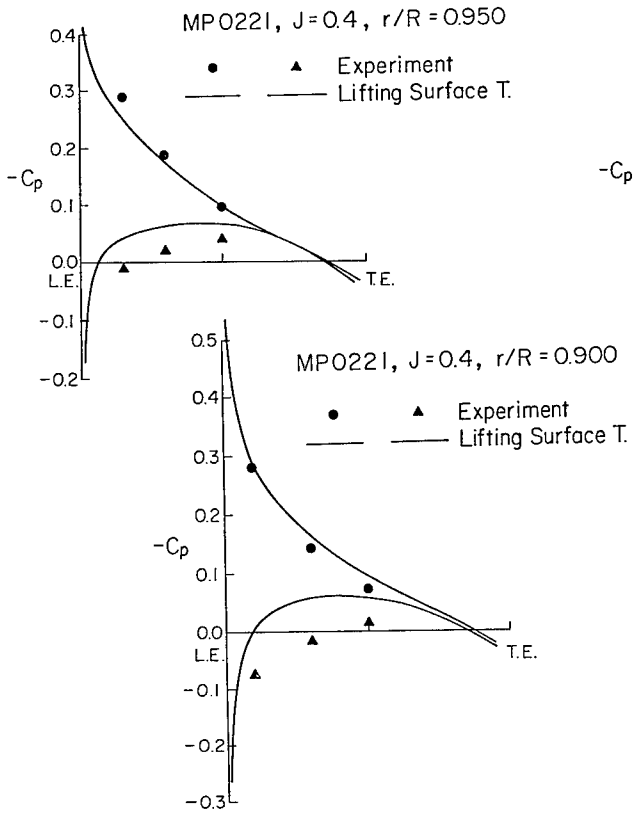


Fig. 5a Pressure Distribution on Blade
(MP0221, J = 0.4)

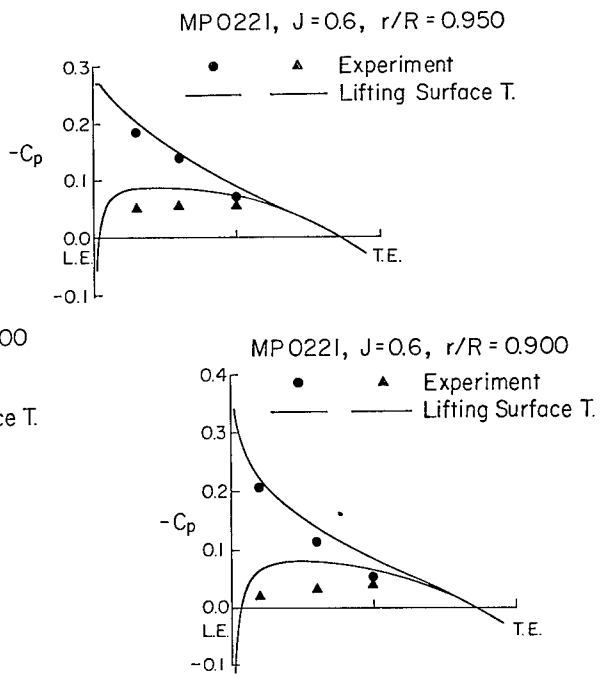


Fig. 5b Pressure Distribution on Blade
(MP0221, J = 0.6)

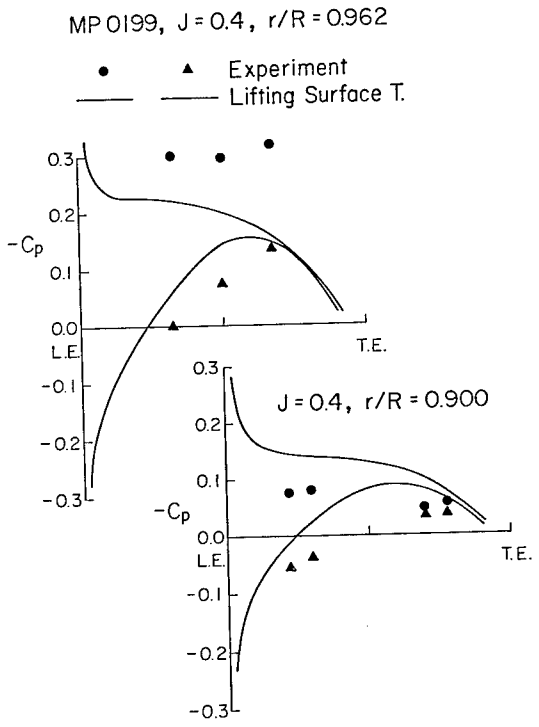


Fig. 6a Pressure Distribution on Blade
(MP0199, J = 0.4)

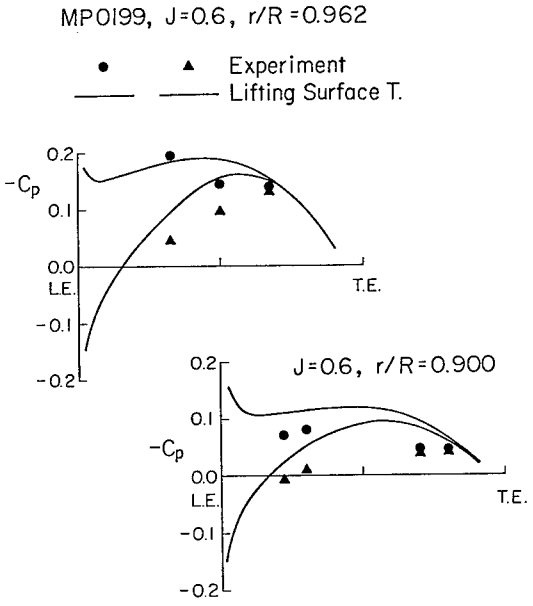


Fig. 6b Pressure Distribution on Blade
(MP0199, J = 0.6)

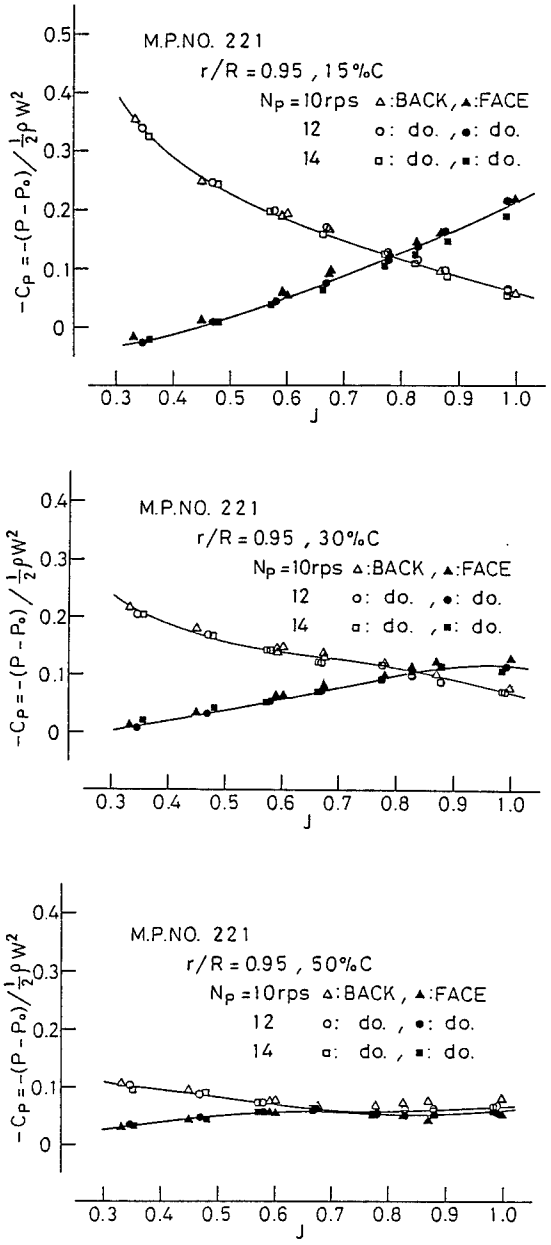


Fig. 7 Measured Value for Pressure on Blade (MP0221, r/R = 0.95)

The theory used in the previous section is composed of the lifting surface theory and thick airfoil theory. The theory removes the leading edge singularity of pressure in the lifting surface theory. Finite value of pressure is obtained near the leading edge. However the three dimensional effect of thickness is not taken into consideration in the theory, though the three dimensional effect of camber is taken into consideration. It is considered that the shortcoming of the theory appears in the comparison between theory and experiment shown in the previous section.

In order to understand the discussion the simple calculation is shown below. Potential flow around an ellipsoid $x^2/a^2+y^2/b^2+z^2/c^2=1$ and an elliptic cylinder $x^2/a^2+z^2/c^2=1$ can be calculated analytically. Flow direction is parallel to the x axis. Three dimensional effect of thickness can be investigated by comparing the pressure of the ellipsoid and the elliptic cylinder. The example of the comparison is shown in Fig.8. The thickness ratio is c/a=0.09. In the figure, the discrepancy between the ellipsoid and the elliptic cylinder is not small in spite of the small thickness ratio. We define β as the three dimensional effect factor which is the ratio of C_p value at the midchord of the ellipsoid to that of the elliptic cylinder. The β values for many combinations of a,b,c values are shown in Fig.9. β value does not tend to unit when thickness ratio c/a becomes zero, and the value varies according to aspect ratio b/a.

Another remarkable result from the measurement is that the measured pressure on the back side near the tip of blade shows very low value. The result is considered to be related to the phenomenon of flow separation at the edge. This must be discussed with more other experimental investigations (Sections 3,4).

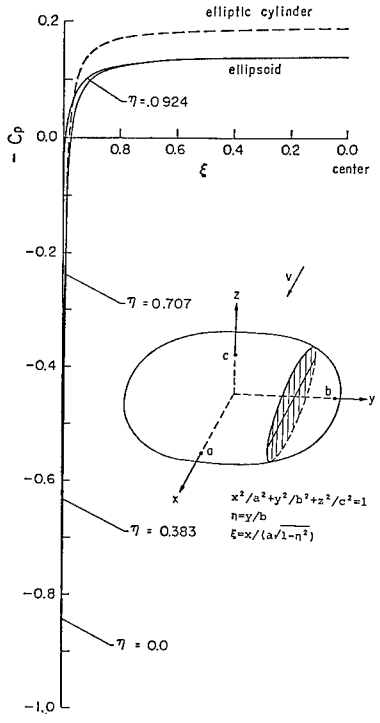


Fig. 8 Pressure Distribution on an ellipsoid (a = 1, b = 1, c = 0.09)

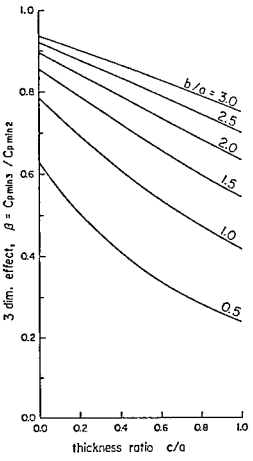


Fig. 9 Three Dimensional Effect on Minimum Pressure Coefficient $C_{p\ min}$

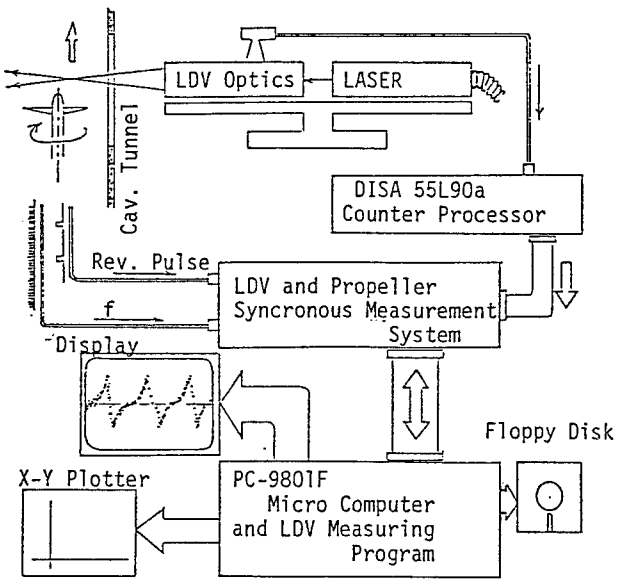


Fig. 10 LDV Measurement System

3 FLOW FIELD MEASUREMENT BY LASER DOPPLER VELOCIMETER

As shown in the previous section the measurement data on the pressure on a propeller blade were very useful in order to evaluate the analysis method. For the same purpose the measurement data on velocity around the blade are useful too and can be used to complement the discussion on the analysis method.

Recent progress in measurement technique with LDV (Laser Doppler Velocimeter) is remarkable, and the technique has provided the ability to measure time-varying velocities without disturbing the flow. Consequently, the technique is being applied to many fields such as flow phenomena in hydraulic machinery, flow around the rotor blade of helicopter(7), flow around the propeller blade (8) and so on. There are also some studies on marine propellers made by using LDV (9). Authors developed an LDV measurement system, in which triggering pulses, synchronized with the propeller rotation, initiate collection of the LDV data, in order to measure the periodically varying velocity field, and succeeded in showing the instantaneous velocity field around operating propeller blades.

The flow field around a propeller is unsteady for the observer on the ship. The mean value of varying flow velocity behind propeller can be estimated with random sampling by the statistical method. However, the flow velocity behind propeller doesn't vary at random, but varies regularly with the lapse of time. So the accurate knowledge of regularly varying flow is useful also for the understanding of the mean value.

The following are the results of the measurements of the flow field around a model propeller operating in a uniform flow, which provide insight into flow structure around a propeller.

3.1 LDV Measurement System

The experiment was performed in a cavitation tunnel with a test section of 0.75 m diameter. The arrangement of the LDV measurement system is shown in Fig.10. The LDV system is composed of DISA 55x, one component backscatter optics, and DISA 55L90a, counter processor, and others. This system enables simultaneous measurement of only one velocity component, thus requiring three sets of measurements to acquire all three components. In the system, after checking whether validated velocity data are acquired or not, the velocity data and the signal for rotating blade angle from the propeller dynamometer are fed to a microcomputer. The continuation of the data accumulation gives the velocity distribution along a circumference drawn by propeller rotation. It is necessary to control the number of tracing particles in the water in order to secure the reliability of the LDV measurement. A commercial water paint was used as particles to be poured into the tunnel. As a result the measurement was performed under the condition that the number of the validated data points per second was 300-500 and that the number was 10-30% of the number of the particles passing through the measuring position.

3.2 Model Propeller and Experiment Condition

We used the model propeller MP0221 for the measurement. Particulars and configuration of the propeller are shown in Table 1 and Fig.1 , respectively. The experiment was performed with the model propeller operating in a uniform flow. Number of propeller rotation was set at $n = 12\ s^{-1}$. Coordinate system is shown in Fig.11. The coordinate x is measured in the backward direction of propeller shaft, the coordinate θ is measured positive in the contra-rotating direction of propeller, and the

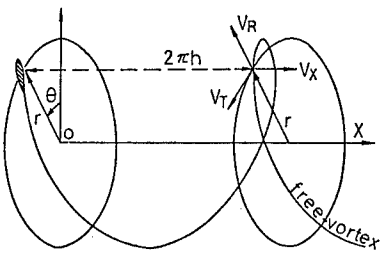


Fig. 11 Cylindrical Coordinates

coordinate r is measured in the radial direction. The velocities V_X, V_T and V_R are velocity components of the coordinate direction.

3.3 Results of the Measurement of Velocity Distribution

The examples of the experimental results of the velocity distribution V_X, V_T and V_R along the circumference at a given radius just behind the propeller blade are presented in Figs.12a, 12b and 12c for the case of J =

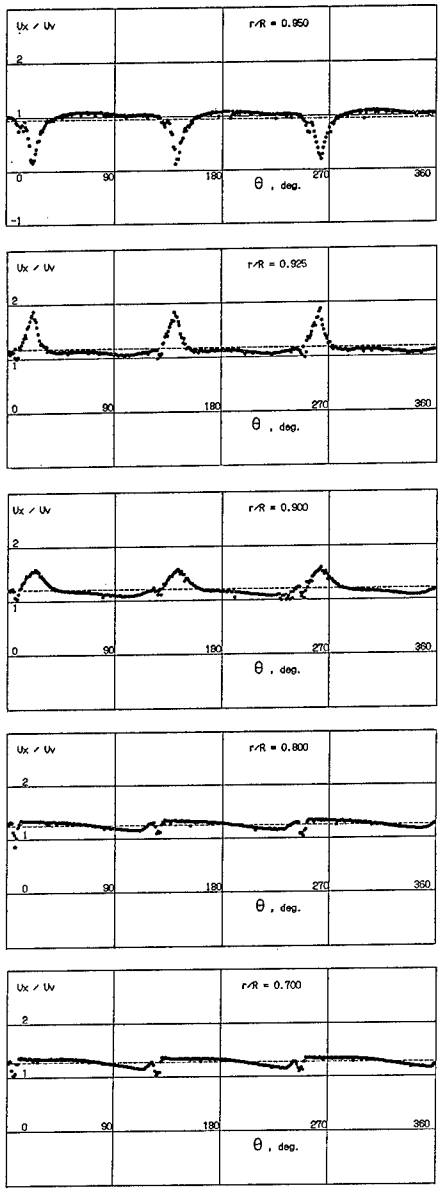


Fig. 12a Circumferential Distribution of Axial Velocity Components V_X
(J = 0.584, x/D = 0.11)

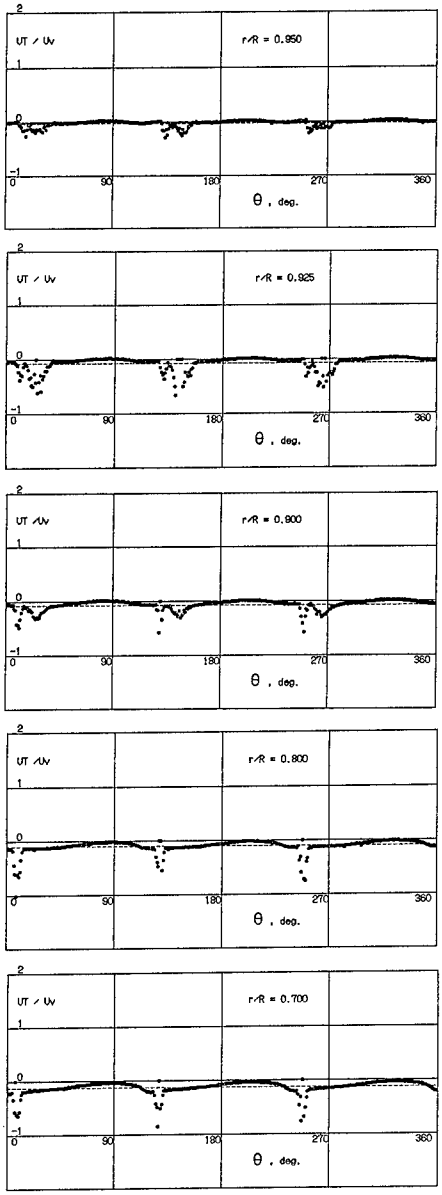


Fig. 12b Circumferential Distribution of Tangential Velocity Components V_T
(J = 0.584, x/D = 0.11)

0.584. Measured values are plotted for every degree of blade angular position θ taken as the abscissa. The tunnel water speed V_v is used for the normalization of velocity. Three bladed propeller causes three periods of the velocity distribution in one rotation. Data in the figures show the velocity field of the strong tip vorticies and weak free vortex sheets. In Fig.12a (V_X), the direction of the velocity peak for r = 0.95R is opposite to that for r = 0.925R. This is because the two measurement positions are at outside and inside of the tip vortex, and the tip vortex takes place between the two measurement positions. Small disturbance shown on the left side of the velocity peak in Fig.12a is considered to be the effect of a free vortex sheet emanating at trailing edge. In Fig.12b (V_T), the velocity valleys corresponding to the blade wake are observed at the position of the free vortex sheets. In Fig.12c (V_R), it is clear that flow direction changes rapidly at the position of the tip vortex. Fig.13 is the plots of vectors composed of V_T and V_R seen from behind. Velocity field behind propeller blade, especially flow around tip vortex can be well understood by this figure.

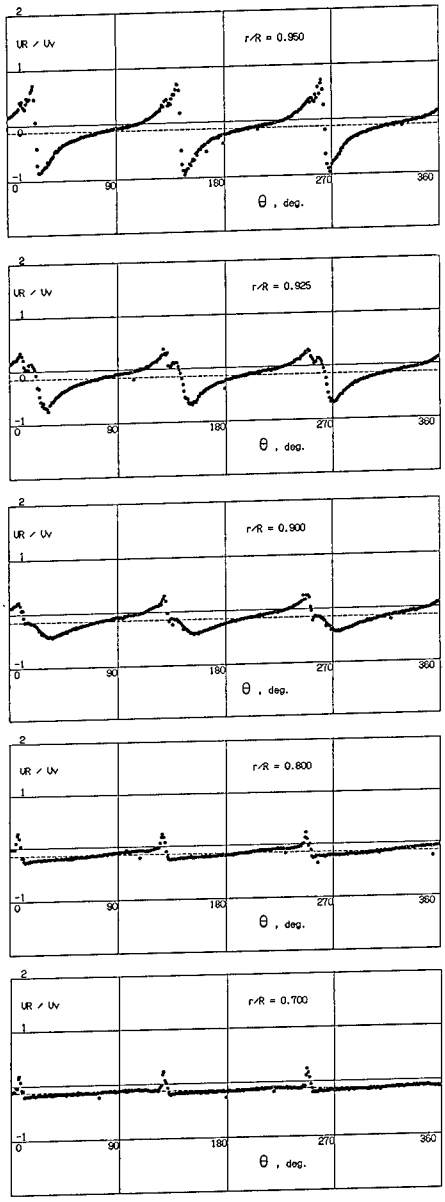


Fig. 12c Circumferential Distribution of Radial Velocity Components V_R
(J = 0.584, x/D = 0.11)

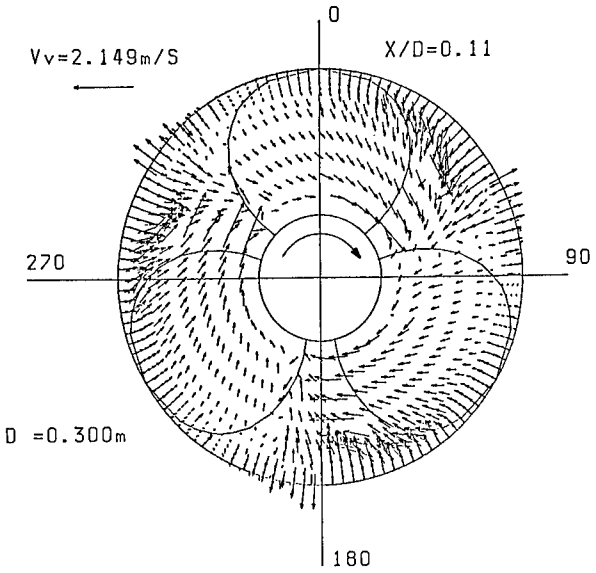


Fig. 13 Velocity Vector Diagram $V_T + V_R$
(J = 0.584, x/D = 0.11)

3.4 Mean Velocity Distribution

Measured circumferential distributions of velocity components V_X, V_T and V_R yield the circumferential mean values $\bar{V}_X$, $\bar{V}_T$ and $\bar{V}_R$.

Fig.14 shows the mean velocity component $\bar{V}_X$ for the case of J = 0.364. The increase of the velocity component $\bar{V}_X$ with increasing axial distance is shown. The accelerated region becomes narrow as the position shifts downstream, which indicates a slipstream contraction. Outside the slipstream, velocity behind the propeller is lower than that before it.

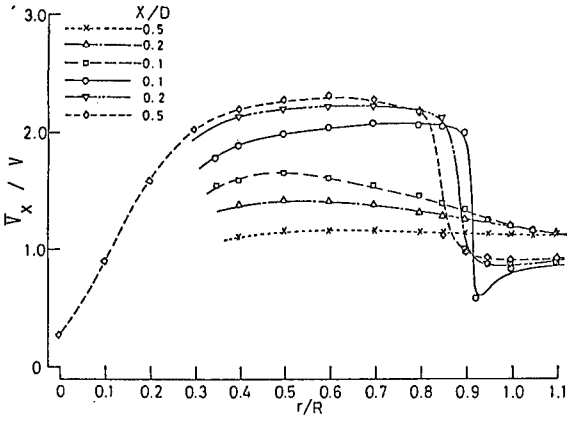


Fig. 14 Radial Distribution of Mean Axial Velocities $\bar{V}_X$ (J = 0.364)

3.5 Pitch Distribution

Pitch $2\pi h$ of the helicoidal flow was calculated using the velocity components $\bar{V}_X$ and $\bar{V}_T$. Radial distribution of the pitch is presented in Fig.15 for the case of J = 0.364. The pitch of observed tip vortex cavitation and the pitch calculated by lifting surface theory (LST) are also plotted. The fact that the pitch of the tip vortex is smaller than the pitch of the inside helicoidal flow, indicates a rolling-up of the edge of the vortex sheet, and makes one imagine easily the shape of the vortex system of the flow separated at the blade tip.

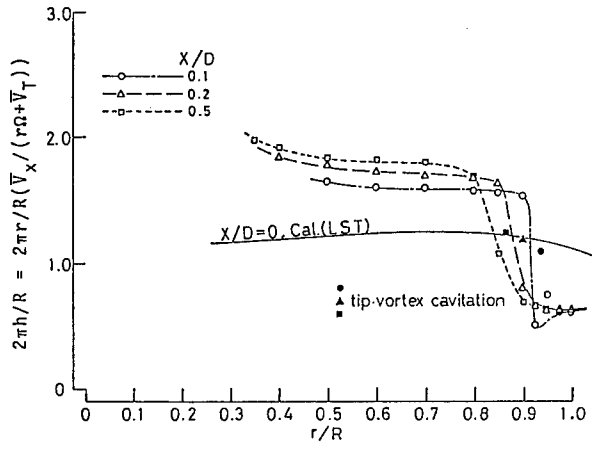


Fig. 15 Radial Distribution of Pitch of Helicoidal Flow (J = 0.364)

3.6 Circulation around Blade Section

Circulation Γ around the blade section at radius r is given by formula (10)

$$\Gamma = 2 \pi r \bar{V}_T / l \qquad (l : \text{number of blades})$$

which is valid on the simple assumption. Radial distribution of the circulation is shown in Fig.16. The values of x/D = 0.1, 0.2 and 0.5 in the figure mean the axial positions where the values $\bar{V}_T$ were measured. The three results should be equal in principle. It is due to the limitation of the formula that the equality of the three results is not sufficient. Also shown is a result calculated by lifting surface theory (LST). Estimated value by the measurement and theoretical value are in good agreement in general. However, high peak and steep gradient of the experimental data near the tip are not followed by the lifting surface theory. The strong circulation near the tip is considered to cause a separated tip vortex which becomes main part of slip stream vortex system.

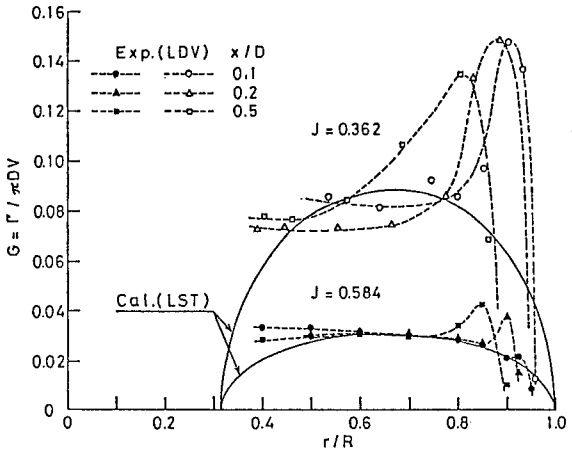


Fig. 16 Radial Distribution of Circulation around Blade Section

3.7 Discussions

A three-dimensional complex flow field around a propeller operating in a uniform flow was measured and an investigation of the measured velocities reveals the complexity of the flow field around a propeller. The comparison between the measured results and the results calculated by lifting surface theory shows that it is necessary to take into account the separated flow in the region near the blade tip, in order to improve the theoretical analysis method. If the measurement as discussed in this section becomes easier and faster in future, the measurement system will

be applicable to analysis of propeller blade performance, and further to improvement of propeller geometry.

4 OIL FLOW OBSERVATION ON THE BLADE SURFACE

Oil flow observation on the blade surface was performed for MP.0221, MP.0222, and MP.0199 (Fig.1). The blade contour of MP0222 is the same as that of MP0221. The blade contour of MP0199 is not the same as that of MP0221, but those are similar. The section forms of MP0221, MP0222, and MP0199 are NACA 4 digit, NACA 16 series and circular arc respectively. The leading edge radius of MP0221 is largest in the three. That of MP0199 is smallest in the three.

Example of the results of the oil flow test is shown in Fig.17 . The region where the flow is considered to be separated is observed near the leading edge. The region is extended along the leading edge to the blade tip. The region is remarkable for the blade of the small leading edge radius such as MP0199

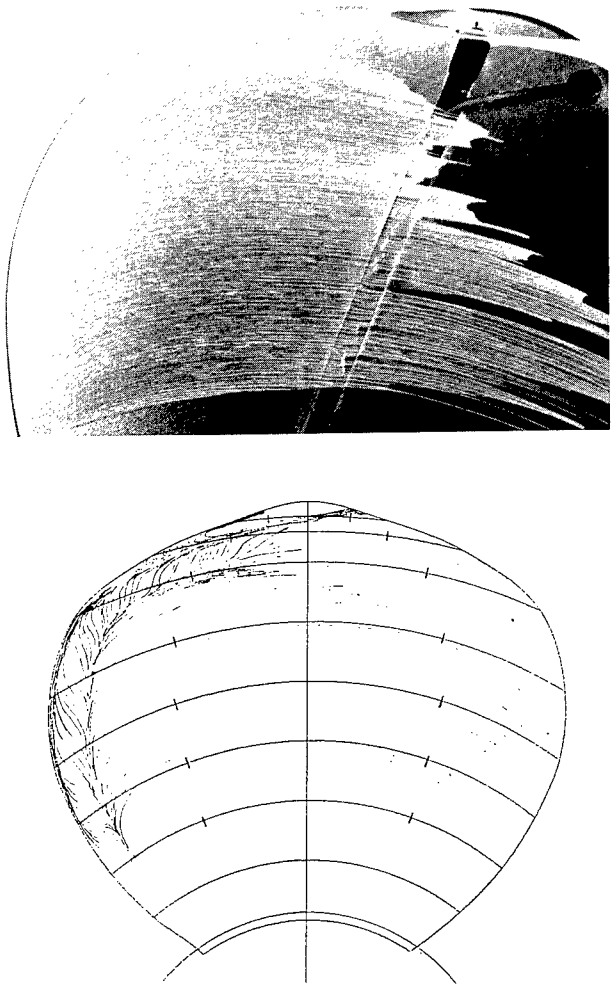


Fig. 17 Photograph and Sketch for Paint-flow Pattern on the Suction Side of Blade (MP0199, J = 0.38)

The observed oil flow pattern is similar to that of the part-span vortex of swept back wing (11). The patterns which are considered to be the secondary separation line and the dead water region are observed near the blade tip. It is known that the pressure in the part-span vortex is very low. The low pressure near the tip on the back side surface of the blade of MP0199 shown in section 2.3 (Fig.6), the strong circulation near the tip shown in section 3.6 (Fig.16), and the separated flow along the leading edge near the tip observed in the oil flow pattern (Fig.17) are considered to be the appearance of one and the same phenomenon.

5. APPLICATION OF PANEL METHOD

In analyzing the flow around a body, the potential flow theory is very useful, provided that the flow scarcely separates and that the boundary layer and the vortex wake are thin enough. The lifting surface theory is one of the example of the potential theory which is utilized successfully. The panel method for arbitrary configurations is considered to be the extension of the lifting surface theory in the sense of the extension from a thin wing to a thick wing.

By using high speed computers with large capacity, the panel method is utilized in the analysis of realistic aircrafts. A review of the panel method is found elsewhere(12). We remember the calculation by Hess and Smith for non-lifting bodies(13). The method is widely used even now. In case of lifting bodies, Morino's direct formulation employing the Green's theorem, is noticed(14). In addition to the calculation by Morino there are many studies on the panel method for the three dimensional lifting body. Maskew showed the method based on the internal Dirichlet formulation (15). The technique of making panels is a key job in the application of panel method. Johnson developed the higher order panel method, in order to overcome the difficulties in making panels (16). In almost all methods the formulation is based on the potential or singularity on the body surface. So the pressure or velocity on the body surface is calculated by the derivertives of the potential which is obtained by solving the integral equation. On the other hand there is a few methods based on velocity formulation. In the methods the integral equation is constructed by using the velocity on the body surface as the unknown (17),(18). However the authors can not find the numerical results by the method for the lifting bodies.

So far as the application of panel method to propeller blade is concerned, Ling's calculation is noticed (19). He studied a propeller theory based on the formulation similar to Morino's method.

In this section the formulation of the

integral equation for the velocity on the body surface is presented as well as the formulation of the potential. Numerical method for higher order panel method is presented. The numerical results are shown for the rectangular wing, the circular wing, and the propeller blade.

5.1 Formulation

It is assumed that the flow is incompressible, inviscid and irrotational. Then there exists the velocity potential Φ and the potential satisfies Laplace's equation

$$\nabla^2 \Phi = 0 . \tag{1}$$

According to Green's identity formula, the velocity potential in the three dimensional flow field is expressed as

$$\Phi = -\frac{1}{4\pi} \iint \frac{\partial \Phi}{\partial n'} \frac{1}{r} \, dS + \frac{1}{4\pi} \iint \Phi \frac{\partial}{\partial n'} \left(\frac{1}{r} \right) dS \tag{2}$$

where the integral domain includes all boundary surface which bounds the flow field and r is defined to be the length of the vector $\bar{r}$ from integral point to observer point. Symbol $\partial/\partial n'$ is the normal derivertive to the integral surface directed into the flow field.

For the body set in the stream, the velocity potential Φ can be written as

$$\Phi = \Phi_D + \Phi_S + \Phi_W + \Phi_\infty \tag{3}$$

$$\Phi_D = \frac{1}{4\pi} \iint_S \mu \frac{\partial}{\partial n'} \left(\frac{1}{r} \right) dS \tag{4}$$

$$\Phi_S = \frac{-1}{4\pi} \iint_S \sigma \left(\frac{1}{r} \right) dS \tag{5}$$

$$\mu = \Phi - \Phi_i \tag{6}$$

$$\sigma = \frac{\partial \Phi}{\partial n'} - \frac{\partial \Phi_i}{\partial n'} \tag{7}$$

$$\Phi_W = \frac{1}{4\pi} \iint_W \left(\Phi_{TU} - \Phi_{TL} \right) \frac{\partial}{\partial n'} \left(\frac{1}{r} \right) dS \tag{8}$$

where,

Φ_D is velocity potential induced by doublet distribution on body surface.

Φ_S is velocity potential induced by source distribution on body surface.

Φ_W is velocity potential induced by vortex wake.

Φ_∞ is velocity potential in case of unperturbed field without body.

Φ_i is fictitious velocity potential inside the body.

S is body surface.

W is upper surface of the vortex wake.

Φ_{TU} is velocity potential at trailing edge on upper side.

Φ_{TL} is velocity potential at trailing edge on lower side.

Flow velocity $\bar{V}$ is obtained by the derivative of velocity potential.

$$\bar{V} = \nabla \Phi = \nabla \Phi_D + \nabla \Phi_S + \nabla \Phi_W + \nabla \Phi_\infty . \tag{9}$$

In the case where the observer point is on the body surface, the integrals for Φ_D, $\nabla \Phi_D$, $\nabla \Phi_S$ become singular. The potential on the body surface inside the flow field induced by doublet distribution Φ_{D+} and the fictitious potential on the body surface inside the body induced by doublet distribution Φ_{D-} are expressed as

$$\Phi_{D\pm} = \pm \frac{1}{2} \mu + \frac{1}{4\pi} \fint\!\!\!\fint_S \mu \frac{\partial}{\partial n'} \left(\frac{1}{r} \right) dS \tag{10}$$

where the symbol $\fint\!\!\!\fint$ indicates that the integration excludes the singular point at which the observer point coincides with the integral point.

The velocity on the body surface inside the flow field $\nabla \Phi_{S+}$, $\nabla \Phi_{D+}$ and the fictitious velocity on the body surface inside the body $\nabla \Phi_{S-}$, $\nabla \Phi_{D-}$ are expressed as (18)

$$\nabla \Phi_{S\pm} = \pm \frac{1}{2} \sigma \bar{n} + \frac{-1}{4\pi} \fint\!\!\!\fint_S \sigma \nabla \left(\frac{1}{r} \right) dS \tag{11}$$

$$\nabla \Phi_{D\pm} = \pm \frac{1}{2} \bar{D}\mu + \frac{1}{4\pi} \fint\!\!\!\fint_S \left(\bar{D}\mu \times \bar{n} \right) \times \nabla \left(\frac{1}{r} \right) dS - \frac{1}{4\pi} \int_{\partial S} \mu \nabla \left(\frac{1}{r} \right) \times \bar{t} \, ds \tag{12}$$

where $\bar{n}$ indicates the unit normal vector to the surface S, $\bar{D}\mu$ indicates the vector which is the gradient of μ within S, symbol $\int_{\partial S}$ indicates the line integral along the boundary ∂S of S, and $\bar{t}$ indicates the unit tangential vector along ∂S. The line integral does not emerge when S is a closed surface.

In the usual panel method, equations (3), (6), and (10) are combined, resulting in (15),

$$-\frac{1}{2} \left(\Phi - \Phi_i \right) + \frac{1}{4\pi} \fint\!\!\!\fint_S \left(\Phi - \Phi_i \right) \frac{\partial}{\partial n'} \left(\frac{1}{r} \right) dS = \Phi_i - \Phi_S - \Phi_W - \Phi_\infty \tag{13}$$

The fictitious potential inside the body Φ_i is assumed suitably and $\partial\Phi/\partial n$ is determined by the boundary condition on the body surface. Then the equation (13) becomes a Fredholm integral equation of the second kind with the

unknown Φ. Velocity on the body surface must be calculated by the delivertive of the velocity potential obtained by solving the integral equation (13).

If the potential Φ_i is assumed to be equal Φ_∞

$$\Phi_i = \Phi_\infty, \tag{14}$$

then

$$u = \Phi - \Phi_\infty \tag{15}$$

$$\sigma = \frac{\partial \Phi}{\partial n'} - \frac{\partial \Phi_\infty}{\partial n'} . \tag{16}$$

The integral equation (13) becomes

$$- \frac{1}{2} (\Phi - \Phi_\infty) + \frac{1}{4\pi} \iint_S (\Phi - \Phi_\infty) \frac{\partial}{\partial n'} (\frac{1}{r}) \, dS = - \Phi_S - \Phi_W \tag{17}$$

The form of this integral equation is the same as Morino's direct formulation which does not require the concept of sources or doublets, or of fictitious internal fields (14).

If the potential Φ_i is assumed to be equal zero

$$\Phi_i = 0, \tag{18}$$

then

$$u = \Phi \tag{19}$$

$$\sigma = \frac{\partial \Phi}{\partial n} . \tag{20}$$

The integral equation (13) becomes

$$- \frac{1}{2} \Phi + \frac{1}{4\pi} \iint_S \Phi \frac{\partial}{\partial n'} (\frac{1}{r}) \, dS = - \Phi_S - \Phi_W - \Phi_\infty . \tag{21}$$

If $\partial\Phi/\partial n = 0$, then $\Phi_S = 0$.

It is considered to be convenient that the formulation can be constructed on the basis of the integral equation using the velocity on the body surface $\bar{V}$ as the unknown.

If the potential Φ_i is assumed to be zero, then

$$\bar{D} u = \bar{V} . \tag{22}$$

Then the equation (12) becomes

$$\nabla \Phi_{D\pm} = \pm \frac{1}{2} \bar{V} + \frac{1}{4\pi} \iint_S (\bar{V}' \times \bar{n}') \times \nabla (\frac{1}{r}) \, dS - \frac{1}{4\pi} \int_{\partial S} u \nabla (\frac{1}{r}) \times \bar{t} \, ds \tag{23}$$

The integral equation for $\bar{V}$ is constructed using the condition that the fictitious velocity on the body surface inside the body is to be zero. The condition is equivalent with the condition that the normal velocity is zero on the body surface outside the body.

$$\bar{t} [- \frac{1}{2} \bar{V} + \frac{1}{4\pi} \iint_S (\bar{V}' \times \bar{n}') \times \nabla (\frac{1}{r}) \, dS] = \bar{t} [- \nabla \Phi_W - \nabla \Phi_\infty] \tag{24}$$

where $\bar{t}$ means unit tangential vector to the surface S. The third term of the right hand side of equation (23) is negrected, because the body surface have no edge, and because $\Phi_{TU} - \Phi_{TL}$ is zero at the blade tip.

We use the orthogonal curvelinear coordinate system (a,b) confined within the surface S. To this system is added the third coordinate n, which is the distance along the normal to S, to form a three dimensional coordinate system (a,b,n) . Then the vector $\bar{t}$ is the linear combination of the unit tangential vectors $\bar{a}$ and $\bar{b}$. If we define,

$$\bar{V}' = V_a' \bar{a}' + V_b' \bar{b}' \tag{25}$$

$$\bar{a}' = a_a \bar{a} + a_b \bar{b} + a_n \bar{n} \tag{26}$$

$$\bar{b}' = b_a \bar{a} + b_b \bar{b} + b_n \bar{n} , \tag{27}$$

then the equation (24) becomes two equations

$$\frac{1}{2} V_a + \iint_S [V_a' n_{aa} + V_b' n_{ab}] \, dS = V_{aW} + V_{a\infty} \tag{28a}$$

$$\frac{1}{2} V_b + \iint_S [V_a' n_{ba} + V_b' n_{bb}] \, dS = V_{bW} + V_{b\infty} \tag{28b}$$

where V_a, V_{aW}, $V_{a\infty}$ are the a-component of the vectors $\bar{V}$, $\bar{V}_W = \nabla \Phi_W$, $\bar{V}_\infty = \nabla \Phi_\infty$, respectively, and V_b , V_{bW} , $V_{b\infty}$ are the b-component of the vectors, and

$$n_{aa} = \frac{-1}{4\pi} \{ b_n \frac{\partial}{\partial b} (\frac{1}{r}) - b_b \frac{\partial}{\partial n} (\frac{1}{r}) \} \tag{29a}$$

$$n_{ab} = \frac{-1}{4\pi} \{ -a_n \frac{\partial}{\partial b} (\frac{1}{r}) + a_b \frac{\partial}{\partial n} (\frac{1}{r}) \} \tag{29b}$$

$$n_{ba} = \frac{-1}{4\pi} \{ b_a \frac{\partial}{\partial n} (\frac{1}{r}) - b_n \frac{\partial}{\partial a} (\frac{1}{r}) \} \tag{29c}$$

$$n_{bb} = \frac{-1}{4\pi} \{ -a_a \frac{\partial}{\partial n} (\frac{1}{r}) + a_n \frac{\partial}{\partial a} (\frac{1}{r}) \} \quad (29d)$$

Equations (28a),(28b) are the simultaneous Fredholm integral equations of the second kind. The advantage of the method based on the integral equations (28a) and (28b) is that the unknown is the velocity on the body surface $\bar{V}$. The disadvantage of the method is that the unknown in the method is about twice the number in the method based on the integral equation (17) or (21).

If unit vectors corresponding to three components of Cartesian coordinates x,y,z are defined as $\bar{i}$, $\bar{j}$, $\bar{k}$ and the notations

$$\bar{a} = a_x \bar{i} + a_y \bar{j} + a_z \bar{k} \quad (30a)$$

$$\bar{b} = b_x \bar{i} + b_y \bar{j} + b_z \bar{k} \quad (30b)$$

$$\bar{n} = n_x \bar{i} + n_y \bar{j} + n_z \bar{k} \quad (30c)$$

$$\bar{a}' = a'_x \bar{i} + a'_y \bar{j} + a'_z \bar{k} \quad (31a)$$

$$\bar{b}' = b'_x \bar{i} + b'_y \bar{j} + b'_z \bar{k} \quad (31b)$$

$$\bar{n}' = n'_x \bar{i} + n'_y \bar{j} + n'_z \bar{k} \quad (31c)$$

are used, then

$$n_{aa} = \frac{-1}{4\pi} [\{ (b_x n_y - n_x b_y) b'_y + (b_x n_z - n_x b_z) b'_z \} \frac{\partial}{\partial x} (\frac{1}{r}) + \{ (b_y n_z - n_y b_z) b'_z + (b_y n_x - n_y b_x) b'_x \} \frac{\partial}{\partial y} (\frac{1}{r}) + \{ (b_z n_x - n_z b_x) b'_x + (b_z n_y - n_z b_y) b'_y \} \frac{\partial}{\partial z} (\frac{1}{r})] \quad (32a)$$

$$n_{ab} = \frac{-1}{4\pi} [\{ + (- b_x n_z + n_x b_z) a'_z \} \frac{\partial}{\partial x} (\frac{1}{r}) + \{ (- b_y n_z + n_y b_z) a'_z + (- b_y n_x + n_y b_x) a'_x \} \frac{\partial}{\partial y} (\frac{1}{r}) + \{ (- b_z n_x + n_z b_x) a'_x \} \frac{\partial}{\partial z} (\frac{1}{r})] \quad (32b)$$

$$n_{ba} = \frac{-1}{4\pi} [\{ (- a_x n_y + n_x a_y) b'_y + (- a_x n_z + n_x a_z) b'_z \} \frac{\partial}{\partial x} (\frac{1}{r}) + \{ (- a_y n_z + n_y a_z) b'_z + (- a_y n_x + n_y a_x) b'_x \} \frac{\partial}{\partial y} (\frac{1}{r}) + \{ (- a_z n_x + n_z a_x) b'_x + (- a_z n_y + n_z a_y) b'_y \} \frac{\partial}{\partial z} (\frac{1}{r})] \quad (32c)$$

$$n_{bb} = \frac{-1}{4\pi} [\{ + (a_x n_z - n_x a_z) a'_z \} \frac{\partial}{\partial x} (\frac{1}{r}) + \{ (a_y n_z - n_y a_z) a'_z + (a_y n_x - n_y a_x) a'_x \} \frac{\partial}{\partial y} (\frac{1}{r}) + \{ (a_z n_x - n_z a_x) a'_x \} \frac{\partial}{\partial z} (\frac{1}{r})] \quad (32d)$$

5.2 Numerical Method

In the panel method, the body surface S is devided into many small panels. Integral calculation is performed for each panel Sl. In this section the numerical method of integration for a panel is shown.

In order to calculate the formulae presented in the previous section, numerical method of calculation of the integrals

$$\Phi_{Dl} = \frac{1}{4\pi} \iint_{Sl} \mu \frac{\partial}{\partial n'} (\frac{1}{r}) \, dS \quad (33)$$

$$\Phi_{Sl} = \frac{-1}{4\pi} \iint_{Sl} \sigma (\frac{1}{r}) \, dS \quad (34)$$

$$\nabla \Phi_{Sl} = \frac{-1}{4\pi} \iint_{Sl} \sigma \nabla (\frac{1}{r}) \, dS \quad (35)$$

$$\nabla_a \Phi_{Dl} = - \iint_{Sl} [V'_a n_{aa} + V'_b n_{ab}] \, dS \quad (36a)$$

$$\nabla_b \Phi_{Dl} = - \iint_{Sl} [V'_a n_{ba} + V'_b n_{bb}] \, dS \quad (36b)$$

should be invented.

Cartesian coordinates X,Y,Z for each panel is used. XY plane approximates the panel surface, and Z axis directs into the flow domain. The panel surface is expressed as follows

$$B(X',Y',Z') = Z' - Z_B(X',Y') = 0 \quad (37)$$

Then

$$\frac{\partial}{\partial n'} = \bar{n}' \cdot \nabla$$

$$= \left(\frac{\partial B}{\partial X'} \frac{\partial}{\partial X'} + \frac{\partial B}{\partial Y'} \frac{\partial}{\partial Y'} + \frac{\partial B}{\partial Z'} \frac{\partial}{\partial Z'} \right) / R_n \quad (38)$$

$$dS = R_n \, dX' \, dY' \quad (39)$$

$$R_n = \sqrt{ \left\{ \left(\frac{\partial B}{\partial X'} \right)^2 + \left(\frac{\partial B}{\partial Y'} \right)^2 + \left(\frac{\partial B}{\partial Z'} \right)^2 \right\} } \quad (40)$$

Unknowns u, σ, V_a', V_b' are assumed to be expressed by the polynomial of X', Y' . For example,

$$u = m_{00} + m_{10} X' + m_{01} Y' + \frac{1}{2} m_{20} X'^2 + m_{11} X'Y' + \frac{1}{2} m_{02} Y'^2 \quad (41)$$

Coefficient m_{ij} is expressed by unknowns u_k which are the value at the control point in the panel distributed around the integral panel. Then

$$u = \sum_{k=0}^{M} W_k u_k \left\{ C_{00}^k + C_{10}^k X' + C_{01}^k Y' + \frac{1}{2} C_{20}^k X'^2 + C_{11}^k X'Y' + \frac{1}{2} C_{02}^k Y'^2 \right\} \quad (42)$$

Coefficients C_{00}^k, C_{10}^k,,, are determined by a kind of a method of least squares and W_k is a weight function. Then in order to calculate the integrals (33)∿ (36), the following integrations should be calculated.

$$G_{Xmn} = \frac{-1}{4\pi} \iint X'^m Y'^n \frac{\partial B}{\partial X'} \frac{\partial}{\partial X'} \left(\frac{1}{r} \right) dX'dY' \quad (43a)$$

$$G_{Ymn} = \frac{-1}{4\pi} \iint X'^m Y'^n \frac{\partial B}{\partial Y'} \frac{\partial}{\partial Y'} \left(\frac{1}{r} \right) dX'dY' \quad (43b)$$

$$G_{Zmn} = \frac{-1}{4\pi} \iint X'^m Y'^n \frac{\partial B}{\partial Z'} \frac{\partial}{\partial Z'} \left(\frac{1}{r} \right) dX'dY' \quad (43c)$$

$$G_{0mn} = \frac{-1}{4\pi} \iint X'^m Y'^n \left(\frac{1}{r} \right) R_n \, dX'dY' \quad (44)$$

$$H_X^{mn} = \frac{-1}{4\pi} \iint X'^m Y'^n \frac{\partial}{\partial X} \left(\frac{1}{r} \right) R_n \, dX'dY' \quad (45a)$$

$$H_Y^{mn} = \frac{-1}{4\pi} \iint X'^m Y'^n \frac{\partial}{\partial Y} \left(\frac{1}{r} \right) R_n \, dX'dY' \quad (45b)$$

$$H_Z^{mn} = \frac{-1}{4\pi} \iint X'^m Y'^n \frac{\partial}{\partial Z} \left(\frac{1}{r} \right) R_n \, dX'dY' \quad (45c)$$

$$I_{Xb_Y}^{mn} = \frac{-1}{4\pi} \iint X'^m Y'^n b_Y' \frac{\partial}{\partial X} \left(\frac{1}{r} \right) R_n \, dX'dY' \quad (46a)$$

$$I_{Xb_Z}^{mn} = \frac{-1}{4\pi} \iint X'^m Y'^n b_Z' \frac{\partial}{\partial X} \left(\frac{1}{r} \right) R_n \, dX'dY' \quad (46b)$$

$$I_{Xa_Z}^{mn} = \frac{-1}{4\pi} \iint X'^m Y'^n a_Z' \frac{\partial}{\partial X} \left(\frac{1}{r} \right) R_n \, dX'dY' \quad (46c)$$

$$I_{Yb_X}^{mn} = \frac{-1}{4\pi} \iint X'^m Y'^n b_X' \frac{\partial}{\partial Y} \left(\frac{1}{r} \right) R_n \, dX'dY' \quad (46d)$$

$$I_{Yb_Z}^{mn} = \frac{-1}{4\pi} \iint X'^m Y'^n b_Z' \frac{\partial}{\partial Y} \left(\frac{1}{r} \right) R_n \, dX'dY' \quad (46e)$$

$$I_{Ya_X}^{mn} = \frac{-1}{4\pi} \iint X'^m Y'^n a_X' \frac{\partial}{\partial Y} \left(\frac{1}{r} \right) R_n \, dX'dY' \quad (46f)$$

$$I_{Ya_Z}^{mn} = \frac{-1}{4\pi} \iint X'^m Y'^n a_Z' \frac{\partial}{\partial Y} \left(\frac{1}{r} \right) R_n \, dX'dY' \quad (46g)$$

$$I_{Zb_X}^{mn} = \frac{-1}{4\pi} \iint X'^m Y'^n b_X' \frac{\partial}{\partial Z} \left(\frac{1}{r} \right) R_n \, dX'dY' \quad (46h)$$

$$I_{Zb_Y}^{mn} = \frac{-1}{4\pi} \iint X'^m Y'^n b_Y' \frac{\partial}{\partial Z} \left(\frac{1}{r} \right) R_n \, dX'dY' \quad (46i)$$

$$I_{Za_X}^{mn} = \frac{-1}{4\pi} \iint X'^m Y'^n a_X' \frac{\partial}{\partial Z} \left(\frac{1}{r} \right) R_n \, dX'dY' \quad (46j)$$

If the order of the value $Z'=Z_B(X',Y')$ is small, then

$$\frac{1}{r} \simeq \frac{1}{\rho} + \frac{Z}{\rho^3} Z' + \frac{1}{2}\left\{ \frac{-1}{\rho^3} + \frac{3Z^2}{\rho^5} \right\} Z'^2 + \ldots \tag{47}$$

$$\frac{1}{r^3} \simeq \frac{1}{\rho^3} + \frac{3Z}{\rho^5} Z' + \frac{1}{2}\left\{ \frac{-3}{\rho^5} + \frac{15Z^2}{\rho^7} \right\} Z'^2 + \ldots \tag{48}$$

$$r = \sqrt{(X-X')^2 + (Y-Y')^2 + (Z-Z')^2} \tag{49}$$

$$\rho = \sqrt{(X-X')^2 + (Y-Y')^2 + Z^2} \tag{50}$$

$$R_n \simeq 1 + \frac{1}{2}\left\{ \left(\frac{\partial B}{\partial X'} \right)^2 + \left(\frac{\partial B}{\partial Y'} \right)^2 \right\} + \ldots \tag{51}$$

$$b'_X R_n \simeq - \frac{\partial B}{\partial X'} \frac{\partial B}{\partial Y'} + \ldots \tag{52a}$$

$$b'_Y R_n \simeq 1 + \frac{1}{2} \left(\frac{\partial B}{\partial X'} \right)^2 + \ldots \tag{52b}$$

$$b'_Z R_n \simeq - \frac{\partial B}{\partial Y'} + \ldots \tag{52c}$$

$$a'_X R_n \simeq 1 + \frac{1}{2} \left(\frac{\partial B}{\partial Y'} \right)^2 + \ldots \tag{52d}$$

$$a'_Z R_n \simeq - \frac{\partial B}{\partial X'} + \ldots \tag{52e}$$

If it is assumed that

$$Z' = Z_B(X',Y') \simeq d_{10}X' + d_{01}Y' + \frac{1}{2} d_{20}X'^2 + d_{11}X'Y' + \frac{1}{2} d_{02}Y'^2 + \ldots \tag{53}$$

and the function H_{mnk} is defined as

$$H_{mnk} = \frac{-1}{4\pi} \iint_{S1} X'^m Y'^n \rho^k \, dX'dY' \tag{54}$$

and if the 2nd order of Z' is negrected, then

$$\begin{aligned} G_{Xmn} \simeq & - d_{10}(X H_{m,n,-3} - H_{m+1,n,-3}) \\ & - d_{20}(X H_{m+1,n,-3} - H_{m+2,n,-3}) \\ & - d_{11}(X H_{m,n+1,-3} - H_{m+1,n+1,-3}) \\ & + \ldots \end{aligned} \tag{55a}$$

$$\begin{aligned} G_{Ymn} \simeq & - d_{01}(Y H_{m,n,-3} - H_{m,n+1,-3}) \\ & - d_{11}(Y H_{m+1,n,-3} - H_{m+1,n+1,-3}) \\ & - d_{02}(Y H_{m,n+1,-3} - H_{m,n+2,-3}) \\ & + \ldots \end{aligned} \tag{55b}$$

$$\begin{aligned} G_{Zmn} \simeq & Z H_{m,n,-3} - d_{10} H_{m+1,n,-3} - d_{01} H_{m,n+1,-3} \\ & - \frac{1}{2} d_{20} H_{m+2,n,-3} - d_{11} H_{m+1,n+1,-3} \\ & - \frac{1}{2} d_{02} H_{m,n+2,-3} \\ & + 3Z^2 d_{10} H_{m+1,n,-5} + 3Z^2 d_{01} H_{m,n+1,-5} \\ & + \frac{3}{2} Z^2 d_{20} H_{m+2,n,-5} + 3Z^2 d_{11} H_{m+1,n+1,-5} \\ & + \frac{3}{2} Z^2 d_{02} H_{m,n+2,-5} \\ & + \ldots \end{aligned} \tag{55c}$$

$$\begin{aligned} G_{0mn} \simeq & H_{m,n,-1} + Z d_{10} H_{m+1,n,-3} + Z d_{01} H_{m,n+1,-3} \\ & + \frac{1}{2} Z d_{20} H_{m+2,n,-3} + Z d_{11} H_{m+1,n+1,-3} \\ & + \frac{1}{2} Z d_{02} H_{m,n+2,-3} \\ & + \ldots \end{aligned} \tag{56}$$

$$\begin{aligned} H_X^{mn} \simeq & - (X H_{m,n,-3} - H_{m+1,n,-3}) \\ & - 3Z d_{10}(X H_{m+1,n,-5} - H_{m+2,n,-5}) \\ & - 3Z d_{01}(X H_{m,n+1,-5} - H_{m+1,n+1,-5}) \\ & - \frac{3}{2} Z d_{20} (X H_{m+2,n,-5} - H_{m+3,n,-5}) \\ & - 3Z d_{11}(X H_{m+1,n+1,-5} - H_{m+2,n+1,-5}) \\ & - \frac{3}{2} Z d_{02}(X H_{m,n+2,-5} - H_{m+1,n+2,-5}) \\ & + \ldots \end{aligned} \tag{57a}$$

$$\begin{aligned} H_Y^{mn} \simeq & - (Y H_{m,n,-3} - H_{m,n+1,-3}) \\ & - 3Z d_{10}(Y H_{m+1,n,-5} - H_{m+1,n+1,-5}) \\ & - 3Z d_{01}(Y H_{m,n+1,-5} - H_{m,n+2,-5}) \\ & - \frac{3}{2} Z d_{20} (Y H_{m+2,n,-5} - H_{m+2,n+1,-5}) \\ & - 3Z d_{11}(Y H_{m+1,n+1,-5} - H_{m+1,n+2,-5}) \\ & - \frac{3}{2} Z d_{02} (Y H_{m,n+2,-5} - H_{m,n+3,-5}) \\ & + \ldots \end{aligned} \tag{57b}$$

$$\begin{aligned} H_Z^{mn} \simeq & - Z H_{m,n,-3} \\ & + d_{10} H_{m+1,n,-3} + d_{01} H_{m,n+1,-3} \\ & + \frac{1}{2} d_{20} H_{m+2,n,-3} + d_{11} H_{m+1,n+1,-3} \\ & + \frac{1}{2} d_{02} H_{m,n+2,-3} \\ & - 3Z^2 d_{10} H_{m+1,n,-5} - 3Z^2 d_{01} H_{m,n+1,-5} \\ & - \frac{3}{2} Z^2 d_{20} H_{m+2,n,-5} - 3Z^2 d_{11} H_{m+1,n+1,-5} \end{aligned}$$

$$- \frac{3}{2} Z^2 d_{02} H_{m,n+2,-5}$$

$$+ \ldots \quad (57c)$$

$$I^{mn}_{Xb_Y} \simeq H^{mn}_X \quad (58a)$$

$$I^{mn}_{Xb_Z} \simeq - d_{01}(X H_{m,n,-3} - H_{m+1,n,-3}) - d_{11}(X H_{m+1,n,-3} - H_{m+2,n,-3}) - d_{02}(X H_{m,n+1,-3} - H_{m+1,n+1,-3})$$

$$- \ldots \quad (58b)$$

$$I^{mn}_{Xa_Z} \simeq - d_{10}(X H_{m,n,-3} - H_{m+1,n,-3}) - d_{20}(X H_{m+1,n,-3} - H_{m+2,n,-3}) - d_{11}(X H_{m,n+1,-3} - H_{m+1,n+1,-3})$$

$$- \ldots \quad (58c)$$

$$I^{mn}_{Yb_X} \simeq 0.0 \quad (58d)$$

$$I^{mn}_{Yb_Z} \simeq - d_{01}(Y H_{m,n,-3} - H_{m,n+1,-3}) - d_{11}(Y H_{m+1,n,-3} - H_{m+1,n+1,-3}) - d_{02}(Y H_{m,n+1,-3} - H_{m,n+2,-3})$$

$$- \ldots \quad (58e)$$

$$I^{mn}_{Ya_X} \simeq H^{mn}_Y \quad (58f)$$

$$I^{mn}_{Ya_Z} \simeq - d_{10}(Y H_{m,n,-3} - H_{m,n+1,-3}) - d_{20}(Y H_{m+1,n,-3} - H_{m+1,n+1,-3}) - d_{11}(Y H_{m,n+1,-3} - H_{m,n+2,-3})$$

$$- \ldots \quad (58g)$$

$$I^{mn}_{Zb_X} \simeq 0.0 \quad (58h)$$

$$I^{mn}_{Zb_Y} \simeq H^{mn}_Z \quad (58i)$$

The formulae mentioned above can be used for the calculation in various higher order panel methods. The function H_{mnk} is calculated using the recurrence formulae (APPENDIX).

The numerical method of calculation of Φ_W for vortex wake is the same as that of Φ_D in principle. In case of Φ_W, the value $\Phi_{TU}-\Phi_{TL}$ is constant along the stream line, and the integral domain is extended to infinity. So the analytical integration along stream line is convenient in case of simple vortex wake such as the wing. The value $\Phi_{TU}-\Phi_{TL}$ is connected to the unknown Φ on the body surface. The description of the analytical integration is omitted here.

5.3 Numerical Calculation

Numerical calculation was performed using the three methods based on the formulae presented in the previous section. Method 1, Method 2, and Method 3 are based on the integral equation (17), the integral equation (21), and the simultaneous integral equations (28a),(28b), respectively. The programs were examined by comparison of the numerical results with the analytical value for a sphere and an ellipsoid.

5.3.1 Rectangular Wing

The calculation was performed for the rectangular wing with aspect ratio 2 and thickness ratio 11% (16). The form of the wing is Boeing TR17 airfoil section and the angle of attack is 0.1 rad.(Fig.18)

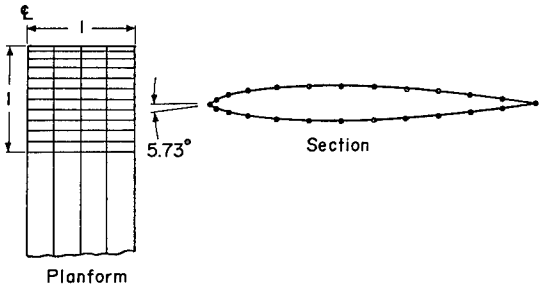


Fig. 18 Configuration of Rectangular Wing

The results of the calculation by Method 1 are shown in Fig.19 with the comparison with the results presented in the reference (16). Number of panels is 12 in chordwise and 10 in spanwise. Low order panel method is used in the calculation. In the low order method the strength of the singularity is constant in a panel and the configuration of the panel is flat. Agreement between the present results and the reference is good except at the panels adjoining to the leading edge, the trailing edge, or the tip.

Results of the calculation by Method 2 are shown in Fig.20. They are similar to that by Method 1 except near the leading edge, the trailing edge, and the tip. In Method 1 and Method 2, special Kutta condition at the trailing edge was not used. Only boundary condition (17) or (21) on each panel was used.

On the other hand Method 3 without Kutta condition can not supply the suitable lift. Method 3 needs the Kutta condition at the trailing edge in addition to the boundary condition (28). Therefore, in case of Method

3, the total number of the boundary conditions is larger than the number of unknowns. The method of least squares was used for minimizing the error of boundary conditions. The pressure condition at the trailing edge was used for the Kutta condition, and consequently Newton Raphson method was employed to satisfy the non-linear condition. As the result Method 3 requires large amounts of computer time and storage. Fig.21 is the results by Method 3. Higher order panel method is employed in the calculation. Number of panels is 8 in chordwise and 10 in spanwise. The results are good in spite of a smaller number of panels.

5.3.2 Circular Wing

The calculation was performed for the circular wing, and the results were compared with the experiment. The form of the section of the wing is NACA0009 (Fig.22). The angle of attack is 5 degrees. Experiment was performed in a wind tunnel. The detail of the experiment is shown in Ref.(5). Pressure coefficients C_p obtained by the measurement, by the panel methods, and by the ordinary method based on the lifting surface theory are compared. The results by Method 1, 2, and 3 are shown in Figs. 23, 24, and 25 respectively.

The value $-C_p$ obtained by the panel method is lower than that by the ordinary method based on the lifting surface theory in general. This result is coincident with the prediction discussed in section 2.4. Near the trailing edge the results by the panel method are closer to experimental one than that by the ordinary method. The results by the panel methods at $y/b = \eta = 0.707$ are close upon experiment. But the results by the three panel methods do not coincide with each other near leading edge and near tip ($\eta = 0.924$). This is a problem by which the numerical technique in the panel method is confronted. The reason of the feature that the experimental results at $\eta = 0.383$ are closer to the results by the ordinary method than to that by the panel method, is not clear.

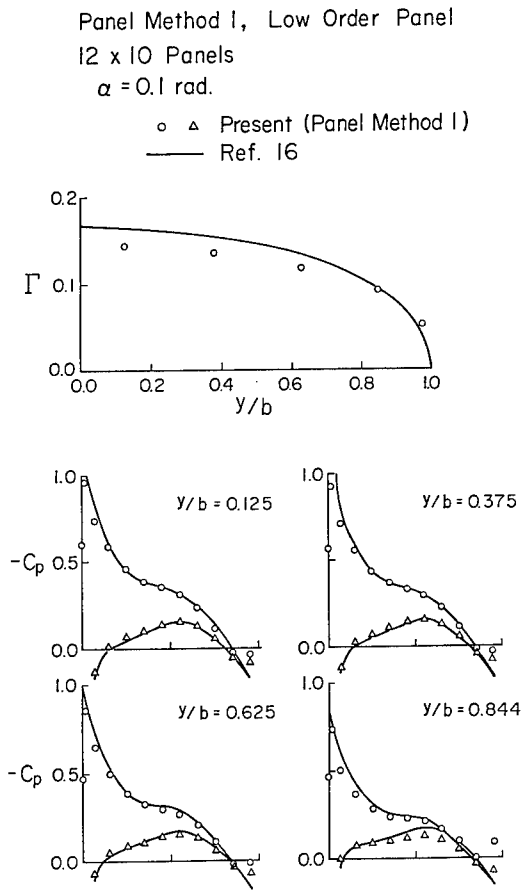


Fig. 19 Calculation for the Rectangular Wing by Method 1 (α = 0.1 rad.)

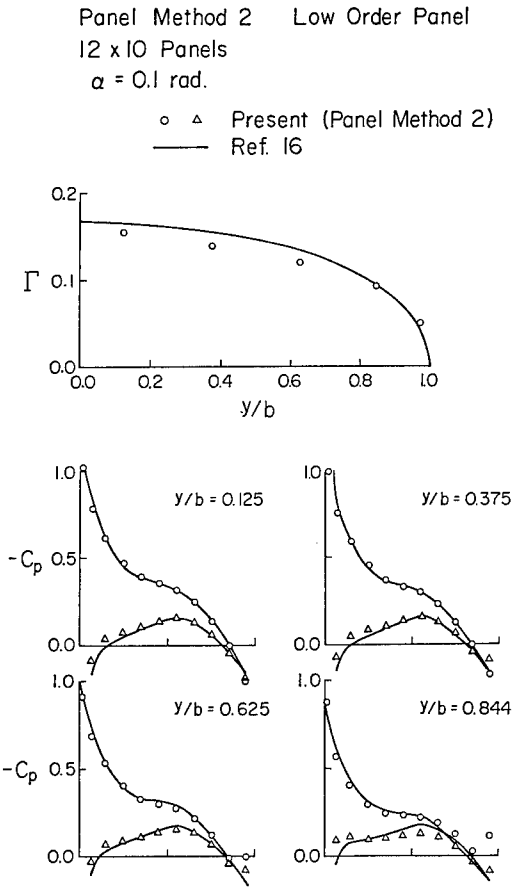


Fig. 20 Calculation for the Rectangular Wing by Method 2 (α = 0.1 rad.)

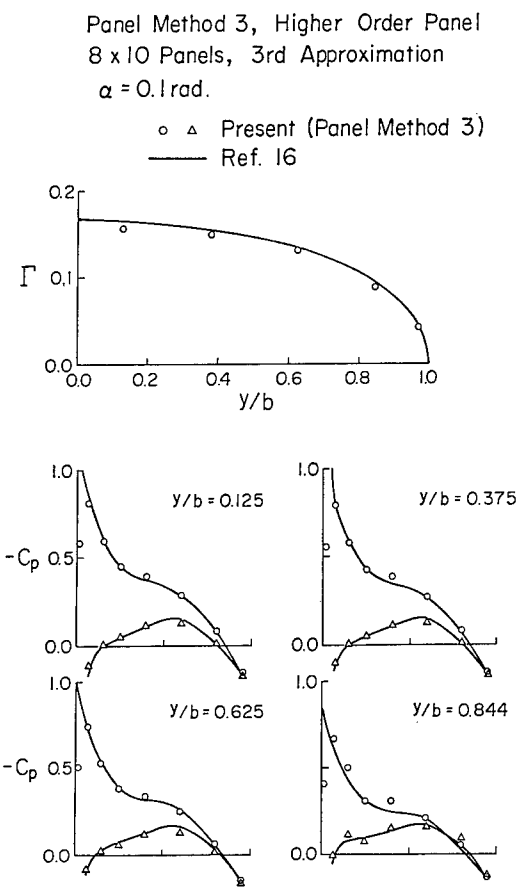


Fig. 21 Calculation for the Rectangular Wing by Method 3 (α = 0.1 rad.)

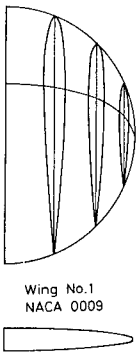


Fig. 22 Configuration of Circular Wing

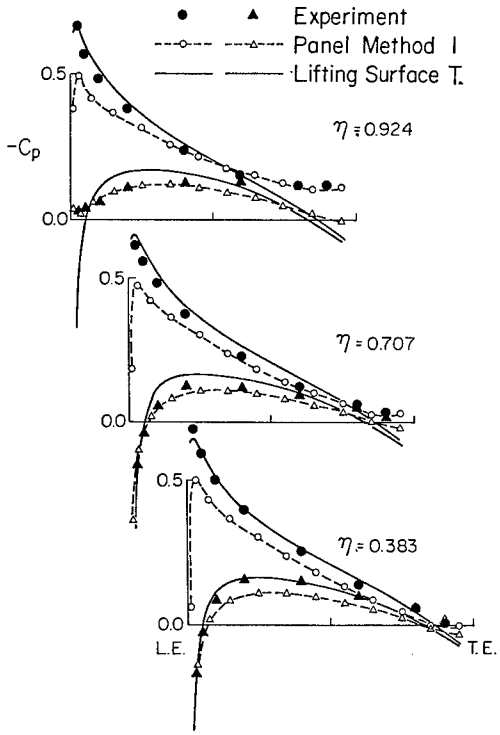


Fig. 23 Pressure Distribution of Circular Wing by Method 1 (α = 5 deg.)

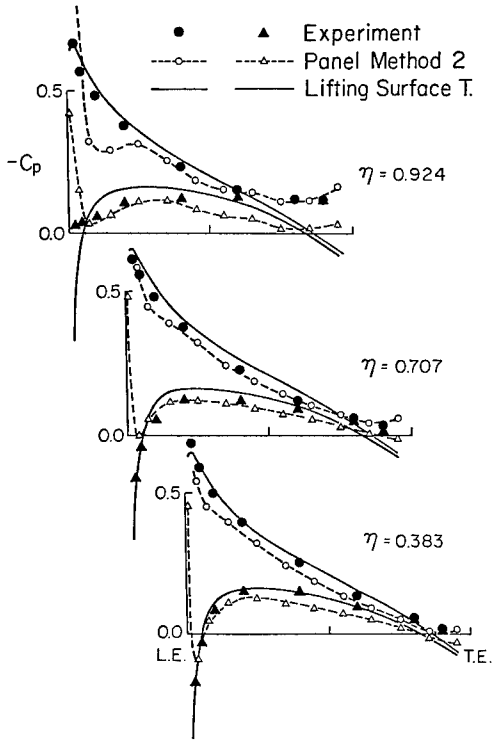


Fig. 24 Pressure Distribution of Circular Wing by Method 2 (α = 5 deg.)

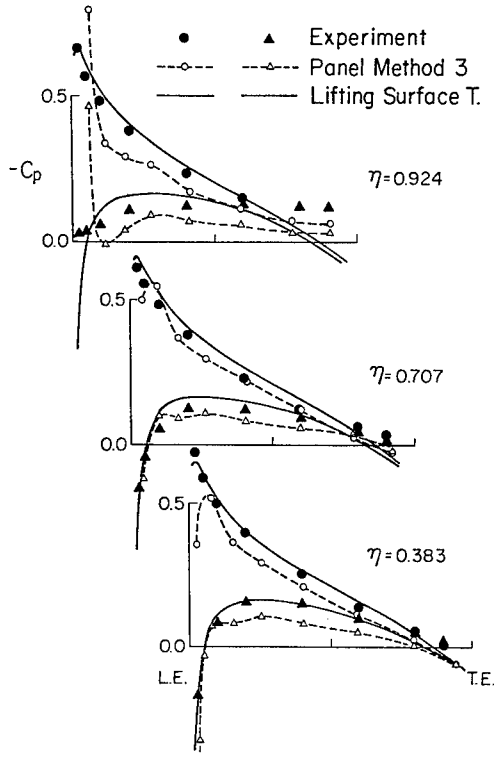


Fig. 25 Pressure Distribution of Circular Wing by Method 3 (α = 5 deg.)

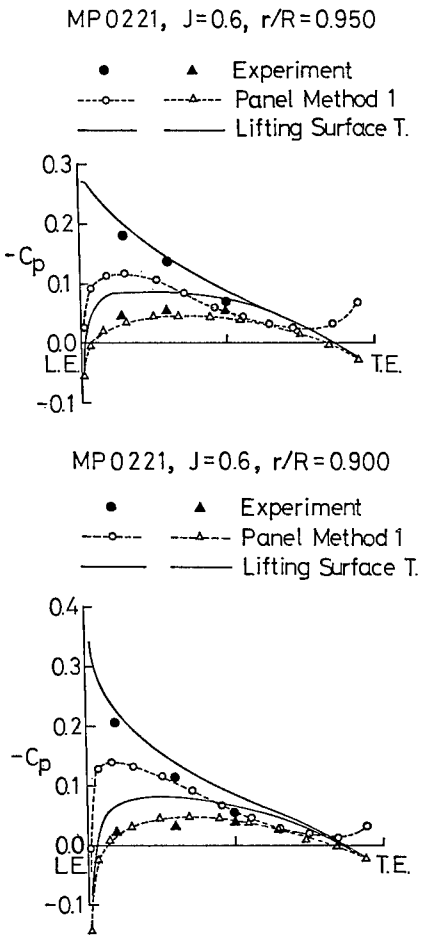


Fig. 26 Pressure Distribution on Propeller Blade by Method 1 (MP0221, J = 0.6)

5.3.3 Propeller Blade

The panel method (Method 1) was applied to the calculation of the propeller blade presented in section 2. The example of the calculation for MP0221 is shown in Fig.26. Unlike the ordinary method based on the lifting surface theory, the result by the panel method is close to the experiment for the face side of the blade. The value $-C_p$ obtained by the panel method is lower than that by the ordinary method, which is coincident with the prediction discussed in section 2.4. It is considered to be the numerical problem to be solved in future that the results by the panel method is not so close to the experiment on the back side near the leading edge and near the tip.

6. CONCLUSIONS

In order to investigate the hydrodynamic characteristics of marine propellers, the experimental study was performed. The measurement of pressure on propeller blades was carried out using small pressure gauges. The measurement of velocity distribution around propeller blade was carried out using Laser Doppler Velocimeter. The comparison between the theory and the experiment showed the direction of the improvement of the propeller theory.

One of the new directions of the improvement was the complete treatment of the three dimensional flow around blades with thickness. In order to analyze the three dimensional potential flow around thick blades of a propeller, a panel method was applied. The panel method surmounted the shortcomings of the ordinary method based on the lifting surface theory. The results of improvement in the pressure on blade by the panel method were presented.

Another new direction of the improvement of the propeller theory is the treatment of the separated flow in the region extended along the leading edge to the blade tip. This is a subject to be studied in future.

In the results of calculations presented in this paper, we can see the state of the accuracy level of the propeller analysis method based on the potential theory.

REFERENCES

1. Takahashi,M. and Oku,M.,"The Cavitation Characteristics of MAU type Propeller, The

First Report: Pressure Distribution on Blade Surface in Uniform Flow," J. of the Society of Naval Architects of Japan, Vol.141, June 1977.

2. Yamasaki,T.,"On Some Tank Test Results with a Large Model Propeller - 0.95m in Diameter - Part 1 -," J. of the Society of Naval Architects of Japan, Vol.144, June 1978.

3. Takei,Y., Koyama,K., and Kurobe,Y., "Measurement of Pressures on a Blade of a Propeller Model", Papers of Ship Research Institute,No.55, March 1979.

4. Versmissen,G.G.P. and Gent,W.van, "Hydrodynamic Pressure Measurements on a Ship Model Propeller," 14th Symposium on Naval Hydrodynamics,Washington,1982.

5. Koyama,K. "On Application of the Lifting Surface Theory to Marine Propellers, 13th Symposium on Naval Hydrodynamics,Tokyo, 1980.

6. Koyama,K., Takei,Y., Kurobe,Y., and Kakugawa,A.,"A Method for Treating the Singularity at the Blade Tip of Marine Propellers (Third Report)", J. of the Society of Naval Architects of Japan, Vol.153, June 1983.

7. Biggers,J.C., Lee,A., Orloff,K.L., and Lemmer,O.J., "Measurements of Helicopter Roter Tip Vortices," Proc. 33rd Annual National Forum of the American Helicopter Society, Washington, D.C. May 1977.

8. Lepicovsky,J. and Bell,W.A., "Aerodynamic Measurements About a Rotating Propeller with a Laser Velocimeter," J. Aircraft, Vol.21, No.4, April 1984.

9. Jessup,S.D.,Scott,C.,Jeffers,M., and Kobayashi,S., "Local Propeller Blade Flows in Uniform and Sheared Onset Flows Using LDV Techniques," 15th Symposium on Naval Hydrodynamics, Hamburg, 1984.

10. van Manen,J.D., "Fundamentals of Ship Resistance and Propulsion - Part B - Propulsion," Int. Shipbuild. Prog., Vol.4, No.34, 1957.

11. Garner,H.C. and Bryer,D.W., "Experimental Study of Surface Flow and Part-Span Vortex Layers on a Cropped Arrowhead Wing," A.R.C., R.& M. No.3107, 1957.

12. Hunt,B.,"The Panel Method for Subsonic Aerodynamic Flows : A Survey of Mathematical Formulations and Numerical Methods and an Outline of the New British Aerospace Scheme," Computational Fluid Dynamics, edited by Kollmann,W., Hemisphere Publishing Corp.,1978.

13. Hess,J.L., and Smith,A.M.O., "Calculation of Potential Flow About Arbitrary Bodies," Progress in Aeronautical Sciences, Vol.8, Pergamon Press, New York, 1966.

14. Morino,L. and Kuo,C.C., "Subsonic Potential Aerodynamics for Complex Configurations : A General Theory," AIAA J., Vol.12, No.2, Feb. 1974.

15. Maskew,B., "Prediction of Subsonic Aerodynamic Characteristics : A Case for Low-Order Panel Methods," J. Aircraft, Vol.19, No.2, Feb. 1982.

16. Johnson,F.T., "A General Panel Method for the Analysis and Design of Arbitrary Configurations in Incompressible Flows," NASA CR-3079, May 1980.

17. Grodtkjaer,E., "A Direct Integral Equation Method for the Potential Flow about Arbitrary Bodies," Int. J. Numerical Methods in Engineering, Vol.6, No.2, 1973.

18. Ebihara,M., "A Method for the Calculation of Lifting Potential Flow Problems (1) Theoretical Basis," Tech. Rep. of National Aerospace Laboratory (Japan),TR-240T, July 1971.

19. Ling,Z.,Sasaki,Y., and Takahashi,M., "Analysis of Three-Dimensional Flow around Marine Propeller by Direct Formulation of Boundary Element Method (1st Report : in Uniform Flow)," J. of the Society of Naval Architects of Japan, Vol.157, June 1985.

APPENDIX Recurrence Formulae for Function H_{mnk}

The function

$$H_{mnk} = \frac{-1}{4\pi} \iint_{SI} X'^{m} Y'^{n} \rho^{K} \, dX'dY'$$

$$\rho = \sqrt{(X-X')^2 + (Y-Y')^2 + Z^2}$$

can be calculated with the aid of the following recurrence formulae, provided that the integral surface SI is a polygon on X'Y' plane.

If we define the function

$$H(M,N,K) = \iint_{SI} \frac{(X-X')^M (Y-Y')^N}{\rho^K} \, dX'dY'$$

then, function H_{mnk} can be expressed with a linear combination of H(M,N,K) . Recurrence formulae for H(M,N,K) is given as follows

$$H(M+2,N,K) = \frac{M+1}{K-2} H(M,N,K-2) + \Sigma \frac{1}{K-2} F_{\xi}(M+1,N,K-2)$$

$$H(M,N+2,K) = \frac{N+1}{K-2} H(M,N,K-2) + \Sigma \frac{1}{K-2} F_{\eta}(M,N+1,K-2)$$

$$(K-M-N-2)H(M,N,K) = K Z^2 H(M,N,K+2) + \Sigma F_{\xi}(M+1,N,K) + \Sigma F_{\eta}(M,N+1,K)$$

where Σ indicates the summation of all sides of the polygon, and

$$F_{\xi}(M,N,K) = \int_{Y_1}^{Y_2} \frac{(X-X_{12})^M (Y-Y')^N}{\rho^K} \, dY'$$

$$F_{\eta}(M,N,K) = -\int_{X_1}^{X_2} \frac{(X-X')^M (Y-Y_{12})^N}{\rho^K} \, dX'$$

$$X_{12} = X_{12}^0 + X_{12}^1 Y'$$

$$Y_{12} = Y_{12}^0 + Y_{12}^1 X'$$

(X_1,Y_1), (X_2,Y_2) indicate the coordinates of the edges of the side.

If we define the functions

$$I_\xi(m,k) = \int_{Y_1}^{Y_2} Y'^m \sqrt{a_X Y'^2 + b_X Y' + c_X}^k \, dY'$$

$$I_\eta(m,k) = \int_{X_1}^{X_2} X'^m \sqrt{a_Y X'^2 + b_Y X' + c_Y}^k \, dX'$$

then, functions $F_\xi(M,N,K)$, $F_\eta(M,N,K)$ are expressed with a linear combination of $I_\xi(m,k)$, $I_\eta(m,k)$, respectively. In order to calculate the functions $I_\xi(m,k)$, $I_\eta(m,k)$, the following formulae are used.

$$I(m,k) = \int x^m \sqrt{a x^2 + b x + c}^k \, dx$$

$$I(m,k) = \frac{1}{(m+k+1)a} \{ x^{m-1} \sqrt{a x^2 + b x + c}^{k+2} - \frac{(2m+k)b}{2} I(m-1,k) - (m-1) c I(m-2,k) \},$$

$$, \quad (m + k \neq -1)$$

$$I(m,k) = a I(m+2,k-2) + b I(m+1,k-2) + c I(m,k-2)$$

$$I(0,k) = \frac{2(2ax+b)}{(k+2)(b^2-4ac)} \sqrt{a x^2 + b x + c}^{k+2} + \frac{4(k+3)a}{(k+2)(b^2-4ac)} I(0,k+2)$$

$$, \quad (k \neq -2)$$

$$I(0,-1) = \frac{1}{\sqrt{a}} \log | 2ax+b+ 2 \sqrt{a(ax^2+bx+c)} |$$

$$, (a > 0)$$

We can calculate the value H(M,N,K) by these recurrence formulae, provided that H(0,0,1) is known. Analytical expressions for H(0,0,1), H(0,0,3), H(1,0,3), H(0,1,3) are given in low order panel method (13)

DISCUSSION

Chang-Gu Kang,
University of Michigan

Your theory removes the leading edge singularity of pressure in the lifting surface theory. How did you remove this singularity?

Why didn't you take into consideration the thickness effects in your theory?

Hyoung-Tae Kim,
Iowa Institute of Hydraulic Research

a. In your measurement of velocity components just behind the propeller (in Fig. 12(a),(b),(c)), peaks in each component seem to show the clear effect of rolled-up tip vortex behind the propeller. Could you explain how this rolled-up vortex influence each of the velocity components? As I know, similar measurements in MIT Cavitation Tunnel (Kobayashi & Wang, 1985) showed the difference of the locations (in θ) of peaks of each velocity components. Could you tell me, what is the reference in Fig. 12(a),(b),(c) and would you comment on the difference between your measurement and those of MIT, with respect to the location of the peaks of velocity components. Did you see the roll-up of vortex-sheet near the hub (blade-root)? Did you examine the hub vortex formulation? Do you have plans to measure the turbulence quantities also?

b. I understand that some propeller programs, for instance MIT-PUF2, PSF2, etc., include modifications to reduce the leading-edge singularity suction force empirically by 1/3. What is the meaning of the paragraph "removes the leading-edge singularity" in your paper. What is the Lifting Surface Method in your paper? Do you solve the lifting problem and non-lifting problem separately? Would you explain how to model propeller wake in your numerical calculation?

Reply -

In reply to Dr. Kang's discussion and Dr. Kim's 2nd discussion, I have to describe the ordinary theoretical method which is employed for the calculation of pressure distribution on a blade in our paper. In this ordinary theoretical method, which is popular in Japan, the camber effect and the thickness effect are treated separately. (Fig. 27 below)

The camber effect is calculated by lifting surface theory which is available for three-dimensional thin wings. The details of the lifting surface theory used in our paper is presented in Ref. 5. The propeller wake is modeled by a doublet distribution on the helical surface with constant stength along the mean streamline, which is of constant radius. The rolling-up of the wake is not taken into account in the model. The calculation supplies the pressure distribution for singularity at the leading edge. The pressure distribution for each blade section corresponds to the two-dimensional camber line, which differs from the geometrical camber line at the blade section.

The two-dimensional camber line and the thickness distribution can compose the two dimensional thick wing. The pressure on the two dimensional thick wing can be calculated by the nonlinear thick airfoil theory whichhas no singularity at the leading edge.

In reply to Dr. Kim's 1st discussion, I would like to share our understanding of the rolling-up tip vortex from our measurement data in Fig. 28.

As written in the main body, the velocity induced by the strong tip vortex is found in the axial velocity component and the radial velocity component. The effect of the blade wake appeared in the tangential velocity component. The appearance in the velocity components can be understood by the schematic figure (Fig. 28). The reference in Fig. 12 (a),(b),(c) is the pulse signal from the rotating propeller shaft which is used for the strobescope in the cavitation observation.

We could not find the rolling-up of vortex sheet near the hub. The hub vortex formulation and the turbulence intensity analysis are considered to be important study in the future.

K. Nakatake,
Kyushu University Hakozaki

According to our experience to calculate the lift and the pressure distribution on the 3-D wing by using Hess, the panel method, it is not easy to get a stable and accurate value of the lift compared with the lifting surface theory. What do you think about it?

The propellers named MP0221, 0222 and 0199 seem to have peculiar shapes and blade sections. What is the reason to select such propellers?

Reply -

In reply to Prof. Nakatake's discussion I would like to describe the panel method. As Prof. Nakatake pointed out, the panel method often gives an inaccurate total lift. Our calculation shows that the shortcoming of the panel method is caused by the inaccurate results of calculation in the region near the leading edge and tip.

Model propellers MP0221,0220,0199 have low aspect ratio blades. The shape of the blade magnifies the hydrodynamic characteristics in the tip region of the conventional propeller blade such as MP0123. Blades of all these three propellers have no camber. One of the function of the propellers is to analyse the effect of thickness separately.

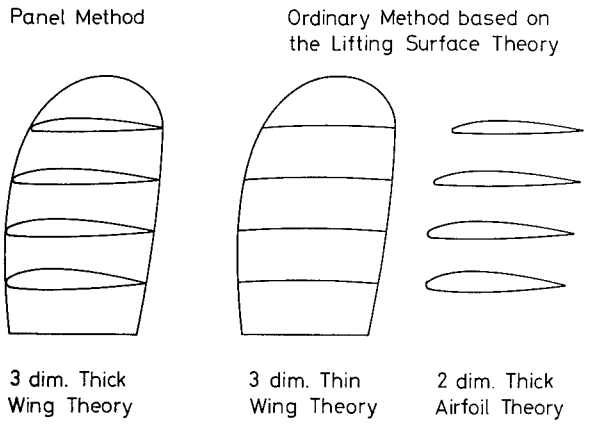


Figure 27. Ordinary theoretical method based on the lifting surface theory.

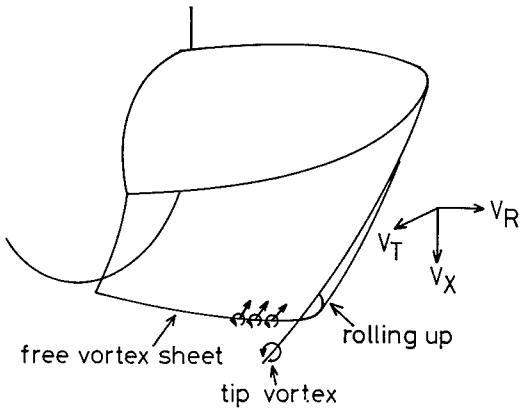


Figure 28. Vortex wake of propeller blade.

Some Time-Dependent Features of Turbulent Appendage-Body Juncture Flows

W.J. DEVENPORT and R.L. SIMPSON

Virginia Polytechnic Institute & State University, U.S.A.

ABSTRACT

The time-dependent and time-averaged features of the wing-body junction flow formed around a wing with a 1.5:1 elliptical nose and a NACA 0020 tail are being studied. The first results of this study are presented.

Surface pressure measurements and oil-flow visualizations have been obtained on the flat wall surrounding the wing. Measurements of mean velocity and turbulent stresses have been made with a single hot-wire probe in the region surrounding the nose of the wing.

Histograms of streamwise velocity fluctuations obtained in the nose region suggest the presence of low-frequency fluctuations in the flow here. These may be due to low frequency changes in the size or position of the junction vortex.

An array of surface hot-wire sensors have been constructed to enable instantaneous spanwise distributions of skin friction to be measured. Some preliminary results of this technique are presented.

NOMENCLATURE

C_p	pressure coefficient, $(p-p_{ref})/(p_o-p_{ref})$
f	frequency, Hz
h	pitch factor of hot-wire probe
k	axial sensitivity of hot-wire probe
n_a	mean frequency of wall-bursting in a turbulent boundary layer
p	static pressure
p_{ref}	static pressure in potential flow at wind tunnel throat
p_o	stagnation pressure in potential flow at wind tunnel throat
Re_θ	Reynolds number based on edge velocity and momentum thickness of approach boundary layer
t	maximum thickness of the wing, 7.17 cm
U	component of velocity in the time-mean flow direction (Fig. 3)
$\bar{U}$	time-mean U
u	fluctuating component of U
U_e	boundary-layer edge velocity
U_{eff}	effective cooling velocity of hot-wire probe
$\bar{U}_{eff}$	time-mean U_{eff}
u_{eff}	fluctuating component of U_{eff}
U_m	shear velocity based on maximum turbulent shearing stress
U_{ref}	velocity of potential flow at wind tunnel throat
U_τ	friction velocity
U^+	$\bar{U}/U_\tau$
V	component of velocity normal to U and W positive away from wall (Fig. 3)
v	fluctuating component of V
W	component of velocity normal to U and parallel to wall (Fig. 3)
w	fluctuating component of W
x	distance measured downstream from the leading edge of the wing (Fig. 3)
y	distance measured normal to the wall (Fig. 3)
y^+	yU_τ/ν
z	spanwise distance measure from the centerline of the wing (Fig. 3)
α	angle between hot-wire probe and mean-velocity vector
δ	boundary-layer thickness
λ_z	spanwise spacing of turbulent-boundary-layer structures
ν	kinematic viscosity, m^2/s
τ	wall-shear stress
$\bar{\tau}$	average time-mean shear stress across the hot-wire array

I. INTRODUCTION

When a laminar or turbulent boundary layer on a surface encounters a protuberance or strut projecting from that surface, a "horseshoe" vortex is formed at the junction of the two surfaces. Upstream of the protuberance the time-averaged vorticity direction in the boundary layer is spanwise

across the surface. In order to satisfy the vortex theorems of fluid dynamics, streamwise legs of this upstream vorticity stretch around the protuberance in a horseshoe shape (Figure 1) with each leg having vorticity of opposite rotational sense. This type of three-dimensional turbulent boundary layer occurs in a number of practical cases, such as in turbomachinery blade and end wall flows, aircraft wing and body junction flows, and ship appendage and hull junction flows.

Dean [1] and Humphreys and vandenBerg [2] reviewed available data for this type of flow in order to select the best test cases for evaluating computational methods [3]. Dean pointed out that little turbulence data had been obtained during 50 years of measurements. Consequently, only the Shabaka [4,5] flow around a flat plate with a 3:1 semi-elliptical nose was recommended as a computational test case for the secondary flow produced by the streamwise vortex legs well downstream of the nose. Humphreys and vandenBerg recommended the Dechow [6] flow as a test case. Turbulence measurements were made in front of and beside the protuberance or obstruction, but not in the presence of adverse pressure gradients. In this case the protuberance was a 320 mm diameter half cylinder with a streamlined afterbody that prevented premature separation upstream of the trailing edge. Pierce's group [7,8,9] have made some time-averaged measurements around the nose of a similar circular-nosed strut.

Computational methods for the mean flow in the corners around a protuberance are not in a satisfactory state, even for the zero pressure gradient case [3]. Dean pointed out the need for measurements of the streamwise vortex corner flow in the presence of adverse pressure gradients for increased understanding and for improvement and verification of computational methods. In many practical applications these adverse pressure gradients cause the vortex strength to be attenuated and the vortex to wander away from the corner [5].

In other work on streamlined struts, Barber [10] showed that the size of the separated flow zone was inversely related to the incident boundary layer thickness (Figure 1). Mehta [11] and Kubendran et al. [12] showed that the circulation in the streamwise corner vortex is much less for a sharp-nosed appendage than for a blunt-nosed one.

McMahon and his co-workers at Georgia Tech [12-15] made measurements on the flow around a protuberance of constant thickness with a 1.5:1 elliptical nose, a case similar to Shabaka's. Dickinson [16] has recently made measurements around a wing with a 1.5:1 elliptical nose and a NACA 0020 tail.

In all of these studies only time-averaged measurements were made. With exception of recent unpublished work by Dickinson, no quantitative measurements were made of flow regions that contain adverse pressure gradients and/or separation. No spectra of the turbulence energy containing frequencies were obtained. No examination was made of the organized time-varying coherent structure of this type of turbulent boundary layer, such as has been done for mean two-dimensional boundary layers, which is briefly discussed in section II below.

Recently, Rood [17] reported relatively low frequency and narrow bandwidth turbulent fluctuations in the three-dimensional boundary layer downstream of a streamlined protuberance with a 1.5:1 elliptical nose. In some practical cases this type of downstream boundary layer passes over other protuberances and structural elements and interacts with them in an undesirable and as yet unpredictable way. Noise is generated when large-scale turbulent structures in this boundary layer interact with these structural elements. When a rotor blade encounters the wake of a strut, tonal noise is generated [18]. It is thought that the organized time-varying coherent structure of these flows may be able to explain such undesirable behavior and to aid in future optimal designs of these structural elements.

Rood found extensive spatial coherence in the vortex flow in two lower frequency bandwidths. Frequencies in one bandwidth ($U_{ref}/f\delta$ = 7 to 24) originated in the nose region of the wing and plate junction. Frequencies in the lower frequency bandwidth ($U_{ref}/f\delta$ = 60 to 600) originated in the trailing edge region of the wing for a circular arc tail section but were not present with a NACA 0020 tail [19]. Hasan et al. [20] also found that the adverse pressure gradient along the flow centerline approaching the 1.5:1 elliptic nose caused the low frequency content of surface pressure fluctuations to increase while decreasing the high frequency content. This effect of an adverse pressure gradient on large-scale structures is the same as observed for two-dimensional flows, as discussed in section II below.

A time-averaged description of the three-dimensional flow downstream of a protuberance, whether from experiments or a calculation method, provides no information on the large-scale time-dependent motions. Since these large-scale time-dependent motions would interact with downstream moving rotor blades differently than for the mean flow, information is needed on the nature of these large-scale structures of a three-dimensional flow downstream of a protuberance. Adverse pressure gradients on the downstream side of a protuberance or strut may cause the individual structures to move away from the corner and agglomerate by pairing, since Shabaka and Bradshaw [5] have noted that the mean flow vortex does wander from the corner under these conditions. Separation, as shown in Figure 1, is likely, with rapidly growing large-scale structure.

Detailed time-averaged measurements, turbulence spectral analysis, and space-time correlations using hot-wire and laser anemometry are needed for a limited number of cases in order to quantify features and to develop scaling relationships for this type of flow. In this continuing research program we

are studying the time-dependent and time-averaged features of the horseshoe-vortex flow around a wing with a 1.5:1 elliptical nose and a NACA 0020 tail. Flows around wings of this shape have also been investigated by Rood [19] and Dickinson [16].

To study the time-mean flow, surface oil-flow visualizations and measurements of wall static pressure are being made. Hot-wire anemometers and a three-component laser anemometer are being employed to measure time-mean velocities and all six components of the Reynolds stress tensor in the region around the leading edge of the wing. These measurements are being made for an approach boundary-layer momentum-thickness Reynolds number Re_θ of 7000. As well as providing information about the flow structure it is hoped that this data will serve as a test case for the development and verification of calculation methods.

We are studying the time-dependent nature of this flow at an approach boundary layer Reynolds numbers between 2500 and 7000. At Re_θ=2500, which occurs in some practical cases, large scale turbulent structures are more clearly coherent than at higher Reynolds numbers [21]. If such structures are amplified or attenuated we would expect to see that at this low Reynolds number. The approach boundary layer is "fully turbulent" at Re_θ=7000. Any turbulent structures observed at this Reynolds number will therefore be representative of high-Reynolds-number flows.

The instantaneous flow is being examined through spectra of the signals of hot-wire probes positioned in the boundary layer. Spectra are being taken upstream, around and downstream of the wing and in the outer part of detached flow regions. We are also using array of surface hot wires arranged across the flow to measure instantaneous distributions of skin friction. Time-averaged skin friction can vary appreciably across a streamwise vortex [22]. As instantaneous variations are even greater we expect the hot-wire array to reveal any meandering of the trailing legs of the junction vortex and any relationship between this movement and the approach boundary layer structure. A similar array of miniature microphones for measuring instantaneous distributions of surface pressure is also being used.

Here we report the first results from this program. The following sections deal with a review of coherent structures in two-dimensional turbulent boundary layers, experimental apparatus and instrumentation, the structure of the approach boundary layer and results of mean pressure measurements, oil-flow visualizations, hot-wire traverses and hot-wire-array measurements made around the wing.

II. COHERENT STRUCTURES IN MEAN TWO-DIMENSIONAL TURBULENT BOUNDARY LAYERS

Mean two-dimensional turbulent boundary layers with a steady freestream are quite complicated themselves and much theoretical and experimental research has been devoted to this subject without complete satisfaction. In this type of flow large-scaled ($1/2\ \delta$) transverse vortex coherent structures [21,23,24,25] are present which govern the bulges in the outer edge of the boundary layer, the entrainment of inviscid free-stream fluid into the boundary layer, the transport of momentum and kinetic energy within the boundary layer, and the quasi-periodicity of the viscous sublayer "bursting" phenomenon. The transverse vortex motions are formed as a result of interactions between low-speed and high-speed fluid elements in the outer region. These vortices grow in size while traveling downstream at a small angle away from the wall. A large-scale structure with greater convection speed will overtake a slower structure and the two will agglomerate or "pair" to form a single large-scale structure after "leap frogging" over one another for a short streamwise distance.

The bursting behavior occurs when low speed fluid lifts off the near wall region into the semi-logarithmic mean velocity profile region of the boundary layer. The frequency of occurrence of the bursting phenomenon scales principally on the mainstream velocity and the shear layer thickness δ. The beginning of a sequence of ejection of low speed fluid from and sweep of higher speed fluid toward the wall region closely correlates with the passage of a transverse vortex [26]. Since the streamwise convection velocity of disturbances in the sublayer is of the order of 12-16 U_τ, these disturbances must emanate from the outer region transverse vortex. This convection velocity is greater than the local mean velocity in the sublayer, while it is less than the mean velocity farther away. The wall region ejections do not move to the outer region and give rise to the contorted edge of the boundary layers [27].

These results suggest a simple flow model for the near wall region. A large scale outer region structure throws some higher velocity fluid toward the wall as a sweep. This fluid has some wallward momentum, so it displaces low velocity fluid that is nearest the wall. The low velocity fluid has lost its streamwise momentum because of viscous stresses near the wall. The displaced fluid forms the ejection which moves up and around the sides of the sweep. A fold between the sweep and ejection fluid results which forms the streamwise rotational motion that has been observed. Because both the low velocity fluid and the high velocity sweep fluid contribute to the average wall shearing stress, then the wall shear velocity U_τ is a normalizing parameter for the spanwise spacing λ_z and the time duration for an ejection to occur. This time is short compared with the lifetime of outer region transverse vortex motions. The time

between sweeps is governed by the large scale outer region structure.

Simpson et al. [25] presented data on the effects of strong adverse pressure gradients on coherent structures. In strong adverse pressure gradient flows, the location of maximum turbulent shearing stress and turbulent mixing is away from the near wall region. Large-scale structures grow rapidly in size due to retardation of the flow and to pairing of upstream large-scale structures. The spanwise size of these structures varies with the square of shear layer thickness. The frequencies of passage of outer region bulges and the wall bursting behavior decrease. The wall bursting mean frequency n_a also scales principally on outer region velocity and length scales with $U_e/\delta n_a \approx 10$. The non-dimensional spanwise spacing of the near wall streamwise rotational motions is given approximately by the relation $\lambda_z U_m/\nu \approx 100$ upstream of separation, where U_m is $(-\overline{uv}_{max})^{1/2}$ or a shear velocity based on the maximum turbulent shearing stress. Simpson et al. [28] show that surface pressure fluctuation spectral content increases at lower frequencies as detachment is approached.

III. EXPERIMENTAL APPARATUS, INSTRUMENTATION AND METHODS

A. Apparatus

1. The wing. The wing shape is shown in Figure 2. It consists of a 1.5:1 elliptical nose and a NACA 0020 tail. The wing is cylindrical, has a maximum thickness of 7.17 cm, a chord of 30 cm and is 22.9 cm high (Figure 3). It was fabricated at VPI on a computer-controlled milling machine. The streamlines produced by the wing in an unbounded potential flow have been calculated and are also shown in Figure 2.

The boundary layer on the wing was tripped to avoid any unsteadiness or uneveness of the flow which might have resulted from natural transition. Trip wires of circular cross-section, 1 mm in diameter, were attached 10 mm upstream of the maximum thickness of the wing. This diameter was chosen according to criteria stated by Schlichting [29] to ensure that the wire would be fully effective at the lowest flow speeds of interest.

2. The wind tunnel. The mainstream flow of the blown open-circuit wind tunnel is introduced into the test section after first passing through a filter, blower, a fixed-setting damper, a plenum, a section of honeycomb to remove the mean swirl of the flow, seven screens to remove much of the turbulence intensity, and finally through a two-dimensional 4:1 contraction ratio nozzle to further reduce the longitudinal turbulence intensity while accelerating the flow to test speed. This tunnel has been used in much previous research both at VPI&SU and earlier at Southern Methodist University.

Figure 4 is a side-view schematic of the 8 m long, 0.91 m wide test section of the wind tunnel. The upper wall is made from plexiglas reinforced with aluminum channel. The side walls are made from float-plate glass (to prevent dispersion of laser anemometer signals) while the test wall was constructed from 19 mm thick fin-form plywood.

In the absence of the wing this flow channel produces a zero-pressure-gradient turbulent boundary layer on the test wall between the locations marked as 1 and 2 on Figure 4. The inviscid core of this flow is uniform to within 0.05% in the spanwise direction and within 1% in the vertical direction with a turbulence intensity of 0.1% at 18 m/s. The test wall boundary layer is tripped by the blunt leading edge of the plywood floor, the height of the step from the wind tunnel contraction to the test wall being 0.63 cm. Smoke can be introduced uniformly into the boundary layer and freestream upstream of this trip for use with the laser anemometer.

The test wall is reinforced every 28 cm with 7.6 x 3.8 x 0.6 cm cross section steel channel. This reinforcement was necessary since test wall vibration amplitudes as small as 0.025 mm can produce up to a 10% error in turbulence measurements in the viscous sublayer near the wall. Such vibrations can be reduced by adding a large amount of mass to the test wall. In the present case the entire weight of the test section rests on the test wall and the steel reinforcements.

The wing was mounted in the center of the test section at zero degrees angle of incidence, with no sweep, with its leading edge 1.39 m downstream of location 1 (Figure 5). As recommended by Dechow [6] a gap of 37 mm was left between the upper end of the wing and the upper wall of the wind tunnel. This gap prevented the formation of a second junction vortex here which could have interfered with the flow on the test wall further downstream. Inserts for the wind-tunnel side walls were constructed to eliminate blockage-induced pressure gradients around the wing. To check that blockage effects were minimal, mean surface pressures obtained from the above potential-flow calculation were compared with measurements made along lines on either side of the wing 22.9 cm from its centerline.

B. Instrumentation and Experimental Methods

1. Oil-flow visualization. Surface-oil-flow visualizations were done on the wind tunnel floor and the wing (Figure 5). To preserve these we used a technique devised by Peter Sutton at Cambridge University for low-speed flows. The technique is as follows.

Opaque black self-adhesive plastic film is applied to the surfaces on which the oil-flow visualization is to be performed. A conventional paint mixture of finely ground titanium dioxide (TiO_2), kerosene and a small amount of oleic acid is used. The relative proportions of these is varied depending on

the magnitude of the shear stresses expected. We found a mixture of 15 parts kerosene, 5 parts TiO_2 and 1 part oleic acid to be ideal for the wing-body junction flow at an approach boundary-layer Reynolds number Re_θ of 7000. After a thin coat of paint has been applied, the wind tunnel is switched on and left running at the desired flow conditions until the paint dries. The plastic film may then be peeled away with the oil-flow record intact on its surface. To make the oil-flow permanent it can be sprayed with a fixer (of the type artists use on charcoal drawings) or it can be covered with clear plastic film. Photocopies may then be made. In fact, a good photocopier can be used to increase or decrease the contrast and improve the record or highlight particular features.

2. Hot wire anemometry. A boundary-layer type single-hot-wire probe (TSI type 1218T1.5) was used to measure mean velocity and three components of the Reynolds stress tensor. The probe was operated using a constant temperature anemometer bridge of the type designed by Miller [30] and modified by Simpson et al. [31]. The frequency response of this combination was found to be flat from zero to 12 kHz at an overheat ratio of 0·7. The bridge output was fed through a TSI amplifier (Type 1015C) into an analogue-to-digital converter and signal processor (Data Precision Data 6000). This was interfaced to an IBM AT computer enabling calibrations and measurements to be made on line.

The probe was fixed in its traverse gear with the sensor wire in the x-z plane parallel to the wind tunnel floor (see Figure 3). The traverse gear allowed the probe to be rotated about an axis normal to the wind tunnel floor passing through the middle of the sensor wire. Thus the sensor wire could be rotated to any angle of yaw while remaining at the same location.

For the purposes of the analysis below and the presentation of measurements we will define U as the component of velocity in the time-mean flow direction, W as the component normal to U and parallel to the wind tunnel floor and V as the component normal to both U and W positive away from the wall, (see Figure 3).

If it is assumed that time-mean velocities normal to the wind tunnel floor are negligible with respect to the magnitude of the mean velocity vector, we may write the effective velocity measured by the above hot-wire as

$$U_{eff}^2 = U^2 (\cos^2\alpha + k \sin^2\alpha) + hV^2 + W^2 (\sin^2\alpha + k \cos^2\alpha) \quad (1)$$

given Jorgensen's equation [32]. Here α is the angle at which the hot-wire probe is yawed relative to the mean-velocity vector. k and h are the axial sensitivity and the pitch factor of the probe respectively.

By ignoring second-order terms equation (1) can be decomposed into

$$\bar{U}_{eff} = \sqrt{A}\,\bar{U} \quad (2)$$

$$\text{and } \overline{u^2}_{eff} = A\,\overline{u^2} + \frac{F^2}{4A}\,\overline{w^2} + F\,\overline{uw} \quad (3)$$

$$\text{where } A = \cos^2\alpha + k \sin^2\alpha \quad (4)$$

$$F = \sin^2\alpha\,(1-k) \quad (5)$$

$$\text{and } U_{eff} = \bar{U}_{eff} + u_{eff} \quad (6)$$

$$U = \bar{U} + u \quad (7)$$

$$W = w \quad (8)$$

So, two measurements of $\bar{U}_{eff}$ (and $\overline{u^2}_{eff}$), made with the probe at two different angles of yaw (about ±30°) can be used to determine the magnitude and relative direction of the mean-velocity vector ($\bar{U}$ and α). A third measurement will yield $\overline{u^2}$, $\overline{w^2}$, $\overline{uw}$ and redundant values of $\bar{U}$ and α. If the third measurement is made with the probe in the near flow direction (α=0) then histograms and spectrum of U may also be obtained.

3. Hot-wire array. An array of surface hot-wires has been constructed to examine the time-dependent structure of the junction vortex by measuring instantaneous distributions of skin friction.

This array (Figure 6) consists of 29 independent sensors, each 2 mm in length, mounted approximately 0.1 mm from the surface. The sensors are arranged in two rows 1 mm apart. The upstream row contains 15 sensors each separated by a gap of 2 mm. The 14 sensors in the downstream row are positioned behind these gaps, the net effect being 29 surface hot wires positioned at 2 mm intervals across the flow.

The array was mounted in a plexiglas block. Stainless steel sewing needles were used for the hot-wire prongs. These were fixed in holes drilled through the block so that their points projected 2 or 3 mm out of the surface. The points were then ground down to produce flat ends 0.1 mm above the surface. The sensors were made from 5 micron-diameter platinum-plated tungsten wire welded to these ends.

15 constant temperature anemometer bridges were available for use with the array. All results presented in this paper were taken with these connected to the upstream row of sensors. The downstream row was not used.

A schematic of the data-acquisition system is shown in Figure 7. The bridge outputs were connected to a 16 channel multiplexer. The output of the multiplexer was fed through an amplifier (Tektronix Type AM502) and into the Data 6000 analogue-to-digital converter and signal processor. The Data 6000 was synchronized using clock and

trigger signals provided by the driving circuits of the multiplexer. The IBM AT computer, interfaced to the DATA 6000, was used to control the system and process and store the data collected. This system allowed a maximum sampling rate of 80 kHz. The 16 multiplexer channels could therefore be scanned as fast as 5000 times a second.

The array was used to measure skin friction by assuming similarity of the instantaneous velocity profile as far as 0.1 mm from the wall. This corresponds to a Y^+ of about 6 for Re_θ=7000 and U_e=26 m/s. It was calibrated in the zero-pressure-gradient turbulent boundary layer produced in the wind tunnel in the absence of the wing. The boundary layer was closely two-dimensional. A regular single hot-wire probe was calibrated (for velocity) and positioned 0.1 mm from the wind tunnel wall at the same streamwise location as the array, but offset 1 cm or so in the spanwise direction. The output from this probe was fed into the unused input channel of the multiplexer. Over 30,000 samples of each multiplexer input were then taken while the edge velocity of the boundary layer was slowly varied. These data were then processed to produce 15 histograms of unlinearized bridge voltage, and one (linearized) histogram of velocity for the regular probe. A calibration curve is then obtained for each of the wires in the array by comparing, percentile by percentile, its unlinearized histogram with the linearized histogram of the regular hot wire. An additional measurement made with the array in the boundary layer, at conditions for which the time-mean skin friction is known (through a Clauser plot for example) then provides the conversion factor between velocity and skin friction. This procedure appears to produce good and consistent calibrations with product-moment correlation coefficients greater than 0.9999.

IV. DESCRIPTION OF THE APPROACH BOUNDARY LAYER

The wing was located more than 30 boundary layer thicknesses downstream of location 1 in Figure 4. This insured the formation of a normal two-dimensional zero-pressure-gradient boundary layer upstream of the wing.

During the first part of this research, detailed turbulence measurements were made of the zero-pressure gradient boundary layer that approaches the wing [33-35]. The temporal structure of this type flow was examined over a range of momentum thickness Reynolds numbers Re_θ between 3200 and 7000. Streamwise spectral and cross-spectral distributions of fluctuations, $\overline{u^2}$, $\overline{v^2}$, $\overline{w^2}$ and $-\overline{uv}$ Reynolds stresses, and surface pressure spectra were obtained to thoroughly document the time-dependent behavior of the zero-pressure gradient turbulent boundary layers approaching the body. This is important so that we can know if the time-dependent narrow frequency bandwidth motions observed by Rood downstream of the wing are due to unusual features of the upstream zero-pressure gradient boundary layer or due to the presence of the wing.

In the absence of the wing, the classical U^+ vs. y^+ "law-of-the-wall" velocity profile with Coles constants exists near the wall. The surface skin friction factor obeys the classical Ludwieg-Tillmann correlation [31]. The mean velocity profile shape factor has the same dependence on skin friction factor as shown in earlier experiments. The flow is a good mean two-dimensional turbulent boundary layer since it closely satisfies the two-dimensional momentum integral equation. The Reynolds shearing stress distributions across this boundary layer were obtained by cross-wire and triple-wire hot-wire anemometer probes [33,35] and are in good agreement with earlier distributions for this type of flow.

Measurements of $\overline{u^2}$ by single, cross-wire, and triple-wire hot-wire anemometers are in good agreement as discussed by Ahn [33].

Measurements of $\overline{v^2}$ by cross-wire and triple-wire probes agree away from the wall where triple-wire measurements are valid [33].

Measurements of triple-wire $\overline{w^2}$ are in agreement with earlier turbulent boundary layer results.

In Figure 8, the streamwise turbulence intensities of the zero pressure gradient flow are shown plotted with inner flow scaling, where the results for Re_θ=5400 are compared with those of Purtell, et al. [36] for the similar Reynolds number (Re_θ=5100). As can be seen, there is a very close agreement between these two data sets. As discussed by Purtell et al., the Reynolds number effect penetrates the boundary layer much deeper in terms of the turbulence intensity than it does for mean velocity. $\frac{\sqrt{u^2}}{U_\tau}$ vs. y^+ is maintained only out to $y^+\sim$20, compared with the mean velocity which is similar throughout the semi-logarithmic region which extends beyond y^+=100. At Re_θ=9000, $\frac{\sqrt{u^2}}{U_\tau}$ vs. y^+ is higher than the other data in the low y^+ region and it is believed to be due to the slight forward-facing step of the wall less than one inch upstream of this particular location. At Re_θ=3300, $\frac{\sqrt{u^2}}{U_\tau}$ vs. y^+ does not collapse on to the other data due to the low Reynolds number effect, as expected.

Figure 9 shows that u fluctuation spectra from single hot-wire data have normal wideband features without any preferred single

frequency [33]. This indicates no appreciable single frequency unsteadiness in this wind tunnel flow. Spectra for v and w obtained by cross and triple wire probes also show normal zero-pressure-gradient flow behavior without any preferred frequency [35].

Ahn [33] shows that u spectral data agree closely with earlier data. From dimensional analysis we know that a n^{-1} or k^{-1} spectral region should exist in the near wall law-of-the-wall region and that a $n^{-5/3}$ or $k^{-5/3}$ "inertial" spectral region should exist at higher frequencies. At the highest frequencies a viscous-dominated spectrum exists. The asymptotic lines 1, 2, and 3 in Figure 9 are those given by Perry et al. [37] as fitting data for these three spectral regions. The data of Ahn for this flow agree with earlier data and have the same dependence on y^+ and Re_θ as shown by Perry et al. The k^{-1} and $k^{-5/3}$ regions intersect at frequencies between 0.7 and 1.4 kHz while the high frequency end of the $k^{-5/3}$ region occurs at 17 kHz to 38 kHz, increasing with Re_θ. Figure 10 shows good agreement of v spectral data with the Klebanoff data at Re_θ=9000.

In work sponsored by NASA, McGrath and Simpson [34] have obtained surface pressure spectra, pressure fluctuation wave speeds, and streamwise and spanwise coherence measurements for this zero-pressure gradient flow. The surface pressure spectra at lower frequencies agree with one another in terms of the outer region non-dimensionalizing variables U_e and the displacement thickness δ_1 (Figure 11). The higher frequency surface pressure fluctuation spectra correlate when non-dimensionalized on wall variables U_τ and ν/U_τ. No discrete preferred frequency was observed in any of these surface pressure fluctuation data. These spectra agree with earlier investigations [34].

V. RESULTS AND DISCUSSION

A. Coordinate System

A right-handed coordinate system (x, y, z) is used to define positions (see Figure 3). Coordinate x is measured parallel to the chord of the wing in the downstream direction, y is measured normal to the wind tunnel floor and z is measured in the spanwise direction normal to x and y. The origin of this coordinate system is the intersection between the wing leading edge and the wind tunnel floor. The maximum thickness of the wing t (7.17 cm) is used to non-dimensionalize distances.

B. Measurements of Time-Mean Wall-Static Pressure

Measurements have been made using the array of static-pressure tappings installed in the test wall around the wing for an approach-boundary-layer Reynolds number Re_θ of 7000. These are presented in Figures 12(a and b) and 13. Pressures are plotted in terms of the coefficient C_p (= $(p-p_{ref})/(p_o-p_{ref})$) based on the static and stagnation pressures (p_{ref} and p_o) measured in the potential flow at the wind tunnel throat using a pitot-static tube (see Figure 5). The uncertainty of these measurements is about $\pm 6 \times 10^{-3}$ in C_p. Measurements made on opposite sides of the wing agree to within their combined uncertainty suggesting that the flow was symmetrical.

Figure 13 shows a perspective view of the pressure distribution. Its basic features, a pressure ridge ahead of the leading edge and deep valleys on either side of the wing near its maximum thickness are qualitatively what would be expected from potential-flow considerations. This pressure distribution bears a close resemblance to that presented by Dickinson [16] for a similar wing-body junction.

C. Oil-Flow Visualization

Oil-flow records obtained at approach-boundary-layer Reynolds numbers Re_θ of 7000 and 4000 are shown in Figures 14 and 15. Ideally the streaks on these diagrams indicate the direction of the time-mean wall shear stress and therefore should lie along the limiting streamlines at the surface. However, pressure forces can be a significant influence if the oil film gets too thick in regions where the shear stresses are small (such as near separation). This effect was minimized by applying the paint very sparingly, but at Re_θ=4000 some accumulation of the oil towards the trailing edge of the wing was unavoidable.

Both figures show a separation point about 0.8 wing thickness upstream of the leading edge, on the centerline of the flow. The separation line springing from this point, as inferred from the streaks, is at first not marked by an accumulation of paint. The paint appears to have accumulated on a line nearer the wing. Large-scale pictures of the nose region (Figures 14(b) and 15(b)) show that this second line is not a separation as the surface streamlines clearly pass through it. The paint streaks suggest that fluid moving upstream from the leading edge, close to the wall, suddenly loses its forward momentum at this second line causing it to be rapidly deflected sideways by steep cross-stream pressure gradients here (Figure 13). This sudden slowing and deflection of the flow appears to have resulted in the build up of paint that forms the second line. These observations are consistent with Dickinson's [16] suggestion that the second line marks the boundary between a region of high surface shear stress close to the wing and one of lower shear stress further away. The distance between the second line and the wing increases with distance downstream. It appears to merge

with the true separation line at about mid chord. At Re_θ=4000 (Figure 15(b)) there is some indication of a secondary attachment line immediately upstream of the leading edge.

Downstream of the maximum thickness the initial separation line grows away from the wing, perhaps indicating some enlargement of the junction vortex in the positive streamwise pressure gradient here. The flow in the corner between the wing and floor separates at about 80% chord at both Reynolds numbers. We noticed that the paint dried quite quickly in the separated flow downstream of the trailing edge suggesting the presence of high time-mean wall shear stresses here.

Figures 14 and 15 give some indication of the effects of the trip on the junction flow. These effects appear to be significantly greater at the lower Reynolds number.

D. Velocity Measurements

Flow velocities have been measured with a single hot-wire probe in the region upstream of the maximum thickness of the wing at an approach boundary-layer Reynolds number Re_θ of 7000. Hot-wire measurements were not made in the region immediately ahead of the wing because instantaneous flow reversals and high velocities normal to the wind tunnel floor were expected here. Velocity measurements are presented in terms of U, the component of velocity in the mean flow direction, W, the component of velocity normal to U and parallel to the wind tunnel floor. The velocity U_{ref} of the potential flow at the wind tunnel throat at location 1 in Figure 4, measured using the pitot-static tube, has been used to non-dimensionalize all velocity measurements.

Figures 16, 17 and 18 show profiles of $\bar{U}/U_{ref}$, $\sqrt{\overline{u^2}}/U_{ref}$ and $\sqrt{\overline{w^2}}/U_{ref}$, measured at locations A, B and C (marked on Figure 14(b)) on the plane of symmetry in the flow approaching separation ahead of the wing. As we would expect, the profiles appear very much as those of a two-dimensional turbulent boundary layer in an adverse pressure gradient. The outer region of the mean-velocity profiles increases in size as separation is neared, while the size of the log-law region decreases. This is accompanied by an increase in the peak turbulence intensity $\sqrt{\overline{u^2}}/U_{ref}$ and in the distance from the wall at which it occurs. In contrast, the profiles of $\sqrt{\overline{w^2}}/U_{ref}$ change little in this region.

Figures 19-22 show profiles of the flow properties measured at locations D, E, F and G (see Figure 14(b)). These locations have been selected as they all lie close to the same limiting streamline at the surface, outside of the line of separation. We would expect the flow along this line to be predominantly pressure driven. Streamwise and cross-stream pressure gradients in a boundary layer exert a much stronger influence on the flow near the wall than on the rest of the flow because of its low velocity. This effect can be clearly seen in the profiles of mean velocity $\bar{U}/U_{ref}$ (Figure 19) and those of flow angle (Figure 20). Here 'flow angle' refers to the angle between the mean-velocity vector and the plane of symmetry.

The mean-velocity profiles (Figure 19) show an acceleration of the flow between locations D and G, under the influence of a favorable streamwise pressure gradient that can be seen in the distribution of wall-static pressure (Figure 13). As we would expect, fluid close to the wall is accelerated most.

The profiles of flow angle measured at D and E show the effects of a cross-stream pressure gradient curving the flow away from the plane of symmetry (Figure 14(b)). As a result flow angles are largest near the wall where the influence of the pressure gradient is greatest. Flow angle decreases rapidly with Y to reach a comparatively small value towards the edge of the boundary layer. Further downstream, at locations F and G, the profiles of flow angle show the effects of a change in sign of the cross-stream pressure gradient and the consequent curvature of the flow back towards the direction of the main stream. As the flow near the wall responds most to this change, the largest flow angle is no longer found at the wall and a peak forms in the distribution of flow angle (Figure 20).

The profiles of turbulence intensity $\sqrt{\overline{u^2}}/U_{ref}$ at locations D, E, F and G are shown in Figure 21. As the flow moves downstream from D to G, a second peak in the turbulence profiles appears very near to the wall. The formation of this peak is accompanied by a fall in the turbulence level over the rest of boundary layer. It seems likely that the new peak is a result of production of turbulence energy close to the wall. This might result from the acceleration of the flow close to the wall observed in the mean-velocity profiles and the increase in the surface shear stress that this implies. The reduction of turbulence intensity over the rest of the boundary layer could also be due in part to the flow acceleration via the same mechanism that reduces the turbulence intensity in a wind tunnel contraction. Figure 22 shows small but significant amounts of the turbulent shear stress $\overline{uw}/U_{ref}^2$ in this region of the flow. The shear stress is positive in all the profiles except very close to the wall at location G.

Figures 23 through 26 compare profiles of flow properties measured outside of the separation line and within the various regions of the separated flow zone 0.35 wing thicknesses downstream of the leading edge. The profile locations are marked in Figure 14(b) as H, I, J and K.

The most noticeable features of the mean-velocity profiles measured within and near the

line of separation (Figure 23) is that they contain minima and maxima, apparently because of some very high velocities close to the wall. Previous workers [16,17] have suggested that this is a result of the junction vortex bringing high velocity fluid from outside the boundary layer into the near-wall region. Near-wall velocities are largest at K, close to the wing, and at J, at the line on which the oil-flow visualization (Figure 14(b)) showed a build-up of pigment. The significance of this line passing through J becomes clearer if we look at the measurements of the turbulence quantities $\sqrt{\overline{u^2}}/U_{ref}$, $\sqrt{\overline{w^2}}/U_{ref}$ and $\overline{uw}/U_{ref^2}$ shown in Figures 24, 25 and 26.

Although the profiles of $\sqrt{\overline{u^2}}/U_{ref}$ (Figure 24) have the same basic form as those measured outside of the separation line, turbulence intensities are unusually high at J, and unusually low at K, closer to the wing. The lateral turbulence intensities $\sqrt{\overline{w^2}}/U_{ref}$ (Figure 25) are also greatest at J, but at all these locations they are unusually large and exceed the streamwise turbulence intensities in the near-wall region. Figure 26 shows that $\overline{uw}/U_{ref^2}$ is still mildly positive in the outer regions of the boundary layer but there is a strong negative shear stress near the wall within the line of separation. At J this negative shear stress is several times greater than elsewhere being of the same order of magnitude as the normal stresses here (Figures 24 and 25).

Results similar to those described above have been obtained in other y-z planes at the leading edge and at the maximum thickness of the wing. Taken together our observations strongly suggest that the line passing through J, observed in the oil-flow visualizations as a build-up of paint, is a line of shear between near-wall fluid of high-velocity close to the wing, and lower velocity further away. This confirms Dickinson's [16] suggestion.

It is almost certain that the high velocity fluid is brought in from outside the boundary layer by the junction vortex. It is difficult to see how this could also be the source of the low velocity fluid. This implies that the line of shear marks the limit of the region in which the junction vortex has a direct influence on the near-wall flow. Consider then flow near the line of symmetry ahead of the wing. The oil flow visualizations (Figures 14 and 15) show a region of separated flow immediately downstream of the line of separation and ahead of the line of shear. The above observation suggests that this separated flow is outside of the direct influence of the junction vortex. We might therefore expect the flow here to be something like that formed by the separation of a two-dimensional boundary layer. The backflow produced by such a separation has little time-mean velocity and produces only small time-mean surface shear stresses. Such a backflow seems a probable source of the low velocity fluid observed outside of the line of shear near location J. In addition, we would expect the nose region to be a source of velocity fluctuations at frequencies characteristic of two-dimensional separated flows. As already noted in the introduction, Rood's [19] measurements show that this is the case.

To further investigate the instantaneous structure of the flow near the line of shear, histograms of streamwise velocity fluctuations were measured close to the wall (Y=0.18 mm) at location J and at location L further upstream (see Figure 14(b)). At L (Figure 27) the histogram has two peaks. At J (Figure 28) the low velocity peak is less marked but still forms a lump on the low-speed side of the distribution. Histograms of this type were not observed further than 0.5 mm from the wall at J or L, nor were they observed at any other locations at which measurements were made.

Double-peaked histograms could be produced by low-frequency coherent side-to-side motions of the line of shear. (These would expose a stationary hot wire at L or J to flow of alternately high and low mean velocity). These could result from low-frequency movement of the junction vortex or perhaps instabilities in the line of shear itself. Work is in progress to examine the possible causes of the double-peaked histograms. At present it seems quite likely that the line of shear is closely associated with a strong source of low-frequency fluctuations in the flow.

E. Measurements Made with the Hot-Wire Array

Preliminary measurements have been made with the array of surface hot wires positioned spanwise across the flow at the trailing edge of the wing (see Figure 14(a)).

Corresponding temporal variations of skin friction for the 15 operational sensors are shown in Figure 29. Figure 30 shows some of the associated instantaneous distributions of surface shear stress (τ). These data have been non-dimensionalized using the average time mean shear stress across the array $\bar{\tau}$. While these figures do not immediately give any clear indication of the spanwise position of the junction vortex they do show some instantaneous spanwise coherence of the flow and large instantaneous fluctuations in the surface shear stress.

Work is underway to establish criteria that will enable us to infer spanwise motions of the junction vortex from these signals or from signals obtained in other parts of the flow.

VI. CONCLUSIONS AND FURTHER WORK

The time-dependent and time-averaged features of the wing-body junction flow formed

around a wing with a 1.5:1 elliptical nose and a NACA 0020 tail are being studied. The first results of this study have been presented.

The boundary layer approaching the wing has been shown to have the statistical and spectral characteritics of a two-dimensional zero-pressure-gradient equilibrium turbulent boundary layer. For an approach boundary-layer Reynolds number Re_θ of 7000 oil-flow visualizations and the distribution of time-mean static pressure on the wall surrounding the wing are similar to those obtained by Dickinson [16] for a wing of the same shape. These measurements demonstrate the symmetry of the time-mean flow.

The oil-flow visualizations show a line of separation that begins at a separation point 0.8 wing thicknesses upstream of the leading edge and extends around the wing. The oil-flow visualizations also highlight a second line. This is formed around the upstream half of the wing a short distance downstream of the line of separation. Measurements of mean-velocity and Reynolds stresses made with a single hot-wire probe in the nose region indicate that this is a line of shear between high velocity fluid near the wing and lower velocity fluid further away. This confirms Dickinson's [16] observations. The line of shear can be seen as the limit of the region in which the junction vortex has a direct influence on the near-wall flow. The high velocity fluid within this region is almost certainly supplied from the free stream by the junction vortex. It is suggested that the low velocity fluid outside this region is supplied from a region of separated flow, near the plane of symmetry ahead of the junction vortex, with characteristics similar to those of a two-dimensional separated flow.

Histograms of streamwise velocity fluctuations measured close to the line of shear exhibit two peaks. These are probably produced by low-frequency side-to-side motions of the line of shear. Such motions could be produced by changes in the size or spanwise position of the junction vortex or by instability in the line of shear itself.

An array of 29 surface hot wires has been built to reveal any spanwise movement or meandering of the junction vortex. A data acquisition system and a calibration scheme have been developed enabling instantaneous spanwise distributions of skin friction to be measured. Preliminary measurements have been made with the array positioned spanwise across the flow at the trailing edge of the wing.

In the near future we intend to use the array at other locations, in particular locations near the maximum thickness of the wing, where the line of shear is still distinct from the line of separation, and in the separated flow downstream of its trailing edge. Work is underway to establish criteria that will enable us to infer spanwise motions of the junction vortex from these results. We hope that simultaneous measurements made with the hot-wire array and a hot-wire probe or microphone positioned in the approach boundary layer will reveal any connection between these motions and the structure of the approach boundary layer. A similar series of measurements is also planned for the array of microphones.

In the near future measurements of mean velocity and all six turbulent stresses will be made with a 3-component laser anemometer in the region upstream of the maximum thickness of the wing. In the longer term hot-wire and laser measurements will also be made downstream of the maximum thickness. Together these data will provide a detailed description of the time-mean flow and will serve as a test case for the development and verification of calculation methods.

ACKNOWLEDGEMENTS

The authors would like to thank Peter Sutton of Cambridge University for his advice on the oil-flow technique and Semih Olcmen of VPI&SU for his help in taking many of the above measurements. This work is sponsored by NAVSEA through NSWC contract N60921-83-G-A165.

REFERENCES

1. Dean, R., "Turbulent Secondary Flow of the First Kind," see Kline et al. [3], 1981, pp. 139-154.

2. Humphreys, D.A. and vandenBerg, B., "Three-Dimensional Turbulent Boundary Layers," see Kline et al. [3], 1980, pp. 162-169.

3. Kline, S.J., Cantwell, B.J. and Lilley, G.M., ed., The 1980-1981 AFOSR-HTTM-Stanford Conferences on Complex Turbulent Flows: Comparison of Computation and Experiment, Vol. 1, 2, and 3, Stanford Univ. Dept. Mechanical Engineering, 1981.

4. Shabaka, I.M.M.A., "Turbulent Flow in an Idealized Wing-Body Junction," Ph.D. Dissertation, Imperial College of Science and Technology, London, 1979.

5. Shabaka, I.M.M.A. and Bradshaw, P., "Turbulent Flow Measurements in an Idealized Wing/Body Junction," AIAA Journal, 19, 1981, pp. 131-132.

6. Dechow, R., Dissertation, Univ. Karlsruhe, see Dechow, R. and Felsch, K.O., Turb. Shear Flows Sym., PA State University, 1977, pp. 9.11-9.20.

7. McAllister, J.E., Pierce, F.J. and Tennant, M.H., "Direct Force Wall Shear Stress Measurement in Pressure-Driven Three-Dimensional Turbulent Boundary Layers," J. Fluids Engrg., 104, 1982, pp. 150-155.

8. Menna, J.D., "Three-Dimensional Turbulent Boundary Layer Upstream and Around a Junction Vortex Flow," Ph.D. Dissertation, VPI&SU, Mechanical Engrg. Dept., 1984.

9. Harsh, M.D., "Experimental Investigation of a Turbulent Junction Vortex," Ph.D. Dissertation, VPI&SU, Mechanical Engrg. Dept., 1985.

10. Barber, T.J., "An Investigation of Strut-Wall Intersection Losses," J. Aircraft, 15, 1978, pp. 576-681.

11. Mehta, R.D., "Effect of Wing Nose Shape on the Flow in a Wing/Body Junction, Aero. J., 1984, pp. 456-460.

12. Kubendran, L.R., McMahon, H. and Hubbartt, J.E., "Turbulent Flow Around a Wing-Fuselage Type Juncture," AIAA-85-0040.

13. Oguz, E.A., "An Experimental Investigation of the Turbulent Flow in the Junction of a Flat Plate and a Body of Constant Thickness," Ph.D. Dissertation, Georgia Inst. Tech., 1981.

14. McMahon, H., Hubbartt, J. and Kubendran, L.R., "Mean Velocities and Reynolds Stresses in a Juncture Flow." NASA CR 3605, 1982.

15. McMahon, H., Hubbartt, J. and Kubendran, L.R., "Mean Velocities and Reynolds Stresses Upstream of a Simulated Wing-Fuselage Juncture," NASA CR 3695.

16. Dickinson, S.C., "Flow Visualization and Velocity Measurements in the Separated Region of an Appendage-Flat Plate Junction," Ninth Biennial Symposium on Turbulence, October 1-3, University Missouri-Rolla, 1984.

17. Rood, E.P., "Experimental Investigation of the Turbulent Large Scale Temporal Flow in the Wing-Body Junction," Ph.D. Dissertation, School of Engineering and Architecture, The Catholic University of America, 1984.

18. Trunzo, R., "The Effect of Inlet Turbulence and Strut-Generated Disturbances on Turbomachinery Noise," M.S. Thesis, Dept. Aero, Engrg., PA State University, 1981.

19. Rood, E.P. and Anthony, D.G., "Tail Profile Effects on Unsteady Large Scale Flow Structure in the Wing and Plate Junction," Forum on Unsteady Flow - 1985, P.H. Rothe, ed., ASME FED-27, 1985, pp. 30-32.

20. Hasan, M.A.Z., Casarella, M.J. and Rood, E.P., "An Experimental Study of the Flow and Wall Preserve Field Around a Wing-Body Junction," Shear Flow-Structure Ineraction Phenomena, A. Akay and M. Reischman, ed., ASME NCA-1, 1985, pp. 89-95.

21. Cantwell, B.J., "Organized Motion in Turbulent Flow," Ann. Rev. Fluid Mech., 13, 1981, pp. 457-515.

22. Westphal, R.V., Eaton, J.K. and Pauley, W.R., "Interaction Between a Vortex and a Turbulent Boundary Layer in a Streamwise Pressure Gradient,: 5th Symposium on Turbulent Shear Flows, August 7-9, Cornell University, 1985, pp. 7.1-7.8.

23. Davies, P.O.A.L. and Yule, A.M., "Coherent Structures in Turbulence," J. Fluid Mech., 69, 1975, pp. 513-537.

24. Smith, C.R. and Abbott, D.E., ed., Lehigh Workshop on Coherent Structures in Turbulent Boundary Layers, 1978.

25. Simpson, R.L., Strickland, J.H. and Barr, P.W., "Features of a Separating Turbulent Boundary Layer in the Vicinity of Separation," J. Fluid Mech., 79, 1977, pp. 553-594.

26. Nychas, S.G., Hershey, H.C. and Brodkey, R.S., "A Visual Study of Turbulent Shear Flow," J. Fluid Mech., 62, 1973, pp. 223-239.

27. Praturi, A.K. and Brodkey, R.S., "A Stereoscopic Visual Study of Coherent Structures in Turbulent Shear Flow," J. Fluid Mech., 89, 1978, pp. 251-272.

28. Simpson, R.L., Ghodbane, M. and McGrath, B.E., "An Experimental Study of Surface Pressure Fluctuations in a Separating Turbulent Boundary Layer," accepted for publication, J. Fluid Mech.

29. Schlichting, H., Boundary-Layer Theory, Sixth Edition, McGraw-Hill, New York, 1968, pp. 511-512.

30. Miller, J.A., "A Simple Linearized Hot-Wire Anemometer," J. Fluids Engrg., 98, 1976, 550.

31. Simpson, R.L., Heizer, K.W. and Nasburg, R.E., "Performance Characteristics of a Simple Linearized Hot-Wire Anemometer," J. Fluids Engrg., 101, 1979, 381.

32. Jorgensen, F.E., "Directional Sensitivity of Wire and Fiber-Film Probes," Disa Information, No. 11, 1971, pp. 31-37.

33. Ahn, S., "Unsteady Features of Turbulent Boundary Layers," M.S. Thesis, Dept. Aerospace and Ocean Engrg., VPI&SU, 1986.

34. McGrath, B., "Some Features of Surface Pressure Fluctuations in Zero and Favorable Pressure Gradients," M.S. Thesis, Dept. Aerospace and Ocean Engrg., VPI&SU, 1985.

35. Chew, Y.-T. and Simpson, R.L., "A Simple Data Reduction Method for Triple Sensors Hot-Wire Anemometers in Three-Dimensional Flow," submitted to J. Fluids Engrg.

36. Purtell, L.P., Klebanoff, P.S. and Buckley, F.T., "Turbulent Boundary Layer at Low Reynolds Number," The Physics of Fluids, Vol. 24, 1981, pp. 802-811.

37. Perry, A.E., Lin, K.L. and Henbest, S.M., "A Spectral Analysis of Smooth Flat-Plate Boundary Layers," 5th Symposium on Turbulent Shear Flows, Cornell Univ., August 7-9, 1985, p. 9.29.

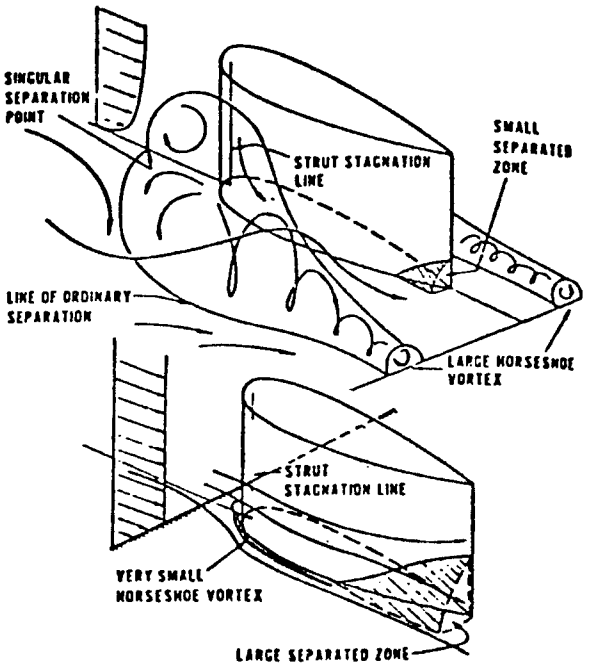


Figure 1. Flow behavior for a thick boundary-layer-strut interaction (top figure) and for thin boundary-layer-strut interaction (lower figure).

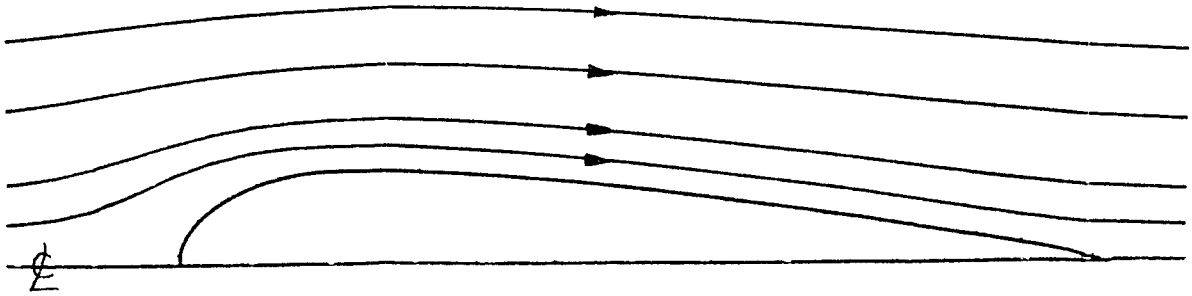


Figure 2. Streamlines produced by a two-dimensional wing with a 1.5 to 1 elliptical nose and a NACA 0020 tail in an unbounded potential flow.

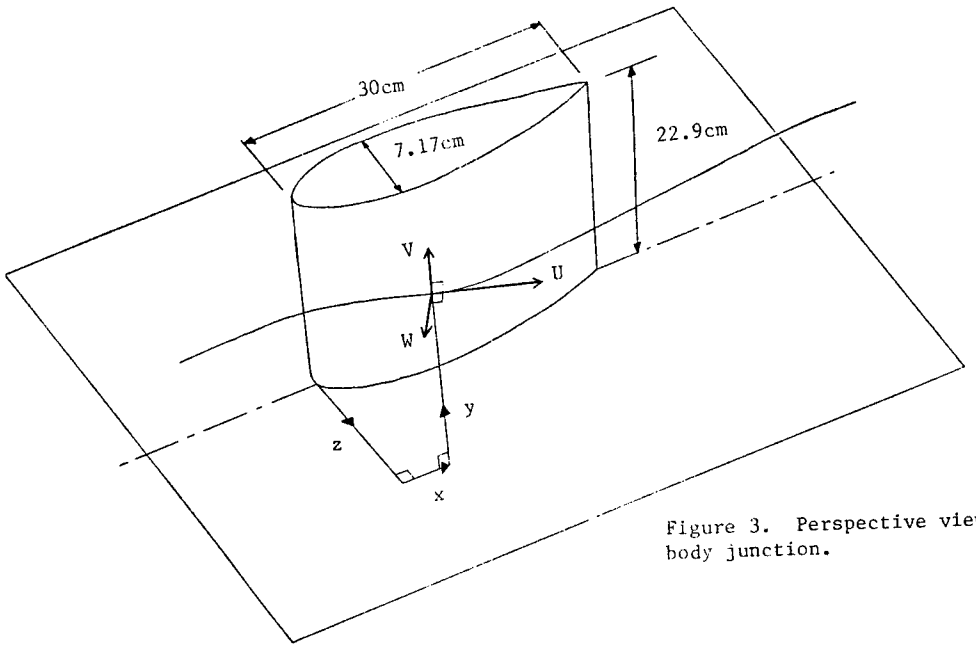


Figure 3. Perspective view of the wing-body junction.

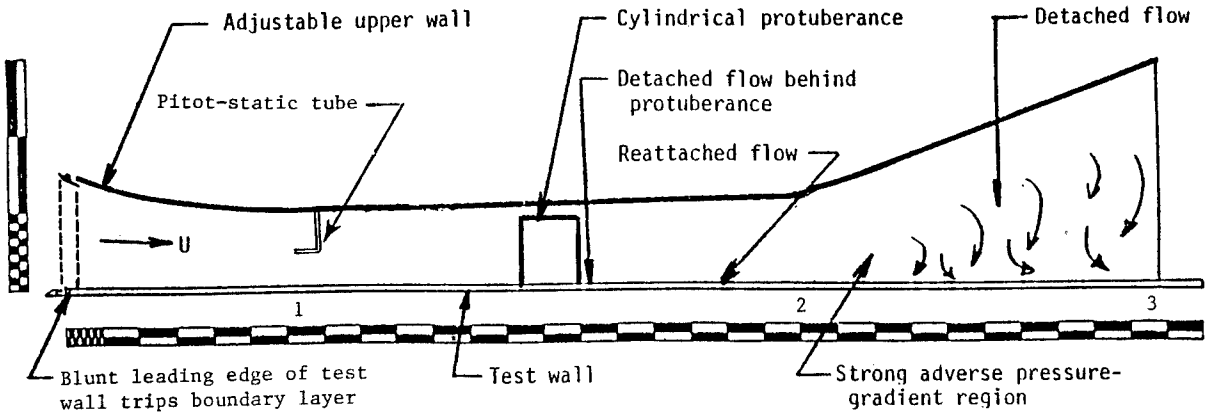


Figure 4. Sideview schematic of the wind-tunnel test section for the wing-body junction experiments. Major divisions on scales: 25.4cm.

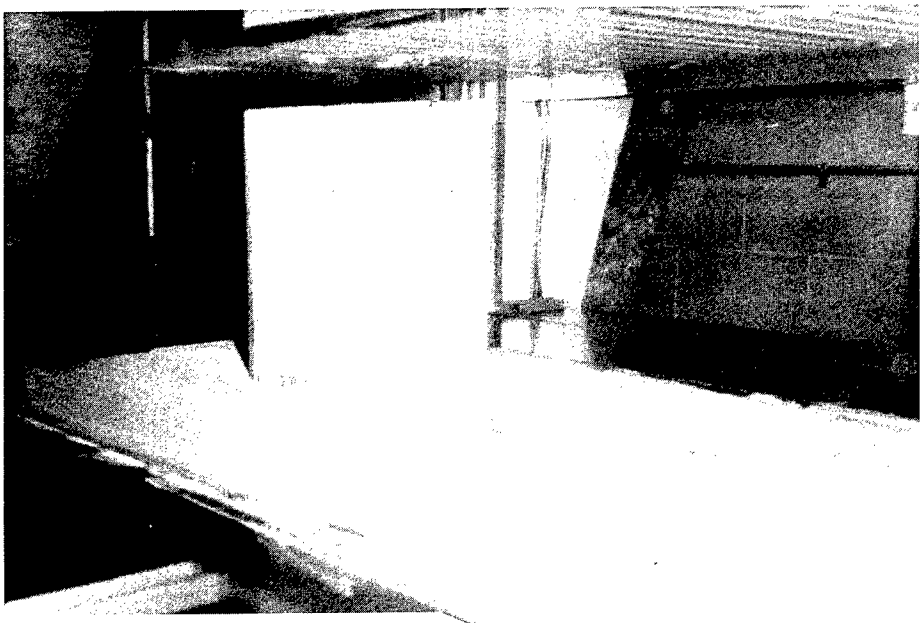


Figure 5. View of the wing-body junction from downstream showing a surface oil-flow visualization.

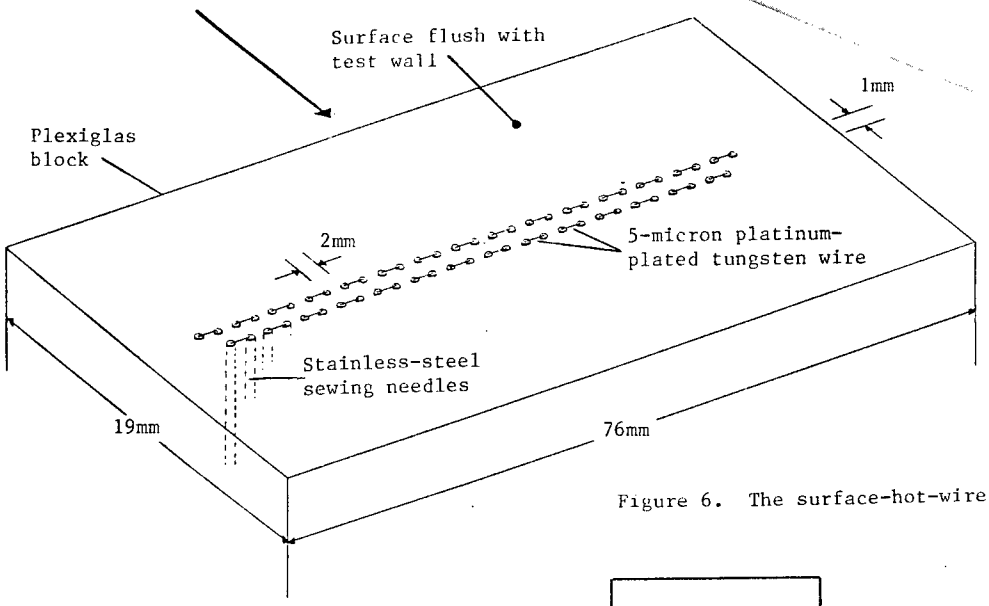


Figure 6. The surface-hot-wire array.

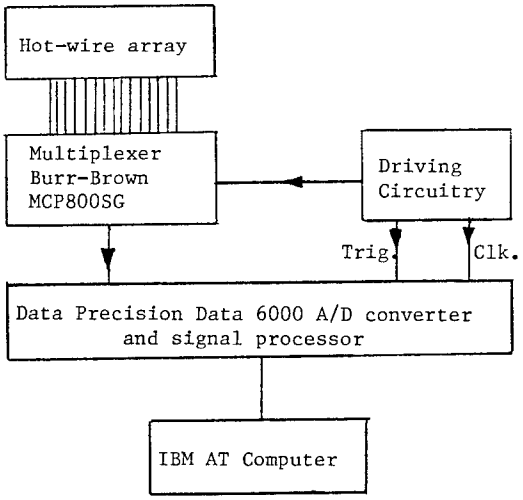


Figure 7. Schematic of the data-acquisition system for the hot-wire array

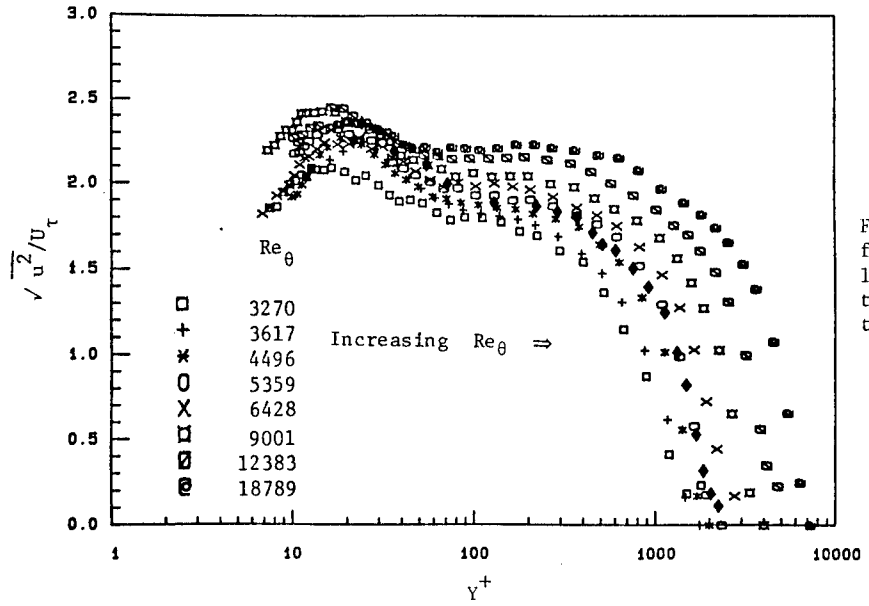


Figure 8. $\overline{u^2}/U$ vs. Y^+ for the test-wall boundary layer in the absence of the wing. Diamonds mark the data of Purtell (36).

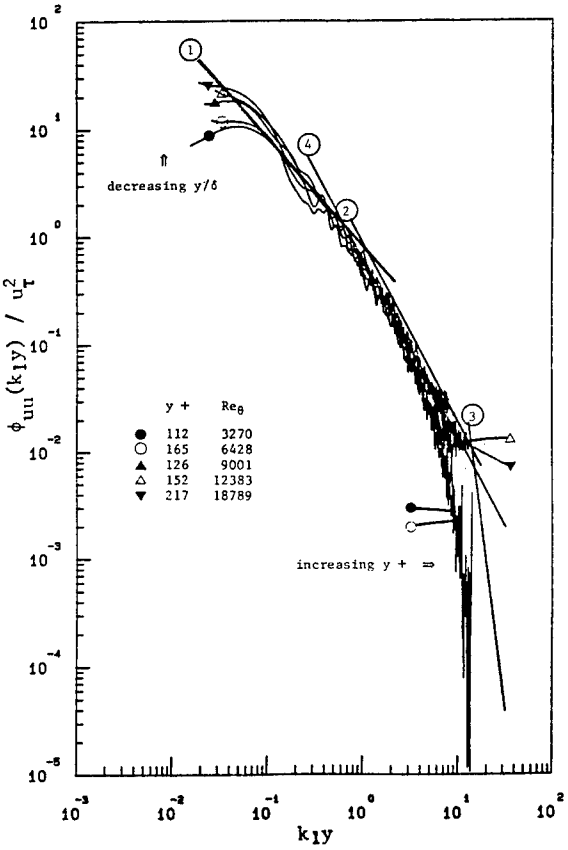


Figure 9. Spectra of streamwise velocity fluctuations in the semi-logarithmic velocity profile region of the test-wall boundary layer in the absence of the wing.

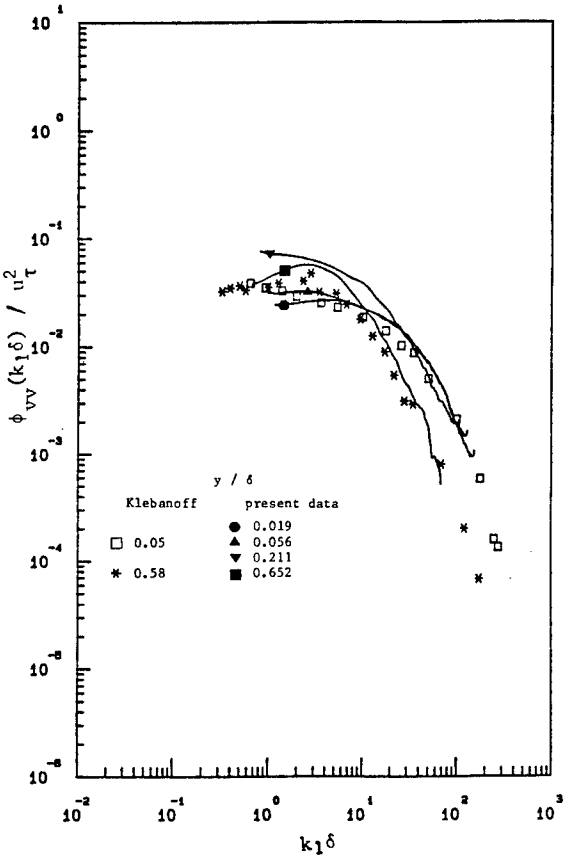


Figure 10. Spectra of v velocity fluctuations in the test-wall boundary layer in the absence of the wing for Re_θ = 9000. Data of Klebanoff for Re_θ = 8000.

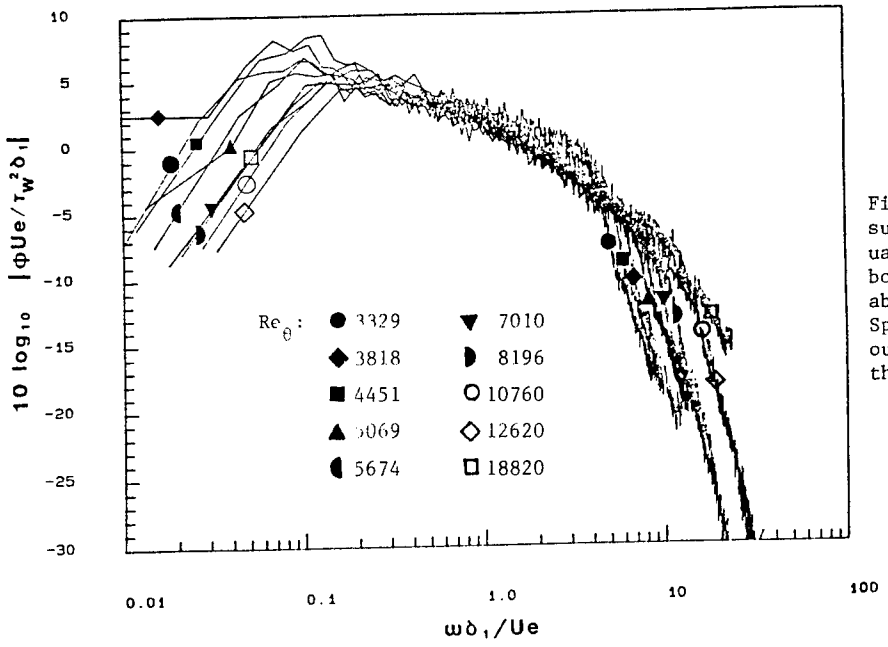


Figure 11. Spectra of surface pressure fluctuations for the test-wall boundary layer in the absence of the wing. Spectra normalized on the outer variables δ_1, U_e and the wall shear stress τ.

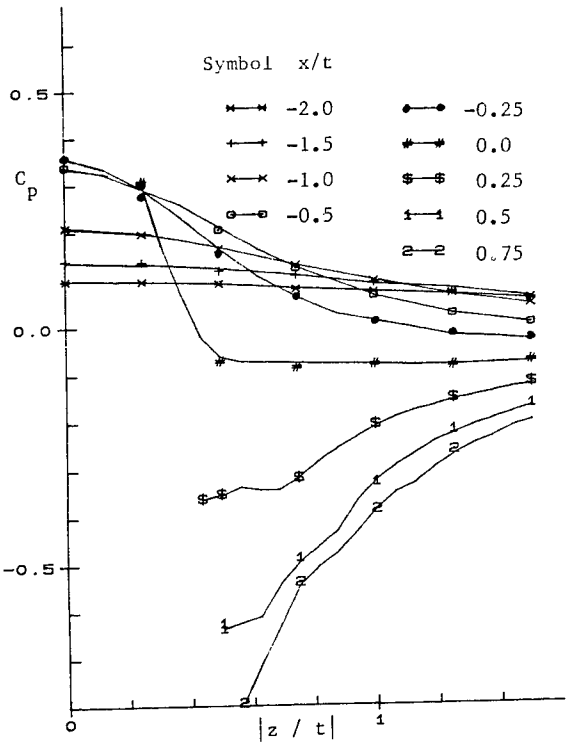


Figure 12(a). Distribution of time-mean static pressure on the wall surrounding the wing for Re_θ = 7000. Lines indicate positive z, points indicate negative z.

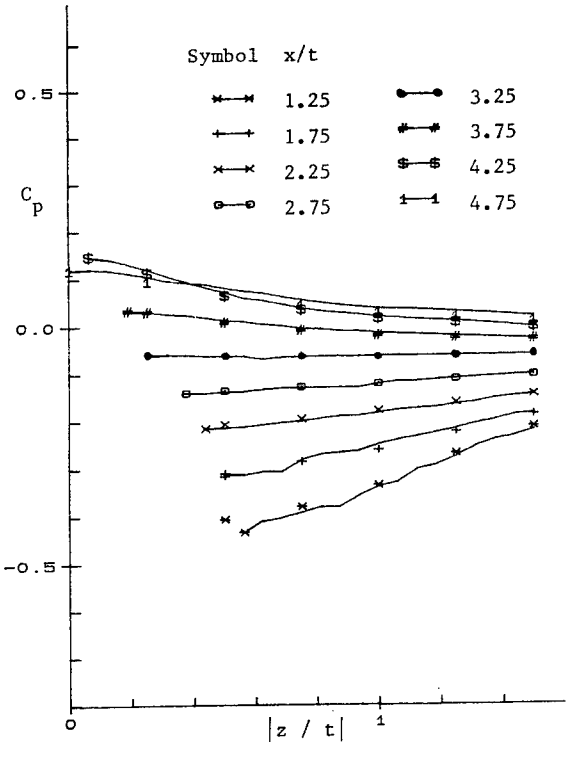


Figure 12(b). Distribution of time-mean static pressure on the wall surrounding the wing for Re_θ = 7000. Lines indicate positive z, points indicate negative z.

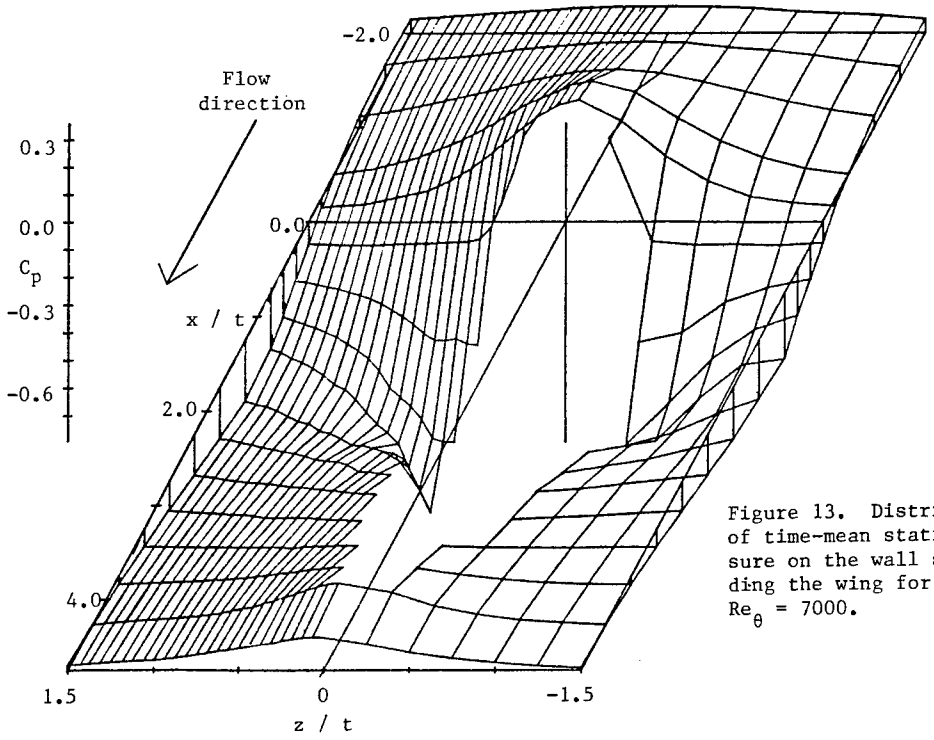


Figure 13. Distribution of time-mean static pressure on the wall surrounding the wing for Re_θ = 7000.

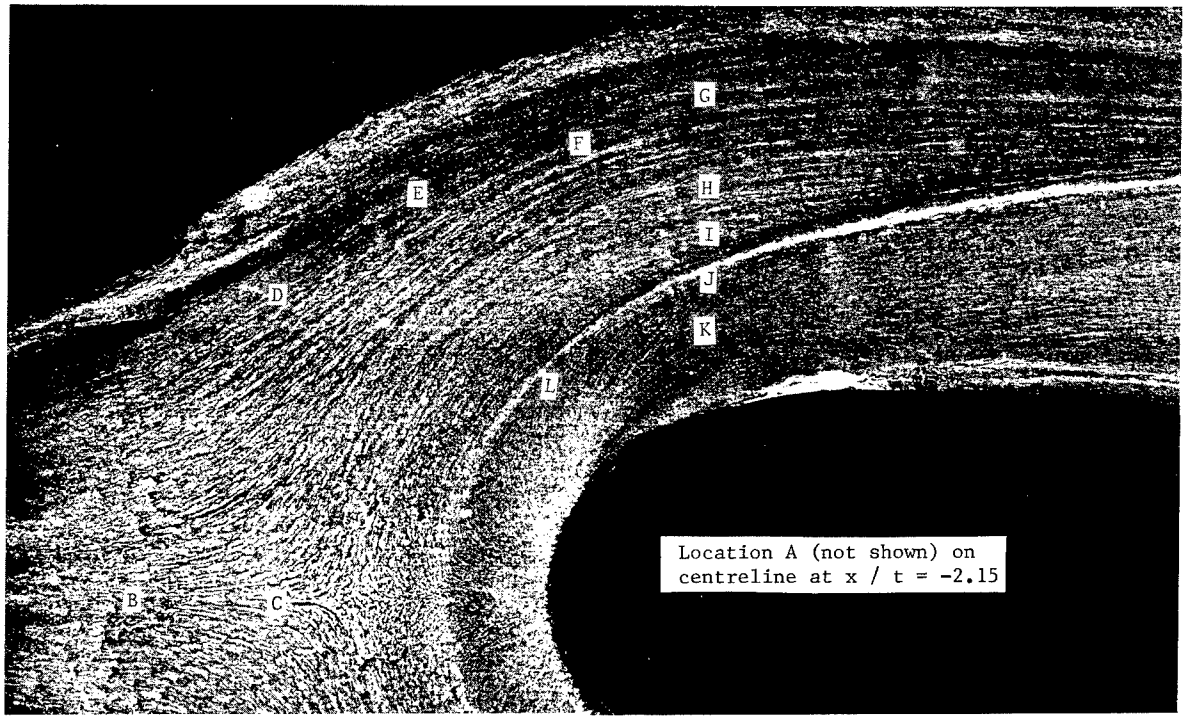


Figure 14(b). Surface oil-flow visualization on the wall surrounding the wing for Re_θ = 7000, detail of nose region.

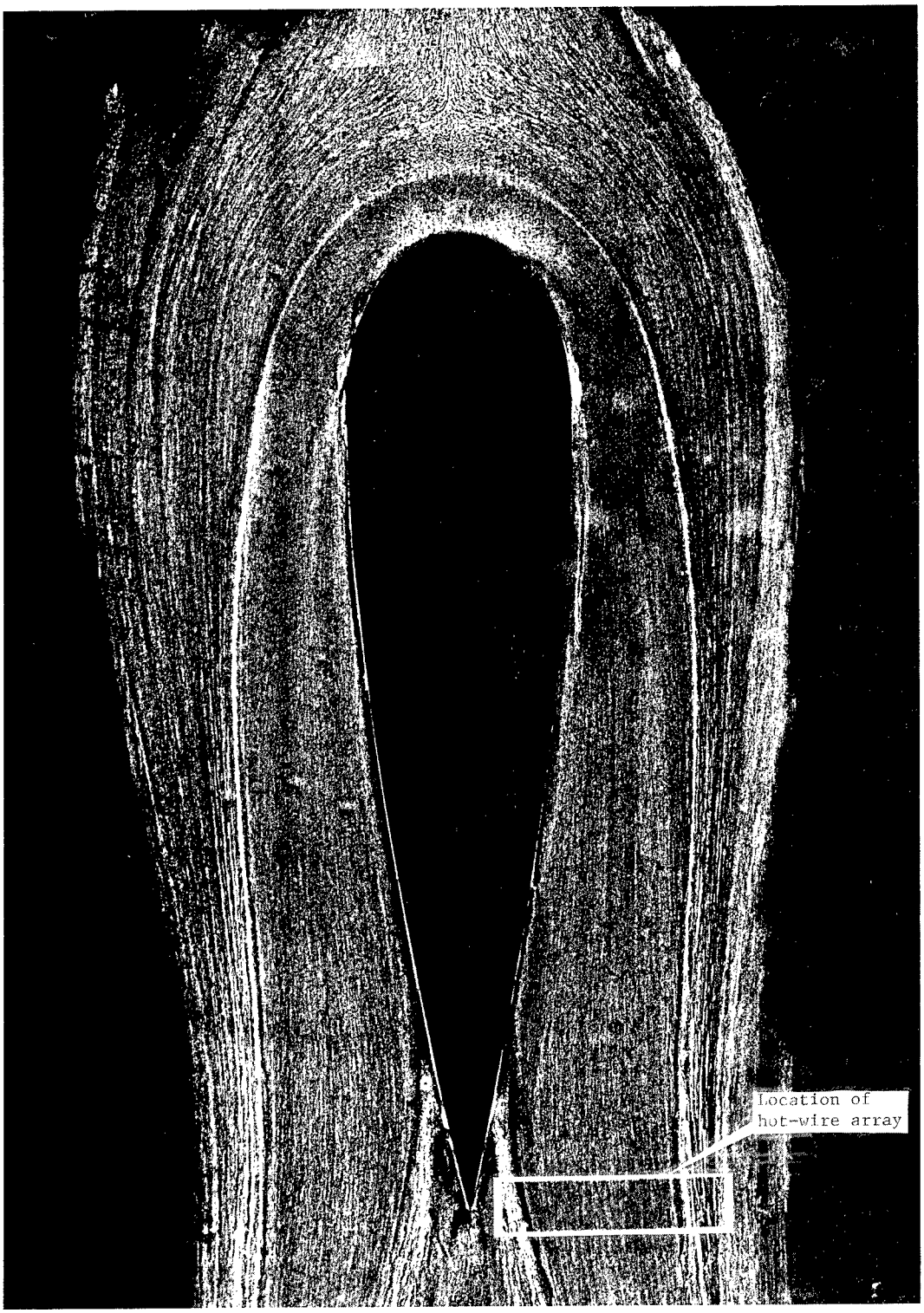


Figure 14(a). Surface oil-flow visualisation on the wall surrounding the wing for Re_θ = 7000.

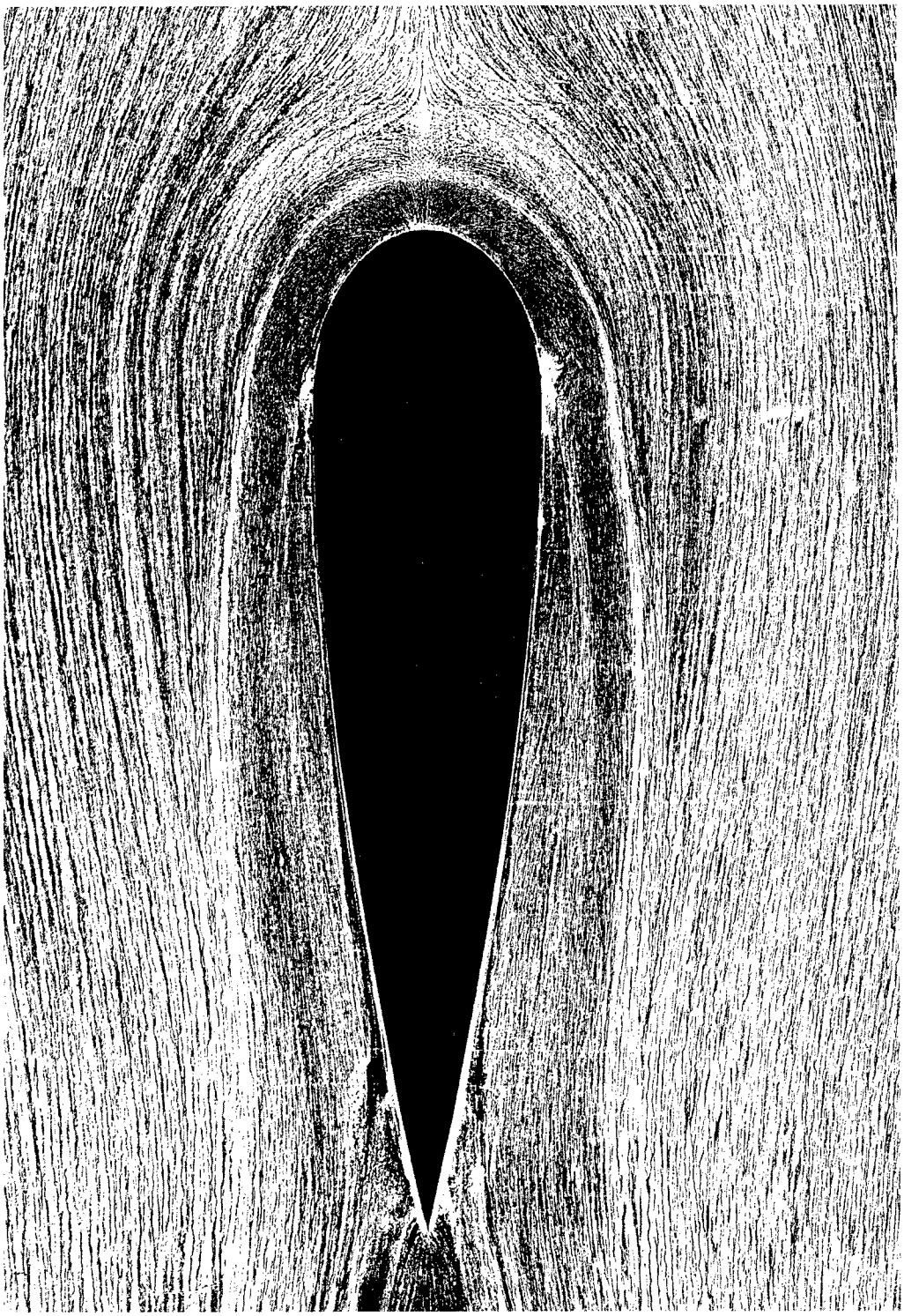


Figure 15(a). Surface oil-flow visualization on the wall surrounding the wing for $Re_\theta = 4000$.

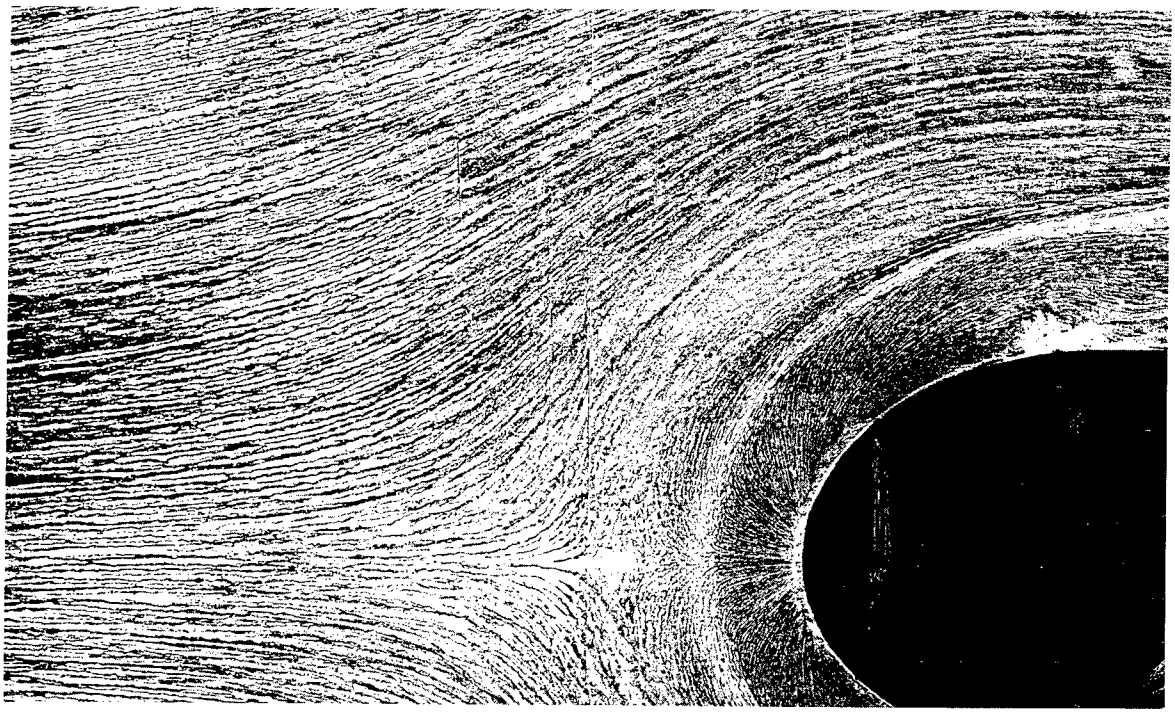


Figure 15(b). Surface oil-flow visualization on the wall surrounding the wing for Re_θ = 4000, detail of nose region.

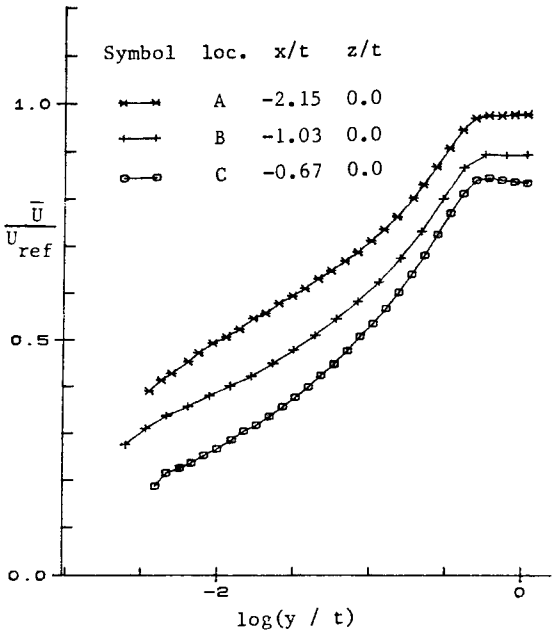


Figure 16. Profiles of $\bar{U}/U_{ref}$ at locations A B and C for Re_θ = 7000.

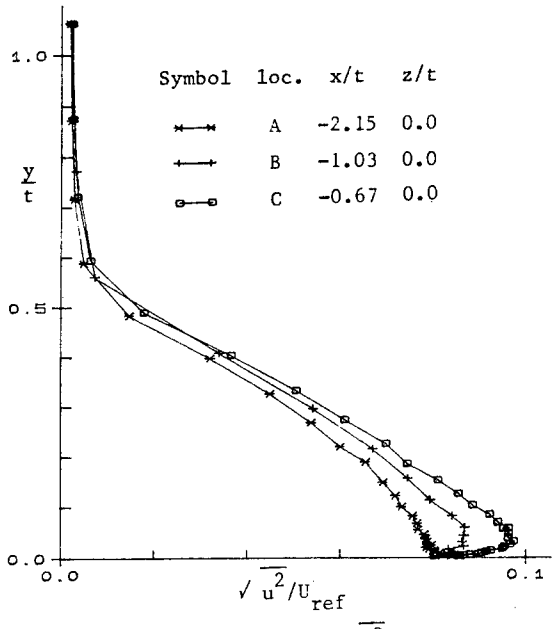


Figure 17. Profiles of $\sqrt{\overline{u^2}}/U_{ref}$ at locations A B and C for Re_θ = 7000.

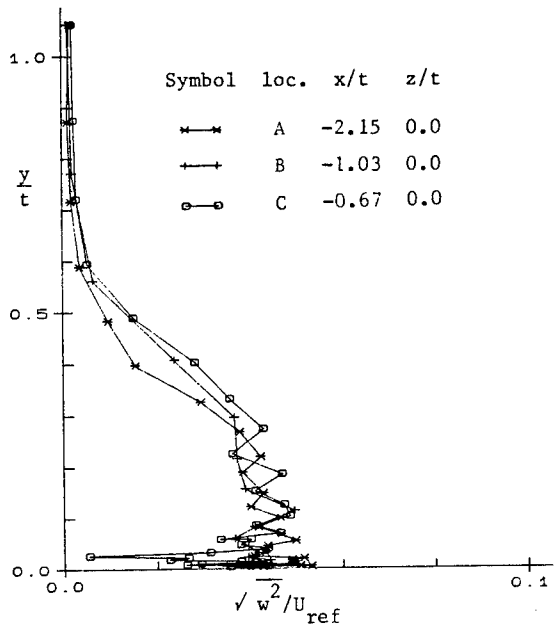


Figure 18. Profiles of $\sqrt{\overline{w^2}}/U_{ref}$ at locations A B and C for Re_θ = 7000.

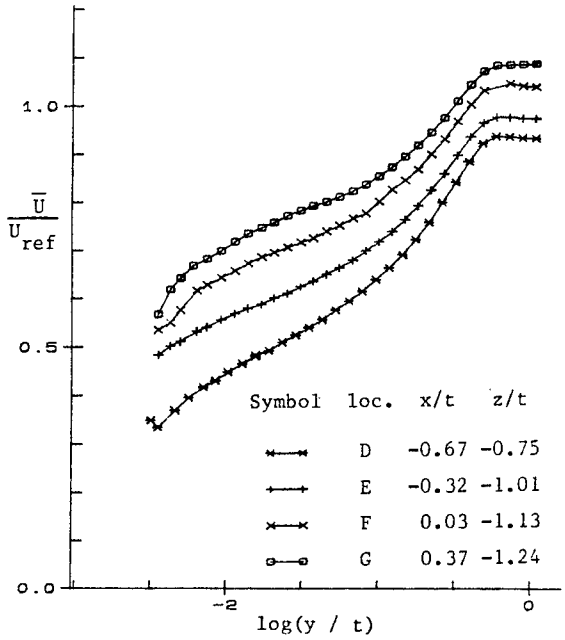


Figure 19. Profiles of $\overline{U}/U_{ref}$ at locations D E F and G for Re_θ = 7000.

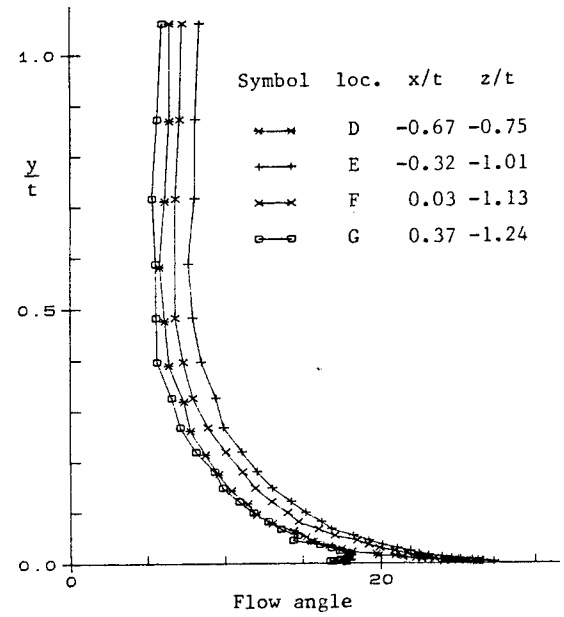


Figure 20. Profiles of flow angle at locations D E F and G for Re_θ = 7000.

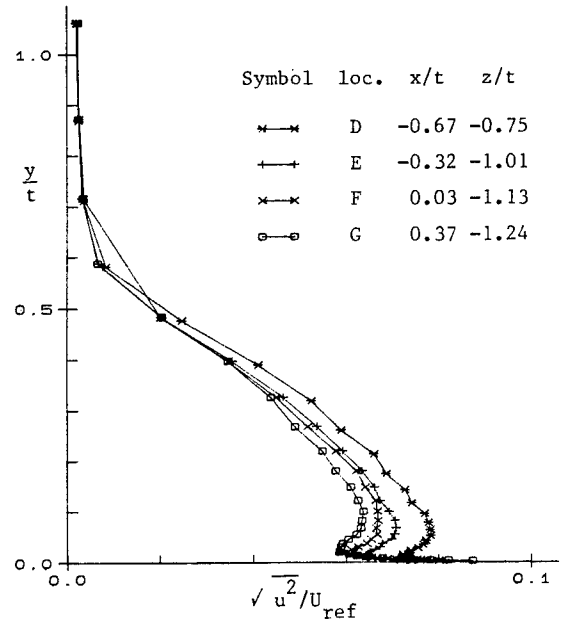


Figure 21. Profiles of $\sqrt{\overline{u^2}}/U_{ref}$ at locations D E F and G for Re_θ = 7000.

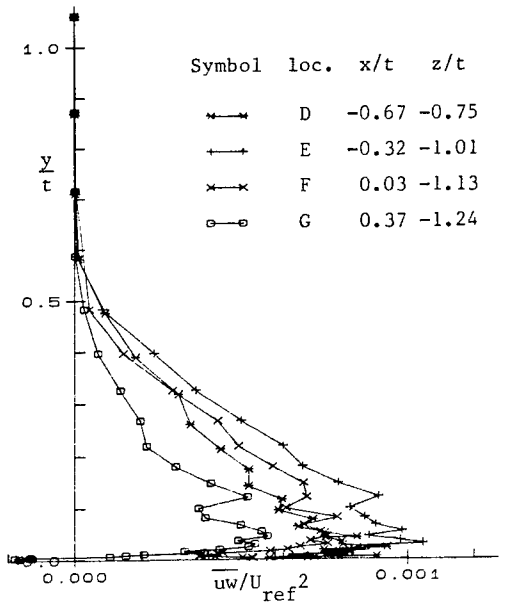


Figure 22. Profiles of $\overline{uw}/U_{ref}^2$ at locations D E F and G for Re_θ = 7000.

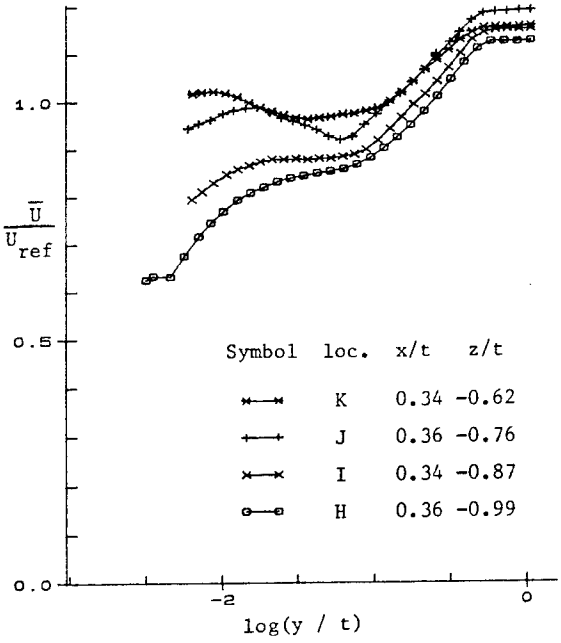


Figure 23. Profiles of $\overline{U}/U_{ref}$ at locations H I J and K for Re_θ = 7000.

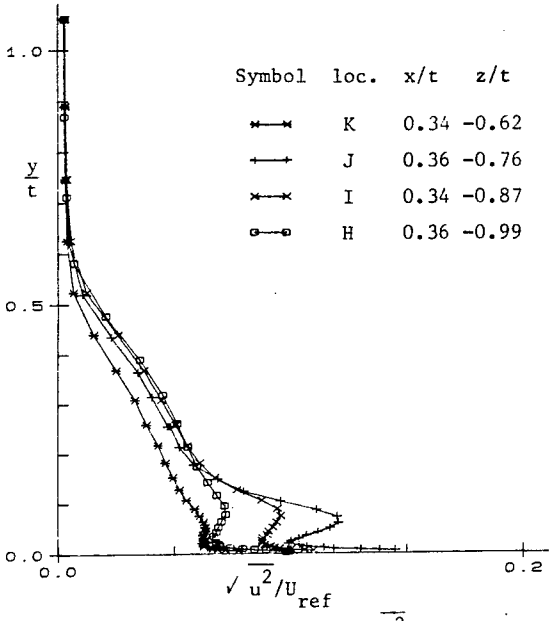


Figure 24. Profiles of $\sqrt{\overline{u^2}}/U_{ref}$ at locations H I J and K for Re_θ = 7000.

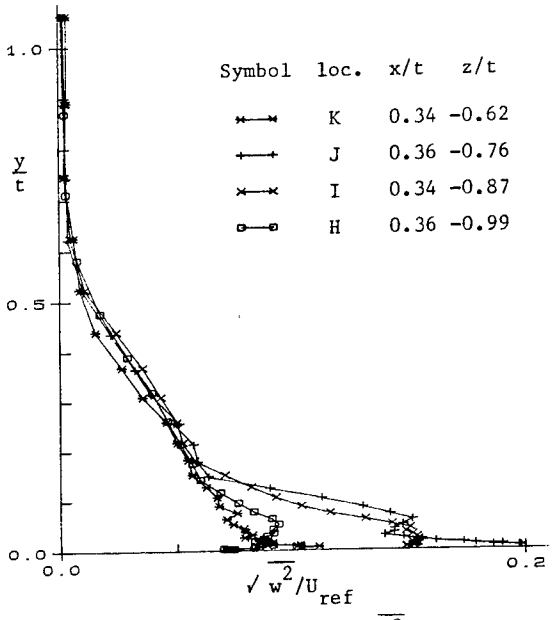


Figure 25. Profiles of $\sqrt{\overline{w^2}}/U_{ref}$ at locations H I J and K for Re_θ = 7000.

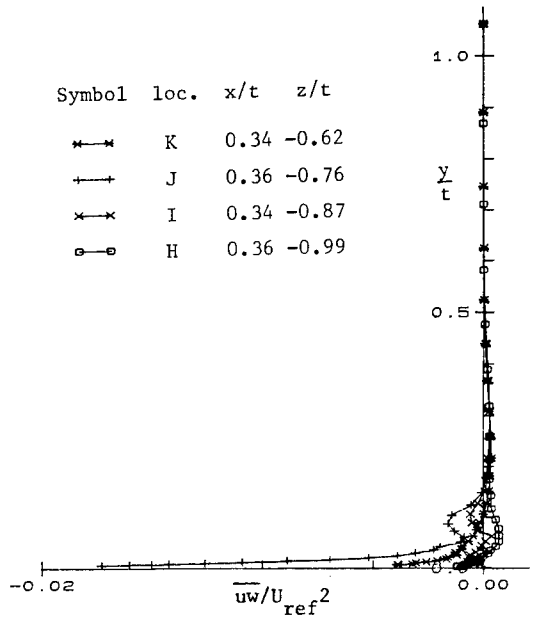


Figure 26(a). Profiles of $\overline{uw}/U_{ref}^2$ at locations H I J and K for Re_θ = 7000.

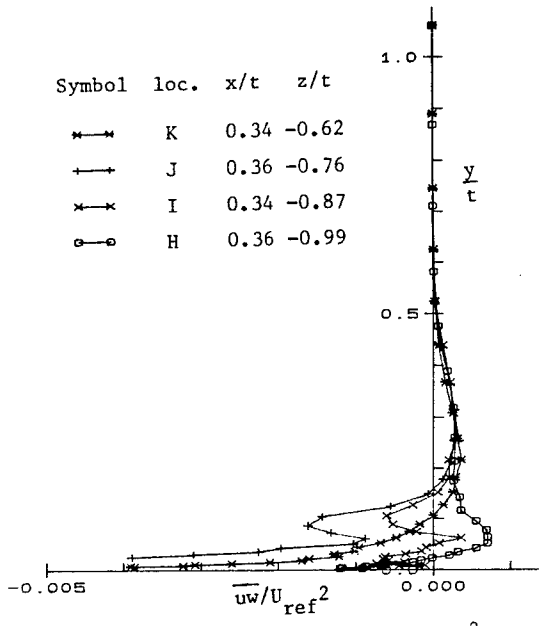


Figure 26(b). Profiles of $\overline{uw}/U_{ref}^2$ at locations H I J and K for Re_θ = 7000.

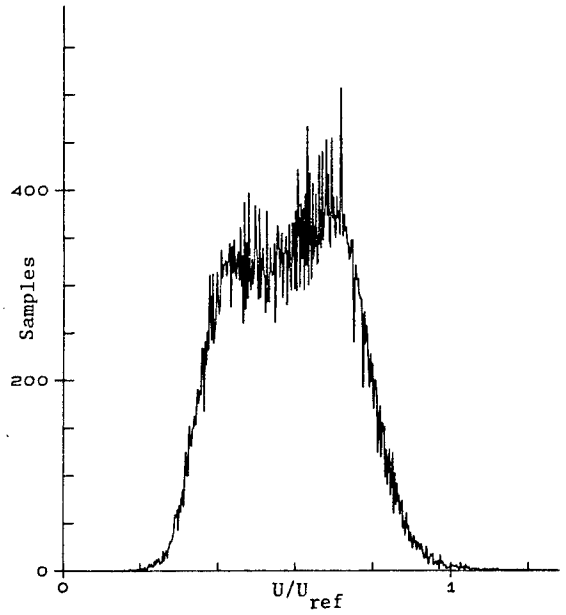


Figure 27. Histogram of streamwise velocity fluctuations 0.18mm from the wall at location L for Re_θ = 7000.

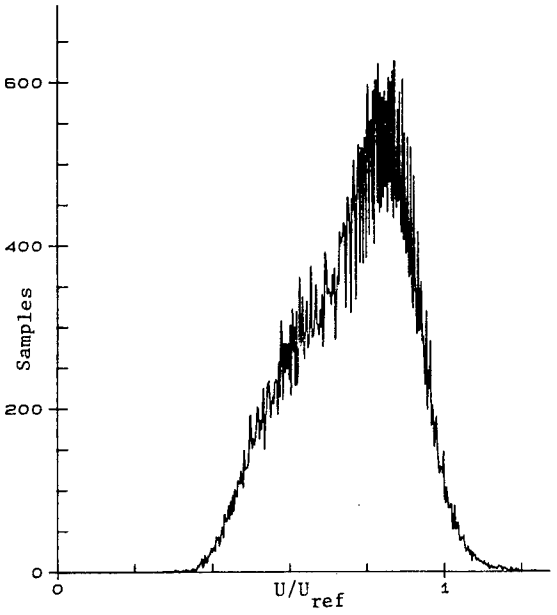


Figure 28. Histogram of streamwise velocity fluctuations 0.18mm from the wall at location J for Re_θ = 7000.

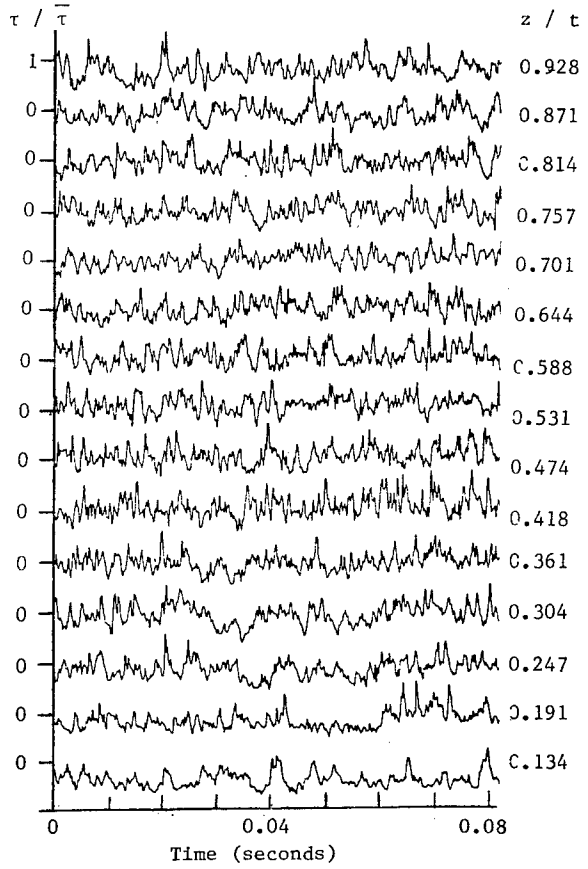


Figure 29. 'Simultaneous' variations of skin friction at spanwise locations across the flow at the trailing edge of the wing (x / t = 4.25), Re_θ = 7000.

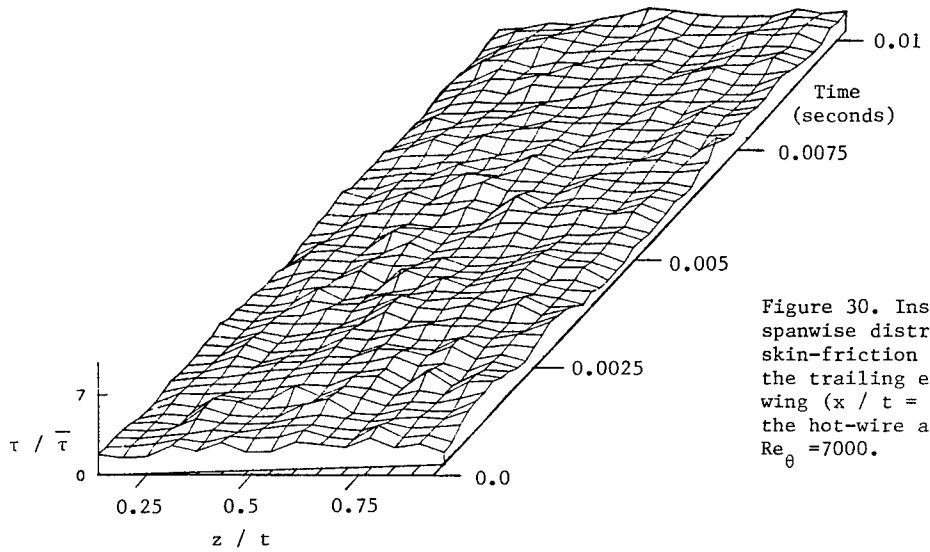


Figure 30. Instantaneous spanwise distributions of skin-friction measured at the trailing edge of the wing (x / t = 4.25) with the hot-wire array, Re_θ =7000.

DISCUSSION

Brian Clayton,
University College London

A major effect of hull-sail interaction is the generation of a horse-shoe vortex adjacent to the streamwise corner. The downstream propagation of the vortex can thus give rise to a self noise source at sonar elements and unsteady conditions at propellers and control surfaces, again giving rise to discrete frequency noise sources. It is important, therefore, to reduce the intensity of these vortex lines and, all other things being equal, this intensity is strongly related to the details of the corner geometry. In this respect a fillet corner, even a small one, can be effective and must therefore substantially modify the surrounding flow characteristics. have the authors examined, or do they plan to examine the effects of radiused corners? If not, would the authors care to speculate on the effects of such geometric changes in the pressence of pressure gradients. Again, on the subject of boundary geometry could the authors discuss the expected sensitivity of the flow behavior to hull transverse nature, noting that in their experiments a plane flow was used in the wind tunnel.

Reply -

Our work is directed towards understanding the complex turbulence structure produced by an appendage-body junction flow, and the mechanisms through which it generates sound. We expect this structure to be qualitatively unaffected by the transverse curvature of a hull. Of course other experiments will be needed to confirm this and determine the magnitude of any quantitative differences. We have no immediate plans to study the effects of fillets on appendage-body junction flows, though we are aware of their probable importance in reducing noise generated by submarines.

Numerical Analysis of the Viscous Flow Field Resulting From a Hull-Sail Interaction

R. LEVY and S. J. SHAMROTH

Scientific Research Associates, Inc., U.S.A.

ABSTRACT

The corner vortex originating in the hull-sail intersection region is an important component of the submarine flow field. The vortex may play a major role in overall drag, wake development and propeller performance, and may be a major acoustic source. The flow itself is a complex one, being three-dimensional, viscous and turbulent. The present paper focuses upon the portion of this flow field downstream of the sail leading edge. The paper first details the analysis which is based upon a three-dimensional, viscous, spatial forward marching approach. The solution procedure which is based upon ADI techniques is described. The discussion then proceeds to the coordinate system, initial conditions and boundary conditions. Finally, calculations for both laminar and turbulent flows are presented.

INTRODUCTION

The complex flow field of the submarine hull-sail interaction represents a difficult hydrodynamics problem which can be divided into three separate regions. The first region is the leading edge region of the sail where the adverse streamwise pressure gradient experienced by the oncoming hull boundary layer results in a complex three-dimensional flow separation ahead of the leading edge. Convection of this fluid around the leading edge sets up a horseshoe vortex. The second region is the hull/sail corner region where the interaction of the horseshoe vortex with the hull and sail boundary layers is of importance and is dominated by streamwise convection and transverse dissipation of vorticity. The third region contains the wake of the sail and downstream wake-vortex-hull interactions.

All three regions contain complex fluid flow patterns in which streamwise vortices and viscous effects play major roles. In the case of the submarine appendage problem, the generation of the horseshoe vortex in the sail leading edge and hull corner region and the subsequent development of the streamwise vorticity as it proceeds downstream have major effects in determining hull drag, wake development, and possible acoustic sources. In addition, this strong streamwise vorticity could impinge upon the propeller and influence the propeller performance. Clearly, a technique for predicting this complex flow field would be a major asset in understanding submarine hydrodynamics as well as a benefit to the design process.

In developing an analysis for this problem, several possibilities of varying complexity can be considered. These include semi-empirical analyses, inviscid analyses with viscous corrections and three-dimensional viscous analyses. Based upon an understanding of the flow field it appears that, in general, semi-empirical analyses cannot be used with confidence for this problem. The strong role played both by viscous effects and three-dimensional flow patterns makes any semi-empirical analysis an unlikely candidate as a general predictive procedure. Similarly, although inviscid analyses can yield realistic flow field predictions in cases where viscous effects are confined to thin layers in the vicinity of no-slip walls, purely inviscid analyses appear unsuitable for the present problem. The horseshoe vortex generation clearly requires a viscous analysis for this part of the problem. Even downstream of the generation region, viscous effects play an important role in the prediction of diffusion and dissipation of the streamwise vortex and in the interaction of the vortex, sail wake and hull. Clearly, an appropriate analysis should be based upon three-dimensional, viscous methods.

In the approach presented here, an existing forward marching, three-dimensional viscous flow, numerical prediction technique has been adopted to simulate the hull sail corner flow field. In this study the calculation is begun downstream of the leading edge region in which the horseshoe vortex originates. The horseshoe vortex at the initial plane of the present calculation has been modeled by constructing forced vortices whose location, strength and extent are input parameters in the viscous flow

computer program. It should be noted that eventually it is anticipated that a Navier-Stokes analysis, such as that of Ref. 1, be used to calculate the horseshoe vortex formation in the leading edge region thus generating initial conditions for the streamwise marching code presently used for the flow calculation downstream of this region.

The present effort focuses upon the detailed flow field of the leading edge vortex as it progresses downstream and is influenced by the hull sail corner. The hull sail geometry is represented by polar-like coordinates in planes normal to the hull centerline. The coordinate system used is a body fitted system leading to boundaries being coincident with coordinate lines. This results in considerable simplification in specifying boundary conditions. The body of the paper first discusses the governing equations and solution techniques, followed by a description of the coordinates used and, finally, results of the flow field simulation are presented.

THE FORWARD MARCHING COMPUTATION PROCEDURE

The forward marching computation procedure used for the solution of the parabolic Navier-Stokes equations provides an economical and accurate method for computing many three-dimensional viscous flow fields. This procedure, initially developed and applied to internal flow fields (Refs. 2-4), has been extended to the computation of external flows such as the ship propeller tip flow field (e.g., see Refs. 5-7) and the hull-sail interaction flow which is the subject of the present endeavor. The governing equations and the computational scheme are presented in this section.

Governing equations are derived through approximations made relative to a curvilinear coordinate system fitted to and aligned with the flow geometry under consideration. The coordinate system is chosen such that the streamwise or marching coordinate either coincides with or is at least approximately aligned with a known inviscid primary flow direction as determined, for example, by a potential flow for the given geometry. Transverse coordinate surfaces must be approximately perpendicular to solid walls or bounding surfaces, since diffusion is permitted only in these transverse coordinate surfaces.

Equations governing primary flow velocity, U_p, and a secondary vorticity, Ω_n, normal to transverse coordinate surfaces are derived utilizing approximations which permit solution of the governing equations as an initial-value problem, provided reversal of the composite streamwise velocity does not occur. Terms representing diffusion normal to transverse coordinate surfaces (in the streamwise direction) are neglected. Secondary flow velocities are determined from scalar and vector surface potential calculations in transverse coordinate surfaces, once the primary velocity and secondary vorticity are known. With the computed velocity field, the pressure field associated with the velocity field can be determined.

Primary-Secondary Velocity Decomposition

In what follows, vectors are denoted by an overbar, and unit vectors by a caret. The analysis is based on decomposition of the overall velocity vector field $\bar{U}$ into a primary flow velocity, $\bar{U}_p$, and a secondary flow velocity, $\bar{U}_s$. The overall or composite velocity is determined from the superposition

$$\bar{U} = \bar{U}_p + \bar{U}_s \tag{1}$$

The primary flow velocity is represented as

$$\bar{U}_p = U_p \hat{i}_p \tag{2}$$

where $\hat{i}_p$ is a known inviscid primary flow direction determined, for example, from an a priori potential flow solution for the geometry under consideration. A streamwise coordinate direction from a body fitted coordinate system could be used as an approximation to this potential flow direction. The primary velocity $\bar{U}_p$ is determined from solution of a primary flow momentum equation. The secondary flow velocity, $\bar{U}_s$, is derived from scalar and vector surface potential denoted ϕ and ψ, respectively. If $\hat{i}_n$ denotes the unit vector normal to transverse coordinate surfaces, if ρ is density, and if ρ_o is an arbitrary constant reference density, then $\bar{U}_s$ is defined by

$$\bar{U}_s \equiv \nabla_s\phi + (\rho_o/\rho)\nabla x\hat{i}_n\psi \tag{3}$$

where ∇_s is the surface gradient operator defined by

$$\nabla_s \equiv \nabla - \hat{i}_n(\hat{i}_n\cdot\nabla) \tag{4}$$

It follows that since $\hat{i}_n \cdot \bar{U}_s = 0$, then U_s lies entirely within transverse coordinate surfaces. Equation (3) is a general form permitting both rotational and irrotational secondary flows and will lead to governing equations which may be solved as an initial-boundary value problem. The overall velocity decomposition (1) can be written

$$\bar{U} = U_p\hat{i}_p + \nabla_s\phi + (\rho_o/\rho)\nabla x\hat{i}_n\psi \tag{5}$$

Surface Potential Equations

Equations relating ϕ and ψ with U_p, ρ, and the secondary vorticity component Ω_n can be derived using Eq. (5) as follows: From continuity,

$$\nabla\cdot\rho\bar{U} = 0 = \nabla\cdot\rho U_p\hat{i}_p + \nabla\cdot\rho\nabla_s\phi + \rho_o\nabla\cdot\nabla x\hat{i}_n\psi \tag{6}$$

and from the definition of the vorticity, Ω_n, based on the secondary flow within the transverse surfaces

$$\hat{i}_n \cdot \nabla \times \bar{U} \equiv \Omega_n = \hat{i}_n \cdot \nabla \times U_p \hat{i}_p + \hat{i}_n \cdot \nabla \times (\rho_o/\rho) \nabla \times \hat{i}_n \psi + \hat{i}_n \cdot \nabla \times \nabla_s \phi \quad (7)$$

Since the last term in each of Eqs. (6) and (7) is zero by vector identity, Eqs. (6) and (7) can be written as

$$\nabla \cdot \rho \nabla_s \phi = -\nabla \cdot \rho U_p \hat{i}_p \quad (8)$$

$$\hat{i}_n \cdot \nabla \times (\rho_o/\rho) \nabla \times \hat{i}_n \psi = \Omega_n - \hat{i}_n \cdot \nabla \times U_p \hat{i}_p \quad (9)$$

Note that the last term in Eq. (9) is identically zero in a coordinate system for which $\hat{i}_n$ and $\hat{i}_p$ have the same direction, and would be small if $\hat{i}_n$ and $\hat{i}_p$ are approximately aligned. In any event, given a knowledge of U_p, Ω_n and ρ, the surface potentials ϕ and ψ can be determined by a two-dimensional elliptic calculation in transverse coordinate surfaces at each streamwise location. In turn $\bar{U}_s$ can be computed from Eq. (3), and the composite velocity $\bar{U}$ will satisfy continuity. Equations for $\bar{U}_p$ and Ω_n are obtained from the equations governing momentum and vorticity, respectively.

The streamwise momentum equation is given by

$$\hat{i}_p \cdot [(\bar{U} \cdot \nabla)\bar{U} + (\nabla P)/\rho] = \hat{i}_p \cdot \bar{F} + \hat{i}_p \cdot \bar{R} \quad (10)$$

where P is pressure and ρF is force due to viscous stress and terms in F representing streamwise diffusion are neglected. $\rho \bar{R}$ is the additional force due to a rotating coordinate system, such as would arise in the ship propeller application; where $\bar{R} = -2\bar{\omega} \times \bar{U} - \bar{\omega} \times (\omega \times \bar{r})$, ω is the angular velocity of the coordinate system and $\bar{r}$ is the radius vector from the rotation axis. The pressure term in the streamwise momentum equation (10) can be taken from a simpler analysis such as an inviscid flow analysis. While this results in a set of equations which can be solved by forward marching, the surface pressures which are due to the pressure field imposed upon the flow are the inviscid flow pressures. Since the actual surface pressures are often of primary interest a new estimate of the actual surface pressure which includes viscous and secondary flow effects can be computed from the resulting velocity field in the following manner.

The momentum equations in the transverse surfaces are:

$$\hat{i}_1 \cdot [(\rho\bar{U} \cdot \nabla)\bar{U} + \nabla P - \rho\bar{F} - \rho\bar{R}] = 0$$
$$\hat{i}_2 \cdot [(\rho\bar{U} \cdot \nabla)\bar{U} + \nabla P - \rho\bar{F} - \rho\bar{R}] = 0 \quad (11)$$

Equation (11) represents components of the momentum vector in the transverse surfaces:

$$\hat{i}_1 (\hat{i}_1 \cdot [(\rho\bar{U} \cdot \nabla)\bar{U} + \nabla P - \rho\bar{F} - \rho\bar{R}]) + \hat{i}_2 (\hat{i}_2 \cdot [(\rho\bar{U} \cdot \nabla)\bar{U} + \nabla P - \rho\bar{F} - \rho\bar{R}]) \quad (12)$$

The divergence of this vector can be written as a Poisson equation for the pressure P at each transverse surface:

$$\nabla_s^2 P = \nabla_s^2 (P_I + P_c) = -\frac{\partial}{\partial x_1} (\hat{i}_1 \cdot [(\rho\bar{U} \cdot \nabla)\bar{U} - \rho\bar{F} - \rho\bar{R}]) - \frac{\partial}{\partial x_2} (\hat{i}_2 \cdot [(\rho\bar{U} \cdot \nabla)\bar{U} - \rho\bar{F} - \rho\bar{R}]) \quad (13)$$

where P_I is the imposed pressure, P_c is a viscous correction to the pressure field and x_1 and x_2 are coordinates in the $\hat{i}_1$ and $\hat{i}_2$ directions, respectively. Equation (13) can be solved for the pressure correction, P_c, at each computational station using Neuman boundary conditions derived from Eq. (12). The use of Neuman boundary conditions requires an additional parameter which is only a function of the normal direction, $P_v(x_3)$, in order to set the level of the pressure field. For external flows $P_v(x_3)$ is set to match the imposed pressure at an appropriate far field location.

Secondary Vorticity

The equation governing Ω is obtained by cross differentiating each of the transverse momentum equations (11). Eliminating the pressure in the two equations results in a single equation for the transport of the vorticity normal to the transverse surface. This equation has the form

$$\bar{U} \cdot \nabla \Omega_n - \bar{\Omega} \cdot \nabla U_n = G_n + C + i_n \cdot (\nabla \times \bar{R}) \quad (14)$$

where G_n is the normal component of

$$\bar{G} = \nabla \times \bar{F} \quad (15)$$

and C is a collection of curvature terms arising from changes in orientation of the transverse surface as a function of streamwise coordinate.

Governing System of Equations

A complete system of five coupled equations governing U_p, Ω_n, ϕ, ψ, and P is given by Eqs. (8), (9), (10), (14) and (13). Ancillary relation (5) is given for the composite velocity. In Ref. 2, these equations are given in general orthogonal coordinates and in Ref. 3 in nonorthogonal coordinates.

Numerical Method

Since techniques for obtaining the basic inviscid flow solution are well known and numerous, they need not be enumerated or discussed here. Instead, the present development concentrates on describing the

numerical method used to solve the system of governing equations. Streamwise derivative terms in the governing equations have a form such as $u_3\partial(\ )/\partial x_3$, and because the streamwise velocity u_3 is very small in the viscous dominated region near no-slip walls, it is essential to use implicit algorithms which are not subject to stringent stability restrictions unrelated to accuracy requirements. Although it is possible to devise algorithms for solution of the governing equations as a fully coupled implicit system, such algorithms would require considerable iteration for the system of equations treated here, and this would detract from the overall efficiency. The present method seeks to reduce the amount of iteration required and yet avoid the more severe stability restrictions of explicit algorithms. The method partitions the system of governing equations into subsystems which govern the primary flow, the secondary flow, and the turbulence model. The primary-flow subset of equations contains the streamwise momentum equation. The secondary-flow subset of equations contains the secondary vorticity equation, the scalar and vector potential equations and the pressure equation. These subsystems are decoupled by linearizing the solution variables in the spatial marching direction.

Summary of Algorithm

The governing equations are replaced by finite-difference approximations. Three-point central difference formulas are used for all transverse spatial derivatives. Analytical coordinate transformations are employed as a means of introducing a nonuniform grid in each transverse coordinate direction to concentrate grid points in the wall boundary layer regions. Second-order accuracy for the transverse directions is rigorously maintained. Two-point backward difference approximations are used for streamwise derivatives, although this is not essential.

The primary flow subsystem of viscous equations is solved via a scalar ADI scheme. In this application this is the streamwise momentum equation. Given the solution for the primary flow, the secondary flow subsystem can be solved. First, the scalar potential equation (continuity) is solved using a scalar iterative ADI scheme. Next, the secondary vorticity and vector potential equations are written as a fully implicit coupled system and solved using an iterative linearized block implicit (LBI) scheme (cf. Briley and McDonald Ref. 9). In selecting boundary conditions for the secondary flow subsystem, care must be taken to ensure that the final secondary velocity satisfies the no-slip condition accurately. Zero normal derivatives of ϕ are specified in the scalar potential equation, and this boundary condition corresponds to zero normal velocity. It is not possible to simultaneously specify the tangential velocity, however, and thus the ϕ-contribution to the secondary velocity will have a nonzero tangential (slip) component, denoted v_t, at solid boundaries. In the coupled vorticity and vector-potential equations, both normal and tangential velocity components can be specified as boundary conditions, since these equations are solved as a coupled system. By choosing (a) zero normal velocity, and (b) $-v_t$ as the ψ-contribution to the tangential velocity, the slip velocity v_t arising from the ϕ calculation is cancelled, and the composite secondary flow velocity including both ϕ and ψ contributions will satisfy the no-slip condition exactly.

A summary of the overall algorithm used to advance the solution a single axial step follows. It is assumed that the solution is known at the n-level x^n and is desired at x^{n+1}.

(1) The imposed streamwise pressure gradient distribution is determined from an a priori inviscid potential flow.

(2) The momentum equation is solved using an iterative scalar ADI scheme to determine u^{n+1}.

(3) Using values now available for u^{n+1}, the scalar potential equation (8) is solved using an iterative scalar ADI scheme, to obtain ϕ^{n+1}. This ensures that the continuity equation is satisfied.

(4) The equations for vorticity (14) and vector potential (9) form a coupled system for Ω^{n+1} and ψ^{n+1} which is solved as a coupled system using an iterative LBI scheme.

(5) Values for the transverse velocities v_s and w_s are computed from Eq. (3).

(6) Using the computed velocity field, the transverse pressure field is computed from Eq. (13) by an iterative scalar ADI scheme.

Computational Coordinate System

Figure 1 presents a view of a typical cross section looking downstream. Around the hull and sail are constant velocity contour lines representing the boundary layer profiles. The approach used to represent this geometry is to use polar-like coordinates in the cross plane. A polar coordinate system was modified as shown in Fig. 2. Grid distributions on the inner and outer coordinate circles are used to place grid point I on the inner boundary and grid point I on the outer boundary at the same y coordinate location. The line connecting them is a vertical line, and is used to define the vertical side of the sail. The radial grid lines are clustered around this line to permit resolution of the sail boundary layer. From symmetry, the line indicated -I is also defined.

Coordinate line J in Fig. 2 is taken as the top of the sail between lines I and -I.

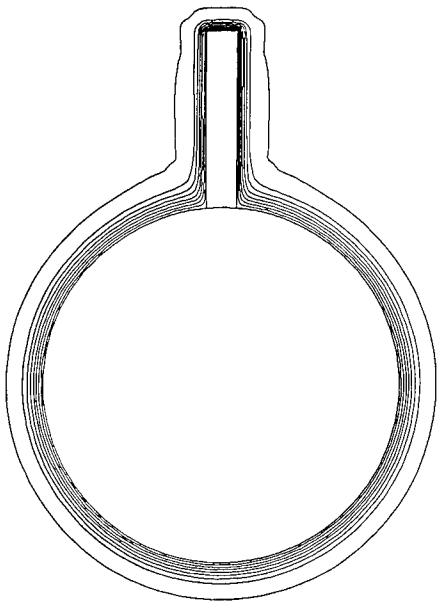


Fig. 1 - Hull-Sail Cross-Section.

The grid is clustered near line J to resolve the flow near the top of the sail. The grid is also clustered near the hull to resolve the hull boundary layer.

The variable sail thickness calculations presented below were accomplished by varying the physical distance between line I and line -I so as to follow the thickness distribution of a modified NACA 16 series foil. This technique allowed the sail surface to be coincident with a coordinate surface providing the required body fitted representation. This approach leads to coordinate lines at each axial station coincident with sail boundaries, as is required by a body fitted coordinate system. Further, grid lines fall within the sail. The points within the sail are clearly external to the flow domain and are treated by separate equations, as is discussed in the following subsection.

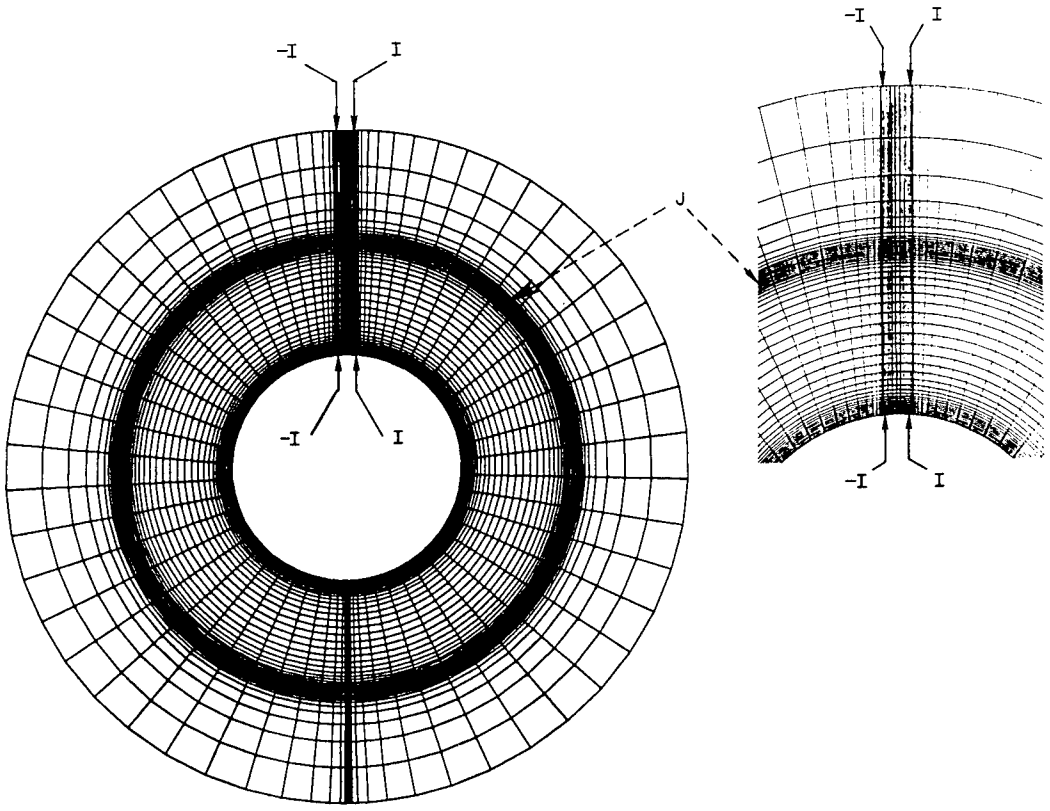


Fig. 2 - Cross-Section Coordinate System.

Boundary Conditions for the Hull-Sail Flow Computations

The cross-sectional computational domain is shown schematically in Fig. 3. Boundaries 1 and 2 are symmetry boundaries. On these boundaries the normal gradient of the streamwise velocity and of the scalar potential were set to zero and the vector potential was set to a constant (normal velocity set to zero). The streamwise vorticity was set to zero as the compatible condition with the vector potential. Boundary 3, the hull surface, and boundaries 5 and 6, the sail surfaces, are all no-slip walls. On these boundaries the no-slip condition was satisfied by setting the normal gradient of the scalar potential (the normal velocity) to zero. In the coupled vector potential and vorticity equations the normal component of the rotational velocity was set to zero and the tangential component was set equal and opposite to the tangential component of the velocity generated by the scalar potential. These conditions allowed an implicit specification of the vector potential and the vorticity on the no-slip boundary, as discussed above in the summary of the algorithm. The resultant secondary velocity field satisfies the no-slip conditions on the boundary. The streamwise velocity was also set to zero at the solid boundary.

Far field conditions were specified on boundary (4). The streamwise velocity was extrapolated from the interior flow field. The scalar potential was set to a constant so that the tangential component of the irrotational velocity was zero. This condition allowed outflow through the boundary due to the displacement effect of the boundary layers. The vector potential was set to zero so that the normal component of the rotational velocity is zero. The streamwise vorticity was set to zero.

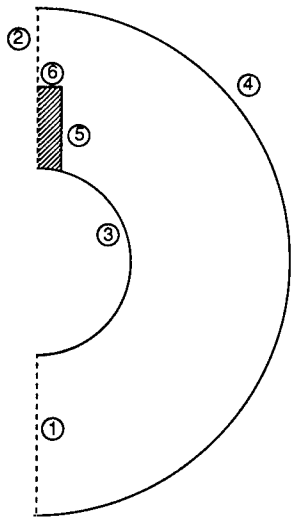


Fig. 3 - Flow Boundaries of the Computational Domain.

The shaded section in Fig. 3 represents regions included within the computational grid which are located physically within the sail. Within the present context there are two obvious techniques for obtaining a solution. The first would set up special purpose code logic so that these points could be excluded from the computational domain. The second would keep these points in the computational domain and specify dependent variable relations at these points consistent with their being points within the sail. Although either approach is viable, the latter is simpler and was chosen. At grid points within the sail, velocity components are set to zero. On the sail surface, boundary conditions are written which do not include information from inside the sail. Replacing the governing equations by these no flow conditions allows the solution of the system of equations to be performed by the existing matrix solvers which are highly efficient subroutines vectorized for the Cray computers. Leaving them intact produces little, if any, run time penalty and confines the code modifications needed to represent the sail to the equation writing subroutines.

Initial Conditions

Hull and sail boundary layer thicknesses are specified. Outside these boundary layers the streamwise velocity is set to unity. Within the boundary layers, the velocity profiles corresponding to flat plate boundary layers at the appropriate Reynolds numbers are used. Near the hull-sail corner, where the two boundary layers merge, an effective boundary layer is approximated at a point in the flow from:

$$\left(\frac{y}{\delta}\right)_{eff} = \left(\left(\frac{\delta_H}{y_H}\right)^{3/2} + \left(\frac{\delta_S}{y_S}\right)^{3/2}\right)^{-2/3} \qquad (16)$$

where δ_H and δ_S are the hull and sail boundary layer thickness and y_H and y_S are the distance to the hull and sail.

The initial vortex distribution is determined by a two-step procedure: first setting a vortex strength and then solving the vorticity-streamfunction equations in the initial cross plane to create a starting secondary flow that is compatible with the hull-sail corner. This is accomplished by first constructing forced vortices of constant strength within the core whose strength, location and core extent are specified through input to the code. The strength and extent of the vortex is first calculated from

$$\Omega = 2\frac{q}{r} \qquad (17)$$

where Ω, the vorticity, is determined as a constant function of q, the magnitude of the edge velocity, and r, the radius of the forced vortex core. Everywhere outside this forced vortex the vorticity is initially set to zero. Second, this constructed vorticity distribution is modified through solution of equations governing streamwise vorticity transport and governing the vector potential in the initial transverse plane subject to appropriate hull

and sail boundary conditions. Solution of these equations results in a new, modified vorticity distribution which includes the effect of the hull and the sail upon the initial plane vorticity profile.

Turbulence Model

In the high Reynolds number flows addressed in this paper it is necessary to specify a turbulence model. Although one of the more sophisticated models, such as a multi-equation model, may eventually be necessary to obtain quantitative simulations, at present, a simpler mixing length type model is used in the analysis. It should be noted that although a k-ε model has been used in internal flow applications of this analysis, quantitatively accurate internal flow simulations have been obtained with a mixing length approach (Refs. 2-4). The mixing-length turbulence model employed here computes an eddy viscosity (μ_T) based upon a mixing length distribution.

$$\frac{\mu_T}{Re} = \rho \ell^2 \left(2\bar{\bar{e}}:\bar{\bar{e}}\right)^{1/2} \qquad (18)$$

where $\bar{\bar{e}}$ is the mean flow rate of strain tensor

$$\bar{\bar{e}} = \frac{1}{2}\left((\nabla\bar{U}) + (\nabla\bar{U})^T\right) \qquad (19)$$

The mixing length (ℓ) is determined from the empiracal relationship of McDonald and Camarata [10] for equilibrium turbulent boundary layers.

$$\ell(y) = 0.09\delta_b \tanh\left[\kappa y/(0.09\delta_b)\right]D \qquad (20)$$

where δ_b is the local boundary layer thickness, κ is the von Karman constant taken as 0.43, y is the distance from the wall and D is a sublayer damping factor

$$D = p^{1/2}(y^+ - \bar{y}^+)/\sigma \qquad (21)$$

where p is the normal probability function, $y^+ = y(\tau/\rho)^{1/2}/(\mu/\rho)$, τ is local shear stress, $\bar{y}^+ = 23$, and $\sigma = 8$. δ_b is taken as the average of the hull and sail boundary layer thickness and (y/δ) is computed from Eq. (16).

RESULTS

The three-dimensional spatial forward marching procedure employed here requires an input approximate streamwise pressure gradient which appears as a source term in the streamwise momentum equation, see Eq. (10). As previously discussed, this pressure gradient must be obtained from an external source. This a priori pressure field serves to provide the elliptic information to the analysis and allows quantitative flow simulations via this three-dimensional forward marching procedure. It should be noted that the streamfunction-vorticity equations which are developed from the transverse momentum equations are not constrained by this assumption and do generate a cross plane pressure field consistent with the computed secondary flow. As previously discussed, the streamwise pressure gradient source term must be obtained from an external analysis. Although a representative pressure field may be required for quantitatively accurate simulations, previous experience has clearly shown that many of the basic physical flow phenomena can be obtained even when this input pressure field is assumed to be a constant (Refs. 5-7). For the cases presented in this paper, the emphasis is upon demonstrating application of the procedure to the hull-sail interaction problem and a constant input pressure field was assumed. Calculations to be performed in the future will include an input applied pressure field based upon an inviscid panel method. It should be noted that in a study of the ship propeller tip flow field, currently being performed at SRA with this same three-dimensional forward marching analysis, an inviscid pressure field of this type is currently being used.

Four test cases were chosen to demonstrate the capability of the forward marching procedure to simulate the vortex-corner flow resulting from a hull-sail interaction. The first two cases use a constant thickness sail and the last two cases use a modified NACA 16 series foil. The cases presented are:

1. Constant thickness sail, laminar flow
2. Constant thickness sail, turbulent flow
3. Variable thickness sail, laminar flow
4. Variable thickness sail, turbulent flow

These cases were chosen to demonstrate the computation of the basic flow processes in the corner region of the hull-sail interaction and to indicate the effects of sail thickness on the flow field.

Case 1: Constant Thickness Sail, Laminar Flow

The initial test case considered is the basic case of laminar flow with a constant thickness sail. Laminar flow was computed in the hull-sail region. A 50 x 50 cross-sectional grid was used in the right half plane to take advantage of the symmetry of the flow. The Reynolds number was 1000, based on hull diameter, D, and freestream conditions, and the sail height was 1/2 hull diameter. The initial hull boundary layer thickness was set to .1 D and the sail boundary layer thickness set to .05D. A streamwise step size of .025D was used. A starting vortex was modeled as described above. The starting flow field is shown in Fig. 4a. On the left is the cross-section of the vehicle showing both the axial velocity on the bottom and the cross flows on the top. The vortex location is evident. The maximum secondary velocity is 0.15 U_∞. As the flow proceeds downstream, Figs. 4b through 4d, the very low Reynolds number causes the viscous losses to be large. The boundary layers on the hull and on the sail are seen to grow, and the vortex strength is seen to suffer very significant decay, as would be expected at this very low Reynolds number. Little distortion of the axial velocity is seen.

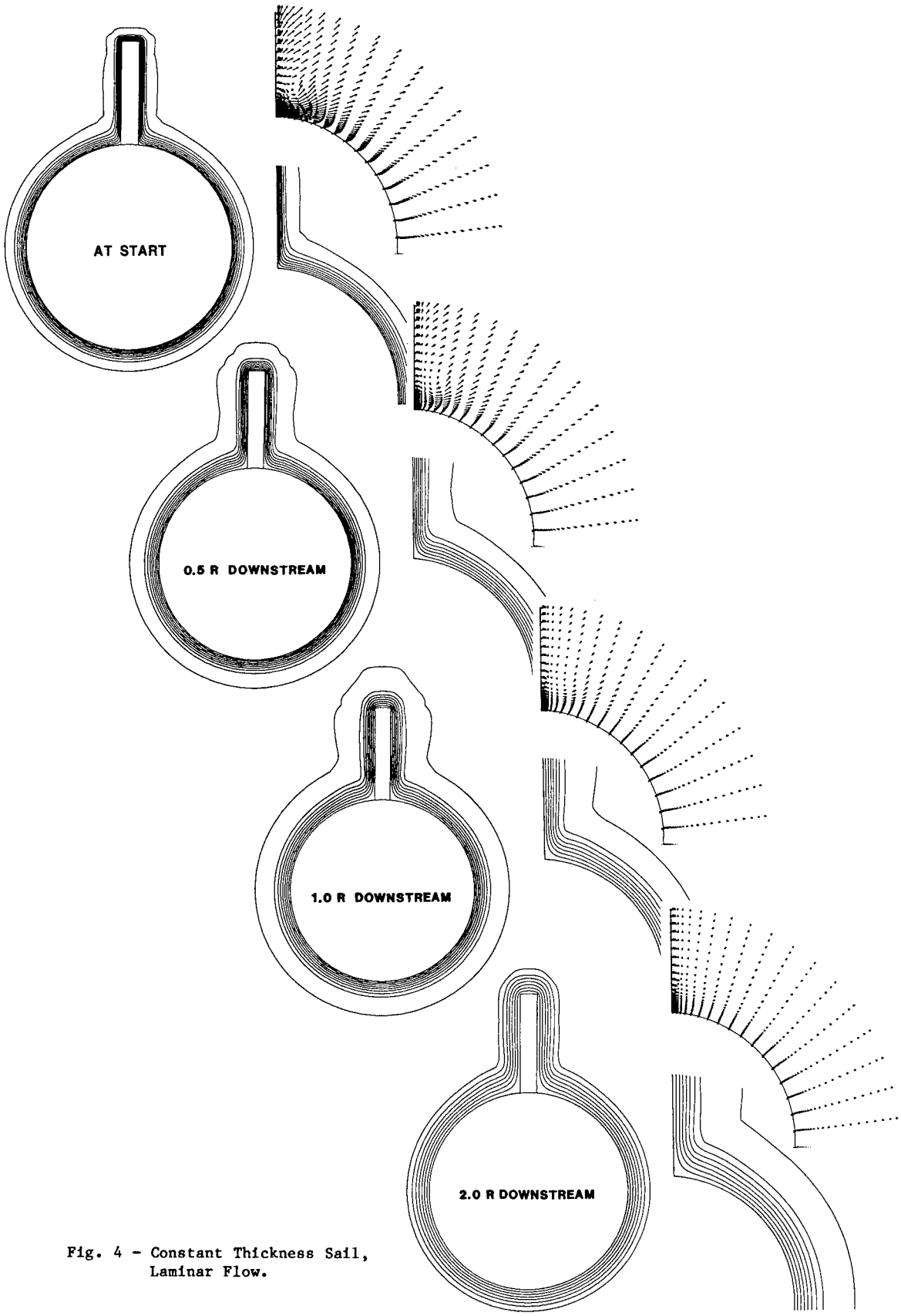


Fig. 4 - Constant Thickness Sail, Laminar Flow.

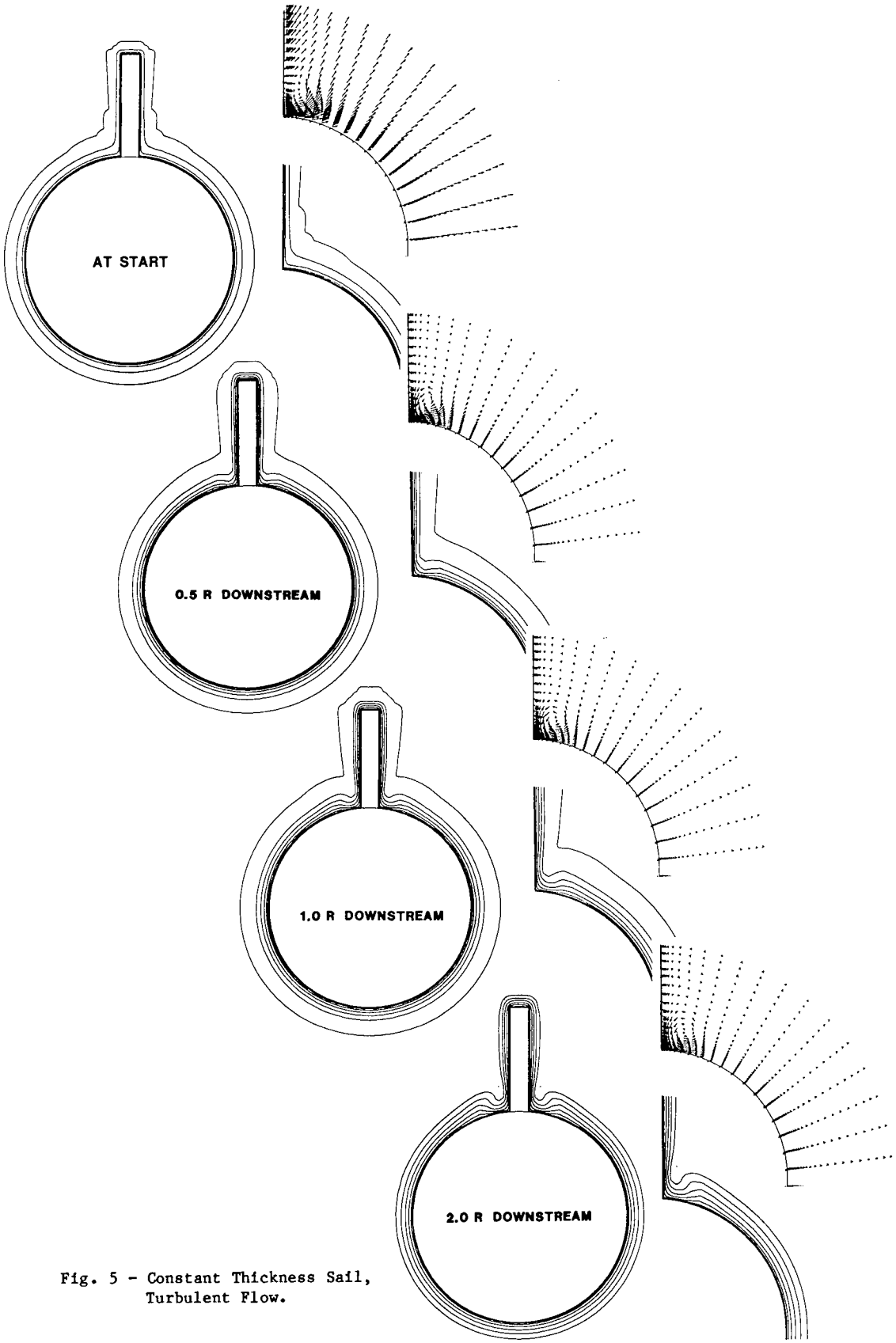


Fig. 5 - Constant Thickness Sail, Turbulent Flow.

Case 2: Constant Thickness Sail, Turbulent Flow

A turbulent flow calculation was performed at a Reynolds number of 10^6, based on hull diameter and freestream velocity. The computational coordinate mesh was the same as in the laminar calculation presented above. Also, the hull boundary layer was .1D, and the sail boundary layer was .05D. A corner vortex was modeled and placed in the starting flow field as shown in Fig. 5a. Although the boundary layer thickness in the laminar and turbulent flow cases were the same, the difference in starting profiles is clearly seen by comparing Fig. 4a and Fig. 5a.

At this high Reynolds number, the vortex persists as it is convected downstream. This vortex distorts the axial flow, as seen by the distortion of the axial velocity contours in Figs. 5b through 5d. This distortion of the primary flow is accompanied by large cross flow velocities along the hull near the corner which appears to result from the vortex-corner interaction.

Although the present results must be regarded as qualitative because (i) the assumed constant a priori pressure field, (ii) the relatively simple turbulence and (iii) the need for further grid refinement particularly along the sail, the results do show considerable correspondence to the experimental turbulent flow data of Rood (Ref. 8). The data of Rood is shown in Fig. 6. It should be noted that the measured and numerically simulated distortions in the axial velocity contours show significant similarity, as do the generated secondary flow characteristics. In particular, note the large cross flows near the hull surface which appear both in the numerical simulation and the measured data.

Case 3: Variable Thickness Sail, Laminar Flow

Although the previous test cases show significant flow field physics, they represent an idealized geometric configuration. The long term objective of this study is to model the flow for realistic configurations at angle of incidence. The next step in realizing this objective is inclusion of variable sail thickness. This is demonstrated in cases 3 and 4.

Since these were the first variable thickness sail calculations, a NACA 16 series foil was modified for use in the calculation to emphasize the basic physical processes involved and to reduce the emphasis on grid generation. The modifications shown in Fig. 7 include a constant thickness upstream extension and an aft fairing to a constant thickness downstream extension. From their experience with the subject flow analysis, the authors believe that future calculations on an unmodified foil could be started near 5% of chord and continued beyond the trailing edge.

For the calculations presented here, the maximum sail thickness was 10% of the hull diameter. A 50x50 cross-sectional coordinate mesh was used with grid clustering near the solid walls. The streamwise step size was 0.1 chord. The hull boundary layer thickness was 0.1D and the sail boundary layer thickness was 0.05D. The Reynolds number based on hull diameter was 10^3.

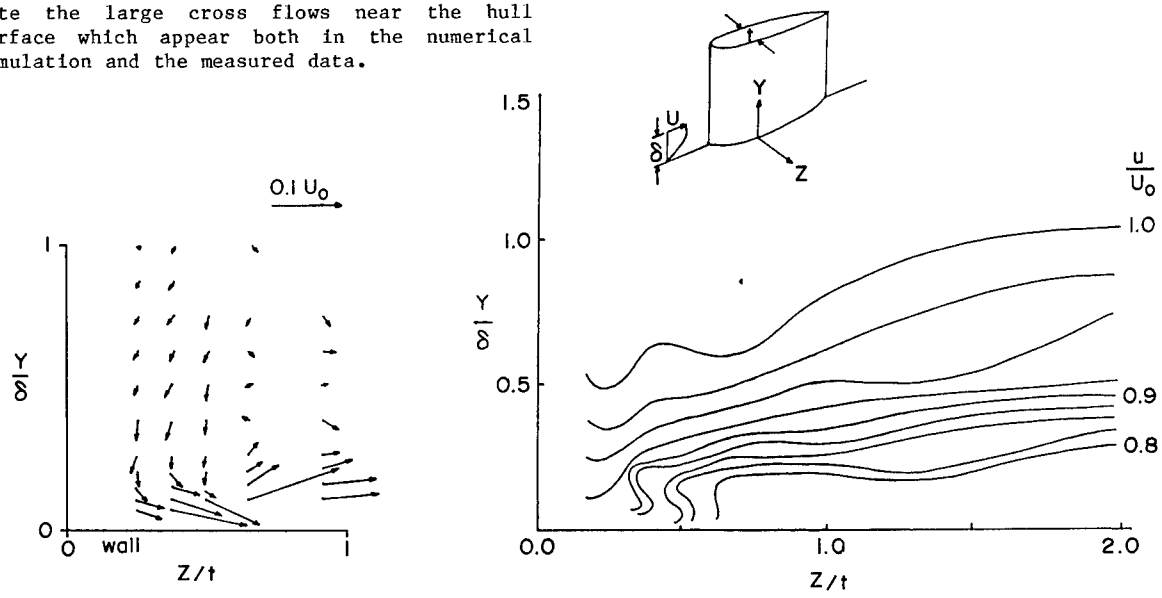


Fig. 6 - Experimental Investigation of Turbulent Flow in a Wing-Body Junction, (From Ref. 8).

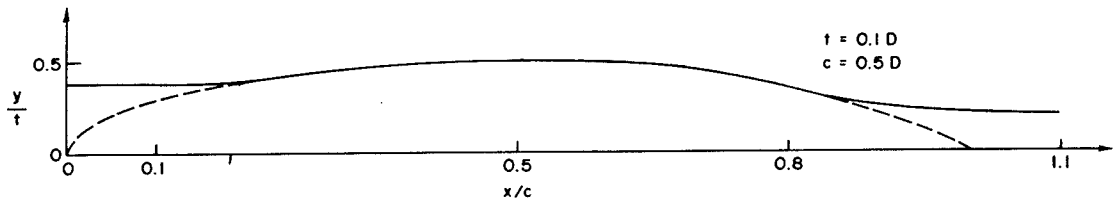


Fig. 7 - Modified NACA 16 Series Foil, a = 0.8.

Results of this calculation are presented in Fig. 8 at the four locations shown in Fig. 7, x = 0.1, 0.5, 0.8, 1.1. Presented in Fig. 8 are cross-sections of the body showing streamwise velocity contours, an enlargement of these contours at the top of the sail, cross flow velocity vectors at the top of the sail and cross flow velocity vectors in the hull-sail corner. The growth of the hull boundary layer is evident in the figures down the left side of Fig. 8. The effect of sail thickness variation on the boundary layer is best seen in the streamwise velocity contours at the top of the sail. Where the sail is thickening, the boundary layer on the side of the sail grows more slowly than the boundary layer on the top, (x = 0.1 to x = 0.5). As the sail thins, the boundary layer on the side of the sail thickens quickly (x = 0.8 and x = 1.1). The cross flow vectors at the top of the sail are seen to move away from the side of the sail as it thickens and to move toward the side of the sail as it thins.

The velocity vectors in the hull-sail corner show the development of the corner vortex. The initial vortex (at x = 0.1) is difficult to see since it is masked by the velocity from the initial growth of the corner boundary layers. However, it should be noted that vorticity need not be associated with a clear circular flow pattern, but rather is associated with transverse flow gradients. The results of Fig. 8 show a clear circular flow pattern appearing by x = 0.5. This pattern persists as the flow proceeds downstream and a clear vortex is still apparent at the last station, x = 1.1 The results of Fig. 8 are quite consistent with those of Fig. 4 at the same streamwise location. When this calculation was carried to x = 2.0 the the vortex decayed almost completely as in the previous case. The rate of decay is determined by the flow Reynolds number, and at higher Reynolds number laminar flows the vortex strength persists to distort the primary flow. This has been demonstrated in this study by calculations which space prevents presenting here.

Case 4: Variable Thickness Sail, Turbulent Flow

The final case considered is a turbulent flow at a Reynolds number of 10^5 based on hull diameter. The geometry and computational grid for this case are the same as for the previous test case. The results are presented in Fig. 9. Although the initial boundary layer thickness on the hull and sail are the same as in the previous laminar flow test case, the turbulent boundary layer profile is evident from the clustering of the streamwise velocity contour lines near the surfaces. Qualitative behavior of the flow is similar to the previous laminar flow test case except in the hull-sail corner. The lower dissipative effects of the higher Reynolds number result in the vortex retaining its strength and beginning to distort the primary flow. This is seen at the bottom of Fig. 9 as a thickening of the streamwise flow boundary layer on the hull near the sail. From the cross flow vectors it can be seen that low velocity flow from along the sail is being convected into the corner and out along the hull surface by the corner vortex. The large region of low velocity fluid along the sail results from the variable thickness of the sail and is not evident in the constant thickness test case presented above, Fig. 5. The secondary flow along the hull is seen to grow large as in the previous turbulent flow test case and as in the data of Rood (Ref. 8) discussed above. In comparing the results of Figs. 5 and 9, the calculations in Fig. 5 were initiated with a stronger vortex, as can be seen by the respective secondary flow vector plots at the starting location.

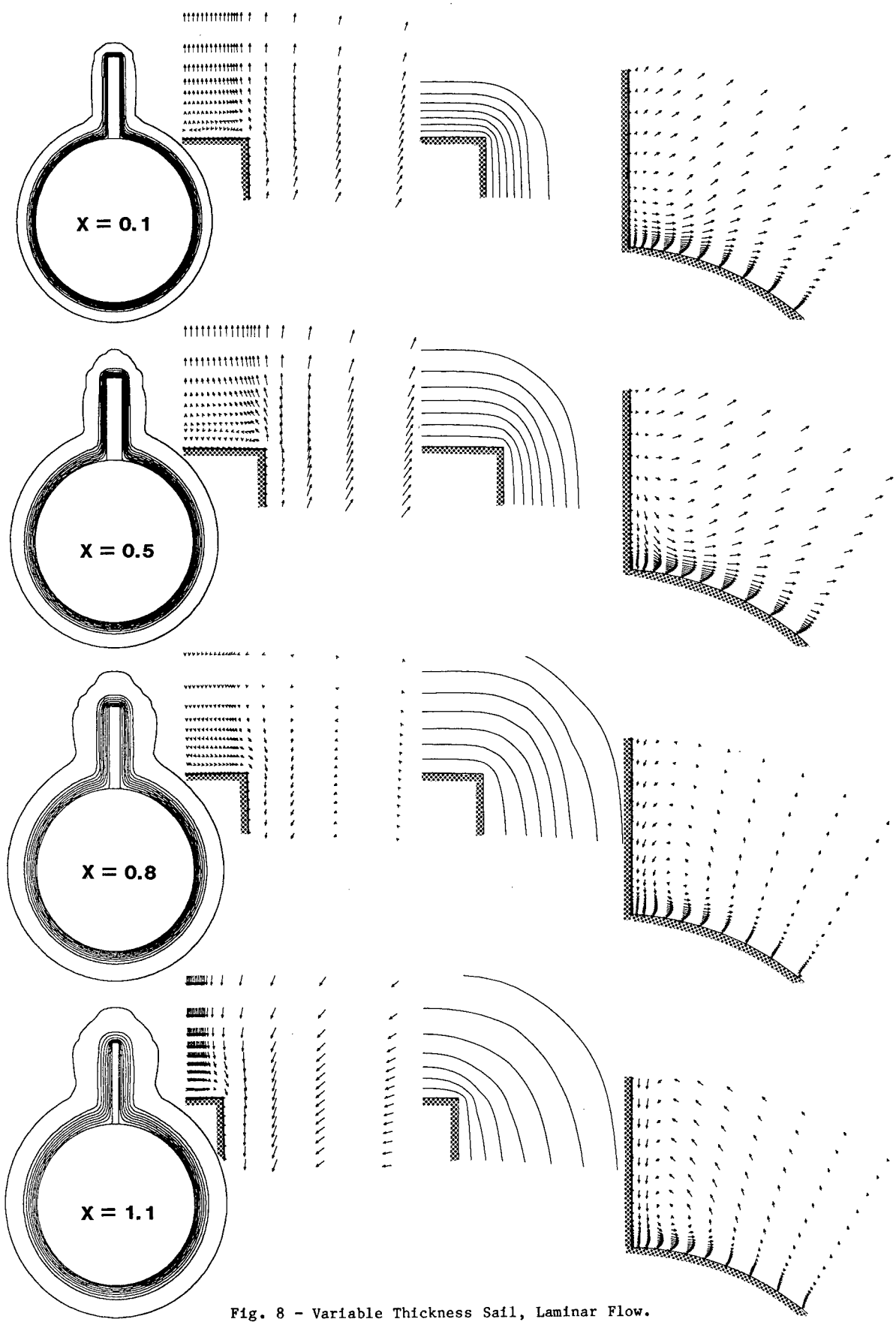


Fig. 8 - Variable Thickness Sail, Laminar Flow.

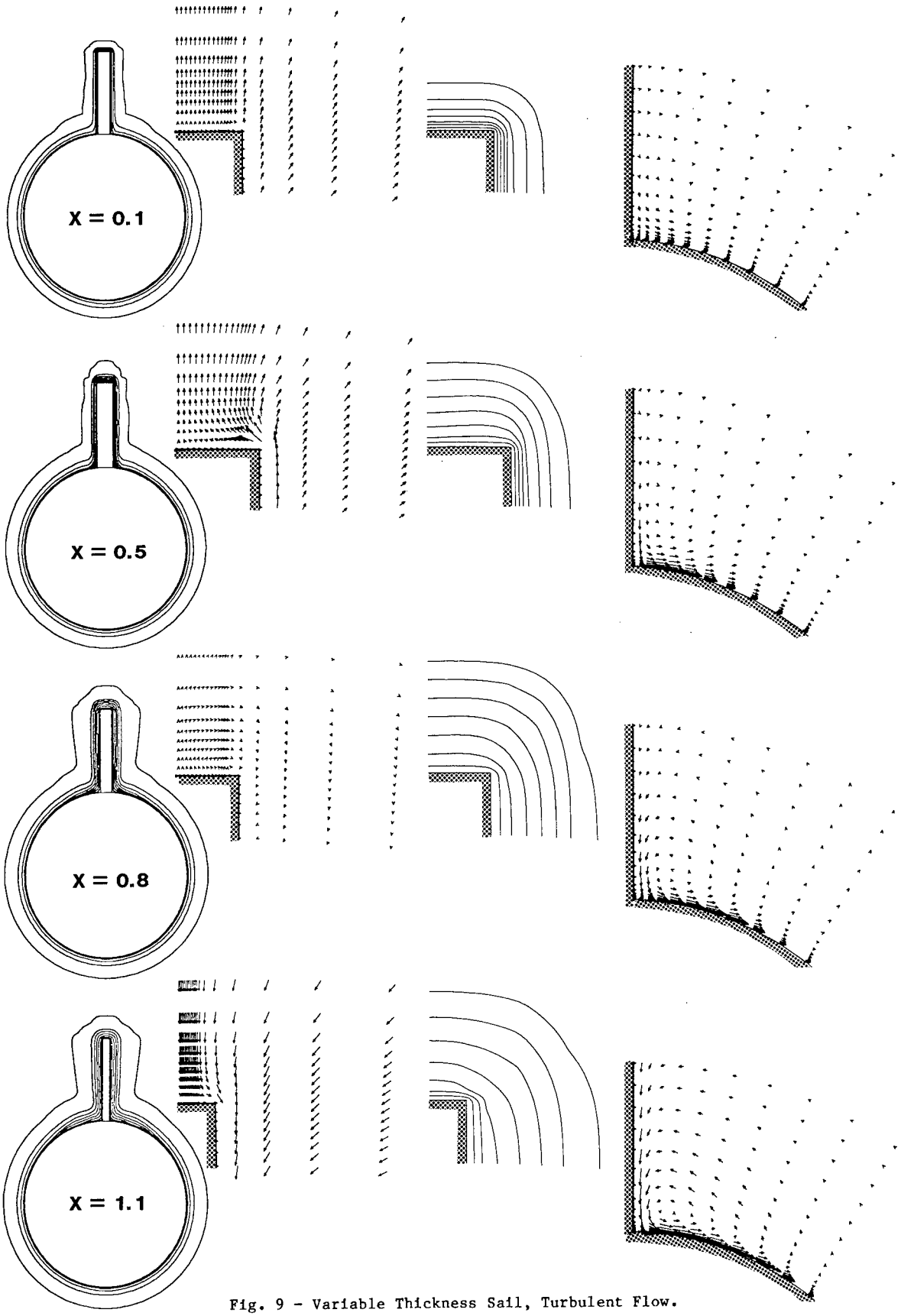


Fig. 9 - Variable Thickness Sail, Turbulent Flow.

CONCLUSIONS

The long range objective of this study is to predict the flowfield resulting from the hull-sail interaction of a submarine at angle of incidence. This includes the sail leading edge, the hull-sail corner and the downstream sail wake-vortex-hull interactions. This paper, reporting the first part of this study, documents the application of an efficient spatial marching, three-dimensional viscous flow analysis to the flow in the hull-sail corner at zero angle of incidence. Starting with an assumed forced vortex in the hull-sail corner aft of the sail leading edge, test calculations were performed for both laminar and turbulent flow for a constant thickness sail and a variable thickness sail. Computed results for the cases presented show the qualitative features of the hull-sail flow-field, and are in qualitative agreement with the turbulent flow data of Rood (Ref. 8). The results show the influence of the sail thickness distribution on the flow around the sail, the acceleration of the cross flow along the hull in the hull-sail corner and the distortion of the streamwise flow by the corner vortex. The computations are economical compared to computing solutions to the full Navier-Stokes equations for this region. Typical computer run times on a Cray XMP using a single processor for 30,000 grid points are approximately 2 minutes for each calculation presented.

Further development of this analysis is needed to compute flow about a submarine at incidence including both pitch and yaw. To accomplish this the computations should incorporate (i) an imbedded Navier-Stokes solution to the sail leading edge, (ii) an a priori pressure field to improve quantitative accuracy, and (iii) a turbulence model suitable for wake flows. Benchmark quality experimental data will be necessary to verify the accuracy of the computational analysis.

ACKNOWLEDGEMENT

This work was sponsored by the Naval Sea System Command under the General Hydrodynamics Research Program administered by the David W. Taylor Naval Ship Research and Development Center under Contract N00014-84-C-0096.

REFERENCES

1. Briley, W.R. and McDonald, H.: Computation of Turbulent Horseshoe Vortex Flow Past Swept and Unswept Leading Edges, Report R82-9200001-F, Contract N000014-77-C-0075.

2. Briley, W.R. and McDonald, H.: Analysis and Computation of Viscous Subsonic Primary and Secondary Flows. AIAA Paper 79-1453, 1979.

3. Levy, R., Briley, W.R. and McDonald, H.: Viscous Primary/Secondary Flow Analysis for Use with Nonorthagonal Coordinate Systems. AIAA Paper 83-0556, 1983.

4. Towne, C.E., Computation of Viscous Flow in Curved Ducts and Comparison with Experimental Data. AIAA Paper 84-0531, 1984.

5. Govindan, T.R., Levy, R. and Shamroth, S.J.: Computation of the Tip Vortex Generation Process for Ship Propeller Blades. Fourth National Conference on Numerical Ship Hydrodynamics, Washington, D.C., 1985.

6. Govindan, T.R. and Levy, R.: Computation of the Tip Vortex Flow Field for Advanced Propellers. Report R85-900046-F, NASA Contract NASA-24532, 1985.

7. Lin, S.-J., Levy, R., Shamroth, S.J. and Govindan, T.R.: A Three-Dimensional Viscous Flow Analysis for the Helicopter Tip Vortex Generation Problem, AIAA Paper 86-0560, 1986.

8. Rood, E.P.: Experimental Investigation of the Turbulent Large Scale Temporal Flow in the Wing-Body Junction, Catholic University of America, 1984.

9. Briley, W.R. and McDonald, H.: On the Structure and Use of Linearized Block Implicit Schemes, Journal of Computational Physics, Vol. 34, 1980.

10. McDonald, H. and Camarata, F.J.: An Extended Mixing Length Approach for Computing the Turbulent Boundary Layer Development, Proceedings of the AFOSR-IFP-Stanford Conference on Boundary Layer Prediction, Stanford, CA, 1986.

DISCUSSION

Hyoung-Tae Kim,
Iowa Institute of Hydraulic Research

I understand that the effect of downstream pressure may be important in a corner flow. Could you show the pressure distribution? Are you sure you don't need to make a pressure correction or to update iteratively to get a more reasonable, converged solution?

Reply -

The treatment of the streamwise pressure gradient, as shown in the streamwise momentum equation, is viewed as a physical approximation rather than a trial guess to be removed by iteration. The present approximating equations determine a new three-dimensional pressure field, consistent with the transverse momentum equations. Multiple streamwise sweeps of the flow domain are not needed to solve the set of approximate flow equations, since this set is a well-posed initial-value problem, and consequently, these approximations lead to considerable economy in the solution procedure.

The approximate equations solved by the forward-marching procedure contain in them the flow features of a hull-sail corner flow. These include the large secondary velocities and the distortion of the primary velocity field, both of which are present in the flow predictions given in the paper.

Not included in the present approximating equations is the effect of the perturbed streamwise pressure gradient on streamwise momentum balance due to the computed pressure field. This effect could be included by solving the Navier-Stokes equations and would be included if a convergent "guess and correct" multiple-sweep iteration procedure were devised such that the (corrected) pressure field computed from the transverse momentum equations converged to that assumed for the streamwise momentum equation. In either case, the approximating equations being solved are elliptic and subject to downstream boundary conditions. In general, elliptic equations are far more costly to solve than well-posed initial-value problems.

Nan King,
U.S. Navy Strategic Systems Programs Office

Your present and future works have important design applications, if successful. In your paper, you comment that "Benchmark quality experimental data will be necessary to verify the accuracy of the computational analysis." (Last paragraph of paper.) With regards to overall total effort, is there an effort to obtain such quality experimental data for verification purposes at particular points in your efforts?

Reply -

Experimental work on related flow configurations is being sponsored by the U. S. Navy. Several experiments are now underway. We hope these programs will continue and grow in scope.

Michael Mendenhall,
Nielsen Engineering & Research

Would the authors care to comment on any numerical difficulties they anticipate when the method is applied to submarine configurations at full-scale Reynolds numbers.

Reply -

The critical requirements for calculation of high Reynolds number flow is the ability to resolve the various length scales that appear. This requires an analysis that can operate efficiently when large numbers of computational grid points are used to resolve the different length scales in different parts of the flow field. The analysis used here is computationally efficient and has the characteristic that run time scales nearly linearly with the total number of grid points. The turbulent flow case presented in this paper was at Reynolds number based on hull diameter of 10^5. In other applications, flow at Reynolds numbers based on diameter of 4×10^7 has been computed with this same analysis. Calculation of flow at full-scale Reynolds numbers of 10^8 to 10^9 based on diameter appear to be achievable.

V.C. Patel,
Iowa Institute of Hydraulic Research

I agree with your assessment that the qualitative features of your results are correct. I have a number of questions which are related to the details of the computations:

a. Why is it necessary to cluster the grid at the bottom of the body in Figure 2?

b. Your computation domain extends up to 2R, which is not too far from the body. Does this mean that the imposed (inviscid) dp/dx should be updated in a second streamwise pass through the solution domain?

c. How sensitive is your solution to the location of the outer boundary?

d. In the turbulence model, how are the distance from the wall (y) and the boundary-layer thickness defined in the corner region?

Reply -

a. The grid was clustered at the bottom to permit a very accurate calculation of the symmetry condition at this line. This is a cautious approach and probably not required for this problem.

b,c. The outer boundary conditions were chosen carefully to permit the outer boundary to be near the body. As a result, the solution is relatively insensitive to the location of the outer boundary. In an alternative application of this analysis, the vortex generation on a propeller tip, flow calculations were made with several choices of outer boundary location. In each case the outer boundary was much closer to the body, both nondimensionally and in physical units, than in the case presented in this paper. The surface pressures, vortex strength and location and the velocity field were found to be insensitive to outer boundary location.

The Navier-Stokes equations are approximated by a set of physical approximations as outlined in this paper. The resulting set of governing equations can be solved as an initial value problem in space with the nominal streamwise direction being the marching direction. There is no second pass in this algorithm.

d. Distance from the wall and boundary layer thickness for the turbulence model are computed as they are for the initial conditions by Equation 16.

Three-Dimensional Flow Separation and the Effect of Appendages

M.-S. CHANG and L. P. PURTELL

David W. Taylor Naval Ship R&D Center, U.S.A.

ABSTRACT

A numerical method for computing flow separation from a long three-dimensional body has been developed based on the potential flow approach. By considering the similarities of the local separating cross-flow to a two-dimensional separation, a Kutta condition was derived and incorporated into the method for calculation of the separated vortex sheet. Computations were compared to experiments for an ogive-cylinder and prolate spheroid at angle of attack. The results show definite improvements over previous attempts.

Since the potential flow model requires that the positions of the separated vortex sheets be specified, a boundary layer model was employed to predict for this purpose the locations of the surface shear convergence lines. The computations compared favorably with published measurements on the spheroid and lend confidence to application of the method to other cases.

To simplify the measurement of the flow around a turning body, a method was developed to transform the body and flow field into a curved body in a straight flow. Recognizing that approximations were involved, the method was tested computationally in terms of pressure distribution (potential flow) and surface shear convergence (separation), both of which validated the approach. Thus a curved model was built and measurements of pressure, velocity, and the location of separation were conducted. Corresponding computations agreed well with the measurements.

The influence of a low aspect ratio vertical appendage on the turning body was investigated using the curved model. The symmetry of the flow around the body without an appendage was significantly distorted by the addition of the appendage. This was apparent in the pressure and convergence line measurements and in the wake velocity measurements which showed a radical repositioning of the streamwise vortices generated by the separation.

INTRODUCTION

When an axisymmetric body moves at a sufficiently large angle of attack, one observes a complicated flow separation quite different from streamwise separation on a planar two-dimensional body. The wide variety of separation phenomena that can occur, depending upon geometry and angle of attack, has prompted a major effort merely to ascertain the topology of the flow field, e.g., Tobak and Peake [1], Hornung and Perry [2], Perry and Hornung [3]. In general, a crossflow develops very near the surface leading to lines of flow convergence across which the surface shear stress is zero. Along these lines the boundary layer vorticity may lift off the surface in sheets and be convected downstream where the sheets rapidly coil into streamwise vortices (Figure 1). This type of separation caused by the crossflow near the surface will be referred to in this paper as cross-plane separation.

Since cross-plane separation will occur on almost all maneuvering bodies, except at very small angles of attack, its consideration is important to proper body design. Cross-plane separation is particularly important in determining the velocity field near the stern for its effect on propulsion and in determining the pressure distribution on the body and its influence on maneuverability and control. The problem is compounded for a vehicle executing a small radius turn. In this case, the local angle of attack varies significantly along the length of the body (see Figure 2) and will, in general, even reverse slightly near the bow. For instance, the local flow angle can vary more than fifteen degrees over the aft twenty percent of a body under a tight turn of 0.8 body lengths in radius.

Though the effects of cross-plane separation are substantial and have been recognized for some time, the flow is so complex that no completely satisfactory analytical tools are available. A comprehensive method would need to calculate the boundary layer development up to the separation lines, then calculate the vortex sheet lift-off, and trajectory, as well as the influence on the outer potential flow requiring a viscous-inviscid interaction calculation capability.

Boundary layer separation of any kind is fundamentally a viscous phenomenon. Yet, in many respects, ideal flow solutions can approximate the real fluid flow phenomena quite well. An outstanding example is the use of ideal wing theory to calculate lift which is physically a result of viscous action. Use of a Kutta condition at the trailing edge permits highly accurate computations of the flow field and resultant lift. Cross-plane separation is also viscous in origin but more complex than the two-dimensional wing. However, this inherently three-dimensional flow can and has been approached using potential flow techniques with the wake being considered as part of the singularity surface. The earlier methods developed were of the marching two-dimensional type, e.g. Mendenhall and Perkins [4]; three-dimensional methods, Kato and Yamaguchi [5], Thrasher [6], were only recently derived. The primary difficulty to be overcome by these methods is the absence of a predetermined location of separation for specifying the appropriate Kutta condition. The sharp trailing edge of a wing fixes separation there, but the generally smooth surface of a body

David W. Taylor Naval Ship • Research and Development Center • Bethesda, MD 20084

at angle of attack has no such characteristic location. Mathematically, there is no singularity in the potential flow solution around the smooth surface, so there is not even a need to apply a Kutta condition to the flowfield. Thus, other physical conditions must be considered in order to establish an appropriate requirement for separation specification. At present, no fundamental theoretical derivation or experimental determination of a Kutta condition has been achieved. Instead, phenomenological methods have been developed which vary from author to author. For example, in Mendenhall and Perkins [4], Kutta conditions are applied at positions determined from a modified two-dimensional separation criterion with vortex strengths equal to the total vorticity generated in the viscous layer and at radial locations which reduce the crossflow velocities to zero at the separation locations on the body. In Tinker [7], the Kutta condition is applied fifteen degrees leeward from the location of minimum pressure and with strengths and radial locations empirically specified. The Kutta condition employed by Kato and Yamaguchi [5], a three-dimensional computation, differs from the others in that the vortex strengths are determined by specifying the velocity directions at given locations estimated from physical and numerical experiments. In Maskew and Dvorak [8], the Kutta condition is the conservation of potential jump from the separation location to the wake.

Experiments on turning models using a rotating arm apparatus are difficult and usually lack detailed velocity measurements. Measurement about a stationary model in a moving flow, such as in a wind or water tunnel, has distinct advantages, but the curving shear flow required for a turn would be nearly impossible to achieve. However, one approach which has been very useful in two-dimensional potential flow is the transformation of the straight body in a curving flow to an appropriate curved body in a straight flow. In two dimensions, this merely involves a logarithmic conformal transformation. Though not so simple in three-dimensional flow, the method was explored with some success at the Central Aero-Hydrodynamical Institute, Moscow, USSR, in 1934 by Gourjienko [9]. The approach was to apply a purely geometrical transformation to physical space based on the concept of maintaining local angle of incidence to the oncoming flow. This is effectively the logarithmic transformation applied to each plane of the body parallel to the plane of motion. The method is not theoretically exact, but the evidence indicates it is a very useful approximation.

A major goal of the present computational work is the prediction of three-dimensional separation based on a more rigorously founded Kutta condition for numerical models. The numerical effort involves the development of a three-dimensional potential flow computer code based on Green's theorem with doublet distributions. It is similar in concept to that of Maskew and Rao [10] but differs importantly in prescribing the Kutta condition. Here, not only is the jump in potential conserved, but also the jump in cross-flow velocity. The method requires information on the location of separation lines either from boundary layer calculations or experiments. Results are shown for the ogive cylinder and prolate spheroid at angle of attack.

A second goal of this work is the extension and improvement of the turning body transformation technique for experimental testing. The technique has been analyzed and modified, and a model has been built and tested in a wind tunnel. Encouraging results have been obtained from velocity measurements, pressure measurements, and flow visualization.

COMPUTATIONAL APPROACH

A simple potential model with proper closure conditions on the wake can compute the flow field around a two-dimensional cylinder in good agreement with experimental measurements, Celik, Patel, and Landweber [11]. If it is thus postulated that the general physics of cross-plane separation is similar to that of two-dimensional separation on a cylinder, then the development of an appropriate potential model should also be possible for this more complex flow. Following this approach, the separated flow around the body is represented as in Figure 1, where the main features are the roll-ups of the vortex sheets downstream of separation. In reality there is a viscous layer on the body surface, and the wake could be somewhat more complicated than is shown. Nevertheless, for the potential flow model, the problem is simplified by neglecting the viscous layer (except in locating the separation lines) and assuming that the trailing vorticity is confined to thin sheets. These simplifications will be justified if pressure distributions and resultant forces (in contrast to fine details of the flow) are adequately predicted.

Assuming an incompressible fluid, the flow field can be generated by singularities on the body surface and by the vortex sheets. From Green's Theorem the velocity potential, ϕ, at a point P (x, y, z) is

$$\phi(p) = -\frac{1}{4\pi}\iint_{S_B + S_{w+} + S_{w-}} G(P,Q)\frac{\partial}{\partial N}\phi(Q)\,dS(Q) + \frac{1}{4\pi}\iint_{S_B + S_{w+} + S_w} \phi(Q)\frac{\partial}{\partial N}G(P,Q)\,dS(Q) \quad (1)$$

where (fig. 3):

x, y, z are space coordinates with x oriented along the axis of the body, positive aft, z upward and normal to the plane of the manuever, and y given to form a right hand system.

G (P,Q) is the Green's function for a source point at Q and field point at P. It equals $1/|PQ|$ where $|PQ|$ is the distance between P and Q.

S_B is the body surface.

S_w is the wake surface where + and − denote upper and lower surfaces.

$N=(N_x, N_y, N_z,)$ is the unit vector normal to the surface,

and dS(Q) is the differential surface element at Q.

If the vortex sheets are thin, then across the wake surface, S_w, there is no discontinuity in the normal component of velocity, $\partial\,\phi\,(Q)/\partial N$, and

$$\iint_{Sw^+ + Sw^-} G\frac{\partial \phi}{\partial N}\,dS = 0.$$

Equation (1) is thus reduced to

$$\phi(P) = -\frac{1}{4\pi}\iint_{S_B} G(P,Q)\frac{\partial}{\partial N}\phi(Q)dS(Q) + \frac{1}{4\pi}\iint_{S_B}\phi(Q)\frac{\partial}{\partial N}G(P,Q)dS(Q) + \frac{1}{4\pi}\iint_{S_w}\Delta\phi(Q)\frac{\partial}{\partial N}G(P,Q)dS(Q) \quad (2)$$

where $\Delta\phi$ is the jump in potential across the surface, i.e., $\Delta\phi=\phi|_{Sw}{}^{+}-\phi|_{Sw}{}^{-}$. Since the potential function is continuous, in steady flow the value of this jump is the same along each streamline and at the body surface across the separation line. Symbolically as a point on the body, S_B, approaches the separation surface, Sw^+ or Sw^-, this can be written

$$\Delta\phi = \phi|_{Sw+} - \phi|_{Sw-} = \phi|_{SB \to Sw+} - \phi|_{S_B \to S_w-} \quad (3)$$

Equation (2) can be solved for the potential function, $\phi(Q)$, if $\partial\phi(Q)/\partial N$ on the body surface is specified and separation lines are given. $\partial\phi(Q)/\partial N$ is related to the body motion by

$$\frac{\partial\phi(Q)}{\partial N} = \underline{V}\cdot\underline{N} \quad (4)$$

where $\underline{V}$ is the velocity vector of point Q on the body surface. A solution of Equation (2) is unique only if the body has sharp corners fixing the location of separation and thus of the Kutta condition application. A smooth body does not require a Kutta condition to be applied *anywhere*; $\Delta\phi=0$ is a perfectly satisfactory solution. Therefore, in order to obtain a nontrivial solution, an auxiliary condition is needed. Some of the numerical methods do not discuss this clearly; in many cases, e.g., Thrasher [6], and Jepps [12], a cross-flow stagnation was established implicitly by the configuring of the wake panels. As seen in Fig. 4, the computed pressure distributions near the separation region do not agree well with corresponding measurements.

Kato and Yamaguchi [5] imposed an explicit condition in their three-dimensional method by specifying the flow direction in the wake region near separation. In their approach, the direction of the flow at some wake locations is set tangent to the body surface at the separation lines. Although this is a physically sound condition, the solutions depend on the locations chosen for specifying the velocity. However, through numerical experiments, locations were determined which lead to numerical results in good agreement with measurements.

In the present method, also, the auxiliary condition is explicit but differs from that of Kato and Yamaguchi [5]. It is a modification of the two-dimensional approach of Maskew and Dvorak [8] and is given as

$$\left.\frac{\partial\Delta\phi}{\partial s}\right|_{S_w \to S_B} = \left.\frac{\partial\Delta\phi}{\partial x}\frac{\partial x}{\partial s}\right|_{S_w \to S_B} = \Delta v\Big|_{S_B \to S_w} = v\Big|_{S_B +} \quad (5)$$

where s is the cross-plane arc length and v the cross-plane velocity. This relates the streamwise variation of circulation, $\partial\Delta\phi/\partial x$, with the cross-flow velocities upstream of the separation.

The panel method described in Maskew and Rao [10] was employed to solve the system of equations (2) and (5) with separation lines on the body being prescribed beforehand. After the potential function, ϕ, is evaluated on the panels of the body surface (Fig. 5), the velocities are computed by a local linear expansion of the potential:

$$d\phi = \frac{\partial\phi}{\partial x}dx + \frac{\partial\phi}{\partial y}dy + \frac{\partial\phi}{\partial z}dz \quad (6)$$

$$\frac{\partial\phi}{\partial x}Nx + \frac{\partial\phi}{\partial y}Ny + \frac{\partial\phi}{\partial z}Nz = \underline{V}\cdot\underline{N} \quad (7)$$

To obtain the unknowns $\partial\phi/\partial x$, $\partial\phi/\partial y$, and $\partial\phi/\partial z$ in Equation (6) with the constraints of Equation (7), the method of Lagrangian multipliers was utilized. With a proper choice of the neighboring panels, the velocities are computed from a set of equations derived from Equations (6) and (7):

$$\sum_{i=1}^{m}(\Delta\phi_i - \frac{\partial\phi}{\partial x}\Delta X_i - \frac{\partial\phi}{\partial y}\Delta y_i - \frac{\partial\phi}{\partial z}\Delta z_i)\Delta X_i - \lambda N_x = 0$$

$$\sum_{i=1}^{m}(\Delta\phi_i - \frac{\partial\phi}{\partial x}\Delta x_i - \frac{\partial\phi}{\partial y}\Delta y_i - \frac{\partial\phi}{\partial z}\Delta z_i)\Delta y_i - \lambda N_y = 0$$

$$\sum_{i=1}^{m}(\Delta\phi_i - \frac{\partial\phi}{\partial x}\Delta x_i - \frac{\partial\phi}{\partial y}\Delta y_i - \frac{\partial\phi}{\partial z}\Delta z_i)\Delta z_i - \lambda N_z = 0$$

and (8)

$$\frac{\partial\phi}{\partial x}N_x + \frac{\partial\phi}{\partial y}Ny + \frac{\partial\phi}{\partial z}Nz = \underline{V}\cdot\underline{N}$$

where m is the number of neighboring panels and λ is the Langrangian multiplier. In the present approach, four neighboring panels were chosen for each velocity computation. Pressures were then computed from the Bernoulli equation and integrated over the body surface to determine the resultant force and moment.

This method was applied to the flow field around an ogive-cylinder at angles of [6] attack and to bodies executing turns. Fig. 6 compares calculated and measured pressures for an ogive-cylinder at an angle of attack of 15 and 20 degrees. The results from the present method generally agree well with the measurements at all three stations along the body and for both angles of attack, whereas the results of Thrasher and Jepps, in [6], suffered inaccuracies at and aft of the separation. The pressure predicted by the present method shows better agreement with measured pressure near separation locations, but the discrepancy between the measured and predicted pressure becomes noticeable at circumferential locations beyond about 150 degrees, especially at x/D=4.5. There is a consistent tendency for the calculated pressures to be higher than the measurements. This is believed to be caused by improper tracking of the vortices. Improvement of the model in this regard is under investigation. The results of the turning body computations are presented in a later section along with a discussion of the measurements.

BOUNDARY LAYER MODEL

A potential flow model requires specification of the separation line locations. These locations can be approximated using a three-dimensional boundary-layer code. A code developed by Cebeci [13] for application to a ship-like

geometry has been updated to compute the separation locations.* The boundary-layer code requires the specification of the velocity vectors at the edge of the boundary layer. These vectors are usually obtained from a potential flow code, such as the vortex lattice code, without including separation. Since the governing boundary-layer equations in the code are formulated in general (non-orthogonal) coordinates, the computational setup is relatively simple.

A prolate spheroid has been selected by many researchers of the three-dimensional boundary layer as their test body since it has a simple shape and an analytical potential flow solution, yet has most of the basic characteristics of a general three-dimensional flow. Likewise, the boundary layer code was applied to this shape to test its performance at computing the convergence or separation lines in the present study. The outer (potential) flow was computed for a 6:1 spheroid at ten degrees angle of attack using the present potential code discussed before. This provided the boundary conditions for the computation of the boundary layer development and the eventual three-dimensional separation. The results are shown as surface shear stress vectors in Fig. 7 which may be compared with Meier's measurements given in Reference 15 on the same body (Fig. 8).

Transition from laminar to turbulent flow was specified from the measurements. As for all boundary layer codes at present, the computations break down when the shear stress gradient becomes too large. Such a breakdown is usually considered to indicate the location of separation (i.e., the convergence lines), and this procedure is followed here. In substantial agreement with the measurements, noticeable convergence of the shear stress vectors first occurs at approximately x/L=0.75 at an azimuthal location of 130 degrees. Further downstream at x/L=0.9 it has moved to about 120 degrees. For these computations, the potential flow solution accounted for the occurrence of flow separation (by iteration). In other trials, attached potential flow around the spheroid was utilized, but the difference in the results was small since the separation here is rather weak. This is not the case for more complex shapes, however, as will be seen for the flow around a curved body (simulating a turning body).

THE TURNING BODY PROBLEM

In transforming the turning body (Fig. 2a) to a space of rectilinear approaching flow (Fig. 2b), Gourjienko [9] performed a simple geometrical transformation preserving the local angle of attack of the approaching flow (from the perspective of a coordinate system attached to the body). This is merely a two-dimensional conformal transformation applied to the horizontal plane through the centerline with circular cross-sections maintained normal to the centerline. As can be seen from the schematic of Fig. 2a, however, the magnitude of the velocity also varies along the body. Thus, as shown in Fig. 2b, which is a schematic of the above transformation, the velocity of any point on the body (or equivalently of an approaching flow for a stationary body) also varies along the length of the body. This velocity is merely the radial distance in the physical plane of Fig. 2a from the center of the turn to a point on the body multiplied by the (constant) angular velocity of the turn. If the flow in Fig. 2b were to represent wind tunnel flow, the approaching velocity would have to vary across the test section (i.e, a mean shear flow). Gourjienko attempted to achieve this condition by actually generating a shear flow in the wind tunnel but had limited success.

*A version of the Cebeci [13] boundary-layer computation code modified by Groves and Chang [14] including the rotational term is also available to compute separation location for rotating bodies.

For the present work, the transformation itself is modified to account approximately for the varying magnitude of the velocity without an actual shear flow in the wind tunnel. The fundamental hypothesis underlying the modification, in accordance with the approach followed in the development of the Kutta condition discussed earlier, is that the separation phenomena on the body are predominantly controlled by the crossflow velocity components (i.e., the components of the approaching velocity which are normal to the centerline of the turning body in Fig. 2a). Thus the modification, shown schematically in Fig. 2c, is designed to maintain approximately the crossflow velocity of Fig. 2a while permitting the approaching (wind tunnel) velocity in Fig. 2c to be constant. If the resultant velocity U* at x=x* is used as the free-stream velocity in the wind tunnel experiment, the centerline of the curved body is transformed according to the following relationship given by

$$\eta = \frac{1}{3}\frac{\sqrt{R_0^2+\chi^2}}{\sqrt{R_0^2+\chi^{*2}}}\,\frac{R_0^2+\chi^2}{R_0} \tag{9}$$

$$\text{and } \frac{d\eta}{d\chi} = \frac{\sqrt{R_0^2+\chi^2}}{\sqrt{R_0^2+\chi^{*2}}}\,\frac{\chi}{R_0} = \tan\theta$$

$$\text{with } \chi = x - x_0$$

The Crossflow, $U_\perp$, and along-body, $U_{||}$, velocities of the curved body are

$$U_\perp = U^*\sin\theta = \omega x\,\frac{\sqrt{1+\left(\frac{\chi^{*2}+\chi^2}{R_0^2}\right)+\left(\frac{\chi^*\chi}{R_0^2}\right)^2}}{\sqrt{1+\left(\frac{\chi^{*2}+\chi^2}{R_0^2}\right)+\left(\frac{\chi}{R_0}\right)^4}}$$

$$\text{and } U_{||} = U^*\cos\theta = -\omega R_0\,\frac{1+\left(\frac{\chi^*}{R_0}\right)^2}{\sqrt{1+\left(\frac{\chi^{*2}+\chi^2}{R_0^2}\right)+\left(\frac{\chi}{R_0}\right)^4}}$$

In this paper, we will present a sample case of R_0=1.3147 L at χ=o (the nose of body is at x_o=+.234 L) and x*=0.54 L (R*=1.421 L), Fig. 2a, L being the total length of the straight body. The distribution of the radius along the body is the same as the offsets for axisymmetric body DTNSRDC Model #1 (Table 1 of 16). For this case, the percentage differences of crossflow and along-body velocities between the curved body and the straight turning body at A (χ=o), B (χ=x*) and C (χ=0.766L) are:

	A(χ=0)	B(χ=x*)	C(χ=0.766L)
$\frac{100(U_\perp - V_\perp)}{V_\perp}$	0	0	−1.8%
$\frac{100(U_{||} - V_{||})}{V_{||}}$	8.1%	0	−8.3%

The curved body almost maintained exactly the same crossflow velocity component of the turning body for the entire length. However, the along-body velocity component is higher than that of the turning body upstream of the

reference point B ($x=x^*$) and is lower than that of the turning body for $x>x^*$. The maximum deviation of the along-body velocity component of the curved body from that of the turning body is less than 10%.

The present curved body is different from that of Gourjienko [9]. If one allows a ten percent inaccuracy in along-body velocity component, the present method can be used to generate a curved body for testing in wind tunnel with uniform flow instead of shear flow proposed by Gourjienko. The objective of the present work is to develop a viscous-inviscid computation procedure for the turning body having crossflow separation. As long as the crossflow velocity component is maintained between the turning body and curved body, the comparison of the predicted and measured flow field of the curved body will provide insight into the hydrodynamics of the turning body and will facilitate the development of an efficient viscous-inviscid computation procedure for the turning body.

As a preliminary test of the method's applicability, purely potential flow (no separation) was computed using a panel method for both a straight body and its deformed equivalent described previously. The results in terms of pressure distributions were very encouraging. For example, as can be seen in Fig. 9, the pressure coefficients are quite close for the two cases. Using the potential flow solution as the outer flow for a boundary layer computation, the shear stress distribution was computed for the two cases giving very comparable results for the location of the convergence lines (Fig. 10a, b). Though some difference is noticeable near the origin of separation, convergence is weak in that region and does not much influence the more important downstream development (as evidenced by agreement downstream of the two cases). It is concluded from these computations that the transformation of the turning body, though approximate, is sufficiently accurate to warrant further use.

A wind tunnel model of a curved, transformed body was thus constructed and then installed in the Dual Test Section Wind Tunnel at the National Bureau of Standards (Fig. 11). The actual model differs slightly at the bow from the transformation discussed above. The transformation, strictly applied, would require the forward part of the model to have a very slight reversed angle of attack compared to the rest of the body. The model was built instead with a zero angle of attack in that region to somewhat simplify the numerical modeling, since that activity was of primary importance. This modification could be easily deleted for other model constructions. The model is 3.05m (120 inches) in length and 0.28m (10.9 inches) in maximum diameters. It is semi-cantilevered from a sting mount with fine wires at the nose, mostly for stability. The boundary layer was tripped by 0.4mm grit roughness, 5.1cm (2.0 inches) in streamwise extent beginning at $x/L=0.05$. To reduce blockage effects, the adjustable wind tunnel walls were set to provide a constant pressure (within 1% of the approaching dynamic pressure) near the walls and away from the body. The wind tunnel was operated at 22.9 and 45.7 m/s (75 and 150 feet per second), giving nominal Reynolds numbers of 0.42×10^6 and 0.84×10^6 based on the maximum diameter of the body. The body was fitted with 24 pressure taps flush to the surface equally spaced around the circumference of the body at each of eleven stations along the curved centerline. The pressure was measured by a pressure transducer attached to the output of a scanning valve system. Velocities in the wake were measured using a x-wire probe and a hot-wire anemometer system. All data was acquired and stored by a minicomputer system. Flow visualization consisted of 0.2mm diameter flexible cotton thread tufts attached to the body by 0.05mm thick double-sided tape. The flowfield was not detectably altered by the tufts.

MEASUREMENTS AND COMPUTATIONS

The base configuration consisting of the bare body, no appendages, provided a background for investigation of the characteristics of the separating flow against which one influence of the appendage could be evaluated. The results of pressure measurements, velocity distributions, and surface flow visualization (tufts) all give a consistent picture of the behavior of the flow around the body. From previous work, the general features of the flow can easily be predicted, and no qualitative differences from this flow pattern were revealed by the measurements. Basically, the boundary layer can be heuristically pictured as a cross-flow being swept along the body, with the magnitude of the cross-flow velocity determined by the angle of attack to the centerline. Thus the cross-flow shear layer separation is not a closed separation (as it would be with no along-body flow), but is instead open. The shear layer is then convected downstream to form streamwise vortices as it wraps up as opposed to transverse vortices as formed when no along-body flow is present.

The development of the boundary layer separation is gradual as indicated by the pressure measurements (Fig. 12) and by the tufts (fig. 13). Until $x/L=0.674$, the pressures show very little indication of separation effects. Further downstream, though, the separation begins to reduce the pressure coefficient on the leeward side. This region of reduced pressure expands around the body until at the aft-most station of pressure measurements ($x/L=0.886$) it occupies about 120 degrees of the circumference. The tuft displacements show a similar development in the convergence of the surface shear lines. By a careful interpolation of the tuft pattern on the surface, convergence lines (separation lines) were recorded along the sides (topside and underside) of the body (Fig. 14). These are in very good agreement with the boundaries of the reduced pressure region.

The calculations of the convergence lines (Fig. 14) using the 3-D boundary layer code are based on shear stress vectors (Fig. 10) as discussed before for the prolate spheroid. Since the boundary layer flow depends on the applied external flow, which, in turn, depends on the boundary layer separation, an iterative technique was employed for these calculations. The first iteration used unseparated potential flow and produced the upper line of boundary layer separation. The outer flow resulting from this computation was then used for a second iteration, and so forth. The method converged quickly; the second iteration produced satisfactory results. The agreement with the measured lines is rather remarkable.

The calculated pressure distributions are shown in Fig. 12 along with the measurements and attached potential flow predictions. The separated flow predictions show significant improvements over the attached flow predictions. In comparison to the measurements, the presently calculated results are very good up to the angle of 135 degrees. Above that angle, the calculated pressures are higher than the measurements. This could be caused by improper tracking of the vortices in the wake as it is for the ogive-cylinder case. Further improvement of the potential model is necessary in order to obtain a better comparison over that region.

As the separating shear layer develops along the body, it rolls up into a pair of streamwise vortices. Those vortices can be most easily seen from the velocity components in the plane which are perpendicular to the centerline of the body. Figure 15 is a plot of those velocity components measured at $x/L=0.936$. It is seen in the figure that at this axial station the separation wake has grown to approximately 0.75D with the center of the vortex at y/D of -1.5. It is also seen that at the centerline there are significant velocities which flow towards the body at y/D less than -1.5. That downward

flow motion caused by the vortex should result in an increase of the streamwise velocity at the centerline. In examining the measured velocity component along the body surface (Fig. 16), the velocity increase is clearly shown; near the centerline, the magnitude of the along-body velocity component close to the body is approximately thirty percent higher than the freestream velocity, while the magnitudes are decreased by twenty percent at z/D of 0.2 where the vortex generated motions are upward (Fig. 15). It should be noted that for practical reasons the velocities were measured in the planes perpendicular to the wind tunnel axis instead of perpendicular to the local centerline of the body. Thus Figures 15 and 16 should be viewed as qualitative when interpreting them as displaying velocity components in a crossflow plane. The effect on the interpretation should be minimal, however.

With this baseline information on the bare body, the influence of an appendage on the flowfield and on the associated pressure forces can be ascertained. This influence may be the result of the vorticity created by the appendage experiencing flow at an angle of attack. The development of separation is once again a gradual process as indicated by the pressure distributions (Fig. 17a) and the tuft photographs (Fig. 18). The pressure shows very little deviation from the bare hull results until $x/L=0.808$ where the trend toward higher pressures on the side opposite the appendage becomes evident.

Figure 17 also presents the pressure distributions computed from the potential flow model. It is seen (Fig. 17a) that the computed pressure coefficients for an attached flow, i.e., without separation wake, are higher on the appendage side than on the opposite side and are not in agreement with the measurements. The pressure coefficients computed with separation show improved agreement. In comparison to the measured data, the calculations again show the need for further improvement in the region above 135 degrees.

The convergence lines (Fig. 19) show an increase in the azimuthal location on the appendage side. This is consistent with the concept of tip vorticity inducing image vorticity on the body which decreases the pressure on the appendage side (Fig. 17a), hence modifying the separation locations. The locations of the observed convergence lines are also consistent with the pressure measurements in terms of the locations where the reduced pressures begin.

The measured velocity field with appendage shows a significant difference from that of the bare body case. The flow topology has not changed in that there are still two regions of vorticity of opposing sense, but both the centers and the strengths of the vortices are altered. In comparison to the bare body case, the appendage vorticity has moved closer to the center and to the body surface while the vorticity at the opposite side has moved upward and become less singular. The relocation of those vortices results not only in the change of the cross-flow velocity field, but also of the along-body velocities. As one can see in Figure 21, the maximum velocities are in this case located at regions near the centerline and y/D of -1.5 where the cross-flow convergence is large.

The significant asymmetry of the flow around the body with an appendage attached is in stark contrast to the nearly perfect symmetry exhibited by the flow around the bare body. The symmetry is displayed in Figures 12 and 15 but may also be seen in a photograph of the leeside of the body near the stern (Fig. 22a). The tufts show a definite divergence in the surface shear and excellent symmetry in the tuft patterns. A similar photograph (Fig. 22b) of the body with an appendage attached indicates substantial crossflow and resulting asymmetry at the same location.

CONCLUDING REMARKS

The concept of considering the three-dimensional separation along a body at an angle of attack or undergoing a turn as a modification of a two-dimensional cross-flow separation has been shown to be useful. It has specifically been utilized to derive an explicit Kutta condition which gives results superior to previous computations for similar flow situations. The computed pressure coefficients were somewhat high in the separated region, however, and further efforts to understand and correct this will be undertaken.

A boundary layer model has been employed to predict the locations of the convergence lines on a prolate spheroid and on the curved body and its transformed equivalent. Results from the spheroid agreed well with previously published measurements, and the turning body calculations were in substantial agreement with those from the curved body. The latter comparison supported the use of the transformation for experimental testing of the difficult case of a submerged body executing a turn.

The transformation utilized for the turning body differed from a previous formulation in that the absence of the mean shear flow on the external stream was accounted for in the transformation itself and not in an attempt to impose such a shear in the external stream. The success of computational tests of the concept led to the construction and testing of an actual windtunnel model. Pressure and velocity measurements and flow visualization showed that the development of the convergence lines is gradual along the body and moves toward the centerlines near the stern. The boundary layer computations of the convergence lines were in substantial agreement with the experiments, and the potential flow model which uses the convergence line locations was able to predict the pressure distributions with accuracy except in the separated region as mentioned before for the spheroid.

The excellent symmetry of the measurements for the bare body configuration was upset when an appendage was added. The pressure show a distinct difference between the sides with and without appendage. The velocity measurements likewise show an asymmetry in the locations of the shed vortices, a result consistent with a concept that the tip vortex on the appendage can be viewed as generating image vorticity on the body surface.

Further work is required on all aspects of this program. The computed pressures in the separated region need to be improved. The boundary layer computations need to be refined and incorporated into an overall scheme. Additional experiments need to be performed to provide more detailed flow conditions near the stern and in the boundary layer. However, substantial progress has been made on all fronts.

ACKNOWLEDGEMENTS

This work was performed under the Naval Sea Systems Command Special Focus Program and was authorized by the General Hydrodynamics Research Program administered by the David W. Taylor Naval Ship Research and Development Center.

The authors would like to acknowledge the cooperation of the National Bureau of Standards for the use of their wind tunnel facility and Dr. Thomas Huang of DTNSRDC for his technical guidance.

REFERENCES

1. Tobak, Murray and David J. Peake, "Topology of Three-Dimensional Separated Flows", Ann. Rev. Fluid Mech, 14, 1982.

2. Hornung, Hans and Authony E. Perry, "Some Aspects of Three-Dimensional Separation, Part I", Z. Flugwiss Weltramforsch, May, 1984.
3. Perry, Authony E. and Hans Hornung, "Some Aspects of Three-Dimensional Separation, Part II", Z. Flugwiss Weltramforsch, May, 1984.
4. Menderhall, Michael R. and Stanley C. Perkins, Jr., "Predictions of the Unsteady Hydrodynamic Characteristic of Submersible Vehicles", Fourth Numerical Conference on Numerical Ship Hydrodynamics, Washington, D.C., 1985.
5. Kato, N. and M. Yamaguchi, "The Vortex on a Submerged Solid of Revolution", Second International Symposium on Ship Viscous Resistance", Sweden, 1985.
6. Thrasher, David F., "Application of the Vortex-Lattice Concept to Flows With Smooth-Surface Separation", Ship Performance Department Research and Development Report, David W. Taylor Naval Ship Research and Development Center, DTNSRDC-85/041, 1985.
7. Tinker, S.J., "Numerical Simulation of Separated Flow Over Bodies of Revolution", Admiralty Research Establishment, Haslar, Gosport, AMTE(H) R85209, 1985.
8. Maskew, Brian and Frank A. Dvorak, "The Prediction of C_{LMAX} Using a Separated Flow Model", Journal of The American Helicopter Society, April, 1978.
9. Gourjienko, G.A., "Method of Curved Models and Its Application to The Study of Curvilinear Flight of Airships", Rep. 182, Part I and II, Central Aero-Hydrodynamical Institute, Moscow, 1934 (Reprinted as NACA TM 829 and 830).
10. Maskew, Brian and B.M. Rao, "Calculation of Vortex Flows on Complex Configurations", Paper 6.2.3 in ICAS proceedings, Seattle, WA, August, 1982.
11. Celik, I., V.C. Patel and L. Landweber, "Calculation of the Mean Flow Past Circular Cylinders by Viscous-Inviscid Interaction", Journal of Fluids Engineering, 1985.
12. Jepps, S.A., "A Theoretical Investigation of the Subsonic Flow Past an Ogive-Cylinder Body", British Aircraft Corporation, Math. Services Note 226, March, 1977.
13. Cebeci, T., K.C. Chang and K. Kaups, "A General Method for Calculating Three-Dimensional Laminar and Turbulent Boundary Layers on Ship Hulls", MDC J7998, 1978.
14. Groves, Nancy C. and M.S. Chang, "A Differential Prediction Method for Three-Dimensional Laminar and Turbulent Boundary Layers of Rotating Propeller Blades", Fifteenth Symposium on Naval Hydrodynamics, National Academy Press, 1985.
15. Patel, V.C. and J.H. Baek, "Calculation of Boundary Layers and Separation on A Spheroid at Incidence", Second Symposium on Numerical and Physical Aspects of Aerodynamic Flows, 1983.
16. Huang, T.T., N. Santelli, and G. Belt, "Stern Boundary-Layer Flow on Axisymmetric Bodies", Paper presented at the 12th Symposium on Naval Hydrodynamics, Washington, D.C., June 5-9, 1978; Also published by National Academy of Sciences, Wash. D.C., pp. 128, 1979.

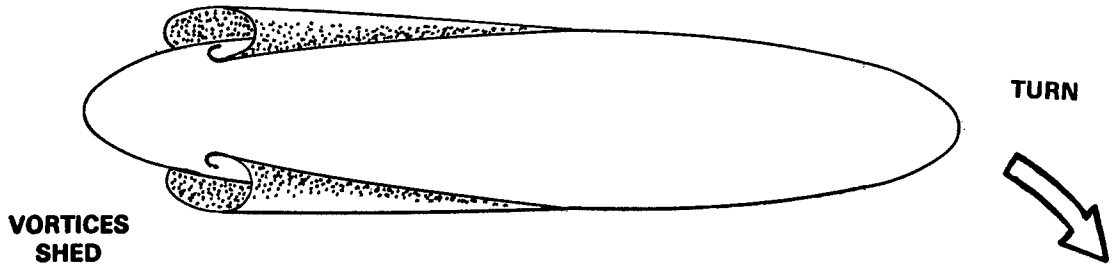


Fig. 1. Streamwise vortices generated by 3-D separation.

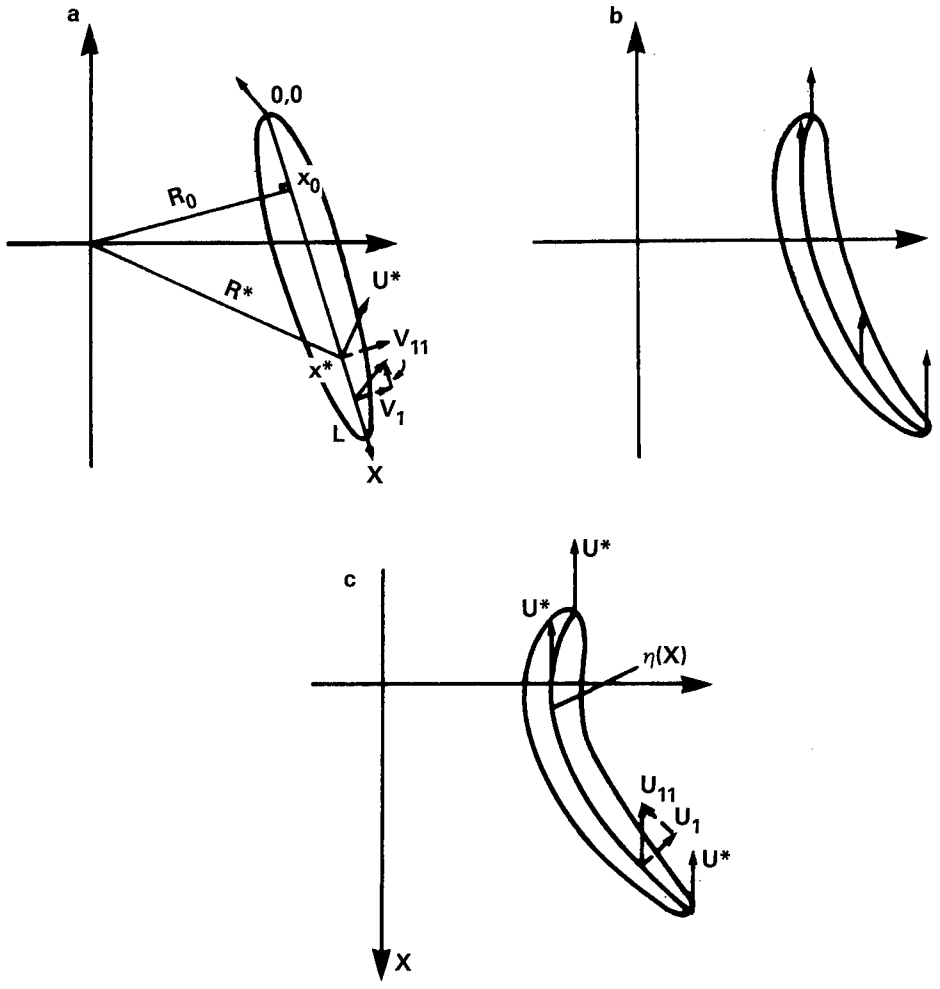


Fig. 2. Turning body. (a) Physical space; (b) Curved body preserving angle of attack but with varying velocity magnitude [9]; (c) Curved body preserving crossflow components and having constant forward velocity.

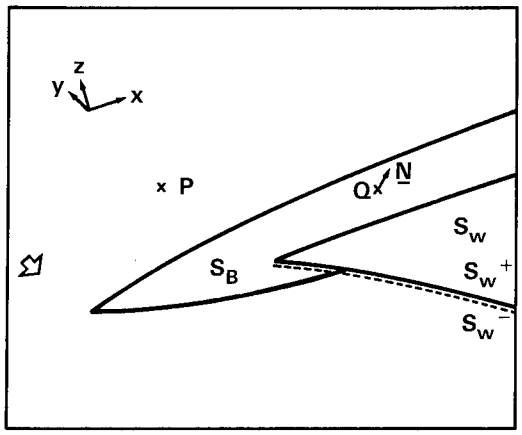


Fig. 3. Schematic of coordinate system.

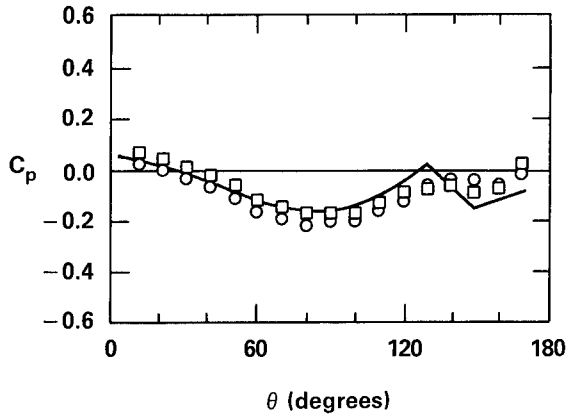


Fig. 4. Cp calculations of Thrasher [6] for 15 deg. angle of attack. x/d=4.5; Experiment, (o) Re=0.44 x 10(6), (□) Re=3.0 x 10(6); (—) computed.

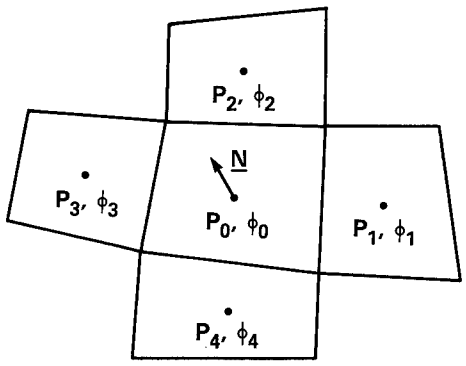


Fig. 5. Panel layout and location of points.



Fig. 11. Model of transformed turning body mounted in windtunnel.

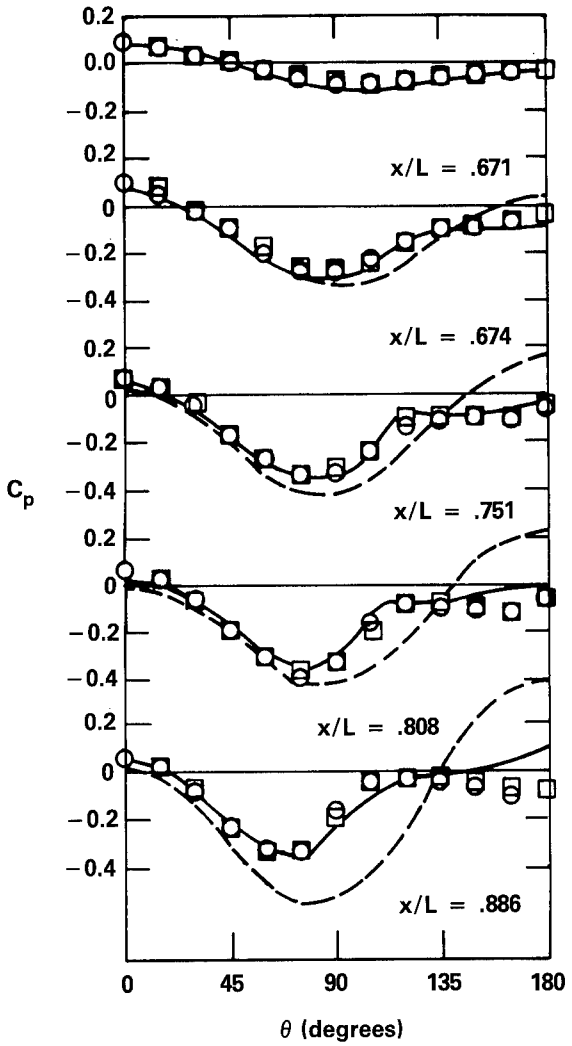


Fig. 12. Cp distributions on transformed body. Measured, (□) top, (○) bottom; nonseparated potential flow (– –); separated potential flow (——).

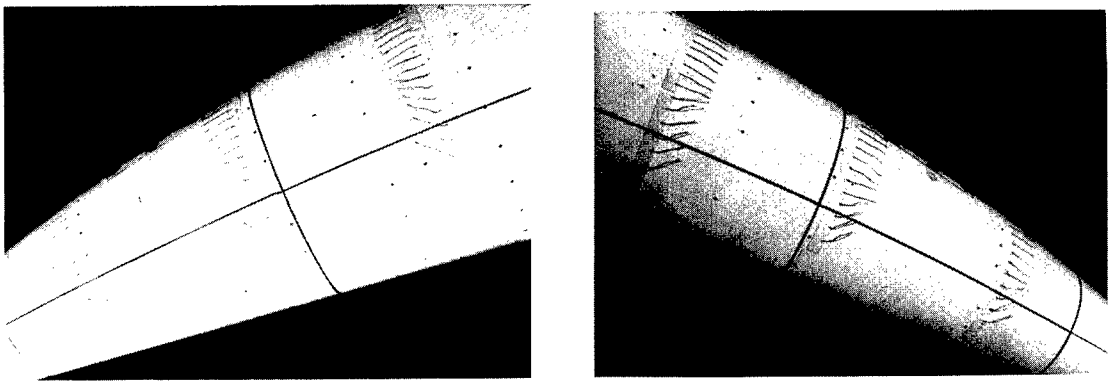
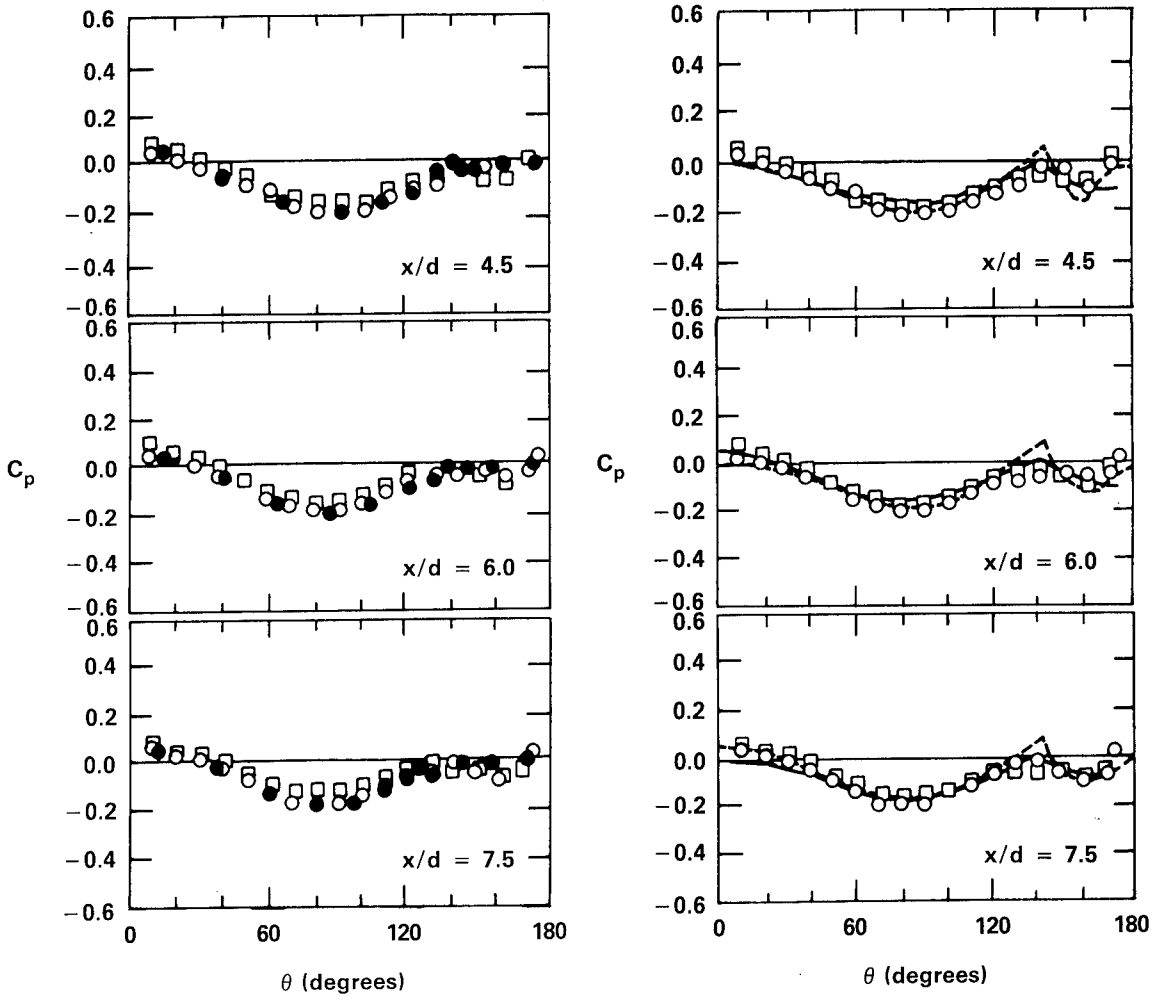
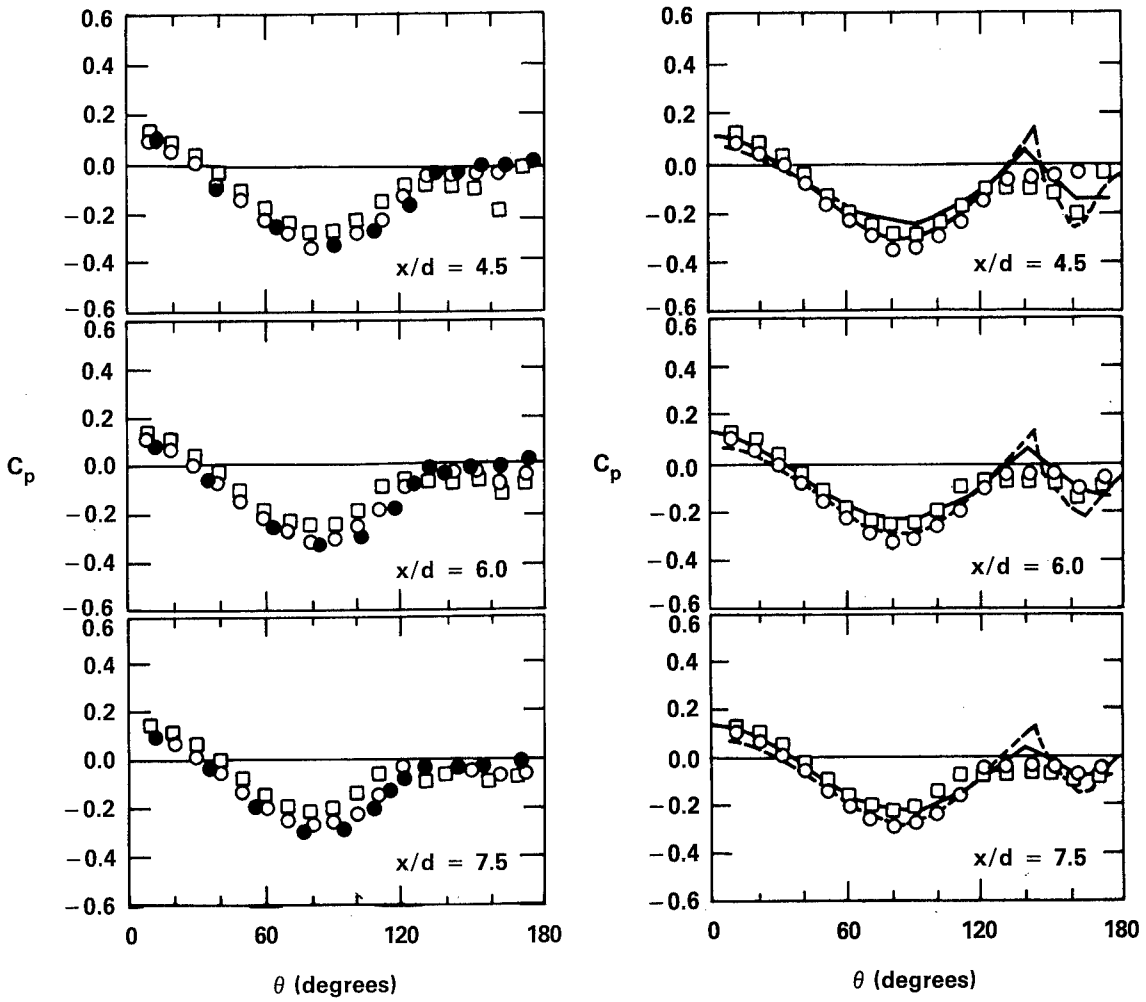


Fig. 13. Tuft patterns, bare hull. (a) top side; (b) other side.



(a) 15 degrees of angle attack.

Fig. 6. Cp for ogive-cylinder at angle of attack. (o,□) same as Fig. 4; (●) present computation; (——) same as Fig. 4; (---) Jepps in [6].



(b) 20 degrees of angle attack.

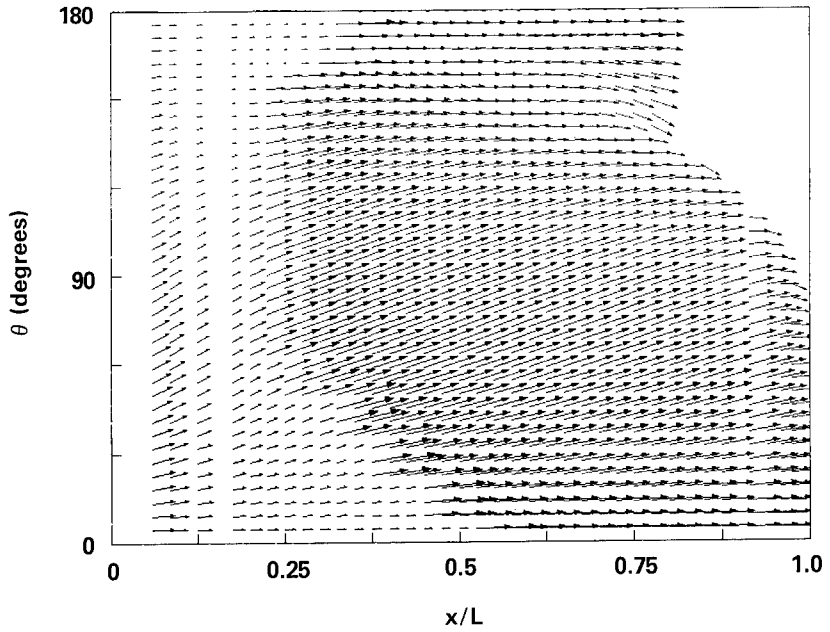


Fig. 7. Surface shear stress calculations (present work) on prolate spheroid of [15].

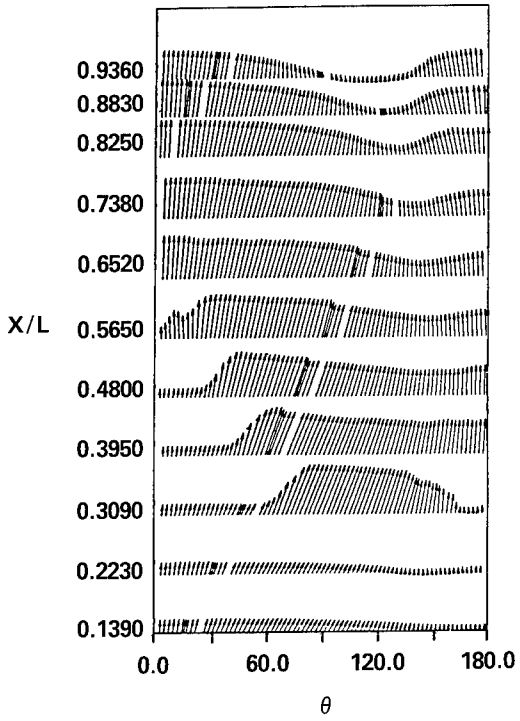


Fig. 8. Measured surface shear stress on prolate spheroid from [15].

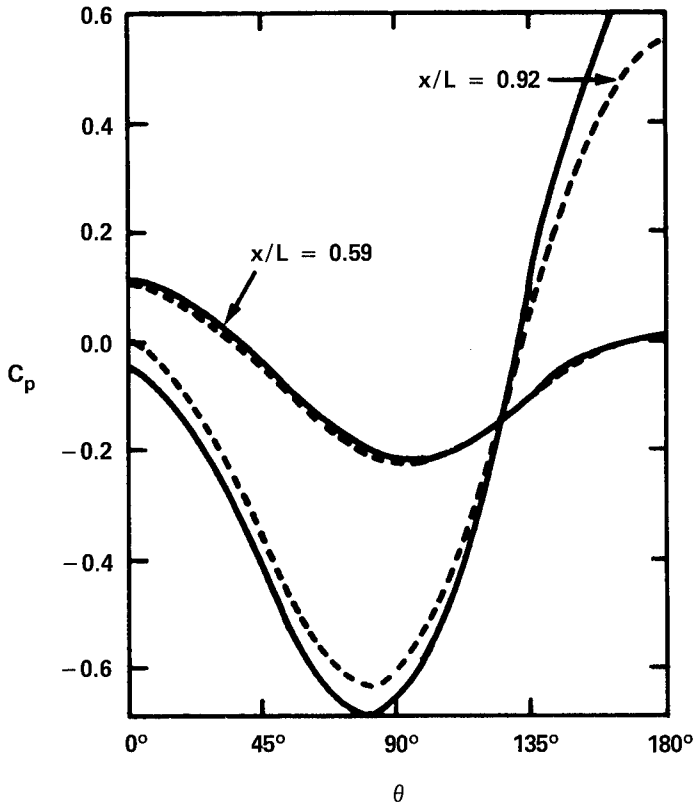


Fig. 9. Cp calculations for a turning body (—) and its transformed equivalent (– –) using nonseparated potential flow.

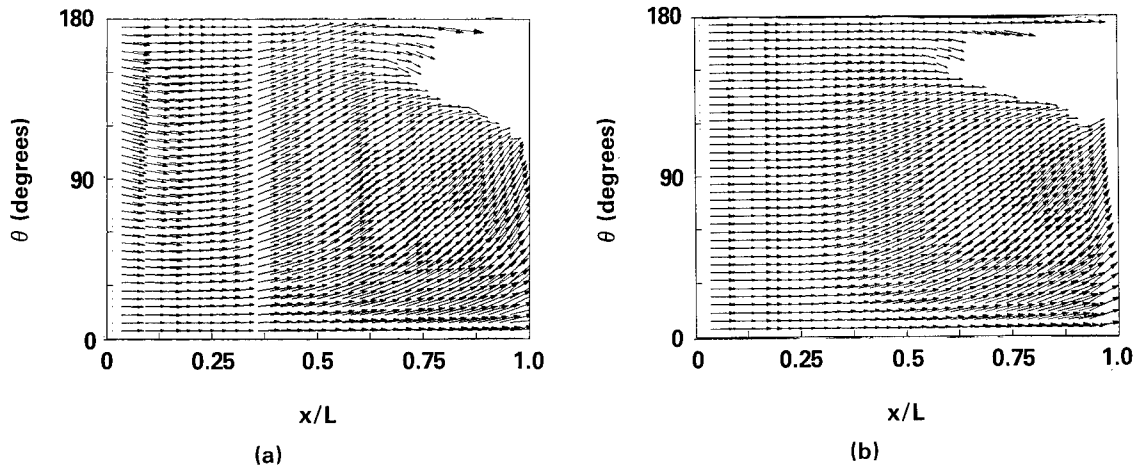


Fig. 10. Surface shear stress computations for (a) turning body and (b) transformed equivalent body, using nonseparated potential flow for outer conditions.

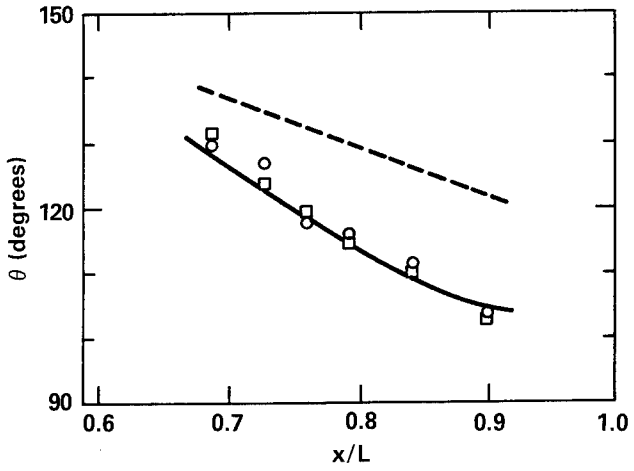


Fig. 14. Convergence line locations. Side with appendage (○); other side (□); calculated, no separation in outer flow (- - -); calculated, final iteration (——).

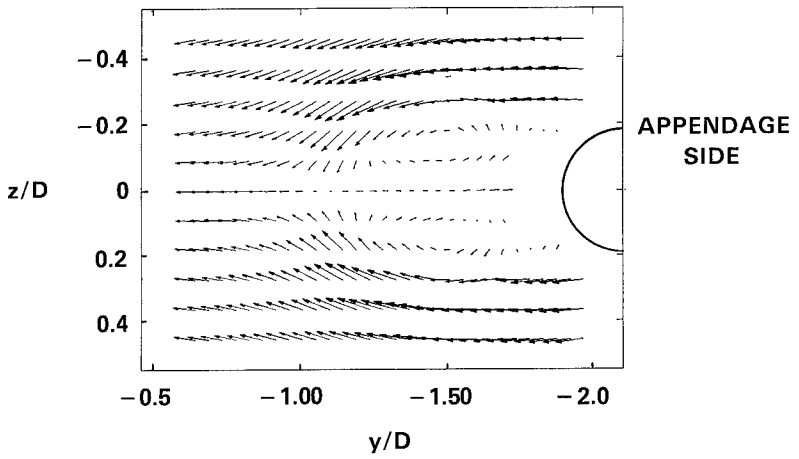


Fig. 15. Cross-stream velocity vectors viewed looking upstream parallel to body centerline. x/L = 0.936.

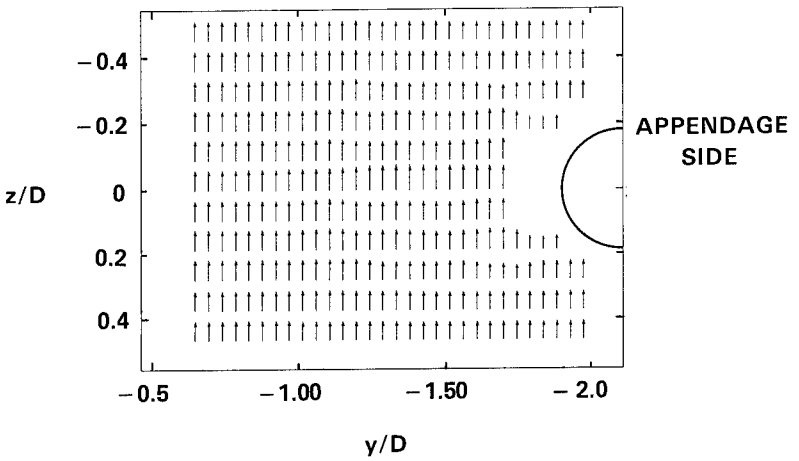


Fig. 16. Velocity component parallel to body centerline. x/L = 0.936. Arrows indicate magnitude only; flow direction is out of page.

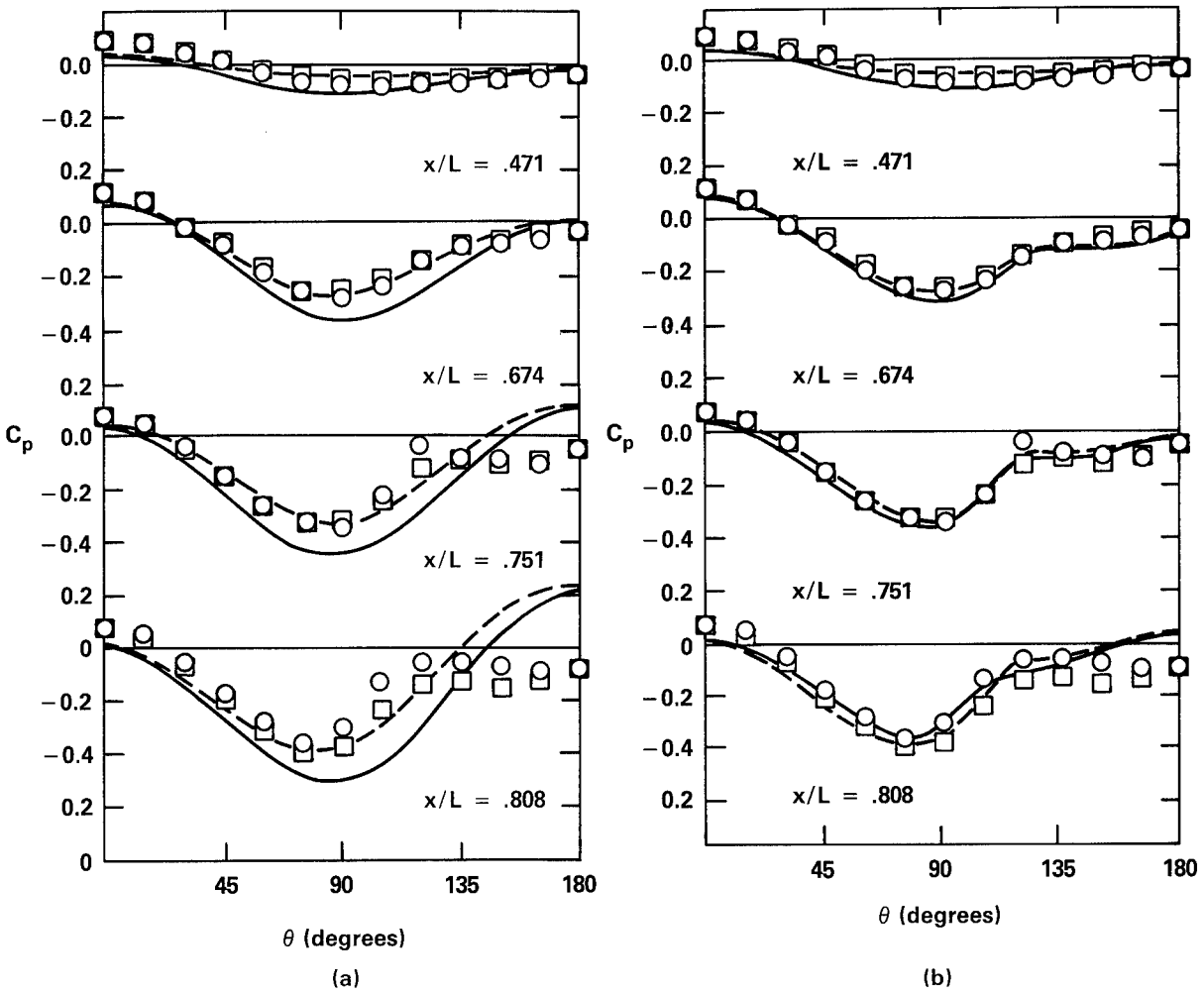


Fig. 17. Comparison of measured and computed Cp distributions with appendage on body. (a) attached flow; (b) with vortex wake. Appendage side: (□) measured; (– –) computed. Other side: (○) measured; (—) computed.

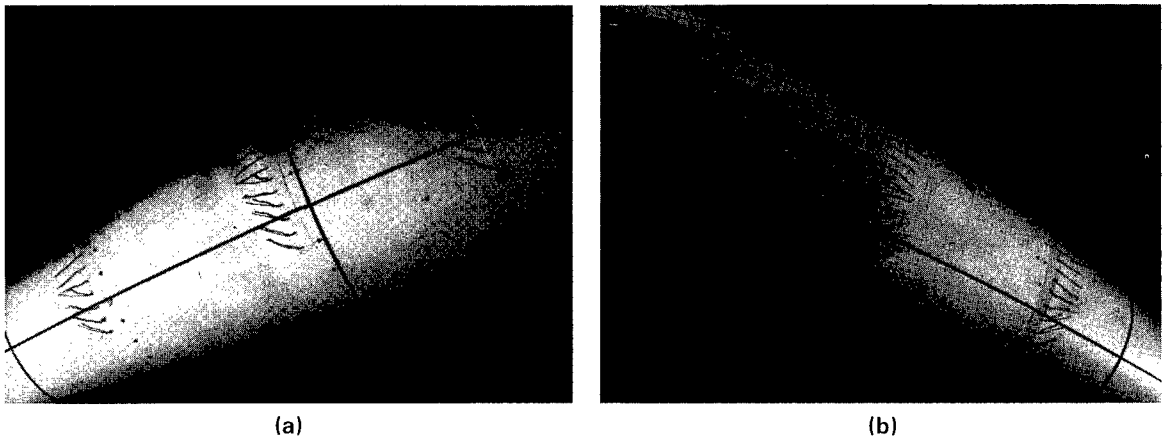


Fig. 18. Tuft patterns, appendage attached. (a) appendage side; (b) other side.

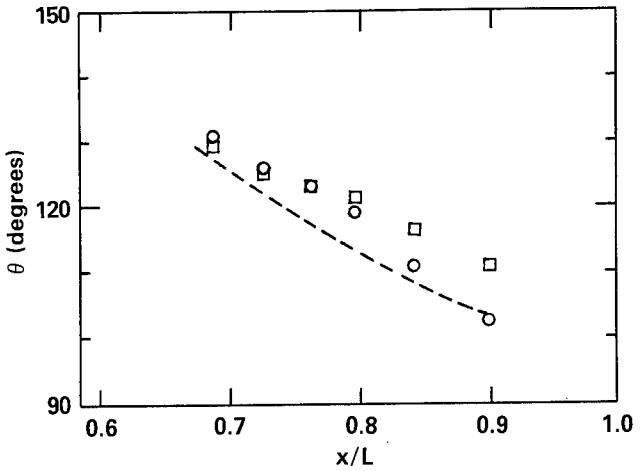


Fig. 19. Convergence line locations. Appendage side (□); other side (○); bare body (– –).

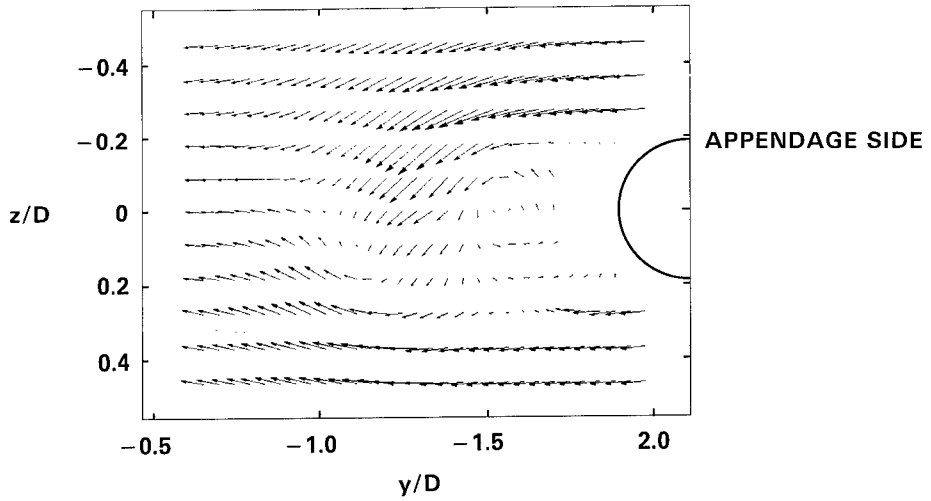


Fig. 20. Cross-stream velocity vectors, appendage attached. See Fig. 16.

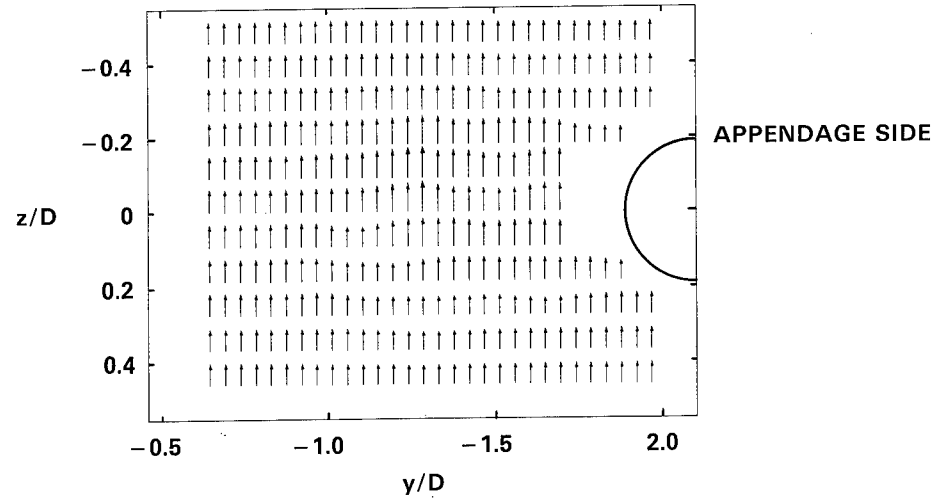
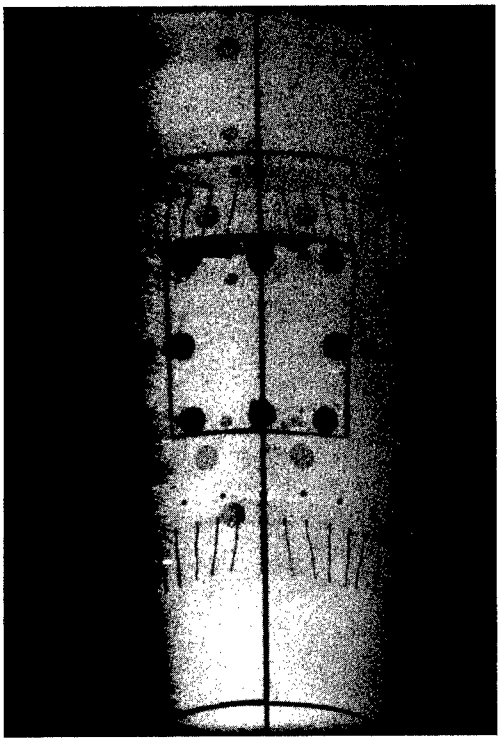
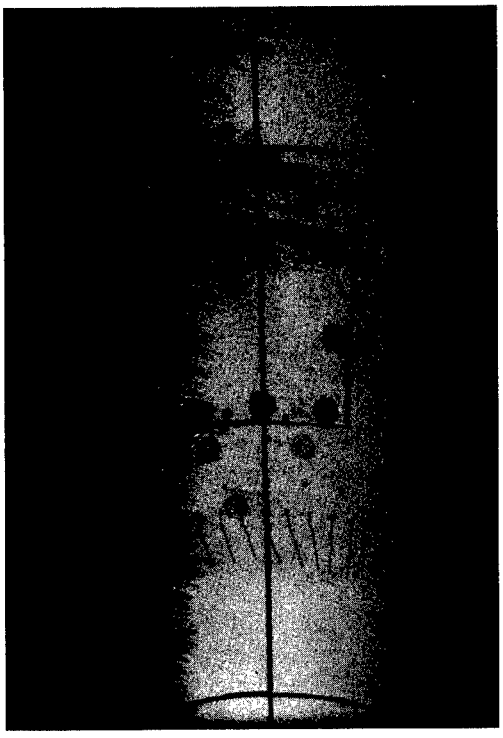


Fig. 21. Velocity component parallel to body centerline with appendage attached. See Fig. 16.



(a)



(b)

Fig. 22. Leeward view of stern. (a) bare hull; (b) appendage attached.

DISCUSSION

Michael Mendenhall,
Nielsen Engineering & Research,

a. Which panel method was used for Fig. 9 results?

b. What effect on the strengths of the hull separation vortices does the appendage vortex have?

c. How does the hull separation vortex sheet roll up? Are there numerical difficulties with the sheet roll-up calculation; e.g., do parts of the sheet try to cross over or overlap?

d. Can your covergence line prediction illustrate the effect of the appendage shown in Fig. 19? The separation criteria described in your Ref. 4 has demonstated a capability to include appendage interference.

e. Is the ogive-cylinder experimental data in Figs. 4 & 6 from the NACA report by Tinling & Allen? If not, where can it be found?

f. Some detail on the appendage size and location on the curved body is needed; e.g., a sketch to illustrate the actual geometry.

Reply -

a. The panel method used for Figure 9 was doublet method described in the second section of this paper.

b. The appendage vortex causes the strengths of the hull separation vortices to be asymmtric. This effect becomes more pronounced at the stern.

c. Tracing the stream lines in the wake requires special care numerically. The problem associated with the present code is not so much that the sheet may try to cross over as that the wake may intersect the body surface. Special checking has been added to the code to avoid this problem.

d. The convergence line prediction technique should also be applicable to the case with appendage. It will be included in a future publication.

e. The ogive-cylinder experimental data in Fig- ures 4 and 6 are taken from reference 6.

f. The appendage is a NACA 0009 foil with a faired tip, 0.05 model lengths in chord and 0.03 lengths in span, located at 0.32 lengths from the nose.

Vladimir Ankudinov,
Tracor Hydronautics

The paper provides an excellent insight into the flow phenomenon around the turning body, and hopefuly will facilitate the development of the practical computational procedure to estimate and velocity field and hydrodynamic forces acting on a body in turn. Perhaps, it is too early to ask about force distribution and / or total force value comparisons of calculations and measurements, but I would like to see at least some results on that matter, particularly for shiplike body configurations. The curved body approximation in turning body problem should be also examined by comparison of the flow/pressure field and hydrodynamic forces obtained experimentally from the rotating arm measurements. Extension of this work to cover the surface ship hulls and in the presence of the free surface will be extremely welcome.

Reply -

The pressure measurements are not sufficiently detailed to determine with any accuracy the total force values for comparison with calculations. Also, the model was constructed to permit the types of measurements that are presented and not, in addition, more complicated and costly force and moment measurements. The curved body technique has been compared to rotating arm experiments, but at this time only for data which is not public. The technique has been developed for the problem of separation from a smooth submerged body and as such is not intended for a hull shape with sharp stern and keel, such as on a surface ship.

Study on the Characteristics of Propeller Cavitation and Its Noise

H. YUASA, H. KAMIIRISA, and T. NOJIRI

Mitsui Engineering & Shipbuilding Co., Ltd., Akishima Laboratory, Japan

ABSTRACT

The cavitation noise radiated from propulsors is the major part of hydrodynamic noise on ships. Our latest research is presented by referring to both full-scale and model experiment results on this subject.

This paper consists of the following parts:

- Relation between cavitation and its noise
- Cavitation noise on controllable pitch propellers (CPP)
- Directivity of cavitation noise
- Evaluation for noise reduction
- Theoretical approach for the prediction of cavitation noise

NOMENCLATURE

D	Propulsor diameter
f	Frequency
K_T	Thrust coefficient $T/\frac{1}{2}\rho n^2 D^4$
n	Propulsor turning rate
P	Free stream pressure
P_V	Vapour pressure
r	Radial position of a propulsor
R	Radius of a propulsor
SPL	Sound pressure level
T	Thrust of a propulsor
TL	Transmission loss
Z	Number of blades
θ	Blade pitch angle
σ_N	Cavitation number $(P-P_V)/\frac{1}{2}\rho n^2 D^2$
λ	Scale factor
ρ	Fluid density

1. INTRODUCTION

The constructions of ocean research and experiment vessels have increased the interest for the problem of underwater radiated noise induced by the cavitation of propulsors.

Controllable pitch propellers (CPP) and side thrusters have been installed on such vessels equipped with dynamic positioning systems (DPS). The underwater radiated noise from their cavitation is getting more danger for interferring the operation of DPS as the working offshore field becomes deeper.

Moreover, it has been pointed out that the influence and disturbances on hydroacoustic equipment due to propeller noise are the most important problems on fishing boats[1].

Our latest research has made clear the complicated phenomena of CPP and side thruster cavitation and its radiated noise in connection with the blade pitch angles by referring to the full-scale and the model experiments.

Through the research, several interesting results were obtained as follows:

a) The relation between cavitation and noise is experimentally clarified by simulation in a cavitation tunnel.
b) The characteristics and the level of the noise from a CPP vary as its cavitation pattern changes due to the variation of its pitch angle.
c) The relation between the underwater radiated noise and the CPP operating condition varying from the non-cavitating to the cavitating is disclosed from full-scale cavitation observations and noise measurements.
d) The directivity and other features of the noise radiated from side thrusters are pointed out from the measurements on actual onboard ships and moreover full-scale tests in a large-sized tank.
e) The theoretical approaches have been tried in an effort to obtain the cavitation noise. This was done by applying the combination of a propeller lifting surface theory and a cavitation theory.

2. PROPELLER

2.1 General Aspect of Propeller Noise

It is quite natural that the propeller cavitation noise increases when the speed becomes higher in case of ordinary vessels with fixed pitch propeller or CPPs operating

at the design pitch angle. Fig. 1 shows the relation between the operating condition of a full-scale propeller and its underwater noise level for SHIP A. The underwater noise was measured by a hydrophone equipped at the bottom hull surface just above the propeller. This figure denotes that tip vortex cavitation firstly, sheet cavitation secondly and then root cavitation occur in succession as the cavitation number σ_N becomes lower along the operation line according to the main engine power increase. While the underwater noise level remains at a rate corresponding to the background noise in a non-cavitating condition in a low speed range 1/10 MCR.

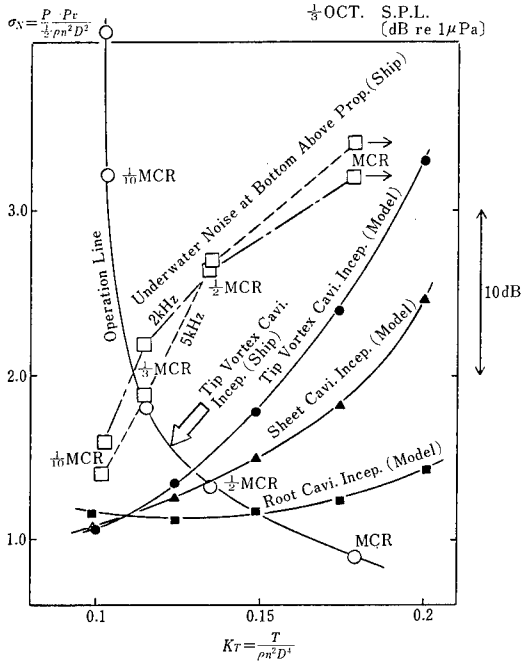


Fig. 1 Relation between the Operating Condition of a Full-Scale Propeller and Its Underwater Noise Level (SHIP A)

Reaching 1/3 MCR, the noise level denotes an increment of about 5 dB (re. 1 μPa, 1/3 OCT. analysis) in spite of non-occurrence of tip vortex cavitation. The tip vortex cavitation inception was observed around the mid-point between 1/3 MCR and 1/2 MCR at the full-scale measurements as an arrow indicates in this figure. As the ship speed becomes higher up to 1/2 MCR, the noise level increases more than 10 dB in comparison with the background noise, while sheet cavitation occurs. Ascending up to MCR, the increment of noise level denotes about 20 dB while root cavitation occurs too.

Hence, the three curves of cavitation inception in this figure were obtained from the cavitation tunnel test using the scale model propeller. The typical difference between the model and full-scale is the tip vortex cavitation inception which of full-scale is located in the lighter loading condition than the model. From the recent study[2] on the cavitation inception, the ratio of Froud Number between the full-scale and the model was reported as 0.89, while about the same value has been obtained in the present SHIP A. Moreover, the ratio of that on the inception of both sheet and root cavitation was claimed nearly equal to 1.0. This value seems to be reasonable from our experiences, however more investigation is needed to evaluate the reliability of the model test depending upon the nuclei distribution and air content of the tunnel water especially for the cavitation inception.

2.2 Simulation by Model Test

The relation between cavitation and its noise would be clarified, if the cavitation condition of the above mentioned propeller could be simulated along the operation line in a cavitation tunnel. However, there is no facility which is available for such tests as both the thrust coefficient K_T and the cavitation number σ_N can continuously be controlled at the same time along the operation line. Therefore, fixing K_T value, σ_N has only been controlled to decrease in the cavitation tunnel in the present study. In order to obtain the acoustic characteristics inside the tunnel, the calibration was in advance carried out by transmitting random noise with the same frequency band from 0.9 radius at the top position of the propeller blade. This result was used for the correction of the measured data.

In Fig. 2 the pressure in the tunnel is gradually decreased from non-cavitating condition $\sigma_N \fallingdotseq 5$, namely the time passes from the right hand side to the left of the horizontal axis, while K_T is fixed at 0.15.

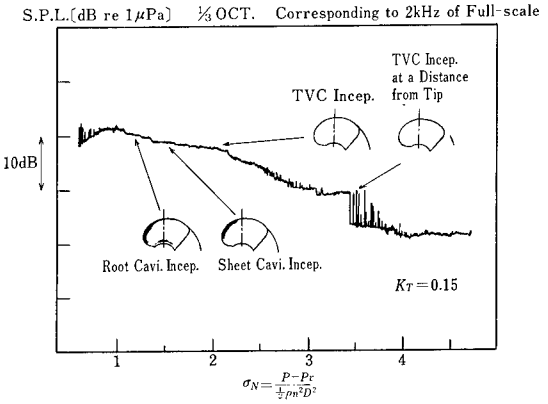


Fig. 2 Simulation of Cavitation and Its Noise Radiation by the Model Test on SHIP A

The cavitation noise has been measured by a hydrophone installed inside the tunnel wall just below the model propeller, and has been analyzed in the 1/3 octave band with the center frequency corresponding to 2 kHz of the full-scale for SHIP A. As shown in the figure, burst or spike noise appears when σ_N becomes lower than 4. The sound pressure level (SPL) increases 5 dB about same as the envelope of the burst noise signals where σ_N passes through the value of 3.5 and tip vortex cavitation (TVC) comes in sight at the certain distance in the downstream of the propeller tip. Around σ_N = 2, TVC connects to the propeller tip. This event is recognized as the cavitation inception by visual observation[3, 4]. The slope of SPL rise seems to slow down after that, even if sheet cavitation occurs at σ_N = 1.5 and root cavitation at σ_N = 1.2. Then the SPL rise from the background noise is about 20 dB which seems like that in the full-scale measurement as shown in Fig. 1.

Thus, it is clarified that the relative rise of SPL against the background noise with cavitation occurrences can approximately be simulated like the operating condition of full-scale propeller by continuously varying σ_N in the cavitation tunnel.

2.3 Influence of CPP Blade Pitch Angle

On the relation between cavitation patterns and its noise level, several papers were published, for example; the study on the three kinds of model propellers which were designed to generate tip vortex, bubble and sheet cavitation respectively[5], and the study on the intensity distribution of noise source along propeller slip stream by using a measuring barge in a lake[6]. These are all in regard with fixed pitch propeller (FPP), and no papers related to CPP could be found by the authors.

In this section, the influence on cavitation noise by CPP blade pitch angle is described by carrying out a cavitation tunnel test of four bladed CPP for SHIP B. Moreover, a typical result on this phenomena in a full-scale measurement is shown for SHIP C with twin CPP.

2.3.1 Model test for SHIP B

The principal particulars of a model propeller of CPP are shown in Table 1. The test was performed in the non-uniform wake of SHIP B simulated by wire-mesh screen in a cavitation tunnel.
The blade pitch angle θ, the propeller loading K_T and the cavitation number σ_N were adjusted to correspond to the full-scale measurement. As well as for SHIP A, cavitation noise was measured by a hydrophone equipped inside the tunnel wall, and was analysed in the overall band.

Table 1 Principal Particulars of the Model Propeller (SHIP B)

Diameter (m)	0.250
No. of Blades	4
Boss Ratio	0.331
Expanded Area Ratio	0.627

Fig. 3 shows the linear and the A-weighted overall noise level versus blade pitch angle for the two couples n and σ_N.

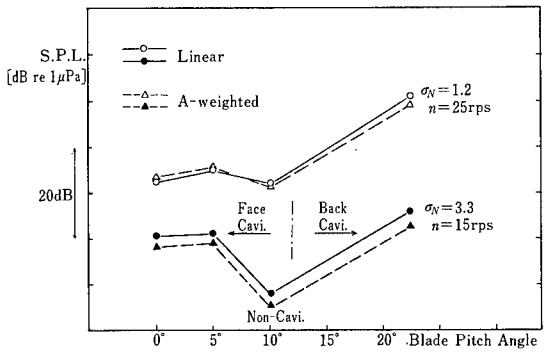
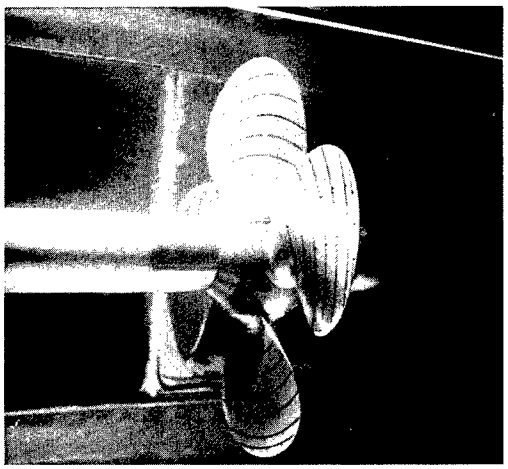
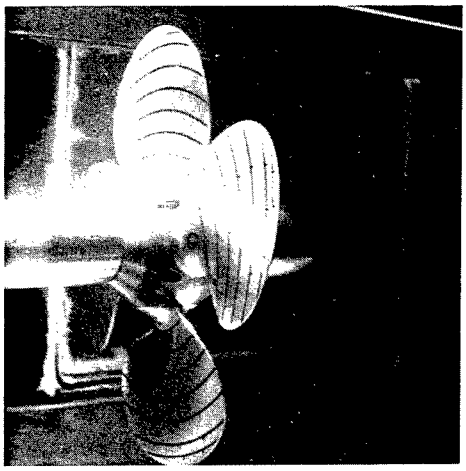


Fig. 3 Relation between Overall Noise Level and Blade Pitch Angle by the Model Test on SHIP B

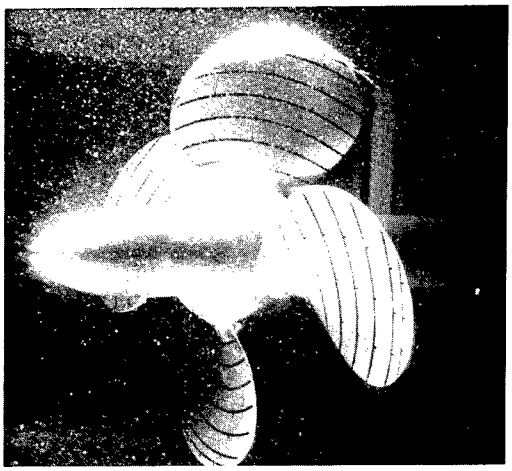
The figure denotes a high noise level at both sides of the high and low blade pitch angles θ with the bottom at the middle around θ = 10° between them. In case of σ_N = 3.3, face cavitation occurs at the leading edge of the propeller blade at θ = 0° and 5° by observing the cavitation patterns (Photo 1).



θ = 0°
σ_N = 3.3



θ = 5°
σN = 3.3



θ = 22°
σN = 3.3

Photo 1 Variation of Cavitation Patterns versus Blade Pitch Angle by the Model Test on SHIP B

It is clear that the face cavitation causes the high SPL in the range of low blade pitch angle. Since no cavitation is observed at θ = 10°, SPL stays low level corresponding to the background noise. Getting to θ = 22°, back sheet cavitation is observed around the propeller top position which causes the high SPL in the range of high blade pitch angle. Fig. 4 is the variation of cavitation map denoting the circumferential distributions of cavitation patterns during one revolution. At θ = 0° and 5° face cavitation occupies over the whole circumference which indicates the weak influence of non-uniform wake. On the other hand, back sheet cavitation affected by the non-uniform wake occurs

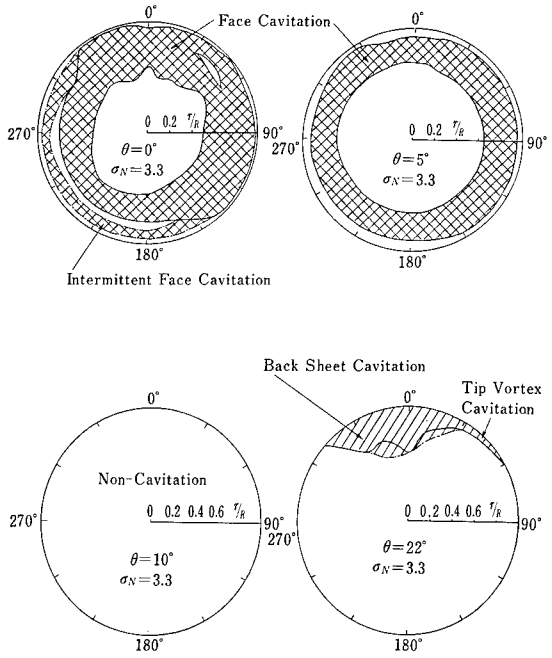


Fig. 4 Variation of Cavitation Map (Circumferential Distributions of Cavitation Patterns) versus Blade Pitch Angle θ by the Model Test On Ship B)

around the top position at θ = 22°. Besides, the latter indicates higher noise level than the formers. It is considered that the higher noise is caused by the greater steepness of circumferential variation of cavitation volume and the amount is larger than the face cavitation of low blade pitch angle.

Photo 2 shows the cavitation pattern at σ_N = 1.2 and θ = 0°, and Fig. 5 its cavitation map.

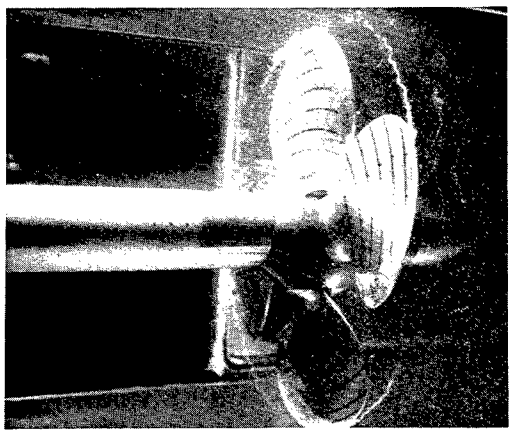


Photo 2 Cavitation Pattern at Blade Pitch Angle θ = 0° by the Model Test on SHIP B, σ_N = 1.2

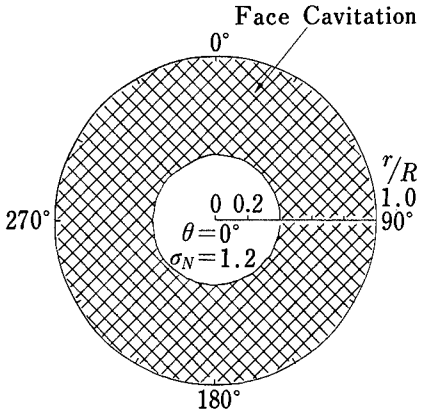


Fig. 5 Cavitation Map by the Model Test on SHIP B, σ_N = 1.2

In comparison with the cavitation at σ_N = 3.3, SPL is rather high as shown in Fig. 3 because of rather large cavitation volume in case of σ_N = 1.2.

2.3.2 Full-scale measurement for SHIP C

In order to see the actual phenomena on board ship with CPP, the full-scale measurement was carried out together with cavitation observation for the portside screw of a twin screwed SHIP C. The cavitation noise was measured by a hydrophone installed at the hull bottom surface of the forebody and analyzed in the 1/3 octave band with the center frequency of 2, 5 and 12.5 kHz. In the low speed range, the ship was controlled by shifting the blade pitch angle. From the medium speed after reaching the design pitch angle, the propeller turning rate was controlled to increase the ship speed.

Fig. 6 shows the variation of cavitation noise level versus the blade pitch angle and the propeller turning rate. In the range of blade pitch control, the SPL is higher as the blade pitch angle is lower, and decreases as the blade pitch approaches to the design pitch angle. The SPL again increases by raising the turning rate in the RPM control range. The SPL variation indicates the difference between each frequency that the variation is smaller as the frequency is lower. These results might be interpreted by taking into consideration of the cavitation patterns.

The cavitation patterns were obtained at the same full-scale measurement as shown in Fig. 7 which shows as the cavitation maps on the propeller disc by looking aftward.

At the $\theta = \frac{2}{7}$ design pitch angle and n = $\frac{2}{5}$MCR, face tip cavitation occurs along the lower part of the disc circumference. This may radiate the noise about the same level

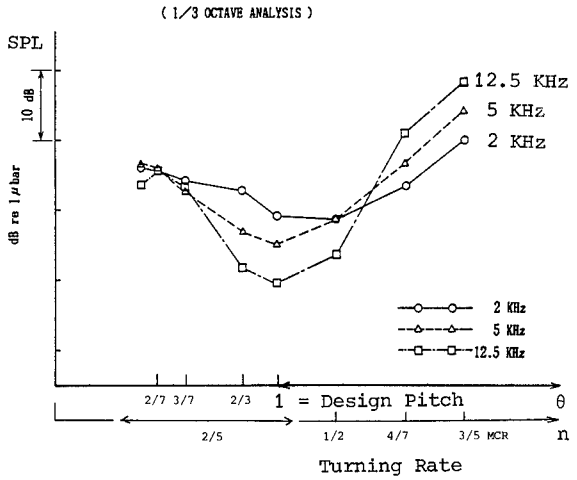


Fig. 6 Variation of Cavitation Noise Level versus the Blade Pitch Angle and Propeller Turning Rate by Full-Scale Test on SHIP C

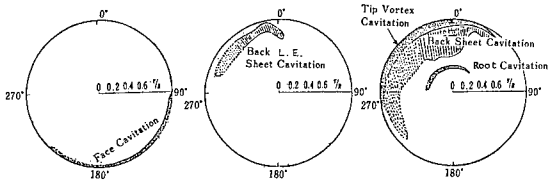


Fig. 7 Variation of Cavitation Map versus Blade Pitch Angle and Main Engine Output by the Full-Scale Test on SHIP C

for each frequency as in Fig. 6. When the pitch angle reaches the design pitch, leading edge sheet cavitation appears on the back surface of the propeller blades on the upper part of the disc. Since the SPL indicates the lowest level especially for the high frequency 12.5 kHz at the condition above, this must approximately be equal to cavitation inception.

In case of $\frac{3}{5}$ MCR in the RPM control range, back sheet cavitation develops so large extent over the upper and left (near center line of the hull because of clock-wise turning by looking forward) part of the disc that the SPL increases higher than the SPL in the range of blade pitch control.

3. SIDE THRUSTER

In this chapter, the state of the arts and the up-to-date problems on the underwater radiated noise from a thruster are firstly outlined. Since the cavitation noise acts the leading part of that, it is investigated and described what kinds of research work are

needed to clarify the characteristics of the cavitation noise and how to reduce it. A full-scale thruster test in a large-sized tank is finally introduced which was conducted in accordance with the guidelines.

3.1 State of the Arts

3.1.1 Cavitation of side thruster

Forcussing the general type of tunnel thruster, the blade must be shaped as flat plate and its pitch angle controlled because it must generate the equal thrust for both right and left directions. When the blade pitch angle is raised in order to generate a thrust, the pitch angle around the blade tip region is excessively increased. This is easy to cause the cavitation because of large angle of attack[7].

The special feature of the thruster cavitation denotes the difference of the cavitation occurrence between the right and left flow directions. Because the one way flow locates the impeller in the upstream and the other in the downstream of the housing of gear equipment[8].

3.1.2 Outline of full-scale measurements

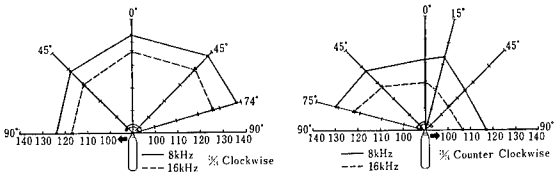
Summarizing our experiences on full-scale measurements[9], the characteristics of the underwater noise radiated from thruster cavitation are as follows:

a) SPL shows the continuous spectrum and has the slope about -5 - -10 dB/octave in the frequency range larger than 2 kHz.
b) SPL line seems to be parallel to or to approach the upperbound of the Brown's formula[10].
c) On the machinery noise in the frequency larger than a few kHz, there are only the possibility that the higher order harmonics of the gearing frequency appear as spike noises. Accordingly, it is natural to consider that the cavitation mainly causes the underwater noise in the frequency range larger than 2 kHz.

3.1.3 Level and directivity of cavitation noise

Fig. 8 shows an example measured result of underwater noise for a full-scale SHIP D. From these results the followings are disclosed:

a) The noise level denotes the difference depending upon the inflow direction (the level is higher in case that the gear housing is located in the upstream position of the impeller)



(a) Pitch ¾, Turning to the Right (b) Pitch ¾, Turning to the Left

Fig. 8 Directivity of Underwater Noise Radiated from the Thruster (SHIP D)

b) The upstream noise level is 10 dB higher than the downstream.
c) Comparing the condition of maximum thrust and non thrust the former is 10 - 15 dB higher noise level at 10 kHz than the latter.
d) The slope of noise spectrum becomes smaller, as the blade pitch angle increases.

3.1.4 Past records of model test

There are quite a few published papers relating the model test of a side thruster for the underwater noise in cavitation tunnel[8]. The authors could not find the papers especially treating the cavitation noise measurements on the tunnel thruster. When the noise would be measured by using a model in cavitation tunnel, there are not any scaling laws to predict the full-scale condition in case of a tunnel thruster. However, the model test in a cavitation tunnel has the great advantages for simplifying the phenomena which seems less convenient for the full-scale test. The model test should positively be applied from now on.

3.1.5 Desired works

In regard with the blade shape a forward skewed blade was proposed as a low noise type[11]. However, the effect was not made clear completely.

Concerning the non-uniformity of the flow inside the tunnel, the velocity distributions were measured in the wake of gear housing where the rather low velocity was revealed[7].

It is not clear what effect can be obtained by applying the air injection for the noise reduction of thrusters, and what influences will appear against the other performances. In case of normal ducted propellers, several data were published on the air injection obtained from model and full-scale tests[12 - 14]. The effect of the air injection in case of thrusters is considered to essentially be about the same as in case of ducted propellers.

Based upon the investigation mentioned above, the followings are to be examined in

order to make clear the characteristics of the cavitation noise.

a) Study on the characteristics of thruster cavitation noise
b) Study on the relation between cavitation and its noise
c) Study on the correlation of the cavitation noise between model and full-scale
d) Study on the effect of the non-uniform flow inside the tunnel on the cavitation noise
e) Study on the effect of the air injection and its influence against the other performances
f) Study on the blade shape for the noise reduction

3.2 Full-Scale Test

The full-scale test has been carried out in a large-sized tank in accordance with the guidelines described in the former section. The purposes of the test are determined as follows:

a) Clarifying the characteristics of thruster cavitation and its noise
   - Cavitation observation and underwater noise measurements by varying the turning rate and blade pitch angle.
b) Grasping the relation between non-uniform flow inside the tunnel and the cavitation noise
   - The influence on the flow by changing the tunnel inlet, i.e., the shape of bellmouth.
c) Defining the effect of the air injection on the cavitation noise
   - The change of the cavitation noise by varying the flow rate of the air injection.

Since the test would be performed in the closed space inside the water tank, the following problems were in advance examined; circulation flow generated by thruster operation, abnormal sound field affected by the interference and the reflection by the bottom and the side walls. The former could be solved by controlling the time interval of thruster operation and by watching the flow rate and the change of the thrust. The latter seemed to be a rather difficult problem that the less reliability of the measurements might be arised depending on their influence.

For that reason, the sound propagation test in the tank has firstly been conducted before the full-scale test for a thruster.

3.2.1 Sound propagation test

Evaluating the propriety of the test in such a closed space, the following characteristics of underwater sound propagation were investigated.

a) The propagation characteristics of underwater sound
b) The transmission loss between the sound generator corresponding to the cavitation noise and the hydrophones located at the same position as the full-scale test

Data were analyzed by using the transmission loss TL indicating the damping rate of the sound due to the distance between the transmitter and the receivers as follows:

$$TL = 10 \log \frac{P_0^2}{P_1^2}$$

hence,

P_0: Sound pressure at 1 m from the transmitter
P_1: Sound pressure at a measuring point.

Fig. 9 shows the test result of pure tone transmission when the receiver was continuously removed along the longitudinal direction of the tank. In this case the irregular changes of TL were detected due to the interference and reflection, and the peak to peak value was 40 dB.

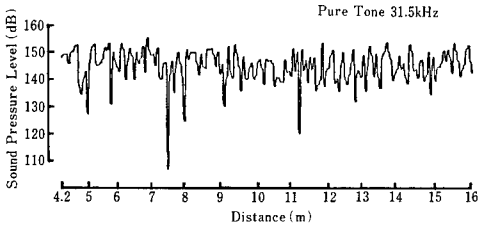


Fig. 9 Transmission Loss of Pure Tone along Longitudinal Direction of the Water Tank

Fig. 10 shows the test result in case of random noise with narrow band along the longitudinal direction of the tank. In this figure the TL at the center frequencies 2 - 31.5 kHz are given, and the irregular changes in case of the pure tone are disappeared.

Besides in the condition of the thruster sunk under the water in the tank, TL has been analyzed by transmitting the random noise from the blade tip. This result indicates that TL is 10 - 12 dB with flat tendency over the frequency concerned.

The underwater noise radiated from thrusters is considered to consist of the spike noise by the machinery vibrations and the cavitation noise. The former has the propagation characteristics of the pure tone and the latter that of the random noise. Consequently, the noise source based on the

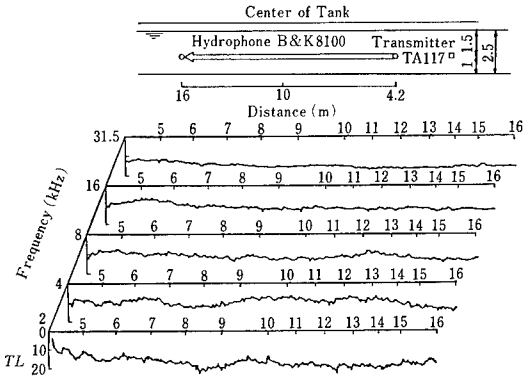


Fig. 10 Transmission Loss of Random Noise along the Longitudinal Direction of the Water Tank

cavitation can be evaluated by applying the 1/3 octave band analysis. Nevertheless the noise source based on the machinery vibrations seems difficult to detect, because the pure tone has the remarkable change of TL due to the location of a measuring point.

3.2.2 Full-scale test

(1) Test equipment

The test was conducted by using a full-scale thruster with a 1 m diameter and the maximum thrust 2 tf (19.6 kN), and was installed in the current water tank (55 m length x 8 m breadth x 2.5 m depth) of Akishima Laboratory (Mitsui E.& S.). The thruster was fixed to the sub-carriage which was freely put on the main structure. In order to measure the thrust, four load cells were used to connect the sub-carriage to the main (Photo 3).

As shown in Fig. 11 two kinds of the tunnel inlet, namely NORMAL type with straight corner and JIS type with the shape of bell-mouth were used in sequence. Moreover inside the tunnel the two rows of orifices for the air injection were provided at the both sides of the impeller center line.

Fig. 12 shows the system for cavitation observation and underwater noise measurement. For the cavitation observation an underwater color TV camera was used.

Photo 4 is an example monitored by the TV camera which operating condition is as follows; impeller turning rate 525 rpm, blade pitch angle 12° and flow rate of air injection 0.43 m^3/min. (MAX).

(2) Test results

a) Cavitation and thrust

Fig. 13 shows the comparison between the cavitation patterns of no air and of MAX air injection at 525 rpm. In case

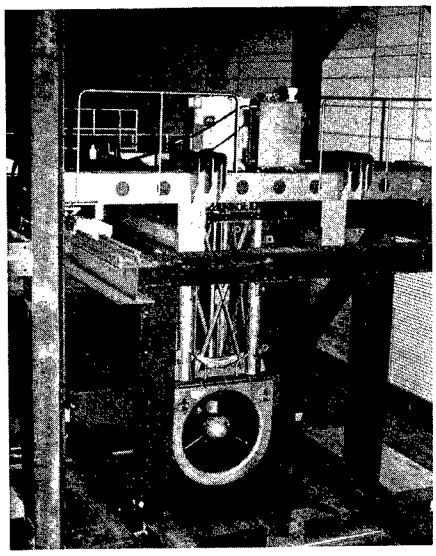


Photo 3 Full-Scale Thruster Installed in the Water Tank

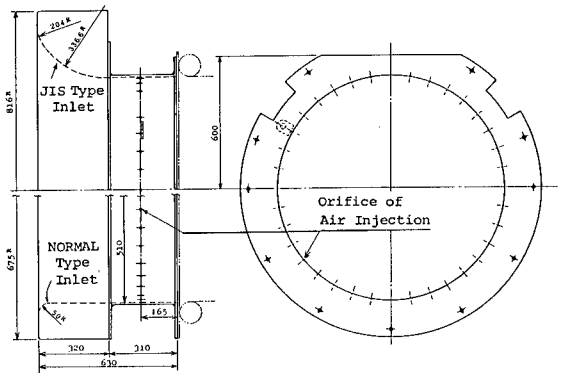


Fig. 11 Shapes of the Tunnel Inlet of the Thruster (NORMAL and JIS Type)

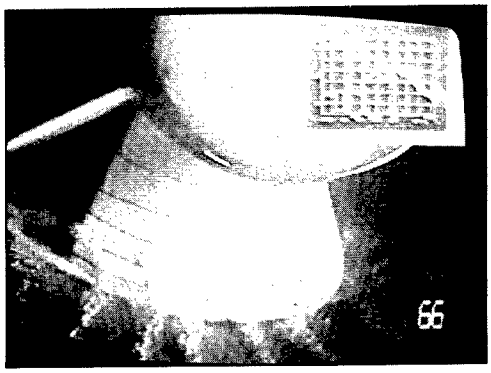


Photo 4 Cavitation on the Blade of the Thruster with Air Injection

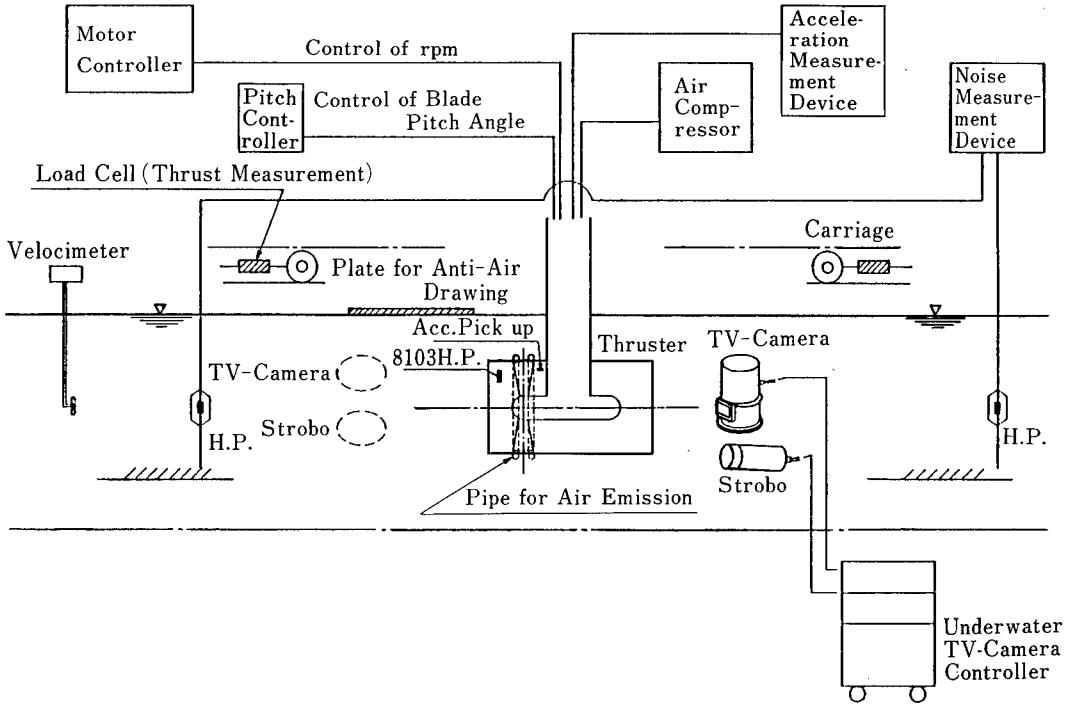


Fig. 12 System for Cavitation Observation and Underwater Noise Measurement on the Phototype of Thruster

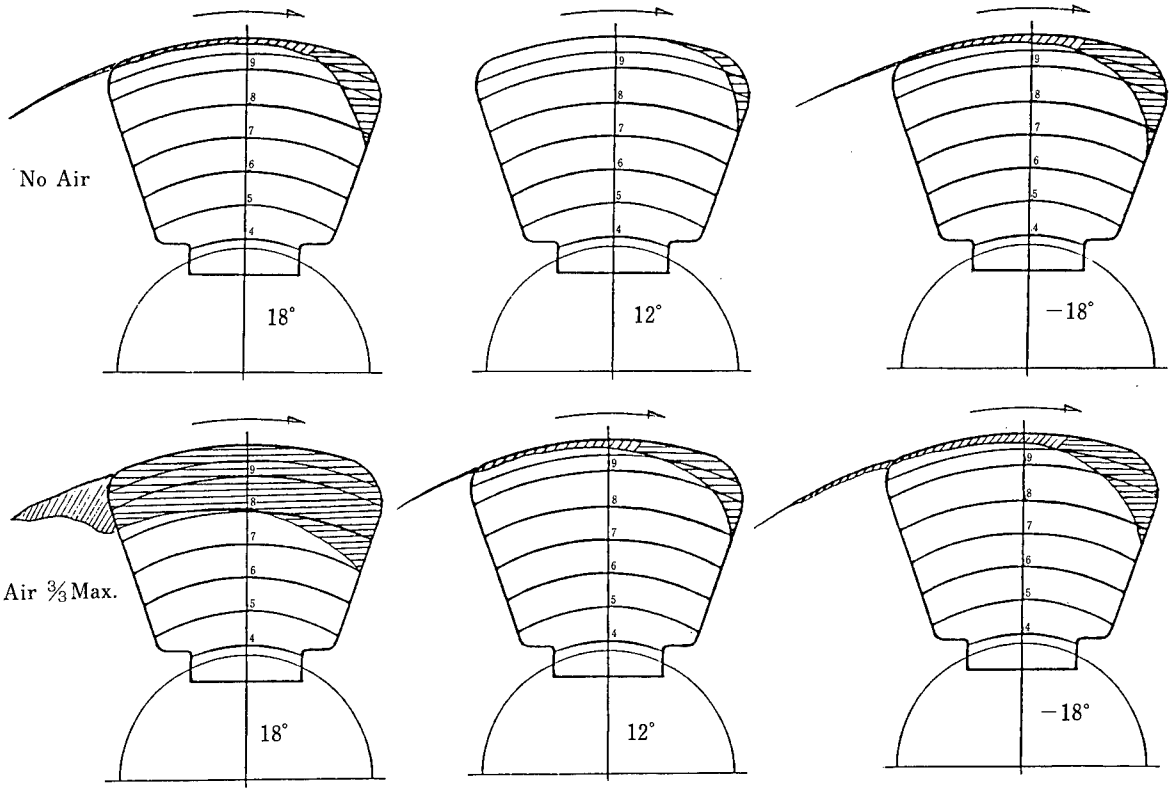


Fig. 13 Comparison between the Cavitation Sketches of No Air and of Max. Air Injection at 525 rpm

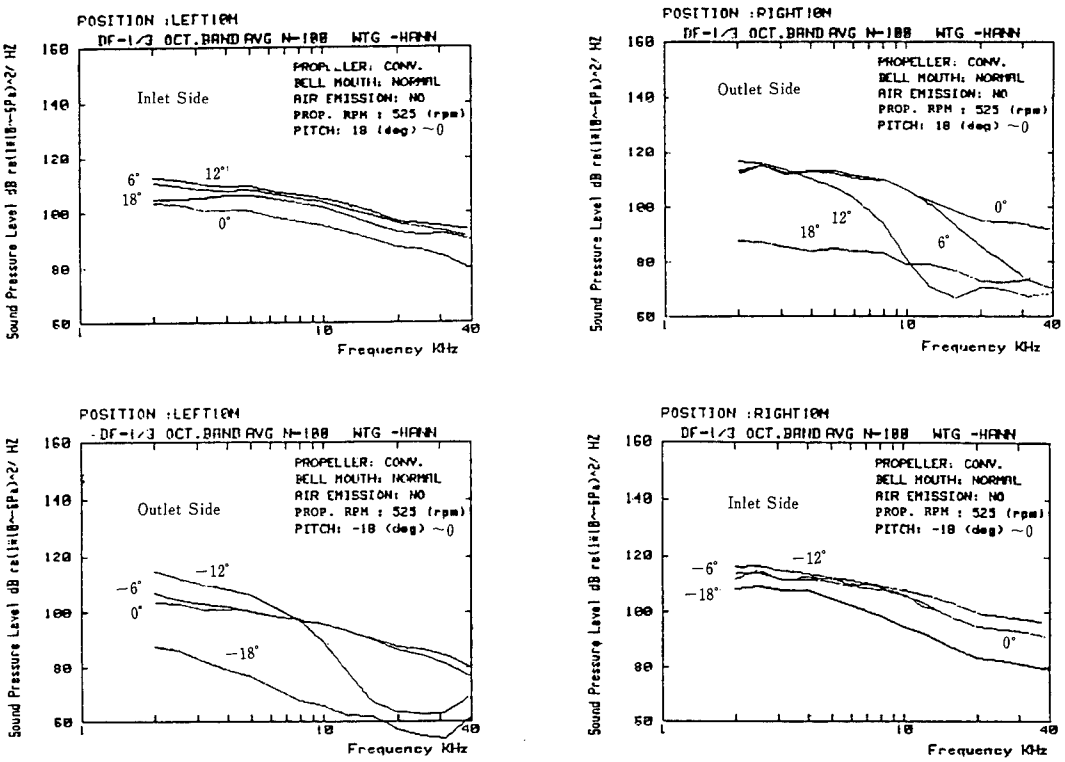


Fig. 14 Measured Underwater Noise Level Radiated from the Thruster (525 rpm, Blade Pitch Angle 18^{o} - -18^{o})

of air injection comparing with no air condition, no change of the cavitation pattern is observed at $\theta = -18^{o}$ (impeller in the downstream position of the housing), tip vortex cavitation somewhat larger develops at $\theta = 12^{o}$ (impeller in the upstream of the housing), and sheet cavitation extremely larger develops at $\theta = 18^{o}$. No difference of the thrusts between no air and MAX air injection was obtained.

b) Cavitation and underwater noise

Fig 14 shows the measured underwater noise analyzed in the 1/3 octave band. The operating condition is of no air at 525 rpm. The SPLs measured in the upstream, i.e. both the positions of LEFT 10M of $\theta = 18^{o}$ - 0^{o} and of RIGHT 10M of $\theta = 0^{o}$ - -18^{o} indicate the similar tendency. Comparing them with the cavitation patterns in Fig. 13, the SPL of $\theta = 12^{o}$ is larger than that of $\theta = 18^{o}$ and -18^{o} with tip vortex cavitation, even if the latters have larger cavitation extents than the formers.

The SPLs measured in the downstream, i.e. both the positions of RIGHT 10M of $\theta = 18^{o}$ - 0^{o} and of LEFT 10M of $\theta = 0^{o}$ - -18^{o} indicate very interesting features. Especially at $\theta = \pm 12^{o}$ the SPLs in the high frequency range larger than 10 kHz are remarkably reduced. As the pitch angle becomes $\theta = \pm 18^{o}$, the reduction rate is emphasized in the lower frequency range too. These levels are definitely lower than that in the upstream. These phenomena must be so-called directivity of the cavitation noise disclosed in case of SHIP D in Fig. 8.

Observing the water in the downstream field of the thruster, the cloudy turburent flow rushed about in frenzy as the pitch angle became larger. Accordingly it is denoted that a lot of air bubbles mixed in the cloudy flow baffle the noise propagation in the downstream.

c) Influence of turning rate

Fig. 15 shows the same as Fig. 14 but at 450 rpm. The SPLs of almost pitch angles at 525 rpm are larger than that at 450 rpm except $\theta = \pm 18^{o}$. This can be explained that the SPL becomes lower when the cavitation develops and becomes stable which can sometimes be seen in the general case of propeller cavitation tests in uniform flow. Tip vortex cavitation must be one of the effects to stabilize the cavitation.

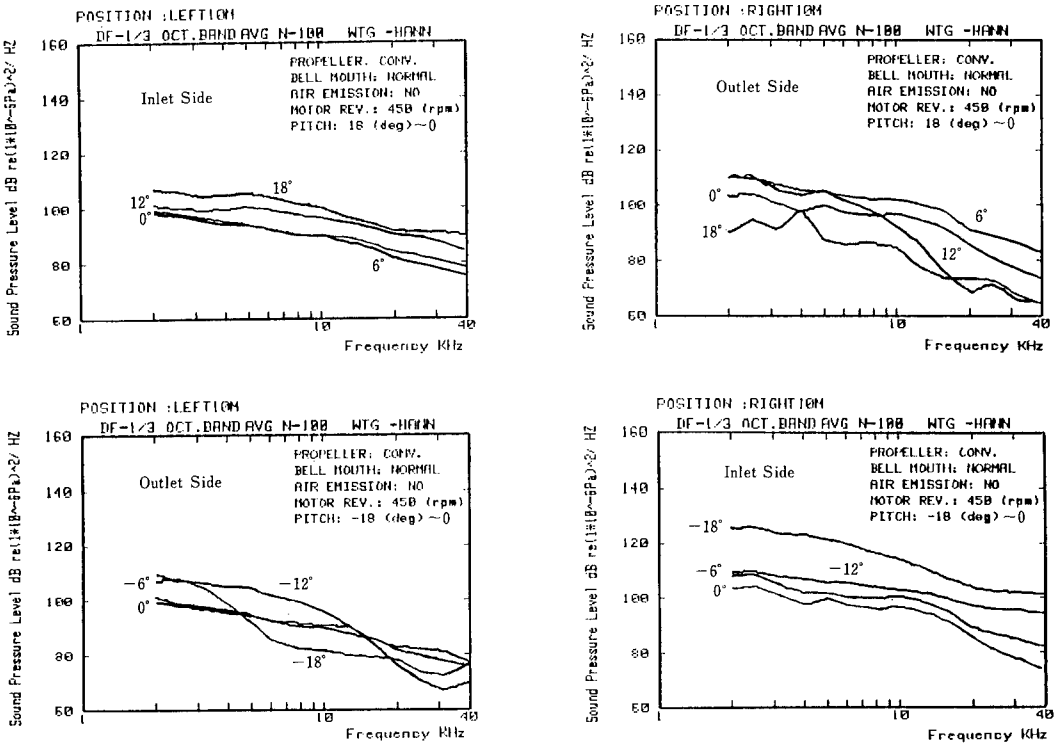


Fig. 15 Measured Underwater Noise Level Radiated from the Thruster (450 rpm, Blade Pitch Angle 18^{o} - -18^{o})

d) Underwater noise and air injection

Fig. 16 shows the SPLs when varying the flow rate of the air injection. At the measuring position in the upstream field of the thruster, 5 - 10 dB noise reduction is obtained by the air injection. On the other hand at that in the downstream the noise reduction is remarkably obtained in the frequency range lower than 10 kHz.

e) Underwater noise and gear vibration

Fig. 17 shows the cross correlation between the underwater noise at LEFT 10M in the upstream field of the thruster and the gear vibration measured by the acceleration pick up fixed on the gear housing at the condition of $\theta = 18^{o}$ and 525 rpm. This analysis denotes that the contribution of the vibration on the underwater noise decreases while that of cavitation increases as the pitch angle becomes larger.

f) Underwater noise and the shape of tunnel inlet

The shape of the tunnel inlet gave no remarkable change on the underwater noise and the thrust. The cavitation extent of the JIS type seemed somewhat larger than that of the NORMAL type, and its SPL at $\theta = 18^{o}$ is slightly higher.

4. PREDICTION

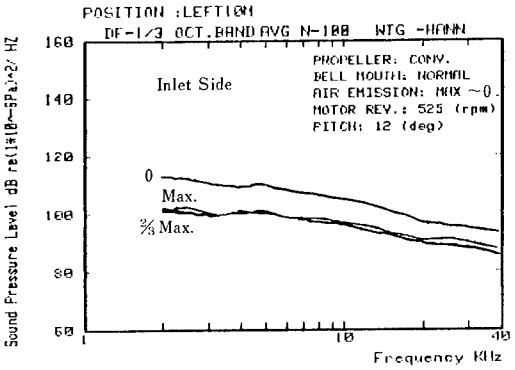
4.1 Scaling from Model to Full-Scale

For SHIP B the model and full-scale spectra of the cavitation noise are shown in Fig. 18 at the condition of $\sigma_N = 1.2$, $\theta = 0^{o}$. The SPL is converted into the power per 1 Hz from the 1/3 octave band analysis. In this figure, the predicted values for the full-scale by well-known two methods[15, 16] are shown. Moreover the value by Brown's formula and the predicted value by an improved method are added too.

The methods of Levkovskii[15] and Björheden et al[16]. give the different frequency shifts from model to full-scale respectively which however conflict with the full-scale measured values. For instance, the latter defines the frequency shift by the scaling law as follows:

$$fs = fm \cdot 1/\lambda. \qquad (1)$$

In general model tests in cavitation tunnels, the propeller turning rate is determined to maintain the hydrodynamic condition to keep Reynolds number as high as



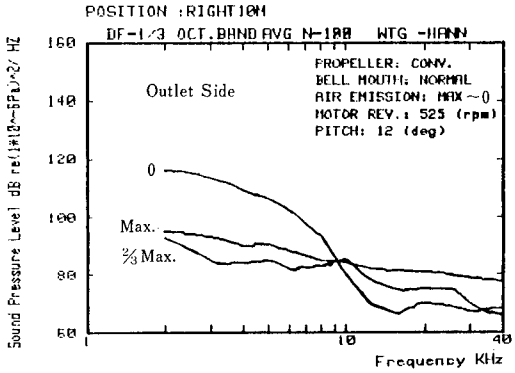
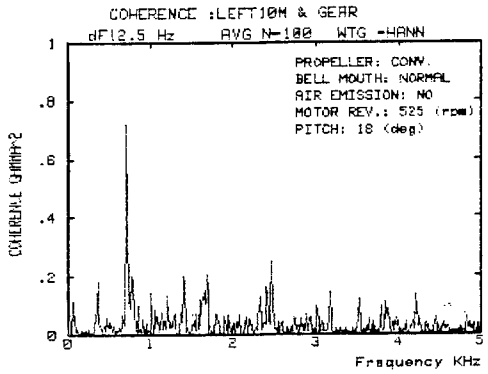


Fig. 16 Measured Underwater Noise Level Radiated from the Thruster (525 rpm, Blade Pitch Angle 12°, Air 0 - Max)



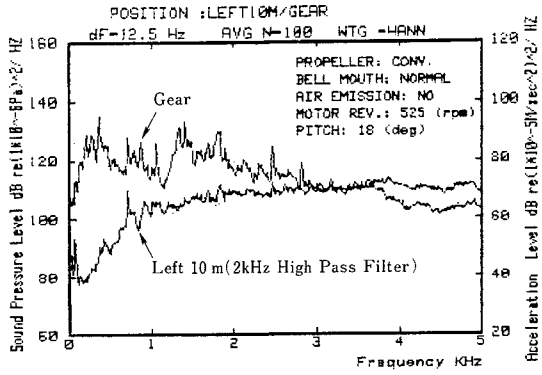


Fig. 17 Coherence between Underwater Noise (LEFT 10 M) and the Vibration of Gear (525 rpm, Blade Pitch Angle 18°)

possible. Therefore, it is unreasonable that f_m is converted by the scale factor to f_S, because the frequency of hydrodynamic phenomena is governed by the blade rate frequency especially in the low frequency range.

For that reason the following relation should be applied for the frequency converted from model to ship denoted by "m" and "s" respectively.

$$f_S = f_m \cdot n_S Z_S / n_m Z_m = f_m \cdot n_S / n_m \quad (2)$$

The sound pressure should also be considered an extension of the free space pressure radiated from the propeller cavitation. Accordingly as the scaling law, the well-known $K_p = P/\rho n^2 D^2$ can be applied at the similar point of both ship and model as follows :

$$SPL_S = SPL_m + 20 \log(n_S/n_m)^2 \lambda^2. \quad (3)$$

These improved expressions have resulted in Bark's[17,18] formulae. The results by these expressions are shown in Fig. 18, and indicate good agreement with the full-scale values.

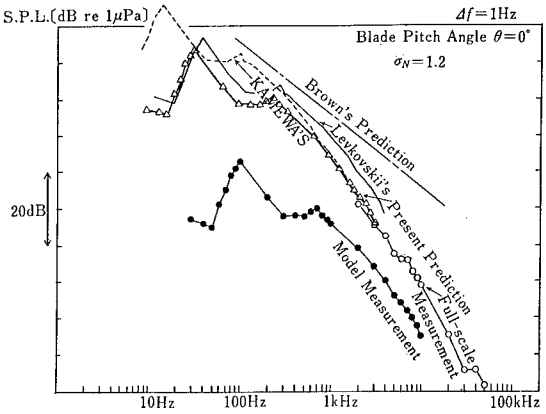


Fig. 18 Comparison between Measured and Predicted Underwater Noise Level on SHIP B

4.2 Theoretical Approach

4.2.1 Method

In order to predict the radiated sound

energy level of air bubbles by cavitation, the following parameters have to be known: the distribution of bubble radii before and after collapsing, the inner pressure of bubbles when collapsing, the duration of sound pulse emission, the probability density of bubble collapse in unit time and volume etc.. Such basic data can hardly be obtained, even if detailed observations and measurements are conducted in cavitation tunnels or on board ships.

It must be useful if the prediction could be done by using the computer program near at hand at least in an available frequency range. Because the radiated sound pressure from cavitation is considered to lie on the extension of the hull surface pressure which is nowaday calculated with certain accuracy in practical use. The basic idea was originated by Tyvand and Persson.[19]

If the SPL of the cavitation noise in the low frequency range is obtained, the SPL in the high frequency range can be approximated by applying Fitzpatrick's work[20], namely the slope of the SPL estimated by -6 dB/octave in the 1/3 octave band. In order to apply this relation, the frequency with the peak value of the SPL has to be determined which gives the turning point between the low and high frequency range. That is to say the upper limit frequency of the theoretical calculation. In other words, this is the resonance frequency of a bubble with the greatest number of the bubble radius distributions.

Referring to the bubble collapsing time T_C obtained from Rayleigh equation, the frequency of the bubble vibration f_{max} is obtained as follows:

$$f_{max} = \frac{1}{2T_C} = \frac{1}{2R_{max}}\sqrt{\frac{P_o}{\rho_o}} \quad , \quad (4)$$

hence,

P_o: static pressure
ρ_o: water density
R_{max}: bubble radius with the greatest number.

For example, as the values P_o = 1 atm, ρ_o = 1 g/cm^3, R_{max} = 1 cm are applied, then f_{max} = 500 Hz is obtained. In the following sample calculation f_{max} = 200 Hz is however used for the time saving.

4.2.2 Calculation

For the sample calculation, the following procedure is applied.

a) Propeller induced pressure is obtained at given field points based on the unsteady lifting surface theory for a propeller and the two-dimensional cavitation theory which are used for the prediction of hull surface pressure[21].

b) This is transformed to the spectrum level with the upper frequency of about the third harmonics of the blade rate frequency (BRF) due to the limited number of time steps during one revolution of the propeller (Fig. 19). In the present case the upper frequency is about 30 Hz.

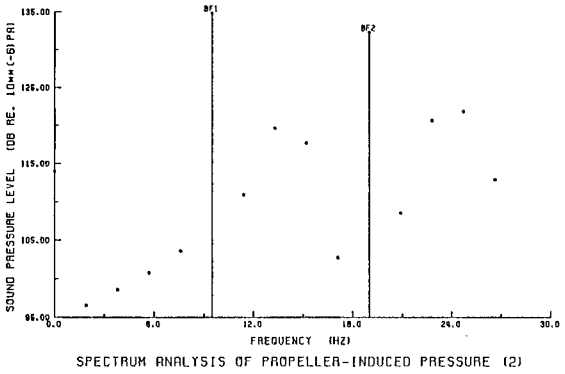


Fig. 19 Calculated Spectrum of Propeller Induced Pressure

c) The detailed wake distributions with the fine interval of time steps are provided to get higher frequency range up to 200 Hz.

d) The transmission function from the wake spectrum to the successive pressure spectrum avoiding the harmonics of BRF is caluclated within the frequency range up to the upper frequency.

e) The transmission function of the range from the upper frequency to 200 Hz is estimated by outerpolating the former. In this case the constant value is used as the same at the upper frequency (Fig. 20)

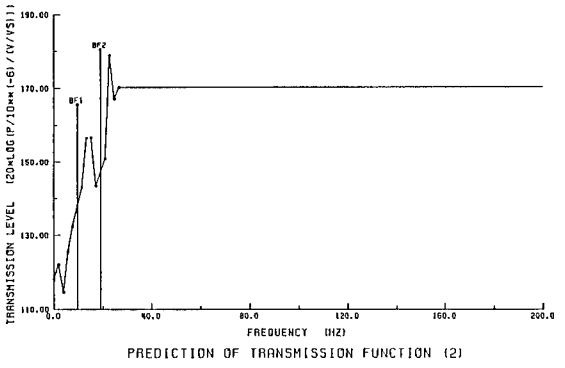


Fig. 20 Transmission Function from the Wake Spectrum to the Propeller Induced Pressure

f) The SPL with Δf = 1 Hz is predicted by multiplying the wake spectrum by the transmission function up to 200 Hz (Fig. 21)

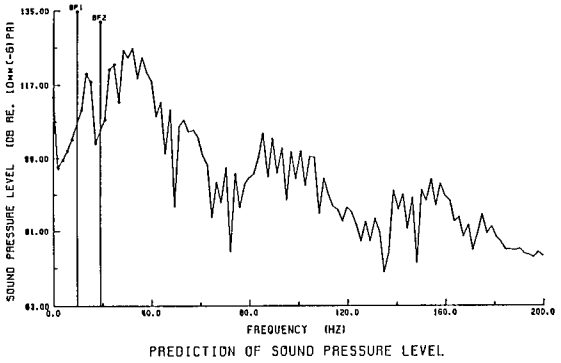


Fig. 21 Calculated Cavitation Noise Spectrum

g) The SPL in the 1/3 octave band is calculated including the harmonics of BRF (Fig. 22).

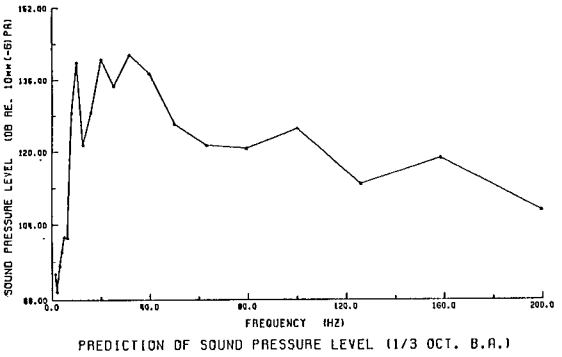


Fig. 22 Calculated Cavitation Noise Level in the 1/3 Octave Band

h) For the higher frequency than 200 Hz, the slope of -6 dB/octave in the 1/3 octave band is applied (Fig. 23).

From the practical point of view, this proposed calculation system seems simple and reasonable. Since the calculation has been made for the sample only, the further investigation is needed to make a comparison with some measured values.

5. CONCLUDING REMARKS

On the characteristics of marine propellers and thrusters, full-scale measurements and model tests have been introduced and taken into consideration. Several experiment results revealed the following conclusions.

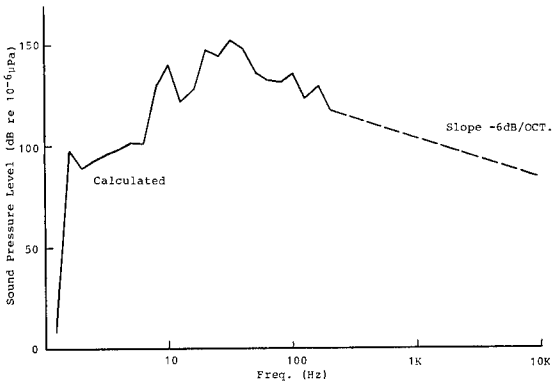


Fig. 23 Calculated Cavitation Noise Level with the Prediction in the High Frequency Range

a) The relation between the process from non-cavitating to cavitating condition and the change of underwater noise level along the operation line of a full-scale propeller has been shown.
b) This process has nearly been simulated by a model test in a cavitation tunnel and the changes of the noise level have been explained by referring to the cavitation occurrences.
c) It is shown that the noise level from controllable pitch propellers varies, as its cavitation pattern changes due to the variation of its pitch angle.
d) Investigating the underwater noise of thrusters the state of the arts and the problems are shown.
e) The directivity of the cavitation noise has been detected by evaluating a full-scale measurement on a thruster.
f) In a large-sized tank cavitation observation and underwater noise measurement have been carried out by using a full-scale thruster.
g) The reliability of the tests in such a closed tank has in advance been confirmed by measuring the propagation loss of underwater sound, i.e. pure tone and random noise.
h) The relation between cavitation and its radiated noise has been made clear under the various parameters i.e. the blade pitch angle, the turning rate of the impeller, the inlet shape of the tunnel, the effect of gear housing wake, air injection, coherence with the gearing vibration.
i) The noise propagation in the downstream field of the thruster may be baffled by the cloudy flow with air bubbles especially in the range of high frequency. The cavitation noise in the upstream of the impeller is larger than that in the downstream from the reason mentioned above together with the

baffling effect of the impeller blades.

j) The scaling law of the cavitation noise was discussed and improved by applying more simple and reasonable shape.

k) Applying a propeller unsteady lifting surface and cavitation theory, the calculation system for the cavitation noise is proposed which is simply and reasonably arranged by taking into account the characteristics of the sound pressure radiated from the propeller cavitation.

ACKNOWLEDGEMENT

The authors would like to express their sincere thanks to Prof. Hiroharu Kato of Tokyo University and Prof. Kiyoshi Nirei of Tokai University for their encouragements and advices throughout the course of the present project.

REFERENCES

1. Løvik, A. and Holden, K.," Noise Reduction by Airinlet in the Propeller Duct", Inter·Noise 83 1983 pp. 779-782.
2. Accardo, L. et. al.", An Integrated Theoretical and Experimental Procedure for Propeller Design", ISSHES, Spain, 1983.
3. Latorre, R., "Experimental Study of Model Propeller Tip Vortex Cavitation Noise", ACUSTICA, Vol. 47, No.2, 1981.
4. Chandraschekhara, N., "Analysis of Tip Vortex Cavitation Inception at Hydrofoils and Propellers", Schiffstechnik, Bd. 23, 1976.
5. Noordzij, L. et. al., "Radiated Noise of Cavitating Propellers", ASME, 1977.
6. Leggat, L. T. et. al., "The Study of Propeller Cavitation Noise Using Cross-Correlation Methods", ASME, Int. Synmp. on Cavitation Noise, 1982.
7. Minsaas, K. J., "Hydrodynamic Design of Thrusters for Safe and Reliable Dynamic Positioning", Proc. of Symp. on Safty and Reliability of DPS, Det Norske Veritas, 1975.
8. Minsaas, K. T. et. al., "Hydrodynamical Characteristics of Rotatable Thrusters", NSFI Report, R-69, 78, 1978.
9. "Report on the Research and Study of Low Noise Thruster", The Association of Industrial Machine of Japan 1982, pp. 30-127.
10. Brown, N. A. "Noise Problems and Solutions", "Int. Symp. on Shipboard Acoustics, 1976.
11. Cumming, R. A. et. al., "Highly Skewed Propellers", SNAME, 1972.
12. Huse, E., "Air Injection to Avoid Cavitation Erosion in Propeller Dust", NSFI Report, R-49, 75, 1975.
13. Narita, H. et. al., "Investigation on the Ducted Propeller Cavitation and the Dust Erosion Prevention by the Air Injection System", Proc. of Symp. on Hydrodynamic and Offshore Propulsion System, 1977.
14. Okamoto, H. et. al., "Cavitation Study of Ducted Propeller on Large Ship", SNAME Vol. 7, 1975.
15. Björheden, O. et. al., "Prediction of Propeller Noise Spectra", Symp. on Hydro. of Ship and Offshore System, 1977.
16. Levkovskii, Y. L. "Modeling of Cavitation Noise", Sov. Phys. Acoustics, Vol. 13, No. 3, 1968.
17. Bark G., "Prediction of Propeller Cavitation Noise from Model Tests and Its Comparison with Full Scale Data", Journal of Fluids Eng., Trans. of the ASME, Vol. 107, March 1985.
18. Johnsson, C. A.," The Cavitating Propeller as a Source of Vibration and Noise", Proceedings of International Symp. on Cavitation, Sendai, Japan, April 1986, pp. 9-20.
19. Tyvand, N.P. and Persson, B. "Prediction of Noise from a Cavitating Propeller", Inter·Noise 79, Warszawa, Polen, Sept., 1979.
20. Fitzpatrick, H. M. et. al., Proc. Second Symp. on Naval Hydrodynamics, ACR-38, ONR, Washington D.C, 1958, pp. 201-205.
21. Yuasa, H. et. al., "Practical Applications of the Discrete Vortex Element Method For Calculation of Propeller Induced Excitation Forces", Proc. 13th Symp. on Naval Hydrodynamics, SRAJ, Tokyo, 1980, pp. 65-88.

DISCUSSION

Neal A. Brown,
Atlantic Applied Research Corporation

This discussor is the "Brown" to whom the upper line is attributed in figure 18 and to whom estimates or limits are attributed in the text. As a limit this line may be appropriate. As an estimate, however, it would differ in several ways.

First, the level of the sloped line in the middle frequencies would be reduced by the ratio of the swept area of cavitaion (as shown in the author's figure 4, and numerous others) to the disk area of the propeller. Secondly, below some "break" frequency the slope of the spectral estimate would be reduced to zero (i.e. flat). That frequency would depend on diameter, submergence and the abovementioned area ratio. Finally, above 10 kHz the slope would be halved.

The authors are quite correct in their description of the cavitation susceptibility of CRP thrusters. In order to maintain port-starboard symmetry in the operating characteristics of these constant speed, controllable-reversible pitch machines, the blades must be flat - that is their mid surfaces must be planar (unpitched). Therefore, when swung for thrust in either direction the blades are overpitched and suffer substantial leading edge sheet cavitation at the outer radii (as well as tip-gap cavitation).

The authors have not cited papers by John Norton of the Bird Johnson Company and myself which were presented at the Olso symposium on Hydrodynamics of Ship and Offshore Propulsion Systems in 1977, [a] and at the San Diego section of SNAME in 1974, later published in Marine Technology, [b]. These papers reported the development of a 3000 HP CRP transverse thruster design for dynamic positioning of acousitcally positioned drillships.

Our solution was largely a hydrodynamic one incorporating large thickness ratios in the blade sections of NACA type and a forward skewed blade outline. The combination greatly increased the blades' cavitation tolerance to angle-of-attack. Model tests showed a complete absence of leading edge or blade surface cavitation within the design thrust range. Only tip-gap cavitation remained.

This development led to U.S. Patent No. 3,972,646 and foreign patents on the thruster blade form which are held by Mr. Norton and me. Twelve of these thrusters were built by the Bird Johnson Company and six were installed in each of two of the largest drillships in service, the DISCOVERER 534 and SEVEN SEAS. Measurements of the underwater radiated noise due to thruster operation on the "534" yielded levels 10 dB lower, typically, than those of comparably powered transverse thrusters, [c]. These units have now been in service successfully for more than ten years.

[a] "Acoustic Performance of Dynamic Positioning Thrusters," N. A. Brown and J. A. Norton, Symposium on Hydrodynamics of Ship and Offshore Propulsion Systems, Det Norske Veritas, Oslo, March 20- 25, 1977.

[b] "Thruster Design for Acoustic Positioning Systems," N. A. Brown and J. A. Norton, Marine Technology, Vol. 12, No. 2, April 1975.

[c] Underwater Noise of Thruster on DISCOVERER 534, N. A. Brown et al., Bolt Beranek and Newman Inc. Technical Memorandum No. 276, December 22, 1975.

Reply -

We thank Mr. Brown for his kind remarks and comments.

Regarding the full-scale noise estimation in figure 18, his suggested method seems to give an agreeable line with the measured one. Unfortunately, we do not know how the method would logically be explained in conformity with the physical phenomena.

We know your published paper in regard with the forward skewed thruster. This type of blade may have the advantage to reduce the thickness or volume of cavitation and to stabilize it.

We have heard that the forward skewed blades do not always reduce the cavitation noise, especially in the high frequency range in connection with the operation of acoustic apparatus. We would like to say that the blade shape should be selected or designed to avoid the noise disturbance in the required frequency range when the cavitation occurence can not be eliminated by whatever possible design procedure.

Experimental and Analytical Techniques for the Study of Unsteady Propeller Sheet Cavitation

J. KERWIN and S. KINNAS, Massachusetts Institute of Technology, and
M. B. WILSON and J. McHUGH, David W. Taylor Naval Ship R&D Center, U.S.A.

ABSTRACT

Results of an experimental investigation carried out in the 24-inch water tunnel at DTNSRDC to determine cavitating propeller-induced surface pressures and reference-area surface forces are presented. New apparatus for the measurement of the reference area surface force on a disc is described. Reciprocity calibration measurements have been carried out and the resulting pressure-to-acceleration transfer function has been used to estimate the blade rate harmonics of the cavity volume velocity. Tests have been run with a seven bladed propeller operating behind a screen generated simulation of a steep axial wake velocity distribution for a single screw ship. A computational procedure for the prediction of three-dimensional unsteady propeller cavitation developed at MIT is briefly reviewed. An extension to this theory to include the non-linear effect of the leading edge radius on the cavity solution is developed. Results are given for the propeller and wake field used in the experimental program. The inclusion of the leading edge radius is seen to reduce the extent of cavitaion, but its effect on the blade rate cavity volume velocity is found to depend on cavitation number. Comparison between measured and predicted cavity extents and cavity volume velocity harmonics shows a consistent trend.

NOMENCLATURE

A_m	Fourier cosine coefficient of the mth harmonic
a	Measured level of acceleration
$a(\rho_L;l)$	Leading edge correction factor
a_z	Vertical clearance between blade tip and nearby surface
B_m	Fourier sine coefficient of the mth harmonic
C_{th}	Thrust loading coefficient; $8K_T/\pi J^2$
D	Propeller diameter
$f(\eta;s)$	Weight function in 2-D cavity solution
$F(\eta)$	Auxiliary function in 2-D cavity solution
$\tilde{F}_S$	Unsteady force amplitude on hull or boundary element
$(F_S)_m$	Unsteady surface normal force amplitude on disc, m'th harmonic component
$h(x)$	Cavity thickness distribution
i	Complex number, $\sqrt{-1}$
J	Advance coefficient; V_A/nD
k	Constant in asymptotic behavior of $F(\eta)$
$(K_p)_m$	Pressure amplitude coefficient of mth harmonic; $(\Delta p)_m/\rho n^2 D^2$
$(K_F)_m$	Disc force amplitude coefficient of mth harmonic; $(F_S)_m/\rho n^2 D^4$
K_T	Propeller thrust coefficient; $T/\rho n^2 D^4$
l	Cavity length
m	Index for harmonic component, $m = \mu Z$
N	Propeller rate of revolution (RPM)
N	Number of vortex panels over the chord
N_c	Number of vortex panels within the cavity
n	Propeller rate of revolution (rps)
P_m	Total amplitude of mth harmonic of unsteady pressure
$\tilde{p}$	Unsteady fluid pressure
p_o	Fluid static pressure at propeller center
p_v	Vapor pressure of water
p_∞	Free-stream pressure
$q(x)$	Cavity source distribution
q_c	Magnitude of total velocity on cavity surface
Q_i	Discrete source in the i'th panel
r	The variable $(1+s^2)^{1/4}$ in 2-D cavity solution
s	Transformed cavity length in cavity solution
T	Propeller mean thrust force
t	Time
t_m	Blade section maximum thickness
u_c	Streamwise perturbation velocity on cavity surface
$u_w^\pm$	Streamwise perturbation velocity for wetted solution
U_∞	Free-stream velocity in 2-D cavity theory
V	Free-stream velocity
V_A	Speed of advance $V(1-w_T)$
V_X	Axial component of nominal wake
w_T	Wake fraction based on thrust identity
x	Chordwise coordinate for 2-D solution
x_{PC}	Longitudinal coordinate from propeller centerline, positive upstream
x_j^D	Control point coordinate–dynamic boundary condition
x_j^K	Control point coordinate–kinematic boundary condition
y	Transverse coordinate from propeller center, positive to starboard
z	Transformed x coordinate in 2-D cavity solution
Z	Number of propeller blades
α	Angle of attack
β_m	Harmonic phase angle of m'th component of disc force
$\gamma(x)$	Vorticity distribution on 2-D hydrofoil
$\gamma_w(x)$	Vorticity distribution for wetted solution
γ_m	Harmonic phase of angle of m'th component of pressure
Γ_i	Discrete vortex in the i'th panel
Δp	Unsteady pressure amplitude, general
$(\Delta p)_m$	Unsteady pressure amplitude–m'th component
$\Delta\xi_i^S$	Width of the i'th source panel
$\Delta\xi_i^V$	Width of the i'th vortex panel
$\Delta U(x)$	Chordwise velocity error function
$\Delta V(x)$	Normal velocity error function
η	Dummy z coordinate in 2-D cavity solution
$\eta(x)$	Hydrofoil mean line coordinate including angle of attack
θ	Position angle for wake velocity, measured positive counterclockwise from 12 o'clock, looking upstream
θ	Transformed x coordinate in 2-D numerical solution
μ	Index for harmonic component of blade rate $\mu = m/Z$
ξ	Dummy x coordinate in 2-D solution
ξ_i^S	Chordwise position of discrete source Q_i
ξ_i^V	Chordwise position of discrete vortex Γ_i

ρ	Fluid mass density
ρ_L	Leading edge radius
σ	Cavitation number in 2-D cavity flow; $(p_\infty - p_v)/1/2\rho U_\infty^2$
σ_L	Cavitation number obtained from linear cavity theory
σ_n	Cavitation number; $(p_o - p_v)/1/2\rho n^2 D^2$
σ_{V_A}	Cavitation number; $(p_o - p_v)/1/2\rho V_A{}^2$
$\tau(x)$	Hydrofoil thickness distribution
Φ_m	Spatial phase angle of m'th harmonic component of pressure
ϕ	Position angle measured clockwise from 12 o'clock looking upstream; ωt
ω	Circular frequency
$\dot{\nabla}_c/nR^3$	Cavity volume velocity coefficient

ABBREVIATIONS

DTNSRDC	David Taylor Naval Ship Research and Development Center
SSPA	(Statens Skeppsprovninganstalt) Maritime Research and Consulting, Goteborg Sweden
BR	Blade rate frequency
MARIN	Maritime Research Institute Netherlands
PUF-3	Propeller Unsteady Force (including cavitation) computer code developed at MIT

INTRODUCTION

Propeller-excitation has long been known as a major source of vibration and noise on ships. Problems arise in the form of excessive hull girder vibrations in the stern area and at the upper levels of deckhouses; unacceptable localized vibrations in important aft end spaces; fatigue damage to hull plating, internal stiffeners, appendages, or other structures near the propeller; high levels of inboard airborne noise; and general crew nuisance. Any one or all of these symptoms could lead to the imposition of speed restrictions, limitations on certain maneuvers, or avoidance of certain propeller RPM regimes. Understanding the hydrodynamic source of fluctuating forces and unsteady pressures is crucial for the eventual prediction of the magnitudes and spatial extent of the excitation. Thus an important aspect of the design of the propeller-hull arrangement, in addition to satisfactory steady propulsive performance, is the proper accounting for the propeller-induced unsteady forces, moments, and periodic hull pressure fluctuations.

There are two main categories of propeller excitation. Both are concerned with the interaction of the propeller blade elements operating in the nonuniform velocity wake inflow conditions. (1) Unsteady shaft-transmitted loads (bearing loads) are forces and moments developed on the propeller and transmitted to the hull through the thrust bearing foundation and reduction gearing system and the aftermost shaft bearing. (2) Unsteady hull surface loads or pressure-transmitted loads are forces and moments that arise from the spatially integrated effect of the fluctuating pressure field induced by the propeller blades passing through a varying inflow velocity pattern. The presence of intermittent blade cavitation causes further magnified pressure fluctuations due to the monopole behavior of the unsteady cavity volume. Under the worst conditions, periodic pressure pulses having nearly constant phase angle may act over a wide expanse of hull surface and on nearby appendages. In this situation, integrated surface forces of very substantial magnitude can be delivered to the hull. Presently, methods for prediction of the exciting loads are different for each of the categories. In the area of unsteady bearing loads prediction capability has been available for some time and it has been well integrated into the propeller design process in the U.S. Navy. The application of bearing load analyses to design has been rather successful because of the development of specific design modifications such as blade skew, warp, etc for reducing excessive unsteady blade loads.

Capability for the analytical prediction of unsteady pressure pulses and distributed surface forces, on the other hand, has just emerged. There is a vast and growing literature on this subject by now, largely stemming from work in the early 1970's after it became clear that unsteady variations of cavity volume in conjunction with large wake velocity gradients could significantly magnify the blade fanning pressures caused by a propeller operating near a boundary. A sampling of important references concerned with prediction of unsteady surface forces and/or periodic hull pressure amplitudes includes Huse (1972), Noordzij (1976), Vorus, et al (1978), Fitzsimmons (1979), Kaplan et al (1979), Hoshino (1982), Kaplan et al (1982), Breslin et al (1982), and Huse and Guoqiang (1982).

The U.S. Navy has been fortunate over many years to have relatively few experiences with the severe vibration and noise problems that can be attributed to surface force excitation. Typically, the merchant ship designs displaying problems (tankers, product carriers, Ro-Ro, ferries, LNG ships) have tended to exacerbate the difficulties because of high installed power (increasing dramatically through the late 1960's and 1970's) and restrictive propeller-hull arrangements, giving rise to steep and deep wake patterns. In contrast, the open stern arrangements of most Naval combatants and many auxiliary ships have wake distributions for which simple vertical tip clearance allowances, such as the values recommended by Navy customary practice, have generally been satisfactory.

Problems of excessive interior noise, early stage blade surface erosion, and heavy localized vibration encountered on the first of the class U.S. Navy Auxiliary Oiler AO-177 have been described by Wilson, et al (1982), and illustrate a case where the neglect of surface force excitation in the original design consideration led to an unsatisfactory mismatch of propeller and hull shape (wake). In this case, intermittent blade cavitation resulted in excessive unsteady pressure pulses over a wide area of the stern near the propeller and unstable cavity flow behavior near the blade tips and trailing edge (cloud cavitation). Among the many lessons learned from the experimental and analytical investigations carried out for the AO-177 project was the observation of how such subtle changes of the blade cavitation extent and appearance could produce improvements in the excitation magnitude. The hydrodynamics of the blade cavity behavior (thickness, total cavity volume variation, and interaction with tip vortex cavity) appeared to be crucial to understanding the magnitudes and character of these changes.

Experiments and analysis are both essential tools for providing fundamental understanding and practical estimates for determining propulsor-induced excitation magnitudes and the cavity flow conditions involved. Experiments are best used to uncover areas of weak fundamental physical understanding, provide crucial validation for prediction methods, and offer the safest practical assessment of final design configurations. Computational hydrodynamics is essential to the progress of accurate analysis in the difficult area of unsteady cavitating flow, and will provide the best means of systematic parametric studies.

The experimental portion of this paper was aimed at development of both test equipment and experimental skills for use in the water tunnels at DTNSRDC for the basic study of the excitation characteristics of unsteady cavitating propulsors and to provide a possible test bed for design assessments. The analysis portion of the paper has been directed at the incorporation of non-linear leading edge effects in the cavitating propeller analysis scheme developed over the past eight years at MIT. The resulting computer code, which is known as PUF-3, is starting to be used at DTNSRDC to assist in the evaluation of propeller designs. The current efforts to improve the capability of the PUF-3 scheme has been motivated by the importance of the details of blade sheet cavity dynamics to determine the exciting pressures and forces produced by a propeller operating near a ship hull.

BACKGROUND

Model experiments are very important to the study of propeller-excitation characteristics that can give rise to ship vibration and inboard noise. Many of the significant milestones in our understanding of the phenomena involved and in the estimation of unsteady loadings for full scale designs of propellers and shafting systems have been achieved through model testing in a variety of experimental facilities.

Full scale experiments are also essential for correlations with model results, for observing flow features, and for crucial data on important measured ship responses such as localized and girder vibration and inboard noise.

CHARACTERIZING EXCITATION

If we confine our attention to the category of surface pressure/surface force and moment excitation, we can characterize the propeller exciting magnitudes by considering several main features.

Fluctuating pressure amplitudes

There is a rotating pressure field associated with the operation of a propeller. Figure 1 is a sketch of this pressure disturbance frozen at an instant in time and it shows a definition of the spatial phase angle Φ_Z measured to the reference line of the blade from the surface point just as the positive peak of the blade rate pressure passes. The amplitude on the surface will appear to fluctuate in time with the blade passing frequency and multiples of that frequency. The surface pressure pulse can reach up to twice the free space magnitude because of reflection effect from the boundary. Point pressure measurements on a nearby hull surface or on appendages of a ship or a model can be obtained experimentally with flush mounted pressure transducers, and provide some picture of the pressure loads delivered to the hull. A single point pressure measurement (over the tip of the propeller at the closest distance to the hull) is sometimes taken as the sole indicator of the magnitude of the surface force excitation. Such a value is certainly interesting for comparisons, but it is generally insufficient to characterize a representative surface force magnitude that would be useful to estimate, for instance, the hull girder vibration response. On the other hand, the distribution of point pressures over a region of hull surface may well be used for the loading excitation for structural vibration predictions. In any case, point pressure pulses should be obtained at several locations forward and aft of the propeller plane and laterally off centerline to have an idea of the character and extent of the loading.

Some examples of measured propeller- induced pressure pulse distributions are provided by Denny (1967), on the model scale and by Taniguchi and Ohtaka (1963), for a full scale destroyer.

Reference-area surface force amplitudes

The periodic surface force experienced by a patch of area of the nearby hull boundary represents a net or integrated effect of the distributed pressure pulses exerted on the surface. Such a quantity can be obtained experimentally with an instrumented surface segment (See for example, Kerwin, et al (1978)), or by integrating measured point pressures over the desired area, accounting for the spatial and temporal (phase angle) variations. A manageable size of the reference area might be on the order of the propeller disc area.

Surface force density

The longitudinal distribution of the induced surface force-per-unit length is called force density. It is a convenient way to represent the fluctuating loading imposed on the hull girder, especially in relation to excitation of overall girder vibration. It cannot be determined by direct measurement, but can be approximated by performing girthwise integration of measured point pressures resolved as vertical or other force components at each section down the length of the hull shape. It is noted here because it is especially useful for displaying the rate of change of exciting surface force as a function of distance in the vicinity of the propeller, and away from it as well.

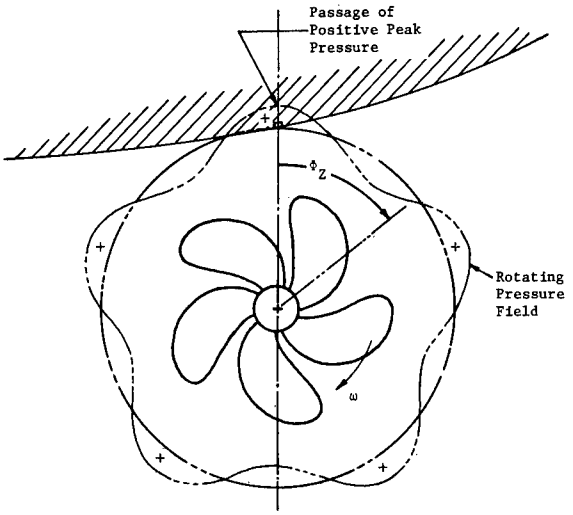


Figure 1 - Definition Sketch of Rotating Pressure field Near an Operating Propeller

Net surface force amplitude

In principle, the total integrated or net surface force amplitudes induced by the propeller can be determined approximately from area integrations of measured point pressure amplitudes. There has never been a direct model experimental measurement made of the total induced vertical surface force (separated from any moment effects), and none accomplished on a full scale ship. The net force magnitude, at various blade rate harmonics, would represent the most condensed parameter for measuring excitation level important to girder vibration, although of less importance to inboard noise. The net vertical force is not likely to act exactly at the propeller plane location because of asymmetries in the longitudinal distribution of force density.

Example discussions of vertical surface force values obtained either from distribution of measured pressure amplitudes or by calculation using computed distributions of pressure pulses can be found in references by Hylarides (1978), Skaar and Raestad (1979), and Huse (1982). Recommendations on the levels of vertical force ratio (total surface force-to-mean propeller thrust) that could cause hull girder vibration problems could be inferred from each of these references, but there is no agreement among them. Recommended ratios for the critical value of surface force-to-thrust ratio for the onset of unacceptable vibration excitation seem to range from about 7 percent to 30 percent. Occasionally values well above 100 percent have been predicted with no report of excessive ship vibration on the ship itself. There is considerable need for improvement on how to interpret and use estimated values of net surface force amplitude

Cavity volume pulsation strength

For a propeller operating with intermittent blade cavitation in a nonuniform flow, the resultant pressure amplitudes are typically cally increased noticeably over noncavitating levels. The increase is relatively even greater for the corresponding amplitudes of, say, the vertical surface force density or the total surface force because they are area- integrated quantities of pressure fluctuations having nearly constant phase angles everywhere . The dominating

feature is the monopole-like pressure source behavior of the fluctuating cavity volume of each blade sheet cavity. Although the primary characteristic of a typical sheet cavity volume variation is similar to that of a pulsating spherical bubble (Breslin et al (1982)), there are contributions from cavitating tip vortices (Weitendorf (1977)), and possibly significant contributions from bulging tip vortices (English (1979)). The term cavity volume variation refers to the total volume within the blade cavities plotted as a function of the circumferential position angle.

A useful representation of the main physical mechanism involved with exciting pressures from cavity pulsation is given in a simple expression for the pressure fluctuation produced at a distance r from the center of a pulsating spherical bubble

$$\Delta p = \frac{\rho}{4\pi r}\frac{d^2\nabla_c}{dt^2} \tag{1}$$

where the cavity volume variation is given by $\nabla_c(t)$. This shows that the spatial rate of decay of the induced pressure amplitude is r^{-1} and that the pulsation strength is proportional to the cavity volume acceleration $\ddot{\nabla}_c$ (or $\omega\dot{\nabla}_c$ for harmonic variations). This spatial variation is also approximately valid for non-spherical pulsating bubbles at relatively large distances. An important difficulty in making use of this type of relationship is obtaining accurate determination of the cavity volume variation, either by analytical prediction or by experiment.

It is possible to determine cavity volume pulsation strength experimentally by an indirect means involving the concept of reciprocal measurements. From the reciprocity principle for linear dynamic systems, a simplified expression is available (see Appendix) to cover the case of the unsteady force on a body or a body surface element fixed in position relative to a fluctuating point source. Then, in a water tunnel or full scale test environment, the "volume velocity" of a fluctuating blade sheet cavity can be approximated by

$$\dot{\nabla}_c = \frac{F_2}{i\omega(p_1/a_2)} \tag{2}$$

where $\dot{\nabla}_c$ is the time rate of change of cavity volume, F_2 is the harmonic amplitude of the measured unsteady force on a body or body element at circular frequency ω, (p_1/a_2) is the transfer function which is defined as the measured ratio of the pressure amplitude at the propeller location to the acceleration amplitude at the body, and $i = \sqrt{(-1)}$.

All the quantities in this formula except ω are regarded as complex. A discussion of this expression and related forms is given in Appendix A.

To implement the reciprocity technique, there are two phases of measurements. During the calibration phase, the body element is forced to oscillate through a range of frequencies of interest. The transfer function ratio (p_1/a_2) is formed for each frequency from the simultaneous measurement of the pressure p_1 measured at a position in the fluid representing the approximate center of cavitation and the vertical acceleration a_2 of the forcing body element. The final measurement phase is run with excitation from the cavitating propeller. Then once the cavitation-dependent component of the vertical surface force blade rate amplitude $(F_s)_Z$ on the body element is determined, the resulting blade rate component of volume velocity can be evaluated from the expression given above.

REVIEW OF EXPERIMENTS

It is useful to outline the scope of some example model experimental investigations that have been used to explore various features of propeller-induced surface pressure/surface force excitation.

Early Experiments on Exciting Loads and Induced Pressures

The earliest work that showed an appreciation of the presence of propeller-induced surface forces in addition to the bearing loads was that of Lewis (1935, 1936). An experimental scheme was devised for testing rigid ship models in a towing basin, where the model vibration response was used to determine the exciting forces under self-propelled conditions by comparing the response to that produced by a calibration vibration exciter located in the stern that delivered known oscillating force levels. Lewis was able to decide that the major contribution to the measured propeller-induced effective vertical force on the hull, for example, was due to the surface force. Similar measurements were made on a model of a cargo ship form and reported by Lewis and Tachmindji (1954). Continuing with an improved rigid model approach, but with smaller models, Lewis presented a summary of results of such experiments for several different examples (1969). Unsteady blade cavitation played no role in these model basin studies, and was not suspected as being important until many years later.

An experimental program to measure the aft end vibratory surface loads and inferred bearing loads was presented by Stuntz, et al (1960). In this case, the stern end of the ship model was mounted on flexures and instrumented to measure the vertical, horizon tal, and torsional unsteady loads induced by the operating propeller as tested in a towing basin. No conditions involving intermittent blade cavitation could be considered.

Early experiments conducted in water to measure the periodic pressure disturbances ahead of, behind, and beside an operating propeller have been presented in reports by Tachmindji and Dickerson (1957 a, b) on the free space pressure pulses near a propeller running in uniform flow and behind a strut; by Pohl (1960) on the fluctuating pressures induced on a flat plate surface mounted parallel to the propeller axis in a water channel and on the pressure pulses acting on the hull surface of a model ship in a towing basin; by Taniguchi (1958) on the pressures induced on a flat plate; and by Weitendorf (1970) on the variations of fluctuating pressures induced on flat and concave curved plates at various tip clearance ratios, on pressure pulses on flat plates with various elastic mountings, and on pressure pulses at locations near the propeller on the hull surface of surface ship models. All these early tests involved non-cavitating flow conditions. Experiments by Nelka (1974) also concerned with the induced pressure amplitudes on a flat plate boundary near a propeller and showed the effects of tip clearance ratio with a series of propellers with increasing blade skew angles and blade warp angles and the effect of nonuniform inflow velocity pattern.

Examples of complete ship model experimental results obtained in towing basin tests for propeller-induced vibratory pressure amplitudes on the hull surface near the propeller have been reported by Keil (1965) for an oceanographic ship; by Huse (1968) for a tanker form; by Weitendorf (1970) for semi- tunnel stern combatant form; and by Jacobs, et al (1972) for a destroyer hull form. All these have been conducted with nonuniform inflows, but noncavitating conditions, so that crucial interaction between nonuniform inflow and intermittent cavity volume variation is missing in each of these investigations.

Experiments with Cavitating Propellers and Modelled Wake Inflow

Simple Boundary Arrangements . Early water tunnel experiments were carried out by Denny (1967) who made extensive measurements of the propeller-induced periodic pressure amplitudes on a flat plate boundary. A number of important effects were studied, including tip clearance ratio, propeller loading, nonuniform inflow, propeller geometry (expanded area ratio and blade skew angle), and cavitation in uniform flow. Extensive comparisons were made with theoretical predictions available at the time, and these were used to check the separate contributions of

loading and thickness. It is interesting that Denny was the first to note that blade cavitation served to accentuate the magnitudes of the induced pressure pulses in the case of uniform inflow and extensive sheet cavitation. The increases of pressure pulse level in the steady cavitating flow were comparable to the increases caused by noncavitating operation in certain of the wake patterns tested. However, the crucial combination of nonuniform flow with blade sheet cavitation was not included by Denny, so the important influence of intermittent blade cavitation was not revealed in these experiments.

The pivotal paper by Takahashi and Ueda (1969) describes measurements of propeller- induced pressure amplitudes on a flat plate in both noncavitating and cavitating conditions and in both uniform and nonuniform wake flow. It is this work that is often credited with first providing the experimental motivation of the connection between intermittent blade cavitation and exaggerated pressure pulses that arise in operation in nonuniform flow.

Other water tunnel experiments concerned with distributions of fluctuating pressure amplitudes induced on a flat plate boundary by a cavitating model propeller in nonuniform flow have been carried out and reported by Weitendorf (1973 a, b), Takahashi (1975), Chiba and Hoshino (1976), Sasajima (1982), Takekuma (1979), Okamoto and Kasahara (1986) and Weitendorf (1977) who provides a summary discussion of a number of different effects.

Water tunnel experiments involving measurement of the localized propeller-induced excitation levels on somewhat more complicated boundaries have been carried out, for example, by Nelka (1974) on the pressure pulses produced on the inside surface of a duct of a ducted propeller system, and by Peck (1974) on the pressure pulses at points on the centerline of a tunnel enclosing 65 percent of the diameter of two different propellers. Lewis and Kerwin(1978) and Kerwin, et al (1978) presented results on the levels of propeller-excited unsteady normal surface force measured on a flat force disc imbedded flush with a flat boundary.

Partial Stern (Dummy Model) Experiments . The use of foreshortened ship hull-models, often termed dummy models, in variable pressure water tunnel experiments with operating propellers has long provided a practical approach to the problem of attempting to model the proper three dimensional wake velocity patterns for model propeller cavitation tests. Since the early 1970's, dummy models have also been used in many laboratories around the world to try to survey the propeller-induced periodic pressures at points near the propeller , with approximate representation of the wake velocities, hull boundary shape, and cavitation number environment.

Some early published investigations using foreshortened hull models in the determination of cavitating propeller-induced pressure pulses include van Manen (1972), Huse (1971), van Oossanen and van der Kooij (1973). and van der Kooij and Jonk (1974). Examples of more recent publications that have either made use of results from dummy model tests or mention this test technique in some fashion are Hylarides (1978), Glover et al (1979),Glover and Patience (1979), Lover and Wills (1979), Chiba, et al (1980), Reed, et al (1981), Lovik (1981), Munk, et al (1982), and Hadler, et al (1984).

Useful and informative work on the test techniques and interpretive problems of dummy model testing in water tunnels has been reported on by English (1979) and by Larsen (1982).

Complete Model Experiments . Because of the importance of the wake velocity pattern to the correct modelling of the intermittent blade cavitation, the idea of using complete ship hull models for cavitation experiments is very appealing. The idea is that, at least on the model scale, the correct wake pattern is represented closely by using the geometrically scaled hull form. There are two prominent facilities actively used for research and engineering assessments of ship propulsion systems using complete ship hull models: the MARIN Depressurized Towing Tank in Wageningen Netherlands, which provides for the simultaneous satisfaction of the Froude number and the cavitation number; and the large cavitation tunnel (Tunnel No.2) at SSPA in Sweden which provides no free surface boundary at the model waterline, but employs typical free stream velocities that lead to relatively high model blade Reynolds numbers. Good summaries of some experimental results and discussions of testing techniques, data analyses, and comparison studies are given by van der Kooij (1979) on the Depressurized Towing Tank, by Lindgren and Bjärne (1980) On the large cavitation tunnel at SSPA, and by Dyne and Hoekstra (1976) on comparisons of results between the two.

Reciprocity Experiments . Application of a simplified form of the reciprocity principle to shipboard measurement of the propeller source strength (volume velocity) was developed in Steenhoek and Ten Wolde (1970) and Ten Wolde and de Bruijn (1975) with particular reference to the problem of inboard noise transmitted by means of ship structure vibration excited by the propeller. The basic ideas for this approach are discussed in the Appendix. Gray (1981) has also demonstrated the use of the reciprocity concept in determining the source strength of cavity pulsation and the estimate of oscillating hull pressure amplitudes on full scale ships. Van der Kooij (1979) has indicated that the same ideas have been used to measure the model scale cavity source strength from model tests in the MARIN Depressurized Towing Basin.

Vorus in a discussion of a paper given by Kerwin, et al (1978) proposed an experimental/analytical method for estimating the unsteady force on a body (any shape) located near a fluctuating point source by exploiting the results of a reciprocity experiment conducted with very simple model geometry in a water tunnel. This suggestion was subsequently followed by experiments carried out with the instrumented force disc described by Kerwin, et al (1978) using a model of a destroyer propeller. The calibration experiment to determine the acceleration-to- pressure transfer function is described by Whalen, et al (1982 a). Description of the wake simulation tests and results of the measurement of the disc force amplitude leading to the determination of cavity volume velocity are presented by Whalen, et al (1982 b). Application of these results to determine the effect of blade tip clearance on the propeller-induced vertical hull surface force for the tested propeller has been summarized by Vorus (1984).

An attempt to exploit a more complete statement of the reciprocity principle has been carried out by des Moutis (1981) in the M.I.T. water tunnel for the experimental determination of cavity volume velocity as well as the six unsteady propeller bearing force and moment amplitudes.

APPARATUS AND INSTRUMENTATION

FACILITY

The particular experimental equipment developed for this work was designed for use in the 24-inch Variable Pressure Water Tunnel at DTNSRDC. This facility provides the basic propeller dynamometry, adjustable ambient tunnel pressure to simulate cavitating flow conditions, and an access chamber on the top side of the open jet section which provides space for the force measuring apparatus.

Mounting Plate and Instrumentation

A one-inch thick, aluminum flat plate insert was positioned horizontally and parallel to the axis of the open jet test section of the water tunnel. This functioned as the representative boundary surface for the initial experiments. With the propeller installed along the tunnel centerline on the downstream shaft, the vertical position of the plate can be varied from 7.5 in.(19.1 cm) to 9.0 in.(22.9 cm) from the centerline to provide vertical tip clearances in the range of $a_z/D = 0.25$ to 0.4 for a nominal 10 in.(25.4 cm) diameter propeller. The upstream end of the plate was faired into the tunnel convergence with a flexible nylon sheet joining the

plate to a nose piece fastened to the tunnel wall. This allowed a simple adjustment of the vertical position of the plate boundary.

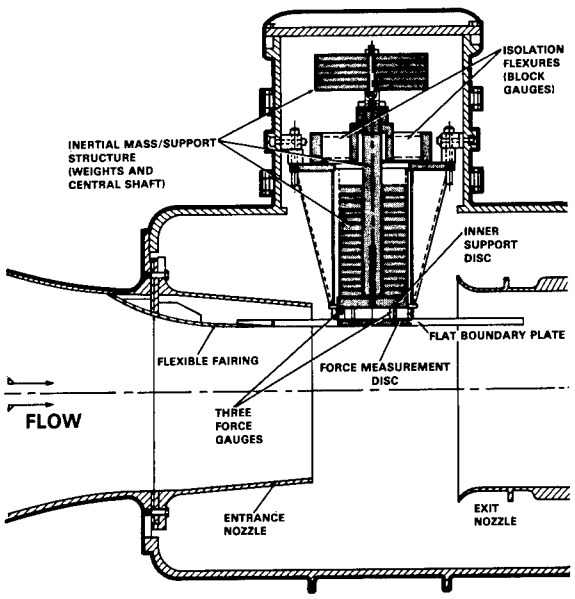


Figure 2 - Schematic of Force Measuring Device Installed in the 24-Inch Water Tunnel Open Jet Test Section

Force Measuring Apparatus

The surface force measuring device is shown in the sketch of Figure 2. It consists of an instrumented force disc connected to a robust inner plate and backup support structure . The entire support system is connected to the water tunnel structure through the flexures of two block gauges.

The force disc itself is a circular aluminum plate with a diameter of 10 in. (25.4 cm) and thickness of 1 in.(2.54 cm) mounted flush with the flat plate boundary. An O-ring was fitted in the gap between the disc and the hole in the mounting plate. The disc is attached to the inner support plate by a tripod arrangement of three piezoelectric force gauges. The particular force gauge (Wilcoxon Model L10) was chosen because it satisfies several important requirements: (a) accurate measurement of oscillatory force levels with amplitudes expected in the range of 5×10^{-2} to 5 lb (0.22 to 22 N) in a frequency range possibly up to 1500 Hz, (b) large value of effective spring stiffness constant, and (c) capability of being driven electrically in a reverse mode in order to be used as a force excitor by placing an oscillatory voltage signal at the input.

Various masses and support stiffnesses of the elements of the force measuring device were chosen to obtain a flat dynamic response characteristic of the force disc in the range of frequency covering the first three harmonics of the blade rate. The force disc mass plus its added mass is about 1 slug (14.6 kg) mounted on the force gauges having a combined spring stiffness of 15×10^6 lb/in.(26.3×10^6 N/cm). The massive support structure includes two stacks of weights and was sized to provide a large inertial mass of about 550 lb (17.1 slug or 249 kg) suspended on the flexures having an effective stiffness of 1×10^5 lb/in. (1.75×10^5 N/cm). The system was designed to accommodate the exciting frequency range of 50 Hz to 650 Hz which brackets the range of the first three blade rate harmonics for any model propellers of interest, operating at the necessary rates of rotation ($14 \leq n \leq 25$ rps).

The force disc could be instrumented with as many as three accelerometers mounted on the top side in order to measure the vertical vibration levels of the disc either during various calibrations or during an excitation experiment with a propeller running in the tunnel. Waterproofing of the accelerometers and all the force gauges was provided by coating them with standard potting material .

Surface Pressures

Mounting holes for flush-mounted pressure gauges were arranged in the pattern shown in Figure 3 in the flat mounting plate and the force disc. There are 52 positions on the flat plate and 13 on the force disc. These provide the possibility of obtaining a comprehensive picture of the distribution of surface pressure amplitudes at points within a rectangle of dimension 1.1D by 2D in the vicinity of the propeller, for a normal 10-inch (25.4 cm) diameter. Special threaded adaptor fittings permitted the use of either of the two different types of pressure gauges available for the experiments. The expected range of maximum fluctuating pressure amplitude at points closest to the tip at the blade rate frequency or any of its higher multiples was on the order of ±1 psi (±6.9 kPa). The two types of gages used were Kulite XTM-190 and the CEC 4-312, with nominal operating ranges of ±10 psi (±69 kPa) and ±25 psi (±172 kPa), respectively. Both gauges are of the strain gauged diaphragm type.

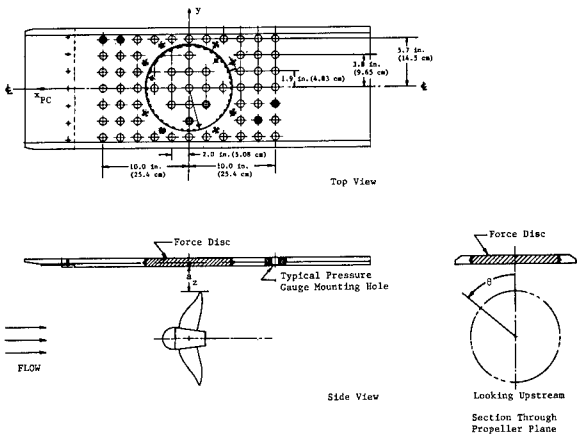


Figure 3 - Flat Plate Boundary, Force Disc, and Pressure Gauge Locations

CALIBRATIONS

The pressure gauges were calibrated in a static pressure test stand to determine the sensitivity (slope = pressure/volt) for each gauge. These slopes were also checked at intervals throughout the experimental program, using tunnel pressure.

Extensive calibrations were performed on the surface force measuring device in order to establish its characteristics as an unsteady dynamometer and for its application in a reciprocity experiment.

It was necessary to establish the correct force slope factors for the three force gauges and to determine the frequency response characteristic for the force disc. An unsteady force was applied to the disc by means of an electrodynamic shaker. The force applied to the disc was measured independently with a precalibrated piezoelectric force gauge. For the case of the tunnel full of water and with the O-ring in place around the edge of the disc, the measured dynamic response is shown in Figure 4, displaying the ratio force output-to-force input plotted versus frequency of excitation. The frequency response curve is essentially flat to around 650 Hz where it begins to rise toward a natural resonance frequency at

930 Hz. This indicates that the desired level response characteristic holds satisfactorily out to frequencies well beyond the third blade rate harmonic for model propellers with as many as seven blades. The flat force response also permitted the final determination of the calibration slopes for the three piezoelectric force gauges with the fully assembled dynamometer .

The second major function of the force disc apparatus is to provide the possibility of determining the characteristic cavity volume variation of a cavitating propeller in nonuniform inflow by means of the indirect method exploiting the reciprocity principle. To make this type of measurement it is necessary first to perform a reciprocity calibration which determines the transfer function relating the fluid pressure response at a field point to the magnitude of vertical vibration of the surface area element (force disc). The reciprocity calibration was carried out by oscillating the force disc vertically along its axis (normal to the surface) by means of a sinusoidally varying voltage placed across the three piezoelectric force gauges which support the disc. This effectively drove the force gauges in a reverse mode so that the disc was itself the electrodynamic shaker for the calibration phase. Excitation frequency covered a wide range from about 70 Hz to 1000 Hz in order to include the frequency variation up to the third harmonic of blade rate. The vertical acceleration of the disc was measured with accelerometers mounted on the back side of the disc. Pressure response in the fluid was measured in the absence of the propeller using a hydrophone located at a point in the 12 o'clock position at a distance 0.9R from the axis. This location corresponds roughly to the expected center of the largest blade cavity volume determined from visual observation .

The resulting calibrated transfer function is shown in Figure 5 as the curve of the logarithm of the ratio of pressure amplitude to vertical acceleration (p/a) plotted versus frequency. There is a variation with frequency apparent in this empirical function, with a local peak occurring at around 500 Hz, and a relative flattening beyond 800 Hz.

For frequencies below 300 Hz the measured values of the transfer function for (p/a) were found to display a variability. Since the reciprocity calibration was obtained from a long analog tape record of the simultaneous measurement of fluid pressure and disc acceleration taken during the same calibration session, several values of (p/a) at a given frequency could be calculated from several different segments of the tape. For the data displayed, each segment consisted of a frequency sweep through the range of interest. This provides a check on repeatability and shows that the values of (p/a) were reliably repeatable for the frequency regime higher than 300 Hz. Below 300 Hz, however, there was a range of values computed for (p/a) at any one frequency, indicating an increased level of uncertainty. In Figure 5, the shaded region shows the range of values of the transfer function computed from several different segments of the measured record.

At this time, there is no conclusive explanation for the variability of the measures transfer function in the low frequency range. One possibility is that under unsteady excitation, there are pressure reflections from structural elements inside the tunnel and test section, such as the nozzles or the installed flat plate. There could be interferring unsteady pressures set up by induced vibrations of the tunnel walls and model structure. A likely contributor to the problem could be poor signal-to-noise ratio for the pressure response to the disc oscillation . This is expected to be worse at the low frequencies because of the very small acceleration levels being produced by the mechanical system in the frequency range involved. It is not likely that the variability of the (p/a) ratio is attributable to changing local properties such as temperature or ambient pressure, because the time scales of these changes are much longer than characteristic time involved with the changes of the transfer function magnitude. This problem requires further study.

For the model propeller experiments reported on here, the blade rate frequency at the convenient operating speed was 98 Hz. At this frequency, the variability of the (p/a) involves a range of about ±34 percent.

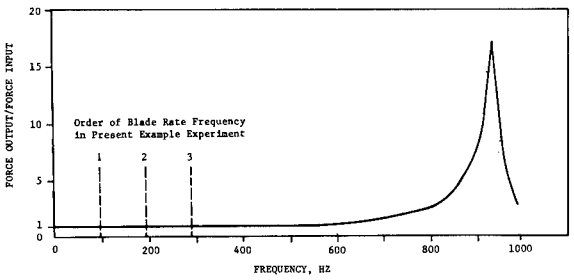


Figure 4 - Calibrated Dynamic Response Curve for Force Measuring Device

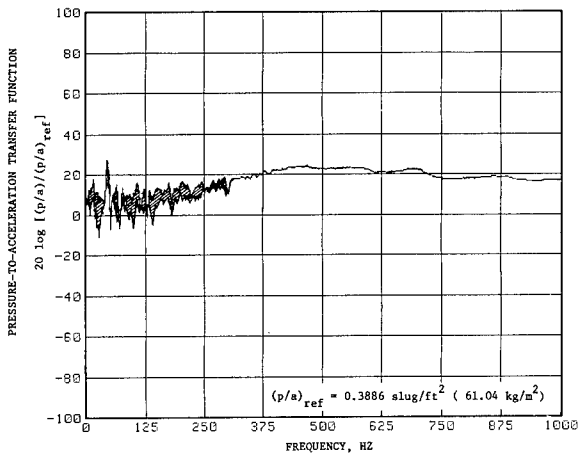


Figure 5 - Reciprocity Calibration for the Driven Force Disc: Pressure-to-Acceleration Transfer Function versus Frequency for the case $a_Z/D = 0.26$

EXCITATION EXPERIMENTS WITH MODEL PROPELLER

PROPELLER

For comparison purposes, it was decided to use the 9.812-in (24.92 cm) diameter DTNSRDC model propeller number 4677 which represents the 21-ft, seven-bladed, skewed propeller for the single screw Naval Auxiliary Oiler AO-177 with the scale ratio 25.682. The wake adapted design of this propeller is described by Valentine and Chase (1976). The particulars of the propeller geometry may be found in Wilson,et al(1982). Drawings of the blade shape are given in Figure 6. Figure 7 shows the propeller open water characteristics presented by Hendrican and Remmers (1976). Appropriate operating conditions for the propeller were selected on the basis of the model powering experiments reported by Hendrican and Remmers (1976).

EXPERIMENTAL PROCEDURE

Wake Simulation

All the experiments shown here were carried out in a non-uniform flow in the tunnel produced by a wake screen which provides for control of the axial velocity component only. The wake screen was designed to simulate the nominal wake distribution V_X/V produced by the AO-177 as determined from a towing basin wake

survey with a scaled model of the ship hull. Wake surveys were conducted in the tunnel with the screen-generated flow using a rake of five, 5-hole spherically-headed pitot tubes. The flat plate boundary was set at two locations corresponding to propeller tip clearances of $a_z/D = 0.26$ and 0.41 . Figures 8, 9, and 10 are example comparisons of the measured axial velocity ratio V_X/V versus θ for r/R = 0.557, 0.774, and 1.178 respectively, showing data obtained from a towing basin wake survey Hampton (1981) and Wilson and Hampton (1981), and the tunnel wake surveys. Definition of the position angle θ is given in Figure 3. These comparisons show that the V_X/V flow patterns behind the wake screen for the two different plate locations are generally similar to the target nominal velocity distributions, but are not identical. One noticeable feature is that there are differences in the level of the V_X/V values when the position angle θ is outside the main velocity defect region (which is contained inside $-90° < \theta < 90°$) . The relatively higher values for the case $a_z/D = 0.26$ are attributable to relatively increased average flow velocity caused by the smaller flow cross section area. This speed-up influence is less pronounced for the case of $a_z/D = 0.41$, because the flow area blockage is less. The narrow velocity defect from the lower skeg region, centered about the position angle $\theta = 180°$, and seen clearly in the towing basin velocity distribution, was not reproduced in the wake screen velocity pattern. The skeg wake velocity feature in this case is much less important than the main hull wake characteristic because there is no known blade cavitation that occurs in that region. For this reason, dense screen material was not applied along the centerline of the lower disc area of the wake screen used for the present experiments.

There are important similarities between the wake screen velocity patterns and the towing basin velocity distributions (the target wake). The values of the minimum V_X/V ratio in the vicinity of θ are nearly the same in the two wake screen distributions as in the target wake, although the precise angular positions may be offset somewhat for the wake screen cases. More importantly, the relative slopes of the main velocity defect with respect to the circumferential angle, denoted by $d(V_X/V)/d\theta$, are approximately the same for the target distribution and the wake screen distributions along the rays, say $\theta = 40°$ and $\theta = 320°$. These similarities are concerned with features of the wake that are most important to the production of unsteady pressures due to cavity volume variation, as noted, for instance in Odabasi and Fitzsimmons (1978). It is concluded that propeller blade cavities should reach approximately the same size at about the same circumferential position, and should grow and diminish at about the same rate in either of the two wake screen velocity patterns as in the towing basin velocity distribution. Since the dominant contribution to the propeller unsteady pressures and surface force comes from the unsteady cavity volume variation, experiments in the wake screen velocity patterns described above could be expected to provide excitation characteristics generally meaningful to the case of the AO-177 propeller and wake combination.

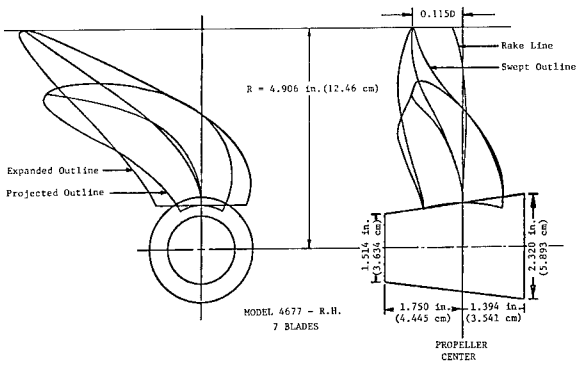


Figure 6 - Drawings of Propeller Model 4677

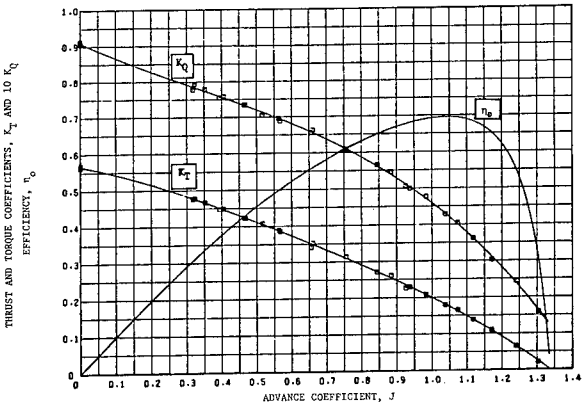


Figure 7 - Open Water Characteristics of Propeller Model 4677

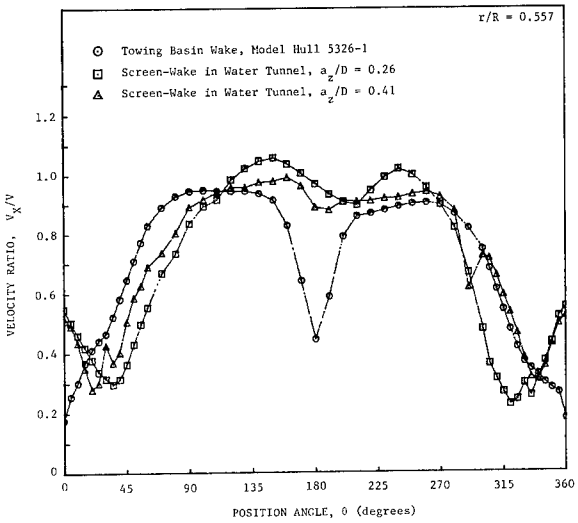


Figure 8 - Comparisons of Measured Axial Velocity Ratios at $r/R = 0.557$

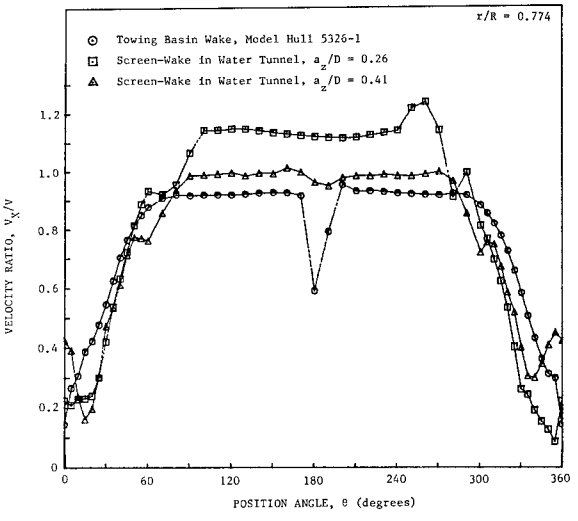


Figure 9 - Comparisons of Measured Axial Velocity Ratios at $r/R = 0.774$

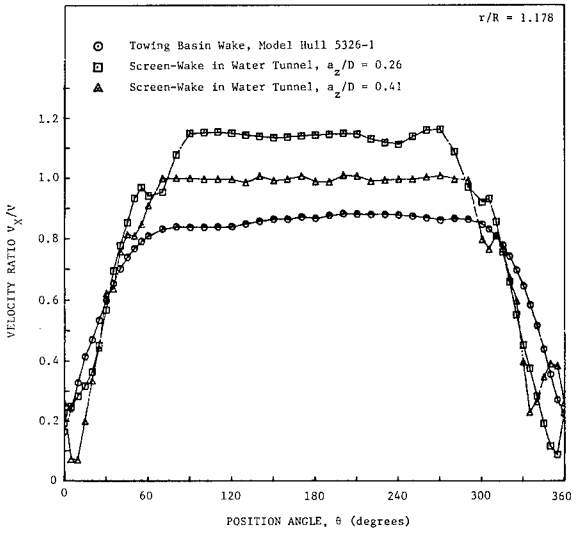


Figure 10 - Circumferential Distribution of Axial Wake Velocity Ratio, Comparison of Measurements in Water Tunnel and Towing Basin at $r/R = 1.178$

Unsteady Pressures and Disc Surface Force

Measurements have been carried out in the 24-inch water tunnel using the newly developed apparatus and propeller Model 4677. The propeller was mounted on the downstream shaft, with the boundary plate arranged parallel to the axis. Pressure gauge measurements were taken at 11 of the locations on the disc and at many locations on the surrounding boundary plane, concentrating on the points along the longitudinal and transverse centerlines (x_{PC} and y axes, respectively) as depicted in Figure 3. The propeller reference center identified in Figure 6 was placed at the longitudinal position of the transverse axis, $x_{PC} = 0$. Thus, the location of a plane through the blade tips was at a distance 0.1l5D downstream of the $x_{PC} = 0$ position.

Unsteady disc force measurements were made with the three piezoelectric force gauges in place, and in some cases, simultaneously with pressure gauge measurements.

All the experiments conducted for this work were performed at the loading condition corresponding to the advance coefficient J = 0.79 and thrust coefficient $K_T = 0.295$, producing a thrust coefficient of $C_{Th} = 1.2$. Test section velocity was set for the target J by using the thrust identity method from the open-water characteristics. This was accomplished by setting the shaft rotation speed for the desired advance coefficient and adjusting the tunnel water speed until the thrust coefficient matched the open-water thrust coefficient. The velocity calibrated in this way was held constant and the tunnel pressure varied to change the cavitation number. Shaft rotation speed was maintained at 14 rps for all the conditions tested. The Reynolds number based on chordlength at the 0.7R and the approximate total velocity was 0.51×10^6 .

The range of cavitation numbers included $\sigma_n = 17.86 \rightarrow 8.36$ ($\sigma_{VA} = 28.6 \rightarrow 13.4$) which covered non-cavitating reference conditions as well as conditions with mixed tip vortex and sheet cavitation characteristic for this propeller. The minimum cavitation number used here was limited by a tunnel flow speed that would not damage the wake screen. With the loading conditions held the same throughout the range of σ_n , the effects of different blade cavitation patterns on the unsteady pressures and disc force could be studied independent of the propeller loading condition.

Total air content of the tunnel water, measured with a Van Slyke apparatus, was held in the range of 24 to 35 percent of saturation at atmospheric pressure, mainly to provide clear visibility. Water temperature varied from 69° to 74° F (20.6° to 23.3° C).

Measurements of both the pressure fluctuations and disc unsteady force were obtained with the flat plate boundary positioned at two different locations corresponding to propeller tip clearance ratios $a_z/D = 0.26$ and 0.41 . The vertical tip clearance ratio on the AO-177 ship is $a_z/D = 0.292$.

The test procedure consisted of recording the pressure and force transducer signals for several minutes at a particular cavitation number, with the simultaneous recording of the data onto magnetic tape. Throughout most of the test conditions, the pressure and force signals were checked online with a time series analyzer to review the character of the pressure and force spectra and the relative contributions at the blade rate frequency and its higher harmonics. Taped pressure and force gauge records consisted of a recorded digitized signal of 256 points around each shaft rotation as triggered from a shaft encoder attached to the propeller shaft. A timing channel, recorded simultaneously with the pressure and force signals, provided a single pulse per shaft rotation that was arranged to indicate the passage of a blade reference line past the 12 o'clock position (point of closest approach to the flat boundary). It was used for the measured phase analysis.

After the recording sessions, the data were analyzed using a Model 70 Interdata computer to provide the Fourier Series harmonic components over a convenient specified time interval, usually 10 seconds. Thus a typical analysis record for these experiments covered 140 propeller revolutions.

It was clear from the harmonic analysis and from the time series analyzer spectra that the signals of the surface pressures and disc force were dominated by the blade rate frequency. Amplitudes of higher multiples of blade rate were always smaller than the blade rate itself, but not necessarily with magnitude decreasing strictly with increasing harmonic order.

Data Analysis

The unsteady behavior of the pressure measured at any location is a periodic fluctuation p(t) and can be represented by the Fourier series,

$$\tilde{p}(t) = \sum_{m=1}^{\infty} (A_m \cos m\omega t + B_m \sin m\omega t) \qquad (3)$$

which can also be written in a form to display total amplitude and phase angle as follows,

$$\tilde{p}(t) = \sum_{m=1}^{\infty} P_m \sin(m\phi - \gamma_m) \qquad (4)$$

where

$\phi = \omega t$ = position angle taken positive clockwise from 12 o'clock, looking upstream

$\omega = 2\pi n$ = shaft circular frequency

$P_m = (A_m^2 + B_m^2)^{1/2}$ = total amplitude of the mth harmonic component of the pressure fluctuation

$\gamma_m = \tan^{-1}(-A_m/B_m)$ = harmonic phase angle of the mth pressure harmonic

The positive peak (maximum positive value) of the mth harmonic component of pressure fluctuation occurs when

$$m\phi - \gamma_m = \frac{\pi}{2} \qquad (5)$$

Thus the spatial phase angle at which, say, the Zth or blade rate harmonic of pressure reaches a maximum positive value is

$$\Phi_Z = \left(\frac{\gamma_Z + \frac{\pi}{2}}{Z}\right) \qquad (6)$$

This phase angle is the angular location of the blade reference line when the blade rate pressure positive peak occurs, measured clockwise looking upstream (see Figure 1).

The amplitude of the mth harmonic pressure component $(\Delta p)_m = P_m$ is made non-dimensional in the following definition

$$(K_p)_m = \frac{P_m}{\rho n^2 D^2} \tag{7}$$

In the present work, we confine our interest to the results for the first three blade rate harmonics, with $m = \mu Z$

$$m = Z,\ 2Z,\ 3Z; \qquad \mu = 1,\ 2,\ 3$$

Similarly, the unsteady reference area surface force on the disc can be expressed in terms of its Fourier series

$$F_S(t) = \sum_{m=1}^{\infty} (F_S)_m \sin(m\phi - \beta_m) \tag{8}$$

where

$\phi = \omega t$ = position angle
$(F_S)_m$ = total amplitude of the mth harmonic component of fluctuating disc force (obtained from the sum of the three force gauge signals)
β_m = harmonic phase angle of the mth disc force component

The nondimensional form of the disc force amplitude for the mth harmonic is

$$(K_F)_m = \frac{(F_S)_m}{\rho n^2 D^4} \tag{9}$$

Using this, the ratio of the unsteady force amplitude to propeller mean thrust, say at blade rate frequency, is the ratio of the coefficients

$$\frac{(F_S)_Z}{T} = \frac{(K_F)_Z}{K_T} \tag{10}$$

RESULTS

Propeller Cavitation

Visual observation of the propeller operated under the test conditions described earlier showed that tip vortex cavitation springing from the blade tips appeared at around $\sigma_n = 13$. As the cavitation number was decreased from this value, the tip vortex increased in size. Sheet cavitation began forming on the suction side near the blade tips at $\sigma_n \sim 12$. At $\sigma_n = 10.5$ there was substantial sheet cavitation on each blade. For the cavitation number $\sigma_n = 8.36$, the lowest value achieved in this test series, the sheet cavity on each blade covered a portion of the outer 25 percent of the propeller radius. The circumferential extent of the blade sheet cavitation was from about 90° before 12 o'clock around to 60° beyond the top-dead-center position.

Unsteady Pressures

Figures 11 and 12 show the variation of pressure coefficient values K_p versus cavitation number for the amplitudes of fluctuating pressure acting at the center of the disc (directly over the propeller center) for the first three harmonics of blade rate. Figure 11 shows data for the tip clearance ratio $a_z/D = 0.26$, with Figure 12 applicable to the larger tip clearance $a_z/D = 0.41$. The pressure amplitude curves are flat in the non-cavitating regime of large σ_n. For values of $\sigma_n < 12$, the pressure amplitude characteristics start to rise with decreasing cavitation number. The noticeable increase in the levels of all the $(K_p)_m$ values coincides with the appearance and growth in size of blade sheet cavities, a fact that confirms our general understanding of the importance of unsteady cavity volume variation to the pressure excitation.

For both tip clearances, the blade rate harmonic component is typically larger than the second and third blade rate contributions. The differences are clearly dependent on the tip clearance ratio. At the smallest tip clearance of $a_z/D = 0.26$ the blade rate amplitudes exceed the higher harmonics by a factor of more than 2.5. For the larger $a_z/D = 0.41$, the higher harmonic amplitude values are comparable to the fundamental blade rate amplitude.

In a comparison of the results of magnitudes of the blade rate component for the two tip clearance ratios, there appears to be a large influence of tip clearance. The smaller tip clearance produces the larger $(K_p)_Z$ levels in both the non-cavitating and cavitating regimes. This is certainly consistent with previous experimental findings. Some of the difference in pressure amplitudes between the two tip clearance cases may be attributed to differences in the screen-generated nominal wakes for the two tip clearance ratios, as seen in Figures 8 through 10. The extremes of the hydrodynamic advance angle away from the mean value are different for the two wakes, and this could influence the variation of blade cavitation. However, visual observation of the blade cavitation for the two tip clearance cases revealed no significant differences. It is plausible that for the gauge location over the propeller center, the measured differences of pressure amplitude are due mainly to the tip clearance variation.

The longitudinal distributions of the blade rate harmonics of fluctuating pressure amplitude coefficient along the centerline of the plate (the x_{PC} -axis shown in Figure 3) are displayed in Figure 13 for tip clearance ratio $a_z/D = 0.26$. The comparable distributions of $(K_p)_m$ versus x_{PC}/D for the tip clearance case $a_z/D = 0.41$ are given in Figure 14. Here, positive values of x_{PC}/D are upstream of the propeller center. The contours in these figures are for five different values of the cavitation number. These plots show the expected fall-off of pressure amplitude both upstream and downstream of the location of the propeller center.

The transverse distributions of the blade rate harmonic of pressure coefficient are plotted versus the nondimensional distance y/D (along the lateral axis in line with propeller center) in Figures 15 and 16 for $a_z/D = 0.26$ and 0.41 , respectively. Here the positive values of y/D are taken to starboard, looking upstream. Generally, the largest blade rate pressure amplitudes occur near the propeller centerline and fall off to either side. It has been observed from published experimental work with a variety of propeller types, that the transverse distributions of blade rate pressure amplitudes are not necessarily expected to be symmetric about the propeller centerline or about a line passing through the location of the peak pressure. Propeller blade skew will tend to accentuate the non-symmetry, particularly for the lower range of n where transient cavitation begins to dominate excitation pressures. The propeller used in the present experiments has 45 deg skew at the tip radius. With blades having positive skew ("skew back"), even with a symmetrical wake, the region of greatest cavitation extent is displaced around to the right hand side of the disc area for a right-handed propeller (see for instance, Wilson et al (1982). For very low cavitation numbers, the largest unsteady pressures are associated with the cavity-collapse portion of the cavity volume variation, which occurs over in the right-hand quadrant of the propeller disc rather than at the 12 o'clock position where the tip clearance is smallest. The displacement and distortion of cavity volume due to effects of skew can influence the higher harmonics of the surface pressure in non-trivial ways as well. In the present experiments, carried out at intermediate values of cavitation number, the location of the peak blade rate pressure amplitude is apparently influenced most by the effect of tip proximity, and occurs at or near the position of closest approach of the blade tip.

Unsteady Disc Force

The measured fluctuating disc force amplitude coefficients for the first three blade rate harmonics are shown plotted versus cavitation number for $a_z/D = 0.26$ in Figure 17, and for $a_z/D = 0.41$ in Figure 18. The symbols plotted in these graphs represent the average values for two or three data spots at each of the tested cavitation numbers. Similar to the trends of the pressure amplitudes, the disc force amplitude curves are flat for σ_n larger than about 12, then there are noticeable increases as the cavitation number is decreased. This characteristic is linked to the appearance and growth of blade sheet cavities.

When comparing the first blade rate harmonic of disc force for the two different tip clearance cases, the force amplitude for $a_z/D = 0.26$ is about 20 percent larger than the force amplitude for $a_z/D = 0.41$. This relative difference of force amplitude is considerably less than that for the pressure amplitude at the disc center for the same tip clearance ratios. For instance, from data displayed in Figures 11 and 12, at $\sigma_n = 8.36$, the blade rate pressure amplitude for the smaller tip clearance ratio is 170 percent larger than that for $a_z/D = 0.41$. Thus, the variation of pressure pulse amplitude versus cavitation number measured at one surface point location is not necessarily indicative of the magnitude of force amplitude variation acting on a surrounding reference area for this propeller and wake.

Simultaneously with the disc force measurements, pressure amplitude and phase angle measurements were obtained at 11 locations on the disc. For the first three blade rate harmonics components, the measured pressure values were integrated over the surface of the flat disc to determine a net normal force estimate on the disc area. Proper account was made for the variation of

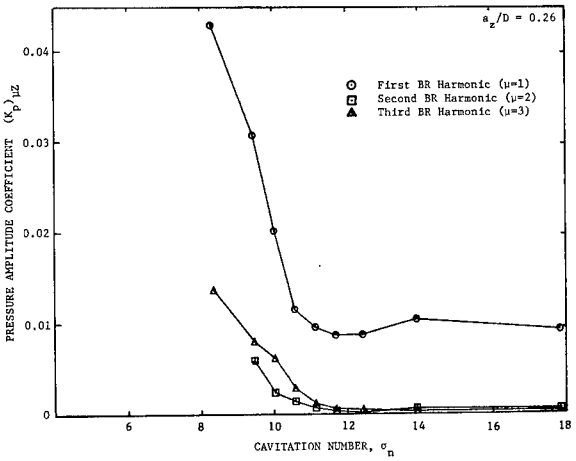


Figure 11 - Three Blade Rate Harmonics of Measured Pressure Amplitude Coefficients Taken at the Disc Center with $a_z/D = 0.26$

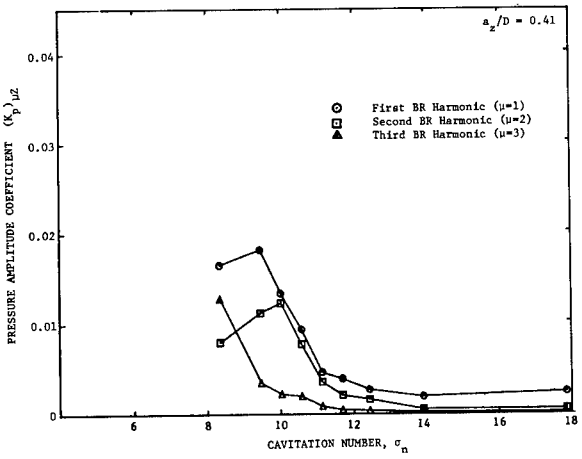


Figure 12 - Three Blade Rate Harmonics of Measured Pressure Amplitude Coefficients Taken at the Disc Center with $a_z/D = 0.41$

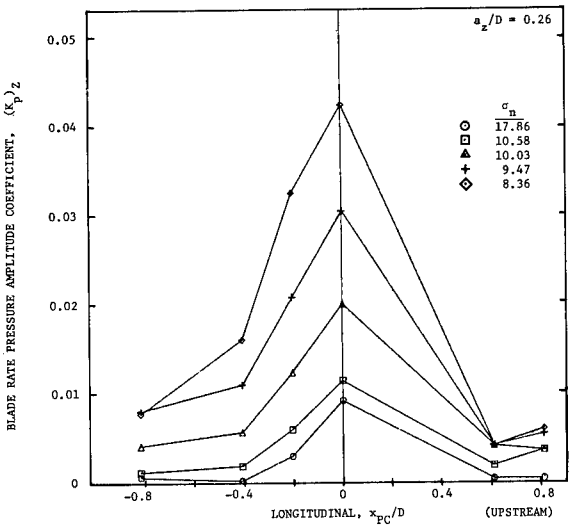


Figure 13 - Blade Rate Harmonic of Measured Pressure Amplitude Coefficient versus Longitudinal Position for Five Cavitation Numbers, with $a_z/D = 0.26$

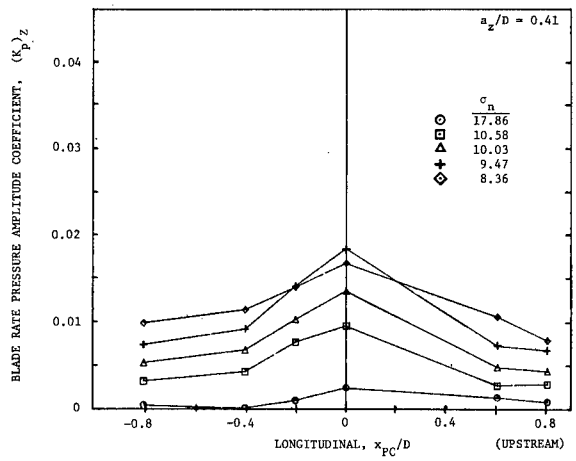


Figure 14 - Blade Rate Harmonic of Measured Pressure Amplitude Coefficient versus Longitudinal Position for Five Cavitation Numbers, with $a_z/D = 0.41$

phase angle for each transducer location, so that the presence of transverse asymmetries of pressure amplitude distributions should not affect the accuracy of the integrated pressure results. The results provide interesting comparisons with the measured force amplitudes at various cavitation numbers at the two different tip clearances.

Figures 19 and 20 compare the blade rate harmonic force coefficient values of measured force and integrated pressure force for the tip clearance ratios $a_z/D = 0.26$ and 0.41 , respectively. The comparisons of twice blade rate harmonic force coefficients for the two tip clearances are given in Figures 21 and 22. In each of the comparisons, the integrated pressure force amplitudes exceed the actual measured disc force amplitudes. The discrepancy is larger for the blade rate harmonic components than for the higher harmonics. This serves as another indication that a single point surface pressure amplitude is not necessarily an accurate representation of the net force acting over a reference area surrounding the point.

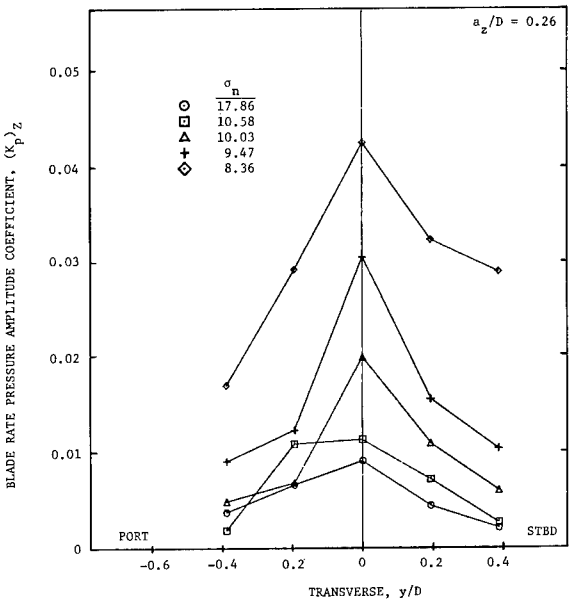


Figure 15 - Blade Rate Harmonic of Measured Pressure Amplitude Coefficient versus Transverse Position for Five Cavitation Numbers, with $a_z/D = 0.26$

Cavity Volume Velocity

Disc force measurements obtained with excitation from the operating propeller, together with the calibrated transfer function (p/a) have been used to make estimates of the cavity volume velocity harmonic from the expression in Equation (2). The unsteady disc force due to the effect of cavity volume variation must be isolated from the measured total force variation (amplitude and phase) by vectorially subtracting away the noncavitating or reference force. At the blade rate frequency of 98 Hz for the seven-bladed propeller, an average value of the pressure-to-acceleration transfer function was determined to be $(p/a) = 0.6747 slug/ft^2 (105.99 kg/m^2)$. This is for the case of $a_z/D = 0.26$, for which the calibrated transfer function of Figure 5 applies.

The blade rate disc force amplitude and phase for the noncavitating propeller at $a_z/D = 0.26$ were found to be $10^3 K_{Fnc} = 0.1622$ and $\phi_{nc} = 1.9°$. Then the following table provides the amplitude and phase data for the disc force characteristics used to obtain the inferred blade rate harmonic of cavity volume velocity given in nondimensional form.

Estimate of Blade Rate Cavity Volume Velocity Using Reciprocal Measurement					
σ_n	Total Force Coeff.	Total Force Phase	Cavitating Force Coeff.	Cavitating Force Phase	Volume Velocity Coeff.
10.03	2.05	−16.4°	1.90	17.9°	0.00081
9.47	3.54	40.6°	3.41	42.3°	0.00146
8.36	5.22	−4.3°	5.06	4.5°	0.00216

The force coefficients in the above table are multiplied by 10^3.

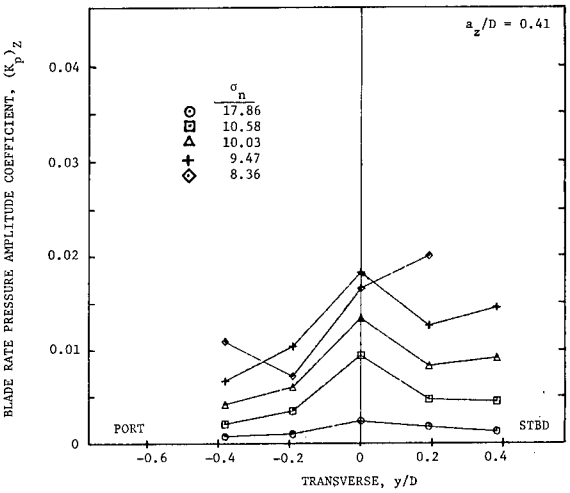


Figure 16 - Blade Rate Harmonic of Measured Pressure Amplitude Coefficient versus Transverse Position for Five Cavitation Numbers, with $a_z/D = 0.41$

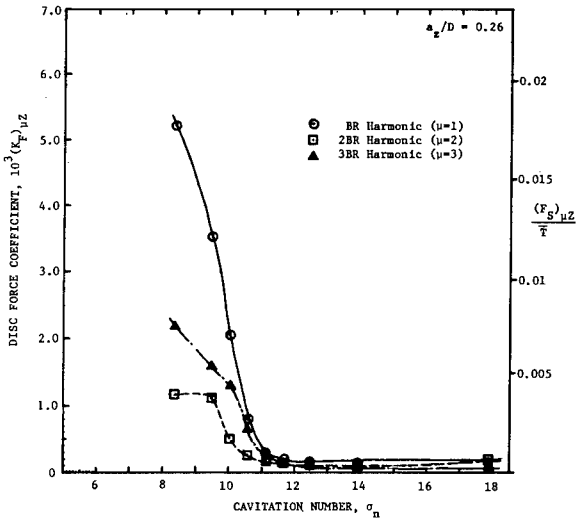


Figure 17 - Three Blade Rate Harmonics of Measured Disc Force Coefficient with $a_z/D = 0.26$

Comparison with Previous Results

Experimental results for the pressure pulse excitation were obtained previously for propeller model 4677 in the large cavitation tunnel at SSPA (Bjärne (1980)) where a complete scale model of the AO-177 hull with appendages was installed in order to produce the desired model wake. Unsteady pressure amplitude measurements were recorded at several locations on the hull surface near the propeller. The nominal wake in the water tunnel flow behind the AO-177 model was not measured, but was assumed to match sufficiently well the nominal wake measured in a towing basin behind a model having the same scale.

Figure 23 shows a comparison of the longitudinal distribution of the blade rate pressure amplitude coefficients along the flat surface from the present 24-inch water tunnel results and along the hull surface from the complete model hull tests in the SSPA tunnel. Although this is not completely consistent because of the difference between the flat plate boundary and the actual hull shape and the mismatch of pressure gauge locations, it does provide an approximate comparison of the general trend of the longitudinal distribution of pressure pulse amplitudes. Measurements taken on the flat plate boundary positioned with tip clearance ratios $a_z/D = 0.26$ and 0.41 are shown in Figure 23 together with measurements obtained with the model hull shape with the vertical tip clearance of $a_z/D = 0.292$, all with the same cavitation number $\sigma_n = 8.36$. The values from the actual hull shape with $a_z/D = 0.292$ fall generally between the values obtained with the flat plate at the two different tip clearances. This indicates that the measurements on a flat plate represent a good order of magnitude approximation for the measurements along the hull. However, the shape of the curve of the $(K_p)_Z$ values versus x_{PC}/D is not the same for the flat plate cases and the hull, and the details of differences are attributable to the difference in wake and boundary geometry (hull shape).

The variations with respect to cavitation number of the blade rate component of pressure amplitudes at or near the tip plane are shown in Figure 24. The values measured on the complete hull shape model were taken over the propeller tip and the values measured on the flat plate boundary were obtained in line with the propeller center. The curves compare favorably in an approximate way, considering the differences in boundary shape and tip clearances.

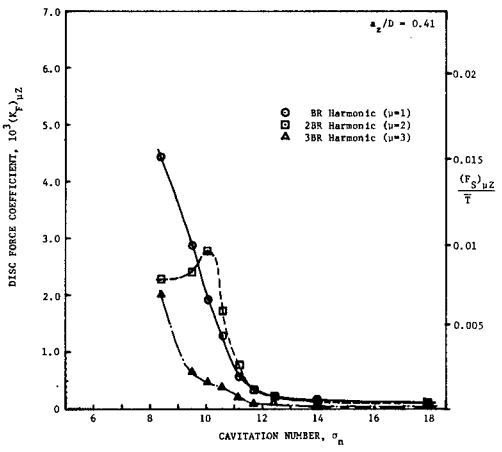


Figure 18 - Three Blade Rate Harmonics of Measured Disc Force Coefficient with $a_z/D = 0.41$

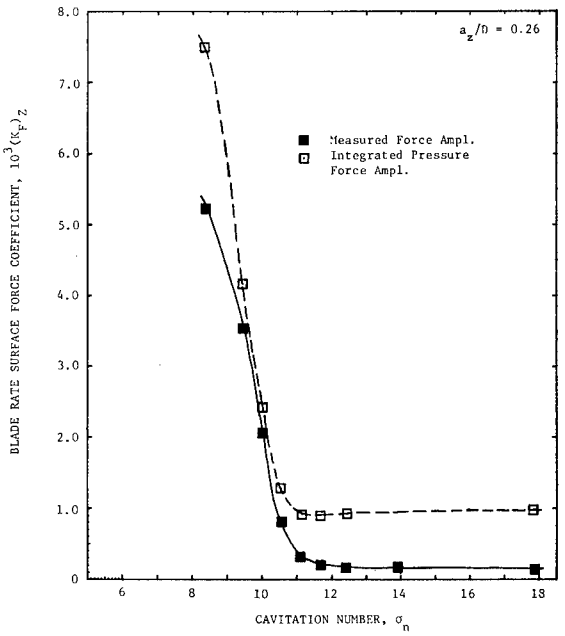


Figure 19 - Blade Rate Harmonic of Disc Force Coefficient versus Cavitation Number, Comparison Between Measured Force and Integrated Pressure, with $a_z/D = 0.26$

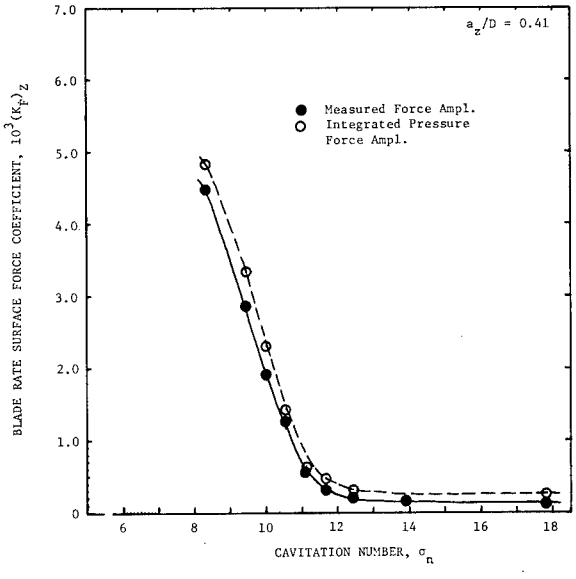


Figure 20 - Blade Rate Harmonic of Disc Force Coefficient versus Cavitation Number, Comparison Between Measured Force and Integrated Pressure, with $a_z/D = 0.41$

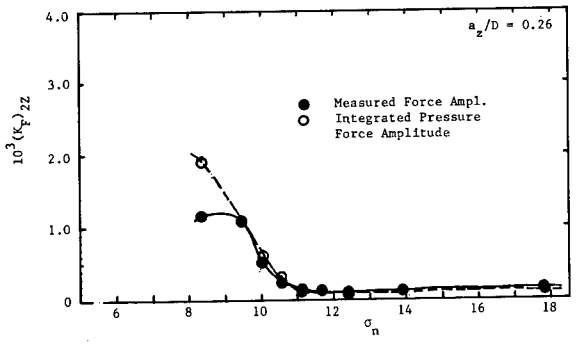


Figure 21 - Twice Blade Rate Harmonic of Disc Force Coefficient versus Cavitation Number, with $a_z/D = 0.26$

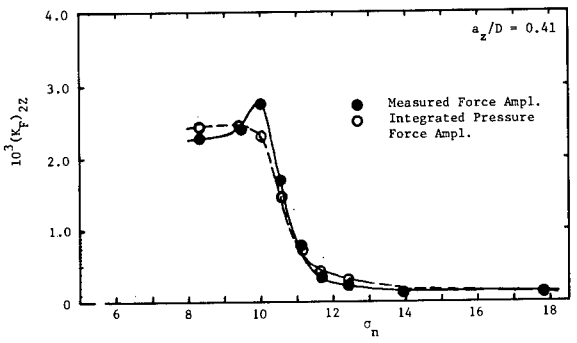


Figure 22 - Twice Blade Rate Harmonic of Disc Force Coefficient versus Cavitation Number, with $a_z/D = 0.41$

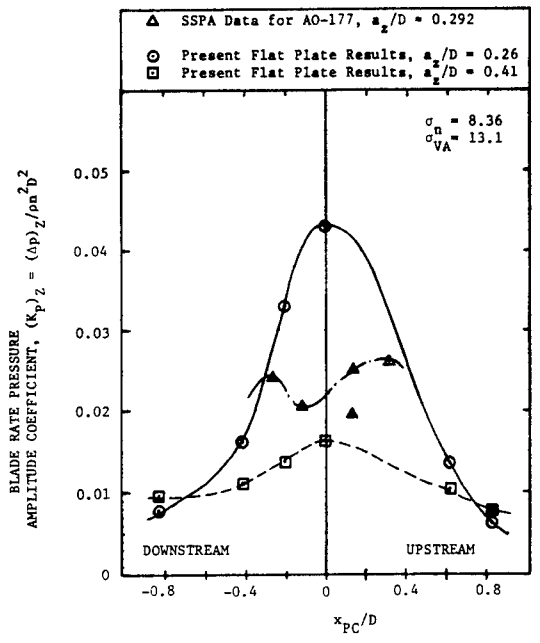


Figure 23 - Comparison of Measured Blade Rate Pressure Amplitude Longitudinal Distribution

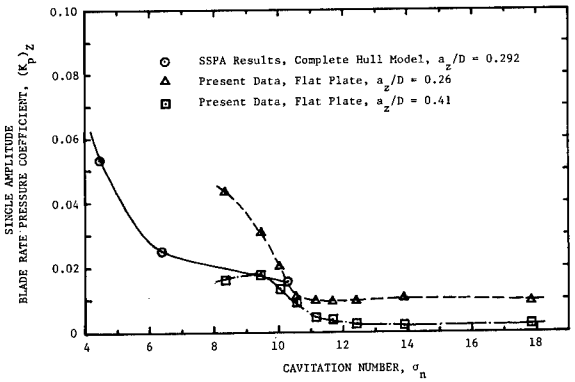


Figure 24 - Comparison of Blade Rate Pressure Amplitude Coefficient Above the Propeller versus Cavitation Number

DISCUSSION

Useful measurements are described for three blade rate harmonics of the unsteady excitating force and pressures on a reference-area disc mounted in a flat boundary above a cavitating propeller operating in a screen-generated wake in the 24-inch variable pressure water tunnel at DTNSRDC. The inflow velocity distribution was intended to simulate the axial velocity pattern of a very severe single-screw ship type of wake, similar to that of the AO-177. Results of measurements are presented for a range of cavitation numbers covering non-cavitating and cavitating conditions and for two different tip clearances. Comparisons are provided between the measured disc force and the force obtained by integrating the pressures over the disc area. The integrated pressure force values are always somewhat larger than the measured force values, principally because of the lack of sufficient detail in defining the variation of phase angles for the pressures over the disc.

Measured results from the complete array of pressure transducers over the flat plate boundary show the longitudinal and transverse centerline distributions of pressure pulse amplitudes in the region around the propeller. In general these show that the largest pressure excitation amplitudes occur near the propeller center.

All the computed harmonics of unsteady disc force and pressures show a noticeable increase with decreasing cavitation number, particularly below the onset of visible blade sheet cavitation at around $\sigma_n = 12$ Unsteady force and pressure amplitudes are largest for the smaller of the two tip clearance values.

A reciprocity experiment was performed to measure the pressure-to-acceleration transfer function (p/a), needed to estimate the time rate of change of cavity volume. The transfer function was found to have a varability at frequencies below about 300 Hz, and this was judged to represent an uncertainty in the capability to approximate the value of cavity volume velocity.

Comparisons between the present measured unsteady pressure amplitudes produced with the AO-77 model propeller on a flat plate boundary and those obtained previously on a complete scale model hull at SSPA show reasonable correlation with respect to the effect of tip clearance at comparable cavitation numbers. The differences between the results in terms of spatial distribution and variation with cavitation number are associated with the detailed differences in wake and boundary geometry.

It should be noted that with the capability developed here, propeller excitation experiments could be carried out with partial

stern or dummy model representations of the near-propeller hull geometry that include characterizations of the reference-area unsteady vertical surface force as well as surface pressures. The disc force measuring system described here could be used to measure the vertical surface force amplitudes on a shaped element imbedded in the surface of a foreshortened hull model. Pressure gauges could be installed flush with the shaped surface as usual. The use of a partial body would provide some help with the simulation of a desired wake configuration, and it could be made less subject to low tunnel speed restrictions imposed by the use of wake screens alone.

THE COMPUTATION OF UNSTEADY PROPELLER CAVITATION

Detailed developments of the procedure used to solve the linear unsteady three-dimensional cavity flow problem have been given by Lee(1979) and by Breslin, VanHouten, Kerwin and Johnsson(1982), while a brief description appears in a review paper by VanHouten, Kerwin and Uhlman(1983). We will therefore will not present a complete development of the procedure here, but will attempt to provide the essential background required to lead into the development of the non-linear leading edge correction.

While unsteady propeller cavitation patterns may take on many forms, it is safe to say that a typical pattern will involve cavity lengths which vary from zero to substantial fractions of the chord during each propeller revolution. This large variation in cavity length makes the problem strongly non-linear, even if one makes the assumption that the flow conditions are such that the cavities are thin.

The steady cavity flow problem in two dimensions can be reduced to a linear problem by prescribing the length of the cavity and solving for the resulting cavity pressure. The two-dimensional steady solution for a prescribed cavity pressure then involves an iterative solution of a succession of linear problems. The extension to the steady three-dimensional problem becomes considerably more complicated since the iterative adjustment of cavity length must now be performed simultaneously over the entire span.

Solution of the three-dimensional unsteady problem requires a similar three-dimensional adjustment of cavity length, and clearly must be carried out in the time domain. The solution obtained *somehow* at a particular time is advanced one time step by adjusting the previously obtained cavity boundary, satisfying the appropriate dynamic, kinematic and cavity closure conditions, as well as the conditions on vorticity associated with the unsteady lifting problem in fully-wetted flow. This time domain solution could, in principle, represent the real transient problem of a hydrofoil or propeller starting from rest. However, since our objective in most cases is to obtain the steady state oscillatory solution, the initial conditions which we will impose are artificial. The propeller is assumed initially to be operating without cavitation in steady flow represented by the circumferential mean inflow of the given wake field. The unsteadiness of the inflow is then turned on and the solution is allowed to proceed until the steady state oscillatory non-cavitating solution is acheived. Finally, the cavity solution is turned on and the solution process continues for sufficient time to acheive a steady state oscillatory cavity solution.

As indicated in Figure 25, the propeller is represented by a lattice of discrete line vortex and source elements placed on the mean camber surface of the blades. The sources represent both the thickness of the blades and the thickness of the cavities. The strength of the former is known at the outset, while the cavity sources must be solved for at each time step. Vortex and cavity source elements are extended downstream of the blades into a

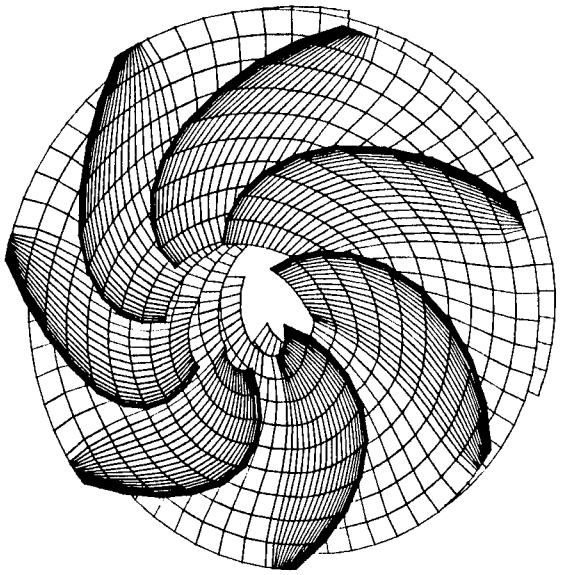


Figure 25 - Vortex Lattice Arrangement on AO-177 Propeller, showing the blades and the transition wake. The ultimate wake hub and tip vortices are not shown.

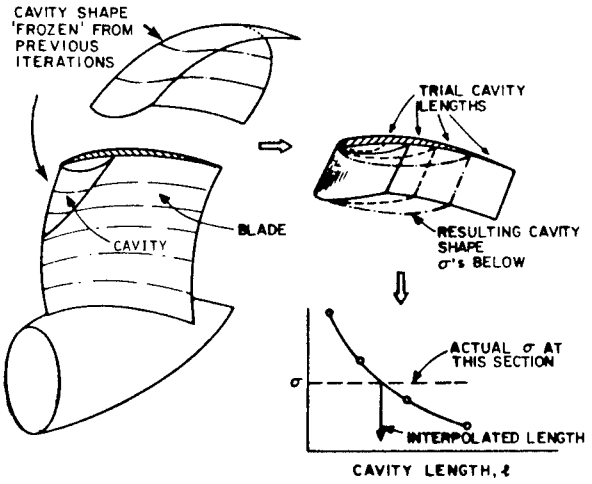


Figure 26 - Pictorial of Iterative Solution for Three-Dimensional Cavity

transition wake region whose angular extent is typically one quarter of a propeller revolution. The cavity source elements in the transition wake are, of course, non-zero only if the flow is supercavitating. Finally, the trailing vortices in the transition wake are collected into concentrated hub and tip vortices which extend to "computational" infinity downstream.

The time-domain solution up to the point where cavitation is turned on follows the procedure presented by Kerwin and Lee (1978). The usual flow tangency boundary condition is solved at a set of control points on the key blade, which then provides the solution for the discrete vortex strengths. While one could solve the boundary value problem for all of the blades simultaneously,

it is more efficient to let the loading on each of the other blades correspond to the values previously found for the key blade at the same angular position.

The numerical procedure which is employed to obtain the cavitating solution is shown schematically in Figure 26. For a given time step, the solution for the loading and cavitation is obtained in an iterative way by solving the problem in one chordwise strip, while the loading and cavitation on all the other strips, and on the other blades is assumed to be known. The solution marches out from the hub to the tip, returns back to the hub and returns again to the tip until convergence is acheived. It is important to note that the solution for each chordwise strip is not a two-dimensional one, but represents the solution for a collection of three-dimensional source and vortex elements placed in a flow field consisting of the sum of the propeller onset flow and the flow induced by all the other chordwise strips. The converged result therefore represents the true three-dimensional solution of the discretized representation of the propeller.

The solution for one chordwise strip requires an additional iteration for cavity length, as discussed earlier in this section. As indicated in Figure 26, the solution of the linearized cavity problem for a prescribed cavity length includes the cavity pressure, as well as the chordwise distribution of vorticity and cavity source strength. Since the cavity pressure at each radius is known from the given flow conditions, the cavity length must be adjusted until the computed cavity pressure agrees with this prescribed value. This is carried out by adjusting the cavity length by integral units of the chordwise discretization until two solutions are obtained yielding cavity pressures which bracket the desired value. The final solution is then formed by a linear interpolation between these two solutions.

The addition of these two levels of iteration brought about by the inherrent non-linearity of the solution with respect to cavity length greatly increases the computation time. It is for this reason that the non-cavitating unsteady solution is found first, to provide the best possible initial estimate of the distribution of blade loading at each time step.

Experience with PUF-3 at MIT and DTNSRDC has indicated that the code may tend to overpredict the extent of cavitation. This may be due to difficulties in effective wake prediction as well as to the limitations of the linear cavity theory incorporated in the code.

The importance of non linear thickness effects was first demonstrated by Tulin and Hsu(1977), who developed a "short" cavity theory in which the cavity flow was treated as a linear disturbance to the non linear wetted flow. Their results showed a considerable reduction in cavitation with increasing section thickness. Uhlman(1983) solved the non linear partially cavitating problem numerically by using surface singularity techniques with an iterative procedure to place the singularities on the exact boundary of the hydrofoil and its cavity. His results showed the same trend as Tulin and Hsu, but showed considerably less sensitivity to thickness. Kinnas(1985) introduced a leading edge correction to linear cavity flow theory, and a review of this development is given in the following sections. This theory is simple enough to be implemented in a three dimensional propeller code, and has been found to give results which are in reasonable agreement with the elaborate numerical calculations made by Uhlman.

THE TWO-DIMENSIONAL CAVITATING HYDROFOIL

Pure Linear Theory

Consider a hydrofoil as shown in Figure 27, with a camber distribution $\eta(x)$ and a thickness distribution $\tau(x)$, operating in a uniform inflow U_∞ with ambient pressure p_∞. A cavity with thickness $h(x)$ is assumed to extend from the leading edge to a point $x = l$. The cavitation number,σ, is defined in the usual way as

$$\sigma = \frac{p_\infty - p_v}{1/2\rho U_\infty^2} \tag{11}$$

where p_v is the pressure in the cavity, which is assumed to be vapor pressure.

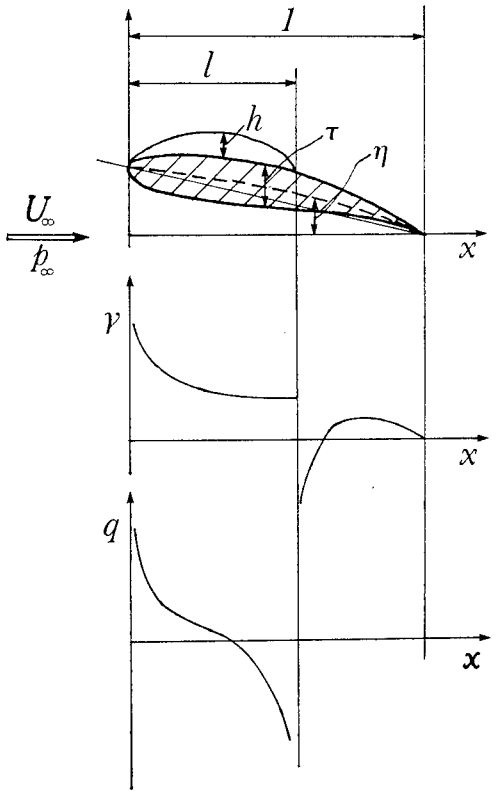


Figure 27 - Cavitating Hydrofoil Coordinate System

Assuming that the hydrofoil and the cavity are *thin*, then linear theory is applicable and the flow can be simulated by a cavity source distribution $q(x)$ and a vorticity distribution $\gamma(x)$, as shown in Figure 27. These singularity distributions must satisfy the following linearized boundary conditions,

The kinematic boundary condition:

$$-\frac{q(x)}{2} + \frac{1}{2\pi}\int_0^1 \frac{\gamma(\xi)d\xi}{\xi - x} = U_\infty \frac{\partial \eta}{\partial x}; \qquad 0 < x < 1 \tag{12}$$

The dynamic boundary condition:

$$\frac{\gamma(x)}{2} - \frac{1}{2\pi}\int_0^l \frac{q(\xi)d\xi}{\xi - x} = \frac{\sigma}{2}U_\infty + \frac{U_\infty}{2\pi}\int_0^1 \frac{\partial \tau / \partial \xi}{\xi - x} d\xi$$

$$0 < x < l \tag{13}$$

The Kutta condition:

$$\gamma(1) = 0 \tag{14}$$

The cavity closure condition:

$$\int_0^l q(x)dx = 0 \tag{15}$$

The cavity thickness distribution $h(x)$ will satisfy the equation:

$$q(x) = U_\infty \frac{\partial h}{\partial x} \qquad ;0 < x < l \tag{16}$$

The inversion of the Cauchy type singular integral equations yields a unique solution for $\sigma, q(x)$and $\gamma(x)$ for a given cavity length,l. As shown by Kinnas(1985), the solution can be expressed in terms of integrals over the cavity length of the streamwise perturbation velocity u_w^+ corresponding to the non-cavitating flow around the hydrofoil. The solution is obtained in terms of the transformed chordwise coordinate

$$z = \sqrt{\frac{x}{1-x}} \tag{17}$$

and the transformed cavity length

$$s = \sqrt{\frac{l}{1-l}} \tag{18}$$

The expression for the cavitation number, σ , is found to be,

$$\sigma = \int_0^s \frac{2u_w^+(\eta)}{U_\infty} f(\eta; s) d\eta \tag{19}$$

where the weighting function $f(\eta; s)$, which depends only on the cavity length, is given by,

$$f(\eta; s) = \frac{2\sqrt{2}}{\pi} \frac{\sqrt{\eta(s-\eta)}}{(1+\eta^2)^2} \frac{r^2}{r^2-1} \left[\sqrt{r^2+1} - \eta\sqrt{r^2-1}\right] \tag{20}$$

where

$$r^2 = \sqrt{1+s^2} \tag{21}$$

The final expressions for the cavity source strength $q(z)$ and the vorticity $\gamma(z)$ can be shown to be

$$q(z) = \frac{1}{\pi} \frac{1+z^2}{\sqrt{z(s-z)}} \int_0^s \frac{F(\eta)}{z-\eta} d\eta; \qquad z < s \tag{22}$$

$$\gamma(z) = -\frac{1}{\pi} \frac{1+z^2}{\sqrt{z(s+z)}} \int_0^s \frac{F(\eta)}{z+\eta} d\eta - \left[u_w^+(z) - \frac{\sigma U_\infty}{2}\right] + \gamma_w(z); \qquad z < s \tag{23}$$

The weighting function $F(\eta)$ in the above equations depends both on the cavitation number, σ, and on the vorticity distribution γ_w and the upper surface streamwise perturbation velocity u_w^+ of the fully-wetted flow around the same hydrofoil. The expression for the weighting function is

$$F(\eta) = \frac{\sqrt{\eta(s-\eta)}}{1+\eta^2} \left[u_w^+ - \frac{\sigma U_\infty}{2}\right] \tag{24}$$

A similar analysis for supercavitating hydrofoils is described by Kinnas(1984).

The Leading Edge Correction

It is known that linear theory gives extremely accurate results for thin fully-wetted hydrofoils, except in the neighborhood of the leading edge. The correction to linear theory developed by Lighthill(1951), however, makes it possible to obtain reasonably accurate pressure distributions over the entire hydrofoil. In particular, Lighthill's rule produces a stagnation point at the leading edge which is totally lacking in the linearized thickness problem.

The idea which is employed here in the cavitating problem is to consider first that one has obtained the linearized cavity solution, using the results of the preceding section. If one now *freezes* the resulting hydrofoil plus cavity and applies Lighthill's rule to obtain the pressure distribution, the result will be that the pressure on the cavity near the leading edge will be much higher than predicted from linear theory. Thus, the boundary condition of vapor pressure on the cavity boundary will not be satisfied.

Suppose instead, that the dynamic boundary condition for the linear problem is modified in such a way that the pressure on the cavity becomes vapor pressure *after* the application of Lighthill's rule. Even though the modification to the dynamic boundary condition will be significant only near the leading edge, this change in the initial conditions for the cavity streamline will have a global influence on the cavity.

According to linear theory , the streamwise perturbation velocity, u_c, on the cavity surface is

$$u_c = \frac{\sigma}{2} U_\infty; \qquad 0 < x < l \tag{25}$$

which is obtained from the exact dynamic boundary condition

$$q_c = \sqrt{1+\sigma}\, U_\infty \tag{26}$$

In order for (26) to be satisfied after the application of Lighthill's correction, the dynamic boundary condition for the linearized problem should not be one of constant streamwise perturbation velocity, but should be as follows,

$$u_c = U_\infty(\sqrt{1+\sigma}\sqrt{\frac{x+\rho_L/2}{x}} - 1); \qquad 0 < x < l \tag{27}$$

where ρ_L is the leading edge radius of the hydrofoil. Because of the local behavior of the cavity source strength near the leading edge , this also represents the leading edge radius of the body defined as the foil and the cavity.

Equations (12) to (15) will remain the same except for (13) where $\frac{\sigma}{2} U_\infty$ is replaced by the right hand side of (27). Defining σ_L as the cavitation number obtained from the solution of the linear problem, the cavitation number, σ , with the leading edge correction will be,

$$\sigma = (\frac{1+\frac{\sigma_L}{2}}{a(\rho_L; l)})^2 - 1 \tag{28}$$

where $a(\rho_L; l)$ is the leading edge correction factor defined by

$$a(\rho_L; l) = \int_0^s \sqrt{\frac{x+\rho_L/2}{x}} f(\eta; s) d\eta \tag{29}$$

The source and vortex distributions $q(x)$ and $\gamma(x)$ will be given by (22), (23) and (24) with u_w^+ replaced by

$$u_w^+ - U_\infty\sqrt{1+\sigma}\left[\sqrt{\frac{x+\frac{\rho_L}{2}}{x}} - 1\right]$$

The effect of the leading edge radius on the solution of the problem of a partially cavitating flat plate at an angle of attack can be seen in Figure 28. One can note a decrease in both the extent and thickness of the cavity as the leading edge radius is increased. The same effect can also be seen in Figure 29, which shows the results obtained for NACA 16 thickness forms with thickness/chord ratios of 6,9 and 12 percent. For comparison, Figure 30 shows the cavities computed for the same NACA 16 sections using linear theory. Here the trend is opposite, with linear theory predicting larger cavities as the thickness is increased. This result of linear theory is clearly incorrect, as indicated from the non-linear theories of Tulin and Hsu(1977), Uhlman(1983) and Hsu(1986), as well as from experiments conducted by Kinnas(1985).

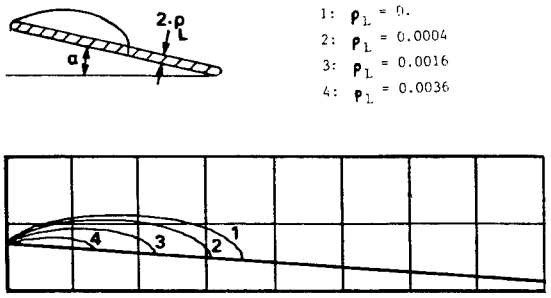


Figure 28 - Cavitating Flat Plate with Different Leading Edge Radii, ρ_L , $\alpha = 4°$, $\alpha/\sigma = 0.06$

A NUMERICAL METHOD FOR SOLVING THE CAVITATING HYDROFOIL PROBLEM

The solution for a two dimensional cavitating hydrofoil of general shape, with or without the leading edge correction, can be obtained by evaluating the integrals in (19),(22) and (23). An efficient and accurate scheme to evaluate these integrals is described by Kinnas(1985).

However, a numerical scheme using discrete vortex and source elements is desirable in order to permit the extension of the theory to the three dimensional propeller problem. Such numerical methods have already been developed by Golden(1975), Lee(1979) and Van Houten(1982) and have formed the basis for the development of PUF-3. However, the goal in developing these earlier methods was limited to the accurate prediction of cavitation number for a given cavity length, rather than the detailed prediction of cavity source and vortex distributions. The purpose of the following section is to develop a numerical scheme which will provide a more accurate representation of the chordwise singularity distributions.

The numerical scheme which we have employed consists of approximating the vorticity and cavity source distributions $\gamma(x)$ and $q(x)$ by discrete vortices Γ_i and Q_i. The values of Γ_i and Q_i are determined by applying (12) and (13) at appropriately selected control points.

The chordwise discretezation, which we refer to as "half cosine" spacing, spaces the singularities in constant increments of the transformed variable θ, which is related to the physical coordinate x as follows:

$$x = 1 - \cos\theta\,; \qquad 0 < \theta < \pi/2 \tag{30}$$

The arrangement of the vortices and sources is shown in Figure 31 . This choice is the outcome of an extensive investigation of different numerical schemes, which is described in detail by Corrado(1986). One obvious attribute of half cosine spacing is the concentration of elements near the leading edge—a desirable feature in obtaining an accurate cavity solution.

The vortices for N panels over the chord are located at the points,

$$\xi_i^V = 1 - \cos\left(\frac{2i-1}{2}\frac{\pi}{2N}\right)\,; \qquad i = 1,\ldots,N \tag{31}$$

while the sources for N_c cavitating panels are located at

$$\xi_i^S = 1 - \cos\left(i\frac{\pi}{2N}\right)\,; \qquad i = 1,\ldots,N_c \tag{32}$$

except for the first source, which is put at the same position as the first vortex.

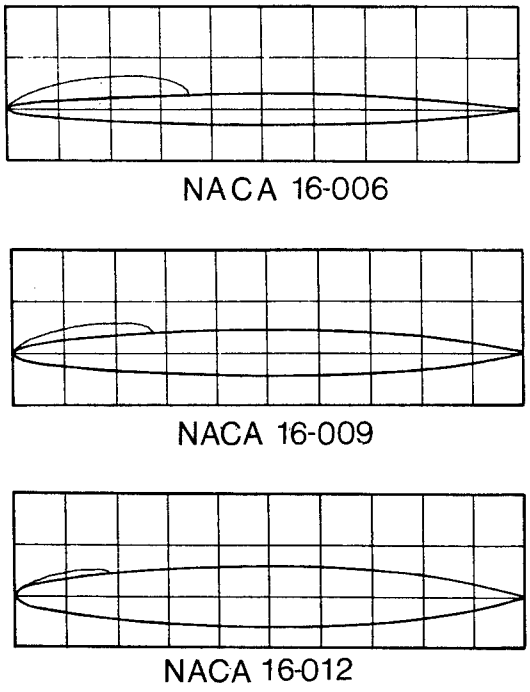


Figure 29 - Linear Theory Including Leading Edge Corrections - All Hydrofoils at $\alpha = 4°$ and $\sigma = 1.07$

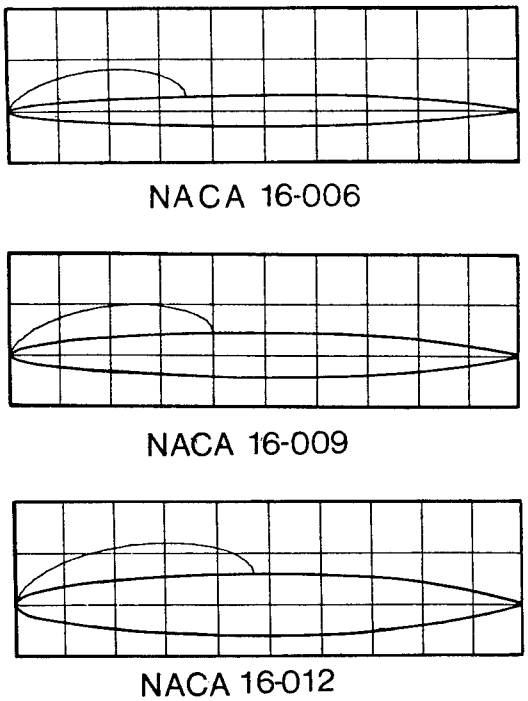


Figure 30 - Pure Linear Theory. All Hydrofoils at α = 4o and $\sigma = 1.07$

The strengths of the discrete vortices and sources are defined as

$$\Gamma_i = \gamma(\xi_i^V)\Delta\xi_i^V \tag{33}$$

$$Q_i = \bar{q}_i\Delta\xi_i^S \tag{34}$$

where $\Delta\xi_i^V$ and $\Delta\xi_i^S$ are the widths of the i'th vortex and source panels, respectively. The boundaries of these panels can be seen in Figure 31 . Notice that we base Q_i on the average $\bar{q}_i$ rather than on the local value $q(\xi_i^S)$, which has been found to be necessary in order to obtain the correct cavity thickness distribution, according to (16). Notice also that the cavity is considered to end between a vortex and source in θ coordinates in order to obtain a better representation of the square root singularities of the vorticity and cavity source distributions at the cavity termination.

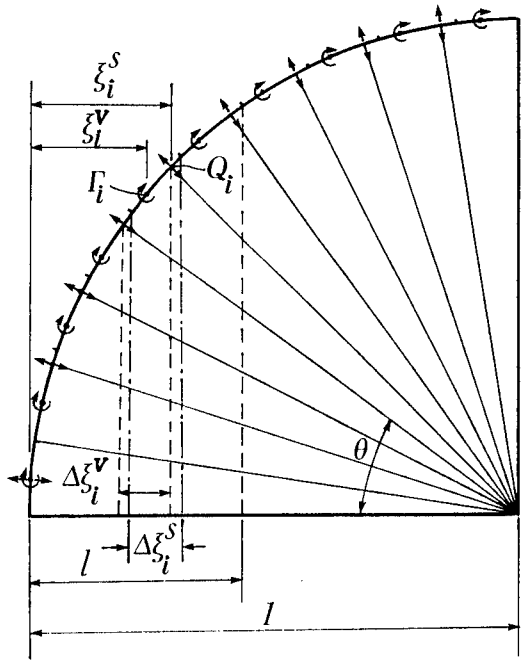


Figure 31 - Arrangement of Vortices and Sources for the Two Dimensional Numerical Scheme

Using an analysis similar to that presented by Lan(1974), the control points for the kinematic boundary condition x_j^K are placed at the zeros of the equation,

$$\Delta V(x) = -\sum_{i=1}^{N}\frac{1}{2\pi}\frac{\Gamma_i}{\xi_i^V - x} + \frac{q(x)}{2} - U_\infty\alpha \tag{35}$$

as indicated by (12) where $\gamma(x)$ and $q(x)$ correspond to the vorticity and cavity source distribution for a cavitating flat plate at an angle of attack α, as given in Appendix B.

Plots of $\Delta V(x)$ as a function of θ over the entire chord for both a non-cavitating and cavitating flat plate are shown in Figures 32 , 33 and 34 . These figures show that the correct location for the control points for the kinematic boundary condition x_i^K is midway between the θ coordinates of the vortices. These are also the points where the sources are located.

Similarly, the control points for the dynamic boundary condition x_j^D are placed at the zeros of the equation,

$$\Delta U(x) = -\sum_{i=1}^{N_c}\frac{1}{2\pi}\frac{Q_i}{\xi_i^S - x} + \frac{\gamma(x)}{2} - \frac{\sigma}{2}U_\infty \tag{36}$$

Plots of $\Delta U(x)$ as a function of θ over the length of the cavity are shown in Figures 35 and 36 This shows that the control points for the dynamic boundary condition x_j^D should be located midway between the θ coordinate of the sources, which is where the vortices are located.

The N values of Γ_i and the N_c values of Q_i, as well as the cavitation number σ will finally be determined by applying the kinematic boundary condition (12) at N points x_j^K and the dynamic boundary condition at $N_c - 1$ points x_j^D.

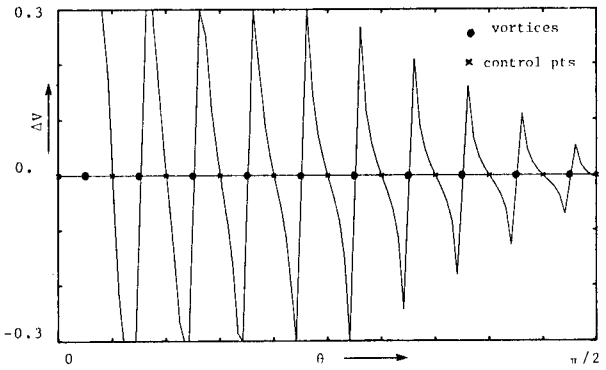


Figure 32 - Plot of Normal Error Function,ΔV for a Non-Cavitating Flat Plate at $\alpha = 4°$, $N = 10$, $N_c = 6$

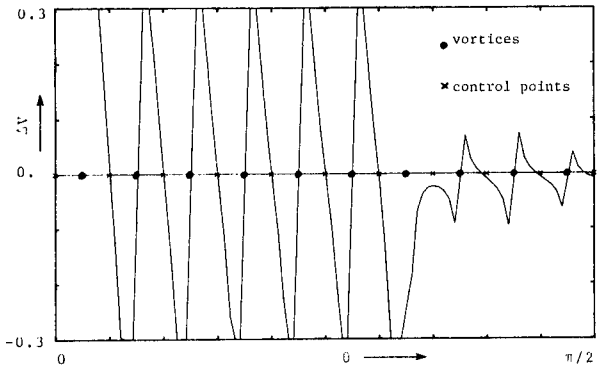


Figure 33 - Plot of Normal Error Function,ΔV , for a Cavitating Flat Plate at $\alpha = 4°$, $N = 10$ $N_c = 6$

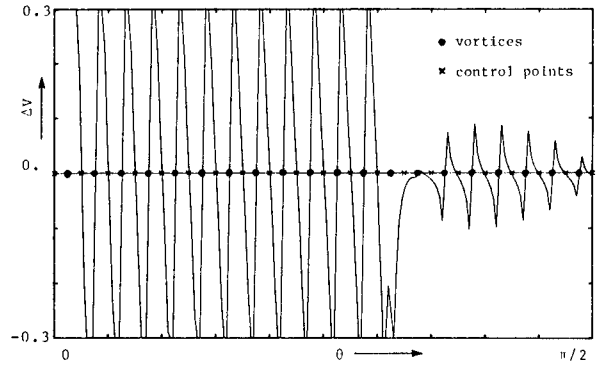


Figure 34 - Plot of Normal Error Function, ΔV, for a Cavitating Flat Plate at $\alpha = 4°$, $N = 20$ $N_c = 12$

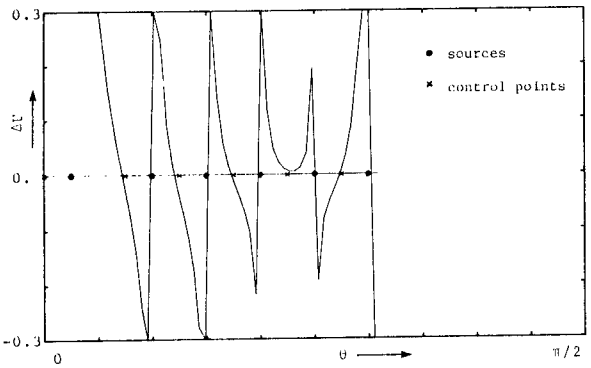


Figure 35 - Plot of Horizontal Error Function, ΔU, for a Cavitating Flat Plate at $\alpha = 4°$, $N = 10$ $N_c = 6$

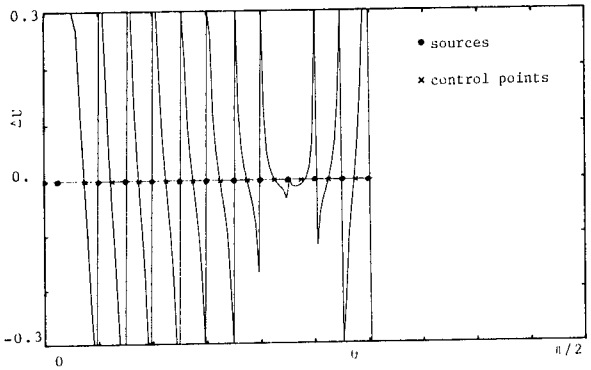


Figure 36 - Plot of Horizontal Error Function, ΔU, for a Cavitating Flat Plate at $\alpha = 4°$, $N = 20$ $N_c = 12$

The closure condition (15) will take the discretized form,

$$\sum_{i=1}^{N_c} Q_i = 0 \tag{37}$$

The one missing equation is obtained from the behavior of $\gamma(x)$ and $q(x)$ at the leading edge. By using (57) with (33) and (34) we obtain the relationship,

$$\frac{3}{4}\frac{Q_1}{(\Delta\xi_1^S)^{3/4}} = \frac{(\xi_1^V)^{1/4}}{\Delta\xi_1^V}\Gamma_1 \tag{38}$$

The Kutta condition (14) is satisfied implicitly as shown for fully wetted vortex lattice flows by James(1972).

The numerical scheme has been applied to the problem of a cavitating flat plate, and the cavitation number, σ, obtained with increasing numbers of elements N and N_c is shown in the following table:

N/N_c	Numerical	Analytical
10/6	0.86	0.85
20/12	0.87	0.87
40/24	0.88	0.88

The convergence seems to be excellent. The numerical vorticity and cavity source distribution for $N = 10$ and $N_c = 6$ can be seen in Figures 37 and 38 plotted together with the analytical values. The accuracy is remarkable, even with a small number of elements. The numerical convergence has also been found to be good for parabolic and NACA $a = .8$ camber lines, as shown by Corrado(1986).

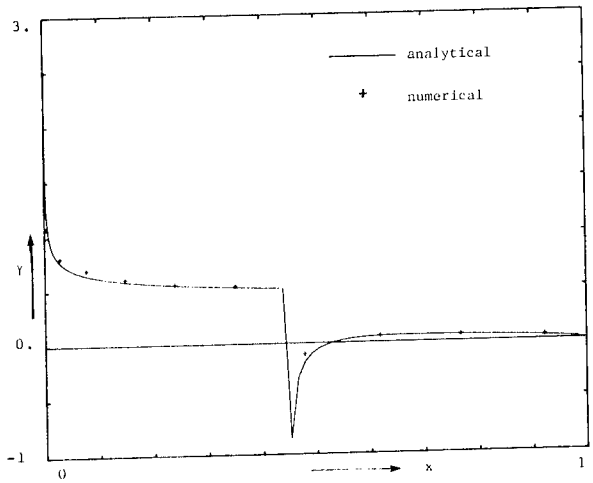


Figure 37 - Analytical and Numerical Vorticity Distribution for a Flat Plate at $\alpha = 4°$, $N = 10$ $N_c = 6$

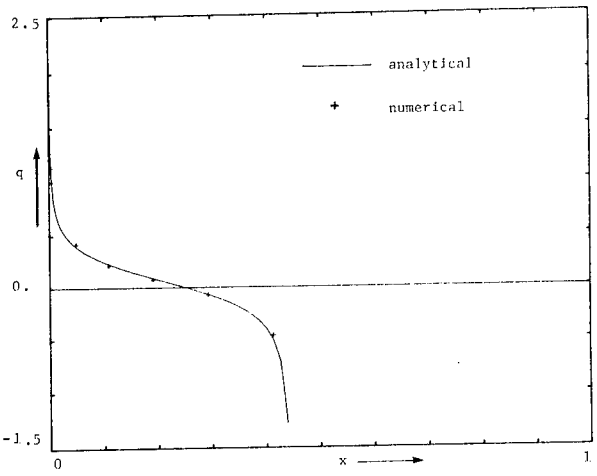


Figure 38 - Analytical and Numerical Cavity Source Distribution for a Flat Plate $\alpha = 4°$, $N = 10$ $N_c = 6$

The numerical scheme has also been applied to the problem of the leading edge radius correction described in the previous section. All the equations remain the same except for the right hand side of (13) in which $\frac{q}{2}U_\infty$ must be replaced by:

$$\left(\sqrt{1+\sigma}\sqrt{\frac{x+\frac{\rho_L}{2}}{x}} - 1\right)U_\infty$$

The results of the computation of the cavitation number, σ, with increasing values of N and N_c are shown for a section leading edge radius $\rho_L = 0.00176$ in the following table:

N/N_c	Numerical	Analytical
10/6	0.73	0.83
20/12	0.81	0.84
40/24	0.85	0.85

The analytical values of the cavitation number were calculated using (28) for the exact values of cavity length corresponding to each combination of N and N_c. It can be noted that convergence is now slower than in the case of no leading edge correction.

This is attributed to the fact that finer discretezation is needed near the leading edge to capture the singular behavior of u_c as given by (27). However, it appears that 20 elements over the chord provide sufficiently accurate results, and this value is acceptable for use in a three-dimensional propeller calculation.

COMPUTED RESULTS FOR THE AO-177 PROPELLER

The numerical scheme described in the preceding section has been incorporated in the PUF-3 code with the option to include the non-linear leading edge correction or to use linear cavity theory. In the latter case, the method is essentially the same as in the original code, but with improved convergence as a result of the change in the position of the control points and in the treatment of the leading edge singularity elements. All calculations were made with 20 panels over the chord and 9 panels over the radius, which is the arrangement shown in Figure 25.

With the leading edge correction included, one would expect to obtain smaller cavities, and this has been found to be the case. Figure 39 shows the computed time histories of cavity volume during one revolution with the propeller operating at a cavitation number of 3, which corresponds approximately to the full speed operating condition of the ship. The leading edge correction clearly results in smaller cavity volumes, and the cavity contour plots shown within the figure show in addition that the cavities at the inner radii are eliminated entirely. The computed cavity patterns are comparable to those observed in the experiments at SSPA reported in Wilson, et al(1982), although one should keep in mind that the present calculations were made for the wake field corresponding to the DTNSRDC experiments.

Figure 40 shows the computed blade rate harmonic of the cavity volume velocity of a single blade as a function of cavitation number. The effect of the leading edge correction reduces the blade rate harmonic at high cavitation numbers, but the curves can be seen to cross at the lowest cavitation number. It is evident from Figure 39 that at the lowest cavitation number the volume is less, but the angular duration of the cavitation is shorter. Therefore, the seventh harmonic of the volume velocity would not necessarily be less.

The results of the present reciprocity experiments are also shown in Figure 40 for comparison. The experimental values are higher than the theory, and this may be due to the role of unsteady tip vortex cavitation which is not accounted for. At the relatively high cavitation numbers of the tests, the observed tip vortex volume was not negligible in comparison to the volume of sheet cavitation on the blades. However, the combined uncertainties in the experimental calibrations and the extreme sensitivity of computed cavity volume to propeller inflow should certainly not be ignored.

Figure 41 shows the variation of the maximum cavity volume per blade as a function of cavitation number, again with and without the leading edge correction. The cavity contour plots shown within the figure, which in this case are shown only with the leading edge correction, indicate the difference in cavity patterns with cavitation number . The results corresponding to the cavitation number range of the tests follow the trend of the observations described earlier.

ACKNOWLEDGMENTS

The experimental portion of the work presented here was supported by the Naval Sea Systems Command under the Ships, Subs and Boats Program and was carried out at the David Taylor Naval Ship Research and Development Center. The theoretical work was sponsored by the Navy's General Hydromechanics Research Program, and was carried out at the Massachusetts Institute of Technology.

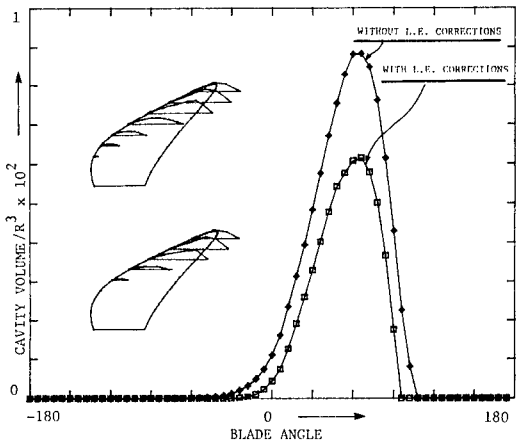


Figure 39 - Cavity Volume per Blade as Predicted from PUF-3 Versus Blade Angle for AO-177 Propeller at $\sigma_n = 3$. The Cavity Plots Correspond to the Maximum Cavity Volume per Blade with (on the bottom) or Without (on the top) the Leading Edge Corrections

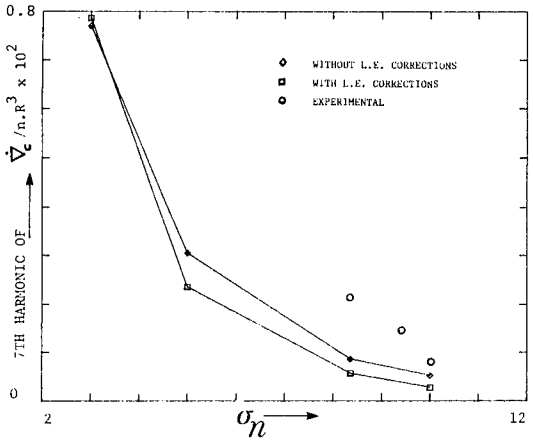


Figure 40 - Seventh Harmonic of the Cavity Volume Velocity Versus σ_n for the AO-177 Propeller

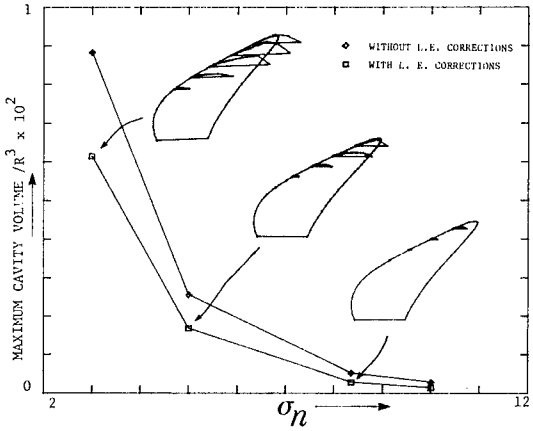


Figure 41 - Maximum Cavity Volume per Blade Versus σ_n for AO-177 Propeller

The authors wish to acknowledge the valuable assistance of Mr. Charles Corrado, graduate student in Ocean Engineering at MIT, who showed remarkable skill and patience in dealing with the complex hydrofoil and propeller codes which lie submerged beneath the results presented here.

The authors also wish to acknowledge the work of Mr. George Gilbert for the detailed design of the force measuring apparatus, and Mr. Steve McQuigan for help with the computer data acquisition and analysis systems.

REFERENCES

Acosta, A. J., "A Note on Partial Cavitation of Flat Plate Hydrofoils," California Institute of Technology Hydrodynamics Laboratory Report No. E-19.9, October 1955.

Bjärne, E., "US Navy Oiler AO 177 Class-Model Tests in SSPA Cavitation Tunnel No. 2," Swedish Maritime Research Centre (SSPA) Report No. 2564-1 (Nov 1980).

Breslin, J. P., et al, "Theoretical and Experimental Propeller-Induced Hull Pressures Arising from Intermittent Blade Cavitation, Loading, and Thickness, Trans. SNAME, Vol. 90 (1982).

Chertock, G., "General Reciprocity Relation," Journal of Acoustical Society of America, Vol. 34, p. 989 (1962).

Chiba, N., and T. Hoshino, "Effect of Unsteady Cavity on Propeller-Induced Hydrodynamic Pressure," Journal of Society of Naval Architects of Japan, Vol. 139 (1976).

Chiba, N., T. Sasajima, and T. Hoshino, "Prediction of Propeller-Induced Fluctuating Pressures and Correlation with Full Scale Data," 13th Symposium on Naval Hydrodynamics, Tokyo (Oct 1980).

Corrado, C., "Investigation of Numerical Schemes for the Evaluation of the Cavitating Flow Around Hydrofoils," Master Thesis, MIT, Department of Ocean Engineering. (To Appear in August 1986).

Denny, S., "Comparisons of Experimentally Determined and Theoretically Predicted Pressures in the Vicinity of a Marine Propeller," NSRDC Report 2349 (May 1967).

des Moutis, E., "Reciprocity Measurements of Dynamic Source Characteristics of Cavitating Propellers Including the Effect of Air Content," M.I.T. Report No. 87620-1 (July 1981).

Dyne, G. and M. Hoekstra, "Propulsion, Cavitation and Propeller-induced Pressure Fluctuations of a Tanker," SNAME Spring Meeting Transactions (June 1976).

English, J., "Cavitation Induced Hull Surface Pressures–Measurements in Water Tunnels," RINA Symposium on Propeller Induced Ship Vibration, London (Dec 1979).

Fitzsimmons, P. A., "Cavitation Induced Hull Pressures: A Comparison of Analytical Results, Ship and Model Measurements," RINA Symposium on Propeller Induced Ship Vibration, London (Dec 1979).

Geurst, J. A. and Timman, R., "Linearized Theory of Two-Dimensional Cavitational Flow Around a Wing Section," IX International Congress of Applied Mechanics, 1956.

Glover, E. J., J. F. Thorn, and L. Hawdon, "Propeller Design or Minimum Hull Excitation," The Naval Architect, pp. 267-275 (Nov. 1979).

Glover, E. J. and G. Patience, "Aspects of the Design and Application of Off-Loaded Tip Propellers," RINA Symposium on Propeller Induced Ship Vibration, London (Dec 1979).

Golden, D. W., "A Numerical Method for Two-Dimensional, Cavitating Lifting Flow," MIT, Department of Ocean Engineering, Report No. 81512-1, May 1975.

Greeley, D. S., "Marine Propeller Blade Tip Flows" Ph.D. Thesis M.I.T., Department of Ocean Engineering (1982).

Gray, L. M., "Investigation intoModelling and Measurement of Propeller Cavitation Source Strength at Blade Rate on Merchant Ships," SNAME Propellers '81 Symposium Virginia Beach (May 1981).

Hadler, J. B., J. W. English, and S. K. Gupta, "Program to Minimize Propeller-Induced Vibration on Converted Maersk 'E' Class Ships," Trans. SNAME, Vol. 92 (1984).

Hampton, G., "Analysis of Wake Survey for Tunnel-Fin and Accelerating Fin Configurations for the Naval Auxiliary Oiler (AO 177) Represented by Model 5326-1," DTNSRDC Departmental Report SPD-0544-18 (April 1981).

Hendrican, A. and K. Remmers, "Powering and Cavitation Performance for a Naval Fleet Oiler, AO-177 Class (Model 5326) and Propeller 4677), DTNSRDC Departmental Report SPD-544-14 (Jan 1976).

Hoshino, T., "A Method to Predict Fluctuating Pressures Induced by a Cavitating Propeller," Mitsubishi Technical Bulletin No. 150 (May 1982).

Hsu, C. C., "Partially Cavitating Flows About Foils," DTNSRDC-86/014 (1986).

Huse, E., "Pressure Fluctuations on the Hull Induced by Cavitating Propellers," Norwegian Ship Model Experimental Tank Publ. No. 111 (March 1972).

Huse, E. and W. Guoqiang, "Cavitation-Induced Excitation Forces on the Hull," Trans. SNAME, Vol. 90 (1982).

Huse, E., "Trykkimpulser fra kaviterende propell," paper presented at Nordisk Skipsteknisk Mote, Abo Finland (1971).

Huse, E., "The Magnitude and Distribution of Propeller-Induced Surface Forces on a Single-Screw Ship Model," Norwegian Ship Model Experimental Tank Publication No. 100 (Dec 1968).

Hylarides, S., "Some Hydrodynamic Considerations of Propeller-Induced Ship Vibrations," Ship Vibration Symposium, SNAME (Oct 1978).

Jacob, W. R., J. Mercier, andS. Tsakonas, "Theory and Measurements of the Propeller-Induced Vibratory Pressure Field," Journal of Ship Research, Vol. 16, No. 2 (1972).

James, R. M., "On the Remarkable Accuracy of the Vortex Lattice Method," Computer Methods in Applied Mechanics and Engineering 2 (1972).

Kaplan, P., J. Bentson, and J. P. Breslin, "Theoretical Analysis of Propeller Radiated Pressure and Blade Forces due to Cavitation," RINA Symposium on Propeller Induced Ship Vibration, London (Dec 1979).

Kaplan, P., J. Bentson, and M. Benatar, "Analytical Prediction of Pressures and Forces on a Ship Hull Due to Cavitating Propellers," 14th ONR Symposium on Naval Hydrodynamics, The University of Michigan (Aug 1982).

Keil, H., "Messung der vom Propeller induzierten Druckschwankingen um Forschungsschiff 'Meteor' und Vergleich mit dem Modellversuch," Vol. 59 pp. 368-377 (1965).

Kerwin, J., S. Lewis, and S. Kobayashi, "Systematic Experiments to Determine the Influence of Skew and Rake on Hull Vibratory Excitation Due to Transient Cavitation," Ship Vibration Symposium, Arlington, VA., SNAME (1978).

Kerwin, J. E., C. S. Lee, "Prediction of Steady and Unsteady Marine Propeller Performance by Numerical Lifting Surface Theory," Transactions SNAME, Vol. 86, (1978).

Kinnas, S. A., "Non-Linear Corrections to the Linear Theory for the Prediction of the Cavitating Flow Around Hydrofoils," PhD Thesis, MIT, May 1985.

Kinnas, S. A., "Cavity Shape Characteristics for Supercavitating Hydrofoils," MIT, Department of Ocean Engineering, Report 84-13, October 1984.

Lan, C. E., "A Quasi-Vortex-Lattice Method in Thin Wing Theory," J. Aircraft, Vol. 11, No. 9.

Larsen, A., "Prediction of Propeller Induced Hull Pressures by Means of a Medium-Size Cavitation Tunnel," Danish Ship Research Laboratory Report (April 1982).

Lee, C. S., "Prediction of Steady and Unsteady Performance of Marine Propellers with or without Cavitation by Numerical Lifting Surface Theory," Ph.D. Thesis, MIT Department of Ocean Engineering, May 1979.

Lewis, F. M., "Propeller Vibration," Trans SNAME, Vol. 43, pp. 252-285 (1935).

Lewis, F. M., "Propeller Vibration," Trans SNAME, Vol. 44, pp. 501-519 (1936).

Lewis, F. M. and A. J. Tachmindji, "Propeller Forces Exciting Hull Vibration," Trans. SNAME Vol. 62 (1954).

Lewis, F. M., and Kerwin, J. E.,"Vibratory Forces on a Simulated Hull Surface Produced by Transient Propeller Cavitation," Journal of Ship Research, Vol. 22, No. 2, June 1978, pp. 89-93.

Lewis, F. M., "Propeller Vibration Forces in Single Screw Ships," Trans. SNAME, Vol. 77 (1969).

Lighthill, M. J., "A New Approach to Thin Aerofoil Theory," The Aeronautical Quarterly 3, November 1951, pp. 193-210.

Lindgren, H. and E. Bjarne, "Ten Years of Research in the SSPA Large Cavitation Tunnel," Stone Manganese Marine/Newcastle University Conference (1979); also SSPA Publication No. 86 (1980).

Lover, E. P. and C. B. Wills, "Cavitation Tunnel Testing for the Royal Navy," Stone Manganese Marine/Newcastle University Conference (1979).

Lovik, A., "Scaling of Propeller Cavitation Noise," Paper D in Noise Sources in Ships I: Propellers, Edited by A. Nilsson and N. Tyvland, Nordforak (1981).

Munk, T., J. Romeling, S. Spangenberg, and C. Aage, "Noise and Pressure Impulses form Cavitating Propellers. A comparative Study on Two Ships in Full Scale and Model Scale," Danish Ship Research Laboratory, Bulletin No. 47 (April 1982).

Nelka, J. J., "Induced Field-Point Pressures of a Ducted Propeller System," Naval Ship Research and Development Center Report 4270 (Oct 1974).

Nelka, J., "Experimental Evaluation of a Series of Skewed Propellers with Forward Rake: Open-Water Performance, Cavitation Performance, Field-Point Pressures, and Unsteady Propeller Loading," NSRDC Report 4113 (July 1974).

Okamoto, Y. and Y. Kasahara, "Experimental and Theoretical Investigations of Hull Pressure Fluctuations Caused by a Cavitating Propeller," Proc. International Symposium on Propeller Cavitation, Wuxi, China (April 1986).

Peck, J. G., "Tunnel Hull Cavitation and Propeller Induced Pressure Investigation," Naval Ship Research and Development Center Departmental Report SPD-597-01 (Nov 1974).

Persson, B., "Theoretical Study of Cavitation on Flat Plate," DnV Technical Report 78/440 (1978).

Pohl, K., "Die durch eine Schiffschraube auf benachbarten Platten erzeugten periodischen hydrodynamischen Drucke," (in German) Schiffstechnik Vol. 7, No. 35, pp 5-18 (1960).

Reed, F. E., N. L. Basset, and J. A. Norton, "Effects of Hull and Propeller Design Changes on the Vibration of a Lakes Freighter," Trans. SNAME, Vol. 89 (1981).

Sasajima, T., "Application of Noise Measurements for Studying Unsteady Cavitation in Cavitation Tunnel," Proc. ASME Symposium on Cavitation Noise, Phoenix (1982).

Skaar, K. and A. Raestad, "The Relative Importance of Ship Vibration Excitation Forces," RINA Symposium on Propeller Induced Ship Vibration, London (Dec 1979).

Steenhoek, H. F. and T. Ten Wolde, "The Reciprocal Measurement of Mechanical-Acoustical Transfer Functions," ACUSTICA, Vol. 23, No. 5, pp. 301-305 (Nov 1970).

Stuntz, G. R., et al., "Series 60 - The effect of Variations in the Afterbody Shape Upon Resistance, Power, Wake Distribution, and Propeller Excited Vibratory Forces," Trans SNAME, Vol. 68 (1960).

Tulin, M. P. and Hsu, C. C., "The Theory of Leading-Edge Cavitation on Lifting Surfaces with Thickness," Symposium on Hydrodynamics of Ship and Offshore Propulsion Systems, March 1977.

Tachmindji, A. J. and M. C. Dickerson, "The Measurement of Oscillating Pressures in the Vicinity of Propellers," DTNSRDC Report No. 1130 (Apr 1957).

Tachmindji, A. J. and M. C. Dickerson, "The Measurement of Thrust Fluctuation and Free Space Oscillating Pressures for a Propeller," DTNSRDC Report No. 1107 (Jan 1957).

Takahashi, H. and T. Ueda, "An Experimental Investigation into the Effect of Cavitation on Fluctuating Pressures Around a Marine Propeller," Proceedings 12th I.T.T.C., Rome (1969).

Takahashi, H., "A Consideration on the Effect of the Propeller Cavitation upon the Surface Force," (in Japanese), Trans. of West-Japan Society of Naval Architects, No. 49 (1975).

Takekuma, K., "Effect of Air Bubbles Entrained from Bow on Propeller-Induced Pressure fluctuation," Mitsubishi Technical Bulletin No. 140 (June 1980); (see also RINA Symposium on Propeller Induced Ship Vibration, London 1979).

Taniguchi, K., "On the Pressure Fluctuation in the Vicinity of Propellers," (in Japanese), Journ of Society of Naval Architects of West-Japan, No. 16 (1958).

Taniguchi, K. and K. Ohtaka, "Measurements of the Propeller-Induced Vibratory Forces on a Destroyer," Journ. of Society of Naval Architects of Japan, Vol. 114, pp. 138-147 (1963).

Ten Wolde, T. and A. de Bruijn, "A New Method for Measurement of the Acoustical Source Strength of Cavitating Ship Propellers," International Shipbuilding Progress, Vol. 22, No. 25 (Nov 1975).

Uhlman, J. S., "The Surface Singularity Method Applied to Partially Cavitating Hydrofoils," Ph.D. Thesis, MIT, Department of Ocean Engineering, January 1983.

Valentine, D. T. and A. Chase, "Highly Skewed Propeller Design for a Naval Auxiliary Oiler (AO 177)," DTNSRDC Departmental Report SPD-544-12 (Sept 1976).

van der Kooij, J. and A. Jonk, "Propeller-Induced Hydrodynamic Hull Forces on a Great Lakes Bulk Carrier. Results of Model Tests and Full Scale Measurements," Symposium on High Powered Propulsion of Large Ships, NSMB Publication No. 490, Part 2 (Dec 1974).

van der Kooij, J., "Experimental Determination of Propeller-Induced Hydrodynamic Hull Forces in the NSNB Depressurized Towing Tank," RINA Symposium on Propeller Induced Ship Vibration, London (Dec 1979).

Van Houten, R. J., "The Numerical Prediction of Unsteady Sheet Cavitation on High Aspect Ratio Hydrofoils," Fourteenth Symposium on Naval Hydrodynamics (1982).

Van Houten, R. J., J. E. Kerwin, J. S. Uhlman, "Numerical Solutions of Lifting Surface Sheet Cavitation. A Review of Research at MIT." American Towing Tank Conference (ATTC), August 1983, Davidson Laboratory, Stevens Institute of Technology, Hoboken, New Jersey.

van Manen, J. D., "The Effect of Cavitation on the Interaction Between Propeller and Ship's Hull, "International Shipbuilding Progress, Vol. 19, No. 209 (Jan 1972).

van Oossanen, P. and J. van der Kooij, "Vibratory Hull Forces Induced by Cavitating Propellers," Trans. RINA (1973)'

Vorus, W. S., "An Analysis of the Vibratory Excitation of a Naval Ship with Variation of Blade Tip to Hull Clearance," Vorus and Associates, Inc. Report No. 84-004 (Sept 1984).

Weitendorf, E., "Cavitation and Its Influence on Induced Hull

Pressure Amplitudes," Symposium on Hydrodynamics of Ship and Offshore Propulsion Systems, Oslo Norway (March 1977)
Weitendorf, E-A., "Experimental Investigations of the Periodic Pressure Variations Produced by Propellers on the Outer Skin," Schiff und Hafen, Vol. 22, No. 1 pp. 11-22 (1970).
Weitendorf, E-A., "Vergleich von propellererregten Druckschwankungen fur Modell and Grossausfuhrung am Beispiel des Frachtschiffes MS 'Hornmeer'" Schif und Hafen, Vol. 25, Part 5, pp. 423-428 (May 1973)
Weitendorf, E-A., "Experimentalle Untersuchungen der durch kavitierende Propeller erzeugten Druckschwankungen," (Experimental investigations on the pressure fluctuations caused by cavitating propeller), Schiff und Hafen, Vol. 25, Part 11 (Nov 1973).
Whalen, M., R. J. Van Houten, and J. E. Kerwin, "A Calibration Procedure to Enable the Derivation of Propeller Cavity Volume from Water Tunnel Measurements," Draft of M.I.T. Ocean Engineering Report to SNAME Purchase Order 6317 (May 1982).
Whalen, M., J. E. Kerwin, and R. J. Van Houten, "Experimental Determination of the Influence of Tip Clearance on Unsteady Propeller Cavitation," M.I.T. Department of Ocean Engineering Report 82-6 (May 1982).
Wilson, M. B. et al., "Causes and Corrections for Propeller-Excited Airborne Noise on a Naval Auxiliary Oiler," Trans. SNAME, Vol. 90 (1982).
Wilson, M. B. and G. A. Hampton, "Measurements of the Effect of Trim on the Nominal Wake of the Naval Auxiliary Oiler AO-177," DTNSRDC SPD-0544-19 (March 1981).

APPENDIX A

RECIPROCITY CONCEPT AND APPLICATION

The reciprocity principle states that for a linear system, there is a reciprocal relationship between the force applied and the system response at any two points. That is, the system vibration velocity response v, say, at a point due to a force applied at point 2 is the same as the response at point 2 due to a force at point 1. Thus,

$$\frac{v_1}{F_2} = \frac{v_2}{F_1} \tag{39}$$

or

$$v_1 F_1 = v_2 F_2 \tag{40}$$

For the assumed linear system, the resulting flow of power monitored at the check points can be expressed in terms of other conjugate variables, for example, volume velocity $\dot{\nabla}$ times fluid acoustic pressure p.

Then

$$\dot{\nabla}_1 p_1 = F_2 v_2 \tag{41}$$

Figure 42 provides a definition sketch and outline for the experiments needed to make the reciprocity calibration and to provide one of several interpretations of the expression given above.

For the calibration phase, a mechanical shaker can be used to provide an input force at point 2 on a body surface element (or within the hull of a complete body). The fluid pressure is measured simultaneously at point 1 in the propeller plane where the center of the unsteady cavity volume is expected to occur. A transfer function is formed as the ratio (F_2/p_1) and this remains a property of the system. Then the measurement of vibration velocity v_2 is made at point 2 in the same direction as the calibration drive force, with the cavitating propeller running as the system excitation. The volume velocity of the cavity at point 1 is thus obtained as

$$\dot{\nabla}_1 = (\frac{F_2}{p_1}) v_2 \tag{42}$$

For harmonic oscillations of the system, the acceleration at point 2 in the same direction as the velocity v_2 is

$$a_2 = i\omega v_2 \tag{43}$$

Thus, another version of the basic reciprocity relationship is expressed as

$$\dot{\nabla}_1 = \frac{F_2 a_2}{i\omega p_1} \tag{44}$$

Note that the variables measured for the calibration and final measurement phases can be rearranged for convenience. For example, suppose that during the calibration phase the acceleration a_2 at the drive point is measured as well as the corresponding fluid pressure p_1 . In this case, the appropriate transfer function is the ratio (p_1/a_2). The the run measurement of F_2 (in the same direction as the calibrating drive acceleration) leads to the determination of the cavity volume velocity $\dot{\nabla}_1$ from equation(44). In either of the forms, the calibrated transfer function is a complex function of the real-valued frequency ω. The other measured quantities involved must also be treated as complex.

The basic form of the simplified reciprocity relationship of (42) or (44) can be derived in a formal way using the second Green theorem following concepts discussed by Chertock(1962).

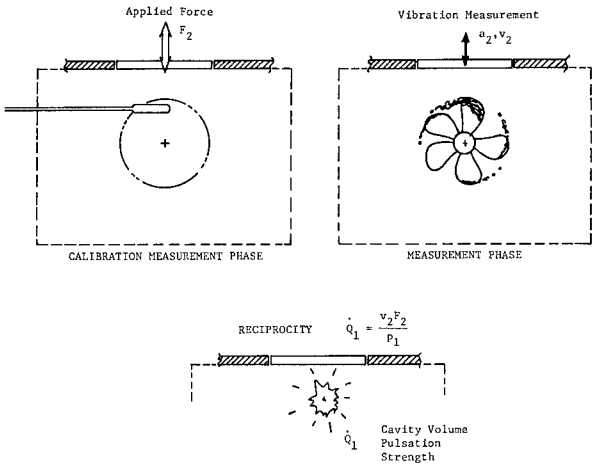


Figure 42 - Schematic of the Measurement of Cavity Volume Velocity by Reciprocal Method

APPENDIX B

Linear Solution for a Flat Plate

In the case of a fully-wetted flow around a flat plate at an angle of attack α,

$$u_w^+ = \frac{\gamma_w(x)}{2} = U_\infty \alpha \sqrt{\frac{1-x}{x}} = \frac{U_\infty \alpha}{z} \tag{45}$$

By substituting (45) in (19), (22) and (23), we obtain the following expressions,

$$\sigma = 2\alpha s \frac{r^2+1}{r^2-1} \tag{46}$$

$$q(z) = \sigma U_\infty \frac{M - Nz}{\sqrt{z(s-z)}}; \qquad z < s \tag{47}$$

$$\gamma(z) = \sigma U_\infty \frac{M + Nz}{\sqrt{z(s+z)}}; \qquad z < s \tag{48}$$

$$\gamma(z) = \sigma U_\infty \frac{M + Nz}{\sqrt{z(s+z)}} + \sigma U_\infty \frac{M - Nz}{\sqrt{z(z-s)}}; \qquad z > s \tag{49}$$

where M and N are

$$M = \frac{1}{\sqrt{2}}\left[\frac{\alpha}{\sigma}\sqrt{r^2+1} + \frac{1}{2}\sqrt{r^2-1}\right] \tag{50}$$

$$N = \frac{1}{\sqrt{2}}\left[-\frac{\alpha}{\sigma}\sqrt{r^2-1} + \frac{1}{2}\sqrt{r^2+1}\right] \tag{51}$$

These results agree with those published previously by Guerst and Timman(1956), Acosta(1955) and Persson(1978) , but are obtained more directly with the present formulation.

APPENDIX C

The Nature of the Singularities at the Leading Edge

The asymptotic behavior of $q(z)$ at $z = 0$ can be determined from (22)

$$q(z) \sim -\frac{1}{\pi}\frac{1}{\sqrt{zs}}\int_0^s \frac{F(\eta)}{\eta}d\eta \qquad as \quad z \to 0 \tag{52}$$

Similarly, the behavior of $\gamma(z)$ near the leading edge can be obtained from (23)

$$\gamma(z) \sim -\frac{k}{z} - \frac{1}{\pi}\frac{1}{\sqrt{zs}}\int_o^s \frac{F(\eta)}{\eta}d\eta - u_w^+(z) + \gamma_w(z)$$

$$as \quad z \to 0 \tag{53}$$

where k is defined as the coefficient in the following asymptotic behavior of the function $F(z)$

$$F(z) \sim \frac{k\sqrt{s}}{\sqrt{z}} \qquad as \quad z \to 0 \tag{54}$$

In the case of linear theory

$$\frac{k}{z} \sim u_w^+(z) \qquad and \qquad \gamma_w(z) = 2u_w^+(z) \tag{55}$$

Therefore,

$$\gamma(z) \sim -\frac{1}{\pi}\frac{1}{\sqrt{zs}}\int_0^s \frac{F(\eta)}{\eta}d\eta \qquad as z \to 0 \tag{56}$$

From (52), (56) and (17) we conclude that

$$q(x) \sim \gamma(x) \sim \frac{const}{x^{1/4}} \qquad as \quad x \to 0 \tag{57}$$

When the leading-edge correction is applied to linear theory, $q(z)$ and $\gamma(z)$ will be given by (22) and (23). In this case u_w^+ must be replaced by

$$u_w^+ - U_\infty\sqrt{1+\sigma}\left[\sqrt{\frac{x+\frac{\rho_L}{2}}{x}} - 1\right],$$

which, when incorpotated in (53) will give the result

$$\gamma(x) \sim 2U_\infty\sqrt{1+\sigma}\frac{\sqrt{\rho_L/2}}{x^{1/2}} + \frac{const}{x^{1/4}} \qquad as x \to 0 \tag{58}$$

$$q(x) \sim \frac{const}{x^{1/4}} \qquad as \quad x \to 0 \tag{59}$$

DISCUSSION

Fred Stern,
Iowa Institute of Hydraulic Research

My discussion is primarily concerned with the second part of the paper in which progress in the development of procedures at MIT for predicting unsteady propeller sheet cavitation are described. The areas of progress are the incorporation of a nonlinear leading-edge correction the their linear propeller/cavity theory and other improved numerical treatments. These improvements are shown to lead to a reduction in the predicted cavity volume variation for the application of the AO-177 propeller. Since the overall method is known to over-predict the extent of cavitation such improvements should be helpful; however, it appears to me that even with the leading-edge correction the predicted cavity volume is still too large. Figure 39 indicates a maximum cavity volume of about 6 cubic feet. This is indeed a very large cavity.

My own prediction for the AO-177 propeller (see figure 7 and the relevant discussion in [a] for further details) indicates a maximum cavity volume of about 2.2 cubic feet (for the without fin condition); i.e., about half the MIT value. Although both the radial and chordwise extent of cavitation compared well with the model, full-scale observations of the cavities appeared to be too thick (also, see discussion of Stern, 1982 by Dr. M. Wilson). A large part of the over-prediction of cavity thickness was attributed to difficulties in predicting the effective wake. Undoubtedly, a part of the cause of the over-prediction of the MIT method can also be attributed to effective wake; however, it seems to me that linear propeller/cavity theory even with leading-edge corrections tends to over-predict the extent of cavitation.

Another very important aspect of unsteady cavitation for which linear theory is suspect is in predicting the cavity dynamics. Although insufficient information is given in the present paper to judge the performance of the MIT method in this regard. Lastly, with regard to the experimental program I would like to stress the importance of developing procedures for measuring cavity volumes (radial and chordwise extent as well as thickness) and volume velocities. Such measurements are clearly imperative for validating cavity prediction methods.

[a] Stern, F., (1982), "Comparison of Computational and Experimental Unsteady Cavitation," Proc. 14th ONR Symp. on Naval Hydrodynamics, Ann Arbor, MI, pp. 613-652.

Reply -

Regarding the comparison of the results of our method to those of Dr. Stern, we would like to point out that the wake input data are not exactly the same. Our results have been obtained by using the experimental wake data shown in the first part of the paper. The purpose of those experiments was to simulate the wake field behind the full-scale ship. However, small differences between the experimental and the actual wake velocities could result in different cavity patterns, especially close to the "twelve o'clock" position, where the cavity volume is expected to be maximum.

The incorporation of the leading edge corrections in the linear theory for the prediction of the flow around cavitating hydrofoils has been shown by Kinnas (1985) to be necessary as well as adequate in order to predict correctly the nonlinear blade thickness effects on cavitation. The results for a two-dimensional hydrofoil using linear cavity theory and including the leading edge corrections, agree quite well with those predicted by numerical nonlinear theory, Uhlman (1983), in which the exact dynamic boundary condition is applied on the exact cavity surface.

Therefore, we believe that our present numerical method for the prediction of the unsteady propeller sheet cavitation with the leading edge corrections included, is adequate as well as efficient for propeller applications.

Dr. Stern has questioned the capability of the present theory to predict cavity dynamics. As shown in Breslin et al. (1982) our propeller code incorporates the exact linearized unsteady three-dimensional dynamic boundary condition on the cavity. As a result, typical cavity volume time histories exhibit a slow growth and rapid collapse, as shown for example in Figure 39. A quasi-steady cavity theory would not show this tendancy.

Finally, we would like to thank Dr. Stern for his suggestions on further experimental investigations and comparisons with the analytical predictions.

H. Mauro,
Yokohama National University

I appreciate such a elaborate analysis of the complicated problem of unsteady cavitation propeller. I should like to make two points:

1. The authors have employed the closure condition of the cavity given by eq. (15). However there are several examples of comparison between computation and measurement of the cavity shape of cavitating hydrofoil. According to these results, the closure condition of eq. (15) is not adequate. This conclusion may be legitimized by the existence of strong wake behind the cavity.

2. The authors have extended the theory of steady cavitation to the unsteady problem. However the cavity repeats the generation, growth and collapsing in the case of unsteady cavitating propeller. Then the cavity mechanics, which is more a physical problem, seems to be important in order to estimate the duration of cavity.

Reply -

First, we would like to thank Professor Maruo for his kind comments on our paper.

With regard to his first point, we agree that the cavity closure condition is very important for the prediction of the cavity characteristics. Furthermore, we believe that the most accurate model is one that can take into consideration the turbulent flow behind the cavity.

To treat the cavitating hydrofoil problem by using a direct viscous flow solution would be hopeless. How-

ever, we can still use an inviscid open cavity model where the openness of the cavity is provided from the global characteristics of the boundary layer behind the cavity. This on the other hand, requires further both analytical and experimental investigation.

In our analysis we decided to consider a closed cavity model which is consistent with the linear cavity theory incorporating a Riaboushinsky or a reentrant jet cavity closure model. We believe, however that there is still room for improvement towards an open cavity model. This is something we are currently investigating and we hope to include it in our propeller code in the near future.

With respect to the second point, it has been shown by Van Houten and al. (1982) that the cavity gas dynamics are not very important for the prediction of unsteady cavities. We also refer Professor Maruo to the last part of our reply to Dr. Stern's discussion.

Neal A. Brown,
Atlantic Applied Research Corporation

The authors need not apologize for the roughness of their reciprocal calibration on frequency. Indeed I am suspicious of the smoothness of the result at the higher frequencies. I would have expected an increasing amount of fluctuation in the p/a ratio with increasing frequency.

Roughness in frequency response is the way of the world, and all the mass in Carderock will not make the tunnel structure rigid nor make the extent of the contained water infinite. The solution may be, I submit, in less, rather than more, precision. By this I mean averaging, both in frequency and in space, through bandwidth and by varying the hydrophone position over the extent of the cavity. A measure of "dither" in the propeller revolution rate would then be appropriate in the measurement in order to match the signal bandwidth to that of the transfer gain.

As a confirmed pusher of reciprocal techniques I remind the authors that the accelerometer measurement is unnecessary. The elecrical parameters of the piezoelectric force transducers can be involved simply in a reciprocal relationship:

$$\frac{p}{i} = \frac{V}{q}$$

where:
i is the current through the force transducer when driven as a source, producing
p, the hydrophone sensed pressure, and
V is the open circuit voltage produced by the force transducer when the plate is subjected to the pressure field produced by
q, the volume flux.

With regard to math-modeling, the authors' analytical correction of the cavity thickness overestimation is brilliant. I feel it demonstrates the value of the analysis with computation in contrast to pure computing. The authors should not be too concerned, however, with the mathematical niceties of cavity closure as any observer will agree that the closure of real cavities is a mass of froth unlike anyone's mathematics.

Reply -

Regarding the reciprocity calibration transfer function, the function displayed in Figure 5 of the paper is a composite of three separate transfer function curves derived from three separate blocks of data. It shows basically the envelope of the variation. Above about 300 Hz, the three results collapse onto the same curve, and the result does indeed tend to level out to a relatively flat curve as noted. The reciprocity calibration obtained by Whalen, Van Houten, and Kerwin (1982) shows very similar behavior in the higher frequency region. It is a bit of a surprise to find out that this relative flatness is not expected in the higher frequency range. We would expect different levels of the curve for different positions of the pressure transducer. Averaging over several positions of the pressure pickup should be carried out to account (at least) for the approximate region of cavity extent in the propeller disc. The suggestions by Dr. Brown for introducing averaging in both frequency and space are interesting and welcome. We hope to try some of these ideas when we get back to these experiments again.

We thank Dr. Brown for the reminder about the use of the electrical parameters of the force transducer in the reciprocal relationship used to determine volume velocity. Certain simple scaling factors still must be applied to make the result dimensionally correct. These factors need to be stated separately. It is satisfying to display the reciprocity result in a form that can be easily understood and can be checked dimensionally and arithmetrically by a reader. It seems that a common and confusing feature of most every presentation of a reciprocal experimental result is either the complete absence of the transfer function or the lack of a complete description of the scaling factors that make it useable.

Hyoung-Tae Kim,
Iowa Institute of Hydraulic Research

In the paper the largest unsteady pressures at very low cavitation numbers are associated with the cavity-collapse portion of the volume variation. However, at intermediate values of cavitation number, the location of the peak blade rate pressure amplitude is apparently influenced most by the effect of tip proximity, and occurs at or near the position of closest approach of the blade tip.

Would you explain what you mean by the effect of tip proximity? And is it true that at this cavitation number, collapse is not important?

Reply -

In the discussion, the effet of tip proximity simply means the influence of distance from the blade tip to the nearby boundary surface. This distance is a minimum when the blade tip passes through the centerline. In the complete absence of an unsteady cavity, the location of the induced surface pressure peak will be dictated by the various phase angles of the doublet-like displacement effect due to blade thickness plus the blade loading effect. Unsteady cavity effects become gradually more important as the amount of cavitation increases. Apparently in the present case, at the moderate cavitation numbers tested, the cavity collapse effect

is present to some degree and is important (see Figure 11), but its phase angle influence is mixed in with the thickness/displacement and blade loading effects in such a way that the peak in the pressure amplitude is roughly centered. It should be noted that at the moderate cavitation numbers of these tests, the blade cavities were observed to be roughly centered circumferentially about the centerplane of the screen-generated wake peak of the tunnel flow.

At much lower cavitation numbers and relatively much more cavitation volume, we expect that the cavity collapse location to become more skewed to the right and to lead to more unsymmetrical pressure amplitude contours.

Two Dimensional Transient Motions with Large Amplitude by Time Domain Method

Y. J. KIM & J. H. HWANG

Seoul National University, Korea

ABSTRACT

In the present work, a two-dimensional large amplitude motion is treated as an initial value problem by satisfying the exact body boundary condition and the linear free surface condition. The present numerical scheme is similar to that described by Chapman(15)[1]. To remove the so-called irregular frequency effect, an artificial lid is placed on the inner free surface of the floating body.

The numerical calcultions are performed for the following problems,

- .Transient waves generated by a wave maker
- .Translation with uniform speed ($U\neq0$, $\omega=0$)
- .Forced harmonic large-amplitude oscillation ($U=0$, $\omega\neq0$)
- .Forced harmonic large-amplitude oscillation with forword speed ($U\neq0$, $\omega\neq0$)

The results are compared with available experimental and analytical results. Generally good agreements are observed.

NOMENCLATURE

A	motion amplitude of body
$A(t,k_n)$	complex function in spectral representation of free surface elevation, Eq.(17) and Eq.(19)
A^*	amplitude of wave-maker motion at y=0
$B(t,k_n)$	complex function in spectral representation of wave potential, Eq.(18) and Eq.(20)
$F(t),F$	hydrodynamic force
F_h	depth Froude number, $U/\sqrt{gh}$
F_{na}	n-th harmonic force amplitude, Eq.(28), n=1, 2, 3,....
F_{nc},F_{ns}	n-th harmonic force components in phase with body velocity and body acceleration respectively, Eq.(28), n=1, 2, 3,....
F_r	Froude number, $U/\sqrt{gr}$
F_t	total hydrodynamic force, $F_\phi+F_v$
F_v	velocity-square force, obtained by integrating P_v
F_o	time-mean force, Eq.(28)
F_ϕ	potential-time-derivative force, obained by integrating P_ϕ
g	acceleration of gravity
$G(p;q)$	Green function, Eq.(13)
h	depth of submergence
$I(t',k)$	complex body-influence function, Eq.(9)
$I^*(\underline{t},k_n)$	mean value of $I(t',k_n)$ during Δt, Eq.(21)-Eq.(23)
k	wave number
k_n	discretized wave number, Eq.(15) and Eq.(16), n=1,2,...,n_w
ℓ	minimum half-length of component wave
L_m	maximum range of computational region from x=0
$\vec{n}$	unit normal vector
n_w	total number of discrete wave components
N_t	total number of body segments
(o,x,y)	coordinate system fixed in space, Fig.1
$p,(x,y)$	field point
P	pressure, Eq.(24)
P_t	total hydrodynamic pressure, $P_\phi+P_v$
P_v	velocity-square pressure, second term of Eq.(24)
P_ϕ	potential-time-derivative pressure, first term in Eq.(24)
$q,(x',y')$	source point
r	radius of circular cylinder
S_b	wetted surface of body
t_n	time of n-th computation step
T	period of body motion
T_m	desired terminal computation-time
T_o	oscillation period of hydrodynamic force, Eq.(26)
U	horizontal translation speed of body
$U^*(y,t)$	horizontal velocity of wave-maker motion, Eq.(25)
$\vec{V}$	velocity vector of body motion
Vg	wave group velocity
δ_n	phase angle of n-th harmonic component force, Eq.(28), n=1, 2, 3,...
Δt	time step size
ε	nondimensional amplitude of body motion, A/r
$\eta(x;t)$	free surface elevation, positive upward, Fig.1
ρ	density of fluid
$\sigma(q)$	source strength

Y.J.Kim*,J.H.Hwang;Seoul National Univ.,Naval Arch. Dept.,Kwanak-Ku,Seoul 151,Korea

*Present address;National Fisheries Univ. of Busan,Naval Arch. Dept.,Nam-ku,Pusan 608,Korea

[1] Underlined numbers designate References at end of paper.

$\sigma_m(t+\Delta t/2)$ uniform source-strength on m-th body segment at time $t+\Delta t/2$
τ speed-frequency parameter, $U\omega/g$
$\phi(x,y;t)$ velocity potential, Eq.(6), $\phi_b+\phi_w$
ϕ_b body potential, Eq.(7) and Eq.(8)
ϕ_w wave potential, Eq.(10)
ω circular frequency, $\omega^2=gk$
ω_n discretized circular frequency, $\omega_n^2=gk_n$

1. INTRODUCTION

There are largely two approaches in treating ship motion problems: a frequency-domain approach and a time-domain approach. The former approach is based on the perturbation method. The linear frequency-domain approach has been successfully applied to many practical engineering problems. There are also the researches using the second-order perturbation method in frequency domain(1-5). The researches have made valuable contributions to the understanding of various nonlinear effects. However, in this approach the body boundary condition is imposed on the mean body surface even in the higher order theories. Therefore, this approach has a restriction in the application to a motion problem with very large motion amplitude. Another disadvantage of this approach is that one can not handle a general time-depenent problems frequently occurring in a typical ship maneuvering problem. The above two restrictions can be overcome by taking the time-domain approach.

As an earlier time-domain analysis, Cummins(6) formulated the motion problem in the time-domain using an impulse response function. This approach was extended by Ogilvie(7) and Wehausen(8). The semi-Lagrangian time-stepping method seems to be one of the more general methods which can treat the free surface and the body boundary conditions exactly at every instance. This method was first introduced by Longuet-Higgins and Cokelet(9) for a breaking wave problem. Later this has been extended to wave-body interaction problems by Faltinsen(10), Vinje and Brevig(11), Vinje, Maogang, and Brevig(12), Lin, Newman,and Yue(13), Greenhow and Lin(14). This method seems to be the most complete numerical method employed so far for the exact nonlinear free-surface flow problem. However, this scheme takes very much computation time in the numerical computation.

The major sources of the nonlinearities in the free-surface flow problem are the free surface and the body boundary conditions. There can be still another type of formualtion which is an intermediate level. That is, the body boundary condition is satisfied exactly at the instantaneous position while the free surface boundary condition is linearized. This type of approach can be justified only when the generated free surface waves are small. An appropriate physical model may be the case when the amplitude of the body motion is very large, but the frequency of the body motion is low and/or the depth of submergence is large. In this approach, a method of spectral free-surface representation with simple source distribution on the body surface can be employed. This method was first used by Chapman(15,16). Loeser, Yue,and Salvesen(17) also discussed this approach applied to the ship motion analysis. The major advantage in this approach is that the computation time is quite reduced compared to the complete numerical method without losing the accuracy when an appropriate physical model is justified.

In the present paper, we follow closely the method used by Chapman(15). However, some modifications are made to the method of Chapman. Specifically, an artificial lid has been introduced on the free surface interior to the body to remove the effect of the inner flow. This remedy has been successfully used previously in frequency-domain approach. Some computational improvements also have been made. As applications of the present method, computations are made for four typical types of free surface problems: a wave-maker problem, a wave resistance problem of a submerged circular cylinder, a large amplitude motion of a floating circular cylinder, and a large amplitude motion of a submerged circular cylinder with forward speed. For a large amplitude motion of a floating cylinder, the computed nonlinear hydrodynamic quantities are compared with those obtained by the frequency-domain approach. For an oscillating and translating circular cylinder, Yamamoto(18) and Park(19) made computations in a linear frequency-domain approach. In this type of a problem there exists an interaction effect between the disturbed steady flow and the oscillatory body motion, as indicated by Timman and Newman(20). However, in the computations in the previous frequency-domain researchs quoted here, this interaction effect was not considered. In the present paper, the interaction term is also computed. It is also of interest to note that the results of hydrodynamic force in our computations show a smooth transition in the neighborhood of the parameter $\tau=0.25$, while the previously computed results show an abrupt change at this value.

2. OUTLINE OF THE MATHEMATICAL FORMULATION AND NUMERICAL METHOD

The present approach is similar to that used in Chapman(15). However, an important modification is made to remove the inner flow effect in a floating body motion and some computational improvements are made. Since more details can be found in the references(15,21), we will give a brief description here.

The coordinate system is fixed in space with the x-axis along the undisturbed waterline and y-axis positive downward as shown in Fig.1. The free surface elevation η is defined positive upward.

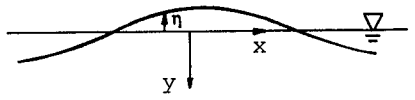


Fig.1 Coordinate System

The fluid is assumed to be inviscid and incompressible, with its motion irrotational. The free surface boundary condition is linear-

ized for the spectral representation of free surface. The spectral technique is more efficient to represent the free surface in the numerical computation compared to the other time-domain methods. The present method has a restriction in the application to a large wave problem due to the linearization of the free-surface boundary condition. On the other hand, there is no restriction on the body motion since the body boundary condition is satisfied exactly at the instantaneous position. Introducing velocity potential Φ , the time-dependent boundary value problem to be treated can be written as

$$\nabla^2\Phi = 0 \qquad y\geq 0,\ t\geq 0 \qquad (1)$$

$$\eta = -\frac{1}{g}\frac{\partial\Phi}{\partial t} \qquad y=0,\ t\geq 0 \qquad (2)$$

$$\frac{\partial\eta}{\partial t} = -\frac{\partial\Phi}{\partial y} \qquad y=0,\ t\geq 0 \qquad (3)$$

$$\frac{\partial\Phi}{\partial n} = \vec{V}\cdot\vec{n} \qquad \text{at the instantaneous body surface, } t\geq 0 \qquad (4)$$

$$\Phi = \frac{\partial\Phi}{\partial t} = 0 \qquad y\geq 0,\ t<0, \qquad (5)$$

with an appropriate infinity condition. Here g denotes the gravitational acceleration, $\vec{n}$ unit normal vector into the fluid, $\vec{V}$ velocity vector of the body motion.

In the present method, the velocity potential Φ is devided into two parts as

$$\Phi = \phi_b + \phi_w \ , \qquad (6)$$

where, the body potential ϕ_b represents the instantaneous effect of the body, and the wave potential ϕ_w represents the wave field. The body potential ϕ_b satisfies the following boundary conditions.

$$\phi_b = 0 \qquad y=0,\ t\geq 0 \qquad (7)$$

$$\frac{\partial\phi_b}{\partial n} = -\frac{\partial\phi_w}{\partial n} + \vec{V}\cdot\vec{n} \qquad \text{at the instantaneous body surface, } t\geq 0 \qquad (8)$$

From Eq.(7) ϕ_b is skew symmetric with respect to y=0 and induces a normal velocity on the x-axis. We introduce a form of the Fourier integral for the upward normal velocity on the free surface(y=0) as follows,

$$-\left(\frac{\partial\phi_b}{\partial y}\right)_{y=0} = \int_0^\infty I(t',k)\ e^{ikx}\,dk \qquad (9)$$

where, the body-influence function I(t',k) is complex. Throughout the paper, only the real part is taken in the right-hand side of Eq.(9) and of similar expressions. Integrating the disturbance of Eq.(9) we obtain the following expressions for the wave elevation η and the wave potential ϕ_w (21).

$$\phi_w = -\int_0^t dt' \int_0^\infty dk\,\frac{g}{\omega}\ I(t',k)\ \sin\omega(t-t')\cdot e^{k(ix-y)} \qquad (10)$$

$$\eta = \int_0^t dt' \int_0^\infty dk\ I(t',k)\ \cos\omega(t-t')\cdot e^{ikx} \qquad (11)$$

where, $\omega^2=gk$. The above expressions are obtained by a similar approach in the Cauchy Poisson problem(22). In the solution procedures for the velocity potential Φ , a method of integral equation is employed in solving for ϕ_b , whereas a spectral method is utilized in the computation for ϕ_w . The solution procedures are described below.

The body potential ϕ_b can be represented by distributing simple sources on the body surface and its negative image as follows,

$$\phi_b(p) = \frac{1}{2\pi}\int_{S_b}\sigma(q)\ G(p;q)\ ds(q) \qquad (12)$$

where,

$$G(x,y;x',y') = \frac{1}{2}\log[(x-x')^2+(y-y')^2] - \frac{1}{2}\log[(x-x')^2+(y+y')^2]. \qquad (13)$$

Here, S_b represents the body surface, p and q are the field point and the source point, respectively. The strength σ of the distributed sources is obtained by solving the Fredholm integral equation of the 2nd kind given as

$$\frac{\partial\phi_b}{\partial n_p} = \frac{\sigma(p)}{2} + \frac{1}{2\pi}\int_{S_b}\sigma(q)\ \frac{\partial G(p;q)}{\partial n_p}\,ds(q) = -\frac{\partial\phi_w}{\partial n_p} + \vec{V}\cdot\vec{n}_p, \qquad (14)$$

Here, $\partial\phi_w/\partial n_p$ is assumed to be known. In the computation, it is obtained from the computed values of ϕ_w to be described later. In the numerical calculation the body is represented by a set of N_t straight segments and σ is assumed to be constant in each segment. The integral equation, Eq.(14), is solved at each time step.

In the numerical calculation for ϕ_w , a discretizing procedure of wave numbers is closely related to the interested range of space and time in the computation(15). Let L_m be the maximum distance from x=0 reached by the disturbances generated by the body. Then the following condition for wave number spacing should be satisfied.

$$k_{n+1} - k_n \leq \frac{\pi}{L_m} \qquad (15)$$

Here, the computational region is assumed to be $|x|\leq L_m$. Similarly, if the desired terminal computation-time is T_m , the following condition should be satisfied.

$$\sqrt{gk_{n+1}} - \sqrt{gk_n} \leq \frac{\pi}{T_m} \qquad (16)$$

To satisfy the above two conditions simultaneously, discretization should be made by the equation which gives smaller spacing. In the computation, the equal signs in the above equations are taken and the generated wave numbers are truncated at a predetermined value.

Once the discretized wave numbers are chosen, η and ϕ_w in Eq.(11) and Eq.(10) can be represented as follows.

$$\eta = \sum_{n=1}^{n_w}\Delta k_n\ A(t,k_n)\ e^{ik_nx} \qquad (17)$$

$$\phi_w = -\sum_{n=1}^{n_w}\Delta k_n\frac{g}{\omega_n}\ B(t,k_n)\ e^{k_n(ix-y)} \qquad (18)$$

where,

$$A(t,k_n) = \int_0^t I(t',k_n)\ \cos\omega_n(t-t')\,dt' \qquad (19)$$

$$B(t,k_n) = \int_0^t I(t',k_n)\ \sin\omega_n(t-t')\ dt' \quad (20)$$

Here n_w is the total number of wave components, and $\omega_n^2 = gk_n$. For time-stepping procedure, we can derive the following relations from Eq.(19) and Eq.(20) by assuming $I(t',k_n)$ is a constant value $I^*(\underline{t},k_n)$ during the time interval Δt.

$$\begin{aligned} A(t+\Delta t,k_n) &= \int_0^t I(t',k_n)\ \cos\omega_n(t+\Delta t-t')\ dt' \\ &\quad + \int_t^{t+\Delta t} I(t',k_n)\ \cos\omega_n(t+\Delta t-t')\ dt' \qquad (21) \\ &= A(t,k_n)\cos\omega_n\Delta t - B(t,k_n)\sin\omega_n\Delta t \\ &\quad + I^*(\underline{t},k_n)\ \frac{\sin\omega_n\Delta t}{\omega_n} \end{aligned}$$

$$\begin{aligned} B(t+\Delta t,k_n) &= B(t,k_n)\cos\omega_n\Delta t + A(t,k_n)\sin\omega_n\Delta t \qquad (22) \\ &\quad + I^*(\underline{t},k_n)\ \left[\ \frac{1\ -\ \cos\omega_n\Delta t}{\omega_n}\right] \end{aligned}$$

In the present calculation $I^*(\underline{t},k_n)$ is computed by the following equation without iteration(21).

$$\begin{aligned} I^*(\underline{t},k_n) &= \sum_{m=1}^{N_t} 2\sigma_m(t+\tfrac{\Delta t}{2})\left[e^{-k_n(ix'_m+y'_m)}\right. \\ &\quad \left. - e^{-k_n(ix'_{m+1}+y'_{m+1})}\right]\cdot\frac{\sinh k_n\ell}{k_n\ell} \\ &\quad \cdot \frac{\left[(x'_{m+1}-x'_m)^2+(y'_{m+1}-y'_m)^2\right]^{\frac{1}{2}}}{k_n\left[i(x'_{m+1}-x'_m)+(y'_{m+1}-y'_m)\right]} \qquad (23) \end{aligned}$$

where, N_t is the total number of body segments, and 2ℓ is the minimum length of component wave. The coordinates (x'_m, y'_m) and (x'_{m+1}, y'_{m+1}) are the end points of the m-th body segment at the time $(t+\Delta t/2)$, and $\sigma_m(t+\Delta t/2)$ on the m-th body segment is calculated by extrapolating the three values of the previous time steps. Through numerical tests, it is found that the approximation error included in Eq.(23) is negligible and the numerical results are stable even for a moderate value of Δt. Then the new values of η and ϕ_w at the next time step can be calculated by using the equations (21) through (23). The new value of ϕ_w is used in the calculation of Eq.(14). This procedure is repeated successively to march forward in time.

The pressure on the body surface is calculated from the following Bernoulli's equation.

$$P = -\rho\frac{D\Phi}{Dt} + \frac{1}{2}\rho\left[\vec{V}^2 - (\nabla\Phi - \vec{V})^2\right] + \rho gy \qquad (24)$$

where ρ is the fluid density, D/Dt denotes the time derivative in a body-fixed system. The first term on the right-hand side is the potential-time-derivative pressure denoted by P_ϕ, the second term the velocity-square pressure denoted by P_v. In the present computation, the total pressure P_t is defined as the sum of P_ϕ and P_v by dropping the hydrostatic pressure. The forces acting on the body are calculated by integrating the pressures. We define the forces F_ϕ, F_v and F_t, corresponding to the pressures P_ϕ, P_v and P_t, respectively.

3. TRANSIENT WAVES GENERATED BY A WAVE MAKER

As a test of the present numerical method, a wave maker problem is treated as a transient problem. The body boundary condition on the wave maker is linearized, and the horizontal velocity of the wave maker at its mean position is given as

$$U^*(y,t)\ \begin{cases} = (1-y)\ A^*\omega\ \cos\omega t \\ = (1-y)\ A^*\omega\ \sin\omega t \end{cases} \qquad (25)$$

$$x=0,\ 1\geq y\geq 0,\ t\geq 0,$$

where, A^* is the amplitude of displacement of the wave maker at y=0. In Eq.(25) we define "cosine mode" and "sine mode" depending on $\cos\omega t$ and $\sin\omega t$, respectively.

In the present calculation the height of wave maker is given as 1m. The wave profile shown in Fig.2 is that for the case of cosine mode operation which has a jump on the velocity at t=0. In the figure we can see some distortion of the wave profile, which is indicated by the arrows. This distortion seems to be generated at the starting instant, and it propagates forward and disperses. However, in Fig.3 the case of sine mode operation which has a jump on the acceleration at t=0, such a distortion is hardly shown. Comparing these two sets of results, it is found that the distortion of wave profile is closely related to the jump on the velocity, but insensitive to the jump on the acceleration.

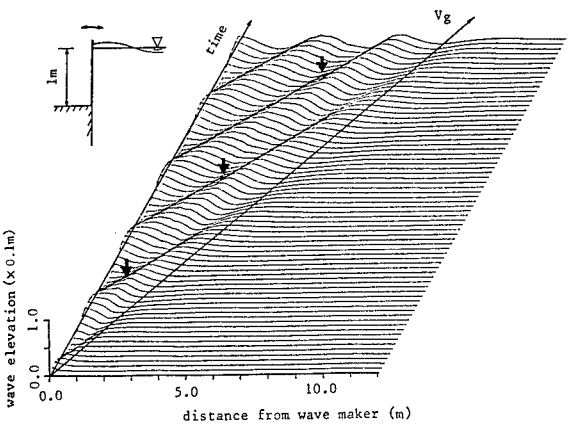


Fig.2 Wave Profile Generated by Flap-Type Wave Maker ($U^*(0,t)=A^*\omega\cos\omega t, \omega=4.5$rad/sec, $A^*=0.01$m)

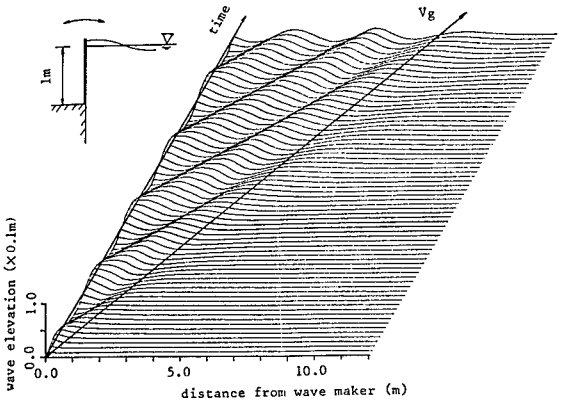


Fig.3 Wave Profile Generated by Flap-Type Wave Maker ($U^*(0,t)=A^*\omega\sin\omega t, \omega=4.5$rad/sec, $A^*=0.01$m)

Fig.2 and Fig.3 also show the dispersion phenomenon in the wave front region. Here, the wave group velocity corresponding to the frequency ω is denoted as Vg. In the present computations, L_m is 1.5 - 2.0 times of the reach of group velocity.

4. TRANSLATION WITH UNIFORM SPEED ($U \neq 0, \omega = 0$)

In this section, wave profiles and hydrodynamic forces for a submerged circular cylinder translating with a uniform speed are studied. The cylinder starts to move with a constant horizontal velocity -U from the state of rest at time t=0. The computation is made specifically for the case of h/r=2.0, where h is the depth of submergence measured from the free surface to the center of cylinder, and the radius of cylinder r is taken as 1m. The body surface is devided into 20 equal segments.

The profiles of generated waves for the depth Froude number F_h =0.4 is shown in Fig.4. Here, $F_h = U/\sqrt{gh}$. In the figure, we can see particular transient waves due to the impulsive start of the body at t=0.

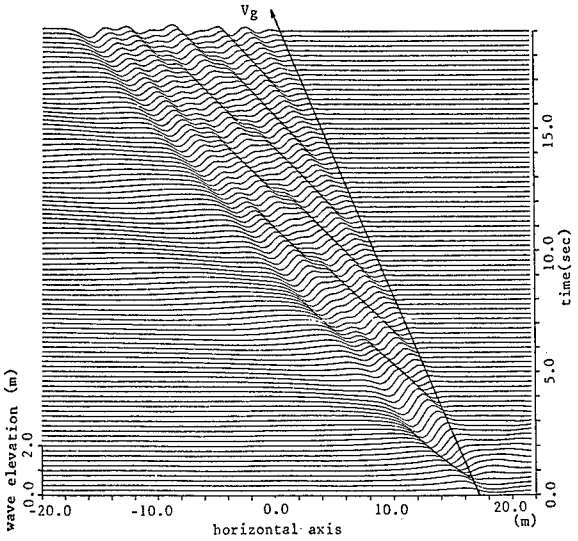


Fig.4 Wave Profile Generated by Uniformly Translating Circular Cylinder (h=2.0r,F_h=0.4)

The time history of the horizontal and vertical hydrodynamic forces, F_t, acting on the cylinder for F_h=0.4 are shown in Fig.5. In the figure we can see oscillatory behavior in the forces due to the transient waves in Fig.4. An approximation formula for the period of this oscillation can be obtained by considering the translation velocity of the body and the phase speed of the transient waves(21). The period of oscillation T_o can be computed by the following equation.

$$T_o = 2\pi / (g/4U) \qquad (26)$$

In deriving the above simple relation, we assumed that during the subsequent time, the body does not interact with the transient waves due to an impulse given at t=0 and the hydrodynamic

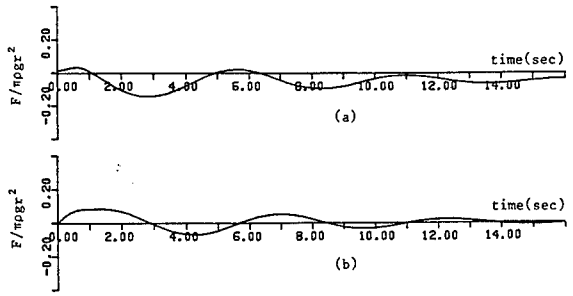


Fig.5 Time History of Forces for Uniformly Translating Circular Cylinder (h =2.0r,F_h =0.4) (a) Vertical Force (b) Horizontal Force

force on the body is directly affected by the wave elevation above the body. The comparison between the periods by Eq.(26) and those in simulation results showed generally good agreement. The agreement was even better in the range of $F_h \geq 0.6$. We leave out the comparisons.

The steady state values of the horizontal and vertical hydrodynamic forces for this uniform translation problem are obtained by taking a mean value of the force at the later time. In Fig.6 these mean values for F_h =0.6, 0.8, 1.0 are compared with the steady state solution of Havelock(23). The present result by Eq.(21) and Eq.(22) with Eq.(23) show fairly a good agreement with the result of Havelock.

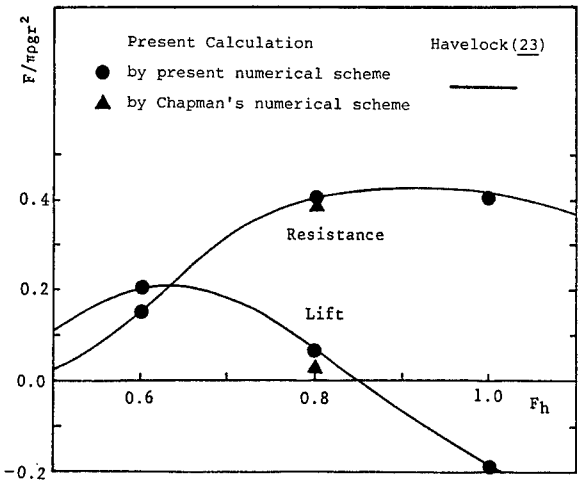


Fig.6 Comparison with Havelock's Result, Uniformly Translating Circular Cylinder (lift being positive, h=2.0r)

In the calculation, the truncation and discretization parameters are taken as L_m=220m, T_m =60sec, ℓ =0.4m, Δt=0.04sec for F_h =0.8. For other cases, these parameters are properly chosen according to the Froude number, the translated distance of the body and etc.. In this figure, the result by Chapman's numerical scheme(15) with the same discretization and truncation parameters is also shown for F_h=0.8. His numerical scheme takes only the contribution of $O(\Delta t)$ in the third terms of Eq.(21) and Eq.(22), and omits $\Delta t/2$ correction in Eq.(23).

5. FORCED HARMONIC LARGE-AMPLITUDE OSCILLATION (U=0, $\omega \neq 0$)

First we applied the present method, as a test, to a linear problem where the body boundary condition is also linearized. The calculated results for a floating circular cylinder showed large waves on the free surface inside of the cylinder(21). The hydrodynamic force also showed a considerable effect due to this inner flow. From this observation and the previous remedies used in frequency domain methods to remove the irregular frequencies, the additional sources are distributed on the inner free surface requiring the following additional condition,

$$\frac{\partial \phi_b}{\partial n} = -\frac{\partial \phi_w}{\partial n} - \frac{n(t_n)}{\Delta t} \qquad t = t_n \qquad (27)$$

on the free surface interior to the body. The second term on the right-hand side in Eq.(27) is a term to correct the accumulation of numerical errors in marching time-steps. Once the integral of the original integral equation for ϕ_b is redefined on the wetted surface of the body and on the inner free surface on which Eq.(27) is imposed, we could control the inner flow in our computed results.

Fig.7 and Fig.8 show respectively the inner and outer free surface elevation and the time history of hydrodynamic force in the nonlinear computation where the body boundary condition is satisfied exactly at the instantaneous position. The specific model treated here is a half immersed circular cylinder of radius 1m and the vertical displacement of the cylinder is given as $-A\cos\omega t$. The time step size Δt was taken as T/100 where T is the motion period. The number of segments on the half of the wetted surface is varying in time with its average number being 15, and the four segments is taken on the half of the inner free surface.

In harmonic oscillation problems, each harmonic component and time-mean force are obtained by the Fourier transform of the calculated forces. Introducing component forces, the periodical force in time is written as follows.

$$\begin{aligned} F(t) &= F_0 + F_{1c}\cos\omega t + F_{1s}\sin\omega t \\ &\quad + F_{2c}\cos 2\omega t + F_{2s}\sin 2\omega t \\ &\quad + F_{3c}\cos 3\omega t + F_{3s}\sin 3\omega t + \cdots \\ &= F_0 + F_{1a}\sin(\omega t+\delta_1) + F_{2a}\sin(2\omega t+\delta_2) \\ &\quad + F_{3a}\sin(3\omega t+\delta_3) + \cdots \\ &\qquad\qquad 0 \le \delta_n \le 2\pi \end{aligned} \qquad (28)$$

In the present results, the body motion as a reference for the above expression is taken as follows,

$$y(t) = A\sin\omega t \qquad (29)$$

where, A is the amplitude of body motion.

The present results for the time-mean force and the second-harmonic force amplitude

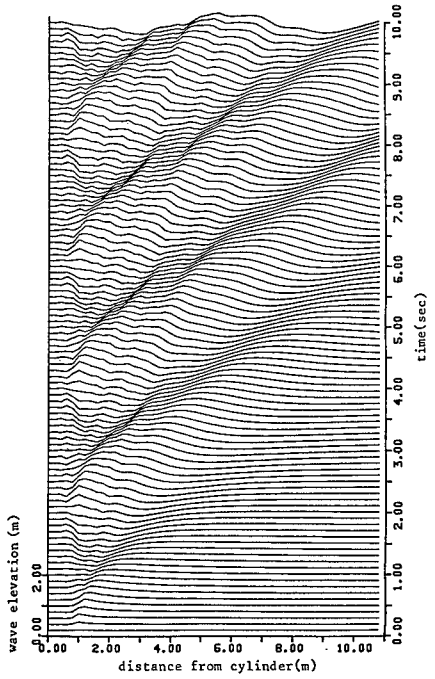


Fig.7 Inner and Outer Free Surface Elevation of Heaving Circular Cylinder, Nonlinear Computation (Floating,Inner Free Surface with Rigid Wall Condition, T = 2.0 sec, A=0.4r)

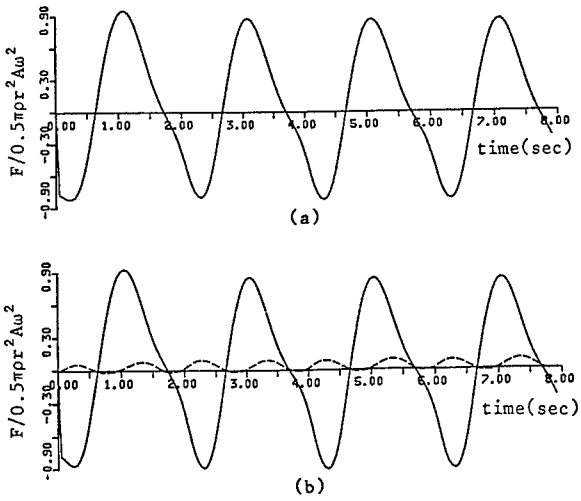


Fig.8 Time History of Forces for Heaving Circular Cylinder, Nonlinear Computation (Floating,Inner Free Surface with Rigid Wall Condition, T = 2.0sec, A = 0.4r)
(a) Total Force F_t (b)F_ϕ(———) and F_v(- - - - -)

are compared with the results of Kyozuka(5) in Fig.9 and Fig.10 respectively, where $\varepsilon = A/r$. The calculated result of Kyozuka was obtained by the second order perturbation method in frequency domain. He has also presented experimental results.

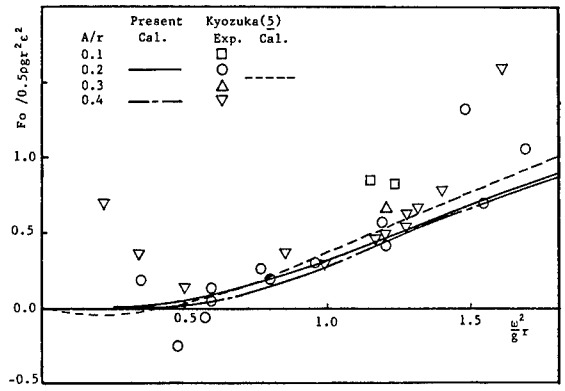


Fig.9 Time-Mean Forces of Heaving Circular Cylinder (Floating)

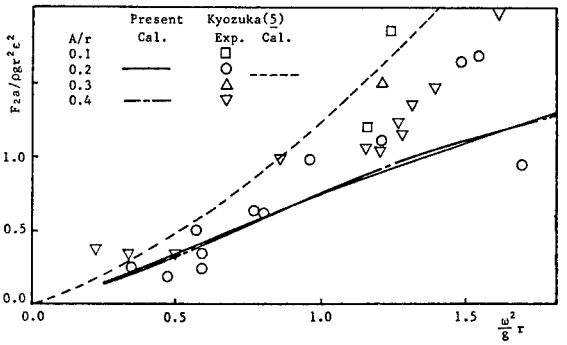


Fig.10 Second-Harmonic Amplitudes of Heaving Circular Cylinder (Floating)

In general, our results of the time-mean forces show good agreement with the calculated results of Kyozuka. However, the comparison in the second-harmonic force amplitude shows a considerable discrepancy between the present result and the calculated result of Kyozuka. It is of interest to note that our results underpredict the experimental results of Kyozuka in the range of $1.0 < \omega^2 r/g < 1.6$, while the computed results of Kyozuka overpredict for the nearly entire range of $\omega^2 r/g$.

6. FORCED HARMONIC LARGE-AMPLITUDE OSCILLATION WITH FORWARD SPEED ($U \neq 0$, $\omega \neq 0$)

In this section, forced harmonic oscillation with forward speed of a submerged circular cylinder is treated. Linear solutions of such a problem were studied in frequency domain by Yamamoto(18) by using the multipole expansion method ,and by Park(19) by using the translating and pulsating sources. Linear and nonlinear computations of the heaving motion with forward speed are performed. The quasi-steady results of linear computation are compared with the results of Park(19).

At time t=0, the body starts to translate with a uniform horizontal speed -U and starts to oscillate vertically with displacement given as $y = -A\cos\omega t$. In calculation, the depth of submergence h is given as 1.5r, where r is the

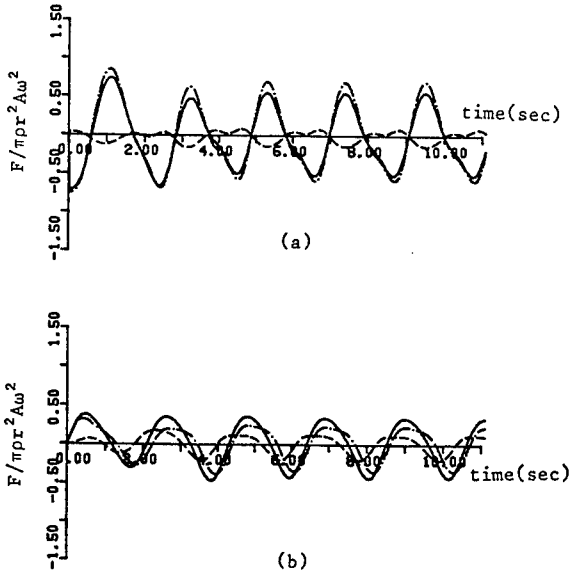


Fig.11 Time History of Forces for Translating and Heaving Circular Cylinder,Nonlinear computation (h=1.5r, F_r =0.25, T=2.1sec, A=0.3r) (a) Vertical Forces (b) Horizontal Forces ;F_t(———), F_ϕ(—·—·—) and F_V(- - - - -)

radius of cylinder, and the Froude number F_r is 0.25. Here $F_r = U/\sqrt{gr}$. The impulsive start of the body results in the transient oscillatory phenomena of hydrodynamic force. At the given depth of submergence and forward speed, the oscillation of hydrodynamic force decays sufficiently after 5 or 6 seconds. Hence, all computations of the oscillatory motions are performed up to the time range which is large enough for the transient effect to disappear. In the present computation, the number of body segments is 20 and the time step size Δt is 1/100 of the given motion period T.

A typical force time-history by nonlinear computation is shown in Fig.11, for A=0.3r, T=2.1sec. In the figure, we can see apparent nonlinearities due to a large-amplitude motion. And it is of interest that the magnitude of horizontal force is comparable with that of the vertical force, in spite of the absence of horizontal oscillatory motion of the body.

In frequency domain anaysis, the wave system and hydrodynamic force show some singular behaviors at τ=0.25. Here $\tau = U\omega/g$. However in the present calculation, no singular behavior appears at or near τ =0.25. And we did not experience any difficulty in the computations at or near τ =0.25.

The present results of the linear first-harmonic component force are compared with the calculated results of Park in Fig.12 and Fig.13, for vertical and horizontal forces, respectively. Corresponding to the pressure of Park's calculation, the pressure in the present calculation is evaluated as $-\rho\partial\Phi/\partial t$ in a linear computation.

In Fig.12, the present result and Park's result of damping coefficient show a very good agreement except in the high frequency range. However, in the result of added mass the

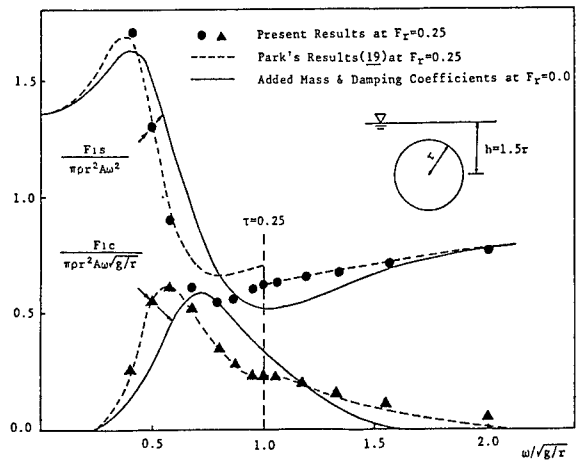


Fig.12 Heave-Induced Heaving Added Mass and Damping Coefficients of Translating and Heaving Circular Cylinder, Linear Computation (h=1.5r)

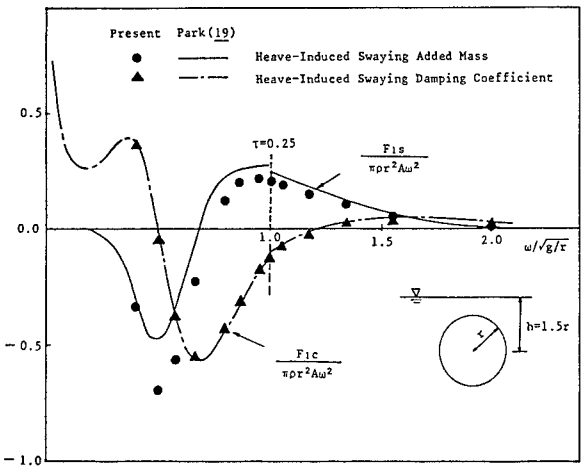


Fig.13 Heave-Induced Swaying Added Mass and Damping Coefficients of Translating and Heaving Circular Cylinder, Linear Computation (h=1.5r)

comparison between two results shows a good agreement in the range of $\tau>0.25$, but shows considerable discrepancy in the range of $\tau< 0.25$. Such a trend is also shown in the coupled added mass and the coupled damping coefficient in Fig.13. Here we note that in the present calculation, the added mass and the damping coefficient are obtained simultaneously by the Fourier transform of the calculated forces in time domain. Another remarkable difference in this comparison is that the variation of the present result vs frequency shows no discontinuity at τ =0.25, but Park's result shows discontinuity there. To examine the effects of the computation-time length and the number of wave components on this discontinuity, we performed a computation up to the 8th period and performed test-runs varying the discretization and truncation parameters at τ =0.25. From this series of numerical tests, it is concluded that the behavior of the smooth transition at τ =0.25 do not change.

By utilizing the Kramers-Kronig relation (24), we have also reevaluated added mass by using the damping coefficients in Fig.12, which show a good agreement with the results of Park. And it is also confirmed that the reevaluated value of added mass agrees well with the present results of added mass in Fig.12. Therefore we conclude that the present result is not likely inaccurate.

The first-harmonic component of vertical force in phase with the body acceleration and that in phase with the body velocity are shown in Fig.14 and Fig.15, respectively. In Fig.16 and Fig.17, those of the horizontal force are shown.

In each figure, the three values in linear case and the other three values in nonlinear case are shown together. In these four figures, the symbols, ⊡ , ⊙ and △ denote the first-harmonic components which are obtained from the three different pressures in a linear computa-

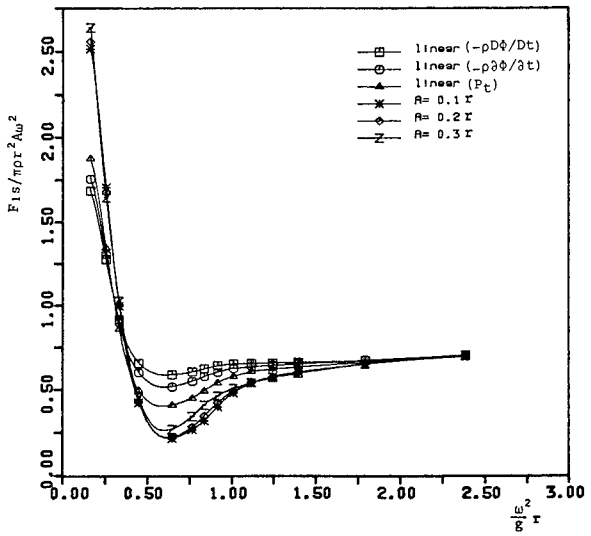


Fig.14 First-Harmonic Component of Vertical Forces for Translating and Heaving Circular Cylinder - Acceleration Phase (h=1.5r, F_r=0.25)

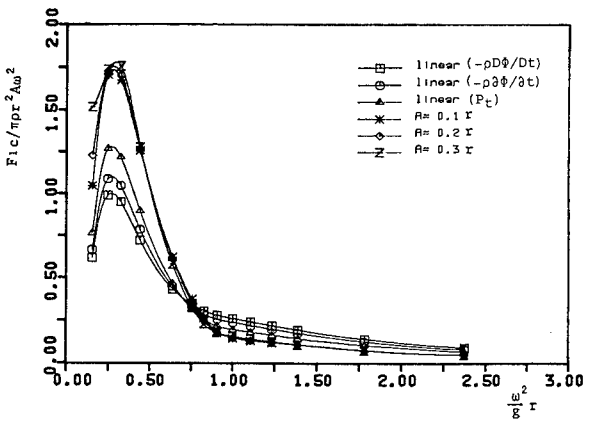


Fig.15 First-Harmonic Component of Vertical Forces for Translating and Heaving Circular Cylinder - Velocity Phase (h=1.5r, F_r=0.25)

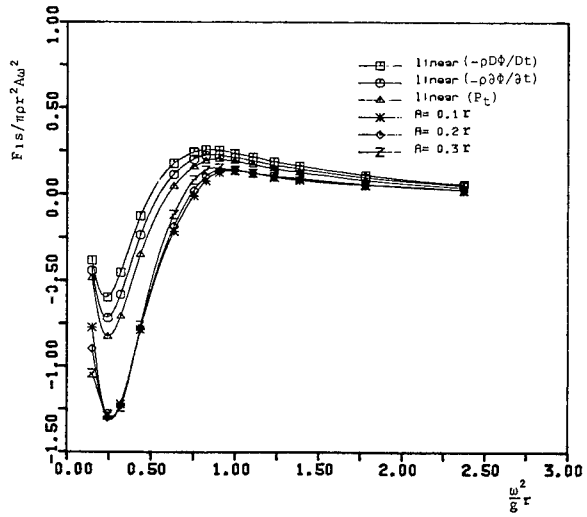


Fig.16 First-Harmonic Component of Horizontal Forces for Translating and Heaving Circular Cylinder - Acceleration Phase (h=1.5r, F_r=0.25)

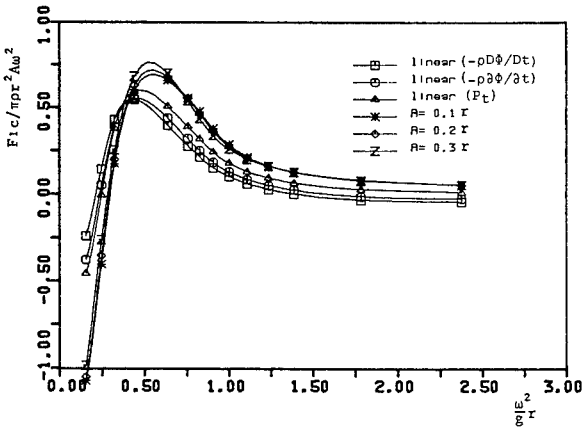


Fig.17 First-Harmonic Component of Horizontal Forces for Translating and Heaving Circular Cylinder - Velocity Phase (h=1.5r, F_r=0.25)

tion, i.e., $-\rho D\Phi/Dt$ and $-\rho\partial\Phi/\partial t$ the total pressure Pt, respectively. Here, the force component denoted by ⊙ has been reproduced from the present results in Fig.12 and Fig.13. The first-harmonic components denoted by the other three symbols are obtained by the Fourier transform of the total force F_t in nonlinear computations with three different motion amplitudes.

In the four figures, the results for nonlinear motions with amplitudes A=0.1r, 0.2r, 0.3r are shown. It is remarkable that discrepancy does exist between the results by linear and nonlinear computations, even when the amplitude of body motion is very small. This discrepancy is due to an interaction effect between the disturbed steady flow and the change of body position in nonlinear computation. This discrepancy is pronounced in the lower frequency region as shown in the figures. In frequency-domain formulation, this interaction effect was pointed out by Timman and Newman(20).

The time-mean and higher harmonic forces in nonlinear computations are shown in Fig.18 through Fig.24, where ε =A/r. The vertical time-mean force in Fig.18 includes the steady lift force due to the forward speed. In Fig.19 and Fig.20, the amplitude and phase of the second-harmonic component of verical force are shown, respectively. Those of the horizontal force are also shown in Fig.21 and Fig.22. It is of interest to note that the second-harmonic amplitude has its minimum value near $\omega^2 r/g$=0.4. The third-harmonic amplitudes of vertical and horizontal forces are shown in Fig.23 and Fig.24, respectively.

In the present calculation, the discretization and truncation parameters are L_m =24m, T_m =10sec, ℓ =0.1m at $\omega^2 r/g$=1.0 for the computation of four periods. For other frequencies, these parameters are properly changed.

The present computations have been carried out on a mini-computer PDP 11/34. A typical computation time for 20 segments on the body boundary and 300 wave number components was approximately 30 seconds(CPU) for one time step.

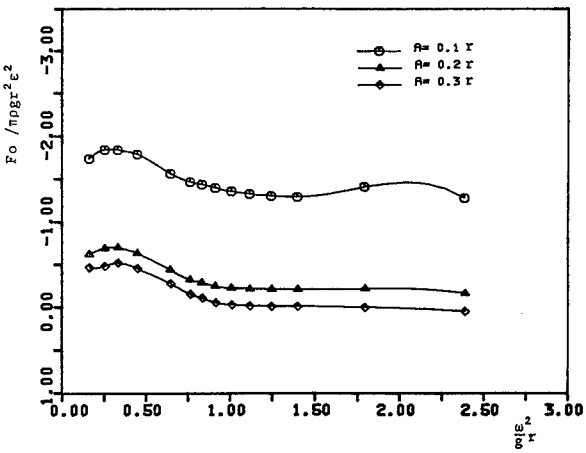


Fig.18 Time-Mean Vertical Forces of Translating and Heaving Circular Cylinder (h=1.5r, F_r=0.25)

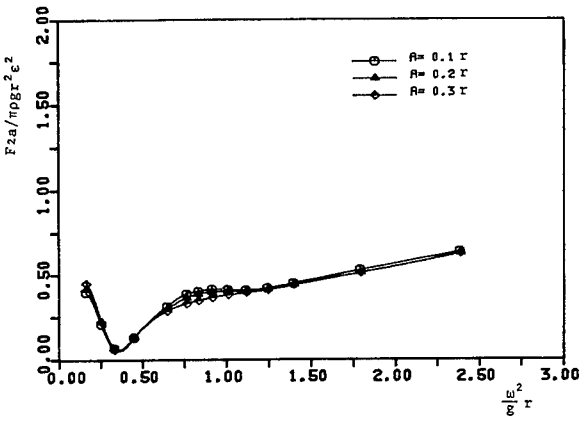


Fig.19 Second-Harmonic Amplitude of Vertical Forces for Translating and Heaving Circular Cylinder (h=1.5r, F_r=0.25)

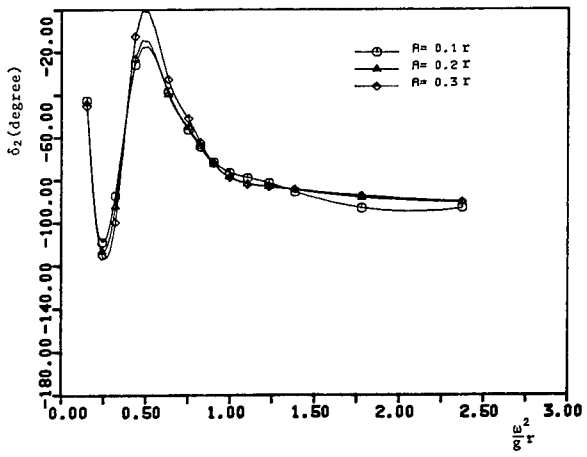


Fig.20 Second-Harmonic Phase of Vertical Forces for Translating and Heaving Circular Cylinder (h=1.5r, F_r=0.25)

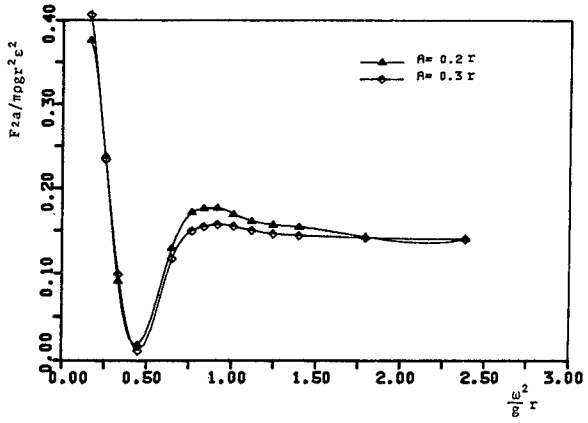


Fig.21 Second-Harmonic Amplitude of Horizontal Forces for Translating and Heaving Circular Cylinder (h=1.5r, F_r=0.25)

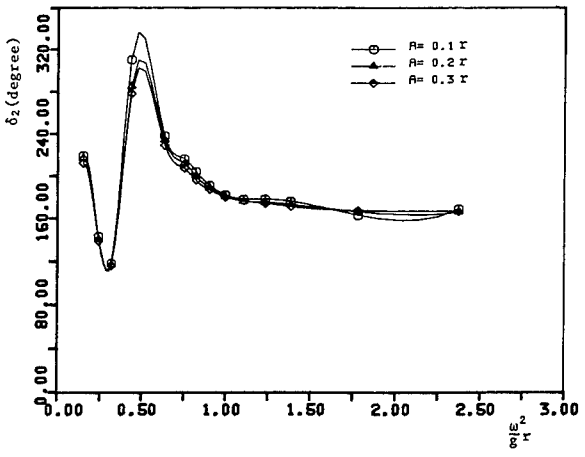


Fig.22 Second-Harmonic Phase of Horizontal Forces for Translating and Heaving Circular Cylinder (h=1.5r, F_r=0.25)

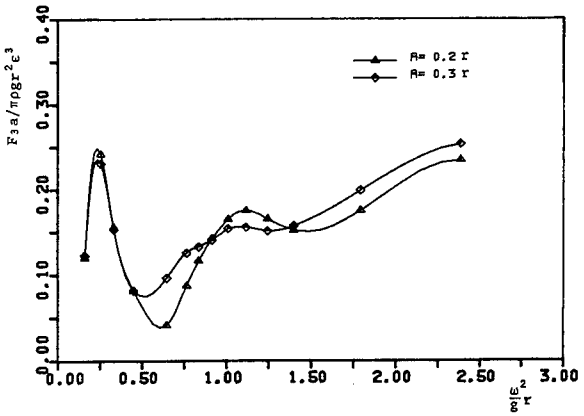


Fig.23 Third-Harmonic Amplitude of Vertical Forces for Translating and Heaving Circular Cylinder (h=1.5r, F_r=0.25)

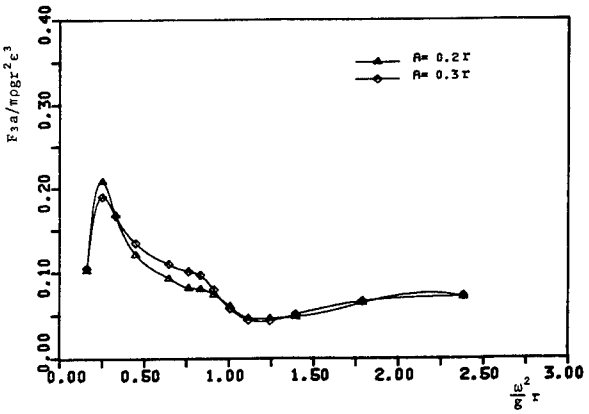


Fig.24 Third-Harmonic Amplitude of Horizontal Forces for Translating and Heaving Circular Cylinder (h=1.5r, F_r=0.25)

7. CONCLUSION

Four typical problems in two-dimensional free-surface flows are studied by using the method of spectral free-surface representation with simple source distribution on the instantaneous body surface. In this work, the free surface boundary condition is linearized, while the body boundary condition is satisfied exactly at the instantaneous position. In comparisons of some calculated results with available experimental data and other analytical results, generally good agreements are observed.

In the present paper, a modified rigid wall condition has been imposed on the inner free surface to remove the so-called irregular frequency effect. This technique removes the effect of the inner flow sufficiently.

In the forced harmonic large-amplitude oscillation problem with forward speed, it is shown that the interaction between the disturbed steady flow and the body oscillation plays a significant role in the values of the added mass and damping coefficients for a bluff body in heave motion. In this case, we did not experience any difficulty in the computation at

or near the τ =0.25, and there is no singular phenomenon in wave profiles and hydrodynamic forces contrary to the results obtained by the frequency-domain approach.

Even though the present method has a restriction in the application to a large-amplitude wave problem, it is an efficient and promising tool for two-dimensional time-dependent motions with large amplitude. It can be easily extended to a three-dimensional problem.

ACKNOWLEDGEMENT

The authors would like to thank Professor K.J. Bai, Seoul National University, for his discussion and help during the execution of this work and preparation of this paper. Thanks are also due to professor H.C. Kim, H.S. Choi and K.P. Rhee, Seoul National University, for their discussions.

REFERENCES

1. Ogilvie,T.F., "First- and Second-Order Forces on a Cylinder Submerged Under a Free Surface," Journal of Fluid Mechanics, Vol. 16, 1963, pp. 451-472.

2. Lee,C.M., "Second-Order Theory of Heaving Cylinders in a Free Surface," Journal of Ship Research, Vol. 12, 1968, pp. 313-327.

3. Potash,R.L., "Second-Order Theory of Oscillating Cylinders," Journal of Ship Research, Vol. 15, 1971, pp. 295-324.

4. Papanikolaou,A. and Nowacki,H., "Second-Order Theory of Oscillating Cylinders in a Regular Steep Wave," Proceedings of the 13th Symposium on Naval Hydrodynamics, Tokyo, 1980.

5. Kyozuka,Y.,"Experimental Study on Second-Order Forces Acting on a Cylindrical Body in Waves," Proceedings of the 14th Symposium on Naval Hydrodynamics, Ann Arbor, 1982.

6. Cummins,W.E., "The Impulse Response Function and Ship Motions," Schiffstechnik, Vol.9, 1962, pp. 101-109.

7. Ogilvie,T.F., "Recent Progress toward the Understanding and Prediction of Ship Motion," Proceedings of the 5th Symposium on Naval Hydrodynamics, Bergen, 1964.

8. Wehausen,V., "Initial-Value Problem for the Motion in an Undulating Sea of a Body with Fixed Equilibrium Position," Journal of Engineering Mathematics, Vol. 1, pp. 1-19.

9. Longuet-Higgins,M.S. and Cokelet, E.D., "The Deformation of Steep Surface Waves on Water, I: A Numerical Method of Computation," Proceedings of the Royal Society of London, Series A, 350, 1976.

10. Faltinsen,O.M., "Numerical Solution of Transient Nonlinear Free-Surface Motion Outside or Inside Moving Bodies," Proceedings of the 2nd International Conference on Numerical Ship Hydrodynamics, Berkeley, 1977.

11. Vinje,T. and Brevig,P., "Nonlinear Ship Motion," Proceedings of the 3rd International Conference on Numerical Ship Hydrodynamics, Paris, 1981.

12. Vinje,T., Maogang,X. and Brevig,P., "A Numerical Approach to Nonlinear Ship Motion," Proceedings of the 14th Symposium on Naval Hydrodynamics, Ann Arbor, 1982.

13. Lin,W.M., Newman,J.N. and Yue,D.K., "Nonlinear Forced Motions of Floating Bodies," Proceeding of the 15th Symposium on Naval Hydrodynamics, Hamburg, 1984.

14. Greenhow,M. and Lin,W.M.,"Numerical Simulation of Nonlinear Free Surface Flows Generated by Wedge Entry and Wavemaker Motions," Proceedings of the 4th International Conference on Numerical Ship Hydrodynamics, Bethesda, 1985.

15. Chapman,R.B., "Large-Amplitude Transient Motion of Two-Dimensional Floating Bodies," Journal of Ship Research, Vol. 23, 1979, pp. 20-31.

16. Chapman,R.B., "Time-Domain Method for Computing Forces and Moments Acting on Three-Dimensional Surface-Piercing Ship Hulls with Forward Speed," Proceedings of the 3rd International Conference on Numerical Ship Hydrodynamics, Paris, 1981.

17. Loeser,D.J., Yue,D.K. and Salvesen,N., "Slender-Body Calculations of Large-Amplitude Ship Motions," Proceedings of the 14th Symposium on Naval Hydrodynamics, Ann Arbor, 1982.

18. Yamamoto,Y., "On the Oscillating Body below the Water Surface," Journal of the Society of Naval Architects of Japan, 1955.

19. Park,S.H., "Oscillation of Cylinders Near the Free Surface of a Deep Fluid in Horizontal Currents," Dissertation, Stevens Institute of Technology, 1983.

20. Timman,R. and Newman,J.N., "The Coupled Damping Coefficients of a Symmetric Ship," Journal of Ship Research, Vol.5, 1962, pp. 1-7.

21. Kim,Y.J., "On Two Dimensional Transient Motions with Large Amplitude by Time Domain Method," Dissertation, Seoul National University, 1985.

22. Lamb,H., Hydrodynamics, 6th edition,Dover Publications Inc., New York, 1932, pp. 384-391.

23. Havelock,T.H., "The Forces on a Circular Cylinder Submerged in a Uniform Stream," Proceedings of the Royal Society of London, Series A, Vol. 157, 1936.

24. Kotik,J. and Mangulis,V.,"On the Kramers-Kronig Relations for Ship Motions," International Shipbuilding Progress, Vol. 9, 1962. pp. 361- 368.

DISCUSSION

Heinrich Söding,
Institute fur Schiffbau Hamburg

Your Fig. 4 seems to indicate waves being generated in front of the body. Is this correct?

(Comment to the authors: I first misunderstood the V_g line as indicating the position of the body. Perhaps, in the answer this could be clarified together with explaining the long waves in front of the body by the impulsive start?)

Reply -

Dr. Soding's question seems to be resulted from our insufficient explanation about Fig. 4. In the figure, the V_g line indicates the wave group velocity which is the half of the body speed, and the body position is, roughly, below the first wave trough from the left. Therefore, the main waves due to the continuous translation of the body appears behind the body. The relatively long waves supperposed on the main waves are the transient waves generated by the impulsive start of the body.

Ronald W. Yeung
University of California, Berkeley

I have a question concerning the discrepancies between the author's results and the results of Park (Ref. 19). Does the author feel that Park's frequency-domain calculations are in error or that the author's time-domain calculations would not necessarily yield the correct frequency-domain results? I would also like to ask whether or not the author has applied the Kramers-Kronig relation test to Park's calculations? I don't feel the Kramers-Kronig relation generally offers a strong enough test for correctness.

Reply -

Concerning the first question of Prof. Yeung, we would like to recall that the present results for zero forward-speed case show good agreement with the well-known results by frequency-domain methods, and the present calculations for non-zero forward-speed case are performed by the same numerical scheme. And the numerical tests for non-zero forward-speed case also show good convergence and stability. Therefore, we believe that the present numerical scheme is reliable in the calculations for both cases. We hope this answers the first question.

The answer to the second question is yes, and the result of the test is conditionally negative. That is, if the singularity at $\tau = 0.25$ in Park (Ref. 19) is a simple discontinuity, then his result seems to be against the Kramers-Kronig relation. However, if the singularity in his result is another type, such as a delta function, other conclusions might be possible. Authors quite agree with Prof. Yeung in his last comment on the Kramers-Kronig relation, and it is also obvious that a correct solution should satisfy the relation.

Quadratic Response to Short-Crested Seas

J. F. DALZELL

David W. Taylor Naval Ship R&D Center, U.S.A.

ABSTRACT

The motivation of the present work was that, in contrast to the situation for linear seakeeping phenomena, there appeared to be no theory for the estimation of common statistical parameters for quadratic nonlinear seakeeping systems subjected to short crested random seas. The quadratic input-output model which has been in use for some time was taken directly from electronics and communication theory where the notion of short crestedness does not exist, and thus it is a "time only" (long crested sea) model. Hasselmann published the basic formulation for a short crested sea model in 1966, and the present development is largely a translation and embellishment of this basic formulation. In this case the linear and quadratic response functions which define the ship dynamics become functions of vectors rather than scalars. Given a directional wave spectrum and the linear and quadratic response functions corresponding to some response of interest, estimating formulae have been developed for a variety of statistics. It was found that the previous restriction of the time only case to the encounter frequency domain may be largely removed. The formula for the mean value of the response in short crested seas is especially simple, in that it is found to be hardly more computationally demanding than estimating the variance of a purely linear system in short crested seas.

INTRODUCTION

Since the first introduction to the field, Hasselmann (1966), Vassilopoulos (1966), there have been developed a number of applications of the quadratic functional model to the prediction or simulation of nonlinear response of ships and platforms to random seas. An abbreviated list of examples includes Brink (1979), Dalzell (1976), (1979), Kim (1981), and Pinkster (1979), and (1980).

The detail of the various current approaches to quadratic nonlinear response varies. However, all now known are essentially single input models. This means that validity is confined to the long-crested sea case. Additionally, in the case of non-zero forward speed the models in use are encounter domain models. In effect, current practice apparently does not include a short-crested sea model for quadratic nonlinear response. In contrast, a short crested sea model for linear response has been available for some 30 years, St.Denis (1953).

It appears that only one attempt at considering the short crested nonlinear case is in the literature, and this was in what is perhaps the first introduction of the quadratic functional model to the field, Hasselmann, (1966). Unfortunately, the main thrust of this work was toward interpretation of nonlinear response in terms of higher order spectra, and the basic treatment was specialized shortly after the formulation to the head or bow sea long crested case. Thus the overall objective of the present work was to refine the development of a statistical model for the quadratic nonlinear response to short crested seas in hopes that some reasonably practical statistical estimators for the effect of quadratic nonlinearities would emerge.

THE INITIAL REPRESENTATION

The general idea is that a ship response to waves is a function of the "wave field", which is itself a function of time and space. The response is thus a functional by definition. Hasselmann's (1966) representation of the response as a functional polynomial comes about quite abruptly as the result of what appears at first sight to be an unusual "Taylor expansion". The mathematical foundations of his representation are very substantial. Some effort at a review of this background is contained in Dalzell (1985).

Very briefly, Volterra (1930) introduced the idea of a Taylor expansion of a functional in which the derivatives with respect to a parameter in the ordinary Taylor expansion of a function are replaced by "functional derivatives" with respect to a function. From this start the theory of generalized functions

(Gel'fand (1964), Rugh (1981)) indicates that under broad restrictions on the input (wave field), the quadratic functional polynomial model which has simply been postulated in most work since 1966 may be interpreted as the result of a Taylor expansion in the neighborhood of zero wave field (no waves). The important difference in the Hasselmann formulation is that the wave field is presumed to be a function of space as well as time. The extension of the single input representation theory to the case of several variables appears to have rigorous mathematical backing, and the arguments of Barrett (1963) with respect to time invariance of the dynamic nonlinear system being excited appear to go over easily to this case.

Suppose in general that a ship system is excited by a wave field, $\zeta(t,x,y)$, a function of time, t, and coordinate position, x,y. Denoting the general response by $\xi[\zeta(t,x,y)]$ to indicate that it is a functional of the wave field, and assuming further that the ship dynamics do not depend upon the absolute values of time or position, the representation theory says that the response may be represented through nonlinearities of the second degree as follows:

$$\xi[\zeta(t,x,y)] = \iiint k_1(t-t_1,x-x_1,y-y_1) \times \zeta(t_1,x_1,y_1)\,dt_1\,dx_1\,dy_1 + \int\cdots\int k_2(t-t_1,x-x_1,y-y_1,t-t_2,x-x_2,y-y_2) \times \zeta(t_1,x_1,y_1)\zeta(t_2,x_2,y_2) \times dt_1\,dx_1\,dy_1\,dt_2\,dx_2\,dy_2 \qquad (1)$$

The kernels in Equation (1) are functions of time and space differences, conceptually contain the dynamics of the system of interest, and again conceptually, correspond to the linear and quadratic response functions of the single input representation. It is worth noting that the representation theory implies that any functional of the form of the left hand side of Equation (1) may be expanded in this way under the presumption of continuity and differentiability of the wave field, and the presumption that the field either vanishes outside a finite region in the space of all admissible such functions, or is square integrable.

It may be noted that the leading term in the Taylor expansion (the response to zero wave field) has been dropped on the presumption that the only responses of interest are caused by waves. There is no mathematical justification for truncating the implied Taylor series expansion at the quadratic term. This is done arbitrarily on the presumption that the resulting model may be useful.

Some further specialization of the definitions of response and wave field are required to complete a representation analogous to Hasselmann's. Nothing is lost if it is assumed that the mean motion of the ship is along the X axis in a fixed (X,Y) frame of reference. If the mean velocity of the ship is U, then a moving coordinate system may be defined:

$$x = X - Ut$$
$$y = Y$$

If the wave field, $\zeta(t,x,y)$ is interpreted as the field relative to the moving ship, $\zeta(t,0,0)$ is the wave field at the ship position (assumed to be the field undistorted by the ship as in most ship response theory). Thus in this space coordinate system the explicit space differences in Equation (1) may be ignored, or what amounts to the same thing, the response may be assumed to be a functional of $\zeta(t,0,0)$. The response thus may be considered a function of time. With the assumptions just outlined it should be emphasized that Equation (1) is an encounter domain representation. Because the assumption will be made that the integrands of Equation (1) differ from zero only in a finite range of the dummy arguments, it is permissible to regard the integrals as infinite. With this additional assumption a simple transformation of the time variables serves to convert Equation (1) to:

$$\xi(t) = \iiint k_1(t_1,x_1,y_1)\zeta(t-t_1,x_1,y_1)\,dt_1\,dx_1\,dy_1 + \int\cdots\int k_2(t_1,x_1,y_1,t_2,x_2,y_2) \times \zeta(t-t_1,x_1,y_1)\zeta(t-t_2,x_2,y_2) \times dt_1\,dx_1\,dy_1\,dt_2\,dx_2\,dy_2 \qquad (2)$$

where all the dummy variables are time or space differences. Equation (2) thus implies an extended functional polynomial similar to that assumed previously (e.g. Dalzell (1976)). In this form the representation is essentially that of Hasselmann, apart from the complications introduced by the fact that he chose to represent the response as a functional of the normal surface velocity, $\partial\zeta/\partial t[\zeta(t,x,y)]$, as well as the wave elevations. It appears that Hasselmann's addition of surface velocity added little in the end and has been omitted.

RESPONSE IN REGULAR WAVES

The most direct way to make an interpretation of the time domain model, Equation (2), is to temporarily assume that the wave field is composed of one or two long crested regular waves. As previously noted, the ship has been assumed to be proceeding at mean velocity U along a fixed X axis. Now additionally it will be assumed that a regular wave is propagating in a direction μ relative to the X axis. These relationships are sketched in Figure 1. The angle μ relative to the ship track corresponds to the usual ship motion convention. As is conventional the

following parameters are defined for the regular wave:

λ = wave length

ω = wave frequency

$\bar{\kappa}$ = vector wave number with components;

$\kappa_X = \kappa\cos(\mu)$

$\kappa_Y = \kappa\sin(\mu)$

μ = wave direction $= \tan^{-1}(\kappa_Y/\kappa_X)$

κ = scalar wave number $= 2\pi/\lambda = |\bar{\kappa}|$

where the scalar wave number and frequency are connected by a dispersion relation.

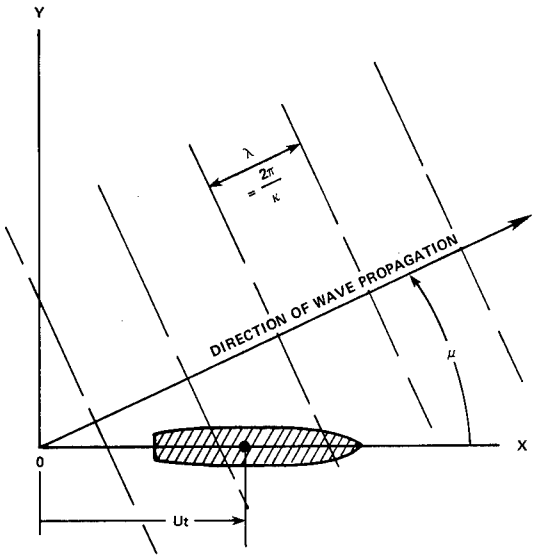


Figure 1 - Component Wave Direction

Supposing the wave to have (small) amplitude, a, the conventional representation for the surface elevations will be taken as the wave field. Thus in fixed axes the wave field becomes:

$$\zeta(t,X,Y) = a\cos(\kappa_X X + \kappa_Y Y - \omega t + \varepsilon) \qquad (3)$$

where ε is an arbitrary phase angle.

The response model (Equation 2) is written for the encounter domain. Thus making the change of space coordinates to those moving with the ship, the encountered wave field becomes:

$$\zeta(t,x,y) = aRe\{\mathrm{Exp}[i(\bar{\kappa}\cdot\bar{x} - \sigma t + \varepsilon)]\} \qquad (4)$$

where: $\sigma = \omega - \kappa_X U$

in which σ is the encounter frequency, and $\bar{x}$ is the vector representation of position relative to the ship.

Because the wave field as defined by Equation (4) is defined for infinite ranges in time and space, the initial assumptions leading to the response model are violated. Strictly, Equation (4) cannot be substituted into Equation (2) unless the representation of the wave field is multiplied by a time and space "window" which is unity over a finite range and zero elsewhere. On the other hand, if the kernels of Equation (2) are non-zero only in a finite range of time and space differences, and the range of time and space of the "window" is very much larger than the range of definition of the kernels, there will come a time in the evolution of the response, Equation (2), when the effect of the window will no longer be felt; that is, starting transients will have died out, and the response will be "steady state". Thus the steady state response may be defined by a direct substitution of Equation (4) into Equation (2).

Before proceeding, some elaboration on the restriction just put on the kernels is in order. As has been noted, the ship dynamics are assumed to be embedded in the kernels. It seems permissible for a wide range of responses to assume that the "memory" of the ship with respect to space as well as time is finite; that is, the response at time t depends upon a finite range of time in the neighborhood of t, and a finite region of the wave field in the neighborhood of the ship. There are responses, the unrestored modes of translation for example, for which the assumption will not hold. It will be assumed, just as in the time only case, that some artifice can be introduced to overcome the problem if it occurs.

When the substitution of Equation (4) into Equation (2) is carried out the result is as follows:

$$\begin{aligned} Z_1(t) = {} & aRe\{T(\bar{\kappa}:U)\mathrm{Exp}[i\sigma t - i\varepsilon]\} \\ & + (a^2/2)R(\bar{\kappa},\bar{\kappa}:U) \\ & + (a^2/2)Re\{Q(\bar{\kappa},\bar{\kappa}:U)\mathrm{Exp}[i2\sigma t - i2\varepsilon]\} \end{aligned} \qquad (5)$$

where $Z_1(t)$ is interpreted as the steady state response to the assumed cosinusoidal wave field.

The form of Equation (5) is precisely what would be expected from previous work. The first term is a linear response at the same frequency as the input wave field, the second and third represent a shift in the mean and a second harmonic response due to the assumed quadratic nonlinearities.

The three new functions appearing in Equation (5) are defined as follows:

$$T(\bar{\kappa}_1:U) = \int\int\int k_1(t_1,x_1,y_1) \times \mathrm{Exp}[-i(\sigma_1 t_1+\kappa_{X1}x_1+\kappa_{Y1}y_1)]dt_1dx_1dy_1 \quad (6)$$

$$Q(\bar{\kappa}_1,\bar{\kappa}_2:U) = \int..\int k_2(t_1,x_1,y_1,t_2,x_2,y_2) \times \mathrm{Exp}[-i(\sigma_1 t_1+\kappa_{X1}x_1+\kappa_{Y1}y_1 +\sigma_2 t_2+\kappa_{X2}x_2+\kappa_{Y2}y_2)]dt_1...dy_2 \quad (7)$$

$$R(\bar{\kappa}_1,\bar{\kappa}_2:U) = \int..\int k_2(t_1,x_1,y_1,t_2,x_2,y_2) \times \mathrm{Exp}[-i(\sigma_1 t_1+\kappa_{X1}x_1+\kappa_{Y1}y_1 -\sigma_2 t_2-\kappa_{X2}x_2-\kappa_{Y2}y_2)]dt_1...dy_2 \quad (8)$$

Existence of these multi-dimensional Fourier transforms is assured by the assumption that the kernels of Equation (2) are non-zero in a finite range of time and space. Given a ship speed and a dispersion relationship the encounter frequency, σ, is determined by the vector wave number. Thus the functions on the left hand sides of Equations (6) through (8) may be considered functions only of vector wave number with the speed parameter, U, given. The background to the basic Taylor expansion suggests that the quadratic kernel should be symmetric in the sense that:

$$k_2(t_1,x_1,y_1,t_2,x_2,y_2) = k_2(t_2,x_2,y_2,t_1,x_1,y_1) \quad (9)$$

This symmetry implies:

$$Q(\bar{\kappa}_1,\bar{\kappa}_2:U) = Q(\bar{\kappa}_2,\bar{\kappa}_1:U) \quad (10)$$

$$R(\bar{\kappa}_1,\bar{\kappa}_2:U) = R^*(\bar{\kappa}_2,\bar{\kappa}_1:U) \quad (11)$$

The transform $T(\bar{\kappa}_1:U)$, Equation (6) is interpreted as the linear frequency response function. Because the arguments involve wave number and direction with ship speed given and the corresponding encounter frequency thus determined, this function is not essentially different from the corresponding function defined by St.Denis (1953) (and it may be remarked that had this result been different something would have been badly wrong). With respect to the linear response the present development contains nothing which has not been state of art for some time.

The form of the nonlinear terms of Equation (5) parallels the form of the corresponding terms of the time only model. In the time only model the shift in the mean is described by a quadratic frequency response function with arguments $(\sigma,-\sigma)$. In the present case the shift in the mean is defined by a similar function with arguments $(\bar{\kappa},\bar{\kappa}:U)$. It may be noted that for the special case of the transform $R(\bar{\kappa},\bar{\kappa}:U)$, the function is purely real since Equation (11) implies that the function is equal to its complex conjugate under this circumstance. In contrast to the time only model, the second harmonic response is described by a different function.

The above results suggest that the interpretation of the transforms of the quadratic kernel, Equations (7) and (8), can be continued in the same manner as the time only case. Thus the assumption is made that the wave field is the superposition of two regular waves with parameters $a_1,\bar{\kappa}_1$ and $a_2,\bar{\kappa}_2$. Substituting the sum of two cosinusoids, each defined as in Equation (4), into Equation (2) and taking account of Equations (6) through (11), results in the following expression for the steady state response to two distinct regular waves:

$$\begin{aligned} Z_2(t) = {} & a_1 Re\{T(\bar{\kappa}_1:U)\mathrm{Exp}[i\sigma_1 t-i\varepsilon_1]\} \\ & +a_2 Re\{T(\bar{\kappa}_2:U)\mathrm{Exp}[i\sigma_2 t-i\varepsilon_2]\} \\ & +(a_1^2/2)R(\bar{\kappa}_1,\bar{\kappa}_1:U) + (a_2^2/2)R(\bar{\kappa}_2,\bar{\kappa}_2:U) \\ & +(a_1^2/2)Re\{Q(\bar{\kappa}_1,\bar{\kappa}_1:U)\mathrm{Exp}[i2\sigma_1 t-i2\varepsilon_1]\} \\ & +(a_2^2/2)Re\{Q(\bar{\kappa}_2,\bar{\kappa}_2:U)\mathrm{Exp}[i2\sigma_2 t-i2\varepsilon_2]\} \\ & +a_1a_2 Re\{Q(\bar{\kappa}_1,\bar{\kappa}_2:U)\mathrm{Exp}[i(\sigma_1+\sigma_2)t-i(\varepsilon_1+\varepsilon_2)]\} \\ & +a_1a_2 Re\{R(\bar{\kappa}_1,\bar{\kappa}_2:U)\mathrm{Exp}[i(\sigma_1-\sigma_2)t-i(\varepsilon_1-\varepsilon_2)]\} \end{aligned} \quad (12)$$

As in the time only case the steady state response of the present model involves six frequencies and a shift in the mean. The first two terms are the linear response to each of the regular waves. The next two are the superposition of the mean shifts induced by the two waves, and the 5th and 6th terms are the superposition of the second harmonic response to the two waves. The 7th and 8th terms denote the response in the sum and difference frequencies. It is clear by analogy with the time only case that the transforms, Equations (7) and (8) may be interpreted as an extended form of quadratic frequency response function. The function $Q(\bar{\kappa}_1,\bar{\kappa}_2:U)$ expresses the normalized sum frequency response which arises in the response to pairs of waves, and the function $R(\bar{\kappa}_1,\bar{\kappa}_2:U)$ expresses the same thing for difference frequency response. Apart from minor notational differences these are the same functions introduced as linear and quadratic transfer functions by Hasselmann (1966). Essentially, the linear response function is a function of vector wave number, and the quadratic functions are functions of pairs of vector wave numbers.

The definition of the functions for a particular response by means of experiment or theoretical analysis is in principle the same as in the time only case. The ship system needs to be excited by single and dual regular wave fields, and the results interpreted in the light of Equations (5) and (12).

There are some significant differences between the present and the time only cases.

In the time only case it is possible to define a single quadratic frequency response function which is a function of two frequencies, and which serves to define quadratic response in both the sum and difference frequencies through the signs of the frequency arguments. This conceptual convenience is not available in the present case since sign changes in component wave numbers define a wave on a different heading, not the abstract reversed time that negative frequencies imply. It will be noted from Equations (6) through (8) that inversion into the time/space domain of the frequency response functions defined here is not the straightforward affair of the time only case.

The physical interpretation given the quadratic functions by Equation (12) lends additional credence to the symmetry assumed for the quadratic kernel of Equation (3). The quadratic response to two waves can not depend upon the order in which they are specified.

WAVE VARIANCE SPECTRA

In common with the long held wisdom, St.Denis (1953), Hasselmann (1966) makes the initial assumption that the random wave field, at least to a linear approximation associated with very mild wave conditions, is stationary in time, homogeneous in space, Gaussian and zero mean. The wave frequency-direction variance spectrum of wave elevations commonly used in the seakeeping field will be denoted $S_{\zeta\zeta}(\omega,\mu)$. The vector wave number variance spectrum which is an alternate representation will be denoted by $F(\kappa_X,\kappa_Y)$. It is usually assumed that both spectra are normalized in such a way that the wave elevation variance may be expressed as follows:

$$\mathrm{Var}(\zeta) = \int_{-\infty}^{\infty}\int_{-\infty}^{\infty} F(\kappa_X,\kappa_Y)\,d\kappa_X\,d\kappa_Y = \int_{\mu=0}^{2\pi}\int_{\omega=0}^{\infty} S_{\zeta\zeta}(\omega,\mu)\,d\omega\,d\mu \qquad (13)$$

An assumed dispersion relationship establishes the relationship between the two variance spectra by a change of variables in one or the other of the two forms of Equation (13).

SPECTRAL REPRESENTATIONS

The basic assumptions about the wave field just made, as well as the existence of a variance spectral density function for the homogeneous random wave field implies that the field has a "spectral representation" (Doob (1953), Yaglom (1962)). This representation is usually written in the form of a Fourier-Stieltges integral in the same form as that of the representation for a stationary (time only) process. Hasselmann (1966) (as well as St.Denis (1953)) found it convenient to work with the corresponding approximating Fourier sum, and modified the basic theoretical representation to account for the dispersive gravity wave case as well as the transformation to moving axes required for the present development. The result is a "spectral representation" for the encountered wave field, $\zeta(t,x,y)$, which may be written as follows:

$$\zeta(t,x,y) = \sum_j Re\left\{W(j)\,\mathrm{Exp}[i(\bar{\kappa}_j\cdot\bar{x}-\sigma_j t)]\right\} \qquad (14)$$

where $W(j)$ is a complex random function of the interval $\Delta\kappa_{Xj},\Delta\kappa_{Yj}$, and has the following properties. ($\langle\cdot\rangle$ denotes the ensemble expected value.)

$$\langle W(j)\rangle \equiv 0 \qquad (15)$$

$$\langle W(j)\,W^*(k)\rangle = 0 \qquad (\text{for } j \neq k) \qquad (16)$$

$$\langle W(j)\,W^*(j)\rangle = 2F(\kappa_{Xj},\kappa_{Yj})\,\Delta\kappa_{Xj}\Delta\kappa_{Yj} \qquad (17)$$

$$\langle W(j)W(k)\rangle \equiv 0 \qquad (18)$$

Now the initial assumption on the wave field of stationarity in time, and the Gaussian process assumption, as well as that of homogeneity imply that the random functions $W(j)$ are Gaussian and statistically independent for different wave numbers and directions of propagation. Thus from the properties of the third and fourth moments of Gaussian variables the following additional relations arise:

$$\langle W(j)W(k)W(m)\rangle = \langle W(j)W(k)W^*(m)\rangle \equiv 0 \qquad (19)$$

$$\langle W(j)W(k)W(m)W(n)\rangle = \langle W(j)W(k)W(m)W^*(n)\rangle \equiv 0 \qquad (20)$$

$$\langle W(j)W(k)W^*(m)W^*(n)\rangle = 0 \qquad (21)$$

unless (j,k = m,n or j,k = n,m)

in which case:

$$\langle W(j)W(k)W^*(j)W^*(k)\rangle = 4F(\kappa_{Xj},\kappa_{Yj})F(\kappa_{Xk},\kappa_{Yk})\,\Delta\kappa_{Xj}\Delta\kappa_{Yj}\,\Delta\kappa_{Xk}\Delta\kappa_{Yk} = 8[F(\kappa_{Xj},\kappa_{Yj})\,\Delta\kappa_{Xj}\Delta\kappa_{Yj}]^2 \qquad (\text{if } k = j) \qquad (22)$$

Returning to the spectral representation of the wave field, the expected value of Equation (14) yields zero as required from the relation, Equation (15). Taking the expected value of the square of Equation (14) to form the variance, and applying Equations (16) through (18) results in:

$$\langle\zeta^2(t,x,y)\rangle = \sum_j F(\kappa_{Xj},\kappa_{Yj})\,\Delta\kappa_{Xj}\Delta\kappa_{Yj} \qquad (23)$$

and it may be seen by increasing the range of j and decreasing the component wave number intervals, that in the limit this last result for the wave elevation variance becomes Equation (13) as required.

A substitution of Equation (14) into Equation (2), yields a spectral representation of the (statistical) steady state response. Carrying out the substitution with utilization of Equations (6) through (11), yields a spectral representation of the response as follows:

$$\xi(t) = \sum_j Re\{T(\bar{\kappa}_j:U)\, W^*(j)\, Exp[i\sigma_j t]\}$$

$$+\sum_j\sum_k \tfrac{1}{2} Re\{Q(\bar{\kappa}_j,\bar{\kappa}_k:U)\, W^*(j)\, W^*(k)\, Exp[i(\sigma_j+\sigma_k)t]\}$$

$$+\sum_j\sum_k \tfrac{1}{2} Re\{R(\bar{\kappa}_j,\bar{\kappa}_k:U)\, W^*(j)\, W(k)\, Exp[i(\sigma_j-\sigma_k)t]\} \qquad (24)$$

Apart from notation this last result corresponds to Hasselmann's spectral representation of the response (as well as that of St.Denis (1953), for the linear part).

THE MEAN VALUE OF RESPONSE

The most practically useful statistic of the quadratic response to random waves is the expected, or mean, value. Thus the next step is to take the ensemble expectation of Equation (24). The expectations of the first and second terms of Equation (24) are zero by Equations (15) and (18). The mean response of a linear system subjected to zero mean excitation is zero. Similarly, the second term involves the generation of high frequency response which does not contribute to a shift in the mean. When the third term of Equation (24) is expanded, the expectations taken, and Equations (11), (16) and (17) are applied the expected value of the response becomes:

$$\langle \xi(t) \rangle = \sum_j R(\bar{\kappa}_j,\bar{\kappa}_j:U)\, F(\kappa_{Xj},\kappa_{Yj})\, \Delta\kappa_{Xj}\Delta\kappa_{Yj} \qquad (25)$$

At this point the complex amplitude functions have disappeared so that increasing the range of j and decreasing the component wave number intervals, the limiting form of the result is an ordinary integral:

$$\langle \xi(t) \rangle = \int\int R(\bar{\kappa},\bar{\kappa}:U)\, F(\kappa_X,\kappa_Y)\, d\kappa_X d\kappa_Y \qquad (26)$$

The form of this result was obtained by Hasselmann (1966), and was buried in the context of the identification of the frequency response functions.

As has been noted, it is not the custom to use vector wave number variance spectra in seakeeping work, so that a change in the variables of Equation (26) is of interest. For present purposes the deep water dispersion relationship has been assumed. Thus the function $R(\bar{\kappa},\bar{\kappa}:U)$ of Equation (26) may be considered a function either of component wave numbers or wave frequency, ω, and direction, μ. This special value of the function appears in Equation (5) and is interpreted as a measure of the shift in the mean response to a single regular wave.

Thus if $\bar{Z}(\omega,\mu:U)$ is defined as the shift in the mean response induced by a regular wave of frequency ω, direction μ, and amplitude a, given ship speed, U, and the equivalents of the component wave numbers are used in the argument of $R(\bar{\kappa},\bar{\kappa}:U)$, Equation (5) implies the following transformation:

$$R(\bar{\kappa},\bar{\kappa}:U) \rightarrow 2[\bar{Z}(\omega,\mu:U)/a^2]$$

A change of variables of Equation (26) to the wave frequency-direction system assuming deep water dispersion results in the following for the expected value of response.

$$\langle \xi(t) \rangle = 2\int_{\mu=0}^{2\pi}\int_{\omega=0}^{\infty} [\bar{Z}(\omega,\mu:U)/a^2]\, S_{\zeta\zeta}(\omega,\mu)\, d\omega d\mu \qquad (27)$$

Within the present state of art the frequency-direction wave variance spectrum is most often represented as the product of a point spectrum $S(\omega)$, say and a spreading function $M(\mu)$; that is,

$$S_{\zeta\zeta}(\omega,\mu) = S(\omega)\, M(\mu) \qquad (28)$$

and substitution of this relation into Equation (28) yields:

$$\langle \xi(t) \rangle = \int_{\mu=0}^{2\pi} \left\{ 2\int_{\omega=0}^{\infty} [\bar{Z}(\omega,\mu:U)/a^2]\, S(\omega)\, d\omega \right\} M(\mu)\, d\mu \qquad (29)$$

To the extent that the shift in the mean response to a regular wave of unit amplitude is definable as a function of both frequency and direction (given speed) Equations (27) and (29) appear to be reasonably practical prediction formulae.

If the wave system is actually long-crested the spreading function in Equation (29) will approach a delta function $\delta(\mu_0-\mu)$, say, and the direction integration will in effect disappear. Under this assumption what is left within the curly brackets appears the same as the long known estimator for the mean of a quadratic system in long-crested waves, since the direction variable becomes a constant parameter. If speed ,U, is zero the expression within the brackets of Equation (29) is exactly the same estimator. What the present development has shown is that it is not necessary to work in the encounter domain when estimating mean added resistance or the like in either long or short crested seas. If the inner integration of Equation (29) is done first, the result prior to the direction integration is just the expected value of response to long-crested waves having a given point spectrum. Given this intermediate result for a range of wave headings, the short crested result for the mean value may be obtained mechanically in exactly the same way as that usually used in computing response variances in short-crested seas according to the established linear theory.

RESPONSE ENCOUNTER SPECTRA

It is not at all clear that estimates of the encountered spectrum of response in short crested seas would be commonly required, but it is of interest to see what is involved in such estimates when quadratic nonlinearities are present, as well as how general spectral moments are effected.

It was convenient to start by deriving the auto-correlation which is the expected value: $\langle \xi(t)\,\xi(t+\tau)\rangle$. Substitution of the spectral representation, Equation (34), for $\xi(t)$ and $\xi(t+\tau)$, expanding the product, taking the ensemble expectation, applying the relations, Equations (16) through (22), and observing the symmetry relations, Equations (10) and (11) results (after some pages of algebra) in the following expression:

$$\begin{aligned}\langle \xi(t)\xi(t+\tau)\rangle \;=\; & \sum_j |T(\bar\kappa_j:U)|^2 \cos(\sigma_j\tau)\, F(\kappa_{Xj},\kappa_{Yj})\,\Delta\kappa_{Xj}\Delta\kappa_{Yj} \\ & + \sum_j\sum_k \Big(\big\{ |Q(\bar\kappa_j,\bar\kappa_k:U)|^2 \cos[(\sigma_j+\sigma_k)\tau] \\ & \qquad + |R(\bar\kappa_j,\bar\kappa_k:U)|^2 \cos[(\sigma_j-\sigma_k)\tau] \big\} \\ & \qquad F(\kappa_{Xj},\kappa_{Yj})\, F(\kappa_{Xk},\kappa_{Yk})\,\Delta\kappa_{Xj}\Delta\kappa_{Yj}\,\Delta\kappa_{Xk}\Delta\kappa_{Yk} \Big) \\ & + \Big[\sum_j R(\bar\kappa_j,\bar\kappa_j:U)\, F(\kappa_{Xj},\kappa_{Yj})\,\Delta\kappa_{Xj}\Delta\kappa_{Yj} \Big]^2 \end{aligned} \qquad (30)$$

where τ is a time difference, and σ_1 and σ_2 are encounter frequencies defined by the corresponding wave frequencies and directions.

The last term of Equation (30) is the square of the mean, Equation (25), so that the first two terms are a spectral representation of the auto-covariance. As before, the complex amplitude functions have gone so that by increasing the ranges of j and k and decreasing the component wave number intervals yields a limiting form in the form of ordinary integrals. Transforming these integrals from the wave number to the wave frequency/direction domain with deep water assumed yields the following result for the auto-covariance of the response:

$$\begin{aligned} C_{\zeta\zeta}(\tau) \;=\; & \int_0^{2\pi}\int_0^{\infty} |\tilde T(\omega_1,\mu_1:U)|^2 \cos(\sigma_1\tau)\, S_{\zeta\zeta}(\omega_1,\mu_1)\, d\omega_1 d\mu_1 \\ & + \int_0^{2\pi}\int_0^{2\pi}\int_0^{\infty}\int_0^{\infty} \big\{ |\tilde Q(\omega_1,\mu_1,\omega_2,\mu_2:U)|^2 \cos[(\sigma_1+\sigma_2)\tau] \\ & \qquad + |\tilde R(\omega_1,\mu_1,\omega_2,\mu_2:U)|^2 \cos[(\sigma_1-\sigma_2)\tau] \big\} \\ & \qquad S_{\zeta\zeta}(\omega_1,\mu_1)\, S_{\zeta\zeta}(\omega_2,\mu_2)\, d\omega_1 d\mu_1\, d\omega_2 d\mu_2 \end{aligned} \qquad (31)$$

where $\tilde T(\omega_1,\mu_1:U)$, $\tilde Q(\omega_1,\mu_1,\omega_2,\mu_2:U)$, and $\tilde R(\omega_1,\mu_1,\omega_2,\mu_2:U)$ denote the linear and quadratic response functions mapped into the wave frequency-direction domain.

It is convenient to define a two sided variance spectrum of response, $\Phi(\sigma)$, such that the the integral over positive and negative encounter frequency equals the response variance. Invoking the standard relation between the spectrum and the auto-covariance, the encounter spectrum then becomes:

$$\begin{aligned} \Phi(\sigma) \;=\; & \frac{1}{2\pi}\int_{-\infty}^{\infty} C_{\zeta\zeta}(\tau)\, Exp[-i\sigma\tau]\, d\tau \\ \;=\; & \frac{1}{2}\int_0^{2\pi}\int_0^{\infty} |\tilde T(\omega_1,\mu_1:U)|^2 \,[\delta(\sigma_1-\sigma)+\delta(-\sigma_1-\sigma)] \\ & \qquad S_{\zeta\zeta}(\omega_1,\mu_1)\, d\omega_1 d\mu_1 \\ & + \frac{1}{2}\int_0^{2\pi}\int_0^{2\pi}\int_0^{\infty}\int_0^{\infty} \Big(|\tilde Q(\omega_1,\mu_1,\omega_2,\mu_2:U)|^2 \times \\ & \qquad [\delta(\sigma_1+\sigma_2-\sigma)+\delta(-\sigma_1-\sigma_2-\sigma)] \\ & \qquad + |\tilde R(\omega_1,\mu_1,\omega_2,\mu_2:U)|^2 \times \\ & \qquad [\delta(\sigma_1-\sigma_2-\sigma)+\delta(-\sigma_1+\sigma_2-\sigma)] \Big) \\ & \qquad S_{\zeta\zeta}(\omega_1,\mu_1)\, S_{\zeta\zeta}(\omega_2,\mu_2)\, d\omega_1 d\mu_1\, d\omega_2 d\mu_2 \end{aligned} \qquad (32)$$

where $\delta(\ldots)$ denotes the Dirac delta function.

As in St.Denis (1953), Equation (32) must be transformed into the encounter domain. Assuming deep water, the transformation of the first (linear) term of Equation (32) may be carried out exactly as in St.Denis (1953). Because encounter frequency is an ambiguous function of wave frequency and direction, the integration of the first term must be broken into three parts which correspond to three non-ambiguous regions where the transformations are one-to-one. Following St.Denis, the three regions in the wave frequency-direction domain are defined as follows:

Region 1; $\quad -\infty < \alpha < 1/2$

Region 2; $\quad 1/2 < \alpha < 1$

Region 3; $\quad 1 < \alpha < \infty$

where $\alpha = (\omega U/g)\cos(\mu)$

The integrations of the second term involve two wave frequency- direction domains, so that there is a nine-fold ambiguity rather than the three fold of the linear term. Table 1 indicates the nine domains into which the integration of the second term must be broken to insure one to one transformations.

The following indicates the form of the transformed two-sided spectrum:

$$\Phi(\sigma) = \frac{1}{2}\sum_{p=1}^{3}\int_{Dp}|\hat{T}^p(\sigma_1,\mu_1)|^2\,[\delta(\sigma_1-\sigma)+\delta(-\sigma_1-\sigma)]\,S^p_{\zeta\zeta}(\sigma_1,\mu_1)\,d\sigma_1 d\mu_1$$

$$+\frac{1}{2}\sum_{p=1}^{3}\sum_{q=1}^{3}\int_{Dp}\int_{Dq}\Big(|\hat{Q}^{pq}(\sigma_1,\mu_1,\sigma_2,\mu_2)|^2\times[\delta(\sigma_1+\sigma_2-\sigma)+\delta(-\sigma_1-\sigma_2-\sigma)]$$

$$+|\hat{R}^{pq}(\sigma_1,\mu_1,\sigma_2,\mu_2)|^2\times[\delta(\sigma_1-\sigma_2-\sigma)+\delta(-\sigma_1+\sigma_2-\sigma)]\Big)$$

$$S^p_{\zeta\zeta}(\sigma_1,\mu_1)\,S^q_{\zeta\zeta}(\sigma_2,\mu_2)\,d\sigma_1 d\mu_1\,d\sigma_2 d\mu_2 \qquad (33)$$

In the above, $S^p_{\zeta\zeta}(\sigma,\mu)$ denotes the encountered directional spectrum in the "p"th region. $T^p(\sigma_1,\mu_1)$ denotes the linear response function corresponding to the "p" th region and considered as a function of encounter frequency and wave direction. Similarly, $Q^{pq}(\sigma_1,\mu_1,\sigma_2,\mu_2)$ and $R^{pq}(\sigma_1,\mu_1,\sigma_2,\mu_2)$ denote the quadratic response functions as functions of encounter frequency in the "pq" th region, Table 1. The integration limits "Dp" and "Dq" symbolize the σ,μ domains corresponding to the relations given in Table 1. It should be noted that the signs of encounter frequency are meaningful in the quadratic term. Thus in working out the corresponding encounter frequencies for each domain a deviation from the detail of the St.Denis treatment is required. St.Denis modified the encounter frequencies corresponding to $1 < \alpha < \infty$ to be positive always. (This makes no difference to the transformation of the linear term since the spectrum is even by definition.) In the present case encounter frequencies in this region are allowed to be negative. This results in a second minor difference in that wave directions in the present case are the same in the wave and the encounter domains.

TABLE 1

DOMAINS OF INTEGRATION

	p = 1	p = 2	p = 3
q = 1	$-\infty < \alpha_1 < 1/2$ $-\infty < \alpha_2 < 1/2$	$1/2 < \alpha_1 < 1$ $-\infty < \alpha_2 < 1/2$	$1 < \alpha_1 < \infty$ $-\infty < \alpha_2 < 1/2$
q = 2	$-\infty < \alpha_1 < 1/2$ $1/2 < \alpha_2 < 1$	$1/2 < \alpha_1 < 1$ $1/2 < \alpha_2 < 1$	$1 < \alpha_1 < \infty$ $1/2 < \alpha_2 < 1$
q = 3	$-\infty < \alpha_1 < 1/2$ $1 < \alpha_2 < \infty$	$1/2 < \alpha_1 < 1$ $1 < \alpha_2 < \infty$	$1 < \alpha_1 < \infty$ $1 < \alpha_2 < \infty$

Clearly, programming the estimate of the encounter spectrum will be an aggravation if it is needed. The expression given is incomplete in the sense that an integration with respect to either σ_1 or σ_2 is needed to remove the delta functions. Nevertheless the estimate would probably be less trouble than obtaining the quadratic frequency response functions required.

SPECTRAL MOMENTS

More often than not, "spectral moments" are of more practical use than the encountered response spectrum itself. The "n"th spectral moment may be defined:

$$m_n = \int_0^\infty \sigma^n[2\Phi(\sigma)]d\sigma \qquad (34)$$

Carrying out the indicated operation on Equation (33) results in the following expression for the spectral moments:

$$m_n = \sum_{p=1}^{3}\int_{Dp}|\hat{T}^p(\sigma_1,\mu_1)|^2\,|\sigma_1|^n\,S^p_{\zeta\zeta}(\sigma_1,\mu_1)\,d\sigma_1 d\mu_1$$

$$+\sum_{p=1}^{3}\sum_{q=1}^{3}\int_{Dp}\int_{Dq}\Big(|\hat{Q}^{pq}(\sigma_1,\mu_1,\sigma_2,\mu_2)|^2\,|\sigma_1+\sigma_2|^n + |\hat{R}^{pq}(\sigma_1,\mu_1,\sigma_2,\mu_2)|^2\,|\sigma_1-\sigma_2|^n\Big)$$

$$S^p_{\zeta\zeta}(\sigma_1,\mu_1)\,S^q_{\zeta\zeta}(\sigma_2,\mu_2)\,d\sigma_1 d\mu_1\,d\sigma_2 d\mu_2 \qquad (35)$$

It may be noted that Equation (35) for the moments may be transformed back into the wave frequency domain, and Equation (36) following is the result.

$$m_n = \int_0^{2\pi}\int_0^{\infty}|\tilde{T}(\omega,\mu:U)|^2\,|\sigma|^n\,S_{\zeta\zeta}(\omega,\mu)\,d\omega d\mu$$

$$+\int_0^{2\pi}\int_0^{2\pi}\int_0^{\infty}\int_0^{\infty}\Big(|\tilde{Q}(\omega_1,\mu_1,\omega_2,\mu_2:U)|^2\,|\sigma_1+\sigma_2|^n + |\tilde{R}(\omega_1,\mu_1,\omega_2,\mu_2:U)|^2\,|\sigma_1-\sigma_2|^n\Big)$$

$$S_{\zeta\zeta}(\omega_1,\mu_1)\,S_{\zeta\zeta}(\omega_2,\mu_2)\,d\omega_1 d\mu_1\,d\omega_2 d\mu_2 \qquad (36)$$

where in order to compress the notation the encounter frequencies instead of the corresponding functions of wave frequency, direction and speed are retained in the equation.

As in the purely linear case, all moments of the encountered response spectrum in short crested seas may be computed in the wave frequency domain rather than in the much more complicated encounter domain. When n=0, 2 and 4 in Equation (36) the variances of the response and its first two time derivatives are recovered, and these results are checked by independent derivation in Dalzell (1985).

DISCUSSION

Had the question concerning what can be done about the weakly nonlinear short crested sea situation been asked earlier, there would likely have been some answers long since because Hasselmann published the basic formulation in 1966. The present development is

largely a translation and embellishment of this basic formulation. As in the case of the purely linear short crested theory, it is assumed that the wave field is a stationary zero mean vector Gaussian process. This assumption, as Hasselmann pointed out in 1966, is inconsistent in the sense that only the ship system is allowed to have quadratic nonlinearities. Work to remove this inconsistency and investigate the effect of quadratic wave-wave interactions upon various statistics of response is presently under way.

Given a directional wave spectrum and the linear and quadratic response functions corresponding to some response of interest, estimating formulae have also been developed for the third degree cumulants of the joint probability density of the response and its first two derivatives, Dalzell (1985). When the quadratic contributions to response are assumed negligible in these estimates as well as the ones shown in the present paper the results of the purely linear short crested theory are recovered to the extent that they are applicable. When the directional wave spectrum is modified to represent long-crested waves it appears that the time only quadratic model is recovered.

Broadly, the fundamental difference between the time only and the present short crested sea model is that a wave field rather than a wave profile must be dealt with. The result is that the kernels in the functional expansion of the nonlinear response are functions of space a well as time. Response functions which describe the linear and quadratic response in the wave number or wave frequency domains are identifiable in much the same way as in the time only model. The difference is that the arguments of these functions are vector rather than scalar. In the present work no attempt has been made to do anything beyond indicate how the quadratic response functions may be obtained. Because of the effective increase in dimensions, it is likely that an actual analytical determination of the quadratic functions will consume more computational effort than nearly any of the estimates which the present work shows may be made from them.

Very little work on time domain simulation of quadratic response in short crested seas has been done. The implied six-fold convolution of Equation (2), as well as the inversion of quadratic frequency response to the corresponding time-space domain kernel, appear to be formidable computational problems. If this has to be done for some reason, a "spectral" approach involving Equation (24) may yield more tractable approximations.

CONCLUSION

Relative to the corresponding results for the time only quadratic model there are no real surprises in the short crested estimation formulae; that is, no fundamental changes in form. All such estimates are more complicated, but this has to do with the additional wave direction parameter.

It was found that in all of the estimates except that of the response spectrum in the encounter frequency domain, there is no necessity to work in the encounter domain. Wave frequency domain estimates represent computationally less demanding approaches. This result also means that many of the formulae for statistical parameters for the time only case may be recast into the wave frequency domain, and consequently that the restriction of the time only case to the nonambiguous portion of the encounter frequency domain may be largely removed.

The formula given for the mean value of the response in short crested seas is especially simple, in that it is hardly more computationally demanding than estimating the variance of a purely linear system in short crested seas. Furthermore, it is probable that the quadratic response functions required for this estimate are state of art.

ACKNOWLEDGMENTS

This work was funded by the Mathematical Statistics Program of the Naval Sea Systems Command, and by the General Hydromechanics Research Program administered by DTNSRDC.

REFERENCES

Barrett, J.F., (1963) "The Use of Functionals in the Analysis of Non-linear Physical Systems", Journal of Electronics and Control, Vol. 15.

Brink, A.W., and Stuurman, A.M., (1979) "Automatic and Manual Control of the "Tripartite" Minehunter in the Hover and Trackkeeping Modes -- A Preliminary Design Study", International Shipbuilding Progress, Vol. 26, No. 300.

Dalzell, J.F., (1976) "Application of the Functional Polynomial Model to the Ship Added Resistance Problem", 11th Symposium on Naval Hydrodynamics, London.

Dalzell, J.F., and Kim, C.H., (1979) "An Analysis of the Quadratic Frequency Response Function for Added Resistance", Journal of Ship Research, Vol. 23, No.3.

Dalzell, J.F. (1985) "Effect of Short-Crested Seas on Quadratic Response", David Taylor Naval Ship Research and Development Center Report DTNSRDC-85/102, A163435.

Doob, J.L., (1953) "Stochastic Processes", John Wiley & Sons, New York.

Gel'fand, I., and Vilenkin, N., (1964) "Generalized Functions; Volume 4", Academic Press, New York, Chapter 1.

Hasselmann, K., (1966) "On Nonlinear Ship Motions in Irregular Waves", Journal of Ship Research, Vol. 10, No. 1.

Kim, C.H., and Dalzell, J.F., (1981) " An Analysis of the Quadratic Frequency Response for Lateral Drifting Force and Moment", Journal of Ship Research, Vol. 25, No. 2.

Pinkster, J.A., (1979) "Mean and Low Frequency Wave Drifting Forces on Floating Structures", Ocean Engineering.

Pinkster, J.A., (1980) "Low Frequency Second Order Wave Exciting Forces on Floating Structures", Publication 650, Netherlands Ship Model Basin.

Rugh, W.J., (1981) "Nonlinear System Theory", Johns Hopkins University Press, Chapter 1.

St.Denis, M., and Pierson, W.J., (1953) "On the Motion of Ships in Confused Seas", Society of Naval Architects and Marine Engineers, Vol. 61.

Vassilopoulos, L.A., (1966) "Application of Statistical Theory of Nonlinear Systems to Ship Motion Performance in Random Seas", Ship Control Symposium, Annapolis.

Volterra, V., (1930) "Theory of Functionals and of Integral and Integro-differential Equations", (Dover Publications, 1959), Chapter 1.

Yaglom,A.M., (1962) "An Introduction to the Theory of Stationary Random Functions", Prentice-Hall, (Dover Publications, 1973).

DISCUSSION

Radoslav Nabergoj,
Institute of Naval Architecture, Trieste

First of all, I would like to express my appreciation to Prof. Dalzell for his valuable paper on ship response in short crested seas. He shows how the Volterra functional method may successfully be used to solve the nonlinear seakeeping problem in quite a simple manner, i.e. by means of a nonlinear transfer function. The way appears to be sufficiently clear, although a lot of work a lot of work remains still to be done.

Would the author explain the advantages of this method with respect to the method based on Focker-Plank equation. The latter allows one to compute both the usual statistics of the response and the distribution of the maxima, frequently required in practical applications. How can this be done by the method here presented?

Moreover, would the author explain why he used a quadratic model instead of a cubic model which, for example, is commonly adopted in any theoretical investigation of the nonlinear rolling.

Reply -

My thanks to Prof. Nabergoj for his kind words. It is agreed that much more could be done.

The approach to nonlinear random systems in the paper is admittedly quite restrictive. It applies only to stable systems having quadratic nonlinearities, and this restricts practical use to problems similar to low frequency drift or added resistance. In my opinion these problems are of sufficient importance in their own right to justify the effort. On the other hand, as Prof. Nabergoj points our, the quadratic model is not appropriate for the study of weak nonlinearities which occur in the restored motions of roll, pitch, or heave, unless the particular geometry involves unusually weak restoration. In order to model this class of nonlinearities the functional expansion has to be truncated after the cubic term at least. Some work similar to that of the paper has been done with a cubic model for the long crested but not the short-crested case. The direct answer to Prof. Nabergoj's last question is that the statistics of a cubic system in short crested seas were not attempted because it was not obvious at the outset that anything useful could be obtained even for the simpler quadratic case.

Approximations, consistent with the order of the expansion, to the most important parameters defining the probability density of response maxima are available with the present method. I must note that my exposure to Fokker-Planck (FP) methods is rather elementary. Ideally, the FP approach to the statistics of system response is far superior to that adopted here. However it appears that the practical implementation of the FP appraoch depends upon two assumptions which are not necessarily appropriate for all ship motions problems. The first is that a single differential equation with constant coefficients is postulated to define the ship system. Most FP work I have seen involves the representation of rolling with Froude's single degree of freedom rolling equation. I do not remember seeing a treatment of anything else. I have also not yet seen the postulation in the FP context of the set of six nonlinear integro-differential equations which we probably have to deal with generally. In the functional expansion approach, system memory and coupled systems are automatically taken care of. Of course, if the degree of the functional expansion is less than that required to describe the physics of the problem the approach is useless. The functional expansion approach cannot possibly deal with strong nonlinearities, and this is a cardinal weakness. The second pivotal assumption in the FP approach is that the system is excited by a white (time-only) noise. This, I think, confines the FP approach at best to the long-crested case, and at worst to wave spectra with unrealistic shapes.

Wave Drift Forces in Current

R. H. M. HUIJSMANS

MARIN, The Netherlands

ABSTRACT

This paper is concerned with the development and application of hydrodynamic theory required for the prediction of the wave damping phenomena as introduced by Wichers in 1979 [1] and in 1982 [2]. The concept of wave damping necessitates the development of forward speed dependent expressions for the mean wave drift forces and a new 3-d diffraction potential algorithm for forward speed. (Wichers and Huijsmans [3], Hearn and Koon [4]).

In this paper the first order calculated motion response functions for heave and pitch for a 200 kDWT tanker moored in deep water head waves with a 4 knot current are compared with results of model test experiments. Also for this situation the computed mean wave drift forces are validated with results from model test experiments as reported by Wichers [5].

The overall comparison between calculations and results from model test experiments for the first order response functions and the mean wave drift forces are generally quite good.

INTRODUCTION

In the last two decades many theories have been developed to compute ship motions. Major attention is directed towards thin and slender ships sailing at forward speed in waves. An important development is the slender body approximation by Newman [6] and Newman and Tuck [7] for both zero and non-zero forward speed.

The unified strip theory introduced by Newman [8] gave again better results in several cases and is extended by several authors.

Meanwhile some powerful programs have been introduced to treat the zero speed case for ship motions, without any geometrical simplifications. One of the first diffraction programs making use of source distributions over the actual hull surface was reported by Van Oortmerssen [9]. Since then several similar programs have been developed.

Some care is needed to evaluate the pulsating wave source. Newman [10] reports a very efficient algorithm for the computation of the pulsating wave source function at zero speed.

Using pressure integration techniques Pinkster [11] showed excellent agreeement of the calculated wave drift forces at zero speed with experiements. An unresolved problem, however, is the estimation of the motions of a moored ship, especially when the mooring is unstable. Wichers and Huijsmans [3] also report that the damping at the natural frequencies of the mooring system have to be considered carefully.

Results of model test experiments showed that a large part of the damping at these natural frequencies could be contributed to the velocity dependency of the wave drift forces. A consideration that also has been supported by Faltinsen et al. [12].

The experimental investigation and validation actually go back to the work of Remery and Hermans [13] in 1971. They reported that a unreasonably large damping coefficient had to be chosen for the correct prediction of the low frequency motion response.

So the effect of forward speed should be accounted for if one wants to evaluate this wave damping phenomena. The forward speed effect can be introduced using the pulsating translating wave source function and certain line integrals. This approach has been attempted by Bougis [14], Chang [15] and Inglis [16]. The computer time involved in their calculations was very large with respect to the zero speed calculations.

An approximative way of introducing forward speed into the problem has e.g. been presented by Inglis [16] and Huijsmans and Dallinga [17]. The total potential function will be split up in the well-known way:

$$\Phi(\underline{x},t) = -Ux + \phi(\underline{x},U) + \overline{\Phi}(\underline{x},U,t) \qquad (1)$$

The steady problem gives rise to a highly non-uniform problem in the case where U tends to zero as has been shown, amongst others, by Hermans [18], Brandsma and Hermans [19] and

R.H.M. Huijsmans, Maritime Research Institute Netherlands (MARIN), Haagsteeg 2, P.O. Box 28, 6700 AA Wageningen, The Netherlands

Eggers [20], especially in the case for non-thin and non-slender bodies.

The time dependent potential $\bar{\phi}(\underline{x},U,t)$ will be written as a source distribution along the ship's hull and the waterline. This expression will then be expanded with respect to small values of the forward speed U. Huijsmans and Hermans [22] give a justification of the use of such a small forward speed expansion.

MATHEMATICAL FORMULATION

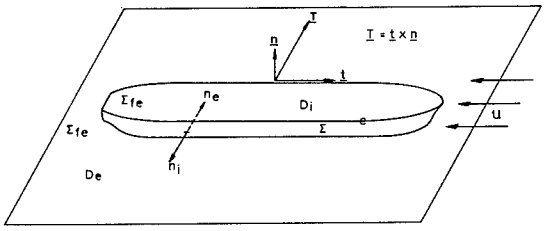


Fig. 1 System of axes

The problem for the time harmonic potential $\bar{\Phi}(\underline{x},U,t)$ can be written as:

$$\Delta\bar{\Phi} = 0 \qquad \text{in the fluid domain} \qquad (2)$$

$$\bar{\Phi}_{tt} - 2U\,\bar{\Phi}_{xt} + U^2\,\bar{\Phi}_{xx} + g\,\bar{\Phi}_z = 0 \text{ at } z=0 \qquad (3)$$

$$(\nabla\bar{\Phi}.n) = V(\underline{x})\,e^{-i\omega t} \qquad \text{at } \underline{x} \in S_o \qquad (4)$$

an appropriate radiation condition

where $V(\underline{x}) = n_x$ if the ship exhibits a unit oscillatory motion in the x-direction. In the case of wave diffraction and motions in the other modes $V(\underline{x})$ is defined accordingly.

We assume $\bar{\Phi}(x,U,t)$ to be oscillatory:

$$\bar{\Phi}(x,U,t) = \phi(\underline{x},U)\,e^{-i\omega t} \qquad (5)$$

The free surface condition (3) results in:

$$-\omega^2\phi + 2i\omega\,U\,\phi_x + U^2\phi_{xx} + g\,\phi_z = 0 \text{ at } z=0 \qquad (6)$$

and the condition on the hull:

$$(\nabla\phi.n) = V(\underline{x})$$

Brard [21] applies Green's theorem to a problem in D_i inside S_o and to the problem D_e, outside S_o, where S_o is the ship's hull. In this way it can be shown that the problem can be described by means of a source and a vortex distribution. Following the analysis as presented by Huijsmans and Hermans [22] one may write:

$$\iint_{S_o} -\gamma(\underline{\xi})\,\frac{\partial}{\partial n}\,G(\underline{x},\underline{\xi})dS_\xi - \iint_{S_o}\sigma(\underline{\xi})\,G(\underline{x},\underline{\xi})dS_\xi$$
$$- 2i\,\frac{\omega U}{g}\int_{WL}\gamma(\underline{\xi})\,G(\underline{x},\underline{\xi})dn + \frac{U^2}{g}\int_{WL}\gamma(\underline{\xi})\,\frac{\partial}{\partial\xi}\,G(\underline{x},\underline{\xi})$$
$$- \{\alpha_t\gamma_t(\underline{\xi}) + \alpha_T\gamma_T(\underline{\xi})\}G(\underline{x},\underline{\xi})dn +$$
$$+ \frac{U^2}{g}\int_{WL}\alpha_n\,\sigma(\underline{\xi})\,G(\underline{x},\underline{\xi})dn = \begin{cases} 4\pi\,\phi_e & x \in D_e \\ 4\pi\,\phi_i & x \in D_i \end{cases} \qquad (7)$$

$\alpha_t = \cos(0x,\underline{t})$
$\alpha_T = \cos(0x,\underline{T})$
$\alpha_n = \cos(0x,\underline{n})$

where n is the normal and $\underline{t}$ is the tangent to the waterline and $T = \underline{t} \times \underline{n}$ the binormal.

It is clear that with the choice of $\gamma(\underline{\xi}) = 0$ the integral along the waterline gives no contribution up to order U. Hence, for our purpose a source distribution is the appropriate choice. The source strength $\sigma(\underline{\xi})$ is then the solution of the following integral equation, where the velocity squared terms have been dropped:

$$-\tfrac{1}{2}\,\sigma(\underline{x},U) + \frac{1}{4\pi}\iint_{S_o}\sigma(\underline{\xi},U)\,\frac{\partial}{\partial n_x}\,G(\underline{x},\underline{\xi})dS_\xi = V(\underline{x}) \qquad x \in S_o \qquad (8)$$

and

$$\phi(\underline{x},U) = \frac{1}{4\pi}\iint_{S_o}\sigma(\underline{\xi},U)\,G(\underline{\xi},\underline{x},U)dS_\xi \qquad x \in D_e \qquad (9)$$

If we consider the case that $\tau = \omega U/g \ll 1$ it can be shown [22]:

$$\sigma(\underline{x},U) = \sigma_0(\underline{x}) + \tau\,\sigma_1(\underline{x}) + \tilde{\sigma}(\underline{x},U)$$
$$\phi(\underline{x},U) = \phi_0(\underline{x}) + \tau\,\phi_1(\underline{x}) + \tilde{\phi}(\underline{x},U) \qquad (10)$$

where $\tilde{\sigma}$ and $\tilde{\phi}$ are $O(\tau^2)$ as $\tau \to 0$.

The Green's function for $\tau < \frac{1}{4}$ is given by Wehausen and Laitone [24]:

$$G(\underline{x},\underline{\xi},U) = -\frac{1}{r} + \frac{1}{r_1} - \psi(\underline{x},\underline{\xi},U) \qquad (11)$$

with

$$\psi(\underline{x},\underline{\xi},U) = \frac{2g}{\pi}\int_0^{\pi/2} d\Theta \int_{L_1} dk\,F(\Theta,k) +$$
$$+ \frac{2g}{\pi}\int_{\pi/2}^{\pi} d\Theta \int_{L_2} dk\,F(\Theta,k)$$

when

$$F(\Theta,k) =$$

$$= \frac{k\,\exp\{k(z+\zeta+i(x-\xi)\cos\Theta)\}\,\cos\{k(y-n)\sin\Theta\}}{gk - (\omega + kU\cos\Theta)^2}$$

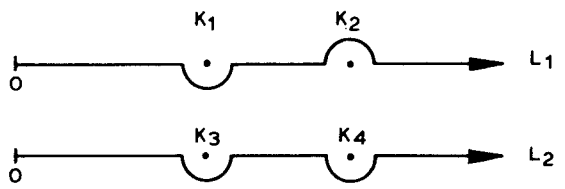


Fig. 2 Contours L_1 and l_2

with k_1, k_2, k_3 and k_4 are the poles of $F(\Theta,k)$.

Developing this Green's function with respect to τ leads to:

$$\psi(\underline{x},\underline{\xi},U) = \psi_0(\underline{x},\underline{\xi}) + \tau\ \psi_1(\underline{x},\underline{\xi})$$

with:

$$\psi_0(\underline{x},\underline{\xi}) = 2g \int_L \frac{k\ e^{k(z+\zeta)}}{gk - \omega^2} J_0(kR)dk \qquad (12)$$

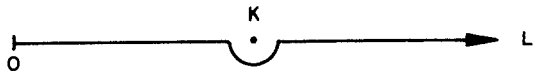
$$\psi_1(\underline{x},\underline{\xi}) =$$

$$= 4ig^2 \cos\Theta' \int_L \frac{k^2\ e^{k(z+\zeta)}}{(gk - \omega^2)^2} J_1(kR)dk \qquad (13)$$

where: $R^2 = (x-\xi)^2 + (y-\eta)^2$

and : $\Theta' = \text{arctg}\left(\frac{y-\eta}{x-\xi}\right)$

and the integration contour L becomes:



Using the expansion given for $\sigma(\underline{x},U)$ and $\phi(\underline{x},U)$ results in equations for σ_0, σ_1, ϕ_0 and ϕ_1. The source functions σ_0 and σ_1 become:

$$-\tfrac{1}{2}\ \sigma_0(\underline{x}) + \frac{1}{4\pi} \iint_{S_o} \sigma_0(\underline{\xi})\ \frac{\partial}{\partial n_x}\ G_0(\underline{x},\underline{\xi})dS_\xi = V(\underline{x}) \qquad (14)$$

and

$$-\tfrac{1}{2}\ \sigma_1(\underline{x}) + \frac{1}{4\pi} \iint_{S_o} \sigma_1(\underline{\xi})\ \frac{\partial}{\partial n_x}\ G_0(\underline{x},\underline{\xi})d\sigma_\xi =$$

$$= +\frac{1}{4\pi} \iint_{S_o} \sigma_0(\underline{\xi})\ \frac{\partial}{\partial n_x}\ \psi_1(\underline{x},\underline{\xi})dS_\xi \qquad (15)$$

Once the Fredholm integral equations for σ_0 and σ_1 are solved the potential functions become:

$$\phi_0(\underline{x}) = \frac{1}{4\pi} \iint_{S_o} \sigma_0(\underline{\xi})\ G_0(\underline{x},\underline{\xi})dS_\xi \qquad (16)$$

and

$$\phi_1(\underline{x}) = -\frac{1}{4\pi} \iint_{S_o} \sigma_0(\underline{\xi})\ \psi_1(\underline{x},\underline{\xi})dS_\xi +$$

$$+\frac{1}{4\pi} \iint_{S_o} \sigma_1(\underline{\xi})\ G_0(\underline{x},\underline{\xi})dS_\xi \qquad (17)$$

The hydrodynamic pressure can be derived from the linearized Bernoulli equation:

$$p(\underline{x},t) = -\rho\left(\frac{\partial}{\partial t}\ \Phi(\underline{x},t) - U\ \frac{\partial}{\partial x}\ \Phi(\underline{x},t)\right) \qquad (18)$$

From this expression the first order hydrodynamic reaction coefficients and wave loads can be determined by integration of the pressure distribution over the mean wetted surface.

From the computed wave loads and added mass and damping coefficients, the motion of the vessel can be determined using Newton's law of inertia.

DERIVATION OF THE MEAN WAVE DRIFT FORCES

Once the velocity potential $\phi(\underline{x},U)$ is known, the fluid pressure is determined from Bernoulli's equation:

$$p = -\rho gz - \rho\ \Phi_t - \tfrac{1}{2}\rho\ |\nabla\Phi|^2 + p_0 + C(t) \qquad (19)$$

where:

p_0 = atmospheric pressure
z = vertical distance below the mean free surface
Φ = velocity potential
$C(t)$ = a constant independent of co-ordinates
ρ = mass density of fluid.

In Bernoulli's equation p_0 and $C(t)$ may be taken zero without loss of generality.

Assuming that the point is carrying out first order wave frequency motion $\underline{X}^{(1)}$ about a mean position $\underline{X}^{(0)}$ and applying a Taylor's expansion to the pressure in the mean position, the following expression is found:

$$p = p^{(0)} + \varepsilon p^{(1)} + \varepsilon^2 p^{(2)} + O(\varepsilon^3) \qquad (20)^1$$

where:

$$p^{(0)} = -\rho g z^{(0)}\ , \qquad (21)$$

the hydrostatic pressure

$$p^{(1)} = -\rho g z^{(1)} - \rho\Phi_t^{(1)}\ , \qquad (22)$$

the first order pressure

$$p^{(2)} =$$

$$-\tfrac{1}{2}\rho\ |\nabla\Phi^{(1)}|^2 - \rho\Phi_t^{(2)} - \rho(\underline{X}^{(1)}.\nabla\Phi_t) \qquad (23)$$

The derivatives of the potential $\Phi^{(1)}$ are taken at the mean postion of the point. The material derivative, D/Dt, results in a $\partial/\partial t$ and a convective term $-U\ \partial/\partial x$ operating on the potential $\Phi^{(1)}$. We will further neglect the influence of the second order velocity potential $\Phi^{(2)}$, since this term does not contribute to the mean wave drift forces.

The force acting on the ship is expressed as:

$$F = -\int_S p\ \underline{n}\ dS \qquad (24)$$

with S the instantaneous wetted surface.

Using a similar perturbation scheme for the wave loads as for the fluid pressure, we can write:

$$F = F^{(0)} + \varepsilon F^{(1)} + \varepsilon^2 F^{(2)} + O(\varepsilon^3) \qquad (25)$$

[1] The superscripts (0), (1) and (2) indicate the zero, first and second order variables as defined by expansion (20).

in which the $F^{(0)}$ is the hydrostatic force obtained from integration of $p^{(0)}$ over the mean wetted surface S_o and $F^{(1)}$ is the first order wave load.

After some algebraic manipulations, the final expressions for the mean wave drift force becomes:

$$F^{(2)} =$$

$$- \int_{WL} \tfrac{1}{2}\rho |\zeta_r^{(1)}|^2 \, \underline{n} \, d\ell + \alpha^{(1)} x \, (M.\ddot{\underline{x}}_g^{(1)}) +$$

$$+ \int_{S_o} \tfrac{1}{2}\rho |\nabla\Phi^{(1)}|^2 \, \underline{n} \, dS + \int_{S_o} \rho (X^{(1)}.\nabla\phi_t^{(1)}) \underline{n} \, dS \qquad (26)$$

which in fact is a complete analogue of the expressions Pinkster [11] obtained. We distinguish four contributions to the total mean wave drift force.

I : First order relative wave elevation

$$-\tfrac{1}{2}\rho g \int_{WL} |\zeta_r^{(1)}|^2 \, n \, d\ell \qquad (27)$$

II : Pressure drop due to first order velocity

$$\tfrac{1}{2}\rho \int_{S_o} |\nabla\Phi^{(1)}|^2 \, n \, dS \qquad (28)$$

III: Pressure due to product of gradient of first order pressure and first order motion

$$\rho \int_{S_o} (\underline{X}^{(1)}.\nabla\Phi_t^{(1)}) n \, dS \qquad (29)$$

IV : Contribution due to products of first order angular motions and inertia forces

$$\underline{\alpha}^{(1)} \times (M.\underline{X}_g^{(1)}) \qquad (30)$$

In expression (26) the forward speed dependent potentials and derivatives of these potentials have to be evaluated at the mean waterline and the mean wetted surface. The expressions we then obtain are of similar nature as those obtained by Hearn and Koon [4], [23]. However, their method is based on 2-d strip theory with adaptions for the incorporations of diffraction effects.

NUMERICAL SCHEME

The calculations of the mean wave drift forces in current following the analysis of the previous chapter involves some extra computational work when considering the computational burden for the zero speed case. As an example the contribution due to the relative wave height will be further explained.

Returning to equation (24) and (25) we are able to write:

$$F^{(2)} = - \int_{S_o} p^{(2)} n \, dS - \underline{\alpha}^{(1)} x \int_{S_o} p^{(1)} n \, dS +$$

$$- \int_{s} p^{(1)} n \, dS \qquad (31)$$

with s an oscillating surface near the free surface and S_o is the mean wetted surface. The last term in (31) will lead to the contribution of the relative wave height.

If one substitutes the first order pressure from (22) and remembering that in the waterline:

$$-\rho \, \Phi_t^{(1)} = \rho g \, \zeta^{(1)} \qquad (32)$$

and writing the surface element as:

$$ds = dz \, d\ell$$

this integral then becomes:

$$- \int_{WL} \int_{z_{WL}^{(1)}}^{\zeta^{(1)}} (\rho g \, \zeta^{(1)} - \rho g z) n \, dz \, d\ell \qquad (33)$$

which then results in:

$$-\tfrac{1}{2}\rho g \int_{WL} |\zeta_r^{(1)}|^2 \, n \, d\ell \qquad (34)$$

in which $\zeta_r^{(1)}$ is the relative wave elevation defined by:

$$\zeta_r^{(1)} = \zeta^{(1)} - z_{WL}^{(1)}$$

with $z_{WL}^{(1)}$ is the local vertical displacement at the waterline, which can be calculated using the previously described potential theory in the previous chapters.

The wave height $\zeta^{(1)}$ can be split up into two components, i.e. the undisturbed incoming wave height $\zeta_i^{(1)}$ and the diffracted wave height $\zeta_d^{(1)}$ with:

$$\zeta^{(1)} = \zeta_i^{(1)} + \zeta_d^{(1)} \qquad (35)$$

Also the following relation holds for $\zeta^{(1)}$ and its components:

$$\zeta^{(1)} = - \frac{1}{g} \left(\frac{\partial}{\partial t} \Phi^{(1)} - U \frac{\partial}{\partial x} \Phi^{(1)} \right) \quad \text{at } z=0 \qquad (36)$$

in which:

$$\Phi^{(1)} = \Phi_0^{(1)} + \tau \, \Phi_1^{(1)} \qquad (37)$$

where $\Phi_0^{(1)}$ and $\Phi_1^{(1)}$ are the velocity potentials for the zero forward speed and the correction potential for forward speed.

The remaining three terms in the mean wave drift force expressions (28), (29) and (30) can be treated in a similar fashion as was explained for the term with the relative wave height contribution.

VALIDATION

For the validation of the described numerical procedure to calculate the mean wave drift forces, a number of model test experiments are analysed. The first order wave loads and added mass and damping coefficients were computed using the algorithm proposed by Huijsmans and Hermans [22].

Calculations were performed for a head sea condition for a tanker moored in deep water in a 4 knot current. The calculated response functions for the heave and pitch mode are in Fig. 3. Also results of model test experiments are depicted in this figure. As shown the calculated heave and pitch motion response compare favourably with the results of model test experiments.

The main particulars of the used 200 kDWT tanker are displayed in Table 1.

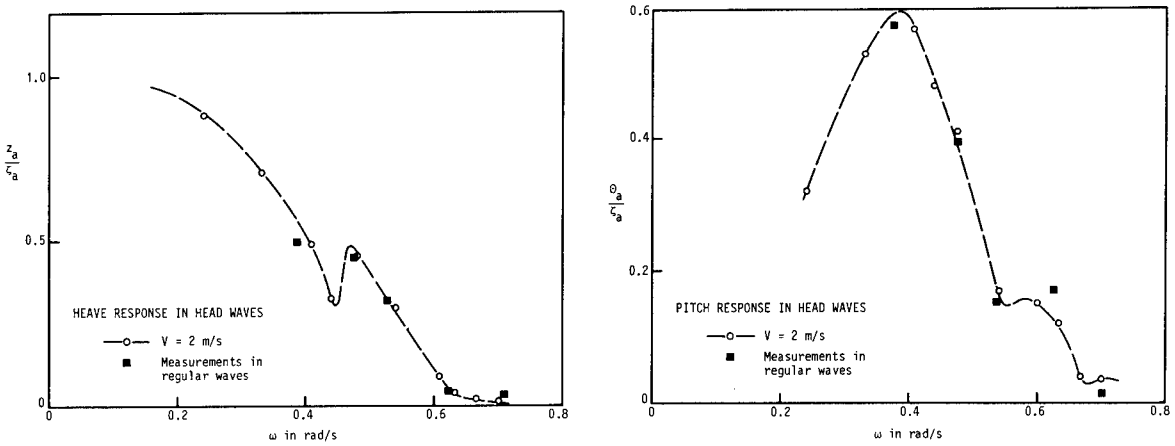
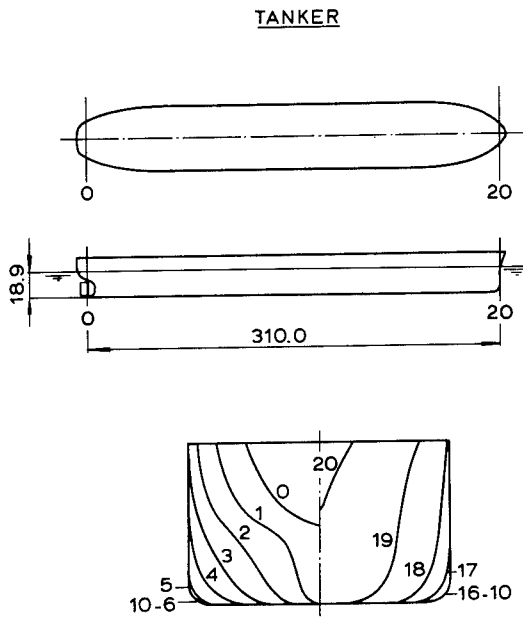


Fig. 3 Response of a 200 kDWT tanker in deep water

Table 1 Main particulars of 200 kDWT tanker



Designation	Symbol	Unit	Tanker	
			Tested	Calculated
Length (between perpendiculars)	L_{PP}	m	310.00	
Breadth	B	m	47.17	
Draft	T	m	18.90	
Displacement volume	∇	m^3	234,826	
Centre of gravity above base	$\overline{KG}$	m	13.32	
Metacentric height	$\overline{GM}$	m	5.78	
Transverse gyradius in air	k_{xx}	m	-	14.77
Transverse gyradius in water	k_{xx}	m	17.02	17.02
Longitudinal gyradius in air	k_{yy}	m	77.47	77.50
Vertical gyradius in air	k_{zz}	m	-	79.30
Natural period of heave	T_z	s	11.8	11.7
Natural period of roll	T_ϕ	s	14.2	14.2
Natural period of pitch	T_Θ	s	10.8	10.6

For the calculations a panel distribution is used as shown in Fig. 4. The number of plane elements amount to 238 and the number of waterlines elements was 60.

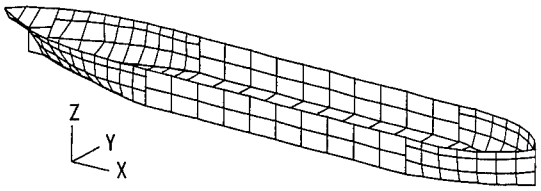


Fig. 4 Facet distribution of 200 kDWT tanker

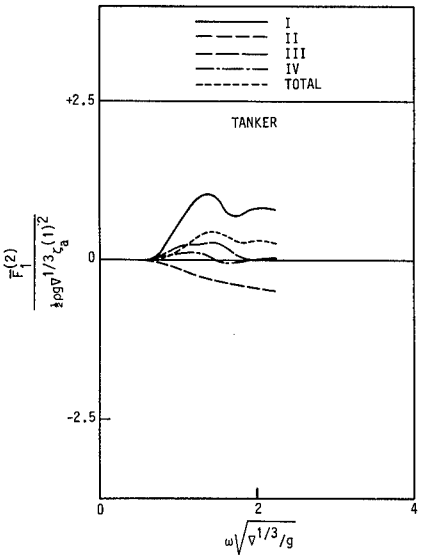


Fig. 5 Contributions to the mean wave drift force (zero speed)

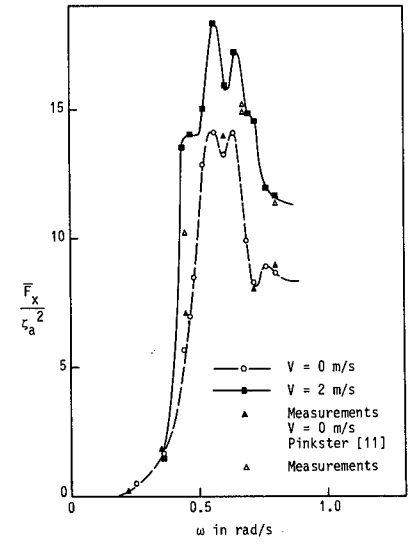


Fig. 7 Mean surge drift force in head waves for 200 kDWT tanker

In Pinkster's study [11] four contributions were identified which add up to the total mean wave drift force at zero speed. These four contributions are stated in equations (27) to (30). Similar contributions can be observed for the 4 knot current case.

The contributions for the zero speed and 4 knot current speed are shown in Figs. 5 and 6. The total mean wave drift force for the zero speed and the 4 knot current case are depicted in Fig. 7.

From the mean wave drift at zero speed and non-zero speed the so-called "wave damping" coefficient can be derived as shown by Wichers and Huijsmans [3]. For the underlying case the wave damping gives the following picture (Fig. 8).

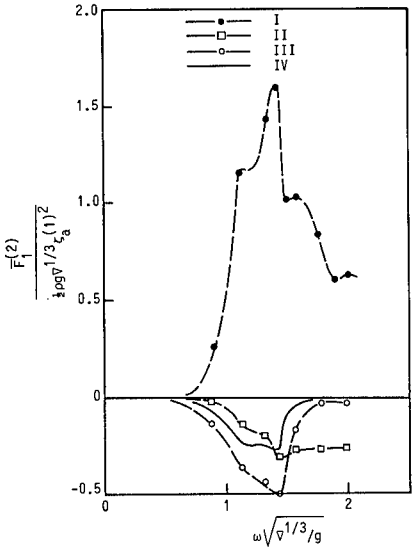


Fig. 6 Contributions to the mean wave drift force (4 knot current)

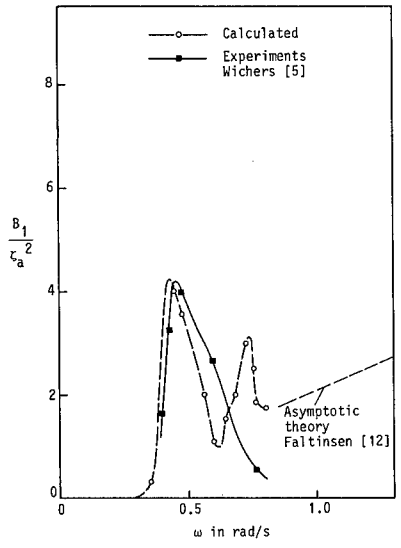


Fig. 8 "Wave damping" coefficient

REFERENCES

1. Wichers, J.E.W., "On the Low Frequency Surge Motions of Vessels Mooring in High Seas", Offshore Technology Conference, Paper 4437, Houston, 1982.
2. Wichers, J.E.W. and Van Sluijs, M.F., "The Influence of Wave on the Low Frequency Hydrodynamic Coefficients of Moored Vessels", Offshore Technology Conference, Paper 2625, Houston, 1979.
3. Wichers, J.E.W. and Huijsmans, R.H.M., "On the Low Frequency Hydrodynamic Damping Forces Acting on Offshore Moored Vessels", Offshore Technology Conference, Paper 4813, Houston, 1984.
4. Hearn, G. and Koon, T., "Second Order Fluid Damping", Progress Report, July 1985, University of Newcastle.
5. Wichers, J.E.W., "Progress in Computer Simulations of SPM Moored Vessels", Offshore Technology Conference, Paper 5175, Houston, 1986.
6. Newman, J.N., "A Slender Body Theory for Ship Oscillations in Waves", Journal of Fluid Mechanics, Vol. 18, 1964.
7. Newman, J.N. and Tuck, E.O., "Current Progress in the Slender-Ship Theory of Ship Motions", 5th Symposium on Naval Hydrodynamics, Washington, 1964.
8. Newman, J.N., "The Theory of Ship Motions", Advance in Applied Mechanics, Vol. 18, 1978.
9. Van Oortmerssen, G., "The Motions of a Moored Ship in Waves", MARIN publication No. 510, Wageningen, 1976.
10. Newman, J.N., "Three Dimensional Wave Interactions with Ships and Platforms", International Workshop on Ship and Platform Motions, Berkeley, 1983.
11. Pinkster, J.A., "Low Frequency Second Order Wave Exciting Forces on Floating Bodies", MARIN publication No. 650, Wageningen, 1980.
12. Faltinsen, O., Dahle, L. and Sortland, B., "Slow Drift Damping and Response of a Moored Ship in Irregular Waves", Offshore Mechanics and Architects Engineering Conference, Tokyo, 1986.
13. Remery, G.F.M. and Hermans, A.J., "The Slow Drift Oscillations of a Moored Object in Random Seas", Offshore Technology Conference, Paper 1500, Houston, 1971.
14. Bougis, J., "Etude de Diffraction-Radiation dans le Cas d'un Flotteur Indeformable Animé par une Houle Sinusiodale de Faible Amplitude", PhD Thesis, Université de Nantes, 1980.
15. Chang, M.S., "Computation of Three Dimensional Ship Motions with Forward Speed", 2nd International Conference on Numerical Ship Hydrodynamics, Berkeley, 1977.
16. Inglis, R.B., "A Three Dimensional Analysis of the Motion of a Rigid Ship in Waves", PhD Thesis, University College, London, 1980.
17. Huijsmans, R.H.M. and Dallinga, R.P., "Non-Linear Ship Motions in Shallow Water", International Workshop on Ship and Platform Motions", Berkeley, 1983.
18. Hermans, A.J., "The Wave Pattern of a Ship Sailing at Low Speed", Report 84A, University of Delaware.
19. Brandsma, F.J. and Hermans, A.J., "A Quasi Linear Free Surface Condition in Slow Ship Theory", Schiffstechnik, April 1985.
20. Eggers, K., "Non-Kelvin Dispersive Waves Around Non-Slender Ships", Schiffstechnik, Vol. 8, 1981.
21. Brard, R., "The Representation of a Given Ship Form by Singularity Distribution When the Boundary Condition on the Free Surface is Linearized", Journal of Ship Research, Vol. 16, 1972.
22. Huijsmans, R.H.M. and Hermans, A.J., "A Fast Algorithm for Computation of 3-D Ship Motions at Moderate Forward Speed", 4th International Conference on Numerical Ship Hydrodynamics, Washington, 1985.
23. Hearn, G. and Koon, T., "Evaluation of Low Frequency Wave Damping", Offshore Technology Conference, Paper 5176, Houston, 1986.
24. Wehausen, J. and Laitone, E., Handbuch der Physic, Vol. 9, 1960.

DISCUSSION

Hajime Maruo,
Yokohama National University

I appreciate the author's elaborate computation of the drift force when the current is present. As the author may be aware, there is a formula for the steady drift force of a ship moving in waves, derived by the energy and momentum analysis. Much simplification of the formula has been suggested by Gerritsma and myself for practical computation purposes. Making use of this method, the drift force, as well as the motion of the ship, can be computed by the strip theory. It has been regarded that this method can give a good assessment of the added resistance of a ship in a seaway. Have you compared your computation with results by the above formula?

Reply -

The distinguished discussor raises the point of the use of other established methods to calculate the mean wave drift forces on ships.

The well-known Gerritsma-Beukelman formulation has ben used in an early stage of this research project, which was reported by Wichers et al. 3] in 1984. The results from this study indicate that the computed mean wave drift force using strip theory and the Gerritsma-Beukelman formulation were not very reliable (i.e. negative wave drift damping coefficients). The same conjecture was made by Hearn et al. [4]. This actually motivated us to go further with a pressure distribution integration technique for the calculation of the wave drift forces at forward speed.

Paul D. Scalvounos,
Massachussetts Institute of Technology

I first would like to congratulate Dr. Huijsmans for an interesting paper which points in a new and perhaps very promising direction for the solution of the forward-speed ship motion problem.

The analytical definition of the "wave drift damping" is given in the article by Wichers and Huijsmans [3]. It would be useful if this definition could be reproduced, so that the reader could relate it to the small approximation developed here.

The forward-speed study carried out in this paper is intended for the evaluation of the wave damping associated with the slow drift oscillations of ships. At the same time, however, it suggests a new approach for the forward-speed seakeeping of ships at finite values (not necessarily small) of the Froude number and frequency of oscillation. A ship in steady forward translation generates trailing surface waves with characteristic wavelength in the direction of translation equal to $2U^2/g$. Let an oscillatory motion at a frequency be superimposed to the forward translation, and assume for the sake of the present discussion that $\tau > 1/4$. Two transverse wave systems trail the ship with substantially different length-scales. One system is associated with the Kelvin waves, and its wavelength decreases relative that at =0 as increases. The second system is associated with the waves radiated at U=0, and their wavelength increases with increasing U. Their amplitudes vary in a manner inversely proportional to their respective wavelengths. These properties suggest that the integrated effect of the former wave system in the evaluation of the added-mass and damping forces is small relative to that of the latter. Moreover, the validity of this decomposition seems to be more valid as τ increases due to the opposite tendencies of the two wavelengths and amplitudes.

The small τ approximation outlined in this paper utilizes these properties to eliminate the rapidly oscillatory component of the wave source potential as a higher-order quantity and reduce the remaining term. At higher values of τ, the elimination of the rapidly oscillatory component is even more justified, but the reduction of the remaining slowly oscillating component of the Green function is no longer possible. Following a decomposition of the exact Green function into fast and slow components, the latter can be regarded as the wave source potential for the forward speed problem. It depends on both wavenumbers ω^2/g and g/U^2, assumed to be of O(1), and consequently is more complex to evaluate in comparison to the functions given by equations (12) and (13) in the present paper which are the leading-order terms in its small- τ approximation. The principal advantage in utilizing a slowly varying Green function is that the number of panels necessary for the discretzation of the ship wetted surface is no larger than that needed at zero speed.

Reply -

First of all I would like to thank the distinguished discussor for both his interesting and stimulating remarks on the forward speed ship motion problem. The definition of the "wave damping" coefficient has been dropped from the text. The definition is related to the wave drift force formulation:

$$F(x, \dot{x}, t) = \overline{F(x, \dot{x}, t)} + \dot{x} \frac{d}{d\dot{x}} [F(x, \dot{x}, t)] \Big|_{\dot{x}=0}$$

in which:

$\dot{x}$ is the slowly varying surge velocity,

$\frac{d}{d\dot{x}} [F(x, \dot{x}, t)] \Big|_{\dot{x}=0}$ is the "wave damping" coefficient, and

$\overline{F(x, \dot{x}, t)}$ is the mean wave drift at zero speed.

The remarks the discusser makes concerning the integrated effects (e.g. added mass damping) of the Kelvin wave system can hold true. However its effect still has to be analysed by using the proper linearized free surface condition. The two wave systems cannot be separated out in the exact linearized free surface condition.

In an approximate sense the influence of the Kelvin wave system on the pressure distribution is of order U^2 for the small τ approximation. This may be also the case for τ values larger than 1/4. However the Green's function that would be involved for τ larger 1/4 cannot be calculated using an efficient zero speed Green's function formulation, which was one of the main advantages of the small τ approximation.

The Dynamics of Waves at the Interface Between a Two-Layer, Viscoelastic Coating and a Fluid Flow

J. H. DUNCAN

Flow Research Company, U.S.A.

ABSTRACT

In this paper the dynamics of two-dimensional waves at the interface between a compliant wall and a boundary layer flow is examined theoretically. The compliant wall consists of two-layers of linear, incompressible, viscoelastic material and is bonded to a rigid plate. The pressure from the flow on the surface of the coating is modeled first by potential theory and then modified to incorporate reduced magnitudes and phase shifts observed in turbulent flow over wavy walls. The coating and the mean flow are coupled at the interface by equating normal velocities and stresses; the shear stress on the interface is neglected. The waves at the interface behave much like those on a single layer coating. However, when the upper layer is thin and stiff, it induces a plate-like behavior which appears as a wrinkle in the dispersion curves. In the presence of a mean flow, waves in the intermediate wavenumber range ($kd \sim 3$ where d is the total coating thickness, k is $2\pi/\lambda$, and λ is the horizontal wave length) are strongly influenced by the flow. For low flow speeds, all the waves are stable if the coating has sufficient damping. For flow speeds above a critical value, which depends on the coating design, the waves in the intermediate wavenumber range can not propagate upstream. These waves are destabilized by the material damping. At still higher flow speeds a Kelvin-Helmholtz or flutter instability appears.

NOMENCLATURE

a	amplitude of the vertical displacement at the coating surface
c	complex wave phase speed
C	dimensionless wave phase velocity ($=c/C_{t2}$)
c_i	imaginary part of the wave phase speed
$C_{\ell n}$	square root of the real part of C^2_{Ln}
C_{Ln}	complex longitudinal wave speed of a Voigt solid - see Equation [3]
c_r	real part of the wave phase speed
C_{tn}	square root of the real part of C^2_{Tn}
C_{Tn}	complex shear wave speed of a Voigt solid - see Equation [3]
d_n	depth of the bottom of coating layer n
i	$\sqrt{-1}$
k	wavenumber ($=2\pi/\lambda$)
K_p	induced pressure coefficient - see Equation [15]
n	a subscript denoting the upper (n=1) or lower (n=2) layer of the compliant coating
P_f	pressure at the coating surface due to the mean flow over the wavy surface of the coating
t	time
t_n	thickness of coating layer n
U_∞	flow speed at $y = \infty$
x	horizontal coordinate (parallel to the coating surface) - see Figure 1
y	vertical coordinate (normal to the coating surface) - see Figure 1
$\tan\delta_n$	loss tangent of a viscoelastic material
ζ_n	horizontal component of the displacement in the coating
$\vec{\zeta}_n$	vector displacement in the coating
η_n	vertical component of the displacement in the coating
$\eta_{\ell n}$	damping ratio associated with longitudinal wave motion - see Equation [4]
η_{tn}	damping ratio associated with transverse wave motion - see Equation [4]
θ_p	phase shift of the flow pressure over the wavy surface of the coating - see Equation [15]
λ	wavelength
π	3.14159
ρ	density of the fluid
ρ_p	density of the layer n of the coating
σ^n_{ij}	i, j component of the stress tensor in layer n of the coating
$\tau_{\ell n}$	material relaxation time associated with longitudinal wave motion in layer n of the coating
τ_{tn}	material relaxation time associated with transverse wave motion in layer n of the coating
ω_r	real part of the frequency of the wave motion

1. INTRODUCTION

The idea of modifying the structure of a turbulent boundary layer through the use of a compliant coating has generated much interest because of the potential for drag and noise reduction. Theoretical models of the system require the coupling of a complicated turbulent flow and a coating design with many degrees of freedom. Since both components of the system and the coupling between the two are difficult to handle theoretically, it is not suprising that a good physical understanding of the problem does not exist at present. This lack of knowledge has hindered the design of systematic experiments that might, for instance, test various classes of coatings for interactive properties. The simplest practical coating design is a single layer of isotropic, incompressible, viscoelastic material. The interaction of a turbulent boundary layer with coatings of this type have been studied experimentally by Hansen and Hunston (1); Hansen, Hunston, Ni, Reischman, and Hoyt (2); Hansen and Hunston (3); and Gad-el-Hak, Blackwelder, and Riley (4). Most of this work has concentrated on unstable interfacial waves which appear when the flow speed is above a critical value. Complimentary theoretical studies on stability have been performed by Duncan, Waxman, and Tulin (5) and Everensel (6). The response under stable flow conditions has been examined experimentally by Chu, Falco, and Wiggert (7) and theoretically by Duncan (8). For coatings with low damping under stable flow conditions, V-shaped interfacial wave patterns appear behind isolated turbulent events (probably turbulent bursts). When the flow speed is high enough this local response is masked by the unstable, two-dimensional wavetrain which covers the surface. The work on single-layer coatings has brought out a fundamental limitation on the response amplitude under stable conditions. The amplitude is proportional to the magnitude of the fluctuating pressures (which are proportional to $\rho_f U_\infty^2$) and inversly proportional to the coating stiffness ($\rho_c C_t^2$ where ρ_c and C_t are the density and shear wave speed of the coating material). However, the stable response amplitude is limited because the coating becomes unstable when this ratio reaches a critical value. Duncan (8) estimates the maximum amplitude to be $0.04\ \delta^*$ at a length Reynolds number of 5×10^5 .

A two-layer coating with a stiff upper layer offers the possibility of interesting variations from the single-layer case. First of all, the upper layer acts like a plate. The wave propagation characteristics of single-layer coatings and plates are quite different. For single layer coatings, the wave group velocity is always less than the phase speed (8). The phase speed of the dominant waves generated by the turbulent event travel downstream with the event. Thus, for the coating, most of the interfacial wave energy will be left behind. For bending waves in plates, the group velocity is greater than the phase velocity and this allows the waves to propagate ahead of the turbulent events. The presence of the stiff upper layer will also postpone instabilities to higher flow speeds. This might result in larger surface displacements under stable flow conditions.

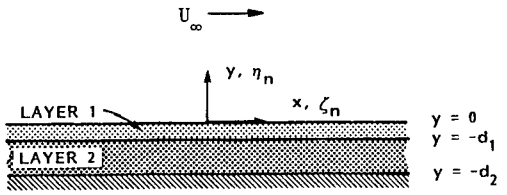


Figure 1. Schematic of Two-Layer Coating

In this paper, a first step is taken toward examining the response of a two-layer coating: the dynamics of waves on the coating surface is examined theoretically. The occurence of instabilities is given detailed attention. The theoretical model is similar to the single-layer coating work by Duncan et al (5). The coating is treated as a two-layer, linear, viscoelastic solid of infinite horizontal extent that is bonded to a rigid surface on its lower boundary. The coating and the flow are coupled through the induced interfacial pressure. The induced pressure is generated by the mean boundary-layer flow over the wavy coating surface. This pressure is modelled by first computing the pressures resulting from a potential flow over the surface and then modifying that distribution to incorporate the reduced magnitudes and phase shifts found experimentally in boundary-layer flows over wavy walls.

2. THEORETICAL DEVELOPMENT

The coating model consists of two arbitrarily thick layers of homogeneous, isotropic, Voigt material. On its lower surface ($y = -d_2$) the coating is attached to a rigid plate, while on its upper surface it is bounded by flowing water (see Figure 1). At the interface between the fluid and the coating we consider a wave of the form

$$\eta = ae^{ik(x-ct)}, \qquad [1]$$

where a is the amplitude, k is the wavenumber (2π divided by the wavelength λ) and $c(=c_r+ic_i)$ is the complex wave speed. The propagation speed is given by c_r and the wave growth rate by kc_i ($c_i > 0$ indicates a growing wave). The differential equation of motion for a Voigt material is [9]:

$$\frac{\partial^2 \zeta_n}{\partial t^2} = C_{Tn}^2 \nabla^2 \zeta_n + (C_{Ln}^2 - C_{Tn}^2)\nabla(\nabla \cdot \zeta_n) \qquad [2]$$

where $\vec{\zeta}_n = \zeta_n \hat{i} + \eta_n \hat{j}$ is the displacement vector and the subscript n can have values of 1 or 2 referring to the upper or lower layers, respectively (see Figure 1). C_{Tn} and C_{Ln} are the complex shear and longitudinal wave speeds of the solid. Considering small displacements proportional to $e^{ik(x-ct)}$, we have

$$C_{Tn}^2 = C_{tn}^2 \left(1 - ikd_n C \eta_{tn}\right)$$

$$C_{Ln}^2 = C_{\ell n}^2 \left(1 - ikd_n C \frac{C_{t2}}{C_{\ell n}} \eta_{\ell n}\right) \qquad [3]$$

where $C = c/C_{t2}$, C_{tn} and $C_{\ell n}$ are the shear- and longitudinal-wave speeds in an ideal elastic solid, and η_{tn} and $\eta_{\ell n}$ are dimensionless damping ratios, defined by

$$\eta_{tn} = \frac{\tau_{tn} C_{tn}}{d_n}, \quad \eta_{\ell n} \frac{\tau_{\ell n} C_{\ell n}}{d_n} \qquad [4]$$

The relaxation times τ_{tn} and $\tau_{\ell n}$ indicate the dissipative properties of the material. For incompressible materials, the damping properties are sometimes reported in terms of the loss tangent, $\tan \delta_n = \tau_{tn} \omega_r$, where $\omega_r = c_r k$.

There are eight boundary conditions for the present problem. In their linearized form they can be written:

$$\zeta_2(x,-d_2,t) = 0 \qquad [5]$$

$$\eta_2(x,-d_2,t) = 0 \qquad [6]$$

$$\sigma_{1yy}(x,-d_1,t) = \sigma_{2yy}(x,-d_1,t) \qquad [7]$$

$$\sigma_{1xy}(x,-d_1,t) = \sigma_{2xy}(x,-d_1,t) \qquad [8]$$

$$\zeta_1(x,-d_1,t) = \zeta_2(x,-d_1,t) \qquad [9]$$

$$\eta_1(x,-d_1,t) = \eta_2(x,-d_1,t) \qquad [10]$$

$$\sigma_{1yy}(x,0,t) = -P_f \qquad [11]$$

$$\sigma_{1xy}(x,0,t) = 0 \qquad [12]$$

where σ_{nyy} and σ_{nxy} are the normal and shear stresses which have the form:

$$\sigma_{nyy} = \rho_n C_{Ln}^2 \frac{\partial \eta_n}{\partial y} + \rho_n (C_{Ln}^2 - 2C_{Tn}^2) \frac{\partial \zeta_n}{\partial x} \qquad [13]$$

$$\sigma_{nxy} = \rho_n C_{Tn}^2 \left(\frac{\partial \zeta_n}{\partial y} + \frac{\partial \eta_n}{\partial x}\right). \qquad [14]$$

Boundary conditions [5] and [6] state that there is no horizontal or vertical displacement at the lower boundary, $y = -d_2$. Equations [7] through [10] are the conditions for the continuity of normal stress, shear stress, and displacements at the interface between the two layers. The continuity of force conditions at the upper boundary are given by Equations [11] and [12]. In the present model, we match the flow pressure and the vertical stress component in the coating at the interface, while the shear stress is taken to be zero.

The induced pressure, P_f, is modeled with a modified potential flow theory as was used by Duncan et al (5):

$$P_f = -K_p \rho_f a k (U_\infty - c)^2 e^{i[\theta_p + k(x-ct)]} \qquad [15]$$

When the empirical constants K_p and θ_p are given the values 1.0 and 0.0, respectively, Equation [15] gives the pressure for potential flow over the wavy wall. With a turbulent boundary layer, the magnitude of the pressure is less than the potential flow value and the phase is shifted. These effects are obtained with the constants K_p and θ_p in the present model. Values are taken from the experimental data of Kendall (10).

The solution of these equations is obtained by standard techniques which can be found in Miklowitz (11) or Duncan et al (5). Basically, the displacement field is broken into irrotational and incompressible parts, the resulting equations are solved and the full displacement field is reconstructed. At this point, the displacement field is known to within eight unknown constants. When the displacement fields are substituted into the boundary conditions, Equations [5] to [12], a set of eight, linear, homogeneous, algebraic equations is obtained. The dispersion relation for the interfacial waves (c=f(k)) results from setting the determinant of the coefficients equal to zero. The zeros of the determinant of the eight by eight complex matrix are found numerically using a contour integration method based on the work of Delves and Lyness (12).

3. RESULTS

In this section, the results of calculations for two-layer coatings are presented. In all cases, the materials are effectively incompressible ($C_{\ell n} = 70.0\ C_{tn}$) and have densities equal to that of the fluid. The thickness and shear wave speed of the upper layer were varied relative to those of the lower layer; however, in all cases C_{t1} was greater than C_{t2}. The pressure magnitude factor, K_p, was taken as 0.25, a value obtained from Kendall's experimental data (10) on flow over moving wavy walls. In Kendall's experiments, the ratio of

interfacial wavelength to boundary layer displacement thickness (λ/δ^*) was in the range 14.0 to 20.0. When calculations where performed with pressure phase shifts, a value of -10.0 degrees was used for waves that moved slowly compared to the flow speed and a value of -20.0 degrees was used for waves that moved at speeds closer to, but still less than, the flow speed. These values were chosen as representative from Kendall's data.

In examining the stability of the waves, it will be useful to calculate the activation energy, ΔE, which is defined as the change in kinetic and potential energy of the coating plus the change in energy of the flow due to the work done on the coating by conservative forces only. In the present case we have

$$\Delta E = \frac{1}{\lambda}\int_x^{x+\lambda}\int_{-d_2}^{\zeta_1}|_{y=0}(SE+KE)dy\,dx + \frac{1}{\lambda}\int_x^{x+\lambda} W_{cons}\,dx \quad [16]$$

where KE and SE, the kinetic and elastic-strain energy of the coating respectively, are defined as

$$SE = \frac{\rho}{2}\left\{c_\ell^2\left[\left(\frac{\partial\zeta}{\partial x}\right)^2+\left(\frac{\partial\eta}{\partial y}\right)^2\right] + 2(c_\ell^2-2c_t^2)\frac{\partial\zeta}{\partial x}\frac{\partial\eta}{\partial y} + c_t^2\left(\frac{\partial\zeta}{\partial y}+\frac{\partial\eta}{\partial x}\right)^2\right\}_{1 \text{ or } 2} \quad [17]$$

$$KE = \frac{\rho}{2}\left[\left(\frac{\partial\zeta}{\partial t}\right)^2+\left(\frac{\partial\eta}{\partial t}\right)^2\right]_{1 \text{ or } 2}$$

To derive the conservative work term, we follow Benjamin's (13) derivation of the work done by a potential flow, however we substite the conservative part of our pressure term

$$P_{cons} = -K_p\rho_f ak(U_\infty-c)^2\cos\theta_p e(ik(x-ct) \quad [18]$$

for the potential-flow pressure in his calculation. Thus we find

$$\frac{1}{\lambda}\int_x^{x+\eta} W_{cons}\,dx = \tfrac{1}{4}K_p\rho_f k\cos\theta_p(cc^*-U_\infty^2)\hat{\eta}^2 \quad [19]$$

where $\hat{\eta}=ae^{kc_i t}$.

The activation energy was first suggested by Benjamin (13). Three classes of waves were identified according to its sign: $\Delta E<0$ class A, $\Delta E>0$ class B, and $\Delta E=0$ class C. The wave classes were discussed in general by Benjamin and, in the specific case of a single-layer coating, by Duncan et al (5). Briefly, in an ideal system, i.e. one with no damping and no irreversible transfer of energy between the wave system and the flow at infinity, class A and B waves are neutrally stable, while class C waves are unstable. Kelvin-Helmholtz instabilities are

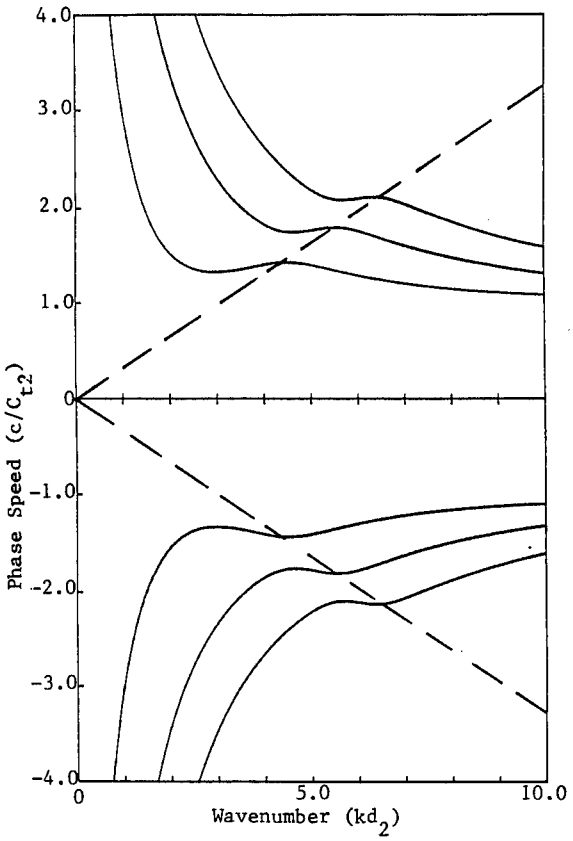


Figure 2. Dispersion curves for a two-layer coating-first three modes $U_\infty/C_{t2}=0.0$, $K_p=0.25$, $\theta_p=0.0$, $\rho_1=\rho_2=\rho_f$, $C_{t1}/C_{t2}=10.0$, $d_2/d_1=10.0$, $C_{\ell1}/C_{t1}=C_{\ell2}/C_{t2}=70.0$, $\eta_{t1}=\eta_{t2}=0$.

class C. Note that ΔE is proportional to the square of the wave amplitude. Thus, for class B waves ($\Delta E>0$), when energy is removed from the wave system by an irreversible process like damping or interaction with the mean flow through the pressure phase shift, the amplitude of the wave must decrease to accommodate the lower ΔE. However, for class A waves, which have $\Delta E<0$, energy removal results in a larger amplitude to accommodate the increased magnitude of ΔE. Irreversible increases in energy caused by interaction with the mean flow through the phase shift cause the amplitude to behave in the opposite manner in each class.

In the first calculations presented here, the damping and the pressure phase shift are zero--a reversible system. Let us first examine a two-layer coating with an upper layer that has one-tenth the thickness of the total coating thickness ($d_2 = 10.0\ d_1$), while the shear wave speed of the upper layer is ten times that of the lower layer ($C_{t_1} = 10.0\ C_{t_2}$). The case with the flow speed set to zero is plotted in Figure 2. For comparison, the corresponding single-layer case is

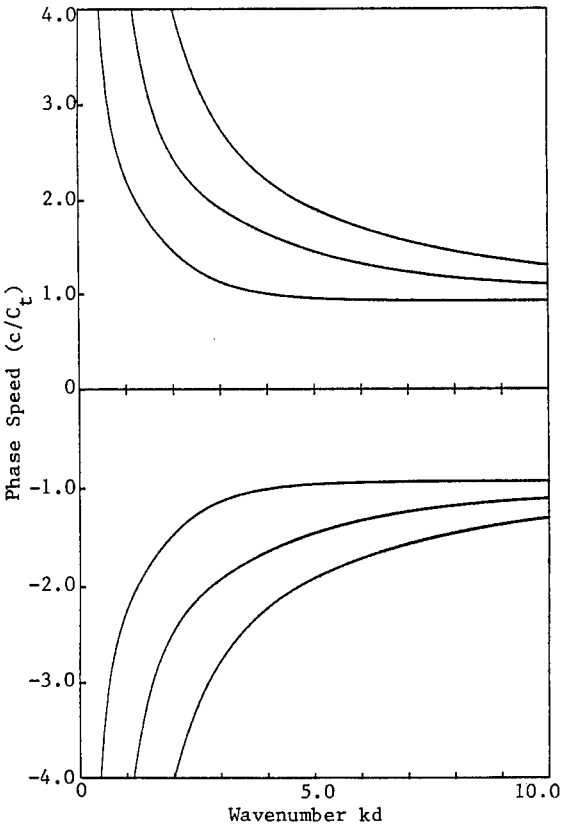


Figure 3. Dispersion curves for a single-layer coating-first three modes $U_\infty/C_t=0$, $K_p=0.25$, $\theta_p=0.0$, $\rho_c=\rho_f$, $C_\ell/C_t=70.0$, $\eta_t=0$.

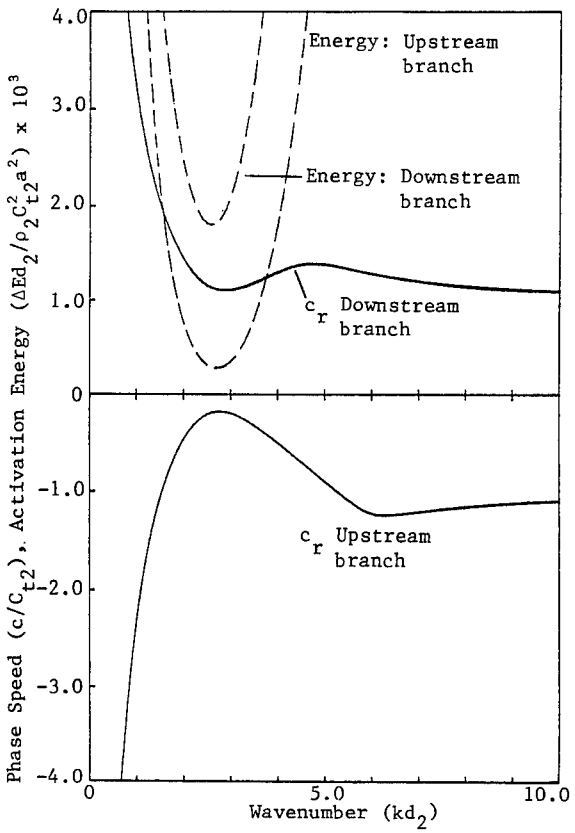


Figure 4. Dispersion curves for a two-layer coating-first mode $U_\infty/C_{t2}=3.4$, $K_p=0.25$, $\theta_p=0.0$, $\rho_1=\rho_2=\rho_f$, $C_{t1}/C_{t2}=10.0$, $d_2/d_1=10.0$, $C_{\ell 1}/C_{t1}=C_{\ell 2}/C_{t2}=70.0$, $\eta_{t1}=\eta_{t2}=0$.

presented in Figure 3. The phase speed, c, is scaled by the shear wave speed of the single-layer coating in Figure 3 and the shear wave speed of the lower layer of the two-layer coating in Figure 2. The wavenumber is scaled by the total coating thickness in both cases. (The total thickness of the two layer coating is d_2). With this scaling, one can easily see[2] the changes in the single-layer dispersion relations when the upper part of the coating is replaced by a layer of stiffer material. Note from the figures that the gross shape of the curves is the same for both coatings: there are an infinite number of modes, c tends to infinity as kd approaches zero, c becomes a constant at large kd, there are no waves with c less than about C_t or C_{t2}. In the two-layer case, there are wrinkles in the curves. A straight line has been drawn connecting the maximas of the wrinkles in each modal curve. Note that the line goes through (0.0, 0.0). The equation for long bending waves in a free plate is also a straight line. In the present case, the upper layer acts like a plate modified by the added mass effect from the fluid on one side and the influence of the soft, lower layer of the coating on the other. The inability of the lower layer to accommodate slow moving waves has prevented the presence of the bending waves in the upper layer at small wavenumbers. Note also that in the vicinity of the wrinkles there are small regions of the dispersion curves with $dc/dk > 0$. Since the group velocity, c_g, can be shown to equal $c + kdc/dk$, the regions with positive dc/dk correspond to regions with $c_g>c$. Bending waves in a plate are also characterized by $c_g>c$. Since the flow speed is zero in the present case, the activation energy is always positive (class B) and, as expected, these waves will decay in the presence of damping.

The first mode dispersion curves and activation energy for the two-layer coating with the flow speed increased to $3.4\ C_{t2}$ are shown in Figure 4. The higher modes are not affected significantly by the flow. Note that the upstream branch ($c<0$) has moved toward the $c=0$ axis in the intermediate wavenumber range. The downstream branch is essentially unaffected. The activation energy for both branches is still positive for all wavenumbers. In the single -layer case, a similar effect occurs, but the

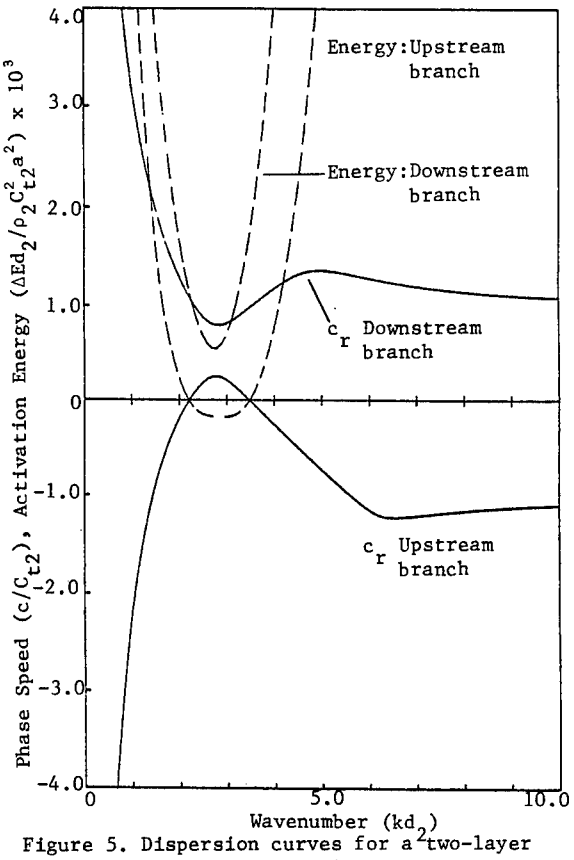


Figure 5. Dispersion curves for a two-layer coating-first mode $U_\infty/C_{t2}=3.8$, $K_p=0.25$, $\theta_p=0.0$, $\rho_1=\rho_2=\rho_f$, $C_{t1}/C_{t2}=10.0$, $d_2/d_1=10.0$, $C_{\ell 1}/C_{t1}=C_{\ell 2}/C_{t2}=70.0$, $\eta_{t1}=\eta_{t2}=0$.

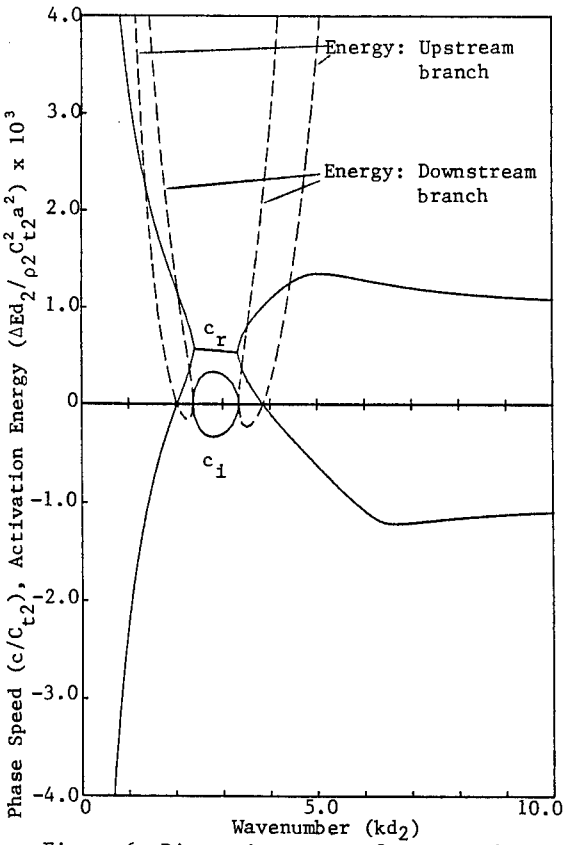


Figure 6. Dispersion curves for a two-layer coating-first mode $U_\infty/C_{t2}=4.0$, $K_p=0.25$, $\theta_p=0.0$, $\rho_1=\rho_2=\rho_f$, $C_{t1}/C_{t2}=10.0$, $d_2/d_1=10.0$, $C_{\ell 1}/C_{t1}=C_{\ell 2}/C_{t2}=70.0$, $\eta_{t1}=\eta_{t2}=0$.

dispersion curve is lifted for all the higher wavenumbers as well (5). When the flow speed is increased to 3.8, Figure 5, the upstream branch has crossed the c=0 axis in the $kd_2=3$ range of wavenumbers. Note that the acitvation energy is positive (class A) for the part of the upstream dispersion curve with c>0. Again, a similar phenomena occurs for the single-layer coating but for all the higher wavenumbers. In the present case, the upstream dispersion curve first crosses the c=0 axis when the flow speed reaches 3.59 C_{t2}, while in the single-layer case it occurs at a flow speed of 2.86 C_t. Thus, the presence of the stiff upper layer has delayed the appearance of the class A waves. When the flow speed is increased to 4.0 C_{t2} the upstream and downstream branches meet for wavenumbers near 3.0 (Figure 6). In this range, the two phase speeds form a complex conjugate pair signaling the appearance of a class C instability. Note also that the activation energy is zero for this range of wavenumbers. For the parts of the upstream branch that propagate downstream with zero imaginary part, the activation energy is positive as in Figure 5. The other waves in the Figure 6 are all class B, $\Delta E>0$. Again, the situation for the single-layer coating is similar, but the dispersion curves meet for all the higher wavenumbers (5). In the two-layer case, class C waves first appear when the flow speed is increased to 3.88 C_{t2} as opposed to 3.04 C_t for the single-layer coating. Thus, the presence of the stiff upper layer has also delayed the appearance of class C waves to a higher flow speed.

The effect of changing the relative shear wave speed and thickness of the two layers is illustrated with Figures 7 through 10. Figure 7 contains three, mode-one dispersion curves for three two-layer coating designs. The flow speed is zero in all three cases and the relative thickness of the two layers is constant ($d_2/d_1=10.0$). The ratio of shear wave speeds of the two layers is different for each curve. Note that as C_{t1}/C_{t2} changes from 5.0 to 10.0 and then to 20.0, the local maximum phase speed increases and occurs at lower wavenumbers. Figure 8 also contains three dispersion curves; however, in this figure the shear wave speed ratio was held constant and the thickness ratio of the two layers was varied ($d_2/d_1=$ 10.0, 5.0, 2.5). Note that increasing the thickness of the

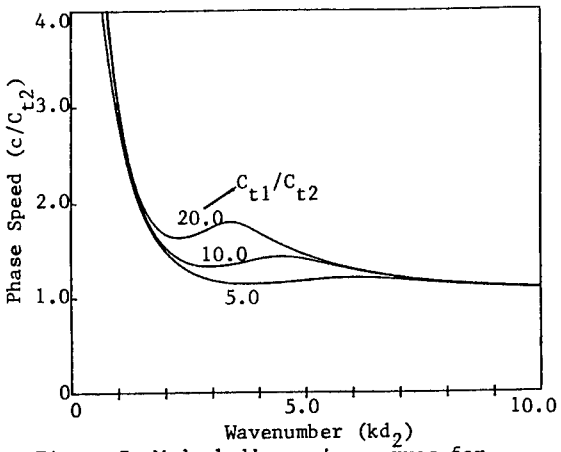


Figure 7. Mode 1 dispersion curves for various values of C_{t1}/C_{t2}
$U_\infty/C_{t2}=0$, $K_p=0.25$, $\theta_p=0.0$, $\rho_1=\rho_2=\rho_f$, $d_2/d_1=10.0$, $C_{\ell 1}/C_{t1}=C_{\ell 2}/C_{t2}=70.0$, $\eta_{t1}=\eta_{t2}=0$.

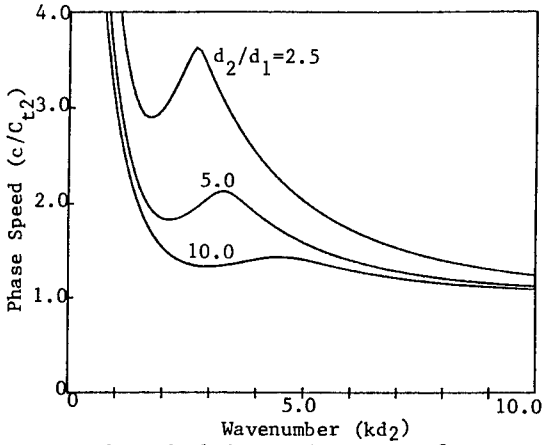


Figure 8. Mode 1 dispersion curves for various values of d_2/d_1
$U_\infty/C_{t2}=0.0$, $K_p=0.25$, $\theta_p=0.0$, $\rho_1=\rho_2=\rho_f$, $C_{t1}/C_{t2}=10.0$, $C_{\ell 1}/C_{t1}=C_{\ell 2}/C_{t2}=70.0$, $\eta_{t1}=\eta_{t2}=0$.

upper layer also moves the position of the local maximum to lower wavenumbers and increases it maximum value. Increasing the shear wave speed or thickness of the upper layer would cause the dashed lines in Figure 2 to have a greater slope as would be expected since this would increase the bending stiffness of the upper layer.

The effect of the upper layer characteristics on the appearance of class A and C waves is summarized in Figures 9 and 10. Figure 9 is a plot of the onset flow speed for class A and C waves versus d_2/d_1 for three values of C_{t1}/C_{t2} (5.0,10.0 and 20.0). Note that the onset flow speeds tend to the single-layer

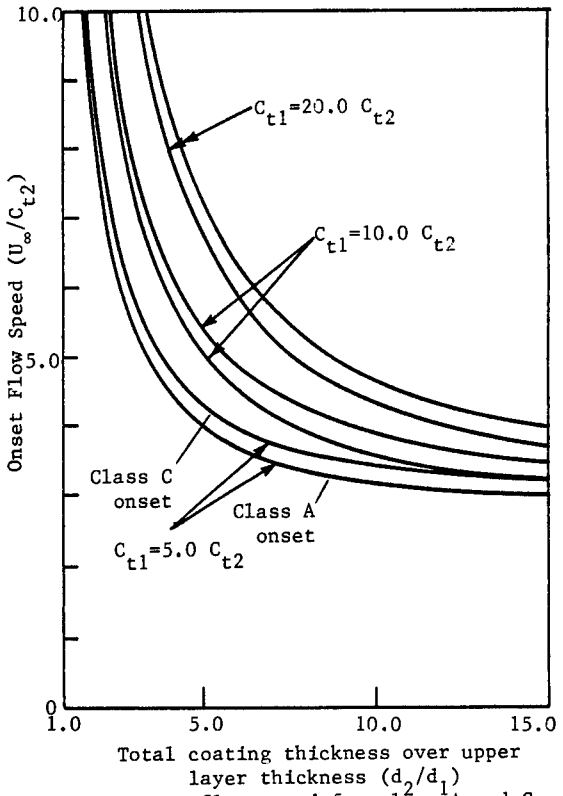


Figure 9. Onset flow speed for class A and C waves versus d_2/d_1 for various values of C_{t1}/C_{t2}
$K_p=0.25$, $\theta_p=0.0$, $\rho_1=\rho_2=\rho_f$, $C_{\ell 1}/C_{t1}=C_{\ell 2}/C_{t2}=70.0$, $\eta_{t1}=\eta_{t2}=0$

values (2.86 C_{t2} for A waves and 3.04 C_{t2} for C waves) as d_2/d_1 tends to infinity (i.e. the thickness of the upper layer tends to zero). As d_2/d_1 tends to 1 the the onset flow speeds also tend to the single layer values, however, with C_{t2} replaced by C_{t1}. Note that increasing C_{t1}/C_{t2} or decreasing d_2/d_1 results in an increase in the onset flow speed of both wave classes. Figure 10 contains a plot of the wavenumber of the class A or C waves at onset versus d_2/d_1 for the same three values of C_{t1}/C_{t2}. Note the onset wavenumber is the same for both wave classes. The wavenumber nondimensionalized by the total coating thickness increases with d_2/d_1 and decreases as C_{t1}/C_{t2} increases.

As an example of the effect of damping and pressure phase shifts on the above results, consider the dispersion curves shown in Figure 11. In this coating design $C_{t1}/C_{t2}=10.0$ and $d_2/d_1=10.0$ as in Figures 2, 4, 5, and 6. However, in the present calculation we have an ideal elastic upper layer and a lower layer with large damping ($\eta_1=0.0$ and $\eta_2=0.5$). The flow speed is 3.9 C_{t2}. The pressure phase shift was taken as -10.0 degrees for the upstream dispersion curve since these waves move upstream or very slowly downstream. For the downstream

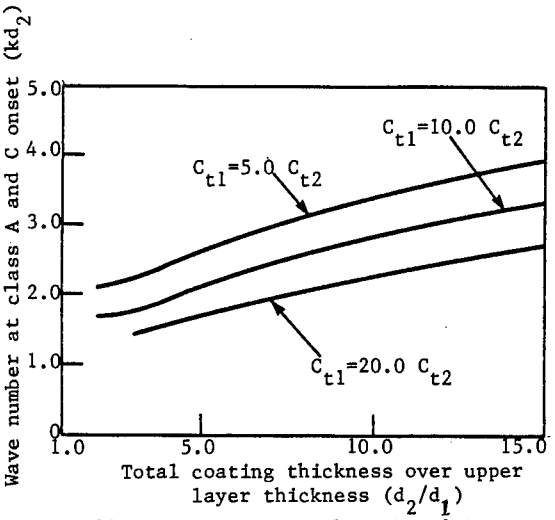


Figure 10. Wave number at class A and C onset versus d_2/d_1 for various values of C_{t1}/C_{t2}
K_p=0.25, θ_p=0.0, $\rho_1=\rho_2=\rho_f$, $C_{\ell 1}/C_{t1}=C_{\ell 2}/C_{t2}$=70.0, $\eta_{t1}=\eta_{t2}$=0

branch, the phase shift was taken as -20.0 since these waves move downstream at about 25% of the flow speed. These characteristic phase shift values were taken from Kendall's data (10). In the ideal case (no damping or phase shifts) a class C instability appeared at 3.88 C_{t2}. In the present case, the rather large damping has stabilized the class C instability. Note in fact that the entire downstream branch has a large negative c_i indicating that these class B waves are decaying. The upstream branch also consists mostly of decaying class B waves. However, in the middle of the range of waves with positve c_r there are some growing (c_i>0) waves (2.3<kd <3.3). These waves are members of class A and are being destabilized by the large damping in the lower layer.

4. CONCLUSION

The dispersion curves for surface waves on a two-layer, incompressible coating bounded by a fluid flow have been examined. The results for a coating with a stiff upper layer are significantly different than for a single-layer coating. The effect of the upper layer appears as wrinkles in the dispersion curves of a single-layer coating. In the vicinity of these wrinkles, the wave group velocity is greater than the phase velocity, as it is for bending waves on a plate. The presence of the stiff upper layer delays the appearance of class A (damping) instabilities and Class C (Kelvin-Helmholtz) instabilties to higher flow speeds when compared to a single-layer coating.

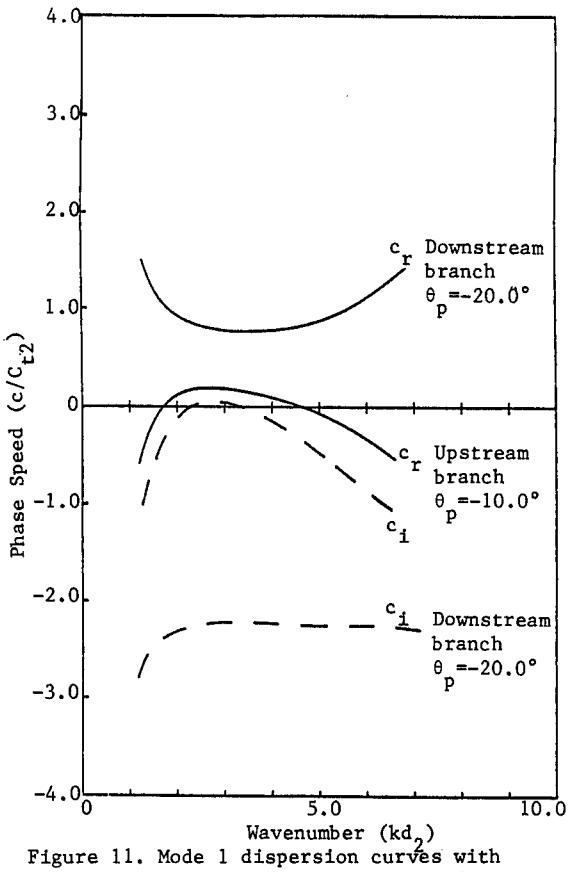


Figure 11. Mode 1 dispersion curves with pressure phase shift and damping U_∞/C_{t2}=3.9, K_p=0.25, $\rho_1=\rho_2=\rho_f$, C_{t1}/C_{t2}=10.0, d_2/d_1=10.0, $C_{\ell 1}/C_{t1}=C_{\ell 2}/C_{t2}$ =70.0, η_{t1}=0, η_{t2}=0.5

REFERENCES

1. Hansen, R. J. and Hunston, D. L. " An experimental study of turbulent flows over compliant surfaces," Journal of Sound and Vibration, Vol. 34(3), pp. 297-308, 1974.

2. Hansen, R. J., Hunston, D. L., Ni, C. C., Reischman, M. M. and Hoyt, J. W. "Hydrodynamic drag and surface deformations generated by liquid flows over flexible surfaces", In Viscous Flow Drag Reduction; Prog. Astro. Aero. Vol 72, pp. 439-451, 1979.

3. Hansen, R.J. and Hunston, D.L. 1983, "Fluid property effects on flow-generated waves on a compliant surface," J. Fluid Mech., vol. 133, pp. 161-177.

4. Gad-el-Hak, M., Blackwelder, R.F., and Riley, J.J. 1984 "On the interaction of compliant coatings with boundary-layer flows," J. Fluid Mech. vol. 140 pp.257-280.

5. Duncan J. H., Waxman, A. M., and Tulin, M. P., "The dynamics of waves at the interface beween a viscoelastic coating and a fluid flow," J. Fluid Mech. vol. 158, pp. 177-197, 1985.

6. Evrensel, C. A. and Kalnins, A. "Response of a compliant slab to inviscid incompressible fluid flow," JASA, December, 1985.

7. Chu, C.C., Falco, R. E. and Chu, C. C., "Experimental determination of drag modification due to an elastic compliant surface using quantitative visual techniques," Ninth Symposium on Turbulence, University of Missouri-Rolla, 1984.

8. Duncan, J. H. "The response of an incompressible, viscoelastic coating to pressure fluctuations in a turbulent boundary layer," to appear in J. Fluid Mech. fall 1986.

9. Fung, Y. C., Foundations of Solid Mechanics, Prentice-Hall, Inc., Englewood Cliffs, New Jersey, 1965, page 188.

10. Kendall, J. M., "The turbulent boundary layer over a wall with progressive surface waves," J. Fluid Mech. Vol. 41, Pt. 2, pp. 259-281, 1970.

11. Miklowitz, J., The Theory of Elastic Waves and Waveguides, North-Holland Publishing Company, N. Y., 1978, page 425.

12. Delves, L. M. and Lyness, J. N. 1967, " A numerical method for locating the zeros of an analytic function," Mathematics of Computation, Vol. 21, pp. 543-560.

13. Benjamin, T. B. "The threefold classification of unstable disturbances in flexible surfaces bounding inviscid flows," J. Fluid Mech. vol. 16, pp. 436-450, 1963.

DISCUSSION

Colin Moore,
University of California, Berkeley

Thank you for your introduction to this interesting area. It seems to me that actual application would involve compressible coatings. Please expand on the role of compressibility.

Reply -

The response of a compliant coating to flow structures in a turbulent boundary layer (for instance turbulent bursts) will be effected significantly by the compressibility of the coating. The differences between the response of a compressible and incompressible coating can be traced to the differences between their respective dispersion relations. Thus, varying the compressibility of the coating will change the wave length, included angle, distribution of wave amplitude, etc. of the wave patterns generated locally on the coating surface by the bursts. The flow speed at which the response becomes unstable may also change. At present, the wave patterns and amplitudes most likely to produce favorable turbulence modification for drag or noise reduction are not known. Thus, though one can say that the use of compressible coatings will change the response (and with some additional work, predict what those changes will be), it is not presently possible to predict how these changes will effect the likelihood of turbulence modification.

Michael M. Reischman,
Office of Naval Research

In your model for the transient pressure force the wall shearing stress is neglected. Could you give a rationale for that omission and how difficult would it be to improve the model to include this input?

Reply -

The difficulty in including both shear stress and pressure fluctuations in the compliant coating response model is one of phasing. The model used here employs a prescribed pressure distribution which is designed to imitate the pressure distribution found under a turbulent eddy. Of course, the shear stress fluctuations that occur simultaneously can also deform the coating. One could easily modify the current theory to compute the response to a prescribed shear stress distribution alone. In order to include both the shear stress and the pressure simultaneously, careful attention must be given to the phasing of the two. This phasing could be obtained from measurements or possibly from a model of the eddy structure that is producing the fluctuations. This model was not addressed in the present study due to lack of time. Since in turbulent flows over rigid walls, measurements have shown that the pressure fluctuations are considerably larger than the shear stress fluctuations, it was decided to explore the effect of pressure fluctuations first.

Ship Maneuvering in Waves

W. R. McCREIGHT
David W. Taylor Naval Ship R&D Center

Conventional frequency-domain methods for predicting motions in a seaway for a ship moving with constant mean heading and speed are not applicable to the more general problem of predicting motions during a maneuver in a seaway. This is important for naval problems such as error analysis of shipboard weapon systems performance during maneuvers. This paper describes the developent of a six-degree-of-freedom time domain theory for predicting the motions of a ship maneuvering in waves and wind, including wave induced motions. The full nonlinear calm water maneuvering equations of motion are combined with wave effects derived from linear ship motion theory. This includes the frequency dependence of the added mass and damping terms, which are represented by high order systems of differential equations having (approximately) the same frequency response to a motion input as the added mass and damping for each mode of motion. The effects of variations of speed and heading on the coefficients in the equations of motion are modelled. Alternate approaches are discussed in this paper.

INTRODUCTION

The motions of a ship at sea, whether caused by waves or by the ship's own maneuvers, can strongly affect the functioning of the ship's systems and consequently its ability to carry out its mission. Weapon and sensor effectiveness, and safety of underway replenishment at sea operations are just two examples of important performance characteristics which can be degraded by ship motions. Thus, ship designers must consider the effects of ship motions while maneuvering.

In order to thoroughly analyze these effects, it is necessary to have analytical predictions in the form of motion time histories. Until the present time, it has been possible to predict the trajectory and attitude of a moving ship at sea only for the separate cases of (a) rudder-induced motions while maneuvering in calm water, and (b) wave-induced motions while moving at a constant (mean) speed along a steady course in a moderate seaway. Models for the first case omitted seaway effects while those for the second neglected (necessarily because of the analytical approach conventionally taken) speed and heading variations, wind, and transient motions due to the rudder. The solution to the important problem of predicting the combined effects of simultaneous maneuvers and waves on the motions of a ship has not been possible. Analyses of motion-sensitive systems could only consider a limited part of the problem at one time.

Most previous work in the area of maneuvering in waves has been concerned with the course keeping ability of ships in waves and with the possibility of broaching and capsizing. Conolly[1] has surveyed these problems. Perez y Perez[2] developed a model for steering in waves which models the effect of frequency dependent coefficients by convolution integrals. Hirano et al.,[3] calculated the trajectory of a merchant ship in regular waves, neglecting oscillatory forces and thus obtained predictions of the mean motion and compared these predictions with experiments, obtaining reasonably good results. Henry[4] has modelled the motions of a submerged torpedo in waves ignoring the frequency-dependent coefficients. Aukudinov[5] presented a simplified maneuvering in waves model, taking account of frequency dependence of the coefficients, but with heave and pitch decoupled from surge as well as from the lateral plane motions. Livingston[6] used a filter fit to the linear motion response to exciting forces and moment at constant speed and heading, and was able to then consider nonlinear damping in the time domain as another external force. This approach has the disadvantage that the speed dependence is imbedded in the model for one fixed speed and cannot model the effect of speed variation on motion responses, except for the frequency of encounter shift. Another method which may be reasonably accurate is a quasi-steady approximation in which the calm water maneuvers would be calculated and the linear wave responses calculated in the same way that the linear wave exciting forces are calculated in the present work and then simply added to the calm water motions. This would be particularly applicable to relatively slow ships whose heading does not change appreciably during one encounter period.

This paper describes a mathematical model for predicting the motions of a ship while maneuvering in waves which takes into account all important disturbances and which includes the effect of past motions on the forces action on the hull (the memory effects). These effects are important for wave-induced motions but are neglected for conventional time-domain maneuvering predictions due to the difficulty of modelling them and to their relative lack of importance for calm water maneuvering.

The approach used combines existing models for calm water maneuvering and linear ship motions in waves. This combined model will reduce in the limit of no waves and of small waves with no maneuvering to these two cases.

EQUATIONS OF MOTION

Coordinate Systems

In developing the equations of motion, the following coordinate systems are used:

W.R. McCreight, Surface Ship Dynamics Branch, Code 1561, David Taylor Naval Ship Research and Development Center, Bethesda, MD 20084

Inertial (x_o,y_o,z_o): right handed, z_o upwards, fixed in space

Upright (x_u,y_u,z_u): parallel to the inertial coordinate system with origin on free surface, coinciding with amidships

Yawed (x',y',z'): upright coordinate system rotated through angle ψ about the z_u axis

Pitched (x'',y'',z''): yawed coordinate system rotated through angle θ about the y' axis

Body (x_b,y_b,z_b): pitched coordinate system rotated through angle θ about the x'' axis

Maneuvering (x,y,z): the conventional SNAME maneuvering coordinate system fixed in the body, x positive forward, z postive downward, origin located at $-x_{sk},0,z_{sk}$) in the body coordinate system. This can be obtained by rotating the body coordinate system by 180° about the x axis and then translating the origin to the point ($-x_{sk},0,z_{sk}$) in the body coordinate system.

Seakeeping (x_s,y_s,z_s): parallel to upright coordinate system rotated about the z axis through yaw angle with origin located at the mean positive of the origin of the body coordinate system. This is the conventional linear seakeeping coordinate system and is meaningful only for a ship moving at constant speed on a constant course.

All of the systems are right-handed. The more important of these systems are shown in Figure 1.

DYNAMICS

The equations of motion assuming (a) transverse symmetry, (b) the principal axes of inertia parallel to the chosen axis system, $I_y = I_z$, and (c) the center of gravity located at (x_G,O,z_G), are, in standard nomenclature,[2,3]

$$m[\dot{u} + qw - rv - x_G(q^2 + r^2) + z_G(pr + \dot{q})] = X$$

$$m[\dot{v} + ru - pw + z_G(qr - \dot{p}) + x_G(qp + \dot{r})] = Y$$

$$m[\dot{w} + pv - qu - z_G(p^2 + q^2) + x_G(rp - \dot{q})] = Z$$

$$I_x\dot{p} - mz_G(\dot{v} + ru - pw) - mx_Gz_G(pq + \dot{r}) = K$$

$$I_y\dot{q} + (I_x - I_z)\,rp + mz_G(\dot{u} + qw - rv) - mx_G(\dot{w} + pv - qu) + mx_Gz_G(p^2 - r^2) = M$$

$$I_z\dot{r} + (I_y - I_x)\,pq + mx_g(\dot{v} + ru - pw) + mz_Gx_G(rq - \dot{p}) = N \qquad (1)$$

Kinematics

Some useful kinematic relations are:

$$\dot{\phi} = p + (q\sin\phi + r\cos\phi)\tan\theta$$

$$\dot{\theta} = q\cos\phi - r\sin\phi$$

$$\dot{\psi} = (q\sin\phi + r\cos\phi)/\cos\theta$$

$$\dot{x}_o = u\cos\theta\cos\psi + v(\sin\phi\sin\theta\cos\psi - \cos\phi\sin\psi) + w(\cos\phi\sin\theta\cos\psi + \sin\phi\sin\psi)$$

$$\dot{y}_o = u\cos\theta\sin\psi + v(\sin\phi\sin\theta\sin\psi - \cos\phi\cos\psi) + w(\cos\phi\sin\theta\sin\psi - \sin\phi\cos\psi)$$

$$\dot{z}_o = -u\sin\theta + v\sin\phi\cos\theta + w\cos\phi\cos\theta \qquad (2)$$

EXTERNAL FORCES AND MOMENTS

Each of the forces and moments X, Y, Z, K, M, and N acting on the ship can be separated into terms according to the cause of the force or moment as follows. For the general force F:

$$F = F_{HS} + F_{CW} + F_{WIND} + F_{WAVE} \qquad (3)$$

The subscript HS indicates hydrostatic force and all six components must be considered due to the changing orientation of the ship axis system. The subscript CW indicates terms other than hydrostatics in the conventional calm water model. This includes various hydrodynamic effects, propulsion forces and rudder forces and moments. The wind terms are rather simple. The wave terms are based on linear ship motion theory, and include frequency effects.

These force and moment terms are separately calculated in a convenient coordinate system and then transformed into the maneuvering coordinate system and summed to obtain the total forces and moments acting on the ship. These models are described in detail below.

Hydrostatic Forces

The hydrostatic forces and moments which represent the difference between the gravitational forces on the ship and the integral of the hydrostatic pressure acting on the hull are calculated using a linear theory in the yawed seakeeping coordinate system. In this sytem the non-zero components of the hydrostatic forces and moments are taken as

$$f_3 = -z_o\,C_{33} - \theta\,C_{35}$$

$$f_4 = -\phi\,C_{44}$$

$$f_5 = -z_o\,C_{53} - \theta\,C_{55} \qquad (4)$$

where z_o is the vertical displacement of the seakeeping origin from its rest position, and ϕ and θ are the (finite amplitude) roll and pitch angles, which for small angles reduce to the corresponding linear seakeeping theory angles. The C_{ij} terms are the conventional linear hydrostatic coefficients defined by, for example, Salvesen, Tuck, and Faltinsen.[7] The resulting forces and moments are then transformed into the body coordinate system.

CALM WATER HYDRODYNAMIC FORCES

The calm water hydrodynamic forces and moments X_{CW}, Y_{CW}, K_{CW}, and N_{CW} are functions of ship velocities and accelerations. The model for these forces and moments which has been adopted is a modification and extension of the model developed by L.E. Motter* for the DD-963. This model is, in turn, an extension of the nonlinear three-degree-of-freedom ship maneuvering model of Smitt and Chislett.[8] After the equations of motion are nondimensionalized using L as the length scale, L/U as the time scale, and ϱL^3 as the mass scale, the hydrodynamic force and moment model is

$$X'_{CW} = X'_{prop} + \dot{X}'_{\underline{u}}\underline{u}' + X'_{\delta\delta}\delta^2 + X'_{\delta\delta\underline{u}}\delta^2\underline{u}' + X'_{vv}v'^2 + X'_{v\delta}v'\delta + X'_{vvF}v'^2F_n + X'_{vvFF}v'^2F_n^2 + X'_{\underline{u}\delta\delta F}\underline{u}'\delta F_n$$

$$Y'_{CW} = Y'_o + Y'_{o\underline{u}}\underline{u}' + Y'_{\dot{v}}\dot{v}' + Y'_{\dot{r}}\dot{r}' + Y'_{\dot{p}}\dot{p}' + Y'_v v' + Y'_r r'$$

*Published in a report with limited distribution.

$$+ Y'_{\delta}\delta + Y'_{\delta\delta\delta}\delta^3 + Y'_{\delta|v|}\delta|v'| + Y'_{\delta\underline{u}}\delta\underline{u}'$$
$$+ Y'_{\delta\underline{u}\underline{u}}\delta\underline{u}'^2 + Y'_{v|v|}v'|v'| + Y'_{v|r|}v'|r'|$$
$$+ Y'_{v\underline{u}}v'\underline{u}' + Y'_{rrr}r'^3 + Y'_{\phi}\phi + Y'_{\phi|r|}\phi|r'|$$

$$K'_{CW} = K'_{\delta}\delta + K'_{\delta\delta\delta}\delta^3 + K'_{\dot{p}}\dot{p}' + K'_{\dot{v}}\dot{v}' + K'_{v}v' + K'_{r}r'$$
$$+ K'_{p}p' + K'_{\delta|v|}\delta|v'| + K_{\delta\underline{u}}\delta\underline{u}' + K'_{\delta\underline{u}\underline{u}}\delta\underline{u}'^2$$
$$+ K'_{v|v|}v'|v'| + K'_{v\underline{u}}v'\underline{u}'$$
$$+ K'_{rrr}r'^3 + K'_{\phi|r|}\phi|r'|$$
$$+ K'_{|\phi|r}|\phi|r' + K'_{pDF}p'F_n^{-1}$$
$$+ K'_{pF}p'F_n + K'_{pFF}p'F_n^2 + K'_{p|p|}p'|p'|$$
$$+ K'_{p|p|F}p'|p'|F_n + K'_{p|p|FF}p'|p'|F_n^2 + K'_{p|p|FFF}p'|p'|F_n^3$$
$$+ K'_{vF}v'F_n + K'_{vFF}v'F_n^2$$

$$N' = N'_{o} + N'_{ou}u' - N'_{\dot{r}}\dot{r}' + N'_{\dot{v}}\dot{v}' + N'_{v}v' + N'_{r}r'$$
$$+ N'_{\delta} + N'_{\delta\delta\delta}\delta^3 + N'_{\delta|v|}\delta|v'| + N'_{\delta\underline{u}}\delta\underline{u}'$$
$$+ N'_{v|v|}v'|v'| + N'_{v|r|}v'|r'|$$
$$+ N'_{v\underline{u}}v'\underline{u}' + N'_{rrr}r'^3$$
$$+ N'_{\phi}\phi + N'_{\phi\underline{u}}\phi\underline{u}' + N'_{|\phi|r}|\phi|r'$$
$$+ N'_{\phi|\delta|}\phi|\delta| \qquad (5)$$

The term X'_{prop} represents the propulsion force model. This may be simply the expression

$$X'_{\underline{u}}\underline{u} + X'_{\underline{u}\underline{u}}\underline{u}'^2 + X'_{\underline{u}\underline{u}\underline{u}}\underline{u}'^3 \qquad (6)$$

A more detailed propulsion force model is based on the difference between the total propeller thrust force and propelled hull resistance, i.e.,

$$X = N_p T - R_T/(1-t) \qquad (7)$$

where N_p is the number of propellers, T is the propeller thrust, R_T is the total ship resistance without propellers and t is the thrust deduction fraction, as a function of ship speed. With the ship effective horsepower P_E and propeller open water thrust and torque coefficients K_T and K_Q represented in the form

$$P_E/(N_p V^3) = a_0 + a_1 V + a_2 V^2 + a_3 V^3 \qquad (8)$$

$$K_T = \frac{T}{pn^2D^4} = b_0 + b_1 J_T + b_2 J_T^2 \qquad (9)$$

$$K_Q = \frac{Q}{pn^2D^5} = c_0 + c_1 J_Q + c_2 J_Q^2 \qquad (10)$$

where J is the advance coefficient V/nD, based on thrust or torque identity, as indicated by the subscripts T and Q respectively.

Knowing the thrust and torque identity wake fractions W_T and W_Q and thrust deduction t, these can readily be solved for n, T, and Q for (a) equilibrium conditions and (b) during maneuvers assuming either constant power $P = 2\pi\, n\, Q$, constant Q or constant n.

In addition to these options, detailed diesel engine and turbine models, including the effects of engine dynamics, governors, torque limiters, and drive train dynamics are available. These models were developed by Propulsion Dynamics, Inc.[9] and details will not be presented here.

The various coefficients may be obtained either by model experiments for a given ship or by independent prediction. Motter, mentioned above, Smitt and Chislett[8] and Mandel[10] discuss the model experiment technique. This model is valid only for a limited range of the variables, but is adequate for the normal values involved in maneuvering. It should be noted that not all coefficients are required for all ships.

Wind Forces

The following model for wind force and moment in the yawed coordinate system has been adopted, based on the data of Aage[11] for nine ships:

$$X'_W = \left(\frac{U_{RW}}{U}\right)^2 \frac{\varrho_a}{\varrho}\frac{A_f}{L^2} C_{X_{W_{MAX}}} \sin\left[\frac{9}{7}\left(|\psi_{RW}| - \frac{\pi}{2}\right)\right] \qquad -\pi \leq \psi_{RW} \leq \pi$$

$$Y'_W = \left(\frac{U_{RW}}{U}\right)^2 \frac{\varrho_a}{\varrho}\frac{A_s}{L^2} C_{Y_{W_{MAX}}} \sin\psi_{RW}$$

$$K'_W = \left(\frac{U_{RW}}{U}\right)^2 \frac{\varrho_a}{\varrho}\frac{A_s H_s}{L^3} C_{K_{W_{MAX}}} \sin\psi_{RW}\cos^2\phi$$

$$N'_W = \left(\frac{U_{RW}}{U}\right)^2 \frac{\varrho_a}{\varrho}\frac{A_s L_{OA}}{L^3} C_{N_{W_{MAX}}} \sin 2\psi_{RW} \qquad (11)$$

where A_f, A_s, ϱ_a, ϱ, and L are frontal projected above water area, lateral projected above water area, air density mass and water mass density, respectively, and the relative wind velocity and direction U_{RW} and ψ_{RW} are given by

$$U_{RW} = \{[U_W \cos(\psi_W - \psi) - u]^2 + [U_W \sin(\psi_W) - v]^2\} \qquad (12)$$

$$\psi_{RW} = \tan^{-1}\left\{\frac{U_W \sin(\psi_W - \psi) - v}{U_W \cos(\psi_W - \psi) - u}\right\} \qquad (13)$$

where U_W and ψ_W are the wind speed and direction relative to the inertial coordinate system and u and v are the longitudinal and lateral velocity components in the coordinate system. The values 0.70, 0.80, 1.30, and 0.10 have been adopted for $C_{X_{MAX}}$, $C_{Y_{MAX}}$, $C_{K_{MAX}}$, AND $C_{N_{MAX}}$, respectively.

The $\cos^2\phi$ dependence of roll moment on roll angle is adopted from Sarchin and Goldberg.[12] Kinoshita and Okada[13] found a similar effect, as well as a relatively smaller decrease of wind-induced sway force with heel, which is neglected here. Eda[14] uses a generally similar model for the X and Y forces and yaw moment. The form adopted for the X force agrees with data presented by Todd[15] showing that the maximum X force occurs with the wind somewhat off the bow or stern.

It should be noted that Aage's data is based on tests in which the boundary layer is not scaled and consequently is intermediate in thickness between a full scale atmospheric boundary layer[16] and a uniform flow. Aage[11] states that this gives realistic results because a ship at sea will operate in a relative wind field which is the sum of the nonuniform flow due to the wind and the forward speed of the ship. This wind field will vary with height and direction as well as

velocity. In the mathematical model for wind effects used here, no correction for the boundary layer is attempted, although schemes for such corrections have been proposed.[17,18]

REGULAR WAVE EXCITING FORCES

The regular wave exciting forces used are those from conventional strip theory (Salvesen, Tuck, Faltinsen[7]), which are calculated in the seakeeping coordinate system assuming that the ship has been proceeding at constant (mean) speed and heading for all time. The instantaneous values of the forces are used, based on the wave elevation at the origin of the seakeeping coordinate system, neglecting memory effects. For the Froude-Krylov terms, this assumption is exact. The amplitude and phase relative to the wave of the diffraction term depends on ship speed and heading, which will vary slowly. Thus this is a reasonable approximation, which also eliminates the difficulty mentioned by Tick[19] that the impulse response function may depend on the "future", if time is indexed at amidships, due to the fact that the wave at the bow will move the ship even though it hasn't yet reached the origin. The exciting forces are obtained in the form of frequency response functions $H_\ell(\omega_e)$ for each mode which are functions of the ship speed and the wave heading and frequency. In a random seaway, the frequency content of the input is preserved in the present approach because the forces due to each component of the seaway are calculated separately and then summed.

WAVE EXCITING FORCES IN RANDOM SEAS

The seaway model adopted is that prescribed in the St. Denis and Pierson[20] model

$$\zeta(x,y,t) = \mathrm{Re} \sum_{j=1}^{n} \sum_{k=1}^{m} \exp\{-ik_k(x_o(t)\cos\mu_j + y_o(t)\sin\mu_j) + i\omega_k t + i\varepsilon_{jk}\} \times (2S_\zeta(\omega_k,\mu_j)\,\Delta\mu_j\,\Delta\omega_k)^{1/2} \quad (14)$$

for short crested seas, where K_k is the number ω_k^2/g of the kth frequency, ω_k of m frequencies, μ_j is the jth direction of n, ε_{jk} is the random phase of each component uniformly distributed over $(0, 2\pi)$ and S_ζ is the Bretschneider [21] spectrum with cosine squared spreading given by

$$s_\zeta(\omega,\mu) = \frac{2}{\pi}\cos^2(\mu-\mu_c)\,S_\zeta(\omega) \qquad -\frac{\pi}{2} \leqslant \mu-\mu_c \leqslant \frac{\pi}{2}$$

$$= 0 \qquad \frac{\pi}{2} < |\mu-\mu_c| < \pi \quad (15)$$

where μ_c is the predominant wave direction and

$$S_\zeta(\omega) = 487.1(\tilde{\zeta}_w)_{1/3}^2\, T_o^{-4}\,\omega^{-5} \exp(-1944.5\, T_o^{-4}\,\omega^{-4}) \qquad m^2 s \quad (16)$$

where $(\tilde{\zeta}_w)_{1/3}$ is the significant wave height and T_o is the modal or peak energy wave period.

The exciting force in the ℓth mode for conditions corresponding to Equation (15) is given by

$$F_\ell(t) = \mathrm{Re} \sum_{j=1}^{n} \sum_{k=1}^{m} A_{jk}\, H_\ell(\omega_k, \psi - \mu_j) \cdot \exp\{-iK_\zeta(x_o(t)\cos\mu_j + y_o(t)\sin\mu_j) + i\omega_k t + i\varepsilon_{jk}\} \quad (17)$$

where H_ℓ is the exciting force transfer function, as discussed in the previous section, for the ℓth mode, $x_o(t)$, $y_o(t)$ are the location of the origin of the seakeeping axis system, and ψ is the heading of the ship.

SECOND ORDER WAVE FORCES

Nonlinear interaction of waves with a ship results in second-order forces and moments acting on the ship. These are relatively small in magnitude and are generally neglected in maneuvering studies. An exception is the study of underway replenishment by Brown and Alvestad[22] in which a very accurate ship track was required over a long period of time. In the present paper, the effect of drift forces and moments and the closely related added resistance in waves will be neglected because of the difficulty in computing them and the relatively small effect they will have on the ship motions, particularly roll, over the short time period of interest. For other problems, notably station keeping, the drift forces will be quite important and must be included in the hydrodynamic model. Aukudinov[5] also included a drift force model in his work.

HYDRODYNAMIC REACTION FORCES

The hydrodynamic reaction forces, that is, the total forces acting on the hull due to forced motion in calm water less the hydrostatic forces, are developed in the seakeeping coordinate system using linear theory and then transformed into the yawed and pitched, or stability, coordinate system.

Frequency Domain

For sinusoidal motions the force component $f_{ij}(t)$ in the ith direction due to forced motion in the jth mode (i,j = 1, 2, 3, 4, 5, 6 for surge, sway, heave, roll, pitch, and yaw, respectively) be given by

$$f_{ij} = -A_{ij}\,\ddot{\xi}_j - B_{ij}\,\dot{\xi}_j \quad (18)$$

In the frequency domain this can be represented by

$$F_i = T_{ij}\,\Xi_j \quad (19)$$

where

$$T_{ij} = \omega^2 A_{ij} - i\omega B_{ij}$$

The Ogilvie-Tuck[23] rational strip theory is used for calculation of heave and pitch added mass and damping. Experiments by O'Dea and Jones[24] on a SL-7 model revealed a considerable discrepancy between measurements and conventional strip theory predictions of heave-pitch cross-coupling coefficients and heave and pitch motions in head seas. For the coefficients, these errors are particularly large for long wavelength and high Froude number. Calculation of these coefficients and motions predicted by a close fit implementation of the Ogilvie-Tuck theory showed a very great improvement for this hull. These results are shown in Figures 2 through 6 for the SL-7 with the O'Dea and Jones experimental results. Faltinsen[25] found similar results for a Series 60 hull form.

It was also found that a constant-coefficient time domain heave-pitch model using added mass and damping terms from conventional strip theory was unstable for long wavelengths and high Froude number. Eigenvalue analysis of the equations of motion confirmed this instability. Use of the added mass and damping predicted by the Ogilvie-Tuck rational strip theory eliminated the instability. While use of a constant-coefficient model is not a strictly accurate representation of real ship motions, due to the well-known frequency dependence of the hydrodynamic coefficients, this instability dramatically ilustrates the inaccuracies of the conventional strip theory at low frequency.

For the lateral modes (sway, roll, and yaw) the standard strip theory of Salvesen, Tuck and Faltinsen[7] is used. The non-zero term, in seakeeping axes, are:

$$
\begin{aligned}
T_{11} &= T_{11}^{(0)} \\
T_{22} &= T_{22}^{(0)} \\
T_{24} &= T_{24}^{(0)} \\
T_{26} &= T_{26}^{(0)} - \frac{U}{i\omega} T_{22}^{(0)} \\
T_{33} &= T_{33}^{(0)} \\
T_{35} &= T_{35}^{(0)} + \frac{U}{i\omega} T_{33}^{(0)} + U\, S_{35} \\
T_{42} &= T_{42}^{(0)} \\
T_{44} &= T_{44}^{(0)} \\
T_{46} &= T_{46}^{(0)} - \frac{U}{i\omega} T_{42}^{(0)} \\
T_{53} &= T_{53}^{(0)} - \frac{U}{i\omega} T_{33}^{(0)} - U\, S_{35} \\
T_{55} &= T_{55}^{(0)} \\
T_{62} &= T_{62}^{(0)} + \frac{U}{i\omega} T_{22}^{(0)} \\
T_{64} &= T_{64}^{(0)} + \frac{U}{i\omega} T_{24}^{(0)} \\
T_{66} &= T_{66}^{(0)} + \frac{U}{\omega^2} T_{26}^{(0)}
\end{aligned}
\qquad (20)
$$

where U is the mean forward speed, $T_{ij}^{(0)}$ indicates the zero forward speed term, and S_{35} is the Ogilvie-Tuck free surface integral term for heave-pitch coupling. Detailed expressions and derivations may be bound in the original references. These coefficients are defined in coordinates fixed in the earth except for a steady motion parallel to the mean motion of the ship. However, a maneuvering ship follows a general curved path and it is not possible to define a "mean" path analogous to that used in the steady forward motion problem. Consequently, we will transform the expressions for these forces into a coordinate system which is yawed and pitched to correspond with the yaw and pitch Euler angles ψ and θ, which are known.

Assuming small angles, the angular velocities and surge velocity are unchanged, while the sway and heave velocities in the new coordinate system, $\dot{\xi}_2$ and $\dot{\xi}_3$, are

$$
\begin{aligned}
\dot{\xi}_2 &= \dot{\eta}_2 + U\eta_6 = \dot{\eta}_2 + \frac{U}{i\omega}\dot{\eta}_6 \\
\dot{\xi}_3 &= \dot{\eta}_3 - U\eta_5 = \dot{\eta}_3 - \frac{U}{i\omega}\dot{\eta}_5
\end{aligned}
\qquad (21)
$$

where η_i and $\dot{\eta}_i$ are the displacements and velocities in the seakeeping coordinate system, $\eta_5 = \theta$ and $\eta_6 = \psi$. After this change of coordinate system, we have

$$
\begin{aligned}
T_{11} &= T_{11}^{(0)} \\
T_{22} &= T_{22}^{(0)} \\
T_{24} &= T_{24}^{(0)} \\
T_{26} &= T_{26}^{(0)} \\
T_{33} &= T_{33}^{(0)} \\
T_{35} &= T_{35}^{(0)} + U\, S_{35} \\
T_{42} &= T_{42}^{(0)} \\
T_{44} &= T_{44}^{(0)} \\
T_{46} &= T_{46}^{(0)} \\
T_{53} &= T_{53}^{(0)} - \frac{U}{i\omega} T_{33}^{(0)} - U\, S_{35}^{(0)} \\
T_{55} &= T_{55}^{(0)} - \frac{U}{i\omega} T_{53}^{(0)} \\
T_{62} &= T_{62}^{(0)} + \frac{U}{i\omega} T_{22}^{(0)} \\
T_{64} &= T_{64}^{(0)} + \frac{U}{i\omega} T_{24}^{(0)} \\
T_{66} &= T_{66}^{(0)} + \frac{U}{i\omega} T_{26}^{(0)}
\end{aligned}
\qquad (22)
$$

While the lateral mode terms in this coordinate system are considerably simplified, the vertical mode terms are more complicated. Schmitke[26] previously applied the same transformation to the lateral mode terms. Note that in the expression for T_{55} two higher order terms have been dropped.

Time Domain

The expressions developed above are for sinusoidal motions of the hull. Due to the presence of the free surface, the coefficients A_{ij} and B_{ij} are functions of frequency and consequently Equation (19) is not valid for arbitrary motions. This situation is discussed at length in, for example, Ogilvie[27], Tick[19] and Cummins.[28] The exact formulation of the time domain model for a system with frequency dependent coefficients is in terms of a convolution integral:

$$
f_{ij}(t) = -A_{ij}(\infty)\ddot{\xi}_j - \int_0^\infty h_{ij}(\tau)\,\dot{\xi}_j(t-\tau)\,d\tau \qquad (23)
$$

where

$$
h_{ij}(t) = \frac{2}{\pi}\int_0^\infty B_{ij}(\omega)\cos\omega t\, d\omega = -\frac{2}{\pi}\int_0^\infty \omega\,[A_{ij}(\omega) - A_{ij}(\infty)]\sin\omega t\, d\omega \qquad (24)
$$

The equations are standard relations in linear system theory. Cummins showed how they could be derived for ship motions from hydrodynamic considerations.

The simplest approach to handling this effect is to neglect the frequency dependence altogether and assume a constant coefficient model, choosing the coefficient values at some appropriate frequency, for example, the roll natural frequency. This has commonly been done for analog computer models of ship roll motion. See, for example, Zarnick and Diskin.[27] For modes of motion which are not as sharply tuned as roll, the errors involved in this assumption are excessive. At the other extreme of complication, it is possible to calculate the impulse response function $h_{ij}(t)$ from added mass and damping data and then evaluate the convolution integral equation for each term in the equations of motion at each time step during the simulation. However, this approach is very tricky to implement for any but the most

primitive ordinary differential equation solver, and in any case can be very time consuming.

An alternative approach has been used here. The repeated evaluation of the convolution integrals is avoided by modelling the frequency-dependent added mass and damping by a filter which has (approximately) the same frequency response as the force and then implementing this filter in the time domain. The effect is to increase the order of the system of equations but to accurately account for the frequency dependence of the hydrodynamic forces. The resulting model is equivalent to a system of hypothetical masses, dashpots, and springs. Tick[19] first proposed this method in the context of ship hydrodynamics, using simple polynomial filters. Schmiechen[30,31] has applied this method to the problem of the collision of ships, in which the excitation (impact) is very broad banded, using the more general rational function filters in the frequency domain. More recently, Jeffreys[32] among others has applied this approach to modelling of wave power devices. Ankudinov[5] reverted to the simple Tick polynomial filter in his approach to maneuvering in waves.

The frequency dependent reaction forces are modelled in the frequency domain by a least squares curve fit of the form

$$i\omega A(\omega) + B(\omega) = \frac{\sum_{k=1}^{m} (i\omega)^{k-1} a_k}{\sum_{k=1}^{n} (i\omega)^{k-1} b_k} + i\omega A_\infty + B_\infty \qquad (25)$$

where $n = m + 1$. For each of the lateral modes, the value of B_∞ is then adjusted to force $B(0)$ to zero. This is done to avoid altering the effective values of the linear maneuvering coefficients in Equation (5). Depending on the specific term being fitted, either A_∞, B_∞ or both may be zero. The transfer function

$$\frac{Y(\omega)}{X(\omega)} = \frac{\sum_{k=1}^{m} (i\omega)^{k-1} a_k}{\sum_{k=1}^{n} (i\omega)^{k-1} b_k} \qquad (26)$$

is equivalent to the system of ordinary differential equations

$$\sum_{k=1}^{n} b_k \frac{d^{k-1}}{dt^{k-1}} y(t) = \sum_{k=1}^{m} a_k \frac{d^{k-1}}{dt^{k-1}} x(t) \qquad (27)$$

which can be written as

$$\sum_{k=1}^{n} b_k \frac{d^{k-1}}{dt^{k-1}} z(t) = x(t)$$

$$\sum_{k=1}^{m} a_k \frac{d^{k-1}}{dt^{k-1}} z(t) = y(t) \qquad (28)$$

Then if $\eta_k = \frac{d^{k-1}}{dt^{k-1}} z(t)$ we obtain

$$\dot{\eta}_k = \eta_{k+1} \qquad k = 1, \ldots, n-2$$

$$\dot{\eta}_{n-1} = \frac{1}{b_n} [x(t) - \sum_{k=1}^{n-1} b_k \eta_k]$$

$$y(t) = \sum_{k=1}^{m} a_k \eta_k \qquad (29)$$

This system of ordinary differential equations is readily implemented and yields the frequency dependent y(t) due to the arbitrary input velocity x(t). The variable $\eta(t)$ and its $m-1$ derivatives increase the order of the system, but the additional terms in the resulting equations of motion are quite simple to evaluate. In applying this force model, the input to the filter representing each term of Equation (22) is the velocity $x_j(t)$ and the resulting force or moment $y_i(t)$ is added to the total force. The $A_{ij}(\infty)$ term from Equation (25) is part of the inertial term.

Modelling the force as a function of velocity simplifies the problem by (a) eliminating unknown acceleration terms if represented in terms of acceleration (Jeffries[32]) and (b) suppressing singularities in the strip theory heave and pitch added mass at $\omega_e = 0$ which will occur if represented as a function of displacement.

The actual curve fitting is carried out using the functional form

$$\sum_{J=1}^{n} \{ \frac{c_j + id_j}{(\omega - a_j - ib_j^2)} + \frac{-c_j + id_j}{(\omega - a_j - ib_j^2)} \} + i\omega A\infty + B\infty \qquad (30)$$

This consists of pairs of poles located symmetrically on either side of the imaginary axis of the complex ω plane to ensure realizability and above the real axis to ensure the stability of the resulting model. Forcing the models of the individual terms to be realizable and stable is not only necessary from a modelling point of view, but is also physically correct.

The processes modelled are the force (moment) responses to a velocity input. The impulse response h_{ij} is thus the force in the i^{th} mode resulting from a velocity impulse in the j^{th} mode. This input is equivalent to a step in the displacement. Stability requires that the impulse response go to zero for large time. For surge and sway, it is clear that this will happen. For heave, roll, and pitch, the resulting force will go to a constant, which is due to hydrostatics, which are not modelled by the fit and thus will not cause an instability. Similarly, a step in yaw angle will result in a constant moment, which is due to circulation effects which again are not modelled. Thus the process being modelled is stable, and it is appropriate to require that the model (curve fit) be stable.

Calculated and filter fitted frequency domain heave added mass and damping at zero speed are presented in Figures 7 and 8 for heave, $T_{33}(\omega)$, and the corresponding impulse response function $h_{33}(t)$ is presented in Figure 9.

INITIALIZATION

The initial conditions for the time domain solution are chosen to represent the steady state solution corresponding to the ship moving at constant speed and heading, subject to the wind assumed, and with the linear seaway induced motions for the assumed seaway added. This is necessary in order to prevent spurious starting transients in the solution.

The initial conditions are determined by a two-step process. First, the calm water steady-state condition is found by minimizing the sum of the squares of the accelerations in six

degrees of freedom. This yields rudder angle, shaft horsepower, heave, roll, pitch, and yaw (drift angle) to balance wind forces and forces due to asymmetry of the ship calm water hydrodynamic model.

In the second step, the linear frequency domain seakeeping equations are solved to obtain initial values of the motions about the above calm water solution. The filter state variables for frequency dependent reaction forces are initialized at the same time. The result is the seaway induced motions (displacements and velocities) as if the ship had been proceeding along a constant course at constant speed from $t = -\infty$ to $t = 0$.

The method adopted for finding initial conditions yields solutions which result in negligible starting transients. This has been demonstrated by running calm water solutions with no steering or speed commands for periods of time up to 1000 seconds (full scale) which resulted in essentially no change in the ship speed, heading, or attitude.

SOLUTION OF THE EQUATIONS OF MOTION

At any time t the equations of motion, see Equation 1, can be solved algebraically for the accelerations in terms of the velocities, displacements and forcing functions.

$$\frac{du}{dt} = g_1\,(u,v,w,p,q,r,x_o,y_o,z_o,\phi,\theta,\psi,t)$$

$$\frac{dv}{dt} = g_2\,(u,v,w,p,q,r,x_o,y_o,z_o,\phi,\theta,\psi,t)$$

$$\frac{dw}{dt} = g_3\,(u,v,w,p,q,r,x_o,y_o,z_o,\phi,\theta,\psi,t)$$

$$\frac{dp}{dt} = g_4\,(u,v,w,p,q,r,x_o,y_o,z_o,\phi,\theta,\psi,t)$$

$$\frac{dq}{dt} = g_5\,(u,v,w,p,q,r,x_o,y_o,z_o,\phi,\theta,\psi,t)$$

$$\frac{dr}{dt} = g_6\,(u,v,w,p,q,r,x_o,y_o,z_o,\phi,\theta,\psi,t)$$

Together with the kinematic relationship of Equation 2 for the position and orientation $x_o,y_o,z_o,\phi,\theta,\psi$, these form the system of differential equations. These are then integrated numerically from the initial condition found as described in the previous section to find the calm water motion of the ship in the horizontal plane. Euler's method is often used, but in the present work an adaptive Runge-Kutta method developed by Merson[33] is preferred.

Test runs in calm water conditions showed that predictions of sharp turns (rudder angle 35 degrees) were practically independent of step size for step sizes ranging from 0.0333 seconds to 5.0 seconds. For step sizes greater than 1.0 second, the step reduction feature came into play in the initial portion of the run when accelerations were largest.

PREDICTIONS

Results of sample computations for a typical high-speed hull form 400 ft (122 m) long operating at a Froude number of 0.22 in regular waves with $\lambda/L = 1.75$ and amplitudes of 0.1 ft, 1.0 ft, and 2.0 ft (0.03 m, 0.31 m, and 0.62 m, respectively). Turning circles are shown in Figure 10. Heave, roll, and pitch are shown in Figures 11, 12, and 13, respectively. The initial wave condition is head seas and the maximum rudder angle is 25 degrees in all cases. Rudder motion begins at $t = 0$. The wave-induced motions are clearly seen to be linear with wave amplitude.

CONCLUSIONS

A mathematical model for the maneuvering of ships in waves taking account of frequency dependent hydrodynamic coefficients has been developed and implemented. Some predicted time histories of motions of a ship while maneuvering in regular waves have been presented. As predictions are correlated with model test results, refinements in the implementation of this model will be carried out.

ACKNOWLEDGMENTS

The author wishes to thank Dr. Woei-Min Lin of ORI, Inc. whose careful checking of the computer code implementing this model was extremely valuable.

This work was sponsored by the Naval Sea Systems Command under the General Hydromechanics Research Program administered by the David W. Taylor Naval Ship Research and Development Center.

REFERENCES

1. Conolly, J.E., "Stability and Control in Waves: A Survey of the Problem," Journal of Mechanical Engineering Science, Vol. 14, No. 7 (Supplementary Issue) (1972).

2. Perez y Perez, "A Time-Domain Solution to the Motions of a Steered Ship in Waves, Journal of Ship Research, Vol. 18, No. 1 (Mar 1974).

3. Hirano, M., J. Takashina, Y. Takaishi, and T. Saruta, Ship Turning Trajectory in Waves, Transactions, West-Japan Society of Naval Architects, No. 60 (Aug 1980).

4. Henry, Charles J., "Simulation of Torpedo Motions in Waves," Report SIT-DL-73-1669, Stevens Institute of Technology (Jul 1973).

5. Aukudinov, V., "Simulation Analysis of Ship Motion in Waves," International Workshop on Ship and Platform Motions, Berkeley, California (1983).

6. Livingston, W., "A Nonlinear Frequency Domain Simulation for SWATH Craft," DTNSRDC Report DTNSRDC/SPD-0893-01 (Mar 1980).

7. Salvesen, N., E.O. Tuck, and O.M. Faltinsen, "Ship Motions and Sea Loads," Transactions of the Society of Naval Architects and Marine Engineers, Vol. 78 (1970).

8. Smitt, L.W. and M.S. Chislett, "Large Amplitude PMM Tests and Maneuvering Predictions for a Mariner Class Vessel," Tenth ONR Symposium on Naval Hydrodynamics, Boston (Jun 1974).

9. Propulsion Dynamics, Inc., "Implementation of Turbine and Diesel Propulsion System Models in a Surface Ship Maneuvering Simulation," DTNSRDC Report SPD-CR-003-82 (Mar 1982).

10. Mandel, P., "Ship Maneuvering and Control," Chapter VII of Principles of Naval Architecture, J.P. Comstock, editor, Society of Naval Architects and Marine Engineers, New York (1967).

11. Aage, C., "Wind Coefficients for Nine Ship Models," Hydro-og Aerodynamisk Laboratorium Report No. A-3 (May 1971).

12. Sarchin, T.H. and L.L. Goldberg, "Stability and Buoyancy Criteria for U.S. Naval Surface Ships," Transactions of the Society of Naval Architects and Marine Engineers (1962).

13. Kinoshita, M. and S. Okada, "Heeling Moment Due to the Wind Pressure on Small Vessels," Proceedings of the Symposium on the Behaviour of Ships in a Seaway, Wageningen (1957).

14. Eda, H., "Studies of Ship Maneuvering - Control in Wind," Proceedings of the Ship Control Symposium, Annapolis (1966).

15. Todd, F.H., "Resistance and Propulsion," Chapter VII of Principles of Naval Architecture, J.P. Comstrock, editor, The Society of Naval Architects and Marine Engineers, New York (1967).

16. Simu, E. and R.H. Scanlan, "Wind Effects on Structures," Wiley-Interscience, New York (1978).

17. Wilson, C.J. and R.F. Roddy, Jr., "Estimating the Wind Resistance of Cargo Ships and Tankers," Naval Ship Research and Development Center Report 3355 (May 1970).

18. Isherwood, R.M., "Wind Resistance of Merchant Ships," Transactions of the Royal Institution of Naval Architects, Vol. 115 (1973).

19. Tick, L.J., "Differential Equations with Frequency-Dependent Coefficients," Journal of Ship Research, Vol. 3, No. 2 (Oct 1959).

20. St. Denis, M. and W.J. Pierson, Jr., "On the Motion of Ships in Confused Seas," Transactions of the Society of Naval Architects and Marine Engineers, Vol. 61 (1953).

21. Bretschneider, C.L., "Wave Variability and Wave Spectra for Wind-Generated Gravity Waves," Technical Memorandum 118, U.S. Army Beach Erosion Board, Washington, D.C. (1959).

22. Brown, S.H. and R. Alvestad, "Sensitivity Study of Control Parameters During Underway Replenishment Simulations Including Approximate Nonlinear Sea Effects," David Taylor Naval Ship R&D Center Report DTNSRDC 77-0003 (Jan 1977).

23. Ogilvie, T. Francis, and Ernest O. Tuck, "A Rational Strip Theory of Ship Motions: Part I," Report O13, The Department of Naval Architecture and Marine Engineering, University of Michigan (Mar 1969).

24. O'Dea, John F., and Harry D. Jones, "Absolute and Relative Motion Measurements on a Model of a High-Speed Containership," Proceedings, Twentieth American Towing Tank Conference, Hoboken, New Jersey (Aug 1983).

25. Faltinsen, Odd M., "A Numerical Investigation of the Ogilvie-Tuck Formulas for Added-Mass and Damping Coefficients," Journal of Ship Research, Vol. 18, No. 2 (June 1974).

26. Schmitke, R.T., "Ship Sway, Roll, and Yaw Motions in Oblique Seas," Transactions of the Society of Naval Architects and Marine Engineers, Vol. 86 (1978).

27. Ogilvie, T.F., "Recent Progress Toward the Understanding and Prediction of Ship Motion," Fifth ONR Symposium of Naval Hydrodynamics, Bergen, Norway (1964).

28. Cummins, W.E., "The Impulse Response Function and Ship Motions," Schiffstechnik, Vol. 9 (1962).

29. Zarnick, E.E. and J.A. Diskin, "Modeling Techniques for the Evaluation of Anti-Roll Tank Devices," Proceedings of the Third Ship Control Symposium, Bath, England (1972).

30. Schmiechen, M. "Zur Kollisionsdynamik von Schiffen," Jahrbuch der Schiffbautechnischen Gesellschaft, 68.Band (1974).

31. Schmiechen, M., "Equations for Non-Quasi-Steady Ship Motions," Seakeeping Committee Report, Proceedings of the 14th International Towing Tank Conference, Ottawa (Sep 1975).

32. Jeffreys, E.R., "Simulation of Wave Power Devices," Applied Ocean Research, Vol. 6, No. 1 (1984).

33. Fox, L., "Numerical Solution of Ordinary and Partial Differential Equations," Addison-Wesley, Reading Massachusetts (1962).

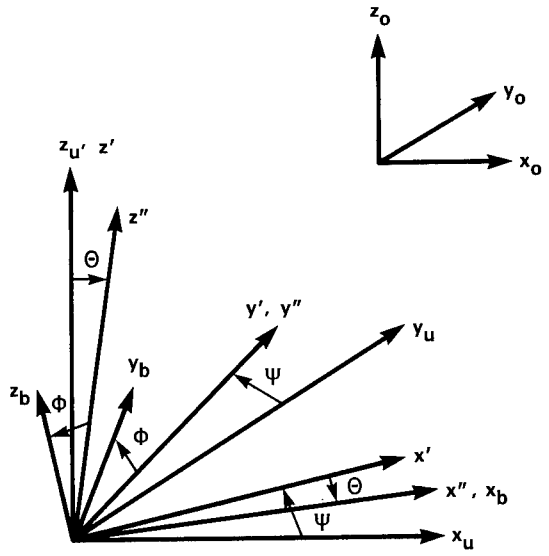


Fig. 1. Coordinate systems.

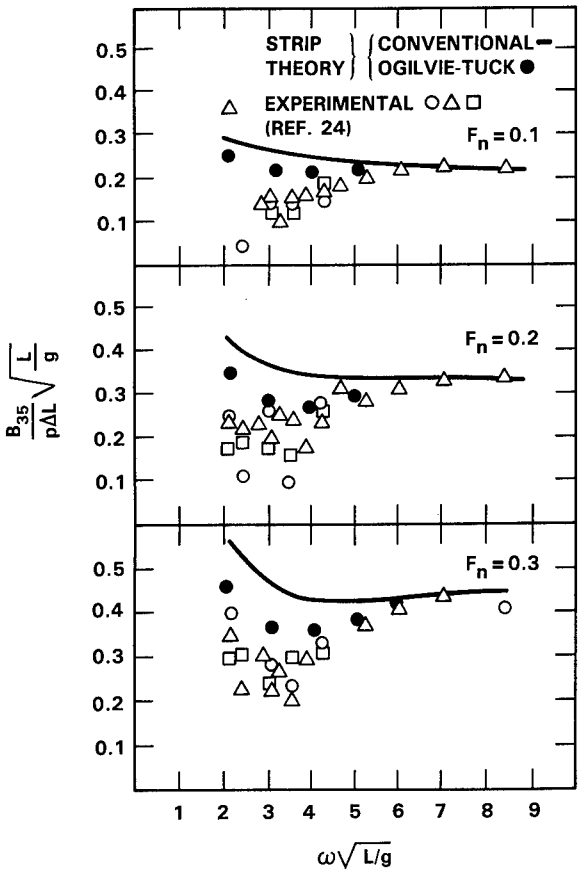


Fig. 3. SL7 heave-pitch coupling coefficient B_{35}.

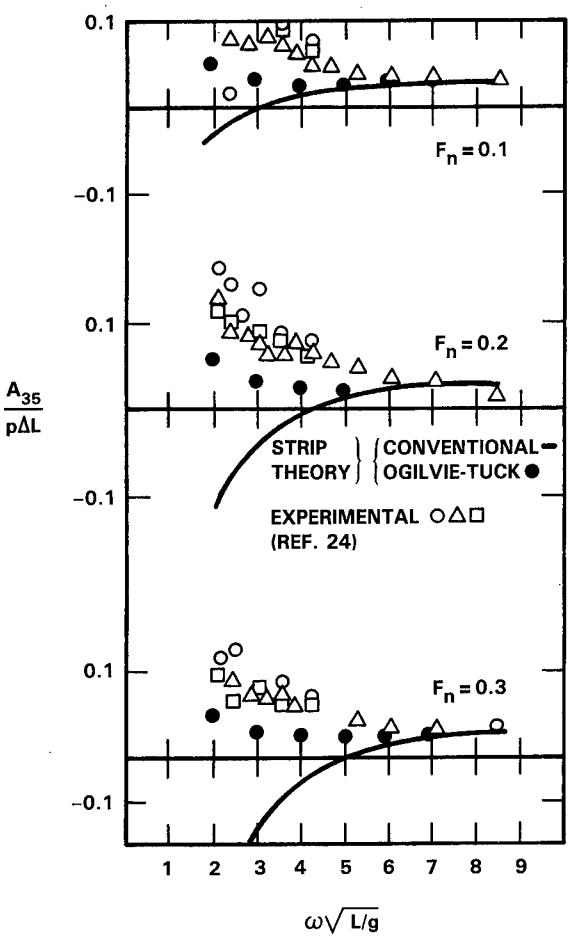


Fig. 2. SL7 heave-pitch coupling coefficient A_{35}.

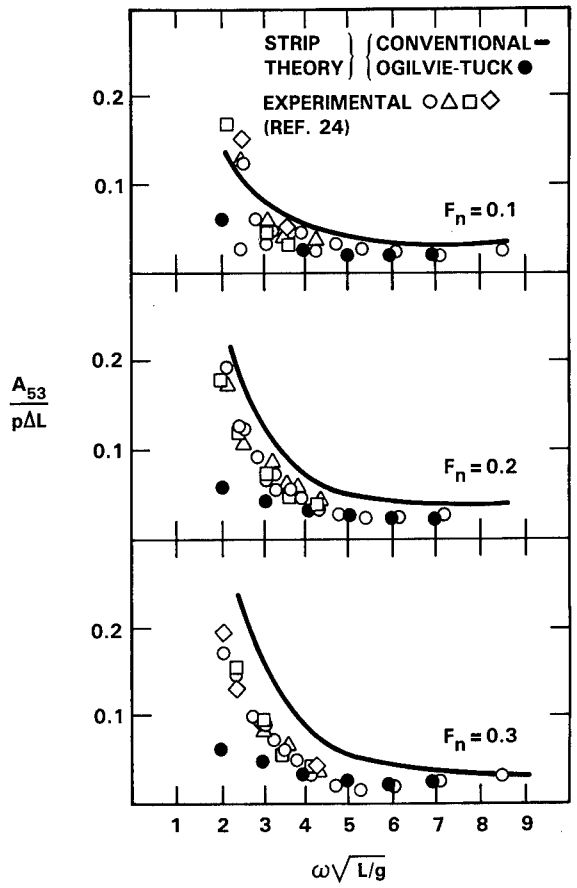


Fig. 4. SL7 pitch-heave coupling coefficient A_{53}.

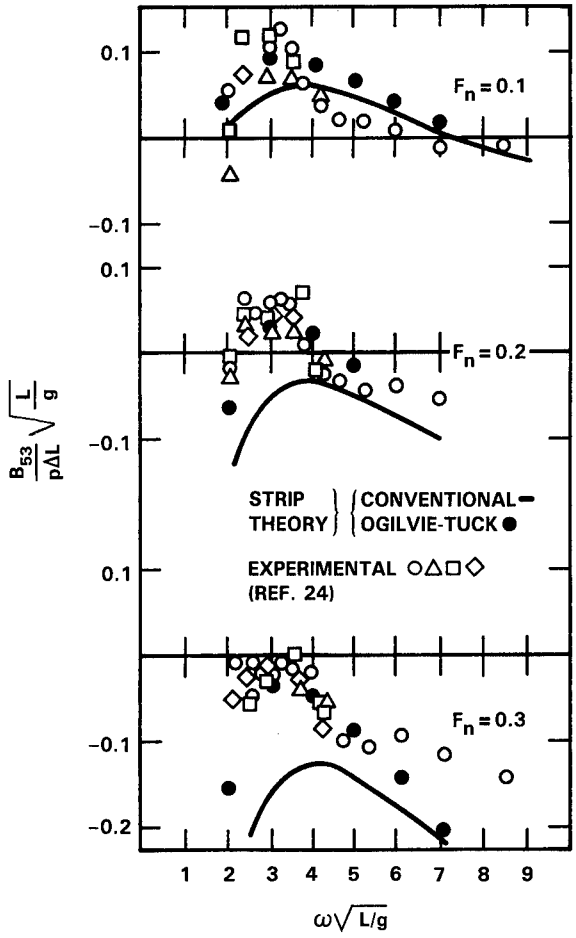


Fig. 5. SL7 pitch heave coupling coefficient B_{53}.

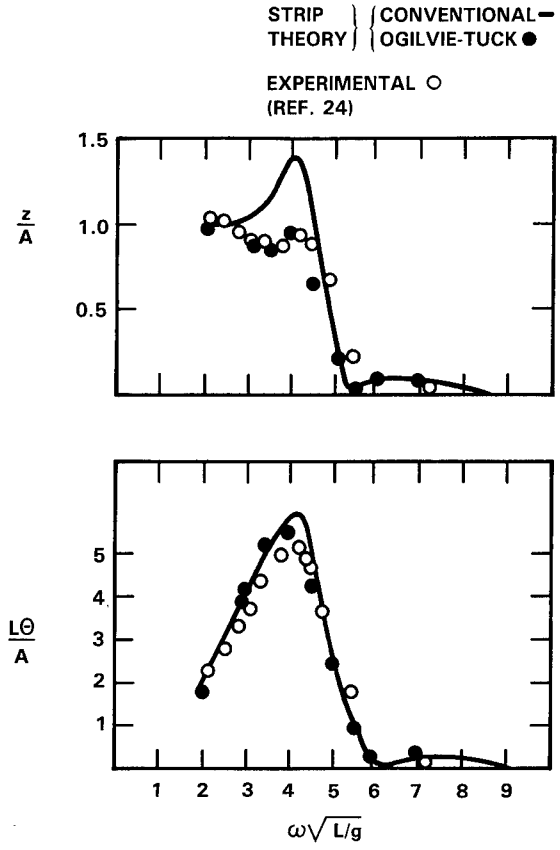


Fig. 6. SL7 heave and pitch transfer functions at Froude number = 0.3.

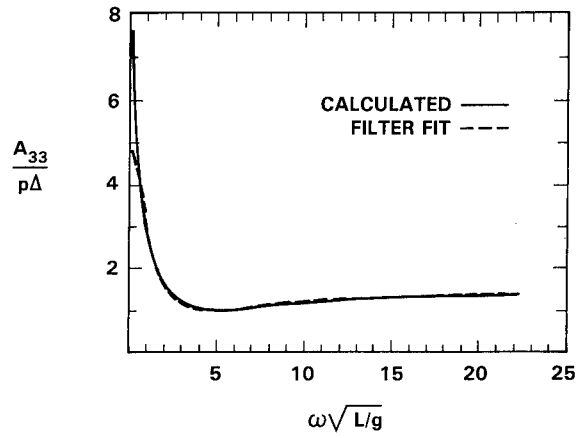


Fig. 7. Heave added mass A_{33} for 400 ft. (122 m.) high speed hull form for zero speed.

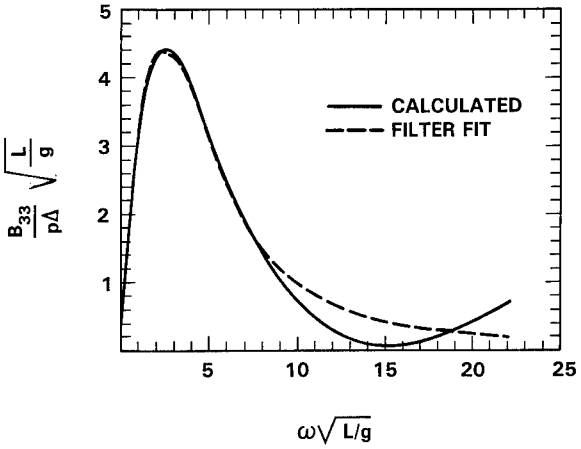


Fig. 8. Heave damping B_{33} for 400 ft. (122 m.) high speed hull form for zero speed.

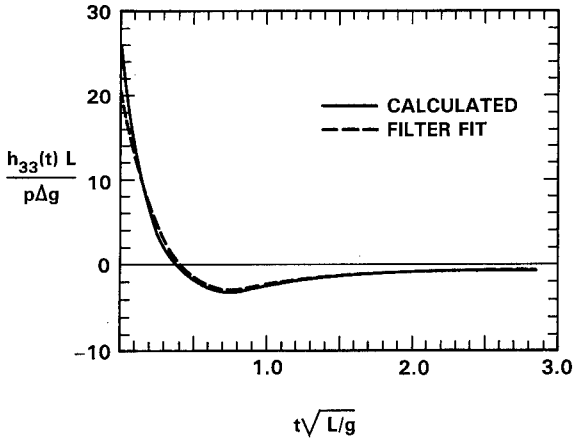


Fig. 9. Heave impulse response function $h_{33}(t)$ for 400 ft.(122 m.) high speed hull form.

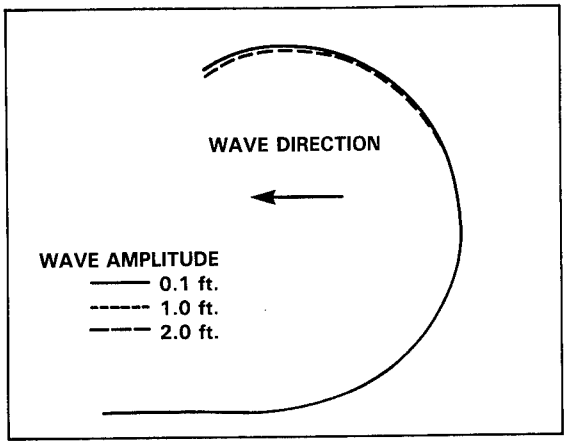


Fig. 10. Turning circles for 400 ft. (122 m.) high speed hull form for Froude number = 0.22 in regular waves for $\lambda/L = 1.75$.

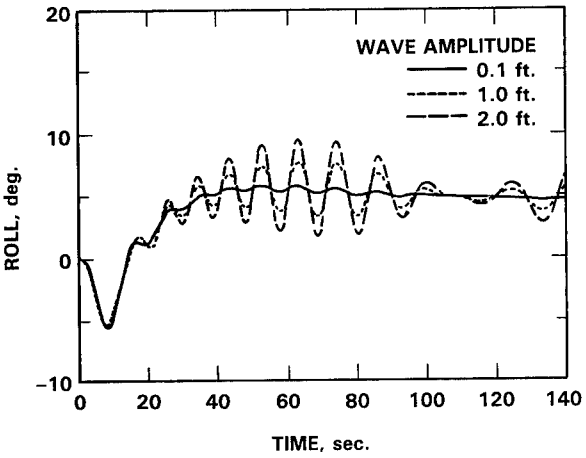


Fig. 12. Roll for 400 ft. (122 m.) high speed hull form for Froude number = 0.22 in regular waves for $\lambda/L = 1.75$.

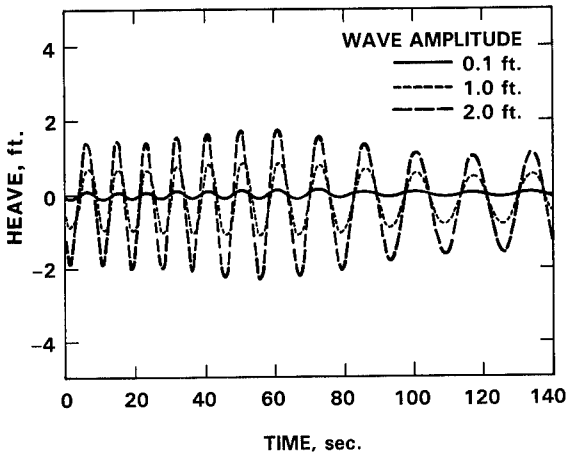


Fig. 11. Heave for 400 ft. (122 m.) high speed hull form for Froude number = 0.22 in regular waves for $\lambda/L = 1.75$.

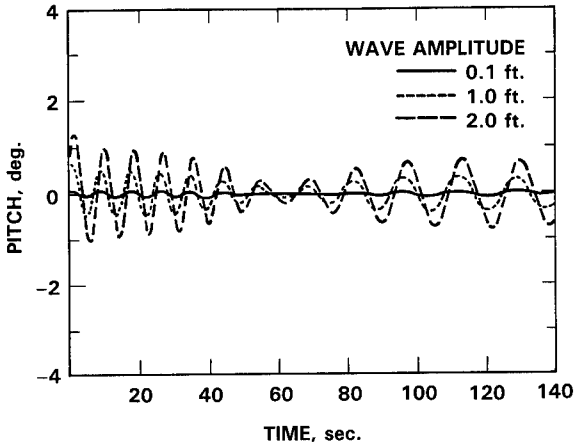


Fig. 13. Pitch for 400 ft. (122 m.) high speed hull form for Froude number = 0.22 in regular waves for $\lambda/L = 1.75$.

DISCUSSION

Vladimir Ankudinov,
Tracor Hydronautics

The paper describes an alternative approximation to simulate ship motions in waves by first applying the linear impulse response operator to represent wave forces, and then by using the fully nonlinear calm water maneuvering equations of water to predict ship motions in six degrees of freedom. The main assumption of the approach as displayed in equation (3) is that the calm water forces, F_{cw}, reflecting "various hydrodynamic effects, propulsion forces and rudder forces," and wave effects forces, F_{wave}, are calculated independently and are quasi-steady for the specified ship heading angle and forward speed. Then the standard second-order differential equations of motions,

$$\frac{d\dot{\zeta}_i}{dt} = F_i(\dot{\zeta}_i, \dot{\zeta}_j, \zeta_i, \zeta_j), \qquad i,j = 1, \ldots, 6 \qquad (31)$$

are solved in terms of the velocities, $\dot{\zeta}_i$, and the displacements, ζ_i.

Although it sounds like an acceptable approach for seakeeping applications (specifically for heave, pitch and roll motions which are dominated by the hydrostatic and wave/inertia forces) there are serious problems to apply it for the analysis of ship manuevering in waves. Here is why.

The wave/inertia forces and wave motion are adequately described by the linear wave theory. The time domain approach leads to convolution integrals typically requiring excessive computational effort for their solutions, as has been demonstrated by Perez & Perez [2]. The equivalent linear system of higher order differential equations (27) can be solved more easily using the well-established techniques of the linear system theory.

On the other hand, maneuvering excitations resulting from the rudder-propulsion system are dominated by non-linear viscous forces, and typically system (1A) with the constant force terms coefficients is used. For the mathematical analysis of ship maneuvering in waves where both excitations are present, system (1A) should also include the additional terms of higher order derivatives associated with the free-surface and viscous "memory" effects, to retain the history of the motion. Solution of such general systems in terms of velocities and displacements is not trivial. Ship manuevering motions in the horizontal plane are strongly nonlinear, and the present approximation to include the linearized wave forces through the impulse force h_{ij} resulting form the velocity impulse in the j^{th} mode, $\dot{\zeta}_i$, which is essentially a result of nonlinear dynamic solution, and then to reintroduce them again to the nonlinear system (1A), appears to be inadequate.

What makes this specific hydrodynamic problem so difficult is that the relatively small (compared to wave's) nonlinear viscous forces have to be evaluated in the variable time/space wave flow, and be integrated with the large wave induced hydrodynamic forces. For instance, the rudder forces, F_R, are typically proportional to the square of the effective velocity over the rudder, v_R. That is, $F_R \approx v_R^2$. In the wave flow in the vicinity of rudder, the velocity v_R can be approximated by the sum: $v_R = v_s + v_w$,where v_s is the flow velocity over the rudder in quiet water, and v_w is the wave-induced flow velocity over the rudder.

In typical seaway operations the oscillating velocity component v_w is comparable to v_s , and at certain times a vessel may become uncontrollable, particularly in high seas, a phenomenon that is well-known to seamen.

There are several other areas of concern in modeling the hydrodynamics of a maneuvering of ship in waves which have not been closely examined by the paper:

a. Wave drift forces have not been accounted for in the present level of effort. Although it is not a trivial problem for a vessel moving with the variable forward speed, there are several practical solutions valid for the practical simulations.

b. Due to the interaction of the wave (v_w) and viscous (v_s) flow, the interaction quadratic forces involving variable groupings such as $v_w|v_w|$ or $v_s|v_w|$ (associated with the cross-flow drag terms in the wave flow) should also be accounted for.

c. Hydrostatic and hydrodynamic forces should be calculated at the instantaneous ship position.

d. Extension of the strip theory even with Ogilvie-Tuck corrections for a wide range of frequencies as required by the author's methods should be done with extreme caution. Particular concern is the vertical force coefficients which could become singular at low frequencies. For simulations of the typical slow speed maneuvering operations at sea, a 3-D calculation seems to be a better choice.

Reply -

The present work was motivated by the desire to predict wave-induced motions of a ship (destroyer, etc.) maneuvering at high speed in "typical" seaways in which shipboard system performance rather than ship survival is at issue. That is, the goal was to incorporate maneuvering effects into predictions of ship motions for the sea conditions usually considered in linear strip theory.

Dr. Ankudinov has raised several issues regarding the modelling of maneuvering in waves under arbitrary conditions. Some of these points are relevant to either the problem of (a) maneuvering at low speeds or (b) survivability in extreme seas. I believe that these are of secondary importance for the problem of interest here. Detailed investigation would be required to determine the degree of importance of these effects in any given case.

In reply to other remarks:

a. Wave drift forces will be relatively unimportant to the motions of a ship maneuvering at high speed.

b. Similarly, the wave and viscous flow interactions can be expected to be second order effects.

c. The hydrostatic and hydrodynamic forces are cal-

culated correctly within limits of linear theory.

d. The well-known zero-frequency-of-encounter singularity of the vertical-mode strip-theory coefficients is not a problem in practice because this behavior is suppressed by multiplication by the encounter frequency or the square of the encounter frequency when calculating the forces. In this connection, use of the Ogilvie-Tuck theory in the vertical plane modes has the effect of dropping terms in the conventional strip theory for which this is not the case.

Strip theory is generally accepted as giving reasonable results for typical "slender" hull forms. For blunt forms, barges and the like, is the superiority of the 3-D potential flow calculations at zero speed is, of course, well established. Three-dimensional theories which include forward speed effects are still in development. The present model can easily be adapted to use the results of such theory, when one becomes available.

In summary, Dr. Ankudinov has provided a list of (mostly unsolved) problems, which may be of importance in some circumstances. Investigation of these effects would be of value.

Chang-Gu Kang,
University of Michigan

Fig. 10 in the paper shows turning circle trajectories in waves. Have you compared the calculated time histories of yaw angle (heading angle) with experiment?

Reply -

I have unfortunately not yet had a chance to compare the predicted results to the available measured model test data.

Dr. Jacek S. Pawlowski,
Institute for Marine Dynamics, NRCC

I would like to congratulate the author on his interesting contribution to the modelling of ship motions in time domain. In this connection it is perhaps relevant to mention that memory effects in diffraction force can be taken into account within the framework used by the author by employing the equivalent motion concept presented in [a].

[a] J.S. Pawlowski, "The estimation of diffraction force components from the equivalent motion concept," International Shipbuilding Progress, Vol. 29, March 1982, No. 331, pp.62-73.

Reply -

Thank you for your comments. I am aware of your paper, but haven't yet studied it in detail. A relative motion approach would allow accounting for memory effects in the diffraction forces, but at the expense of introducing other approximations. I don't believe that the memory effects will be too important for exciting forces, since the exciting forces will not be affected by the wave-induced motions, except for higher-order effects. The frequency content of the seaway, and consequently of the excitation, is of course included because of these are modeled by summing sine waves, each with an appropriate amplitude.

Michael Schmiechen,
VWS Berlin Model Basin

I am very pleased to see the state space description being more widely applied after all. I myself have only recently written a program to coherently identify the parameters of a multidimensional model. Although low-order models are sufficient for many purposes, high-order models are necessary to fit the "given" transfer functions in detail. My question is what order model has been cited in the study presented. A second question is whether attempts have been make to extend the approach to nonlinear problems. In this area I see a great potential of the state space approach as opposed to the functional polynomial or Volterra series description.

Reply -

The fits are generally 4 terms over 5 terms (3rd order over 4th order). For 5 of the 18 separate functions fitted, 6 terms over 7 terms were used. The resulting fits are generally quite good. I have not attempted to apply this approach to nonlinear problems.

Periodic and Multiple Periodic Behavior of Locked-In Vortex Shedding

Y. LeCOINTE and J. PIQUET

Laboratoire d'Hydrodynamique Navale ENSM, France

ABSTRACT

The numerical solution of the unsteady two-dimensional Navier-Stokes equations is used to investigate the vortex-shedding characteristics behind a circular cylinder immersed in a uniform stream and performing superimposed in-line or/and transversed oscillations of given reduced amplitude.

1. INTRODUCTION

The common features of unsteady laminar flows at moderate Reynolds numbers are investigated by means of the unsteady two-dimensional Navier-Stokes equations written in their vorticity-stream function formulation and solved numerically with compact schemes for several geometries. Attention is focussed on the study of vortex-shedding characteristics at several values of the Reynolds number behind an oscillating circular cylinder. Oscillations can be either in line or transverse at a frequency close to the Strouhal frequency or close to an harmonic of it. The effects of the Reynolds number $Re = U_\infty D/\nu$, of the reduced frequency $F = f_c D/U_\infty$ and of the reduced amplitude a/D of the oscillations on the laminar periodic or quasiperiodic wake evolution are studied. The inherent unsteadiness of these well separated flows implies that Navier-Stokes equations are a valuable tool to investigate such a problem in that very complete simultaneous data are easily observed and analyzed on a level of detail no possible with experimental techniques. The work is outlined as follows. Section 2 briefly summarizes the equations, the characteristics of the numerical methods and the cases which have been used to validate the code. Section 3 is concerned by a presentation of results obtained for a pure oscillating motion without mean flow. Section 4,5,6 consider the study of the unsteady wake behind a circular cylinder. The locking-on phenomenon is examined both for transverse (sect. 4), in line (sect 5) and composite -in line + transverse- (sect 6) superimposed motions of high reduced amplitude.

2. THE EQUATIONS AND THE NUMERICS.

The body B is a circular shaped cylinder, the axis **k** of which is orthogonal to the plane of the flow induced by a (uniform) oncoming stream $V_\infty \mathbf{i}$. B has a motion characterized by its translation velocity $\mathbf{u_B}$ in an absolute frame so that the velocity **V** with respect to the body is connected to the absolute velocity $\mathbf{V_a}$ by (1)

$$\mathbf{V_a} = \mathbf{U_B} + \mathbf{V}. \qquad (1)$$

Streamlines defined by $\mathbf{dr} \times \mathbf{V_a} = 0$ are therefore not invariant with respect to a change of frame so that streamline patterns in different frames differ from each other. The body contour being a relative streamline, the relative frame is the most convenient to discuss flow separation (although the definition of separation in the steady state $\zeta=0$; $d\zeta/ds<0$ does not hold since the flow is still time dependent in the relative frame). Therefore, understanding of events constituting the shedding phenomenon and determining the evolution of forces and moments will be more easy in this relative frame. A direct consequence of (1) is that vorticity fields are identical $\mathbf{curl}\ \mathbf{V_a} = \mathbf{curl}\ \mathbf{V}$ so that equivorticity patterns are invariant. After a conformal mapping, the Navier-Stokes equations can be written in the computational plane $Z = \lambda + i\eta$:

$$g\zeta_t - \psi_\eta \zeta_\lambda + \psi_\lambda \zeta_\eta = \frac{2}{Re}\nabla^2\zeta$$

$$\nabla^2\psi + g\zeta = 0$$

ψ is the relative streamfunction such that $\mathbf{V} = \mathbf{curl}\ (\psi\mathbf{k})$, $\zeta = \mathbf{k}.\mathbf{curl}\ \mathbf{V}$; $g(Z) = (dz/dZ)^2$ $z=x+iy$) is the square of the jacobian of the transformation for a circular cylinder $g = \exp(2\lambda)$. Physical components of the velocity (u-radial, v-circumferential) result from $u = -g^{-1/2}\psi_\eta$; $v = g^{-1/2}\psi_\lambda$. In the computational Z-domain, the wall boundary is specified by the line $\lambda=0$ and the megh is of 0-type. The factor 2/Re comes from the fact that lengths are adimensionalized with the radius of the cylinder in the computational domain while Re is defined with the diameter.

Several numerical schemes have been tested. Spatial discretization of the vorticity equation is of compact type : an upwind conservative scheme (Daube & Ta Phuoc [1978]) with second order corrections (UCh^2) or a centered conservative scheme (CCh^2) can be used with an ADI Peaceman Rachford time discretization. Alternatively, an OCI scheme ($UOCI\ h^4$) which is fourth order accurate in space and uses a one step approximate factorization of Beam & Warming in time has been considered. Such a spatial discretization is known to be free of

mesh Reynolds number restrictions at a standard point as it automatically switches its form from a Numerov scheme when the mesh Reynolds number R_c is zero to an upwind scheme when $Re \to \infty$ (Berger et Al [1980]).

Moreover, because of the Δ-form of the splitting, the time procedure is second order accurate in time in contrast to Peaceman-Rachford method which is only Δt-accurate. The Poisson equation is solved by an optimized ADI method, the convergence of which rests on the predetermination of optimized Wachpress parameters. The spatial discretization is of OCI type so that fourth order accuracy on ψ is obtained.

Detailed features of the schemes and systematic comparisons have been outlined in Lecointe & Piquet [1984] where test problems include the impulsively started circular cylinder problem (Re=200, 550) (symmetric flow) and the problem of vortex shedding behind a circular cylinder with or without superimposed oscillations at Re=200. Fourth order accurate schemes were proved to lead to the best results especially for long time resolutions as indicated by the value of the Strouhal number S_0 : but only second order schemes were able to provide numerical solutions at high Re. This was evidenced for the symmetric flow past an impulsively started circular cylinder both at Re=3000 and Re=9500 (Lecointe & Piquet [1985a, b]. For the free vortex shedding problem (unsymmetric flow) it was found that a high grid resolution was necessary with second-order schemes (Lecointe & Piquet [1985b] and despite of this, because of their robustness at high Reynolds number, they will be systematically used under a conservative form in the following.

The outputs of the numerical computation are analyzed by means of an harmonic analysis in which functions of time are identified under the following form:

$$f(t) = A\sum_{n=0}^{N} a_n \cos\left(2\pi f_n (t'-t'_a) + \phi_n\right)$$

$$= A\sum_{n=0}^{N} a_n \cos\left(\pi S_n (t-t_a) + \phi_n\right)$$

where $t'=tU_\infty/R$; $S_n=f_n . D/U_\infty$; $D=2R$; $a_0=1$; $N < 3$ usually; f_n are the frequencies of the numerical signal while the phase angles are determined within an arbitrary constant so that only phase shifts are significant. The identification of the signal is performed for $t_a \leq t \leq t_b$ following the procedure of Sulmont & Rajaona [1985]. Therefore frequencies less than $F_k=2/(t_b-t_a)$ cannot be validated while frequencies which differ by less than $2F_k$ cannot be distinguished. Nevertheless, the identification of the frequencies occuring was found very accurate (usually the error is of order 1%.). The amplitudes a_n indicate the relative amount of each term of the decomposition with respect to the fundamental contribution n = 0 from which the Strouhal frequency is found.

3. PURE OSCILLATING CASE

The Reynolds number is defined by $Re = S\omega D/\nu$ where S is the amplitude of the cylinder vibration and $\omega = 2\pi f_c$. At small vibration amplitudes, S/D (or equivalently at small Keulegan-Carpenter numbers $U_{max}T/D=2\pi S/D$) only viscous waves are generated near the cylinder and a steady flow component is not observed. When the vibration amplitude is increased, a secondary steady flow component is observed in addition to viscous waves when certain threshold values $2S < D$ are reached (see e.g Rosenhead [1965] chap.VII for a review). The aim of the following computations is twofold : (i) verify the conditions of occurrence of the transition from the non separated regime to the separation regime and the related existence of the acoustic streaming ; (ii) verify whether a symmetric configuration (with respect to the direction of the vibration) is stable or not.

3.1. Low Reynolds number cases.

The following cases taken from Sorokodum [1983] are detailed: OSCL1 refers to Re=18.85 ; S/D=.25 ; OSCL5 refers to Re=62.83 ; S/D=0.833 ; the motion of the cylinder is $\kappa = 2 \cos \omega t$ of adimensionnal period $2\pi S/D$.

The harmonic analysis has been first applied on the force coefficients C_x, C_y and C_M which appear to be periodic at the frequency of the motion. The wall vorticity ζ_{wr} in the direction orthogonal to the vibration oscillates only at the reduced frequency of the motion for the lowest Reynolds case studied (Re=15.08 ; S/D=.2). For the OSCL1 test a frequency at 2F is present with a maximum amplitude of 10%. For the OSCL5 case, the 2F harmonic has a 40% contribution and contributions at 3F and 4F are also present. In both cases the vorticity is damped when the distance to the cylinder increases. The velocity components along the axis of the vibration are controlled by the frequency of the motion with a mean value slightly different from zero.

More interesting is the consideration of the radial component of the velocity in the direction orthogonal to the vibration at 1, 2, 3 and 4 radii of the cylinder. For a low Reynolds number, this component stays negative corresponding to a streaming away from the cylinder (fig. 1a) in the direction orthogonal to the vibration. For the higher Re case corresponding to OSCL5, the velocity oscillates around a mean value which is positive both at 1, 2, 3, 4 radii from the cylinder indicating a streaming away from the cylinder in the direction of the vibration (fig. 1b). For the closest locations (0.12, 0.226, 0.47 radii from the cylinder), it appears that the mean velocity is negative, indicating a streaming away from the cylinder in the direction orthogonal to the vibration and therefore a streaming towards the cylinder in the direction of the vibration. (see fig. 1c where a schematic representation of the flow is also given). This means that the generated vortices can be evacuated away from the cylinder. This is confirmed by streamline plots and lines of constant vorticity which are now considered. The following levels are plotted: for ψ_a: ±.001; ±.05; ±.1; ±.15; ±.2; ±.25; ±.3; ±.35; ±.4; ±.6; ±.8; ±1.; ±1.2; ±1.4; ±1.6. For ψ : values from -5. to +5. with increments of .25 ; for ζ : ±100.; ±50.; ±25.; ±10.; ±5.; ±3.; ±2.; ±1.; ±.075; ±.05.

Fig. 2 details the time evolution of the flow for the OSCL1 case. Starting at t = 1.18 the relative streamlines exhibit an unseparated flow while isovorticity lines show a "double banana" structure on each side of the cylinder. During the "leftwash" motion of the cylinder two primary vortices arise about t = 1.55. At t = 1.63 the streamline structure has collapsed (vortices are nevertheless present has can be seen from the kinks arising on streamlines). The situation appears quasisteady until t = 2.08. Then the "rightwash" is sufficiently strong enough to induce primary vortices clearly visible at t = 2.15. The same evolution results until the streamline structure collapses (before t = 2.38). The second most outer "banana" disappears about t = 2.53. Endly the return back to a "double banana structure" is already accomplished at t = 2.68.

Fig. 3 considers the time evolution for the OSCL5 case. The studied sequence starts during the "leftwash" (t = 19.63) with a more elaborated vorticity structure. Because of the higher velocities, the upstreaming flow appears more slowly : at t = 20.63 the wall is completely isolated from the outerflow region while the outer downstream vorticity structure has been swept away ; the sequence terminates after t = 20.88 as can be seen from sequence t = 21.13 where kinks apparent from streamline plots indicate high vorticity regions. At t = 21.63 the "rightwash" has just begun and new primary vortices appear at t = 21.88. The same sequence is repeated symmetrically with respect to before. isovorticity contours confirm the tendency of the maxima to drift away from the cylinder in the direction of the vibration: after half a cycle, the vorticity maximum A has been slightly swept rightwards as an effect of the streaming.

3.2. High Reynolds number cases.

First let us consider the case OSCL6 of a motion along the y-axis under the following conditions: Re=500 ; S/D=2. ; F=0.16 ; Δt=.01 ; r_∞=30. ; 151x101 grid . The flow appears symmetric: C_x and C_M stay of order 10^{-6} until t=50 . The fact that the flow is well established is seen from C_y and ζ_{wr} plots which appear to be locked-in at F=0.16 . The following harmonics are present ; for C_y: 5F (14.4%), 7F (12.3%), 9F (7.4%) ; for ζ_{wr}: 3F (37.2%), 5F (28.9%), 7F (21%), 9F (10%), 11F (4.3%), 13F (9.2%), 15F (10.2%) . A streaming similar to that found at lower Re is also present but far more intense.

Now, if the symmetry of the flow is destroyed at earlier times by a pitching motion of the cylinder (cases OSCL8, OSCL10), while the same parameters as in OSCL6 are kept (apart from r_∞), C_x and C_y evolutions show that the flow experiences difficulties in evolving towards an established regime ; neither does it return to a symmetric configuration. Moreover numerical problems are found: the computation breaks down shortly after t=100 if r_∞=30 (OSCL8) and at t=45 if r_∞=60 (OSCL10). Therefore confinement effects cannot be excluded at least in the OSCL8 case. Moreover, the harmonic analysis is difficult to interpret because the Nyquist frequency is roughly 0.032 for a window [43,104]. Two driving frequencies seem to be present, one at F, the other close to f=.1 so that 2f and F cannot be distinguished. Other numerical tests are therefore needed to interpret this situation.

4. UNSTEADY WAKE BEHIND A CIRCULAR CYLINDER, HEAVING SUPERIMPOSED MOTION .

4.1. The subject of unsteady bluff body flow has received a great deal of attention as reported in several review papers (King [1977], Sarpkaya [1979]). The case Re = 200 has been mainly considered in the following as it corresponds to the highest Reynolds number for which the wake of the cylinder remains laminar. In the case of a classical free vortex shedding (no superimposed motion) the lift coefficient C_y and the moment coefficient C_M are found to oscillate at the Strouhal frequency S_0 while the drag coefficient C_x oscillates at 2 S_0. The following table gives the value of S_0 together with the levels of C_x, C_y, C_M found by means of an harmonic analysis at four values of the Reynolds number :

Re	S_0	C_x	C_y	C_M
140	0.18	1.26±0.002	±0.356	±0.017
200	0.2	1.27±0.04	±0.55	±0.024
500	0.226	1.35±0.14	±1.012	±0.043
1000	0.241	1.5 ±0.25	±1.37	±0.084

Let us now consider the case when a transverse vibration is superimposed at or near the shedding frequency S_0. The heaving motion (set in at $t=t_p$) of the cylinder is described by:

$$y = -(2a/D)\cos \pi F (t - t_p)$$

$$V_{max} = 2a\pi F/D$$

F is the reduced frequency of the motion: $F=f_c D/U_\infty$ and a its amplitude. In this situation, experiments show that the superimposed motion increases the vortex strengh, the drag force and the two dimensional character of the wake. Moreover, it forces the frequency of the vortex shedding to change from the free Strouhal frequency characterized by S_0 to the cylinder heaving frequency F. This lock-in effect was first documented by Bishop & Hassan [1964] and measured for low Reynolds number by Koopman [1972]. Locking on is apparent from C_y and C_M which oscillate at F while C_x oscillates at 2 F. Two parameters determine the synchronization zone : the reduced amplitude a/D of the motion and its reduced frequency F. This zone in the plane F/S_0, a/D has usually a triangular shape peaking at:

[$(F/S_0)_{min} = (F/S_0)_{max} = 1$; a/D = 0], the broadening when a/D increases with $(F/S_0)_{max} - (F/S_0)_{min}$, its boundaries $(F/S_0)_{min}$ or $(F/S_0)_{max}$ slightly depend on Re. It has been shown that high grid resolution was necessary in order to get a good coherence of the wake (Lecointe & Piquet [1985 a,b]).

The case Re = 200 ; a/D = .5 ; F = .2 has been first studied for a 151 x 101 conformal mesh (with r_∞ = 100, Δt = .025). The lock-in phenomenon was found to need some delay to establish itself. It was found that C_x = 1.82 ± 0.55

$C_y = \pm 2.9$; $C_M = \pm 0.1$ and that the lift leads the motion by less than 100° indicating weak aerodynamic stability (Lecointe & Piquet [1985a].

The case of high reduced amplitudes (Re=200 ; a/D = .1) was investigated in Lecointe & Piquet [1985c] with a 151 x 151 grid, $r_\infty = 80$, $\Delta t = .0125$. For a reduced frequency F = .17, the flow is roughly established for t>30. C_y, C_M and ζ_{wr} oscillate classically at F but a 13% harmonic at 3F is present both on C_y and C_M ; C_x oscillates at 2F with an harmonic at 4F of 11.8 %. ; ζ_{wr} oscillates at F with several harmonics at 3F (25 %), 5F (27 %), 7F (17 %), 9F (6 %). The motion leads the drag by 161° indicating strong damping and stability. Moreover, $C_x = 1.85 \pm 0.75$; $C_y = \pm 1.55$; $C_M = \pm 0.11$.

4.2. F higher than S_0.

If the reduced frequency is doubled: F=.34, the time step must be halved: $\Delta t = .00625$. Although the flow is not completely established at t = 80, (especially on C_M) locking on is also found: $C_x = 3.6 \pm 6.2$ oscillates at 2F with a 4F harmonic of 14.6% ; $C_y = \pm 6$ and C_M oscillate at F with an harmonic at 3F (of 14.5 % on C_y and 11.5 % on 3F). Such a result shows that locking-on is also found when the reduced frequency of the transverse motion is close to an harmonic of the Strouhal frequency.

Let us now return for F=.34 to the case of a moderate amplitude (a/D = .5). $C_y = \pm 5$, $C_M = \pm 0.16$ oscillate at F and ζ_{wr} (rear component of the vorticity at the wall) oscillates at F with a 20 % harmonic at 3F. The oscillations on the drag are more complex (see fig.4). The fundamental oscillation is at 2F but a 95 % harmonic is present at S_0 ; another important contribution (73.3 %) is found at $0.48 = 2F - S_0$. Less important harmonics are also present at $0.87 \sim 2F + S_0$ (17.3 %), at $0.592 \sim 2F - f$ (18.2 %). $0289 \sim S_0 + f$ (16.3 %), with $f = 0.091 \sim S_0/2$ (19.3 %). Unfortunately, because of the window [29.5 - 70.44] used for the harmonic analysis, the Nyquist frequency is $F_k = .0488$ so that if f is validable, frequency differences of order f are not significant.

The influence of the Reynolds number is clearly visible if one considers now the same case as before (F = .34 ; a/D = .5) at Re = 500. Locking-on is found both on $C_x = 1.84 \pm 0.5$ which oscillates at 2F with a 4F harmonic (28.6 %), on $C_y = \pm 4.1$ and $C_M = \pm 0.145$ which oscillate at F with a 5 % harmonic for C_y and 10.5 % harmonic for C_M at 3F. The motion leads the lift by 132°.8 indicating strong damping and stability.

The reordering phenomenon clearly visible on C_x (Fig.4,5) is a consequence of the fact that $(F/S_0)_{min}$ value is closer from 1 at Re = 500 than at Re= 200.

4.3. F less than S_0.

Let us now investigate results corresponding to a reduced frequency close to $S_0/2$ and therefore to a slow velocity of the cylinder with respect to the oncoming stream.

(i) Case of low amplitude a/D =.25.
Two reduced frequencies have been studies at Re = 200 : F =.12 and F =.14 ; the situation which results does not appear to be locked-in. In the case F =.12 for an harmonic analysis resting on $F_k = .039$, C_y and C_M oscillate at .0185 ($\sim S_0 \sim 3F/2$) with an F harmonic of 43.3 % for C_y and 80.5 % for C_M. C_x oscillates at f =.066 ($\sim F/2$) with undistinguishable harmonics from several differences between nS_0 and f or nF and f: at .231 ($\sim$ 2F ; 18.3 %) ; .302 ($\sim 3S0/2 \sim 5F/2$) and .365 ($\sim$ 3F ; 43.8 %).

In order to get some insight on these troubling results, relative streamline, accompanying streamlines and lines of constant vorticity are presented on Fig.6. The following levels of ψ are given for relative streamlines: ±1.6; ±1.4; ±1.2; ±1.0; ±.80; ±.60; ±.40; ±.35; ±.25; ±.25; ±.2; ±.15; ±.1; ±.05; ±.001 . Lines of constant vorticity correspond to the following levels of ζ: ±100. ; ±50. ; ±25. ; ±10. ; ±5. ; ±3. ; ±2. ; ±1. ; ±.75; ±.50; ±.25; ±.10; ±.075; ±.05; ±.025 . Plots will be given with these values unless specified.

The bubble A seen at t = 90 grows and induces a diminishing drag and an increase of C_y and C_M until it disrupts in the outer flow, isolating a secondary eddy B with negative circulation. A change of sign on C_y and C_M results after t = 82, but the loss of momentum decreases as the primary bubble A moves downstream, therefore the drag is minimum at t = 83. B now substitutes to A and alignes itself with the axis of the flow inducing a decreasing lift and moment. B grows asymmetrically but the growth and disruption phase it encounters for $86 \leq t \leq 90$ is slower than the corresponding phase for A $81 \leq t \leq 83$. The drag is maximum about t = 87 as B does not communicate yet with the outer flow while it isolates already a bubble A' which gets therefore more time to grow and manifests an important momentum defect. Discrepancies are evidenced from the comparison of accompanying streamlines at t = 83 and t = 90. The change of the sign of C_y and C_M appears for the same reasons as before but vortex untensities and therefore C_y and C_M values are higher. A secondary counterrotating bubble B' already present at t = 90 grows now.

At this moment, A' is already very developped while B is not far enough ; B' generation anticipates the isolation phenomenon which led to the birth of B about t = 82. The drag is minimum and varies only a little. After t = 91, B' grows and counterclockwise circulation is created, it induces a growth of C_M and C_y which change their sign. Although the described evolution manifests a lack of periodicity, the whole sequence repeats itself in a similar way but the complex variations of C_x are connected to the variations of the intensity of the just shedded primary bubble and of the growing secondary bubbles.

Case F =.14. The computation has been performed until t = 210 in order to get a Nyquist frequency as low as possible : $F_k \sim .011$. A leading frequency of f = 0.04 is found independently of the window. The evolution of C_x is, once again, the most complex (Fig.7): the fundamental is at f while the following sequence of harmonics is

present: 2f (32.5%), .118~3f (15.6%), 4f (8.8%), .213~5f (1.1%), .242~6f~2F-f (3.4%), .281~7f~2F (34.4%), .321~8f~2F+f (37.8%), .360~9F~2F+2f (20.5%), .400~10f~2F+3f (10.5%). f can be interpreted as $F-S_0/2$; therefore at least two different frequencies interplay whatever the interpretation. Similar results are found both on C_y which is driven by F+f with important harmonics at F (46.4 %) at F+2f (24.1 %) and F-f (15.5 %) and minor contributions at 4f, F-2f, F+4f, while C_M is driven by F with important harmonics at F-f (13.2 %) ; F+f (44.4 %) ; F+2f (10.6 %). The vorticity ζ_{wr} is driven by F and by F+f (96.9 % of the F contribution) with important harmonics at F-2f (10.4 %) ; F-f (18.8 %) ; F+2f (19.8 %) ; 3F+f (9.8 %) ; 3F+2f (8.2 %) and minor contributions at F+3f and F+4f.

It is therefore found that the study of this biperiodic vortex shedding needs a long time computation in order to lower enough the Nyquist frequency of the harmonic analysis.

The influence of the Reynolds number is now considered by studying the case Re = 500, F = .12 with an harmonic analysis such that F_k = .025.

Locking on is not found as S_0 appears to drive the forces : C_x oscillates at S_0-F with important harmonics at $2S_0$ (82.7 %), S_0+F (63.8 %) and other contributions at $3S_0$-F (17.8 %) and S_0 (7 %). C_y, C_M and ζ_{wr} oscillate at S_0 with an harmonic at F for C_y (22.4 %) for C_M (28.5 %) and for ζ_{wr} (15.6 %). Another contributions are also found for C_M (F+S_0 : 8.7%) and ζ_{wr}.

The evolution of streamlines is more complex in this case (Fig.8). If one considers the situation after t = 107.3 (upwash motion of the cylinder) ; apart from a primary bubble A to be shed, two secondary eddies B_1 and B_2 are present. A shedding ends at t = 108.3 which correspond to a minimum of C_x and to an increase and change of sign of C_y and C_M. B_1 and B_2 grow simultaneously, inducing an increase of C_x ; they coalesce about t = 110.3 which corresponds to maximum lift. B_{12} = B_1 + B_2 is violently ejected outwards because of the upwash motion of the cylinder. C_x decreases after t = 111.3 followed by C_y and C_M which change of sign as the highest location of the cylinder is attained (t = 113). Two new secondary eddies B'_1 and B'_2 emerge and a similar sequence leading to their coalescence into B'_{12} develops. Nevertheless B'_{12} is more intense as seen from a comparison of isovorticities between t = 110.3 and t = 114.3. The ejection of B'_{12} about t = 116.3 is followed by the occurence of two new secondary eddies B''_1 and B''_2 but their growth is not equal and B''_2 is slaved to B''_1 which subsists alone. The drag which had decreased increases slightly. At t = 119.3 the moment leads the lift which is maximum. As B''_1 become more intense at t = 120.3, the momentum loss and the drag increase. C_M and C_y abruptly "stall" and change their sign as secondary bubbles C_1 and C_2 appear. B_{12} has been ejected subsequently leading to a decreasing drag about t = 121.3 because the downwards motion of the cylinder is achieved. The classical isolation of a secondary bubble D is a result of the ejection. A complex structure appears with two twin eddies C_1 and C_2 on one side while D on the other side grows enough quickly to coalesce with C_2, C_1 retaining its identity. Endly, a situation similar to that already seen at t = 106.30 results at t = 124.

(ii) Case of moderate amplitude : a/D = .5 ; F = 0.12 ; Re = 200.

This case performed with a 151 x 151 mesh, Δt = 0.01 does not appear to be completely established at t = 70. The resulting consequence is that the interpretation of the harmonic analysis is not easy. Nevertheless lock-in is not found in this case (Lecointe & Piquet [1985e]).

(iii) Case of high reduced amplitude : a/D = 1 ; F = 0.16 ; Re = 200.

Although more complex, the situation is similar to that presented in Lecointe & Piquet [1985c] where F = 0.17. Locking on is found : C_x oscillates at 2F with very important harmonics at F (44 %) and 3F (62.7 %) and significant contributions close to 4F (.624 at 22.7 % and .635 at 8.9 %).

The lift leads the motion by 128°32 indicating damping and stability. It oscillates at F with a 57.4 % harmonic at 2F and a 8.2 % harmonic at 3F. C_M oscillates at F with a 48.9 % harmonic at 2F. ζ_{wr} oscillates also at F with the whole set of multiples up to 9F. Fig.9 shows the corresponding evolution with time of forces. The sequence of streamline plots is not presented as it does not differ significantly from the abovementionned F = .17 case treated in Lecointe & Piquet [1985c]

5. UNSTEADY WAKE BEHIND A CIRCULAR CYLINDER. IN LINE MOTION .

The surging motion, which is set in at $t=t_p$, is defined by

$$x = -(2a/D)\cos \pi F (t - t_p)$$

$$U_{max} = 2\pi F a/D$$

In this case, experiments indicate also the existence of a lock-in regime : two types of instability are known depending on the values of the reduced frequency: for $F < 2S_0$, (e.g F = .35) the flow is characterized by the emission of twin counterrotating eddies on each side of the cylinder during each cycle of the motion. This was confirmed by numerical experiments at a/D = .5 ; Re = 200 reported in Lecointe & Piquet [1985a, b].

For $F > 2S_0$ (e.g. F = .45) only one vortice per cycle is shed leading to a classical vortex street downstream of the cylinder but only if the reduced amplitude a/D is low enough (e.g. 0.1 - 0.3). The lift oscillates at F while Cy, C_M and ζ_{wr} oscillate at F/2 with an harmonic at 3F/2 the strength of which depends on the level of the reduced amplitude (Lecointe & Piquet [1985b], Hurlbut et Al [1982]). The motion leads the drag by about 100° indicating positive damping and stability.

More striking is the fact that for moderate reduced amplitudes (a/D = .5, Re = 200), a symmetric shedding similar to that found for $F < 2S_0$

is obtained (Lecointe & Piquet [1985b]. Moreover this symmetric pattern is stable in the sense that if the computation is started from an asymmetric pattern, the solution evolves back to a symmetric wake flow.

In order to investigate the effect of the reduced frequency close to a subharmonic of $2S_0$ new tests have been performed with a 151 x 101 mesh ; $\Delta t = .0125$; $r_\infty = 80$ at $F = .16$; $a/D = .25$; $Re = 200$.

The results appear to lead in this case to an asymmetric shedding and the flow does not evolve back to a symmetric wake flow as can be seen from Fig. 10 which depicts the evolution with time of force coefficients. Moreover lock-in is found for this low reduced amplitude : C_x oscillates classically at F with an harmonic of 12 % at 2F ; C_y, C_M, ζ_{wr} oscillate also at F (instead of F/2) with harmonics at 2F (26.5 % for C_y, 33.8% for C_M, 9.6% for ζ_{wr}) and 3F (5.9 % for C_y, 6.3 % for C_M). These new results which confirm the time evolution of forces are enlightened by the consideration of streamline plots which are shown in Fig. 11 for $96.88 \leq t \leq 109.38$. The fact that the asymmetry has been initially triggered by a pitching motion of the cylinder is not forgotten: the bubble to be shed is always generated on the same rearside of the cylinder but if the pitching destabilizing motion was reversed, the bubble would be shed from the other rearside.

The specificity of this last case is confirmed by the consideration of the case MC11 : $a/D = .25$; $F = .32$; $Re = 200$ where the reduced frequency has been doubled and is therefore such that $S_0 < F < 2S_0$. The harmonic analysis confirms the well established character of the flow as evidenced from force evolutions which are presented in Fig. 12. C_x oscillates at F with very small harmonics at F/2 (2.3%) and 2F (7.9%). C_y oscillates at F/2 with harmonics at 3F/2 (39.2%) and 5F/2 (5.1%). C_M and ζ_{wr} oscillate also at F/2 with a 3F/2 harmonic (21% for C_M and 22.1% for ζ_{wr}). Relative streamlines and equivorticity plots are presented in Fig. 13 for $96.88 \leq t \leq 103.13$ in order to allow a comparison with Fig. 11 (the shedding evolves symmetrically for $103.13 \leq t \leq 109.38$ and configurations at 96.88 and 109.38 are almost identical). Because of the higher frequency, the shedding and the circumferential motion are more intense, therefore the bubble is shed at $t \sim 102$.

6. UNSTEADY WAKE OF A CIRCULAR CYLINDER. COMPOUND MOTION .

Both in-line and transverse harmonic vibrations are first superimposed at the same frequency $F_1 = F_2 = .16$ and $Re = 200$. The following equations describe the motion of the cylinder ($F = \omega D/2\pi U_\infty$):

$$x = a \cos(\omega_1 t - \phi_1) \qquad U_{max} = a\omega_1$$

$$y = b \cos(\omega_2 t - \phi_2) \qquad V_{max} = b\omega_2$$

The numerical characteristics of the tests are the same as retained previously. The following table describes the considered parameters:

test	a/D	b/D	Φ_1	Φ_2
MC1	.25	1.	0°	0°
MC2	.25	1.	0°	45°
MC3	.25	1.	0°	90°

While MC1 is a rectilinear motion of the cylinder $y = bx/a$, cases MC2 and MC3 correspond to elliptic motions. $b = 0$; $a/D = .25$ is the pure in-line case already considered in §5. $a = 0$; $b/D = 1$. is a pure transverse motion which leads to results equivalent to the similar heaving case considered at F=.17 by Lecointe & Piquet [1985c], this is the reason for which it is not considered here.

(i) Case MC1

Although the flow is not completely established as evidenced from force evolutions, locking-on is found but a small frequency shift seems to result from the non established character of the flow. The transverse motion which is of the highest reduced amplitude controls the whole flow. C_x oscillates at $0.37 \sim 2F$ with $0.165 \sim F$ (76.4 %) and $.474 \sim 3F$ (47.6 %) harmonics. C_y, C_M and ζ_{wr} oscillate at $0.157 \sim F$ with harmonics at $0.311 \sim 2F$ (34.6 %) and $0.483 \sim 3F$ (15.2 %) for C_y ; harmonics at $0.313 \sim 2F$ (36.7 %) and $0.468 \sim 3F$ (9.5 %) for C_M ; harmonics at $0.312 \sim 2F$ (45 %) and $.47 \sim 3F$ (42 %). Several other frequencies of less importance need the occurence of at least $f \sim .06$ to be explained. Endly the motion leads the drag by 93° and the lift by 173°, therefore neutral stability is approximately found for the in line motion in this case.

(ii) Case MC2

The locked in regime corresponding to this case appears very well established and results here again from the transverse motion (Fig. 14). The harmonic analysis leads to very clear results : C_x oscillates at 2F with harmonics at F (62.8 %), 3F (40.4 %), 4F (19.3 %), 5F (4.7 %). C_y, C_M and ζ_{wr} oscillate at F with several harmonics : for C_y : at 2F (30.5 %) and 3F (19.4 %) for C_M : at 2F (32.2 %) and 3F (17.2 %). The vorticity ζ_{wr} exhibits the following series 3F (39.8 %), 4F (29.8 %), 5F (40 %), 6F (27.2 %), 7F (22.9 %), 8F(13.7%) and 9F (7 %).

Corresponding relative streamlines are presented in Fig. 15. Their evolution shows that the shedding mechanism is similar to what would occur in the absence of heaving motion, but the isolated secondary eddy (resulting from the disruption of the primary eddy into the outerflow at t = 99.38) sees its size diminish once the primary eddy is shed because of the heaving motion. It seems to be shed before t = 104.38 before the upstroke of the cylinder.

(iii) Case MC3

Here again, a well established lock-in is found as indicated from force evolutions (Fig. 16). C_x oscillates at F (instead of 2F) with harmonics at 2F (46.5 %), 3F (46.8 %), 4F (12.1 %) and at 3F/2 (8 %), 5F/2 (8.2 %), 7F/2(7.6%). C_y, C_M and ζ_{wr} oscillate also at F being apparently controlled by the transverse motion with the following harmonics : F/2 (4.7 %), 3F/2 (20 %), 2F (62.2 %),

5F/2 (5.7 %) for C_y ; 2F (52.6 %), 5F/2 (5.4 %) for C_M ; 2F (88.2 %), 5F/2 (7.6 %), 3F (45 %), 7F/2 (7.2 %), 4F (46.8 %), 9F/2 (7.5 %), 5F (19.7 %), 6F (24.3 %), 13F/2 (6.10 %) for ζ_{wr}.

The occurrence of half order harmonics on C_y and C_M is an indication of the influence of the in-line motion. Corresponding relative streamlines are presented in Fig. 17 . They indicate the influence of the phase shift on the shedding.

Let us now consider cases where the frequency of the in-line motion is twice the frequency of the transverse motion. Synchronization should be easier to get than with only one transverse superimposed motion as the two frequencies correspond to a resonant case.

case	a/D	F_1	b/D	F_2	ϕ_1	ϕ_2
MC6	.25	.32	1.	.16	0°	0°
MC10	.25	.32	.25	.16	0°	45°

The main difference between the two cases comes from the orbit which is a segment of parabola of x axis for MC6 while the orbit of MC10 draws a closed eight. The corresponding pure in-line motion MC11 has been considered in §5. The pure transverse motion corresponding to MC10 has not been examined but similar studied cases indicate that it should correspond to a standard locked-in regime.

(iv) Case MC6

A well established lock-in regime is found in this case (fig. 18). C_x oscillates at $2F_2$ with harmonics at $4F_2$ (27.4%), $F_2=F_1/2$ (6.7%), $3F_2=3F_1/2$ (3.6%). C_y and C_M oscillate at F_2 with $3F_2$ (28%) and $5F_2$ (7.9%) harmonics for C_y ; $2F_2$ (6.7%) and $3F_2$ (33.5%) harmonics for C_M. The situation is more interesting for ζ_{wr} which oscillates at $3F_2=3F_1/2$ with the following series of harmonics: F_2 (57.2%), F_1 (22.3%), $4F_2$ (22.3%), $5F_2=5F_1/2$ (65.1%), $6F_2$ (13.9%), $7F_2$ (31.9%), $8F_2$ (7.5%), $9F_2$ (10.8%). Half harmonics on C_x and on ζ_{wr} indicate that the lock-in regime should be considered as dominated rather by the in-line motion. The vortex shedding mechanism appears quite different and, for this case, simpler than that resulting for a single vibration (fig. 19)

(v) Case MC10.

Here again, the locked-in regime is well established but it is controlled by the surging motion as shown by a comparison on forces evolution (fig. 20) with case MC11 . It is found that C_x oscillates at $2F_2$ with a 4% harmonic at $4F_2$. C_y, C_M and ζ_{wr} oscillate at F_2 with harmonics at $3F_2$ (42.7%) and $5F_2$ (7.1%) for C_y, at $3F_2$ (25.1%) for C_M and at $2F_2$ (4%), $3F_2$ (30%), $5F_2$ (6.8%) for ζ_{wr}. The vortex shedding mechanism is quite similar to what has been found in the pure in-line MC11 case (fig. 21).

The main result of these tests is that the phase shift between the in-line and the transverse motion leads to significantly different mechanisms for the shedding and consequently for the frequencies of force evolutions, but no influence of this phase shift on the controling frequency has been found probably because of lock-in. Some more extensive tests are obviously needed to understand more completely the conditions determining the leading influence of one motion or another.

6. CONCLUSION.

The unsteady laminar viscous flow round circular cylinders oscillating in-line or/and orthogonally to uniform oncoming stream has been investigated. Vortex shedding characteristics have been studied by means of an harmonic analysis of the signals obtained from the numerical solution of the unsteady Navier-Stokes equations written in the vorticity-stream function formulation.

For pure oscillations of the cylinder (no oncoming uniform stream : §3), two regimes are evidenced, one at low Reynolds number characterized by " multiple banana " configurations ; the other at higher Reynolds numbers. In this last case, the main characteristics is the existence of a streaming (steady component of the flow) in the direction of the vibration and with a progressive " sweeping away " of the generated vortices.

If the Reynolds number is increased to 500, things appear less clear in the case where the symmetry of the flow is broken at earlier times by a pitching motion of the cylinder. Multiple periodicity is evidenced although its detailed analysis is forbidden by the fact that the flow is not established if not perturbed by numerical troubles. Some more numerical tests are obviously needed.

In the case of transverse vibrations (heaving motion of the cylinder), lock-in has been found at high reduced amplitudes, not only for reduced frequencies close to the Strouhal frequency but also for reduced frequencies close to twice or half the Strouhal frequency. This phenomenon is characterized by an intensification of the shedding and by the fact that the lift, the moment and the transverse velocity component oscillate at F while the drag and the in-line velocity component oscillate at 2F.

For moderate reduced amplitudes, the lock-in is more complex: while the lift, the moment and the transverse velocity component oscillate at F, the drag appears more complex especially for Re=200 while it is reordered for Re=500. This reordering phenomenon evidenced at F=.34 can be easily explained by the fact that the Strouhal frequency increases with Re so that, for fixed a/D, F ; an increase of Re moves test conditions closer from the synchronization zone in the plane [F/S_0, a/D]. At F=.12, a similar phenomenon is found: S_0 controls the flow for Re=500 but not for Re=200 where, again, the drag evolution is the most complex. Here, an increase of Re moves test conditions farther from the synchronization zone and the drag does not oscillate at twice the frequency of the lift but rather at about the same frequency! It is therefore clear that at least two frequencies control the flow close to the boundary of the synchronization zone.

In the case of in-line vibrations (surging motion of the cylinder), it has been confirmed that,

for high reduced amplitudes, the shedding is symmetric and that the symmetry is stable. For moderate reduced amplitudes implying lock-in, the vortex shedding is asymmetric for frequencies higher than twice the Strouhal frequency: the drag oscillates at F while the lift and the moment oscillate at F/2 with significant harmonics at 3F/2 and, possibly, 5F/2. A distinct type of asymmetry has been evidenced for frequencies lower than the Strouhal frequency. In this last case, both the lift, the moment and the drag oscillate at the reduced frequency of the motion because only one vortice per cycle is shed and always on the same rearside of the cylinder.

For superimposed in-line (indexed 1) and transverse (indexed 2) vibrations, several locked-in tests have been considered. The influence of the phase shift between the two vibrations did not appear to be too important when $F_1=F_2$ probably because of the high considered reduced amplitudes. For the resonant case $F_1=2F_2$, either the in-line motion or the transverse motion could control the shedding. This point should deserve further attention especially in cases where one motion corresponds to lock-in and the other implies a natural shedding controlled by S_0. Also, a more realistic study of the hydrodynamic stability and of the possible occurrence of self excited motions should be of valuable interest, considering the mechanical equation of the cylinder motion.

REFERENCES

Berger, A. E., Solomon, J. M., Ciment, M., Leventhal, S. H. & Weinberg, B. C. [1981] "On Generalized OCI schemes for Boundary Layer Problems." *Maths. of Comp.* ; Vol. 35 ; pp. 695-731.

Bishop, R. E. D. & Hassan, A. Y. [1964] "The Lift and the Drag Forces on a Circular Cylinder in a Flowing Field." *Proc. Roy. Soc. (London) Ser. A* ; Vol. 277, pp. 51-75.

Daube, O. & Ta Phuoc, L. [1978] "Etude Numérique d'Ecoulements Instationnaires de fluides visqueux incompressibles autour de corps profilés par une méthode combinée d'ordre $O(h^2)$ et $O(h^4)$." *Journ. Méca.* ; Vol. 17 ; pp. 651-678.

Griffin, O. M. & Koopman, G. H. [1977] "The vortex-excited Lift and Reaction Force on resonantly Vibrating Cylinders". *Journ. Sound and Vibration* ; Vol. 54 ; pp. 435-448.

Hurlbut, S. E. ; Spaulding, M. L. & White , F. M. [1982] "Numerical Solution for Laminar Two-dimensional Flow about a Cylinder Oscillating in a Uniform Stream". *Journ. Fluids Eng.* ; Vol. 104 ; pp. 214-222.

King, R. [1977] "A Review of Vortex Shedding Research and its Applications." *Ocean Engineering* ; Vol. 4 ; pp. 141-172.

Koopman, G. H. [1967] "The Vortex Wakes on Vibrating Cylinders at low Reynolds Numbers." *J. Fluid Mech.* ; Vol. 66 ; pp. 501-512.

Lecointe, Y. & Piquet, J. [1984] "On the Use of several Compact Methods for the Study of Unsteady Incompressible Viscous Flow around Circular Cylinders" *Comp. and Fluids* ; Vol. 12 ; N°4 ; pp. 255-280.

Lecointe, Y. & Piquet, J. [1985a] "Numerical Solution of Unsteady Incompressible Viscous Flow around Bodies." *Proc. Third Symp. Num. Phys. Aspects Aerod. Flows.* Ed. Cebeci, T. Cal. State Univ. Long Beach. pp. 5-15/29.

Lecointe, Y. & Piquet, J. [1985b] "Compact Finite-Difference Methods for Solving Incompressible Navier-Stokes Equations around Oscillating Bodies" *Von Karman Lecture Series 1985-04;* Computational Fluid Dynamics; 210 pages.

Lecointe, Y. & Piquet, J. [1985c] "Unsteady Viscous Flow Round Moving Circular Cylinders and Airfoils" *AIAA Paper 85-1490* in AIAA-CP 854 ; Proc. AIAA 7th. Comp. Fluid Dyn. Conf; Cincinnati.

Lecointe, Y. & Piquet, J. [1985d] "Unsteady Viscous Flow round moving Circular Cylinders and Airfoils II" *Proc. Int. Symp. Refined Flow Modelling & Turbulence Measurements* Univ. Iowa. F14-1/10.

Lecointe, Y. & Piquet, J. [1985e] "Ecoulement Visqueux Instationnaire autour de Corps Cylindriques en Mouvement Oscillant." *XXIième Colloque AAAF d'Aérodynamique Appliquée"* ; Paper 28/3AF-AA-85.

Rosenhead, L. [1965] "Laminar Boundary Layers." Fluid Motion Memoirs ; *Oxford at the Clarendon Press* Pt. VII : "Unsteady Boundary Layers."

Sarpkaya, T. [1979] "Vortex Induced Oscillations, A selective Review." *ASME Journ. of Applied Mech.* ; Vol. 46 ; pp. 241-258.

Sorokodum, E. D. [1983] "Flow near a Vibrating Cylinder." *Fluid Dynamics* ; Vol. 17 ; N° 4 ; pp. 654-656.

Sulmont, P. & Rajaona, R. D. [1985] "A Method of Spectral Analysis applied to Periodic and Pseudo-periodic Signals." *Journ. Comp. Phys.* Vol. 61 ; N°1 ; pp. 186-193.

Tanida, Y., Okajima, A. & Watanabe, Y. [1973] "Stability of a Circular Cylinder Oscillating in Uniform Flow or Wake". *Journ. Fluid Mech.* ; Vol. 61 ; pp. 769-784.

ACKNOWLEDGMENTS.

Some computations were performed on Nas-9080 of CIRCE; other facilities on CRAY1-S have been provided by the Scientific Committee of " Centre de Calcul Vectoriel pour la Recherche ".

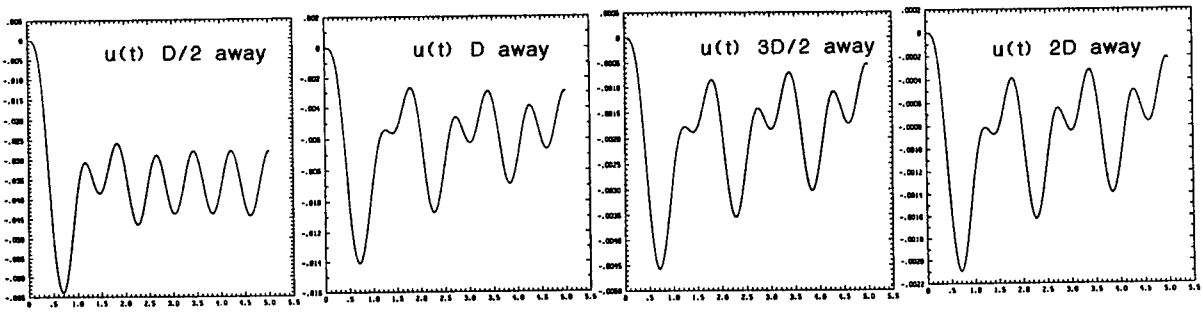


fig. 1a. OSCL1 : radial component of **V** along an axis normal to the vibration.

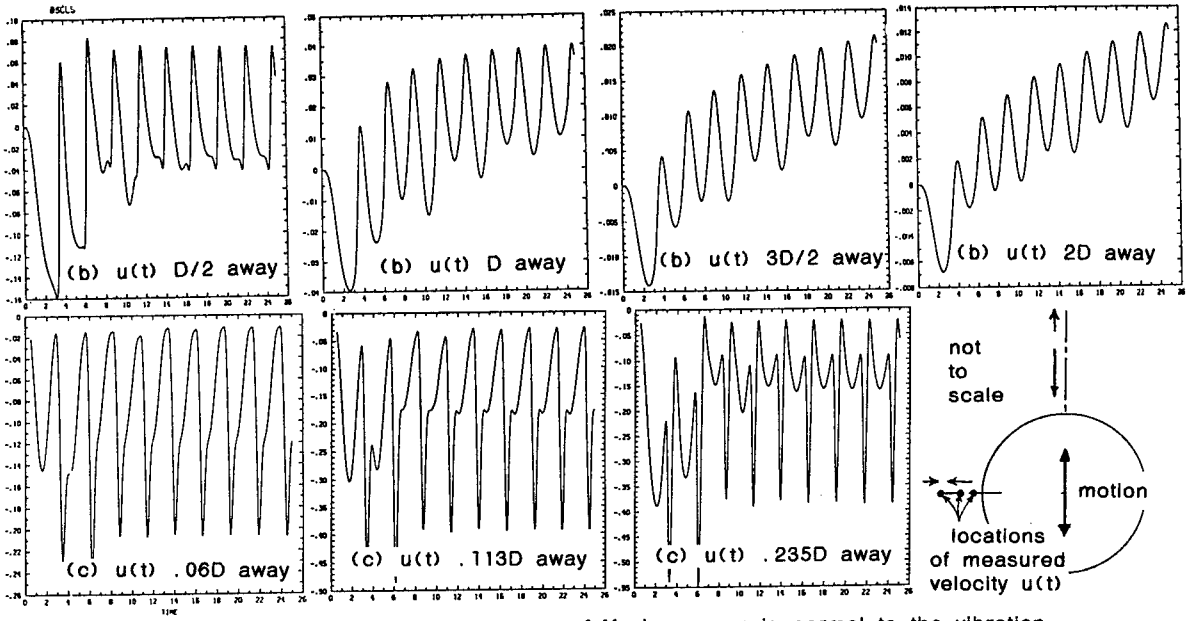


fig. 1b, c. OSCL5 : radial component of **V** along an axis normal to the vibration.

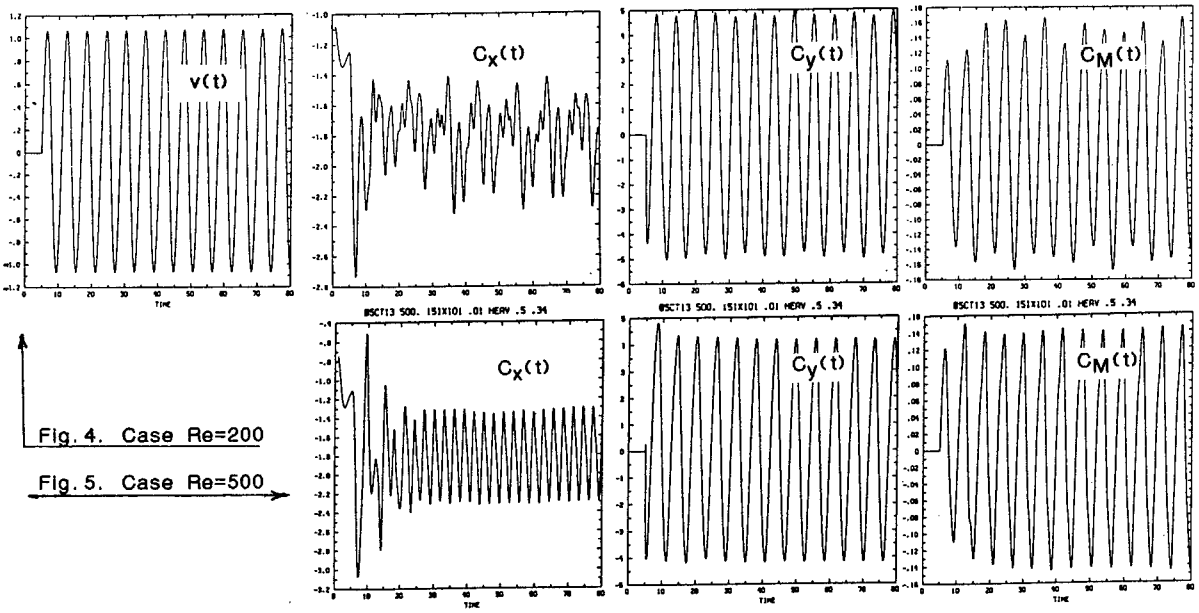


Fig. 4, 5. Heaving Motion. F=.34 ; a/D=.5 ; reordering phenomenon.

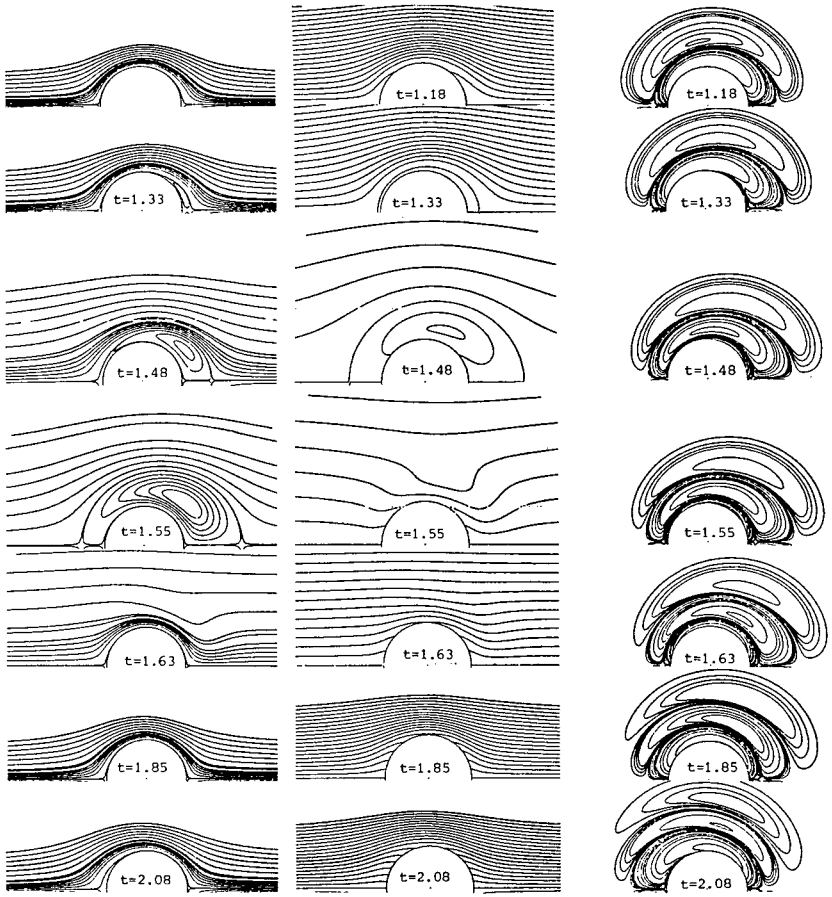


Fig. 2. OSCL1. Evolution with time of relative streamlines (left), absolute streamlines (center), isovorticity lines (right).

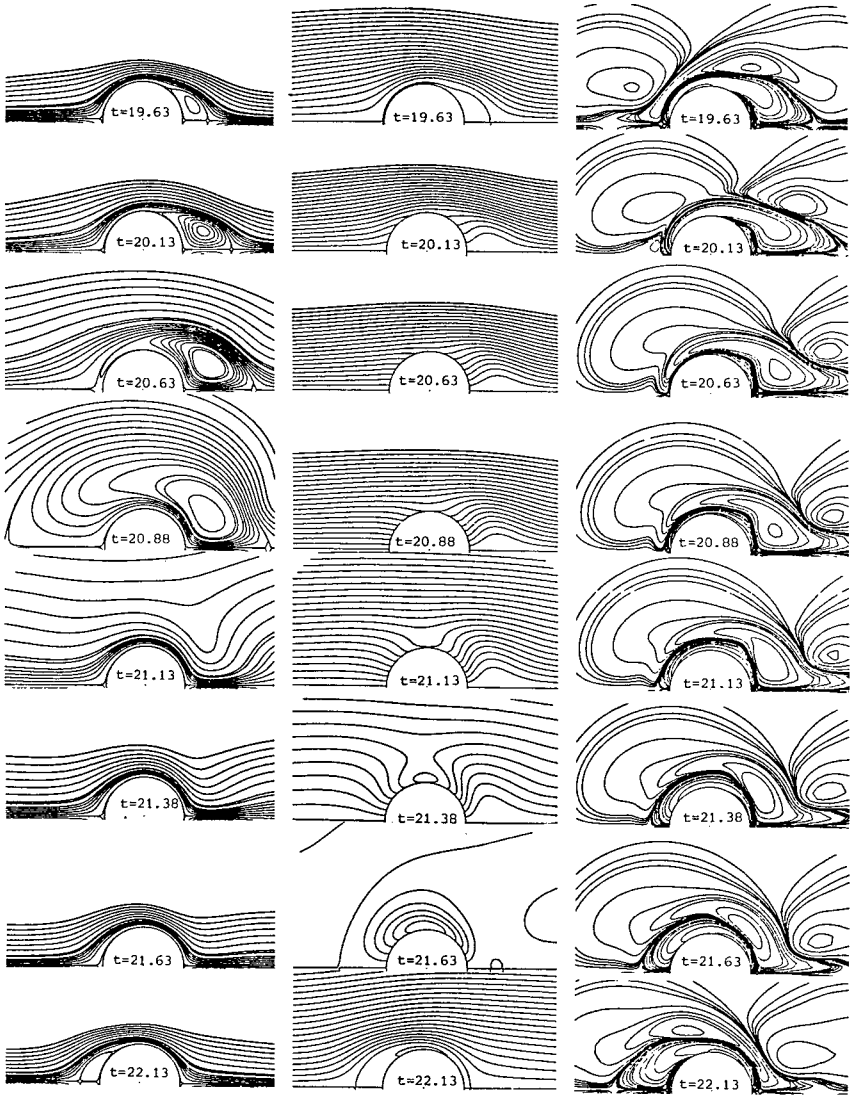
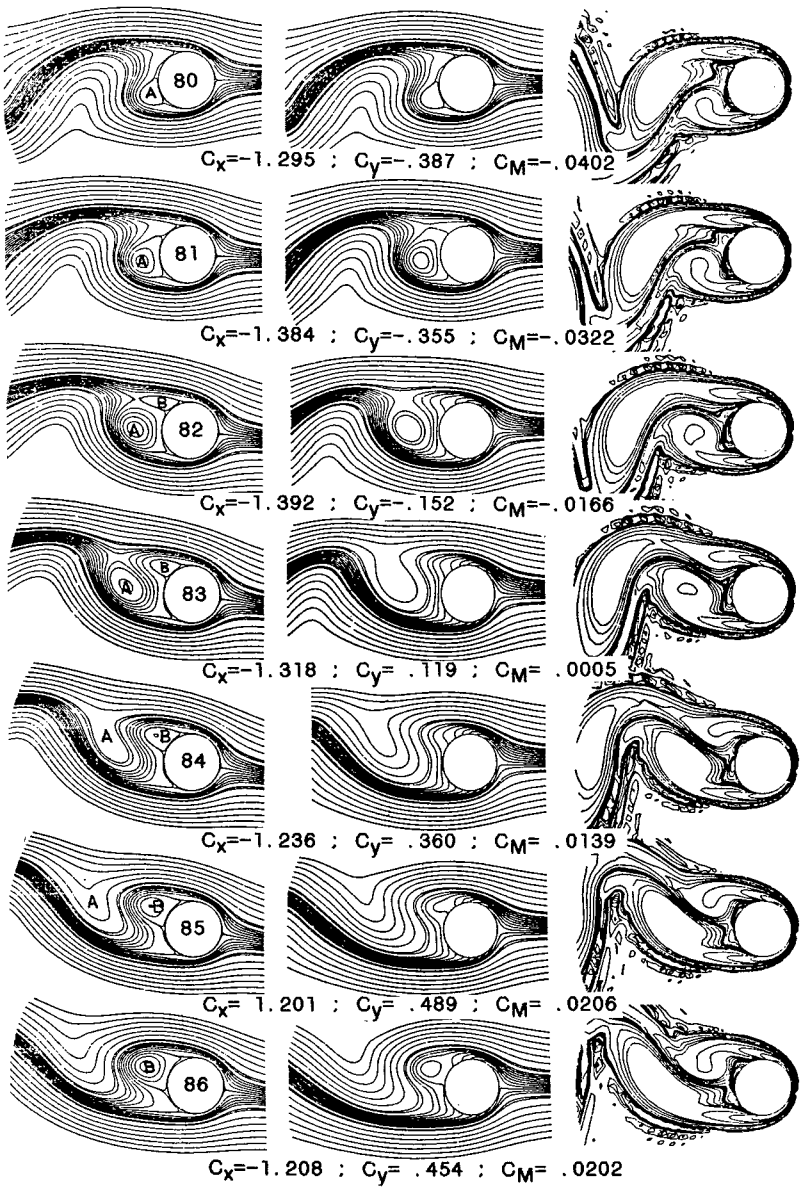


Fig. 3. OSCL5. Evolution with time of relative streamlines (left), absolute streamlines (center), isovorticity lines (right).



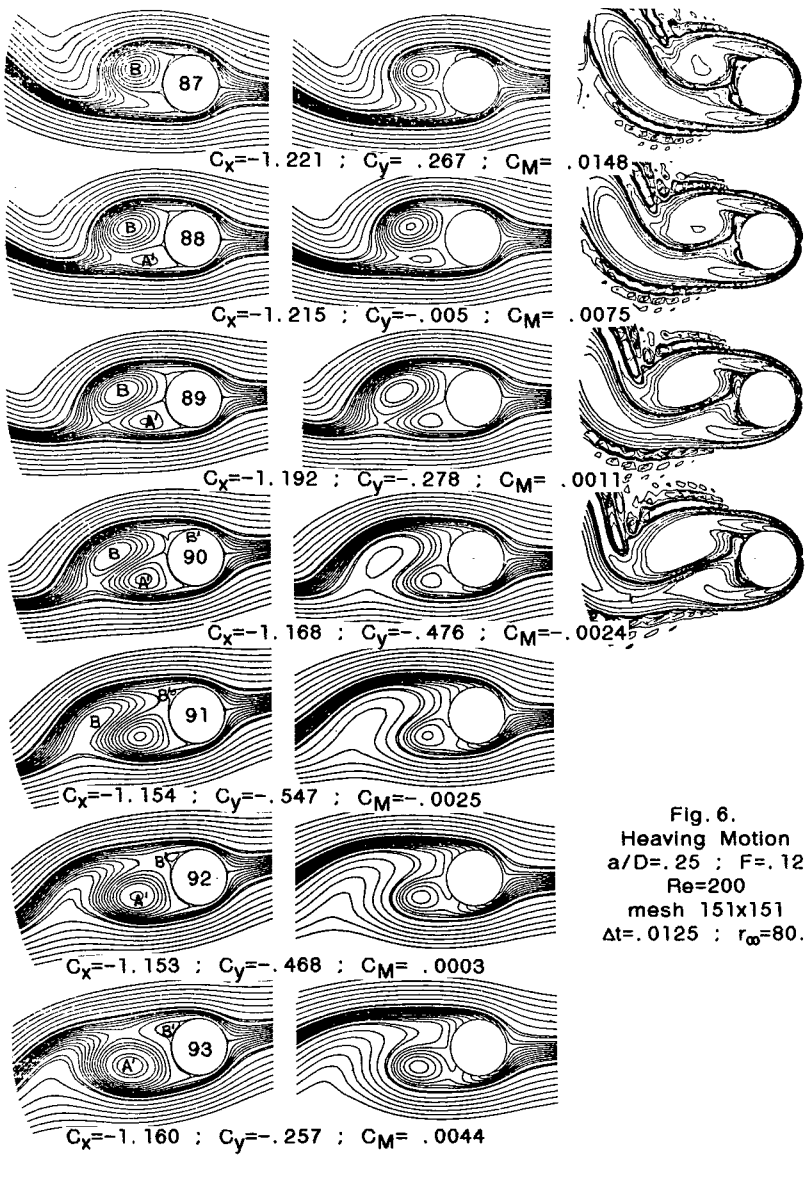


Fig. 6.
Heaving Motion
a/D=.25 ; F=.12
Re=200
mesh 151x151
Δt=.0125 ; r_∞=80.

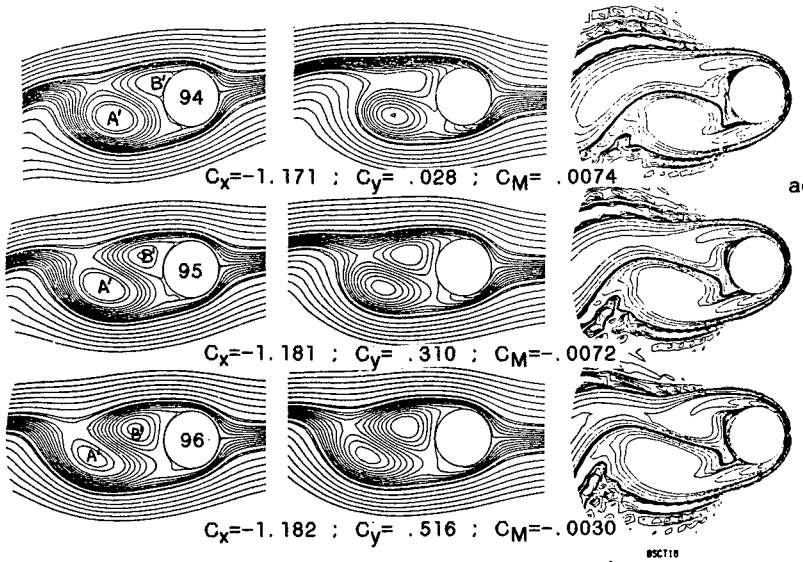


Fig. 6. Heaving Motion.

Evolution with time of
relative streamlines (left)
accompanying streamlines (center)
equivorticity lines (right)

a/D=.25 ; F=.12
Re=200
mesh 151x151
Δt=.0125 ; r_∞=80.

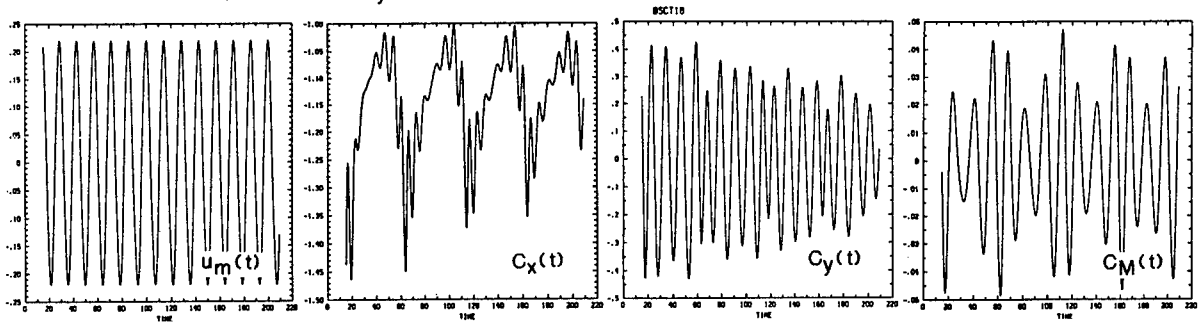


Fig. 7. Heaving Motion ; a/D=.25 ; F=.14 ; Re=200 ; Force Evolutions.

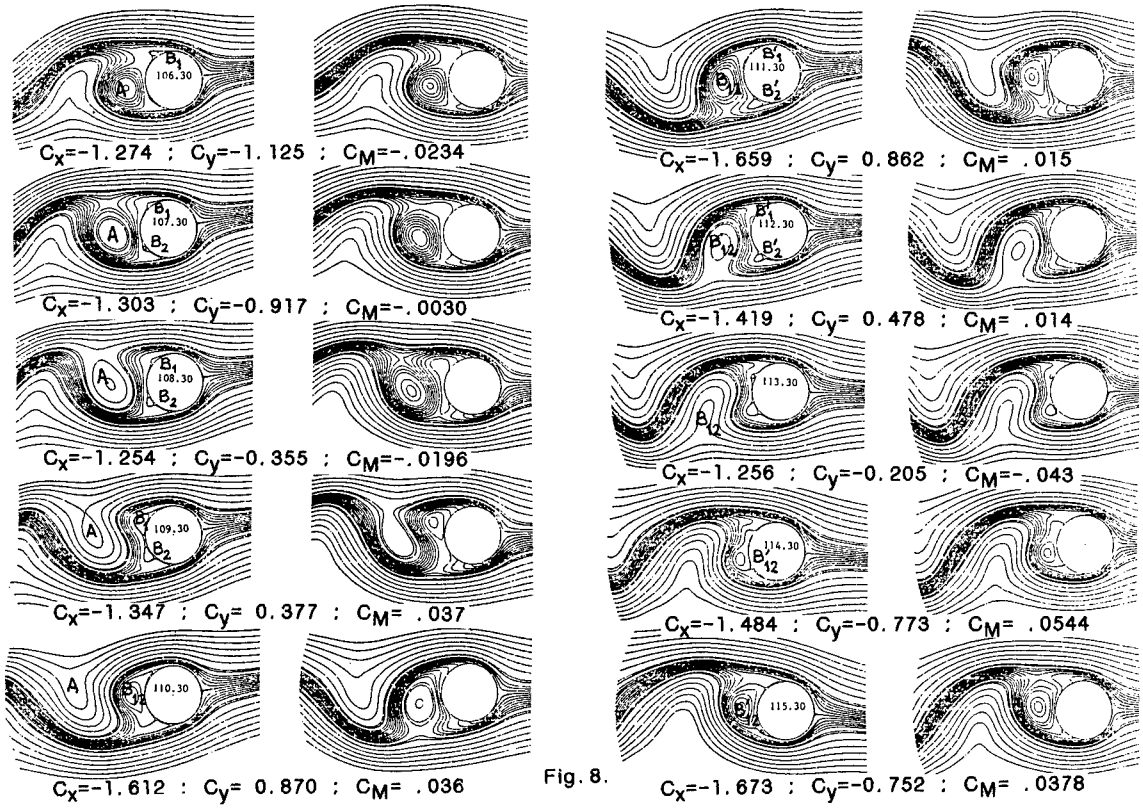


Fig. 8.

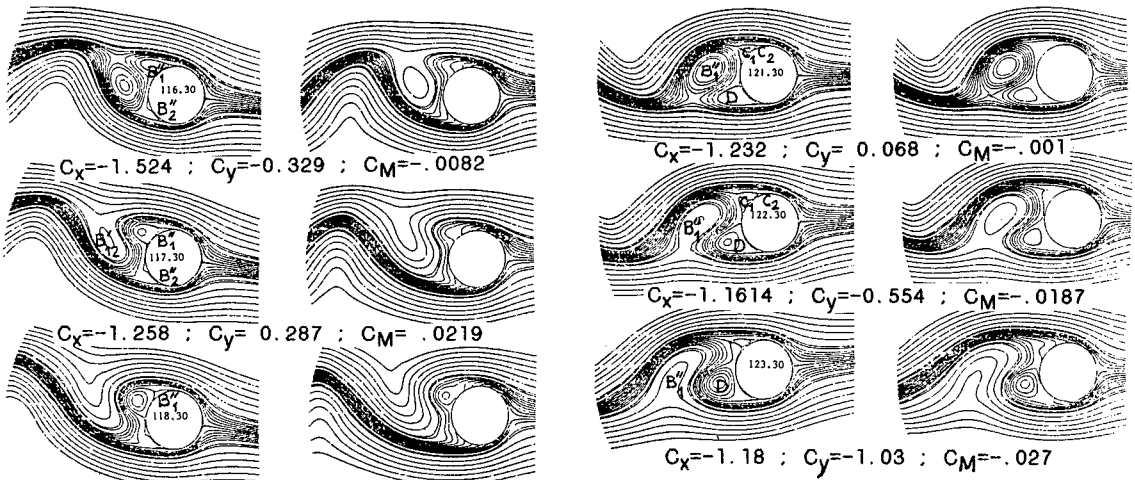


Fig. 8. Evolution with time of relative streamlines (left) and accompanying streamlines (right) Heaving Motion. a/D=.25 F=.12 Re=500 Δt=.02 ; r_∞=110 ; 171x101 grid.

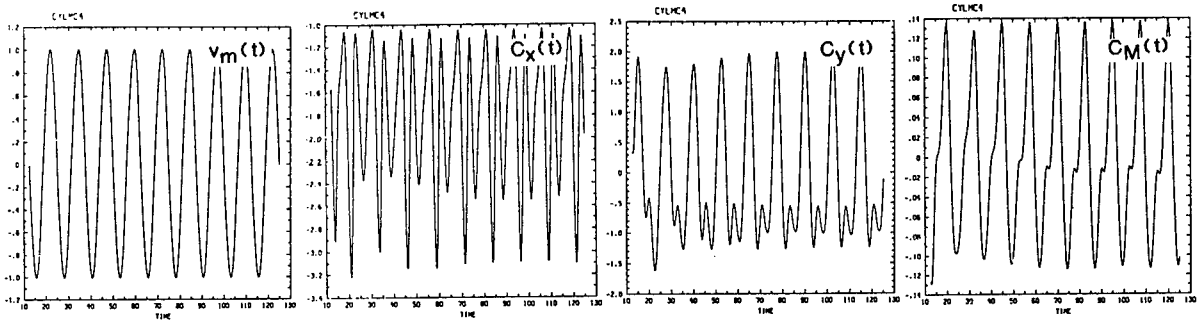


Fig. 9. Heaving Motion. Evolution of Forces. a/D=1. ; F=.16 ; Re=200 .

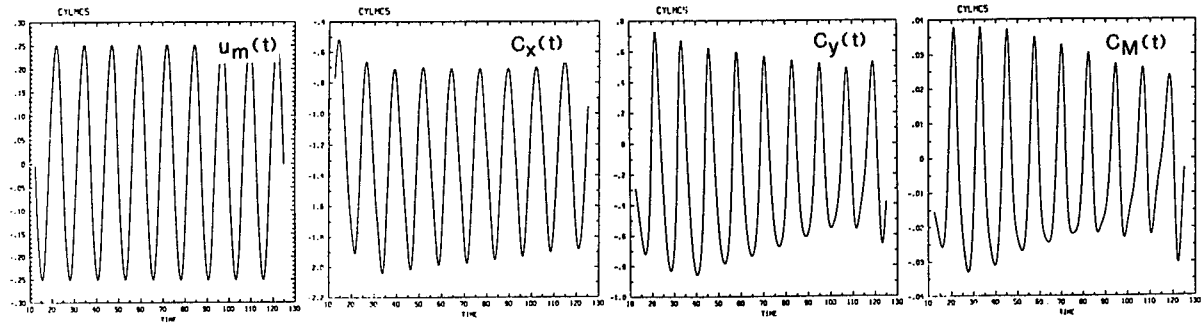


Fig. 10. Surging Motion. a/D=.25 ; F=.16 ; Re=200 . Evolution of Forces.

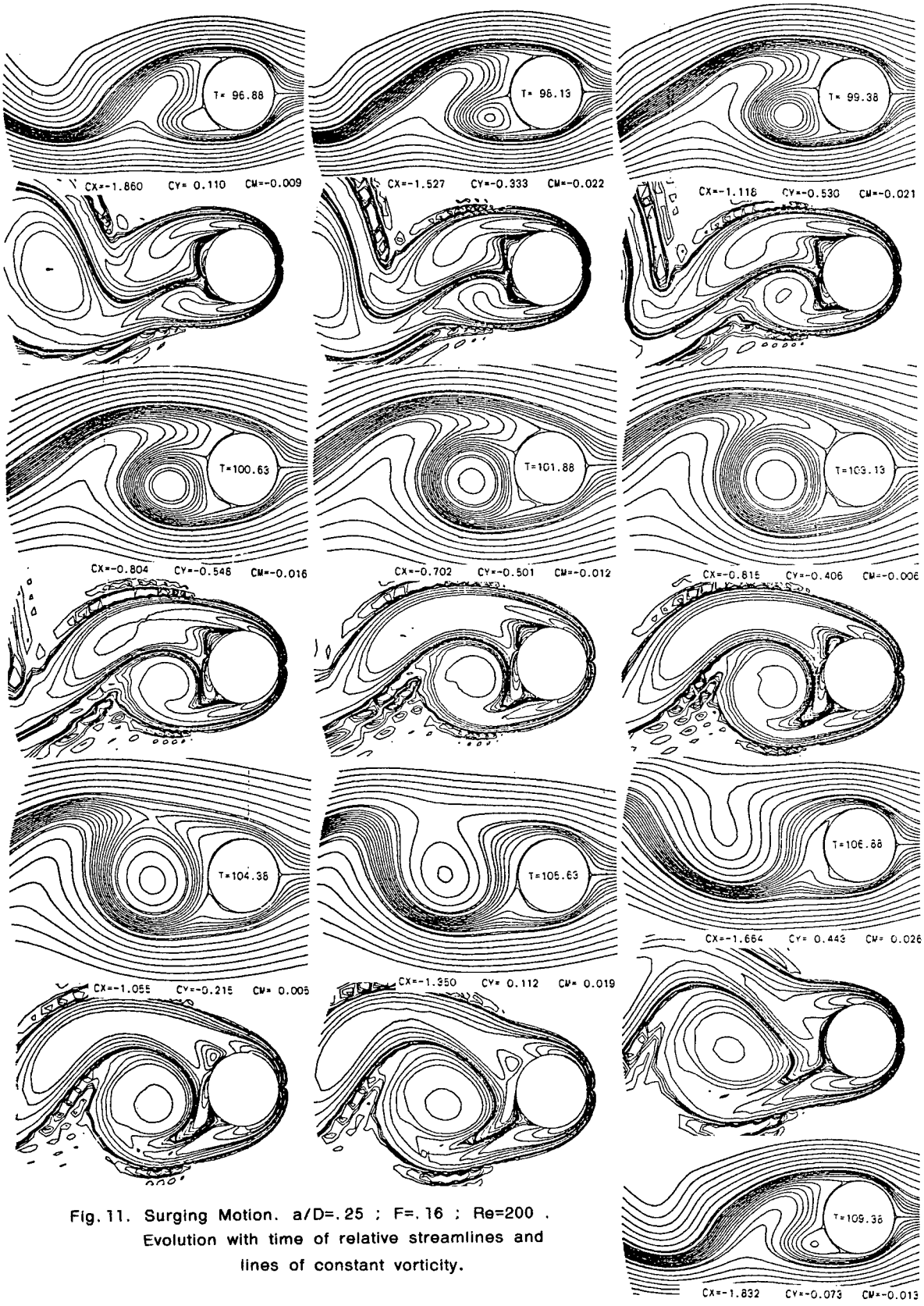


Fig. 11. Surging Motion. a/D=.25 ; F=.16 ; Re=200 . Evolution with time of relative streamlines and lines of constant vorticity.

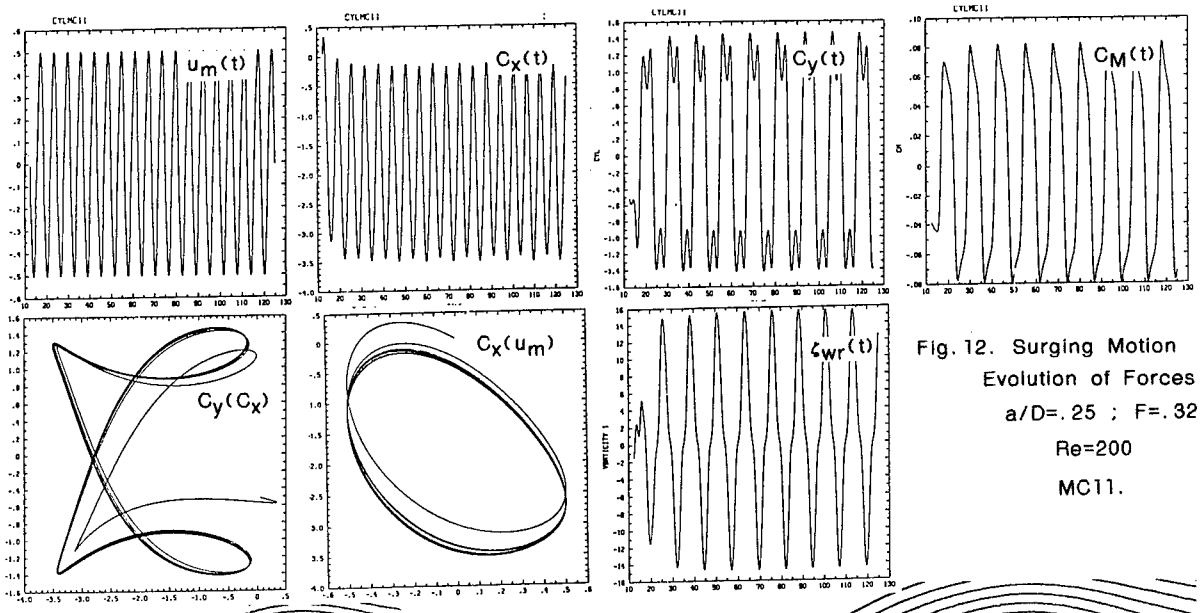


Fig. 12. Surging Motion
Evolution of Forces
a/D=.25 ; F=.32
Re=200
MC11.

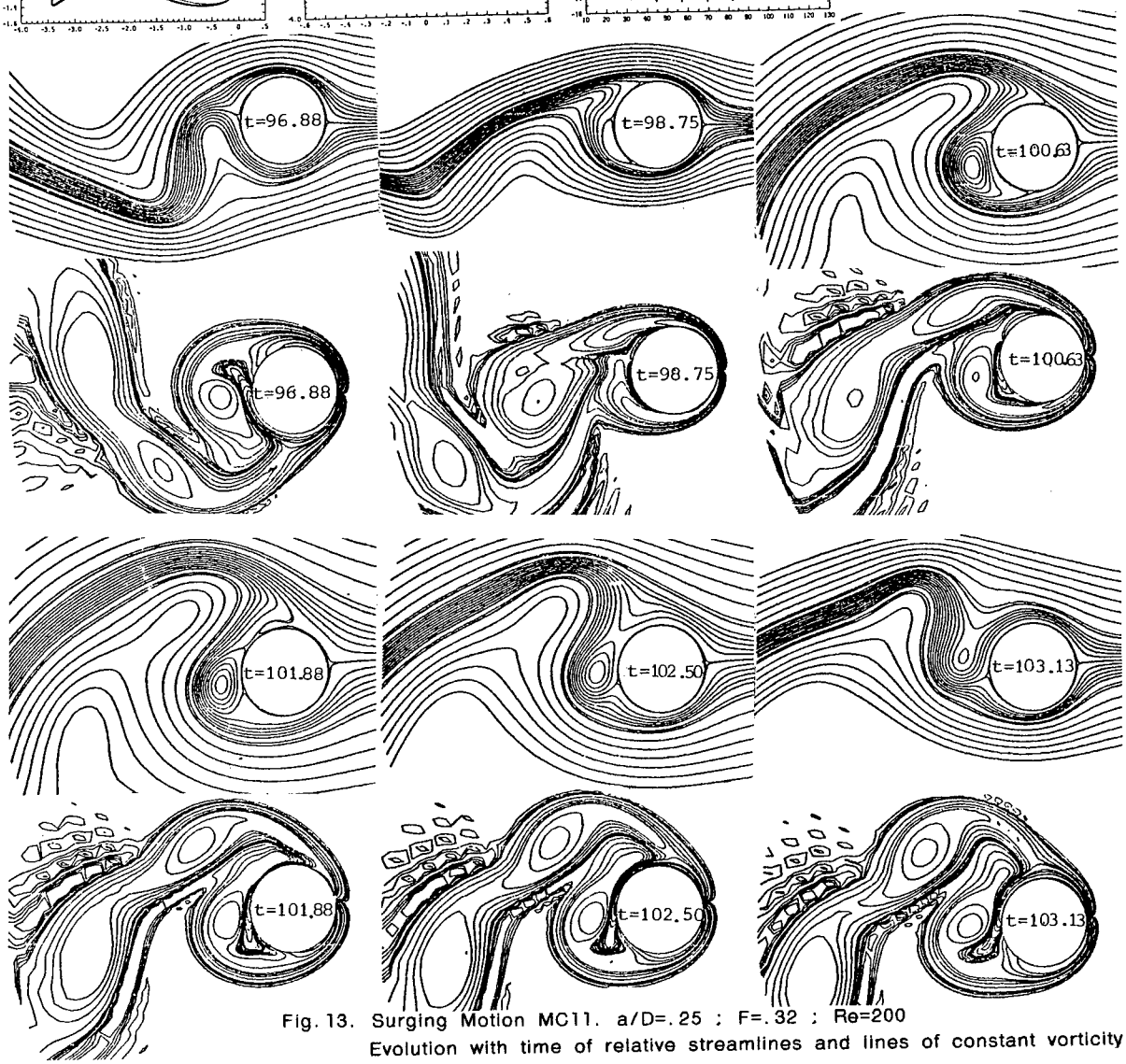


Fig. 13. Surging Motion MC11. a/D=.25 ; F=.32 ; Re=200
Evolution with time of relative streamlines and lines of constant vorticity

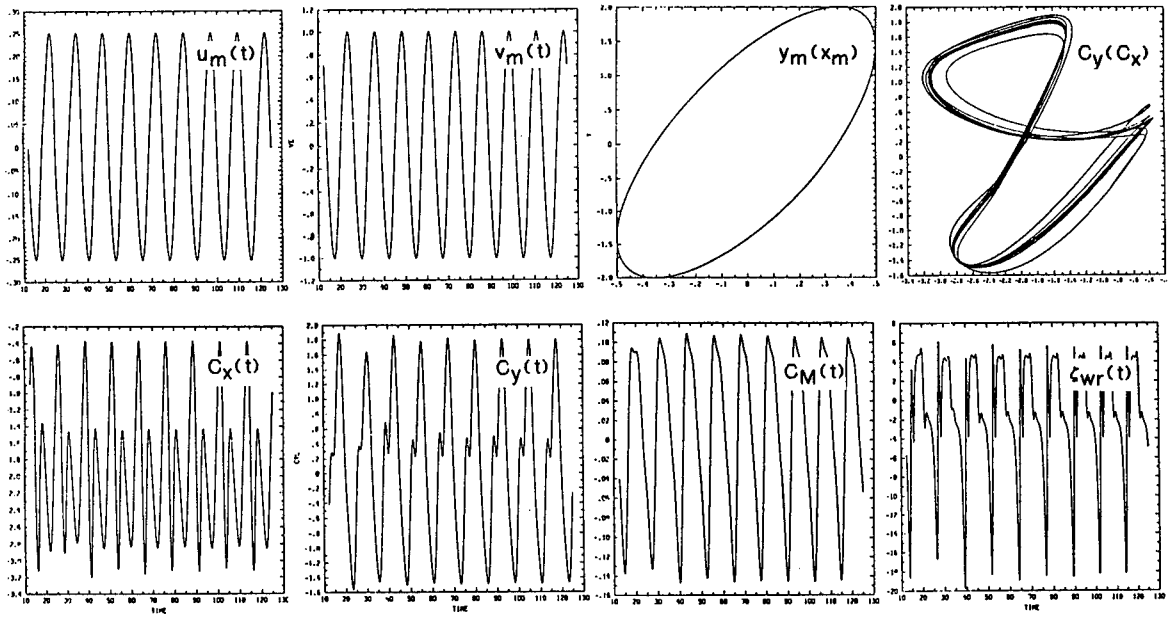


Fig. 14. Oblique Elliptic Compound Motion MC2. Evolution of Forces.

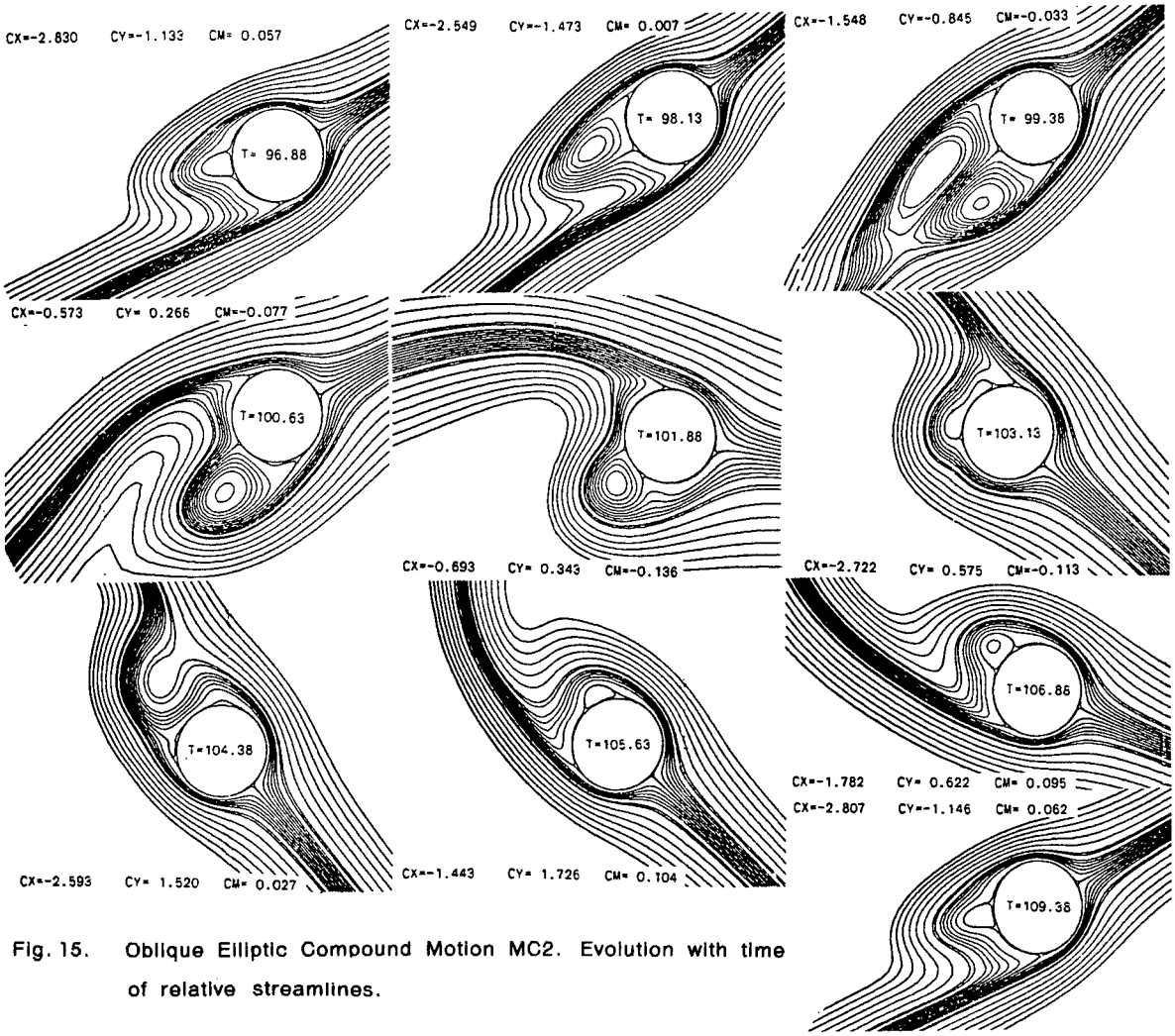


Fig. 15. Oblique Elliptic Compound Motion MC2. Evolution with time of relative streamlines.

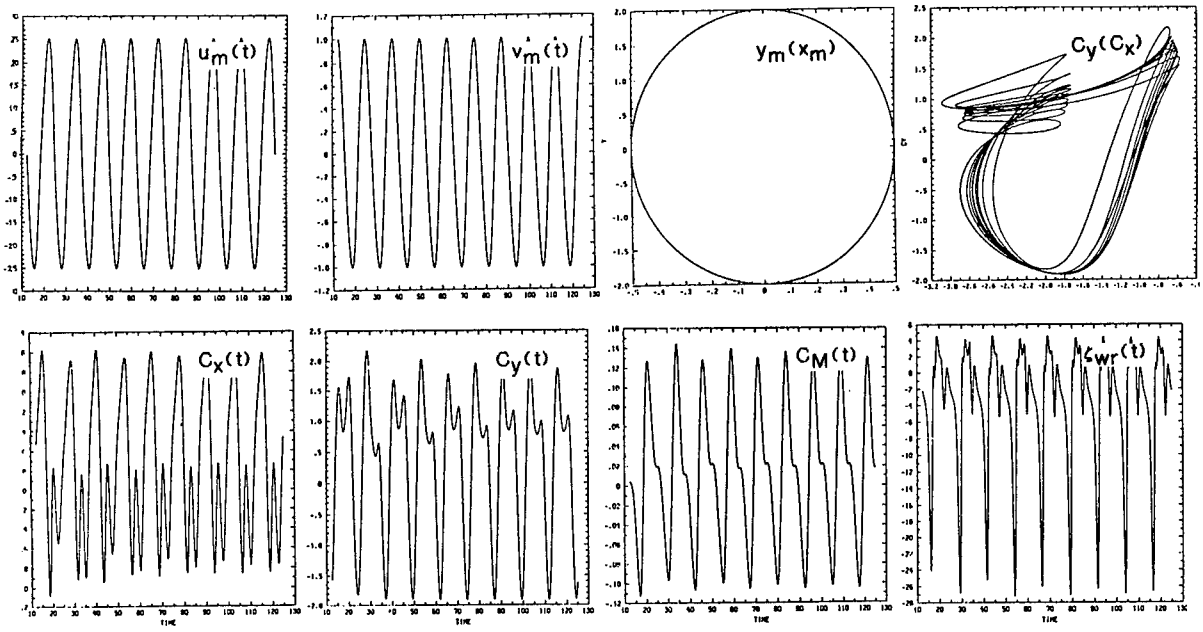


Fig. 16. Circular Compound Motion MC3. Evolution of Forces.

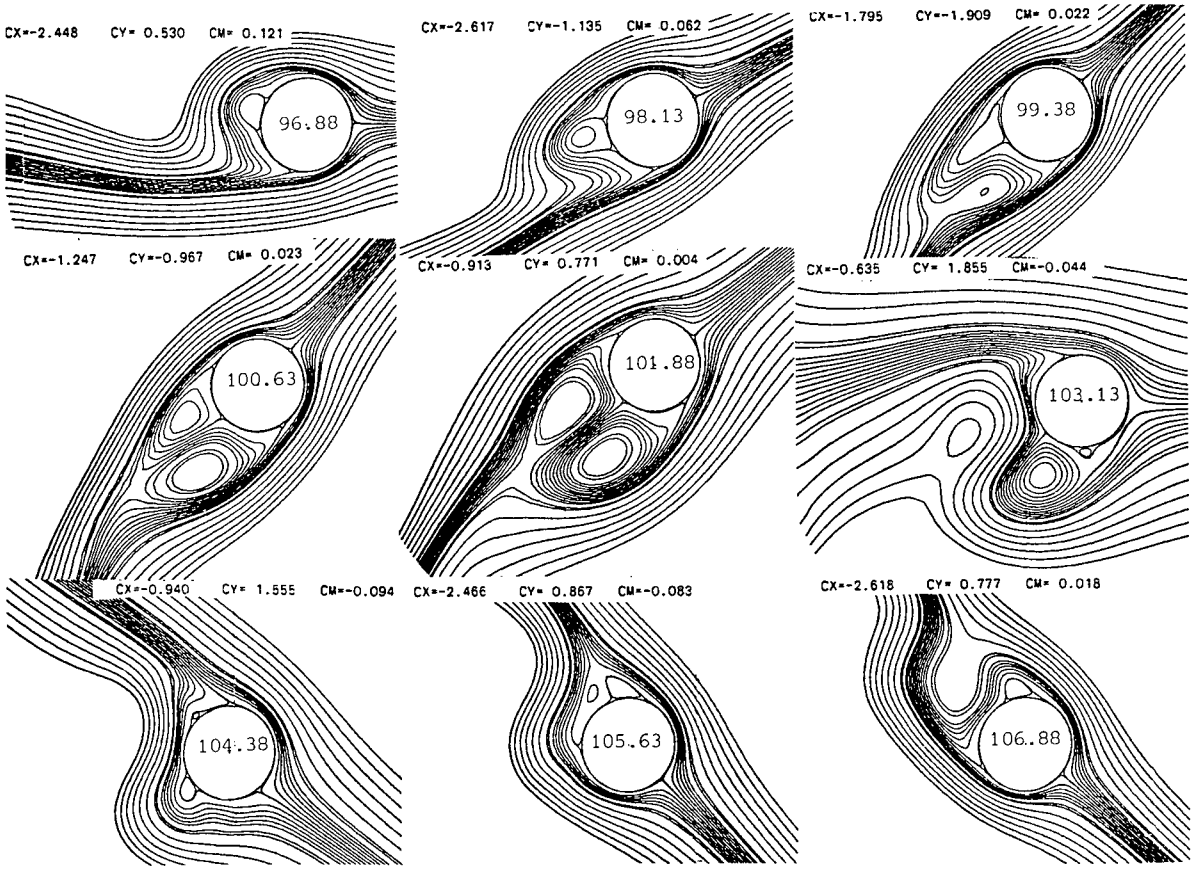


Fig. 17. Circular Compound Motion MC3. Evolution with time of relative streamlines.

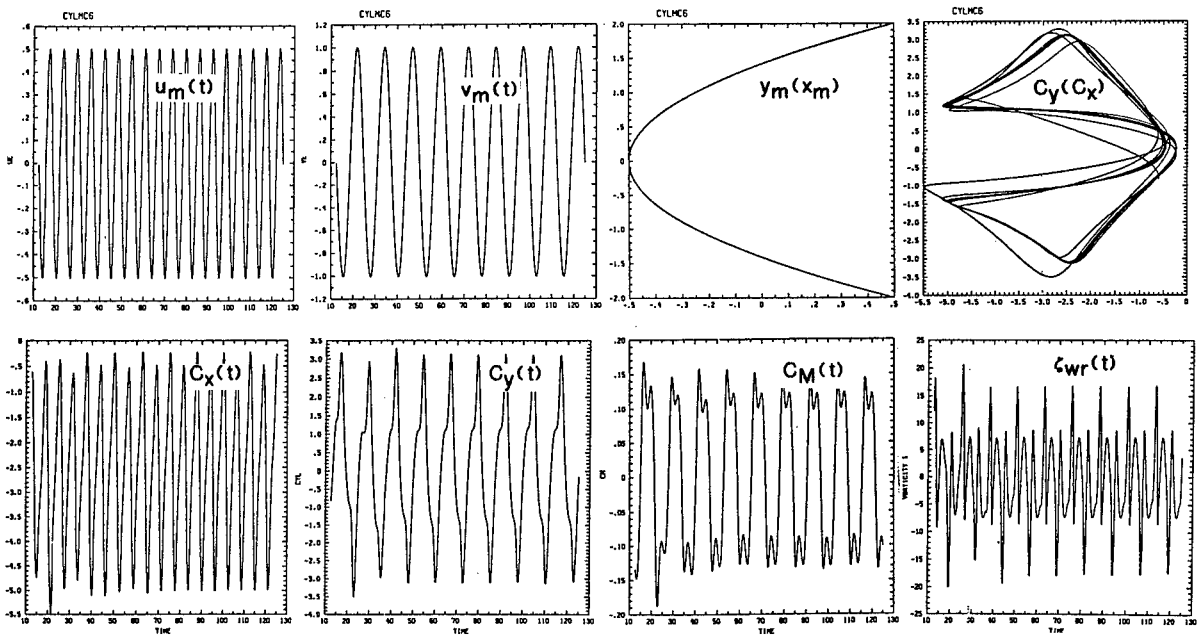


Fig. 18. Piecewise Parabolic Compound Motion MC6. Evolution of Forces.

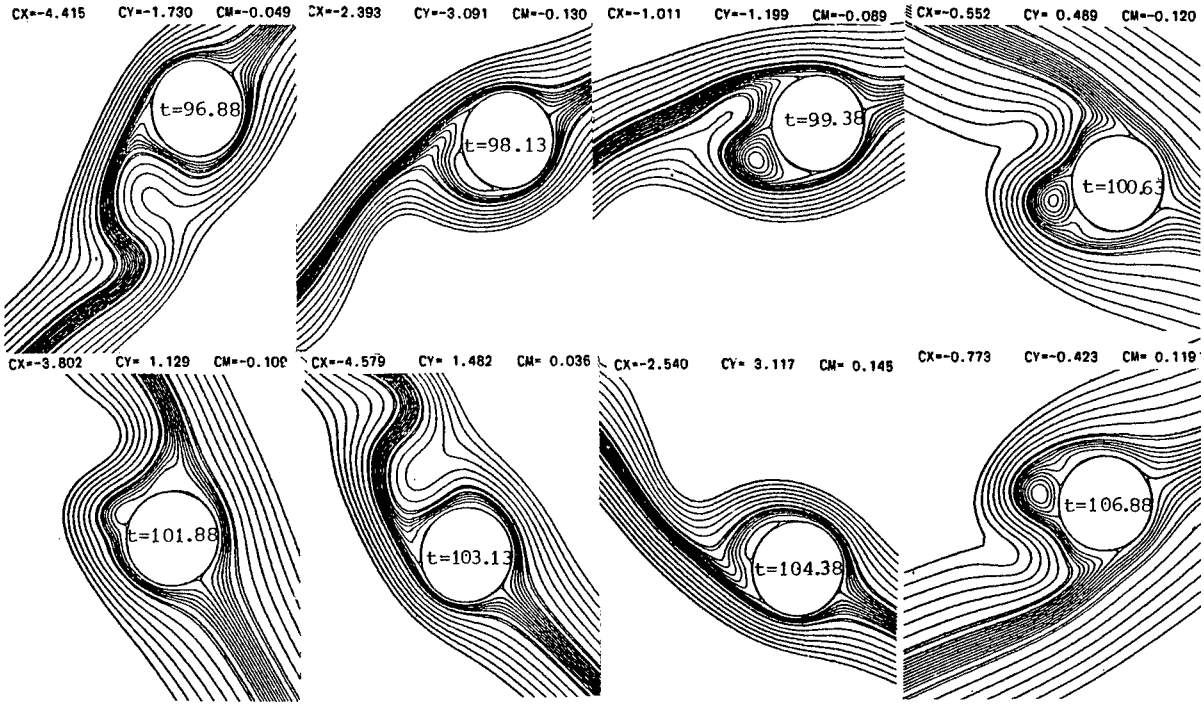


Fig. 19. Piecewise Parabolic Compound Motion MC6. Evolution with time of relative streamlines.

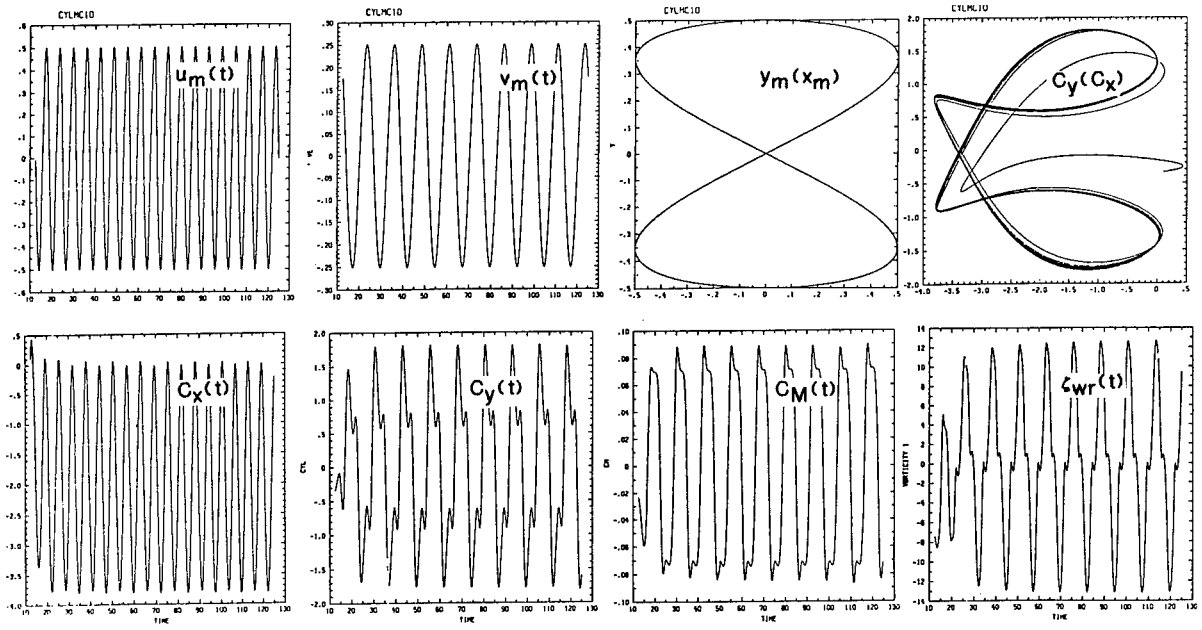


Fig 20. Eight type Compound Motion MC10. Evolution of Forces.

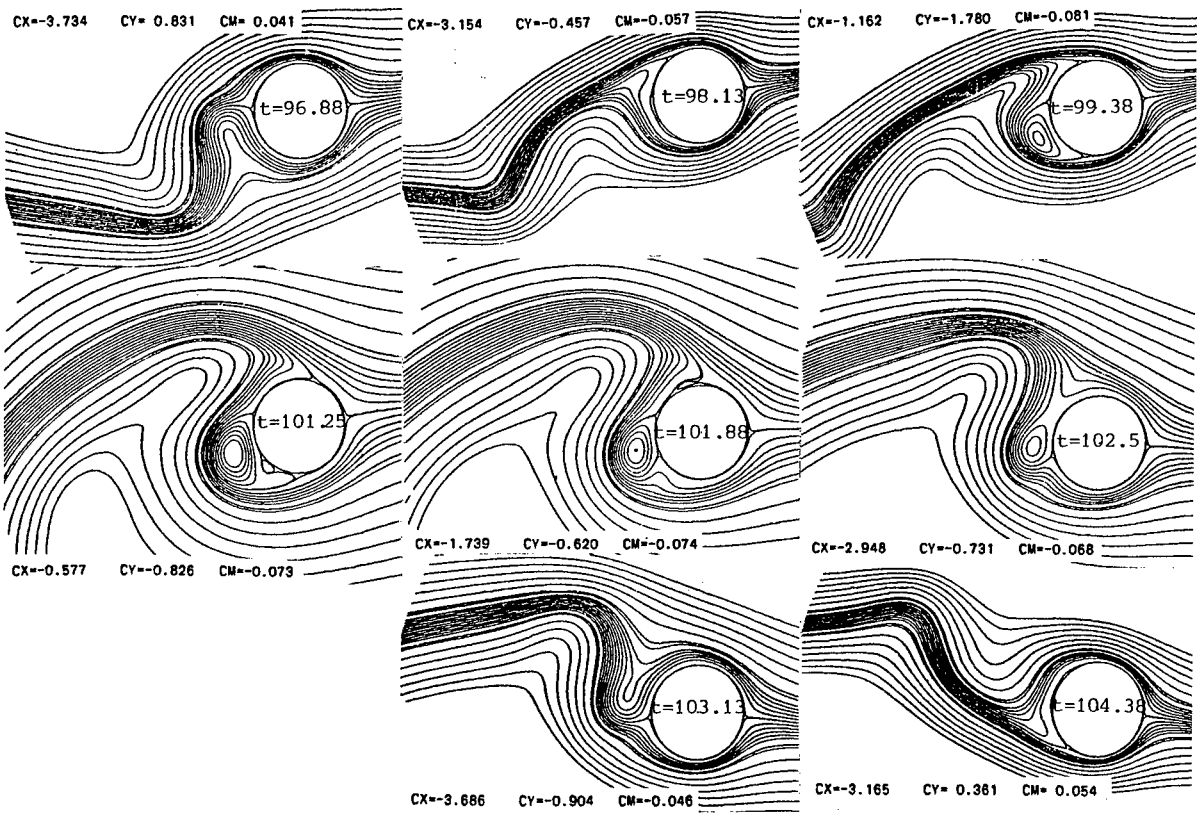


Fig. 21. Eight type Compound Motion MC10. Evolution with time of Relative Streamlines.

DISCUSSION

Hyoung-Tae Kim,
Iowa Institute of Hydraulic Research

In your numerical scheme, what order of approximation is used for body boundary condition of vorticity?

In the calculation of the impulsive start motion, did you use any artificial disturbance to trigger the vortex shedding?

Reply -

At the boundary, the vorticity is computed by means of a local finite difference relation for the second deriative of the stream-function. The order is h^2 but some other relations in higher order were tested. This point is extensively discussed in the reference Lecointe & Piquet (1985-b). In fact, the influence on the flow structure was not found significant. Nevertheless, as the computation of the vorticity derivative is necessary to obtain the forces, a weak influence on their level is found.

In the case of an impulsive motion of a circular cylinder, even if an upwind scheme is used in the whole domain, the flow remains symmetric. If one wants to get a vortex shedding, it seems necessary to impose to the cylinder a pitching perturbation which is taken as:

$$u_w = 0.15, \quad \text{for } 3.0 < t < 3.5, \text{ and}$$
$$u_w = -0.25, \quad \text{for } 3.5 < t < 5.0$$

where u_w is the pitching velocity.

Simulation of the Viscous Flow Over a Cylinder in a Wave Field

E. C. TIEMROTH

University of California, Berkeley, U.S.A.

ABSTRACT

The random vortex method is applied to the problem of wave induced flow over a transversely oriented circular cylinder, with and without a current. The method is seen to have many advantages over competing methods. It is grid free and allows for the rigorous decomposition of the resultant force into "potential" and "viscous" components. One of the major problems with the method is the amount of computation required for the convection calculation. A Lagrangian scheme based on series expansion is successfully used to combat this problem. The method is capable of reducing the required number of operation from $O(N^2)$ to $O(N^{1.5})$, where N is the number of computational elements present. The simulated forces are compared with experimental results and found to agree well.

NOMENCLATURE

Vector and matrix quantities are indicated in bold face.

A	=	wave amplitude
b	=	vortex blob core function
b	=	$n\times1$ vector $[1, 1, ..., 1]^T$
c	=	wave speed
C(t)	=	stream function integration constant
C_D	=	drag coefficient = $X/(\rho g\pi D^2/4)$
C_L	=	lift coefficient = $Y/(\rho g\pi D^2/4)$
D	=	cylinder diameter
F(z)	=	complex potential
g	=	acceleration due to gravity
h	=	vortex sheet segment half-length
H	=	depth of fluid below free surface
i	=	$\sqrt{-1}$
k	=	wave number
K	=	influence matrix
l	=	sheet layer thickness
M	=	number of singularity panels
N	=	number of blobs
p	=	number of Laurent series terms retained
q	=	number of neighbor cells
Re	=	Reynolds number
s_{max}	=	maximum allowable slip velocity for which no vorticity is generated
u	=	fluid velocity vector
u_∞	=	velocity at the outer edge of the sheet layer
V	=	boundary velocity
w(z)	=	complex velocity u-iv
X	=	x component of the force on the body
$\mathbf{X}_i$	=	Lagrangian coordinate of i^{th} blob
Y	=	y component of the force on the body and submergence of cylinder below free surface
γ	=	vortex sheet circulation per unit length
$\boldsymbol{\gamma}$	=	vector of unknown panel strengths
γ_{max}	=	maximum allowable vortex sheet strength
Γ	=	circulation
Γ_0	=	total circulation of the vortex blobs
δ	=	DVIC grid dimension
$\delta(x)$	=	Dirac delta function
Δt	=	time step
ζ_i	=	complex coordinate of i^{th} blob
θ	=	singularity panel tangent angle
λ	=	wave length
ν	=	fluid kinematic viscosity
ξ	=	vorticity
ρ	=	fluid density
σ	=	vortex blob radius
Φ	=	velocity potential
Ψ	=	stream function
ω	=	wave angular velocity
∂_α	=	differentiation with respect to "α"
∂B	=	body boundary
$'$	=	denotes derivative with respect to z

1. INTRODUCTION

The prediction of fluid forces on bluff, cylindrical members is one of the most important problems in offshore engineering. Acceptable analytical and/or numerical methods for predicting such forces have not yet been found for the flow regimes in which "viscous effects" are significant. In the following, the application of a relatively new method, known as the "random vortex method" (RVM), to the simulation of the flow about a circular cylinder in various regular wave fields is described. This problem is particularly interesting because, depending on the values of certain parameters, viscous effects may or may not be important.

Potential theory has been successful for analyzing flows around bodies when viscous effects, such as separation and vortex shedding, are negligible. To properly account for the presence of viscosity one must abandon potential theory and turn to the notoriously intractable Navier-Stokes (N-S) equations. In deference to the problems associated with the N-S equations, engineers have traditionally used force prediction schemes in which potential theory is combined with empirical factors to account for viscous effects. The epitome of this approach is the Morison equation [1]. The Morison equation was originally

proposed in 1950 to explain the measured forces on piles caused by incident free surface waves. Its functional form is based on simple theoretical ideas and the equation is fitted to data with empirically determined coefficients. The Morison equation became the standard means of calculating waves loads on bluff members when viscous effects are expected to be important, and remains so today.

The popularity of the Morison equation reflects its ability to make fairly accurate predictions of forces under a variety of flow conditions. There are, however, situations in which its predictions are poor. Fallon [2] measured the forces on cylinders subject to regular free surface waves. Tests were made with a cylinder in various orientations and with waves of various wave lengths and amplitudes. He found that the Morison equation accurately predicted the forces for the vertical (perpendicular to the free surface) and longitudinal (parallel to the free surface and perpendicular to the wave crests) orientations over the entire range of wave lengths and amplitudes he measured, but that the predicted forces differed from the measured forces by as much as 40-50% for the transverse (parallel to the free surface and wave crests) cylinder (figure 1). Furthermore, Morison's equation is often applied to complicated geometries, such as configurations involving multiple cylinders, for which there is little or no experimental evidence of its applicability. Clearly, there is a need for more sophisticated means of predicting wave loads on cylinders that can be used independently for fundamental research, and to validate the applicablity of Morison's equation to new flow configurations for engineering uses.

Finite difference and, to a lesser extent, finite element methods have been the most common techniques for simulating the N-S equations. These methods have been very successful for simulating low Reynolds number flows but serious impediments remain to extending them to high the Reynolds number range that is of practical interest. The main obstacles are [3]: the large computational requirements which grow rapidly with Reynolds number, stability problems, difficulty in implementing boundary conditions and artificial viscosity.

The class of methods called "vortex methods" represents a different approach to simulating viscous flows from the finite difference and finite element methods. Vortex methods attempt to solve high Reynolds number viscous flow problems within the context of classical inviscid, irrotational flow theory. This is done by introducing known distributions of vorticity into an otherwise irrotational flow. The approach dates back to the Kirchhoff-Helmholtz free streamline theory [4]. Some of the more notable early applications were: the Kutta-Joukowski thin wing theory [5], Prandtl's lifting line theory [5], von Kármán's analysis of the von Kármán vortex street[4], Rosenhead's analysis and simulation of the Kelvin-Helmholtz instability [6], and Westwater's vortex sheet roll-up simulation [7]. Modern applications include the work of Abernathy & Kronauer [8], Deffenbaugh & Marshall [9], Sarpkaya [10,11,12], and Clements & Maull [13]. A review of the literature [14] shows that some good results have been obtained over the years with vortex methods for bluff body flow simulations but that most of the methods were largely "ad-hoc" in nature. This characteristic made the application of a given technique to a new problem uncertain, which prevented the wide spread use of these schemes.

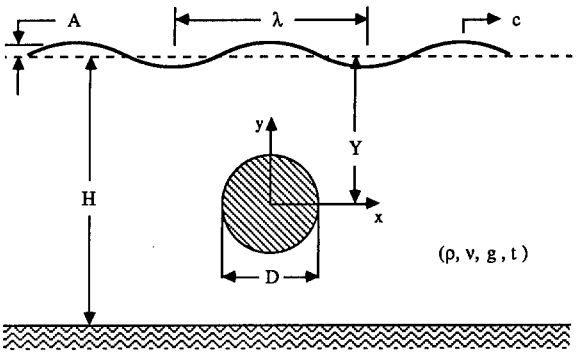


Fig. 1 Transversely oriented cylinder in a wave field.

Chorin [15] made an important contribution to the evolution of the vortex methods by introducing an algorithm with an explicit link to the Navier-Stokes equations. Chorin's original ideas were further developed by himself [16, 17] and a number of other authors, and were used successfully by them on a variety of problems (see [14] and [18] for reviews).

The vortex methods avoid many of the problems of the Eulerian finite difference and finite element methods but are subject to some of their own. Chief among these is the cost of the convection calculation. One of the great strengths of the vortex methods based on Chorin's work is that they lend themselves to hybridization with other numerical techniques. In particular, these methods are compatible with most potential theory techniques.

2. THE RANDOM VORTEX METHOD

The purpose of the random vortex method is to simulate flows governed by the Navier-Stokes Equations and the continuity equation,

$$\partial_t \mathbf{u} + (\mathbf{u}\cdot\nabla)\,\mathbf{u} = -\,1/\rho\,\nabla p + \nu\nabla^2\mathbf{u}, \qquad (1)$$

$$\nabla\cdot\mathbf{u} = 0, \qquad (2)$$

and appropriate boundary conditions. The only boundary condition that enters in the present work is the kinematic condition on a rigid surface which may be expressed as

$$\mathbf{u}(\mathbf{x}_b) = \mathbf{V}(\mathbf{x}_b) \qquad \forall\, \mathbf{x}_b \in \partial B\ . \qquad (3)$$

The continuity equation (2) can be implicitly satisfied by introducing a stream function, Ψ, and solving for it instead of the velocity, $\mathbf{u}$. The velocity can then be found from the stream function by the definition, $\mathbf{u} = \nabla \mathbf{x} \Psi$. The pressure, p, can be eliminated by introducing the vorticity, $\xi = \nabla \mathbf{x} \mathbf{u}$, taking the curl of (1) and using the resulting vorticity transport equation as the governing equation of the fluid in place of (1). Only two-dimensional problems will be considered in the following, and in this case Ψ and ξ have only one component and may be considered scalars. The vorticity transport equation in two-dimensions is

$$\partial_t \xi + (\mathbf{u}\cdot\nabla)\xi = \nu\nabla^2\xi\ . \qquad (4)$$

The stream function is determined from the vorticity distribution by solving Poisson's equation

$$\nabla^2\Psi = -\xi \quad . \tag{5}$$

The original boundary value problem, (1), (2), and (3), in which the primary unknown is the velocity, $\mathbf{u}$, has now been manipulated into a new form, (3) and (4), in which the vorticity, ξ, is the primary unknown. The major advantage of the new "vorticity form" of the boundary value problem derives from the way (3) and (4) can be used to interpret the evolution of the flow in terms of vorticity kinematics. These interpretations have been known for some time and particularly influential accounts of them are given in Lighthill [19] and Batchelor [20]. Equation (4) is essentially kinematic in character unlike the dynamic N-S equations (1). It is a transport equation for the vorticity and may be interpreted as describing the simultaneous convection and diffusion of ξ. When the viscosity is identically zero, (4) reduces to the vorticity form of Euler's equation which describes the pure convection of the vorticity and implies that vorticity is a material property of the fluid.

$$\partial_t\xi + (\mathbf{u}\cdot\nabla)\xi = 0 \tag{6}$$

This case will henceforth be referred to as the convection problem. In cases in which $(\mathbf{u}\cdot\nabla)\xi$ is identically zero, (4) reduces to the diffusion or "heat" equation.

$$\partial_t\xi = \nu\nabla^2\xi \tag{7}$$

In the absence of viscosity, only the normal component of the boundary condition (3), called the no-leak condition, can be satisfied because Euler's equation only involves the first derivatives of ξ. When finite viscosity is present, the tangential component of (3), which is called the "no-slip" condition, must also be satisfied. The physical manifestation of the no-slip condition is the production of vorticity at the boundary, which does not occur in the inviscid case.

A nonlinear decomposition of (4) into the convection and diffusion sub-problems can be made using the fractional step method, sometimes called "time-splitting". In this approach the simultaneous convection and diffusion process is modeled by a number of sequential diffusion and convection steps, with the idea that the solution will converge in the limit as the time step approaches zero. The resulting algorithm is known as a "product formula" and a more detailed and rigorous discussion is given in [21]. The application of time-splitting significantly simplifies the problem by replacing the N-S equations with the more tractable Euler and diffusion equations. The diffusion equation is a linear partial differential equation which is relatively easy to solve. The Euler equation, however, involves a nonlinear convective term that makes it difficult to simulate.

Adopting a Lagrangian view of the vorticity field facilitates the solution of both convection and diffusion problems. The vorticity field is assumed to be represented by the sum of N Lagrangian interpolation functions called "vortex blobs"

$$\xi(\mathbf{x},t) = \sum_{i=1}^{N} \Gamma_i\, b(\mathbf{x}-\mathbf{X}_i) \tag{8}$$

where $\mathbf{X}_i$ is the location of the i^{th} blob, b is the normalized blob core-function, and Γ_i is the circulation of the i^{th} blob. Note that (8) would represent the familiar point vortex field if $b = \delta(x-X_i)\,\delta(y-Y_i)$. In the convection problem it is assumed that each interpolation function follows the material particle located at its reference point $\mathbf{X}_i$. With this assumption, Euler's equation describing the evolution of the vorticity field is replaced with the simple linear ordinary differential equation,

$$\partial_t\mathbf{X}_i = \mathbf{u}(\mathbf{x}(\mathbf{X}_i(t)), t), \tag{9}$$

for the motion of the particles, which is easily solved by a variety of numerical integration methods.

The diffusion of the blobs can be conveniently simulated using the "random walk" algorithm. This technique was originally developed by Einstein [22] and a thorough discussion with application to vortex methods is given in [23]. Briefly, one exploits the similarity of the whole space diffusion Green function to the Gaussian probability distribution to deduce that the diffusion of an initially concentrated quantity can be approximated by the motion of a number of particles which are given "random walks" at each of a number of small time steps. The random walk is a displacement whose magnitude in each coordinate is given by the value of Gaussian random variables. Einstein showed that if the variance of the random walks is $2\nu\Delta t$, then the simulated motion of the particles converges to the solution of (7) as $\Delta t \to 0$ and $N \to \infty$ for problems in which there are no boundaries. The effect of boundaries can be included in the random walk algorithm and the method for doing this will be described shortly.

The no-leak boundary condition is satisfied in the convection problem by enforcing it in solving Poisson's equation (5) and it is satisfied in the diffusion problem by a method yet to be described. The no-slip condition (tangential component of (3)) cannot be satisfied in an analogous manner because neither Poisson's equation nor the diffusion equation are able to satisfy arbitrary normal and tangential velocity boundary conditions simultaneously. Instead, new vorticity must be introduced at the boundary in such a way that the slip velocity is nullified and no normal flow is introduced. Chorin [15] originally placed vortex blobs on the boundary to do this but he later developed a better method known as the "sheet algorithm" [16]. In the sheet algorithm, a vortex sheet is placed on the boundary at each time step. The sheet is divided into a number of straight line segments whose strengths are determined from the condition that the tangential velocity be zero at the boundary point coincident with the center of each newly formed sheet segment. The no-slip condition is thus satisfied exactly at a finite number of discrete boundary points. As time progresses, the sheet segments move away from the wall and metamorphose into blobs when they reach a predetermined distance from the wall. The region containing the sheets is called the "sheet layer". The sheet layer is a mathematical artifice not to be confused with the physical boundary layer (figure 2).

The flow in the sheet layer is assumed to be governed by the Prandtl boundary layer equations [20]. In discussing this region, x, y and u,v shall represent the tangential and normal coordinates and velocities relative to the boundary. The boundary layer equations in two-dimensional vorticity form are

$$\partial_t\xi + (\mathbf{u}\cdot\nabla)\xi = \nu\,\partial_{yy}\xi \tag{10}$$

$$\nabla\cdot\mathbf{u} = 0 \tag{11}$$

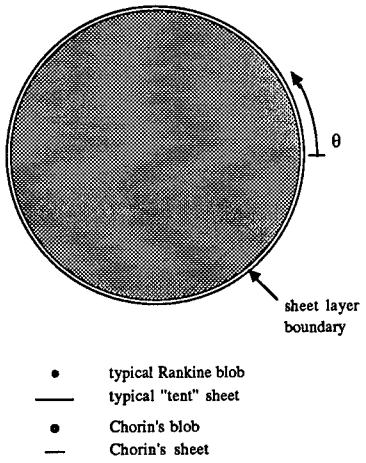


Fig. 2 The sheets, blobs, and sheet layer thickness are shown to scale. "Chorin's" sheet and blob show the sizes his scheme would give with an equivalent discretization.

where

$$\xi = -\partial_y u \,. \tag{12}$$

Time-splitting is applied to the boundary layer equations just as was done for the N-S equations governing the outer flow, and the sheet segments are transported by diffusion and convection steps. The boundary layer approximation leads to significant simplification of both convection and diffusion problems. The convection velocities are, from (3), (11), and (12)

$$\begin{aligned} u(x,y) &= u_\infty(x,l) + \int_y^l \xi(x,s)\, ds \\ v(x,y) &= -\partial_x \int_0^y \xi(x,s)\, ds \end{aligned} \tag{13}$$

and the diffusion equation now involves only one spatial dimension, y. $u_\infty(x,l)$ is the velocity due to all sources except the sheets, evaluated at the edge of the sheet layer above the boundary point with tangential coordinate, x. The assumption $u_\infty(x,l) \approx u_\infty(x,0)$ is consistent with the boundary layer approximation and may be used if convenient. The integrals in (13) are simple to evaluate because the only vorticity in the sheet layer consists of the singular distributions that constitute the sheets, and the integrals are simple the sum of the velocity "jumps" across the sheet segments that lie above the point (x,0) and between the limits of the integral. The differentiation in the tangential (x) direction can be evaluated by simple differencing.

Before discussing the details of the blob and sheet distribution functions, the diffusion problem in the presence of boundaries will be treated. The probability of a computational element moving more than a few standard deviations, say two or three, in a single walk is very small. As a result, if the sheet layer is, say, two standard deviations thick, then the blobs will almost never tend to move through the wall and the presence of the boundaries can be ignored for the blobs. The sheet layer can still be made arbitrarily thin with the correct choice of time step, since the walk standard deviation depends on both the kinematic viscosity and the time step. The few blobs that do move through the wall can either be reflected back into the flow or discarded. Though either procedure is strictly incorrect, only a small error will be introduced since very few blobs will be affected. The sheets exist close to the wall and it is consistent with the boundary layer approximation to assume that the wall is locally flat. In this case the the presence of the boundary on the one-dimensional diffusion equation can be accounted for by using a simple reflection principle [23, 14]. If a sheet passes through the wall during a random walk, it is simply reflected about the wall and back into the flow.

Choice of Vorticity Distributions

To select the blob core functions ($b(\mathbf{x})$ in equation (8)) and the sheet segment distributions, one must consider each separately and the metamorphosis process that takes place at the sheet layer boundary. Sheets and blobs are closely related computational elements, however there are important differences. Each is specified by a fixed distribution with variable position and circulation. The sheets induce a velocity field that only effects their immediate vicinity, reflecting the parabolic character of the boundary layer equations. The blobs, on the other hand, induce velocities over a larger area, a behavior associated with the elliptic N-S and Poisson equations. One objective in the choice of the blob core functions was to eliminate singularities in the velocity and vorticity fields as much as possible and the other was to obtain a reasonable metamorphosis behavior. A Rankine vortex (figure 3) was chosen for the blob core function. It consists of a uniform distribution of vorticity over a circular blob of radius σ and has no singularities in either its vorticity or velocity fields. It is interesting to note that all radially symmetric normalized core functions, including the delta function, induce the same velocity field outside the blob core ($r > 1$). For the Rankine blob with $r^2 = [(x-X_i)^2+(y-Y_i)^2] / \sigma^2$

$$\begin{aligned} &\xi(r) = \Gamma_i/\pi \qquad \Psi(r) = -\Gamma_i r^2/4\pi \qquad r < 1 \\ &\xi(r) = 0 \qquad\quad \Psi(r) = -\Gamma_i \ln(r)/2\pi \quad \text{otherwise.} \end{aligned} \tag{14}$$

The corresponding velocity field is given by the generalized Biot-Savart law [14]

$$\begin{aligned} &u = \Gamma_i (y-Y_i)/2\pi \qquad v = -\Gamma_i (x-X_i)/2\pi \qquad r < 1 \\ &u = \Gamma_i (y-Y_i)/2\pi\, r^2 \quad v = -\Gamma_i (x-X_i)/2\pi\, r^2 \text{ otherwise.} \end{aligned} \tag{15}$$

"Tent" functions were chosen for the vortex sheet segments. Tent functions vary from unity at the center of the sheet to zero at each end. As such, they give a continuous velocity field, unlike the constant strength sheet segments used by Chorin [16, 17] and others [24, 25]. When the vortex sheet is formed on the boundary, the tents are arranged to overlap such that distribution of vortex sheet strength is continuous and forms a linear approximation of the true distribution. This is superior to the piecewise continuous approximation obtained with the constant strength sheets. Mathematically, the sheet segments are specified by

$$\begin{aligned} \gamma_i(x,y) &= (\Gamma_i/h)\,[1-|x-X_i|/h\,]\,\delta(y-Y_i)] \quad ; \quad |x-X_i| < h \\ &= 0 \qquad\qquad\qquad\qquad\qquad\quad ; \text{ otherwise} \end{aligned} \tag{16}$$

where γ_i is the circulation per unit length of the i^{th}

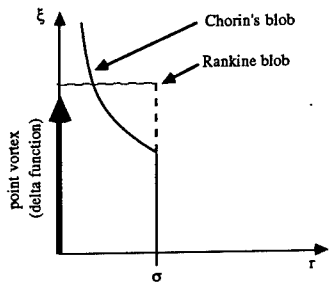


Fig. 3a

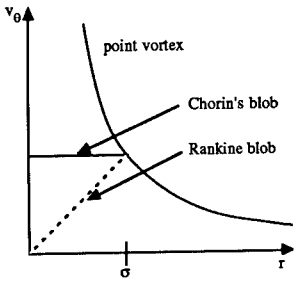


Fig. 3b

Fig. 3 Comparison of Blob Core Functions. Fig. 3a shows a comparison of vorticity distributions. Fig. 3b shows the corresponding tangential velocity distributions. Note that differences between the distributions only exit for r <σ.

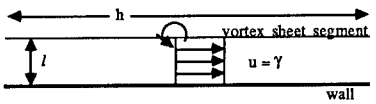


Fig. 4a

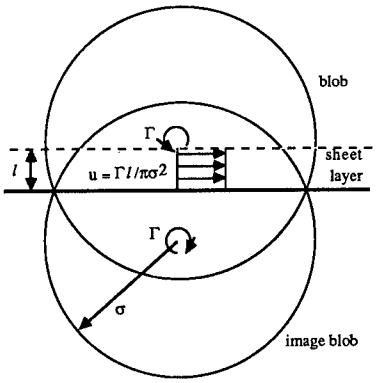


Fig. 4b

Fig. 4 Metamorphosis Between Sheets and Blobs. Fig. 4a shows a sheet segment at the sheet layer boundary. Fig. 4b shows a blob and its image at the same position. The velocity fields are equivalent if (17) is satisfied.

sheet segment whose center lies at (X_i,Y_i) and whose half length is h.

The sheet parameters h and Γ_i are determined in the sheet generation process. h is the distance between the collocation points at which the no-slip condition is enforced and Γ_i is the strength required to annul the slip. As the sheets reach the sheet layer boundary and turn into blobs, their circulation should be conserved. This requirement has already been used in the definitions (14) and (16) to relate the strengths of the sheets and blobs. The only remaining unknown is the blob radius, σ. Following Chorin [17], σ is determined from the requirement that the tangential velocity induced by a sheet segment at the sheet layer boundary, and that induced by a blob located at the same point, and its image, be the same throughout the depth of the sheet layer (figure 4). Direct calculation [14] shows that this requirement leads to the following relation between σ and h:

$$\sigma = \sqrt{hl/\pi} \qquad (17)$$

where l is the sheet layer thickness.

Chorin [17] used a different blob core function which is shown in figure 3. His choice has the advantage that the blob radius is independent of the (arbitrary) sheet layer thickness parameter, l, but it also has the disadvantage of having a singularity in the vorticity field.

The simplest fractional-step algorithm was presented in the preceding discussion. Beale & Majda [26] showed that the convergence of this scheme in the absence of boundaries is $O(\nu\Delta t)$ and presented a second order accurate method that converges $O(\nu\Delta t^2)$. In the latter algorithm, one makes a diffusion step followed by a convection step and a second diffusion step. The variance of the random walk steps in this method is $\nu\Delta t$, half that of the two step algorithm. The three step algorithm was used in the present work together with modified Euler time integration for the convection problem (9). This combination produces a consistent algorithm in which both convection and diffusion errors are $O(\Delta t^2)$.

The overall algorithm for the flow over a rigid body, as presented so far, may be summarized as follows:

- The body surface is discretized into a number of straight line sheet generation panels of length h.
- Initially there are no blobs or sheets present in the domain and the velocity is simply calculated by solving (5) subject to the no-leak condition.
- The tangential velocity at the center of each sheet generation panel is calculated and vortex sheet segments are generated to nullify the slip. It is sufficient to generate one sheet at each panel to eliminate the slip velocity, but the modeling of the diffusion process is improved if several weaker panels are generated. Normally, a maximum sheet segment strength is specified and the number of sheets generated is then equal to the slip divided by the maximum allowable strength, plus one. The sheet strengths are adjusted so that the cumulative strength of the newly created sheets exactly nullifies the slip.
- A random walk step is given to each computational element. If a sheet penetrates

the boundary it is reflected back into the flow.
- Each computational element is convected using modified Euler time integration to solve (9). The velocity field for the blobs is determined by solving Poisson's equation (5) and the velocity field for the sheets is computed from(13). Whether a computational element is treated as a sheet or a blob depends on its height above the boundary. If it lies outside the sheet layer it is a blob.
- A second diffusion step is made.
- The process is repeated as long as desired

Theoretical Considerations

The convergence of the random vortex method has not yet been proven, but important strides towards doing so have been made. Beale & Majda [26] have given a convergence proof of the fractional-step algorithm for the Navier-Stokes equations in the absence of boundaries. The proof assumed that the convection and diffusion problems are solved exactly at each step. Their result is, of course, not applicable to the present algorithm but the result is nevertheless encouraging.

A good deal of theoretical work has focused on the application of the convection part of the algorithm to solve Euler's equation. Hald [27] proved convergence for infinite domains and Beale & Majda [28] and Anderson & Greengard [29] have made some extensions to Hald's proof but no one has yet accounted for the presence of boundaries.

3. SOLUTION OF THE CONVECTION PROBLEM

One of the most problematical aspects of the random vortex method involves the solution of the convection problem, for it is here that one pays the price for the Lagrangian representation of the vorticity field. As time progresses, the number of vortex blobs increases and the number of calculations required to convect them becomes prohibitive.

Only the body boundary condition (3) will be considered in the this section. Treatment of the free surface and/or bottom boundary conditions will be discussed after the basic convection procedure has been presented.

The convection of the blobs is determined by numerically integrating (9) using the modified Euler method. This integration requires the evaluation of the velocity field, $\mathbf{u}$, which is obtained by solving the Poisson equation (5) subject to the boundary condition(3). The problem is linear so the stream function may be decomposed into three parts: the particular solution ψ_p, the incident stream function ψ_I, and a perturbation stream function ψ_b. The sum of the incident and perturbation stream functions is often called the homogeneous solution. ψ_I is presumed known and ψ_p and ψ_b are determined from the following boundary value problems:

$$\nabla^2 \psi_p = -\xi \quad ; \quad \lim_{r \to \infty} \psi_p(r) = 0 \tag{18}$$

$$\nabla^2 \psi_b = 0$$
$$\psi_b(\mathbf{x}_b) = C_i(t) - \psi_I(\mathbf{x}_b) - \psi_p(\mathbf{x}_b) \quad \forall\, \mathbf{x}_b \in \partial B_i \tag{19}$$

The boundary condition on for ψ_b expresses the no-leak requirement and contains the implicit assumption that the rigid boundaries are fixed relative to the coordinate system. Each B_i bounds a simply connected part of the exterior domain upon which (3) is enforced. The functions C_i will generally be different, and one of them is arbitrary. In the present work, there is at most one body, so C_i can be set equal to zero for convenience. In general, $C_i - C_j$ is equal to the flux across any rectifiable Jordan arc, lying in the domain, and connecting B_j and B_i.

Particular Solution of Poisson's Equation

The particular solution is not affected by the boundary conditions so it may be determined once and for all. Green theory is used to solve the problem using the whole space Green function and the solution for a single blob has already been given in (14). The stream function for a collection of blobs is simply the sum of the individual blob stream functions. This solution is gratifyingly simple but not very efficient computationally. Calculating the particular solution velocity component at each blob requires $O(N-1)$ computations, making the total operation count $O(N^2)$. This characteristic is unfortunate because N is expected to be large - indeed the convergence limit is approached as $N \to \infty$!

There are two general approaches to dealing with the operation count problem: reduce the effective value of N and/or replace the Biot-Savart law (15) with an approximate solution that requires fewer operations. In problems in which the blobs tend to be convected away from the region of interest, one might simply discard the blobs that have moved "far enough" away. This method tends to keep N around a constant value and has been used by Chorin [17] and Teng [30] among others. The problems with the method are that the error has not been analyzed and that it is not applicable to general problems. Coalescing blobs to reduce N has been done [31, 32], but again theoretical justification is lacking. The second approach is embodied in the "vortex-in-cell" (VIC) method [18, 33-35]. The VIC method is an Eulerian scheme in which the vorticity contained in the blobs is interpolated onto a grid. Poisson's equation is then solved using fast-Fourier transforms. If the grid contains m nodes, then the operation count for the basic algorithm is $O(m \log(m))$. The enforcement of boundary conditions on the edge nodes and the interpolation of the vorticity add $O(N\sqrt{m}+N)$ operations, making the total operation count $O(m \log(m)+N\sqrt{m}+N)$. There are a host of theoretical and practical considerations that make comparing the VIC algorithm with Lagrangian schemes difficult. The VIC algorithm was rejected in the current work in favor of a series expansion method called the "discrete-vortex-in-cell" (DVIC) method. Comparison of the two algorithms is best postponed until after the DVIC method has been presented.

Consider a group of k blobs lying relatively close together. Outside the smallest circle that contains all the blobs, a holomorphic complex potential $F(x+iy) = F(z) = \Phi+i\Psi$ exits and is given by

$$F(z) = \frac{1}{2\pi i} \sum_{j=1}^{k} \Gamma_j \ln(z-\zeta_j) \tag{20}$$

Making a Taylor expansion in ζ_j about an arbitrary point, z_0 leads to

$$F(z) = w_0 \ln(z-z_0) - \sum_{n=1}^{\infty} \frac{w_n}{n\,(z-z_0)^n} \tag{21}$$

where

$$w_n = \frac{1}{2\pi i} \sum_{j=1}^{k} \Gamma_j (\zeta_j - z_0)^n \ . \qquad (22)$$

The series is absolutely convergent at all points outside the smallest disk that contains all the blobs and the point $z = z_0$. The complex velocity $w(z) = u(z) - iv(z)$ necessarily exits and is holomorphic outside the "disk of divergence". It is given by the Laurent series

$$w(z) = \sum_{n=0}^{\infty} \frac{w_n}{(z-z_0)^{n+1}} \ . \qquad (23)$$

Equations (22) and (23) imply that, as one moves away from the group of blobs, the induced velocity becomes closer and closer to that of a single vortex located at z_0 with strength equal to the cumulative strength of the group (w_0). This observation suggests a scheme in which the first few terms of (23) are used to evaluate velocities outside some disk containing the group. Savings in calculation will result if the number of blobs in the group exceeds the number of retained terms.

To develop a general algorithm, consider an arbitrary distribution of blobs in the complex plane. A grid is introduced with which to group the blobs, as illustrated in figure 5. It is emphasized that this is not an Eulerian grid but rather a means of grouping the Lagrangian blobs. The grid is chosen to have equal x and y spacing, δ, and the term "cells" is used to denote the squares defined by the grid. The grid serves to associate each blob with a cell. Each cell will generally contain a group of blobs, located at $\{\zeta_1, \zeta_2, \ldots, \zeta_k\}$, which will necessarily have the property that $|\zeta_j - z_0(n)| \leq \delta/\sqrt{2}, \forall j$, where $z_0(n)$ is the center of the n^{th} cell. An expansion of the form (23) can be made for the groups of blobs in each cell. The radius of divergence for these expansions will be at most $(\sigma+\delta/\sqrt{2})$.

The Biot-Savart law (15) is used to evaluate the velocity at a particular blob in the n^{th} cell due to its cell mates. This cannot be avoided since the blob of interest may lie in the non-analytic core region of its cell mates and/or because an expansion of the form (23) for the cell mates is not convergent within the cell. Equation (15) must also be used for all of the blobs within cells whose centers lie closer than $\{\sigma+\delta(1+\sqrt{2})/2\}$ from the center of the n^{th} cell since the disks of divergence for these cells overlap the n^{th} cell. The Laurent expansions are used for all of the other cells instead of accounting for the influence of each blob separately. The series (23) converges very rapidly and it is expected that only the first few terms will be needed to obtain an accurate estimate of $w(z)$. The DVIC algorithm effectively replaces a potentially large collection of simple vortices with a single vortex and, perhaps, a small number of higher order singularities (vortex dipole, etc.), all located at z_0.

The number of operations involved in the DVIC algorithm depends on a number of factors. The distribution of the blobs, the cell size, the blob core size and the number of terms retained in the Laurent expansions as well as the number of blobs will effect the speed of the algorithm. For a given distribution of blobs, one suspects that an optimum cell size will exist. It is interesting to note that both the limit $\delta \to \infty$ and the limit $\delta \to 0$ lead back to the Biot-Savart law. In the first limit, one cell will contain all the blobs while in the second limit each cell will contain at most one blob, so the Laurent expansions will be exact with only one

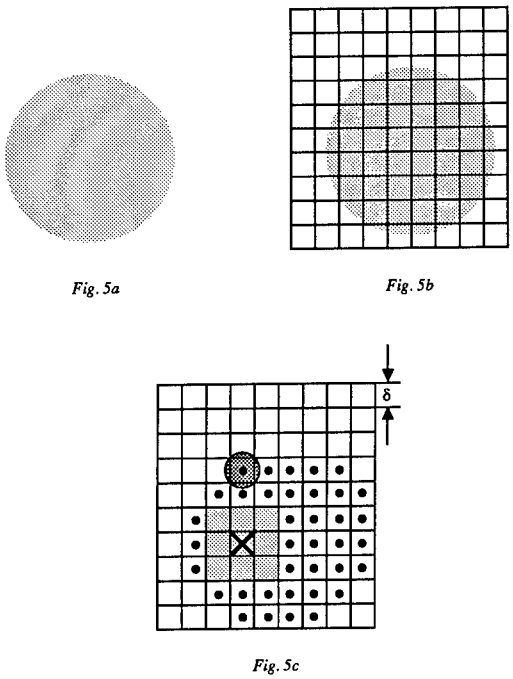


Fig. 5a

Fig. 5b

Fig. 5c

Fig. 5 The Discrete Vortex-in-Cell Concept. Fig. 5a shows a distribution of blobs in space. Fig. 5b illustrates the introduction of a grid to group the blobs into cells of dimension δ. In Fig. 5c the velocity is being evaluated at a point in the cell marked "X". The large dots denote the cells whose blobs are represented by a Laurent series. The shaded circle is a typical "disk of divergence" of a series. The Biot-Savart law is used for the cells filled with small dots.

term. Cells that do not contain any blobs never have to be dealt with and one is always free to treat any blobs one chooses by Biot-Savart, if this is expedient. The gridded region will be finite in practice. If a blob happens to wander outside this region it is simply treated by the Biot-Savart law so the calculation does not have to stop for re-griding of the domain, as would have to be done in the VIC method.

To get an idea of the operation count for the DVIC algorithm, one can examine the case of a uniform distribution of blobs over a square. Suppose there are a total of N blobs with n blobs per cell. For each cell a list is made of the blobs which lie within it. This process requires O(N) operations = KN. To compute the velocity at each blob will require qn-1 Biot-Savart calculations and (N/n - q)p Laurent series calculations, where q is the number of "neighbor" cells for which the Biot-Savart law is always used and p is the number of terms being retained in the Laurent expansions. The total number of operations is therefore proportional to $N\{K + qn-1 + (N/n-q)p\}$. Minimizing the operation count with respect to n gives,

$$n = \sqrt{Np/q} \ . \qquad (24)$$

Substituting this result back into the operation count formula yields,

$$\#\text{ operations} \propto N^{1.5}(\sqrt{pq} + \sqrt{q/p}) + N(K-pq) \ . \qquad (25)$$

Equation (25) shows that the number of operations for a uniform distribution of blobs with an optimal cell size is

$O(N^{1.5})$ - a major improvement over the N^2 figure for the Biot-Savart law. p and q are determined by accuracy considerations. Typical values are p=9 and q=3. Numerical experiments [14] have shown that the 3/2 power growth rate is realized in practice for the uniform distribution (figure 6) and that very high accuracy is achieved.

The DVIC algorithm is accurate, easy to implement, Lagrangian and significantly reduces the number of operations required to evaluate the velocity field compared to the exact Biot-Savart law, but how does it compare to other available algorithms? Spalart & Leonard [31] introduced a similar algorithm based on series expansion some time ago. These authors later dropped it and returned to using the Biot-Savart law claiming that the latter method was more efficient on the vector computers they were using [32]. It is conjectured that the DVIC algorithm could be vectorized to a large extent, though it has not been possible to verify this in the present work. Since the benefits of vectorization increase faster than linearly with the size of the "vector" one expects that, for a given number of blobs, the Biot-Savart law's efficiency will see relatively greater improvement with vectorization than the DVIC algorithm. It is not clear, however, that overall efficiency will be greater than that of the DVIC method, especially for large numbers of blobs.

It is felt that the VIC algorithm is not really compatible with the random vortex method, though numerical schemes employing it may have some practical value. First of all, one of the key parameters of the RVM, the blob core-function, does not enter in the basic VIC scheme. Theoretical and numerical studies [27, 36, 37] have shown that the choice of this function has a major impact on the accuracy and convergence behavior of the RVM, so one must question the appropriatness of a velocity evaluation algorithm that eliminates this important parameter. Furthermore, re-introducing an Eulerian scheme seems counter-productive since the Lagrangian view provided the key advantages of the RVM over the finite difference and finite element methods. A general comparison of the efficiency of the VIC and DVIC methods is impossible because the value of m required to achieve a given level of accuracy depends on the distribution of the blobs as well as the number of blobs. For any value of m, one could construct a distribution of blobs for which the VIC methods would produce unacceptably large errors, where as the DVIC and Biot-Savart laws would not. Stansby & Dixon [33] used the VIC method to compute flow over a cylinder and obtained reasonable looking results, however van der Vegt & Huijsmans [34] later claimed that their scheme involved velocity errors as great as 50%. The latter authors used a different VIC scheme that they claimed reduced the error level to 5%, but their published results did not show fine scale flow structures - the resolution of which is the hallmark of the RVM [14, 16 17, 25]. In both of the cited papers the efficiency of the VIC methods was vastly better than the Biot-Savart law, but the accuracy does not seem to have been comparable. From a theoretical point-of-view it is not yet clear that the VIC methods give comparable accuracy for less cost. However, the VIC schemes may be sufficiently accurate for various practical uses and thus more cost effective from a practical perspective.

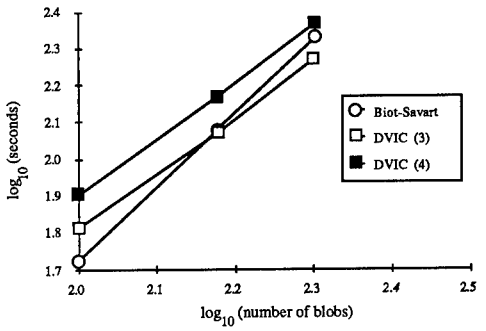


Fig. 6 CPU Seconds per Time Step as a Function of the Number of Blobs. These log-log plots show how CPU time vs. number-of-blobs varies with the number of Laurent series terms retained for the case of an approximately uniform distribution of blobs. The number of retained terms is shown parenthetically in the legend.

Homogeneous Solution of Poisson's Equation

The boundary value problem for the homogeneous solution, (19), was solved using the classic singularity distribution technique. The solution is detailed in [14] and is similar to the formulation used in [33]. For the present work, only the formulation for a single body in an infinite domain will be needed. The application of Green theory leads to several possible singularity distributions involving sources and/or dipoles. (When solving for the stream function, the natural "source" is the point vortex and similarly, the "dipole" is a vortex dipole.) The source only distribution was chosen in which submerged, straight-line panels are used. The use of submerged panels leads to a Fredholm integral equation of the first kind instead of one of the second kind like one obtains with surface panels. While integral equations of the first type are not supported by as strong existence and uniqueness results as those of the second kind, the submerged panels often require less computation to achieve a given level of accuracy [38] and were chosen for this reason.

There has been some confusion in the literature about why a circulation constraint is needed to make the solution unique and what this constraint should be. Both Stansby & Dixon [33] and van der Vegt & Huijsmans [34] gave circulation constraints as afterthoughts, stating that such a constraint is necessary to make the solution unique. This is indeed true, but it should have been pointed out that the circulation constraint occurs naturally in the derivation of the integral equation and is a necessary condition for discarding the integral over infinity. Stansby & Dixon [33] asserted that the correct circulation condition was that the total circulation be zero, to satisfy Kelvin's circulation theorem. The invocation of Kelvin's theorem is not appropriate in an algorithm that involves the production of vorticity at the boundaries and presumes to simulate the Navier-Stokes equations. The correct condition is the no-slip condition. The two conditions are equivalent when only one body is present and when the initial condition has zero circulation, so Stansby's & Dixon's results are still valid. However, when multiple bodies are present this is no longer true. The no-slip condition requires the circulation on each body to be zero separately, which Stansby's & Dixon's condition does not.

Straight line panels and collocation were used in the present work and [33, 34] to discretize the integral

equation into a system of linear algebraic equations. In [33, 34] the circulation constraint was incorporated by replacing one of the collocation equations with the constraint equation. This approach can lead to large errors in the vicinity of the discarded collocation point. In the present work, a more accurate method employing a Lagrange multiplier was used. Discretizing the singularity distribution into n straight-line, constant strength panels and application of the collocation method leads to the system of n algebraic equations

$$\mathbf{K}\gamma = -\psi \tag{26}$$

where $\mathbf{K}$ is the $n \times n$ influence matrix, γ is the vector of (unknown) panel strengths and ψ is a vector containing the values of the right-hand-side of (19) at each of the collocation points. The circulation constraint equation is

$$\mathbf{b}^T\gamma + \Gamma_0 = 0 \tag{27}$$

where $\mathbf{b}^T = [1,1,1,1,...,1]$ and Γ_0 is the net strength of the blobs in the flow. The Lagrange multiplier λ is introduced and the functional I is formed.

$$I = [\mathbf{K}\gamma + \psi]^T[\mathbf{K}\gamma + \psi] + \lambda(\mathbf{b}^T\gamma + \Gamma_0)$$

Minimizing I with respect to γ and λ leads to a system of equations for γ and λ whose solution is

$$\begin{bmatrix} \mathbf{K}\mathbf{K}^T & \mathbf{b} \\ \mathbf{b}^T & 0 \end{bmatrix}^{-1} \begin{bmatrix} \mathbf{K}^T & 0 \\ 0 & 1 \end{bmatrix} \begin{bmatrix} -\psi \\ -\Gamma_0 \end{bmatrix} = \begin{bmatrix} \gamma \\ \lambda \end{bmatrix} \tag{28}$$

The first two matrices depend only on the geometry of the body and may, therefore, be computed and multiplied together once and for all at the beginning of the simulation.

Calculation of Forces

The forces consist of two components: force due to the normal pressure and force due to viscous shear stresses. The shear stresses were ignored because, for the Reynolds numbers of interest, the resultant force is known to be insignificant compared to the pressure force [14]. The pressure force is computed by a potential theory method based on Blasius' theorem. The method is nearly the same as that given by Graham [40] for singular vortices but is extended to include the singularity panels. A complete derivation is given in [14]. The fact that the blobs have a finite core is only a problem where they overlap the boundary. In this area, the blobs are effectively modeled as point vortices for the force computation. The resulting formula for the force on the body is

$$X+iY = i\rho\{\sum_{j=1}^{N} \Gamma_j [\, \partial z_j/\partial t - \overline{F'_I(z_j)}\,] + \sum_{k=1}^{M} 2hz_k\, \partial\gamma_k/\partial t - \gamma_k e^{i\theta_k} [\, \overline{F_I(z_k+he^{i\theta_k}) - F_I(z_k-he^{i\theta_k})}\,]\} \tag{29}$$

where an overbar denotes the complex conjugate, F_I is the incident complex potential, z_k is the coordinate of the center of each singularity panel, θ_k is the angle the singularity panel makes with the x-axis and γ_k is the strength of the k^{th} panel.

Numerical differentiation is required to evaluate the forces. Doing so for the time derivatives of the blob positions was not a problem because the velocity fields varied smoothly in time. Accurate results for the time derivatives of the panel strengths, however, could not be obtained because of the rapid variation of the panel strengths in the presence of blobs. Knowledge of the exact solution was used to overcome this difficulty. One can deduce by the method of images that the singularity panels, in the presence of blobs, are equivalent to a system of image blobs plus the singularity distribution one would obtain in the absence of blobs. This result can be used to obtain the force in a two step process. First, the force due to the latter singularity distribution can be computed in a simulation in which no vorticity is generated. When no blobs are present, the panel strengths are periodic and vary smoothly enough that accurate numerical differentiation can be done. (The additional simulation does not add significant expense.) Next, a normal simulation is made but only the first term in (29) is evaluated. The force due to the images is included by extending this first summation to include each blob and its image.

4. SIMPLIFICATION OF BOUNDARY CONDITIONS

The only boundary condition which has been treated so far is the body boundary condition (3). To compute the flow around a cylinder in a wave field one must also deal with the free surface boundary condition. In this work, the linearized free surface boundary condition was imposed on the incident stream function but not on the particular solution or disturbance stream function. There is no theoretical reason why the free surface condition could not be imposed on all the stream function components. The approximation was made for the sake of economy. To properly satisfy the linearized free surface boundary conditions would involve the use of the time dependent Green function which is laborious to compute [39]. In light of the fact that the RVM is already computationally intensive, it seemed prudent to see what could be learned from a simplified analysis.

From analysis of the harmonic free surface Green function [14], it is known that the error introduced by neglecting the free surface in calculating the perturbation stream function decays twice as fast as the incident wave velocity field does with increasing kY. This observation suggests that, for a given submergence of the cylinder, there will be a range of wave lengths that cause significant excitation around the cylinder but for which the error due to the approximation will be small. The foregoing argument is not made to justify the approximation but rather to motivate it. Justification will come through comparison with experiments.

The water in Fallon's experiments was shallow enough to have a measurable effect on the longest waves. In the numerical simulations, the bottom was treated much like the free surface - its effects were included in calculating the incident waves but neglected in calculating the perturbation stream function and the particular solution. Again, one can make an argument for doing this based on decay rates [14].

5. PHYSICAL AND NUMERICAL PARAMETERS

The physical parameters associated with the general problem are shown in figure 1. The wave length and wave speed can be replaced with the derived quantities $k = 2\pi/\lambda$ and $\omega = ck$. It is assumed that linear wave theory is applicable. From this theory it is

known that ω and k are related through the dispersion relation, so one parameter involving ω or k can be eliminated from the list of independent parameters. This leaves the following set of non-dimensional parameters:

$$(kA, kD, \omega t, Y/D, H/D, A\omega D/\nu)$$

The last parameter is a "Reynolds number" for the problem. In addition to the physical parameters there are the non-dimensional numerical parameters,

$$(l/D, \gamma_{max}/V_m(0), \omega\Delta t, h/D, \delta/D, p, M, s_{max}/\gamma_{max}) =$$

$$(l^*, \gamma_m^*, \Delta t^*, h^*, \delta^*, p, M, s^*).$$

The quantity $V_m(0)$ is the maximum velocity at the center of the cylinder due to the incident flow. As such, it is a derived quantity of kA, kD, Y/D, and H/D. $V_m(0)$ would not ordinarily occur in the dimensional analysis but it proved to be the most sensible quantity with which to nondimensionalize the maximum sheet strength. The advantage of using $V_m(0)$ is that it makes γ_m^* comparable with similarly defined parameters for other problems, such as uniform flow over a cylinder, in which $\gamma_m^* = \gamma_{max}/U_\infty$.

The following values of the numerical parameters were used in the simulations reported below: $l^* = 0.0125$, $\gamma_m^* = 0.255$, $\Delta t^* = 0.24$, $h^* = \tan(\pi/20)/2$ (forty sheet generation panels), $\delta^* = 0.125$, $p = 3$, $M = 50$, $s^* = 0.25$. These choices were based on experience with the problem of uniform flow over a cylinder and some parametric variations [14]. The singularity panels were submerged 0.005D below the cylinder surface.

6. RESULTS AND DISCUSSION

The goal of this work was to investigate Fallon's experimental results [2] numerically. To put the numerical results in context, a short summary of some of Fallon's findings is in order.

Summary of Fallon's Experiments

As mentioned in the introduction, Fallon found that only the transverse configuration (figure 1) demonstrated significantly nonlinear force histories for the range of parameters he investigated. Figure 7 shows the variations in the first harmonic of the force amplitude with kA and kD obtained by Fallon. The force response is linear for small kD and/or small kA and agrees well with linear potential theory predictions (not shown here). As kA increases, the force curves flatten and the measured forces are less than those predicted by linear potential theory. For longer waves ($kD < 0.206$) the force curves later steepen, forming a "step" shape. Comparison of the force curves with potential theory calculations implies that the viscous effects are unimportant in the initial linear range but become increasingly significant with increasing kA. Fallon used dye injection from a pipet for flow visualization. It is only possible to see the gross flow behavior in the resulting video tapes and structures like macro-vortices cannot be consistently detected. Further, one cannot infer the motion of the fluid initially near the boundary because dye was not injected in this neighborhood. In shorter waves, one can clearly see that separation never really develops and the fluid initially near the boundary stays close to the cylinder for many wave periods. Separation clearly occurs in the longer waves and dye initially near the cylinder is quickly dispersed.

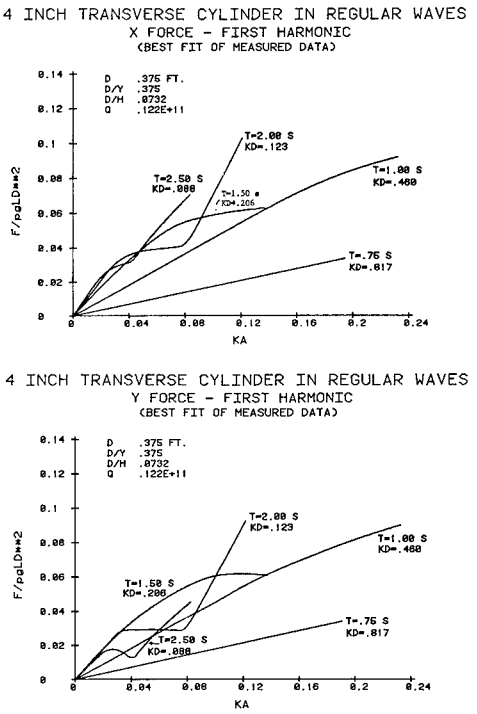


Fig. 7 Experimentally Measured Force Coefficients. The magnitude of the first harmonic component of the drag (x force) and lift (y force) forces measured by Fallon are shown. The force coefficients may be converted to drag and lift coefficients by multiplying by $4/\pi$. (From Fallon [2].)

Simulation of Fallon's Experiments

Simulations for each of three representative regions in figure 7 are presented. Two of the simulations were made for $kD = 0.1232$ - one with $kA = 0.114$, $Re = 35{,}240$ and one with $kA = 0.058$, $Re = 17{,}773$. The first case corresponds to a point on the "steep" part of a step shaped curve and the second lies in the middle of the "flat" part of the same curve. In deference to the partial neglect of the boundary conditions described above, it was desired to use the shortest waves possible. $kD = 0.1232$ was chosen because it is the shortest wave for which the experimentally measured force history was clearly non-harmonic. The third simulation was of $kD = 0.4602$, $kA = 0.218$, $Re = 35{,}774$ which lies in the nonlinear region of a typical "plateau" shaped curve. In all cases $H/D = 13.67$ and $Y/D = 2.67$

An estimate of the error caused by the partial neglect of the free surface and bottom boundary conditions can be made by comparing the predictions of the present panel method with linearized potential theory. For this comparison, no vorticity was generated. Fallon made force calculations using three-dimensional potential theory in which the linearized free surface boundary condition was satisfied. The predicted Froude-Krilov plus added mass forces are naturally harmonic. For the longest waves simulated ($kD = 0.1232$), which should give rise to the largest error, Fallon found the drag and lift coefficient amplitudes to be 0.179 and 0.155, respectively. These

results compare with the values of 0.169 and 0.146 computed by the simplified method. The difference is less than 6% in both cases, which implies that the boundary condition simplification is reasonable, at least in the vicinity of the cylinder when no vorticity is present.

The flow development is best understood by studying the evolution of the vorticity field. The three simulations show grossly similar development. The main difference between them is the degree to which the vorticity is able to move away from the cylinder. The kD = 0.1232 , kA = 0.114 case shown in figures 8 and 9 will be described first. The figures labeled "positive vorticity" are plots of the positions of the blobs with positive sign and the "negative vorticity" is similarly defined. The direction of wave propagation in the figures is left to right.

Initially, the flow is parallel to the x-axis moving from left to right. Vorticity is generated all around the boundary of the cylinder with the highest concentrations around the top and bottom where the slip velocity is greatest. As time proceeds, the forward stagnation point moves around the cylinder in a clockwise sense, as demanded by the incident waves. As this happens, the vorticity of positive sign (counter-clockwise), which initially lies on the lower part of the cylinder, is "peeled" off the surface and begins to collect into a macro-vortex. The negatively signed vorticity that was initially formed at the top of the cylinder also forms into a large cloud, but it remains close to the boundary. All the while, new vorticity is being formed. The macro-vortex is able to move well away from the cylinder. It interacts with the negative macro-vortex lying close to the cylinder, forming a jet through the region between them. The macro-vortex moves far enough away from the cylinder that it is not smashed into the cylinder during the second half of the wave cycle. The predominantly positive macro-vortex tends to entrain vorticity from the predominantly negative cloud lying close to the cylinder resulting in a pair of oppositely signed macro-vortices.

In the second simulation (kD = 0.1232, kA = 0.058), a distinct macro-vortex forms but it does not move sufficiently far from the cylinder to avoid being washed back into it and broken up. The break-up process tends to weaken the vortex by mixing it with oppositely signed vorticity lying near the cylinder. The jet is present in this case too, but it is not as extensive.

The short wave case does not form a distinct macro-vortex but rather a "bulge" in the vorticity field. The net strength of the vorticity field remains small and only the part of the velocity field in the immediate area of the cylinder is disturbed by the presence of the vorticity. The differences in the extents of the vorticity fields in the three simulations is illustrated in figure 10 which compares these fields at non-dimensional time 10.8 (after about 1 3/4 wave cycles).

Comparison of the calculated forces with Fallon's measured forces for the (kD = 0.1232 , kA = 0.114) simulation is a bit problematical. Both calculated and measured forces are non-harmonic, so a time series analysis is required to properly compare them. Such an analysis could not be performed on the calculated results because the simulation was so short (three cycles). The simulation could not be extended because of the tendency of the vorticity to move through the free surface after about two cycles. The calculated forces (figure 11) show the double peaks an inflection points evident in Fallon's measurments. A crude quantitative comparison can be made by estimating and comparing the average of the peak amplitudes. The calculated forces show an average of about 0.08 for both lift and drag coefficients vs. about 0.12 for Fallon's results.

The other simulations produce nearly harmonic force histories so the amplitudes can be directly compared with the experiments. For the (kD = 0.1232 , kA = 0.058) case (figure 12) the calculated and measured lift and drag coefficients were (0.051, 0.039) and (0.051, 0.038) respectively. The (kD = 0.4602, kA = 0.218) case (figure 13), gave (0.012, 0.012), calculated vs. (0.012, 0.011) measured.

The difference between the simulated forces and those that would be predicted by linear potential theory can be seen by comparing the total force coefficients with the "potential force" component. The linearity of (29) allows one to decompose the total force into components. Figures 11-13 show the total lift and drag force coefficients and components labeled "vorticity force" and "potential force". The potential force is the force that would be computed by linear potential theory with the boundary condition approximations discussed above. The vorticity force is the force due to the presence of the vorticity which might also be called the "viscous effects" (though no skin friction is included). The vorticity force contains contributions from both summations in (29) because the presence of the vorticity affects the time history of γ. The fact that the present numerical method allows a rigorous decomposition of the total force is significant since many people think qualitatively about flow problems this way and because many empirical force predictors, like the Morison equation use it. Thus, it would seem that the random vortex method, as formulated here, might be ideal for studying Morison's equation and perhaps developing correction terms to make it more accurate.

Using the simulation results, it is possible to associate characteristic flow behavior with the distinctive areas of Fallon's force response curves (figure 7). The typical "step" shape of these curves has three distinct regions: an initial linear part, a plateau, and a later steep region. Equation (29) shows that the force due to the vorticity is the product of the strength of the vorticity and the velocity at the vortex due to the other vorticity and the body. The incident velocity enters only indirectly through its effect on the body source panel strength.

In the linear region, a fairly thin Stokes-type layer forms in which vorticity of both signs is continually generated. The vorticity is unable to escape the region immediately outside the boundary and it is soon annihilated through mixing. The vorticity induces little force on the cylinder because isolated regions of vorticity of a dominant sign are unable to form. The necessity of such formations for force production can be inferred from equation (29).

Flows in the plateau region are characterized by macro-vortex formation near the boundary. These vortices are unable to move far enough from the cylinder to avoid being pushed back up against it during the rest of the wave cycle. When the macro-vortices are pushed against the boundary they tend to break up and mix with oppositely signed vorticity, thus dissipating themselves. Nevertheless, the result is a significant force component due to the vorticity. This force is out of phase with the Froude-Krilov and added-mass forces leading to a reduced total force. The vorticity induced force stays fairly periodic, probably because the convection of the vorticity is dominated by the wave induced potential flow rather than vortex-vortex interaction.

In the steep part of the force response, flows are characterized by vortex shedding. Vorticity accumulates into lobes of a dominant sign that are peeled off the cylinder and are able to move away from it. These macro-vortices tend to suck oppositely signed vorticity out of the vorticity pool in the wake of the cylinder to create near-dipole pairs. The pairs tend to mix and annul each other's effect on the velocity field in time. The forces produced in these flows tend to be irregular, which likely reflects the increased importance of vortex-vortex interaction in the convection.

In a typical simulation, the number of computational elements after two cycles was around 5000 and the rate of increase of the total number is linear with time. The number of vortex sheets reaches a quasi-steady value after only a few time steps (a typical value is 200). The required CPU time to perform a typical simulation (say 50-80 time steps) was around 1 hour on an IBM 3081 model K computer.

Effect of Current/Forward Speed

To get and idea of the effect of a current or forward speed on the problem, the simulation with $kD = 0.1232$, $kA = 0.114$ was re-run with a current. The current was scaled to be equivalent to a 1/2 knot current acting on a 1.0 foot diameter cylinder (Froude number $v/\sqrt{gD} = 0.149$). The current direction was chosen to be in the direction of wave propagation (left to right in the figures) and the wave frequency was adjusted to frequency of encounter. At the depth of the center of the cylinder, the ratio of the current velocity to the maximum wave induced velocity (in the absence of the cylinder) is 0.59.

A comparison of the simulations with and without current is shown in figures 14 and 15. The times shown are both nondimensionalized with the wave frequency (not frequency of encounter) and thus correspond to equal dimensional times. One sees about what one would expect. In the presence of the current, more computational elements are generated because the slip is greater on the average. A similar vorticity evolution occurs but the current tends to wash the vortex structures downstream and the wake behind the cylinder is bigger at every time step. The increased perturbation of the velocity field caused by the current corresponds to higher drag forces as shown in figure 14. The lift forces are also somewhat larger in the presence of the current.

7. CONCLUSIONS

The major conclusions of the preceding may be summarized as follows:

- The random vortex method algorithm was developed to simulate the flow of a viscous fluid governed by the Navier-Stokes equations. It was seen to have a much sounder theoretical basis than earlier vortex methods and to have important advantages over Eulerian methods, such as finite difference and finite elements methods, for high Reynolds number flows.
- The RVM is very flexible and can be hybridized with the full repertoire of potential theory methods to accommodate most any incident flow and boundary conditions.
- One of the most difficult problems with the RVM is the cost of the convection calculation. It was argued that Eulerian schemes for accelerating these calculations, such as the vortex-in-cell VIC method, are not appropriate for use with the random vortex method. Instead, a Lagrangian method based on series expansion, dubbed the discrete-vortex-in-cell method (DVIC), was introduced. This method was shown to be capable of reducing the computational burden from $O(N^2)$ to $O(N^{1.5})$, where N is the number of vortex blobs, while maintaining very high accuracy.
- Numerical simulations were made of the wave flow over a transversely oriented cylinder. The results were compared with the experiments of Fallon [2]. Agreement was good, especially considering the fact that a fairly crude treatment of the free surface boundary condition was given. The predicted forces showed all of the qualitative behavior observed by Fallon and quantitative error was about 30% at worst, and less than 10% for two out of the three simulations.
- It was possible to interpret the characteristic regions of the force response curves obtained by Fallon with the behavior of the vorticity field. The ability of the vorticity to escape the immediate area around the cylinder was seen to be necessary for significant nonlinear force response to occur.
- A simulation including waves and a current showed an increase in both drag and lift forces over the waves-only case.

The work presented here is not an exhaustive study, but rather an exploration of the applicablity of the random vortex method to the study of the problem of wave flows over bluff bodies. In general the results were quite favorable and would seem to warrant further application of the method to this important problem.

ACKNOWLEDGEMENTS

I would like to thank Professors W. C. Webster and F. S. Sherman of U. C. Berkeley for their many helpful discussions during the course of this work. I also gratefully acknowledge the generous support of the organizations that sponsored this research. The principal sponsor was the Office of Naval Research under contract N000014-84-K-0026. Mainframe and micro-computer support were provided by IBM under the DACE grant at U. C. Berkeley.

REFERENCES

1. Morison, J. R., O'Brien, M. P., Johnson, J. W. and Schaaf, S. A. 1950. The force exerted by surface waves on piles. AIME Pet. Trans. 189, pp. 149-154.

2. Fallon, W. J. 1984. An experimental study of some of the fundamental aspects of wave induced forces on cylindrical objects. Ph.D. Dissertation, University of California, Berkeley.

3. Roache, P. J. 1976. Computational fluid dynamics. Albequerque: Hermosa.

4. Lamb, H. 1945. Hydrodynamics. New York: Dover.

5. Thwaites, B., ed., 1960. Incompressible aerodynamics. Oxford: Oxford University Press.

6. Rosenhead, L. 1931. Formation of vortices from a surface of discontinuity. Proc. R. Soc. Lond. ser. A 134, pp. 170-192.

7. Westwater, F. L. 1935. The rolling up of a surface of discontinuity behind an aerofoil of finite span. ARC R&M 1692.

8. Abernathy, F. H. and Kronauer, R. E. 1962. The formation of vortex streets. J. Fluid Mech. 13, pp. 1-20.

9. Deffenbaugh, F. D. and Marshall, F. J. 1976. Time development of the flow about an impulsively started cylinder. AIAA J. 14, pp. 908-913.

10. Sarpkaya, T. 1968. An analytical study of separated flow about circular cylinders. J. Basic Engr.

ser. D 90, pp. 511-520.
11. Sarpkaya, T. 1975. An inviscid model of two-dimensional vortex shedding for transient and asymptotically steady flow over an inclined plate. J. Fluid Mech. 68, pp. 109-128.
12. Sarpkaya, T. and Schoaff, R. L. 1979. Inviscid model of two-dimensional vortex shedding by a circular cylinder. AIAA J. 71, pp. 1193-1200.
13. Clements, R. R. and Maull, D. J. 1975. The representation of sheets of vorticity by discrete vortices. Prog. Aero. Sci. 16, pp. 129-146.
14. Tiemroth, E. C., 1986. The simulation of the viscous flow around a cylinder by the random vortex method. Ph.D. Dissertation, University of California, Berkeley.
15. Chorin, A. J. 1973. Numerical study of slightly viscous flow. J. Fluid Mech. 57, pp. 785-796.
16. Chorin, A. J. 1978. Vortex sheet approximation of boundary layers. J. Comp. Phys. 27, pp. 428-442.
17. Chorin, A. J. 1980. Vortex models and boundary layer instability. SIAM J. Sci. Stat. Comput. 1, pp. 1-21.
18. Leonard, A. 1980. Vortex methods for flow simulation. J. Comp. Phys. 37, pp. 289-335.
19. Lighthill, M. J. 1963. Introduction: Boundary layer theory. Chapter 2 in Laminar Boundary Layers, ed. L. Rosenhead, Oxford: Oxford Univ. Press.
20. Batchelor, G. K. 1967. An introduction to fluid dynamics. Cambridge: Cambridge University Press.
21. Chorin, A. J., Hughes, T. J. R., McCracken, M. and Marsden, J. E. 1978. Product formulas and numerical algorithms. Comm. Pure Appl. Math. 31, pp. 205-256.
22. Einstein, A. 1956. *Investigations on the theory of brownian movement.* New York: Dover.
23. Ghoniem, A. F. and Sherman, F. S. 1985. Grid-free simulation of diffusion using random walk methods. J. Comp. Phys. 61, pp. 1-37.
24. Cheer, A. Y. 1983. Numerical study of incompressible slightly viscous flow past blunt bodies and airfoils. SIAM J. Sci. Stat. Comput. 4, pp. 685-705.
25. Cheer, A. Y. 1983. Numerical analysis of time dependent flow structures generated by an impulsively started circular cylinder in a slightly viscous incompressible fluid. Ctr. Pure Appl. Math. U. C. Berkeley PAM-145.
26. Beale, J. T. and Majda, A. 1981. Rates of convergence for viscous splitting of the Navier-Stokes equations. Math. Comp. 37(156), pp. 243-259.
27. Hald, O. 1979. Convergence of vortex methods for Euler's equations. II. SIAM J. Numer. Anal. 16, pp. 726-755.
28. Beale, J. T. and Majda, A. 1982. Vortex methods II: Higher order accuracy in two and three dimensions. Math. Comp. 39(159), pp. 29-52.
29. Anderson, C. and Greengard, C. 1985. On vortex methods. SIAM J. Numer. Anal. 22, pp. 413-440.
30. Teng, Z. H. 1982. Elliptic-vortex method for incompressible flow at high Reynolds number. J. Comp. Phys. 46, pp. 54-68.
31. Spalart, P. R. and Leonard, A. 1981. Computation of separated flows by a vortex-tracing algorithm. AIAA 14th Fluid and Plasma Dynamics Conf., Palo Alto.
32. Spalart, P. R. 1984. Two recent extensions of the vortex method. AIAA 22nd Aero. Sciences Meeting, Reno.
33. Stansby, P. K. and Dixon, A. G. 1983. Simulation of flows around cylinders by a Lagrangian vortex scheme. Appl. Ocean Res. 5, pp. 167-178.
34. van der Vegt, J. J. W. and Huijsmans, R. H. M. 1984. Numerical simulation of flow around bluff bodies at high Reynolds numbers. Fifteenth Symp. Naval Hydro., Hamburg, pp. 569-585.
35. van der Vegt, J. J. W. and de Boom, W. C. 1985. Numerical simulation of flow around circular cylinders at high Reynolds numbers. BOSS , pp. 227-238.
36. Beale, J. T. and Majda, A. 1985. High order accurate vortex methods with explicit velocity kernels. J. Comp. Phys. 58, pp. 188-208.
37. Pearlman, M. 1985. On the accuracy of vortex methods. J. Comp. Phys. 59, pp. 200-223.
38. Webster, W. C. 1975. The flow about arbitrary, three-dimensional smooth bodies. J. Ship Res. 19, pp. 206-218.
39. Yeung, R. W. 1982. Numerical methods in free-surface flows. Ann. Rev. Fluid Mech. 14, pp. 395-442.
40. Graham, J. R. M. 1980. The forces on sharp-edged cylinders in oscillatory flow at low Keulegan-Carpenter numbers. J. Fluid Mech. 97, pp. 331-346.

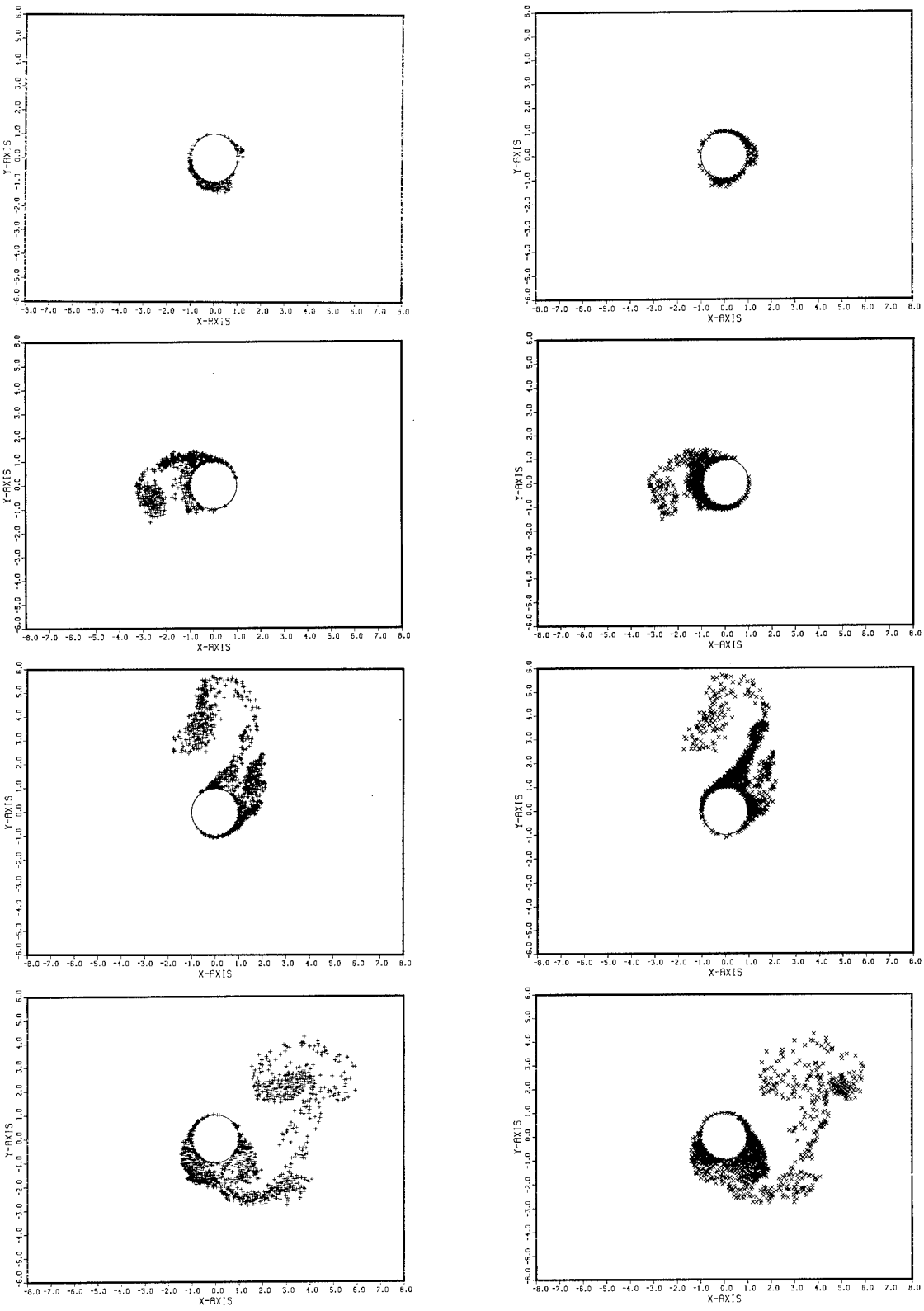


Fig. 8 Simulated Vorticity Field for: kD = 0.1232, kA = 0.114, $\Delta t^* = 0.24$. The left column shows the positive vorticity and the right column shows the negative vorticity. Times shown on this page are (from top to bottom): $t^* = 1.2, 3.6, 6.0, 8.4$.

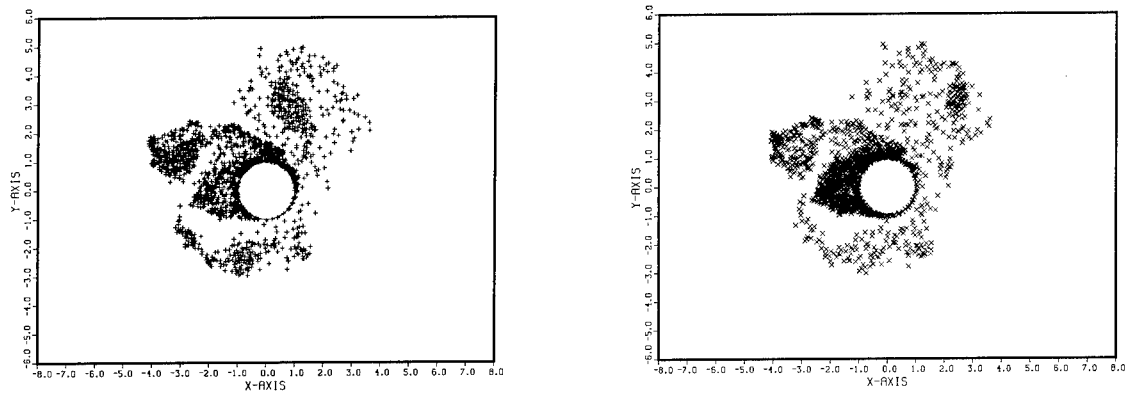


Fig. 8 (cont) t = 10.8 is shown.*

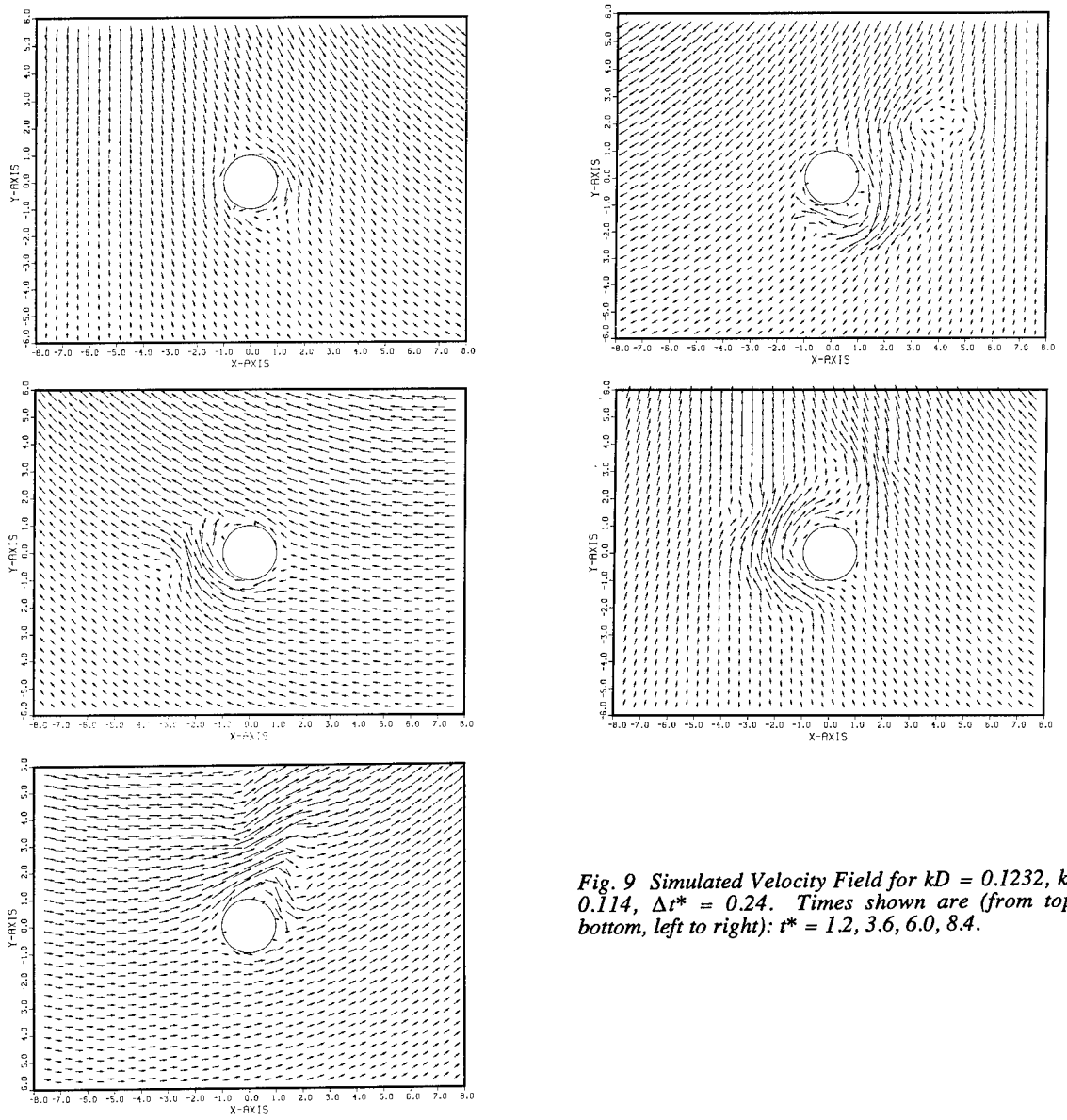


Fig. 9 Simulated Velocity Field for kD = 0.1232, kA = 0.114, Δt = 0.24. Times shown are (from top to bottom, left to right): t* = 1.2, 3.6, 6.0, 8.4.*

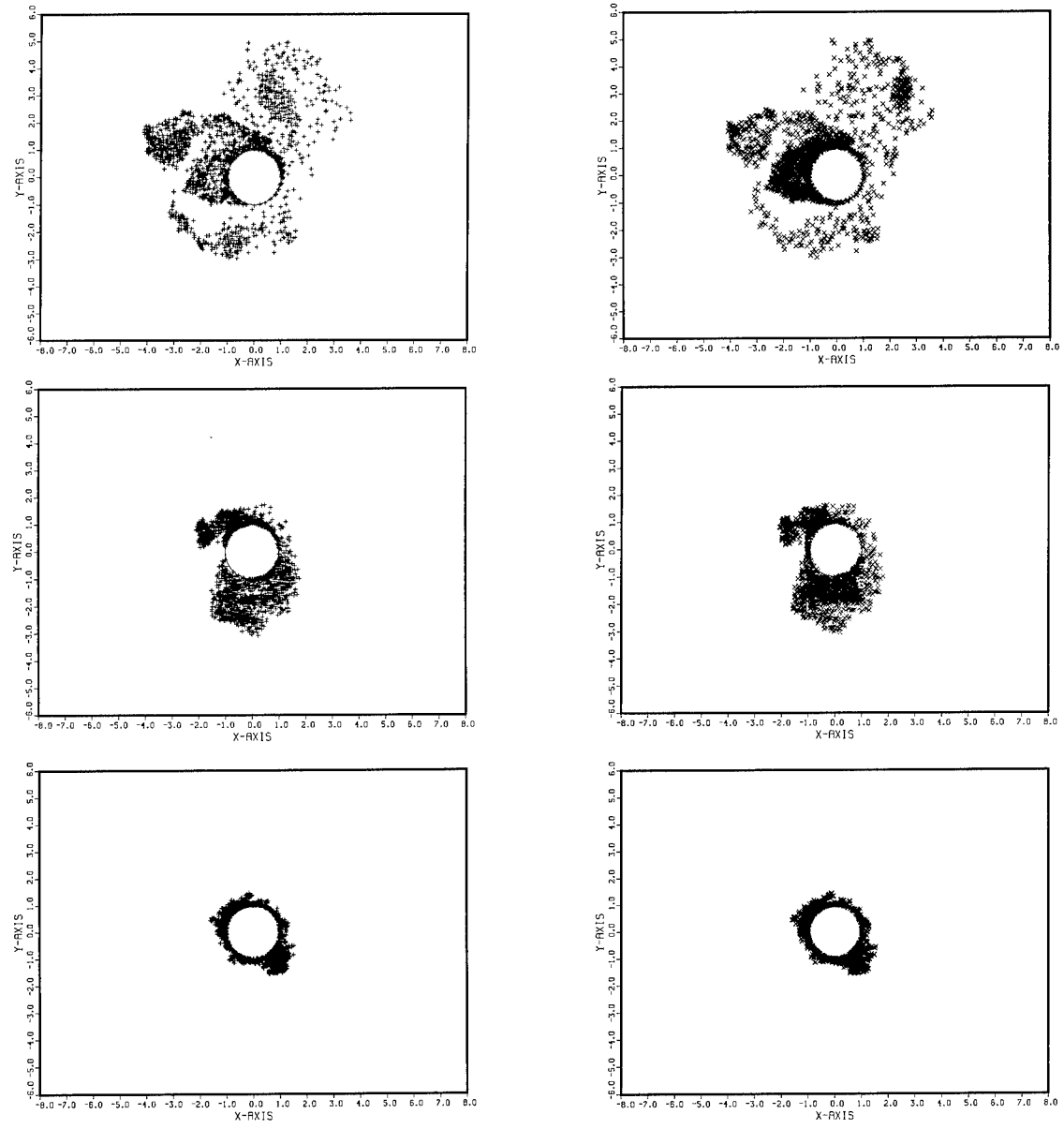


Fig. 10 Comparison of Vorticity Fields. The vorticity fields at t = 10.8 are shown for (from top): (kD = 0.1232, kA = 0.114), (kD = 0.1232, kA = 0.058), and (kD = 0.4602, kA = 0.218). Positive and negative vorticity distributions are shown in the left and right columns, respectively.*

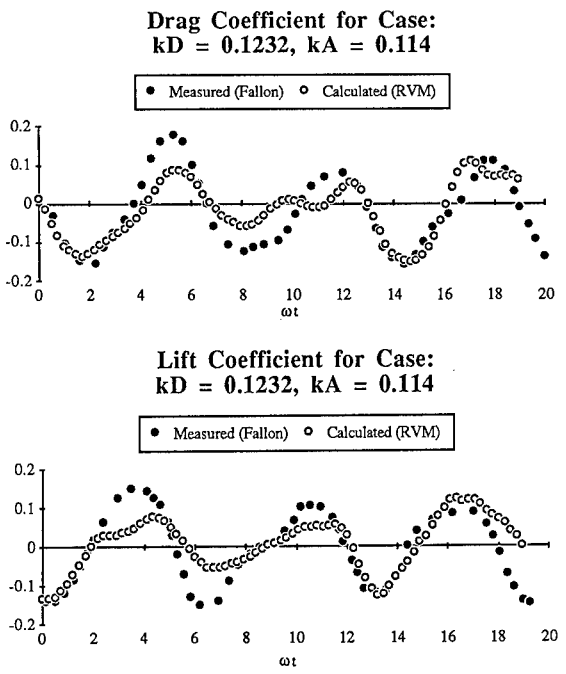


Fig. 11a Comparison of measured and calculated force coefficients.

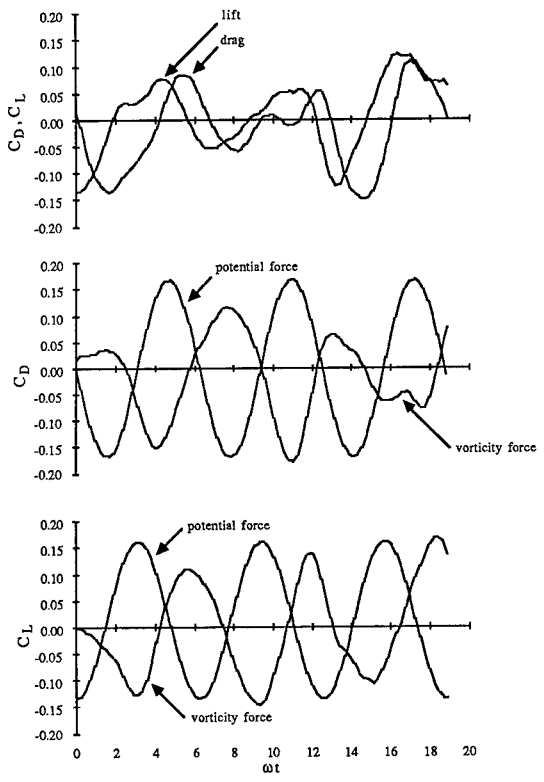


Fig. 11b Force History for kD = 0.1232, kA = 0.114. The top graph shows the total drag and lift coefficients and the lower plots show the force components.

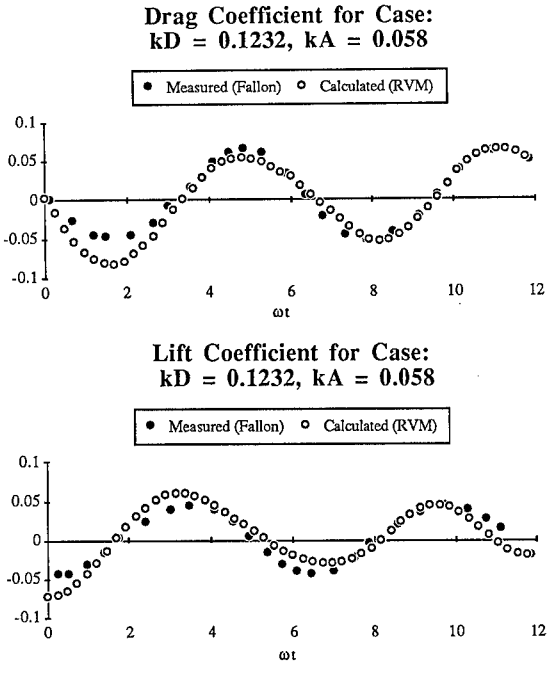


Fig. 12a Comparison of measured and calculated force coefficients.

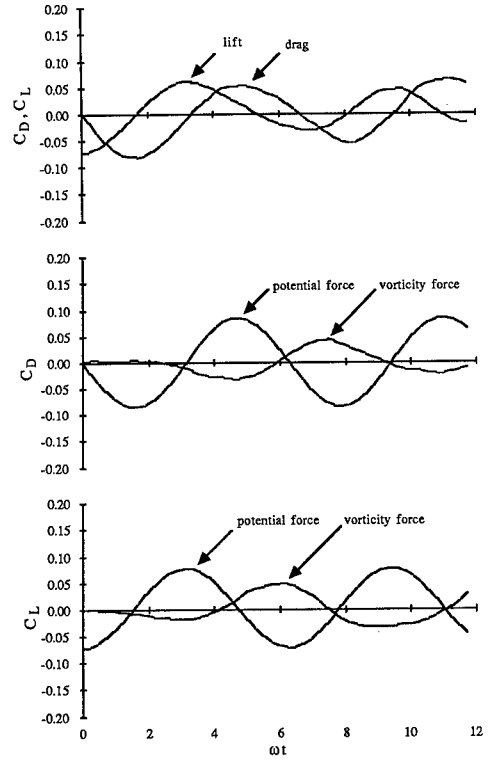


Fig. 12b Force History for kD = 0.1232, kA = 0.058. The top graph shows the total drag and lift coefficients and the lower plots show the force components.

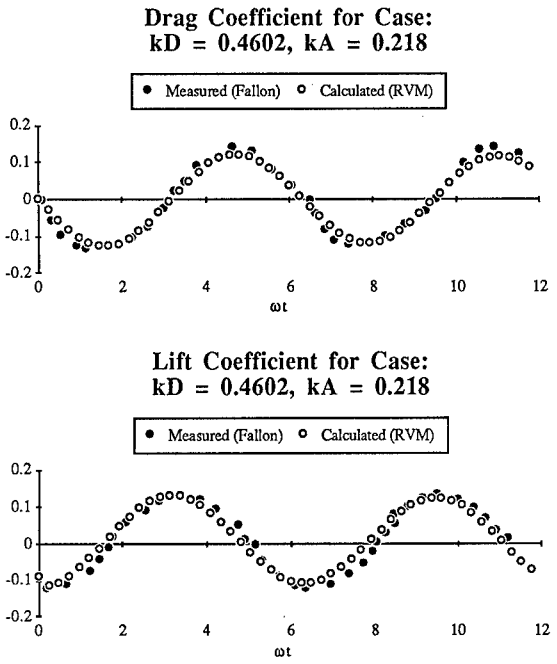


Fig. 13a Comparison of measured and calculated force coefficients.

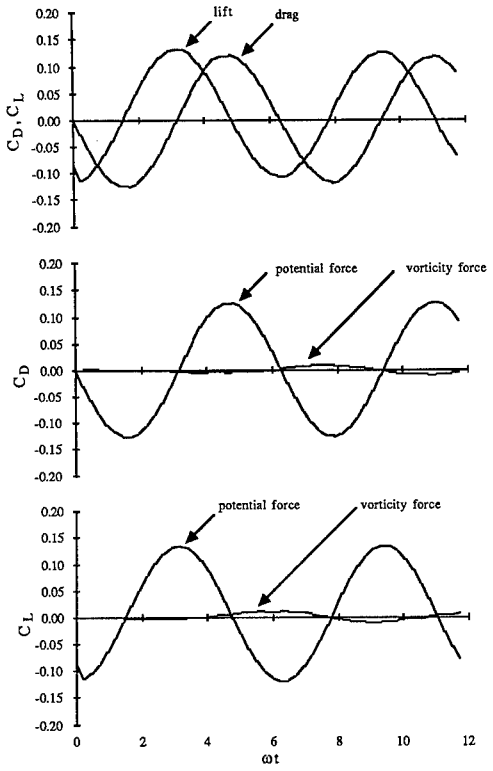


Fig. 13b Force History for kD = 0.4602, kA = 0.218. The top graph shows the total drag and lift coefficients and the lower plots show the force components.

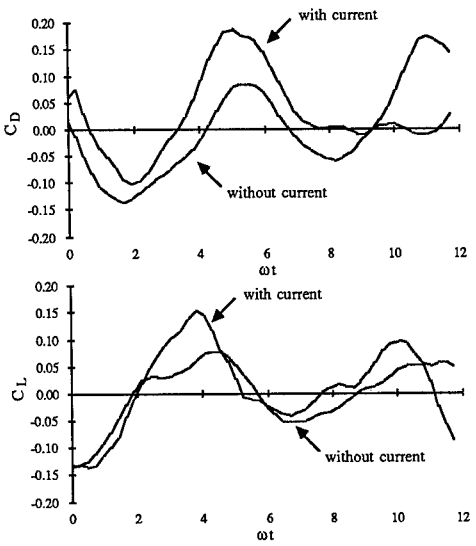


Fig. 14 Force History for kD = 0.1232, kA = 0.114 With and Without a Current. The current flows in the direction of wave propagation with Froude number 0.149.

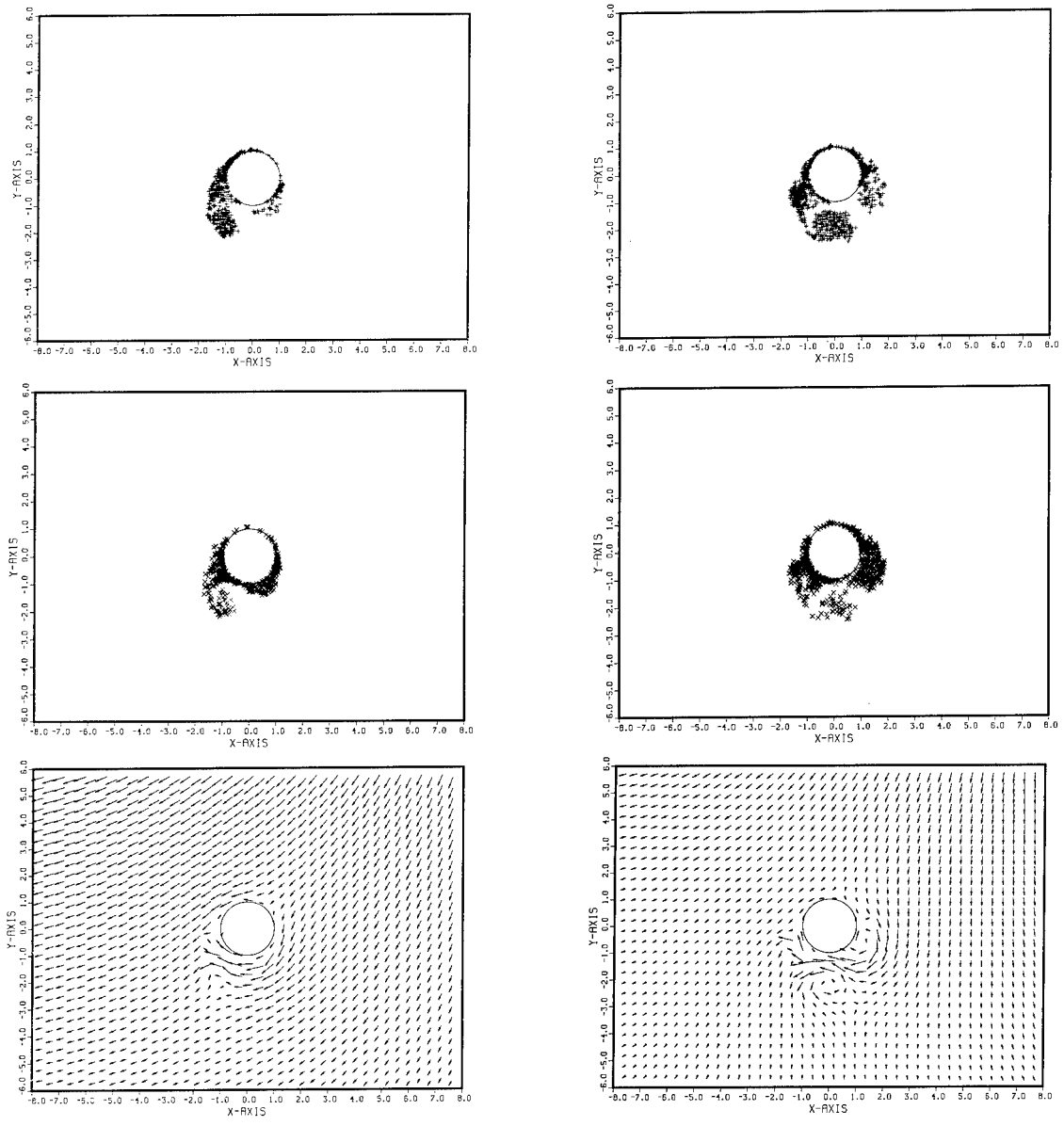


Fig. 15a Effect of Current, kD = 0.1232, kA = 0.114, t = 2.4. The left column shows the Froude number = 0 case and the right column shows Froude number = 0.149. Shown are (from the top): the positive vorticity field, the negative vorticity field, and the velocity field.*

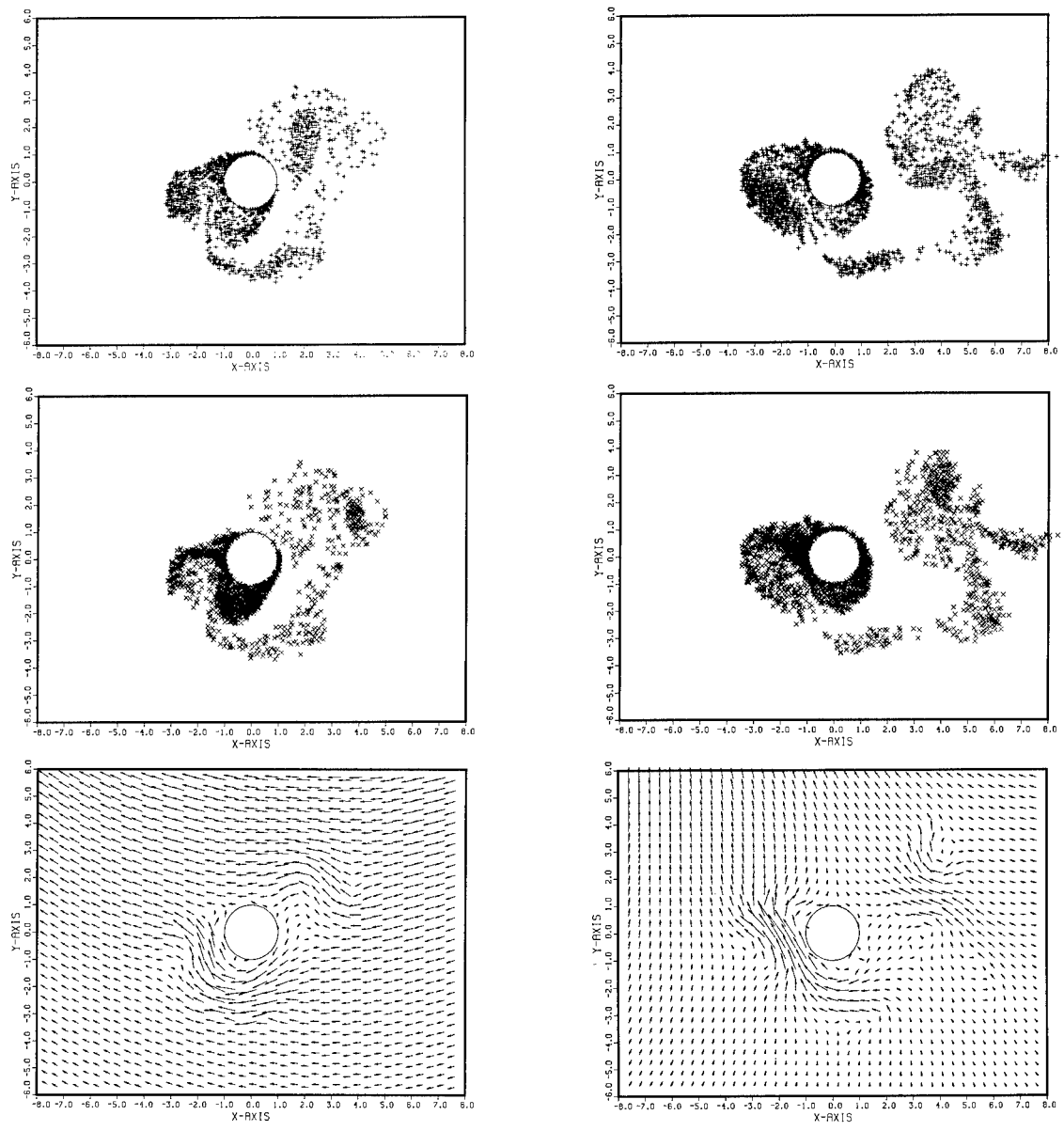


Fig. 15b Same as 15a but for t = 9.6.*

DISCUSSION

Alexandre Chorin,
University of California, Berkeley

I would like to congratulate Tiemroth on his excellent paper, and add the following comment: the convergence of the random vortex method has been proved. In the absence of boundaries there are two proofs: J. Goodman, in press, Comm. Pure Appl. Math, and D.G. Long, Ph.D. Thesis, Math Dept., UC Berkeley, 1986. With a flat boundary, there is an analysis in a paper by G. Benfatto and M. Pulvirenti, in press, Comm. Math. Phys., and for a general boundary, still unpublished results by C. Anderson of UCLA.

R. H. M. Huijsmans & J. J. W. van der Vegt,
Maritime Research Institute Netherlands

We first want to congratulate the author with his of the paper regarding an interesting topic. We would like the author to react regarding a few comments and a few questions we would like to pose.

Diffusion

The necessary boundary condition for diffusion is reflection of vortices at the boundary (Chorin [21]), therefore, vortices reentering the body may not be discarded.

It is in our opinion impossible to decrease the diffusion time step in order to remove the effect of the wall by reducing the variance. The diffusion time step is related to the convection time step, this restriction would result in an unnecessarily small time step.

A question regarding the boundary condition applied by the author: Will the blobs become sheet elements when they reenter the boundary layer?

A more fundamental question with respect to the sheets is that boundary layer theory (which describes the sheet) is not valid close to separation points. How did the author overcome this problem?

Considering the operator splitting algorithm: Did the author update the velocity field after each diffusion step and after the creation of vortices, otherwise, convergence is not $O(t^2)$?

Choice of Kernel

The choice of the kernel of the blob has been known to give an accurate solution only for very small time steps (Hald [26]) it is also possible to use a gaussian blob core diameter. This blob core could easily have been incorporated in the present study, using results as e.g. given by van der Vegt and Huijsmans [34]. The accuracy of the VIC method employed by van der Vegt et al. [34], [35] is much higher than reported by the author. In ref [35] the reported max error amounts to .05% (not 5%!). In the same articles a variational method was discussed in which the gaussian vorticity distribution in the blob core was related to the VIC method, through the use of the filter in their method.

Operational Count

The operational count of the DVIC method is in our opinion still a quadratic process, because the minimization process of the number of vortices per cell is incorrect; the number of vortices per cell is controlled by the physics of the flow. The advantage of this reported method is than that the coefficient of this $O(N^2)$ process is decreased to $O(N^2/n)$. The key item in vectorization of the presented algorithm will be the sorting and regrouping process of the vortices per cell. These type of processes do vectorize well. The situation can be even worse if the code would be completely vectorized, because the number of vortices per cell can be very small, leading to an operational count lower than in SCALAR mode, due to the short vector length.

The justification of the use of a source layer for the representation of the body is not clear to the discusser - why not use a mixed vortex/source layer ([34], [35]) ? The use of a vortex distribution is more consistent with the description of the flow. Unclear is also the motivation for solving the integral equation for the source layer using a first kind Fredholm representation.

Calculation of the forces

The paper discusses the simulation of a viscous flow. Why not use a viscous force formulation instead of the "potential" theory formulation based on the Blasius equation?

Discussion of results

The presented pictures of the flow field lack resolution, which is claimed to be the main advantage of the DVIC? A somewhat strange behaviour of the far field of the flow is observed in fig. 9. Is the chosen time step of 0.24 to large for accurate results?

Reply -

I would like to thank all of the discussants for their insightful questions and comments. Professor Chorin has provided a timely update on the theoretical aspects of the method and I am indebted to him for that. Let me now turn to the questions raised by Drs. Huijsmans and van der Vegt.

The effect of the boundary on the diffusion problem is a subtle one. The proper procedure depends upon the type of computational element being considered. One of the principal advantages of the vortex sheet algorithm is the applicability of a simple reflection principle for sheets which tend to diffuse through the wall.

The vortex sheet segments are assumed to be governed by the Prandtl boundary layer equations. Two approximations implicit in the use of the boundary layer equations are the definition of the vorticity given in equation (12), and the assumption that the wall is locally plane. It is these two assumptions that allow a reflection principle to be derived. Following Chorin [17], the velocity field can be continued anti-symmetrically across the (locally) plane wall and the "vorticity" defined by (12) then becomes symmetric about the wall. The diffusion problem associated with the boundary layer equations is one-dimensional in the direction normal to the wall. Discretization of the well-known Green function solution to this problem leads to the reflection principle.

The vortex blobs are governed by the full Navier-

Stokes equations. In this case the appropriate definition for the vorticity ($\xi = \nabla \times \mathbf{u}$) involves both normal and streamwise derivatives of the velocity. As a result, if one continues the velocity field anti-symmetrically as previously described, the vorticity field is generally neither symmetric nor anti-symmetric about the wall. Further, the associated diffusion problem is no longer one-dimensional. Thus, the reflection principal used for the sheets is not applicable to the blobs and, apparently, no similar principal has been derived for them. The random vortex method seeks to avoid the problem of accounting for the effect of the the boundary on the diffusion of the blobs by preventing the blobs from getting close enough to the boundary to be affected by it, as described in section 2. There is of course always the possibility that a blob could take a large enough random walk to broach the boundary, however, if this is a rare occurrence and since there are many blobs, one expects that the treatment of that blob would not significantly effect the simulation.

As Messrs. Huijsmans and van der Vegt have noted, it is necessary to reduce the time step, as the sheet layer thickness is reduced, in order to prevent too many blobs from broaching the boundary. This certainly could lead to a small time step, but I am not sure that it would be "unnecessarily small". In using this term I assume that the discussants mean that the time step required to obtain accurate diffusion steps might be much smaller than the time step required to obtain accurate convection steps. This could be the case, but regardless of whether the diffusion simulation or the convection simulation requires the smallest time step, one must necessarily use a small enough time step that the overall algorithm produced an acceptably accurate simulation.

When the blobs enter the sheet layer, they do become sheets. I emphasize that the sheet layer and boundary layer are two different things. The boundary layer is a physical entity which has a small thickness scale but is, in reality, always infinite in extent. The sheet layer, in contrast, is a mathematical artifice that is always of small finite thickness. In general, the two are not coincident and the sheet layer should usually be thinner than the boundary layer. This is an important point in regard to the question of the applicability of the boundary layer equations to determining the motion of the vortex sheet segments.

Perhaps the question of the applicability of the boundary layer equations in the sheet layer is settled in the recent work cited by Professor Chorin, which I am sure the discussants will consult. Unfortunately, I cannot comment on it, as I have not seen the papers. Instead, I shall give the reasoning that stands behind my own work.

The primary reason for combining the vortex sheet algorithm with the vortex blob algorithm is empirical evidence that the hybrid algorithm works better [17]. This is generally attributed to improved modeling of the vorticity generation and the motion of the vorticity in the immediate vicinity of the boundary. I believe these improvements are due to the more suitable shape of the sheet segments, as compared to the circular blobs, and the diffusion model associated with the boundary layer equations discussed above.

The random vortex method relies on the vortex blobs to simulate both the boundary layers and any separated flow regions. In order for this to be possible, the sheet layer is made thin compared to the boundary layer. For most practical problems, including the ones addressed in this paper, it is not essential that every detail of the flow in the sheet layer region be modeled. It is only necessary that the vorticity flux through this region be well approximated. If the latter requirement is satisfied, the overall flow will be properly simulated since it differs from the potential flow only by the dynamics of the vorticity which is generated at the boundary. The predicted pressure forces will also be accurate because, according to the Navier-Stokes equations [31], the pressure only depends on the flux of vorticity through the boundary. The shear stress force may be inaccurate, but it is not significant compared to the pressure force in flows involving large scale separation, so one can live with this deficiency. In summary, the boundary layer equations are not being used to model the entire boundary layer, but rather to model a "vorticity generation layer". The model seems to be successful, and heuristic arguments have been made to explained its success. I should add that the expected "drag crisis" was not observed in simulations of steady incident flow over a cylinder reported in [14], though, the approximation of two-dimensional flow is at least as suspect in this regard as the sheet layer model.

With regard to the time stepping procedure, the velocity field was updated after each diffusion step.

In selecting the vortex blob core function, one seeks the choice that will make the algorithm as accurate as possible. That choice is not necessarily the same for problems in which boundaries are present as for problems in which boundaries are absent. The studies cited by the discussants as well as others ([36], [37]) have shown that, for problems without boundaries, certain classes of core functions give more accurate simulations than others. Apparently, no similar studies have been done in which boundaries have been present. It would be sensible to use one of these higher order core functions for problems with boundaries, as long as such a choice does not interfere with other parts of the algorithm. In the random vortex method, however, one must consider the metamorphosis between the sheets and blobs in choosing a core function. The sheets and blobs induce different velocity fields. As a result, there is a discontinuous change in the induced velocity field at the instant of metamorphosis. This effect can be minimized with the proper choice of core function. The flow between the sheet and the wall is the most important part of the sheet's induced velocity field because it strongly influences the generation of vorticity on the wall below it. The discontinuity in this part of the velocity field is greatly reduced by choosing a Rankine core function. As mentioned in the paper, a Rankine core function of appropriate strength (plus its image) induces the same velocity field between its center and the wall as a vortex sheet segment does, while, for example, the Gaussian core function suggested by the discussants does not. Thus, I have chosen to forego the probable, but unproven, improvements associated with the higher order core functions in order to obtain better behavior of the algorithm in the critical boundary region.

The stated accuracy of 5% for the modified Vortex-In-Cell method used by van der Vegt et. al was correctly cited from section 4 of reference [34]. In reference [35]

computations were made using a much finer grid which resulted in the lower error figure of 0.05%. This is not surprising since one expects to be able to make the error of a convergent numerical method arbitrarily small by choosing a fine enough discretization. In the paper I am interested in communicating van der Vegt's & Huijsmans' comparison [34] of their method with the standard VIC method used in [33], and it is in this comparison that the 5% and 50% figures arise. I infer that the 5% and 50% error figures correspond to similar discretizations. It would not have been correct for me to give the 50% error figure for Stansby's & Dixon's [33] method together with the 0.05% figure for van der Vegt et al., since different discretizations were used. As far as comparing the method of van der Vegt et al. with the DVIC scheme is concerned, I can only reiterate the comments I made in the paper concerning the difficulty in comparing Eulerian and Lagrangian schemes in a rational way.

The discussants have conjectured that the operation count of the DVIC algorithm for a general distribution is actually quadratic in N. The discussants' expression, $O(N^2/n)$, cannot be correct because, as n approaches infinity, the operation count approaches the Biot-Savart limit of $O(N^2)$ - not zero! Since I have not been able to make an analysis of the algorithm for a general configuration of blobs, I cannot give a definitive answer as to what the operation count will be with a non-uniform distribution of blobs. Instead, I can only report that I have performed numerical experiments [14] for the "realistic" problem of steady flow over a cylinder and observed growth rates of CPU time with N of between 1.5 and 1.6.

The question of "vectorize-ability" of the algorithm is an important one. I agree with the discussants' that some parts of the algorithm will not vectorize well, however that does not necessarily mean that the algorithm would lose all of its relative speed advantage on a vector computer. The only way to settle the question is to try the algorithm on a vector computer, which I have so far not had the opportunity to do.

As mentioned in the paper, discussion of the singularity solution of the potential problem is clouded by the fact that the term "source" has several interpretations. "Source" is sometimes used to mean the fundamental solution or Green function, and sometimes used to name the flux emitting singularity. If the potential problem is posed in terms of the velocity potential, then the Green function is the flux emitting singularity, and there is no confusion. If the problem is formulated in terms of the stream function, as it is here, then the Green function "source" is actually a discrete vortex. As stated in the paper, the terms "source" and "dipole" are used to refer to the Green function and its first spatial derivatives - which are actually vortices and vortex-dipoles, respectively. Thus, the "source layer" is actually a vortex layer.

The justification for using the "source"-only singularity distribution is as follows: The use of two singularity distributions will always involve more computation for a given number of collocation points than the use of a single distribution. The use of a "dipole"-only distribution is not possible because the circulation condition cannot, in general, be satisfied by such a distribution. This arises from the fact that a "dipole" (vortex-dipole) has zero net circulation. Thus, one is led to choose the "source" (vortex layer) distribution. I shall add one caveat: while the first justification is true, it may be that a combined "source"-"dipole" distribution can produce a more accurate solution, such that fewer collocation points are required to achieve a given accuracy. In such a case, the combined distribution could be superior. In the present work I experimented with the combined distribution and found it to be less efficient in achieving a given accuracy level than the source-only scheme, but this may not be the case in every situation.

The advantage to using the a submerged singularity distribution, which results in a Fredholm integral equation of the first kind, is, as was stated in the paper, that one can often obtain higher accuracy for a given number of singularity panels than with a surface distribution. Another advantage is that the entire fluid domain, including the boundary, is analytic. Since this technique is not part of the original work contained in my paper, I shall limit my discussion of it and refer the discussants to reference [38].

The key factor in the choice of force evaluation method was the ability to decompose the total force in to "potential" and "vorticity induced" components. Equation (29) enables one to do this and shows very explicitly how the interaction of the blobs with the irrotational flow gives rise to the latter force component. Such a decomposition is important because popular methods for force prediction that one might like to study through simulation, like Morison's equation, use it. As stated in the paper, the only part of the total viscous force that is neglected is the viscous "skin friction" which is known to be small compared to the pressure force. For many uses, a viscous flow based force evaluation procedure would be more direct and theoretically appealing, and I know that Dr. van der Vegt has used one [35]. A Navier-Stokes based method for computing the pressure force that only requires the observation of the flux of vorticity through the boundary is given in [31].

I claimed that the random vortex method, not the DVIC velocity evaluation scheme, gave better flow resolution than the VIC based schemes. It should be possible to substitute any sufficiently accurate velocity evaluation scheme into the basic RVM algorithm in place of the DVIC method and still obtain good flow resolution. The plotting scale chosen for the figures is somewhat small so that the whole vorticity distribution at the later times can be shown. This scaling puts a certain lower limit on detail that can be seen in a velocity vector plot. I refer the discussants to chapter 4 of reference [14] for larger scale plots that can be compared with experimental flow visualization pictures made by Bouard & Coutanceau 1980 (J. Fluid Mech. 101:583-607). Most of the flow structures seen in the experiments are also seen in the calculated velocity fields.

I guess that the discussants are referring to the dipole structure seen in figure 9, $t^* = 6.0$, when they speak of "strange behavior". The fact that this structure is essentially a dipole can be seen in the corresponding vorticity plot in figure 8 where a concentration of positive vorticity lies close to, but is separate from, a concentration of negative vorticity in the base of the "mushroom cloud" shaped area of the vorticity plot. I find the phenomenon physically reasonable considering both vorticity dynamics and my own observation of

wakes, in which one sees numerous "lumpy" flow structures. Similar structures can be seen in other calculations [14]. They are transient and usually disappear shortly after their creation, as the one in figure 9 does by $t^* = 8.4$. In reference to the discussants last comment, it would be nice to have a detailed streamline plot of the region, since the vector plots do not resolve the details of the velocity very well here.

As far as the time step is concerned, I made some variations of the time step which are reported in [14] to investigate the adequacy of the 0.24 value and found it to give an accuracy consistent with other aspects of the algorithm. How much accuracy is sufficient depends, as always, on one's interest. I think that figures 11-13 show that the algorithm was accurate enough to satisfy the stated desire of producing simulations comparable with Fallon's [2] experiments.

Nonlinear Forces Caused by Breaking Waves

H.MIYATA, H. KAJITANI, M. ZHU, and T. KAWANO

University of Tokyo, Japan

ABSTRACT

Nonlinear features of waves interacting with shallowly submerged obstacles and resultant nonlinear wave-induced forces are studied both experimentally and numerically. The behavior of waves around two kinds of horizontal cylinder placed in regular incident waves are observed from outside and inside of the flow-field and forces and pressure on the cylinder surface are measured. The experimental results show the occurrence of bore-like wave formation, wave breaking with wave crest splitting, vortex generation due to breaking, the negative drifting forces and other nonlinear features of waves. The finite-difference method based on the Navier-Stokes equations is used for the numerical simulation. A higher-order accurate differencing scheme and a turbulence model are incorporated to raise the appropriateness and the accuracy of the simulation. The simulated results agree qualitatively well with the above observed nonlinear features of the waves. However some discrepancy is still left between measured and predicted forces.

1. INTRODUCTION

The wave breaking phenomenon is of significant importance in the fields of naval architecture, offshore and coastal engineering. The wave energy concentrated on the breaking wave front causes forces of great magnitude on structures and it sometimes gives rise to disastrous effects.

However, due to the nonlinear features of the phenomenon both experimental and theoretical investigations have not succeeded in the whole elucidation of the phenomenon or the precise evaluation of the forces as yet.

One of the simplest cases appears in the problem of wave-induced forces on a 2D submerged of floating body. When the body is deeply submerged it does not receive any drifting force from the incident regular waves of which wavelength is larger than the body length, but when the submergence is decreased and the upper surface of the body is in the proximity of the free-surface, a remarkable negative drifting force is generated. This remarkable variation of drifting force due to waves cannot be explained by analytical methods so far developed. It is mostly because an analytical method cannot explain the nonlinear phenomena of wave breaking, vortex generation, turbulence generation and so forth which take place on the body near the free-surface.

In this paper the complicated flow dynamics about a shallowly submerged 2-dimensional obstacle is experimentally studied by a variety of experimental methods, namely, flow visualization, pressure and force measurement. The complicated flow-fields are numerically simulated by a finite-difference method called TUMMAC method. A higher-order scheme and a sub-grid-scale (SGS) turbulence model are incorporated so that higher degree of resolution is achieved.

2. DESCRIPTION OF EXPERIMENTS

Experiments were conducted at the Experimental Tank of the University of Tokyo. The length, width and depth are 86m, 3.5m and 2.5 m, respectively and a flap-type wavemaker is installed on one side of the tank. In order to realize a 2-dimensional flow-field a rectangular channel is used and a cylindrical obstacle is set in this channel as shown in Fig.1. The length and inner width of the channel are 2.4m and 0.53m. The cylindrical obstacle is rigidly fixed to a carriage through a strut and a box of gauge system for the measurement of forces.

Two cylindrical models shown in Fig.2 are used, both having same area of cross-section. The model A has 16 pressure taps in which strain-gauge type pressure transducers are attached. The submergence of the obstacles is varied and the distance from the top of the obstacles to the undisturbed free-surface is 75mm on the most typical condition of d/b=1.375 for model A and d/b=0.76 for model B, where d is the submergence and b is the half-length of the obstacles as shown in Fig.2. The incident angle of model B is varied by rotating about the center of buoyancy. The incident angle of 180° means that the larger semi-circle is oriented to the upwave direction.

The flow-field beneath the free-surface is visualized by equipments shown in Fig.3 and polystyrene beads, the diameter of which is approximately 1mm, as tracers. In the slide-projector a film with a thin slit is set to produce a parallel vertical beam of 10mm thickness.

Regular waves of which length is 1.57m and 3.14m are generated by the wavemaker and the amplitude (h_0) is 6cm in common with both waves. Therefore the wave period is 1.003s and 1.419s, respectively. Assume that the obstales are simplified models of lower-hulls of semi-submergibles, then the wavelength is 2.6 to 7.9 times longer than the width of the lower-hulls, which marginally coincides with the actual situation of full-scale semi-submergibles. The averaged slope of the incident waves is 0.153 or 0.076, with which a lot of nonlinear features of waves interacting with the obstacles are expected.

The measured force and pressure are instantaneously digitized and stored in a transient memory, and then they are copied onto a magnetic disk, which is conveyed to the computer center where the analysis of measured data including Fourier analysis is executed. The sampling time is 2 and 1 millisecond for force and pressure measurements, respectively.

3. OBSERVATION OF WAVE MOTION

3.1 Free-Surface Appearance

The appearance of waves on model A is shown in Fig.4. Since the incident wave has steep slope and the water depth from the top of the obstacle is only 75mm in this case, the wave shows violent breaking motion. A discontinuous wave profile similar to a bore or hydraulic jump is formed on the upwave part of the obstacle, and a plunging breaker occurs on the rear end of the obstacle. It is interesting to note that wave splitting occurs and two wave crests are produced after the plunging wave front impinges the free-surface below at about 0.3m downwave from the center of the obstacle. Wave splitting phenomenon appears to be one of the consequences of wave breaking.

In the present case wherein the wavelength is much longer than the obstacle length the wave breaking phenomenon is used to take place on the rear part of the obstacle. Therefore it is anticipated that wave set-up, wave impact pressure and other effects of nonlinear features of waves are recognized in this region.

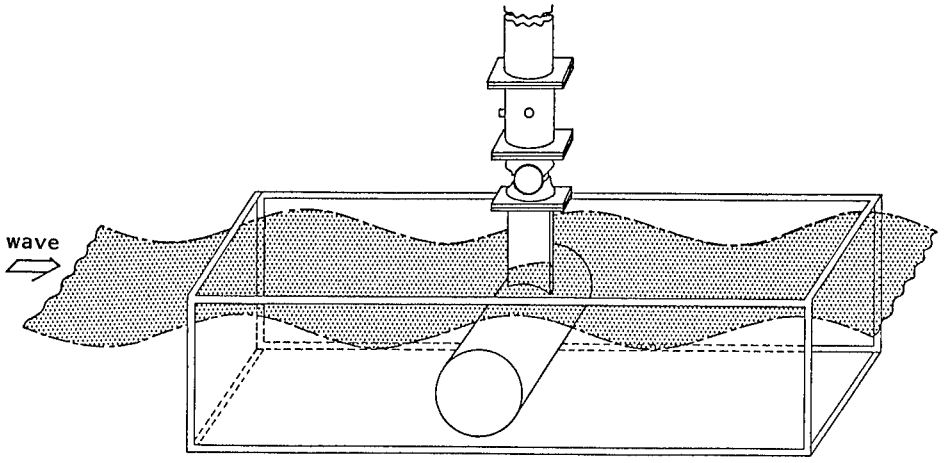


Fig.1 Experimental setup.

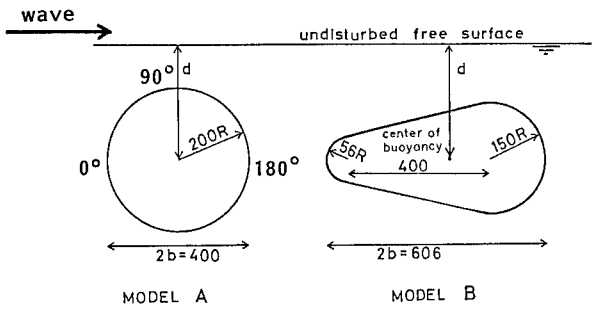


Fig.2 Cross-sections of tested models.

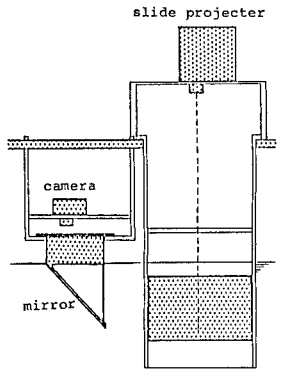


Fig.3 Experimental setup for flow visualization, front view.

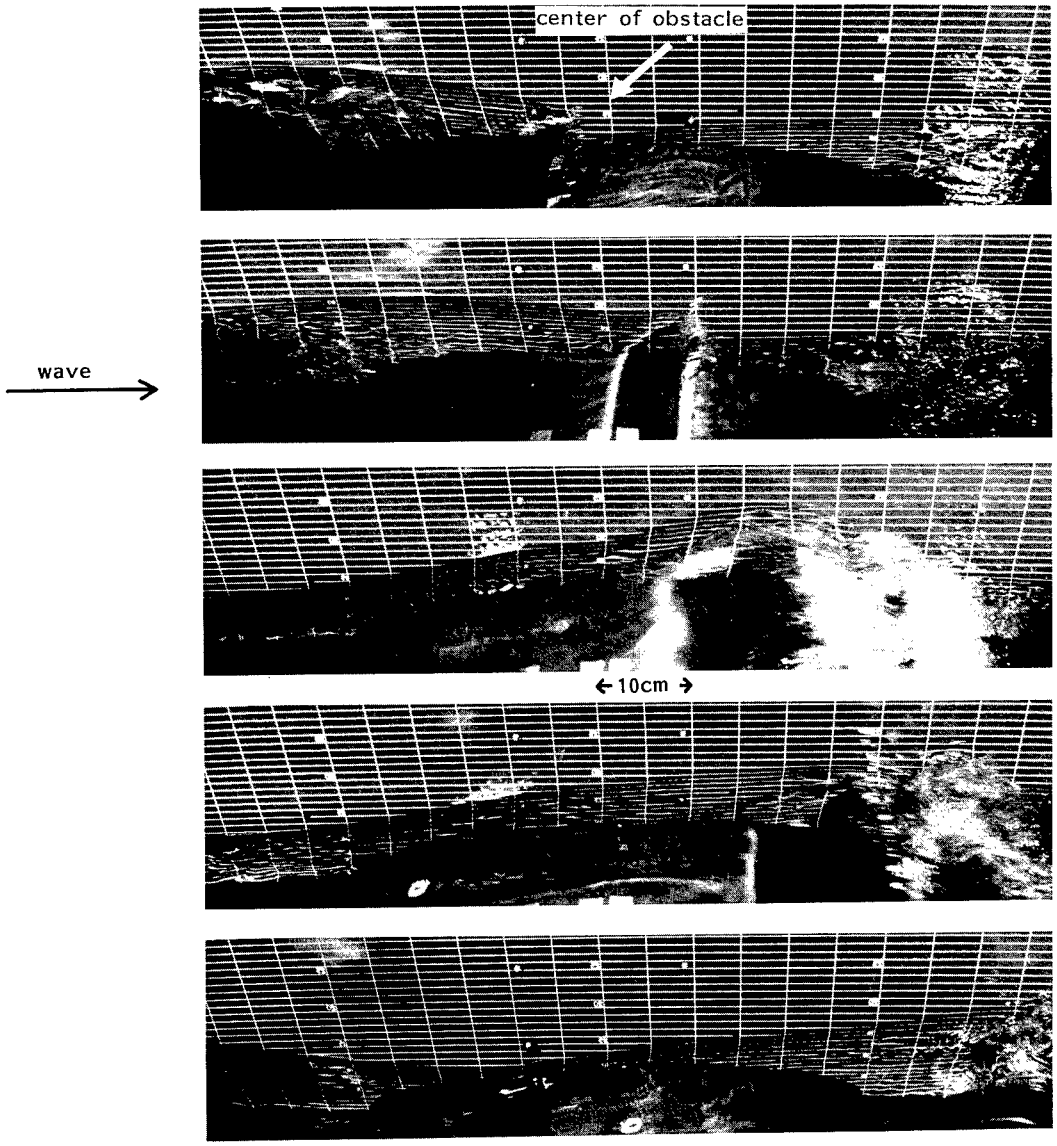


Fig.4 Appearance of waves on model A, d/b=1.375, λ =1.57m, h_O=0.06m.

3.2 Flow-Field Beneath the Free-Surface

Typical three pictures of the flow-field beneath the breaking wave are shown in Fig.5. The exposure time of a 35mm camera is 1/2 second.

Remarkable vortical motions are observed near the free-surface and the obstacle surface. The most dominant vortices near the free-surface are supposed to be generated by wave breaking. Since the wave motion is periodical, the vortices are successively generated and then one pair of vortices are observed in the picture at the top. The vortex near the obstacle surface seems to be generated by the complicated flow including the viscous effect on the obstacle surface in the narrow restricted region in the proximity of the obstacle.

4. FORCE AND PRESSURE MEASUREMENT

4.1 Force Measurement

Some records of measured forces are shown in Fig.6 for the case of model A and in Fig.7 for the case of model B.

Since approximately sinusoidal waves are generated by the wavemaker, the records of measured forces also show approximately sinusoidal fluctuations when the obstacle is deeply submerged without showing nonlinear effects. However the record of horizontal force on a shallowly submerged condition shows very peaky wave profiles as shown in Fig.6. The nonlinear features of waves observed in Section 3 are supposed to give important influences on the wave-induced forces.

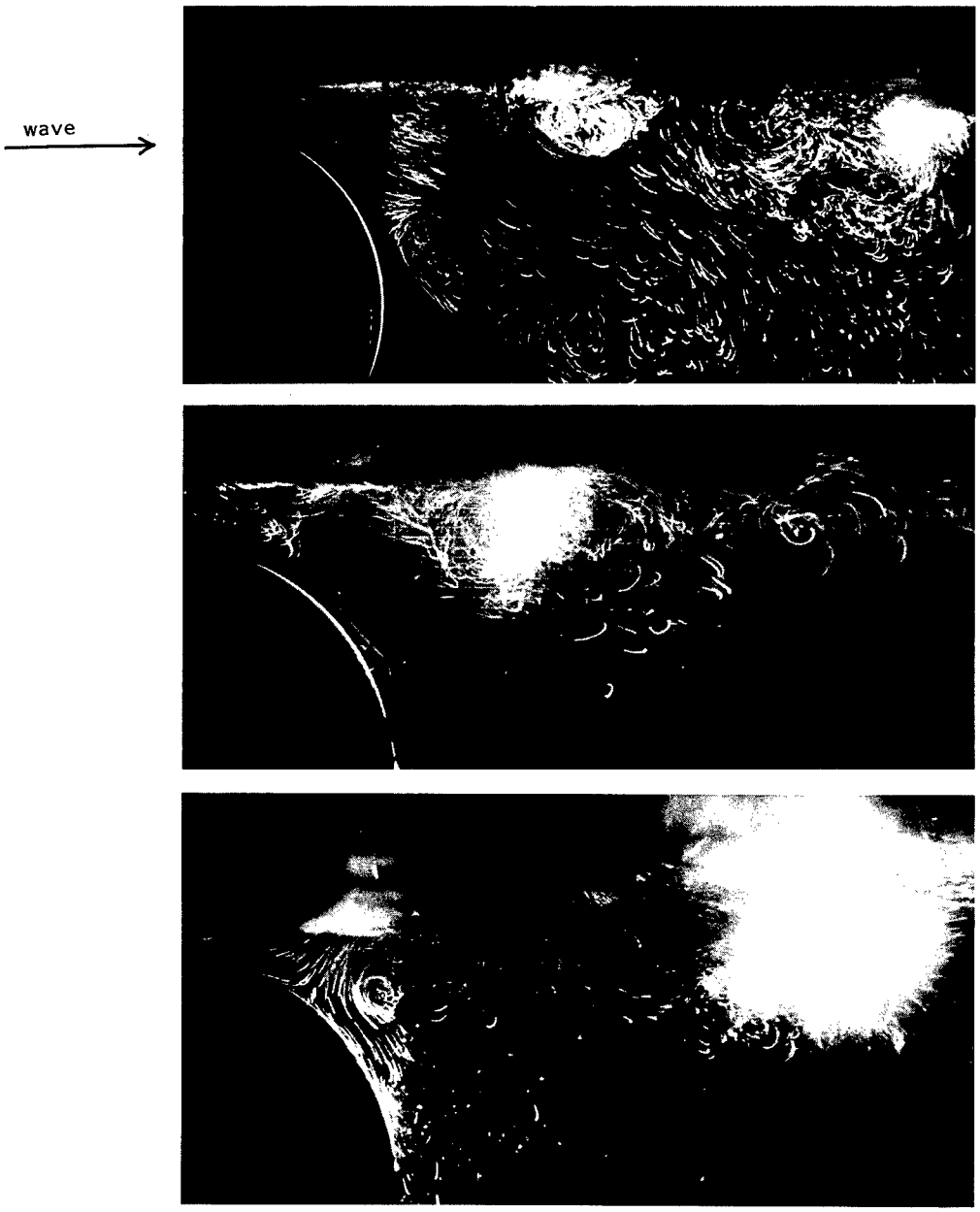


Fig.5 Visualized flow-field behind model A, d/b=1.375, λ=1.57m, h_o=0.06m.

In the case of the unsymmetrical model B the fluctuation of the horizontal force is more modest as shown in Fig.7, and it varies owing to the variation of incident angle.

The time-averaged mean horizontal and vertical forces are shown in Figs.8 and 9 for model A and in Figs.10 and 11 for model B. These forces are made dimensionless with respect to the half-length of the obstacles b and the width L which is 0.52m. In Figs.8 and 9 the model A is fully submerged when d/b is larger than 1.25 and it emerges when d/b=1.0.

The general tendency of the variation due to the change of submergence is that upwave and upward mean forces rather abruptly increase with the decreasing submergence and they suddenly decrease when a part of the obstacle surface emerges above the free-surface. The agreement with the results by Inoue and Kyozuka [1] is satisfactory.

The forces remarkably vary owing to the change of incident angle especially when the submergence is small as shown in Figs.10 and 11. Higher angle of incidence often leads to larger mean forces but this also depends on the wavelength. When the obstacle B is placed in opposite direction, namely θ=180°, a large negative drifting force occurs and it shows larger value on the deeper condition.

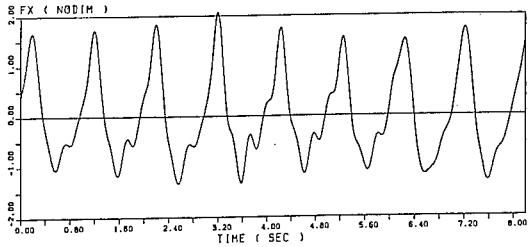


Fig.6 Measured horizontal force on model A, d/b=1.375, λ=1.57m, h_o=0.06m.

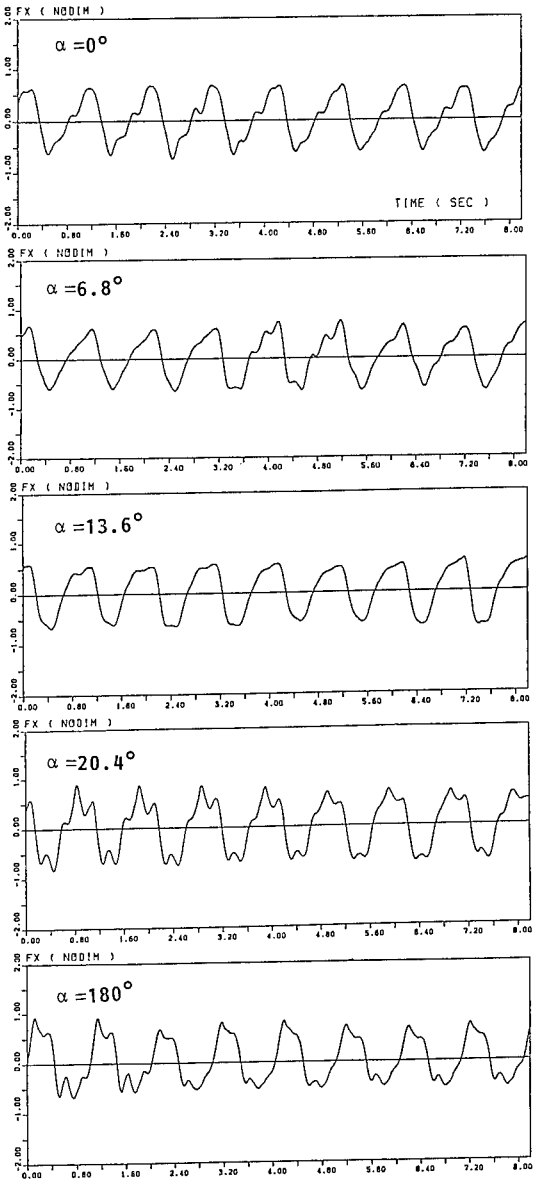


Fig.7 Measured horizontal force on model B at five incident angles, d/b=0.76, λ=1.57m, h_o=0.06m.

4.2 Pressure Measurement

Measured records of pressure on model A in the vicinity of the top (θ=90°) are shown in Figs.12 and 13. They are made dimensionless with respect to $\rho g h_o$. The steep increase of pressure seems to be related with the bore-like wave profiles on the obstacle and this is more remarkable when the incident waves are steeper.

Time-developmental variations of pressure distribution on model A are shown in Figs.14 and 15 for the period of one cycle. Since the pressure at only three points is simultaneously measured, the unrealistic fluctuation is mostly attributable to the phase difference in the measurement. It is noted that the suction pressure has magnitude larger than the compressive pressure.

5. FINITE-DIFFERENCE SIMULATION METHOD

5.1 TUMMAC-Vbk Method

A modified MAC method called TUMMAC method has been continuously developed for various wave problems at the Experimental Tank Laboratory of the University of Tokyo. For instance, the TUMMAC-IV method is proved to be successful for the simulation of nonlinear ship waves [2][3]. In this study another version called TUMMAC-Vbk for 2-dimensional breaking waves is applied with some modifications to raise the degree of appropriateness and accuracy. Since the datailed description of the TUMMAC-Vbk method is already present in Ref.[4][5], the computational method is only briefly described here, except for the modified parts, to which detailed description is made in the subsequent sections.

By forward differencing in time and centered differencing in space the Navier-Stokes equations for incompressible flow in 2-dimensions are written in the following time-marching forms.

$$u^{n+1}_{i+\frac{1}{2},k} = \xi_{i+\frac{1}{2},k} - \frac{\Delta t}{\Delta x}(\phi_{i+1,k} - \phi_{i,k}), \tag{1}$$

$$w^{n+1}_{i,k+\frac{1}{2}} = \zeta_{i,k+\frac{1}{2}} - \frac{\Delta t}{\Delta z}(\phi_{i,k+1} - \phi_{i,k}),$$

where

$$\xi_{i+\frac{1}{2},k} \equiv u_{i+\frac{1}{2},k} - \Delta t \cdot UC_{i+\frac{1}{2},k} + \nu \cdot \Delta t\left\{\frac{u_{i+3/2,k} - 2u_{i+\frac{1}{2},k} + u_{i-\frac{1}{2},k}}{\Delta x^2} + \frac{u_{i+\frac{1}{2},k+1} - 2u_{i+\frac{1}{2},k} + u_{i+\frac{1}{2},k-1}}{\Delta z^2}\right\}, \tag{2}$$

$$\zeta_{i,k+\frac{1}{2}} \equiv w_{i,k+\frac{1}{2}} - \Delta t \cdot WC_{i,k+\frac{1}{2}} + \cdots\cdots$$

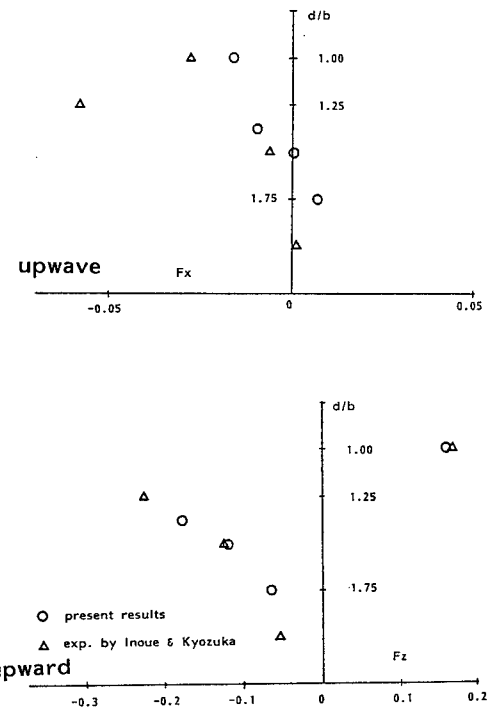


Fig.8 Measured mean horizontal and vertical forces on model A at various submergence, made dimensionless with respect to $\rho g h_o b L$, λ=1.57m, h_o=0.06m.

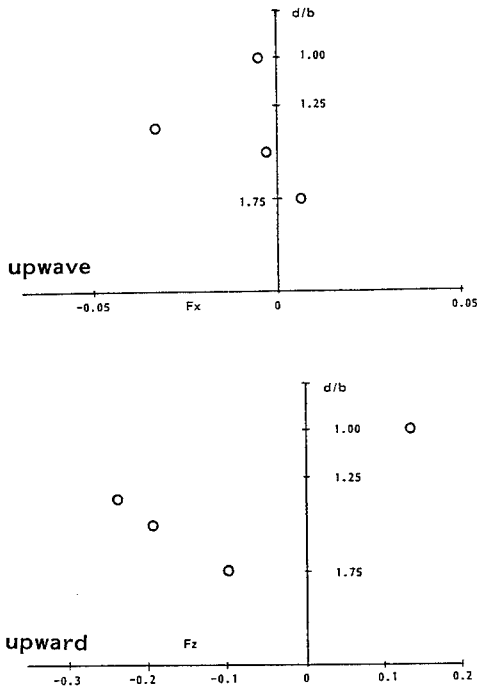


Fig.9 as Fig.8, model A, λ =3.14m, h_o=0.06m.

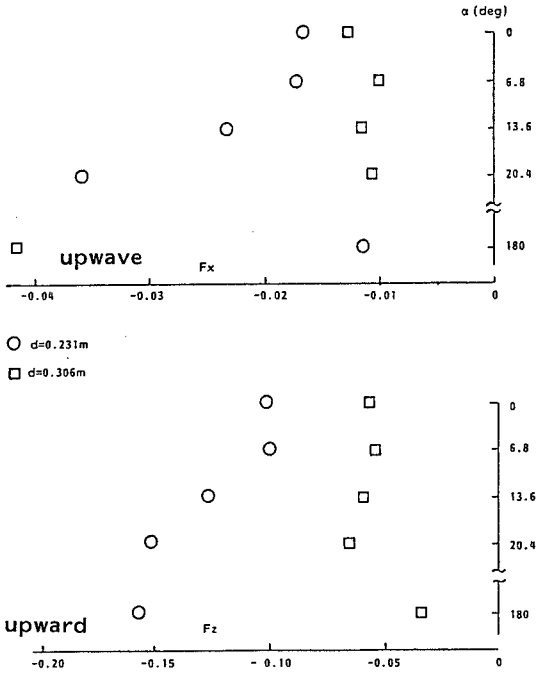


Fig.10 Measured mean horizontal and vertical forces on model B at various incident angles, made dimensionless with respect to $\rho g h_o b L$, λ =1.57m, h_o=0.06m.

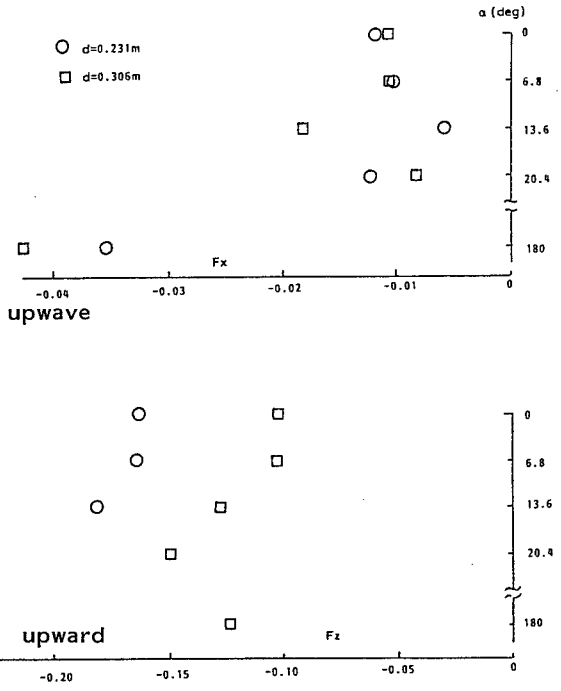


Fig.11 as Fig.10, λ =3.14m, h_o=0.06m.

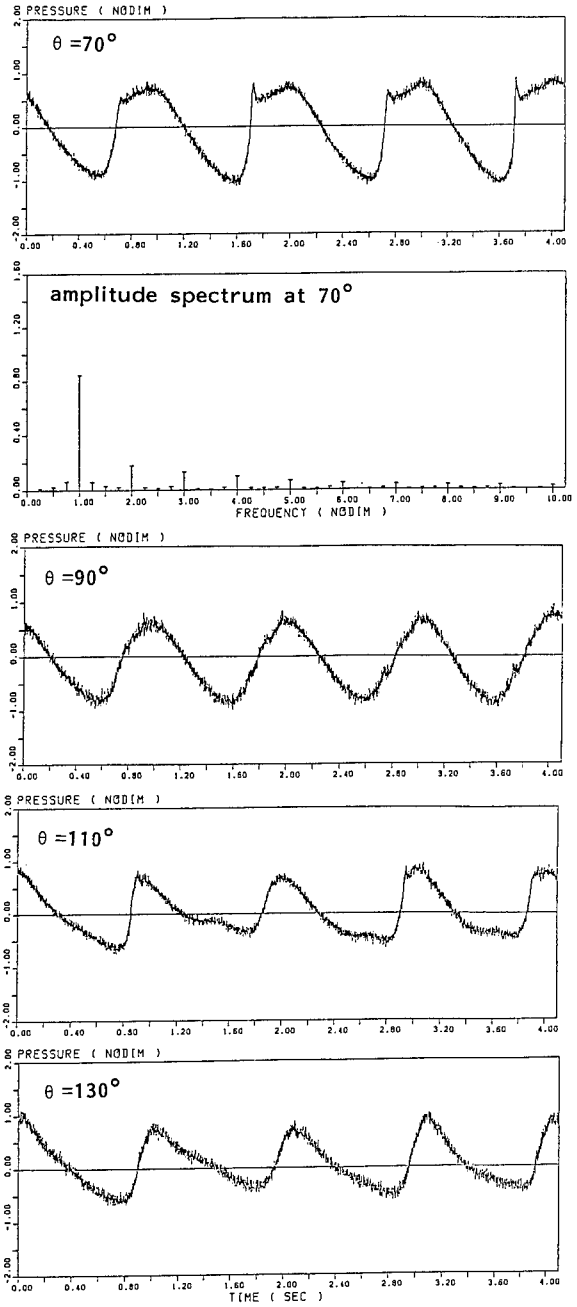


Fig.12 Measured pressure at four points of model A, made dimensionless with respect to $\rho g h_o$, and analysed spectrum of the case of $\theta=70°$; d/b=1.375, λ=1.57m, h_o=0.06m.

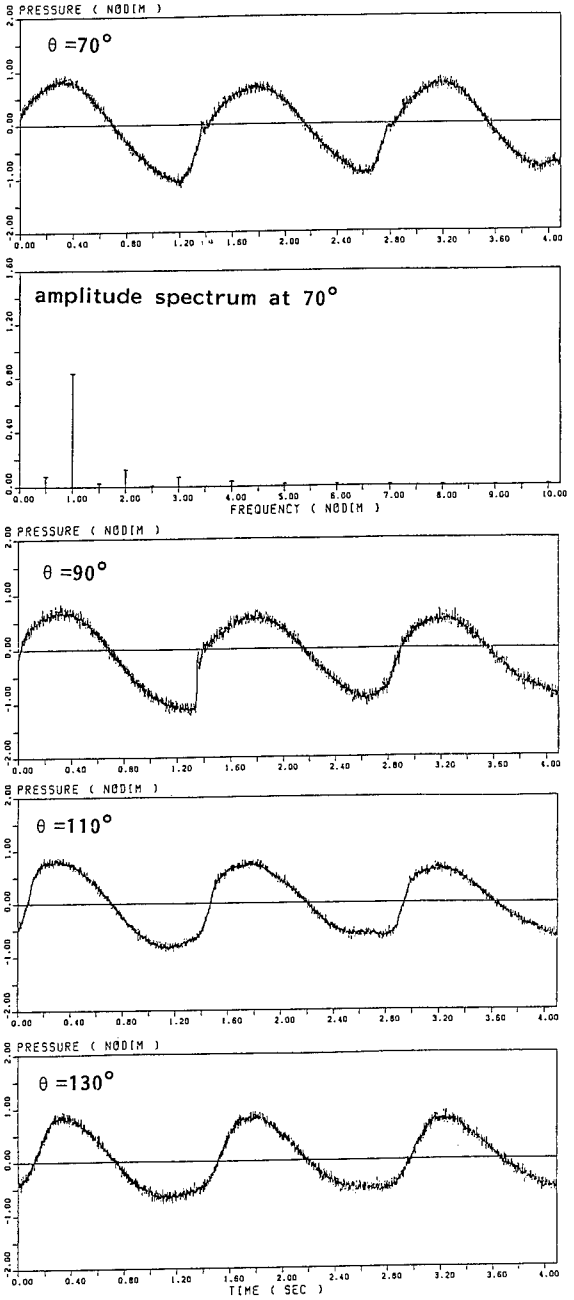


Fig.13 as Fig.12, λ =3.14m, h_o=0.06m.

Here Δt, Δx and Δz are time increment, horizontal and vertical spacing of the inflexible orthogonal cell system, ϕ is pressure divided by the density ρ. Subscripts are used for the cell location and superscripts for the time level. The new velocities are updated by Eq.(1) in the time-marching solution procedure. UC and WC are convective terms in a difference form, to which detailed description is made in the subsequent section.

By taking the divergence of a cell and letting the divergence at the (n+1)th time step zero the Poisson equation for pressure is derived as

$$\phi_{i,k} = \frac{1}{2(1/\Delta x^2 + 1/\Delta z^2)}\left(\frac{\phi_{i+1,k} + \phi_{i-1,k}}{\Delta x^2} + \frac{\phi_{i,k+1} + \phi_{i,k-1}}{\Delta z^2} - R_{i,k}\right) , \quad (3)$$

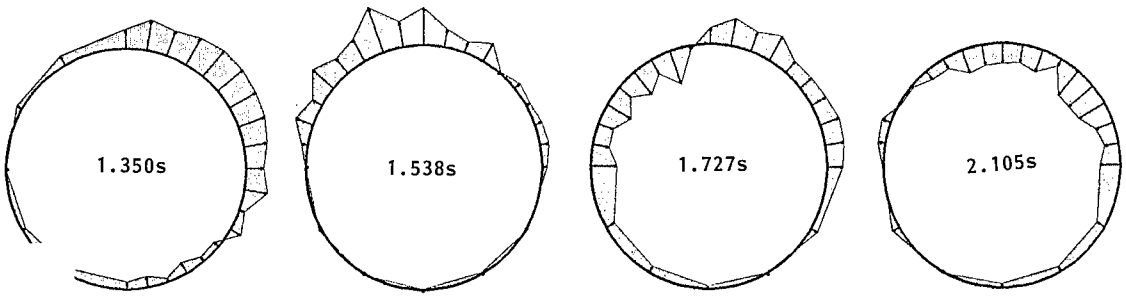


Fig.14 Measured time-sequential pressure distribution on model A, λ=1.57m, h_o=0.06m.

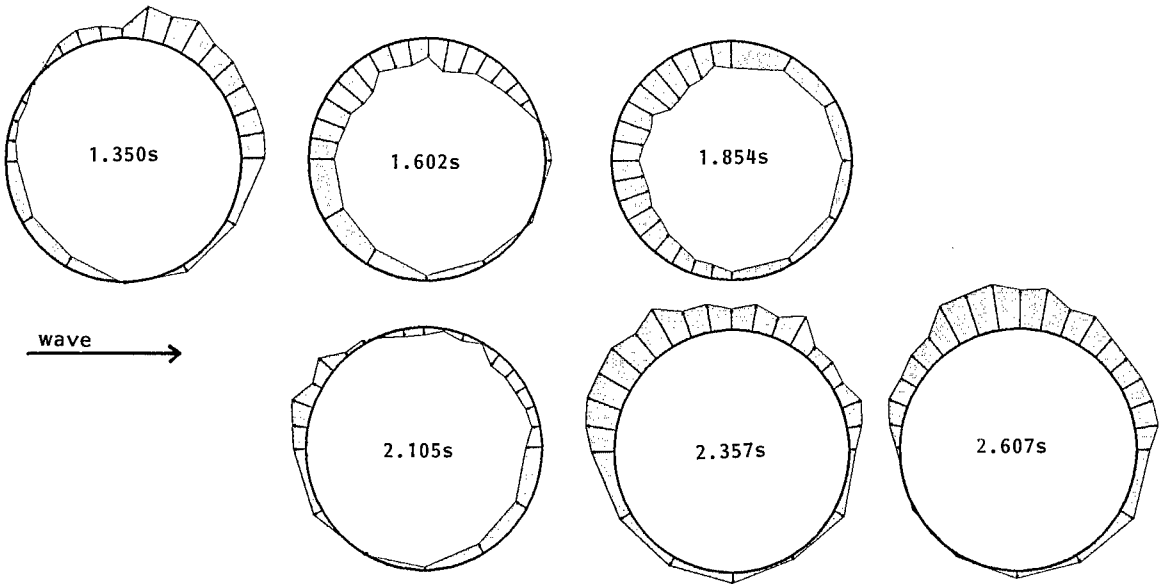


Fig.15 as Fig.14, λ=3.14m, h_o=0.06m.

where

$$R_{i,k} \equiv \frac{\xi_{i+\frac{1}{2},k} - \xi_{i-\frac{1}{2},k}}{\Delta t \cdot \Delta x} + \frac{\zeta_{i,k+\frac{1}{2}} - \zeta_{i,k-\frac{1}{2}}}{\Delta t \cdot \Delta z} . \quad (4)$$

The new pressure field is determined by iteratively solving Eq.(3) with the updated velocity field. The solution is advanced in time by a series of repeated time steps.

5.2 Cell System

An inflexible orthogonal cell system is used in the TUMMAC-Vbk method. In the present problem complicated fluid motions take place near the free-surface and the body, while they are assumed to be very modest in the deeper region. Therefore the numerical simulation becomes more effective and economical when a variable mesh system in the vertical direction is employed.

The computational domain is 2m long 1m deep, and the horizontal spacing Δx is 10mm. The vertical spacing Δz is given by the following equation

$$\Delta z(k) = 1.530 \times 10^{-7} \times (k-304.5)^2 \ (m) . \quad (5)$$

Here k is the vertical location of a cell and it is 100 for a cell just beneath the undisturbed surface. The smallest height of a cell is and the spacing above the undisturbed free surface is set equally at this value. The total number of cell is about 25000.

5.3 Difference Scheme

In order to raise the accuracy and resolution of the TUMMAC-Vbk method some improvements in the differencing scheme are made. One is the employment of the Adams-Bashforth differencing in time and the other is the development of a third-order upstream differencing for the variable mesh system.

The forward differencing in Eqs.(1) and (2) has a first-order truncation error of second derivative in the form $1/2\,\Delta t.u^2.\partial^2 u/\partial x^2$[6]. This contaminates the viscous diffusion terms. Therefore the use of the second-order accurate differencing method such as Adams-Bashforth method [7] is necessary for the solution of a flow that includes viscous effects. This differencing sheme is written as

$$u^{n+1} = u^n + \Delta t\{\frac{3}{2}(\frac{\partial u}{\partial t})^n - \frac{1}{2}(\frac{\partial u}{\partial t})^{n-1}\} . \quad (6)$$

This differencing in time is applied to the convective terms of Eq.(2) and therefore the UC and WC at the previous time step must be preserved.

Two third-order upstream differencing scheme are proposed, one by Agarwal [8] and another by Kawamura and Kuwahara [9]. These two schemes approximate, for instance, the space derivative $\partial w/\partial z$ in the following manner, respectively, when w is positive.

$$\{\frac{\partial w}{\partial z}\}_k = (2w_{k+1} + 3w_k - 6w_{k-1} + w_{k-2})/6\Delta z, \quad (7)$$

$$\{\frac{\partial w}{\partial z}\}_k = (w_{k+2} - 2w_{k+1} + 9w_k - 10w_{k-1} + 2w_{k-2})/6\Delta z. \quad (8)$$

Here the subscript i is dropped for simplicity. The truncation error of these two shemes are respectively

$$\frac{1}{12}\Delta z^3\frac{\partial^4 w}{\partial z^4} + O(\Delta z^4) , \quad (9)$$

$$\frac{1}{4}\Delta z^3\frac{\partial^4 w}{\partial z^4} + O(\Delta z^4) . \quad (10)$$

These schemes have the third-order truncation error of fourth-derivative. However this third-order accuracy is degraded to the second-order when a variable mesh system is used.

The third-order upstream differencing scheme devised for a variable mesh system by the authors is, for example, written as

$$\{\frac{\partial w}{\partial z}\}_k = Aw_{k+2} + Bw_{k+1} + Ew_k + Cw_{k-1} + Dw_{k-2} . \quad (11)$$

The five coefficients are derived by solving the following simultaneous equations.

$$\begin{bmatrix} 1 & 1 & 1 & 1 \\ (\Delta z_k+\Delta z_{k+1}) & \Delta z_k & -\Delta z_{k-1} & -(z_{k-1}+\Delta z_{k-2}) \\ (\Delta z_k+\Delta z_{k+1})^2 & \Delta z_k^2 & \Delta z_{k-1}^2 & (\Delta z_{k-1}+\Delta z_{k-2})^2 \\ (\Delta z_k+\Delta z_{k+1})^3 & \Delta z_k^3 & -\Delta z_{k-1}^3 & -(\Delta z_{k-1}+\Delta z_{k-2})^3 \end{bmatrix} \begin{bmatrix} A \\ B \\ C \\ D \end{bmatrix} = \begin{bmatrix} -E \\ 1 \\ 0 \\ 0 \end{bmatrix} \quad (12)$$

The coefficient E is set at $3/(2\,\Delta z_k)$ so that the scheme accords with Eq.(8) when equal spacing is used. With this scheme the third-order accuracy is assured in the variable mesh system. Since the coefficients A to E depend on the vertical location, they are calculated beforehand when the cell system is determined.

5.4 Turbulence Model

A sub-grid-scale(SGS) turbulence model is employed following Deardorff [10] and modifying into the 2-dimensional case. In partial analogy to the molecular case the SGS stress Rij is expressed as

$$R_{ij} = \frac{1}{2}\overline{u^{\ell\prime}u^{m\prime}}\delta_{\ell m} - \nu_s(\frac{\partial \overline{u_i}}{\partial x_j} + \frac{\partial \overline{u_j}}{\partial x_i}) . \quad (13)$$

Here the primes denote deviations from local grid-volume means, overbars are grid-scale averaging operators and ν_s is the SGS eddy viscosity coefficient.

From Smagorinsky's et al.[11] assumption ν_s is derived as

$$\nu_s = (C_1\Delta)^2\{\frac{\partial \overline{u_i}}{\partial x_j}(\frac{\partial \overline{u_i}}{\partial x_j} + \frac{\partial \overline{u_j}}{\partial x_i})\}^{\frac{1}{2}} , \quad (14)$$

where $\Delta \equiv (\Delta x\cdot\Delta z)^{1/2}$. (15)

The normal stress in Eq.(13) is given by the following equation.

$$\frac{1}{2}\overline{u^{\ell\prime}u^{m\prime}}\delta_{\ell m} = K = \nu_s^2/(C_2\Delta)^2 . \quad (16)$$

Here K is the turbulent kinetic energy. The values of coefficients C_1 and C_2 are set at 0.1 and 0.094, respectively, simply following the previous works.

These SGS stresses are incorporated in the Navier-Stokes equations (1) and (2) in finite-difference form. The value of K is set at zero on the body boundary.

5.5 Boundary Conditions

On the free-surface special treatments of the boundary conditions are necessary so that not only the overturning motion but also the more complicated breaking motions in the stages after the overturning can be simulated. All the cell are flagged and the free-surface profile is represented by a succession of segments. The segments are moved in a Lagrangian manner and the atmospheric pressure on the free-surface is taken into account making use of the "irregular star" technique.

On the body boundary a no-slip boundary condition is approximately satisfied, although the grid system is not so fine as to resolve the boundary layer. On the inflow boundary a numerical wavemaker is installed by simply giving fluctuating velocities according to the linear wave equations. On the open boundaries the condition of zero-normal-gradient is imposed on the velocities. For details see Ref.[4].

6. SIMULATED RESULTS

Numerical simulations are performed at a shallow submergence condition. The water depth measured from the top of the obstacle is 75mm. The wavelength and amplitude of the numerically generated regular waves are 1.57m and 60mm, respectively. The time increment is 1.247millisecond and the simulation is continued to the 1500th time step.

6.1 Model A

The time sequence of the velocity vector field of the typical case is shown in Fig.16 for the period of one wave cycle at the almost steady state. The third wave generated by the numerical wavemaker is approaching the obstacle in the first stage of this figure and the fourth wave is incoming at the final stage.

At N=1140, where N denotes the time step, a remarkable vortex caused by the breaking motion in the previous cycle is present on the right of the obstacle in the vicinity of the free-surface. The incoming wave is deformed into a bore-like profile by the interaction with the obstacle at N=1200. Since the wave energy is concentrated on the wave crest, the velocities show large magnitude, while the flow on the right of the obstacle has velocities of opposite sign at this stage. A kind of fluid collision takes place above the center of the obstacle and accelerates the breaking motion. It is also noted that the vortex that stays at about x=0.35 m causes free-surface deformation. The overturning motion is observed at N=1260 and the overturning wave front collapses to make a damped wave profile at N=1320. Wave splitting starts to occur at N=1380 and two wave crests appear at N=1440, the forward crest making secondary breaking motion. The vortex generated in the previous cycle is involved in the violent breaking flow-field.

The time sequence of pressure contour map at the stages of Fig.16 is shown in Fig.17. The hydrostatic pressure is subtracted and negative values are contoured in dashed lines. The pressure in kg/m^2 is divided by the density of water and then the interval of the contour is 0.02 m^2/sec^2.

The vertical contour lines of the incoming wave on the obstacle at N=1200 rather suddenly change into approximately horizontal lines owing to the formation and the propagation of the bore-like wave at the next stage of N=1260. The gradient of pressure is very steep on and beneath the overturning wave front, which is partly due to the colliding flow velocities observed in Fig.16. The vortex generated in the previous cycle shows pressure hole with negative value. The high pressure caused by the impinging motion of the overturning wave onto the free-surface below seems to generate another wave crest at N=1380, which implies that wave splitting is one of the consequences of the breaking motion. After the breaking process ceases a remarkable part of the wave energy seems to be dissipated and a pressure hole due to a vortex motion appears again at N=1500.

6.2 Model B

The simulated results for the model B are shown in Figs.18 and 19. The computational conditions are common with the previous case of the model B. The distance measured from the top of the obstacle to the undisturbed free-surface is 75mm, which is also common with the previous case.

The overall wave motion about the obstacle does not show significant difference from the case of the model A. However some different features are observed owing to the difference of the obstacle shape. Although the velocities seem to collide on the center of the obstacle at N=1200, the bore-like wave profile is not likely to reach the breaking stage until the wave front passes over the obstacle. It seems to be interesting to note that the pressure contour maps show vertical straight contours for a certain period when the bore-like wave advances on the slope of the obstacle. Since the wave motion on the slope is supposed to have partial similarity with a shallow water wave, the propagation speed of the bore-like wave is influenced by the value of the shallow water case which is approximately proportional to the square root of the water depth above the obstacle in the short restricted region. This delays the wave phase, as noted by comparing the wave profiles in Fig. 19 with Fig.17.

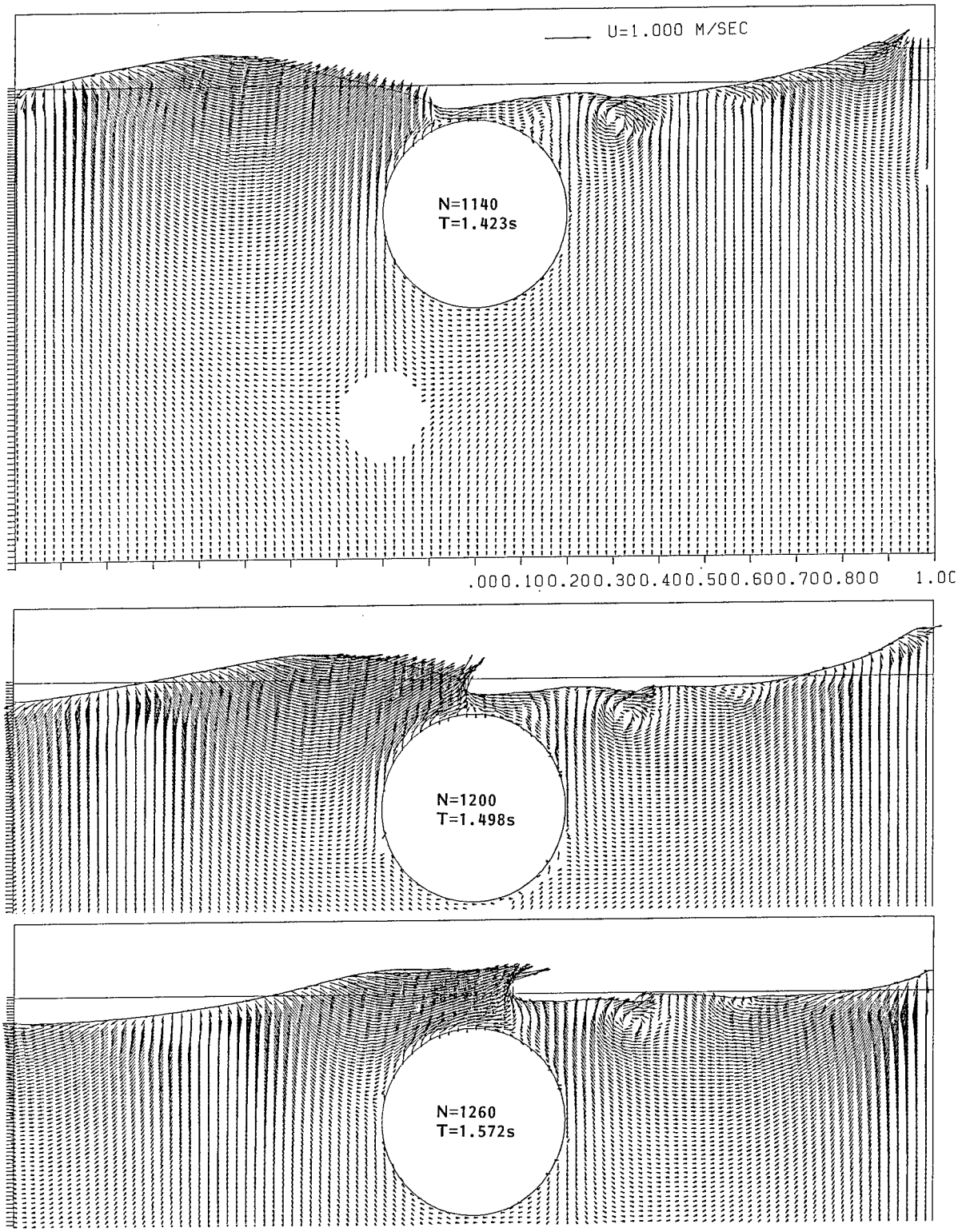


Fig.16 Time sequence of computed velocity vector field about model A, d/b=1,375, λ =1.57m, h_O=0.06m.

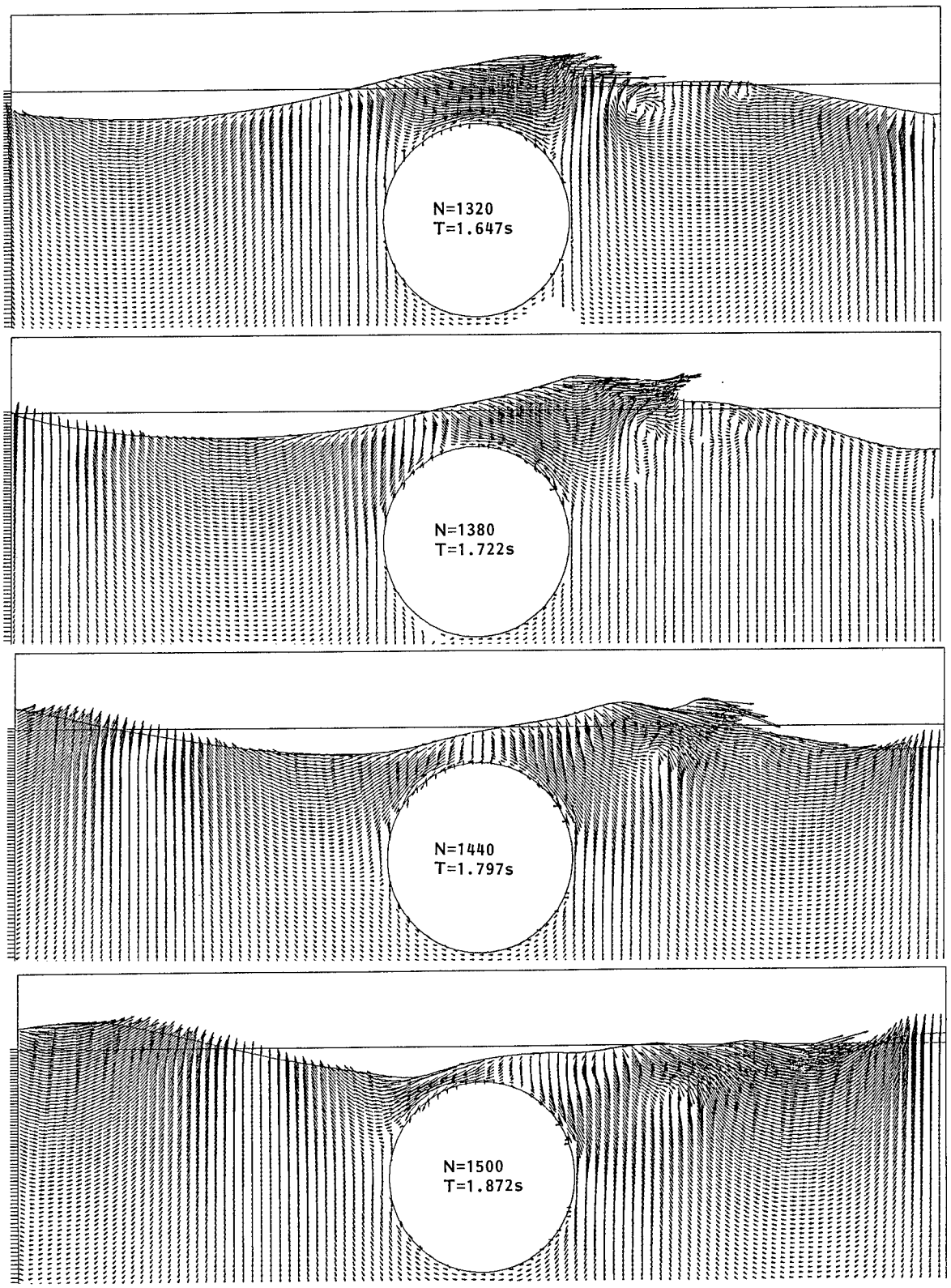


Fig.16 continued.

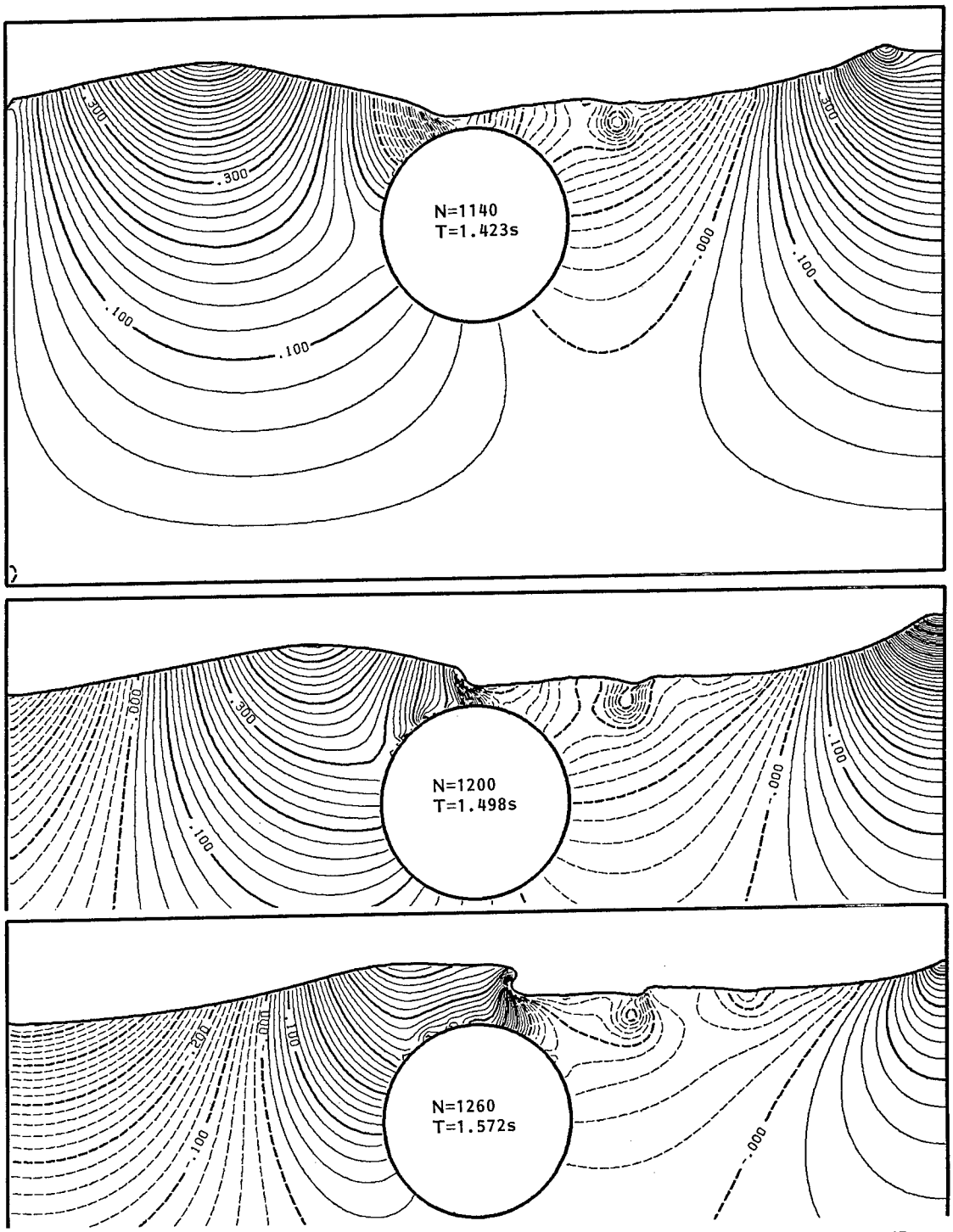


Fig.17 Time sequence of computed pressure contour map about model A, d/b=1.375, λ =1.57m, h_o=0.06m.

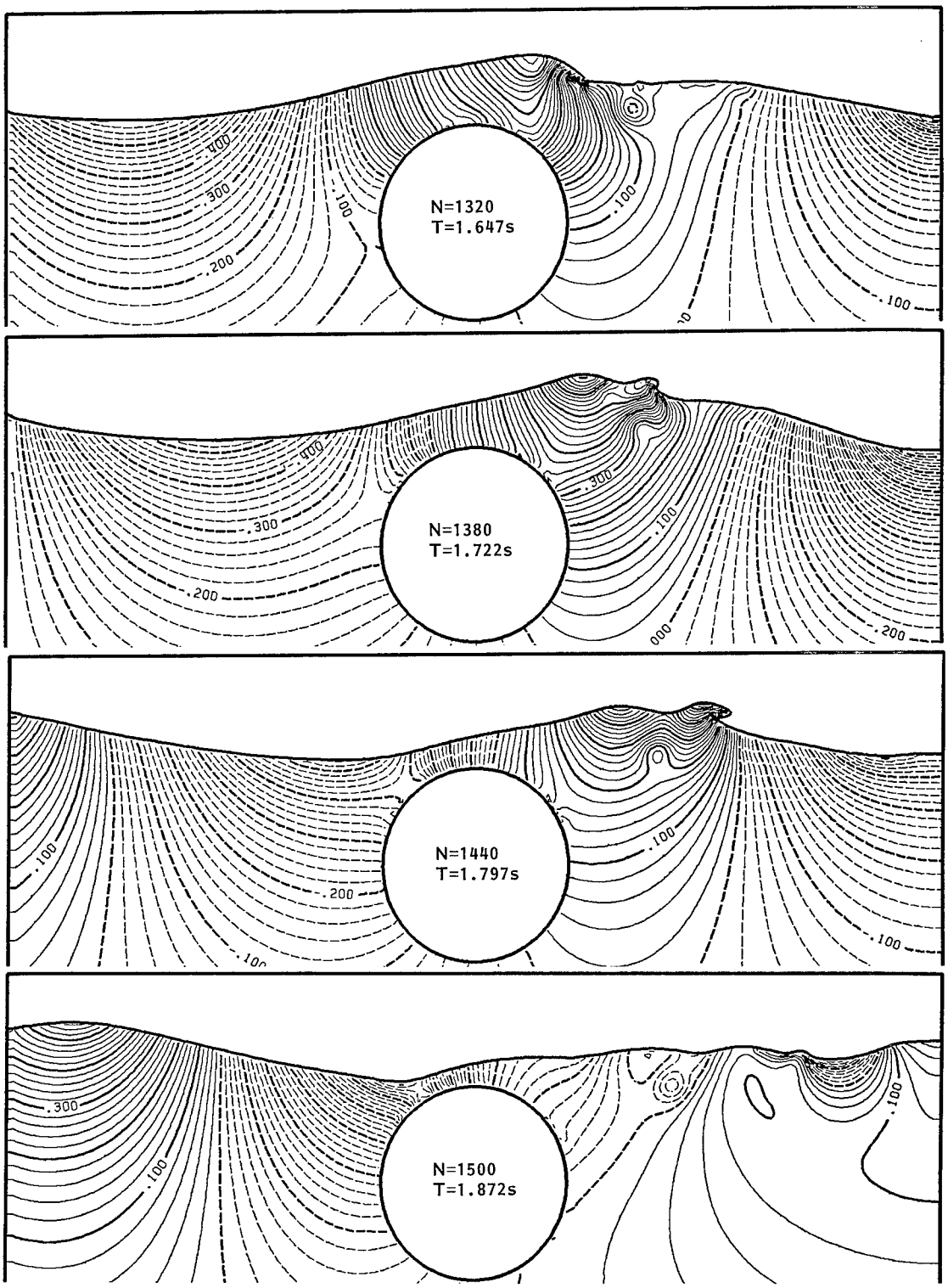


Fig.17 continued.

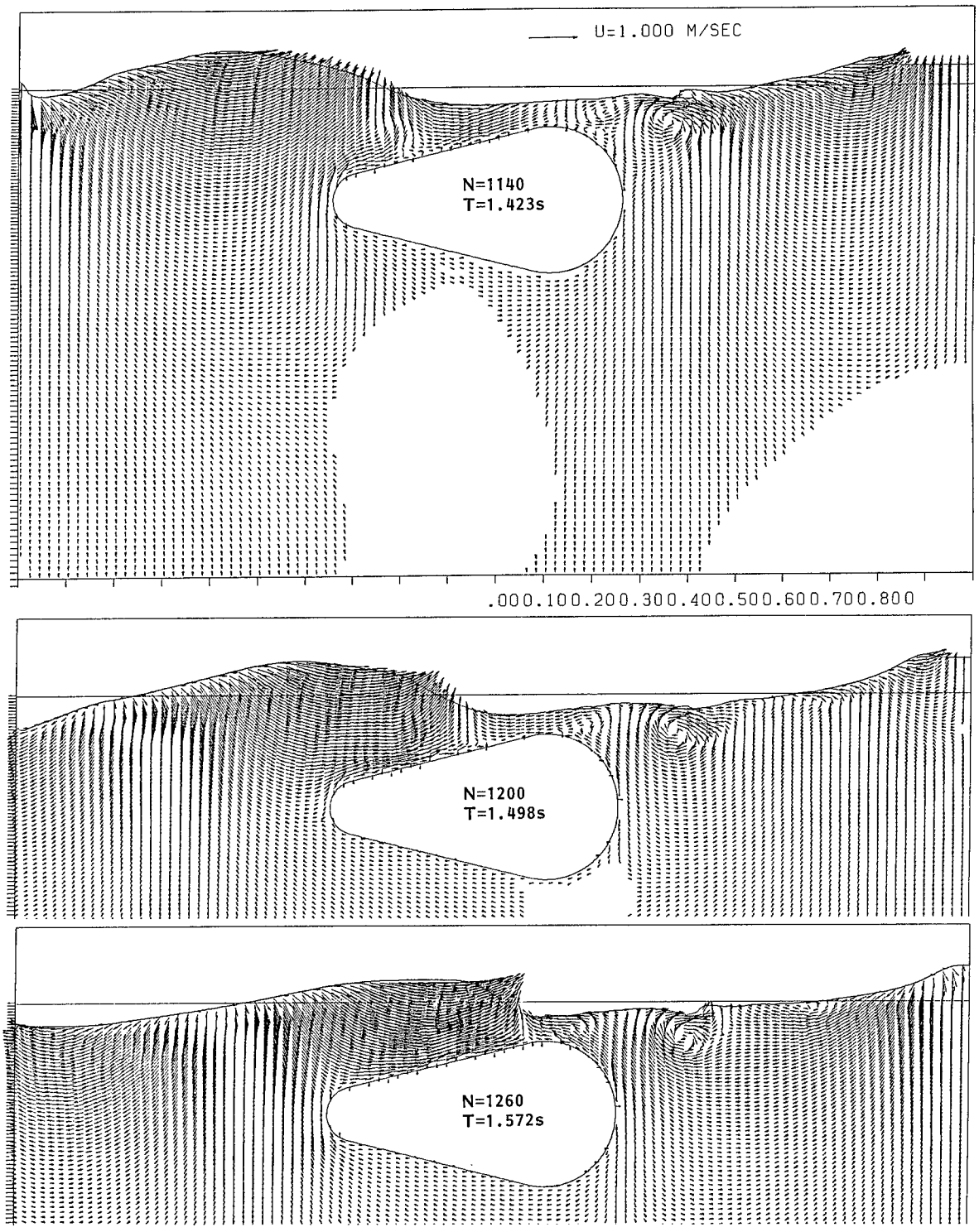


Fig.18 Time sequence of computed velocity vector field about model B, d/b=0.76, λ =1.57m, h_o=0.06m.

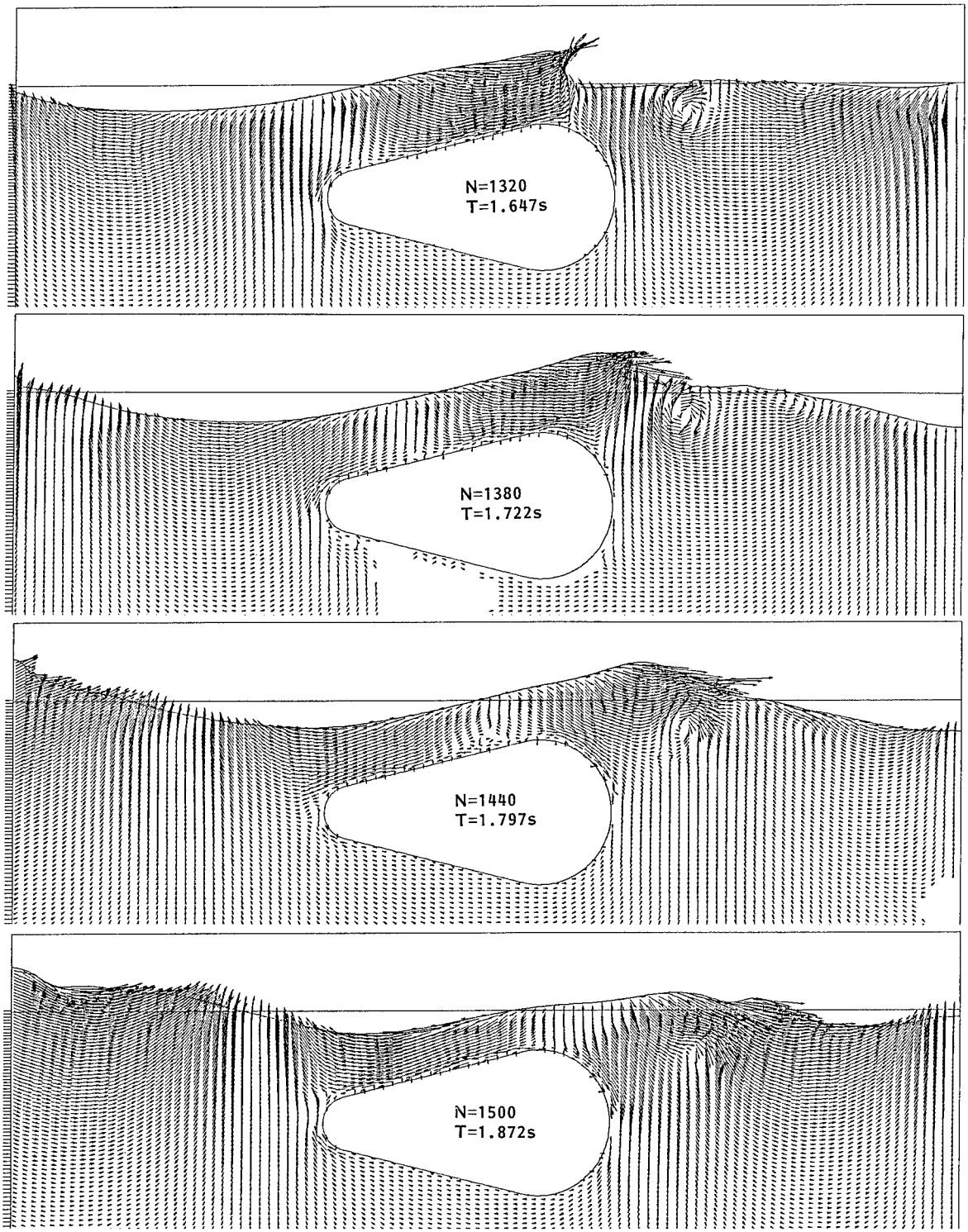


Fig.18 continued.

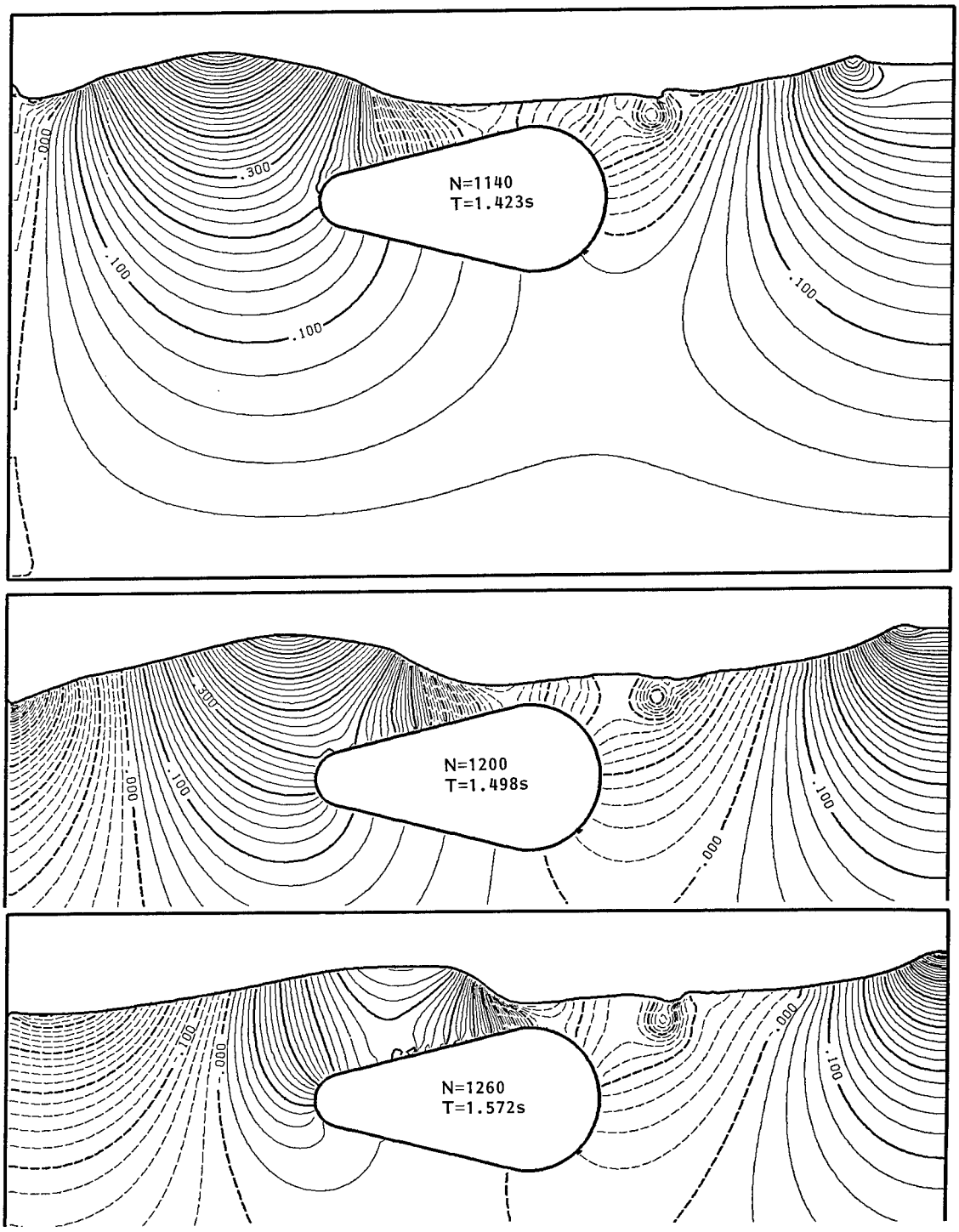


Fig.19 Time sequence of computed pressure contour map about model B, d/b=0.76, λ=1.57m, h_o=0.06m.

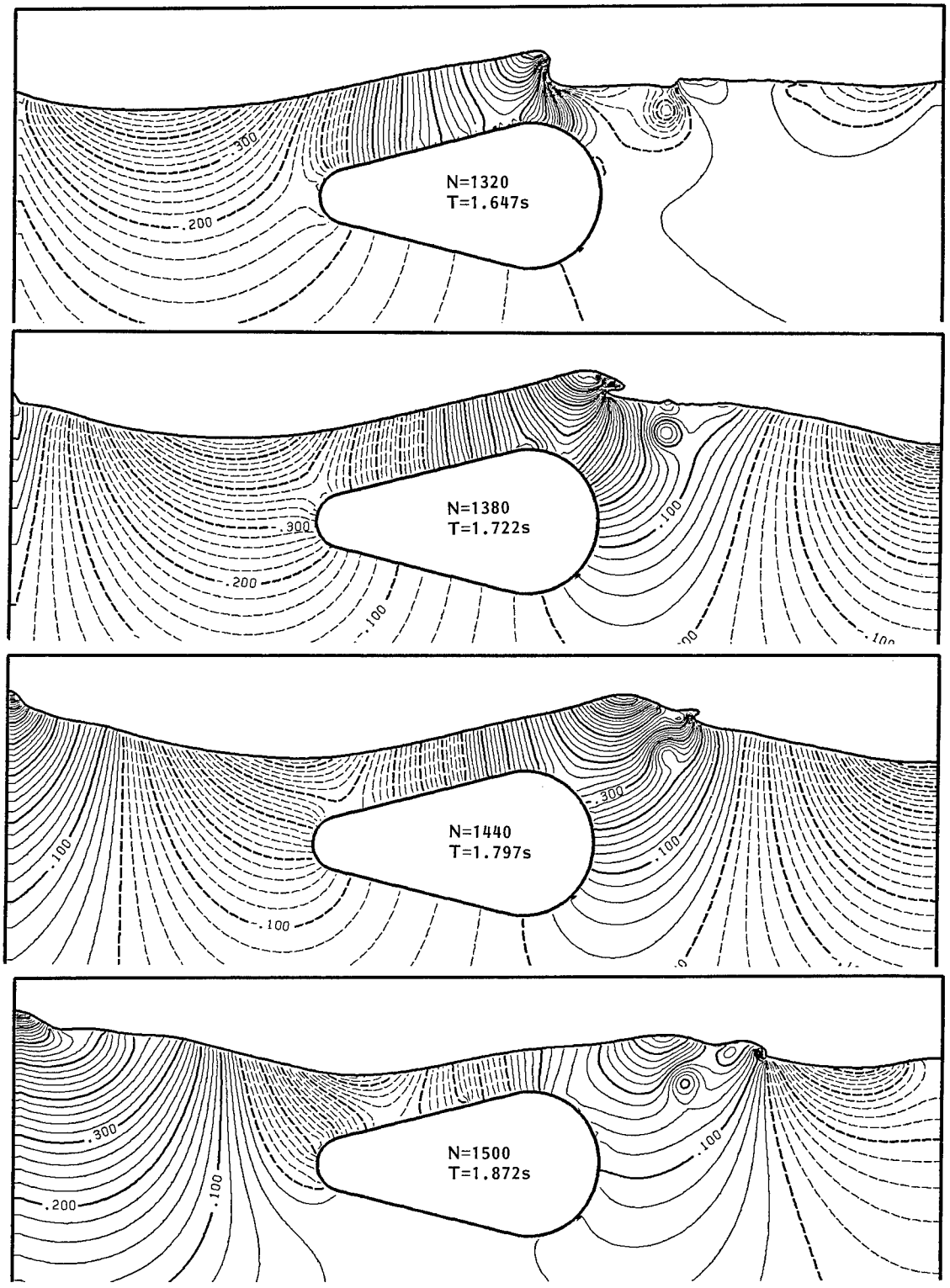


Fig.19 continued.

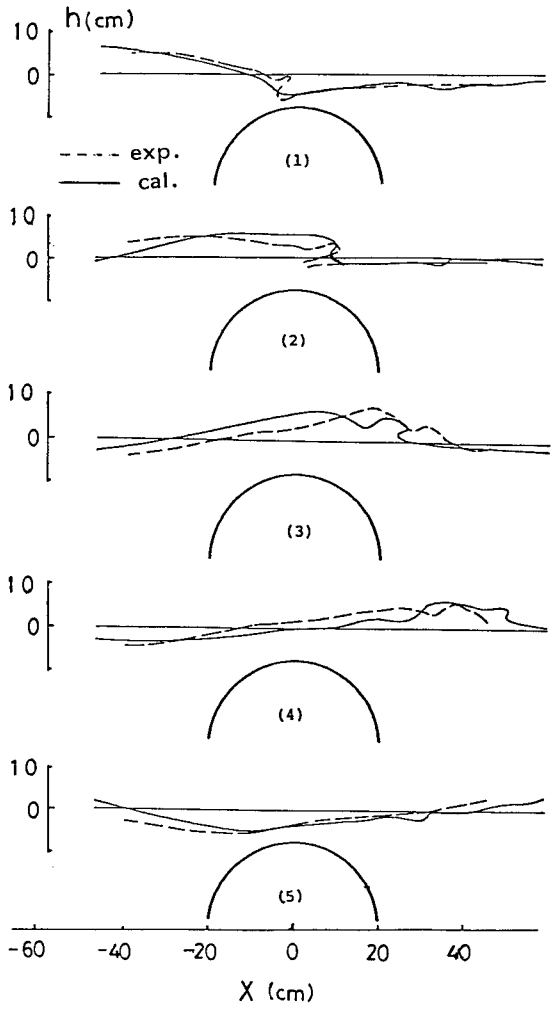


Fig.20 Comparison of measured and computed waves profiles on model A, d/b=1.375, λ=1.57m, h_o=0.06m.

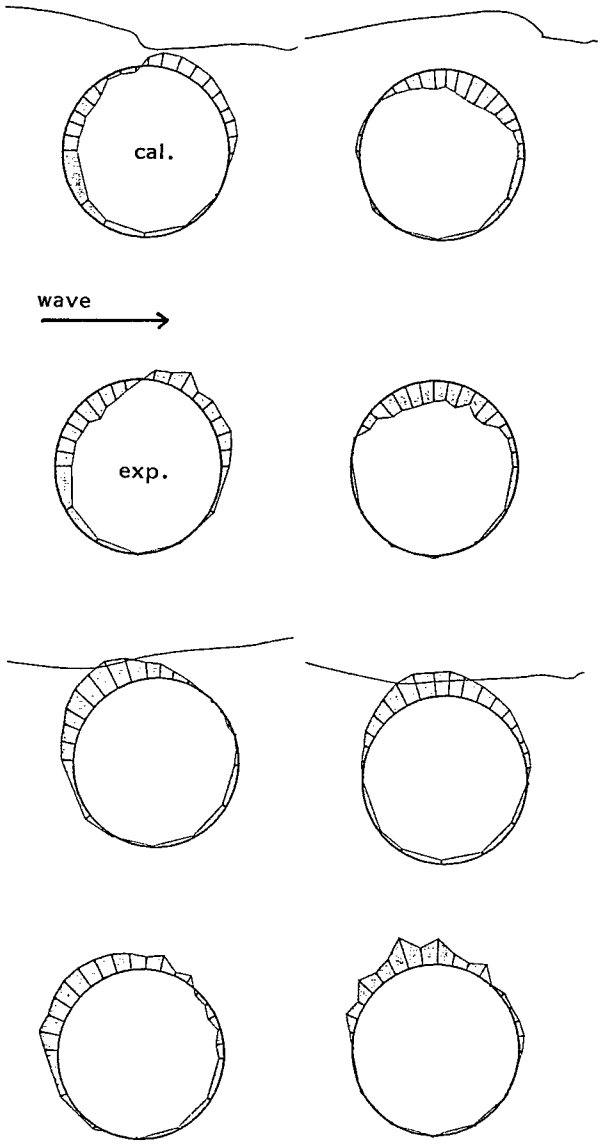


Fig.21 Comparison of computed and measured pressure distribution on model A, d/b= 1.375, λ=1.57m, h_o=0.06m.

7. COMPARISON BETWEEN EXPERIMENT AND SIMULATION

The wave profiles of the case of model A are compared in Fig.20. The experimental wave profiles are made from the pictures in the video-tape-recorder with a precise clock. The overall agreement is good but significant discrepancy is noted at the stage of wave splitting.

Beneath the breaking point a noticeable vortex is generated as shown in the simulation in Fig.16 and this qualitatively agrees well with the visualized results seen in Fig.5.

The pressure distributions on the model A are compared at four moments in Fig.21. The agreement seems to be satisfactory considering that the unrealistic fluctuation in the measured results is attributed to the phase difference in the measurement.

However the simulated forces which is derived from the integration of the pressure on the obstacle surface do not show satisfactory agreement as seen in Figs.22 to 25 for the two models A and B. The amplitude of simulated forces is generally smaller than the measurement. The discrepancy is most significant in the horizontal force on model B, to which further detailed examination will be necessary.

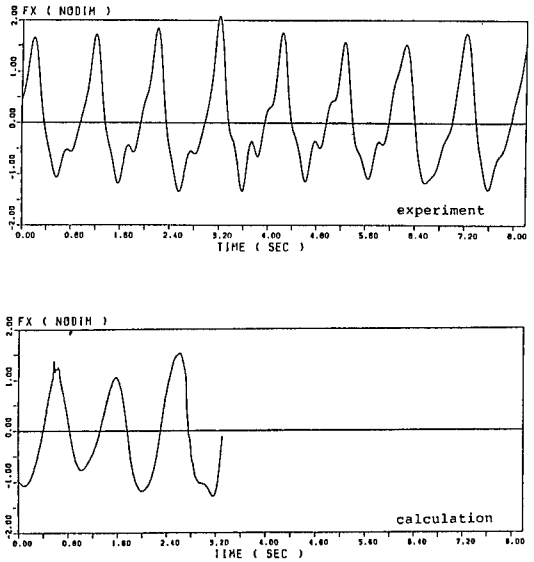


Fig.22 Comparison of measured (above) and computed (below) horizontal forces on model A made dimensionless with respect to $\rho g h_o b L$, d/b=1.375, λ =1.57m, h_o=0.06m.

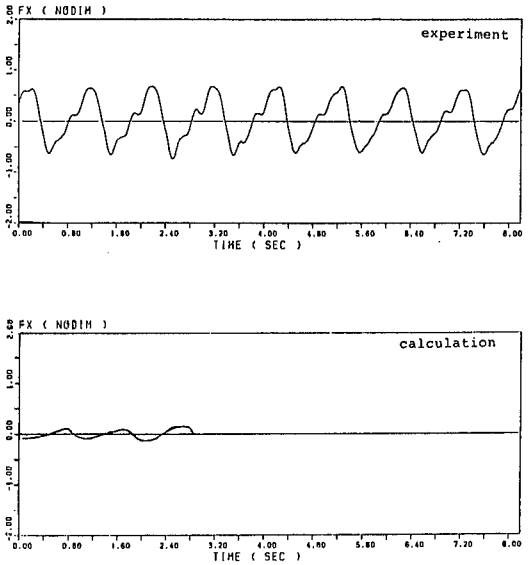


Fig.24 Comparison of measured and computed horizontal forces on model B, d/b= 1.375, λ=1.57m, h_o=0.06m.

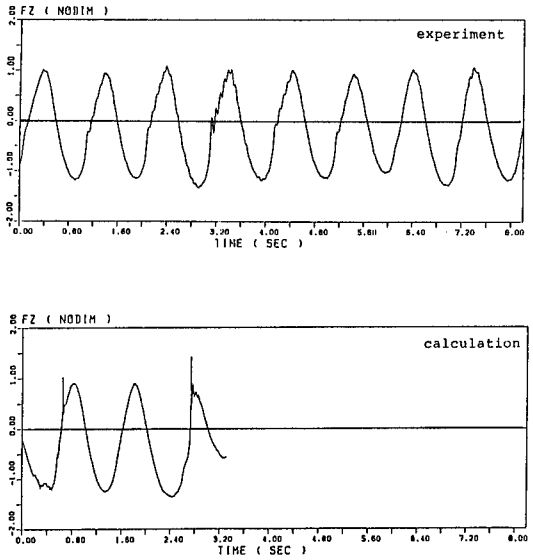


Fig.23 as Fig.22, vertical forces.

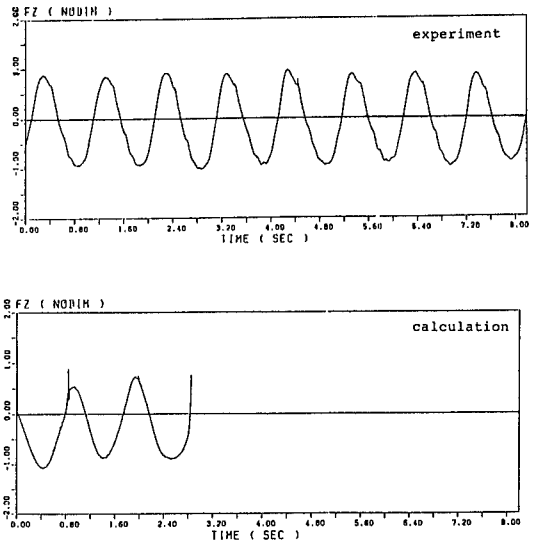


Fig.25 as Fig.24, vertical forces.

8. CONCLUDING REMARKS

A boundary element method is considered to be an alternative method of analysis, but it will not be able to cope with the complicated fluid motions after the overturning stage such as the impinging of the wave front and vortex generation. Furthermore the effect of the viscous flow on the obstacle cannot be interpreted by this kind of method. Therefore the capability of a finite-difference method based on the Navier-Stokes equations is superior to a boundary element method, as is demonstrated by the present simulations and their comparison with the experimental results in this paper. A finite-difference method seems to be cultivating a new research field of wave dynamics. A lot of fluid motions which have been considered impossible to be theoretically explained are going to be simulated by a finite-difference method. Furthermore numerical simulations can elucidate what experimental measurements cannot do even if the degree of accuracy is satisfactory. This may be understood when we find it difficult to make velocity vector fields of an unsteady fluid flow similar to Figs.16 and 18 from experimental measurement.

However it is also proved that the achievement of quantitative agreement in forces is difficult notwithstanding the quite excellent qualitative agreement in many nonlinear features of the waves. The way from the qualitative agreement to the quantitative agreement seems to be longer than expected.

The employment of the Adams-Bashforth method, the third-order upstream differencing method for a variable mesh system and the introduction of the SGS turbulence model enable us to simulate viscous fluid motions emanating from the free-surface and the body surface. However there are some other motions which are still left unconsidered. For instance the turbulence on the free-surface which is not isotropic and the air-entrainment which may cause complicated free-surface motions must be considered in order to attain better agreement.

The computations were performed by HITA C M-280H of the Computer Centre, the University of Tokyo. The CPU time required by the simulation of 1500 time steps was about 5 hours. Further improvement of the numerical technique is also necessary for the reduction of computational time, so that the application of a finite-difference method to engineering purposes is promoted in the near future.

This research is supported partly by the Grant-in-Aid for Scientific Research of the Ministry of Education, Science and Culture and partly by the LINEC group of shipbuilders.

References

1. Inoue, R. & Kyozuka, Y. On the nonlinear wave forces acting on submerged cylinders. J. Soc. Nav. Archit. Jpn. 156 (1984), 115-127. (in Japanese).
2. Miyata, H, Nishimura, S. & Masuko, A. Finite difference simulation of nonlinear waves generated by ships of arbitrary three-dimensional configuration. J. Comput. Phys. 60-3 (1985), 391-436.
3. Miyata, H. & Nishimura, S. Finite-difference simulation of nonlinear ship waves. J. Fluid Mech. 157 (1985), 327-357.
4. Miyata, H. Finite-difference simulation of breaking waves. J. Comput. Phys. (to appear).
5. Miyata, H., Matsukawa, C. & Kajitani, H. Shallow water flow with separation and breaking wave. J. Soc. Nav. Archit. Jpn. 158 (1985), 11-23.
6. Roache, P. J. Computational Fluid Dynamics, Hermosa, Albuquerque, N. M. (1976)
7. Lilly, D. K. On the computational stability of numerical solutions of time-dependent non-linear geophysical fluid dynamics problems. Mon. Weath. Rev. 93 No.1 (1965), 11-26.
8. Agarwal, R. K. A third-order-accurate upwind scheme for Navier-Stokes solutions at high Reynolds numbers. AIAA paper 81-0112 (1981).
9. Kawamura, T. & Kuwahara, K. Computation of high Reynolds number flow around a circular cylinder with surface roughness. AIAA paper 84-0340 (1984).
10. Deardorff, J. W. A numerical study of three-dimensional turbulent channel flow at large Reynolds numbers. J. Fluid Mech. 41 (1970), 453-480.
11. Smagorinsky, J., Manabe, S., & Holloway, J. L. Numerical results from a nine-level general circulation model of the atmosphere. Mon. Weath. Rev. 93 No.12 (1965), 727-768.

DISCUSSION

Sridhar Jagannathan,
Glosten Associates, Inc.

You noted that the use of the finite difference method is preferable to the use of the boundary integral method since viscous effects can be included. It is not however clear from your paper how important the viscous effects are. My questions therefore are as follows:

a. Have you done finite difference simulations with viscosity set to zero, and if so, what are the results?

b. Is the effect of viscosity and shedding of vortices to (a) increase the peak forces on the body, (b) cause forces at high frequency due to vortex shedding, especially in the horizontal force case (see Figures 22 and 24), or (c) cause any change in the wave breaking process?

If the viscous effects are not very significant then it would be computationally far less intensive to use the boundary integral method.

Hyoung-Tae Kim,
Iowa Institute of Hydraulic Research

In the paper, it was said that the no-slip boundary condition is approximately satisfied Would you explain it with more detail?

You used the 25,000 cells for the calculation. Could you show the calculation domain in your calculation? What time step did you use?

Did you consider the transition region from the laminar to the turbulent flows in your turbulent flow calculation? Otherwise, did you presume the whole flow is turbulent?

William W. Schultz,
University of Michigan

In earlier discussion, you mentioned that viscous stresses are ignored at the free surface. Assuming that surface tension is ignored, what boundary conditions do you use that allows strong pressure gradients along the free surface (as shown in Figs. 17 & 19)?

Stephen Shamroth
Scientific Research Associates

Could you elaborate on the downstream boundary condition. Did you notice any wave reflection from this boundary?

Fred Stern,
Iowa Institute of Hydraulic Research

The authors show discrepancies between their measured and computed pressure distributions. I would like to know if the authors also performed experiments and calculations for cylinders sufficiently submerged such that no wave breaking occured. If the comparison between the experiments and the computations is good for such conditions, then the discrepancies shown in the paper can be attributed to the modeling of the wave breaking phenomena; however, if the comparison is not good, then other aspects of the numerical procedure (e.g., treatment of the free-surface boundary conditions and grid resolution) must also be scrutinized. It appears that the authors have neglected the viscous and turbulent stresses in the free-surface boundary conditions. Would the authors please comment on the possibility of including these stresses and what influence they might have on the predictions? Lastly, concerning grid resolution, it appears that the grid used is too coarse to resolve the cylinder boundary layer. What influence do the authors expect this to have, especially for calculating bluff body flows where the boundary layer/vortex shedding characteristics are known to be important?

Erik C. Tiemroth,
University of California, Berkeley

I would like to compliment the authors on their very interesting paper. I am perplexed by the pressure contours shown in figures 17 and 19. The authors describe the plotted quantity as the total pressure minus the hydrostatic pressure. In the "pressure contour maps" presented in the figures, the free-surface is not an isobar. From this observation I infer that the plotted quantity, which I shall denote by $\hat{p}$, is defined as: $\hat{p}=(p + \rho g z)/\rho$, where p is the total pressure, and ρ is the density of the fluid. Is this correct?

The use of $\hat{p}$ to present the pressure results strikes me as an odd choice. For the points within the fluid that are above the undisturbed free surface (z=0), one is subtracting a negative pressure quantity from the total pressure. Furthermore, one cannot see how well the dynamic free-surface boundary condition is being satisfied since $\hat{p}$, unlike p, is not expected to be constant on the free-surface. It seems to me that it would be more useful to plot either the total pressure or the total pressure minus the pressure due to the instantaneous free surface head: $\hat{p}= [p + \rho g(z-Z(x,t))]/\rho$, where Z(x,t) is the instantaneous position of the free surface. I recognize that integrating $\hat{p}$ over the cylinder gives the force due to the waves (total force minus hydrostatic force), but it is not clear to me that $\hat{p}$ has significance away from the body boundary. Could the authors please comment on their choice of $\hat{p}$?

Reply -

The authors wish to thank discussors for their questions. They seem to clarify what is not sufficiently clear in our paper.

We have not performed a simulation without viscosity in the present case. However, we have presented in Ref. [4] a clear example, in which a viscous separated flow is influential to the free-surface flow involving wave breaking. Since the importance of the viscous flow depends on the problem, you may apply a boundary integral method to a problem for which a viscous flow does not play a significant role. However, it does not seem to us reasonable to neglect viscous motion in the breaking waves, since they are flow separation on the free-surface will lead to more precise estimation of forces due to breaking waves. Alot of effort must be focused on this problem.

In the present computations the whole flow is assumed turbulent and no initial condition for turbulence is employed. This is one of the points to which further improvement is necessary to complete simulations of viscous flows at high Reynolds numbers.

In order to approximately implement the no-slip body boundary condition, the velocities at the velocity points in the proximity of the body surface are extrapolated by quadratic equations with horizontal or vertical axes so that velocities on the segments, which represent the body surface, are set at zero. The use of the rectangular mesh system inevitably gives limitations on the resolution of the viscous flow on the curved surfaces.

Since the viscous stresses are ignored on the free-surface, the dynamic free-surface condition is a very simple one that gives the atmospheric pressure (equal to zero here) on the free-surface. This condition is satisfied quite well by the use of the irregular star technique. However, this is not clearly observed in figures 17 and 19, since the contours of total pressure minus statical head are shown, as Dr. Tiemroth pointed out. This choice of pressure is convenient to understand the magnitude of pressure caused by wave motions. The use of the total pressure seems to be a reasonable alternative, but it does not seem to be proper to use the total pressure minus the instantaneous statical head.

The computational domain is as illustrated in figures 16 to 19, namely 2m long and 1.2m high. The numerical wavemaker is located 1m upwave and the outflow boundary is 1m downwave from the center of the body. The short distance between the two boundaries is one of the causes of the inadequate accuracy in forces. The simple open boundary condition of giving zero-normal-gradient of variables works well in cooperation with the upstream differencing scheme for the convective terms. Since the unfavorable effects due to the imperfect open boundary conditions are supposed to give influences on the region of half wavelength upwave of the boundary at most, the enlargement of the computational domain leads to the elimination of the error from the open boundary conditions. This is one of the advantages of using the upstream differencing scheme, which implies that we have far less difficulties in the case of uniform stream.

Further details of the computational method are described in Ref. [4] which appeared in Journal of Computational Physics vol. 65, pp. 179 in July 1986.

Better agreement in forces is attained in the case of an elliplic obstacle as seen in Ref. [4], although the grid system is coarser than the present case and the subgrid-scale turbulence model is not introduced. The source of the discrepancies in the present computational results does not seem to lie in the modelling of the breaking motion or other substantial aspects of the simulation method. The enlargement of the computational domain will remarkably improve the accuracy by the reason described above.

However it appears safe to say that viscous effects on the free-surface and the body must be more rigorously implemented so that the accuracy is raised. Since the use of a rectangular mesh system gives difficulties in the resolution of boundary layers on the two surfaces, another method that uses boundary-fitted coordinate system is more appropriate for the problems in which boundary layer or vortex shedding play an important role. However it seems to be very difficult to generate a boundary-fitted grid system which is fitted to the moving free-surface that involves breaking motions

Hydrodynamic Impact Loads on Three-Dimensional Bodies

A.W. TROESCH and C.-G. KANG

University of Michigan, U.S.A.

ABSTRACT

The three dimensional aspects of hydrodynamic impact are discussed. Theoretical and experimental results for a sphere and a cusped body are presented. The cusped body is axisymmetric and resembles the bow profile of a ship with flare. The sphere was subjected to both vertical and oblique impact angles while the cusped body experienced only vertical motion. Three dimensional calculations using normal dipole distributions and an equi-potential free surface are compared with experimental results. The theoretical boundary value problem was solved using a known interior flow. This procedure reduced computation times significantly. Comparisons between theory and experiment show that, depending upon the body shape theoretical estimates of the maximum impact force may be larger or smaller than the experimental values.

INTRODUCTION

The hydrodynamic loads imposed upon a vessel experiencing large amplitude motions can be severe. Structural damage to the forebodies of ships with large flare angles has occurred in head and bow quartering seas indicating that both vertical and horizontal (and possibly torsional) impact loads are important.

While the impact problem has been investigated in various forms for years, most theories have dealt with two-dimensional, vertical aspects. The classical impact problem was formulated by von Karman (1929) and modified to include the effects of surface wetting by Wagner (1931). These two papers serve as the initial references for much of the later studies. Some authors, such as Payne (1981), suggest that the modifications to von Karman's work were not necessarily improvements. Sarpkaya and Isaacson (1981) review the literature of ocean engineering applications for von Karman-type impact solutions. These are important when considering the wave-slam on horizontal or nearly horizontal circular cylinders. More recently, the two-dimensional problem including gravitational effects and the non-linear free surface boundary condition has been solved numerically. Yim (1985), Gallagher and McGregor (1985), and Greenhow (1986), among others, have used various numerical time stepping techniques to get good descriptions of two-dimensional wedge impact including the spray jet.

Relatively few attempts have been made to rigorously solve impact problems dealing with three dimensional bodies. Examples of three dimensional solutions are Shiffman and Spencer (1951), Chuang (1969), and Miloh (1981). Shiffman and Spencer (1951) and Chuang (1969) developed general expressions for the pressure distributions and slamming forces on a cone. Using similar assumptions, Miloh (1981) analytically derived the added mass coefficients for a double spherical bowl. From these coefficients the impact force on a sphere was calculated assuming that the free surface is represented by an equi-potential or zero gravity surface. Miloh (1981) or Greenhow (1986) offer good reviews of the relevant literature.

Of practical engineering interest are the impact forces in the bow region of a ship. Due to the complexities associated with three-dimensional boundary value problems, it has been common practice to use simplifying assumptions that reduce the calculations of hydrodynamic forces to a two-dimensional strip theory. Examples of this are given by Ochi and Motter (1969) and (1973), Yamamoto, et. al. (1980), Belik, et.al. (1982), and

Oliver (1983). These types of hydrodynamic theories assume that the ship is of sufficient length and cross sectional uniformity to allow the hull to be divided into segments, each of which is assumed to act independently of any other. A number of two-dimensional solutions are then summed to yield the total impact force. Techniques such as these are questionable in the bow region where the assumed two-dimensionality of the flow may not be valid. An illustration of the relative error of the two-dimensional approximation for three-dimensional bow loads can be seen in Figure 1. There the nondimensional impact force for a sphere, defined by C_S = 2 (impact force)/$\rho\pi R^2V^2$, is calculated using results similar to Miloh's (1981) three dimensional theory and a strip theory based upon Kaplan and Silbert's (1976) or Sarpkaya and Isaacson's (1981) formulas for a circular cylinder. The slam coefficient is plotted as a function of z/R , the normalized vertical distance. In both cases, the free surface is represented by an equi-potential surface and the velocity of the body is constant. While the strip theory approximation of the sphere represents an extreme example, it demonstrates the need to exercise caution when applying two-dimensional solutions in areas where three dimensional effects are large.

This paper will present the results of an investigation dealing with the three dimensional hydrodynamic impact problem. The approximate theory of von Karman (1929) will be used in three dimensions in both the vertical and horizontal planes of motion. Two different body shapes will be examined: the sphere, for comparison with previously published results and an axisymmetric cupsed body, similar in shape to the bow profile of a ship's forebody with large flare. The sphere will be evaluated with zero and non-zero horizontal velocity components. Both theoretical and experimental results are presented. A numerically efficient technique for the solution of the hydrodynamic three-dimensional boundary value problem will be described.

PROBLEM FORMULATION

Consider an ideal fluid domain below the surface given by

$$z = \zeta(x,y,t) \tag{1}$$

where (x,y,z) is a right-handed coordinate system with z positive upwards and the origin located at the mean free surface. Then the complete non-linear free surface condition that the velocity potential, ϕ , must satisfy is given by (see Newman (1977))

$$\frac{\partial^2\phi}{\partial t^2} + g\frac{\partial\phi}{\partial z} + 2\nabla\phi\cdot\nabla\frac{\partial\phi}{\partial t} + \frac{1}{2}\nabla\phi\cdot\nabla(\nabla\phi\cdot\nabla\phi) = 0 \tag{2}$$

where Eq. (2) must be true on the surface defined by Eq. (1). Following von Karman (1929), we assume that when the motion of a body on the free surface occurs over a very short time interval, the temporal derivatives of the velocity potential are large compared to the spacial ones and the free surface boundary condition can be approximated as

$$\phi = 0 \tag{3}$$

on $z = 0$. The body boundary condition follows from

$$\frac{\partial\phi}{\partial n} = \underline{V}\cdot\underline{n} \tag{4}$$

on the instantaneous surface of the body. Here $\underline{V}$ is the velocity vector of the body with components (U,V,W) and $\underline{n}$ is the outward unit normal vector.

This boundary value problem is similar to the one proposed by von Karman (1929). It ignores effects due to changes in the local water surface elevation such as the spray jet. However, Payne (1981) demonstrated that this analytical model actually produced results that compared better with experiments than later "improved" theories, such as Wagner's splash-up factor. One possible cause for concern, though, is that this theory will not predict pressures and consequently forces on any part of the object's surface that has not passed the mean free surface. For bodies with concave shapes, such as ships with large flare, the spray sheets may contribute significantly to impact forces. In the following sections, experimental results for a flared body will be compared with theoretical calculations indicating the usefulness and limitations of this relatively simple theory.

The pressures, and subsequent forces, are found from Bernoulli's equation. Bernoulli's equation is given as

$$\frac{p}{\rho} + \frac{\partial\phi}{\partial t} + \frac{1}{2}\nabla\phi\cdot\nabla\phi + gz = \text{const} \tag{5}$$

where in a consistent theory, the quadratic term is of higher order and assumed small. The pressure may be integrated to find the forces acting on

the body. In an alternative derivation, Faltinsen (1977) has re-derived the traditional result that the force on a body is given by

$$\text{Vertical Impact Force} = -\frac{d}{dt}(A_{33}\,\dot{z}_o(t)) + \iint_S ds\ \rho g\ z\ n_3 \qquad (6)$$

In Eq. (6), A_{33} is the heave infinite frequency added mass coefficient as a function of submergence and $z_o(t)$ is the vertical displacement as a function of time. It is common practice to assume that the velocity of the body is constant over the time of impact. The impact force then becomes the time derivative of the added mass. By time stepping the body through the free surface, the body boundary condition can be satisfied exactly on the below-mean-waterline portion of the hull. The assumption of constant velocity is not a necessary condition but rather one of convenience. As will be demonstrated in later sections, it may be appropriate for bodies such as the sphere, but less so for the axisymmetric cupsed body used in this study.

Conceptually, the pressure release problem defined by Eq. (3) and (4) may be solved in a straightforward manner using distributions of surface singularities. This has been done in the field of hydroballistics using source distributions by Wardlaw, et al (1977) for the forces acting on spheres, cones, and disks due to high-speed oblique water entry. In practice, the computational difficulties associated with three dimensional ship-like shapes and the required large number of time steps seem to have prevented researchers from actually using this method to calculate forces for arbitrary bodies. Oliver (1983) gives one example of large computer time estimates for solving extreme ship motion problems.

In this work, the hydrodynamic boundary value problem at each time step will be solved using a normal dipole distribution with a corresponding interior flow. This technique is an expansion of that outlined by Chang and Pien (1975) and Yeung (1982). It has the advantage of being up to 40% faster than the traditional Hess and Smith (1967) method. In particular, from the classical use of Green's Theorem the dipole strength is equal to the difference between the interior and exterior potentials. Solving for the dipole strength with a known interior flow immediately yields the exterior potential and thus the pressures. Breslin, et al (1982) has shown that the interior problem is equivalent to the interior fluid moving vertically as a solid mass of water. For horizontal motion, it will be demonstrated in the following paragraphs that the interior problem is represented by a dipole sheet on the inner free surface with the interior fluid mass moving horizontally.

PROBLEM SOLUTION

Consider a body with bounding surfaces and outward unit normal $\underline{n}$ as shown in Figure 2. The exterior and interior domains are R_e and R_i respectively. The exterior bounding surfaces on the free surface, body, and at infinity are given as S_{Fe}, S_B, and S_∞. The interior bounding surfaces are the interior free surface, S_{Fi}, and the body, S_B. The usual governing equations for the velocity potential, $\phi(\underline{X})$, and a Green function $G(\underline{X};\underline{Y})$, are

$$\nabla^2\phi(\underline{X}) = 0$$

$$-\nabla^2 G(\underline{X};\underline{Y}) = \delta(\underline{X}-\underline{Y}) \qquad (7)$$

where $\underline{X}$ is the vector to the field point, $\underline{Y}$ is the vector to the source point, and $\delta(\underline{X}-\underline{Y})$ is the Dirac delta function. Through the application of Green's second identity in R_e the exterior potential is given as

$$\phi_e(\underline{X}) = -\iint_{S_B+S_{Fe}+S_\infty} \left(G(\underline{X};\underline{Y})\frac{\partial\phi_e(\underline{Y})}{\partial n} - \phi_e(\underline{Y})\frac{\partial G(X;Y)}{\partial n}\right)ds \qquad (8)$$

When Green's second identity is applied again in R_i, the result is

$$0 = -\iint_{S_B+S_{Fi}} \left(G(\underline{X};\underline{Y})\frac{\partial\phi_i(\underline{Y})}{\partial n} - \phi_i(\underline{Y})\frac{\partial G(\underline{X};\underline{Y})}{\partial n}\right)ds \qquad (9)$$

Subtracting Eq. (9) from Eq. (8) gives

$$\phi_e(\underline{X}) = -\iint_{S_B} \left[G(\underline{X};\underline{Y})\left(\frac{\partial\phi_e(\underline{Y})}{\partial n} - \frac{\partial\phi_i(\underline{Y})}{\partial n}\right) - \left(\phi_e(\underline{Y}) - \phi_i(\underline{Y})\right)\frac{\partial G}{\partial n}(\underline{X};\underline{Y})\right] ds$$

$$- \iint_{S_{Fe}} \left[G(\underline{X};\underline{Y}) \frac{\partial \phi_e(\underline{Y})}{\partial n} - \phi_e(\underline{Y}) \frac{\partial G(\underline{X};\underline{Y})}{\partial n}\right] ds$$

$$+ \iint_{S_{Fi}} \left[G(\underline{X};\underline{Y}) \frac{\partial \phi_i(\underline{Y})}{\partial n} - \phi_i(\underline{Y}) \frac{\partial G(\underline{X};\underline{Y})}{\partial n}\right] ds$$

$$- \iint_{S_{\infty}} \left[G(\underline{X};\underline{Y}) \frac{\partial \phi_e(\underline{Y})}{\partial n} - \phi_e(\underline{Y}) \frac{\partial G(\underline{X};\underline{Y})}{\partial n}\right] ds \qquad (10)$$

For the pressure release problem, the appropriate Green function is

$$G(\underline{X};\underline{Y}) = \frac{1}{4\pi}\left(\frac{1}{|\underline{X}-\underline{Y}|} - \frac{1}{|\underline{X}-\underline{Y}'|}\right) \qquad (11)$$

where $\underline{Y}'$ is an image vector of $\underline{Y}$ about $z=0$. Since both $G(\underline{X};\underline{Y})$ and $\phi_e(\underline{X})$ are zero on S_{Fe} and far from the body both go to zero at a sufficient rate, the integrals S_∞ and S_{Fe} contribute nothing in Eq. (10). The interior potential is arbitrary and selected such that the normal derivatives of the interior and exterior problems are continuous. In other words,

$$\frac{\partial \phi_e}{\partial n} - \frac{\partial \phi_i}{\partial n} = 0 \quad \text{on} \quad S_B .$$

The resulting surface dipole distribution has a strength defined as μ where $\mu = \phi_i - \phi_e$ on S_B . From Eq. (10), the following form for the exterior potential is

$$\phi_e(\underline{X}) = - \iint_{S_B} \mu(\underline{Y}) \frac{\partial G(\underline{X};\underline{Y})}{\partial n} ds$$

$$+ \iint_{S_{Fi}} \left[G(\underline{X};\underline{Y})) \frac{\partial \phi_i(\underline{Y})}{\partial n}\right.$$

$$\left. - \phi_i(\underline{Y}) \frac{\partial G(\underline{X};\underline{Y})}{\partial n}\right] ds \qquad (12)$$

As $\underline{X}$ approaches a boundary point on the surface S_B , the exterior potential becomes

$$\phi_e(\underline{X}) = - \frac{\mu(\underline{X})}{2} - \iint_{S_B} \mu(\underline{Y}) \frac{\partial G(\underline{X};\underline{Y})}{\partial n} ds$$

$$+ \iint_{S_{Fi}} \left[G(\underline{X};\underline{Y}) \frac{\partial \phi_i(\underline{Y})}{\partial n} - \phi_i(\underline{Y}) \frac{\partial G(\underline{X};\underline{Y})}{\partial n}\right] ds \qquad (13)$$

for $\underline{X}$ on S_B . Since $\phi_e(\underline{X}) = \phi_i(\underline{X}) - \mu(\underline{X})$ on S_B , the above equation becomes

$$\phi_i(\underline{X}) = \frac{\mu(\underline{X})}{2} - \iint_{S_B} \mu(\underline{Y}) \frac{\partial G(\underline{X};\underline{Y})}{\partial n} ds$$

$$+ \iint_{S_{Fi}} \left[G(\underline{X};\underline{Y}) \frac{\partial \phi_i(\underline{Y})}{\partial n} - \phi_i(\underline{Y}) \frac{\partial G(\underline{X};\underline{Y})}{\partial n}\right] ds \qquad (14)$$

which is a Fredholm Integral Equation of the second kind.

Determination of the Interior Potentials

The governing equation for the interior potential, ϕ_i , in R_i is the Laplace equation. On the body surface, S_B , the boundary condition for ϕ_i is

$$\frac{\partial \phi_i}{\partial n} = \frac{\partial \phi_e}{\partial n} = \underline{V} \cdot \underline{n} .$$

By also setting

$$\frac{\partial \phi_i}{\partial n} = \underline{V} \cdot \underline{n}$$

on the interior free surface, S_{Fi} , ϕ_i is determined uniquely in R_i except for an arbitrary constant. The special cases of rigid body motion in heave and sway are discussed below.

For heave, let the interior potential be given as

$$\phi_i(\underline{X}) = Wz \qquad (15)$$

where W is the vertical velocity component and $\underline{X}$ is in R_i . By inspection, it is clear that the condition of

$$\frac{\partial \phi_i}{\partial n} = \underline{V} \cdot \underline{n}$$

is satisfied on both S_B and S_{Fi} . Since both $\phi_i(\underline{X}) = 0$ and $G(\underline{X};\underline{Y}) = 0$ on S_{Fi} , Eq. (14) becomes

$$\phi_i(\underline{X}) = \frac{\mu(\underline{X})}{2} - \iint_{S_B} \mu(\underline{Y}) \frac{\partial G(\underline{X};\underline{Y})}{\partial n} ds \qquad (16)$$

for $\underline{X}$ on S_B .

For sway, let the interior potential be given as

$$\phi_i(\underline{X}) = Vy \qquad (17)$$

where V is the horizontal velocity component and $\underline{X}$ is in R_i. Again by inspection, it is clear that the condition of

$$\frac{\partial \phi_i}{\partial n} = \underline{V} \cdot \underline{n}$$

is satisfied on both S_B and S_{Fi}. The integral equation in this case is somewhat more complex than for heave since ϕ_i is not zero on S_{Fi}. Using the fact that $G(\underline{X};\underline{Y}) = 0$ on S_{Fi}, or alternatively that

$$\frac{\partial \phi_i}{\partial n} = 0$$

on S_{Fi}, Eq. (14) becomes

$$\phi_i(\underline{X}) + \iint_{S_{Fi}} (Vn)\frac{\partial G(\underline{X};\underline{Y})}{\partial n}\, ds$$

$$= \frac{\mu(\underline{X})}{2} - \iint_{S_B} \mu(\underline{Y})\frac{\partial G(\underline{X};\underline{Y})}{\partial n}\, ds \qquad (18)$$

for $\underline{X}$ on S_B.

The dipole strengths for the heave and sway problems are given as the solutions to Eq. (16) and Eq. (18) respectively. With these strengths known and the interior potential given, the relation $\phi_e(\underline{X}) = \phi_i(\underline{X}) - \mu(\underline{X})$ may be used to find the exterior potentials. This method of solving boundary value problems eliminates to need to find both the values of the Green Function and its normal derivative as in the standard Hess and Smith (1967) method.

Determination of the Impact Pressures

Once the potential is known, the pressures may be found by applying Eq. (5), Bernoulli's Equation. Bernoulli's equation is derived for variables relative to an inertial coordinate system. However, it is convenient for the purpose of solving the impact boundary value problem to use body fixed coordinates. Under these circumstances, spacial differentiation is invariant with coordinate transformation, but temporal differentiation is not. If $\underline{X}$ is a position vector in the inertial coordinates and $\underline{X}'$ is a position vector in the body axis coordinates, then they are related by

$$\underline{X}' = \underline{X} - \int_0^t \underline{V}(t)dt \qquad (19)$$

where $\underline{V}(U,V,W)$ is the velocity vector of the body and

$$\frac{\partial x'}{\partial t} = -U(t)\,, \quad \frac{\partial y'}{\partial t} = -V(t)\,,$$

$$\frac{\partial z'}{\partial t} = -W(t)\,, \qquad (20)$$

Let $\phi(\underline{X},t)$ be the potential in inertial coordinates and $\phi'(\underline{X}',t)$ the potential in body axis coordinates, then by virtue of the chain rule of calculus

$$\frac{\partial \phi_e(\underline{X},t)}{\partial t} = \frac{\partial \phi_e'(\underline{X}',t)}{\partial t} -$$

$$U(t)\frac{\partial \phi_e'(\underline{X}',t)}{\partial x'} - V(t)\frac{\partial \phi_e'(\underline{X}',t)}{\partial y'}$$

$$- W(t)\frac{\partial \phi_e'(\underline{X}',t)}{\partial z'} \qquad (21)$$

Bernoulli's Equation, then, in body fixed coordinates is

$$\frac{p(\underline{X}',t)}{\rho} = -\Big[\frac{\partial \phi_e'(\underline{X}',t)}{\partial t}$$

$$- \Big(U(t)\frac{\partial \phi_e'(\underline{X}',t)}{\partial x'}$$

$$+ V(t)\frac{\partial \phi_e'(\underline{X}',t)}{\partial y'} + W(t)\frac{\partial \phi_e'(\underline{X}',t)}{\partial z'}\Big)$$

$$+ \frac{1}{2}\nabla\phi_e'(\underline{X}',t) \cdot \nabla\phi_e'(\underline{X}',t) + gz\Big] \qquad (22)$$

Integrating $\frac{\partial \phi_e'}{\partial t} n_3$ over the body, where n_3 is the vertical component of the unit normal, yields the time derivative of the added mass as discussed previously. The force resulting from the convective terms in Eq. (22) does not appear in the traditional calculations. (See Eq. (6).) The influence of the various force components are discussed in later sections. The time differential in Eq. (22) is found through numerical differentiation of the potential at various time steps. The fluid velocity vector in body axis coordinates, $\nabla(\phi_e')$, with components (u,v,w) is found by using the vortex lattice concept. Following Thrasher (1983) and others, the jump in velocity vector, $\underline{V}_e - \underline{V}_i$, across a normal dipole sheet can be represented by the vector cross product between the unit surface normal, $\underline{n}$, and the vorticity vector, $\underline{\omega}$, or

$$\underline{V}_e = \underline{V}_i - \underline{n} \times \underline{\omega} \qquad (23)$$

Here $\underline{V}_e$ and $\underline{V}_i$ are the surface velocity vectors on the exterior and interior surfaces respectively. The numerical determination of the vorticity vector is described in the next section.

Given the pressures by Eq. (22), the forces and consequently the accelerations may be found through integration. The usual relations for the accelerations, velocities, and displacements are shown below.

$$F_Z = m\,\ddot{Z} = -\iint p\, n_Z\, dS$$

$$F_Y = m\,\ddot{Y} = -\iint p\, n_Y\, dS \qquad (24)$$

$$\dot{Z}(t) = \int_o^t \ddot{Z}(t)dt \qquad \dot{Y}(t) = \int_o^t \ddot{Y}(t)dt$$

$$Z(t) = \int_o^t \dot{Z}(t)dt \qquad Y(t) = \int_o^t \dot{Y}(t)dt \qquad (25)$$

Computational Details

The surface description of the body and the solutions to the integral equations, Eqs. (16) and (18), follow the method of Hess and Smith (1967). In the interest of computational efficiency, the body was divided vertically into four or five large blocks. The boundary value problems were solved and the velocity potential and velocity vector on the body were calculated in 8-10 time steps for each block. For the particular examples used in this paper, symmetry reduced the number of elements by a factor of four. In any particular block, the number of circumferential elements, M, was fixed and the number of vertical (azimuthal) elements was increased by one for each time step. Thus, at time t_1 the number of elements was MxN and at time $t_1 + \Delta t$ the number was $Mx(N+1)$. For the examples considered in this paper, the range of N was 8 to 16 and the range of M was 6 to 8. When elements were required on the inner free surface, as in the sway problem, the number of surface elements was $(M-1)$. The velocity potential for body fixed coordinates was assumed to locally follow a second order polynomial with respect to time. The partial derivative was easily found as shown below

$$\frac{\partial \phi_e'(\underline{X}',t_1)}{\partial t} =$$

$$= \frac{t_1 - t_2}{(t_0-t_2)(t_0-t_1)}\,\phi_e'(\underline{X}',t_0)$$

$$+ \frac{2t_1 - t_2 - t_0}{(t_1-t_2)(t_1-t_0)}\,\phi_e'(\underline{X}',t_1)$$

$$+ \frac{t_1 - t_0}{(t_2-t_1)(t_2-t_0)}\,\phi_e'(\underline{X}',t_2) \qquad (26)$$

The vorticity vector, $\underline{\omega}$, used in the determination of the velocity vector $\underline{V}_e$, is found using the vortex lattice method (Thrasher (1983)). Since the doublet strength is assumed to be constant over a panel, the local induced velocity is equivalent to the line integral of the vortex filament strengths. As shown in Figure 3, the net vortex strength is found by superimposing adjacent elements. The vorticity vector at the jth panel null point, $\underline{\omega}_j$, is given by

$$\underline{\omega}_j = \sum_{i=1}^{m} \frac{\underline{\ell}_i \Gamma_i}{A_j + A_i} \qquad (27)$$

where $\underline{\ell}_i$ denotes the vectors connecting consecutive nodes of the jth panel, Γ_i is the branch circulation of the corresponding vortex segments, A_j is the area of the jth panel, A_i is the area of the adjoining panel on the ith side, and m is the number of panel edges, either three or four.

The velocity at the free surface $(z=0)$ in the idealized double body problem is infinite for non-wallsided shapes. Numerically this is represented by large values for the vortex strengths on the panels next to that equi-potential surface. Based upon the physics of the problem, and the two dimensional results for the pressure distribution in the spray jet (see Yim (1985), Gallagher and McGregor (1985), and Greenhow (1986)), the vortex strengths for filaments at the free surface were equated to the lower adjacent ones.

The computer program was verified by comparing results with the works of Miloh (1981) and Hulme (1982). For the later, a 20×20 segmented quarter hemisphere gave a result that was within 0.9% of the published value for the sway added mass coefficient (0.2732) and within 0.2% for the heave added mass coefficient (0.500).

THEORETICAL AND EXPERIMENTAL COMPARISONS

Impact experiments were conducted

in the Ship Hydrodynamics Laboratory at the University of Michigan. As mentioned in the INTRODUCTION, two different body shapes were tested: a sphere, and an axisymmetric cupsed body, similar in shape to the bow profile of a ship's forebody with large flare.

The sphere was a composite construction of plexi-glass, concrete, wood, and metal. It was ballasted to float as a hemisphere. The outside diameter was 0.502m (19.8in). The cupsed body was of similar construction. Both the sphere and cupsed body dimensions and profiles are shown in Figure 4. Also shown are the panel distributions used in the computations. The cupsed body had a total weight of 74.7N (16.8 lbs) and floated at approximately 90% of the total height of the body. A transferable instrument packet containing two accelerometers, one for vertical acceleration and one for horizontal acceleration, was used in both bodies. With these measurements the time history of the impact force can be easily determined since the force is equal to the mass of the object multiplied by the instantaneous acceleration. The accelerometers were of the piezo-electric type with a natural frequency in excess of 35 K Hz.

The test matrix included dropping the sphere and cupsed body from three heights, 0.61m (2 ft), 1.22m (4 ft), and 1.83m (6 ft). These corresponded to impact velocities of 2.46m/s (11.3 ft/s), 4.89m/s (16.0 ft/s), and 5.99m/s (19.7 ft/s) respectively. For the 0.61m (2 ft) and 1.22m (4 ft) heights, the sphere was also dropped from a moving carriage with a speed that corresponded to the vertical impact velocity. This resulted in an oblique entry angle of 45 degrees. Each drop was performed two or three times as a check on repeatability. The level of repeatability was good as discussed in the Appendix.

Experimental Results

Both the dimensional and non-dimensional results are displayed in the following figures. Figures 5 and 6 show the dimensional acceleration in multiples of the gravitational constant plotted as a function of elapsed time in milliseconds. They show the vertical acceleration for the sphere and cupsed body with zero horizontal velocity respectively. All three drop heights are included.

The dimensional results of Figures 5 and 6 are replotted in non-dimensional form in Figures 7 and 8. Figure 9 is a plot of nondimensional vertical and horizontal accelerations for the sphere with a 45 degree entrance angle. Both drop heights for this case are included.

The vertical slamming coefficient, C_{VS}, replaces the vertical acceleration. It is defined as

$$C_{VS} = 2\, m\ddot{Z}/\rho\, \pi\, L^2 V_O^2 \qquad (28)$$

where

- m is the mass,
- $\ddot{Z}$ is the vertical acceleration,
- ρ is the water density,
- L is some representative length, (the radius for the sphere and half the top transverse dimension for the cupsed body, 0.195m (7.7 in)),
- $D = 2L$

and V_O is the initial vertical impact velocity.

The time axis has been normalized by V_O/D. For oblique entry impact, the horizontal slamming coefficient, C_{hs}, is defined. In it, the horizontal acceleration, $\ddot{Y}$, replaces the vertical acceleration.

In the non-dimensional plots for the sphere (Figure 7), the normalized accelerations have approximately the same maximum value. However, the normalized maximum impact for the cupsed body (Figure 8) is dependent on the drop height. As time or the depth of immersion increase, the buoyancy becomes relatively more significant for bodies dropped from the lower heights. Also, if the body accelerates and the velocity fails to remain constant, then the normalization is not completely valid. This is consistent with Eq. (22), Bernoulli's equation, where the velocity potential terms for constant velocity may be normalized by the velocity squared, but the hydrostatic term, gz, follows the Froude scaling law.

The non-dimensional maximum vertical impact force for the oblique entry test (Figure 9) does not differ significantly from the normal entry results. This indicates that the coupling force for the sphere (the vertical force due to horizontal impact velocity) is not large. The maximum of the horizontal force is somewhat smaller relative to that of the vertical force and occurs at a latter time. The above conclusions are clearly hull-form dependent and would not necessarily hold for long, slender shapes experiencing oblique slamming.

Theoretical Results

The effect of the buoyancy terms is shown in Figures 10 and 11 for the sphere and cupsed body respectively. Constant velocity during the entire

immersion was assumed. The hydrostatic term has been separated from the rest of the theoretical pressure terms in Eq. (22). The velocity potential contributions were integrated and plotted as the solid line, labeled SUBTOTAL. The normalized buoyancy forces for three different drop Froude Numbers are shown as the dashed lines. (The drop Froude Number is defined as $V_o/\sqrt{(gL)}$ where V_o and L are defined in Eq. (28). All the force components were normalized by the factors $0.5\ \rho\pi L^2 V_o^2$, consistent with Eq. (28). Similar to the experimental results, the buoyancy terms normalized with respect to the velocity squared become relatively more important for the impact forces with lower initial velocities.

The various force components of the different pressure terms in Eq. (22) are shown in Figures 12 and 13 for the sphere and cusped body respectively. Initial velocities corresponding to drop Froude Numbers of 3.8158 for the sphere and 4.3320 for the cusp were assumed. These velocities remained constant during the impact fall. It is of interest to note that numerically, the term associated with the coordinate transformation of the time derivative, V*DPHI/DZ (see Eq. (21)), approximately cancels the quadratic velocity term, $0.5*Q^2$. The solid line in Figure 12, representing the time derivative of the velocity potential in body fixed coordinates, has a maximum of $C_{VS} \approx 0.952$. This value compares well with the results published by Miloh (1981) where an equation analogous to Eq. (6) was used to find the vertical slam coefficient. The maximum value of the slam coefficient for a sphere including all the terms of Eq. (22) except buoyancy, is $C_{VS} \approx 0.903$. See Figure 10.

Simulations of the velocity time histories for the two bodies are shown in Figures 14 and 15. Three different drop heights corresponding to drop Froude Numbers of 2.2030, 3.1156, and 3.8158 for the sphere and 2.5011, 3.5371, and 4.3320 for the cusped body are displayed. The instantaneous velocity has been normalized by the initial impact velocity. For each time step, the forces, accelerations, velocities, and displacements were calculated using Eqs. (24) and (25). Clearly, the velocities do not remain constant during the fall. The maximum impact force for the sphere occurs at a non-dimensional time (TV_o/D) of 0.062, a point where the velocity has been reduced by approximately 5.0%. For the cusped body, the maximum is at $TV_o/D = 0.63$ and the velocity has been reduced by 23.1%. These curves suggest that impact calculations should include the acceleration and velocity changes due to body dynamics. This is particularly true for flared bodies where the location of maximum force corresponds to a significant decrease in velocity.

Comparison Between Theory and Experiment

A comparison of the theoretical and experimental non-dimensional results are shown in Figures 16, 17, and 18. In Figure 16, the sphere test results with a perpendicular entrance angle are given for the three different drop heights. Figure 17 shows the cusped body results for similar conditions. The sphere test results with the 45 degree oblique entrance angle are shown in Figure 18 for two drop heights. The velocities used in the theoretical calculations varied in time as described in the previous section. The theoretical maximum slam coefficients in Figures 16 - 18 differ from the ones in Figures 10 and 11 due to the decrease in velocities and the addition of the buoyancy terms.

Generally, the theory seems to under predict the maximum vertical impact force for the sphere by approximately 5 to 10%. Conversely, the theory over predicts the maximum vertical force of the cusped body. This is possibly a result of the spray jet impinging upon the flared upper sections, acting to decelerate the mass. As a result, the body has an experimental velocity that is lower than the theoretical one when the flared part of the hull passes the mean water surface. The lower velocity would produce lower flare impact forces. The theory also tends to stretch the duration of the impact out when compared with experiment. This is true for both the sphere and cusped body.

The theoretical horizontal slam coefficient, C_{hs} , does not predict the sharp rise in impact force. While it approaches the same maximum value, it does so at a much later time. The experimental results may be due to the sphere impacting on the water in the forward spray sheet. This, of course, is not contained in the theoretical model.

SUMMARY AND CONCLUSIONS

The three dimensional characteristics of the impact problem have been discussed. Two different hull shapes, a sphere and a cusped body, were evaluated for impact forces. Theoretical and experimental comparisons were made. The theoretical calculations were done using dipole distributions with a known interior

flow and an equi-potential free surface condition. The addition of the interior flow reduced the computation time significantly. The contributions from the various terms in Bernoulli's equation were described. Theory under predicted the maximum force of the sphere but over predicted the force for the cusped body. The presence of the spray jet, which was not included in the theory, may be important in attenuating the maximum impact force in flared bodies.

ACKNOWLEDGMENT

This work was supported by the Maritime Administration University Research Program, contract DTM91-83-C-50118 and the Department of Naval Architecture and Marine Engineering, The University of Michigan.

REFERENCES

Belik, O., Bishop, R.E.D., Price, W.G. (1982), "A Simulation of Ship Responses Due to Slamming in Irregular Head Seas," RINA, Vol. 124.

Breslin, J. et.al. (1982), "Theoretical and Experimental Propeller-Induced Pressures Arising from Intermittent Blade Cavitation, Loading, and Thickness," SNAME Transactions, Vol. 90.

Chang, M.S. and Pien, P.C. (1975), "Hydrodynamic Forces on a Body Moving Beneath a Free Surface," 1st International Conference on Numerical Ship Hydrodynamics, National Bureau of Standards, Gaithersburg, Maryland, pp. 539-559.

Chuang, S.L. (1969), "Theoretical Investigations on Slamming of Cone-Shaped Bodies," Journal of Ship Research, Vol. 13, No. 4.

Faltinson, O. (1977), "Numerical Solution of Transient Nonlinear Free-Surface Motion Outside or Inside Moving Bodies," Second International Conference on Numerical Ship Hydrodynamics, University of California, Berkeley, California.

Gallagher, P. and McGregor, R.C. (1985), "Slamming Simulations: An Application of Computational Fluid Dynamics," Fourth International Conference on Numerical Ship Hydrodynamics, Washington, D.C.

Greenhow, M. (1986), "Wedge Entry into Initially Calm Water," Marintek, Report No. OR 530030.12, Trondheim, Norway.

Hess, J.L. and Smith, H.M.O. (1967), "Calculation of Potential Flow About Arbitrary Bodies," Progress in Aeronautical Sciences, Vol. 8 , pp. 1-138, Pergamon Press, New York, New York.

Hulme, A. (1982), "The Wave Forces Acting on a Floating Hemisphere Undergoing Forced Periodic Oscillations," Journal of Fluid Mechanics, Vol. 121, pp. 443-463.

Kaplan, P. and Silbert, M.N. (1976), "Impact Forces on Platform Horizontal Members in the Splash Zone," OTC Paper No. 2498, Houston, TX.

Kaplan, W. (1962), Operational Methods for Linear Systems, Addison-Wesley, Reading, Massachusetts.

Miloh, T. (1981), "Wave Slam on a Sphere Penetrating a Free Surface," Journal of Engineering Math., Vol. 15, No. 3, pp. 221-240.

Newman, J.N. (1977), Marine Hydrodynamics, MIT Press, Cambridge, Massachusetts.

Ochi, M.K. and Motter, L.E. (1969), "Prediction of Extreme Values of Impact Pressure Associated with Ship Slamming," Journal of Ship Res., Vol. 13, No. 2.

Ochi, M.K. and Motter, L.E. (1973), "Prediction of Slamming Characteristics and Hull Responses for Ship Design," SNAME Transactions, pp. 144-176.

Oliver, J.C. (1983), "Advanced Method for Ship Motion and Wave-Load Predictions," Ship Structure Committee Project, SR 1277, Giannotti and Assoc., Annapolis, Maryland.

Payne, P.R. (1981), "The Vertical Impact of a Wedge on a Fluid," Ocean Engineering, Vol. 8, No. 4, pp. 421-436.

Sarpkaya, T. and Isaacson, M. (1981), Mechanics of Wave Forces on Offshore Structures, Van Nostrand Reinhold Co., New York, New York.

Shiffman, M. and Spencer, D.C. (1951), "The Force of Impact on a Cone Striking a Water Surface," Comm. Pure Appl. Math., Vol. 4, pp. 379-417.

Thrasher, D.F. (1983), "Application of the Vortex-Lattice Concept to Flows with Smooth-Surface Separation," Fourteenth Symposium on Naval Hydrodynamics, The University of Michigan, Ann Arbor, Michigan, pp. 1089-1113.

von Karman, T. (1929), "The Impact on Seaplane Floats During Landing," NACA TN 321.

Wagner, H. (1931), "Landing of Seaplanes," NACA TN 622.

Wardlaw, A.B., Morrison, A.M., and Baldwin, J.L. (1977), "Prediction of Impact Pressures, Forces, and Moments During Vertical and Oblique Water Entry," Naval Surface Weapons Center, White Oaks Laboratories NSWC/WOL/ TR 77-16.

Yamamoto, Y., Fujino, M., and Fukasawa, T., (1980), "Motion and Longitudinal Strength of a Ship in Head Seas and the Effects of Nonlinearities," Naval Architecture and Ocean Engineering, Vol. 18, Soc. of Nav. Arch. of JAPAN.

Yeung, R. (1982), "Numerical Methods in Free Surface Flows," Ann. Rev. Fluid Mech., Vol. 14, pp. 395-442.

Yim, B. (1985), "Numerical Solution for Two-Dimensional Wedge Slamming With a Nonlinear Free-Surface Condition," Fourth International Conference on Numerical Ship Hydrodynamics, Washington, D.C.

Yung, T.-W. (1982), by personal communication.

APPENDIX - EXPERIMENTS

The experiments which were conducted at the Ship Hydrodynamics Laboratory (SHL) investigated both vertical and oblique angles of impact. For the vertical impact tests, two shapes (a sphere and a cusped body) were dropped from three heights. For the oblique impact tests, the sphere was dropped from the SHL towing carriage. The carriage speed matched the vertical component of the initial impact velocity resulting in an oblique entrance angle of 45 degrees.

The vertical accelerations were measured for the vertical impact tests while the vertical and horizontal accelerations were measured for the oblique tests. The accelerometer transducers (PCB Piezotronics Inc., model no. 302A02) had natural frequencies exceeding 35KHz. An instrument package was constructed to expedite the transfer of the accelerometers between the sphere and cusped body. This package could be bolted into the top of either shape and the whole assembly made watertight.

Analog signals from the accelerometers were digitized at a sampling rate of 21KHz. Due to the flexibility of the sphere or cusped body, the total system natural frequency was considerable lower than the natural frequency of the individual transducers. Natural frequencies of approximately 450 hz and 275 hz were estimated for the sphere and cusped bodies respectively. These frequencies resulted in adequate rise times for the lower drop heights where the initial velocities were relatively small and the duration of impact stretched out. However, at the higher drop heights, the steep rise time produced significant dynamic system response increasing the measured maximum acceleration.

In order to get the acceleration of the center of gravity of the impact body from an accelerometer suspended inside that body, the entire system was modeled as a single degree-of-freedom spring-mass-damper system experiencing base excitation. (This method is similar to one suggested by Yung (1982)). A schematic of the experimental model is shown in Figure A1. The displacements of the accelerometer transducer and the center of gravity of the body are denoted as X_1 and X_2 respectively. The transducer acceleration, $\ddot{X}_1$ was measured while the base acceleration, $\ddot{X}_2$, was the desired output. Since the accelerometer package accounted for less than 6% of the total system mass, the motion of the center of gravity of the sphere was assumed to be independent of the package motion. The linear equation of motion for the accelerometer package is then

$$m\ddot{X}_1 = k(X_2-X_1) + c(\dot{X}_2-\dot{X}_1) \qquad (A1)$$

or separating the response, X_1, from the excitation, X_2,

$$m\ddot{X}_1 + c\dot{X}_1 + kX_1 = c\dot{X}_2 + kX_2 \qquad (A2)$$

where the mass of the accelerometer package is m. Define now

$$\omega_n^2 = k/m \qquad c/m = 2\zeta\,\omega_n$$

Then Eq. (A2) becomes

$$\ddot{X}_1 + 2\zeta\omega_n\dot{X}_1 + \omega_n^2 X_1 = 2\zeta\omega_n\dot{X}_2 + \omega_n^2 X_2 \qquad (A3)$$

Following linear system analysis, the excitation, $\ddot{X}_2$, and the response, $\ddot{X}_1$, are related by the frequency system response function $H(\omega)$ where

(transducer accel.)/(base accel.) =

$$(-\omega^2 X_1)/(-\omega^2 X_2) = X_1/X_2 = H(\omega) \quad \text{(A4)}$$

and, from the solution for Eq. (A3)

$$H(\omega) = \frac{i\omega 2\zeta\omega_n + \omega_n^2}{-\omega^2 + i\omega 2\zeta\omega_n + \omega_n^2} \quad \text{(A5)}$$

The impulse response function, $h(t)$, is given as the Inverse Fourier Transform of $H(\omega)$. (See Kaplan (1962) or any other book on the calculus of linear systems.) It can be easily shown that the Inverse Fourier Transform of Eq. (A5) is

$$h(t) = e^{-\zeta\omega_n t} \left\{ 2\zeta\omega_n \cos\omega_d t + \frac{\omega_n^2 - 2(\zeta\omega_n)^2}{\omega_d} \sin\omega_d t \right\} \quad \text{(A6)}$$

where $\omega_d = \omega_n\sqrt{1-\zeta^2}$ is the damped natural frequency. The damping factor, ζ, and the damped natural frequency, ω_d, were calculated from the experimental time history.

For the linear system shown in Figure A1, the transducer acceleration, $\ddot{X}_1(t)$, is related to the base acceleration, $\ddot{X}_2(t)$, by the convolution integral

$$\ddot{X}_1(t) = \int_0^t d\tau\ h(t-\tau)\ddot{X}_2(\tau) \quad \text{(A7)}$$

In the application discussed in this paper, $\ddot{X}_1(t)$ was the measured quantity while $\ddot{X}_2(t)$, the acceleration of the body center of gravity, was the unknown. Through discretization, the following approximation for Eq. (A7) may be written:

$$\ddot{X}_1(t_k) = \sum_{j=1}^{k} \ddot{X}_2(t_j) \int_{t_{j-1}}^{t_j} d\tau\ h(t_k-\tau) \quad \text{(A8)}$$

The integral term in the above equation has a closed form expression. Eq. (A8) may then be inverted to yield the body acceleration $\ddot{X}_2$ at time step t_j.

One example of the data reduction technique is shown in Figure A2. There the measured impact acceleration time history is plotted with the results of Eq. (A8). The experimental accelerometer response is plotted as the solid line while the simulated base acceleration is plotted as the dashed line. The reliability of the data was established in two ways. First, the tests at the various drop heights were repeated two or three times. When superimposed upon each other, the resulting time histories showed a high degree of repeatability. Next, the results for the different drop heights, when normalized by the velocity squared, showed approximately the same maximum accelerations. See, for example, Figure 7.

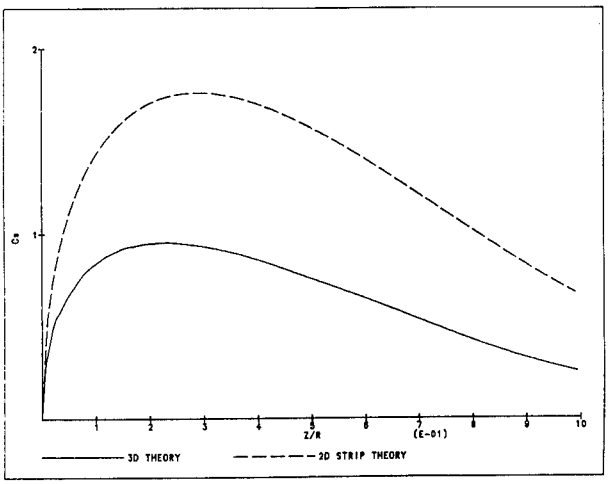


Figure 1: Comparison Between Strip Theory (2-D) and Three Dimensional Theory.

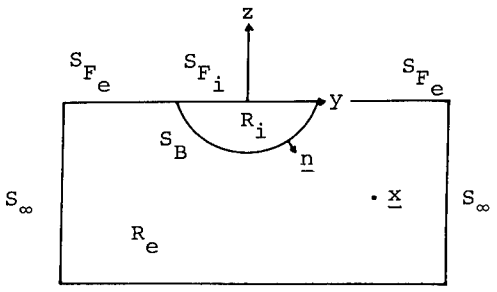


Figure 2: Coordinate System and Bounding Surfaces.

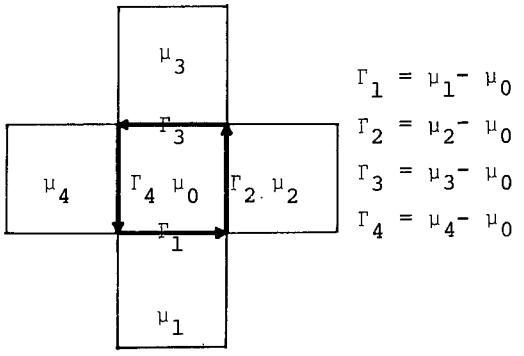


Figure 3: Determination of Vortex Filaments from Normal Dipole Surface Distributions.

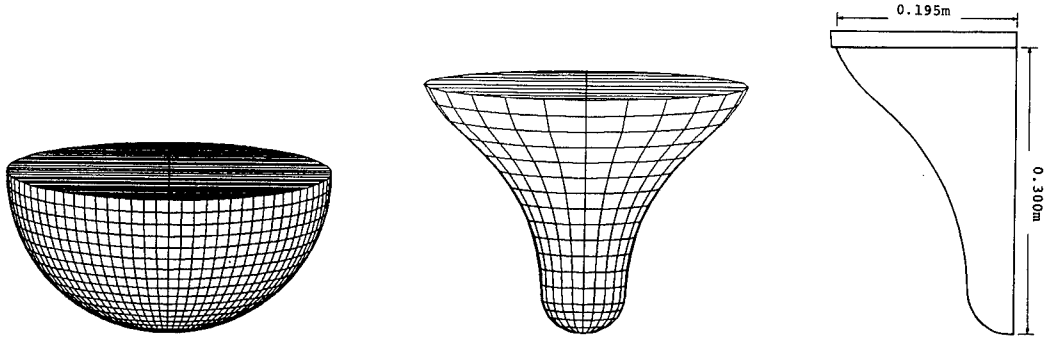


Figure 4: Sphere and Cusped Body Panel Distributions and Dimensions.

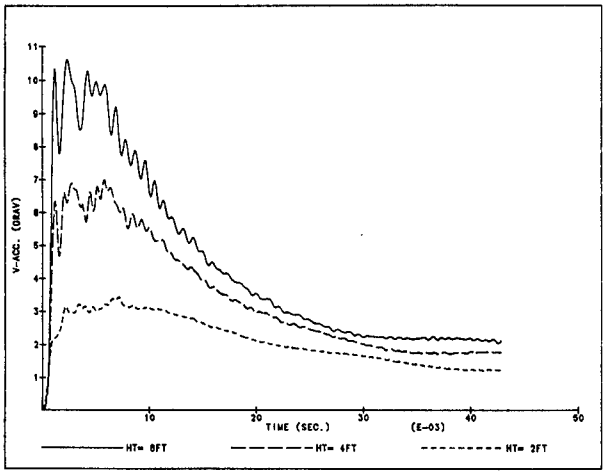


Figure 5: Experimental Impact Accelerations for a Sphere (Dimensional) - Three Drop Heights.

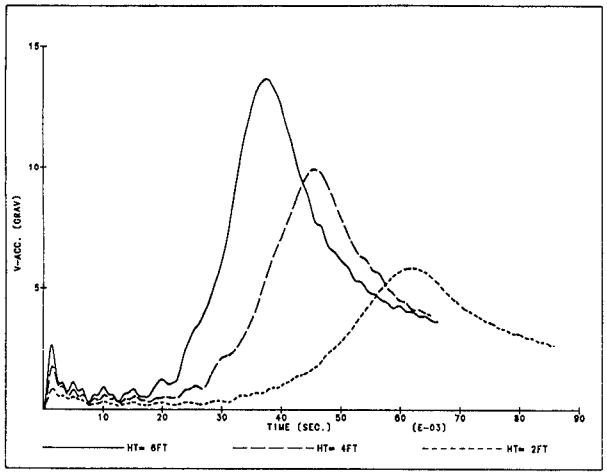


Figure 6: Experimental Impact Accelerations for a Cusped Body (Dimensional) - Three Drop Heights.

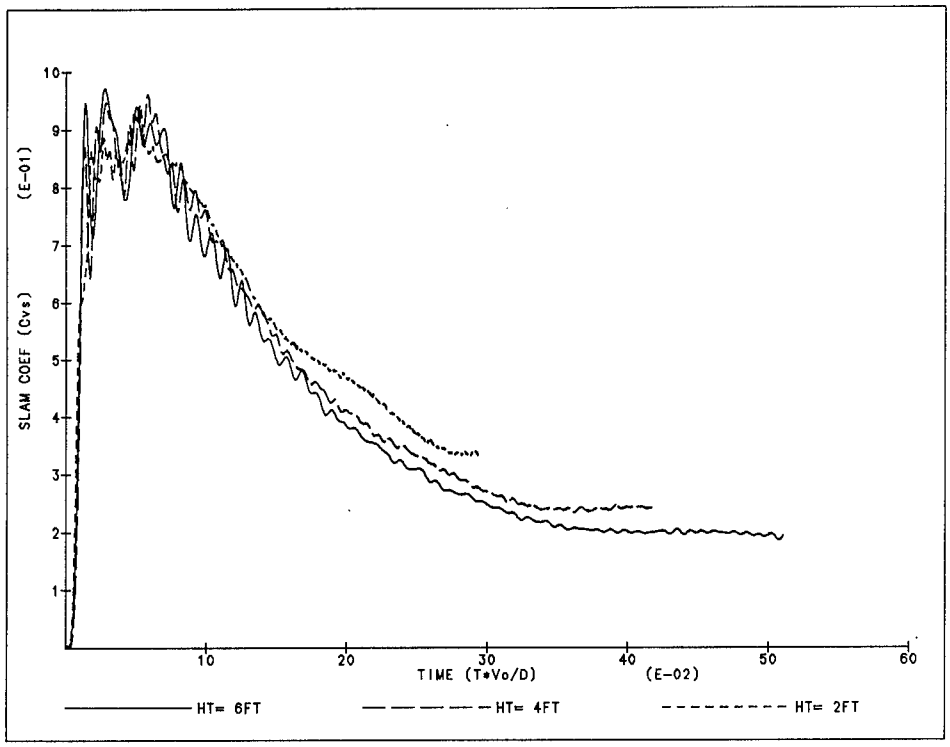


Figure 7: Experimental Non-Dimensional Vertical Slam Coefficients for a Sphere - Three Drop Heights.

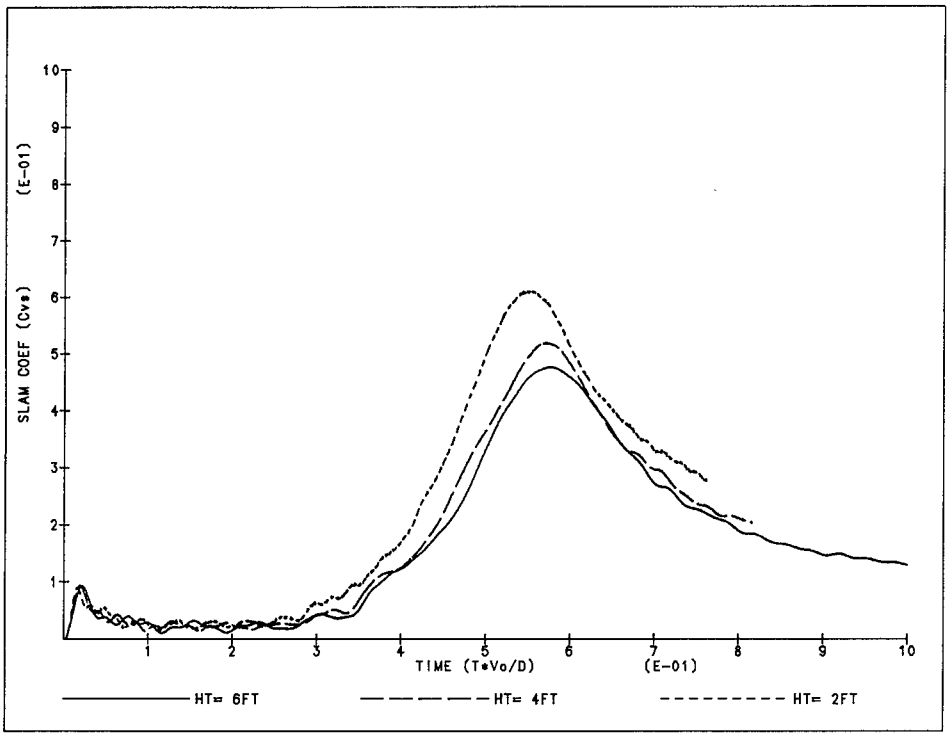


Figure 8: Experimental Non-Dimensional Vertical Slam Coefficients for a Cusped Body - Three Drop Heights.

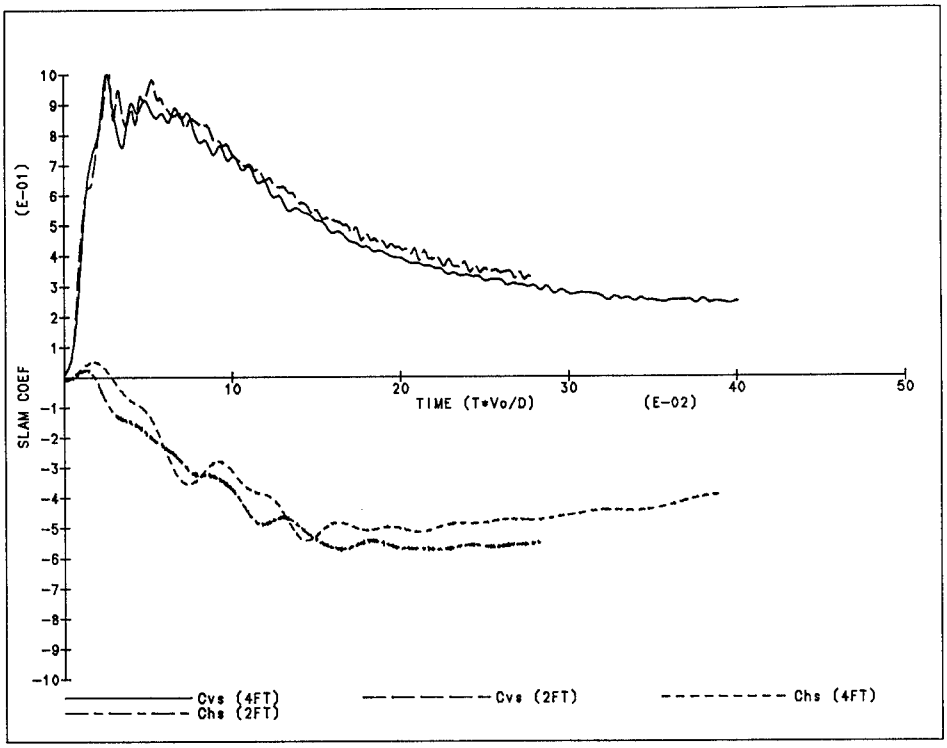


Figure 9: Experimental Non-Dimensional Vertical and Horizontal Slam Coefficients for a Sphere - Two Drop Heights.

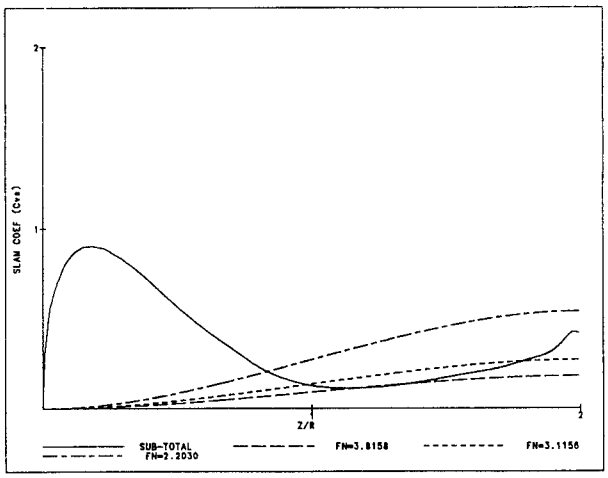


Figure 10: Effect of Buoyancy in the Vertical Impact Force of a Sphere - Three Drop Froude Nos.

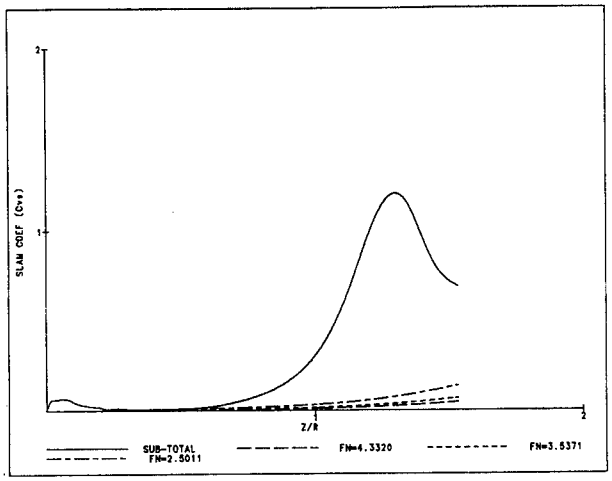


Figure 11: Effect of Buoyancy in the Vertical Impact Force of a Cusped Body - Three Drop Froude Nos.

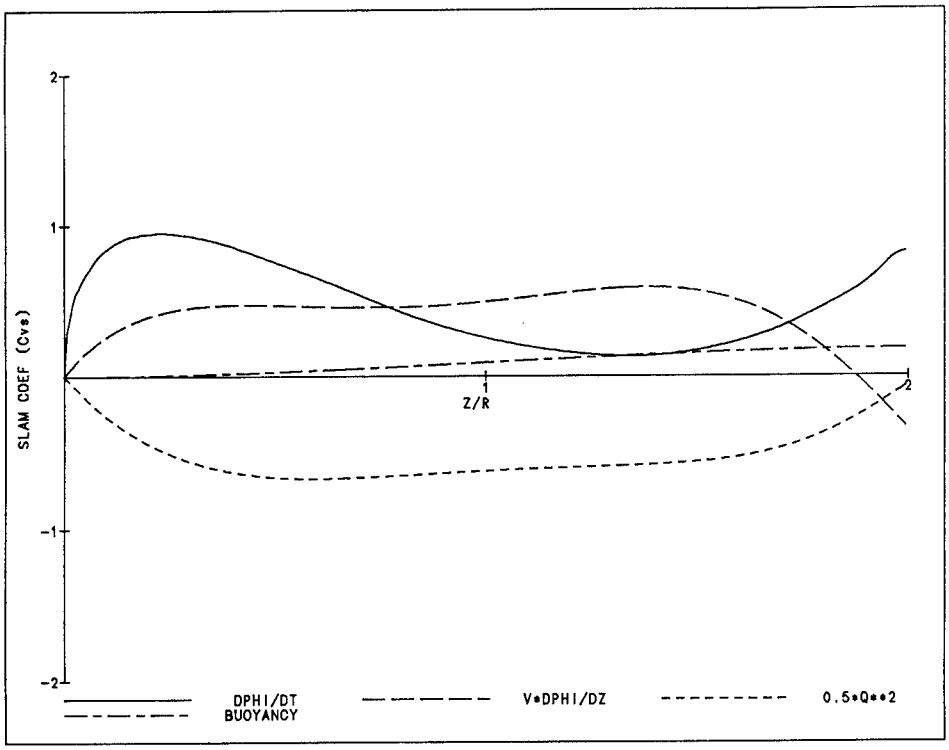


Figure 12: Various Force Components Acting on a Sphere During Vertical Impact (FN=3.8158).

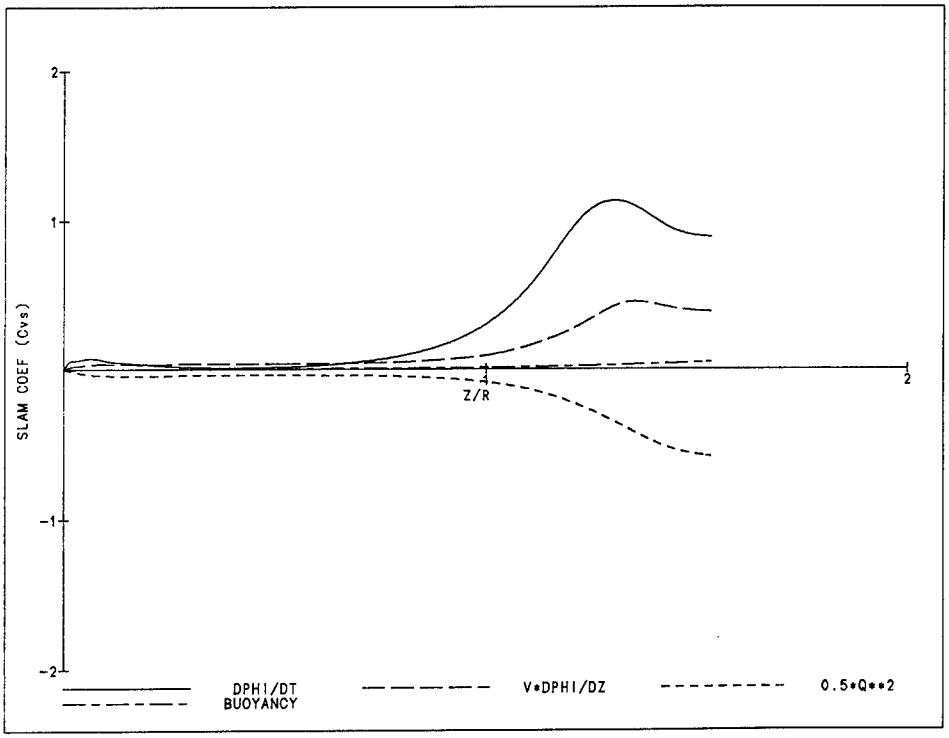


Figure 13: Various Force Components Acting on a Cusped Body During Vertical Impact (FN=4.3320).

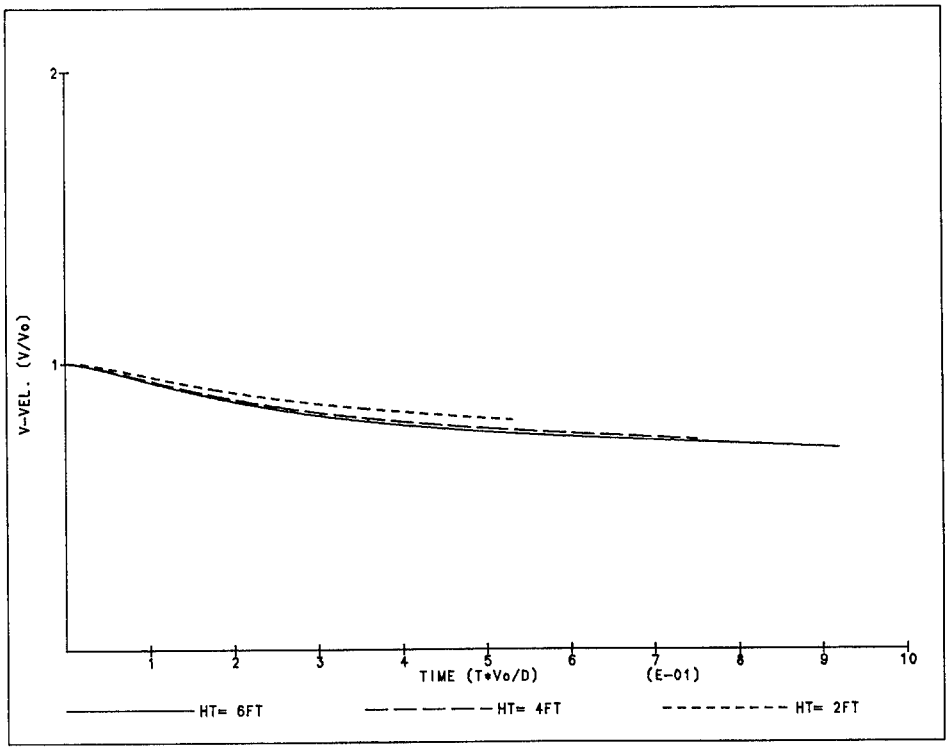


Figure 14: Time Simulation of the Vertical Velocity of a Sphere Dropped from Various Heights (FN=2.2030, 3.1156, 3.8158).

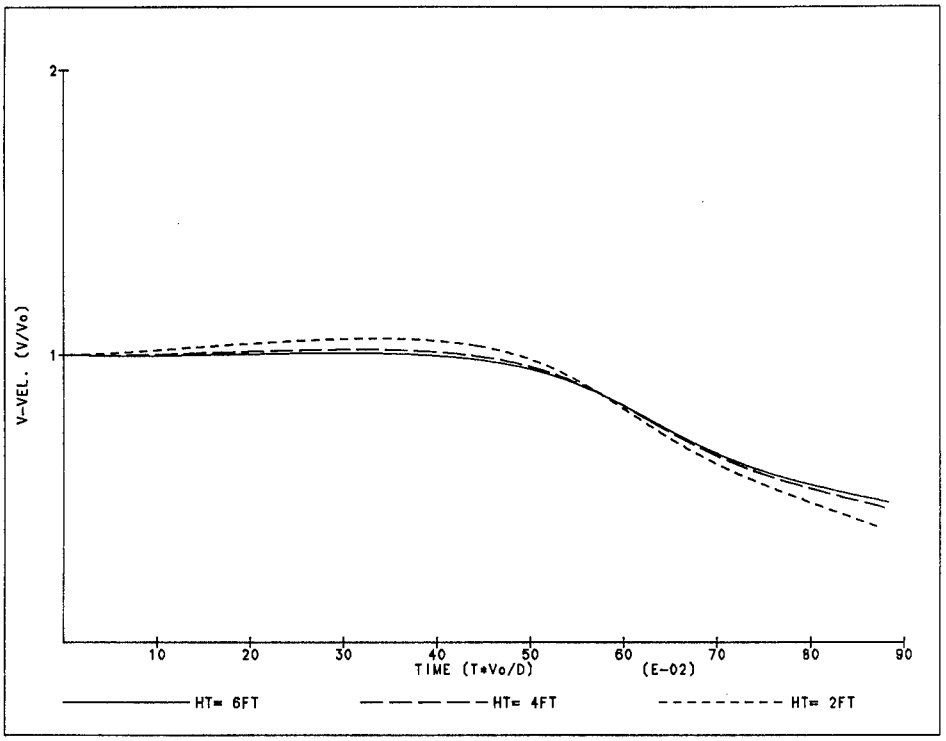


Figure 15: Time Simulation of the Vertical Velocity of a Cusped Body Dropped from Various Heights (FN=2.5011, 3.5371, 4.3320).

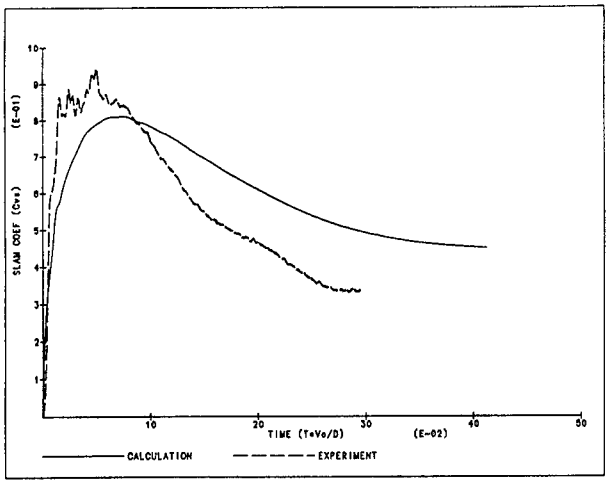


Figure 16a: Comparison Between Theory and Experiment of the Vertical Slam Coefficient for a Sphere (FN=2.2030).

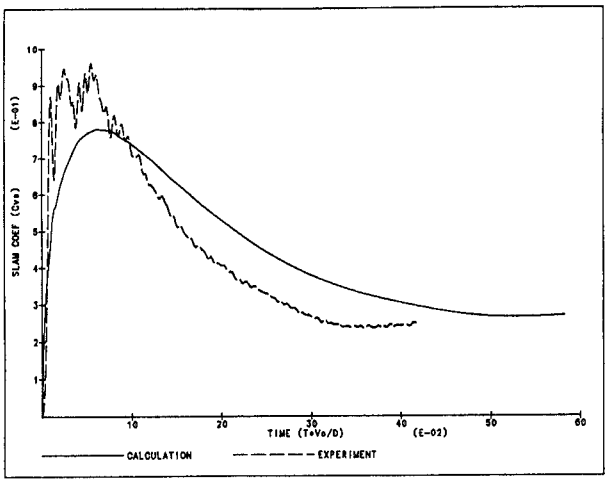


Figure 16b: Comparison Between Theory and Experiment of the Vertical Slam Coefficient for a Sphere (FN=3.1156).

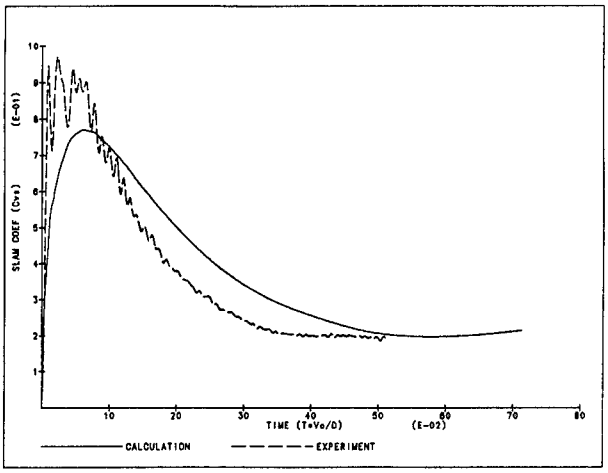


Figure 16c: Comparison Between Theory and Experiment of the Vertical Slam Coefficient for a Sphere (FN=3.8158).

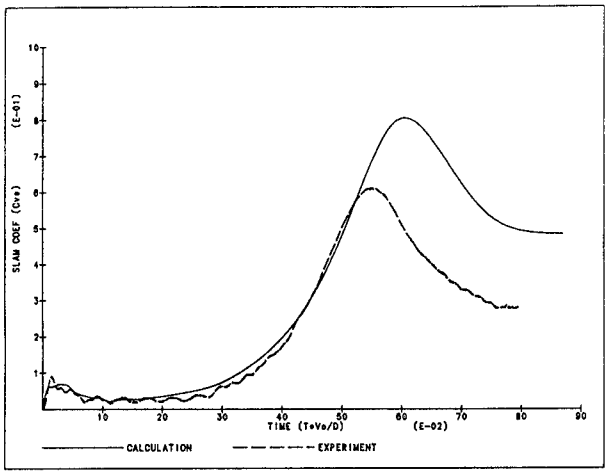


Figure 17a: Comparison Between Theory and Experiment of the Vertical Slam Coefficient for a Cusped Body (FN=2.5011).

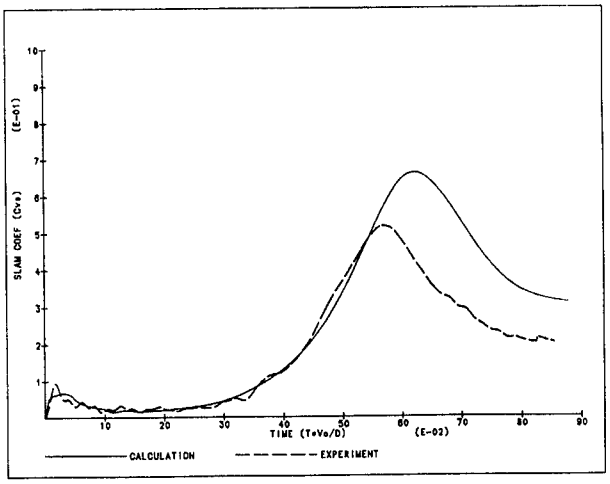


Figure 17b: Comparison Between Theory and Experiment of the Vertical Slam Coefficient for a Cusped Body (FN=3.5371).

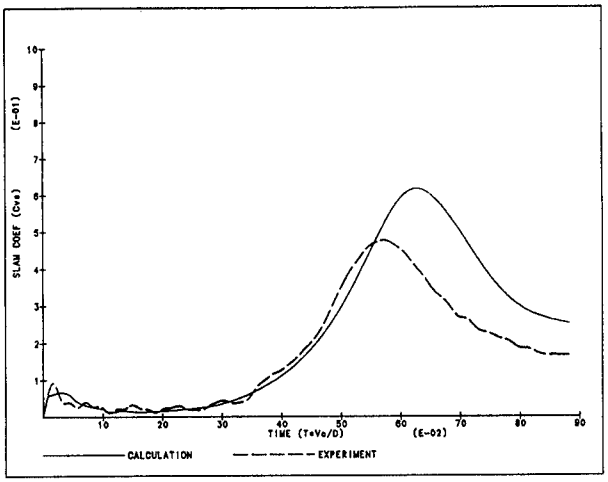


Figure 17c: Comparison Between Theory and Experiment of the Vertical Slam Coefficient for a Cusped Body (FN=4.3320).

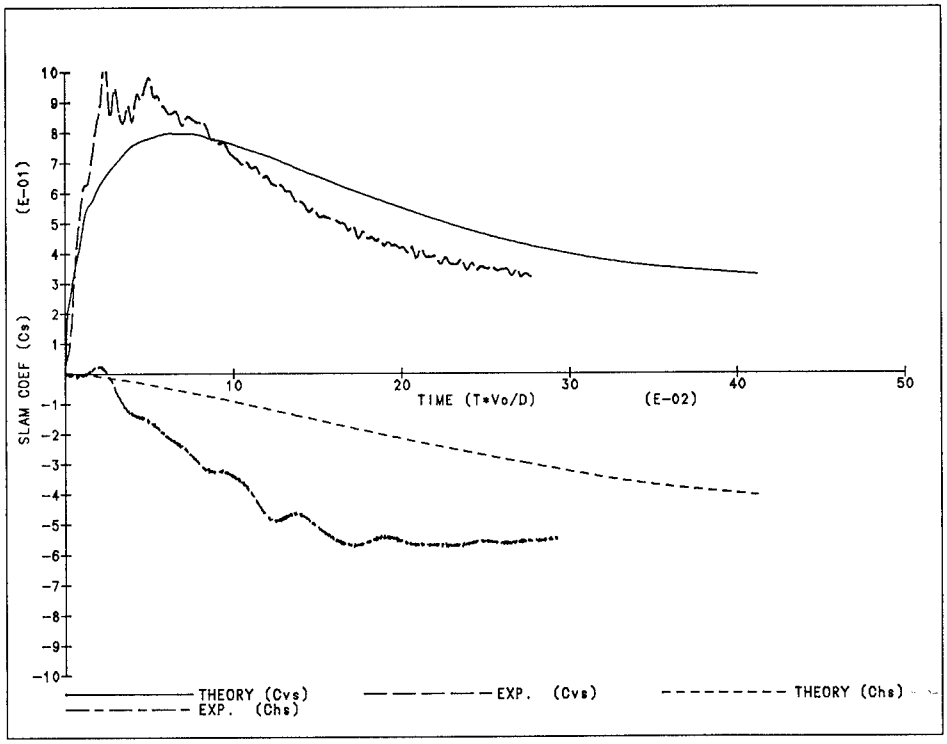


Figure 18a: Comparison Between Theory and Experiment of Vertical and Horizontal Slam Coefficients for a Sphere at an Oblique Angle of Impact (FN=2.2030).

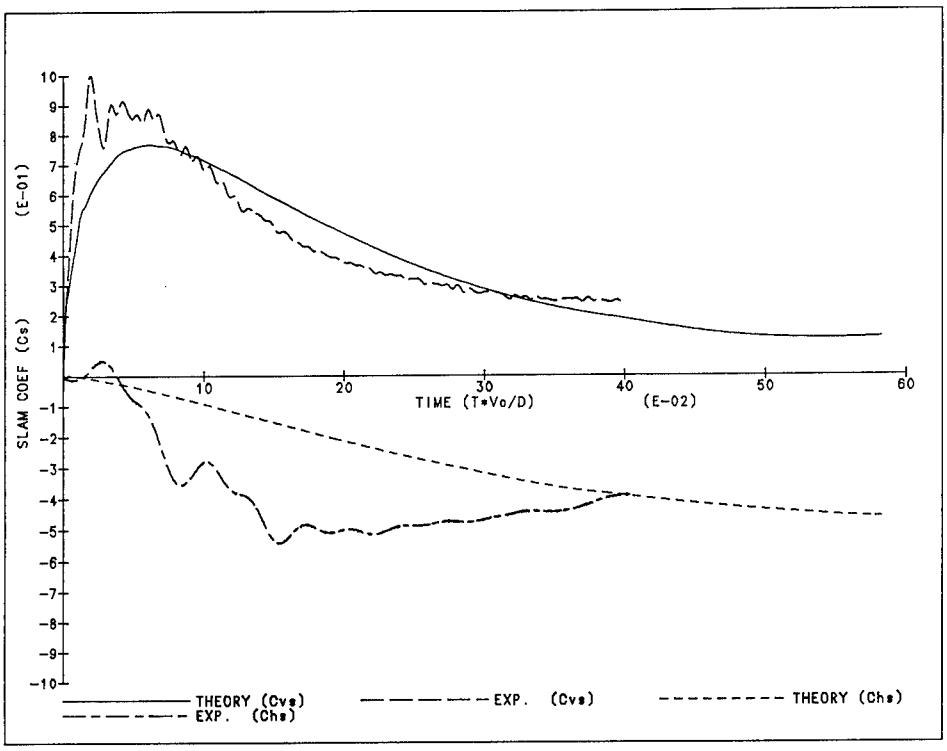


Figure 18b: Comparison Between Theory and Experiment of Vertical and Horizontal Slam Coefficients for a Sphere at an Oblique Angle Impact (FN=3.1156).

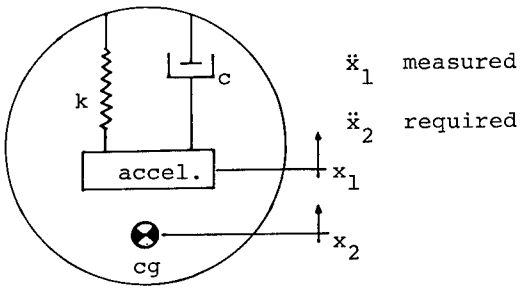


Figure A1: Dynamic Model of the Experimental Apparatus.

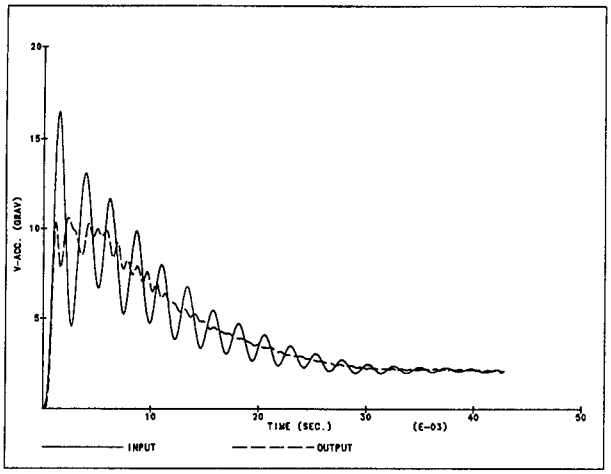


Figure A2: Experimental Impact Time History - Measured Transducer Acceleration (Input) and Acceleration of Body Center of Gravity (Output).

DISCUSSION

Garrett Birkhoff,
Harvard University

If viscosity, gravity, compressibility, and surface tension are neglected, the paper by H. Wagner (ZaMM 12 (1932), 193-215) gives a method for determining the exact self-similar flow induced in otherwise calm water by the vertical impact of a wedge or cone. His solution goes far beyond that of von Kármán (1929). A brief summary is given in [a] Chap. XI, 8-9; a very thorough discussion in [b].

[a]. G. Birkhoff and E. H. Zarantonello, "Jets, Wakes, and Cavities", Academic Press, 1960.

[b]. M. Shiffman add D.C. Spencer, Comm. pure appl. math. 4 (1951), 379-418.

Reply -

Prof. Birkhoff is correct in pointing out that Wagner's (1932) and later Shiffman and Spencer's (1951) formulation of the impact problem is exact for self-similar flows by vertical wedges or cones. Shiffman and Spencer also gave relations that determined the impact force if the shape of the free boundary and the values of the velocity potential on the straight line of the cone were known. Numerical results for their solution to this problem were achieved through an iterative procedure. However, due to the complexity of their solution technique, only the flow for a cone with a vertex angle of 120 degrees was given. As an illustration of the difficulty associated with their method, three theoretically equivalent relationships were used to calculate the fluid momentum during impact. The resulting values had a variation of 10%. Recognizing the large computational effort needed to obtain impact loads for cones with other vertex angles, Shiffman and Spencer suggested an "approximate theory". It is in this approximate theory that elements common to many impact load calculations may be found. To determine the momentum of the fluid they made the following assumptions:

- At each instant in time, the cone is replaced by a circumscribing ellipsoid as in Figure 1 shown below.

- The momentum of the fluid is approximated by the velocity of the ellipsoid multiplied by its classical added mass value.

- The free surface effects are included in a "wetting correction" and a "free surface correction." The wetting correction increases the depth at which the ellipsoidal added mass is determined. See Figure 2.

The following are observations on Shiffman and Spencer's approximate theory. Replacing the cone with an ellipsoid was an assumption of convenience. If the closed-form representation of the added mass for a cone had been known to Shiffman and Spencer, this approximation would likely have not been made. Equating the impact force to the time rate of change of the fluid momentum is fundamentally correct. However, representing that force by the time derivative of the product of the infinite-fluid added mass and the body velocity ignores the convective terms of Eq. (22) given in the paper. This can be justified for the force calculation at the instant of contact when the body penetration draft is small but not for later times when the draft is relatively large. The "wetting correction" to the impact force is also a small-draft apporximation correct only in the asymptotic limit of zero draft. (See the article by Armand and Cointe (1986) referenced by R. Cointe below.) As can be seen from Figure 8 of the paper, the maximum impact force for flared bodies does not occur during the initial stages of immersion in the drop test but rather much later. While von Kármán's approximate theory does not include the exact treatment of the free surface effects as given by Wagner or the first part of Shiffman and Spencer's work, it does allow one to numerically evaluate impact forces for arbitrarily shaped bodies based upon explicit assumptions stated in the boundary value problem. In summary, since typical ship sections with flare do not readily admit to self-similar solutions and since "wetting corrections" to the impact force are correct only in the limit of small draft, it is not clear that an extension of the Shiffman and Spencer results to the ship flare impact problem for arbitrary forebody shapes would provide superior results.

Raymond Cointe,
University of California, Santa Barbara

Your experimental results for the sphere show that the maximum impact force is greater than predicted by the classical von Kármán's theory and that it decreases more rapidly in time. Similar discrepancies are well known for the circular cylinder and are related to the improper treatment of the free surface boundary conditions ($\varphi = 0$ on the undisturbed free surface).

Using modern asymptotic theories, we have made a mathematical study of the problem for the circular cylinder [a] which, for small penetration depth, justifies Wagner's wetting correction and shows that a drag correction, including non-linear free surface effects such as the creation of a jet, has to be included to predict accurately the behavior in time of the impact force. Agreement with experimental data is good.

I would like to know if you plan to incorporate such corrections in your model.

[a] Armand, J.-L., & Cointe, R., "Hydrodynamic Impact Analysis of a Cylinder," Proceedings, 5th OMAE Symposium, Tokyo, 1986 (also to appear in the ASME Journal of Energy Resources).

Reply -

Mr. Cointe and co-author Prof. Armand (Armand and Cointe (1986)) have completed a careful analysis of the impact problem of a cylinder using matched asymptotic expansions. Unfortunately we were unable to review their work in detail before our article was submitted but would like to comment on it now. I does indeed show that Wagner's wetting correction is valid at the instant of impact. However as Figure 1 of their paper demonstrates, the Wagner model quickly deviates from experiments as the penetration depth increases. They then rationally derive higher order correction terms that produce better agreement between theory and experiment for larger immersion depths. The two dimensional impact of a circular cylinder is characterized by a maximum force at the instant of contact

between body and fluid. Due to the three dimensionality of the flow, the sphere maximum occurs at a relatively later time. In predicting maximum impact loads, the rational method of matched asymptotic expansions used by Armand and Cointe is most valid for the circular cylinder. The method should also be applicable for the sphere, though the sphere would presumably require more terms in the second and higher order expansions to achieve similar levels of comparison between experiment and theory. However, it is not clear what form the expansions should take for the cusped body shown in Figure 4 of the paper since for that shape the maximum impact force occurs at a large draft. The usefulness of the von Kármán-type theory presented in our paper is its relative computational simplicity for arbitrary three dimensional bodies. This theory does ignore the effects of the free surface and spray jet which are important as can be seen in Figure 17. There the theoretical impact maximum overestimates experimental values by approximately 25%. We intend to investigate possible solutions to this problem in future work.

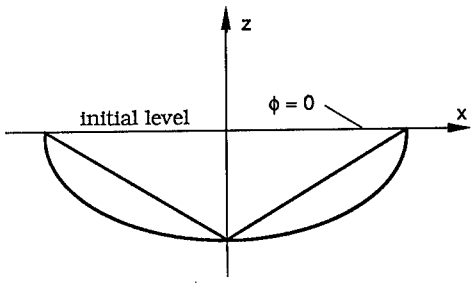


Figure 1. Ellipsoid approximation for a cone.

T. Francis Ogilvie,
Massachusetts Institute of Technology

When a flat-bottomed body impacts on a free surface, it is sometimes crucial to consider effects of air between the body and the water. During the time when the body is approaching the surface, the air acts as a cushion and starts the acceleration of the water surface downward. This entirely changes the physics of the problem studied by the authors.

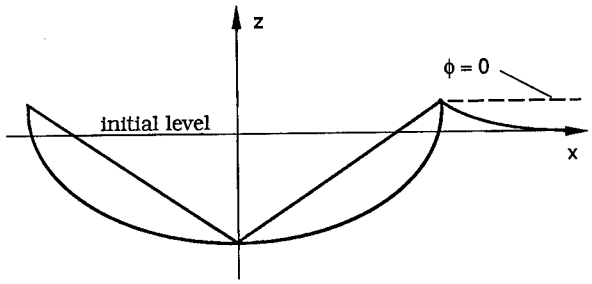


Figure 2. Increased Effective Depth Due to "Wetting Correction"

In such cases, I do not believe that it is generally necessary to consider compressibility of the air, since the speed of the moving air is likely to be much less than the speed of sound in air. But dynamic pressure in the air can be very important. The problem was studied in doctoral dissertations about 20 years ago by Robert S. Johnson (here at Berkeley) and by Grant Lewison at Cambridge University. Both of them considered air compressibility as well, but I think it is fair to say that, under the conditions that make compressibility important, their physical models lose much of their validity for still other reasons.

As others note in this discussion, the problem in this paper has been rather exhaustively studied analytically and numerically. What has not been done satisfactorily to date, I believe, is inclusion of the effects of the air cushion. One might even be able to make considerable progress on that with a linearized model.

Reply -

Professor Ogilvie describes yet another component to the impact problem. The air cushion contribution was not considered in our formulation since the paper's primary objective was to predict bow-flare loads. For this type of impact, it was assumed that the dynamic pressure due to air was not as important as it might be in the impact of flat-bottomed bodies.

We wish to thank the discussors for their interest in the subject and their comments which led to the rather spirited question and answer period.

Theoretical Investigation on the Wave Impact Loads on Ships

I. WATANABE

Ship Research Institute, Japan

ABSTRACT

A general expression for the pressure distribution on the inclined shiplike bodies penetrating the water surface is derived by matched asymptotic expansion on the bases of the shallow draft and the gravity free assumptions which are essentially equal to those used by von Karman or Wagner in the 2-D theories. The flow field divided into two regions, the outer region where the linearity assumption holds and the edge region where the impact phenomena occur. 3-D flat plate formulation is utilized to have the solution in the former region. For the solution in the latter region, its flow similarity to 2-D planing plate flow of which solution is known analytically is made use of. Both solutions are matched asymptotically to make them determinate and a composite solution valid in the entire region is obtained. The calculated results are compared with the experiments which are conducted to measure the pressure distribution over the inclined hypothetical ships such as a circular cylinder or a wedge-shaped cylinder. Agreements in the behavior of the pressure in time domain as well as in space are excellent if considerations are made to the fact that the measured pressure has averaged value over the pressure gauge membrane.

NOMENCLATURE

A_n	coefficients in the doublet distribution
a	radius of the pressure gauge membrane
B_n	$A_n b^{2n}$
b	breadth of the ship
C_p, C_{po}, C_{pe}	pressure coefficient $1/2\rho V^2$, suffix o is for the outer value and e for splash region value respectively
c	$1/(1+\nu)$
d_0	maximum draft of the ship
E	complete elliptic integral of the second kind
F	elliptic integral of the first kind
G_n	kernel of the integral equation,(29)
H,H',H''	defined in eq.(31)
K	complete elliptic integral of the first kind
$\bar{K}$	doublet distribution in η direction,(33)
k	argument in E( ) and K( ),(25)
ℓ_0	longitudinal length of the waterplane, $=\ell(0)$
$\ell, \ell(\eta)$	equation of the waterplane with respect to η
N	order of the polynomials of the doublet distribution
P, P_o, P_e	pressure on the hull,suffix o is for the outer value and e for splash region value respectively
q	$\sqrt{1+\nu}$
R	$\sqrt{(x-\xi)^2+(y-\eta)^2+z^2}$
r	radius of the circular cylinder used in the experiment
S	stretched coordinate in the splash region
t	time and also used as a parameter in the planing plate flow
U	velocity of the flow in the splash region
Ω	normalized rate of change of ℓ with respect to V ,(33)
V	impact velocity of the ship
w	complex velocity potential used for the planing plate flow
x,y,z	space fixed coordinate system
x_0, y_0, z_0	body fixed coordinate system
x_b, y_b	position on the waterline
x_β, y_β	stretched variables in the intermediate region
X,Y,Z	stretched coordinate system in the splash region
$\bar{Y}$	$\eta - y$
β	order function of ε defining the intermediate region
γ	reduction ratio of pressure peak, Fig.16
δ	splash thickness of the planing plate flow

Δ	unkown parameter in the splash region solution to be determined by matching
ε	ℓ_0/d_0, infinitesimal parameter
ζ	complex variable of the planing plate flow
ζ_B	location of the stagnation point of the planing plate flow, real number
ξ, η	location of the doublet distribution
θ	local inclination of the ship hull
$\lambda, \lambda(\eta)$	$\ell(\eta)/2b$
λ_0	$\ell(0)/2b$
μ	density of the doublet distribution
ν	$\cos\theta$
Π	elliptic integral of the third kind
ρ	density of water
τ	tangent of deadrise angle for the experimented wedge
ϕ	velocity potential in the outer region
Φ	velocity potential in the splash region
χ	direction of the normal vector on z=0 in the waterline
ψ	trim angle of the ship

1. INTRODUCTION

In taking up fluid structure interaction such as slamming and subsequent structral responses of a ship in rough seas, it is crucial to know the behavior of impact forces upon the hull in detail. For that purpose, von Karman or Wagner's theories[1,2] have been used for the forces and the pressure assuming that the impact phenomena are two dimensional in the transverse section. And their theories are known to give good estimation for the most hull forms if no air entrapping is involved. There arise, however, some difficulties in calculating impact pressure for the actual cases. Namely, for hull sections having the flat bottom, these theories predict infinite impact pressure because the waterline varies at infinite rate in the two dimensional sense. Of course this is not the case in reality. Existing remedies for it is to introduce empirical pressure in connection with local bottom configuration [3,4]. It seems to the author that the sound treatment should comprise of due consideration to the three dimensionality of the field. Theoretical researches on this aspect are rather scarce and an axisymmetric case is examined[5] so far to this author's knowledge. If we are to treat the three dimensional impact in perfect fluid as in those two dimensional theory, the momentum exchange should be major mechanism for the impact. In other words,von Karman or Wagner's three dimensional version would be powerful if it were presented.

Recently present author[6] has examined the two dimensional problem in the light of matched asymptotic expansion technique and presented that the impact pressure can be better described by combination of the expanding flat plate model and the planing plate model. And it is natural to extend this two dimensional flat plate model to three dimensional flat plate model combined with splash region flow. The author subsequently extended this idea successfully to the three dimensional impact on the flat bottom ship and have shown that peak impact pressure is proportional to $\cot^2\psi$ (ψ:trim angle) in good agreement with experiments.[7] Since the paper was limited to the case where the impact travels only longitudinally, there occured necessity to develope the theory to cover the problem where the impact travels both longitudinally and transversely.

This paper starts with assumptions adopted by those theories in two dimensional impact problem. Namely, Basic assumptions are

(1) that effects of graviy to the free surface can be neglected since perturbed fluid acceleration is much larger than that of gravity (gravity free) and

(2) that the ratio of draft to breadth is so small that flow variation in the vertical direction along the body surface is negligibly smaller than that of horizontal direction.(shallow draft)

The argument should be raised whether the water surface should be treated in the calm condition or in "piled-up water" condition. The difference between von Karman and Wagner in making impact model lies in this point. And for the three dimensional cases ,effect of perturbed water is not to be ignored in any of events. But it is formidable work to calculate instantaneous water elevation caused by body immersion. Therefore as a first attempt to the three dimensional impact problem, we will follow von Karman's way instead of Wagner's. Namely, we will assume

(3) that so-called "pile-up" effect presented by Wagner in calculating expanding velocity of the waterline is negligibly small that the instantaneous waterline can be computed by using water surface at rest.

2. THEORETICAL TREATMENT

Firstly,we will define a problem to be treated here. Flow field around a ship plunging with vertical velocity V into the water at rest will be discussed. The ship is assumed to keep constant trim angle during the motion. The ship may experience expanding waterplane in the rear and the sides as well as in the frontal part. But we will assume that the expansion in the rear and the sides is too small to be related to the occurance of the impact. This means the waterplane of the ship runs forward and the impact occurs only the. We call this region splash region since the impact accompanies the occurance of the splash.

Let us define space fixed coordinate system (x,y,z) as is shown in Fig.1. The origin is located at the aft of the ship with x-axis forward, z-axis upward and y-axis transversely. The fluid is assumed inviscid and irrotational.

2.1 Boundary conditions

Free surface

The acceleration of the fluid caused by the impact is much greater than that of the gravity by assumption. The dynamic condition on the free

surface, therefore, can be written

$$\frac{\partial\phi}{\partial t} + \frac{1}{2}|\nabla\phi|^2 + \frac{p}{\rho} = 0 \ . \qquad (1)$$

where ϕ is the velocity potential.
Take the lowest order term, then

$$\frac{\partial\phi}{\partial t} = 0. \qquad (2)$$

If we integrate (2) ,taking into account of the fact that the motion start with the calm surface at t = 0,

$$\phi = 0 \qquad (3)$$

is derived as the linear free surface condition.

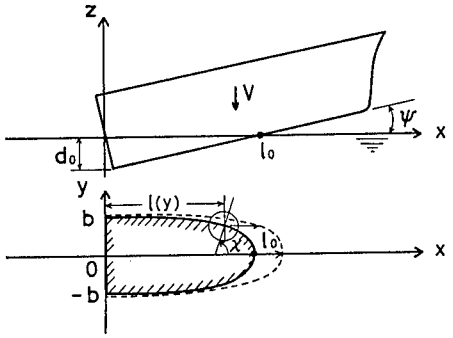


Fig. 1 Schematic view of the problem

Body Boundary

Let us define ε as the ratio of the maximum draft (d_0) to the longitudinal waterline length (ℓ_0)

$$\varepsilon = d_0/\ell_0 << O(1).$$

Let the body be

$$z_0 = \varepsilon f(x_0,y_0) \ . \qquad (4)$$

Here the origin of the body fixed coordinate (x_0,y_0,z_0) is taken to coincide with that of the space fixed coordinate at t=0.
Relation to the space fixed coordinate (x,y,z) is

$$\begin{aligned} z &= z_0 - Vt \\ x &= x_0 \\ y &= y_0 \ . \end{aligned} \qquad (5)$$

Kinematic condition on the body is

$$\frac{D}{Dt}\{ z+Vt-\varepsilon f(x,y)\} = 0 \ , \qquad (6)$$

or

$$\phi_z - \varepsilon (f_x\phi_x + f_y\phi_y) = -V \ . \qquad (7)$$

If we drop the higher order terms,

$$\frac{\partial\phi}{\partial z} = -V \qquad (8)$$

is derived as the linear body boundary condition. This is a boundary value problem for a moving flat plate at right angle. As is well known, the flat plate solution becomes singular as approaching to the edge. Thus, terms left behind in making linearised body condition (8) become order of unity near the edge by $O(\varepsilon^2)$ and the body condition ceases to be valid in the region where the impact phenomena occur(Splash region).

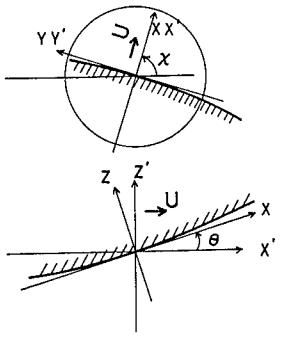


Fig.2 Stretched view of Splash region

Let us consider the boundary value problem in the splash region(x_b,y_b) as shown in Fig.2. Since we have neglected "pile-up" of the water caused by the body motion, the equation of the waterline is

$$\varepsilon f(x_b,y_b) = Vt \ . \qquad (9)$$

We will make an additional assumption that the body hull changes smoothly in the tangential direction on z=0 so that the variation of the velocity in that direction is negligibly smaller than in the other directions. The 2-D normal vector in xy plane is

$$n_2 = \frac{1}{|\nabla f|}(f_x,f_y) = (\cos\chi,\sin\chi) \ . \qquad (10)$$

Introduce stretched coordinate system (X,Y,Z) in the region as

$$\begin{aligned} x-x_b &= \varepsilon^2\{X\cos\chi\cos\theta - Z\cos\chi\sin\theta - Y\sin\chi\} \\ y-y_b &= \varepsilon^2\{X\sin\chi\cos\theta - Z\sin\chi\sin\theta + Y\cos\chi\} \\ z &= \varepsilon^2\{X\sin\theta + Z\cos\theta\} \ . \end{aligned} \qquad (11)$$

where

$$\theta = \tan^{-1}(\varepsilon\sqrt{f_x^2+f_y^2}) \ . \qquad (12)$$

By this coordinate, Z-axis is taken normal to the body surface, Y-axis tangent to the waterline and X-axis normal to the waterline on the surface as is shown in Fig. 2. Substitute them into body boundary condition and expand near X = Y = Z = 0,

$$\varepsilon^2\{X\sin\theta+Z\cos\theta\}+Vt-\varepsilon f(x_b,y_b)$$
$$-\varepsilon^3 f_x\{X\cos\chi\cos\theta-Z\cos\chi\sin\theta-Y\sin\chi\}$$
$$-\varepsilon^3 f_y\{X\sin\chi\cos\theta-Z\sin\chi\sin\theta+Y\cos\chi\}=0 \qquad (13)$$

$$\{\sin\theta-\varepsilon\cos\theta(f_x\cos\chi+f_y\sin\chi)\}X$$
$$+\{\cos\theta-\varepsilon\sin\theta(f_x\cos\chi+f_y\sin\chi)\}Z$$
$$+\varepsilon(f_x\sin\chi-f_y\cos\chi)Y = 0 \qquad (14)$$

The first and the third terms are null in the region respectively, Thus

$$Z = 0 \ , \qquad (15)$$

which means the body can be approximated as an inclined flat plate.

Correspondingly, the body boundary condition becomes

$$\frac{\partial\Phi}{\partial Z} = 0 \ . \qquad (16)$$

In addition to these two conditions, we will impose another condition that there exists splash along the body surface. Although it is not deductible from basic conditions mentioned before, it necessarily accompanies actual impact.

The governing equation is now reduced to 2-D Laplace equation from 3-D Laplace equation since we have assumed slow changes of the velocity in the tangential direction(Y).

Now we have obtained two kinds of the boundary value problem which are complementary each other. In the following sections, two problems will be treated independently to the point where both solutions are to be matched.

2.2 Flat plate solution(outer solution)

As was shown in the last section, the flow field in the outer region is well described by the expanding flat plate in impulsive motion. Let the waterplane be denoted by S. By virtue of Green's theorem, the velocity potential can be described by a distribution of doublet with its axis toward z-direction on the z=0 plane,

$$\phi = \int_S \mu(\xi,\eta)\frac{\partial}{\partial z}\left(\frac{1}{R}\right) ds \qquad (17)$$

where $R=\sqrt{(x-\xi)^2+(y-\eta)^2+z^2}$

and

$$\mu(\xi,\eta) = \frac{1}{4\pi}\{\phi(\xi,\eta,0+)-\phi(\xi,\eta,0-)\}$$
$$= -\phi(\xi,\eta,0-)/2\pi \ . \qquad (18)$$

The density of the doublet $\mu(\xi,\eta)$ is determined through

$$V_B = -\lim_{z\to 0}\frac{\partial\phi}{\partial z} = -\lim_{z\to 0}\int_S \mu(\xi,\eta)\frac{\partial^2}{\partial z^2}\left(\frac{1}{R}\right)ds$$
$$= \oint_S \frac{\mu(\xi,\eta)}{\{(x-\xi)^2+(y-\eta)^2\}^{3/2}}\, ds$$
$$= \oint_{-b}^{b}\int_0^{\ell(\eta)} \frac{\mu(\xi,\eta)}{\{(x-\xi)^2+(y-\eta)^2\}^{3/2}}\, d\xi d\eta, \qquad (19)$$

where $\xi = \ell(\eta)$ ($-b \le \eta \le b$) describes the doublet plane (S).

V_B is given by the body boundary condition (8) and the second integral should be understood as an improper integral whose finite part is defined as

$$\oint_S \frac{\mu(\xi,\eta)}{\{(x-\xi)^2+(y-\eta)^2\}^{3/2}}\, ds$$
$$= \int_S \frac{\mu(\xi,\eta)-\mu(x,y)}{\{(x-\xi)^2+(y-\eta)^2\}^{3/2}}\, ds$$
$$+ \mu(x,y)\lim_{z\to 0}\int_S \frac{1}{\{(x-\xi)^2+(y-\eta)^2+z^2\}^{3/2}} ds \ . \qquad (20)$$

$\mu(\xi,\eta)$

Following the standard scheme of the aerodynamic wing theory, We will assume for the doublet distribution

$$\mu(\xi,\eta) = \frac{V}{b}\sqrt{\xi(\ell-\xi)}\sqrt{b^2-\eta^2}\sum_{n=0}^{N-1} A_n\eta^{2n} \ . \qquad (21)$$

It has only even power components with respect to η because of y-symmetry of the flow. Substitute (21) into (19), then we have

$$V(x,y) = \sum_{n=0}^{N-1}\left(\frac{V}{b}\right)A_n\oint_{-b}^{b}\eta^{2n}\sqrt{b^2-\eta^2}\int_0^{\ell}\frac{\sqrt{\xi(\ell-\xi)}}{\{(x-\xi)^2+Y^2\}^{3/2}}d\xi \qquad (22)$$

where $Y = \eta - y$.

A_n are determined by solving the equation numerically after evaluating these integrals. The problem is reduced to the linear equation. There may be various kinds of methods for solution. Collocation method will be used here. Since we have assumed only one mode of variation with respect to x or ξ direction, single control point in x-direction , $x = \ell/2$, is sufficient for the equation.

Then,

$$V = \sum_{n=0}^{N-1}\left(\frac{V}{b}\right)A_n\int_{-b}^{b}\eta^{2n}\sqrt{b^2-\eta^2}\int_0^{\ell}\frac{\sqrt{\xi(\ell-\xi)}}{\{(\xi-\ell/2)^2+Y^2\}^{3/2}}d\xi. \qquad (23)$$

Here we normalize ξ, x, η and y by b and hereafter the same notations will be uses for normalized variables as far as connotations are clear.
Integration with respect to ξ can be made analytically as is shown in Appendix B. The result is

$$\int_0^{\ell} \frac{\sqrt{\xi(\ell-\xi)}}{\{(\xi-\ell/2)^2+Y^2\}^{3/2}} d\xi = \frac{\lambda^2}{b}\int_{-1}^{1} \frac{\sqrt{1-\xi^2}}{\{\lambda^2\xi^2+Y^2\}^{3/2}} d\xi$$

$$= \frac{2}{b\sqrt{\lambda^2+(\eta-y)^2}} \{-K(k^2) + \frac{\lambda^2+(\eta-y)^2}{(\eta-y)^2} E(k^2)\} \quad , (24)$$

where $\lambda(\eta) = \frac{\ell(\eta)}{2b}$, (25)

$$k^2 = \frac{\lambda(\eta)^2}{\lambda(\eta)^2+(\eta-y)^2} \quad .$$

$K(k^2)$ and $E(k^2)$ are the complete elliptic integrals of the first and the second kind respectively.
Therefore

$$V_j = \sum_{n=0}^{N-1} B_n G_n(y_j), \quad j=1,N \quad , \qquad (26)$$

where

$$V_j = V(0,y_j) \quad ,$$
$$B_n = A_n b^{2n} \quad , \qquad (27)$$

$$G_n = 2[-\oint_{-1}^{1} \eta^{2n} \frac{\sqrt{1-\eta^2}\, K(k^2)}{\sqrt{(y-\eta)^2+\lambda^2}} d\eta$$

$$+ \oint_{-1}^{1} \eta^{2n}\sqrt{1-\eta^2}\sqrt{(y-\eta)^2+\lambda(\eta)^2} \frac{E(k^2)}{(y-\eta)^2} d\eta \ ] \quad . \quad (28)$$

Special care is needed in evaluating the integral numerically since it behaves improperly near $\eta = y$. We will extract the finite part integral and evaluate it separately.
After some algebra as is shown in Appendix B, G_n's are given by

$$G_n = 2[-G_{1n} + G_{2n}] \quad ,$$

$$G_{1n} = \int_{-1}^{1} [\eta^{2n} \frac{\sqrt{1-\eta^2}}{\sqrt{(y-\eta)^2+\lambda(\eta)^2}} K(k^2)$$
$$- y^{2n} \frac{\sqrt{1-y^2}}{\lambda^2(y)} \ln\frac{4\sqrt{(\eta-y)^2+\lambda(y)^2}}{|\eta-y|}] d\eta$$
$$+ y^{2n}\frac{\sqrt{1-y^2}}{\lambda(y)}[(1-y)\ln\frac{4\sqrt{(1-y)^2+\lambda(y)^2}}{|1-y|}$$
$$+ (1+y)\ln\frac{4\sqrt{(1+y)^2+\lambda(y)^2}}{|1+y|}$$
$$+ \frac{\lambda(y)}{2}\{\tan^{-1}(\frac{1-y}{\lambda(y)})+\tan^{-1}(\frac{1+y}{\lambda(y)})\} \qquad (29)$$

and

$$G_{2n} = \int_{-1}^{1} \frac{H(\eta)-H(y)-H'(y)\bar{Y}-H''(y)\bar{Y}^2\ln\{(\bar{Y}^2+\lambda^2)/\bar{Y}^2\}}{\bar{Y}^2} d\eta$$
$$-H(y)\{\frac{1}{1-y} + \frac{1}{1+y}\}+H'(y)\ln(\frac{1-y}{1+y})$$
$$+2H''(y)[(1-y)\ln\frac{\sqrt{(1-y)^2+\lambda^2}}{|1-y|}$$
$$+ (1+y)\ln\frac{\sqrt{(1+y)^2+\lambda^2}}{|1+y|}$$
$$+ \frac{\lambda(y)}{2}\{(1-y)\tan^{-1}(\frac{1-y}{\lambda}) + (1+y)\tan^{-1}(\frac{1+y}{\lambda})\}]. \quad (30)$$

where

$$\lambda = \lambda(y) \quad ,$$
$$H(\eta) = \sqrt{\bar{Y}^2+\lambda(\eta)^2}\ \eta^{2n}\sqrt{1-\eta^2}\ E(k^2)$$
$$H(y) = \lambda(y)y^{2n}\sqrt{1-y^2},$$
$$H'(y) = \{2n\lambda y^{2n-1}+ \frac{d\lambda}{dy}y^{2n}\}\sqrt{1-y^2} - \frac{\lambda y^{2n+1}}{\sqrt{1-y^2}}, \quad (31)$$
$$H''(y) = \frac{y^{2n}}{4\lambda}\sqrt{1-y^2},$$

These integrals are integrable in ordinary sense. Any numerical procedure can be applicable for the evaluation and subsequent solution of the equation if we avoid to take y=1 as a collocation point.

Pressure

Pressure is equal to time derivative of the velocity potential. Since our main concern is the pressure over the ship hull, it is sufficient for the purpose to know the potential over the waterplane. Namely, the doublet density just obtained is all to be needed.

$$\frac{P}{\rho} = -\frac{\partial\phi}{\partial t} = 2\pi\frac{\partial\mu}{\partial t}$$
$$= 2\pi V\frac{\partial}{\partial t}\sqrt{x(\ell-x)}\sqrt{1-y^2}\sum_{n=0}^{N-1} B_n y^{2n}$$
$$= \pi V\{\frac{\partial\ell}{\partial t}(\frac{x}{\ell-x})^{1/2}\sqrt{1-y^2}\sum_{n=0}^{N-1} B_n y^{2n}$$
$$+2\sqrt{x(\ell-x)}\sqrt{1-y^2}\sum_{n=0}^{N-1}\frac{\partial B_n}{\partial t} y^{2n} \}$$
$$= \frac{1}{2}V^2\{ \hat{u}\tilde{K}(y)(\frac{x}{\ell-x})^{1/2} + 4\sqrt{x(\ell-x)}\ \frac{1}{V}\frac{\partial\tilde{K}}{\partial t}\}. \quad (32)$$

where

$$\hat{u} = \frac{1}{V}\frac{\partial\ell}{\partial t} \qquad (33)$$

and $\tilde{K} = 2\pi\sqrt{1-y^2}\sum_{n=0}^{N-1} B_n y^{2n}$.

The contribution of the second term of eq.(32) to the pressure is little in the splash region and significant away from the region as is clear from the formula.Since our main concern is the behavior around the peak pressure, we will ignore this term for simplification in further discussion.

As approaching to the traveling waterline edge, the pressure behaves like

$$\frac{P}{\rho} \to \pi V \frac{\partial \ell}{\partial t} \sqrt{\ell} \, \frac{\sqrt{1-y^2}}{\sqrt{\ell - x}} \sum_{n=0}^{N-1} B_n y^{2n} \quad . \tag{34}$$

The pressure diverges in the order of square root of ℓ-x and has no peak value in the region. This is the reflection of shortcoming of the linear solution as mentioned before. We will try to find another solution to describe the singular region.

Numerical example

In order to show how the flat plate solution works, two kinds of the waterplane are taken as examples. One is a half of an ellipse, which corresponds to the waterplane of the inclined circular cylinder in impact motion. Fig.3 shows effects of the number of terms to convergence of $\bar{K}(y)$, the variation of doublet strength along the y-axis. It is seen that $\bar{K}(y)$ varies little with respect to N if N is greater than 4. Thus N=4 was taken for the standard value for later calculations. Fig.4 shows $\bar{K}(y)$ for ellipses of various length beam ratio λ_0 (= $\ell_0/(2b)$). It is seen that the $\bar{K}(y)$ keeps almost constant value up to the splash corner region where abrupt decrease take place. As λ_0 increases, $\bar{K}(y)$ is decreased in average. The other example is a triangular waterplane model which corresponds to an inclined wedge entry problem. Calculated results are shown in Fig.5. $\bar{K}(y)$ in this case varies more clearly an vanishes at the splash corner. The dependence o $\bar{K}(y)$ to λ_0 is similar to the former model.

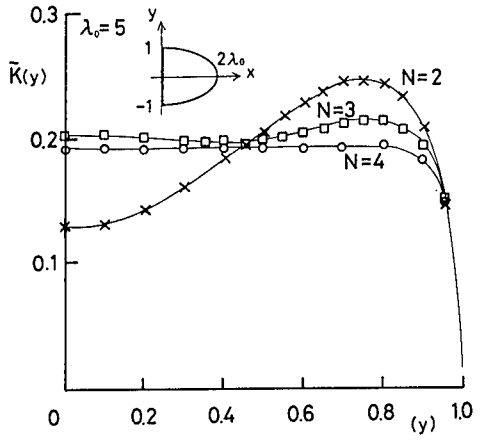


Fig.3 Convergence of K(y) with respect to N

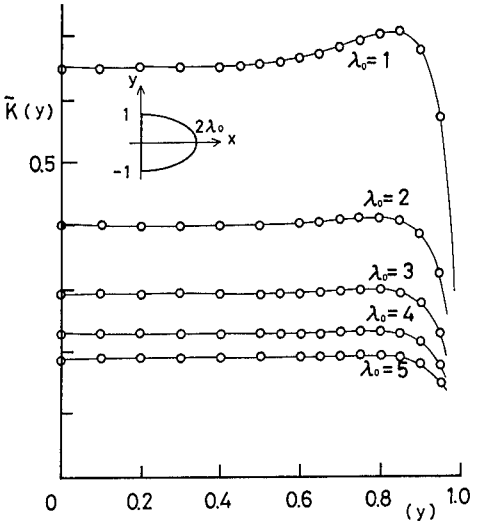


Fig.4 Transverse distribution of the doublet strength for half-elliptic waterplane

2.3 Splash region solution(inner solution)

Let us examine the flow defined by the conditions (15), (16) and the splash condition that there exist splash running away along the body. The exact solution for it is not known and may be indeterminate because of the ill condition at infinity that the flow has different direction upstream and downstream. However,except for its plate length, the conditions are the same for the planing plate problem of which solution is known. It is reasonable to assume that the splash region of the both flow has analogy each other. If we extract an asymptotic expression of the planing plate solution in the splash region, it will satisfy above boundary conditions and will be taken as a inner solution.

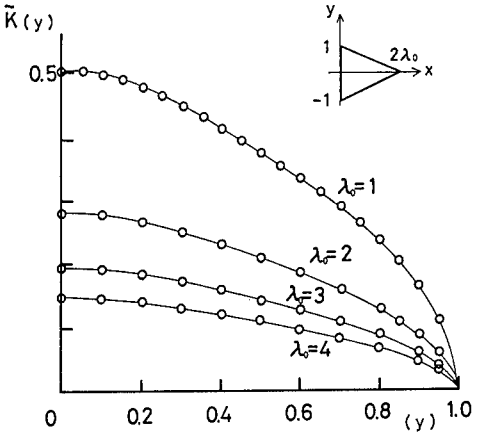


Fig.5 Transverse distribution of the doublet strength for traiangular waterplane

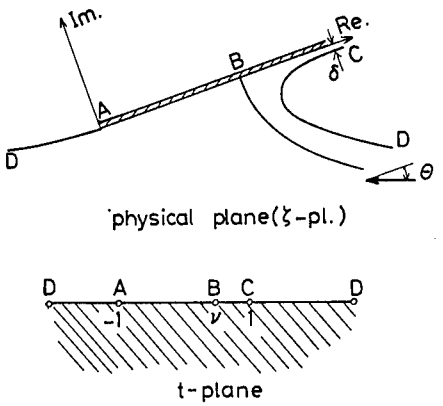


Fig.6 Coordinates of planing plate flow

Planing plate solution

The flow field around a steady planing plate at an attack angle θ has been solved analytically and its velocity distribution will be found in literatures.[9,10,11] Taking coordinate system as shown in Fig.6 and uniform velocity U, the velocity distribution in the fluid is given by

$$\frac{dw}{d\zeta} = U\,\frac{1-\nu t - \sqrt{(1-\nu^2)(1-t^2)}}{t-\nu}\,, \qquad (35)$$

where $\nu = \cos\theta$.
The relation between physical space (ζ) and parameter t is

$$\frac{\pi}{\delta}\zeta = \frac{1}{(1-\nu)}\{\nu(1+t) - (1-\nu)\log(\frac{1-t}{2}) + \sqrt{1-\nu^2}(\frac{\pi}{2} + \sin^{-1}t - \sqrt{1-t^2})\}\,, \qquad (36)$$

where t moves in the lower half plane and δ is the thickness of splash.

Pressure distribution on the planing plate is ,knowing that the quadratic term of the velocity is dominant, given by

$$\frac{P}{\rho} = \frac{U^2}{2}\{1 - (\frac{1}{U}|\frac{dw}{d\zeta}|)^2\} \qquad (37)$$

Taking into account that t is real and moves between -1 and 1 on the plate, the pressure distribution over it is

$$\frac{P}{\rho} = \frac{U^2}{2}[1 - \{\frac{1-\nu t-\sqrt{(1-\nu^2)(1-t^2)}}{t-\nu}\}^2] = \frac{U^2}{2}[1 - \{\frac{t-\nu}{1-\nu t+\sqrt{(1-\nu^2)(1-t^2)}}\}^2]. \qquad (38)$$

The flow defined above satisfies all the boundary conditions in the splash region stated in Sec.2.1 except body length scale.

Splash region solution

In making use of the expression (38) for the solution in the splash region, both (36) and (38) have to be expanded near the stagnation point. Firstly, eq.(36) is expanded about the splash root (ζ_B) assuming sin θ is small. After some algebraic operations, we have

$$\zeta - \zeta_B = \frac{5+3\nu}{2(1-\nu)}\,\frac{\delta}{\pi}(t-\nu) = \Delta(t-\nu). \qquad (39)$$

Instead of δ, we define a new unknown constant Δ for further convenience as

$$\Delta = \frac{5+3\nu}{2(1-\nu)}\,\frac{\delta}{\pi}\,, \qquad (40)$$

which will be determined by matching with the outer solution.

In order to have stretched picture near $\zeta = \zeta_B$, take a new inner variable S as

$$S = \frac{\zeta_B-\zeta}{(1-\nu^2)} = \frac{\Delta(\nu-t)}{(1-\nu^2)}\,, \qquad (41)$$

and substitute it into (38). We have an expansion after dropping higher order terms

$$\frac{P}{\rho} = \frac{U^2}{2}\,\frac{(S/\Delta)^2 - (1+\nu S/\Delta - q\sqrt{S/\Delta+c})^2}{(S/\Delta)^2} = \frac{U^2}{2}\,\frac{(1+\nu S/\Delta+q\sqrt{S/\Delta+c})^2 - (S/\Delta)^2}{(1+\nu S/\Delta+q\sqrt{S/\Delta+c})^2}\,, \qquad (42)$$

where $q = \sqrt{1+\nu}$ and $c = 1/(1+\nu)$. (43)

There are unknown constants U and Δ as well as unknown location of the origin of S in (35). They will be determined by matching.

Fig.7 shows an example of pressure distribution given by (42). It is seen that the pressure rises very sharply to the peak at S = 0 and then gradual descent is followed.

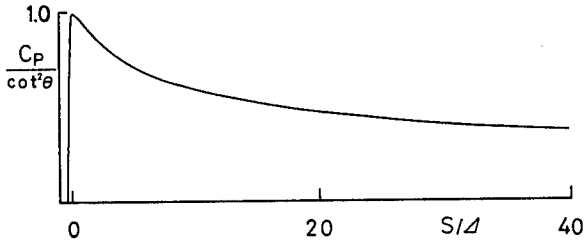


Fig.7 Pressure distribution in the slash region

2.4 Matching and composite solution

Among unknown constants, U can be determined easily by inspection as

$$U = V\cot\theta = \frac{V}{\varepsilon}\,\frac{\nu\varepsilon}{\sqrt{1-\nu^2}}\,, \qquad (44)$$

and the origin of S may be taken at (x_b, y_b). In order to determine Δ, we need a matching principle. Unlike ordinary perturbation problem,

this perturbed flow becomes infinite as ε approaches zero since flow intensity is proportional to $1/\varepsilon$. Thus in the intermediate region, we impose

$$\lim_{\varepsilon\to 0} \frac{1}{\cot\theta}(P_e - P_o) \to 0, \tag{45}$$

instead of

$$\lim_{\varepsilon\to 0} (P_e - P_o) \to 0.$$

We will define intermediate variable X_η in connection with outer and splash region variables as follows

$$\begin{aligned} x &= x_b - \beta(x_\beta \cos\chi - y_\beta \sin\chi) , \\ y &= y_b + \beta(x_\beta \sin\chi + y_\beta \cos\chi) , \end{aligned} \tag{46}$$

$$\beta/\varepsilon^2 \, x_\beta = S \quad , \tag{47}$$

$$\text{where } O(\varepsilon^2) < O(\beta) < O(1) .$$

Substituting these relations into (32) and the second line of (42), expanding with respect to ε and taking leading order terms of both solutions, we have from the outer solution

$$P_o \sim \rho V^2 \hat{u} K(y_b) \left(\frac{\ell(y_b)\cos\chi}{\beta x_\beta}\right)^{1/2} . \tag{48}$$

The asmptotic expansion (48) is valid under the condition that the factor in it is of the order of 1.
Likewise, the intermediate expansion of the splash region solution is

$$P_e \sim 2\rho V^2 \cot^2\theta \, \frac{\nu q \varepsilon \sqrt{\Delta}}{\sqrt{\beta x_\beta}} \tag{49}$$

In order that both expansions are equal, Δ has to be

$$\Delta = \frac{K^2 \ell}{\nu^4 q^2} \left(\frac{\cos\chi}{4}\right) \left(\frac{\sqrt{1-\nu^2}}{\varepsilon}\right)^2 . \tag{50}$$

This determines an unknown constant Δ. The flow field is now completely described by these expansions.

Composite solution

It is convenient to construct a composite expansion which is valid throughout the whole region by following procedure:

$$C_{pc} = C_{po} + C_{pi} - C_{pm} , \tag{51}$$

$$\text{where } C_p = \frac{P}{\rho V^2/2}$$

and C_{pm} is a common part in the both expansions at matching.

The result is

$$C_{pc} = \cot\theta \left[\hat{u} K(y) \left(\frac{x}{\ell - x}\right)^{1/2} + \cot\theta \, \frac{2D}{(S/\Delta)^2 + 2D} - \hat{u} K(y) \left(\frac{\ell}{\ell - x}\right)^{1/2} \right], \tag{52}$$

where

$$D = q^2(S/\Delta + c) + q(1 + \nu S/\Delta)\sqrt{S/\Delta + c} \text{ and}$$

$$S = \frac{(\ell - x)\cos\chi + (y - y_b)\sin\chi}{\varepsilon^2} . \tag{53}$$

As was stated in making the asymptotic expasions, this expansion is not expected to be valid in the sides of the waterplane($\ell << O(1)$),where factors in the outer expansion becomes smaller order than of unity.

The maximum pressure occurs at S=0 ($x = \ell(y)$) and its magnitude is

$$C_p = \cot^2\theta. \tag{54}$$

The point where C_p becomes zero is at

$$S = -c , \tag{55}$$

where local water elevation starts.

Transverse variation of the pressure is obtained simply moving y between $-y_b$ and y_b while keeping x fixed. Take a triangular waterplane as an example to show how the pressure behaves transversely.
Let the equation of waterline be

$$\ell(y) = (b - y) \quad \text{for } y > 0, \tag{56}$$

Substituting in (52), we have

$$C_p = \cot\theta \left[\hat{u}\sqrt{x} \, \frac{K(y)}{\sqrt{y_b - y}} + \cot\theta \, \frac{2D}{(S/\Delta)^2 + 2D} - \hat{u} K(y) \left(\frac{b - y}{y_b - y}\right)^{1/2} \right], \tag{57}$$

where

$$S = \frac{(y - y_b)\sin\chi}{\varepsilon^2} . \tag{58}$$

It is seen that the pressure has peak at the edges which is in accordance with 2-D theory.[6] Only difference is that the derivative of the pressure is discontinuous at the centerline. This is reflection of the discontinuity of y-derivative of the waterline. If we take a smooth shaped body at the centerline like ellipse, the pressure varies smoothly.

3. COMPARISONS WITH EXPERIMENT

3.1 experiment

In order to verify the applicability of the present calculation, experiments were carried out to measure the pressure distribution and their time history in detail over bodies in three dimensional condition. As is shown in Fig.8 , two kinds of cylinders were prepared for the experiment. One has a semi-circluar section of 0.25m in radius(r) and the other one has wedge type cross section of 15.6 deg. in dead rise angle.

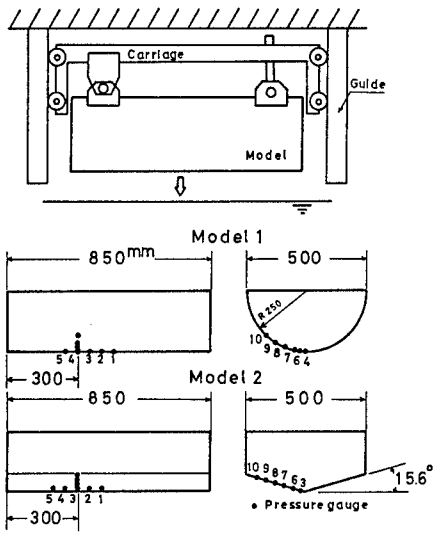


Fig.8 General view of the experiment

Each has ten pressure gauges distributed over the bottom longitudinally and transversely. The pressure gauges are of strain gauge type. The model was dropped freely with fixed trim condition. The trim angles were 0, 5, 10 and 15 deg.. Impact velocity was evaluated from vertical displacement by potentiometer and verified by the integration of vertical acceleration by the acceleration probe. Fig.9 shows an example of the time histories of the various positions on the circular cylinder at trim angle of 5 deg. with impact velocity of about 2 m/sec.

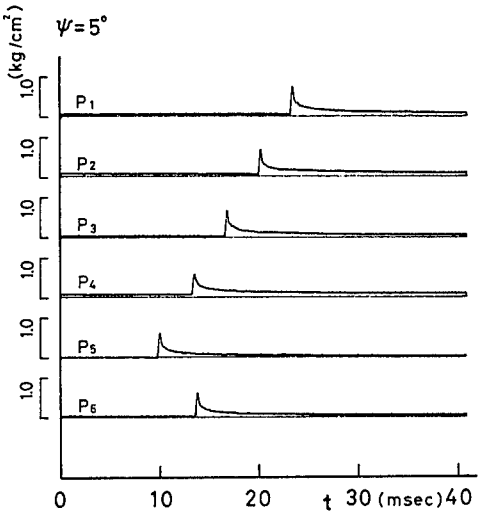


Fig.9 Example of time histories of the pressure

3.2 Calculation

Numerical results to be compared to the experiments can be derived by only specifying body shape and waterplane configuration at the instantaneous position. For the inclined circular cylinder by trim angle ψ with fore-up, by using the coordinate with its origin at the aft keel, the waterline is given by

$$\ell(y) = \ell_0 - \frac{1}{\sin\psi}(r - \sqrt{r^2-y^2}) \qquad (59)$$

for $-b<y<b$,

where $$b = \sqrt{r^2 - (r-\ell_0\sin\psi)^2} \ , \qquad (60)$$

$$\ell_0 = Vt\cot\psi \qquad (61)$$

and r is the radius of the cross section.

χ, the argument of the normal vector of the waterline in the waterplane and θ, the local inclination of the body at the waterline are

$$\chi = \tan^{-1}\left(\frac{y}{\sin\psi\sqrt{r^2-y^2}}\right) \quad \text{and} \qquad (62)$$

$$\theta = \tan^{-1}\left(\frac{\sqrt{y^2 + r^2\tan^2\psi}}{\sqrt{r^2 - y^2}}\right) . \qquad (63)$$

Likewise for the wedge-shaped cylinder with trm angle ψ, the waterline is

$$\ell(y) = \ell_0 - \frac{\tau}{\sin\psi}|y| \qquad (64)$$

for $-b<y<b$,

where τ is the tangent of the deadrise angle and

$$b = \frac{\ell_0\sin\psi}{\tau} . \qquad (65)$$

For χ and θ, we have

$$\chi = \tan^{-1}\left(\frac{\tau}{\sin\psi}\right) \tag{66}$$

and

$$\theta = \tan^{-1}\left(\frac{\sqrt{\sin^2\psi + \tau^2}}{\cos\psi}\right) . \tag{67}$$

3.3 Comparisons

effects of pile-up water

In order to have a look at the pile-up effects which is neglected in the present theory, the travel of the impact pressure is plotted against the longitudinal and transverse distance in Figs.10 through 13. Fig.10 and 11 show the results for the circular cylinder and Fig.12 and 13 are for the wedge. If the pile-up is significant, the impact travels at much higher speed than the estimated speed using the geometric position with respect to the calm water. It is clear from the figures that the actual traveled time is in the same order with geometric estimation for the longitudinal direction for both cylinders, while the actual time in the transverse direction is much shorter than the estimation. It shows that the pile-up effects are negligible longitudinally but not in the transverse direction. Further improvements is needed to take this effects into consideration.

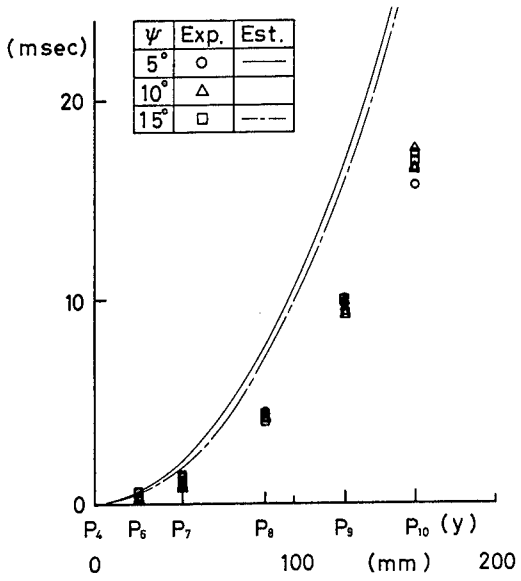


Fig.11 Travel of impact over the circular cylinder in transverse direction

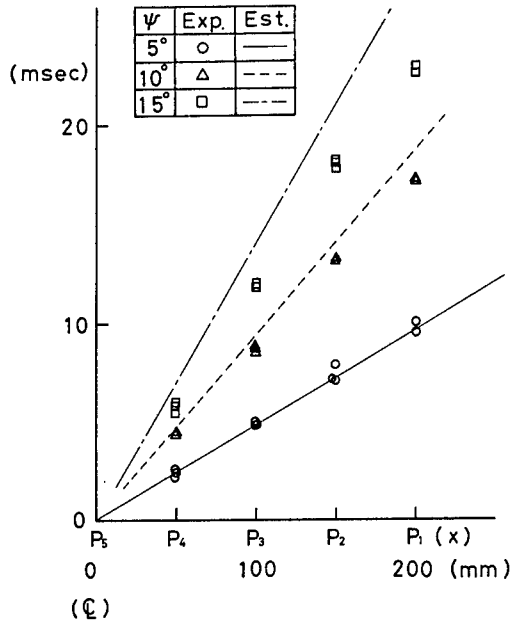


Fig.10 Travel of impact over the circular cylinder in longitudinal direction

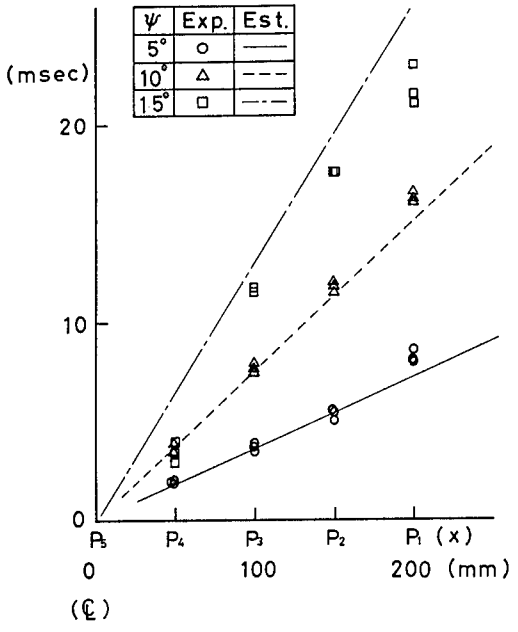


Fig.12 Travel of impact over the wedge in longitudinal direction

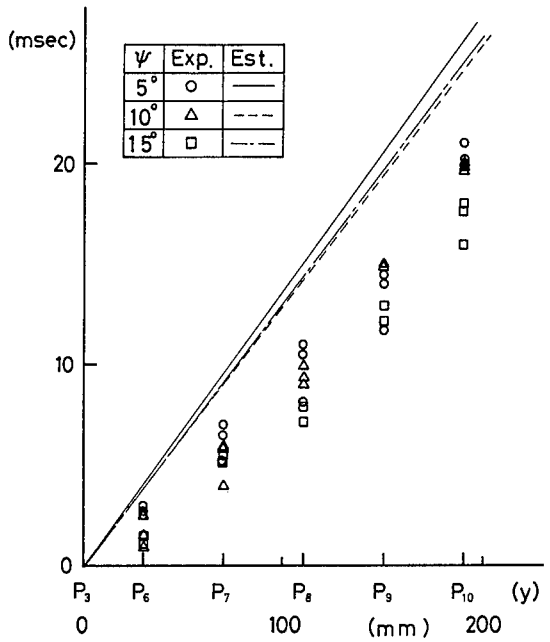


Fig.13 Travel of impact over the wedge in transverse direction

peak value

Fig.14 through 15 show longitudinal and transverse distributions of peak pressure for the inclined circular cylinder. it is seen that the peak gradually decreases transversely. Fine line shows prediction by present theory, which is equal to $\cot^2\theta$ (θ = local body inclination). Discrepancies are clear. The reason for it is thought as follows.[12] The pressure reaches its peak and then declines at very high rate of change as was shown in Fig.7. The high pressure zone is so narrow that the even very small pressure gauges catches averaged peak values. This means that the measured pressure peak is rounded-off. Fig.16 shows how measured peak values are rounded off if we apply calculated pressure on the gauge membrane used in this experiments. Ratio of the gauge diameter to the $\varepsilon^2\Delta$ is taken for abscissa and γ, the ratio of measured peak to applied peak is taken as an ordinate. The pressure gauge is supposed to have circular membrane with diameter a. (a is 5mm in our experiment.) As the ratio becomes very small, which means the high pressure zone becomes narrower, the measured peak is much lowerer than actually applied value. Based on this result , the calculated peak has been corrected and is shown by thick lines in the Figures 14 and 15. Agreements between the calculation and the experiment are improved considerably.

Fig.17 and 18 show peak pressure distributions for the wedge type cylinder. It is seen that the distribution is flattened compared to the circular cylinder case.Since present theory estimates uniform peak value over the bottom surface of the wedge, the estimation is in agreement with the experiment in this respect. On the other hand, contrary to the circular cylinder, the measured pressure is larger than the calculation which is plotted in fine lines. The reason for it can be attributed to the "pile-up" effects in transverse direction if we take into account of the facts that the major flow direction is transverse because of the large deadrise angle and the waterline in that direction travels faster than assumed by the present theory as was shown in Fig.11 and 13. In fact the differences can be made small if we tentatively correct the peak value by $(\pi/2)^2$ following Wagner,as is shown by thick lines. This correction is tentative by all means. Further improvements are needed for full understanding of the discrepancy. The reduction ratio of the peak pressure is not large in this case since the deadrise angle is comparatively large (15.6deg)

duration

Next let us examine how long high pressure stays temporally. In Fig.19 is shown the elapsed time($T_{1/2}$) during which the pressure stays above one half of the peak value. The relation between the elasped time and the trim angle is shown for the pressure(P_4) on the centerline of the circular cylinder. The agreement between the experiment and the present estimation is amazingly good. It is to be noticed that any corrections have not been made on the rounded-off effect of the pressure gauge in this figure.

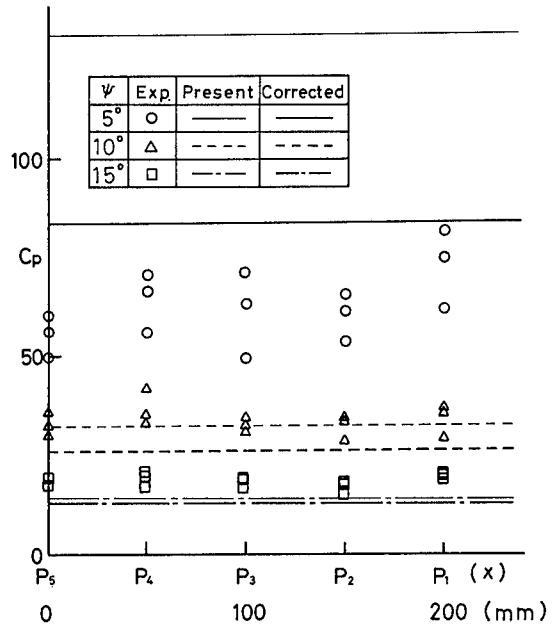


Fig.14 Longitudinal distribution of peak pressure over the circular cylinder

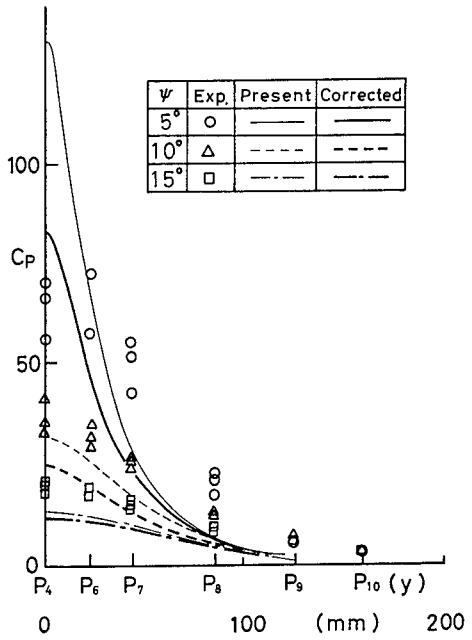


Fig.15 Transverse distribution of peak pressure over the circular cylinder

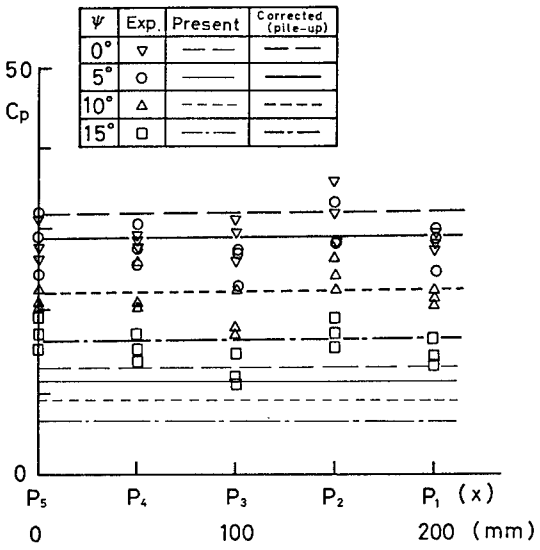


Fig.17 Longitudinal distribution of peak pressure over the wedge type cylinder

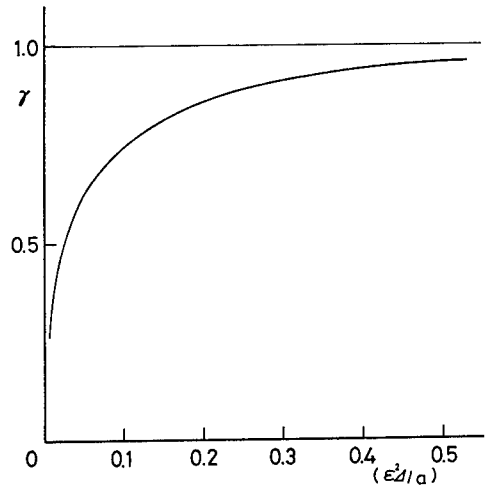


Fig.16 Reduction ratio of the measured peak pressure to the applied peak pressure

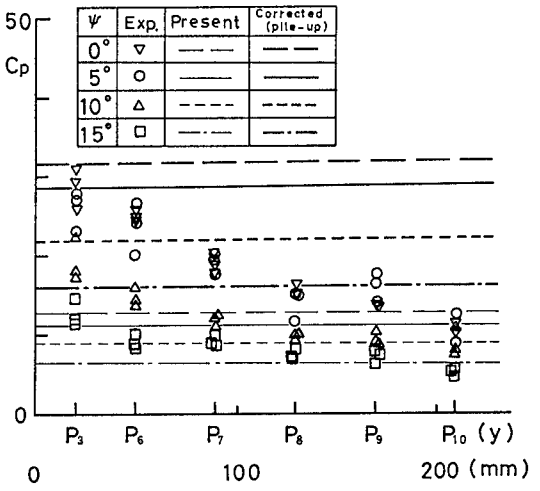


Fig.18 Transverse distribution of peak pressure over the wedge type cylinder

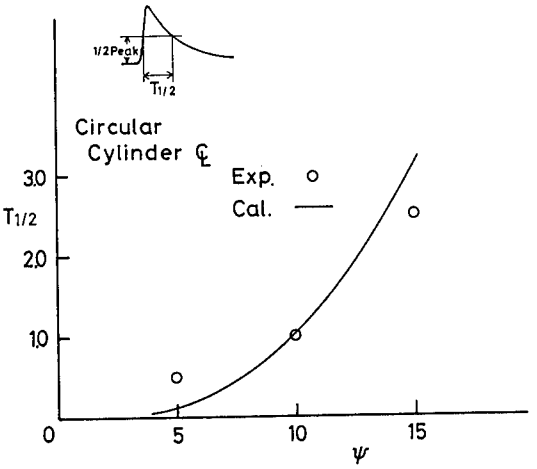


Fig.19 Elapsed time while the pressure being above one half of the maximum pressure

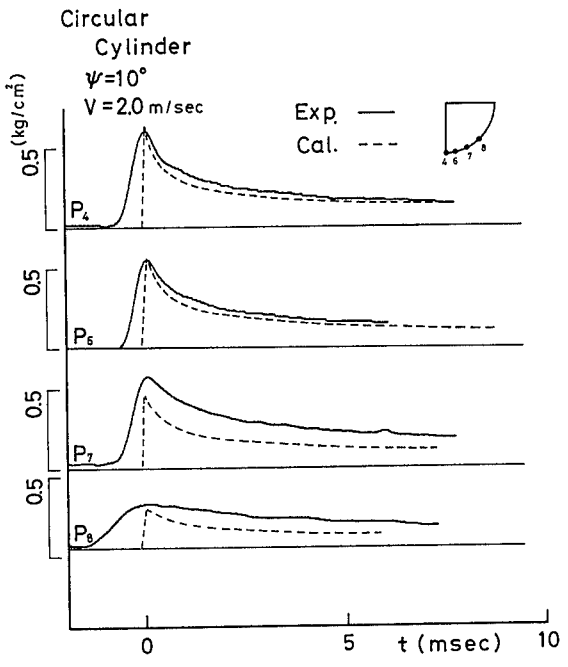


Fig.20 Comparison of calculated and measured pressures in time domain

time history

Fig.20 shows an example of measured time histories and the corresponding calculations of the pressure at various locations. They are aligned in time irrespective of the sequense. Physical unit(kg/cm²) is used in the figure. It is seen that the agreement among them is excellent in spite of negligence of the pile-up effects. It indicates that the flow model of the present theory works well and further improvements along this line would give us more realistic understanding of the phenomena.

4.CONCLUSIONS

A new calulation for the impact pressure over arbitrary three dimensional bodies has been presented and its numerical results have been compared with experiments.Conclusions are

(1) this method can tell the effects of the longitudinal flow upon the impact pressure.

(2) the present composite solution is in good agreement with experiments except the peak pressure value.

(3) the predicted peak pressure value is $\cot^2\theta$ while the experiments show lower value. Agreements are improved,however,if we take into account of the fact that the peak pressure is rounded off due to the finiteness of the pressure gauge.

(4) the pile-up effects can not be neglected at least transversely. Thus,the present theory should be improved in this respect.

(5) the rate of change of the pressure becomes greater when the local body inclination gets larger.

ACKNOWLEDGEMENT

The auhtor is grateful to Dr.Tatsuro Hanaoka, Dr.Kazuo Sugai and other colleagues of our Institute for their supports and encouragements in completing this paper. Especially the author wishes his deep appreciation of their support given by Mr. Michio Ueno, Mr. Hiroshi Sawada and Mr. Tokutaro Yamamoto during the experiment and subsequent data analyses. He also thanks Prof. Masataka Fujino of the University of Tokyo for his suggestion and advises in persuing this theme.

REFERENCES

1.von Karman,Th.,"The Impact of Seaplanes Float During Landing,"NACA TN321,Oct.,1929,pp.1-8.

2.Wagner,H."Über Stoss- und Gleitvorgänge an der Oberfläcke von Flüssigkeiten," ZAMM,band 4,heft 4,1932,pp.193-235.

3.Ochi,M.K.and Motter,L.E.,"A Method to Estimate Slamming Characteristics for Ship Design," Marine Technology, Vol.8,No.2,1971, pp.219-232.

4.Stavovy,A.B.and Chuang,S-L,"Analytical Determination of Slamming Pressures for High-Speed Vehicles in Waves," Journal of Ship Research,Vol.20,No.4,1976,pp.190-198.

5.Chuang,S-L,"Theoretical Investigations on Slamming of Cone-Shaped Bodies," Journal of Ship

Research,Vol.13,No.4,1969,pp.276-283.
6.Watanabe,I,"Anatytical Expression of Hydrodynamic Impact Pressure by Matched Asymptotic Expansion Technique," Transaction of the West-Japan Society of Naval Architects, No.71,March 1986,pp.77-85.
7.Watanabe,I,"On Hydrodynamic Impact Pressure Acting upon Flat Bottomed Ships,"(in Japanese) Journal of the Society of Naval Architects of Japan, No.159,June 1986,pp.201-210.
8.Cole,J.D."Perturbation Methods in Applied Mathematics," Blaisdell (1968)
9.Milne-Thomson,L.M.,"Theoretical Hydrodynamics," Macmillan, 1955.
10.Sedov,L.I.,"Two-dimensional Problems in Hydrodynamics and Aerodynamics," Interscience, 1950.
11.Kochin, N.E.,Kibel,I.A. and Roze.N.V.," Theoretical Hydromechanics," Interscience, 1955.
12.Takemoto,H,"Some Considerations on Water Impact Pressure,"(in Japanese) Journal of the Society of Naval Architects of Japan, No.156,Dec. 1984,pp.314-322.
13.Abramowitz,M and Stegun,I.A., " Handbook of Mathematical Functions," Dover, 1970.

Appendix.A Evaluation of (24)

$$\int_{-1}^{1} \frac{\sqrt{1-\xi^2}}{\{\lambda^2\xi^2+\Upsilon^2\}^{3/2}}\,d\xi = 2\int_{0}^{1} \frac{u^2}{\{(\lambda^2+\Upsilon^2)(1-k^2u^2)\}^{3/2}} \frac{du}{\sqrt{1-u^2}}$$

$$= 2\frac{1}{(\lambda^2+\Upsilon^2)^{3/2}}\int_{0}^{1} \left(\frac{u^2}{1-k^2u^2}\right)\frac{du}{\{(1-u^2)(1-k^2u^2)\}^{1/2}}$$

$$= \frac{2}{\lambda^2}\frac{1}{\sqrt{\lambda^2+\Upsilon^2}}\left[-F\left(\frac{\pi}{2},k\right) + \Pi\left(\frac{\pi}{2};-k^2,k\right)\right], \qquad (A\text{-}1)$$

where $F(\theta,k)$ and $\Pi(\theta,a,k)$ are elliptic integral of the first and the third kind respectively and

$$k^2 = \frac{\lambda^2}{\lambda^2+\Upsilon^2}, \quad \Upsilon = \eta - y .$$

As is well known[13],

$$F\left(\frac{\pi}{2},k\right) = K(k^2),$$
$$\Pi\left(\frac{\pi}{2};-k^2,k\right) = \frac{1}{1-k^2}E(k^2), \qquad (A\text{-}2)$$

where K and E are complete elliptic integral of the first and the second kind respectively. Thus

$$= \frac{2}{\lambda^2\sqrt{\lambda^2+\Upsilon^2}}\left\{-K(k^2) + \frac{\lambda^2+\Upsilon^2}{\Upsilon^2}E(k^2)\right\}. \qquad (A\text{-}3)$$

Appendix.B Reduction of (29) and (30)

As $y \to \eta$ or $k^2 \to 1$, Integrals G_{1n} and G_{2n} become singular. We will examine these singular behaviors and obtain numerically integrable formula for them.
First we take G_{1n}

$$G_{1n} = \int_{-1}^{1} \eta^{2n}\frac{\sqrt{1-\eta^2}}{\sqrt{\Upsilon^2+\lambda(\eta)^2}}K(k^2)d\eta \qquad (B\text{-}1)$$

$$\lim_{k^2\to 1} K(k^2) \to \ln\frac{4}{\sqrt{1-k^2}} = \ln\frac{4\sqrt{\Upsilon^2+\lambda(y)^2}}{|\Upsilon|} \qquad (B\text{-}2)$$

Therefore G_{1n} can be rewritten as

$$G_{1n} = \int_{-1}^{1}\Bigg[\eta^{2n}\frac{\sqrt{1-\eta^2}}{\sqrt{\Upsilon^2+\lambda(\eta)^2}}K(k^2) - y^{2n}\frac{\sqrt{1-y^2}}{\lambda(y)}\ln\frac{4\sqrt{\Upsilon^2+\lambda(y)^2}}{|\Upsilon|}\Bigg]d\eta + y^{2n}\frac{\sqrt{1-y^2}}{\lambda(y)}\int_{-1}^{1}\ln\frac{4\sqrt{\Upsilon^2+\lambda(y)^2}}{|\Upsilon|}\,d\eta . \qquad (B\text{-}3)$$

The second integral can be evaluated analytically as

$$\fint_{-1}^{1} \ln\frac{4\sqrt{\tilde{Y}^2+\lambda(y)^2}}{|\tilde{Y}|}\,d\eta$$

$$= (1-y)\ln\frac{4\sqrt{(1-y)^2+\lambda(y)^2}}{|1-y|}$$

$$+ (1+y)\ln\frac{4\sqrt{(1+y)^2+\lambda(y)^2}}{|1+y|}$$

$$+\frac{\lambda(y)}{2}\{\tan^{-1}(\frac{1-y}{\lambda(y)}) + \tan^{-1}(\frac{1+y}{\lambda(y)})\} \quad \text{(B-4)}$$

Putting (B-3) and (B-4) together, we have eq.(29).

As for G_{2n}, introduce $H(\eta)$ as

$$H(\eta) = \eta^{2n}\sqrt{1-\eta^2}\sqrt{\tilde{Y}^2+\lambda(y)^2}\;E(k^2) \qquad \text{(B-5)}$$

and write

$$G_{2n} = \fint_{-1}^{1} \frac{H(\eta)}{\tilde{Y}^2}d\eta \; . \qquad \text{(B-6)}$$

$H(\eta)$ behaves near $\tilde{Y}=0$ or $\eta=y$ like

$$H(\eta) \to \lambda(y)y^{2n}\sqrt{1-y^2} + \{2n\lambda y^{2n-1}\sqrt{1-y^2}$$

$$+ \frac{\partial\lambda}{\partial y}y^{2n}\sqrt{1-y^2} - \frac{\lambda y^{2n}}{\sqrt{1-y^2}}\}(\eta-y)$$

$$+ \frac{y^{2n}}{4\lambda}\sqrt{1-y^2}\;\tilde{Y}^2\ln\frac{\tilde{Y}^2+\lambda^2}{\tilde{Y}^2} + \text{higher order terms}$$

$$= H(y) + H'(y)\tilde{Y} + H''(y)\tilde{Y}^2\ln\frac{\tilde{Y}^2+\lambda^2}{\tilde{Y}^2}, \qquad \text{(B-7)}$$

where

$$H(y) = \lambda y^{2n}\sqrt{1-y^2} \; , \qquad \text{(B-8)}$$

$$H'(y) = 2n\lambda y^{2n-1}\sqrt{1-y^2} + \frac{\partial\lambda}{\partial y}y^{2n}\sqrt{1-y^2}$$

$$- \frac{\lambda y^{2n+1}}{\sqrt{1-y^2}} \; . \qquad \text{(B-9)}$$

$$H''(y) = \frac{y^{2n}}{4\lambda}\sqrt{1-y^2} \; . \qquad \text{(B-10)}$$

Since

$$\fint_{-1}^{1}\frac{d\eta}{(\eta-y)^2} = -\{\frac{1}{1-y} + \frac{1}{1+y}\}, \qquad \text{(B-11)}$$

$$\fint_{-1}^{1}\frac{d\eta}{\eta-y} = \ln(\frac{1-y}{1+y}) \qquad \text{(B-12)}$$

and

$$\fint_{-1}^{1}\ln\frac{\sqrt{(\eta-y)^2+\lambda^2}}{|\eta-y|}\,d\eta = (1-y)\ln\frac{\sqrt{(1-y)^2+\lambda(y)^2}}{|1-y|}$$

$$+ (1+y)\ln\frac{\sqrt{(1+y)^2+\lambda(y)^2}}{|1+y|}$$

$$+\frac{\lambda(y)}{2}\{\tan^{-1}(\frac{1-y}{\lambda(y)}) + \tan^{-1}(\frac{1+y}{\lambda(y)})\} \; , \qquad \text{(B-13)}$$

G_{2n} can be written

$$\int_{-1}^{1}\frac{H(\eta)-H(y)-H'(y)\tilde{Y}-H''(y)\tilde{Y}^2\ln\{\tilde{Y}^2+\lambda(y)^2\}/\tilde{Y}^2]}{\tilde{Y}^2}d\eta$$

$$-H(y)\{\frac{1}{1-y} + \frac{1}{1+y}\} + H'(y)\ln(\frac{1-y}{1+y})$$

$$+2H''(y)[\;(1-y)\ln\frac{\sqrt{(1-y)^2+\lambda(y)^2}}{|1-y|}$$

$$+ (1+y)\ln\frac{\sqrt{(1+y)^2+\lambda(y)^2}}{|1+y|}$$

$$+\frac{\lambda(y)}{2}\{\tan^{-1}(\frac{1-y}{\lambda(y)}) + \tan^{-1}(\frac{1+y}{\lambda(y)})\}\;]. \qquad \text{(B-14)}$$

DISCUSSION

Raymond Cointe,
University of California, Santa Barbara

Your splash region solution, given by the flow below a planning plate, is only an approximation of the inner boundary value problem (it has a free surface downstream which, of course, is absent from the inner problem) so that you first expand the solution near the stagnation point (Eqs. (39) & (42)). Moreover, in this solution the plate is inclined and the inclination angle β is of order ε so that your inner solution is a function of ε, whereas, in the formal matched asymptotic expansion procedure, each successive approximation should be independent of ε. This appears in the value of Δ you find (Eq. (50)) which is a funcion of ε.

I wonder why you do not use as inner solution the flow with a jet below an infinite plate at zero inclination angle which was obtained by Wagner (1932, [2]). This solution was actually shown to be the exact solution of the lowest-order inner problem in the case of an impacting circular cylinder by Armand and Cointe [a]. It would lead to a different value for the thickness of the jet and to a smoother behavior (exponential decay) of the pressure in the jet.

[a] Armand, J-L. & Cointe, R. "Hydrodynamic Impact Analysis of a Cylinder," Proceedings, 5th OMAE Symposium, Tokyo, 1986 (also to appear in the ASME Journal of Energy Resources).

Reply -

Thank you for your discussion. I believe you have raised three questions:

a. Where I have taken the origin of the inner coordinate S,

b. Should eq. (50) should be independent of β, and

c. Why I have not made use of Wagner's infinite plate solution as an inner solution.

The origin of S or the stagnation point is taken at the point where the outer solution tells us the body surface meets the free surface. Therefore, if we take the piled-up water effect into account, the stagnation point moves at the rate which Wagner presented. There might be a possibility to choose another location as the origin, but I think that would cause little difference as far as my experimental observations goes.

I know an asymptotic sequence with respect to ε should be independent of ε, as you mentioned. But I would like to point out that β is a constant of order of ε in the inner region, not the order function. It has to be understood that eq. (50) has been expressed in the ratio of β to ε, not β itself. You can see Δ is of order unity from the equation.

The reason why I have made use of planing plate solution to get the inner solution rather than Wagner's infinite plate solution lies in that I wished the inner solution be sensitive to the attack angle which can not be taken care of by the Wagner's formula. By doing so, we can equate the incoming velocity (U) in the inner solution to the expanding velocity ($V\cot\beta$) of water plane in the outer solution, since they are in the same direction asymptotically at infinity. On the other hand, if we take Wagner's solution, there would be no way of taking care of it since his velocity at infinity flows tangential to the body surface, which is not in agreement with outer solution contemplated here.

Rankine Source Methods for Numerical Solutions of the Steady Wave Resistance Problem

G. JENSEN and H. SÖDING, Institut für Schiffbau, Germany
Z.-X. MI, Jiao Tong University, China

Abstract

The steady potential flow past a body in or near the free surface of an ideal fluid is computed by superimposing the potential of triangular source panels inside the hull surface and above a part of the free surface. The free surface condition is linearized with respect to the differences between exact values and approximations of surface height and the potential there; this leads to an iteration scheme to sastisfy the nonlinear condition. Based on theoretical reasoning and numerical experiments, a novel, accurate method to satisfy the radiation condition is proposed. Results for the flow past a submerged vortex and preliminary results for the Wigley parabolic hull are presented.

Nomenclature and Coordinate System

x, y, z	right handed coordinate system. (x and y are in the undisturbed water plane; x is pointing upstream; z is pointing vertically downward)
U	free stream velocity
$\vec{n}$	$= (n_x, n_y, n_z)$ unit normal vector on the body surface
ϕ	velocity potential
Φ	velocity potential approximation
φ	correction potential
$\bar{\phi}$	$\phi + Ux$
ϕ_N	numerical approximation of $\bar{\phi}$
ζ	z-coordinate of the free surface
$\bar{\zeta}$	approximation of ζ
ψ	weight function

Subscripts:

x, y, z	denote partial derivatives
l	denotes the derivative in direction of a streamline of Φ
i	number of approximation function or source number
j	number of weight function or collocation point
v	refers to vortex.

Introduction

The steady potential flow past a body in or near the free surface, i. e. the wave-resistance problem, is treated frequently by superimposing source potentials satisfying Laplace's equation and the condition of vanishing disturbance far below the surface. If only a linearized free-surface condition is to be satisfied, source potentials which comply with this condition may be the best choice; if, however, one tries to satisfy a nonlinear free-surface condition, we prefer to use the simple Rankine source potential. In this case, the boundary condition on the body (no flow through its surface) and the free-surface conditions (no flow through the surface; constant pressure; waves radiating only to a sector behind the body) have to be satisfied numerically by choosing appropriate strengths of sources arranged along the wetted hull and a part of the free surface. Dawson [1] and Gadd [2] succeeded with such a method, producing reasonable results inspite of using simplified free-surface conditions. To increase the accuracy and decrease, if possible, the computational effort of these methods, we try to satisfy iteratively the exact non-linear free-surface condition, and we apply different numerical methods for several crucial details.

Heinrich Söding and Gerhard Jensen, Institut für Schiffbau of the University of Hamburg, Lämmersieth 90, 2000 Hamburg 60
Zhen-Xing Mi, Shanghai-Jiatong, University, Department of Navel Architecture and Ocean Engineering, Huashan-Road 1954, Shanghai 20030, PR. China

Problem

We want to determine the steady, symmetrical, vortex-free potential flow of an incompressible fluid with a free surface around a surface-piercing ship with velocity U on deep water. The flow potential ϕ and the surface elevation ζ satisfy the following conditions:

$$\Delta\phi = 0 \qquad \text{for } z > \zeta; \tag{1}$$

$$\vec{n}\nabla\phi = 0 \qquad \text{on the wetted hull surface;} \tag{2}$$

$$\frac{1}{2}(\nabla\phi)^2 - g\zeta = \frac{1}{2}U^2 \qquad \text{on } z = \zeta \tag{3}$$

$$\nabla\phi\nabla\zeta = \phi_z \qquad \text{on } z = \zeta \tag{4}$$

(For simplification, $\zeta(x,y,z)$ with $\zeta_z = 0$ is assumed here.)

$$\lim_{x^2+y^2+z^2\to\infty} \nabla\phi = (-U,0,0)\ . \tag{5}$$

Waves may appear only behind the ship (radiation condition).

Eliminating ζ from (3) and (4) results in the free-surface condition

$$\frac{1}{2}\nabla\phi\nabla(\nabla\phi)^2 - g\phi_z = 0 \qquad \text{on } z = \zeta \tag{6}$$

Linearization

In the problem constituted by (1), (2), (5) and (6), only (6) is nonlinear. It is to be satisfied iteratively by linearizing (6) around approximations Φ and $\bar{\zeta}$ of ϕ and ζ resp. To that end, we substitute $\phi = \Phi + \varphi$, neglect terms nonlinear in φ and $\zeta - \bar{\zeta}$ and develop the resulting condition into a truncated Taylor expansion about $\bar{\zeta}$. This yields the condition

$$\nabla\Phi\nabla\left(\frac{1}{2}(\nabla\Phi)^2 + \nabla\Phi\nabla\varphi\right) + \nabla\varphi\nabla\left(\frac{1}{2}(\nabla\Phi)^2\right) \tag{7}$$
$$- g(\Phi_z + \varphi_z) + \left[\frac{1}{2}\nabla\Phi\nabla(\nabla\Phi)^2 - g\Phi_z\right]_z (\zeta - \bar{\zeta}) = 0$$

on $z = \bar{\zeta}$. Here, ζ has to be substituted by an expression depending on $\bar{\zeta}$, $\Phi(\bar{\zeta})$ and $\phi(\bar{\zeta})$ only. This expression is derived from (3):

$$\begin{aligned} \zeta &= \frac{1}{2g}\left[(\nabla\phi)^2 - U^2\right]_{z=\zeta} \qquad (8)\\ &= \frac{1}{2g}\left[(\nabla\phi)^2 + 2\nabla\Phi\nabla\Phi_z(\zeta - \bar{\zeta}) - U^2\right]_{z=\bar{\zeta}} \end{aligned}$$

Thus

$$\zeta - \bar{\zeta} = \frac{\frac{1}{2g}\left[(\nabla\Phi)^2 + 2\nabla\Phi\nabla\varphi - U^2\right] - \bar{\zeta}}{1. - \nabla\Phi\nabla\Phi_z/g} \tag{9}$$

with Φ and φ to be taken at $z = \bar{\zeta}$.

Inserting (9) into (7) and backsubstituting $\varphi = \phi - \Phi$ yields the linearized free surface condition

$$\nabla\Phi\nabla\left[-(\nabla\Phi)^2 + \nabla\Phi\nabla\phi\right] + \frac{1}{2}\nabla\phi\nabla(\nabla\Phi)^2 - g\phi_z$$
$$+ \left[\frac{1}{2}\nabla\Phi\nabla(\nabla\Phi)^2 - g\Phi_z\right]_z \tag{10}$$
$$\cdot \frac{\frac{1}{2g}\left[-(\nabla\Phi)^2 + 2\nabla\Phi\nabla\phi - U^2\right] - \bar{\zeta}}{1. - \nabla\Phi\nabla\Phi_z/g} = 0$$

on $z = \bar{\zeta}$. The denominator in the last term is zero if the vertical particle acceleration $\nabla\Phi\nabla\Phi_z$ is equal to g, i. e. if the approximated flow becomes unstable.

Comparison with Dawson's Free-Surface Condition

Dawson [1] proposed a linearization of the free-surface condition around the approximations $\bar{\zeta} = 0$ and Φ = double-body potential; thus $\Phi_z = 0$. In this case, (10) simplifies to

$$\nabla\Phi\nabla\left[-(\nabla\Phi)^2 + \nabla\Phi\nabla\phi\right] + \frac{1}{2}\nabla\phi\nabla(\nabla\Phi)^2 - g\phi_z = 0. \tag{11}$$

Following Dawson, we introduce the notation $(\nabla\Phi\nabla)H = \Phi_l H_l$ for arbitrary scalar or vector fields. The index l denotes a derivative in the streamline direction of the double-body flow. Using this notation, (11) transforms to

$$\Phi_l\left(-\Phi_l^2 + \Phi_l\phi_l\right)_l + \frac{1}{2}\nabla\phi\nabla\left(\Phi_l^2\right) - g\phi_z = 0. \tag{12}$$

The second term in (12) may be further transformed to $\Phi_l(\nabla\Phi)_l\nabla\phi$. If the curvature of the streamlines of Φ is small, we can approximate $(\nabla\Phi)_l$ by $\nabla(\Phi_l)$. (Dawson does this without mentioning.) Then we obtain from (12):

$$\Phi_l\left(-\Phi_l^2 + \Phi_l\phi_l\right)_l + \Phi_{ll}\Phi_l\phi_l - g\phi_z = 0, \tag{13}$$

which is easily transformed to Dawson's condition

$$\left(\Phi_l^2\phi_l\right)_l - g\phi_z = 2\Phi_l^2\Phi_{ll}. \tag{14}$$

Thus, besides requiring $\Phi_z = 0$, Dawson's free-surface condition is not an exact linearization. However, many applications have shown that it is a very reasonable approximation for wave-resistance calculations. The exact condition for $\Phi_z = 0$, written in a form corresponding to (14), is

$$\Phi_l\left(\Phi_l\phi_l\right)_l + \Phi_l(\nabla\Phi)_l\nabla\phi - g\phi_z = 2\Phi_l^2\Phi_{ll}. \tag{15}$$

Numerical approximation theory

$\bar{\phi} = \phi + Ux$, the perturbation of the parallel stream is introduced here. We approximate $\bar{\phi}$ by

$$\phi_N = \sum_{i=1}^{I} a_i \phi_i \tag{16}$$

The functions ϕ_i are chosen to satisfy exactly (1) and $\lim_{x^2+y^2+z^2\to\infty} \nabla\phi_i = 0$, whereas the a_i are to be determined such that (2), (6) and the radiation condition are satisfied approximately. The approximation is defined here to be optimal if

$$\int_S \left(\bar{\phi} - \phi_N\right)^2 ds = \underset{a_i}{\text{Minimum}} \tag{17}$$

The integration surface S in (17) is the wetted hull surface and a part of the free surface surrounding the ship. Inserting (16) into (17), a partial derivation of (17) with respect to one a_i (termed a_j) leads to

$$\sum_{i=1}^{I} a_i \int_S \phi_i \phi_j \, ds = \int_S \bar{\phi}\phi_j \, ds \tag{18}$$

for $j = 1, \ldots, I$.

The radiation condition, (2) and (6) are now written formally as

$$B(\bar{\phi}) = f \qquad \text{on S,} \tag{19}$$

with B being the homogeneous and f the inhomogeneous part of the boundary conditions.

Let us define an adjoint operator B^* by the equation

$$\int_S B(\bar{\phi})\psi \, ds = \int_S \bar{\phi} B^*(\psi) \, ds \tag{20}$$

for arbitrary functions $\bar{\phi}$ and ψ to which the operators are applicable. Further, we choose a special set of functions ψ_j by the equations

$$B^*(\psi_j) = \phi_j, \quad j = 1, \ldots, I. \tag{21}$$

Inserting (21) into (18) and using (20) and (19), we obtain

$$\sum_{i=1}^{I} a_i \int_S B(\phi_i)\psi_j \, ds = \int_S f\psi_j \, ds. \tag{22}$$

(22) is the essence of the well-known weighted-residual methods for the determination of the coefficients a_i . The above derivation shows, however, that the weight functions ψ_j should be chosen according to (21) to obtain the optimum approximation possible with the chosen set of functions ϕ_i.

Approximation of Optimum Weight Functions

The application of (22) with ψ_j acc. to (21) seems computationally ineconomical compared to the collocation method, i. e. to choosing $\psi_j = \delta(x - x_j)$, thereby satisfying the boundary conditions at the collocation points x_j only; therefore the collocation method requires much less evaluations of the complicated function $B(\phi_i)$. However, it seems worthwhile to get at least an idea of the optimum weight functions. To that end, we omit the body boundary condition, drop the third dimension (in y direction) and substitute (10) by the simple linear free-surface condition

$$U^2\bar{\phi}_{xx} - g\bar{\phi}_z = 0 \qquad \text{on } z = 0. \tag{23}$$

The radiation condition is now

$$\lim_{x\to+\infty} (\bar{\phi}, \bar{\phi}_x, \bar{\phi}_z) = 0. \tag{24}$$

(Note that in the two-dimensional case, $\bar{\phi}$ does not approach 0 for $x \to -\infty$.)

To determine B^*, we investigate the left-hand side of (20):

$$LH(20) = \int_{-\infty}^{\infty} \left(U^2\bar{\phi}_{xx} - g\bar{\phi}_z\right)\psi \, ds \text{ on } z = 0. \tag{25}$$

A twofold partial integration of the first term in (25) gives

$$U^2 \int_{-\infty}^{\infty} \bar{\phi}_{xx}^2 \psi ds = U^2[(\bar{\phi}_x\psi)_{-\infty}^{\infty} - (\bar{\phi}\psi_x)_{-\infty}^{\infty} + \int_{-\infty}^{\infty} \bar{\phi}\psi_{xx} \, dx]. \tag{26}$$

Using (24) eliminates the first two terms for $x = \infty$. Additionally, we require

$$\lim_{x\to-\infty} (\psi, \psi_x, \psi_z) = 0 \tag{27}$$

to eliminate the first two terms also for $x = -\infty$.

Correspondingly, the second term in (25) is transformed by Green's identity. Using (1), (24), (27) and requiring the further conditions

$$\Delta\psi = 0 \qquad \text{for } z > 0 \tag{28}$$

and

$$\lim_{z\to\infty} \nabla\psi = 0, \tag{29}$$

we obtain

$$g \int_{-\infty}^{\infty} \bar{\phi}_z\psi \, dx = g \int_{-\infty}^{\infty} \bar{\phi}\psi_z \, dx. \tag{30}$$

Thus, from (25) we obtain with (26) and (30):

$$LH(20) = \int_{-\infty}^{\infty} \bar{\phi} \left(U^2 \psi_{xx} - g\psi_z \right) \, ds \qquad (31)$$

Comparing (31) with (25) and (20) shows

$$B^* = B \qquad (32)$$

as far as the free-surface condition is concerned; however, the radiation condition (24) of B has to be changed to (27) in B^*. Taking this together with the conditions (21), (28) and (29), we see that ψ_j is the potential which satisfies the Laplace condition, the depth condition $\lim_{z\to\infty} \nabla\psi_j = 0$ and

1. an inhomogeneous free-surface condition, corresponding to a horizontal pressure gradient proportional to ϕ_j;
2. a radiation condition requiring no waves *behind* the pressure disturbance.

Thus, the optimum weight function ψ_j is expected to have small absolute values only behind the disturbance ϕ_j and a wavy character in front of it. Therefore, we expect that a collocation method approximates the optimum if x_j is positioned in front of the disturbances ϕ_j , at a position where ψ_j deviates substantially from zero.

Numerical Approximation Test

To test this idea numerically, the two-dimensional flow past a submerged vortex at the location x_v, z_v was investigated, at first using the linear free-surface condition (23) together with conditions (1) and (5). For this problem, (16) changes to

$$\phi_N = \sum_{i=1}^{I} a_i \phi_i - Ux + \gamma \arctan \frac{z - z_v}{x - x_v}; \qquad (33)$$

the boundary condition (19) is now

$$\sum_{i=1}^{I} a_i \left(U^2 \phi_{ixx} - g\phi_{iz} \right) = \qquad (34)$$
$$- \frac{U^2 \gamma 2 (x - x_v)(z - z_v)}{r^4} + \frac{g\gamma (x - x_v)}{r^2}$$

with

$$r^2 = (x - x_v)^2 + (z - z_v)^2 . \qquad (35)$$

For ϕ_i we choose combinations of three simple source potentials:

$$\phi_i = \qquad (36)$$
$$\sum_{k=-1}^{1} \log \left[\left(x - x_i + \frac{k\Delta x}{2} \right)^2 + (z - z_i)^2 \right] \left(1 - 0.5k^2 \right)$$

The locations (x_i, z_i) of the central sources were positioned in constant distance Δx above the free surface according to Fig. 1 at different horizontal displacements $\Delta\xi$ with respect to the collocation points $(x_j, 0)$ on the mean surface. Equations (34), satisfied at the collocation points $x_j, j = 1, \ldots, I$, constitute a linear system of equations for the coefficients a_i which define ϕ_N by means of (33). Considerations not recalled here indicate that not only errors due to the finite number accuracy of the computer, but also a part of the approximation error (17) is minimum if the absolute value of the determinant D of the coefficient matrix of this system of equations is maximized. The variation of this determinant with $\Delta\xi$ is shown in Fig. 2. Due to the symmetry of the problem, D is a symmetric function of $\Delta\xi$.

Using the D maximum at $\Delta\xi = 0$ results, as expected, in a symmetrical, wavy surface computed by the linearized version of (3):

$$\varsigma = \frac{U}{g} (\phi_x - U) . \qquad (37)$$

Using the D maximum at $\Delta\xi = \Delta x$ yields the linearized surface deformation shown in Fig. 1. It satisfies the radiation condition (24); it coincides accurately with linear perturbation results by Salvesen and

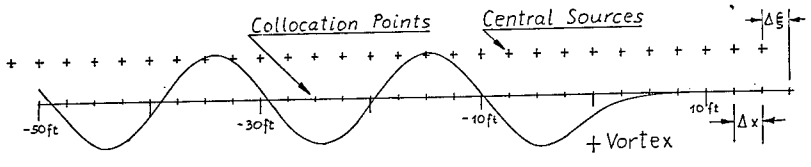


Fig.1 Linearized surface elevation due to a submerged vortex in uniform stream of $U = 10ft/s$

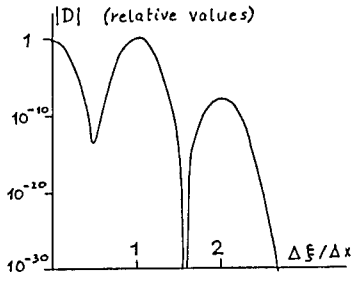


Fig.2 Determinant of the coefficient matrix depending on the offset $\Delta\xi$ between collocation points and central sources relative to the collocation point distance Δx

v. Kerczek [5]; and it shows for $x \ll 0$ constant amplitude waves of very accurate wavelength $2\pi U^2/g$. It is, therefore, the physically correct solution. $\Delta\xi$ values between, say, $0.8\Delta x$ and $1.2\Delta x$ lead to results differing by less than 1% from those with $\Delta\xi = \Delta x$. The D maximum of $\Delta\xi = -\Delta x$ leads to a solution satisfying the 'opposite' radiation condition (27). Using $\Delta\xi = 2\Delta x$ did not result in a reasonable solution.

Compared to the numerical differencing in Dawson's method, we see the following advantages in the above method of satisfying the free-surface and radiation conditions:

1. Excellent accuracy is attained with 8 collocation points per wavelength and very simple triple source potentials for ϕ_i .
2. No damping at the rear end or modifications at the front end of the computational region are necessary.
3. The scheme is simpler.
4. The extent of the computational region may be smaller than in Dawson's method.

Vortex with Nonlinear Free-Surface Condition

Instead of (23) we use now (10) as the free-surface condition in combination with (33). For Φ we begin with (33), using $a_i = 0$. In the following iteration cycles the approximation ϕ_N of the previous cycle may be used as Φ. ζ was determined from (3) applied to Φ. For moderate vortex strengths, this scheme converges nicely. For a stronger vortex, however, the changes of ϕ computed from (10) are excessive. Therefore, a weighted average Φ_N between Φ and ϕ_N is better used as approximate potential in the next iteration cycle, with weights depending on the maximum errors E_1, E_2 of the exact boundary condition (6), applied to Φ or ϕ_N, resp., in all collocation points:

$$\Phi_N = \frac{E_1\phi_N + E_2\Phi}{E_1 + E_2} \qquad (38)$$

This 'more cautious' iteration was tried on the cases investigated in [5] by means, besides others, of a finite-difference method. For positive γ up to more than $2.7ft/s$ and for $\gamma \geq -2.5ft/s$, the errors E may be reduced from their starting value by many orders of magnitude, which means that the exact free-surface condition is accurately satisfied in all collocation points. Between collocation points, the errors are larger, but also small. The case $\gamma = -2.7ft/s$ investigated in [5], however, is hard because waves are near to breaking. For this case, an error reduction to 1/24 of its starting value, i.e. to $E_2 = 0.75ft^2/s^3$, was attained after 24 iteration steps; thereafter, the iteration scheme (38) causes practically no changes any more. Fig. 3 compares our results with those of [5]; the latter refer to a finite water depth of $9.5ft$ whereas our results are for deep water.

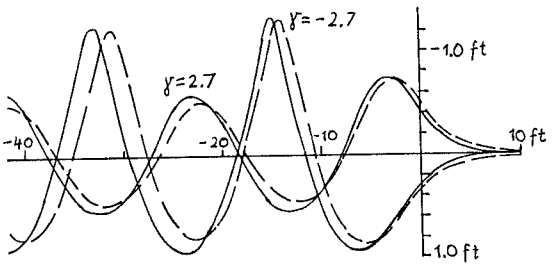


Fig.3 Wave elevations due to a submerged vortex at $x_v = 0$, $z_v = 4.5ft$ in a uniform stream of $U = 10ft/s$ according to [5] (continuous lines) and own investigation (broken lines)

Wave Resistance Calculations

The preceeding investigations are aimed to further develop the 3-dimensional ship resistance calculation method of Dawson [1]. This work is still in progress. At the moment, we can present only results of a method which differs from Dawson's by the following points:

1. As ϕ_i we use not the potential due to constant-strength quadrilateral source panels according to Hess and Smith, but a triangular panelation with continuous source strength varying linearly within each triangle, according to Webster [6]. For numerical accuracy some alterations in the formulae for the velocities due to a source panel were made, similar to those suggested by Yeung [7]. The panels are arranged inside the hull and above the water surface at a distance of not more than half the smallest surface curvature radius. The hull panelation was continued to more than twice the maximum expected wave height above the undisturbed surface, and the free-surface panelation was extended by 10% of the breadth into the hull.
2. The nonlinear free-surface condition (6) is approximated iteratively by means of a simplified version of (10) which disregards the complicated last term, i.e. by (11).
3. Instead of taking mirror images of the sources within the hull, the source panels are extended above the free surface with constant strength. This is done to avoid strong vertical velocities beeing induced by the body sources.

The numerical difference scheme of Dawson for second derivatives in streamline direction was still used.

For tests the Wigley parabolic hull defined by

$$y = \frac{B}{L}\left[1-\left(\frac{2x}{L}\right)^2\right]\left[1-\left(\frac{z}{H}\right)^2\right]$$
$$-\frac{L}{2} \le x \le \frac{L}{2}, \quad 0 \le z \le H$$

with $B/L = 0.1$ and $H/L = 0.0625$, is used. This hull has sharp edges at bow, stern and keel. The block coefficent is 0.44 and the prismatic coefficent is 0.6667. The sides were extended vertically above the undisturbed waterplane.

Since the method of arranging source panels within the hull has problems with sharp edges, the hull was rounded at the bow and at the stern. Fig. 4 and Fig. 5 show the grid on the free surface and on the hull.

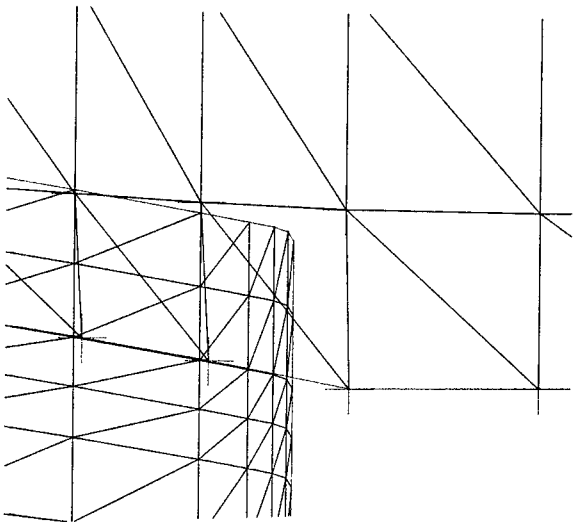


Fig.5 Detail of grid near bow

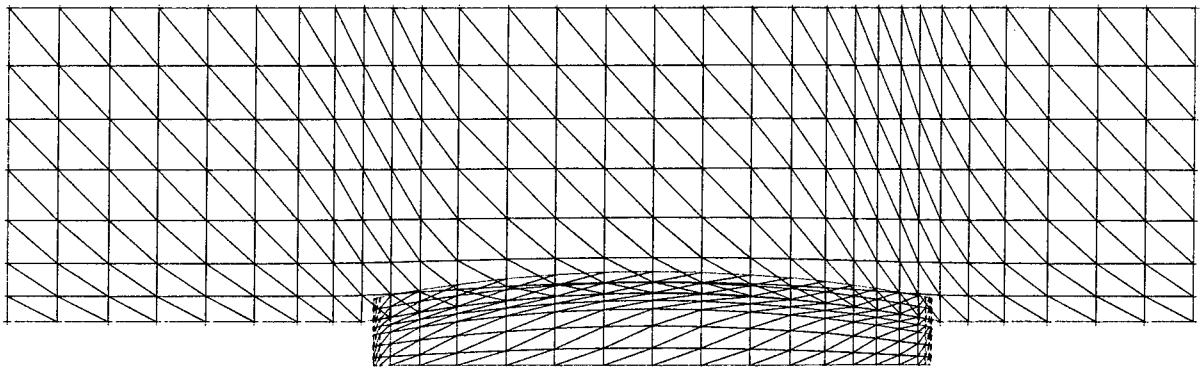


Fig.4 Surface and Hull grid for Wigley parabolic hull with 182 points on the body and 341 points on the free surface

The results are not satisfactory yet; the iteration diverged in most cases. Therefore we only show a result for $Fn = 0.35$. Fig. 6 shows contour lines for the first step, Fig. 7 for the third step. The corresponding values for the wave resistant coefficient are $1.97 \cdot 10^{-3}$ and $2.24 \cdot 10^{-3}$. Trim and sinkage were corrected. This compares only poorly to the $1.79 \cdot 10^{-3}$ given by Landweber [3] from measurements.

Acknowledgement

Part of this work was financed by Deutsche Forschungsgemeinschaft. Contributions of Dipl.-Ing. V. Bertram and Kapt. J. Kleinwächter are gratefully acknowledged.

References

[1] Dawson, C.W.
A Practical Computer Method for Solving Ship-Wave Problems
Second International Conference on Naval Hydrodynamics, University of California, Berkeley (1977)

[2] Gadd, G.E.
A Method of Computing the Flow and Surface Wave Pattern Around Full Forms
The Royal Institution of Naval Architects, Vol. 118 (1976)

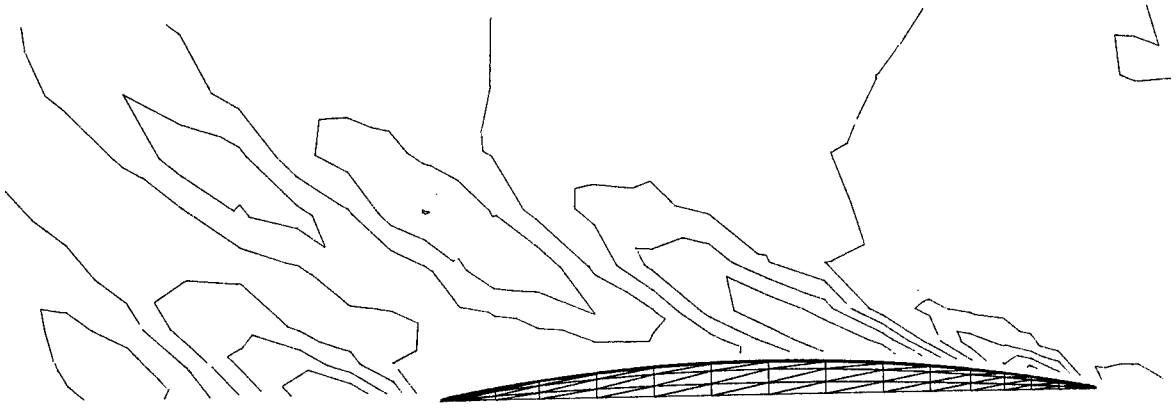


Fig.6 Contour lines of wave elevation in first step of iterarion. The height steps are 0.05 $\frac{1}{2}gU^2$



Fig.7 Contour lines of wave elevation in third step of iterarion. The height steps are 0.05 $\frac{1}{2}gU^2$

[3] Landweber,L.
Wigley Parabolic Hull Group Discussion Proceedings of the Workshop on Ship Wave-Resistance Computations, Vol.1
David Taylor Naval Ship Research and Development Center Bethesda,Maryland, U.S.A. (1979)

[4] Mi, Z.-X.
Wave resistance computations by means of a modified Dawson method (in German)
Institut für Schiffbau der Universität Hamburg, Rep. 460 (1985)

[5] Salvesen, N. and C.H. von Kerczek
Comparison of Numerical and Perturbation Solutions of Two-Dimensional Nonlinear Water-Wave Problems
Journal of Ship Research, Vol. 20, No. 3 (1976)

[6] Webster, W.C.
The flow about Arbitrary Three-Dimensional Smooth Bodies
Journal of Ship Research Vol. 19, No. 4 (1975)

[7] Yeung, R.W. and Bai, K.J.
Numerical Solutions to the Free Surface Flow Problems
10th Symposium on Naval Hydrodynamics
Massachusetts Institute of Technology (1974)

DISCUSSION

Vladimir Ankudinov,
Tracor Hydronautics

Dawson approximation has been further extended by O. Daube and A. Daulieu [a], and in similar effort by Tracor Hydronautics. The non-linear condition,

$$\frac{\partial^2\varphi}{\partial\sigma^2} + \nu\frac{\partial\varphi}{\partial z} = 0, \quad \text{on the free surface,}$$

where

σ is the streamline abscissa,

$\nu = \frac{g}{V^2}$, the wave number, and

$\vec{V} = \vec{\nabla}\varphi$

reduces to Dawson's equation (14) for the double-body flow approximation which is, in turn, used by this method as a first step in the iterative procedure. In further steps Rankine sources are distributed over the instantaneous wetted surface and finite part of the free surface around the ship hull. Comparisons of the experimental and calculated results have been also somewhat disappointing because improvement over the Dawson's approximation are typically marginal, and often worse particularly towards higher Froude number. We have been unable to identify the problem so far but it appears that the numerical procedure requires a very high accuracy in case of significant sinkage and trim. Furthermore, I would like to encourage the authors to continue their work an this challenging hydrodynamic and numerical problem and to extend their computation for other ship hulls (perhaps, will be a good candidate vessel) and to include calculation of sinkage, trim and wave profile along the hull for further analysis of wave induced forces.

[a] Daube, O., and Daulieu, A., "A Numerical Approach of the Nonlinear Wave Resistance Problem," Third International Conference on Numerical Hydrodynamics, Paris, June, 1981.

Reply -

The iterative procedure proposed by Daube and Daulieu is based on a differential equation which is not a linearization of the non linear free surface condition by means of a truncated Taylor expansion. From certain considerations of the error in the nonlinear boundary condition for two succesive approximations we deduce, that there are certain areas where the iteration increases the error for such an equation and therefore will not converge.

Chang-gu Kang,
The University of Michigan

I have calculated the wave resistance due to a submerged vortex in uniform stream by method similar to yours. The difficult problem was numerical instability of upstream part. How did you remove the numerical instability of upstream part?

Reply -

There was no instability in the upstream part. Moving the collocation points upstream effectively ensures that no disturbances may enter from there.

K. Mori,
Hiroshima University

Iteration computations sometimes require introducing a weighting factor explicitly. I think a direct introduction of a weighting function to the wave elevation may make the iterations more stable, for Eq. (10) is modi- fied.

Reply -

We tried to introduce a weighting factor of .25 to the expression for $\zeta - \bar{\zeta}$, (9), which modifies the boundary condition (10). With this alteration the iteration fails to converge even in the less critical case of positive γ.

Ronald W. Yeung,
University of California, Berkeley

The device used by the authors in obtaining downstream waves in the two-dimensional problem is reminiscent to an "analogous" treatment in the modeling of lifting flow about a flat plate by discrete vortices. The so called "quarter-point and three-quarter point" locations of vortex and collocation point in the Weissinger approximation is known to be able to effectively control the direction of the flow and the Kutta condition. The condition for the free-surface problem apparently requires the upstream behavior to be specified, hence upstream collocation points. Can the authors comment on how sensitive is the "optimal collocation arrangement" to the vertical location of discrete sources above the free surface?

Reply -

We agree, that our treatment of the radiation condition is analogous to the modeling of lifting flow with discrete vortices.

We have performed test computations about the value of $\Delta\xi/\Delta x$ for the second maximum of $|D|$ for vertical distances z_q of the sources above the free surface range of $1\Delta x$, ... ,$5\Delta x$. Within this range the position of the maximum varied between $\Delta\xi/\Delta x = -0.996$ and -1.056. This shows, that the dependence on z_q is very small.

A Calculation Method for the Lifting Potential Flow Around Yawed, Surface-Piercing 3-D Bodies

F. XIA and L. LARSSON, SSPA

Maritime Research and Consulting, and Chalmers University of Technology, Sweden

ABSTRACT

A method especially developed for investigating hulls and keels of sailing yachts at an angle of attack is described in the paper. The method may be considered to be an extension of the Hess panel method for lifting, unbounded potential flows to include the effect of the free surface, which may play an important role in the optimization of the design.

The free surface is taken into account in the manner suggested by Dawson, i e not only the hull, but also part of the free surface, is covered by panels. However, rather than using double model streamlines on the surface for defining the panels, a user-specified body-fitted grid is employed. Lift is generated by distributing doublets on the lifting parts and this distribution is determined so as to satisfy the Kutta condition at the trailing edge.

Test calculations show that the method may be a very useful design tool, although some care is needed to avoid the free surface grid dependence problem.

NOMENCLATURE

$[A]$	coefficient matrix for the linear equation systems
B	constant of proportionality for the dipole strength along the arc length of a lifting strip
C	right-hand side array for the linear equation system
CA, CB, CC, CD	coefficients of the finite difference operator
C_D	drag coefficient
C_L	lift coefficient
C_W	wave resistance coefficient
F_n	Froude number
L	number of lifting strips
L_x, L_y, L_z	components of the double model flow direction vector
M	total number of source panels
N	number of panels on the body
N_x, N_y, N_z	components of the normal vector to the body surface
$\bar{n}$	normal to the body surface
U	magnitude of the uniform onset flow velocity
$\bar{V}$	total flow velocity and a vector (X, Y, Z) matrix with X, Y, Z defined as below
$\bar{V}_\infty$	velocity of the uniform onset flow
$\bar{V}^{(o)}$	velocity of the combined onset flow
$\bar{V}^{(k)}$	velocity of the k-th circulatory onset flow
$[X], [Y], [Z]$	matrices of velocity components generated by a unit source distribution
x, y, z	coordinates of the ship coordinate system
β	yaw angle
ζ	wave elevation
σ	source density
ϕ	total velocity potential
Φ	double model flow velocity potential

Subscripts and Superscripts

i, j	subscripts denoting a quantity related to the i-th or j-th panel
ij	double subscript denoting effect of the j-th panel at the i-th control point
(k)	superscript denoting a quantity related to the circulatory onset flow
1	subscript denoting differentiation along a streamline of the double model flow
(∞)	superscript denoting a quantity related to the uniform onset flow

1. INTRODUCTION

In the past decade considerable efforts have been made at SSPA and Chalmers University of Technology to develop ship flow calculation methods useful for design purposes. Results of these efforts have been reported in a series of papers presented at the 11th, 13th, 14th and 15th Symposiums on Naval Hydrodynamics, [1]-[4], and in several other publications. Until 1983 the research was exclusively directed towards viscous flow methods, i e methods for thin, [1], and thick, [2], [3], boundary layers as well as partially parabolic, [4], and fully elliptic, [5], methods. However, the need for useful potential flow computer programs, considering the free surface effect, was felt more and more strongly in the early eighties, and in 1983 a project for developing such programs was started.

The first result of the project was a computer program based on Dawson's approach, [6], and reported in [7]. To investigate its usefulness a number of test cases were computed, including considerable numerical experimentation and parametric studies. Since the results were quite promising the work was continued and a new method, partly using the same ideas, was developed for the potential flow around yawed surface-piercing bodies, generating lift. In another extension of the work the exact free surface problem was investigated and a new iterative method (for the zero lift case) was developed. Very recently the first Dawson type method was extended to include the propeller effect. All work within the potential flow project has been reported in a PhD thesis by Xia, [8]. The present paper deals with the method for lifting flows.

The interest in computer programs for free surface lifting flows around surface-piercing bodies has arisen from the recent activity in the research on sailing yachts, particularly yacht keels. As is well known, the Australian 12 m yacht Australia II, for the first time in the long history of America's Cup, was able to defeat the American defender in the 1983 America's Cup races. The radical wing keel on Australia II was by many considered the main cause of the victory, and an unparalleled interest in yacht research was created. A number of countries turned out to be interested in challenging the Australians and, particularly in America, large amounts of money have now been spent on tank testing of different hulls and keels for the 1987 races. Obviously a computational method especially designed for investigating sailing yacht hull-keel combinations should be most useful.

To the knowledge of the authors no suitable method for such calculations has been reported in the literature. Most aircraft companies and research laboratories seem to have calculation methods for lifting unbounded potential flows, but it is likely that a major factor in the optimization of the keel is the interaction between the keel vorticity and the free surface, so available methods should be of limited value. In two papers by Slooff, [9], [10], reference is made to a method including the free surface, but it does not seem to have been reported in the open literature.

One of the most well-known methods for lifting, unbounded potential flows is the first order panel method developed by Hess, [11], at the Douglas Aircraft Co. The present method may be considered an extension of Hess' to include the free surface, in a manner similar to Dawson's extension of the original Hess & Smith method, [12], for non-lifting flows.

The theory of the method is explained in Section 2 and in Section 3 test results are reported and discussed. In Section 4, finally, some conclusions are drawn.

2. THEORY

2.1 Formulation of the Problem

The flow field around ship configurations may be described by a velocity potential, ϕ, which satisfies the following conditions:

$$\nabla^2\phi = 0 \qquad \text{in the fluid} \qquad (1)$$

$$\phi_n = 0 \qquad \text{on the hull} \qquad (2)$$

$$\nabla\phi \to (U\cos\beta, U\sin\beta, 0) \qquad \text{at infinity} \qquad (3)$$

$$g\zeta + \tfrac{1}{2}(\nabla\phi \cdot \nabla\phi - U^2) = 0 \qquad \text{on the free surface} \qquad (4)$$

$$\phi_x\zeta_x + \phi_y\zeta_y - \phi_z = 0 \qquad \text{"-} \qquad (5)$$

where x, y and z are the coordinates in a Cartesian coordinate system oxyz fixed in the ship, with x parallel to the centreplane and directed from bow to stern, z vertically upwards and the origin at the intersection of the planes of the undisturbed free surface and the midship section. U is the uniform onset flow and β is the yaw angle. β is positive when the y-component of U is positive. ζ is the wave elevation. n denotes the outward normal to the hull surface, see Fig 1.

Further, a radiation condition should be applied. Thus, no upstream waves are permitted.

Eliminating ζ from (4) and (5) and linearizing about the double model potential the free

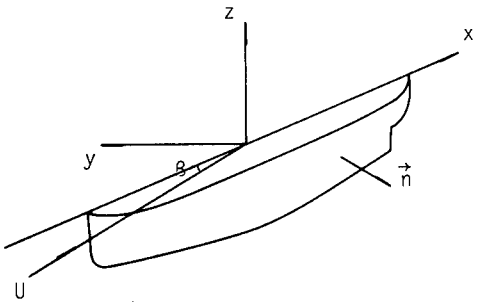


Fig 1 Coordinate system

surface boundary condition may be written

$$(\Phi_1^2\phi_1)_1 + g\phi_z = 2\Phi_1^2\Phi_{11} \quad \text{on } z = o \qquad (6)$$

where Φ is the double model potential. 1 denotes differentiation along a streamline of the double model flow on the undisturbed free surface. See [7] for details of derivation.

2.2 Numerical Procedure for Solving Unbounded Flow Problems - the Hess Method

Since the present method may be considered an extension of the Hess method some familiarity with the latter is needed to understand the paper. A short description of the Hess method for unbounded lifting flows is therefore given in this subsection.

The body configuration is divided into lifting and non-lifting sections and the lift is introduced into the potential flow by applying the Kutta condition at the trailing edge. In addition to the source distribution on the body surface, a vorticity distribution is introduced on the lifting section and its trailing wake. The vorticity distribution generates a circulatory flow superposed onto the uniform onset flow. The source distribution on the body must satisfy the boundary condition in terms of the compound onset flow, so the following integral equation must be satisfied

$$2\pi\sigma(p) - \iint_S \frac{\partial}{\partial n}\left(\frac{1}{r(p,q)}\right)\sigma(q)\,dS =$$

$$= -\bar{n}(p)\left(\bar{V}_\infty + \bar{V}_\mu(p)\right) \qquad (7)$$

where σ is the source density, r is the distance from the integration point q on the body surface S to the point p where the velocity is being evaluated. ∞ denotes the uniform onset flow, μ the induced circulatory flow.

In the numerical discretization of the problem the body surface is approximated by a large number of panels on which the source strength is constant. The body boundary condition corresponding to (7) is applied at a control point on each panel. This point is assumed to be the centre of the panel. On the lifting sections of the body the panels are organized in strips, which should essentially be in the streamwise direction. Vorticity is generated on

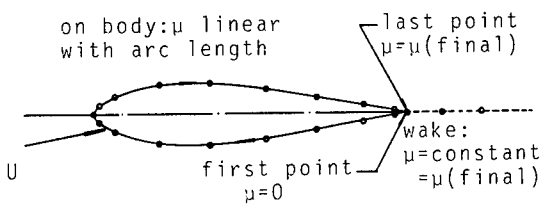


Fig 2 Variation of doublet strength along a lifting strip

each strip by a distribution of doublets, whose strength is assumed to vary linearly with the arc length from the trailing edge forward, around the nose and backward to the trailing edge. Zero strength is thus assumed at the starting point, and the non-zero value obtained at the other side of the trailing edge is kept constant in the wake, see Fig 2. In the spanwise direction the doublet strength is constant on each strip. This distribution is equivalent to a distribution of spanwise vortices with constant strength in the chordwise direction.

Obviously the only additional unknown introduced by the doublets on each strip is the strength derivative, which in principle may be determined by the Kutta condition at the trailing edge. In Hess' method, rather than adding a number of non-linear equations to the linear system of equations for the source strengths, a number of linear solutions for the σ's are obtained. These are then linearly combined to yield a total solution which satisfies the Kutta condition on each lifting strip.

The first of the σ-solutions is obtained from the uniform onset flow, neglecting the doublets, while all other solutions are obtained keeping the doublet strength derivative equal to unity on one strip, neglecting the uniform onset flow and the doublets on the other strips. These other solutions are thus obtained considering the flow generated by the doublets on one strip as an onset flow. If there are L lifting strips there will be L + 1 onset flows and solutions.

If $\bar{V}_{ij}$ is taken to represent the velocity at the i-th panel generated by unit strength sources at the j-th panel a scalar N x N matrix, [A], may be defined by

$$A_{ij} = \bar{V}_{ij} \cdot \bar{n}_i \qquad \begin{matrix} i = 1, \ldots, N \\ j = 1, \ldots, N \end{matrix} \qquad (8)$$

where N is the total number of panels on the body. The normal velocity, generated by all sources, at the control point of the i-th panel may be written

$$\sum_{j=1}^{N} A_{ij}\sigma_j \qquad i = 1, \ldots, N \qquad (9)$$

where the source densities, σ , are as yet unknown. The σ's are determined by the boundary conditions imposed at the control points, i e (9) is set equal to the negative of the normal component of the onset flow. This is done for each onset flow. Normal components of the onset flows are obtained as

$$N_i^{(k)} = \bar{n}_i \cdot \bar{V}_i^{(k)} \qquad \begin{matrix} k = 1, \ldots, L \\ i = 1, \ldots, N \end{matrix} \qquad (10)$$

and

$$N_i^{(\infty)} = \bar{n}_i \cdot \bar{V}_\infty \qquad i = 1, \ldots, N \qquad (11)$$

The linear equations for the source density are thus

$$\sum_{j=1}^{N} A_{ij}\sigma_j^{(k)} = -N_i^{(k)} \qquad \begin{matrix} i = 1, \ldots, N \\ k = 1, \ldots, L+1 \end{matrix} \qquad (12)$$

These are solved by a direct elimination procedure. Thus, there is a set of N values of σ_j for each onset flow. A linear combination in the form

$$\sigma_j = \sigma_j^{(\infty)} + \sum_{k=1}^{L} B^{(k)}\sigma_j^{(k)} \qquad j = 1, \ldots, N \qquad (13)$$

yields the entire source distribution, while there is a combined onset flow

$$\bar{V}_i^{(0)} = \bar{V}_i^{(\infty)} + \sum_{k=1}^{L} B^{(k)}\bar{V}_i^{(k)} \qquad i = 1, \ldots, N \qquad (14)$$

The total velocity at any point is

$$\bar{V}_i = \sum_{j=1}^{N} \bar{V}_{ij}\sigma_j + \bar{V}_i^{(0)} \qquad i = 1, \ldots, N \qquad (15)$$

The constant $B^{(k)}$ appearing above is the dipole strength derivative of strip k, i e the only additional unknown introduced by the doublets. There are L such constants and they are determined by the Kutta condition applied on each lifting strip. In the numerical method the condition is applied to the two aftermost control points on each strip, and it is assumed that the pressure is the same at these points. Making use of the total velocity from (15) expressions for the pressure may be found, and the equal pressure condition may be formulated. The reader is referred to Hess original paper, [11], or Xia's thesis for the exact expression. L non-linear equations are thus obtained and they are solved for $B^{(k)}$ using an iterative method.

2.3 Numerical Procedure for Solving Free Surface Flow Problems - the Present Method

The presence of a free surface gives rise to problems concerning (1) the discretization of the free surface, and (2) the satisfaction of the boundary condition on the free surface. Since for non-zero yaw the ship centreplane is not a symmetry plane of the flow field, the panels should cover the free surface and the hull surface on both sides. Advantage cannot be taken of the symmetry of the hull, as in the non-lifting case, so the number of panels is doubled. The boundary condition on the free surface, Eq (6), is in a compound form. It is therefore treated as follows:

With the present notation, the potential in question, ϕ, is written in a linear combination form

$$\phi = \phi^{(\infty)} + \sum_{k=1}^{L} B^{(k)}\phi^{(k)} \qquad (16)$$

where ∞ again denotes the potential of the uniform onset flow and k the circulatory flow associated with each lifting strip. Accordingly, Eq (6) becomes

$$\left[\Phi_1^2\left(\phi^{(\infty)} + \sum_{k=1}^{L} B^{(k)}\phi^{(k)}\right)_1\right]_1 + g\left(\phi_z^{(\infty)} + \sum_{k=1}^{L} B^{(k)}\phi_z^{(k)}\right) =$$

$$= 2\,\Phi_1^2\Phi_{11} \qquad (17)$$

It can be rewritten as

$$\left(\Phi_1^2\phi_1^{(\infty)}\right)_1 + g\phi_z^{(\infty)} + \sum_{k=1}^{L} B^{(k)}\left[\left(\Phi_1^2\phi_1^{(k)}\right)_1 + g\phi_z^{(k)}\right] = 2\,\Phi_1^2\Phi_{11} \qquad (18)$$

Eq (18) is satisfied if the following system of equations is satisfied.

$$\begin{aligned} &\left(\Phi_1^2\phi_1^{(\infty)}\right)_1 + g\phi_z^{(\infty)} = 2\,\Phi_1^2\Phi_{11} \\ &\left(\Phi_1^2\phi_1^{(k)}\right)_1 + g\phi_z^{(k)} = 0 \end{aligned} \qquad k = 1, \ldots, L \qquad (19)$$

The same procedure is applied to the hull boundary condition:

$$\phi_n = \phi_n^{(\infty)} + \sum_{k=1}^{L} B^{(k)}\phi_n^{(k)} = 0 \qquad (20)$$

It may be resolved as

$$\begin{aligned} \phi_n^{(\infty)} &= 0 \\ \phi_n^{(k)} &= 0 \end{aligned} \qquad k = 1, \ldots, N \qquad (21)$$

The technique of finding a solution to the compound boundary condition (18) by splitting it into several equations (19) is borrowed from the original Hess' method, where the body boundary condition (20) is split into (21). It is obviously possible to obtain one solution in this way, but other solutions may exist. These have not been investigated in the present work.

It should be pointed out that, when splitting the original equation, each new equation has to be independent of the $B^{(k)}$:s which are not known at this stage.

The individual sub-potentials are defined at each control point as

$$\begin{aligned}
\phi_{xi}^{(\infty)} &= U\cos\beta + \sum_{j=1}^{M} \sigma_j^{(\infty)} X_{ij} \\
\phi_{yi}^{(\infty)} &= U\sin\beta + \sum_{j=1}^{M} \sigma_j^{(\infty)} Y_{ij} \qquad i = 1, \ldots, M \\
\phi_{zi}^{(\infty)} &= \sum_{j=1}^{M} \sigma_j^{(\infty)} Z_{ij}
\end{aligned} \tag{22}$$

$$\begin{aligned}
\phi_{xi}^{(k)} &= V_{xi}^{(k)} + \sum_{j=1}^{M} \sigma_j^{(k)} X_{ij} \\
&\qquad\qquad k = 1, \ldots, L \\
\phi_{yi}^{(k)} &= V_{yi}^{(k)} + \sum_{j=1}^{M} \sigma_j^{(k)} Y_{ij} \\
\phi_{zi}^{(k)} &= V_{zi}^{(k)} + \sum_{j=1}^{M} \sigma_j^{(k)} Z_{ij}
\end{aligned}$$

where X_{ij}, Y_{ij} and Z_{ij} are the source velocity components. $V_{xi}^{(k)}$, $V_{yi}^{(k)}$ and $V_{zi}^{(k)}$ are the velocity components due to the dipole distribution on the k'th lifting strip. M is the total number of control points. The L + 1 sets of source densities, σ, are determined so as to satisfy the boundary conditions (19) and (21).

Applying the boundary conditions yields a system of equations linear with respect to σ for each sub-potential in the form

$$[A] \cdot \sigma^{(\infty,k)} = C^{(\infty,k)} \qquad k = 1, \ldots, L \tag{23}$$

where [A] is an M x M matrix common to all sub-potentials. C is the right-hand side array, which has different components for different potentials.

The upper part (corresponding to the hull boundary condition) of the A matrix is easily generated by setting

$$\begin{aligned}
A_{ij} = \bar{V}_{ij} \cdot \bar{n}_i &= X_{ij}N_{xi} + Y_{ij}N_{yi} + Z_{ij}N_{zi} \\
&\qquad i = 1, \ldots, N \\
&\qquad j = 1, \ldots, M
\end{aligned} \tag{24}$$

where N is again the number of control points on the hull surface. N_{xi}, N_{yi} and N_{zi} are the components of the unit normal vector to the hull surface.

The lower part (corresponding to the free surface boundary condition) is generated as follows, [7],

$$\begin{aligned}
A_{ij} &= CA_i\Phi_{1i}^2 (X_{ij}L_{xi} + Y_{ij}L_{yi}) + CB_i\Phi_{1i-1}^2 \\
&\quad (X_{i-1j}L_{xi-1} + Y_{i-1j}L_{yi-1}) + CC_i\Phi_{1i-2}^2 \\
&\quad (X_{i-2j}L_{xi-2} + Y_{i-2j}L_{yi-2}) + CD_i\Phi_{1i-3}^2 \\
&\quad (X_{i-3j}L_{xi-3} + Y_{i-3j}L_{yi-3}) \\
&- \begin{cases} 2\pi g & \text{as } i = j \quad i = N+1, \ldots, M \\ o & \text{as } i \neq j \quad j = 1, \ldots, M \end{cases}
\end{aligned} \tag{25}$$

where

- L_{xi} and L_{yi}, which are the double model flow velocity directions on the free surface, are calculated from the double model velocity components, Φ_{xi}, Φ_{yi} as

$$\begin{aligned}
L_{xi} &= \Phi_{xi} / (\Phi_{xi}^2 + \Phi_{yi}^2)^{\frac{1}{2}} \\
L_{yi} &= \Phi_{yi} / (\Phi_{xi}^2 + \Phi_{yi}^2)^{\frac{1}{2}}
\end{aligned} \tag{26}$$

  Since $\Phi_{zi} = o$ on the mean free surface, $L_{zi} = o$ and

$$\Phi_{1i} = \Phi_{xi}L_{xi} + \Phi_{yi}L_{yi} = (\Phi_{xi}^2 + \Phi_{yi}^2)^{\frac{1}{2}} \tag{27}$$

- CA_i, CB_i, CC_i and CD_i, the coefficients of the four point operator, are calculated from the distance between the successive points in a free surface strip, see [7].

A similar procedure is followed in the generation of the right-hand side arrays of Eq (23), i e,

$$\begin{aligned}
C_i^{(\infty)} &= -U\cos\beta N_{xi} - U\sin\beta N_{yi} \qquad i = 1, \ldots, N \\
C_i^{(\infty)} &= 2\Phi_{1i}^2 (CA_i\Phi_{1i} + CB_i\Phi_{1i-1} + CC_i\Phi_{1i-2} + \\
&\quad + CD_i\Phi_{1i-3}) - \\
&\quad - [CA_i\Phi_{1i}^2 (U\cos\beta L_{xi} + U\sin\beta L_{yi}) + \\
&\quad + CB_i\Phi_{1i-1}^2 (U\cos\beta L_{xi-1} + U\sin\beta L_{yi-1}) + \\
&\quad + CC_i\Phi_{1i-2}^2 (U\cos\beta L_{xi-2} + U\sin\beta L_{yi-2}) + \\
&\quad + CD_i\beta_{1i-3}^2 (U\cos\beta L_{xi-3} + U\sin\beta L_{yi-3})] \\
&\qquad\qquad i = N+1, \ldots, M
\end{aligned} \tag{28}$$

and

$$\begin{aligned}
C_i^{(k)} &= -V_{xi}^{(k)}N_{xi} - V_{yi}^{(k)}N_{yi} - V_{zi}^{(k)}N_{zi} \qquad i = 1, \ldots, N \\
C_i^{(k)} &= -[CA_i\Phi_{1i}^2 (V_{xi}^{(k)}L_{xi} + V_{yi}^{(k)}L_{yi}) + \\
&\quad + CB_i\Phi_{1i-1}^2 (V_{xi-1}^{(k)}L_{xi-1} + V_{yi-1}^{(k)}L_{yi-1}) + \\
&\quad + CC_i\Phi_{1i-2}^2 (V_{xi-2}^{(k)}L_{xi-2} + V_{yi-2}^{(k)}L_{yi-2}) + \\
&\quad + CD_i\Phi_{1i-3}^2 (V_{xi-3}^{(k)}L_{xi-3} + V_{yi-3}^{(k)}L_{yi-3})] \\
&\qquad\qquad i = N+1, \ldots, M \\
&\qquad\qquad k = 1, \ldots, L
\end{aligned} \tag{29}$$

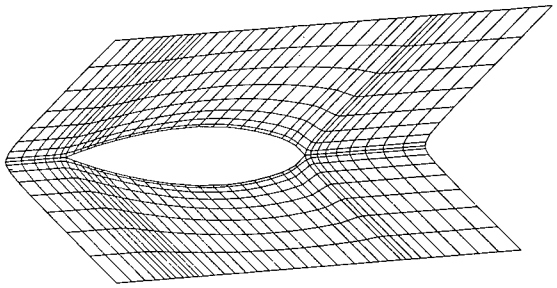


Fig 3 Illustration of the body-fitted free surface grid

As pointed out by Dawson, upstream waves are prevented by the use of upstream finite difference operators like the present one.

2.4 The Body-Fitted Free Surface Grid

The solution procedure given above requires a streamline grid on the free surface, but, as mentioned earlier, it is not always possible to get good resolution of the free surface using such a grid. The difficulty may be circumvented using a non-streamline, body-fitted grid.

An example of the body-fitted grid developed in the present method is given in Fig 3. As in the streamline grid suggested by Dawson, [6], the transverse lines are hyperbolas, while the longitudinal lines are changed from double model streamlines to another set of lines which better follow the shape of the body. There is thus a gradual change from the straight lateral edge, in the main flow direction, to the shape of the water-line, extended forwards and backwards by straight lines, also parallel to the main flow.

The disadvantage of changing from the streamline system is that derivatives with respect to l in the free surface boundary condition (6) cannot be expressed simply by finite differences in one direction. On the other hand, they may be expressed by finite differences in the two directions of the grid, without too much increase in complexity.

Thus, if t and n represent the coordinates of a local non-orthogonal coordinate system with t in the longitudinal and n in the transverse direction, the l-derivatives of any function F may be expressed as

$$F_l = F_t \cdot t_l + F_n \cdot n_l \qquad (30)$$

The derivatives t_l and n_l follow by simple alegbra from the slopes of the t-, n- and l-lines in the z = 0 plane.

The generation of the A matrix and the right-hand side arrays are changed accordingly. Using ΔN and ΔT to denote the finite difference operators along the transverse and longitudinal lines respectively, Eqs (25), (28) and (29) are replaced by

$$A_{ij} = n_{li}\,\Delta N_i[\Phi^2_{li}(X_{ij}L_{xi} + Y_{ij}L_{yi})] + t_{li}\,\Delta T_i[\Phi^2_{li}(X_{ij}L_{xi} + Y_{ij}L_{yi})] - \begin{cases} 2\pi g & \text{as } i = j \quad i = N+1, \ldots, M \\ 0 & \text{as } i \neq j \quad j = 1, \ldots, M \end{cases} \qquad (31)$$

$$\begin{cases} C_i^{(\infty)} = -U\cos\beta\, N_{xi} - U\sin\beta\, N_{yi} \quad i = 1, \ldots, N \\ C_i^{(\infty)} = 2\Phi^2_{li}[n_{li}\,\Delta N_i\Phi_{li} + t_{li}\,\Delta T_i\Phi_{li}] - [n_{li}\,\Delta N_i\Phi^2_{li}(U\cos\beta\, L_{xi} + U\sin\beta\, L_{yi}) + t_{li}\,\Delta T_i\Phi^2_{li}(U\cos\beta\, L_{xi} + U\sin\beta\, L_{yi})] \quad i = N+1, \ldots, M \end{cases} \qquad (32)$$

$$\begin{cases} C_i^{(k)} = -V_{xi}^{(k)}N_{xi} - V_{yi}^{(k)}N_{yi} - V_{zi}^{(k)}N_{zi} \quad i = 1, \ldots, N \\ C_i^{(k)} = -[n_{li}\,\Delta N_i\Phi^2_{li}(V_{xi}^{(k)}L_{xi} + V_{yi}^{(k)}L_{yi}) \\ \qquad t_{li}\,\Delta T_i\Phi^2_{li}(V_{xi}^{(k)}L_{xi} + V_{yi}^{(k)}L_{yi})] \quad i = N+1, \ldots, M \end{cases} \qquad k = 1, \ldots, L \qquad (33)$$

3. RESULTS AND DISCUSSION

So far, the present method has been applied to three hulls: two sailing yachts at various angles of yaw and the Wigley hull at zero yaw, [8]. Since the topic of this paper is lifting potential flow, only the results for the sailing yachts will be presented. Unfortunately, reported experimental data are very rare, so some of the computed results cannot be compared with experiments. Interesting numerical tests may, however, be made. The sailing yachts are a 12 m yacht of the type used in the America's Cup and a 5.5 m yacht, Antiope, which has been used as a standard model for yacht testing for many years. To reduce the number of parameters only upright cases have been considered.

3.1 The 12 m Yacht

For proprietary reasons the exact lines of the 12 m yacht cannot be shown, but in Fig 4 the panel distribution, projected onto the x-z plane may be seen. There are two lifting sections on the body: the keel and the rudder. Four lifting strips are used on the former and

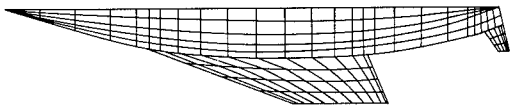


Fig 4 Panel distribution, 12 m hull

three on the latter. The hull is thus non-lifting, but the keel and rudder vorticity is carried to the waterline by extra strips inside the hull, having the same B-value as the strip adjacent to the bottom.

Calculations were carried out for both types of free surface grids. In fact, when the calculations started only the streamline grid was available, and it was only after realizing its disadvantages that the body-fitted grid was developed.

The disadvantages of the streamline grid are immediately clear from Fig 5, in which the yaw angle is 9^{o}. Particularly on the pressure side it is obvious that this grid is not useful. In grid I a reasonable panel width is obtained near the stern, while the panels close to the bow are far too wide to resolve the bow wave properly. Grids II and III represent attempts to improve the resolution at the bow, but it is seen that already for grid II the innermost streamline seems to merge with the hull contour close to the stern. For grid III also the second streamline seems to merge with the other two lines. Not even in this case is the resolution at the bow sufficient.

Results from the three grids are shown in Table 1. Calculations have been made at two Froude numbers, 0.35 and 0.40. The computed drag coefficient is given in the left column, while the lift is shown in the right column. One problem encountered in the interpretation of results of the present kind is that induced resistance cannot be separated from wave resistance, since both are obtained through pressure integration. The only way to get an impression of the wave resistance is to subtract the double model value of the pressure drag from the one calculated at non-zero Froude numbers. This difference is exactly equal to the wave resistance only if the induced resistance is independent of the Froude number. In the central column $C_D - C_{D\,DM}$ is given.

Grid	$10^3\ C_D$		$10^3\ (C_D - C_{D\,DM}) =$ "C_W"		$10^2\ C_L$	
	0.35	0.40	0.35	0.40	0.35	0.40
I	3.77	8.22	0.76	5.21	5.26	5.65
II	4.16	8.36	1.15	5.35	5.26	5.68
III	4.97	10.08	1.96	7.07	5.37	5.75

Table 1 Comparison between results obtained using the three different streamline grids of Fig 5. 9^{o} yaw. (C_L at $F_n = 0$ is 5.15×10^{-2})

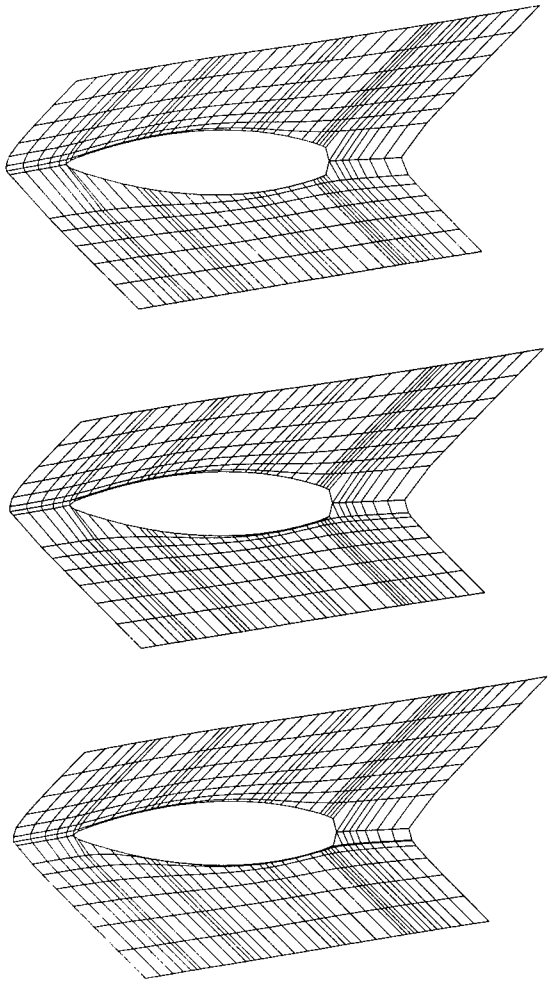


Fig 5 Variation of the streamline grid around the 12 m yacht. 9^{o} yaw.
Upper: Grid I, Middle: Grid II,
Lower: Grid III

It is seen from the table that the lift coefficient is quite independent of the grid. An interesting increase with Froude number is also noted. The drag coefficient, and particularly the "wave resistance" coefficient are, however, quite grid dependent, the latter being changed as much as a factor 2.6 between grids I and III. Admittedly, 9^{o} is a very large yaw angle, which may put too severe demands on the method, but still the grid dependence must be considered too large to be acceptable.

To reduce this problem the body-fitted grid was developed and a new grid dependence study was made. Also in this case the innermost longitudinal line was moved closer and closer to the hull contour. Thus the ratio of the widths of the innermost panel row and one half of the panelled region (the "width ratio") was 1/24, 1/36 and 1/54 respectively. The three grids are seen in Fig 6. Since the grids of

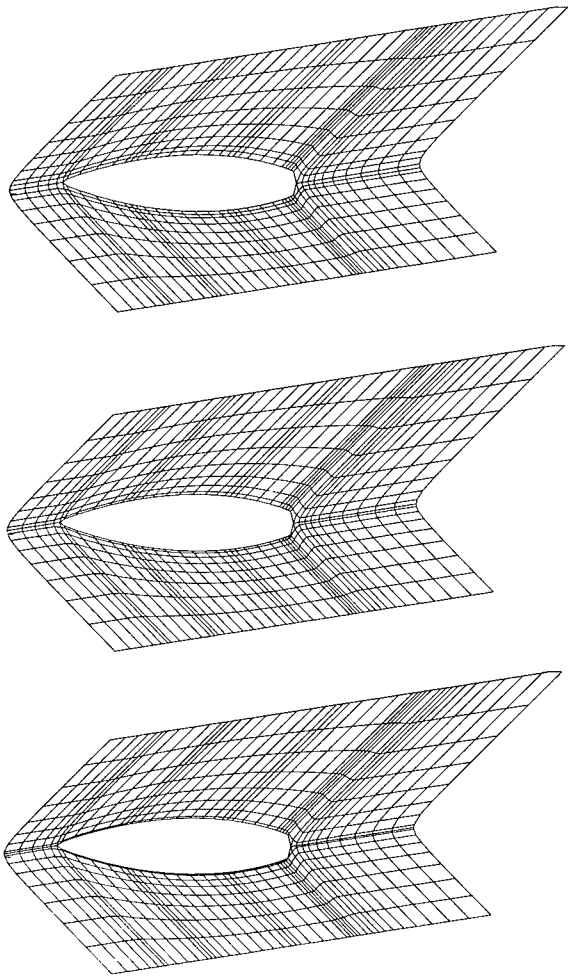


Fig 6 Variation of the body-fitted grid around the 12 m yacht. 9^{o} yaw.
Upper: Grid I, Middle: Grid II,
Lower: Grid III

Figs 5 and 6 are so different it is impossible to say whether or not the variation in grid geometry is equally large in both cases, so it may be difficult to compare directly the grid dependency of the results. However, from previous experience from panel methods, the width variation of the innermost row of panels seems to be quite large in Fig 6.

Grid	Width ratio	$10^3\ C_D$	$10^3(C_D - C_{D\,DM}) =$ "C_W"	$10^2\ C_L$
I	1/24	7.09	4.08	5.41
II	1/36	7.83	4.82	5.52
III	1/54	8.84	5.83	5.61

Table 2 Comparison between results obtained using the three different body-fitted grids of Fig 6. 9^{o} yaw. $F_n = 0.35$

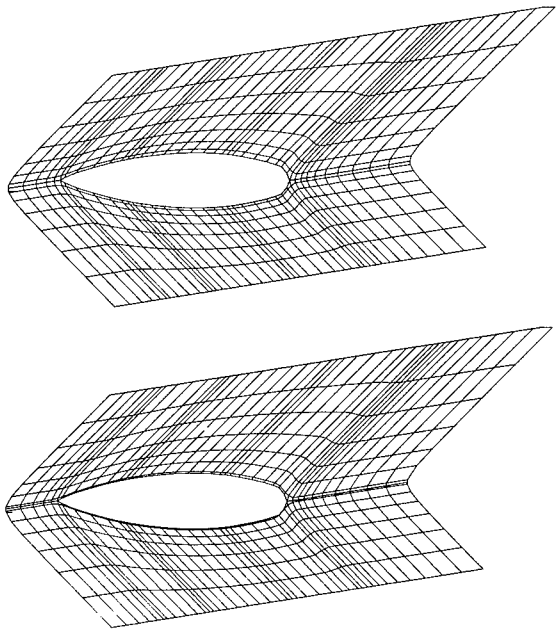


Fig 7 Variation of the body-fitted grid around the 12 m yacht. Smooth contour. 9^{o} yaw.
Upper: Grid I, Lower: Grid II

Also in these results the lift is quite grid-independent. A considerable grid dependence is, however, still found in the drag coefficients, whose level has increased from the streamline grid. Comparing the "wave resistance" of the finest grid (III) with the one from the coarsest (I) a 30% reduction in "wave resistance" from 5.83 to 4.08 x 10^{-3} is noted. Although this change is considerably smaller than the one from the streamline grid it is still large.

This result was at first considered surprising, since similar test runs, carried out for the other yacht, indicated a very small dependence on the grid. The only principal difference between the two cases was the sharp corner in the hull contour near the 12 m stern, so in order to check this effect, a smoother representation of the waterline in this region was tested. Results for one coarse and one fine grid, see Fig 7, are given in Table 3.

Grid	Width ratio	$10^3\ C_D$	$10^3(C_D - C_{D\,DM})$	$10^3\ C_L$
I	1/28	6.21	3.20	5.35
II	1/56	6.39	3.38	5.40

Table 3 Comparison between results obtained using the two grids of Fig 7. Smooth hull contour. 9^{o} yaw. $F_n = 0.35$

Obviously the sensitivity has now been reduced considerably and may be considered acceptable. The effects of the sharp corner

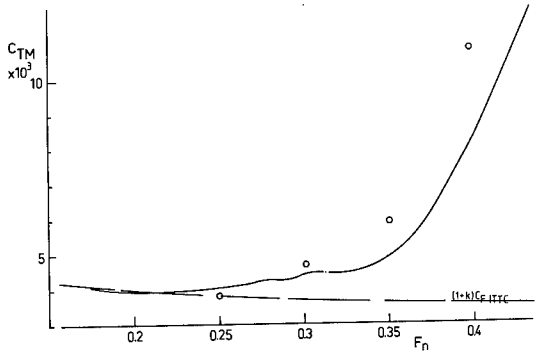


Fig 8 Comparison between calculated and measured resistance at zero yaw. 12 m yacht

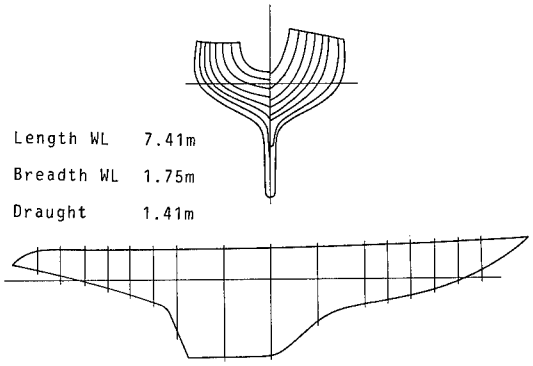


Fig 9 Lines of the Antiope hull

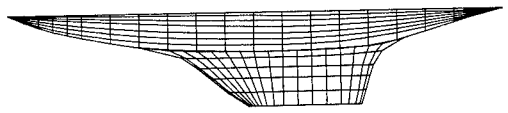


Fig 10 Panel distribution, Antiope

are not, of course, satisfactory, since they seem to destabilize the solution. On the other hand, the result is not entirely unexpected, since the accuracy of the calculations of derivatives must be very low near the corner. Sharp changes in the curvature should therefore be avoided, or represented by a large number of panels. It should also be pointed out that some grid dependence may be tolerated in comparative calcultions, provided all grids are generated in the same way. Further, in many cases, i e in keel and rudder optimization, the free surface grid does not change at all.

No comparisons can be made with measurements at an angle of attack, due to the lack of data, but a resistance curve for zero yaw is available, and in Fig 8 comparisons between calculations and measurements are made. In the figure the calculated wave resistance has been added to the viscous resistance obtained from the ITTC-57 line and a form factor of 1.24, and the sum is compared with the measured total resistance for a 1/3 scale model.

It is seen that the calculated resistance increases faster with Froude number than the measured one. This is to be expected, since the waterline length of a 12 m yacht increases appreciably at higher speeds, due to both sinkage and waves. In the calculations the nominal waterline length is kept at all speeds. It is, of course, possible to reposition the hull to account for the computed sinking force, and this has been done in earlier work, using the non-lifting method, [7]. It then appeared that the resistance increase due to the extra displacement was more than compensated by the increase in waterline length, even if the effect of waves was neglected. At $F_n = 0.4$ the waterline may increase by 25%, corresponding to a Froude number change of about 12%. This is about twice as much as required to make the calculations and measurements coincide. Obviously some "effective" waterline length must be used for a hull of this kind if an absolute value of the resistance is required.

3.2 The 5.5 m Yacht Antiope

The lines of the 5.5 m yacht Antiope are shown in Fig 9 together with some data. The panel distribution is seen in Fig 10. Five lifting strips are used on the keel and there is no separate rudder. As for the 12 m yacht the hull is non-lifting.

To verify the grid independence for this hull seven different grids were tested in the way explained in section 3.1. Now the width ratio was varied within very wide limits, from 1/144 to 1/12, and the results for the "wave resistance" coefficient are given in Fig 11. It is seen that over a range of widths the resistance is almost constant, while it increases when the innermost row of panels becomes extremely thin and decreases when the opposite is true. The drop is caused by the reduced resolution, while the increase may be due to the problems encountered when the control points on the free surface panels get very close to the edge created along the waterline by the upper and lower halves of the double model. In practical cases neither of the two sources of error should be present. The 1/36 grid used in the further calculations is shown in Fig 12.

It should be remarked that all grid dependence studies have been made varying only one of many possible parameters. However, experience shows that it is variations of the grid close to the hull, which have the greatest

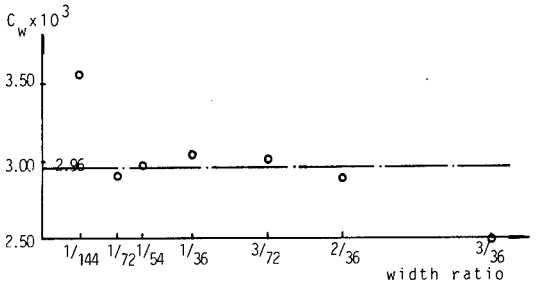


Fig 11 Variation in "wave resistance" with width ratio. Antiope, 9^o yaw

influence, so the method chosen should be appropriate if the number of runs has to be kept to a minimum. In the previous report on the non-lifting method, [7], a number of other parametric studies are reported.

In Dawson's original work, [6], a four-point upstream operator was recommended for the calculation of derivatives along the streamlines. Such an operator is given explicitly in the formulas (25), (28) and (29). However, for the body-fitted grid, derivatives have to be computed in two directions, and it is not obvious that the four-point operator is the best choice in both directions. Therefore, equations (31), (32) and (33) are given without specifying the operator. Further, the slopes of the grid lines have to be computed at all grid points and this could conveniently be done using finite difference operators.

Results of a systematic variation in all operators are reported in [8]. It was found that more fluctuating waves were encountered using the body-fitted grid and four-point formulas throughout. As in Dawson's work the fluctuations were reduced when the order of the difference operator was lowered and it was finally decided to use a three-point operator for the longitudinal derivative while two points were used for the transverse derivative and the line slopes.

Detailed flow calculations for the Antiope hull have been carried out earlier by Larsson, [13]. Through repeated boundary layer calculations the frictional resistance, as well as the viscous pressure resistance, were obtained at one Froude number and zero yaw and heel. Wave resistance was computed at zero yaw and the induced resistance at zero Froude number. The interaction between the lifting vorticity and the free surface was thus neglected.

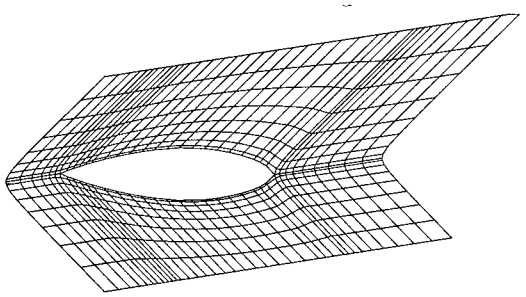


Fig 12 Body-fitted grid around Antiope. Width ratio 1/36, 9^o yaw

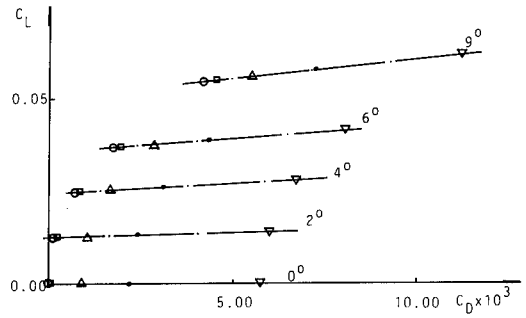


Fig 13 Calculated force coefficients, Antiope. Symbols for Froude numbers: ○ : 0.0, □ : 0.20, △ : 0.30, · : 0.35, ▽ : 0.40

In the present work this interaction is of special interest and a systematic variation of both Froude numbers and yaws was made. All combinations of the F_n:s 0.0, 0.20, 0.30, 0.35 and 0.40 and the β:s 0^o, 2^o, 4^o, 6^o and 9^o were thus computed. The results are summarized in Fig 13, which shows a very regular pattern. As for unbounded flows, the change in drag with lift seems to be parabolic for all Froude numbers and the lift for a given angle of yaw increases linearly with this number. The slope of the straight lines increases monotonically with yaw angle.

Although results are available from measurements at several angles it is difficult to compare the calculated and measured resistance. The viscous resistance is of course included in the measured results but it has not been calculated here. It should be noted that it may vary with both parameters.

In Fig 14 the calculated increase in drag with lift is compared with the measured one for three Froude numbers. The latter are not exactly the same in calculations and measurements but the small difference should have a negligible influence. The lines represent

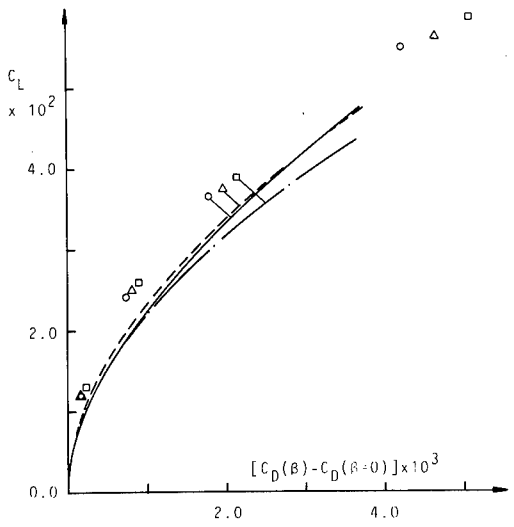


Fig 14 Comparisons between calculated and measured force coefficients, Antiope. Symbols for Froude numbers: Measurements: —— : 0.12, ---- : 0.30, —•— : 0.36, Calculations: 0 : 0.0, Δ : 0.30, □ : 0.35

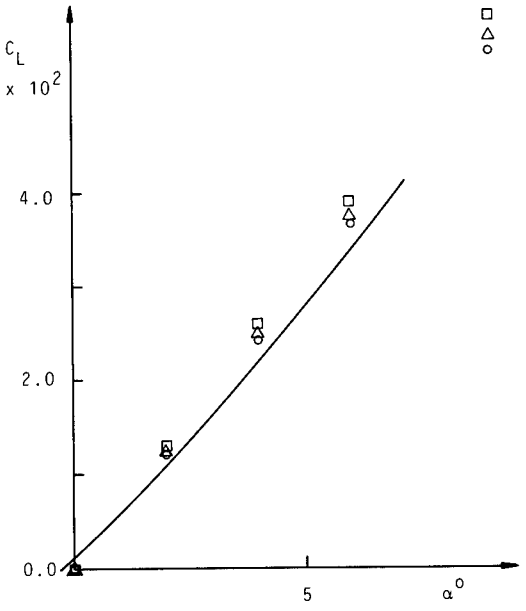


Fig 15 Comparison between calculated and measured lift coefficients, Antiope. Full line: average of measurements. Symbols for calculations as in Fig 14

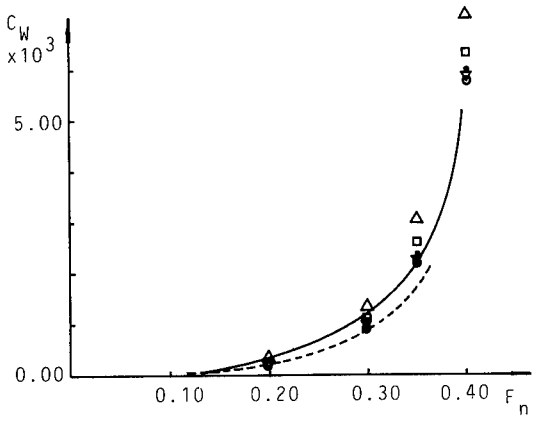


Fig 16 Comparison between calculated and measured wave resistance, Antiope. Symbols for yaw angles: 0 : 0°, ∇ : 2°, • : 4°, □ : 6°, Δ : 9°. Measurements (at zero yaw): —— : Herreshoff & Newman, ---- : Kirkman

averages of the measurements as obtained by Letcher, [14], in his reanalysis of older results. It appears, as expected, that the predicted increase in drag with lift is smaller than the measured one. The viscous resistance should increase with yaw angle, and this may well account for the differences in the figure.

Calculated and measured lift coefficients are compared in Fig 15. The scatter in the measurements is larger than the variation with Froude number, so Letcher has only attempted to draw a mean curve, which is shown in Fig 15. Analyzing the data it is, however, possible to detect a Froude number dependent increase. The calculations, also as expected, overpredict the lift to some extent. Viscous effects should reduce the lift, so at least the low Froude number results should be reasonable. Possibly the increase in lift with Froude number is somewhat too large, but in general the correspondence between calculations and measurements must be considered satisfactory.

The zero yaw resistance from two sets of full scale experiments is compared with calculations in Fig 16. There is, unfortunately, a considerable difference between the two sets of data and the maximum Froude number is quite low, but the tendency of the correspondence with calculations can still be judged. Obviously, also in this case, the slope of the predicted curve is larger than the ones from the measurements. The difference is, however, smaller than for the 12 m yacht and this is to be expected, since the increase in waterline length with speed is much smaller. In the figure the predictions for non-zero yaw are also given for comparison.

In Fig 17 the final results from the Antiope predictions are shown. The wave profile on the two sides of the hull are plotted for four different Froude numbers at 4° yaw. There are no measurements available, but the tendency

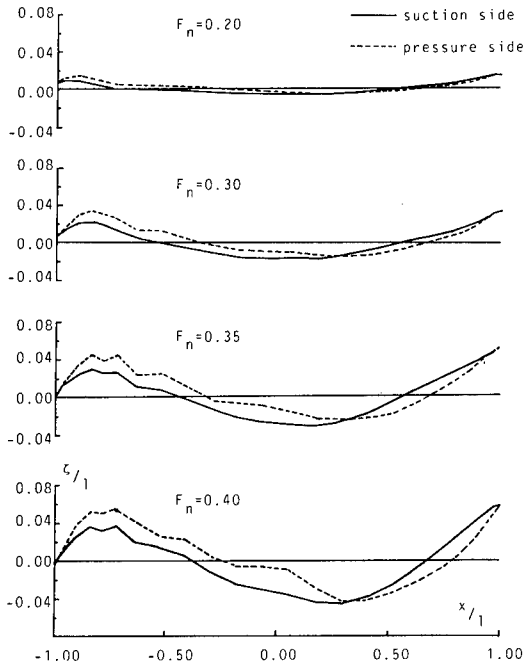


Fig 17 Calculated wave profiles along the two sides of the hull, Antiope. 4° yaw

of the difference between the two sides seems right.

4. CONCLUSIONS

A method for calculating the potential flow around yawed, surface piercing bodies has been presented. Test calculations for two sailing yachts have indicated the following:

1. A free surface streamline grid of the type normally used in Dawson-type methods cannot be used at large yaw angles, where the bad resolution, particularly at the bow, causes a strong grid dependence of the solution. The problem can be solved by applying a body-fitted grid described in the paper.

2. Systematic variations in Froude number and yaw angle for the Antiope hull produced regular variations in the lift and drag. Comparisons with measurements indicated an overprediction of the lift and an underprediction of the drag. The differences were not large, however, and may well be explained by the neglect of the viscous flow effects, which may be taken into account using boundary layer methods.

3. The predicted wave resistance curve at zero yaw showed a larger slope than the measured one, particularly for the 12 m hull. This effect is due to the decrease in effective Froude number caused by the combined sinkage and wave effects for the real hull. For yachts with large overhangs, slightly sunk hulls could therefore be used at high Froude numbers. If comparative calculations, i e for keels and rudders, are being carried out this effect can be neglected.

ACKNOWLEDGEMENTS

The authors are indebted to Dr John L Hess for valuable discussions at the early stages of the project.

Financial support from SSPA and the Swedish Board for Technical Development is also gratefully acknowledged.

REFERENCES

1. Larsson, L, "An Experimental Investigation of the Three-Dimensional Turbulent Boundary Layer on a Ship Model", Proceedings of the 11th Symposium on Naval Hydrodynamics, London, 1976, pp 161-185

2. Larsson, L, and Chang, M-S, "Numerical Viscous and Wave Resistance Calculations Including Interaction", Proceedings of the 13th Symposium on Naval Hydrodynamics, Tokyo, 1980, pp 707-728

3. Larsson, L, and Johansson, L-E, "A Streamline Curvature Method for Computing the Flow near Ship Sterns", Proceedings of the 14th Symposium on Naval Hydrodynamics, Ann Arbor, 1982, pp 953-998

4. Broberg, L, and Larsson, L, "A Calculation Method for Ship Stern Flows Using an Analytical Body-Fitted Coordinate System", Proceedings of the 15th Symposium on Naval Hydrodynamics, Hamburg, 1984, pp 525-538

5. Janson, C-E, and Larsson, L, "Ship Flow Calculations Using the PHOENICS Computer Code", Proceedings of the Second International Symposium on Ship Viscous Resistance, Göteborg, 1985, pp 17:1-17:24

6. Dawson, C W, "A Practical Computer Method for Solving Ship-Wave Problems", Proceedings of the Second International Conference on Numerical Ship Hydrodynamics, Berkeley, 1977, pp 30-38

7. Xia, F, "Calculation of Potential Flow with a Free Surface", SSPA Report No 2912-1, 1984, SSPA Maritime Research and Consulting, Göteborg, Sweden

8. Xia, F, "Numerical Calculations of Ship Flows, with Special Emphasis on the Free Surface Potential Flow", PhD thesis, 1986, Division of Marine Hydrodynamics, Chalmers University of Technology, Göteborg, Sweden

9. Slooff, J W, "On Wings and Keels", International Shipbuilding Progress, Vol 31, No 356, April 1984, pp 94-104

10. Slooff, J W, "On Wings and Keels (II)", Proceedings of the AIAA Symposium on the Aero/Hydrodynamics of Sailing, Seattle, 1986, pp 67-86

11. Hess, J L, "Calculation of Potential Flow about Arbitrary Three-Dimensional Lifting Bodies", Douglas Report N00019-71-C-0524, 1972, Douglas Aircraft Company, USA

12. Hess, J L, and Smith, A M O, "Calculation of Non-Lifting Potential Flow about Arbitrary Three-Dimensional Bodies", Douglas Report No E S 40622, 1962, Douglas Aircraft Company, USA

13. Larsson, L, "Theoretical Performance Predictions for the 5.5 m Yacht Antiope", Proceedings of the Symposium on Yacht Architecture, Amsterdam, 1979, pp 101-134

14. Letcher, J S Jr, "Sailing Hull Hydrodynamics, with Reanalysis of the Antiope Data", Transactions of the Society of Naval Architects and Marine Engineers, Vol 83, 1975, pp 22-40

DISCUSSION

Bruce Johnson,
U.S. Naval Academy

The authors are to be congratulated for reporting on a computational technique for investigating sailing yacht hull-keel combinations. This paper removes some of the mystery surrounding the numerical methods which supported the successful challenge of "Australia II" for the America's Cup.

Since sailboats can be driven to Froude numbers approaching 0.4 when beating to windward and above 0.4 off the wind, the effects of sinkage and trim become important. The change in resistance caused by sinkage is discussed briefly in the paper, but the effects of trim are not discussed. Since this is a difficult problem in numerical hydrodynamics, could the authors shed some light on how these effects may be accounted for?

Also, how was the form factor of 1.24 for the 12m yacht established?

Small changes in resistance between yacht hull forms can account for the "winning edge." Can the authors compare the sensitivity of existing numerical methods to that of towing tank tests in detecting the significance of small changes in hull form and keel design?

Reply -

There is no difficulty calculating the sinkage and trim of the hull using the present method. In fact, it is considerably simpler to compute these two quantities than the wave resistance, since the former result from the addition of all pressure forces on the hull, while the latter is found from the small difference between the high pressures at the stern and the bow. Sinkage and trim have been studied extensively during the development of the calculation method and the results are quite good for both. For proprietary reasons these results have been left out of the paper.

The form factor of 1.24 was obtained from a Prohaska Plot based on the measured resistance at moderately low speeds.

In order to compete with the towing tanks, the numerical methods must be able to resolve differences of about 1% in resistance. When developing the present method and others for the viscous flow, it is certainly the ultimate goal to be able to beat the measured accuracy, but too few evaluations have been made so far to indicate how far we have come in this direction. Even if the calculations are not yet as accurate as the measurements there is, however, an obvious use for the former. At a preliminary design stage choices between fairly different designs have to be made rapidly and without too much cost. Numerical calculations may then be a very interesting alternative to model tests.

Hyoung-Tae Kim,
Iowa Institute of Hydraulic Research

First, I want to congratulate the authors on such nice work. I have several questions that I would like to pose to the authors:

a. As I understand, you use doublet strips, with a constant strength along the span for the keel. Could you explain why you don't use doublet panels, so that the doublet strength is allowed to vary along the span?

b. My understanding is that even in a steady flow situation, the free vortex (or the "trailer") should separate from the lifting body, which in the paper, is simulated by a doublet distribution. How did you treat these shed trailing vortices for the body and keel in the yawed-body calculation?

c. Fig. 8 showed the good agreement with the experimental results and calculations. Since we have alot of data for Wigley hull, I would like to know if you tested your method for this hull?

Heinrich Söding
Institut fur Schiffbau Hamburg

In case of oblique flow, did you include a dipole distribution also in the wake of the ship?

Reply -

The lifting strips on the keel and the rudder are in the horizontal (chordwise) direction. Along these strips the doublet strength is proportional to the arc length. The constant of proportionality is determined simultaneously for all strips in such a way that the Kutta condition is satisfied at the trailing edge of all strips. There are thus, in general, different constants for different strips, and thus a variation in the spanwise direction.

Since the spanwise variation is in the form of steps, free vorticity is generated at the junctions between the strips. The location of this free vorticity is specified in the wake by adding a few wake panels aft of each lifting strip. These wake panels have a constant doublet strength (which is different from strip to strip) so the bound vorticity is zero there.

The Wigley hull has in fact been used as a test case for the present method. In particular, the effect of introducing the new body-fitted grid was tested at zero yaw. The results, which were quite satisfactory, are reported in Dr. Xia's thesis. (Fei Xia: "Numerical Calculations of Ship Flows with Special Emphasis on the Free Surface Potential Flow", Ph.D. thesis, Chalmers University of Technology, Department of Marine Hydrodynamics, 1986.)

K. Mori
Hiroshima University

1. The boundary conditions are split into (L+1) conditions in Eqs. (19) and (20) to solve simultaneous equations (L+1) times. Even so, each lifting strip is required to satisfy the boundary conditions independently. Because $B^{(k)}$'s are known, you could have solved for the sources all at once and obtained more strict results.

2. By the adoption of the body-fitted coordinate system, the differentiations with respect to n appear which have not been examined numerically in detail. How much do the final solutions depend on differencing

schemes in the n-direction, non-reflecting conditions on the lateral boundaries and grid sizes?

Reply -

In the present method the final solution is obtained from a linear combination of a set of solutions for simplified boundary conditions. This is done to save computer time, which would have been very considerable, had the free surface and hull boundary conditions been satisfied simultaneously with the Kutta condition in one solution. A non-linear system of about 1,000 equations would then have had to be solved.

The present approach is based on the observation that there is one possible way of satisfying the free surface and hull boundary conditions **for any value of** the dipole strength derivative $b^{(k)}$. Satisfaction of these two boundary conditions is therefore ensured first (i.e., before the $B^{(k)}$'s have been computed). Thereafter the Kutta condition is employed to obtain the $B^{(k)}$'s.

The choice of a three-point backward difference operator in the longitudinal direction and a two-point operator in the transerse direction was made after condsiderable numerical experimentation. In order not to confuse the reader with too many details this part of the work was excluded in the paper, but it is reported in Dr. Xia's thesis, referenced above.

Minimization of Resistance of Slowly Moving Full Hull Forms in Short Waves

T. SAKAMOTO and E. BABA

Nagasaki Technical Institute, Mitsubishi Heavy Industries, Ltd., Japan

ABSTRACT

A theoretical investigation was made on the minimization of resistance of a slowly moving full hull form in short waves. First, the exact nonlinear free-surface condition was split into steady and unsteady linear free-surface conditions under the assumption of small perturbation over the double body flow around a ship as done in the low speed theory for steady wave-making problem. The unsteady linear free-surface condition newly derived in the present study was found to coincide with that introduced in Faltinsen's asymptotic theory for prediction of added resistance in short waves. Then the sum of steady wave-making resistance calculated by use of the low speed theory and added resistance based on the Faltinsen's theory was minimized by the nonlinear programming technique. It was shown that principal geometric parameters of a full ship have dominant effect on the added resistance in short waves as well as on the steady wave-making resistance. Under the specified values of principal geometrical parameters the added resistance does not vary sensitively with the local minor change of hull forms when it is compared with steady wave-making resistance.

NOMENCLATURE

A_w	waterplane area
B	ship breadth
C_b	block coefficient
d	ship draught
g	gravitational acceleration
h_w	incident wave height ($h_w = 2\zeta_a$)
k_0	incident wave number
L	ship length
R	resistance
R_w	steady wave-making resistance
R_{aw}	added resistance due to wave reflection
U	ship speed (uniform current)
u_{ro}	value of u_r on $z = 0$
V	double body flow velocity along the waterline
$\mathbf{v} = (u,v,w)$	velocity vector
$\mathbf{v}_r = (u_r,v_r,w_r)$	velocity vector of double body flow
$\mathbf{v}_0 = (u_0,v_0,w_0)$	velocity vector of steady wave motion
$\mathbf{v}_1 = (u_1,v_1,w_1)$	velocity vector of unsteady wave motion
v_{r0}	value of v_r on $z = 0$
α	wave direction ($\alpha = 0$ deg. is head wave)
ζ	wave height
ζ_a	amplitude of incident wave
ζ_r	fictitious wave height of rigid-wall flow
ζ_0	wave height of steady wave
ζ_1	wave height of unsteady wave motion
ρ	density of water
λ	incident wave length
Φ	total velocity potential
ϕ_D	diffraction wave potential
ϕ_I	incident wave potential
ϕ_r	velocity potential for double body flow
ϕ_0	velocity potential for steady wave-making
ϕ_1	velocity potential for unsteady wave motion
χ	wave direction ($\chi = 180° - \alpha$)
ω_e	circular frequency of encounter waves
ω_0	circular frequency of incident waves

1. INTRODUCTION

A ship hull form which is designed to have the best propulsive performance in calm sea is

not necessarily be the best one in waves. In the case of large ships, the length of waves which they encounter with high probability is small when it is compared with ship's dimensions. In the short waves, ship motions are negligibly small and resistance component due to wave reflection at the bow part is added and increases as the fullness of the entrance part of a ship becomes large.

Therefore a more rational design objective for the large full ship form should be the minimization of resistance not only in calm sea condition but also in short waves. As a first step to this problem, a theoretical investigation was made in the present study on the optimum entrance form of full ships which has the minimum resistance in short waves within the framework of potential theory and neglecting the ship motion.

First, the assumptions used in the low speed theory for the steady wave-making problems /1,2/ were extended into the unsteady problem, and consequently the exact non-linear free surface condition was separated into two independent linear free surface conditions, i.e. one for the steady wave-making flow and the other for the time dependent wave motion. It was found that the former is identical with the one in the low speed theory and the latter differs from the conventional free surface condition used in the linear ship motion theory hitherto. The characteristic of the time dependent free surface condition newly introduced in the present study is that the equation is formulated on double body flow around a ship as done in the low speed theory for the steady wave-making problem.

If turned out that the free-surface condition introduced by Faltinsen for added resistance calculation in short waves /3/ can be derived from the newly derived free-surface condition when it is applied to the vicinity of hull surface.

Next, discussions were made on the calculation methods of resistance when applying to conventional full hull forms. Finally, the optimum hull forms of least resistance in short waves were determined, where the resistance is the sum of the steady wave-making resistance calculated by the low speed theory and the added resistance due to wave reflection calculated based on Faltinsen's theory.

2. BASIC EQUATIONS

2.1 Coordinate System and Free Surface Condition

Let us consider a ship running in short waves so that the ship motion is neglected. In that case, it is convenient to define a coordinate system fixed with respect to the ship. The coordinate system is defined as shown in Fig. 1. x-axis coincides with the direction of steady uniform stream whose velocity U is identical with the ship speed. The origin of the axis is at the point of intersection of still water surface, midship section and center plane of the ship. y-axis is horizontal and

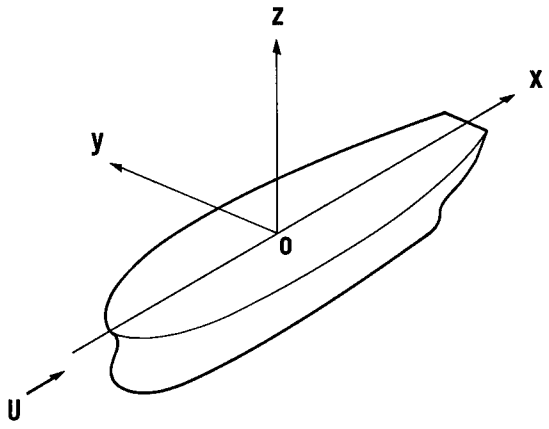


Fig. 1 Coordinate system

normal to x-axis, and z-axis directing vertically upwards.

Supposing a ship is in an inviscid, irrotational, incompressible fluid, the velocity potential Φ, which represents flow around the ship and satisfies Laplace's equation $\nabla^2\Phi = 0$, is introduced. The velocity vector $\mathbf{v}$ is expressed as:

$$\mathbf{v} = \nabla\Phi. \tag{1}$$

The free surface is defined by its elevation

$$z = \zeta(x,y,t).$$

The kinematic and dynamic boundary conditions on this free surface are written respectively as:

$$\frac{D}{Dt}(\zeta - z) = 0 \quad \text{on } z = \zeta, \tag{2}$$

where

$D/Dt \equiv \partial/\partial t + \nabla\Phi\cdot\nabla$, the substantial derivative and

$$\Phi_t + \frac{1}{2}(\nabla\Phi\cdot\nabla\Phi) + gz = \frac{1}{2}U^2 \quad \text{on } z = \zeta, \tag{3}$$

where g is the gravitational acceleration. Since the equation (3) is satisfied on the free surface for all time, its substantial derivative can be set equal to zero. Combining this with eq. (2), the exact non-linear free surface boundary condition is expressed as

$$\Phi_{tt} + 2\nabla\Phi\cdot\nabla\Phi_t + \frac{1}{2}\nabla\Phi\cdot\nabla(\nabla\Phi\cdot\nabla\Phi) + g\Phi_z = 0 \quad \text{on } z = \zeta, \tag{4}$$

where ζ is reduced from (3) as:

$$\zeta(x,y,t) = \frac{1}{g}\left[\frac{1}{2}(U^2 - \nabla\Phi\cdot\nabla\Phi) - \Phi_t\right] \quad \text{on } z = \zeta. \tag{5}$$

2.2 Basic Assumptions

In the low speed theory for steady wave-making problems, the total velocity potential was assumed to be the sum of the rigid-wall potential and the steady wave potential which represent the double body flow and the steady wave motion near the free-surface around a ship respectively. In the present study, the low speed theory is extended to an unsteady problem. Here, we assume that the total velocity potential Φ can be separated into the following three components:

$$\Phi(x,y,z,t) = \phi_r(x,y,z) + \phi_0(x,y,z) + \phi_1(x,y,z,t) \qquad (6)$$

where

ϕ_r : velocity potential representing double body flow in calm water. This is regarded as a base flow on which the following perturbation potentials are superimposed.

ϕ_0 : velocity potential representing steady wave-making.

ϕ_1 : velocity potential representing unsteady wave motion.

And the velocity components corresponding to those potentials are

$$\mathbf{v}_r = (u_r,v_r,w_r) = \nabla\phi_r,$$
$$\mathbf{v}_0 = (u_0,v_0,w_0) = \nabla\phi_0,$$
$$\mathbf{v}_1 = (u_1,v_1,w_1) = \nabla\phi_1, \qquad (7)$$

and

$$\mathbf{v} = \mathbf{v}_r + \mathbf{v}_0 + \mathbf{v}_1. \qquad (8)$$

In the low speed theory for steady wave-making problem, the following assumptions are made about orders of magnitude for the double body flow and the steady wave motion in the low speed limit of ship speed U.

$$\phi_r(x,y,z) = O(U),$$

$$\frac{\partial}{\partial x}, \frac{\partial}{\partial y}, \frac{\partial}{\partial z} = O(1) \text{ when operating on } \phi_r, \qquad (9)$$

then

$$u_r, v_r, w_r = O(U).$$

$$\phi_0(x,y,z) = O(U^5),$$

$$\frac{\partial}{\partial x}, \frac{\partial}{\partial y}, \frac{\partial}{\partial z} = O(U^{-2}) \text{ when operating on } \phi_0, \qquad (10)$$

then

$$u_0, v_0, w_0 = O(U^3)$$

In the present study the order of magnitude of the unsteady wave potnetial ϕ_1 is denoted by ε , which should be fixed later:

$$\phi_1(x,y,z,t) = O(\varepsilon) \qquad (11)$$

For the differential operator, following assumptions are newly introduced in the present study:

$$\frac{\partial}{\partial x}, \frac{\partial}{\partial y}, \frac{\partial}{\partial z} = O(U^{-2}), \text{ when operating on } \phi_1, \qquad (12)$$

$$\frac{\partial}{\partial t} = O(U^{-1}), \qquad (13)$$

then

$$u_1, v_1, w_1 = O(\varepsilon U^{-2}), \qquad (14)$$

where (12) implies that wave length of the unsteady wave motion is as short as that of the steady wave.

The wave height ζ is also expressed as the sum of two parts in the low speed theory for the steady wave-making problem,

$$\zeta(x,y) = \zeta_r(x,y) + \zeta_0(x,y)$$

where ζ_r is the fictitious wave height due to the rigid-wall potential ϕ_r,

$$\zeta_r(x,y) = \frac{1}{2g}\left[U^2 - (u_r^2+v_r^2+w_r^2)\right]_{\text{on } z=\zeta_r}, \qquad (15)$$

and ζ_0 is the steady wave height. In the present study, the wave height is also assumed to be the sum of the above two components and the unsteady component ζ_1,

$$\zeta(x,y,t) = \zeta_r(x,y) + \zeta_0(x,y) + \zeta_1(x,y,t). \qquad (16)$$

Considering (5), ζ_0 and ζ_1 may be defined by the following two equations:

$$\zeta_0 = \frac{1}{2g}\left[U^2 - (u_r^2+v_r^2+w_r^2) - (u_0^2+v_0^2+w_0^2) - 2(u_ru_0+v_rv_0+w_rw_0)\right] - \zeta_r, \quad \text{on } z = \zeta_r+\zeta_0, \qquad (17)$$

$$\zeta_1 = \left[\frac{1}{2g}\left\{U^2 - (u_r^2+v_r^2+w_r^2) - (u_0^2+v_0^2+w_0^2) - 2(u_ru_0+v_rv_0+w_rw_0) - (u_1^2+v_1^2+w_1^2) - 2(u_ru_1+v_rv_1+w_rw_1) - 2(u_0u_1+v_0v_1+w_0w_1)\right\} - \frac{1}{g}\phi_{1t}\right] - \zeta_r - \zeta_0, \quad \text{on } z = \zeta_r+\zeta_0+\zeta_1. \qquad (18)$$

From (15) the order of magnitude of ζ_r is found to be $O(U^2)$. By applying Taylor expansion to eqs. (15), (17) and (18), the wave heights can be expressed as

$$\zeta_r(x,y) = \frac{1}{2g}\left[U^2-u_{r0}^2-v_{r0}^2\right] + O(U^6), \qquad (19)$$

$$\zeta_0(x,y) = -\frac{1}{g}\left[u_{r0}u_0+v_{r0}v_0\right]_{z=\zeta_r} + O(U^6), \qquad (20)$$

$$\zeta_1(x,y,t) = -\frac{1}{g}\left[u_{r0}u_1+v_{r0}v_1+\phi_{1t}\right]_{z=\zeta_r} + O(\varepsilon U). \qquad (21)$$

In this derivation the following relations are used, e.g.

$$u_r = u_{r0} + \zeta_r\left(\frac{\partial u_r}{\partial z}\right)_{z=0} + O(U^5),$$

$$O(U) \qquad \text{Zero}$$

$$w_r = w_{r0} + \zeta_r\left(\frac{\partial w_r}{\partial z}\right)_{z=0} + O(U^5),$$

$$\text{Zero} \qquad O(U^3)$$

where u_{r0} and v_{r0} are velocity components of the double body flow at $z = 0$, and the order of magnitude of ζ_0 and ζ_1 are $O(U^4)$ and $O(\varepsilon U^{-1})$ respectively. It should be noted here that the order of magnitude of the unsteady wave potential ϕ_1 must be much smaller than $O(U^3)$ in order to derive (21). Further, the order of magnitude of ζ_1 must be lower than $O(U^6)$ which is the order of residual terms of ζ_r and ζ_0. So, we assume the following relation hereafter,

$$\varepsilon = U^n, \quad 3 < n < 7. \tag{22}$$

2.3 Derivation of Linearized Free Surface Boundary Conditions

The exact free surface boundary condition (4) is rewritten as

$$\phi_{1tt} + 2(\mathbf{v}_r\cdot\mathbf{v}_{1t}+\mathbf{v}_0\cdot\mathbf{v}_{1t}+\mathbf{v}_1\cdot\mathbf{v}_{1t}) + \{\mathbf{v}_r\cdot\nabla Q_r+\mathbf{v}_r\cdot\nabla Q_0+\mathbf{v}_r\cdot\nabla Q_1+\mathbf{v}_0\cdot\nabla Q_r+\mathbf{v}_0\cdot\nabla Q_0+\mathbf{v}_0\cdot\nabla Q_1 +\mathbf{v}_1\cdot\nabla Q_r+\mathbf{v}_1\cdot\nabla Q_0+\mathbf{v}_1\cdot\nabla Q_1\} + g\{w_r+w_0+w_1\} = 0$$

$$\text{on } z = \zeta_r+\zeta_0+\zeta_1. \tag{23}$$

In the case of steady wave-making problem, it can be written as

$$\{\mathbf{v}_r\cdot\nabla Q_r+\mathbf{v}_r\cdot\nabla Q_0+\mathbf{v}_0\cdot\nabla Q_r+\mathbf{v}_0\cdot\nabla Q_0\} + g\{w_r+w_0\} = 0$$

$$\text{on } z = \zeta_r+\zeta_0, \tag{24}$$

where Q_r, Q_0 and Q_1 are defined as follows,

$$Q_r = \frac{1}{2}(u_r^2+v_r^2+w_r^2),$$

$$Q_0 = \frac{1}{2}(u_0^2+v_0^2+w_0^2) + (u_ru_0+v_rv_0+w_rw_0),$$

$$Q_1 = \frac{1}{2}(u_1^2+v_1^2+w_1^2) + (u_ru_1+v_rv_1+w_rw_1) + (u_0u_1+v_0v_1+w_0w_1). \tag{25}$$

Taking the lowest order terms, which are of order $O(U^3)$, of (24) by use of the assumptions (9) and (10), equations for the wave heights (19) and (20), Taylor expansion, and the relation:

$$w_r = \zeta_r\left(\frac{\partial w_r}{\partial z}\right)_{z=0} = -\zeta_r\left(\frac{\partial u_r}{\partial x} + \frac{\partial v_r}{\partial y}\right)_{z=0},$$

we have the following linear free surface condition for the steady wave potential ϕ_0:

$$\frac{1}{g}\left\{u_{r0}\frac{\partial}{\partial x} + v_{r0}\frac{\partial}{\partial y}\right\}^2\phi_0 + \frac{\partial}{\partial z}\phi_0 = D(x,y) \qquad \text{on } z = \zeta_r, \tag{26}$$

where

$$D(x,y) = \frac{\partial}{\partial x}(u_{r0}\zeta_r) + \frac{\partial}{\partial y}(v_{r0}\zeta_r). \tag{27}$$

These equations are found to be identical with those derived by one of the authors in calculating steady wave-making resistance for low speed ships /2/.

Subtracting (24) from (23), and taking the lowest order terms, which are of $O(\varepsilon U^{-2})$, by use of the assumptions (9) through (14) and (22), equations for the wave heights (19) through (21) and the Taylor expansion, we have also the following linear free surface condition for the unsteady wave potential ϕ_1:

$$\frac{1}{g}\left\{\frac{\partial}{\partial t} + u_{r0}\frac{\partial}{\partial x} + v_{r0}\frac{\partial}{\partial y}\right\}^2\phi_1 + \frac{\partial}{\partial z}\phi_1 = 0 \qquad \text{on } z = \zeta_r. \tag{28}$$

It should be noted that in eqs. (26) and (28), terms including differentiation of double body flow components u_{r0} and v_{r0}, such as

$$u_{r0}\frac{\partial v_{r0}}{\partial x}\frac{\partial \phi_0}{\partial y} \text{ in (26) or } u_{r0}\frac{\partial v_{r0}}{\partial x}\frac{\partial \phi_1}{\partial y} \text{ in (28)}$$

should be neglected as higher order terms.

In general, we have to solve the eqs. (26) and (28) on $z = \zeta_r(x,y)$ simultaneously with Laplace's equation, the body boundary condition, and the radiation condition. Here however for the simplicity of treatment, we introduce a following non-conformal transformation of coordinates:

$$x' = x, \quad y' = y, \quad z' = z - \zeta_r(x,y)$$

The Laplace's equations for ϕ_0 and ϕ_1 are written as

$$0 = \underbrace{\frac{\partial^2\phi_0}{\partial x'^2} + \frac{\partial^2\phi_0}{\partial y'^2} + \frac{\partial^2\phi_0}{\partial z'^2}}_{O(U)} - \underbrace{2\frac{\partial\zeta_r}{\partial x'}\frac{\partial^2\phi_0}{\partial x'\partial z'} - 2\frac{\partial\zeta_r}{\partial y'}\frac{\partial^2\phi_0}{\partial y'\partial z'}}_{O(U^3)} + O(U^5) \tag{29}$$

$$0 = \underset{O(\varepsilon U^{-4})}{\frac{\partial^2\phi_1}{\partial x'^2}} \quad \underset{}{\frac{\partial^2\phi_1}{\partial y'^2}} + \underset{}{\frac{\partial^2\phi_1}{\partial z'^2}}$$

$$- \underset{O(\varepsilon U^{-2})}{2\frac{\partial\zeta_r}{\partial x'}\frac{\partial^2\phi_1}{\partial x'\partial z'}} - 2\frac{\partial\zeta_r}{\partial y'}\frac{\partial^2\phi_1}{\partial y'\partial z'} + O(\varepsilon) \tag{30}$$

Thus, to leading order, ϕ_0 and ϕ_1 satisfy the usual Laplace's equation in terms of the new variables x', y', z'. Taking the lowest order terms and dropping the primes on the new variables, the linearized free surface conditions for the steady wave potential ϕ_0 and the unsteady wave potential ϕ_1 are written as:

$$\frac{1}{g}\left\{u_{r0}\frac{\partial}{\partial x} + v_{r0}\frac{\partial}{\partial y}\right\}^2\phi_0 + \frac{\partial}{\partial z}\phi_0 = D(x,y) \quad \text{on } z=0, \tag{31}$$

and

$$\frac{1}{g}\left\{\frac{\partial}{\partial t} + u_{r0}\frac{\partial}{\partial x} + v_{r0}\frac{\partial}{\partial y}\right\}^2\phi_1 + \frac{\partial}{\partial z}\phi_1 = 0 \quad \text{on } z=0, \tag{32}$$

respectively. In these equations, the free surface condition for ϕ_0 does not have the effect of ϕ_1, and vice versa. So these equations can be solved independently on the common base flow around a ship expressed by (u_{r0}, v_{r0}).

The equation (31) corresponds to the basic equation for the steady low speed wave-resistance theory, and the eq. (32) has been derived newly in the present study, which makes a pair with the equation (31) for steady motion and can be applied to full ship forms. For reference, when we put $u_{r0}\to U$, and $v_{r0}\to 0$ the equations (31) and (32) become the conventional linearized steady and unsteady free surface boundary conditions, respectively.

For reference, it is noted as follows that the free surface condition (28) is derived also by applying the present assumptions on order of magnitude to the free surface condition presented by Newman for small unsteady motion which is superimposed on a general steady flow around ship /4/. In terms of Newman's original notations, the unsteady velocity potential is governed by the following first-order free-surface condition:

$$-(\varphi_t + \mathbf{W}\cdot\nabla\varphi)\left[\frac{1}{2}\frac{\partial}{\partial z}(\mathbf{W}\cdot\nabla W^2) + g\bar{\phi}_{zz}\right]/(g + \mathbf{W}\cdot\mathbf{W}_z)$$

$$O(\varepsilon U^{-1})$$

$$+ \underset{O(\varepsilon U^{-2})}{\varphi_{tt}} + \underset{O(\varepsilon U^{-2})}{2\mathbf{W}\cdot\nabla\varphi_t} + \underset{O(\varepsilon U^{-2})}{\mathbf{W}\cdot\nabla(\mathbf{W}\cdot\nabla\varphi)}$$

$$+ \underset{O(\varepsilon)}{\frac{1}{2}\nabla\varphi\cdot\nabla(W^2)} + \underset{O(\varepsilon U^{-2})}{g\varphi_z} = 0 \quad \text{on } z = \bar{\zeta}, \tag{33}$$

where the following relations exist between Newman's notations and those in the present study:

$$\varphi = \phi_1 \ , \ \mathbf{W} = \mathbf{v}_r + \mathbf{v}_0 \ , \ \bar{\phi} = \frac{1}{U}(\phi_r + \phi_0 - Ux)$$

$$\bar{\zeta} = \zeta_r + \zeta_0 .$$

As shown above the lowest order terms, which are of $O(\varepsilon U^{-2})$, are written as:

$$\varphi_{tt} + 2\mathbf{W}\cdot\nabla\varphi_t + \mathbf{W}\cdot\nabla(\mathbf{W}\cdot\nabla\varphi) + g\varphi_z = 0$$

$$\text{on } z = \zeta_r,$$

which coincides with the equation (28) using the relation

$$\mathbf{W}\cdot\nabla = u_{r0}\frac{\partial}{\partial x} + v_{r0}\frac{\partial}{\partial y} .$$

3. RESISTANCE FORMULAE

3.1 Steady Wave-making Resistance

In the present study, steady and unsteady velocity potentials superimposed on the double body base flow are governed by independent linearized free-surface conditions eqs. (31) and (32). In this linearized problem, the wave-making resistance due to steady flow and the added resistance, which is determined as a time average value in the periodic wave motion, can be calculated separately /5/. Based on the solution of the equation (31) a formula for the steady wave-making resistance of a slow ship was given by

$$R_w = \pi\rho U^2 \int_0^{\pi/2} |C(\theta)+iS(\theta)|^2 \cos^3\theta \, d\theta \tag{34}$$

where

$$C(\theta)+iS(\theta) = -\frac{g}{\pi U^3}\sec^3\theta \int_{-\infty}^{\infty}\!\!\int d\xi d\eta \, D(\xi,\eta)$$

$$\times \exp\left\{i\frac{g}{U^2}\sec^2\theta(\xi\cos\theta+\eta\sin\theta)\right\}, \tag{35}$$

and i denotes imaginary unit and ρ is the density of water.

Though the integral of (35) with respect to ξ and η extends over the infinite domain outside of the hull surface, we have an asymptotic expression of the amplitude function in the low speed limit by partial integration of (35) with respect to ξ :

$$C(\theta)+iS(\theta) = -i\frac{\sec^2\theta}{\pi U} \oint D(\xi_0,\eta_0)\exp\left\{i\frac{g}{U^2}\sec^2\theta\right.$$

$$\left.\times(\xi_0\cos\theta+\eta_0\sin\theta)\right\} d\eta_0, \tag{36}$$

where (ξ_0,η_0) is a point on the intersection of the hull surface and the still waterplane.

As shown above, the steady wave-making resistance may be evaluated only from the velocity of double body flow on the intersection of the hull surface and the still water surface. It is considered, further, that the steady wave motion of a low speed ship appears only in the region close to the still water surface. Also for the unsteady wave motion, only the part of a ship hull close to the water surface will have an effect when the wave length is small and the wave motion decayes depthwise rapidly in the fluid. So we may replace the ship hull by a vertical, infinite-depth cylinder supposing the ship has sufficiently deep draught and nearly vertical sides.

Then the double body flow around the hull may be approximated as a two-dimensional flow and be calculated by the conformal mapping technique. Suppose that the intersection of the hull surface and the waterplane may be transformed into the unit circle by a mapping function as

$$\frac{\xi_0}{L/2} = \sum_{n=1}^{N} a_n \cos(2-n)\beta,$$

$$\frac{\eta_0}{L/2} = \sum_{n=1}^{N} a_n \sin(2-n)\beta, \qquad (37)$$

where L is the waterplane length and β denotes argument. And then, the tangential velocity V of the double body flow on the hull surface is given by

$$\frac{V(\beta)}{U} = 2a_1\sin\beta/\Big[\Big\{\sum_{n=1}^{N} a_n(2-n)\cos(1-n)\beta\Big\}^2 + \Big\{\sum_{n=1}^{N} a_n(2-n)\sin(1-n)\beta\Big\}^2\Big]^{1/2}. \qquad (38)$$

u_{r0} and v_{r0} in (19) and (27) can be calculated from V.

Further, for the sake of simplicity of calculation, we assume that the waterplane form is convex and symmetrical with respect to the y-axis. This simplification does not seem to effect the result so much, since our aim is to determine an entrance form which has the least value of the sum of the steady wave-making resistance and the added resistance in short waves.

By applying the stationary phase method in the integrals (36) and (34), we have a simple formula for wave-making resistance /6/ :

$$R_w = \frac{1}{2}\rho U^2 L^2 \times 8\left(\frac{U}{\sqrt{gL}}\right)^6 \times \int_0^{\pi/2} F(\beta)^2 \frac{\eta_0'(\beta)d\beta}{\{\xi_0'(\beta)\}^2+\{\eta_0'(\beta)\}^2}, \qquad (39)$$

where

$$\eta_0'(\beta) = d\eta_0/d\beta\ ,\quad \xi_0'(\beta) = d\xi_0/d\beta\ ,$$

$$F(\beta) = \frac{v_{r0}(\xi_0,\eta_0)}{U}\,\frac{V}{U}\,\frac{dV}{Ud\beta}\ .$$

3.2 Added Resistance in Short Waves

There is a trend that measured values of added resistance for full ship models in short waves are greater than those predicted theoretically under the assumptions of slender ship. To improve the shortcoming of the theory Fujii and Takahashi introduced an additional term which takes account of wave reflection at ship's bow /7/. In their study Havelock's formula for the drifting force based on the wave reflection /8/ was used together with empirical corrections.

A formula proposed by Fujii and Takahashi for resistance increase Raw due to wave reflection at bow part is given by

$$R_{aw} = \alpha_1(1+\alpha_2)\frac{1}{2}\rho g\zeta_a^2 B\,\overline{\sin^2\theta} \qquad (40)$$

$$\overline{\sin^2\theta} = \frac{1}{B}\int_{-B/2}^{B/2}\sin^2\theta\ dy, \qquad (41)$$

where α_1 and α_2 are empirical correction factors considering the effect of finite draught d and that of the advance velocity:

$$\alpha_1 = \pi^2 I_1^2(k_0d)/\{\pi^2 I_1^2(k_0d) + K_1^2(k_0d)\}, \qquad (42)$$

$$\alpha_2 = 5\left(\frac{U}{\sqrt{gL}}\right)^{1/2} \qquad (43)$$

where I_1 and K_1 are the modified Bessel functions, k_0 is wave number of incident wave, B the breadth of the waterplane, ζ_a the amplitude of incident wave, and θ denotes the inclination of the waterline to the centerline as shown in Fig. 2.

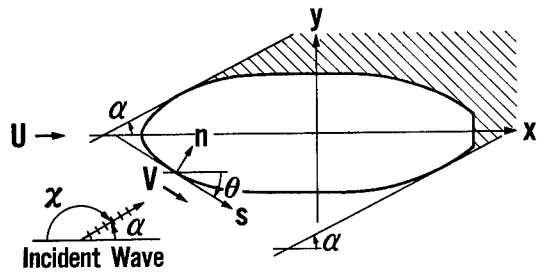


Fig. 2 Coordinate system along waterline

The empirical constants in (42) and (43) were modified later based on additional experimental data obtained in the Nagasaki Experimental Tank as

$$\alpha_1 = \pi^2 I_1^2(1.5k_0d)/\{\pi^2 I_1^2(1.5k_0d) + K_1^2(1.5k_0d)\}, \qquad (44)$$

$$\alpha_2 = 3.5\left(\frac{U}{\sqrt{gL}}\right)^{1/2}. \qquad (45)$$

Though the above formulas are for added resistance in head waves, they may be applied also in oblique waves by a modification of $\sin^2\theta$ as

$$\overline{\sin^2(\theta-\chi)} = \frac{1}{B}\int \sin^2(\theta-\chi)\, dy, \qquad (46)$$

where χ is the wave direction as shown in Fig. 2, and the integration is to be performed in the non-shadow part.

Years later, an asymptotic theory to calculate added resistance of a ship in slow speed forward motion in short waves was prsented by Faltinsen /3/. Looking into wave motions near the ship's hull, he introduced a linearized free-surface condition for diffraction velocity potential ϕ_D along the streamline close to the ship's hull side:

$$\left(\frac{\partial}{\partial t} + V\frac{\partial}{\partial s}\right)^2\phi_D + g\frac{\partial}{\partial z}\phi_D = 0 \quad \text{on } z = 0, \qquad (47)$$

where s is the coordinate along the waterline and V the velocity along s as shown in Fig. 2.

It turned out that this free-surface condition (47) coincides with the equation (32) which was newly derived in the present study. At present, however, the equation (32) together with body boundary condition has not been solved yet by the present authors. But Faltinsen solved approximately this unsteady free-surface problem. He considered the effect of flow distortion around a body on the diffraction wave alone in solving this boundary value problem. Then an asymptotic formula was derived to estimate added resistance in short waves at low speed limit. This theory is regarded as a theoretical extension of Havelock's theory for a case of moving bodies.

In the present study, added resistance in short waves is calculated based on this Faltinsen's theory. In this theory added resistance in short waves is given by

$$R_{aw} = \int \overline{F_n}\sin\theta\, d\ell, \qquad (48)$$

$$\overline{F_n} = \frac{1}{2}\rho g\zeta_a^2\frac{1}{2}\left[\frac{k_1}{k_0} - \cos^2(\theta+\alpha) + \frac{k_2}{k_0}\sin(\theta+\alpha)\right], \qquad (49)$$

$$k_1 = \{\omega_e - Vk_0\cos(\theta+\alpha)\}^2/g, \qquad (50)$$

$$k_2 = \sqrt{k_1^2 - k_0^2\cos^2(\theta+\alpha)}, \qquad (51)$$

where $\overline{Fn}$ is wave force acting on an infinitely small vertical element of the hull, ω_e is the circular frequency of encounter, k_0 and ζ_a are wave number and amplitude of the incident wave, $\alpha = \pi - \chi$ is the wave direction and θ is the inclination of the waterline as shown in Fig. 2. k_1 and k_2 are wave number components of diffraction wave, which is assumed to be expressed in a form:

$$\phi_D \sim A\, e^{-i\omega_e t}\exp\left[k_1 z + i\{k_0 s\cos(\theta+\alpha) - nk_2\}\right]$$

where n and s are coordinates normal and along the waterline. The integration of (48) is along the waterline in the non-shadow part as shown in Fig. 2. An asymptotic formula was also derived in the low speed limit for the wave force on an infinite small element $\overline{Fn}$ of (49) as

$$\overline{F_n} = \frac{1}{2}\rho g\zeta_a^2\left[\sin^2(\theta+\alpha) + \frac{2\omega_0 U}{g}\{1-\cos\theta\cos(\theta+\alpha)\}\right], \qquad (52)$$

where the following approximation is used:

$$V = U\cos\theta. \qquad (53)$$

From (49) the authors have derived a little different expression from (52) as:

$$\overline{F_n} = \frac{1}{2}\rho g\zeta_a^2\left[\sin^2(\theta+\alpha) + \frac{2\omega_0 U}{g}\{\cos\alpha - \cos\theta\cos(\theta+\alpha)\}\right]. \qquad (54)$$

Now let us consider a case of a surface piercing vertical circular cylinder. In this case, the added resistance can be expressed analytically by use of the asymptotic expression in the low speed limit. Exact velocity of the double body flow along the circular cylinder is given by

$$V = 2U\cos\theta. \qquad (55)$$

Then from eqs. (48) through (51), we have in the low speed limit

$$R_{aw} = \frac{1}{2}\rho g\zeta_a^2\, r\left[\frac{4}{3}\{\cos\alpha + \frac{\omega_0 U}{g}(1+\sin^2\alpha)\}\right], \qquad (56)$$

where r is the radius of the circular cylinder. When using Faltinsen's approximation (53), we have

$$R_{aw} = \frac{1}{2}\rho g\zeta_a^2\, r\left[\frac{4}{3}\{\cos\alpha + \frac{\omega_0 U}{g}(1+\cos^2\alpha)\}\right], \qquad (57)$$

Depending on the approximation of the flow around a body, the effect of advance speed in eqs. (56) and (57) appears differently, e.g. the effect of advance speed in head wave ($\alpha = 0°$) is estimated twice as large as when use is made of Faltinsen's approximation (53).

In Fig. 3 the sum of steady wave-making resistance and added resistance due to wave reflection is shown for different incident angles, where the steady wave-making resistance is calculated by the equation (39) as:

$$R_w = \frac{1}{2}\rho U^2(2r)^2 \times \frac{8192}{315}\left(\frac{U}{\sqrt{2gr}}\right)^6$$

for a surface piercing vertical circular cylinder.

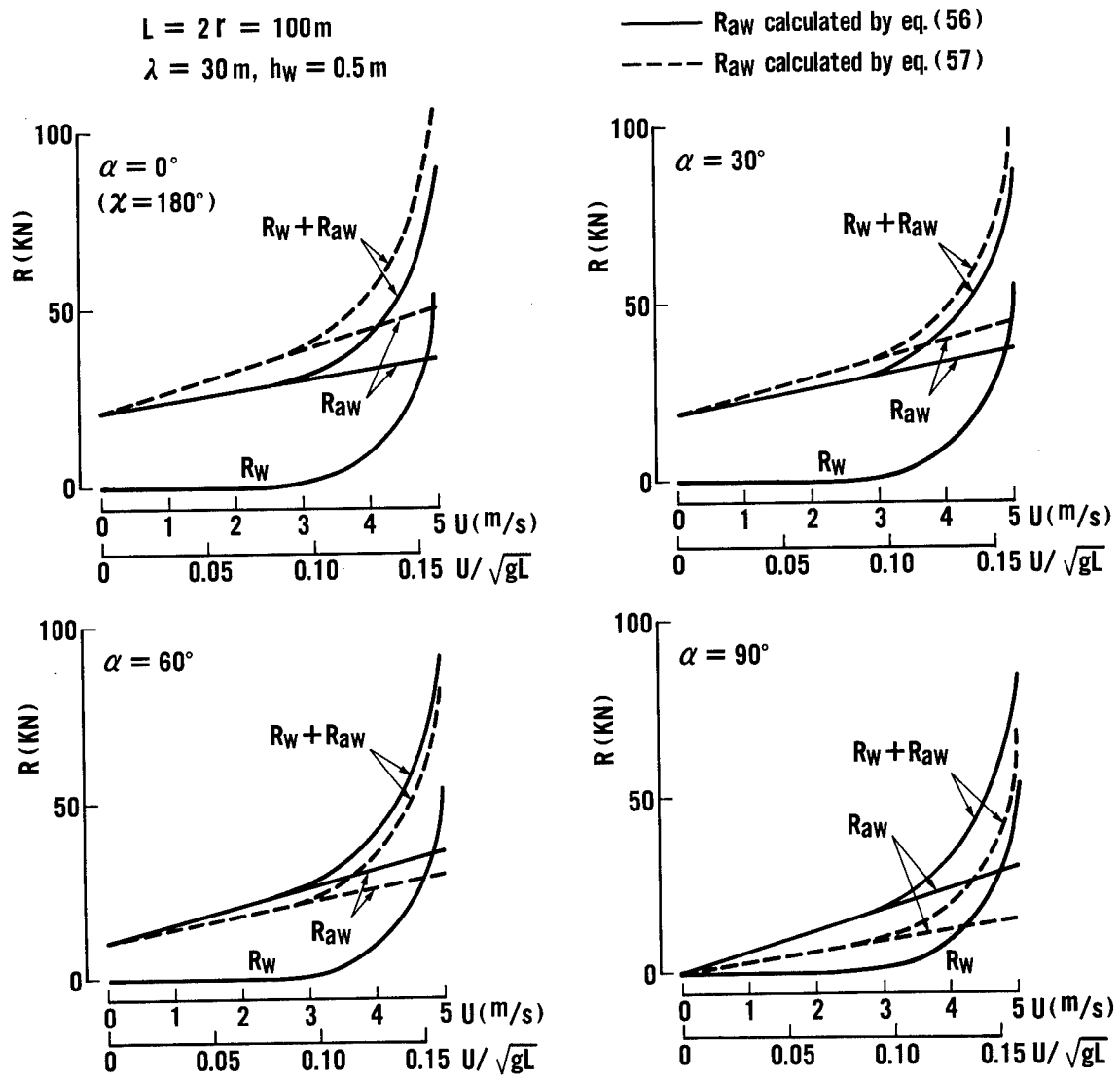


Fig. 3 Resistance of surface piercing vertical circular cylinder

From the Fig. 3 it is found that the added resistance due to the wave reflection is dominant in the low speed region while the steady wave-making resistance increases rapidly with increase of Froude number. As considered previously, the calculated values of added resistance appear differently with respect to the incident wave angles depending on the approximation of the values of base flow around the body. This difference is large for extremely blunt forms such as the present case (circular cylinder) but it may be small for conventional ships as shown later.

It is also a characteristic of Faltinsen's theory that the added resistance does not vanish even when an obstacle symmetrical with respect to midship section, such as a circular cylinder, is running in beam waves. This is attributed to the effect of advance speed. The effect of advance speed appears to make the wave field asymmetrical with respect to front and rear parts of the body due to the change of wave number by the curved flow around a body. The change of wave number k_1/k_0 and k_2/k_0 are shown in Fig. 4 in the case of the surface piercing vertical circular cylinder in beam waves. In the figure, k_1/k_0 and k_2/k_0 are not drawn in the regions where circumferential angle on the cylinder is larger than around 120 deg. They are the regions where the value of k_2 calculated by (51) is imaginary and they are excluded from the range of integration of (48). It should be mentioned here that this sort of considerations about the value of k_2 and the region of integration of (48) were not made in deriving the asymptotic expressions (56) and (57).

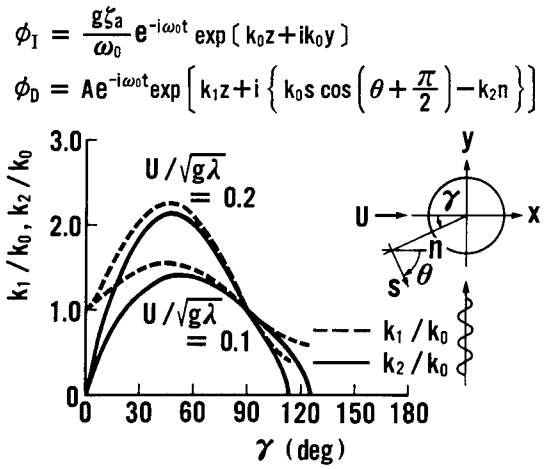


Fig. 4 Variation of wave number around a surface piercing vertical circular cylinder in beam waves

3.4 Application to Ordinary Ship Hull Forms

In Fig. 5 values of steady wave-making resistance calculated by eq. (39) are compared with the experimental values. In the calculation, ship hull forms were approximated by infinite vertical cylinders symmetrical with respect to midship section, which have the same waterplane curves as those of the fore part of original ship hull forms. Assuming that contribution to the steady wave-making resistance from the run part is small, a half of the calculated resistance by eq. (39), that is the contribution from the entrance part only, is compared with the experimental value. Considering the approximation adopted in the theoretical calculation, wave-making resistance coefficients of full ship models which have comparatively U-shaped frameline and nearly vertical sides at the waterplane are shown in the figure.

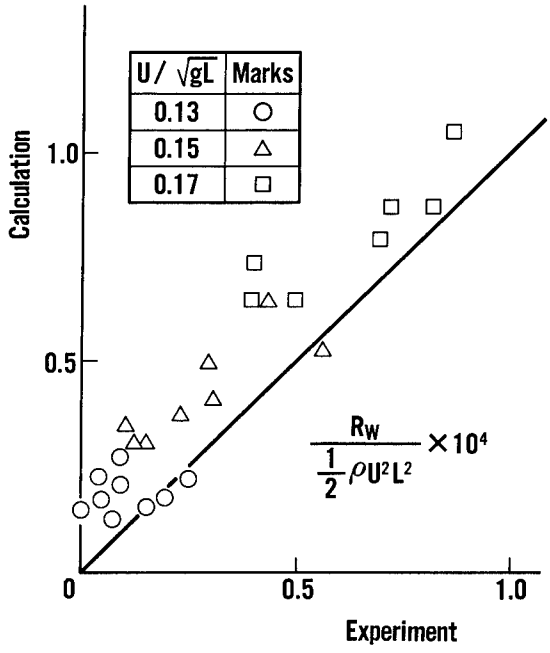


Fig. 5 Comparison of wave-making resistance of full hull forms

In spite of the rough approximations mentioned above, it is observed that the calculated values of wave-making resistance agree well with the experimental values. Therefore, it is considered that the present calculation method of steady wave-making resistance is applicable to the optimization problem of a hull form which has U-shaped frameline form.

In Figs. 6 and 7, experimental values of added resistance of conventional full hull forms are compared with calculated values in a non-dimensional form:

$$\sigma_{aw} = R_{aw}/(\rho g \zeta_a^2 B^2/L) \qquad (58)$$

Solid lines represent σ_{aw} values calculated by eqs. (48) through (51), where the basic flow velocity V in eq. (50) is calculated by the conformal mapping technique replacing the hull form by an infinite depth vertical cylinder which has the same waterplane curve as the original hull form. This method based on Faltinsen's theory is called the present method hereafter for the sake of convenience. On the other hand, chain lines represent σ_{aw} values calculated by eqs. (48) and Faltinsen's asymptotic formula (54), where V is assumed as $U\cos\theta$. Added resistance in short waves was calculated also by Fujii - Takahashi's formulas (40),(44),(45) and (46). The results are shown by dotted lines in the figures.

In the region where $U/\sqrt{gL}$ is less than o.15 in Fig. 6, Fujii-Takahashi's formula predicts somewhat larger added resistance value than that of the present method. Faltinsen's asymptotic formula (54) gives the values almost same as those of other formulas. The difference of the calculated results is small compared with the scatter of the experimental data.

As for the results in oblique waves, the difference of added resistance for various wave directions is relatively small in the calculation by the present method and the tendency coincides with that of the experimental values. In the experiments shown in Fig. 6 and Fig. 7, periodic ship motion was negligibly small but measured values of added resistance in oblique waves may include some effect of steady drift and check helm taken to cancel yaw moment, which are not considered in the theoretical calculation.

Though Faltinsen's theory is an approximate theory, it is found that it can predict the added resistance in the same level of agreement with experiments as Fujii-Takahashi's empirical formula. The present method of calculation of added resistance based on Faltinsen's theory was used in the optimization problems of hull forms in the followings.

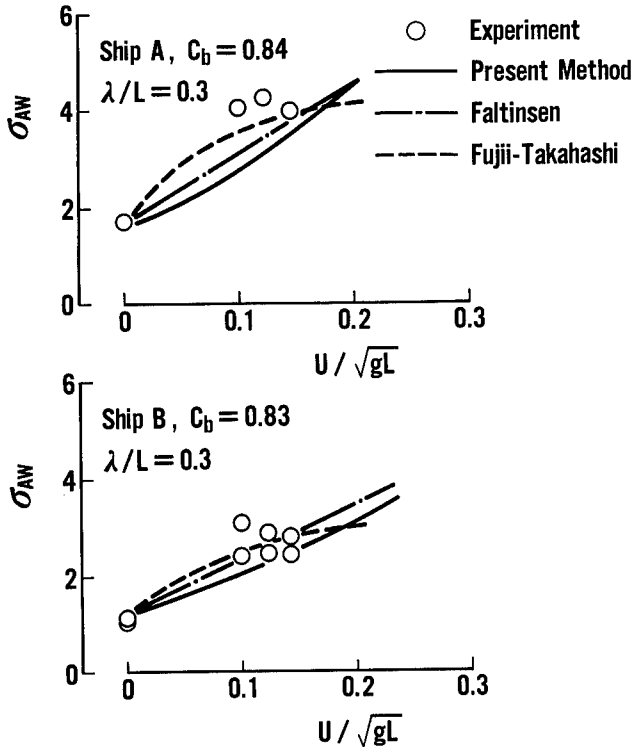


Fig. 6-a Added resistance in head wave

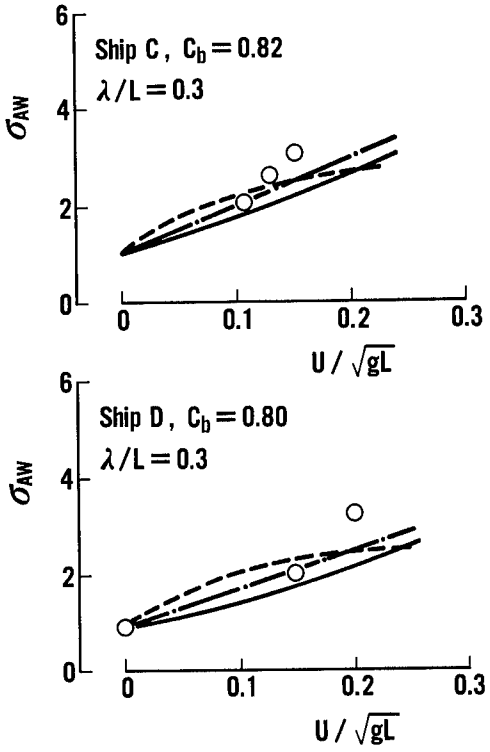


Fig. 6-b Added resistance in head wave

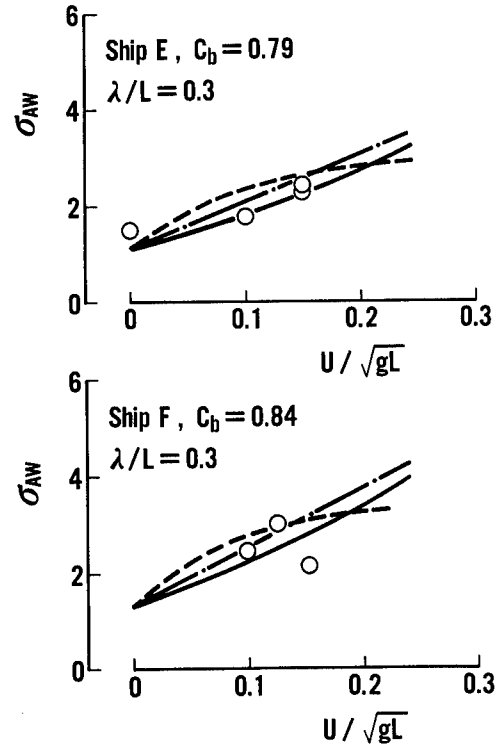


Fig. 6-c Added resistance in head wave

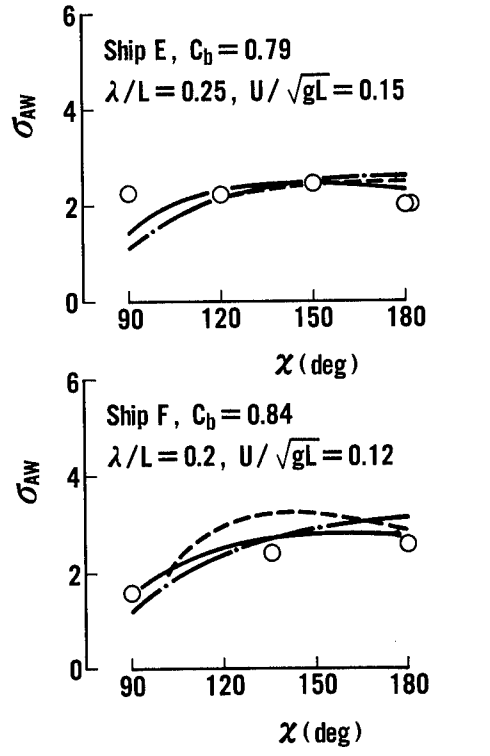


Fig. 7 Added resistance in oblique waves

4. MINIMIZATION OF RESISTANCE

4.1 Optimization Method

Optimum hull forms are determined in such a way that the sum of steady wave-making resistance and added resistance becomes minimum in a certain wave condition. For this calculation a non-linear programming technique, i.e. Hooke and Jeeves' direct search method with external penalty technique /9/ was used. The objective function, which should be minimized in the optimization problem is the sum of the steady wave-making resistance calculated by the eq.(39) and the added resistance due to wave reflection in short waves.

In the same manner as examined in the previous section, a ship hull form was replaced by an infinite-depth vertical cylinder and the double body flow V was calculated by the conformal mapping technique. For the sake of simplicity, the cylinder is assumed to have symmetrical waterplane curve with respect to midship section, which is identical with that of the entrance part of the subject ship, since our interest is in the entrance form whose resistance, namely the sum of steady wave-making resistance and added resistance, is minimum. The constraint of constant waterplane area was satisfied generally in the following ploblem.

4.2 Optimization of Length-breadth Ratio of Elliptic Cylinders

Within the framework of the low speed wave resistance theory there is a tendency that the steady wave-making resistance does not necessarily decrease with increase of length-breadth ratio. Considering this tendency, length-breadth ratio of vertical elliptic cylinders was optimized as a simple case in waves. The waterplane curve of an elliptic cylinder is expressed as

$$\frac{\xi_0}{L/2} = a_1\cos\beta + a_3\cos\beta, \tag{59}$$

$$\frac{\eta_0}{L/2} = a_1\sin\beta - a_3\sin\beta, \tag{60}$$

where a_1 and a_3 are the coefficients of conformal mapping function (37) and should satisfy

$$a_1 + a_3 = 1. \tag{61}$$

a_1 was chosen as a design variable of the optimization problem. In order to satisfy the constraint of constant waterplane area, length of the cylinder L was determined by the following relation:

$$A_W = \frac{L^2}{4}\pi(2a_1 - 1). \tag{62}$$

The waterplane form of minimum steady wave-making resistance was chosen as the initial form for the optimization procedure. The conditions of the calculation are

Length (initial value) : L = 185.6 m
Breadth (initial value): B = 53.9 m
Waterplane area : A_W = 7854 m
Ship speed : U = 7.2 m/sec (14 Kn)
Wave length : λ = 60 m (λ/L=0.323)
Wave height : $h_W = 2\zeta a$ = 0.5 ~ 2.0 m
Wave direction : χ = 180° (head wave)
~90° (beam wave)

Optimum waterplane curves are shown in Fig. 8 for various wave heights and in Fig. 9 for various wave directions.

From Fig. 8, it may be found that length-breadth ratio of the optimum forms increases as the wave height becomes large. Though the steady wave-making resistance component of the optimum forms is a little larger than that of the original form, the total resistance is smaller. This is due to the decrease of added resistance due to wave reflection.

In Fig. 9, length-breadth ratios of optimum forms in oblique waves do not change much from that in head wave. So it seems that an optimum waterplane form designed in head wave will be a nearby optimum form also in oblique waves.

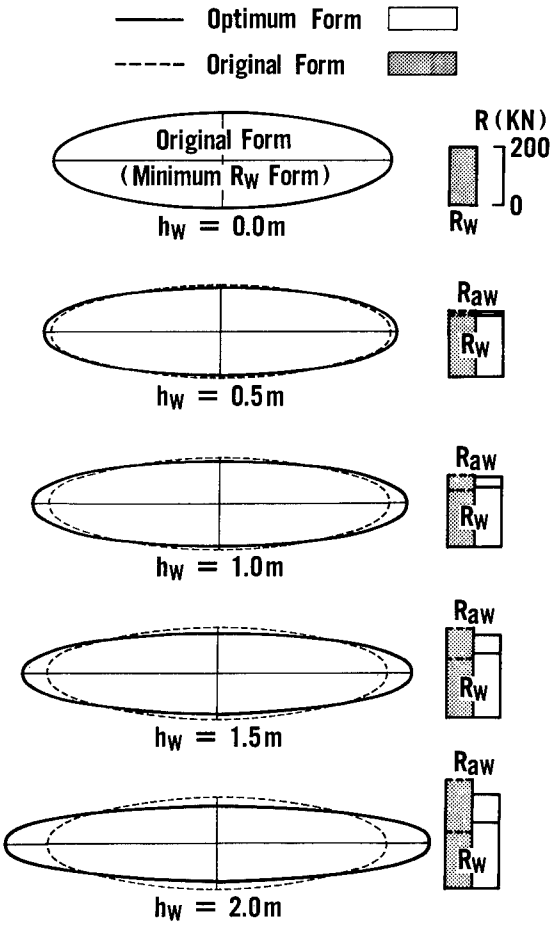


Fig. 8 Optimum form for various wave heights (wave direction χ = 180°, head wave)

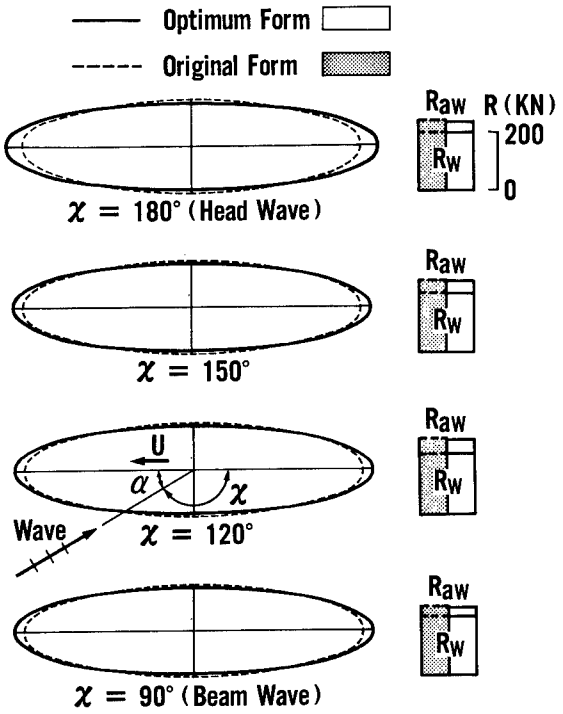


Fig. 9 Optimum form for various wave directions (h_w=1.0 m)

4.3 Optimization of Waterplane Form

As a next step, waterplane form was optimized under the constraints of constant length, breadth and waterplane area. In the caluculation, waterplane form was expressed by 5th polynomials /10/.

$$\tilde{\eta} = A + Bt + Cw, \tag{63}$$

$$A = 1 - 40\tilde{\xi}^3 + 75\tilde{\xi}^4 - 36\tilde{\xi}^5, \tag{64}$$

$$B = -\tilde{\xi}^3(2-3\tilde{\xi})(1-\tilde{\xi}), \tag{65}$$

$$C = 60\tilde{\xi}^3(1-\tilde{\xi})^2, \tag{66}$$

where $\tilde{\xi}$ and $\tilde{\eta}$ are the coordinates normalized by the length of entrance ℓ, and the half breadth of waterplane B/2 as shown in Fig. 10:

$$\tilde{\xi} = |x-x_\ell|/\ell, \tag{67}$$

$$\tilde{\eta} = y/(B/2). \tag{68}$$

w is the area coefficient of entrance and run parts, and t is the inclination of the waterplane curve at the fore and aft ends respectively:

$$w = \int_0^1 \tilde{\eta} d\tilde{\xi} \tag{69}$$

$$t = \frac{d\tilde{\eta}}{d\tilde{\xi}} \quad \text{at } \tilde{\xi} = 1 \tag{70}$$

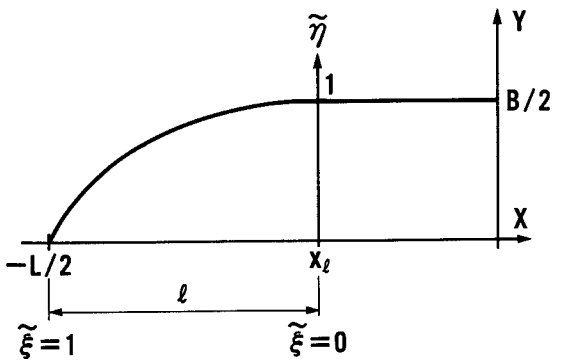


Fig. 10 Expression of waterplane curve

Waterplane curves expressed by (63) satisfy the following conditions:

$$\left.\begin{aligned} &\tilde{\eta} = 1 \\ &\frac{d\tilde{\eta}}{d\tilde{\xi}} = \frac{d^2\tilde{\eta}}{d\tilde{\xi}^2} = 0 \end{aligned}\right\} \text{ at } \tilde{\xi} = 0,$$

$$\tilde{\eta} = 0 \quad \text{at } \tilde{\xi} = 1$$

In the present calculation w and t were chosen as design variables and ℓ was determined by the following equation in order to satisfy the constraint of constant waterplane area:

$$\frac{L}{2}\left(1 - \frac{A_w}{LB}\right) = \ell(1 - w) \tag{71}$$

Further an inequality constraint was imposed so that the waterplane curve is convex everywhere between $\tilde{\xi} = 0$ and $\tilde{\xi} = 1$ in order to calculate the steady wave-making resistance by use of the stationary phase method:

$$\frac{d^2\tilde{\eta}}{d\tilde{\xi}^2} < 0 \quad \text{for} \quad 0 < \tilde{\xi} < 1 \tag{72}$$

Within this inequality constraint the optimum values of w and t are determined.

Calculations were made for the following conditions. Length and advance speed of the ship, wave length and incident wave height are fixed:

L = 300 m, U = 7.2 m/sec (14 Kn)
λ = 60 m (λ/L = 0.2),
h_w = 1.2 m (h_w/λ = 1/50),
while length-breadth ratios and fullness of waterplane area are varied:
L/B = 6, 5,
A_w/LB = 0.7, 0.8, 0.9.

Optimum waterplane forms were determined for the following three cases:
(1) Minimization of steady wave-making resistance alone
(2) Minimization of added resistance alone
(3) Minimization of total resistance, i.e. the sum of steady wave-making resistance and added resistance.

In Fig. 11 optimum waterplane forms of the above three cases are compared. The values of resistance components for the optimum forms are also compared in the figure.

It is observed that optimum waterplane forms of minimum total resistance are close to those of minimum steady wave-making resistance. On the other hand, the optimum waterplane forms of minimum added resistance are somewhat different from the others as shown in the figures.

It is found further that steady wave-making resistance R_w and added resistance R_{aw} change largely with the variation of principal geometrical parameters such as L/B and A_w/LB. However, no appreciable difference is observed for R_{aw} with respect to the local minor change of waterplane forms. In other words, R_{aw} seems insensitive to the change of local form. On the other hand, R_w changes according to the variation of waterplane form. Therefore, in the minimization procedure, the steady wave-making component R_w plays an important role on the determination of waterplane form of minimum total resistance (R_w+ R_{aw}). As a result, the waterplane forms of minimum total resistance come close to those of minimum steady wave-making resistance.

From this study it may be said that under the specified principal geometric parameters the waterplane form of minimum steady wave-making resistance is considered as an optimum form even in short waves.

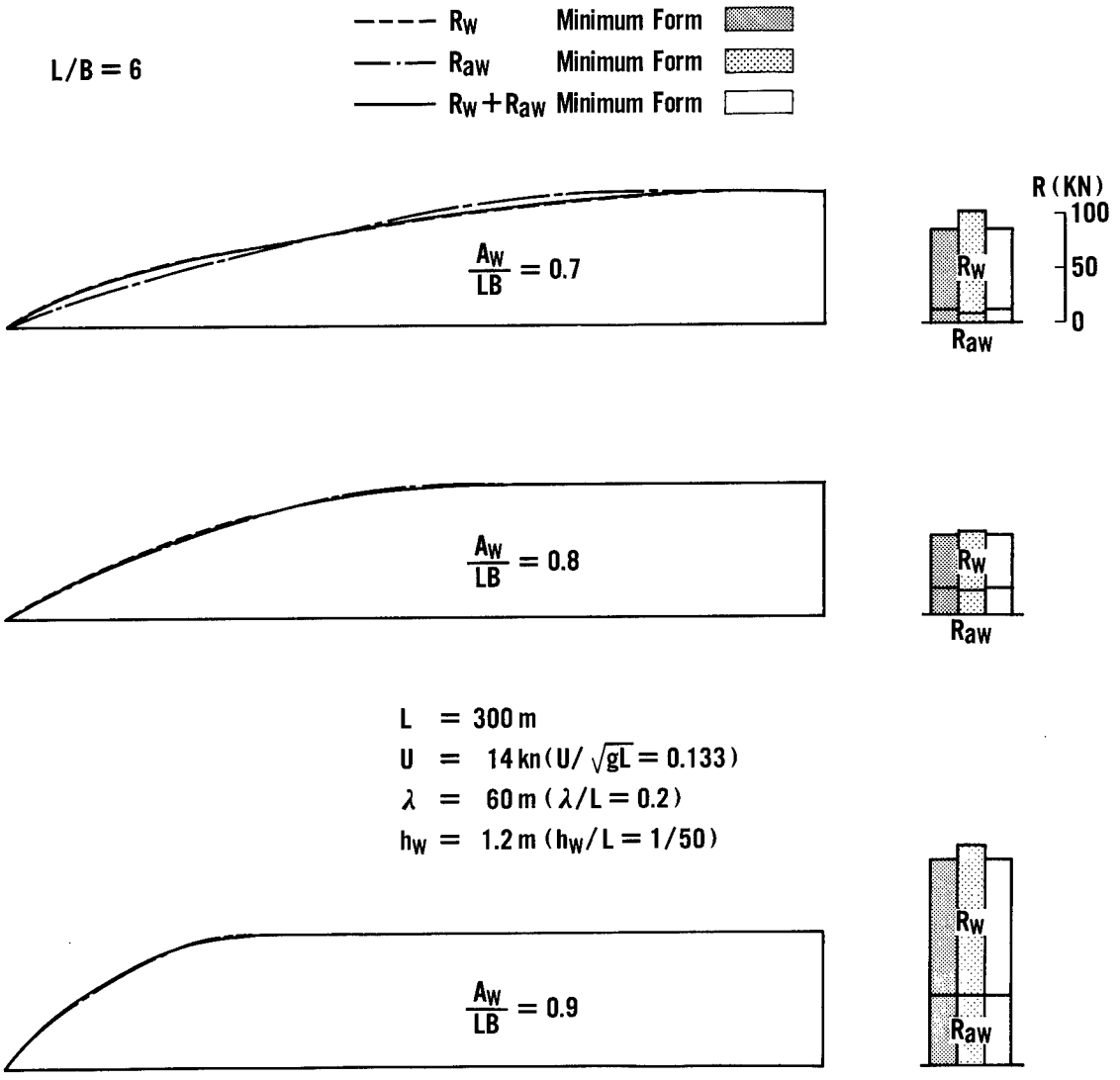


Fig. 11-a Comparison of waterplane forms of minimum resistance (L/B = 6)

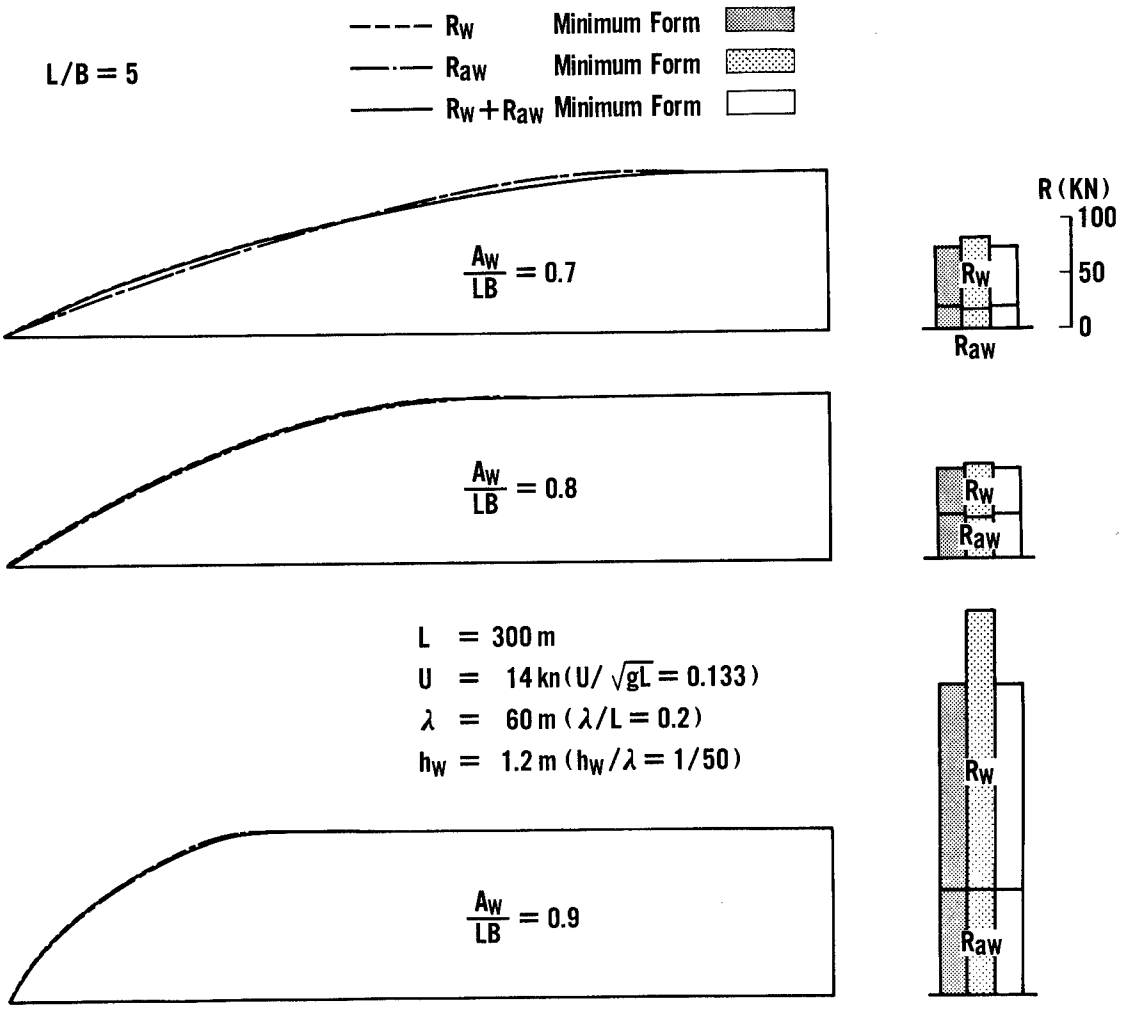


Fig. 11-b Comparison of waterplane forms of minimum resistance (L/B = 5)

5. CONCLUDING REMARKS

In the first part of the present paper, a linear free-surface condition for unsteady wave motion was newly introduced. This linear equation is formulated on the double body flow around a ship and makes a pair with that of the low speed theory for steady wave-making problem. In the region near the hull this equation coincides with that introduced by Faltinsen for a diffraction problem in short waves. In the present study, therefore, Faltinsen's asymptotic solution was used for the calculation of added resistance. Recently, with relation to Faltinsen's theory, Ohkusu and Naito et al. discussed the effect of curved bow flow and breaking waves around a ship /11,12/. Further study remains for deeper understanding of flow phenomena around a ship's bow. It is hoped that the free surface condition introduced in the present study would be a basis for the study.

In the latter part of the present paper, attempts were made to minimize ship resistance in short waves by use of the nonlinear programming technique. The results obtained through the calculation are summarized as follows. Both steady wave-making resistance and added resistance due to wave reflection change widely with the variation of principal geometric parameters such as length-breadth ratio and fullness of waterplane form. So the principal geometric parameters of a full ship should be determined considering the added resistance due to wave reflection as well as the steady wave-making resistance. While for the local change of waterplane forms, the added resistance is rather insensitive when it is compared with the steady wave-making resistance. Therefore, under the specified principal geometric parameters, the waterplane form of minimum steady wave-making resistance is regarded approximately as an optimum form even in waves. It should be reminded that these results are applied only to the ships whose motions in waves are negligibly small.

ACKNOWLEDGEMENTS

The authors would like to express their sincere gratitude to Mr. T. Takahashi, Project Manager of Ship Hydrodynamics Laboratory of Nagasaki Technical Institute, Mitsubishi Heavy Industries for his instructive discussions in preparing this paper.

REFERENCES

1. Ogilvie, T.F., "Wave Resistance : The Low Speed Limit," Univ., of Michigan, Naval Architecture and Marine Engineering, No.002, 1968.

2. Baba, E. and Takekuma, K., "A Study on Free Surface Flow around the Bow of Slowly Moving Full Forms," Journal of the Society of Naval Architects of Japan, Vol.137, 1975, pp.1-10.

3. Faltinsen, O.M., Minsaas, K.J., Liapis, N. and Skjordal, S.O., "Prediction of Resistance and Propulsion of a Ship in a Seaway," Proc. 13th Symposium on Naval Hydrodynamics, 1980, pp.505-529.

4. Newman, J.N., "The Theory of Ship Motions," Advances in Applied Mechanics, Vol.18, Academic Press, 1978, pp.221-283.

5. Maruo, H., "Resistance in Waves," 60th Anniversary Series, The Society of Naval Architects of Japan, Vol.8, Chapter 5, 1963, pp.67-102.

6. Baba, E., "Application of Ship Resistance Theories to the Design of Full Hull Forms," Centenary Conference on Marine Propulsion, NEC 100, North East Coast Institution of Engineers and Shipbuilders, 1984.

7. Fujii, H. and Takahashi, T., "Experimental Study on the Resistance Increase of a Large Full Ship in Regular Oblique Waves," Journal of the Society of Naval Architects of Japan, Vol.137, 1975, pp.132-137.

8. Havelock, T.H., "The Pressure of Water Wave upon Fixed Obstacle," Proc. of the Royal Society of London. Series A, No.963, Vol.175, 1940, pp.409-421.

9. Parsons, M.G, "Optimization Methods for Use in Computer-Aided Ship Design,"Proceedings of First Ship Technology and Research (STAR) Symposium, SNAME, 1975.

10. Gertler, M., "A Reanalysis of the Original Test Data for the Taylor Standard Series," DTMB Report 806, 1954.

11. Ohkusu, M., "Added Resistance in Waves of Hull Forms with Blunt Bow," Proc. 15th Symposium on Naval Hydrodynamics, 1984, pp.135-148.

12. Naito, S., Nakamura, S. and Nishiguchi, A., "Added Resistance in Short Length Waves on Ship Forms with Blunt Bow," Journal of the Kansai Society of Naval Architects, Japan, No.197, 1985, pp.39-45.

DISCUSSION

Hideaki Miyata
University of Tokyo

I have a small comment on this interesting work on added resistance of a slowly moving full hull by short waves.

Recently I have observed the occurrence of very peculiar waves about a slowly moving full hull in short waves. When the Froude number based on L_{pp} (2.8m) is 0.07 and 0.12 on a fully-loaded condition, the steady wave making and resultant wave resistance is negligibly small as is well known, but when the model, which is firmly fixed to the carriage, is in incident waves of 1.5m wavelength and 0.02m wave-amplitude, peculiar waves are formed about the bow as shown in the pictures, which are taken with aluminum powder film on the free-surface. These waves are usually very steep with the maximum slope of 1/2 and they often break. The formation seems to systematically vary with the parameters. They are supposed to have common properties with the free-surface shock waves of the steady case. Experimental investigations on the nonlinear diffraction by an advancing body seem to help obtain a sound understanding of the added resistance problem.

Reply -

Thank you very much for your valuable comment and presenting the interesting experimental data. For the investigation into the change of the incident waves due to the curved bow flow, such experimental data is very valuable.

With relation to the breaking of unsteady waves around the bow of slowly moving full forms, Prof. Naito, Osaka University (Ref. 12), also made an interesting study by making the use of ray theory. I would hope you to refer to this work. These sorts of experimental and theoretical studies are required for the deeper understanding of flow phenomina around a full ship. We would hope that the theory introduced in the present study will be a basis for the study.

Heinrich Söding,
Institute fur Schiffbau Hamburg

In your results, the shapes which are optimum with respect to R_w and to $R_w + R_{aw}$, respectively, hardly deviate from each other. I expect you would have obtained much more impressive results if you had used a higher wave steepness. Were there special reasons for using the low steepness of 1/50?

Reply -

The added resistance due to wave reflection is proportional to square of wave height, so the wave height may be regarded as weighting parameter of the added resistance in the minimization of $R_w + R_{aw}$.

In Fig. 11, optimum waterplane forms with respect to R_{aw}, which may be regarded as the extreme case that the weighting parameter of the added resistance is large, are also shown. And they don't deviate much from the optimum waterplane forms with respect to R_w or $R_w + R_{aw}$.

Even if the optimum waterplane form with respect to $R_w + R_{aw}$ was calculated with higher wave height, the result would have been between the present $R_w + R_{aw}$ minimum form and the R_{aw} minimum form.

There is no special reason for using the wave steepness of 1/50. The wave height used in the optimization was chosen following our intention to investigate into the optimum form in the moderate sea condition, which ships encounter with high probability.



Figure A. Model proceeding at $\mathbf{F_r} = 0.07$.

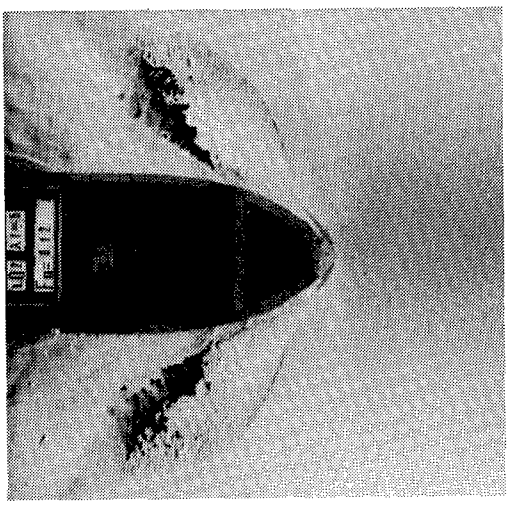


Figure B. Model proceeding at $\mathbf{F_r} = 0.12$.